MMT2017
CAIRO-EGYPT

The 10th International Conference on Mobile Mapping Technology

Mobile Mapping For Sustainable Development

6-8 May 2017, Conrad Cairo Hotel, Cairo, Egypt

Sponsored by

LEADOR 立得空间

ZOYON 武大卓越

ME Micro Engineering Group

Zone Technologies

Trimble

Surveying Systems
Total Survey Systems

TOPCON

MMT2017
CAIRO-EGYPT

The 10th International conference on Mobile Mapping Technology

Mobile Mapping For Sustainable Development

6-8 May 2017, Conrad Cairo Hotel , cairo, Egypt

isprs International Society for Photogrammetry and Remote Sensing

IAG International Association of Geodesy

FIG International Federation of Surveyors

ICA ACI International Cartographic Association

Sponsored by

LEADOR 立得空间

ZOYON 武大卓越

ME Micro Engineering Group

Zone Technologies Trimble

Surveying Systems Total Survey Systems TOPCON

Table of Contents

Geospatial Information: State of the Art and Future Trends 1
Christian Heipke

The Role of Surveying and of Surveyors in Sustainable Development 3
Chryssy A Potsiou

From Mobile Mapping Systems to Intelligent Mapping Robots 5
Deren Li

Comprehensive Road Detection Technology in China 7
Qingquan Li

Spatial Land Data Infrastructure for Sustainable Development 8
Muhamad Alrajhi

Utilizing Mobile Mapping in Navigating Historical Locations: Hijrah Route as a Case Study 10
Abdullah Alkadi

The Performance Analysis of Using Smartphone and Geo-Referenced Image for Space Resection Aided Pedestrian Dead Reckoning 12
Jhen-Kai Liao, Shih-Huan Huang, Kai-Wei Chiang and Chien-Hsun Chu

Relative Orientation and Essential Matrix of Spherical Panorama Images 18
Yi-Hsing Tseng and Tsung-Che Huang

Statistical Analysis of LiDAR Data for Land Cover Classification 24
Nagwa El-Ashmawy and Ahmed Shaker

Rapid Initialization With Image Based Indoor Localization Based On Artificial Neural Network Using Smartphones 35
Shih-Huan Huang, Jhen-Kai Liao and Kai-Wei Chiang

A Dual-Channel CAMShift Algorithm for Embedded Real-time Visual Servoing Applications 42
Islam Alaa, Amr Wassal, Omar Rayan, Osama Rashad and Amr Eldieb

Performance Analysis of Indoor Positioning using Differential Distance Correction based on Bluetooth Low Energy 48
Yun-Tzu Kuo, Jhen-Kai Liao and Kai-Wei Chiang

THE PERFORMANCE ANALYSIS OF LiDAR-BASED UNMANNED AERIAL VEHICLES FOR DISASTER REDUCTION MAPPING APPLICATIONS 55
Guang-Je Tsai, Min-Chuan Tsai, Kai-Wei Chiang and Naser El-Sheimy

THE GENERATION OF WELL GEO-REFERENCED FLOOR PLANS FOR INDOOR NAVIGATION WITH INERTIAL SENSORS AIDED SLAM ALGORITHMS .. 62
Min Chuan Tsai, Guang Je Tsai, You Liang Chen, Kai Wei Chiang and Naser El-Sheimy

A LOW-COST IMAGE BASED MOBILE SYSTEM USING SLAM 69
Ahmed Youssef and Moustafa Baraka

Low-Cost GNSS/MEMS Sensors integrated Vision System for Motion and Position Estimation of a bicycle 77
Hsiu-Wen Chang

Accelerating the convergence period of GPS/GLONASS precise point positioning using pseudorange multipath and noise mitigation 83
Mohammed Abou Galala, Mosbeh Rashid Kaloop, Mostafa Mousa Rabah and Zaki Mohammed Zidan

Road Test Results and Analysis on Integrating Visual Odometry with Car Motion Sensors for Positioning and Navigation 91
Muhammed Tahsin Rahman, Tashfeen Karamat, Sidney Givigi and Aboelmagd Noureldin

Low cost structures oscillation monitoring using terrestrial photogrammetry 97
Omar El Kadi and Adel Hassan Youssef El-Shazly El Shazly

3D RECONSTRUCTION WITH 2D TILTING LIDAR USING VISION ONLY POSITIONING METHOD 101
Cyril Joly, Bruno Ricaud and Arnaud de La Fortelle

A New Platform for Activity Tracking in Smart Health Sensor Monitoring Systems 109
Allaa Hussien, Sherin Youssef and Cherine Fathy

Tuning of the Error Covariance Parameters in EKF-Based INS/GPS Systems: A Practical Approach 112
Mostafa Mahmoud, Islam Alaa, Amr Wassal, Aboelmagd Noureldin and Amr Eldieb

Mobile-based Remotely Veichle Tracking System 118
Essam Mohamed and Sherin Youssef

Preliminary Study of A Time Dependent Model For Exterior Orientation Of Hyperspectral Image Cubes 122
Adilson Berveglieri and Antonio Tommaselli

A cooperative localization system for Unmanned Aerial Vehicles: Prototype development and analysis 127
Salil Goel, Allison Kealy, Bharat Lohani and Guenther Retscher

An Improved model for Multi-Constellations GNSS Single Frequency Precise Point Positioning 134
Mahmoud Abd Rabbou and Adel El-Shazly

Accuracy Assessment Of Different Algorithms Used For Deriving Bathymetry From Landsat 8 Satellite Images, Applied In Egypt, Case Study (Soma Bay, Red Sea) 139
Esalm Saleh, Adel El-Shazly, Mohamed El-Ghazaly and Kamal Ahmed

Separability Analysis for Multiple Simultaneous Faults in GNSS and GNSS/INS Integration Systems 146
Ali Almagbile and Jinling Wang

Performance Analysis of Real Time Precise Point Positioning in Egypt 153
Ahmed Mansour, Mahmoud Abd Rabbou and Adel El-Shazly

Mapping and Analysis of Terrain Geomorphology Using Simulated Airborne LiDAR Data Capture of Low Point Cloud Densities 161
Fahmy Asal

COMPARISON OF AIRBORNE LIDAR SYSTEM CALIBRATION ALGORITHMS 170
Megan Miller and Ayman Habib

On the Development of A Regional Ionospheric Correction Model For Low-Cost Single Frequency GNSS Users 178
Mohamed Abdelazeem, Rahmi Nurhan Çelik and Ahmed El-Rabbany

Segmentation-based Classification of Point Cloud Data 182
Yun-Jou Lin and Ayman Habib

A Structure-from-Motion Approach Using UAV-based Imagery for Precision Agriculture Applications 187
Fangning He, Weifeng Xiong and Ayman Habib

Indoor surveying with low cost UWB devices 192
Andrea Masiero, Francesca Fissore, Alberto Guarnieri and Antonio Vettore

Alternative Approaches for Feature-based Down-Sampling of Irregular Point Clouds for Fine Registration 204
Fangning He, Ayman Habib and Yun-Jou Lin

Monitoring Ionospheric Perturbations over Egypt Based on National GNSS Network 211
Mahmoud Abd Rabbou and Adel El-Shazly

Comparative Analysis of Image and LiDAR-Based Elevation Maps from a UAV Platform for Agriculture Management 217
Fangning He, Magdy Elbahnasawy, Tamer Shamseldin, Weifeng Xiong and Ayman Habib

Combined Pixel/Object Based Building Extraction Technique from High Resolution Remote Sensing Satellite Images 224
Mahmoud A. Shawky, Ahmed S. Elsharkawy, Essam Hamza and Hassan Elhifnawy

Cooperative Localization in Indoor Environments Using Constrained Differential Wi-Fi and UWB Measurements 232
Guenther Retscher, Allison Kealy, Vassilis Gikas, Hannes Hofer, Andreas Ettlinger and Franz Obex

Change Detection Analysis of Urban Land Cover Changes Using SPOT5 of Arar City, Saudi Arabia 234
Saleh Mesbah Elkaffas, Khaled Mahar and Sultan Alenezi

EXTRACTION OF FAÇADE ELEMENTS BASED ON WAVELET ANALYSIS USING POINT CLOUDS 239
Fuxun Liang, Bisheng Yang and Zhen Dong

Dynamic Variation Effects on The Stochastic Performance of Smartphone Sensors Using Allan Variance and Generalized Method of Wavelet Moments 244
Ahmed Radi, You Li, Naser El-Sheimy and Abu Sesay

Automatic Registration of Panoramic Sequence and Mobile LiDAR Point Clouds via Similarity Measurements 252
Jianping Li, Xianghong Zou, Bisheng Yang and Ronggang Huang

iNavSetA benchmark of indoor navigation using smartphones 260
Liu Kun, Pei Ling, Deng Zhantao, Qian Jiuchao, Liu Peilin and Yu Wenxian

Three Levels Security Model for Secure Cloud Storage 268
Sheren Elbooz, Gamal Attiya and Nawal Elfishawy

Novel Highly Isolated Triplexer Antenna to Integrate Aviation and Radio Navigation Satellite Services Including GPS, GLONASS, Galileo, BEIDOW And Sar With Different Communications Applications 275
Mohamed Oweis, Wael Swelam and Mohamed Abd El Azeem

Evaluation of Distinctive Features for Land/Water Classification from Multispectral Airborne LiDAR Data at Lake Ontario 280
Salem Morsy, Ahmed Shaker and Ahmed El-Rabbany

A NOVEL APPROACH FOR STEP DETECTION USING A FREE-MOVING HANDHELD DEVICE 287
Maan Khedr and Naser Elsheimy

LOW-COST UAV IMAGERY SYSTEM FOR SITE-SPECIFIC WEED MANAGEMENT 295
Mohamed Hassanein and Naser El-Sheimy

REMOTE HEALTHCARE MONITORING SYSTEM THROUGH MOBILE APPLICATION 302
Alaa El-Shazli, Nancy El-Gamil and Sherin Youssef

Feasibility Study of a Backpack Mobile Terrestrial System with A Low Cost Omnidirectional Camera 308
Mariana Campos, Antonio Tommaselli and Eija Honkavaara

GNSS/INS integrated with intelligent vision system for path reconstruction of a bicycle. . 314
Tz-Chiau Su and Hsiu-Wen Chang

Visual Surveillance Systems For Tracking Multiple Moving Objects 321
Essam Mohamed, Sheren Youssef and Hany Hanafy

Developing a New Technique for Detecting Two Critical-Nodes in Adhoc Networks 327
Ibrahim Fayed, Mokhtar Ahmed, Gamal Attiya and Nawal El-Fishawy

Positioning Accuracy Improvement Using Low-Cost Inertial Sensors 333
Abdalla El-Desoky, Ahmed Kamel, Mohamed Elhabiby and Hadia Elhennawy

Filter Architectures for Indoor Localization Using Gaussian Process on Smartphones 341
Mostafa Sakr and Naser El-Sheimy

Comparative Analysis of Potential Calibration Alternatives for a Multi-Unit LiDAR System 349
Yun-Jou Lin, Darcy Bullock, Ayman Habib, Radhika Ravi, Tamer Shamseldin and Magdy Elbahnasawy

CORNER FEATURES AIDED INDOOR SLAM FOR UNMANNED VEHICLES 357
Haytham Mohamed, Adel Moussa, Mohamed Elhabiby, Naser El-Sheimy and Abu-Bakarr Sesay

PREDICTION OF INERTIAL POSITIONING ERRORS BASED ON GAUSSIAN PROCESS FOR UAVS IN GNSS DENIED ENVIRONMENT 366
Mostafa Mostafa, Adel Moussa, Naser El-Sheimy and Abu B Sesay

A novel adaptive Kalman filter for MEMS-IMU/Magnetometer fusion 373
Qifan Zhou, Hai Zhang, Maan Khedr and Naser El-Sheimy

PAVEMENT DEFLECTION ASSESSMENT USING DOPPLER LASERS ON A MOBILE PLATFORM 379
Michael Chapman, Cao Min, Deijin Zhang and Qingquan Li

Tightly Coupled Integration of Multi-Constellation GNSS PPP And Mems Based Inertial System Using Non-Linear Filtering 384
Mahmoud Abd Rabbou and Ahmed El-Rabbany

Vision Based Techniques for Building Facade Monitoring 391
Andrea Masiero, Francesca Fissore, Francesco Pirotti and Antonio Vettore

Localization using Region-based Convolution Neural Network: A Comparison Study 402
Charles Toth, Zoltan Koppanyi, Haowei Xu and Dorota Grejner-Brzezinska

Swarm Mapping: Investigation on Strategies to Explore Building Interiors 408
Zoltan Koppanyi, Charles Toth and Grejner-Brzezinska Dorota

Low-Cost Magnetometers Calibration using Proportional Integrator Technique for mobile devices 415
Abdelrahman Ali, Salwa Ahmed, Naif Alsubaie and Naser El-Sheimy

Remote Sensing Images Self Recovery Authentication Watermarking Technique 423
Salwa Ahmed, Abdelrahman Ali and Naser El-Sheimy

Modern tramway track geometric quality inspection by aided INS 430
Qijin Chen and Xiaoji Niu

Comparative Analysis of Wheat Area Estimation using Landsat and Sentinal-2 Satellite Imagery 439
Abdelraouf Massoud Ali, Ayman Fawzy Habib, Mohamed A. Aboelghar and Mohammed Elshirbeny

Random Linear Network Coding Over Cloud Computing Network in Data Transmission .. 445
Omayma Farouk Younis, Rowayda Sadek and Hadya El Hennawy

Multimedia Cloud Computing Based Network Coding 451
Omaima Farouk Younis, Rowayda Sadek and Hadya El Hennawy

The benefit of using high-rate GNSS in precise kinematic positioning 458
Ming Yang, Feng-Yu Chu and Shu-Chen Cheng

Framework Feature Extraction of Building Interiors Using Indoor Mobile Mapping Systems 459
Shiwei Hou, Chenglu Wen, Zheng Gong, Cheng Wang and Jonathan Li

A Backpack Mobile Mapping System Based on Velodyne LIDAR 461
Zheng Gong, Jonathan Li, Cheng Wang and Chenglu Wen

An IMU/LiDAR/PCG-Map Integrated 2D Positioning method for 3D Indoor Mobile Mapping 462
Jian Tang, Chuang Qian, Xiaoji Niu and Rong Zou

FPGA FOR INTELLIGENT CONTROL SYSTEMS: SMART AGENT FOR ELDERLY PEOPLE SUPPORT 463
Nahla El-Araby, Sahar Hamed, Abdelhalim Mohamed, Islam Gamal and Mostafa Nageeb

A LOW-COST BOAT-BASED MOBILE MAPPING SYSTEM FOR MAPPING COASTAL REGIONS 467
Abdullah Arslan and Ayman Habib

An OGC Standard-based Internet of Things Prototype for Vegetation Recovery Monitoring in Northern Alberta 468
Steve Liang, Sara Saeedi, James Badger and Luo Kan

Invited Keynote Speeches

Geospatial Information: State of the Art and Future Trends

Christian Heipke
Institute of Photogrammetry and GeoInformation (IPI)
Leibniz Universität Hannover
President, ISPRS - International Society for Photogrammetry and Remote Sensing

ABSTRACT

The presentation will explore the role of geospatial information in today's internet age and in the grand challenges facing our societies, including global change, sustainable development, mobility, energy, food security, health, biodiversity and demographic change. In the following research trends in photogrammetry, remote sensing and GI science will be discussed, and it will be shown how new and better sensors, sensor networks, including high resolution satellites and satellite constellations and web-enabled 3D cameras as well as unconventional platforms such as mobile mapping systems and unmanned aircraft systems have shaped the discipline in the past years and will continue to do so.

This is the context in which ISPRS, the International Society for Photogrammetry and Remote Sensing, strives to fulfil its role as the foremost scientific body to deliver information from imagery. ISPRS is an international non-governmental organization that promotes international cooperation between the worldwide organizations with interests in the photogrammetry, remote sensing and spatial information sciences. Established in 1910, ISPRS is the oldest international umbrella organization in its field, which may be summarized as addressing "information from imagery".

ISPRS achieves its aims by:

- Advancing knowledge in the areas of interest of ISPRS by encouraging and facilitating research and development, scientific networking and inter-disciplinary activities.
- Facilitating education and training with particular emphasis in less developed countries.
- Promoting public recognition of the contributions of the photogrammetry, remote sensing and spatial information sciences for the benefit of humankind and the sustainability of the environment.

The ISPRS scientific and technical programs are organized by Technical Commissions. Each Commission is sponsored by an ISPRS Member organization for the four-year period between Congresses. The Technical Commissions currently have established approximately 60 Working Groups which are responsible for particular topics within the Commissions' areas of responsibility. All Technical Commissions will hold a Symposium within their country in 2018. In September 2017 the ISPRS Geospatial Week will take place in Wuhan, China. The same year will also see smaller workshops being organized by the Working Groups, such as the "ISPRS Hannover Workshop" next month. The next ISPRS Congress will be held in June/July 2020 in Nice, France.

Biography: Christian Heipke is a professor of photogrammetry and remote sensing at Leibniz Universität Hannover, wherehe currently leads a group of about 25 researchers. His professional interests comprise all aspects ofphotogrammetry, remote sensing, image understanding and their connection to computer vision and GIS. His hasauthored or co-authored more than 300 scientific papers, more than 70 of which appeared in peer-reviewedinternational journals. He is the recipient of the 1992 Otto von Gruber Award, the 2012 Fred Doyle Award, bothfrom the International Society of Photogrammetry and Remote Sensing (ISPRS), and the 2013 Photogrammetric(Fairchild) Award from ASPRS.

From 2004 to 2009, he served as vice president of EuroSDR (European Spatial Data Research, formerly knownas OEEPE). From 2011-2014 he was chair of the German Geodetic Commission (DGK), from 2012-2016 ISPRSSecretary General. Currently he serves as ISPRS President.

The Role of Surveying and of Surveyors in Sustainable Development

Dr. Chryssy A Potsiou
FIG President, UN ECE WPLA bureau member
National Technical University of Athens

ABSTRCAT

A brief overview is given of global trends in the changing economies and markets of the world, changing societal needs and a changing technology, together with an emphasis on the important role of surveying and of surveyors.

Geospatial information is recognized as the tool to address issues like the so called "mega-topics" in order to achieve the sustainable development goals of the UN 2030 Agenda. Such "mega-topics" include population growth and the need for food and water security and poverty eradication; the rapid urbanization of the world's cities and the need to respond rapidly and intelligently in terms of security, housing, mobility and transport, city and building modeling, energy saving, health care, water and waste management, and governance in general; the tendency of development to cluster within the coastal zones of the oceans, the seas and the major river deltas and the need for rapid response to natural disasters and to manage the impact of climate change; the interconnectivity in all areas of our economies, cultures, governmental operations and private lives and the need for harmonization, compatibility and security of procedures.

The use of new developments in technology that will allow capture, assessment, processing and management of geospatial information and the development of appropriate land tools that will allow solution functionality, reliably and affordably (i.e., fit-for-purpose processes) for a complex and rapidly changing world is of significant importance for the future of surveying and mapping. Current and future challenges in mapping include, among other important issues, the compilation of cadaster and registration of property rights for the rest of the world, the formalization of property markets and their sustainability, and the increased capacity in real-time mapping for disaster management and recovery from disasters.

In the globalization era, a globalization of the sciences is also taking place. Surveyors should be prepared to cooperate with several other disciplines and allied professions, and in some cases, there may be severe competition from neighboring disciplines. This is a challenge that surveyors must face through development of their own new skills. Surveyors should be prepared to deal with data inflation, to cope with large amounts of information; they should also maintain in-depth technical research, better education and cooperation with other professions. Today, mobile devices are available to more people, the cost of high resolution satellite imagery is coming down and there is a renewed awareness of the importance of authoritative spatial data at all levels of government. There is a fast-growing civil demand but also a changing culture for authoritative spatial information published on the web, a culture that changes the administrative concept. Authoritative data today can be provided and assured by government agencies but also by crowdsourcing with the engagement of surveyors. The relationship between quality and cost has been significantly improved today by new technologies and it will continue to improve. We need to investigate and be aware of these achievements but also of the challenge of adapting to new technologies while encouraging further improvements.

Biography: Dr Chryssy Potsiou studied at the School for Rural & Surveying Engineering, National Technical University of Athens (NTUA), Greece. In 2005 she became a NTUA Lecturer teaching Cadastre, Land Management and Property Valuation courses. She attended the MIT (Massachusetts Institute of Technology) professional education courses on Real Estate Markets in 2006. In 2010 she was promoted to the position of Assistant Professor and in 2013 she became Associate Professor, in NTUA. She has 30-year experience in education, training and international capacity building. She was a member of the board of directors of the Hellenic Mapping and Cadastre Organization (2009-2010) and of KTIMATOLOGIO SA (2009-2013). She has been an elected member of the bureau of the Hellenic Association of Rural and Surveying Engineers (2013-2015). Since 1982 she is active in the International Federation of Surveyors (FIG) especially in the work of Commission 7 (Cadastre and Land Management) and Commission 3 (Spatial Information Management). She was the Chair of FIG Commission 3 for the period 2006-2010, the ACCO representative at the FIG Council for the periods 2006-2008 and 2008-2010, FIG Vice President (2011-2014), FIG Task Force chair on Property and Housing (2012-2014), and FIG President (2014-2018). She was the chief editor for the FIG peer reviewed papers for the period 2007-2009. Since 2001 she has been an elected UNECE WPLA bureau member. She has organized more than 25 international conferences. She has participated in more than 30 research projects as main researcher or coordinator. She has been contributor, co-author or main author of 15 international books, and she has written more than 150 scientific papers.

From Mobile Mapping Systems to Intelligent Mapping Robots

Prof. Dr. Deren Li

Wuhan University

Academician, Chinese Academy of Sciences

Academician, Chinese Academy of Engineering

ABSTRCAT

Mobile mapping technology (MMT) has evolved from a developmental technology into a well-established mapping solution over the past three decades, and it has revolutionized the surveying and mapping industry. With the rapid advancements in sensors technology and the emergence of mini-grade LIDAR and POS, the first generation street level mobile mapping systems (MMS) have shifted from the integration of digital camera and GPS to the integration of digital camera, IMU, LiDAR, and GNSS. Hundreds of commercialized street level MMS, such as LYNX, RIEGL's VMX, Leador's MMS, and Street Mapper, are being widely used to collect vast amounts of geospatial data and serve for many purposes. On the one hand, with the decreasing of prices, sizes, weights of LiDAR sensors and IMU in the past few years, both fixed-wing and roto-copter platforms open new application areas and represent the largest current user market in the geospatial industry. Quite a lot of such kind of UAV platforms mounting with mini-grade LiDAR (ranging from 50 meters to 400 meters) and IMU are being used for forest investigation, precision agriculture, power lines corridor mapping, and so on. On the other hand, with the emergence of backpack MMS that provide a complimentary and flexible solution between street level MMS and UAV MMS, it is now evolving towards compact, agile and flexible solutions for mapping complex environments (e.g., 3D indoor mapping, 3D cadastral mapping). Last but not least, we are witnessing a transition from street level, UAV, and backpack mobile mapping systems to intelligent robot mapping systems due to the tremendous advancements in Artificial Intelligence (AI), Deep Learning, and Cloud Computing. The integration of image geo-referencing and low-cost 3D sensors for 3D data capture (e.g., mini-grade LiDAR, Kinect) with a robot platform will serve high-end mapping tasks and new application fields, such as building information modeling (BIM) and urban infrastructure management, autonomous vehicles. I will share a lot of project examples on mobile mapping systems undertaken in Wuhan University, ranging from the first generation MMS (image based) to street level, to UAV based and to mapping robot. In the near future, I expect great progress in intelligent mapping robots and great opportunities for academic and industrial communities.

Biography: Li Deren, male, Han nationality, is a native of Dantu, Zhenjiang, Jiangsu Province. He received his doctorate from Stuttgart University in 1985, and was awarded the title of honorary doctor from ETH Zürich, Switzerland in 2008.

In the 1980s, Li mainly engaged in the study of measuring error theory and treatment methods. In 1982, he initiated the selection iteration method, which deducted the rough difference positioning from the variance estimation. In 1985, he put forward the expandability and reliability theory based on two multi-dimensional optional hypotheses, including the error discovered and differential. He also scientifically "solved the pended problems for more than one hundred years of measurement science." For this research, he received the best monograph prize from Germany's Photogrammetric and Remote Sensing Society in 1988, the "Hansa Aerial Photogrammetric Award".

Since the 1990s, Li mainly engaged in the space information science based on the integration of remote sensing, global satellite positioning system (GNSS) and geographical information system (GIS) and the scientific research and teaching works of multimedia communication technology.

Since 1989, Prof. Deren Li has supervised over 170 Ph.D students. Five Ph.D theses by students under the supervision of Prof. Li won the “Best Doctoral Thesis Award” respectively in 1999, 2001, 2002, 2005 and 2011. So far, he has supervised 18 post doctoral candidates. He has published over 700 papers, 11 books, one piece of translation work and 8 pieces of compiling works. He has won more than ten of national and ministerial level prizes, such as the National Science and Technology Progress Award, the National Excellent Textbook Award, Award of the Excellent Educational Achievements, and etc. Prof. Deren Li served as President of ISPRS Technical Commissions III andVI from 1988-1992 and 1992-1996 respectively. He worked for CEOS in2002-2004 and was the first president of Asia GIS Association (2003-2006).He received the Samuel G. Gamble Award at the ISPRS XXI Congress in2008 and was awarded ISPRS Honorary Member at the IPRRS XXII Congress in 2012. Prof. Deren Li worked for CEOS in 2002-2004 and was the first president of Asia GIS Association (2003-2006). He got an award in appreciation and recognition of the outstanding contribution to the success and achievements of the MOST/ESA Dragon Programme 2004 to 2007.

Comprehensive Road Detection Technology in China

Professor Qingquan Li
President of Shenzhen University
Member of the International Eurasian Academy of Science
Former Executive vice-president of Wuhan University
Chairman of Key Laboratory for Geo-Environmental Monitoring of Coastal Zone of the National Administration of Surveying, Mapping and Geo-Information
Chairman of Shenzhen Key Laboratory of Spatial Smart Sensing and Services, Shenzhen University

ABSTRACT

With the rapid construction of transportation infrastructures in the past decade, the China's highway mileage has surpassed 120,000 km. Efficient and automatic maintenance of the highways has become an urgent demand. The research performed at Shenzhen University and commercialized by Zoyon Co. Ltd. has made breakthroughs on the key technologies of high-precision dynamic road testing and measurement, and developed a series of testing equipments with largely improved performance over the competing products. (1) In high-precision dynamic measurement of road bearing capacity, an inversion method is developed to calculate the road deflection by using the deformation velocity captured by laser Doppler sensors. The invention achieves a real-time, non-contact, and dynamic measurement of the road deflection at a speed of 15-90 Km/h, with an accuracy of 0.01mm. (2) In automatic pavement defect detection, laser imaging techniques are employed to model the pavement surface with 3D dense point clouds, and smart computer-vision algorithms are developed to localize and classify the pavement defects such as crack, bump, hole, subsidence, loose and rutting, which improves the efficiency over 20 times, and significantly promotes the pavement defect detection from human interaction to machine automation. (3) In tunnel defect detection, LED arrays are used to solve the problem of poor lighting conditions within the tunnel, and high-precision image-registration algorithms have been proposed to mosaic the adjacent images captured by CCD camera arrays. Assisted by infrared sensors, the invented equipment can effectively detect the tunnel defects such as water seepage, frost damage and cracking. The above research and development have significantly promoted the automation level of China's road maintenance and measurement.

Biography: Prof. Qingquan Li, was born in Jan. 1965, is the president of Shenzhen University since 2012. He is a valid member of the International Eurasian Academy of Science. Prof. Li entered Wuhan Technical University of Surveying and Mapping in 1981 and got his PhD in 1998. Prof. Li has been working in the engineering surveying field over thirty years. One of his outstanding research achievements is related to intelligent road detecting and measurement.

The research has made breakthroughs in the key technologies of high-precision dynamic pavement detecting and measurement, and developed a series of detection equipments with independent intellectual property rights, which fills the technology gap between domestic and abroad, and achieves a leap from the static to the dynamic with regarding to the precise road engineering measurement. His research interests are GIS-T, three dimensional and dynamic data modeling, location-based services, ITS, and surveying engineering, etc. Prof. Li has published 5 books, around 400 papers, and owns about 35 patents in his research field.

“Spatial Land Data Infrastructure for Sustainable Development”

Dr. Ing. Muhamad ALRAJHI

ISPRS Regional Coordinator for the Arab States

Assistant Deputy Minister For Land & Surveying

Ministry of Municipal & Rural Affairs, Kingdom of Saudi Arabia

ABSTRACT

“Saudi Arabia’s Vision 2030” was adopted as a roadmap for socio-economic development to achieve prosperous future and sustainable development. National Transformation Program 2020 is a step towards the ambitious goals of the vision; Most important strategic objective of the program is to “Improve Land Management System, Protect Government Land, and Provide Accurate Spatial Information” to achieve the highest levels of transparency, as well as good governance in all sectors and support the sustainable development.

Establishing Infrastructure for Land Information builds and integrates different types of data once and uses it many times for many applications, which provides increased access to land information through geospatial standards. “Spatial Land Data” infrastructure (SLDI) provides base to support sustainable developmental processes at all levels in the Kingdom of Saudi Arabia. This is important because the rational and successful implementation of various projects depend largely on the availability of geospatial information. MOMRA focuses on establishment of SLDI based on the integration of different types of geospatial data, which will be ready for spatial analysisand integration with businesses process and will increase the return on investment (ROI) in Geoinformation technology by improving interoperability, decision making and service delivery. High rate of urbanization and rapid change in urban infrastructure is the biggest challenge for maintaining and managing the geospatial data. Mobile mapping is a fast and economical alternative of accurate spatial data collection and updating of existing data. At the same time new capability parameters are being identified. The future of Geospatial Infrastructure is also being impacted by the advancement of geospatial technology offerings, including the "mass market" (as depicted by Google Earth, Microsoft Virtual Earth and others). The broader Information Technology (IT) market acceptance of powerful, light weight standards, combined with the IT standards community's awareness of the importance of spatial data at all levels of the internet stack raise new opportunities and challenges for the build out of a truly local to national spatial land data infrastructure. We are coming closer to realizing the vision of accurate and up-to-date "Spatial Land Data Infrastructure".

Biography: Dr. Ing. Muhamad N. ALRAJHI was born and raised in the Kingdom of Saudi Arabia. After graduating with a degree in Civil Engineering, he joined the General Directorate of Surveying and Mapping (GDSM) under the Ministry of Municipal and Rural Affairs (MOMRA), Kingdom of Saudi Arabia. Early in his professional career, he assumed the responsibility for technical and administrative management of large scale projects to fulfill the need for Aerial Photography, Large Scale Digital Photogrammetric Mapping, Municipal Surveying activities, Multipurpose Cadastre Registration as well as Development of Geographic Information System in MOMRA in support of regional and urban planning activities in a timely and effective manner. He steered the General Directorate of Surveying and Mapping as Director General for over 15 years during which state-of-the-art geomatic technologies were successfully implemented, which culminated in the ISO certification and has made GDSM an eminent civilian survey authority of the Kingdom.

He is currently Assistant Deputy Minister for Land and Surveying in MOMRA and under his guidance, the modernization and updating of the Geospatial Information Infrastructure is effectively serving its key role as the most fundamental tool for decision makers and planners in the Kingdom. In step with his administrative and executive responsibilities, his efforts towards professional development have lead to his completing M.Sc. in Geomatics and is working towards PhD in Geomatics at Leibnitz University, Hannover, Germany. He is a member of several Professional Organizations including AGU, FIG, ISO TC211, ASPRS, ISPRS, EAGE, European Academy of Sciences and Saudi GIS National Committee. He has contributed, presented and published many papers Kingdomwide and internationally.

Utilizing Mobile Mapping in Navigating Historical Locations: Hijrah Route as a Case Study

Prof. Abdullah Alkadi

Vice President for Development, Studies and Community Services

Imam Abdulrahman Bin Faisal University

Kingdom of Saudi Arabia

aalkadi@uod.edu.sa

ABSTRACT

Historical locations are very important and essentials to many people who are in the field of history, geography, planning, archeology, economics … etc. Historical locations are scattered all over the globe including the two major religious cities Makkah and Madinah. In Makkah and Madinah, there are historical locations and routes. There are only few people who know those historical locations and routes. As a result, the technology of the mobile mapping is utilized in order to help in locating those historical locations and routes. An app was developed to help laymen in finding the historical locations and routes. The Hijrah Route is taken as a case study to test the app.

Prof Abdullah Alkadi recieved his B. Sc. in Architecture and Planning form King Faisal University, Dammam, Saudi Arabia Then he joined Portland State University, Portland, U.S.A. He finished his Ph. D. Degree in Urban and Regional Planning. Dissertation title: "Hedonic Analysis of Housing Prices Near The Portland Urban Growth Boundary, 1987-1990," 1994.

He have a wide spectrum of interests starting from overall Strategic and Policy Planning issues to technical and detailed design and program and project implementation issues., including the following areas: Planning and Housing Strategies, Land Use Planning, Growth Management, Urban Planning Legislations, Planning Methods and Techniques, Housing, Affordable Housing, Statistical Analysis, Geographic Information Systems (GIS), eServices, and Surveying and Mapping.Gained a very rich administrative experience required to sustain academic and civil society public institutions through holding several posts in King Faisal University and Public Sector agencies includ ing:

Over the past ten years I have conducted more than 50 academic research expeditions and travelled more than 96,000 kilometers over a total of approximately180 days.

Full Length Papers

The Performance Analysis of Using Smartphone and Georeferenced Image for Space Resection Aided Pedestrian Dead Reckoning

Jhen-Kai, Liao *, Shih-Huan Huang, Kai-Wei Chiang, Chien-Hsun, Chu

Dept. of Geomatics, National Cheng-Kung University, No. 1, University Road, Tainan 701, Taiwan - (p68011050, p66044031, kwchiang, p68991030)@ mail.ncku.edu.tw

Commission VI, WG VI/4

KEY WORDS: Indoor Navigation, Space Resection, Smartphone, Pedestrian Dead Reckoning

ABSTRACT:

Mobile mapping system (MMS) plays an important role in modern survey and mapping application since the integration of inertial navigation system (INS) and Global Navigation Satellite System (GNSS) has become mature. With photogrammetry technology, MMS significantly improves the time-consuming procedure of traditional survey. Meanwhile, MMS has been applied on various vehicles to adapt for different environments. As the applied vehicle becomes portable, MMS can be used to mapping indoor environment. Therefore, the georeferenced image of indoor environment can be efficiently collected. On the other hand, indoor navigation is popular in recent years since the smartphone becomes an indispensable device in our daily life. The smartphone has the potential to confront the challenges of a GNSS-denied environment based on the various embedded sensors. This research proposes an indoor navigation system based on the smartphone sensors and the integration of space resection and pedestrian dead reckoning (PDR). Space resection can be considered as an image-based localization which determines the user position by the use of georeferenced image. The proposed integrated system overcomes the challenges of single system based on PDR or image. The result shows the proposed system is able to provide long-term accurate indoor localization, and the system construction is efficient by using MMS.

1. INTRODUCTION

Mobile mapping technology has been developed for many years and widely applied for spatial applications. The prototypes of mobile mapping system (MMS) have been firstly developed for land-based application in United States and Canada (El-Sheimy, 1996; Goad, 1991). Nowadays, because the quality of sensors and the performance of algorithms progress significantly, the application and platform of MMS are more flexible. The portable MMS was appeared and has the ability of indoor mapping (Chu et al., 2013; Ellum, 2001; Keller and Sternberg, 2013). Meanwhile, since the efficiently mapping procedure of mobile mapping technology and the increased requirement of accurate indoor map and building model, the indoor mobile mapping application has attracted more attentions in recent years. On the other hand, one of the extended applications is indoor navigation that utilizes the indoor spatial information such as georeferenced image. In addition to map and building model, georeferenced image is also the production of MMS. Georeferencing means the coordinate system of a map or image can be related to a ground coordinate system (Wolf and DeWitt, 2000). In the other words, the ground coordinates of an object in an image can be directly measured. Space resection is a photogrammetry method that estimates the position and attitude of the camera based on single georeferenced image, collinearity equations and at least three control points with known ground coordinates. Obviously, the portable MMS can provide the required information for space resection and further applied for indoor navigation.

For more detailed, space resection is used to determine the six exterior orientation parameters (EOPs) of the exposure center of a single photograph. The EOPs include the ground coordinates (X, Y, and Z) and rotated angles (omega, phi and kappa) of camera. They are solved by the collinearity equations and the known interior orientation parameters (IOPs) of used camera. In addition, at least three control points are needed which the ground coordinates are known and also appear in the image. The collinearity equations are based on the condition which the camera, the control point and its corresponding image point are all lie on a straight line. Since the collinearity equations are nonlinear, and have been linearized using Taylor's theorem, initial values of EOPs are needed for iterative calculation. Moreover, space resection is a purely numerical method, and permits the least squares method for optimal estimation with redundant of control point. The positioning accuracy achieves centimeter level when the intersection geometry and accuracy of control point are good. It's worth to mention that the coordinate system of estimated position by space resection is an absolute system. Li *et al.* propose a hybrid image-based localization for seamless navigation based on Global Navigation Satellite System (GNSS), compass, calibrated camera and space resection with georeferenced images (Li et al., 2013). However, they mentioned the challenge of initial value of space resection for indoor case. In addition, a large number of applied image, feature recognition and image matching procedure are also the heavy burden of all the image-based localization. Therefore, this research considers the integration of pedestrian dead reckoning (PDR) and space resection to reduce the necessary images and to provide the initial values of space resection for continuous indoor navigation.

PDR estimates two dimensional location of pedestrian based on the accelerometer, gyro and magnetometer. It suffers the error from the following factors: firstly, the algorithm cannot perfectly fit the users and their behaviour because the properties of steps at different stages are typically different, then causes the missed steps (Agata and Robert); Secondly, the step length is often derived from empirical formulas with acceleration,

* Corresponding author

characteristics of individual and corresponding coefficients. Unfortunately, most of step length estimations fail to accurately meet individual users' characteristics and walking habits (Weinberg, 2002). The accurate estimations of step count and step length need pre-calibration, post-processing analysis or mount accurate sensors on specific parts of body for each individual to decide the optimal model parameters (Ho et al., 2016; Lan and Shih, 2013; Liu et al., 2011; Tsai et al.). Those methods are inconvenient for general user that without professional knowledge and adequate budget. Meanwhile, the system that depends on tuning parameters usually has poor generalization ability, which represents the risk that the demonstration system performs better than the production system due to the uncertainty of parameters (Groves et al.); thirdly, in addition to above errors that related to distance, the third error source is heading. Magnetometer and gyro are generally used to provide heading and rotation, respectively. The derived heading from magnetometer is based on the measurement of Earth's magnetic field, and no error accumulated with time. However, the measured magnetic fields are usually affected by the hard- and soft-iron effects (Afzal, 2011). Those effects usually been calibrated because the relation between magnetometer and other magnetic components is fixed in a device. However, they are not easy to perfectly accomplish in real-time by a general user who lacks the basic knowledge. Therefore, the heading based on magnetometer still possible to lose accuracy in a magnetic-hostile environment, and sometimes produces an abnormal value. Gyro is a relatively environment-independent sensor. It indicates that the measurements from gyro are not affected by environment. But the characteristic of gyro makes it requires an initial heading, and its error will accumulate with time. Consequently, magnetometer and gyro are complementary for better heading estimation according to their characteristics. However, even the integrated heading is used, the performance still depends on the tuned parameters of integrated algorithm which related to environmental magnetic field as well as the specification of gyro. In order to maintain the navigation accuracy, the PDR integrated with other external positioning system is needed. Space resection is a good candidate for this requirement.

Smartphone has the required sensors for both PDR and space resection: inertial sensors and camera. Nowadays, the appearance of smartphone encourages the new technological revolution of indoor navigation. The various sensors have been embedded in smartphone such as GNSS chip, Wi-Fi, Bluetooth, accelerometer, gyroscope, magnetometer, camera and even barometer and ambient light sensor. Retscher and Hecht show the feasibility of using different smartphones for tracking in location-based service (LBS) and other navigation applications (Retscher and Hecht). Liu *et al.* propose a smartphone based indoor positioning engine which only uses the built-in hardware and computational resources (Liu et al., 2012). Although the accuracy of such micro electro mechanical system (MEMS) sensors leave much to be desired, but the better performance and smaller size can be expected in the near future. In addition to various sensors, the high popularity is another reason that making smartphone became an ideal personal and mobile navigator. Many users who use smartphones for outdoor navigation applications are based on GNSS. However, people actually spend their daily time about 90% in indoor which is a GNSS-denied environment (Klepeis et al., 2001). Fortunately, the various sensors embedded in the smartphone enable the integrated technologies for pedestrian indoor navigation by utilizing their complementarity, such as the proposed space resection aided PDR.

Unlike most of indoor image-based localizations require multi cameras or successively taking images, space resection only need single image for position estimation. It's more convenient for general users who only navigating with their smartphones. Meanwhile, space resection reduces the heavy burdens of the feature recognition and image matching. In addition, space resection integrated with PDR also further reduce the required images and has the ability of seamless navigation. For seamless purpose, Liang *et al.* propose an image-based localization based on georeferenced image (Liang et al.); Li *et al.* propose a navigation approach based on georeferenced image database, GNSS and INS to facilitate continuous and robust vehicle navigation under harsh environment (Li et al., 2016).

Generally speaking, this research proposes a novel use of space resection to aid PDR in a previously mapped environment. Space resection provides independent location estimation with absolute coordinates (Taiwan Datum 1997, TWD97) to update the navigation solution and reset the accumulated error of PDR. On the other hand, PDR provides the continuous navigation between every implementation of space resection to reduce the burden of image processing of space resection. Moreover, PDR also provides the initial values of iterative calculation for space resection in indoor. Therefore, this algorithm overcomes some major challenges of indoor pedestrian navigation in a GNSS-denied environment such as the requirement of environmental infrastructures and wearable sensors, individual model tuning, fast accumulated error, heavy burden of image processing and poor ability of seamless navigation. The indispensable smartphone is the only needed device since the camera and inertial sensors are originally embedded. Therefore, the proposed algorithm is low cost, convenient and easy to use for general users with their smartphones who only need to take some images. In addition, the proposed algorithm has the ability of seamless navigation based on georeferenced image that produced by MMS. The MMS is used for efficiently mapping the applied environment with the absolute coordinate system. The traditional survey with total station is used for check points to evaluate the position accuracy of proposed algorithm. The preliminary results show the proposed algorithm is suitable for universal pedestrian indoor navigation. It provides the loop closure error about 3% and the improvement of absolute position error about 50% when only few space resections are implemented during a long travel.

2. METHODS

2.1 Pedestrian Dead Reckoning

This research constructs an architecture that integrated with space resection based on PDR. As shown in Figure 1, this architecture has two Kalman filters (KFs) for heading and position estimations, respectively.

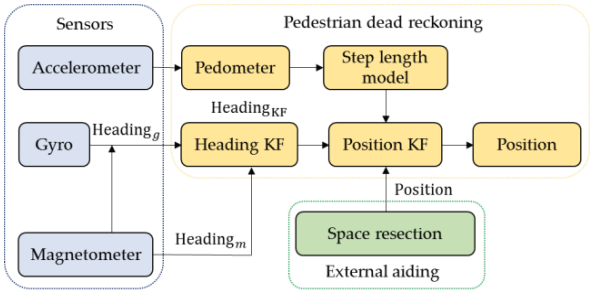

Figure 1. The architecture of proposed algorithm

The pedometer is based on threshold peak detection along with time interval to identify the steps. In addition to pedometer, the

heading KF is based on two kinds of heading measurement: $heading_m$ and $heading_g$ which calculated by magnetometer and gyro, respectively. The gyro heading needs the initial heading from magnetometer at the beginning. Meanwhile, the gyro heading is smooth and independent to the environment, but the error accumulated quickly over time; the magnetic heading is affected by the environment which causes the unsmooth heading measurement, but without accumulated error. Therefore, the heading KF combines the advantages of both heading to obtain a smooth estimation and to reduce the error drift. The used heading KF estimates the errors of integrated heading and gyro bias. The state vector of the heading KF is shown in the following:

$$x_k^h=\begin{bmatrix}\delta\psi_k\\ \delta b_{\psi,k}\end{bmatrix}=\Phi_{k-1}x_{k-1}=\begin{bmatrix}1 & \Delta t\\ 0 & 1\end{bmatrix}\begin{bmatrix}\delta\psi_{k-1}\\ \delta b_{\psi,k-1}\end{bmatrix}+w_k,\ w_k \sim N(0, Q_k) \quad (1)$$

where x_k^h = state vector of heading KF at k epoch
$\delta\psi$ = heading error
δb = gyro bias error
w_k = system noise assumed to be Gaussian distribution
Φ = transition matrix
Q = covariance matrix of system noise

The observation model of heading KF is shown as follows:

$$z_k^h = A_m - A_g \quad (2)$$

where z_k^h = observation model of heading KF
A_m = magnetic heading
A_g = gyro heading

The observation model of heading KF is based on the difference between the magnetic heading and gyro heading at k epoch. After the heading estimation, ones the step is detected, PDR estimates the position based on the integrated heading and step length. The used empirical formula of step length that has better performance with various coefficients can be found in (Chen et al.).

$$L_s=(0.7+a(H-1.75)+b\frac{(F_s-1.79)H}{1.75})c \quad (3)$$

where L_s = step length of s step
a, b and c = model parameters
H = user height
F_s = walking frequency at s step

Moreover, space resection is used as the external aiding in position KF in order to reduce the error accumulated of PDR, as well as avoid the model tuning processing. In the other words, the parameters of the step length formula are default which were trained by 33 walking scenarios of 11 peoples in the reference. The state vector and observation model of position KF are shown in the following equations:

$$x_s^p=[E_s \quad N_s \quad L_s \quad b_{E,s} \quad b_{N,s} \quad b_{L,s}] \quad (4)$$

where x_s^p = state vector of position KF at s step
E_s = eastern coordinate
N_s = northern coordinate
L_s = step length
$b_{E,s}$ = bias of eastern coordinate
$b_{N,s}$ = bias of northern coordinate
$b_{L,s}$ = bias of step length

$$z_s^p = [E_s^{sr} - E_s^{pdr}, N_s^{sr} - N_s^{pdr}] \quad (5)$$

where z_s^p = observation model of position KF at s step
E_s^{sr} = eastern coordinate from space resection
E_s^{pdr} = eastern coordinate from PDR
N_s^{sr} = northern coordinate from space resection
N_s^{pdr} = northern coordinate from PDR

The position KF is used to estimate the integrated position based on space resection and PDR. The observation model is based on the difference between the positions of PDR and space resection. However, the initial position is required for enabling the PDR algorithm and further used in the space resection iterative calculation. Therefore, the start location is given by GNSS in outdoor. Then the PDR further provides the initial values for space resection during later navigation in indoor. Once the image is taken, the solution of space resection can as the constraint for PDR to reset the accumulated error.

2.2 Space Resection

Space resection is a photogrammetry method based on the collinearity equations for solving the EOPs. The collinearity equations are shown as following:

$$x_a=x_p-c\left[\frac{m_{11}(X_A-X_L)+m_{12}(Y_A-Y_L)+m_{13}(Z_A-Z_L)}{m_{31}(X_A-X_L)+m_{32}(Y_A-Y_L)+m_{33}(Z_A-Z_L)}\right] \quad (6)$$

$$y_a=y_p-c\left[\frac{m_{21}(X_A-X_L)+m_{22}(Y_A-Y_L)+m_{23}(Z_A-Z_L)}{m_{31}(X_A-X_L)+m_{32}(Y_A-Y_L)+m_{33}(Z_A-Z_L)}\right] \quad (7)$$

where X_A, Y_A, Z_A = ground coordinates of object point A
m_{ij} = the elements of a rotation matrix
X_L, Y_L, Z_L = ground coordinate of the camera
x_a, y_a = image coordinate of object point A
x_p, y_p = principle point offsets
c = principal distance of camera

The matrix m is a rotation matrix that includes the elements composed of three attitude angles: omega, phi and kappa. The three attitude angles and the location of camera are the elements of EOPs. The principle point offsets and the principal distance of camera are compose the IOPs. The principle of space resection is that the object point, corresponding image point and camera are collinear. The concept of space resection is shown in Figure 2.

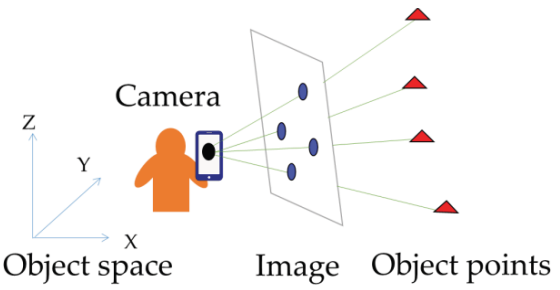

Figure 2. Space resection

In addition, each object point with known ground coordinate is also called control point. At least three control points are needed to solve the unknown EOPs (six parameters). Meanwhile, more control points are needed as the redundant measurement for optimal estimation with least squares. However, the relation between observations and unknowns is nonlinear, so the equations should be linearized by using Taylor theorem. The

collinearity equations are taking partial derivatives with respect to the unknown EOPs, where the exact form can be found in (Wolf and DeWitt, 2000). Therefore, the initial values of unknown EOPs are needed for iterative calculation since linearized equations. The initial values of EOPs in terms of attitude and position are given by the orientation sensor (accelerometer and magnetometer) and PDR algorithm in this research, respectively. The special case is the first location at the beginning of navigation which cannot be provided by PDR because of its characteristic of relative positioning. Therefore, the initial location is provided by GNSS in outdoor.

2.3 Mobile Mapping System

Since the traditional survey for georeferenced images is time-consuming that depending on how much desired control points. The purpose of indoor mobile mapping in this research is to efficiently generate the georeferenced images for space resection. The mobile mapping procedure is one kinds of the photogrammetric technology so-called direct georeferencing. This procedure needs an accurate position and attitude of camera on a moving vehicle. Therefore, a self-developed software was used to precisely estimate the trajectory of MMS based on the Extend Kalman Filter (EKF), Non-Holonomic Constraint (NHC), Zero Velocity Update (ZUPT) and Rauch-Tung-Striebel (RTS) smoother. The state vector of the EKF is shown in the following:

$$x_k^m = \left[\delta r_{1\times3}\ \delta v_{1\times3}\ \delta \emptyset_{1\times3}\ b_{1\times3}^{acc}\ b_{1\times3}^{gyro}\ s_{1\times3}^{acc}\ s_{1\times3}^{gyro}\right] \quad (8)$$

where x_k^m = state vector of EKF for MMS
$\delta r_{1\times3}$ = position errors
$\delta v_{1\times3}$ = velocity errors
$\delta \emptyset_{1\times3}$ = attitude errors
$b_{1\times3}^{acc}$ = biases of accelerometer
$b_{1\times3}^{gyro}$ = biases of gyro
$s_{1\times3}^{acc}$ = scale factor errors of accelerometer
$s_{1\times3}^{gyro}$ = scale factor errors of gyro

After EKF estimation, the RTS smoother is applied. Briefly, RTS combines the forward and backward solutions of EKF to provide the optimal estimations of state vector. Moreover, the fact that the velocities of y-axis and z-axis of the cart should be zero when the cart is moving along, is applied to restrict the error in horizontal velocities. Therefore, NHC can be written as following:

$$z_k^n = [\hat{v}_y^b - 0; \hat{v}_z^b - 0] \quad (9)$$

where z_k^n = observation model of NHC
$\hat{v}_y^b$ = estimated velocities of y-axis in body frame
$\hat{v}_z^b$ = estimated velocities of z-axis in body frame

Similarly, the velocities of three axes of the cart should be zero when the cart is stopped. Therefore, ZUPT can be expressed as following:

$$z_k^{zu} = [\hat{v}_N - 0; \hat{v}_E - 0; \hat{v}_D - 0] \quad (10)$$

where z_k^{zu} = observation model of ZUPT
$\hat{v}_N$ = estimated velocities in north direction
$\hat{v}_E$ = estimated velocities in east direction
$\hat{v}_D$ = estimated velocities in height direction

About the system components, the MMS developed by National Cheng Kung University (NCKU) is an INS/GNSS integration system which consists of GNSS, navigation-grade INS, a panoramic camera, a power supply and an industrial computer, as shown in Figure 3. The similar systems can be found in (Chu et al., 2013; Ellum, 2001; Haala et al., 2011).

However, a large GNSS-denied environment is a harsh space for an INS/GNSS integration system, even using EKF, smoothing, NHC and ZUPT. Therefore, according to the specification of the used INS, velocity of vehicle and past experience, some control points are surveyed by the total station. Those control points are measured in an image for space resection, then the position and attitude of MMS can be estimated to update the EKF solution at that epoch. The MMS starts on the known point which surveyed by real time kinematic (RTK) GNSS at outdoor. Then MMS goes down to mapping the underground parking (experimental field) and go back to the origin. The software is used subsequently to produce the georeferenced images with TWD97 coordinates, as shown in Figure 3. Then the ground and image coordinates of control points can be measured for space resection. Some check points are selected from direct georeferenced images which are later compared to the observed results from traditional survey for accuracy analysis.

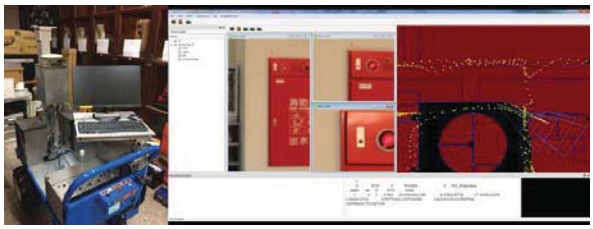

Figure 3. The developed MMS and software interface

3. RESULTS

In order to let the proposed system is easy to use, the space resection uses the IOPs without the camera calibration. In the other words, the used IOPs are from the recording of image file or assumed to be zero. Tables 1 shows the accuracy of space resection in the experimental field with georeferenced images that provided by MMS. The errors shown in Table 1 represent the root mean square error (RMSE) of six locations that implemented the space resection in terms of east, north and horizontal direction. In the other words, only 6 images were used during the navigation. The accuracy of space resection in this field is about one meter, which is acceptable and effective for PDR (without any model calibration, parameter tuning and accurate sensors).

User	East (m)	North (m)	Horizontal (m)
A	0.674	0.865	0.775
B	0.811	0.851	0.831
C	0.846	0.926	0.887
D	0.748	0.866	0.809
Mean	0.770	0.877	0.826

Table 1. The accuracy of space resection in the testing field

The proposed space resection aided PDR is name as S-PDR in the following figure and table. Figures 4 shows the estimated trajectories of four participants (A, B, C and D) using iPhone 5S (Apple Inc., Cupertino, CA, USA). They took the phone and walked along the experimental route. The total walking distance was around 566 m. The black square indicates the start location. In fact, the true trajectory is a closed path but the estimated error causes the offset of end point. Therefore, the red and blue squares are the end locations of PDR and space resection aided PDR, respectively. The green triangle represents the six locations that implemented the space resection update PDR. The red line represents the trajectory estimated by basic PDR algorithm

without any model tuning. The blue dotted line represents the trajectory estimated by proposed space resection aided PDR. The trajectories of two algorithms are overlap at the beginning then become different after the first space resection update. The coordinate system is TWD97, and all the solutions of trajectory are minus the coordinate of start location for clear illustration.

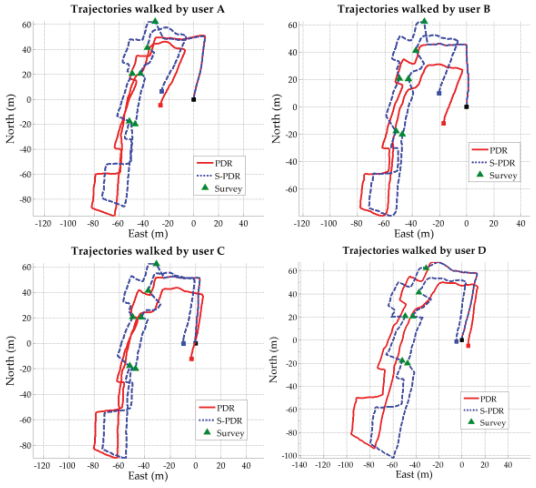

Figure 4. The trajectories of four participants using iPhone 5S

In order to evaluate the improvement of proposed algorithm and verify the better practicality, all the used parameters of PDR are default values. Therefore, the position error caused by step length and step count is obvious because the corresponding parameters are not tuned. Table 2 shows the percentage of loop closure error for analysis of trajectories. The percentage of loop closure error represents the difference between start and end position divided by the total walking distance for a closed path. For example, loop closure error of 1% represents every one hundred meters travelled there will have one-meter error accumulated.

	iPhone 5S	
User	PDR (%)	S-PDR (%)
A	4.803	4.713
B	3.665	3.987
C	2.222	1.730
D	1.292	0.878
Mean	3.00	2.83

Table 2. The percentages of loop closure error of trajectories

However, the improvement of loop closure error after space resection aiding is not significant. Meanwhile, this indicator cannot totally represent the accuracy of complete trajectory. In addition, because it is hard for the user to hold the smartphone and equip the accurate sensors simultaneously, the accurate reference trajectory is difficult to create at the same time. Therefore, we chose some points at the corners as the check points, which can be easily measured on the estimated trajectory. Those reference positions of check point are surveyed by the total station with the accuracy of centimeter level. Then, the absolute accuracy can be further analysed. Tables 3 shows the RMSE of horizontal accuracy of six check points for all the trajectories. The result indicates the space resection aided PDR makes the complete trajectory more coincide with the real walking route, and the absolute accuracy has the average improvement about 52%. The average horizontal RMSE of space resection aided PDR is about 6.2 meters. It's worth mentioning that the large error is usually emerged from the corner, and the four check points in the south (a square part) are without space resection update in the long time. General speaking, the proposed system provides long-term accurate indoor localization after travelled about 566 meters.

User	PDR (m)	S-PDR (m)	Improvement (%)
A	11.545	5.784	49.900
B	13.935	9.861	29.236
C	9.491	3.995	57.907
D	18.381	5.343	70.932
Mean	13.338	6.246	51.994

Table 3. The absolute accuracy of trajectories

Therefore, the result shows better performance of proposed algorithm without any individual calibration, parameters tuning, more accurate wearable sensors and environmental infrastructures. The results also indicate the proposed algorithm is more convenient, lower cost and with higher generalization ability for general user when using their smartphone for seamless navigation. The integration of PDR solves the problem of initial values indoors for the convergence of space resection, and avoids frequent image taking. Meanwhile, space resection provides the error control for PDR without any complex calibration and model.

The more accurate PDR can be considered for a longer gap between two images taken for space resection in the future. In addition, there are some positioning technologies based on RSSI such as magnetic fingerprinting and Wi-Fi positioning. Since the Wi-Fi access point is common indoors and the smartphone usually has a magnetometer, those technologies can be considered in the future to integrate with space resection. However, their accuracies should be acceptable for the convergence of space resection. There is also a large challenge in determining the proposed algorithm for practical and real-time applications using a smartphone due to hardware limitations. The image processing such as feature detection and matching are performed manually in this research. Therefore, the automation process will be considered in future work. The development of cloud servers is one solution for the near future, as they can receive the query image and perform feature extraction and image matching. Another solution is using some designed feature, such as a bar code, to improve the performance of image processing, which is our ongoing work.

4. CONCLUSION

This research proposes the space resection aided PDR in order to develop an algorithm that is low cost, easy to use, high generalization ability and better accuracy for universal indoor pedestrian navigation. By using the proposed algorithm, the user only need one smartphone which embeds the inertial sensor and camera to estimate location. Meanwhile, the user doesn't require to implement any advance calibration and parameters tuning in post-processing, as well as to buy any additional infrastructure and equipped sensors. In addition, space resection provides the position with absolute coordinates for seamless navigation. The MMS is used to fast map environment for the production of georeferenced image. Then the space resection provides estimated position with one-meter accuracy as the update measurement for PDR. On the other hands, PDR provides the initial values for iterative calculation of space resection in indoor once the start location is known. PDR also reduces the requirement of frequently taking images for space resection, and provides the continuous navigation. The preliminary results indicate the proposed algorithm provides the average percentage of loop closure error about 2.8 % and the average error of check points about 6.2 meters, which travelled almost 566 meters.

Meanwhile, the experiments verify the indoor information collected by MMS can be used for indoor navigation. However, there still are some challenges and future works such as image processing and maintaining the accuracy of initial values to make sure the convergence of space resection.

ACKNOWLEDGEMENTS (OPTIONAL)

The authors would like to acknowledge the financial support through the project (SYC1050121) funded by the Department of Land Administration, Ministry of Interior, Taiwan and field support from National Cheng Kung University.

REFERENCES

Afzal, M.H., 2011. Use of Earth's Magnetic Field for Pedestrian Navigation, Geomatics Engineering. University of Calgary, Calgary, Alberta, Canada, p. 247.

Agata, B., Robert, H., Walk detection and step counting on unconstrained smartphones, Zurich, Switzerland, pp. 225-234.

Chen, R., Pei, L., Chen, Y., A Smart Phone Based PDR Solution for Indoor Navigation, Portland, OR, USA, pp. 1404-1408.

Chu, C.H., Chiang, K.W., Lin, C.A., 2013. The Performance Analysis of a Portable Mobile Mapping System with Different GNSS Processing Strategies, Nashville, TN, USA, pp. 689-703.

El-Sheimy, N., 1996. The development of VISAT-A mobile survey system for gis applications. University of Calgary.

Ellum, C.M., 2001. The Development of a Backpack Mobile Mapping System, Department of Geomatics Engineering. University of Calgary, Calgary, Alberta, Canada.

Goad, C.C., 1991. The Ohio State University highway mapping project: the positioning component, Proceedings of the 47th Annual Meeting of The Institute of Navigation, pp. 117-120.

Groves, P.D., Pulford, G.W., Littlefield, C.A., Nash, D.L.J., Mather, C.J., Inertial Navigation Versus Pedestrian Dead Reckoning Optimizing the Integration, Fort Worth, TX, USA.

Haala, N., Fritsch, D., Peter, M., Khosravani, A.M., 2011. Pedestrain Mobile Mapping System for Indoor Environments Based on MEMS IMU and Range Camera. Archives of Photogrammetry, Cartography and Remote Sensing 22, 159-172.

Ho, N.H., Truong, P.H., Jeong, G.M., 2016. Step-Detection and Adaptive Step-Length Estimation for Pedestrian Dead-Reckoning at Various Walking Speeds Using a Smartphone. Sensors (Basel) 16.

Keller, F., Sternberg, H., 2013. Multi-Sensor Platform for Indoor Mobile Mapping: System Calibration and Using a Total Station for Indoor Applications. Remote Sensing 5, 5805-5824.

Klepeis, N.E., Nelson, W.C., Ott, W.R., Robinson, J.P., Tsang, A.M., Switzer, P., Behar, J.V., Hern, S.C., Engelmann, W.H., 2001. The National Human Activity Pattern Survey (NHAPS): A Resource for Assessing Exposure to Environmental Pollutants. Journal of Exposure Analysis and Environmental Epidemiology 11(3), 231-252.

Lan, K.C., Shih, W.Y., 2013. On calibrating the sensor errors of a PDR-based indoor localization system. Sensors (Basel) 13, pp. 4781-4810.

Li, X., Wang, J., Li, T., 2013. Seamless positioning and navigation by using geo-referenced images and multi-sensor data. Sensors (Basel) 13, pp. 9047-9069.

Li, Y., Hu, Q., Wu, M., Gao, Y., 2016. An Imaging Sensor-Aided Vision Navigation Approach that Uses a Geo-Referenced Image Database. Sensors (Basel) 16, 166.

Liang, J.Z., Corso, N., Turner, E., Zakhor, A., Reduced-Complexity Data Acquisition System for Image-Based Localization in Indoor Environments, Montbéliard, France.

Liu, J., Chen, R., Pei, L., Guinness, R., Kuusniemi, H., 2012. A hybrid smartphone indoor positioning solution for mobile LBS. Sensors (Basel) 12, 17208-17233.

Liu, Z., Aduba, C., Won, C.-H., 2011. In-plane dead reckoning with knee and waist attached gyroscopes. Measurement 44, 1860-1868.

Retscher, G., Hecht, T., Investigation of location capabilities of four different smartphones for LBS navigation applications. IEEE, Sydney, NSW, Australia, pp. 1-6.

Tsai, G.-J., Liao, J.-K., Chu, H.-J., Chiang, K.-W., The Performance Analysis of a Smartphone Based Three Dimension Pedestrian Dead-reckoning and Map-Matching Algorithm for Indoor Navigation Applications, Tampa, Florida, USA, pp. 2191-2201.

Weinberg, H., 2002. Using the ADXL202 in Pedometer and Personal Navigation Applications, Norwood, MA, USA.
Wolf, P.R., DeWitt, B.A., 2000. Elements of Photogrammetry: with Applications in GIS, Third ed. McGraw Hill, Boston, MA, USA.

Moons, T., 1997. Report on the Joint ISPRS Commission III/IV Workshop “3D Reconstruction and Modelling of Topographic Objects”, Stuttgart, Germany http://www.radig.informatik.tu-muenchen.de/ISPRS/WG-III4-IV2-Report.html (28 Sep. 1999).

RELATIVE ORIENTATION AND ESSENTIAL MATRIX OF SPHERICAL PANORAMA IMAGES

Yi-Hsing Tseng [a*] and Tsung-Che Huang [b]

[a] Department of Geomatics, National Cheng Kung University, Taiwan – tseng@mail.ncku.edu.tw
[b] Department of Geomatics, National Cheng Kung University, Taiwan – qaz30162@gmail.com

MMT 2017

KEY WORDS: Spherical Panorama Image, Omnidirectional Camera, Relative Orientation, Essential Matrix, Epipolar Geometry, Photogrammetry, Image Navigation, Computer Vision.

ABSTRACT:

Nowadays, a number of commercial multi-camera sensors are capable of capturing images that have complete viewing coverage of the surrounding landscape, which are called spherical panorama images (SPIs), or omnidirectional images. The complete field of view (FOV) is certainly an advantage of SPI over a frame image on the applications of photogrammetry, image navigation and computer vision. For those applications, recovering the relative orientation of a pair of stereo images is one of the important tasks. It is well known that the relative orientation (RO) of two overlapped frame images can be modelled with the essential matrix, and their RO parameters can be solved by using the essential matrix. The objective of this study is to develop an equivalent theory which can be applied to model the RO of two overlapped SPIs. In this paper, we first define the image coordinates, RO parameters and epipolar geometry of SPIs to set up the mathematical basis. Followed the definitions we expound the establishment of the essential matrix of SPIs. Finally, we also describe the derivation of the solution of RO parameters of SPIs with the essential matrix. We demonstrate the computational solutions of RO parameters from the known essential matrices of some SPI pairs. To see the effects of random errors, random errors were added into the tie points to verify the computation as well. We expect that the proposed theory will promote the applications of SPIs.

1. INTRODUCTION

The popularity of 360-degree or omnidirectional cameras has initiated a wide range of applications of spherical panorama images (SPIs) (Lee et al., 2013; Nguyen et al., 2011; Zhang et al., 2012). Featured with the complete viewing coverage of the surroundings, SPIs contain much more image information than frame images. Installing omnidirectional cameras onto a mobile mapping system (MMS) especially enhances the versatility of the system. For example, the photogrammetric mapping ability and efficiency of an MMS can be highly promoted (Tseng et al., 2016). An MMS may also be featured with visual-based navigation and environmental representation with an omnidirectional camera (Gaspar et al., 2000; Hoang and Jo, 2016). Furthermore, an SPI can be applied as a visual compass to guide a robot (Mariottini et al., 2012). For all of the applications mentioned above, the SPI geometry should be solved through the detection and matching corresponding feature points between a pair of overlapping SPIs. Especially, how to solve the relative orientation of an SPI pair is one of the most important issues.

The image geometry of an SPI is different from that of a frame image. Regarding the formation of an SPI, object points are supposedly projected onto the spherical image surface perpendicularly. However, a frame image is formed by the perspective projection of object points onto the image plane. Therefore, conventional photogrammetric theories applied for frame images are no longer valid for SPIs. Focused on the problem of solving the relative orientation of an SPI pair, the first task of this paper is to reformulate the essential matrix of the image pair. The new essential matrix plays an important role for finding corresponding image features between a pair of overlapping SPIs and for solving the relative orientation of an SPI pair. This paper proposes a novel algorithm of SPI matching to find corresponding image features. The solution of the relative orientation of an SPI pair is developed and tested as well.

2. THE SPI GEOMETRY

By definition, an SPI has a spherical image surface, on which the surrounding objects are mapped perpendicularly. An example of SPI and its geometry can be described in Figure 1, where R_{SPI} denotes the spherical radius of an SPI, ρ denotes the zenith angle from the z-axis and α denotes the horizontal angle from the x-axis. Figure 2 show he projected plane image of an SPI. Eq. (1) formulates the coordinates of an image point defined in the image frame (I-Frame).

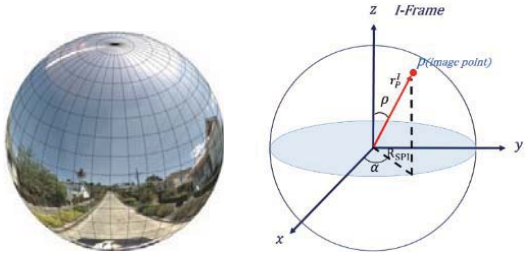

Figure 1 The SPI spherical coordinate system.

Figure 2 The projected plane image of an SPI.

[*] Corresponding author

$$r_P^I = \begin{bmatrix} x_p^I \\ y_p^I \\ z_p^I \end{bmatrix} = \begin{bmatrix} R_{SPI} \sin\rho\cos\alpha \\ R_{SPI} \sin\rho\sin\alpha \\ R_{SPI} \cos\rho \end{bmatrix} \quad (1)$$

So far, ideal sensors to take a perfect SPI have not been available yet. Currently available sensors to capture panoramic images mainly include rotation cameras, multi-camera sensors, and catadioptric cameras (Figure 3). Captured SPIs with those sensors mentioned above may contain a certain amount of geometric distortion from a perfect SPI. The geometric distortion may be reduced by calibrating the sensors (Bastanlar, 2016). The formulas developed in is paper are based on the assumption of the perfect SPI geometry.

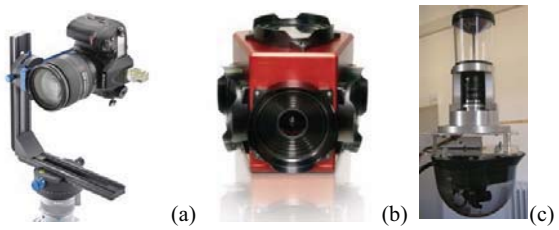

(a) (b) (c)

Figure 3 available sensors to capture panoramic images: (a) a rotation camera, (b) the Ladybug 5, (c) a catadioptric camera.

Suppose there is an ideal SPI, the geometric relationship of an image point and the corresponding object point can be described as an image ray. When the image ray is defined in *I*-Frame and the corresponding object point is defined in object frame, *O*-Frame, the geometric relationship between the image ray and object point can be described in Figure 4. It means that the vector of an object point *P* is the combination of the vector of SPI center and the image ray. This relationship can be expressed as Eq. (2).

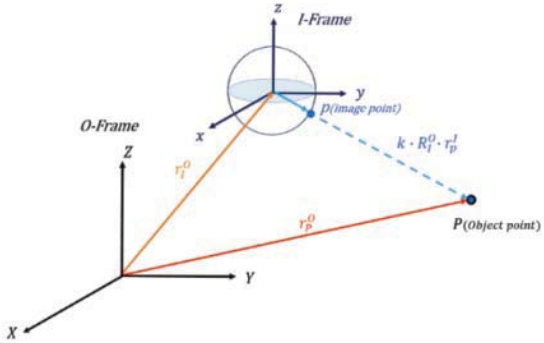

Figure 4 The geometric relationship of an image point and the corresponding object point of an SPI.

$$r_P^O = r_I^O + \mathrm{k} \cdot R_I^O \cdot r_P^I \quad (2)$$

3. GEOMETRY OF AN SPI PAIR

3.1 Relative Orientation

Similar to a stereo pair of frame images, the relative orientation between a pair of overlapping SPIs can be formulated and estimated with conjugate points. Relative orientation defines the position and attitude of one image with respect to the other overlapping image (Ressl, 2000). Figure 5 shows the geometric relationship of an SPI pair. The relative baseline vector and rotation can be formulated as Eq. (3) and Eq. (4) respectively.

$$r_{I1\to I2}^O = r_{I2}^O - r_{I1}^O \quad (3)$$

$$R_{I2}^{I1} = R_O^{I1} R_{I2}^O \quad (4)$$

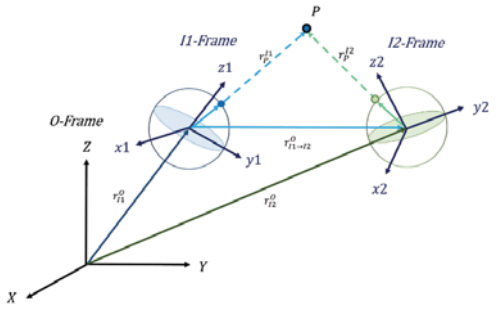

Figure 5 the geometric relationship of an SPI pair.

Both translation and rotation include three parameters, so there are totally six elements of relative orientation. However, since the uncertainty of a scale factor, the base vector between two SPIs cannot be determined and the number of independent parameters is only five. It means that give different scale factors, different translation parameters will be obtained. This will cause the solution infinite if there is no scale factor to be the constraint condition.

3.2 Essential Matrix

The relative orientation between two overlapped SPIs may be retrieved from the essential matrix, and scale factor can be computed by the ray intersection method with more SPIs which the exterior orientation (EO) parameters are known. To extract the relative orientation parameters, we assume the first camera is at the origin and does not contain rotation, which means *I1*-Frame equals to *O*-Frame. The epipolar condition can be depicted in Figure 6, in which the volume of the parallelepiped is the scalar triple product of the three vectors, namely the image rays of two conjugate points and the base vector, is zero. The coplanar condition can be expressed as Eq. (5). By transforming the baseline vector into a skew-symmetric matrix, the coplanar condition can be reformed to Eq. (6). Extracted from the middle part of Eq. (6), Eq. (7) shows the essential matrix, which can be considered as the relative orientation of the image pair (Scaramuzza, 2012).

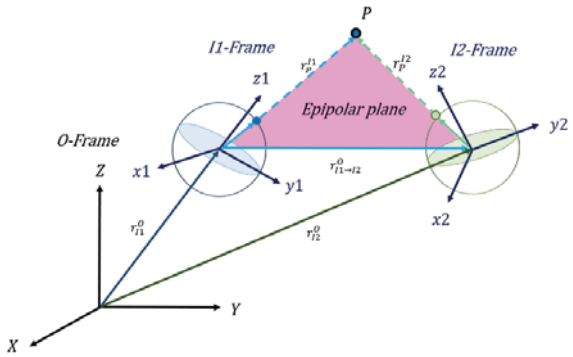

Figure 6 Concept of coplanar condition of an SPI pair.

$$(R_{I1}^O r_P^{I1})^T \cdot [r_{I1\to I2}^O \times R_{I2}^O r_P^{I2}] = 0 \quad (5)$$

$$(r_P^{I1})^T R_O^{I1} \cdot T \cdot R_{I2}^O r_P^{I2} = 0 \quad (6)$$

where

$$T = \begin{bmatrix} 0 & -\Delta Z & \Delta Y \\ \Delta Z & 0 & -\Delta X \\ -\Delta Y & \Delta X & 0 \end{bmatrix}$$

$$E = R_O^{I1} \cdot T \cdot R_{I2}^O = \begin{bmatrix} e_{11} & e_{12} & e_{13} \\ e_{21} & e_{22} & e_{23} \\ e_{31} & e_{32} & e_{33} \end{bmatrix} \quad (7)$$

4. IMAGE MATCHING

It is important to find enough number of corresponding image features between an image pair for solving the relative orientation (Stewenius et al., 2006). This process is called image matching. Image matching techniques have been developed very well (Horn, 1990; Se et al., 2002). However, matching panoramic images is still challenging. De Carufel and Laganiere (2011) have proposed an algorithm for matching cylindrical panorama images. In this paper, we propose a new method to match an SPI pair.

The automatic process of image matching can be divided into two steps. In the first step, image features are detected on the projected images of the SPI pair. Image features are matched by finding the highest similarity of corresponding feature descriptors between the image pair. Scale-invariant feature transform (SIFT) (Lowe, 1999) and speeded up robust features (SURF) (Bay et al., 2002) are the two most famous image feature detectors and descriptors. In this paper, we applied the SURF because it runs faster and more robust than the SIFT.

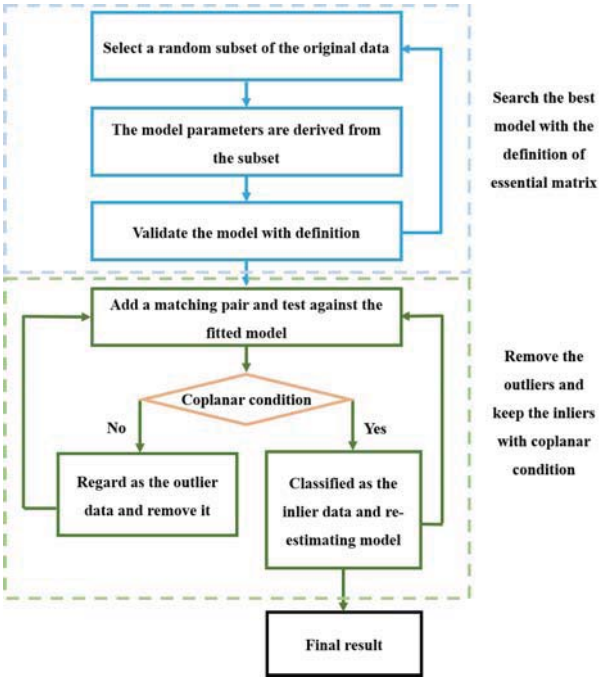

Figure 6 The flow chart of RANSAC for elimination.

The second step is removing outliers from a set of observed data (matched pairs of image features) based on the estimated mathematical model of coplanar condition. In this paper, we adopted a well-known iterative algorithm, the random sample consensus (RANSAC) (Fischler and Bolles, 1981), to achieve this goal. The flow chart of the repeating procedure in shown on Figure 6. The first part of the algorithm is a procedure to test the fitness of a small set of data repeatedly selected to the mathematical model. The mathematical model plays a significant role in RANSAC algorithm. It is the criterion to distinguish between inliers and outliers from the data. The relationship between two frame images may be described by affine transformation. In this paper, the mathematical model is the coplanar condition expressed in Eq. (6). The second part of the algorithm is testing the other data by the coplanar condition to remove outliers. By testing a fixed number of times, the best-fit data set, that generates the largest number of matched image feature pairs, is accepted to determine the relative orientation of the SPI pair, i.e., to estimate the essential matrix expressed in Eq. (7).

It is important to recognize that the geometric relationship between a pair of SPIs is different from that between a pair of frame images. We have to use the correct mathematical model of the geometric relationship for image matching to find as many as possible of matched image features.

5. ESTIMATION OF RO PARAMETERS

As mentioned in section 2.1, the number of independent RO parameters is 5, so we need at least 5 image tie points to solve the parameters (Nister, 2004). However, the solution functions will be nonlinear. Alternatively, the solution functions can be linear by applying the essential matrix, but it needs at least 8 image tie points for the solution. A simple and straightforward solution is the eight-point algorithm proposed by Longuet-Higgins (1981). The solution functions are expressed as Eq. (8). One pair of tie points forms a function. The least squares adjustment is applied when there are more than 8 image tie points.

$$\begin{bmatrix} \vdots \\ xx_i \;\; xy_i \;\; xz_i \;\; yx_i \;\; yy_i \;\; yz_i \;\; zx_i \;\; zy_i \;\; zz_i \\ \vdots \end{bmatrix}_{i=1\sim n} \begin{bmatrix} e_{11} \\ e_{12} \\ e_{13} \\ e_{21} \\ e_{22} \\ e_{23} \\ e_{31} \\ e_{32} \\ e_{33} \end{bmatrix} = 0 \quad (8)$$

where $xx_i = x_i^{I1} \cdot x_i^{I2}$; $xy_i = x_i^{I1} \cdot y_i^{I2}$; $xz_i = x_i^{I1} \cdot z_i^{I2}$; $yx_i = y_i^{I1} \cdot x_i^{I2}$; $yy_i = y_i^{I1} \cdot y_i^{I2}$; $yz_i = y_i^{I1} \cdot z_i^{I2}$; $zx_i = z_i^{I1} \cdot x_i^{I2}$; $zy_i = z_i^{I1} \cdot y_i^{I2}$; and $zz_i = z_i^{I1} \cdot z_i^{I2}$.

Combining all available functions with respect to the tie points gives the matrix form of the combined linear equations, $AE = 0$. By solving the matrix system by the theory of the singular value decomposition (SVD), the parameters of E can be estimated. The solution of the essential matrix can be expressed as $E = U_E D_E V_E^T$, and has $diag(D) = \{d, d, 0\}$, which means that the first and second singular values are equal and the third one is zero. Because the two singular values are equal, the SVD is not unique. In fact, there is a one-parameter family of SVDs for E. Possible solutions to the essential matrix can be obtained by giving an extra constraint, i.e., the essential matrix is $E = Udiag\{1, 1, 0\}V^T$.

The RO parameters can be derived from the estimated essential matrix. It is assumed that the RO parameters of the image pair are composed of the elements of a translation vector and a rotation matrix of the second image with respect to the first image. Converted from Eq. (7), the essential matrix can be rewritten as:

$$E = T \cdot R_{I2}^{I1} \quad (9)$$

The way to recover the translation vector and the rotation matrix has been addressed by Horn (1990). The solution to T is

formulated as Eq. (10). Because of taking the square root, However, there two possible solutions of taking plus or negative signs. After T is determined, the solution to the rotation matrix can be obtained with Eq. (11). It has two possible solutions as well due to the given T. Therefore, there are 4 possible solutions in total.

$$T = \pm\sqrt{\frac{Trace(EE^T)I - EE^T}{2}} \quad (10)$$

$$R_{I2}^{I1} = \frac{Cofactors(E)^T - TE}{T \cdot T} \quad (11)$$

where

I : the identity matrix;

$Cofactors(E)^T = (e_2 \times e_3 \quad e_3 \times e_1 \quad e_1 \times e_2)^T$;

e_i : the i-th column of E.

The 4 possible solutions are resulted from the ambiguity of image ray intersection. Hartley and Zisserman (2004) have illustrated the intersection ambiguity for the case of frame images with a given one intersected object point. The correct solution should be the one has the forward intersection with respect to the both camera. However, the intersection ambiguity is a different situation in SPI case, because of the sphere image plane. Similarly, the four possible solutions due to intersection ambiguity for an SPI pair can be illustrated on Figure 8.

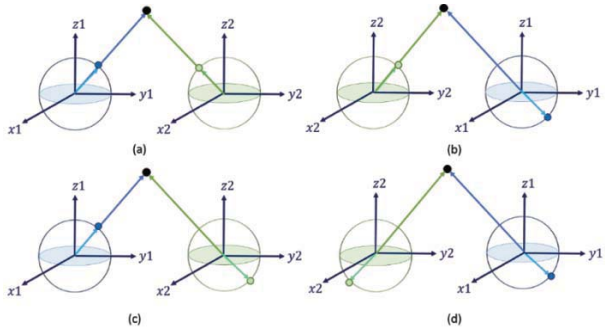

Figure 8 Intersection ambiguity of an SPI pair.

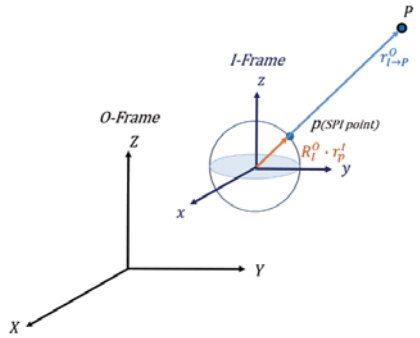

Figure 9 The check angle relationship for solving the intersection ambiguity problem.

This proposes a method to deal with the intersection ambiguity of an SPI pair. Figure 9 shows r_P^I can be transformed into O-Frame by using rotation matrix R_I^O. Vector $r_{I\to P}^O$ also can be computed since we know the position of SPI centre and the intersecting object point. If both rotation and translation of second camera are correct, the angle between $(R_I^O \cdot r_P^I)$ and $r_{I\to P}^O$ will be close to zero rather than close to 180˚. We can use this check angle to solve the intersection ambiguity. The only one correct solution is the one has the both check angles of the two SPIs to be small. The check angle of each SPI can be computed by using inner product computation.

6. EXPERIMENTS

6.1 Image Matching Tests

The test images were captured with a Ladybug 5 sensor. Three test cases of different SPI pairs were tried in the experiments. Case I is an SPI pair that were taken simply in different positions. The distance between the two image positions is about 0.95m (Figure 10). Case II is an SPI pair taken in different rotations. The rotational angle is about 90˚ clockwise (Figure 11). Figure 3(b) shows the concept of cases II. Case III is an SPI pair taken in different tilts. The tilt angle is about 10˚ (Figure 12).

Image features were detected and matched with the SURF detector and descriptor for all SPI pairs. First, the traditional RANSAC algorithm with affine model were tried for the 3 cases to remove outliers. Second, the proposed RANSAC algorithm based on the use of the essential matrix were also performed. Figures 13, 14 and 15 show the test results with respect to the 3 test cases. It is obvious that the number of matched image features can be largely increased with the use of the essential matrix. Table 1 shows the numbers of successfully matched image features for the 3 test cases with RANSAC based on affine model and the essential matrix.

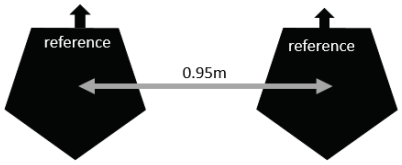

Figure 10 Case I: an SPI pair taken in different positions.

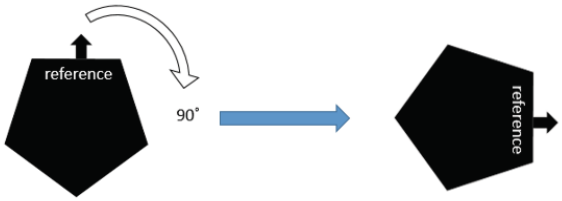

Figure 11 Case II: an SPI pair taken in different rotations.

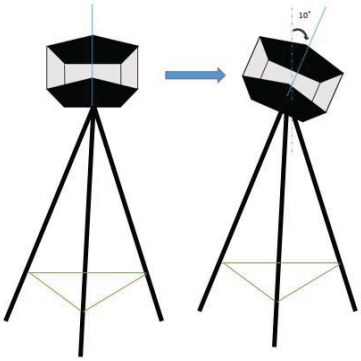

Figure 12 Case III: an SPI pair taken in different tilts.

(a)

(b)

Figure 13 Case I: Image matching with RANSAC based on (a) affine model; (b) the essential matrix.

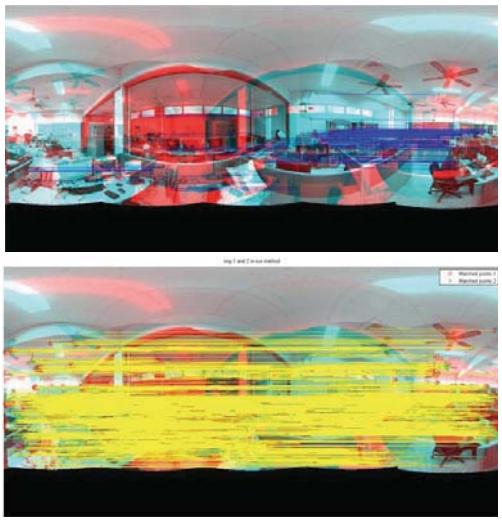

(a)

(b)

Figure 14 Case II: Image matching with RANSAC based on (a) affine model; (b) the essential matrix.

(a)

(b)

Figure 15 Case III: Image matching with RANSAC based on (a) affine model; (b) the essential matrix.

Table 1 The numbers of matched image features for the 3 test cases with affine model and the essential matrix.

	Case I	Case II	Case III
Image matching with affine model	130	680	358
Image matching with essential matrix	360	1831	1040

6.2 Estimation of Relative Orientation

We validated the computation of solving the relative orientation of an SPI pair with a set of simulated data. Table 2 shows the EO parameters of the simulated SPI pair, and Table 3 shows the true values of the translation vector (scaled to unit length) and the rotation matrix. In addition, there were 400 simulated tie points in total generated.

Table 2 The EO parameters of the simulated SPI pair.

	X_0(m)	Y_0(m)	Z_0(m)	$\omega(°)$	$\varphi(°)$	$\kappa(°)$	$R_{SPI}(m)$
First SPI	0	0	0	0	0	0	1
Second SPI	3	5	4	0.64	1.15	25.56	1

Table 3 The true values of the translation vector (scaled to unit length) and the rotation matrix of the simulated SPI pair.

Translation Vector	Rotation Matrix		
0.424	0.9019523	0.4316075	-0.0140387
0.707	-0.4313691	0.9020123	0.0171612
0.566	0.0200699	-0.0094227	0.9997542

Solving the essential matrix with the simulated data, the estimates values of the translation vector and the rotation matrix are listed in Table 4, which shows numbers very close to that in Table 2. In order to see the effects of random errors, we added 0.1 m random errors into the tie points and repeated the computation. Table 5 shows the results of the data with simulated random errors. In this case, the check angles were not perfectly corresponding to the simulated numbers. They are 0.07° and 4.60° with respect to the first and second SPIs.

Table 4 The estimated values of the translation vector and the rotation matrix of the simulated SPI pair.

Translation Vector	Rotation Matrix		
0.424	0.9019524	0.4316075	-0.0140386
0.707	-0.4313690	0.9020123	0.0171612
0.566	0.0200699	-0.0094227	0.9997542

Table 5 The estimated values of the translation vector and the rotation matrix of data with simulated random errors.

Translation Vector	Rotation Matrix		
0.454	0.9273055	0.4291541	-0.0137653
0.739	-0.4265103	0.9151791	0.0479896
0.581	0.0245764	-0.0162586	1.0099651

7. CONCLUSION

The availability of SPI sensors leads to many new applications of mobile mapping and navigation. The geometry of SPIs is very different from that of traditional frame images. Conventional photogrammetric theories developed for frame images may not be valid for the applications of SPI sensors. Focused on the fundamental theory, this paper has dealt with the relative orientation of a pair of SPIs. Based on the definition of SPI coordinate system, the epipolar geometry and the relative orientation of an SPI pair have been redefined and formulated.

This paper has also reformed the essential matrix that representing the relative orientation of an SPI pair. It is validated that the new essential matrix is critical to performing image matching and to solving the RO parameters of SPIs.

To find corresponding image features between an SPI pair, the SURF and RANSAC algorithms were applied in this paper. The experiments show that Traditional RANSAC with affine model used for frame images is not valid for matching SPIs. We demonstrated that the matching results can be largely improved by using the new essential matrix in the RANSAC algorithm. According to the results of the 3 test cases, the numbers of successfully matched image features may increase for about 40%-60%. This will largely help the solution of the RO parameters of an SPI pair.

This paper has also developed an algorithm to solve the RO parameters of an SPI pair by using the essential matrix. We have also illustrated the method to solve the intersection ambiguity. To validate the computation, simulated data without and with random errors were tested to compare with the true data. The computation results demonstrate the correctness of the proposed method and the reliability of solving the intersection ambiguity. We expect that the proposed theory will promote the applications of SPIs.

ACKNOWLEDGMENTS

This research has been sponsored by the Ministry of Science and Technology (MOST) of Taiwan under the project number of MOST 104-2622-E-006-042-CC2 and supported by the Ministry of Interior (MOI) of Taiwan under the project number of SYC1060117.

REFERENCES

Bastanlar, Y. (2016). A Simplified Two-view Geometry Based External Calibration Method for Omnidirectional and PTZ Camera Pairs, Pattern Recognition Letters 71, pp. 1-7.

Bay, H., T. Tuytelaars and L. Van Gool (2008). SURF: Speeded Up Robust Features, Computer Vision and Image Understanding, 110(3), pp. 346-359.

De Carufel, J. and R. Laganiere (2011). Matching Cylindrical Panorama Sequences using Planar Reprojections, IEEE International Conference on Computer Vision Workshops, pp. 320-327.

Fischler, M.A. and R.C. Bolles (1981). Random Sample Consensus: A Paradigm for Model Fitting with Applications to Image Analysis and Automated Cartography. Comm. Of the ACM, Vol. 24, pp. 381-395.

Gaspar, J., N. Winters and J. Santos-Victor (2000). Vision-Based Navigation and Environmental Representations with an Omnidirectional Cameras, IEEE Transactions on Robotics and Automation, Vol. 16, No. 6, pp. 890-898.

Hartley, R. and A. Zisserman (2004). Multiple View Geometry in Computer Vision, Cambridge Univ., pp.257-260.

Hoang V.D. and K.H. Jo (2016). A Simplified Solution to Motion Estimation Using an Omnidirectional Camera and a 2-D LRF Sensor, IEEE Transaction on Industrial Informatics, Vol. 12, No. 3, pp. 1064-1073.

Horn, B.K.P. (1990). Recovering baseline and orientation from essential matrix. MIT AI Memo.

Lee, Y., S. Lee, D. Kim and J.K. Oh (2013). Improved Industrial Part Pose Determination Based on 3D Closed-Loop Boundaries. IEEE International Symposium on Robotics (ISR), pp.1-3.

Longuet-Higgins, H.C. (1981). A Computer Algorithm for Reconstructing a Scene from Two Projections. Nature, 293(10), pp.133-135.

Lowe, D.G. (1999). Object Recognition from Local Scale-Invariant Features, Proc. Of the International Conference on Computer Vision, (Sept. 1999).

Mariottini G.L., S. Scheggi, F. Morbidi and D. Prattichizzo (2012). An Accurate and Robust Visual-Compass Algorithm for Robot-Mounted Omnidirectional Cameras, Robotics and Autonomous Systems 60, pp. 1179-1190.

Nguyen, V.V, J.G Kim and J.W Lee (2011). Panoramic Image-Based Navigation for Smart-Phone in Indoor Environment. Springer-Verlag, Berlin Heidelberg, pp.370-376.

Nister, D. (2004). An Efficient Solution to the Five-Point Relative Pose Problem. IEEE Transaction on Pattern Analysis and Machine Intelligence, 26(6):758-759.

Ressl, C. (2000). An Introduction to the Relative Orientation Using the Trifocal Tensor. International Archives of Photogrammetry and Remote Sensing, Vol. XXXIII, Part B3:769-776.

Stewenius, H., C. Engels, D. Nister (2006). Recent Developments on Direct Relative Orientation. ISPRS Journal of Photogrammetry and Remote Sensing, 60(4), pp. 284-294.

Scaramuzza, D. and F. Fraundorfer. (2012). Visual Odometry: Part I - The First 30 Years and Fundamentals. IEEE Robotics and Automation Magazine, 18(4), pp.85-87.

Se, S., D.Lowe and J, Little (2002). Global Localization using Distintive Visual Features. IEEE/RSJ International Conference on Intelligent Robots and Systems, pp.226-231.

Tseng, Y.H., Y.C. Chen and K.Y. Lin (2016). Bundle Adjustment of Spherical Images Acquired with a Portable Panoramic Image Mapping System (PPIMS), Photogrammetric Engineering and Remote Sensing, Vol. 82, No. 12, pp. 934-943.

Zhang, Chi J. Xu, N. Xi, Y.Y Jia and W.X. Li (2012). Development of an Omni-direction 3D Camera for Robot Navigation. IEEE/ASME International Conference on Advance Intelligent Mechartronics, pp.262-267.

STATISTICAL ANALYSIS OF LIDAR DATA FOR LAND COVER CLASSIFICATION

Nagwa El-Ashmawy[a] , Ahmed Shaker[b],

[a] Survey Research Institute, National Water Research Center, Cairo, Egypt – (nagwa.elashmawy@gmail.com)
[b] Ryerson University, Civil Engineering Department, Toronto, Canada - (ahmed.shaker)@ryerson.ca

KEY WORDS: LiDAR, Point Clouds, Kurtosis Change Curve, Land Cover Classification, Segmentation.

ABSTRACT:
LiDAR technology becomes recently one of the most used technologies in environmental and engineering applications. Near infrared signals, which can be used to distinguish various materials, is one of different wavelengths that are used by LiDAR to detect objects on ground. The reflected signals are then recorded as Intensity (I). Image classification techniques, such as the Maximum Likelihood classifier, can be used to classify LiDAR data based on range and intensity for land cover classification. Statistical analysis segmentation techniques have been introduced to separate terrain and non-terrain points. This paper aims at introducing an innovative approach for classifying LiDAR data. The proposed approach is based on both the statistical analysis segmentation technique and the maximum likelihood classifier for automatically classify LiDAR data into several land cover classes. A complex urban area scanned by airborne laser scanner was selected to test the proposed approach. Four different land cover classes were distinguished and identified using the new approach with overall accuracy of 75%.

INTRODUCTION:
Light Detection And Ranging (LiDAR) has contributed to various environmental and civil engineering applications. Generating Digital Terrain Model (DTM), 3D city modeling, terrain separation, building extraction, road extraction, tree species identification, power lines detection are among many of LiDAR applications [1,2,3,4,5,6,7,8,9,10,11,12,13,14]. Urban land cover classification is one of the applications that LiDAR data has proved its ability to contribute to, [15]. Utilizing the near Infrared (NIR) signals, LiDAR data can help in distinguishing the materials of the illuminated spots on the ground, [16]. Traditionally, image classification techniques have been used in the classification of LiDAR data, [17,18]. However, converting the 3D point data into 2D raster grids causes loss in some details of the data, [7,14,19]. Thus, classifying LiDAR data with the Point-based classification logic demonstrated advantages over converting LiDAR point clouds into raster image and then conducting the classification, [19]. An efficient classification technique is required to deal with the special characteristics of LiDAR data. Recently, statistical analysis segmentation approaches have been introduced to deal with LiDAR data. The introduced segmentation techniques were able to separate the ground and non-

ground points, and to extract features such as roads, vegetation, power lines, and buildings, [6,7,8,9,10, 11,12,13,14].

The statistical analysis segmentation techniques were built on the probability distribution of the data. The normal distribution is uniquely described by its mean and variance, however, the higher order moments (skewness and kurtosis) can be used to characterize other distributions, [20]. Based on the Central Limit theorem, Duda et al., 2001, assumed that the naturally measured samples will lead to normal distribution, and hence, the elevation values of the terrain points will follow a normal distribution, [8]. Bartles and Wei (2006) assumed that the elevation values of the object points may disturb the normal distribution of the terrain points, and by removing the object points, the terrain points will have a normal distribution. Consequently, the skewness value will be equal to (or very near to) zero if the object points will be filtered out, [8,9,10]. Accordingly, they introduced the "Skewness Balancing" technique to separate the terrain points, [8,9,10].

Bao et al., (2008) introduced another statistical analysis approach for segmentation of LiDAR point clouds. This approach depended on Skewness and Kurtosis Change algorithm. The *Kurtosis Change Curve* is a plot of the kurtosis values verses cycle numbers. Where the first cycle the kurtosis value was calculated based on the whole point data, then for each cycle the point with the highest value is removed and the kurtosis value is recalculated until the data were exhausted, [6,7]. This *Kurtosis Change Curve* approach is based on the assumption that if the data of a flat terrain contain terrain points only, the change of the skewness and kurtosis change curves will be smooth; otherwise, there will be inflexions in the change curves. Based on that assumption, the last inflexion point is used as a separation between the objects and terrain, [6,7].

Crosilla et al., 2011 introduced an iterative approach that studying the skewness and kurtosis values of the elevation and intensity, [12,13]. In applying this approach the distribution of the elevation and intensity values are analysed, for each small area, to decide which attribute value to start with. The attribute value which data distribution has distinguishable modes was considered firstly. For example, when the area contained Asphalt road in a flat bare ground area, the intensity was used to distinguish these two classes (road, and ground). On the other hand, when the area contained several features; ground, vegetation, road, and part of a roof. The decision taken to start with the elevation values to separate the building, then the intensity values of the remaining points were considered to separate the road points. Then, the elevation values of the remaining ground points, after removing the road, were considered again to separate the terrain and vegetation areas.

The paper consists of six sections. Section 1 is an introduction, and a description of the previous work. Section 2 explains the purpose and objective of this paper. The third section comprises the methodology used in this research. In Section 4, the study area and the data sets are described. Section 5 includes the classification results of the experimental work and further analysis. The paper is concluded by a summary of the work in Section 6.

OBJECTIVES:

The previously introduced statistical analysis segmentation techniques were adequate for separating the terrain, and for distinguishing one type of features at a time. Thus, the data had to be examined each time to determine the characteristics of the feature type (class) that was required to be separated. For that, this paper proposes an innovative approach for automatically classifying LiDAR data, into different classes, based on the statistical analysis segmentation technique without the necessity of examining the data each time. The procedure for the proposed approach is included in the methodology section.

METHODOLOGY:

The proposed approach is a Point-based logic classifier, which classify the 3D point data without resampling the points into raster grid. This approach is built based on the change in the kurtosis of the elevation and intensity attribute values of LiDAR point data, independently of the spatial locations of the points. To initiate the statistical analysis segmentation technique, *Skewness Balancing* and *Kurtosis Change Curve* approaches are presented with some preliminary assumptions. These assumptions are; (1) The elevation data of the ground points follow normal distribution, [9, 10, 11], (2) A homogeneous class is expected to contain data that are normally distributed, [12, 13], (3) kurtosis and skewness change curves will change smoothly if the points are of ground only in a flat ground (homogeneous class), [6, 7]. The proposed approach in this paper depends on the underlying assumptions that the kurtosis change curve changes smoothly between the cycles if the point data are belonging to a homogeneous class.

The workflow of the proposed approach consists of two stages. Firstly, the point cloud data are segmented using *Kurtosis Change Curve* segmentation approach based on both, the elevation and intensity attribute values of the LiDAR point data. Secondly, the segments produced are classified using the Maximum Likelihood (ML) supervised classification technique, with the aid of training data that are collected from same or similar area. Figure1 shows the procedure of the introduced approach for land cover classification of LiDAR data. The details of the work flow are described in the following subsections.

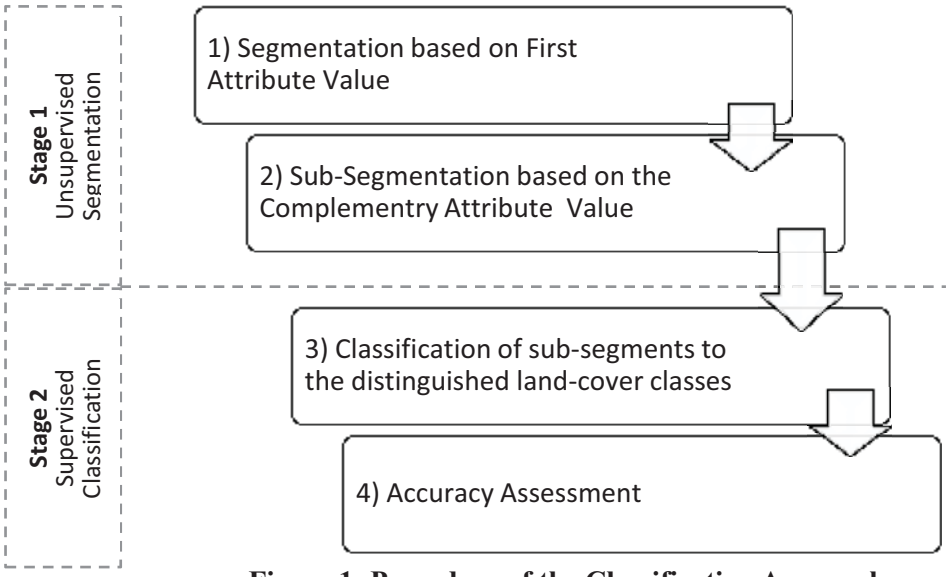

Figure 1: Procedure of the Classification Approach

Unsupervised Segmentation Stage

In the unsupervised segmentation process, the *Kurtosis Change Curve* algorithm is applied on the data twice. Firstly, it is applied on the data based on one of the attribute values, e.g. the elevation, to produce a number of segments. Then, the algorithm is applied again on the produced segments based on the complimentary attribute values, e.g. intensity, to produce sub-segments. If there are more than these two attribute values (elevation and intensity), the segmentation process can be conducted number of times based on each of the considered attribute value.

Since it is assumed that the kurtosis change curve will change smoothly if the point data are belonging to a homogeneous class. Therefore, the prominent changes in the kurtosis change curve (peaks and pits) are used as separators between the different segments, therefore, the local minima and maxima of the curve are determined. The attribute value corresponding to the cycle at last peak or pit is considered as a critical point to separate the higher points into a unique segment. This process works iteratively on the remained points to separate another segment, and so on until all points are segmented. Figure 2 depicts an example of how this process works. The workflow of the unsupervised segmentation process based on the *Kurtosis Change Curve* algorithm is illustrated in Figure 3.

a) Segment 1

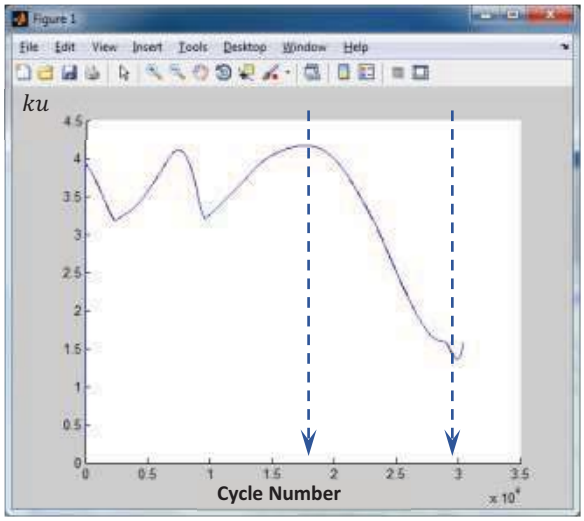

b) Segment 2

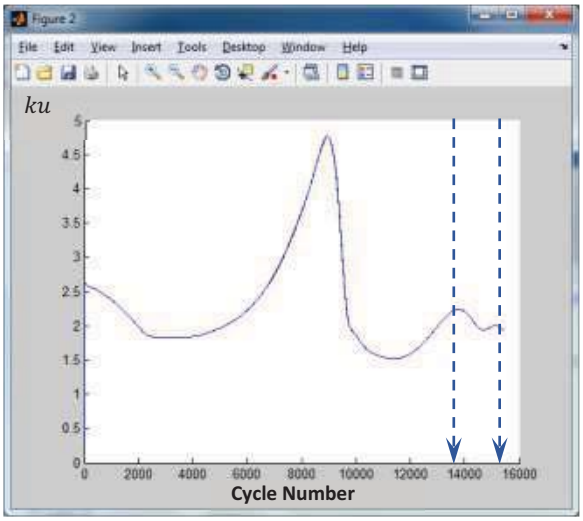

c) Segment 3

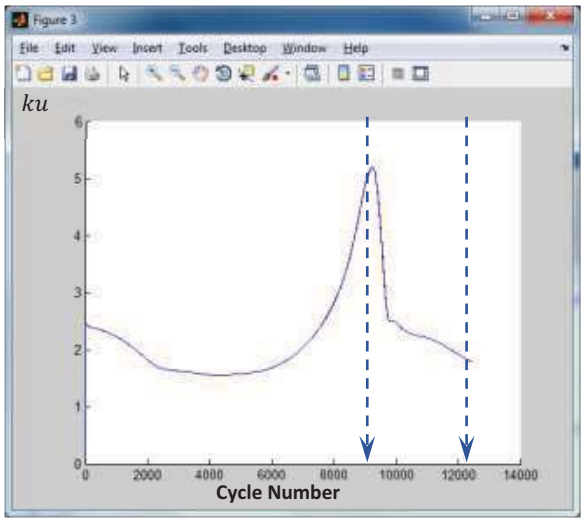

d) Segment 4

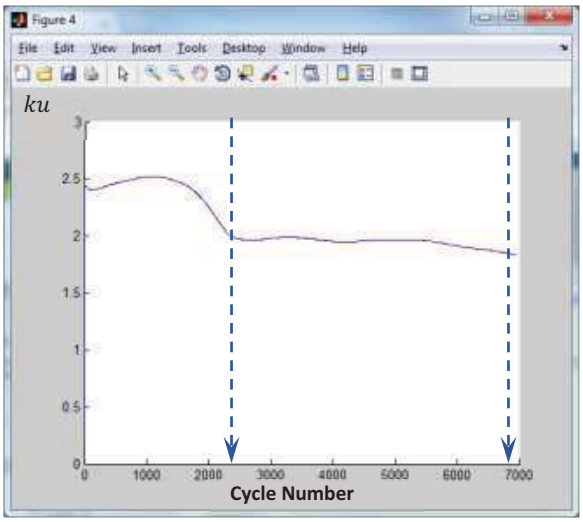

e) Segment 5

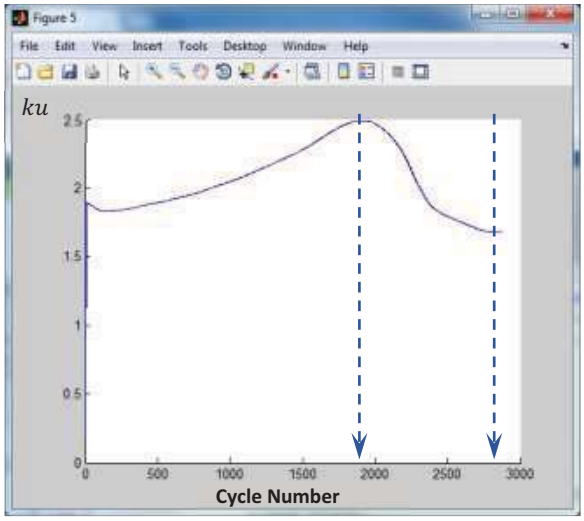

Figure 2: Example of the Proposed Kurtosis Change Curve Segmentation Approach

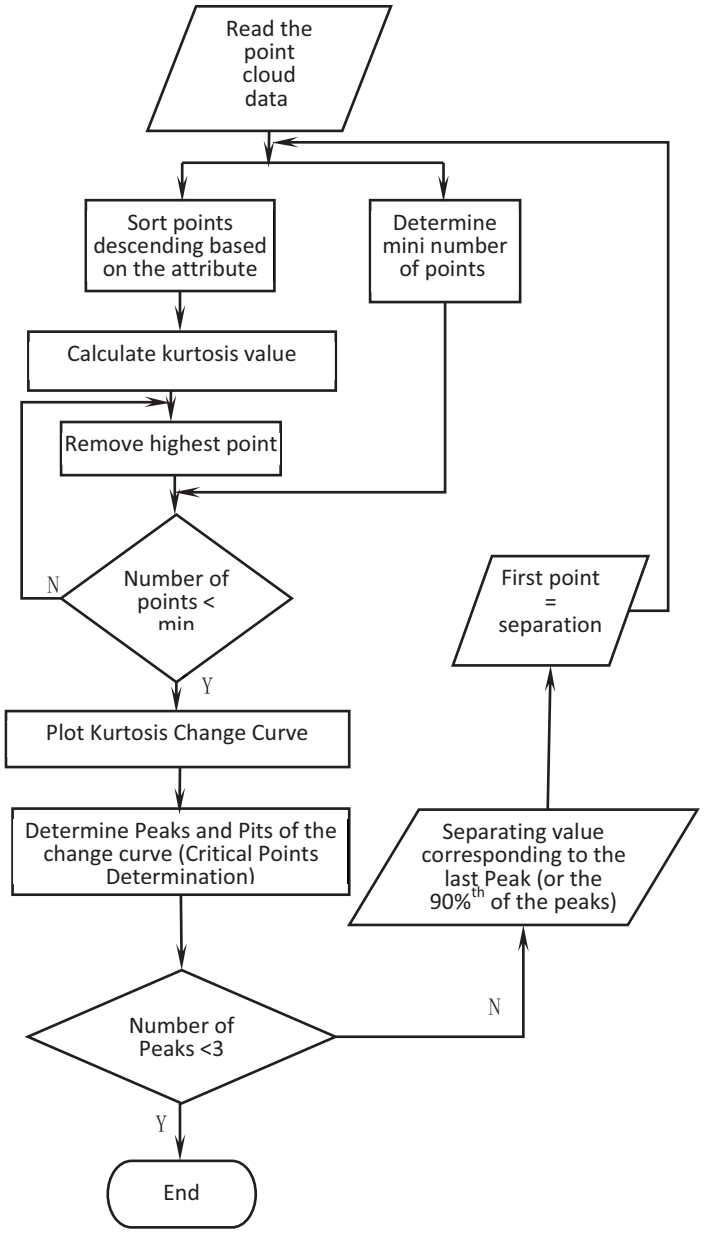

Figure 3: Work Flow of Unsupervised Segmentation of the Point Cloud LiDAR Data

Supervised Classification Stage

The second stage was assigning classes to the sub-segments using one of the supervised classification techniques. In this stage each sub-segment produced in the first stage will be treated as a single pixel or a single object that will be assigned to one of the distinguished classes. The spectral center (the vector of means of each attribute value) of the sub-segment will be determined. The Center point of the segment will be classified, and then all points of this segment will be assigned to the same class. Figure 4 illustrates the steps of the supervised classification.

A MATLAB code was developed to use this new approach for land cover classification of the LiDAR data based on elevation and intensity attribute values.

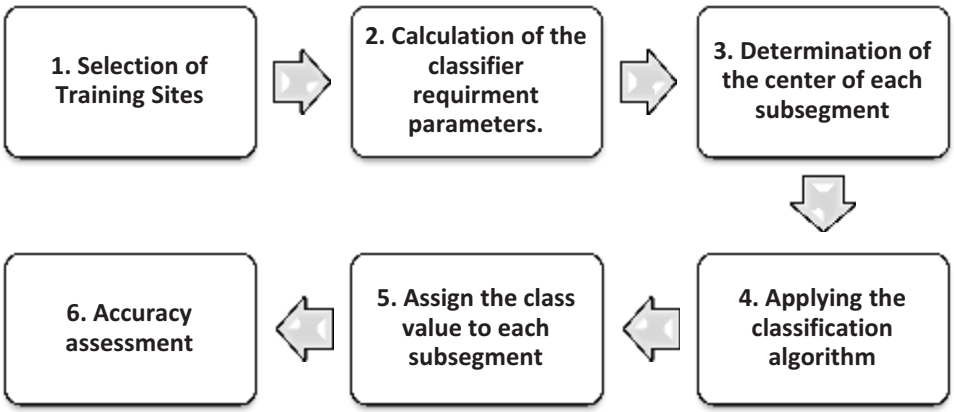

Figure 4: Steps of Supervised Classification Process for Sub-Segments

STUDY AREA AND DATA SETS

Urban district area covering the British Colombia Institute of Technology (BIT), at Burnaby, British Colombia, Canada, was selected to test the proposed classification approach. A Leica ALS50 sensor operating in 1.064 μm wavelength, 0.33 mrad beam divergence and 83 kHz pulse repetition frequency was used to acquire the LiDAR data. The acquisition mission was conducted from around 540 m flying altitude. The LiDAR point density of the LiDAR data was around 4-5 point/m^2. Aerial imageries were captured at the same time of the LiDAR mission. Figure 5 demonstrates the study area and its location as appeared in Google Map, [22].

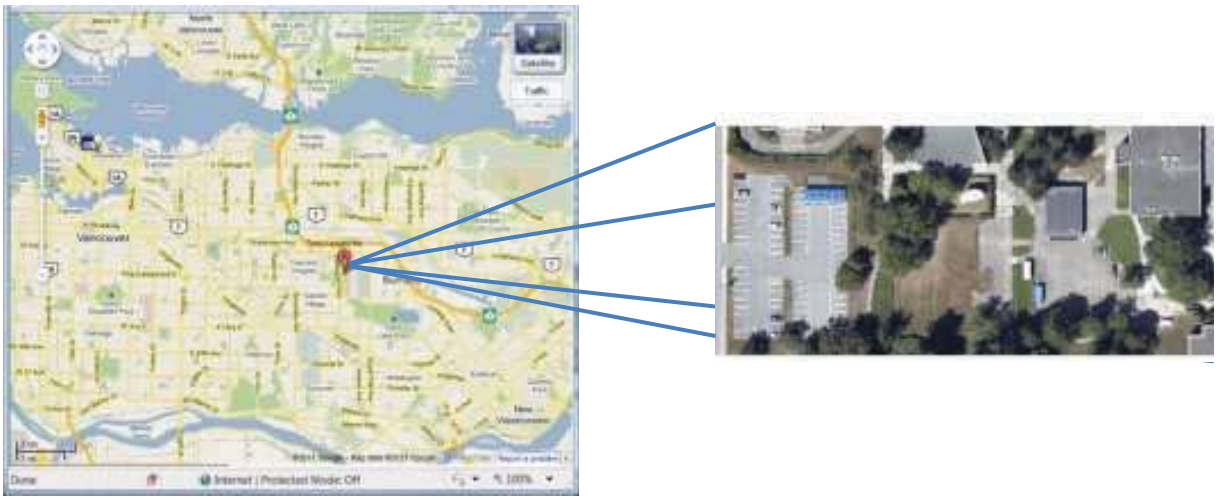

Figure 5: The Location of Study Area as Appeared in Google Map, and the Ortho-Image of the Study Area

A small area of around 150 m x 85 m with around 65,000 point was clipped out to test the proposed classification approach. The study area had complex land cover types comparing to its

size, where different types of roof surfaces and different ground elevations were found within the small area. Four different land cover classes were distinguished in this area: buildings, roads and parking areas, trees, low vegetation (grass) and bare soil.

CLASSIFICATION RESULTS

The Kurtosis Change Curve segmentation technique was applied on the entire dataset based on the elevation values first, producing 11 different segments. By applying the segmentation approach again on the produced segments to cluster them into sub-segments based on the intensity values, total of 42 sub-segments were produced. Then, for the supervised classification stage, the Maximum Likelihood supervised classification technique was applied to assign the produced sub-segments into four distinguished classes; Buildings, Grass or Bare Soil, Roads, and Trees. Figure 5 illustrates the classification results of the study area using the approach proposed.

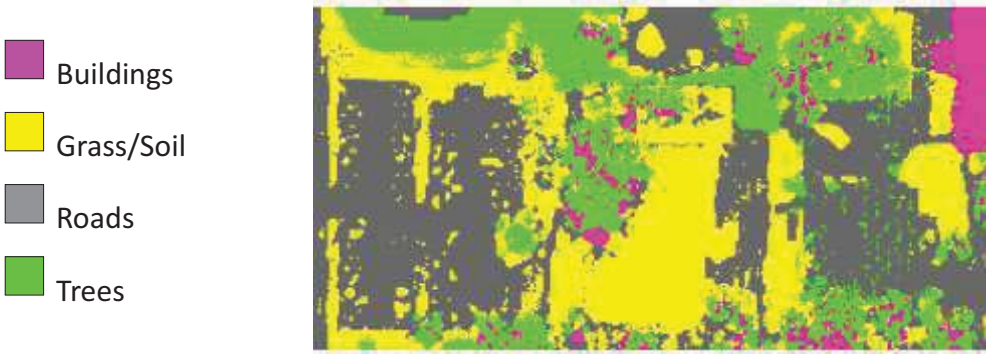

Figure 6: Classification Results Using the Approach Proposed

For assessing the classification results, 220 points randomly distributed over the study area were used. The validation data of the checkpoints was collected from the ortho-rectified aerial imagery. The confusion matrix method was used and the overall accuracy was calculated. The overall accuracy that is achieved of the classified data was around 75%. Table 1 illustrates the confusion matrix of the classified data.

Table 1: Confusion Matrix of Classified Data using the Proposed Approach

	Build	Grass/Soil	Road	Tree	
Build	2	0	0	11	**13**
Grass/Soil	2	61	7	4	**74**
Road	7	11	80	7	**105**
Tree	3	0	3	23	**29**
	14	**72**	**90**	**45**	**221**
OA					**75%**

For comparison reasons; same area was classified by applying the Maximum Likelihood classification algorithm on two-band image (intensity and DSM). Figure 6 shows the classification results of the study area using the supervised image classification technique based

on the Maximum Likelihood classifier. The classified 2-band image was assessed based on same checkpoints. It is found that the overall accuracy of the results was reduced to67%. By analyzing the results over the reference ortho-image of the study area, we can observe that classes produced using the proposed approach match better the aerial ortho-imagery than the classes produced by the traditional image classification technique (Pixel-based classifier).

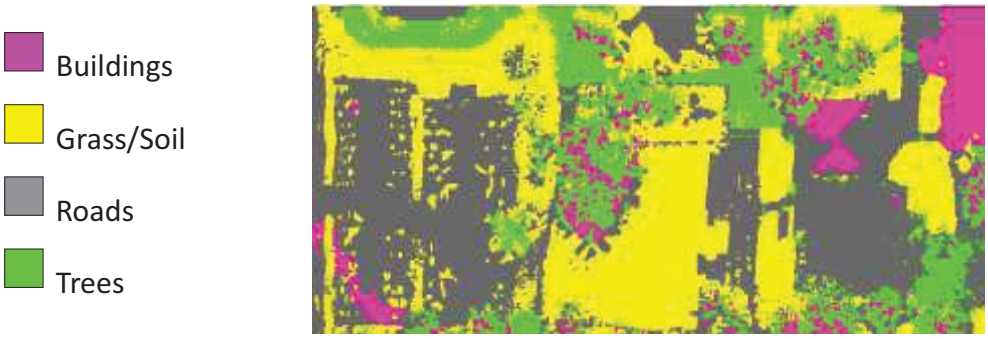

Figure 7: Classification Results Using the ML Classifier

CONCLUSIONS

A two-stage classification approach is proposed, where an unsupervised segmentation of LiDAR point data is conducted on both elevation and intensity data, then a supervised classification technique is used to assign the land cover classes to each segment. The proposed approach starts by a *Kurtosis Change Curve* segmentation algorithm based on one of the attribute values of LiDAR data (elevation or intensity) in an iterative process, where each iteration separates one segment. Then the statistical analysis segmentation algorithm is re-conducted on each produced segment based on the complimentary attribute value, producing sub-segments. In the supervised classification stage, each sub-segment is treated as a single pixel where the center of the sub-segment is classified using the Maximum Likelihood classifier to one of the distinguished classes. Then, all points of this sub-segment are assigned to same class of the sub-segment center. The accuracy achieved of the classified data was 75%, based on 220 checkpoints. With a comparison to the traditional Pixel-based image classification technique, the approach proposed demonstrated advantages over the image classification technique by around 8%.

Generally, the results show that the proposed approach is promising, further investigation is required for enhancing the approach to improve the classification results. The supervised classification of the sub-segments needs more investigation and trials with other classifiers.

ACKNOWLEDGEMENT

This research work is supported by the Discovery Grant from the Natural Sciences and Engineering Research Council of Canada (NSERC) and the GEOIDE Canadian Network of Excellence, Strategic Investment Initiative (SII) project SII P-IV # 72. The authors would like to thank McElhanney Consulting Services Ltd, BC, Canada, for providing the LiDAR and image datasets.

REFERENCES

1. G. Sithole and G. Vosselman, "Experimental Comparison of Filter Algorithms for Bare-Earth Extraction from Airborne Laser Scanning Point Clouds," ISPRS Journal of Photogrammetry and Remote Sensing, Vol. 59, Issues 1–2, pp 85-101, 2004.
2. R. Ma, "DEM Generation and Building Detection from LiDAR Data," Photogrammetric Engineering & Remote Sensing Vol. 71. No.7, pp. 847-854, 2005.
3. N. Haala, and C. Brenner. "Generation of 3D City Models from Airborne Laser Scanning Data." Proceedings EARSEL Workshop on LIDAR remote sensing on Land and Sea, Tallinn/Estonia. 1997.
4. C. Frueh, and A. Zakhor, "Constructing 3D city Models by Merging Ground-Based and Airborne Views," Computer Vision and Pattern Recognition, Proceedings. 2003 IEEE Computer Society Conference on , vol.2, pp.562-9, 2003.
5. N. Haala, N., and C. Brenner, " Extraction of Buildings and Trees in Urban Environments," ISPRS Journal of Photogrammetry & Remote Sensing, 54, pp. 130–137, 1999.
6. Y. Bao , C. Cao, C. Chang, X. Li, E. Chen, Z. Li, "Segmentation to the point clouds of LIDAR data based on change of Kurtosis", International Symposium on Photoelectronic Detection and Imaging, Beijing. (2007)
7. Y. Bao, G. Li, C. Cao, X. Li, H. Zhang, Q. He, L. Bai, and C. Chang, "Classification of LIDAR Point Cloud and Generation of DTM from LIDAR Height and Intensity Data in Forested Area", In: The International Archives of the Photogrammetry, Remote Sensing and Spatial Information Sciences, Beijing, China, Vol. 37, Part B3b. 2008
8. M. Bartels, and H. Wei, "Threshold-Free Object and Ground Point Separation in LiDAR Data", Pattern Recognition Letters, 31, pp. 1089-1099, 2010.
9. M. Bartels, and H. Wei, Segmentation of LIDAR data using measures of distribution, Internat. Arch. Photogram. Remote Sensing Spatial Inform. Sci., XXXVI (7) (2006), pp. 426–431.
10. Bartels, M., Wei, H., and Mason, D.C., 2006, DTM Generation from LiDAR Data using Skewness Balancing, Proceeding of the 18th International Conference on Pattern Recognition (ICPR'06), pp. 566-569.
11. Bartels, M., Wei, H., and Ferryman, J. 2006. Analysis of LiDAR Data Fused with Co-Registered Bands. In Proceedings of the IEEE International Conference on Video and Signal Based Surveillance, (AVSS'06).
12. Crosilla, F., Macorig, D., Sebastianutti, I., Visintini, D., (2011) Points classification by a sequential higher—order moments statistical analysis of LIDAR data. Int Arch Photogramm Remote Sens Spat Inf Sci 38(5/W12).
13. Crosilla F, Macorig D, Scaioni, M., Sebastianutti, I., and Visintini, D., (2013), LiDAR Data Filtering and Classification by Skewness and Kurtosis Iterative Analysis of Multiple Point Cloud Data Categories, Applied Geomatics, Volume 5, Issue 3, September 2013, pp. 225-240.

14. Liu et al., 2009, Liu, Y, Li, Z., Hayward, R., Walker, R., Jin, H., 2009. Classification of Airborne LiDAR Intensity Data Using Statistical Analysis and Hough Transform with Application of Power Line Corridors, In Proceedings of the IEEE International Conference on Digital Image Computing: Techniques and Applications, Australia. IEEE.
15. W.Y. Yan, A. Shaker, and N. El-Ashmawy. "Urban Land Cover Classification Using Airborne LiDAR Data.", Remote Sensing of Environment, Volume 158, pp. 295-310, 2015.
16. N. El-Ashmawy, N., A. Shaker, and W.Y. Yan, "Pixel vs Object-Based Image Classification Techniques for LiDAR Intensity Data," International Archives of the Photogrammetry, Remote Sensing and Spatial Information Sciences, Volume 38, pp. 43-48, 2011.
17. A. Charaniya, R. Manduchi, and S. Lodha, "Supervised Parametric Classification of Aerial LiDAR Data," In: Proceedings of the 2004 IEEE Computer Society Conference on Computer Vision and Pattern Recognition Workshops, (CVPRW'04), 2004.
18. J. Song, S. Han, K. Yu, and Y. Kim, "Assessing the Possibility of Land-Cover Classification Using LiDAR Intensity Data," ISPRS Commission III, Symposium, Graz, Austria. P.B-259ff, 2002.
19. N. El-Ashmawy and A. Shaker, "Raster vs Point Cloud LiDAR Data Classification," International Archives of the Photogrammetry, Remote Sensing and Spatial Information Sciences, Volume 40, pp.79–83, 2014.
20. M. Stricker, and M. Orengo, "Similarity of Color Images," in SPIE Conference on Storage and Retrieval for Image and Video Databases. vol. 2420, pp. 381-392, 1995.
21. Duda, R. O., Hart, P. E. and Stork, D. G., 2001. Pattern classification New York: Wiley.
22. Google Maps, https://www.google.ca/maps/place/BCIT

RAPID INITIALIZATION WITH IMAGE BASED INDOOR LOCALIZATION BASED ON ARTIFICIAL NEURAL NETWORK USING SMARTPHONES

Shih-Huan Huang *, Jhen-Kai Liao , Kai-Wei Chiang

Dept. of Geomatics, National Cheng-Kung University, No. 1, University Road, Tainan 701, Taiwan - (p68011050, p66044031, kwchiang)@ mail.ncku.edu.tw

Commission VI, WG VI/4

KEY WORDS: Indoor navigation, Image-based localization, Smartphone, Rapid initialization, Artificial neural networks

ABSTRACT:

In recent years, indoor localization and navigation have become an important issue because the concept of the smart city appears. Meanwhile, they can achieve location-based service (LBS). There are several methods in indoor navigation in order to overcome the problem in Global Navigation Satellite System (GNSS) denied environment. As the popularization of smartphone, image-based localization is a convenience way because all of the smartphone are embedded with the high-resolution image sensor. With the image-based localization, other signal infrastructure are not needed to reduce the cost of indoor localization. In the indoor localization, the most challenging problem is to initialize in an unknown environment. The main object of this research is to solve this problem with smartphone camera. Image recognition plays an important role in image-based localization. Once the specific marker is recognized, the corresponding navigation parameters will be obtained. Moreover, the distance information and distortion information is implied in a known distance and it can used to carry out rapid initialization with proposed method. The research utilizes the self-design marker in image recognition. Some of the image processing method is used to deal with the projection distortion and vertices detection. The proposed method is robust even in a complicated environment with the effective distance of 10 meters. Previous study has used the space resection method integrated with Pedestrian Dead Reckoning (PDR). However, the accuracy requirement of the initial value in space resection is quite high in some case and it leads to divergent. Therefore, the research adopts Artificial Neural Networks (ANN) in indoor localization. ANN-aided localization is based on the distortion caused by different viewpoint. ANN is applied to estimate the distance between marker and camera. The user position is computed with estimated distance and inertial sensor orientation. The advantage is that it reduce the computational amount and have better localization performance than other image-based localization. The results shows that the ANN-aided image-based localization has smallest error with respect to space resection and similar triangle method. It meets the accuracy of indoor localization and rapid initialization in an unknown environment without other infrastructure.

1. INTRODUCTION AND RELATED WORK

In recently year, the concept of location-based service (LBS) becomes a hot issue because of the popularity of mobile device such as smartphone, smart watch and smart glasses. Localization plays an important role to carry out LBS. The most common way to conduct outdoor localization is Global Navigation Satellite System (GNSS) and it can achieve high accuracy localization in an unsheltered environment. However, it does not work in some GNSS-hostile environment such as urban canyon or indoor environment. Fortunately, several kinds of indoor localization technologies are used in the area without GNSS. There are many kinds of indoor localization methods based on different algorithms and infrastructure.

Inertial navigation system (INS) is often used to compensate the shortcoming of GNSS. The measurement of INS and GNSS are usually integrated using Kalman Filter (KF). However, the shortcoming of INS is that the error may be accumulated as time. As a result, some external aiding position updating such as signal-based localization, image-based localization, map matching or control point updating should be adopted to prevent the accumulation of error caused by inertial sensors. Signal-based localization depends on the external infrastructures. The precision is related to the density of the infrastructures that generate some costs. In addition, the navigation device should be able to receive the signal. As the popularity of smartphone, almost everyone has a smartphone which is equipped with a digital camera. Therefore, vision-based localization is convenient for pedestrian navigation using smartphone. Compared to other localization methods, vision-based localization is more cheap and convenient. It does not need other signal transmission device. It can be categorized into two method. (Kim et al., 2010) One is feature-based localization while the other is marker-based localization. The former one needs a huge amount of database which contains some object space position or navigation information in the environment. The feature extraction and feature matching technique should be used to search the information from the database. The indoor environment image database and feature database should be established in advance. It will cost some time to search the database. Sometimes, mismatching may be occurred that obtains a wrong position or even cause the localization algorithm diverge. Marker-based localization is simpler to be recognized and the computational cost is low. The markers contain 2D barcode with particular ID that we just use some basic image

* Corresponding author

processing algorithms to get the ID from the bar code. Besides, the navigation parameters such as the vertices information or relative orientation corresponding to the ID of marker can be obtained. The marker-based localization can meet the need of rapid initialization in an unknown indoor environment.

Once the marker is recognized, the distance between the marker and camera can be computed using distance estimation algorithm. (Werner et al., 2011) While using the distance estimation algorithm, the camera plane should be parallel in order to estimate more accurately. If the camera plane is not parallel to the marker, the distance estimation error may be increased. In other words, the distance estimation method will have a large error while the image is taken in oblique. Therefore, artificial neural networks (ANN) is used to reduce the distance estimation error caused by oblique in this research. In the previous research, ANN is used in indoor localization in many researches. Farid et al. (2016) used the ANN technique for position calculation in Wifi (RSS) based localization. Gukhwan et al. (2010) adopted ANN to recognize the English alphabet letters that used in image-base localization. Compared to space resection algorithm, initial value is not needed to carry out ANN-aided image-based localization. Besides, ANN-aided method has better performance and lower computation burden than space resection methods. This research utilizes ANN to estimate more accurate reduce distance that enable user to take a picture in approximately 10 meters and reduce the localization error caused by tilt.

There are many kinds of image-based localization method. Space resection is adopted in this research. The basic concept of space resection is collinearity condition. (Wolf et al., 2004) The space resection is used in aerial survey in the past year. Pervious research adopted the space resection method in indoor localization Space resection method is combined with the pedestrian dead reckoning (PDR) to reduce the accumulated error caused by inertial sensor. In this research, there are some square regions in the self-made marker and its vertices points of the square regions can be used in space resection as feature points. Last, the research compare three kinds of image-based localization method in accuracy performance. The results show that ANN-aided method have the lowest localization error even when the distance is large.

2. METHODOLOGY

2.1 Research Framework

The research designs a novel marker which can decrease the computation burden of feature extraction and feature matching, and applied for space resection. The proposed method is divided to two parts. One is the marker recognition stage. The other is localization stage. Marker recognition adopts several kinds of image processing algorithms to recognize the specific marker. Localization stage is to estimate the accurate location using the proposed method. The proposed method contains distance estimation, artificial neural network and space resection. The following figure shows the flowchart of this research.

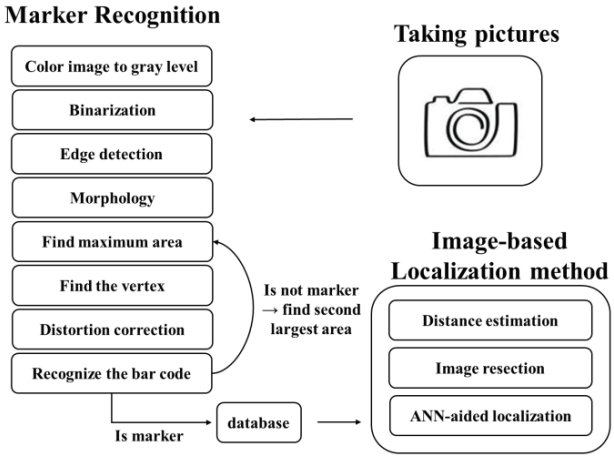

Figure 1. The flowchart of proposed method

2.2 Marker recognition

2.2.1 Marker design

There are two kind of vision based localization method in indoor position. Some researches work on indoor localization system using Scale Invariant Feature Transform (SIFT) method. The SIFT feature are independent of camera viewpoint so they are proper to be used as landmarks. However, the method cause sever burden on computing time including feature extraction and feature matching. (Kim et al., 2010)

Another method is marker-based localization. The advantage is that the principle of recognition is simple and the computation time is less than feature-based localization. The proposed method can detect the marker automatically and it is feasible in a complicated environment as long as the marker is visible. The effective distance of marker-based localization is short generally. There is a limit of recognition distance due to the blurry of image. Besides, the self-designed marker has advantage to provide the vertices points that can be used in space resection. The following figure shows the makers we designed:

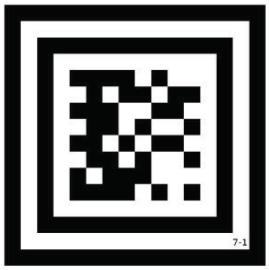

Figure 2. The marker used in this research

There are two square frames containing 16 vertices points that can be used in space resection in the specific marker. The marker also contains data matrix code. Once the specific marker is recognized, the corresponding information such as the object space coordinate of vertices, orientation, building information… etc.

2.2.2 Image segmentation

To recognize the marker, several image processing algorithm should be used to detect the marker in RGB image. First of all, the RGB imaged should be converted to grayscale image. The transformation equation is as follow:

$$I = 0.2989 \times R + 0.5870 \times G + 0.1140 \times B \quad (1)$$

where I is the grayscale digital numbers; R, G, B are the digital values from 0 to 255 of red, green, blue respectively. (coefficients are from the Image Processing Toolbox, MATLAB R2011b, MathWorks®, Natick Massachusetts, USA)

After grayscale image is obtained from the above method, the binarization is used to conduct the image segmentation. The fixed threshold value is selected by experience. Image will become black and white and it represents background region and non-background region, respectively. The advantage is that it can be stored as a binary map saving the memory and computing time.

2.2.3 Edge detection

The edge will be more obvious to be extracted after the binary image is obtained. To extract the edge of the marker, well-knwon Sobel operators are used. Sobel operator is a discrete differentiation operator, computing an approximation of the gradient of the image intensity function. (Zhang et al., 2009) The operator uses two kinds of 3 by 3 kernels to conducting convolution with the source image. Two kernels are horizontal and vertical derivative approximations, respectively, so each pixel in image will have its gradient in two direction. The Sobel kernels can be described as following figure:

-1	0	1
-2	0	2
-1	0	1

G_x

-1	-2	-1
0	0	0
1	2	1

G_y

Figure 3. Sobel operators

The gradient magnitude of each pixel can be calculated using the following equation:

$$G = \sqrt{{G_x}^2 + {G_y}^2} \quad (2)$$

The gradient magnitude can also be approximated as:

$$G = |G_x| + |G_y| \quad (3)$$

Then, the edge pixels can be found using threshold method.

2.2.4 Morphology

Morphology is usually used in image processing and it is based on mathematical theory for operation. The outputs of morphology are some features or attributes. Morphologic image processing only depends on the relative pixel digital value. The basic operation of morphology is erosion and dilation and other operations are extended from these two methods. Kernels are also used to do the weighting operations. In this research, morphology is used to fill the hole after the edge is extraction so that the marker region can be found more easily in the image.

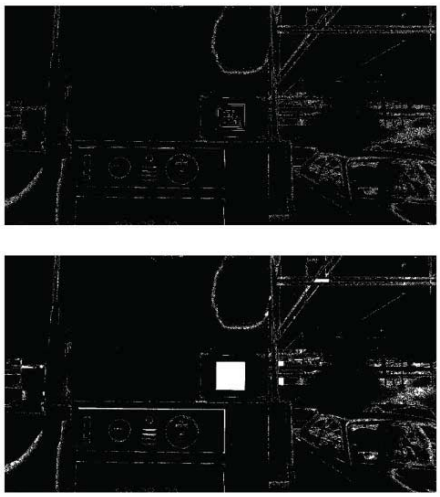

Figure 4. Extract marker region with morphology

In the above figure, there are thousands of small white region, but there are just one correct marker region. The common characteristic of marker is that it usually contains the most pixels, so we can distinguished the marker region from other regions by this property. However, sometimes the marker region is not the maximum region. As a result, this research adopts an iteration method to prevent this situation. If the region it found is not the marker after proposed marker recognition method, the second largest will be a new candidate of marker. The iteration will be stopped when the proper marker region is found or it arrived the maximum number of iteration. If the iteration time reaches maximum, it means that there is no marker in this image.

2.2.5 Vertices detection

When the specific marker region is extracted, its four vertices should be marked automatically in order to conduct the distortion correction in the next step. In other words, the pixel coordinate of four vertices will be detected automatically with the proposed algorithm. The schematic diagram of the proposed method is shown as following figure:

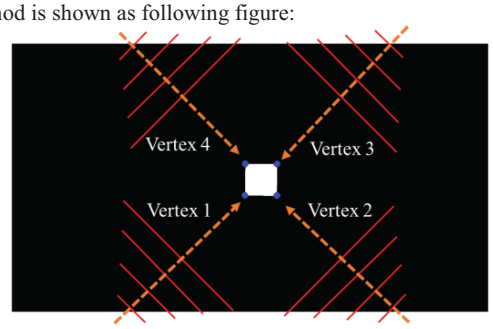

Figure 5. Schematic diagram of proposed method

In the above figure, four direction of diagonal line (red line) is moving from the edge of the image to the middle to find the first encountered white pixel. They will be the vertices of the white region and the coordinate of vertices are recorded to calculate the transformation parameters in the next step.

2.2.6 Distortion correction

The concept of camera is central perspective projection, so the projection distortion will exist. In order to recognize the bar code, the image should be orthogonal. As a result, projection distortion should be eliminated using perspective projection

transformation. To conduct the distortion correction, the vertices of marker that are obtained from previous steps is used to calculate the transformation matrix. The equation of perspective projection transformation is as follow:

$$\begin{bmatrix} up \\ vp \\ wp \end{bmatrix} = \begin{bmatrix} A & B & C \\ D & E & F \\ G & H & I \end{bmatrix} \begin{bmatrix} x \\ y \\ 1 \end{bmatrix} \quad (4)$$

$$u = \frac{up}{wp} = \frac{Ax+By+C}{Gx+Hy+I} \quad (5)$$

$$v = \frac{up}{vp} = \frac{Dx+Ey+F}{Gx+Hy+I} \quad (6)$$

From the above equation, (x,y) is the original coordinate of the marker in image. (u,v) is the coordinate after transformation which makes the marker orthogonal. The four vertices position of marker are used as the measurement to estimate the transformation matrix using least square. As a result, the inverse transformation can be used in sampling the digital values. The nearest neighbour interpolation is adopted to obtain the digital values in the image after distortion correction. After the distortion, the marker will be corrected to its original shape, a square as follow figure:

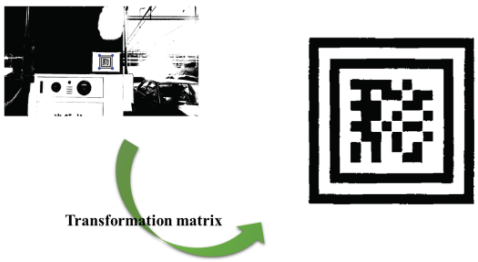

Figure 6. Distortion correction

Next step is to recognize the data matrix code. Then, user can get the navigation information such as the marker's ID, corresponding direction, orientations and object space coordinates of vertices points. The above information can be used in the proposed localization algorithm in the next chapter. If the decoding procedure failed, the region will be removed and go back to find the biggest region until the correct marker is recognized. The effective distance of the proposed method is approximate 10 meters because of the insuffivient resolution of the smartphone camera. If the distance is farther than 10 meters, the image will be too blurred to recognize.

2.3 Localization algorithm

2.3.1 Distance estimation

First, the rough distance between the marker and the centre of projection (COP) is estimated with the similar tringles. When the image plane is parallel to the marker, the distance from COP to image plane and to marker will be proportional to the length in image and in the real world. The schematic diagram is as follow:

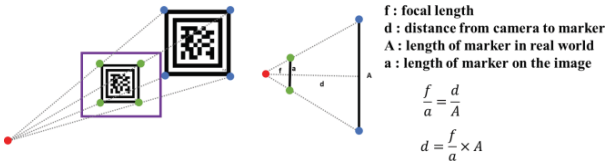

Figure 7. Distance estimation method

The focal length (which is also called principle distance) of camera and the length of real marker is known. The length of the marker on the image can be measured automatically, so distance from the COP to the marker will be obtained from the above equation. The position of user can be calculated from the above figure. The relative angle with respect to the marker can be obtained from the inertial sensors. However, while the image plane is not parallel to marker plane, the estimated distance will be inaccurate.

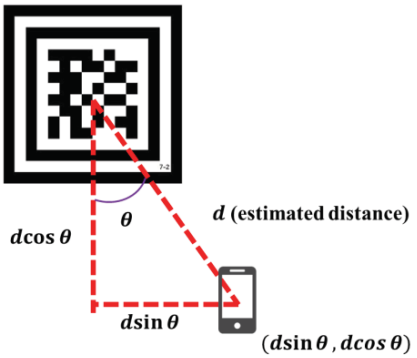

Figure 8. Position estimation method

2.3.2 Artificial neural network

The previous step details the method to estimate the rough distance, but that method can just be used when the image plane is parallel to the marker plane. When the image is taken in oblique, they are not parallel. The estimated distance error may increase while the tilt angle increases. Artificial neural network (ANN) is used to decrease the distance estimation error when the image is taken in oblique. Unlike other studs adopts ANN in image processing.

In this research, multilayer perception (MLP) is selected as the ANN structure because it can deal with some non-linear supervised learning with the back-propagation algorithm. MLP consists of input, hidden and output layer. In this research, there are eleven neurons in input layer which eleven features are extracted from the image. The features contain four normalized coordinates of vertices points, normalized coverage on the image, the estimated distance and camera orientation. The output is the actual distance between marker and camera. There are one hidden layer, which contains eight neurons with an activation function. The activation functions are sigmoid function in hidden later and linear function in output layer. The following figure shows the ANN structure this research adopts.

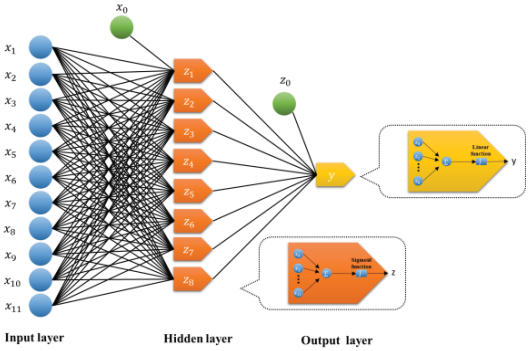

Figure 9. Multilayer Perception structure

In the above figure, each of neuron in hidden layer and output layer will be operated by activation function which is a mathematical operation to evaluate the influence of the neuron. The back-propagation (BP) Momentum Optimize is used as the training algorithm that its learning rate is set to 0.05 and momentum is set to 0.2. The ANN model is established by a large amount of image taken in different distance and tilt angle with the known accurate distance. Then user can take the picture in arbitrary position and angle to get the accurate distance using ANN.

2.3.3 Space resection

The basic concept of space resection is collinearity equation. It assumes that the object point, corresponding image point and optical will be in the same line. The equation is shown as follow : (Wolf et al., 2004)

$$x_a = x_0 - f\left[\frac{m_{11}(X_A - X_L) + m_{12}(Y_A - Y_L) + m_{13}(Z_A - Z_L)}{m_{31}(X_A - X_L) + m_{32}(Y_A - Y_L) + m_{33}(Z_A - Z_L)}\right] \quad (1)$$

$$y_a = y_0 - f\left[\frac{m_{21}(X_A - X_L) + m_{22}(Y_A - Y_L) + m_{23}(Z_A - Z_L)}{m_{31}(X_A - X_L) + m_{32}(Y_A - Y_L) + m_{33}(Z_A - Z_L)}\right] \quad (2)$$

In the above equation, (x_0, y_0, f) are inter orientation parameters (IOPs). It can be obtained from camera calibration. (X_A, Y_A, Z_A) is the object point used in space resection, and it should be measured by high precision instrument. (x_a, y_a) is the corresponding image coordinate used as the measurement. (X_L, Y_L, Z_L) is the object space coordinate of the camera. It indicates where the camera is in the real world. m_{11}~m_{33} are the elements of rotation matrix which is composed of three rotation angles: omega, phi, kappa. The rotation angle is used to describe the relative amount of rotation with respect to the coordinate system. The position and the rotation angle of camera is composed of exterior orientation parameters (EOPs) which are unknown in least square. Because the relationship between measurements and unknown are nonlinear, the observation equation should be linearized with the Taylor expansion equation and it needs initial values to conduct least square. The rotation angles are given from the orientation sensor and the position can be given by the ANN aided method, pedestrian dead reckoning (PDR) algorithm or GNSS. The concept of the space resection is shown in the following figures:

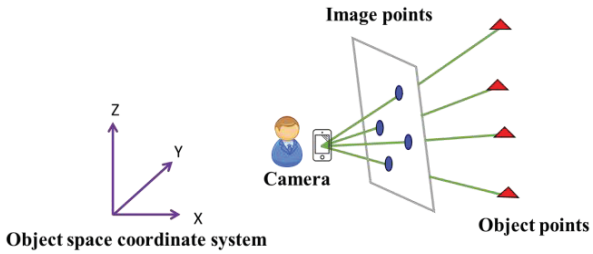

Figure 10. Space resection with smartphone

In the above figure, a feature point can provide two observations. The EOPs are the unknowns in space resection, so there are six unknowns. As a result, at least three feature points should be used to estimate the unknowns. More feature points are needed as redundant measurement for better estimation.

2.3.4 Comparison of different image-based localization

In this research, we used three kinds of image-based localization method: distance estimation, ANN aided method and space resection method. Each of them has its advantage and shortcoming. Distance estimation used the similar triangle geometry to compute the distance. It is simple and rapid, but the accuracy will decrease dramatically while the pictures is taken in oblique. Space resection method can get the high accuracy position and attitude of the camera. However, the initial value is needed to conduct least square. If the initial value is not accurate enough, the algorithm will lead to divergence. The ANN-aided image-based localization shows the high performance in accuracy. The accurate distance can be obtained using the trained model. The model is trained using the distortion information of the marker. It can also deal with the situation that the pictures are taken in oblique.

3. EXPERIMENT AND RESULTS

3.1 Experimental smartphone

The experimental smartphone device is Sony Z3. The results of camera calibration and official specification is as follow table:

Table 1. Specification of Sony Z3

Calibrated principle distance (mm)	4.5398
Principle point offsets	(0.0006,-0.0388)
Radial distortion (K1, K2, K3)	(1397,-575.8,31.56)*10^(-6)
Decentering distortion (P1, P2)	(-136.1,-54.10e)*10^(-6)
Recording principle distance (mm)	4.6
Pixel size (mm)	0.0011
Image size (pixel)	5248*3936

From the above table, recording principle distance, pixel size and image size are the official specification and others are obtained from the camera calibration. The smartphone camera should be calibrated because it is non-metric digital camera. As a result, the IOPs is unstable. Accurate IOPs is needed to eliminate the error caused principle points offsets or lens distortion.

3.2 Practical test of marker

The image is taken in an indoor environment. The results of the proposed method in each steps is shown in following figures:

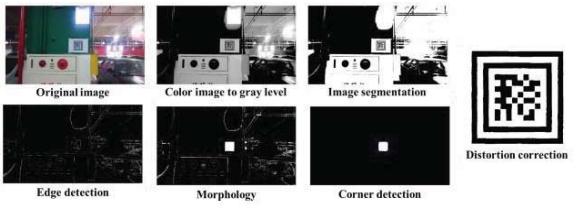

Figure 11. Result of proposed marker recognition method

The above figure shows the result of proposed method in each step. If every steps are worked well, the marker region in orthogonal successfully can be obtained and it can be recognized correctly.

In order to verify the proposed method, pictures are taken in a complex environment. There are even some people in the room and the distance between marker and camera is around 10 meters to examine the recognisability.

Figure 12. The robustness test of proposed method

The result indicates that the marker is detected successfully even the environment is complicated or someone is in the image as long as the marker is visible. It also verify that pictures can be taken in a far distance or in oblique. Because of the image blurry caused by camera resolution, there will be an effective distance in this proposed method. The following figure shows the phenomenon of image burry.

Figure 13. Image burry caused by resolution

The experiment is conducted to find the limit distance to recognize the marker. Many pictures are taken in different distance with respect to the marker. The result indicates that the effective distance of proposed method is around 10 meters.

3.3 Distance estimation experiment

The previous chapter mentions the distance estimation method using similar triangles. The aim of this experiment is to evaluate the distance estimation error in different range. Many images are taken in every one meter. Three different tilt angle are selected to evaluate the distance estimation error caused by oblique. The error in different distance is shown in following figure.

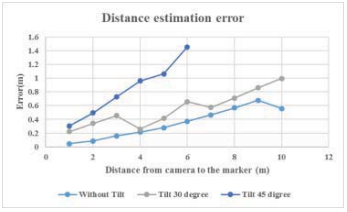

Figure 14. Distance estimation in different tilt angle

The tendency of distance estimation error increases while the distance increases. Because image becomes blurry caused by insufficient of resolution while the distance increases. Besides, the figure shows that while the tilt angle increase, the increasing tendency of error is more obvious. In conclusion, ANN is needed to correct the distance when image is taken in oblique.

3.4 ANN improved distance experiment

ANN is used to correct the estimated distance computed by the aforementioned method. Firstly, we need to collect a large amount of input data with the selected features. The input images are taken in different angle and distance surrounded the marker. We take the pictures from one meter to eleven meters with all many angles for training dataset and extracts their feature for input neurons. The features are the normalized coordinate of vertices points, normalized area, the distance estimation result and orientation given by magnetometer. The real distance is given as target in training dataset. There are 200 training data shown in following figures.

Figure 15. Training data in ANN

MLP(14-8-1) structure is used to be the model which the activation function is set to be sigmoid function and linear function in hidden layer and output layer, respectively. BP Momentum Optimize is chosen as training algorithm that the learning rate is set to 0.05 and momentum is set to 0.2. The following shows the training result with the network error. It can be found that the networks error decrease dramatically first and then converge to a small value in thousands of iteration times.

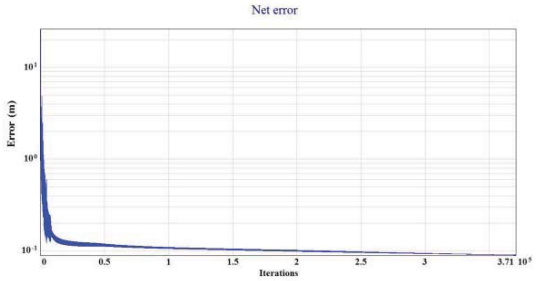

Figure 16. Training result

Testing data is obtained from another scene proving that trained model can be used in different environment. Thirty-two images are taken toward the marker in arbitrary position and tilt angle. The training model is used to estimate the improved distance. The testing data is shown as follow.

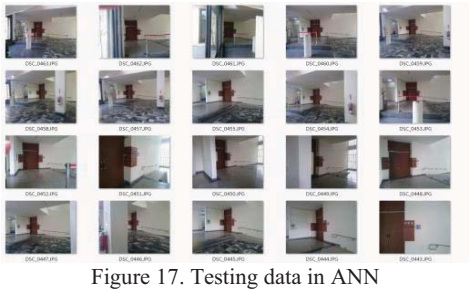

Figure 17. Testing data in ANN

The testing result is shown as following table.

Table 2. The result of testing data

Sample	Distance estimation error(m)	ANN-aided error(m)	Sample	Distance estimation error(m)	ANN-aided error(m)
1	1.170	0.149	17	1.293	0.137
2	0.747	0.598	18	1.245	0.040
3	0.514	0.098	19	0.378	0.427
4	0.369	0.184	20	0.957	0.233
5	1.033	0.080	21	1.246	0.269
6	0.914	0.157	22	2.342	0.299
7	1.369	0.374	23	2.300	0.251
8	0.734	0.544	24	1.307	0.190
9	1.351	0.413	25	1.818	0.373
10	0.994	0.242	26	1.794	0.496
11	0.817	0.055	27	1.254	0.790
12	1.376	0.292	28	1.260	0.055
13	1.065	0.059	29	1.355	0.156
14	1.903	0.020	30	1.699	0.182
15	1.664	0.059	31	1.624	0.015
16	1.892	0.154	32	2.349	1.113
			RMSE	1.414	0.357

The above table shows the distance estimation error and the ANN improved distance error of every samples. Most of the error decreases using ANN. The RMSE before and after using ANN are 1.414 and 0.357 meters. The promotion rate of accuracy using ANN improved distance estimation is 74.8%.

In order to find the relationship among distance, tilting angle and error, 3D error fitting graph is shown as follow. It is obvious that error becomes larger when distance is short and angle is large. It is because that the distortion of the marker will increase dramatically in that case. The proposed method can rudece this kind of situation.

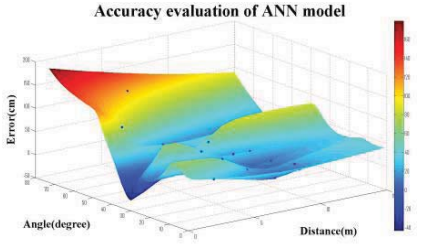

Figure 18. Accuracy evaluation of ANN model

3.5 Accuracy evaluation of different method

In this chapter, three kind of image-based localization methods are compared in their accuracy. Firstly, the positioning accuracy of each image-based positioning is shown in following figure:

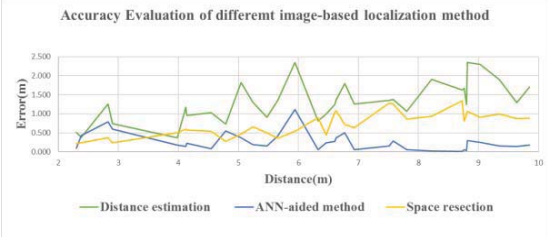

Figure 19. Accuracy evaluation of different image-based localization method

Random 18 samples are collected in different distance and different tilt angle. Then, we take the picture and calculate the position with three image-based localization methods. The results shows that the ANN-aided method shows the high accuracy than other two methods. Besides, ANN aided method does not affected by the distance while distance estimation and space resection method have higher error when the distance is farther. Besides, compared to the image resection method, ANN-aided method does not need initial value. It just need to train the model in advance. The other advantage is that the model can used in different environment even it just need to be trained one time.

4. CONCLUSION

The research proposed a rapid initialization method using smartphone camera. Inertial sensors are used to provide the relative orientation with respective to the self-designed marker. The self-designed marker is recognized using a series of image processing algorithm. Some practical test confirmed that the proposed recognition method is robust and fast. The effective distance is around 10 meters, so that the user does not need to walk approach the marker. Besides, the experiment indicates that it can also be recognized while image is taken in oblique. In the indoor navigation part, the research compares different kinds of image-based localization method using the ANN and space resection and distance estimation. The ANN-aided method shows the best performance in accuracy. Its model is trained using many images with different distance and angle. The model can be used in different scenes and the accuracy of the proposed localization method is below than one meter in average. It can also solve the problem of initialization in an unknown environment. In the future, we will build an ANN model that can be used in different smartphone so that it is no need to do training for all smartphone.

ACKNOWLEDGEMENTS

The authors would like to acknowledge the financial support through the project (SYC1050121) funded by the Department of Land Administration, Ministry of Interior, Taiwan and field support from National Cheng Kung University.

REFERENCES

Farid, Z., Nordin, R., Ismail, M., Abdullah, N.F., 2016. Hybrid indoor-based WLAN-WSN localization scheme for improving accuracy based on artificial neural network. Mobile Information Systems 2016.

Huang, S.H., Liao, J.K., Chiang, K.W., Chang, H.W., Duong, T.T., 2015. Development of Vision Aiding Pedestrian Dead Reckoning with Smartphone for Indoor Navigation, International Symposium on Mobile Mapping technology, Sydney, Australia.

Jin-Yu, Z., Yan, C., Xian-Xiang, H., 2009. Edge detection of images based on improved Sobel operator and genetic algorithms, Image Analysis and Signal Processing, 2009. IASP 2009. International Conference on. IEEE, pp. 31-35.

Kim, G., Petriu, E.M., 2010. Fiducial marker indoor localization with artificial neural network, Advanced intelligent mechatronics (AIM), 2010 IEEE/ASME international conference on. IEEE, pp. 961-966.

Werner, M., Kessel, M., Marouane, C., 2011. Indoor positioning using smartphone camera, Indoor Positioning and Indoor Navigation (IPIN), 2011 International Conference on. IEEE, pp. 1-6.

Wolf, P.R., Dewitt, B.A., 2000. Elements of photogrammetry: with applications in GIS. McGraw-Hill New York.

A DUAL-CHANNEL CAMSHIFT ALGORITHM FOR EMBEDDED REAL-TIME VISUAL SERVOING APPLICATIONS

Islam Alaa[a,*], Amr Wassal[b], Omar Rayan[a], Osama Rashad[a], Amr ElDieb[a]

[a] Systems Design Group, Si-Ware Systems, 3 Khaled Ibn Al-Waleed Street, Heliopolis, Cairo 11361, Egypt - (islam.alaa, omar.rayan, osama.rashad, amr.eldieb)@si-ware.com
[b] Computer Engineering Department, Cairo University, Cairo University Road, Giza 12613, Egypt - wassal@eng.cu.edu.eg

KEY WORDS: Visual Target Tracking, Visual Servoing, CAMShift, Dual-Channel Histogram, Embedded Real-time Application

ABSTRACT:

Visual target tracking has been gaining a great importance recently with the introduction of UAVs, drones and similar vehicles in many new civilian applications such as package delivery, video and movie recording, and emergency response applications among many others. This drives the need to have algorithms that can run on the onboard embedded system in real time. One of the most challenging ensuing problems is visual target tracking and servoing on these platforms. In this paper, some of the existing tracking algorithms are reviewed qualitatively with an emphasis on their suitability to and their performance on embedded platforms. Accordingly, the Continuously Adaptive Mean Shift (CAMShift) algorithm is selected and modified to fit real-time visual servoing applications. The proposed Dual-Channel CAMShift algorithm is presented along with its integration in our implementation of the visual servoing control algorithm and its results. The proposed algorithm utilizes 2-D histograms for target detection and tracking, the hue color channel, and adds another channel for edges orientation. It also adds three-stage filtering to the resultant probability map (PM) to suppress false positives and background noise. This three-stage filtering technique comprises low probability pixels thresholding, probability map smoothing using low-pass filtering, and true-positive emphasis using contrast enhancement. Tuning the three-stage filtering parameters and their impact on the performance is discussed. Other filtering techniques that were tested but did not yield as well in terms of tracking accuracy are also reviewed. A procedure for retaining the target in case of total occlusion or loss is also presented. The Dual-Channel CAMShift algorithm was able to track different targets achieving a frame rate of $6 \sim 8$ FPS on the ARM-based mini-computer embedded board in an indoor testing environment. This frame rate allowed the integrated visual tracking and servoing system to run in real-time. Subsequently, the system achieved an error level of less than 0.5° resulting in high-stability accuracy.

1. INTRODUCTION

Visual target tracking is one of the most important computer-vision blocks that exists in a lot of todays application. Its accuracy and suitability for the intended task plays a vital role in defining the limitation as well as the overall system performance. Different tracking and matching techniques are utilized in the algorithms spanning from direct template matching such as NCC (Briechle and Hanebeck, 2001), to discriminative classification such as TLD (Kalal et al., 2012), STR (Hare et al., 2015), and Real-time CT (Zhang et al., 2012) among others. A review of different visual target tracking algorithms and their performance is presented in (Wu et al., 2013) and (Smeulders et al., 2014). The algorithms that were evaluated on our ARM Cortex-A9 based mini-computer board setup included two implementations of NCC, STR, Real-time CT, and CAMShift. Most of them did not yield in our implementation in most cases because of complexity, memory usage and adaptability to environment changes and target deformations.

1.1 Adaptive Mean-Shift (CAMShift) and Its Derivatives

The original CAMShift tracking algorithm uses the color histogram of the target for matching. This enables it to adapt for dramatic scaling, rotation, and deformation of the target relative to the environment. The algorithm is also known for its lightweight execution that makes it suitable for real-time applications. Simply, the algorithm computes the hue-color histogram of the target in the HSV color space, and back-project this histogram onto each new frame. The result from this back-project is a probability map (PM) indicating the probability of each pixel to be in the target. Then, the CAMShift searches for the center of mass of the probabilities, moving from the old target center, and defines the size based on the probability distribution. Given the fact that the original CAMShift relies only on the hue-channel of the image, the algorithm tends to be prone to tracking errors in case of the existence of the same colors in the background. In order to solve that, several enhancements were proposed and they mainly fall in two categories. The first category is to increase the dependency on the unique colors in the target and decrease the dependency on the colors that appear in the background using background subtraction or background normalization. The other category is to add another feature beside the hue-color channel in order to discriminate the target from the surroundings by means of 2D histograms. Some of the added features include saturation color channel, local binary patters (LBP) to represent the target texture, target edges, and target edges orientation among others. There exist some trials generalize the CAMShift algorithm to use a single channel other than the color such as the edges orientation histogram alone with background manipulation techniques presented in (Yang et al., 2010) and (Ho et al., 2014) among others. Some researchers proposed adding learning methods to the original CAMShift. However, these methods may result in losing the suitability for real-time applications because of the added complexity. Some of the methods mentioned worked well in certain environment conditions, but did not yield in others. Therefore, means of post-processing on the resulting PM is necessary. In

*Corresponding author

addition, some of them suffer from the boundary box explosion problem, while others cannot retain the target in case the target was fully occluded by other objects or by camera motion.

1.2 Visual Servoing

Visual servoing is the process of using the processed visual sensor data feedback to control a robotic manipulator. There exist many variations of visual servo controllers based on the position of the visual sensor used, the number of cameras, and the plane coordinate used among others. In (Chaumette and Hutchinson, 2006), basic techniques for visual servo control were reviewed including image-based visual servoing (IBVS) and position-based visual servoing (PBVS). In (Chaumette and Hutchinson, 2007), advanced techniques for visual servo control were reviewed including hybrid visual servo and partitioned visual servo among others.

1.3 Image Based Visual Servoing (IBVS)

The classical IBVS controller is a control scheme that operates in the image plane and utilizes the image features of a certain target in the scene as the control values. The IBVS controller produces the velocity commands vector, also known as the velocity screw (Hutchinson et al., 1996), (Gans and Hutchinson, 2002), to different robotic manipulator present in the system to bring the image feature to a desired value (Hashimoto et al., 1991). The following equations summarize how the velocity commands vector, which will be sent to the manipulators, is generated from the visual sensor feedback for controlling only two degrees of freedom. The complete derivation and the approximation used can be found in (Hashimoto et al., 1991) and (Hashimoto et al., 1991).

The main goal of any visual servoing system is to minimize the error signal $e(t)$, which is defined as:

$$e(t) = s(m(t), a) - s^* \tag{1}$$

where $m(t)$ is a set of image measurements, a is a set of extra parameters (e.g. camera intrinsic parameters), $s(m(t), a)$ is a vector of k features derived from the image, and s^* is the desired value of the features vector.

The feature velocity describes the motion of the target as viewed by the camera, and it can be represented by the camera velocity as follows:

$$V_c = (v_c, \omega_c) \tag{2}$$

$$\dot{s} = L_s V_c \tag{3}$$

where L_s is the interaction matrix related to s, V_c is the camera velocity, V_c is the linear velocity that represents the transitional motion of the camera frame, and ω_c is the angular velocity that represents the rotational motion of the camera frame. After projecting 3D points in the camera frame onto the 2D image plane, and taking the time derivative of the projection equation to relate the velocity of the 3D point to the camera velocity, the camera velocity can be represents as follows:

$$\dot{x} = L_x v_c \tag{4}$$

The interaction matrix L_x related to x is defined as:

$$L_x = \begin{bmatrix} -1/Z & 0 & x/Z & xy & -(1+x^2) & y \\ 0 & -1/Z & y/Z & 1+y^2 & -xy & -x \end{bmatrix} \tag{5}$$

where (x, y) are the current image feature value in the 2D image plane, and (X, Y, Z) are the coordinates of the 3D point in the camera frame. The Z parameter represents the distance from the camera to the target and is essential to be measured or approximated. Utilizing (1) and (4), the final formulas to get the velocity commands vector after approximations can be given by:

$$v_c = -\lambda L_e^+ e \tag{6}$$

$$L_e^+ = ({L_e}^T L_e)^{-1} {L_e}^T \tag{7}$$

Where L_e^+ is the pseudo-inverse of the interaction matrix L_e. The interaction matrix provided in (5) can only control two degrees of freedom using an image featured formed of a single point. In order to control more degrees of freedom more points are to be added, and other interaction matrices are to be cascaded vertically.

2. DUAL-CHANNEL CAMSHIFT ALGORITHM WITH PROBABILITY MAP FILTERING

As mentioned, the original CAMShift algorithm is not sufficient to handle visual target tracking tasks due to its dependency on the hue color channel only. In (Yue et al., 2009), the integration of the edges orientation histogram was proposed beside the hue channel to add some extra information to the target tracking engine. This resulted in a more stable and robust target tracking in case of the existence of other objects with the same color in the background. In our implementation, this integration was utilized int the computer vision part of the system.

The Dual Channel histogram of the hue and edges orientation is computed for the target image that needs to be tracked in the scene. For each new image received, it is required to generate a new image with two channels: the hue color channel and the edges orientation channel. The target 2-D histogram is then back projected onto the 2-D generated image stream to produce the probability map (PM) indicating the probability of each pixel to belong to the real target.

2.1 Hue Color Channel and Edges Orientation Channel Extraction

The extraction of the hue color channel is straight forward: the RGB image is converted to the HSV color space. Then, the hue color channel is separated from the converted image. On the other hand, to extract the edges orientation from the image, the image should first be converted to gray scale. The sober operator, which is essentially a 3x3 kenrel that is convoluted with the image, is then used in order to get the horizontal derivative G_x and vertical derivative G_y of the gray scaled image. After that, the magnitude $|G|$ and phase θ of the image are calculated to get its edges orientation representation. The resulted edges orientation matrix is then thresholded and dilated in order to suppress any weak information or random noise. The following equations summarize the process of the edges orientation extraction.

$$G_x = \begin{bmatrix} -1 & 0 & +1 \\ -2 & 0 & +2 \\ -1 & 0 & +1 \end{bmatrix} * I(x, y) \tag{8}$$

$$G_y = \begin{bmatrix} +1 & +2 & +1 \\ 0 & 0 & 0 \\ -1 & -2 & -1 \end{bmatrix} * I(x, y) \tag{9}$$

$$|G| = \sqrt{G_x^2 + G_y^2} \tag{10}$$

$$\theta = arctan(\frac{G_y}{G_x}) \tag{11}$$

2.2 Three-Stage Probability Map Filtering

Experiments showed that the resulting (PM) from the Dual-Channel CAMShift algorithm still has a scattered residual noise distributed randomly in it. This noise appears in different forms in the PM as follows:

1. High probability pixels outside the real target.
2. Average to low probability pixels inside and outside the real target.
3. Low probability pixels inside the real object.

So, In order to suppress this scattered noise, a three stage filtering post-processing steps are applied on the resulting including:

Stage I: Low-Probability Pixels Thresholding Which is essential in order to suppress and eliminate the weak pixels with low probabilities both inside and outside the target.

Stage II: Low-Pass Filtering of the Probability Map Which is essential to smooth the probability map and either enhance a certain low probability pixel inside the target or deteriorate a high probability pixel outside the real target.

Stage III: Contrast Enhancement Which is essential to increase the intensity difference between high probability pixels and low probability ones and help differentiating to which category average pixels belong. That's to avoid the tracker confusion between real targets and random noises.

Other Probability Map Filtering Techniques Other possible techniques like high-pass filtering, histogram equalization, and dilation of the image didn't help much in enhancing the tracking accuracy. However, proper tuning of the mentioned three steps as well as the the other methods may result in better filtering combination and thus, a positive impact on the tracking task in general. Moreover, other morphology based contrast enhancement techniques can be tested as mentioned in (Thapar and Garg, 2012).

2.3 Total Target Occlusion and Bounding Box Explosion Handling

Two of the main problems that exist in the original CAMShift as well as the Dual-Channel CAMShift are the problems of how the algorithm can retain the locking on the real target in case of total target occlusion and bounding-box explosion. Both issues can be detected by monitoring the size of the target bounding box. Upon the detection, corrective procedure can be under taken in order to allow the tracker to retain real target locking. The corrective procedure enforces the bounding box to fill the image scene minus a small margin from all four corners. This resets the search window for the CAMShift and allows it to re-start the center-of-mass search based on all information provided in the filtered probability map.

Algorithm 1 Target Occlusion Resolver

procedure TOR($bBox : boundBox$)
  if $bBox.W < 5pixels$ **then**
    $bBox.UprL \leftarrow (5, 5)$
    $bBox.W \leftarrow 310pixels$
    $bBox.H \leftarrow 200pixels$
  end if
  return $bBox$
end procedure

Algorithm 2 Bounding Box Explosion Resolver

procedure BBER($bBox : boundBox$)
  if $bBox.W >= 320pixels$ or
    $bBox.H >= 240pixels$ or
    $bBox.UprL.x >= 320$ or
    $bBox.UprL.y >= 240$ or
    $bBox.UprL.x + bBox.W <= 0pixels$ or
    $bBox.UprL.y + bBox.H <= 0pixels$ or
    $bBox.W * bBox.H < 1pixels$ **then**
      $bBox.UprL \leftarrow (0, 0)$
      $bBox.W \leftarrow 320pixels$
      $bBox.H \leftarrow 240pixels$
  end if
  return $bBox$
end procedure

Total Target Occlusion The first problem the tracker confronts is what to track in case of total target occlusion due to the non-existence of the target inside the camera field of view. This causes the bounding box size to shrink to a very small size with few pixels in width. Algorithm 1 describes the detection procedure as well as the corrective action.

Bounding Box Explosion The second problem happens in case of the existence of a lot of noise in the background, causing the bounding-box size to grow beyond the size of the captured image itself or to shrink and have negative values in width and height. Algorithm 2 describes the detection procedure as well as the corrective action.

3. REAL-TIME IBVS INTEGRATION WITH DUAL-CHANNEL CAMSHIFT ALGORITHM ON ARM-BASED MINICOMPUTER EMBEDDED BOARD

The visual target tracking and servoing integrated system from a software point of view consists of four main steps: initialization step, sensing step, visual target tracking and servoing loops, and the actuation step. Figure 1 illustrates these steps and their interaction in more details. System components include: a 3-axis angular velocity sensor (i.e. 3-axis gyroscope), a 5MP embedded OEM camera attached to a mini-computer embedded board with a cortex A9 ARM-based processor running an embedded operating system, a mini-computer embedded board running on bare-metal, three motor drivers, and 3 brush-less DC motors. Figure 2 shows the hardware components present in the system as well as their interactions with each other.

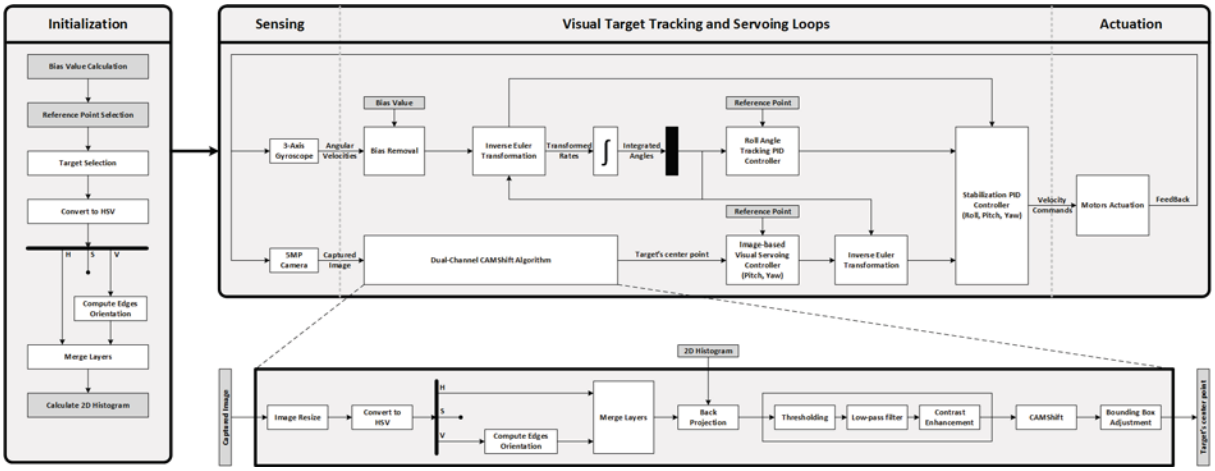

Figure 1. Detailed block diagram of the real-time visual target tracking and servoing integrated system

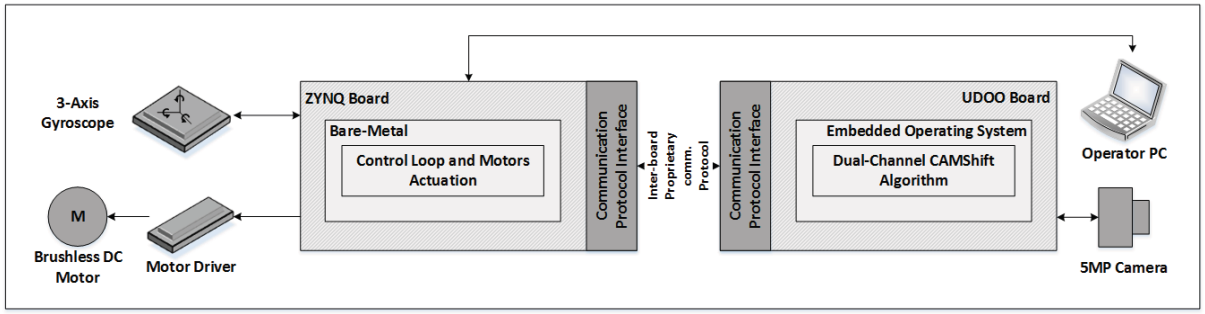

Figure 2. Hardware System Block Diagram

3.1 Initialization

The initialization phase starts by calculating a new bias value for the 3-axis gyroscope present in the system. This is simply done by averaging a number of samples while the whole set up is at rest. This bias values are passed to the next sensing phase. Moreover, the reference point on which the controller should stabilize upon is entered to the system, and the target is selected from the initial scene. After that, the hue and edges orientation histogram is calculated for the target in order to be used in the tracking phase. The initialization phase is done only at the start of the operation and is repeated with each re-start or re-set.

3.2 Sensing

The sensing step includes data acquisition from both the 3-axis gyroscope as well as the camera. The ZYNQ board is used to acquire the 3-axis gyroscope data, scaling them to doubles and forwarding their values to the next phase. While the UDOO board is responsible for the image acquisition from the camera and feeding it to the Dual-Channel CAMShift Algorithm.

3.3 Visual Target Tracking and Servoing Loops

After the sensing step, the Dual-Channel CAMShift algorithm is initiated with the image received from the camera, and the target dual-channel histogram. This results in the center point of the target in th e format of (x, y) pair. This pair is then sent to the IBVS controller to generate the velocity commands for the stabilization loops. On the other hand, and for the roll angle, we only need to stabilize the roll angle on the initial value, so, a tracking PID is provided and its output is then fed to the stabilization loops too. Different physical quantities provided in the system are all presented in their own body frames, so inverse euler transformations are used transform them to a unified frame which is the initial pose of the system. In order to do this transformation simple integration block of the angular velocities provided by the 3-axis gyroscope is provided to get different angles (i.e. pitch, roll, and yaw).

3.4 Actuation

The velocity commands generated from the stabilization loops are then fed to a pulse-width modulation engine to generate motor commands. These commands are passed to the motor drivers and then to the motors.

3.5 System Parameters and Tuning Variables

The system has various parameters and variables which can play a vital role in defining its final performance, including: the accuracy of the bias values, image size, dual-channel histogram ranges, filtering stages ordering and thresholds, IBVS controller gain among others. An extensive study on the effect of each parameter on the system performance can be done to suggest the proper mix of parameters and variables.

4. RESULTS

Figure 3 shows the tracking accuracy of different targets in indoor environment. Three different targets were used for the evaluation of the tracking accuracy including fixed color target (3a -

Figure 3. Tracking Results of the Dual-Channel CAMShift Algorithm with IBVS Intrgaration.
(a-h) 1^{st} target, (i-l) 2^{nd} target, (m-p) 3^{rd} target.

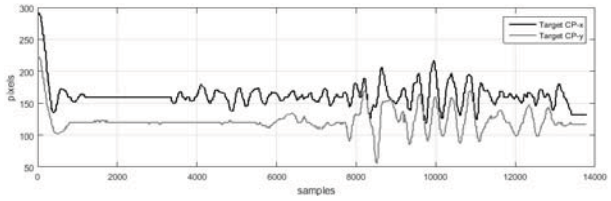

(a) Stabilization accuracy in pixels of both static and dynamic conditions in the same experiment

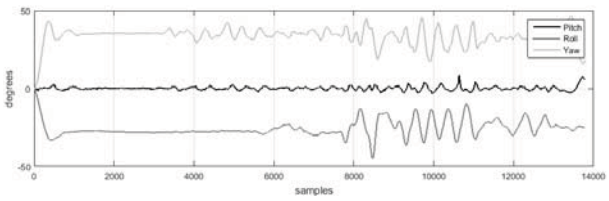

(b) Stabilization accuracy in degrees of both static and dynamic conditions in the same experiment

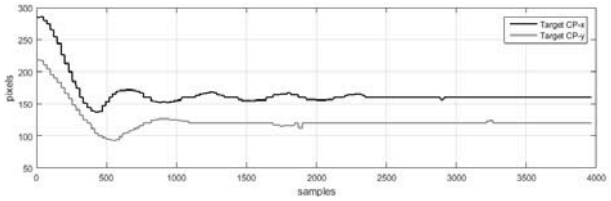

(c) Stabilization accuracy in pixels in static conditions only

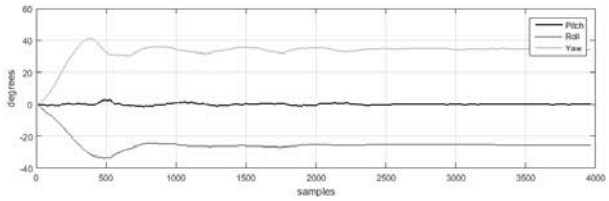

(d) Stabilization accuracy in degrees in static conditions only

Figure 4. Plots of the target center points and angles in static and dynamic conditions

3h), and two multi-color target with background interference (3i - 3p). It shows that the integration of the hue and edges orientation channels managed to detect and track targets of different natures in noisy environment with scaling, rotation, and deformation conditions. Figure 4a and 4b shows the stabilization accuracy of the integrated visual tracking and servoing system, in pixels and degrees, in static conditions for the first 3700 samples and in dynamic conditions afterwards. It shows that the system achieved a stabilization accuracy of 0.5° after the compensation for any setup anomalies. Moreover, and in order to evaluate the system in static conditions only for long periods, the target was kept stationary as well as the carrier of the system resulting in a similar stabilization and pointing accuracy of 0.5° after compensation of any setup anomalies. Figure 4c and 4d shows the results of the later experiment. The system sampling time using the hardware previously mentioned ranges from $6 \sim 8$ FPS satisfying the real-time requirements of such systems.

5. CONCLUSION

In this paper, the Dual-CAMShift algorithm with probability map filtering was proposed. The algorithm utilizes the hue color channel and the edges orientation histograms for target detection and tracking. The probability map filtering includes low probability pixels thresholding, probability map smoothing using low-pass filtering, and true-positive emphasis using contrast enhancement. A real time integration between the Dual-Channel CAMShift tracking algorithm and the IBVS control scheme was presented. The integration was realized on an dual-board embedded mini-computer system running on an operating system for the vision part, and on bare-metal for the sensing and control part. The system included an embedded 5MP camera and a 3-Axis Gyroscope as system sensors and was used to actuate a manipulator with three rotational degrees of freedom. The paper showed that this system was able to run in real-time environment and to achieve high pointing and stabilization accuracy.

6. FUTURE WORK

The visual tracking and servoing integrated system provided can be enhanced from different aspects. CAMShift algorithm can be enhanced by utilizing a third channel such as saturation channel or LBP channel.Moreover, The basic IBVS used can be replaced with other hybrid servoing methodologies to achieve better stability and pointing accuracy. Finally, More performance can be squeezed out from the embedded mini-computer platform used in the system by using means of multi-core concepts.

ACKNOWLEDGEMENT

This work was partially supported by a Collaborative Funded Project (CFP) grant, number **PDP2014.R16.2**, from ITIDA's Information Technology Academia Collaboration (ITAC) program. The authors appreciate this generous support and acknowledge it.

REFERENCES

Briechle, K. and Hanebeck, U., 2001. Template matching using fast normalized cross correlation. *Proceedings of SPIE: Optical Pattern Recognition* XII, pp. 95–102.

Chaumette, F. and Hutchinson, S., 2006. Visual servo control. i. basic approaches. *IEEE Robotics & Automation Magazine* 13(4), pp. 82–90.

Chaumette, F. and Hutchinson, S., 2007. Visual servo control. ii. advanced approaches. *IEEE Robotics & Automation Magazine* 14(1), pp. 109–118.

Gans, N. and Hutchinson, S., 2002. A switching approach to visual servo control. *Proceedings of the IEEE International Symposium on Intelligent Control* 2002, pp. 770–776.

Hare, S., Golodetz, S., Saffari, A., Vineet, V., Cheng, M.-M., Hicks, S. and Torr, P., 2015. Struck: Structured output tracking with kernels. *IEEE Transactions on Pattern Analysis and Machine Intelligence* pp. 263–270.

Hashimoto, K., Kimoto, T., Ebine, T. and Kimura, H., 1991. Manipulator control with image-based visual servo. *IEEE Transactions on Robotics and Automation* 13, pp. 2267 – 2271.

Ho, H.-C., Fuh, C.-S. and Lian, F.-L., 2014. Object tracking algorithm based on combination of edge and color information.

Hutchinson, S., Hager, G. and Corke, P., 1996. A tutorial on visual servo control. *IEEE Transactions on Robotics and Automation* 12(5), pp. 651–670.

Kalal, Z., Mikolajczyk, K. and Matas, J., 2012. Tracking-learning-detection. *IEEE Transactions on Pattern Analysis and Machine Intelligence* 34(7), pp. 1409–1422.

Smeulders, A., Chu, D., Cucchiara, R., Calderara, S., Dehghan, A. and Shah, M., 2014. Visual tracking: An experimental survey. *IEEE Transactions on Pattern Analysis and Machine Intelligence* 36(7), pp. 1442–1468.

Thapar, S. and Garg, S., 2012. Study and implementation of various morphology based image contrast enhancement techniques. *International Journal of Computing & Business Research*.

Wu, Y., Lim, J. and Yang, M.-H., 2013. Online object tracking: A benchmark. *Proceedings of the IEEE conference on Computer Vision and Pattern Recognition (CVPR)* 2013, pp. 24112418.

Yang, Y., Wang, Z., Sun, D., Zhang, M. and Cheng, N., 2010. Automatic object tracking using edge orientation histogram based camshift. In: *2010 Third International Conference on Information and Computing*, Vol. 4, pp. 231–234.

Yue, Y., Gao, Y. and Zhang, X., 2009. An improved camshift algorithm based on dynamic background. In: *2009 First International Conference on Information Science and Engineering*, pp. 1141–1144.

Zhang, K., Zhang, L. and Yang, M.-H., 2012. Real-time compressive tracking. *A. W. Fitzgibbon, S. Lazebnik, P. Perona, Y. Sato & C. Schmid (eds.), Springer.* ECCV (3), pp. 864–877.

Revised March 2017

PERFORMANCE ANALYSIS OF INDOOR POSITIONING USING DIFFERENTIAL DISTANCE CORRECTION BASED ON BLUETOOTH LOW ENERGY

Yun-Tzu Kuo [a, *], Jhen-Kai Liao [b], Kai-Wei Chiang [c]

[a] Department of Geomatics, National Cheng-Kung University, No. 1, Daxue Road, East District, Tainan, Taiwan – yuki31210@gmail.com
[b] Department of Geomatics, National Cheng-Kung University, No. 1, Daxue Road, East District, Tainan, Taiwan - cacalut1690@gmail.com
[c] Department of Geomatics, National Cheng-Kung University, No. 1, Daxue Road, East District, Tainan, Taiwan - kwchiang@mail.ncku.edu.tw

Commission VI, WG VI/4

KEY WORDS: Bluetooth Low Energy, beacon, differential distance correction, indoor positioning

ABSTRACT:

This research utilizes Bluetooth Low Energy (BLE) for indoor positioning due to its advantages such as low cost, low power consumption and widely supported by mobile devices. Beacons are one kind of BLE devices which are able to broadcast information to nearby portable electronic devices. One of the transmitting information from beacons called Received Signal Strength Indication (RSSI) can be converted to distance by using the RSSI propagation model. As the distances between beacons and the receiver are determined, the unknown position can be subsequently calculated by trilateration. However, the signal strength tends to be influenced by surrounding environments, i.e. reflection, shadowing, and multipath effect, which may cause the estimated distance and position incorrect. Therefore, a novel method named differential distance correction is proposed which aims at optimizing positioning accuracy in indoors or reducing the number of beacons while maintaining similar accuracy. In this paper, it will focus on its ability to enhance the indoor accuracy. The concept of the proposed method is similar to the differential technique used in Differential Global Navigation Satellite System (DGNSS) which corrects the distance by differential information from a reference station. Finally, the experimental results show that the positions after using proposed differential distance correction are closer to the real position in terms of overall accuracy.

1. INTRODUCTION

Indoor positioning has become a popular issue recently since the Global Navigation Satellite System (GNSS) positioning is disabled in the indoor environment due to the signal interruption. Moreover, people spend most of their time in indoors (Kang, 2012), so it is necessary to locate one's position precisely inside a building. Nowadays, many researchers have developed various indoor positioning technologies such as infrared (IR), Radio Frequency Identification (RFID), Wi-Fi and so on (Liu, 2007). However, IR has poor penetration which makes it difficult to use in complicated indoor environments (Song, 2011) while RFID is restricted for extra equipment for positioning, i.e. relatively expensive readers to identify tags (Wang, 2016). In addition, Wi-Fi lacks sufficient accuracy and has high power consumption which may not be a suitable positioning tool in some cases (Zou, 2016). Bluetooth Low Energy (BLE), a new version of Bluetooth (Cabarkapa, 2015), is another candidate for indoor positioning. Its advantages include low cost, low energy consumption, and short scanning time. Furthermore, most of the mobile devices provide the Bluetooth functionality with which users are familiar. Therefore, the widespread BLE is a high potential technology to realize indoor positioning.

At present, there are three main positioning approaches that are based on the BLE technology, including proximity, trilateration, and fingerprinting (Zhuang, 2016). All these techniques use Received Signal Strength Indication (RSSI) to estimate the target's position. RSSI, which is one of the received data from the BLE transmitter, is the indicator of the power level and often used in positioning application. In the proximity algorithm, a triggering threshold is previously set. If the received RSSI value is stronger than the threshold, it will determine that the user is near the BLE transmitter, i.e. BLE beacons (Feng, 2015). On the other hand, trilateration is a common approach that uses estimated distance between the target and the BLE transmitter to locate the target's position (Boukerche, 2007). The required distance is converted from the RSSI propagation model and the solution of the location can be obtained from least squares or Kalman filtering. Fingerprinting algorithm consists of two stages: off-line stage and on-line stage. In the off-line stage, a database with RSSI collected at the absolute positions is constructed, while in the on-line stage the positioning of the target is estimated by matching the RSSI in the database (Kriz, 2016).

This paper develops an indoor positioning system with BLE technology and the positioning technique is realized by the trilateration. After collecting RSSI information from beacons, the distances converted from RSSI can be further calculated a solution by applying non-linear least squares method. However, the accuracy using trilateration is dependent on the accuracy of estimated distance. Therefore, to improve the performance of the positioning technique, this paper proposes differential distance correction method to revise the estimated distance which may contain some errors from the indoor environment. According to the experimental result, the location after correction is closer to the real position which proves that the proposed method is able to optimize the positioning accuracy.

* Corresponding author

The rest of this paper is organized as follows: The information about the BLE and BLE beacons is provided in Section 2. The methodology of positioning technique along with a novel method named differential distance correction are presented in Section 3. Section 4 describes the experimental setup. The performance analysis of utilizing differential distance correction is further discussed in Section 5. Finally, the conclusions will be given in Section 6.

2. BLUETOOTH LOW ENERGY AND BLE BEACONS

2.1 Bluetooth Low Energy

BLE, which is the version 4.0 of Bluetooth announced by Bluetooth Special Interest Group (SIG) in 2010, serves as an emerging wireless personal area network technology (Cabarkapa, 2015). Compared to previous Bluetooth standard, it is designed for low cost, low energy consumption, short scanning time, and transmission of a small amount of data with short range communication. Table 1 shows the brief comparison between classic Bluetooth and BLE. The main idea of BLE is to provide a suitable tool for monitoring application with a little data transmission in a cost-optimal way. Therefore, BLE is widely used in various areas, such as health care, push advertising, smart factory, and indoor positioning.

Property	Classic Bluetooth	BLE
Frequency	2.4GHz	2.4GHz
Power Consumption	Low	Very low
Battery life	Multiple weeks	Multiple months
Cost	Medium	Low
Smartphones	Supported	Supported
Positioning Accuracy	2-5 m	1-3 m

Table 1. Comparison of classic Bluetooth and BLE

In the definition of BLE protocol, it operates in 40 channels around 2.4 GHz with each channel width of 2 MHz. There are two kinds of channels among the 40 ones: advertising and data. Advertisement messages are broadcasted in three advertising channels (37, 38, and 39) while the remaining 37 data channels are used for communication between connected devices (Mackensen, 2012). The RSSI information is from the three advertising channels and this study uses aggregate RSSI from all the three channels.

Moreover, BLE acts either in master or slave role. A master can manage multiple slave devices simultaneously and control the data transmission between the slaves. However, a slave can have only one connection to a single master device (Johansson, 2001). Instead of having a connection for a long time, both types of devices stay in sleep mode in most of the time until a slave requires a link connection to the master. In other words, only when the data needs to be transmitted or exchanged do both devices wake up and link with each other. Therefore, this property brings about not only keeping the power consumption as small as possible but also extremely maintaining the stability of the system. Beacons are one of the applications based on BLE technology. A beacon (slave role) can be placed at a fixed point and broadcasts radio signals to nearby portable electronic devices (master role), such as smartphone, tablet, or notebook.

2.2 BLE Beacons

Owing to the rapid development of Android and iOS system, BLE technology is widely supported by most of the mobile devices and provides plenty of applications. The best realization of BLE is the beacon. Beacons are hardware transmitters that are able to broadcast a small amount of data to neighboring mobile devices (Martin, 2014). One of the applications using beacons is indoor positioning which can locate the approximate positions of smartphones. Mobile apps can listen for the signals broadcasted by beacons. Once they hear an appropriate signal, it can trigger an action on the smartphone. Compared to other equipment used in indoor positioning, beacons have the advantages of light weight, small size, and flexible to be deployed in different kinds of environment; therefore, this study chooses beacons to build an indoor positioning system.

3. METHODOLOGY

The indoor positioning system developed in this paper is based on BLE technology. Figure 1 shows the positioning processes. RSSI broadcasted by BLE beacons will be converted to distance by the distance model after filtering its noise. Next, trilateration is adopted to locate the position of the unknown point. Moreover, the proposed differential distance correction is used to revise the distance measurement derived from the model and enhance the accuracy of estimated positions. To have more knowledge about the positioning processes, the details are described in each part below.

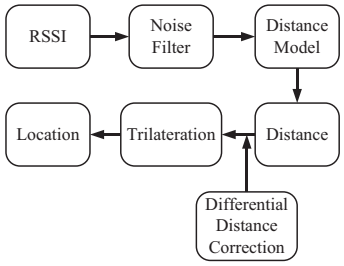

Figure 1. The flow chart of the positioning process

3.1 Noise Filter

During the transmission of the signals broadcasted by beacons, it may suffer from the environmental influence which causes vibrant and unstable signals. Low-pass filter (LPF) is adopted to reduce the high-frequency noise. LPF attenuates high frequency and makes the signal smooth. The adopted LPF is shown as follows:

$$F_n = \alpha F_{n-1} + (1-\alpha) R_n \quad (1)$$

where F_n = the result of the LPF
F_{n-1} = the previous result of the LPF
α = the parameter of the LPF, which value is between 0 and 1
R_n = the n^{th} receiving data

Here, the RSSI values are processed by LPF and the impact of noise will be reduced.

3.2 Distance Model

The distance model utilized in this paper is based on the RSSI propagation model, also called the lognormal shadowing model. Due to the characteristic of the RSSI which decreases exponentially with the increase of the distance, the relationship between RSSI value and corresponding distance can be expressed as follows (Li, 2006):

$$RSSI(D) = RSSI(D_{ref}) - 10 \times n \times log_{10}\left(\frac{D}{D_{ref}}\right) + X_{dBm} \quad (2)$$

where $RSSI(D)$ = the received RSSI value at the distance D between the beacon and the receiver
$RSSI(D_{ref})$ = the received RSSI value at the reference distance D_{ref}
n = the path-loss exponent
X_{dBm} = the Gaussian random variable with zero mean

This RSSI propagation model works well for line-of-sight scenarios. After calibrating the parameters of the model, the model can be exploited to convert the processed RSSI values to distances between beacons and the receiver. The distance is calculated through Equation (3), which is the mathematical transformation of Equation (2).

$$\mathrm{D} = D_{ref} \times 10^{\frac{RSSI(D_{ref}) - RSSI(D) + X_{dBm}}{10 \times n}} \quad (3)$$

Note that the notations are the same as Equation (2).

3.3 Trilateration

Trilateration is a classical positioning technique that determines the location by the estimated distances from the reference points (Yang, 2008). In order to locate the horizontal position of the target, at least three reference points are required. Using the geometry of 2D circles, which the radiuses are the exact distances, the intersection of the circles is the solution of the target. Figure 2 (a) depicts this ideal situation. However, the estimated distance must have some error in it; therefore, in reality, the intersection shows an area instead of a point, as shown in Figure 2 (b). In this paper, beacons are arranged at the reference points while a target smartphone is put at the unknown point, receiving RSSI information from beacons.

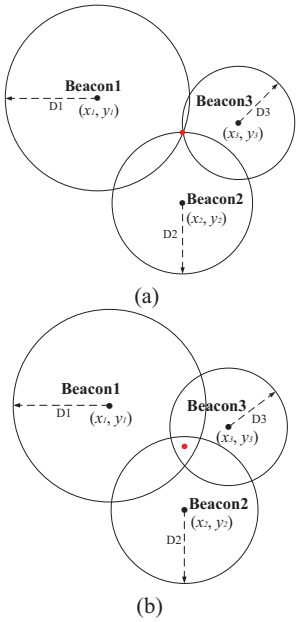

Figure 2. The diagram of trilateration (a) Ideal situation; (b) Real situation

In the real situation, there will be various possible points existing in the area of intersection. The non-linear least squares method is utilized to determine the optimal position of the unknown point (Murphy, 2007). A circle with a radius equal to the exact distance at each beacon can be represented by the Equation (4).

$$(x - x_i)^2 + (y - y_i)^2 = D_i^2 \quad (4)$$

where (x, y) = the true coordinate of the unknown point
(x_i, y_i) = the position of the i[th] beacon
D_i = the exact distance between the receiver and the i[th] beacon

Therefore, the exact distance and the estimated distance are given by

$$D_i = f_i(x, y) = \sqrt{(x - x_i)^2 + (y - y_i)^2} \quad (5)$$

$$\widehat{D}_i = f_i(\hat{x}, \hat{y}) = \sqrt{(\hat{x} - x_i)^2 + (\hat{y} - y_i)^2} \quad (6)$$

where $(\hat{x}, \hat{y})$ = the estimated coordinate of the unknown point
$\widehat{D}_i$ = the estimated distance between the receiver and the i[th] beacon.

A good initial guess for $(\hat{x}, \hat{y})$ can be obtained from the linear least squares method; however, in this paper $(1, 1)$ is used as the initial value due to the small size of the experimental field. The values of $(\hat{x}, \hat{y})$ related to the true solution are shown as follows:

$$x = \hat{x} + \delta x, y = \hat{y} + \delta y \quad (7)$$

where $\delta x, \delta y$ = errors on x, y coordinates

Furthermore, the non-linear Equation (5) needs to be linearized and the first-order Taylor expansion of D_i is:

$$D_i \approx \widehat{D}_i + \left(\frac{\partial f_i}{\partial x}\right)_{x=\hat{x}} \delta x + \left(\frac{\partial f_i}{\partial y}\right)_{y=\hat{y}} \delta y \quad (8)$$

The next equation is the vector and matrix form of Equation (8). In Equation (8), f_i needs to be differentiated with respect to x and y and then generates the Jacobian matrix A.

$$\delta\vec{D} = D_i - \widehat{D}_i = \frac{\hat{x} - x_i}{\widehat{D}_i} \delta x + \frac{\hat{y} - y_i}{\widehat{D}_i} \delta y = A\, \delta\vec{E} \quad (9)$$

$$\text{where } A = \begin{bmatrix} \frac{\partial f_1}{\partial x} & \frac{\partial f_1}{\partial y} \\ \frac{\partial f_2}{\partial x} & \frac{\partial f_2}{\partial y} \\ \vdots & \vdots \\ \frac{\partial f_n}{\partial x} & \frac{\partial f_n}{\partial y} \end{bmatrix}_{x=\hat{x}, y=\hat{y}} = \begin{bmatrix} \frac{\hat{x} - x_1}{\widehat{D}_1} & \frac{\hat{x} - x_1}{\widehat{D}_1} \\ \frac{\hat{x} - x_2}{\widehat{D}_2} & \frac{\hat{x} - x_2}{\widehat{D}_2} \\ \vdots & \vdots \\ \frac{\hat{x} - x_n}{\widehat{D}_n} & \frac{\hat{x} - x_n}{\widehat{D}_n} \end{bmatrix}; \ \delta\vec{E} = \begin{bmatrix} \delta x \\ \delta y \end{bmatrix} \quad (10)$$

Because the Jacobian matrix A is not a square matrix which cannot be inversed. Therefore, Least squares estimation is adopted to minimize the sum of the squares of the errors on x, y coordinates.

$$\delta\vec{E} = (A^T A)^{-1} A^T \delta\vec{D} = \begin{bmatrix} \delta x \\ \delta y \end{bmatrix} \quad (11)$$

Finally, the optimal solution of the unknown point using non-linear least squares can be determined by Newton iteration. As shown in Equation (12), the $k + 1$ denotes the data after updating while k denotes the data before updating.

$$\begin{bmatrix} \hat{x} \\ \hat{y} \end{bmatrix}_{k+1} = \begin{bmatrix} \hat{x} \\ \hat{y} \end{bmatrix}_k + \begin{bmatrix} \delta x \\ \delta y \end{bmatrix}_k \quad (12)$$

3.4 Differential Distance Correction

Although trilateration is able to locate the position of the unknown point, it is assumed that the distance converted from RSSI includes some error caused by the indoor environment such as reflection, shadowing, and multipath effect, which makes the estimated distance and position incorrect. To reduce this kind of effect, this research proposes differential distance correction to revise errors from the estimated distance. This method is similar to the differential principle of DGNSS which also aims at better positioning accuracy by correcting the range using differential information from a reference station Figures 3 represents the concept of differential distance correction.

First, the reference station established at the known position continuously collects the data from beacons and then the estimated distance can be derived from the RSSI propagation model. Since the position of the reference station and beacons are known, the exact distance can also be obtained. Therefore, the difference, which is also called the residual, between estimated distance and the exact distance is regarded as the error caused by the environment. The residual can be thereby used for the correction of the estimated distance from other receiving stations. When the distance to beacons at the receiving station is corrected, the positioning result determined from trilateration will be closer to the real position, which means that the proposed method has the ability to improve the positioning accuracy.

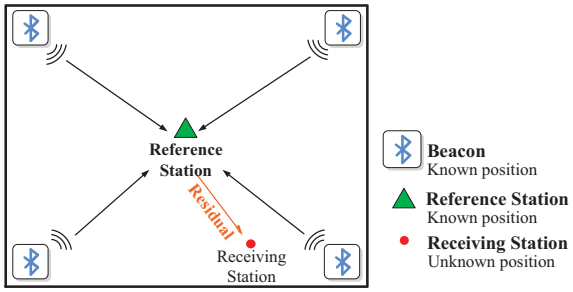

Figure 3. The diagram of differential distance correction

4. EXPERIMENTAL SETUP

This experiment is carried out at the Department of Geomatics in National Cheng Kung University. The experimental field is an indoor environment with the length of 14 m and the width of 8 m. Beacons used in this research are produced by THLight and they include the battery beacon and the USBeacon, which are shown in Figure 4. Six battery beacons are worked as transmitters and attached on the wall with the height of 2.5 m in order to avoid shelters on the path of signal transmission. One USBeacon set in the USB port of the notebook is used as a reference station. It can make the device be a receiver and its data can be automatically stored in the notebook. Moreover, a Sony Xperia Z5 Android smartphone is adopted as another receiver at the checkpoint, which can be regarded as a receiving station.

Figure 4. THLight beacons used in this research

To revise the distance error caused by the noise from the environment, the differential method is applied to determine the residual of distance. The reference station is set near the center of the experimental field and continuously receives data from beacons so as to compute the average distance between the reference station and each beacon. The residual of distance is consequently calculated by subtracting the exact distance from the average of distance observation. The receiving station at the checkpoint can obtain the more accurate distance to beacons after removing the residual. When the correction of the distance at the receiving station is completed, results by the trilateration will be closer to the true position. Figure 5 shows the arrangement of the experimental field. P1, P2, P3, P4, P5, and P6 are the checkpoints and the real position of them will be used in the evaluation. Note that P1, P2, P3, and P4 are near the reference station, while P5 and P6 are farther away from it.

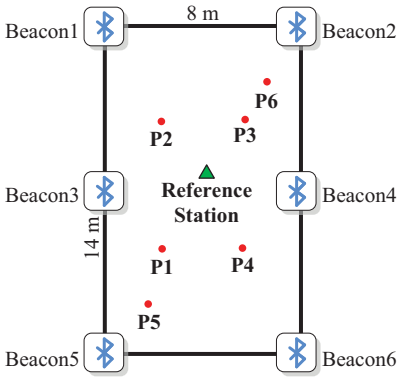

Figure 5. The arrangement in the experimental field

5. RESULTS AND DISCUSSION

This section mainly focuses on the performance of the indoor positioning strategy that the proposed differential distance correction method is exploited. Two different results are compared, including using uncorrected distance (before differential distance correction) and using corrected distance (after differential distance correction). Figure 6 shows the estimated positions of each checkpoint using trilateration technique. Green points show the results of using uncorrected distance while blue points show the results of using corrected distance. The red cross stands for the real position of each checkpoint and the red triangle represents the reference station with the same position.

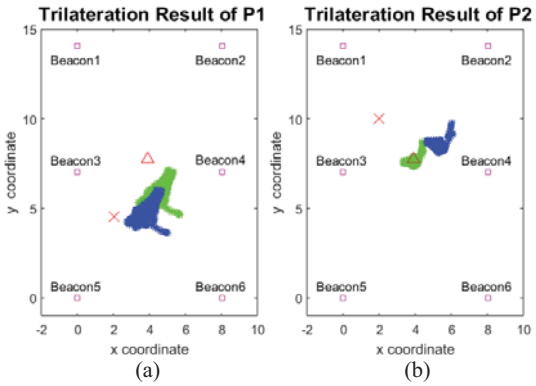

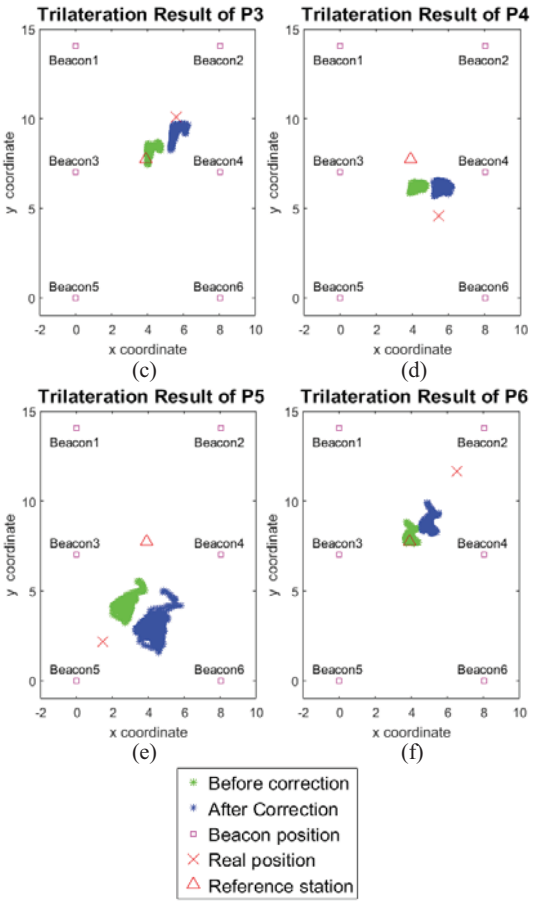

Figure 6. Trilateration results of each checkpoint
(a) P1; (b) P2; (c) P3; (d) P4; (e) P5; (f) P6;
(g) Legend of Figure 6

Figure 7 shows the Cumulative Distribution Function (CDF) of positioning errors of the corresponding checkpoint. Using uncorrected distance (in blue line) and using corrected distance (in red line) are compared in Figure 7. Table 2 summarizes the positioning errors of P1 to P6 using two different distances. Note that the Root Mean Square Error (RMSE) is utilized to evaluate the positioning accuracy. It indicates the difference between the positioning result and the real position. The accuracy is high if the RMSE is small. Moreover, 90% means the 90% positioning error of two estimated positions which use different distances and the two types of improvement in Table 2 are calculated from both RMSE and 90% positioning error.

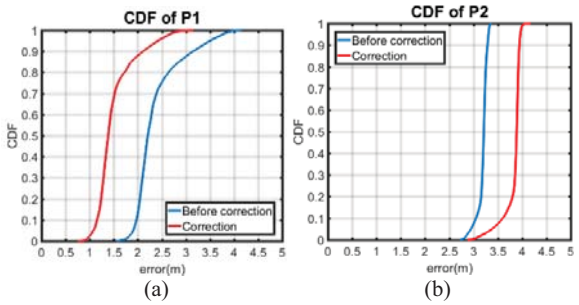

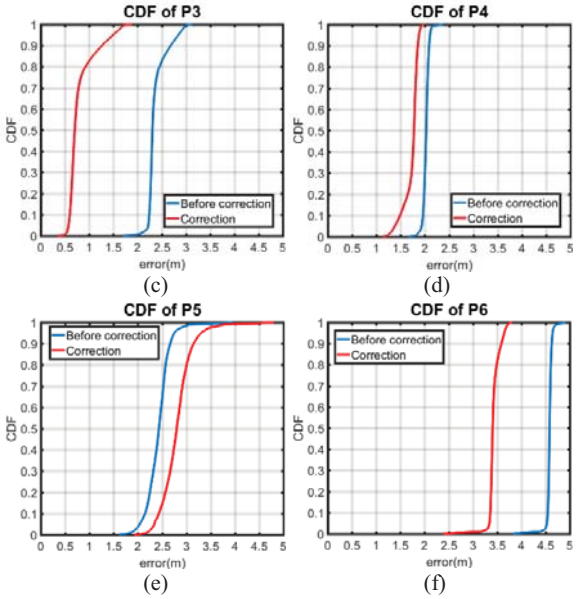

Figure 7. CDFs of positioning errors of each checkpoint
(a) P1; (b) P2; (c) P3; (d) P4; (e) P5; (f) P6

		RMSE (m)	90% (m)	Improve-ment of RMSE (%)	Improve-ment of 90% (%)
P1	Before	2.42	3.15	35.95%	32.70%
	After	1.55	2.12		
P2	Before	3.19	3.28	-20.06%	-20.12%
	After	3.83	3.94		
P3	Before	2.38	2.69	64.29%	53.16%
	After	0.85	1.26		
P4	Before	2.02	2.09	14.36%	11.48%
	After	1.73	1.85		
P5	Before	2.43	2.66	-16.05%	-18.42%
	After	2.82	3.15		
P6	Before	4.58	4.63	25.11%	22.46%
	After	3.43	3.59		

Table 2. Evaluation of positioning results at each checkpoint

According to Figure 6, Figure 7 and Table 2, most of the estimated positions are closer to the real point, except P2 and P5. The discussion here will focus on P1, P3, P4, and P6 while the results of P2 and P5 will be further discussed in the next part.

As shown in Table 2, it is obviously that the horizontal positioning results of P1, P3, P4, and P6 are closer to the real position owing to the smaller RMSE values and 90% positioning errors after correction. The RMSE values of using corrected distance at P1, P3, P4, and P6 are 1.55m, 0.85m, 1.73m, and 3.43m, which improve 35.95%, 64.29%, 14.36% and 25.11% in respect of using uncorrected distance, respectively. At the same time, the 90% positioning errors of using corrected distance at P1, P3, P4, and P6 are 2.12m, 1.26m, 1.85m, and 3.59m, which reduce 32.70%, 53.16%, 11.48% and 22.46% in respect of using uncorrected distance, respectively. In brief, the positioning accuracy at these checkpoints is enhanced after using the proposed method.

However, the positioning errors of P2 and P5 are increased after using differential distance correction. Generally, the beacon, which is the closest to the checkpoint, strongly influences the positioning result. Due to BLE's narrow channel space, the signal strength of BLE fades rapidly. The farther away from the beacon, the more errors of estimated distance converted from the model exist. In other words, the estimated distance to the closest beacon has the least error so that it should have a better result if the corrected distance to the closest beacon is used. However, if the corrected distance between the closest beacon and the checkpoint is not revised to real distance, the positioning result will easily get worse, as shown in Figure 6 (b) and (e). Therefore, this study tries not to consider the distance observation from the closest beacon if the result deteriorates when all distances to beacons are taken into account. Consequently, it shows better results after the re-calculation which are given in Figure 8, Figure 9, and Table 3.

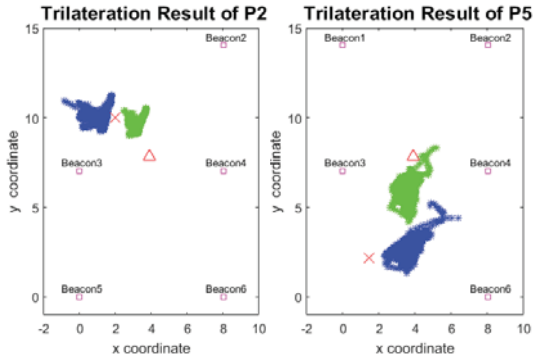

Figure 8. Trilateration results of P2 and P5 when the closest beacon is not considered
(a) P2; (b) P5

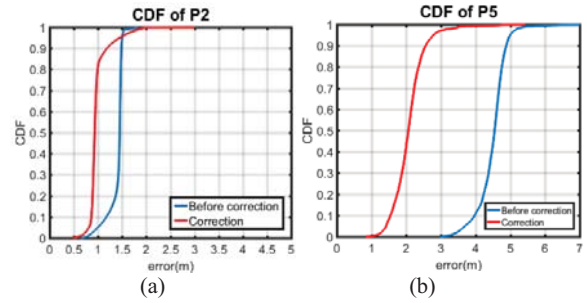

Figure 9. CDFs of positioning errors of P2 and P5 when the closest beacon is not considered
(a) P2; (b) P5

	(m)	RMSE	90%	Improve-ment of RMSE (%)	Improve-ment of 90% (%)
P2	Before	1.40	1.48	28.57%	20.27%
	After	1.00	1.18		
P5	Before	4.50	4.88	52.67%	47.54%
	After	2.13	2.56		

Table 3. Evaluation of positioning results at P2 and P5 when the closest beacon is not considered

As shown in Table 3, it is clear that the results of P2 and P5 when the closest beacon is not considered are improved due to the smaller RMSE values and 90% positioning errors after correction. The RMSE values of using corrected distance at P2 and P5 are 1.00m and 2.13m, which improve 28.57% and 52.67% in respect of using uncorrected distance, respectively. Moreover, the 90% positioning errors of using corrected distance at P2 and P5 are 1.18m and 2.56m, which decrease 20.27% and 47.54% in respect of using uncorrected distance, respectively.

If the estimated distance is properly revised, the overall improvements of using differential distance correction are 1.10m (38.19%) in RMSE and 1.06m (33.65%) in 90% positioning errors as shown in Table 4. In summary, the proposed method has the ability to enhance the accuracy in the BLE-based indoor positioning system.

		RMSE (m)	90% (m)	Improve-ment of RMSE (%)	Improve-ment of 90% (%)
Mean	Before	2.88	3.15	38.19%	33.65%
	After	1.78	2.09		

Table 4. The overall evaluation of positioning results with the accuracy improved

6. CONCLUSION

This paper proposes a novel method named differential distance correction which mainly aims at optimizing the positioning accuracy in the indoor positioning system built by BLE technology. The concept of the proposed method is similar to the DGNSS and it corrects the estimated distance that may contain errors caused by the environment. A reference station is established at a known position and continuously receives RSSI from surrounding beacons. The received RSSI value can be converted to estimated distance by RSSI propagation model. The residual at the reference station can be calculated by subtracting the exact distance from the estimated distance. This differential information is further used for correction of the estimated distances to beacons at other receiving stations. The position will be determined by trilateration based on the uncorrected and corrected distance.

According to the experimental result, most of the positions at the checkpoints are improved when differential distance correction is utilized. However, some of the positions worsen if using all corrected distances. Take a closer look at these distances; it is found that the corrected distance to the closest beacon isn't revised to the real distance. Therefore, the distance to this closest beacon is not taken into account and then calculate the position at the checkpoints again. The results show that the positioning accuracy is also enhanced. The overall improvements of differential distance correction are 1.10m (38.19%) in RMSE and 1.06m (33.65%) in 90% positioning errors. In the future, a system will be developed to detect the improper distance correction automatically, and only use suitable differential information to determinie the position. To conclude, the proposed differential distance correction method is capable of improving the accuracy in the BLE-based indoor positioning system if the estimated distance is properly revised.

ACKNOWLEDGEMENTS

This paper deeply presents the gratitude to Ministry of Interior (SYC1060117) for the grant support.

REFERENCES

Boukerche, A.; Oliveira, H. A. B.; Nakamura, E. F.; Loureiro, A. A. F., 2007. Localization Systems for Wireless Sensor Networks. *IEEE Wireless Communications*, 14(6), pp. 6-12.

Cabarkapa, D.; Gruji, I.; Pavlovi, P., 2015. Comparative analysis of the bluetooth low-energy indoor positioning systems. *In Proceedings of the 12th International Conference on Telecommunication in Modern Satellite, Cable and Broadcasting Services (TELSIKS)*, Nis, Serbia, 14-17 October 2015, pp. 76-79.

Feng, Y.; Yuxin, Z.; Gunnarsson, F., 2015. Proximity report triggering threshold optimization for network-based indoor positioning. *In Proceedings of the 18th International Conference on Information Fusion (Fusion)*, Washington, DC, USA, 6-9 July 2015, pp. 1061-1069.

Johansson, P.; Kazantzidis, M.; Kapoor, R.; Gerla, M., 2001. Bluetooth: an enabler for personal area networking. *IEEE Network*, 15(5), pp. 28-37.

Kang, W.; Nam, S.; Han, Y.; Lee, S., 2012. Improved heading estimation for smartphone-based indoor positioning systems. *In Proceedings of the IEEE 23rd International Symposium on Personal Indoor and Mobile Radio Communications (PIMRC)*, Sydney, Australia, 09-12 September 2012, pp. 2449-2453.

Kriz, P.; Maly, F.; Kozel, T., 2016. Improving indoor localization using bluetooth low energy beacons. *Mobile Information Systems*, Article ID 2083094.

Li, X., 2006. RSS-based location estimation with unknown pathloss model. *IEEE Transactions on Wireless Communications*, 5(12), pp.3626-3633.

Liu, H.; Darabi, H.; Banerjee, P.; Liu, J., 2007. Survey of wireless indoor positioning techniques and systems. *IEEE Transactions on Systems, Man, and Cybernetics, Part C (Applications and Reviews)*, 37(6), pp. 1067-1080.

Mackensen, E.; Lai, M.; Wendt, T. M., 2012. Bluetooth low energy (BLE) based wireless sensors. *In Proceedings of the IEEE Sensors*, Taipei, Taiwan, 28-31 October 2012, pp. 1-4.

Martin, P.; Ho, B. J.; Grupen, N.; Muñoz, S.; Srivastava, M., 2014. An iBeacon primer for indoor localization: demo abstract. *In Proceedings of the 1st ACM Conference on Embedded Systems for Energy-Efficient Buildings*, Memphis, TN, USA, 3-6 November 2014, pp. 190-191.

Murphy, J. W.; William, S., 2007. *Determination of a Position using Approximate Distances and Trilateration*. Master's thesis, Colorado School of Mines, Golden.

Song, Z.; Jiang, G.; Huang, C., 2011. A Survey on Indoor Positioning Technologies. *In Proceedings of the Theoretical and Mathematical Foundations of Computer Science, ICTMF '11*, Singapore, 5-6 May 2011, pp. 198-206.

Wang, Y.; Yang, Q.; Zhang G.; Zhang P., 2016. Indoor positioning system using Euclidean distance correction algorithm with Bluetooth low-energy beacon. *In Proceedings of the Internet of Things and Applications (IOTA)*, Pune, India, 22-24 June 2016, pp. 243-247.

Yang, Z.; Liu, Y., 2010. Quality of trilateration: Confidence based iterative localization. *IEEE Transactions on Parallel and Distributed Systems*, 21(5), pp. 631-640.

Zhuang, Y.; Yang, J.; Li, Y.; Qi, L.; El-Sheimy, N., 2016. Smartphone-Based Indoor Localization with Bluetooth Low Energy Beacons. *Sensors*, 16(5), pp. 1-20.

Zou, H.; Jiang, H.; Luo, Y.; Zhu, J.; Lu, X.; Xie, L., 2016. BlueDetect: An iBeacon-Enabled Scheme for Accurate and Energy-Efficient Indoor-Outdoor Detection and Seamless Location-Based Service. *Sensors*, 16(2), pp. 268.

THE PERFORMANCE ANALYSIS OF LIDAR-BASED UNMANNED AERIAL VEHICLES FOR DISASTER REDUCTION MAPPING APPLICATIONS

G. J. Tsai [a, *], M.C. Tsai [a], K. W. Chiang [a], N. El-Sheimy [b]

[a] Dept. of Geomatics Engineering, National Cheng-Kung University, No. 1, Daxue Road, East District, Tainan, Taiwan - tpp1114@gmail.com
[b] Dept. of Geomatics Engineering, The University of Calgary, 2500 University Dr NW, Calgary, AB T2N 1N4, Canada, naser@geomatics.ucalgary.ca

KEY WORDS: Unmanned Aerial System, LiDAR-based UAS, Direct Georeferenced, Iterative Closest Point (ICP) registration

ABSTRACT:

For disaster management, the primary objectives are to quickly collect the geospatial data and reconstruct the environment. Unmanned Aerial System (UAS) is nowadays used for many scenarios and most of them typically used the camera to be the main mapping sensors. Although these camera-based UASs provide the high accurate geospatial information for surveying or engineering, it is not quite suitable for disaster applications due to the time-consuming process. This paper presents the LiDAR-based UAS and the quick point cloud procedure for disaster reduction. To improve the capabilities, we introduce unmanned helicopter and design the multi-sensor payload architecture for Direct Georeferenced (DG). Since the higher stability of helicopter, it is more suitable to access and deploy in the environmental disaster areas. On the other hand, the proposed architecture achieves the DG applications for recreate the disaster environment. Generally, LiDAR-based system is limited by the navigation sensors. This paper proposes the INS/GNSS integration system with Iterative Closest Point (ICP) registration to reduce the error from traditional DG method and provide the feedback mechanism for integration system as well. Based on the feedback mechanism, the remaining misalignments and vibrating problems can be reduced between each consecutive scan. In order to test the whole integration system, two kinds of testing fields, rough terrain and city area, are selected in this paper. In summary, the proposed ICP feedback integration system for LiDAR-based UAS provides the well results of two testing fields and generating the well geo-referenced point cloud for disaster applications.

1. INTRODUCTION

To analyse or assist the disaster reduction, researchers have devoted to these issues in last decades. Mobile Mapping System (MMS) is one of the approaches to collect geospatial data in short time and provide the adequate information for Geographic Information System (GIS) for disaster applications. The mapping system can be used with different kinds of mobile vehicles, such as automobiles, aircraft, water-based vessels and Unmanned Aerial Vehicles (UAV). UAV was introduced in the beginning of the 19th century for applications of military mission and now are the popular platform for commercial applications or mass-market products. In recent years, this technique is in wide use in terms of disaster, mapping and investigation.

UAV enables to be used in some areas, where are inaccessible to land vehicle and has a great potential for large-scale mapping and detection due to its flexibility and mobility. For radiation investigation, researchers used the UAV to investigate the eastern Japan after events of March 2011 at the Fukushima Daiichi Nuclear Power Plant (Martin, 2016). For other applications, UAV also has the capability to investigate the landslide and generate Digital Terrain Model (DTM) based on the high-resolution of the images (Niethammer, 2012). UAV-Photogrammetry mapping systems not only provide the 3D geospatial data, but also contribute to 3D model generation (Neitzel, 2012). In addition to photogrammetry, new technique, Structure-from-Motion (SfM) had been introduced to enhance the accuracy with the digital SLR camera in helicopter-mounted payload (Dietrich, 2016).
On the other hand, LiDAR-based UAV takes advantage of the remote sensing. LiDAR is the sensor by which receiving the scattered and reflected light to find or measure the distant as well as intensity of the object (Abe, 1981). For high-resolution LiDAR system, most LiDAR-based mapping systems incorporate the Global Positioning System/Inertial Navigation System (GPS/INS) to acquire the high accurate DTM. In coastal environment, it is also the tough task to high-density measurements of bathymetry and topography (Irish, 1998). To get the fine observations, it is important to study the effects of wave patterns on point cloud from LiDAR bathymetry footprints. Such those researches concentrate on Airborne LiDAR bathymetry (ALB) to model the terrain under the water (Westfeld, 2016). In order to extend the applications of LiDAR-based UAS, the combination system with the LiDAR and hyperspectral imaging is proposed to the research of different aspects of issues, like landslides, monitoring, security tasks, surveillance, and remote sensing (Gallay, 2016). Besides, other research also reveal the improvement by registration of Digital Surface Models (DSMs) and Terrestrial Laser Scanners (TLS) according to the descriptor of matching keypoints (Persad, 2016).

Helicopter is one of the popular UAV which takes advantage of the vertical landing and taking off. Another superiority of helicopter is the mobility that allows the vehicle to hover, go forward and backward, even move laterally. With LiDAR sensor, helicopter achieves the long-range travel even in some GPS-denied area. Combining with inertial navigation and normalized cross-correlation (NCC) DTM matching algorithm to prevent the INS drifting problem (Hemann, 2016). Moreover, LiDAR-based helicopter shows the capability of tree height estimation, road extraction and DTM refinement (Lin, 2011). In addition, the autonomous cargo transportation by using helicopter has been

* Corresponding author

proposed (Wang, 2015). Those autonomous systems use the LiDAR sensor and camera to precisely locate itself and land, or adopt the 3D Convolutional Neural Networks (CNN) to detect the reliable landing area (Maturana, 2015).

Due to the rapid development of mapping and inertial sensors, more and more researches focus on developing the low-cost payload to implement mapping system (Goel, 2016 and Sakr, 2016). UAV with the low-cost and low-weight sensors is capable of mapping not in outdoor but also in indoor environment (Wang, 2013 and Shi, 2016).

In this paper, we design the low-cost mapping payload for helicopter with light and small LiDAR and Micro-Electro-Mechanical Systems (MEMS) GPS/IMU system from scratch. Based on the Direct Georeferenced (DG), the proposed method produces the point cloud data in short time and introduces the Iterative Closest Point (ICP) for registration and reducing error. The contributions of this paper are system design of low-cost LiDAR-based UAV mapping system and DG point cloud processing with ICP registration.

2. METHODOLOGY

For data fusion, the proposed approach integrates the GNSS/INS and LiDAR system together to generate the geo-referenced point cloud data. Data fusion is divided into two parts, GNSS/INS/LiDAR integration and the optimization of point cloud by using ICP algorithm. The first part is the Position and Orientation System (POS) that used the EKF/RTS-smoothing combines the LiDAR measurements to generate the DG point cloud. After the first round of point cloud processing, the current DG point cloud would be matched at a frequency of 10Hz with the previous points which are considered as the model points for ICP process. Figure 1 shows the point cloud production and the detail is described below.

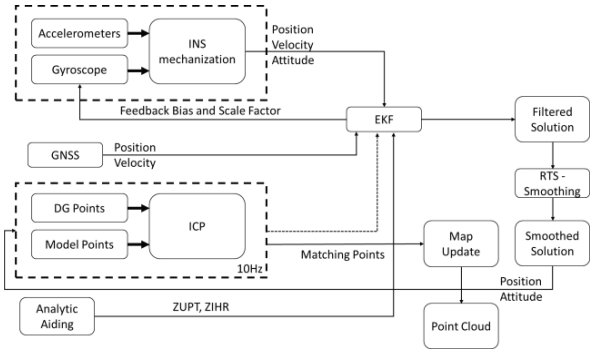

Figure 1. The flow chart of DG point cloud production

2.1 GNSS/INS/LiDAR Integration

The integration scheme is shown in Figure 1. INS is an independent and self-contained positioning system that derives the position and attitude from integrating the acceleration and angle rate provided by accelerometers and gyroscopes. In the conventional approach, the KF is applied in real-time applications to fuse different data from various sensors while optimal smoothing is applied in the post-mission mode. The primary concept is updating the system state with the measurement from different type of sensor.

Fusing independent and redundant sources of navigation information which the measurement models are discrete-time is the basic idea of using the KF in INS integration. The KF equations could be originally linear or linearized, as follows:

$$x_k = \Phi_{k-1,k} x_{k-1} + \omega_k \quad (1)$$

$$z_k = H_k x_k + v_k \quad (2)$$

where x_k is the state vector including position error, velocity error, attitude error, accelerometer bias, gyroscope bias, accelerometer scale factor, and gyroscope scale factor, respectively at time k, $\Phi_{k-1,k} x_{k-1}$ is the state transition matrix from time $k-1$ to k, ω_k is the system noise, z_k is the measurement, H_k is the measurement mapping matrix, and v_k is the measurement noise.

There are two main steps including prediction and update for KF calculation written as:
Prediction:

$$\hat{x}_{k|k-1} = \Phi_{k-1,k} \hat{x}_{k-1} \quad (3)$$

$$P_{k|k-1} = \Phi_{k-1,k} P_{k-1} \Phi_{k-1,k}^T + Q_k \quad (4)$$

Update:

$$K_k = P_{k|k-1} H_K^T \left[H_k P_{k|k-1} H_K^T + R_k \right]^{-1} + Q_k \quad (5)$$

$$\hat{x}_k = \hat{x}_{k|k-1} + K_k \left[z_k - H_k \hat{x}_{k|k-1} \right] \quad (6)$$

$$P_k = P_{k|k-1} - K_k H_k P_{k|k-1} \quad (7)$$

where $\hat{x}_{k|k-1}$ is the predicted state, , $P_{k|k-1}$ represents the covariance, both of two are at time k given information at time $k-1$, $\hat{x}_k$ and P are estimated states and covariance, Q_k, R_k are the covariance matrix of system and measurement noise with zero mean assumed by Gaussian distribution.

The LiDAR-based UAV direct geo-referencing is illustrated in Figure 2. The object point in mapping frame (m-frame) is computed by the relationship between body and LiDAR frame (b-frame and s-frame) based on the direct geo-referencing. The geo-referencing formula can be written as:

$$r_i^m = r_{nav}^m(t) + R_b^m(t) \times (R_s^b r_i^s + r_{nav}^b) \quad (8)$$

where r_i^m is the coordinate vector of i-th interesting point in the m-frame; $r_{nav}^m(t)$ is the coordinate vector at time t of the INS/GNSS in the m-frame; $R_b^m(t)$ is the rotation matrix between the navigation system b-frame and the m-frame; R_c^b is the differential rotation matrix between the s-frame and the b-frame, determined by calibration; r_i^s is the coordinate vector of i-th object point in the s-frame; r_{nav}^b is the vector between INS/GNSS centre and LiDAR, determined by calibration.

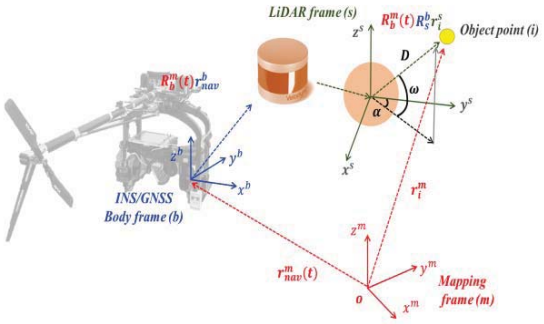

Figure 2. LiDAR-based UAV direct geo-referencing

In s-frame, the r_i^S in s-frame is written as follows:

$$r_i^S = \begin{bmatrix} X_i^S \\ Y_i^S \\ Z_i^S \end{bmatrix} = \begin{bmatrix} D * \cos(\omega) * \sin(\alpha) \\ D * \cos(\omega) * \cos(\alpha) \\ D * \sin(\omega) \end{bmatrix} \quad (9)$$

where X_i^S, Y_i^S and Z_i^S are the point coordinate in s-frame; D is the distance between object and LiDAR; ω is the vertical angle according to the laser channel, and α the horizontal angle between y^S-axis and object.

2.2 Iterative Closest Point (ICP)

Point cloud matching is the popular as the laser scanner or LiDAR has been rapidly developed 3D mapping is not used in mapping system, also applied in autonomous vehicle or robot. One of the most popular method to align the two consecutive point cloud is ICP algorithms. By searching the nearest neighbor, the overall goal is set to find the transformation from one point cloud set to another point cloud set as close as possible (Kjer, 2010). In order to minimize the matching error, the most common error metrics are point-to-point and point-to-plane (Pomerleau, 2013).

To optimize the error metric, this paper uses the Generalized-ICP (G-ICP) in Point Cloud Library (PCL) to implement the registration (Segal, 2009). The difference of error metric in G-ICP is using the Gaussian distribution which represents the probabilistic model in error minimization.

The distribution of two point cloud sets are modelled as:

$$\begin{aligned} n_i &\sim \mathcal{N}(\hat{n}_\iota, C_i^N) \\ m_i &\sim \mathcal{N}(\hat{m}_\iota, C_i^M) \end{aligned} \quad (10)$$

where n_i and m_i are the measured points and C_i^N and C_i^M are the covariance matrices of two different measured points.

The transformation error from transformation (T) that includes the rotation and translation is defined as:

$$d_i^{(T)} = n_i - T \cdot m_i \quad (11)$$

The distribution of correct transformation (T^*) is drawn:

$$d_i^{(T^*)} \sim \mathcal{N}(\hat{n}_\iota - T^* \cdot m_i, C_i^N + (T^* \cdot C_i^M (T^*)^T) \quad (12)$$

Thus, the final error metric is derived from the maximum likelihood estimate:

$$\begin{aligned} T &= \underset{T}{\operatorname{argmax}} \prod_i p(d_i^{(T)}) \\ &= \underset{T}{\operatorname{argmax}} \textstyle\sum_i \log(p(d_i^{(T)})) \\ &= \underset{T}{\operatorname{argmin}} \textstyle\sum_i (d_i^{(T)})^T \cdot (C_i^N + T \cdot C_i^M (T)^T)^{-1} \cdot d_i^{(T)} \end{aligned} \quad (13)$$

In our case, G-ICP performs well compared with ICP method based on the plane-to-plane that takes into account the surface normal and covariance matrix. To reduce the aligning time and increase the robustness, the DG point is adopted in registration process that is given by the initial value to G-ICP. Two of the filters are applied in data filtering process. First, the statistical outlier removal filter is to solve the irregularities in point cloud set. Based on the distribution of distances between neighbours, the outliers are determined by the predefined mean and standard deviation and removed after the determination. The voxel grid filter is to cut down the dataset that speeds up the G-ICP process. In G-ICP step, we also set up the outlier rejection threshold by using Random Sample Consensus model (RANSAC). After the G-ICP iteration, the matched points are considered as the model points for next registration.

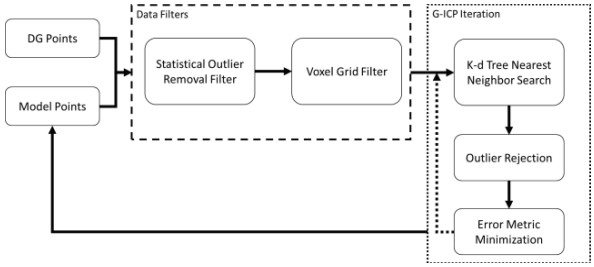

Figure 3. The registration process of DG and G-ICP

3. MAPPING PAYLOAD DESIGN

The proposed UAV platform is designed by Department of Geomatics, NCKU, AVIX Technology Inc. and GEOSAT Aerospace & Technology Inc. in Taiwan. Figure 4 and Table 1 show the platform and specifications of proposed UAV respectively. In order to reduce the weight of payload, the proposed mapping system uses the lightweight and low-cost sensors.

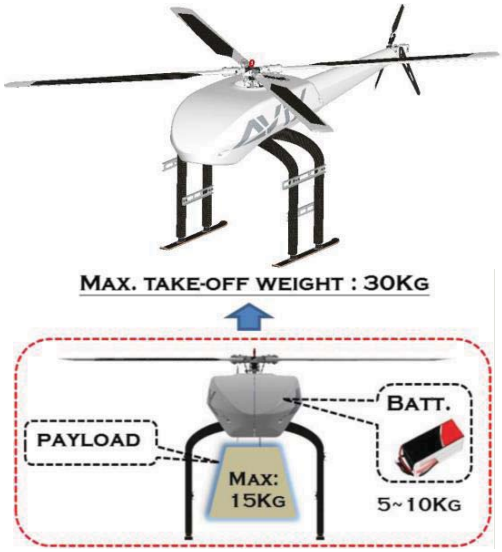

Figure 4. The proposed UAV platform

Table 1. The specifications of proposed UAV platform

Only Helicopter Weight	9 kg
Max. Take-off Weight	30 kg
Battery Weight	5~10 kg
Payload	15 kg
Max. Operational Range	40 km
Max. Cruise Speed	85 km/hr
Max. Endurance	1 hr
Power Voltage	45V~50V (12S Li-Po)

As shown in Figure 5, the mapping system is made up of tactical grade IMU, C-MIGITS with the dual frequency GPS receiver and the low-cost LiDAR, VLP-16. To overcome the vibration from UAV rotor engine, we use the Panasonic Toughbook that is

incorporated temperature, pressure and vibration resistant technology. For LiDAR configuration, we deploy the VLP-16 in the bottom of designed frame, and suspend the LiDAR to scan the object below the UAV as shown in Figure 6. It is worth mentioning that the whole mapping system payload is only 6 KG and is suitable for proposed UAV platform.

Figure 5. The configuration of proposed mapping payload

Figure 6. The scanning field of view of mapping system

4. EXPERIMENT

The proposed UAV platform uses the autopilot module incorporated with the advances neural network theory and adaptive theory in the basic control logic to perform the inertial autonomous navigation control. Furthermore, there are two important utilizations in our experiment. The GPS aiding with Real Time Kinematic (RTK) technique and the ground control station achieve the high-level accuracy of position. With these two assistance, the proposed UAV platform perform the automatic take-off and landing flight patterns as shown in Figure 7. And the Table 2 gives the information of autopilot module. The module is with the 9-axis MEMS sensors (3-axis gyroscope, 3-axis accelerometer and 3-axis magnetic sensor) to aid the system to perform well.

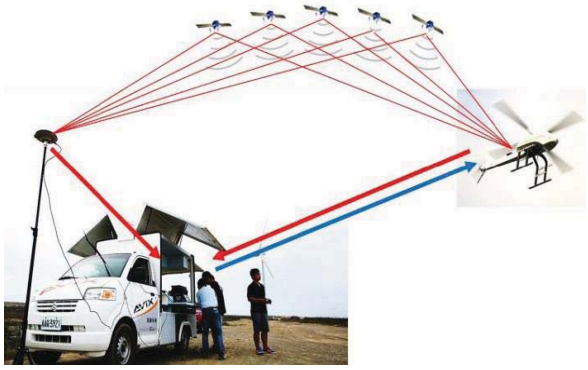
Figure 7. Ground control station for RTK

Table 2. The specifications of autopilot module

GNSS Receiver	Update Frequency	10 Hz
	Receivable	GPS/GLONASS
	RTK Accuracy	1 cm + 1 ppm
3-axis Gyroscope	Measurement Range	±300 deg/s
	Noise Density	0.02 deg/s/sqrt(Hz)
3-axis Accelerometer	Measurement Range	±18 g
	Noise Density	0.006 mg/ sqrt(Hz)
3-axis Magnetic Sensor	Measurement Range	±8 Gauss
Attitude Accuracy	Roll and Pitch	0.5 deg
	Heading	1.5 deg
Waypoints		1000+
Input Voltage		8~26 V
Power Consumption		< 7 W
Size		125 x 85 x 50 mm

The Experimental areas are determined at National Cheng Kung University Kuei-Jen Campus that includes the building and terrain in the paper. The flight path and the satellite images are shown in Figure 8. The time of each experiment is about 15 minutes and the flight speed is set six (m/s).

(a) (b)
Figure 8. Experimental areas, (a) building, (b) rough terrain

5. RESULTS AND DISCUSSIONS

To evaluate the performance of the proposed LiDAR-based UAV, two different areas are selected in this paper. The first experiment is conduct at the area where we set the flight path along with the buildings. The other one is scanning the flat terrain with trees and part of buildings.

As shown in Figure 9, GPS/INS integrated result is almost as same as the planned flight path. The flight height is about 60 meters above the ground, and the integrated result shows the stable the performance of proposed system.

Figure 9. GPS/INS integrated result of building experiment

Figure 10 shows the DG results compared with the DG+ICP results in the first experiment. The color of point clouds is according to the different level of height. As can be clearly seen from this figure, the DG point clouds with the ICP adding are matched at the precise place. In this result, we divided the whole point clouds into the three parts to assess the performance in detail.

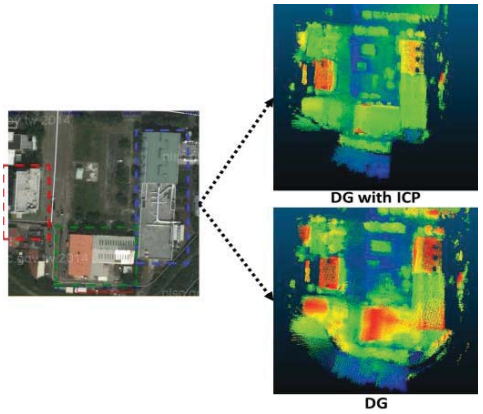

Figure 10. The scanning results of building with DG and DG+ICP

The detail of red, green and blue frame as shown in Figure10 is presented in Figure 11-13 respectively. In Figure 11, the DG with ICP achieve the better performance compared with the only DG result. As you can see form the lower part of DG result, the shape of buildings is blur due to the error from position or attitude. With the ICP assistance, the algorithm matches the each point cloud at 10Hz to reduce the outlier and positioning error. The Figure 12 shows the building with triangle shape of roof. The color of the DG+ICP result at roof part is consistent which means the height of roof is at the same level. However, the DG result shows the different color, the height of point clouds at the roof part is not smooth. The last part of building results focuses on the long rectangle building. It is clearly to see that the result of roof is smooth by using DG+ICP, the result only using DG is not as good as combined algorithm. It is worth to mention that the wall of building in DG+ICP results is distinct. By contrast, it seems like there is the extra layer outside the building with different color in DG result.

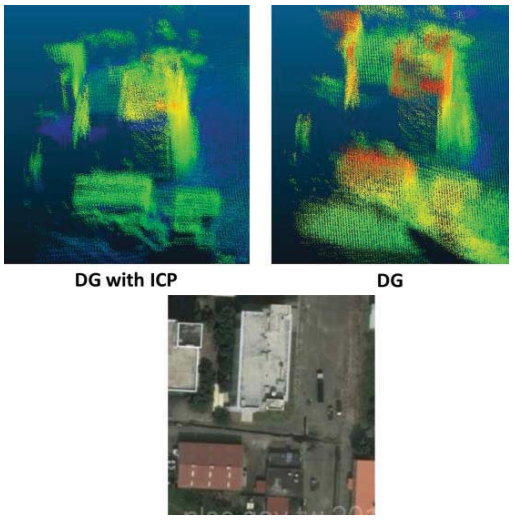

Figure 11. The magnified results of building in red frame

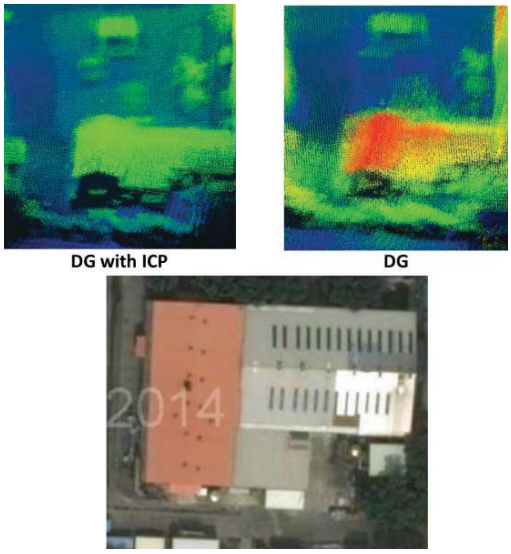

Figure 12. The magnified results of building in green frame

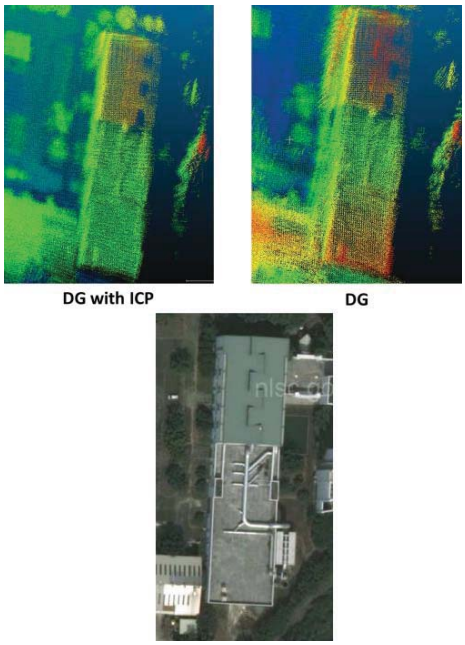

Figure 13. The magnified results of building in blue frame

In terrain experiment, we focus on reconstruct the flat plane and some objects on the ground such as tress or shanties. The second experiment is determined at the other side of building area. The trajectory is shown in Figure 14 and the height profile is presented in the lower place of figure as well. The height of flight is also at around 60 meters. The overview of the terrain experiment is shown in the Figure 15. The color of each points is changed according to its height. In this part, the result is presented in three places to evaluate. In general, the shape of tree or the building in DG+ICP is more clear than the only DG. As you can see from the Figure 15, the satellite image is closer to the combining result.

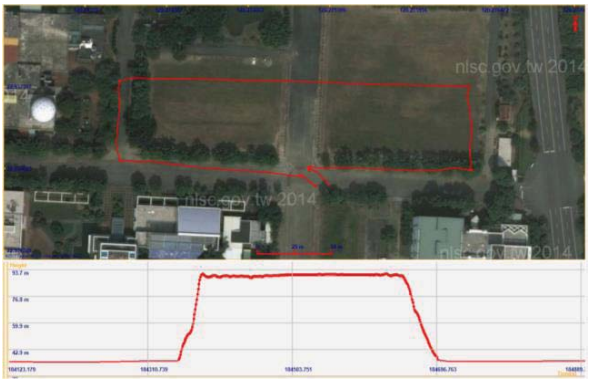

Figure 14. GPS/INS integrated result of terrain experiment

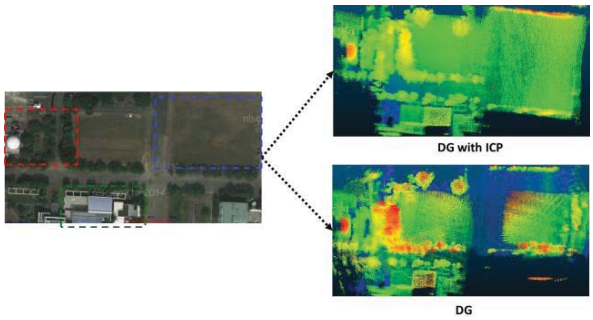

Figure 15. The scanning results of terrain with DG and DG+ICP

As zooming up at the red frame, Figure 16 shows the tree and part of circle shape object. In DG result, the tree along with the intersection and road is unclear. By using DG+ICP method, the point clouds are matched tightly with each other. The circle object and the road is more distinct. Figure 17 represents part of the building including the different roofs. The boundary of each building is clearer in DG+ICP result compared with DG result. The adjacent structures cause some problems as we reconstruct the buildings. The laser beam does not easily scan through all the appearance of building when each one is connected with each other. Therefore, the left side of two results are not distinct. Most of the airborne Lidar systems concentrate on generating the DTM and it needs to be capable of steadily generating the smooth point clouds. As it can be seen form Figure 18, the proposed DG+ICP method can achieve the steady performance to generate the smooth point clouds. Only using the DG result might involve a lot of error from position or attitude. The proposed method can remove most error of the registration.

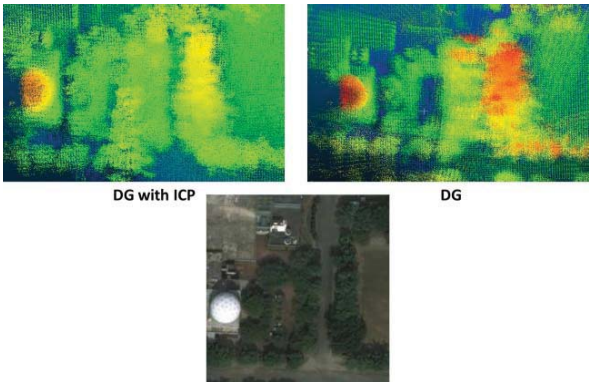

Figure 16. The magnified results of terrain in red frame

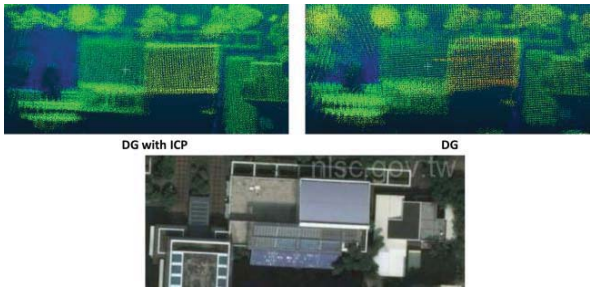

Figure 17. The magnified results of terrain in green frame

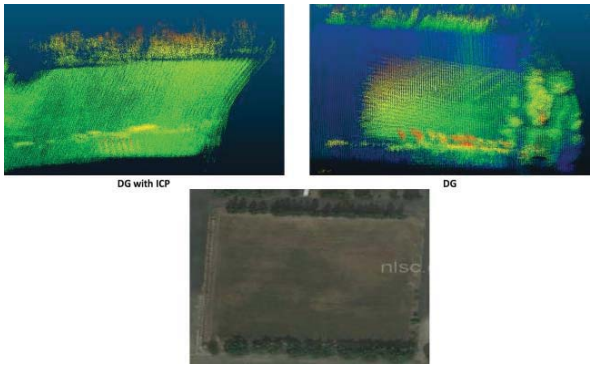

Figure 18. The magnified results of terrain in blue frame

6. CONCLUSIONS

This paper proposed the LiDAR-based UAV system to quickly reconstruct the environment for disaster or mapping applications. The mapping payload is designed for scanning the ground object based on the suspension LiDAR system. By using the low-cost and light sensors, the total weight of whole system is only about 6 KG. By using the autopilot module and ground station, it allows the auto take-off and landing during the experiments.

In addition to design the LiDAR-based UAV system, the proposed DG point clouds with ICP registration achieve the higher accurate performance. The DG point clouds plays the important to reduce the matching error and time in ICP process and improve the consecutive point clouds registration based on the overlapping features. Although the ICP can remove most part of error, it still needs to set up a threshold to prevent the matching divergence. In the future, we would like to enhance the performance by using the tightly integrated system between GPS/INS and ICP to increase the robustness whole system and acquire the higher accurate point clouds.

ACKNOWLEDGEMENTS

The author would acknowledge the financial supports provided by the Ministry of Science and Technology (MOST 105-2221-E-006-017), and technical supports provided by AVIX Technology Inc. and GEOSAT Aerospace & Technology Inc.

REFERENCES

Martin, P.G., Kwong, S., Smith, N.T., Yamashiki, Y., Payton, O.D., Russell-Pavier, F.S., Fardoulis, J.S., Richards, D.A. and Scott, T.B., 2016. 3D unmanned aerial vehicle radiation mapping for assessing contaminant distribution and mobility. *International Journal of Applied Earth Observation and Geoinformation*, 52, pp.12-19.

Niethammer, U., James, M.R., Rothmund, S., Travelletti, J. and Joswig, M., 2012. UAV-based remote sensing of the Super-Sauze landslide: Evaluation and results. Engineering Geology, 128, pp.2-11.

Neitzel, F.; Klonowski, J., 2012. Mobile 3d mapping with a low-cost uav system. In: *International Conference on Unmanned Aerial Vehicle in Geomatics (UAV-g)*, Vol. XXXVIII-1/C22, pp 39-44.

Dietrich, J.T., 2016. Riverscape mapping with helicopter-based Structure-from-Motion photogrammetry. Geomorphology, 252, pp.144-157.

Abe, S., Fujitaka, K., Abe, M. and Fujimoto, K., 1981. Extensive field survey of natural radiation in Japan. Journal of Nuclear Science and Technology, 18(1), pp.21-45.

Irish, J.L. and White, T.E., 1998. Coastal engineering applications of high-resolution lidar bathymetry. Coastal Engineering, 35(1), pp.47-71.

Westfeld, P., Richter, K., Maas, H.G. and Weiß, R., 2016. ANALYSIS OF THE EFFECT OF WAVE PATTERNS ON REFRACTION IN AIRBORNE LIDAR BATHYMETRY. *International Archives of the Photogrammetry, Remote Sensing & Spatial Information Sciences*, 41.

Gallay, M., Eck, C., Zgraggen, C., Kaňuk, J. and Dvorný, E., 2016. HIGH RESOLUTION AIRBORNE LASER SCANNING AND HYPERSPECTRAL IMAGING WITH A SMALL UAV PLATFORM. *ISPRS-International Archives of the Photogrammetry, Remote Sensing and Spatial Information Sciences, pp.823-827.*

Persad, R.A. and Armenakis, C., 2016. CO-REGISTRATION OF DSMs GENERATED BY UAV AND TERRESTRIAL LASER SCANNING SYSTEMS. *International Archives of the Photogrammetry, Remote Sensing & Spatial Information Sciences, 41.*

Hemann, G., Singh, S. and Kaess, M., 2016, October. Long-range GPS-denied aerial inertial navigation with LIDAR localization. In *Intelligent Robots and Systems (IROS), 2016 IEEE/RSJ International Conference on* (pp. 1659-1666). IEEE.

Lin, Y., Hyyppa, J. and Jaakkola, A., 2011. Mini-UAV-borne LIDAR for fine-scale mapping. *IEEE Geoscience and Remote Sensing Letters*, 8(3), pp.426-430.

Wang, F., Liu, P., Zhao, S., Chen, B.M., Phang, S.K., Lai, S., Pang, T., Wang, B., Cai, C. and Lee, T.H., 2015. Development of an unmanned helicopter for vertical replenishment. *Unmanned Systems*, 3(01), pp.63-87.

Maturana, D. and Scherer, S., 2015, May. 3d convolutional neural networks for landing zone detection from lidar. *In Robotics and Automation (ICRA), 2015 IEEE International Conference on* (pp. 3471-3478). IEEE.

Goel, S., Kealy, A. and Lohani, B., 2016. Cooperative UAS localization using low cost sensors. *ISPRS Annals of Photogrammetry, Remote Sensing and Spatial Information Sciences*, pp.183-190.

Sakr, M., Lari, Z. and El-Sheimy, N., 2016. DESIGN AND IMPLEMENTATION OF A LOW-COST UAV-BASED MULTI-SENSOR PAYLOAD FOR RAPID-RESPONSE MAPPING APPLICATIONS. *ISPRS-International Archives of the Photogrammetry, Remote Sensing and Spatial Information Sciences*, pp.1017-1022.

Wang, F., Cui, J., Phang, S.K., Chen, B.M. and Lee, T.H., 2013, May. A mono-camera and scanning laser range finder based UAV indoor navigation system. In *Unmanned Aircraft Systems (ICUAS), 2013 International Conference on* (pp. 694-701). IEEE.

Shi, J., He, B., Zhang, L. and Zhang, J., 2016, October. Vision-based real-time 3D mapping for UAV with laser sensor. In *Intelligent Robots and Systems (IROS), 2016 IEEE/RSJ International Conference on* (pp. 4524-4529). IEEE.

Kjer, H.M. and Wilm, J., 2010. *Evaluation of surface registration algorithms for PET motion correction* (Bachelor's thesis, Technical University of Denmark, DTU, DK-2800 Kgs. Lyngby, Denmark).

Pomerleau, F., Colas, F., Siegwart, R. and Magnenat, S., 2013. Comparing ICP variants on real-world data sets. *Autonomous Robots*, *34*(3), pp.133-148.

Segal, A., Haehnel, D. and Thrun, S., 2009, June. Generalized-ICP. In *Robotics: science and systems* (Vol. 2, No. 4).

THE GENERATION OF WELL GEO-REFERENCED FLOOR PLANS FOR INDOOR NAVIGATION WITH INERTIAL SENSORS AIDED SLAM ALGORITHM

Min-Chuan Tsai [a, *], Guang-Je Tsai [a], You-Liang Chen [a], Kai-Wei Chiang [a], Naser El-Sheimy [b]

[a] Dept. of Geomatics Engineering, National Chang Kung University, Tainan, Taiwan- sandytsai888@gmail.com, eltonboy78, tpp1114@gmail.com, kwchiang@mail.ncku.edu.tw
[b] Dept. of Geomatics Engineering, University of Calgary, Calgary, Canada- elsheimy@ucalgary.ca

KEY WORDS: Mobile Mapping System (MMS), Floor plans, Indoor mapping, SLAM, Inertial sensors, zero velocity update (ZUPT), integration

ABSTRACT:

Spatial data has been ubiquitously used in mobile mapping and navigational positioning technique. Such as the Mobile Mapping System (MMS), the technique getting popular is really a revolution among the fields of Geomatics. It features the enhancement of efficiency that overcomes the great amount of labor and time consuming problems of traditional measurements. However, the applications of MMS service for the outdoor spaces are adequate but relatively limited for the indoor environments due to the size of MMS. This research is then based on the MMS, laser scanner, Inertial Measurement Unit (IMU) and portable multi-sensor device, trying to build up a cost down system with various sensors and enhanced accuracy. Laser scanner is loaded on the robotic platform as the scanner for the indoor environment mapping. Combining Simultaneous Localization And Mapping (SLAM) can promote precision of indoor navigation and make automatic mobile mapping system possible. However, it would still drift by time as it runs as relative positioning algorithms. This research modifies the drift trajectories of the indoor plans by using IMU with zero velocity update (ZUPT) using post processed smoothed trajectories. The floor plans can somehow get rid of the errors from drifting problem as smoothed aided inertial solutions not only offer the original attitude during the scanning process but back up the system in the positioning state. In other words, with the assistant of inertial sensors, the attitude data helps and increases the flexibility of the system. To sum up, as the floor plans are necessary for indoor navigation, the plans and methods in this research try hard to prove the availability with low cost and enough precision for navigation use. This research provides the method and platform to map the indoor environment with low cost sensors and can produce plans in a meter level precision with inertial sensors.

1. INTRODUCTION

Due to the growing of telecommunication network and widespread mobile devices, the geo-spatial information is getting its reputation on various applications and even commercial benefits. Consequently, mobile mapping has been raised and valued, not only the collecting of geospatial data but also the concept of remote sensing which speeds up the time course. Furthermore, MMS is increasing gaining its popularity from outdoor to indoor. In the past few decades, the technique focuses on the mapping vehicle for such as street view application. Currently, the market of maps is saturated with outdoor services and increasing urban environment and considerable smart buildings promote the need of indoor maps and indoor location based services (Nikoohemat, 2013). Motivated by the necessary for indoor navigation, the development of indoor floor plans turns out to be in need. This paper builds the MMS for corresponding environments and puts efforts on improvement of the floor plans for georeferenced level. The concept of georeferenced is the solution to connect navigation operation between indoor floor plans and existing outdoor maps.

Typically, maps are always required for navigation application to know the users' location and the relationship between the destinations. So far, the utilized maps cover mostly the roads and streets outdoor but only shapes displaying for buildings. So as to make use of navigation function in indoor environment with large regions, indoor floor plans are imperatively in need. Not only technology platform but also cartographic and well-designed maps are all in demand for implementing comprehensive indoor navigation systems especially for mobile devices (Shayan Nikoohemat, 2013).

Generally, the environment is first reconstructed by many point clouds captured from various stations and their spatial relationships. Currently, there is a lack of an accurate, rigorous, and speedy method for relating point clouds in indoor, urban, satellite-denied environments. A novel and automatic way for fusing calibrated point clouds obtained using a terrestrial laser scanner and the Microsoft Kinect with a low-cost inertial measurement unit has been applied (Jacky C.K. Chow, 2014).

Instead of 3-dimentional scenes, using 2-dimentional plans is sufficient to apply. Although there are blueprints for the buildings, a lack of integration between one sketch maps to another is really a critical problem to meet up to the georeferenced goal. Moreover, the uncompensated errors can cause inconsistencies between the map and reality. Thus, MMS plays an important role to generate indoor floor plans in this research.

The core techniques of mobile mapping can be divided into two parts, the techniques on positioning and mapping (Oliver, 2012). Typically, the most common positioning algorithm is the integration of Global Navigation Satellite System (GNSS) and INS (GNSS/INS). The heading angles and velocity information from GNSS/INS are able to make the positioning accuracy of SLAM solution better (Chuang Qian, 2016). However, the indoor environments that this research focusing on are satellite-denied. But the same idea for solving error drifting problem in INS is unchanged. With the arrangement of Kalman filter and RTS smoother, the integrated solution is also valid within satellite-denied areas (Chiang, 2012). When it comes to mapping technique, laser scanner offers high precision and high

density data that make it become one of the emphasises for research and development.

The use of MMS has increased over the last few years, with integrated GNSS/INS solution as the common approach to preserving the quality of measurement mostly for outdoor usage. However, for satellite signals unavailable environments, such as in tunnels, urban areas and indoor buildings, additional sources of aiding need to be considered. This sort of GNSS lacking environments should struggle hardly on accuracy, reliability and generalizability for navigation (Chang, 2017). Land-surveyed features, known as adjustment points, are typically utilized to preserve the requested accuracy in most projects with the defects of costly and less efficient procedure (Johnsbråten, I. 2015). On the other hand, even portable system had been proposed, the affordable weight for the human beings restricts the amount and types of the sensors. Besides, the navigation tracks are prone to be affected by the complicated patterns of the pedestrians.

Even the floor plans are extremely vital for indoor navigation and other request, generating seamless maps among all of the regions is the final intent. In spite of powerful methods to derive indoor maps, independent coordinate systems to different areas or different generation ways lead to unavailable global use. Since the outdoor maps have nearly completed, the indoor floor plans generated by this research would be in the same datum to these maps as well as they can. This kind of maps are so called geo-referenced floor plans as they would be aligned to a certain coordinate system involving shifting, rotating, scaling and skewing with the aided IMU data.

In robotic research, most robotic navigation tasks rely greatly on building maps, hence, the methods for generating relatively reliable floor plans has been in high demands. Robot mapping concentrates on real-time localization, sensing and measuring simultaneously that SLAM algorithm following up.

SLAM is an algorithm to overcome the problem that positioning and mapping should operate at the same time to support each other for mobile robot. Literally, these two operations could process with interchangeable data by SLAM algorithm during scanning. Starting from an unknown position, there is a range measurement device to sense the environments and to update the position of the robot. The positioning stage is accomplished by extracting features from the scenes and conducting re-observation when the robot moves around. The features, commonly known as landmarks, are the keys for each scan to register with each other through the position and attitude feedback from navigation filter.

Maps of 2D SLAM applications can generally be classified as landmark-based maps and occupancy grid maps. The FastSLAM algorithm uses landmark-based maps to improve localization accuracy and efficiency (Montemerlo, 2002). Landmark-based maps merely record the position of natural landmarks, and therefore relatively low computing time and power is required. Such maps assist the robot to avoid obstacles and extend response time. From another point on the robot map, occupancy grid maps record all environment information from sensors and divide the environment into small cells, each of which includes different attributes to represent the environment. Gmapping is a popular open source grid-based SLAM algorithm (Grisetti, 2007). It was designed to make use of Rao-Blackwellized particle filters (RBPFs) while incorporating position information and scanning observations. RBPFs are widely used in SLAM to solve localization and mapping problems efficiently. On the other hand, Hector SLAM is an algorithm developed for laser scanners (Kohlbrecher, 2011). The main differences between Gmapping and Hector SLAM algorithms are that the latter uses 6-DOF motion estimation without odometry and the type of scan-matching method.

SLAM has been developed for several years, and most algorithms achieve the robust performance on mapping system as well as localization. The generated maps are often used in navigating the robot and implementing the autonomous motion planning. The well known global localization problem that puts the robot into the known environment and has to localize itself. The primary issue shows in the generation of different reference frames for maps. This problem also occurs when users apply the robot map on different applications. Another problem is that without any landmarks or absolutely aiding information, the accuracy of robot mapping would degrade with time.

Since SLAM algorithm remains to be insuficient to generate navigational geo-referenced floor plans, the INS is then aided toward the system. Moreover, even Kalman Filter eis able to fuse the data from different sources, the result still can't meet the demand of the goal. In addition, smoothing process is proposed to further imrove the outcoming maps. Overall, the integration of INS and SLAM algorithm with smoothing process would be illustrated through out the research. For the next section, the design of the payload would be discribed in detail. Later on in the following two sections would be the methodolegy and experiment related works. Final, in section five and six show the results and make the conclusion and future work to this research.

2. PAYLOAD DESIGN AND STRUCTURE

2.1 Equipment

Laser scanner based SLAM can reach greater positioning accuracy in a feature-abundant environment, and is usually implemented in satellite-denied indoor environment (Chuang Qian, 2016). To scan the data of the environments, the 3D laser scanner is used to collect the spatial information in point clouds format. As the intent of this paper is to combine inertial navigation system with the SLAM algorithm and to deal with the spatial data, the link between scanning data and the inertial navigation raw data would be the time synchronization. Owing to the reason, the laser scanner should be assisted with a GPS antenna receiver to obtain the GPS time. Although the experiments are for indoor environments, there must be a short period of time either outdoors or through broadcast system to get enough GPS receiving time for synchronism. The laser scanner used in this paper has the specification as Table 1.

The device		3D laser scanner
Specification		Velodyne Puck VLP-16
Size		circumference 103.3mm, height 71.7mm
Weight		830 grams
Channel amount		16 channels
Measurement range		Up to 100 meters range
Points' density		300,000 points per second
FOV	Horizontal	360°
	Vertical	15° up and down, total 30°
Advantages		Low power consumption (8W)
		Calibrated reflectively measurements

Table 1.The specification about the laser scanner

As for inertial navigation system (INS) standing in for generating more geo-referenced floor plans, CMIG IMU is taken into use. IMU is combined with two main devices: one is gyroscope which gives out the exterior orientation and another one is accelerometer with three axes accelerations for outputs. In addition, GPS antenna is in demand for the time synchronization as well. With the absolute information

mentioned above, the positions of the experimental devices are better known instead of predicting by SLAM algorithm. Then it could moderate the drifting problem since the SLAM algorithm tracks the positions relatively to a set of landmarks with small errors and causes obvious drift problem over a certain time or a long trajectory.

The device	IMU	
Specification	CMIG-310	
Size (Volume)	54.0 in^3	
Weight	1.1kg (2.4lbs)	
Inner components	Gyroscope	Accelerometer
Bias	1~3°/hr	200μg
Random walk noise	$0.035°/\sqrt{hr}$	$60\mu g/\sqrt{Hz}$

Table 2.The specification about the IMU

Apart from laser scanner for scanning and IMU for more precise pose results, AntiLog is required for IMU control and its data storage. All the equipment mentioned above is combined and loaded on the platforms for experiments. The platforms are shown beneath in 2.2.

2.2 Platform

For indoor environments, the size can be widely ranged from rooms to floors and even from underground streets to tunnels. In order to suit various situations, two distinctive platforms are chosen to carry the payload in different experimental fields. TurtleBot is a personal robot kit with open-source software that is easy to control. About 354 mm wide and long in horizontal and 420mm in vertical height, the robotic body fits the scanning need in regular buildings within 100 meters. The speed can go up to 0.65m/s and 5kg-payload is available. TurtleBot is implemented on the 2nd floor of Geomatics department around 20m by 50m in National Cheng Kung University. When it comes to a larger indoor condition, the vehicle is definitely a convenient platform. A van is better to load the laser scanner higher and help get rid of the complicated scenes in the parking lot, avoiding the reflection from other cars' windows and the feature lines blocked by the obstacles.

Platform	TurtleBot
Size	354 × 354 × 420mm
Max payload	5kg
Max speed	0.65m/s

Table 3.The specification about the TurtleBot

3. METHODOLOGY

When it comes to mobile robot mapping, there is an interesting problem to consider. The robot should localize itself and do mapping at the same time. However, mapping needs self-localization to get the original position and map is also required for robot to build up its cognition for knowing where it is. Therefore, the whole system can be divided into two main parts, localization subsystem and mapping subsystem. The former collects data from navigation filters and provides attitude and initial pose. The latter has the scan data as input and produces maps by SLAM algorithm. Two subsystems keep interchanging the post information with each other to accomplish the tasks. The following Figure 1 shows the architecture of the MMS used in this paper.

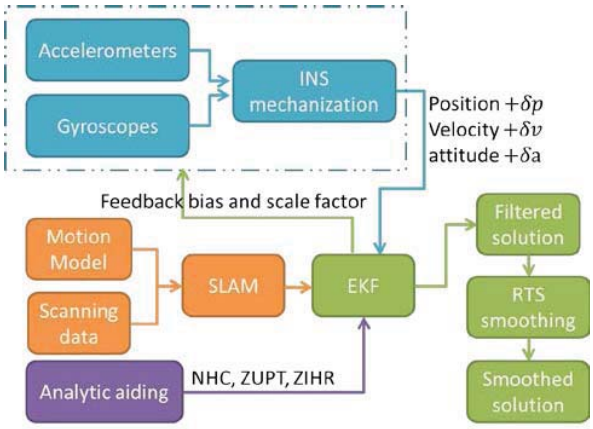

Figure 1.The architecture of the methodology

3.1 Indoor Positioning

Although SLAM is a quite favourable solution to the problem of positioning and mapping at the same time, this paper hopes to improve the indoor positioning issue by the aided INS. Besides, there are several assumptions and skills to enhance positioning process. Positioning process would be done by the localization subsystem with several kinds of aiding information as revealed in Figure 1. Such as the heading data derived from compass, height difference generated by atmospheric pressure, or the velocity and attitude states from the sequential images, could help update the navigation filter.

3.1.1 Data Fusion

To deal with the navigation problem and to analyse the results from different situations, a data fusing program is developed by our lab. The toolbox is a set of libraries written for Matlab software. The parameters of alignment and performance can be revised. Several functions to ameliorate are added in to meet multiple needs. This research handles the drift problem by the application of INS with Kalman Filter (KF) and Rauch-Tung-Striebel (RTS) smoother. In addition, zero velocity update (ZUPT) and non-holonomic constraints (NHC) are the aims for this paper as well. The details would be covered in section 3.1.2 to 3.1.4 for INS/KF/RTS combination and ZUPT/NHC respectively.

3.1.2 INS/ KF/ RTS

Fusing independent and redundant sources of navigation information with discrete-time measurement models is the fundamental idea of employing the KF in INS integration (Tsai, 2012). Figure 2 illustrates the integration scheme of the self-contained positioning system INS and the fusing tool KF for various sensors' data. The equations of KF could be initially linear or being linearized. The concept and the formulas are as follow:

$$x_k = \Phi_{k-1,k}\, x_{k-1} + \omega_k \quad (1)$$

$$z_k = \mathrm{H}_k\, x_{k-1} + v_k \quad (2)$$

where x_k is the state vector composed of position error, velocity error, attitude error, accelerometer bias, gyroscope bias, accelerometer scale factor, and gyroscope scale factor, with respect to time k; $\Phi_{k-1,k}\, x_{k-1}$ is the state transition matrix from time k - 1 to k; ω_k stands for system noise; z_k stands for the measurement; H_k is the measurement mapping matrix and v_k is the measurement noise.

The following equations can divided into prediction and update steps for KF calculation.

Prediction:

$$\hat{x}_{k|k-1} = \Phi_{k-1,k}\,\hat{x}_{k-1} \quad (3)$$

$$P_{k|k-1} = \Phi_{k-1,k}\,P_{k-1}\,\Phi^{T}_{k-1,k} + Q_k \quad (4)$$

Update:

$$K_k = P_{k|k-1}\,H_k^T\,[\mathrm{H}_k\,P_{k|k-1}H_k^T + R_k]^{-1} + Q_k \quad (5)$$

$$\hat{x}_k = \hat{x}_{k|k-1} + \mathrm{K}_k[z_k - H_k\,\hat{x}_{k|k-1}] \quad (6)$$

$$P_k = P_{k|k-1} - K_k H_k P_{k|k-1} \quad (7)$$

as $\hat{x}_{k|k-1}$ represents the predicted state, $P_{k|k-1}$ means the covariance, the mentioned two are at time k given the information at time *k-1*; $\hat{x}_k$ and P in update section are estimated states and covariance; Q_k , R_k are the covariance matrix of system and measurement noise with zero mean assumed by Gaussian distribution.

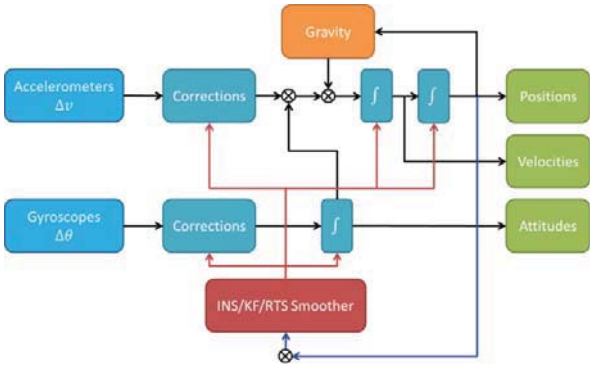

Figure 2.INS/KF/RTS integration scheme

3.1.3 Rauch- Tung- Striebel Off-line Smoothing

To improve the indoor POS estimation, filtering is used in the first step. An optimal smoothing method, such as the Rauch-Tung-Striebel (RTS) backward smoother, can be applied (Tsai, 2015). RTS smoother is an efficient two-pass algorithm for fixed interval smoothing among optimal smoothing types. The forward pass is same as the regular Kalman filter algorithm and filters out a-priori and a-posteriori state estimates and covariances for the backward pass. According to Figure 3, the red curve demonstrates the error of Kalman filter from forward pass. After getting the estimates and covariances from previous step, the cyan reveals the sequel of backward pass. Significantly, the error of the second half of this time interval plummets under RTS smoother operation.

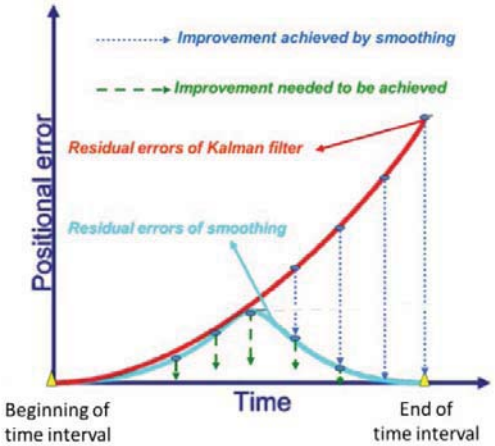

Figure 3.The illustration of RTS

3.1.4 ZUPT/ NHC

INS is completely self-contained and independent that instantaneously gives out the position and velocity information by integrating acceleration and angle rate from accelerometers and gyroscopes. Yet, there is always a problem for inertial elements that the outputs information would degrade with time. Upon to the experimental situations, few techniques can be applied to reduce the effect.

The error model of INS shows the errors increase with respect to incremental time. As we first stay still at the original position for a certain time to conduct alignment, the output information has drifted away instead of being static owing to the problem of inertial units. Setting the velocity and position to zero for this time section is so call zero velocity update.

The platform we use in this paper should not have any apparent side displacements along the pitch axis. Nevertheless, the drift problem from INS leads the motion to be out of the physical law. In classical mechanics, holonomic constraints represent the relations between the position variables. For the mentioned status, NHC is here to revise the mistake and dramatically reduce the horizontal positioning error (Shin, 2003).

3.2 Indoor mapping

Mapping process is conducted by remote sensing devices to derive the scan data. The primary equipment for this research is the laser scanner with scan data output. It can also be the RGB-D sensor like Kinect. With the spatial data collected from the sensors, the detected feature lines can reconstruct the indoor environments and later on generate the maps. As the landmarks are the basic elements for reconstruction, the more the feature points are, the better each scan can register with each other. It is important for the mapping system to conduct preprocessing and calibration before the mapping process to improve accuracy. The data from each scan is combined with position and attitude information in order to register the different datasets together with the position and attitude feedback to the navigation filter. Scan matching is conducted repeatedly for entire robot moving process with the attitude information keeps feeding in from localization subsystem. Owing to the exchanged information between two subsystems, SLAM algorithm is really a convenient technique to produce the maps in real time and the enhanced map accuracy with the aided INS.

3.2.1 Proposed Grid-based SLAM Algorithm

This paper proposed a new model of SLAM based on occupancy grid-based SLAM to solve the divergence of algorithm. There is a problem from experience that the fault tolerance of grid-based SLAM is too small to catch up the speed in a larger environment and so on failing to detect the errors. To give a better initialization for solution, our SLAM algorithm builds up a motion model to receive better results as illustrated in Figure 4. This model estimates the position and heading information based on the feedback from grid-based SLAM which assumes the platform moves in the same pattern.

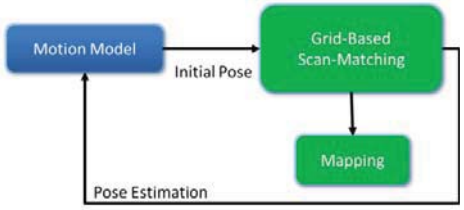

Figure 4.Motion model for SLAM algorithm

Based on the system mentioned in 3.1.1, we can make use of SLAM algorithm for mapping with aided INS positioning to improve the results. As SLAM algorithm itself has no ability to handle the geo-referenced problem, INS information integrated with GNSS can be inserted as the global coordinate reference.

4. EXPERIMENT

4.1 Workflow and Architecture

After building up the MMS with INS and laser scanner, the experiments can put into practice. While the MMS moving around the fields, laser scanner scans the scenes and Antilog collects the INS raw data from IMU. The scanning data and IMU raw data collected in real-time should go further post-process. For the map generation purpose, scanning data would be the input of SLAM algorithm. However, in order to take a look at the performance of INS addition, the trajectories are extracted out for comparison. On the other hand, both data sets are combined with each other by time synchronization and computed by Extended Kalman Filter for trajectories. To get better results, the research takes few methods to constrain, including NHC, ZUPT, ZIHR and RTS smoothing. More details would be mentioned beneath in the following sections. Figure 5 depicts the flow of the whole process and the interaction between each function.

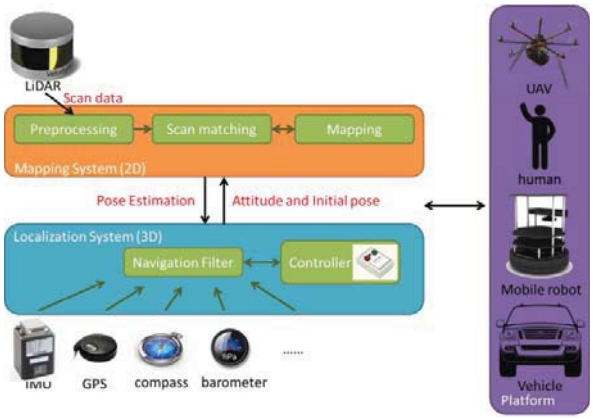

Figure 5.The workflow of the main experiment

4.2 Mobile Mapping System

The experiment started from setting up the MMS for corresponding indoor experimental field. The whole payload setups are displayed in Figure 6 and Figure 7 separately for the two experimental fields. Depending on the size of the field, the platform differs from case to case. For the one on a single and regular building floor, TurtleBot is adequate to move around and complete the mission with acceptable time. The parking lot space is then too large for TurtleBot so a car is replaced instead.

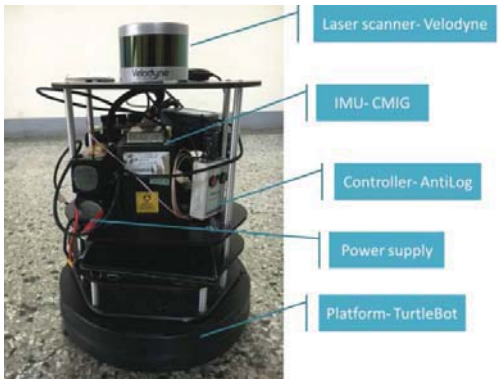

Figure 6.The payload and architecture of the MMS

Figure 7.The architecture of the MMS for larger field

4.3 Positioning Parameters Adjustment

After having the spatial data from MMS, there are several setting and constraints to be set up. There are various parameters to be tilt: the time sections for ZUPT, the original position, velocity and attitude for alignment, bias and scale factor for gyroscope and accelerometer in IMU performance, processing with smoothing or not.

4.4 Trajectory Extractions

Having all of the spatial information, the positions of the MMS during the experiment can be traced down into trajectories. Although the purpose of this research is to generate the floor plans for indoor navigation, the first stage would begin from assuring that the trajectories performs better with the aiding of INS.

5. RESULTS AND ANALYSIS

As the aided IMU is primarily used to overcome the drifting problem and to obtain relatively absolute position, the outcomes would first be the trajectories to observe detailed improvements. The results would be separated into two sections, the consequents for the constraints and the comparisons of different trajectory extractions. There are two scenes being tested in the research, 2nd floor of our department building and an underground public parking lot with corresponding platform.
The common in two experimental fields would be the loop closure assurance. Both experiments have their own starting and ending point at the same position. The trajectories should illustrate as loops corresponding to the reality. However, Figure

8 displays the results of SLAM algorithm without constraints that rebels this principle. The diverse of the parking lot on the right side tells the drift problem with distance of SLAM algorithm. Since the area of the left figure is tinier than the right one, it shows less obvious problem within the experiment. As the result, SLAM algorithm is unable to make loop closure, the following 5.1 and 5.2 would explain the effects of the constraints and do comparison.

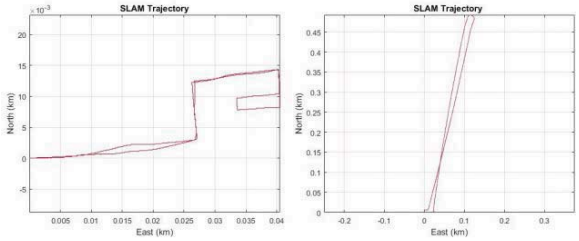

Figure 8.The comparison of trajectories extracted differently

5.1 The result of a floor

This experimental field is on the second floor of the department of Geomatics in National Cheng Kung University in Taiwan. The region is about 45 meters in width and 15 meters in length. In the experiment, TurtleBot carrying IMU moved along the predesign path shown in Figure 9 in orange as the reference. It started from the left of the figure and went for a loop back to the original position. The total length of the route is around 140 meters. First extract the trajectory with pure SLAM algorithm as display in color blue. And the one from IMU only with original position from GPS information is demonstrated in purple. Finally, the result fusing SLAM algorithm and IMU data reveals in green.

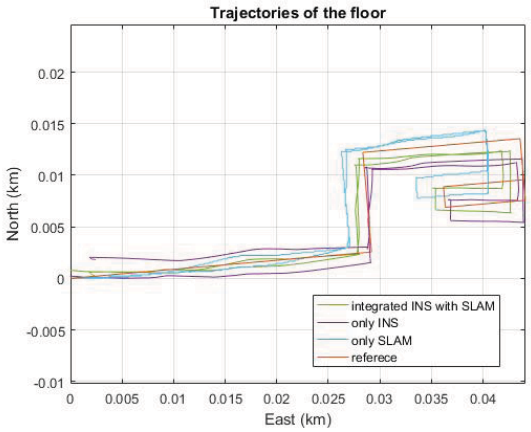

Figure 9.The comparison of trajectories extracted differently

The route is designed in advance in orange and the robot is controlled to go along the path. Take the orange reference as standard, Figure 9 illustrates that merely SLAM algorithm caused more obvious scale problem than the one with only INS. The appearance proves that inertial navigation yet holds a certain level of quality to preserve the accuracy. Nevertheless, there is still a gap between the trajectories of the reference and the single INS. It shows the existing rotational drift problem; the problem hasn't been solved. The merge of having both methods did meet in the middle to improve the result. But the scale of the segment in the middle part along north direction is sacrificed to compromise between two constrains and fail to choose the better one from only INS output.

5.2 The result of the parking lot

The public parking lot locates at the area around tourist sites in Tainan. The total length goes up to 800 meters and 30 meters width with about 900 parking spaces. To avoid the parking cars blocking the outlines for the scanner to detect, a higher position on the car ceiling was necessary as the platform. And a car vehicle is also convenient to complete this huge area in short time. The outcome trajectories is displayed below in Figure 10, devised beforehand in orange as reference, blue representing SLAM result, purple illustrating IMU output and the green one being the integration of the above two.

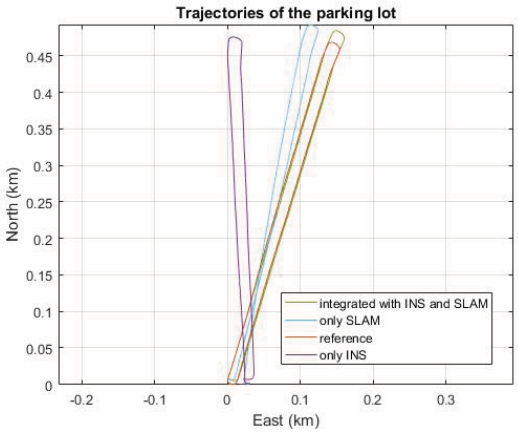

Figure 10.The comparison of different trajectory outcomes

For merely SLAM algorithm, the result fails to close even the route came to an end as a loop during the experiment. As for the result of purely IMU, it shows defeat on the starting and ending location without having a good reference point from the GPS. From the result of the integration, it perfectly matches the reference path despite the scale lapses.

5.3 Loop Closure

To take a look at the loop closure results, Table 4 shows the distance differences between the starting and ending position that should ideally be the same.

		SLAM only	SLAM aided INS
Department floor	North	-0.111m	-0.763m
	East	-2.153m	2.675m
	Total	2.156m	2.782m
Parking lot	North	-6.866m	6.729m
	East	29.324m	1.131m
	Total	30.117m	6.823m

Table 4.The inspection of loop closure problem improvement

In order to make sure the aided INS really improves the results of SLAM algorithm, one of the methods could be the loop closure detection. Comparing the distances between the start point and end point, a great amount of enhancement to the parking lot experiment is obvious since the value drops down from 30.117m to 6.823. However, as for the department floor, it can be viewed as slightly worsen or being relatively even. This phenomenon can be explained by the property of SLAM error model. The errors accumulate through the increasing distances of the path. The path of the experiment at the parking lot is way much longer to the department floor, thus it is reasonable to get the outcomes.

6. CONCLUSION AND FUTURE WORK

Based on the demand of accurate indoor floor plans, this paper proposes the payload design of indoor MMS. For spatial data collection, IMU is the main aiding sensor for positioning and laser scanner primarily scans within point clouds format to work for mapping. SLAM is in charge of mapping in 2-dimention which is enough for navigation use. Later on, the data would be post-process by INS/KF/RTS direct geo-referencing method and ZUPT/NHC/ZIHR constrains. At last, this research aims to prove the combination of INS with SLAM algorithm can improve the quality and generate geo-referenced maps ultimately.

The proposed integrated system is mainly utilized to take advantages of each component. MMS keeps labor and consuming time less, SLAM algorithm is good at providing the mapping method from environmental landmarks, INS keep tracks on the attitudes of the robot along the way and the constraint methods hold the drifting problem tight within a certain value. Each part performs their own duty and also complementary in data currency.

So far in the stage, the trajectories extracted by different combination are show in the content to inspect and to compare the quality. The results prove that the constraints of ZUPT and NHC do make all the trajectories better and get closer appearances to the reality. The constraints mentioned above both amend and restrict the drifting problem of SLAM algorithm and inertial sensors.

Although only trajectory improvements are proposed so far, the mapping outcomes may derive corresponding enhancements based on this research achievement. Based on more accurate trajectories and the precise measurements from laser scanner, the environments can be reconstructed in better scale and fit the geo-referenced goal. The profit would continuously carries out as future work. The ultimate target shoots at the generation of global position information for the mapping system and enables the user to move seamlessly from outdoor to indoor environments based on the produced floor plans with global coordinate system.

ACKNOWLEDGEMENT

The authors would acknowledge the financial support by the Ministry of Science and Technology, ROC (Taiwan) (MOST project)

REFERENCES

Chow, J. (2014). *Multi-Sensor Integration for Indoor 3D Reconstruction* (Doctoral dissertation, University of Calgary).

Johnsbråten, I. (2015). *Mobile mapping system positioning in GNSS denied environments* (Master's thesis, Norwegian University of Life Sciences, Ås).

Tschorn, G. (2013). *Extracting Indoor Map Data From Public Escape Plans On Mobile Devices*.

Nikoohemat, S. (2013). *Smart Campus Map* (Doctoral dissertation, Technical University of Munich).

Qian, C., Liu, H., Tang, J., Chen, Y., Kaartinen, H., Kukko, A., ... & Hyyppä, J. (2016). An Integrated GNSS/INS/LiDAR-SLAM Positioning Method for Highly Accurate Forest Stem Mapping. *Remote Sensing*, *9*(1), 3.

Oliver, A., Kang, S., Wünsche, B. C., & MacDonald, B. (2012, November). Using the Kinect as a navigation sensor for mobile robotics. In *Proceedings of the 27th Conference on Image and Vision Computing New Zealand* (pp. 509-514). ACM.

Okorn, B., Xiong, X., Akinci, B., & Huber, D. (2010, May). Toward automated modeling of floor plans. In *Proceedings of the symposium on 3D data processing, visualization and transmission* (Vol. 2).

Chiang, K. W., Liao, J. K., Huang, S. H., Chang, H. W., & Chu, C. H. (2017). The Performance Analysis of Space Resection-Aided Pedestrian Dead Reckoning for Smartphone Navigation in a Mapped Indoor Environment. *ISPRS International Journal of Geo-Information*, *6*(2), 43.

Chiang, K. W., Duong, T. T., Liao, J. K., Lai, Y. C., Chang, C. C., Cai, J. M., & Huang, S. C. (2012). On-line smoothing for an integrated navigation system with low-cost MEMS inertial sensors. *Sensors*, *12*(12), 17372-17389.

Lucas, B. D., & Kanade, T. (1981). An iterative image registration technique with an application to stereo vision.

Litomisky, K. (2012). Consumer rgb-d cameras and their applications. *Rapport technique, University of California*, *20*.

Chong, K. S., & Kleeman, L. (1997, April). Accurate odometry and error modelling for a mobile robot. In *Robotics and Automation, 1997. Proceedings., 1997 IEEE International Conference on* (Vol. 4, pp. 2783-2788). IEEE.

Shin, E. H., & El-Sheimy, N. (2003). *Accuracy improvement of low cost INS/GPS for land applications*. National Library of Canada= Bibliothèque nationale du Canada

Tsai, G. J., Chiang, K. W., Chu, C. H., Chen, Y. L., El-Sheimy, N., & Habib, A. (2015). The Performance Analysis of An Indoor Mobile Mapping System with RGB-D Sensor. *The International Archives of Photogrammetry, Remote Sensing and Spatial Information Sciences*, *40*(1), 183.

Riisgaard, S., & Blas, M. R. (2003). *SLAM for Dummies. A Tutorial Approach to Simultaneous Localization and Mapping*, 22(1-127), 126.

Montemerlo, M.; Thrun, S.; Koller, D.; Wegbreit, B. *Fastslam: A factored solution to the simultaneous localization and mapping problem* Proceedings of the AAAI National Conference on Artificial Intelligence, 2002; Menlo Park, CA, USA, pp 593-598.

Kohlbrecher, S.; von Stryk, O.; Meyer, J.; Klingauf, U. *A flexible and scalable slam system with full 3d motion estimation.* In Safety, Security, and Rescue Robotics (SSRR), 2011 IEEE International Symposium on, IEEE: Kyoto, 2011; pp 155 - 160.

Revised March 2017

A LOW-COST IMAGE BASED MOBILE SYSTEM USING SLAM

Ahmed. A. Youssef [a], Moustafa A. Baraka [b]

[a] Department of Geomatics Engineering, Schulich School of Engineering, University of Calgary, 2500 University Dr. NW, Calgary, AB T2N 1N4, Alberta, Canada – ahmed.youssef1@ucalgary.ca
[b] Civil Engineering Program, Faculty of Engineering and Materials Science, German University in Cairo (GUC), Cairo Governorate 11432, Egypt

Commission VI, WG VI/4

KEY WORDS: Mobile Mapping, SLAM, Image-based, Collinearity, Least Squares Adjustment, Root Mean Square Error

ABSTRACT:

Typical mobile mapping systems are more productive and precise for large scale mapping applications, in comparison to traditional land mapping techniques. However, typical mobile mapping systems are high in cost, and are composed of highly sensitive components that require trained personnel and special work frames to execute mapping applications. In this research, a standalone low cost image-based mobile system is proposed to perform mapping and localization for map scales 1:2500 and smaller. The proposed mobile mapping system implements an integration of Simultaneous Localization and Mapping (SLAM), and basic photogrammetric solution for image space resection, and object space intersection. The proposed system was evaluated for mapping in two different experiment realizations, and with different configurations. The system has shown a root mean square error in object space coordinates ranging from ± 1.5 cm to ± 14.0 cm.

1. INTRODUCTION

1.1 Overview

Mobile mapping, as a terminology, refers to being able to perform mapping from motion. Traditional land mapping techniques require fixed known position of the mapping sensor, such as total stations, terrestrial laser scanners, etc. The fixed position of the mapping sensor references the mapped points to a certain coordinate system. Nonetheless, mobile mapping overcomes the problem of static-mode mapping, by determination of mapping sensor position as a function of time.

Consequently, typical Mobile Mapping Systems (MMS) consists of a set of navigation and mapping sensors mounted on a moving platform. The different sensors have accurate synchronized data streams. The navigation sensors provide position and orientation of the system directly with respect to a designated reference frame with respect to time. Hence, the mapping sensors can provide referenced coordinates during motion (Li, 1997).

Mapping sensors include a combination of laser scanner(s), camera(s). While navigation sensors might include Global Positioning Satellite System (GNSS), and a full Inertial Measurement Unit(s) (IMU), thus sensitive to 6 degrees of freedom. Whereas, Image based mobile mapping systems consist of a configuration of a set of metric cameras, usually between 6 to 18 Cameras mounted on a vehicle with a GNSS receiver, and IMU (El-Sheimy, et al., 2007).

MMS allow an optimized data flow scheme, with potential of real-time solution. MMS provide a flux of observations that are directly georeferenced. MMS surpasses problems that are encountered by traditional mapping techniques. For instance, photogrammetry, as a mapping technique, requires the estimation of exterior orientation parameters (EOPs) of camera stations to perform its mapping functionality (El-Sheimy, et al., 2007). Consequently, MMS are stand-alone systems which are relatively more productive, and precise for large scale mapping applications. However, MMS are of relatively high cost in comparison to traditional mapping techniques. Additionally, MMS components are of high sensitivity which require special platforms, workflows, and trained personnel to execute mapping applications.

This research introduces a design process for a low-cost image-based MMS, which depends on Simultaneous Localization and Mapping (SLAM) concept. The concept is basically concerned with indoor navigation of robots. Nonetheless, this research tries, to a certain extent, to broaden the spectrum of SLAM application to outdoors applications.

SLAM is a concept that was first introduced in robotics. SLAM, as a concept, seeks the answer to a basic question in robotics, which is how to navigate a robot within an unknown environment depending only on mapping sensors. The concept implies that a robot would create a map of its surroundings, then use that very map to navigate to a new position. The process is repeated sequentially, such that the mapping sensor would provide both navigation and mapping data simultaneously (Durrant-Whyte, et al., 2006).

Visual SLAM is concerned with the problem of using images as the only source for external information, by which the platform acquires its position and orientation, and simultaneously construct a map of the explored zone (Fuentes-Pacheco, et al., 2012).

One of the main visual SLAM algorithms is Structure from Motion (SfM). SfM is a computer vision algorithm that seeks the determination of the cameras 3-D positions and orientations. Then, use the known relative camera poses, the algorithm reconstructs the 3-D scene (Siciliano, et al., 2008).

SfM can be applied using only on camera and is referred to as monocular SLAM. SfM can also be applied using a

stereoscopic pair of cameras, to provide scale for the reconstructed 3-D scene. (Fuentes-Pacheco, et al., 2012)

Typical visual SLAM platforms use SfM to solve the SLAM problem, for its computational efficiency and adequacy for real-time applications. SfM is insensitive to initial values for the camera poses, on the contrary to typical estimation algorithms that requires linearization of the mathematical model, as least squares. The least squares adjustment solves in an iterative manner, which requires close initial value for the states, especially for visual SLAM models, which are highly non-linear.

However, SfM can be described to be sensitive noises in image points coordinates; which implies the enforcement of a set of constraints upon the solution. Such constraints might distort the estimated states depending on how noisy the image points are.

Moreover, the monocular SLAM solution using SfM endures a scale problem, by which the 3D scene is reconstructed relatively without any metric representation. Consequently, it is required to provide an external information to define the scale of the generated map. Nonetheless, this drawback is overcome by using stereoscopic SfM.

This research uses least squares adjustment applied with collinearity condition to perform the SLAM solution. Since the proposed system is intended for mapping, the SLAM solution is performed off-line. Consequently, the computational intensive nature of the collinearity condition using least squares estimation algorithm can be tolerated for off-line operation nature of the system.

The chosen system design overcomes the scale problem in opposition to monocular SLAM, and the coverage area is of the system is increased such that it would be adequate for outdoor applications.

Different from typical MMS, the proposed system does not contain any navigation sensors. However, the system consists of mapping sensors, specifically different configurations of low cost non-metric cameras. The proposed system integrates SLAM with photogrammetry. The cameras perform navigation and mapping processes simultaneously based upon collinearity condition, and its applications, specifically image space resection and object space intersection. This research targets the generation of a map with precision sufficient for scale 1:2500 or smaller.

2. THEORETICAL BACKGROUND

2.1 Collinearity Condition

The collinearity condition states that for a perspective camera model the perspective center, image point, and object space point, all lie on the same straight line. For each object space point, there are two collinearity condition equations relating the object space point to its image space projection. The collinearity condition can be applied to solve for different parameters included in the mathematical model. The collinearity condition equations can be used to solve for EOPs of a camera, which is known as image space resection. The collinearity condition equations can also be used to solve for object space coordinates, which is known object space intersection (Mc Glone, et al., 2004).

$$x - x_o = -f * \frac{m_{11}.(X - X_p) + m_{12}.(Y - Y_p) + m_{13}.(Z - Z_p)}{m_{31}.(X - X_p) + m_{32}.(Y - Y_p) + m_{33}.(Z - Z_p)} \quad (1)$$

$$y - y_o = -f * \frac{m_{21}.(X - X_p) + m_{22}.(Y - Y_p) + m_{23}.(Z - Z_p)}{m_{31}.(X - X_p) + m_{32}.(Y - Y_p) + m_{33}.(Z - Z_p)} \quad (2)$$

$$M = \begin{bmatrix} m_{11} & m_{12} & m_{13} \\ m_{21} & m_{22} & m_{23} \\ m_{31} & m_{32} & m_{33} \end{bmatrix} \quad (3)$$

M rotation matrix is function of rotational parameters of EOPs (ω, φ, χ) representing rotation angles about X, Y, and Z axis respectively. The rotation matrix can be deduced through various methods, among of which is by sequential rotation about X, Y, and Z respectively. (x, y) are the image space coordinates, and (x_o, y_o) are the principal point coordinates, and (f) is the principal distance of the camera.

2.2 Least Squares Adjustment

Generally, there are higher values of redundancy in observations in mathematical models based on photogrammetric conditions. In case of resection, number of image space coordinates and object space coordinates of points represents observations, which happen to be much more than number of unknowns included in the EOPs of an image. Also in case of intersection, number of image space coordinates, and EOPs of an image outnumber number of unknowns in object space coordinates of points.

Consequently, Least Squares Adjustment is applied to the Collinearity condition equations to adjust the values obtained from the mathematical model according to redundancy in observation. Since the mathematical model is a non-linear one, it must be linearized according to Taylor's expansion because least squares adjustment cannot be applied to non-linear mathematical models.
Parametric Least Squares adjustment technique is applied to the mathematical model of Collinearity condition to be in the form shown in equation 4 (Mikhail, et al., 1981).

$$v + B.\Delta = F \quad (4)$$

Where v is the residuals vector, B is design matrix containing the partial derivatives of the mathematical model with respect to the unknowns, and F is the misclosure vector. Δ is the updates vector to the unknown states.

The elements of the formula shown in equation 4 vary as per the application of Collinearity condition being used. The unknowns and observations are interchanged within each application. Consequently, for the image space resection the updates vector would be as shown in equation 5. However, the updates vector for the object space intersection would be as shown in equation 6.

$$\Delta^T = [\delta X_p \quad \delta Y_p \quad \delta Z_p \quad \delta\omega \quad \delta\varphi \quad \delta\chi]^T \quad (5)$$

Where $(\delta X_p, \delta Y_p, \delta Z_p)$ are the update elements for the 3-D object space coordinates of the perspective center. Whereas, $(\delta\omega, \delta\varphi, \delta\chi)$ are the update elements for the rotation angles.

$$\Delta^T = [\delta X \quad \delta Y \quad \delta Z]^T \quad (6)$$

Where $(\delta X, \delta Y, \delta Z)$ are the update elements for the 3-D object space coordinates of the object points.

2.3 Similarity Transformation

Three dimensional coordinates transformation is used to transform between coordinate systems taking into consideration the third dimension. Consequently, equation 7 shows transformation mathematical model between two orthogonal 3-dimensional coordinate systems (X, Y, Z) and (U, V, W). This transformation can also be called seven transformation parameters, as it includes three translational parameters, three rotational parameters, and one scale factor, assuming lone scale factor for all dimensions (Mortenson, 2007).

$$\begin{bmatrix} U \\ V \\ W \end{bmatrix} = kM \begin{bmatrix} X \\ Y \\ Z \end{bmatrix} + \begin{bmatrix} U_o \\ V_o \\ W_o \end{bmatrix} \quad (7)$$

M is a 3×3 orthogonal matrix that is function of three rotation angles about X, Y, and Z axis respectively. (U_o, V_o, W_o) is the translation vector between the two coordinate systems, and k is the scale factor between the two coordinate systems.

3. SYSTEM DEVELOPMENT

3.1 System Design and Configuration

The system configuration was chosen to be linear with nearly parallel focal planes of digital cameras. Since the system operate in close range with respect to objects, the configuration geometry was chosen such that geometric and radiometric distortions, due to perspective projection, are minimized. The minimized distortions result in more efficient and robust image matching. The image matching obtains conjugate points in images captured by the system on the move. Consequently, image matching provides higher potential for the proposed system to operate automatically. However, system automation to obtain near real-time results is not considered in this paper.

The system configuration requires a proper mechanical assembly to ensure fixed relative EOPs among the system components. Relative EOPs include base distances, and constant rotation angles among the digital cameras with respect to each other.

Hence, the set of cameras should form a rigid body to enable direct mapping for simultaneous view taken by the cameras at each time epoch.

To ensure proper experimentation, the proposed mechanical assembly should provide scalability and adjustability for base distances, cameras orientations, and system orientation with respect to the vehicle. The system orientation with respect to the vehicle includes the boresight rotation matrix to transfer from the image space coordinate system to the body frame, and the lever arm translation vector between image space coordinate system and body frame.

Mapping is performed by applying object space intersection between overlapping area with images taken by digital cameras within the system.

As mentioned before, object space intersection has unknown values for 3-D object space coordinates that are computed from relative EOPs, interior orientation parameters (IOPs) of cameras, as well as image space coordinates of points.

Therefore, if the relative EOPs are kept constant, the system can then map its field of view instantly. Moreover, the IOPs of cameras are determined from pre-calibration.

3.2 System Realization

The realization for the system design is mainly concerned with achieving the design considerations at the least possible cost.

The system requires only a set of digital cameras to perform navigation and mapping processes. The proposed system consists of a set of 2~4 non-metric consumer-grade cameras that can be mounted on a moving car with a set of designated configurations. The configuration of cameras is fixed to a constant relative geometry as shown in Figure 1. The cameras were fixed relative to each other to provide constant relative orientation parameters that should not change with time.

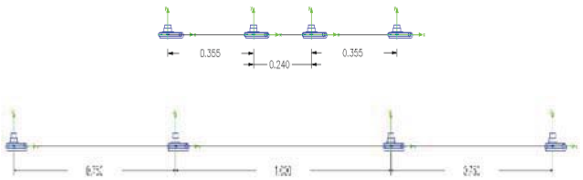

Figure 1. Schematic for System Configuration

The system consists of a longitudinal aluminum bar that is pierced at fixed positions. Standard screws were used to fix the digital cameras along the longitudinal bar. The screws provided fixation of digital cameras as per designated spacings to set base distances among digital cameras.

However, the use of screws to fix cameras to longitudinal bar does not provide full fixation for cameras from rotation about their vertical axis. Hence, relative rotational orientation parameters cannot be kept constant using the introduced mechanical assembly of the system.

The cameras were mounted in different configurations of 2 and 4 cameras to determine the optimum configuration. The cameras were fixed to a linear geometry with nearly parallel focal planes.

The cameras were fixed with respect to each other at different values of base distances to determine the optimum base to object distance ratio. The challenge was to provide an optimum base distance between cameras that would fit to be mounted on a moving car. The system was tested for base distances of 0.25

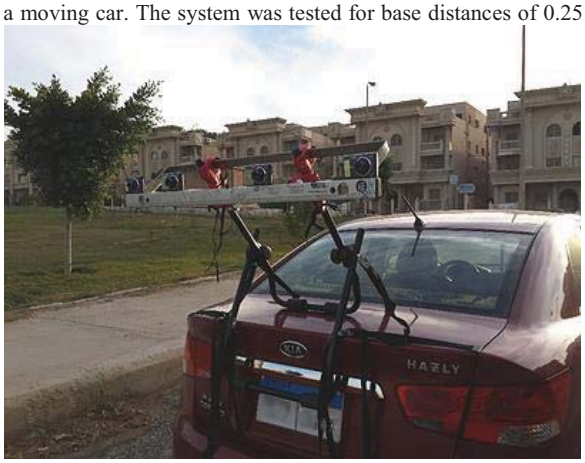

m, 1.00 m, and 2.50 m between the outermost cameras within the system configuration. Figure 2 shows the system configuration mounted on a car.

Figure 2. System mounted on car using standard bicycle mount

The overall cost of the mechanical setup of the system was 50 U.S. dollars. However, the cost of the digital cameras used is 150 U.S. dollars per camera. The system consisted different configurations of low cost consumer grade cameras. The used cameras were Samsung ST150F cameras. Samsung ST150F cameras are non-metric digital cameras with a maximum pixel resolution of 16 megapixels for still imagery, and 720p resolution for video imagery. The cameras were pre-calibrated to determine their IOPs using self-calibrating bundle adjustment. The system includes 4 cameras which were calibrated and marked by numbers. The resulting IOPs from the calibration are shown in Table 1.

IOP	Camera 1	Camera 2	Camera 3	Camera 4
x_o (mm)	0.0886335	-0.033836	-0.015939	-0.034736
y_o (mm)	0.013069	0.055813	-0.03265	-0.129083
f (mm)	4.949072	4.927463	4.668422	4.922182
k_1	-1.85E-04	-6.36E-04	-7.57E-05	-0.000169
k_2	1.59E-05	4.67E-05	3.93E-05	0.0000509
p_1	-1.71E-03	6.26E-04	-1.14E-05	0.000325
p_2	-5.31E-04	-6.96E-04	8.31E-04	0.00193

Table 1. IOPs Results for each of the four cameras within the system

3.3 System Limitations

System stability is not guaranteed at any operating speed of moving vehicle, because of the proposed mechanical assembly of the system. Therefore, the moving vehicle's speed should be limited to ensure as much stability for system configuration.

To adopt the simple and extremely cost effective mechanical design of the system, additional computational process should be implemented to compensate for system stability. During experimentation, image space resection was applied for each set of images taken simultaneously by digital cameras to provide updated values for relative EOPs of the system for each view of the cameras.

3.4 System Workflow

3.4.1 System Calibration Phase: The first process is to perform a system calibration. The system is held still in front of calibration set of points. The purpose is to apply image space resection. Image space resection defines cameras 3D orientation parameters, as mentioned previously, as depicted by figure 3.

However, it is implied that the system should be provided with a set of control points at its initial location. Otherwise, the initial system calibration phase can be held by applying the coplanarity condition.

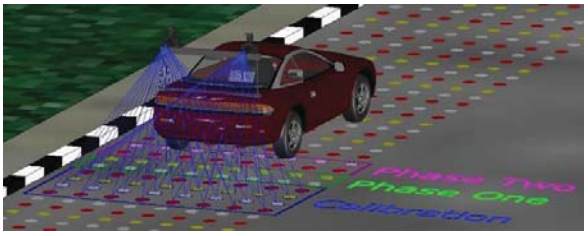

Figure 3. System Calibration Phase for Outdoors Experiments using Image Space Resection

3.4.2 System Motion Phase: The system is then moved from its initial location to face first set of unknown points, in addition to calibration set of points, referred to as phase one of motion.

The system uses its initially computed EOPs that can be considered relatively accurate in computing object space coordinates of the first set of unknown points, as well as, re-computing object space coordinates of calibration set as shown in figure 4. The resulting object space coordinates are considered relatively correct.

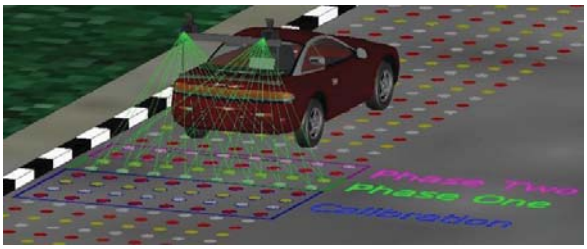

Figure 4. Mapping and georeferencing processes for first set of points using object space intersection and coordinate system transformation

However, the computed object space coordinate needed to be absolutely referenced with respect to global object space coordinate system. Consequently, a set of points from calibration set of points are used once more to geo-reference the computed object space coordinates of first set of unknown points, which are bordered by rectangle for illustration in figure 4. The georeferencing process is performed by applying 3-D similarity transformation. The georeferencing process is performed by computing transformation parameters between actual object space coordinates of calibration set of, and the re-computed values from system new location.

Finally, the EOPs are computed for the new location based on georeferenced object space coordinates of first set of points. Image space resection is applied to determine EOPs of each camera within the proposed system configuration.

The system is then moved to repeat the previously explained process. However, for this case, the system is positioned such that it faces a second set of unknown points, referred to as phase two of motion. The new field of view should be overlapping with first set of points that should be at that stage of known object space coordinates, as shown in figure 5. The system is then used similarly to determine object space coordinates of the second set of points, and then determine EOPs of system upon movement for second time.

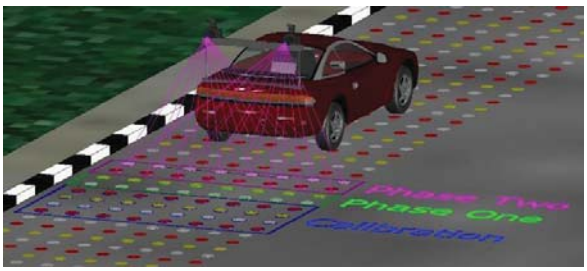

Figure 5. Mapping and georeferencing processes for second set of points using object space intersection and coordinate system transformation

Finally, the calibration phase is repeated to account for any anomalies induced to the relative EOPs. The entire workflow is repeated recursively to perform mapping and tracking for the whole system trajectory.

3.4.3 Data Acquisition and Processing: The data was processed using a self-developed MATLAB code. The code was written to perform image space resection based on least squares adjustment to determine EOPs of cameras required for system calibration and tracking process. Then, the code performs object space intersection based on least squares adjustment to determine object space coordinates required for mapping process. Finally, the code performs a 3-D similarity transformation to geo-reference each

4. EXPERIMENTAL VALIDATION

The objective of the experimental validation was to determine the adequacy of the proposed system to generate maps of scale 1:2500. The system was tested through two sets of experiments. The first set was an indoors set of experiments, and the second was an outdoor set of experiments.

The experiments were designed such that the system was used to map a target field consisting of points of well-known object space coordinates. The system was tested through two sets of experiments. The system was tested indoors to provide a controlled environment for testing. The second set of experiments were performed outdoors to test the system performance in real mapping situation.

For both experiments, the target field points were mapped with respect to local coordinate systems. The local coordinate systems were chosen to be right handed systems. The Y-axis is chosen along the direction of motion. The Z-axis is chosen to be along the zenith direction, and the X-axis is to complete a right-handed coordinate system.

4.1 Validation Criteria

The experiments held aims at validating the results obtained from using the proposed system opposing to using total station in performing same applications. Total station is chosen as a validation tool as it is considered traditional reliable large scale mapping tool. The used total station for indoor applications was SOKKIA set 3X. The expected accuracy of targets coordinates obtained via the SOKKIA set 3X total station is ± 0.005m. The total station that was used for outdoor applications was Leica TC 1103. The accuracy of targets coordinates obtained via the Leica TC1103 total station is ±0.010 m.

4.2 Testing Parameters

A set of parameters were investigated to observe their effect on proposed system results precision as per the stated validation criteria, and with respect to evaluation methods that were chosen.

4.2.1 Base to Object Ratio: defines the quality of intersection geometry, given that the internal geometry of cameras is well known. The internal geometry of cameras can be assumed constant, and are predetermined from camera calibration.

Therefore, during the experiments base distances between cameras within system configuration are changed to investigate the effect of ratio between base distances and average distance between cameras and object, on system precision.

4.2.2 Number of Cameras: The proposed system is designed to use multiple digital cameras with overlapping fields of view to image the same object simultaneously.

The solution is based on least squares adjustment. Therefore, redundancy of observations is expected to enhance the least squares solution, and provide better errors distribution and increase precision of obtained outputs.

Consequently, number of cameras should be tested as a factor to determine the optimum number of cameras that should be used into the proposed system. The number of cameras should fulfill maximum achievable precision with minimum number of cameras providing adequate redundancy for least squares solution.

Vibration and Instability Effects: It refers to the relative motion of the system components with respect to each other. Relative motion of system components occurs due to the vehicle motion, and the chosen low cost mechanical assembly. Nonetheless, there are no direct means to estimate such effects as per the chosen system design and cost.

However, the vehicle speed was reduced to maximum of 50 km/hr to limit such effects. Furthermore, the residual vibration effects are eliminated by the applying the system calibration phase, as explained in sub-section 3.4.1

4.2.3 System Drift: Since SLAM is the underlying concept of the proposed system, then system drift is considered a crucial factor that occurs inevitably. Since, the operation is repetitive, therefore the measurements would endure accumulation of errors that would increase by motion.

The system drift should be monitored in both quantities to be obtained from the system. Theses quantities include 3D object space coordinates of mapping points, and tracking data of system EOPs with respect to global object space coordinate system.

Synchronization Errors: The use of video imaging mode leads to a huge number of images that can be acquired during mapping processes. The chosen data processing method for the system is to shoot same object using digital cameras within the system simultaneously. Consequently, the videos obtained from digital cameras must be synchronized to provide a set of images from which mapping process can be performed.

The data processing is done under the assumption that the images taken from different cameras are of known relative EOPs. Since the system is in motion, and images are acquired in video mode, the corresponding images taken from digital cameras simultaneously must be specified accurately. Otherwise, the system results would be affected due to the variation. In case that images are not exactly synchronized, the EOPs should vary due to relative variation in synchronization

time, such that the variation is translation value obtained from the product of speed of moving vehicle multiplied by variation synchronization time.

Nonetheless, the system calibration phase of the system maintains synchronization errors, as explained in sub-section 3.4.1, which is held at the initial location of the system. Consequently, there are no additional precautions that are required to maintain extremely precise synchronization between video frames for the proposed system.

4.3 Experimental Setups

4.3.1 Indoors Experiments: The test was designed such that the system should provide the object space coordinates of a set of black and white targets from three different sequential positions. The targets were placed on ground with spaces of approximately 0.50 m, as shown in Figure 6.

Figure 6. Targets Pattern for Indoors Experiments

The targets pattern was chosen to be grid in shape with spacing between each two targets of nearly 50 cm. The targets surveyed using total station for validation. The grid of targets consisted of 8 lines in longitudinal direction by 8 lines in transversal direction. The total number of targets was 64 targets. The experiments follow the same procedure previously explained in section 3.4. The images were taken manually in image mode using the non-metric digital cameras.

4.3.2 Outdoor Experiments: The experiment was designed such the system would map a set of designated targets that were marked on real road surface from three sequential positions for different number of cameras and base distances, as shown in Figure 7.

Figure 7. Targets Pattern for Outdoors Experiments

The targets pattern was chosen, like indoor experiments, to be grid in shape with spacing of nearly 50 cm. The grid of targets consisted of 500 points represented such that each transversal line contained 8 points. Each line of targets was painted red, yellow, or white. However, the experiment was performed upon 64 targets that resembles the grid pattern used in indoors experiment. Therefore, the total number of used targets was 64 targets.

The experiments follow the same procedure previously explained in section 3.4. However, since the cameras were used in video mode, IOPs had to be modified to fit aspect ratio of video imagery. Aspect ratio for video imagery is 16:9, while it is 4:3 for still imagery for the used digital cameras.

5. RESULTS AND ANALYSIS

The results of both sets of experiments were assessed in comparison to 3D object space coordinates that were obtained using total station measurements.

The experiments were held with five sets of configurations. Table 2 describes each configuration used within the validation experiments.

Configuration (Config.) Number	Configuration Description
Configuration 1	2 Cameras with maximum base distance 25 cm
Configuration 2	2 Cameras with maximum base distance 100 cm
Configuration 3	2 Cameras with maximum base distance 250 cm
Configuration 4	4 Cameras with maximum base distance 100 cm
Configuration 5	4 Cameras with maximum base distance 250 cm

Table 2. Configuration Descriptions used for System Experimentation

The system was evaluated as per the Root Means Square Errors (RMSE) of differences between system results and total station measurements in X, Y, and Z direction respectively. The RMSE provide an assessment for the absolute position, and provide a measure for the system drift.

Figure 8 shows the RMSE for differences between the proposed system results and total station measurements in X, Y, and Z coordinates for the indoors experiments. While, figure 9 show the RMSE for differences between the proposed system results and total station measurements in X, Y, and Z coordinates for the outdoors experiments.

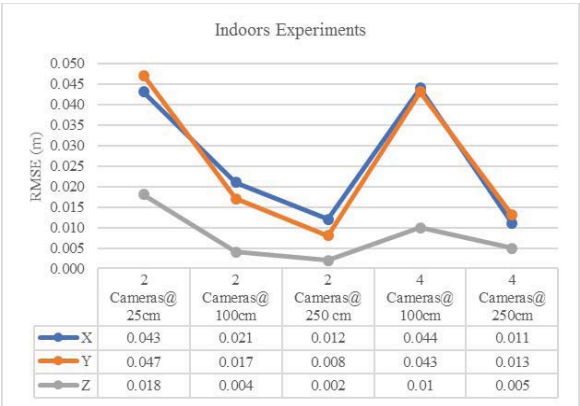

	2 Cameras@ 25cm	2 Cameras@ 100cm	2 Cameras@ 250 cm	4 Cameras@ 100cm	4 Cameras@ 250cm
X	0.043	0.021	0.012	0.044	0.011
Y	0.047	0.017	0.008	0.043	0.013
Z	0.018	0.004	0.002	0.01	0.005

Figure 8. RMSE for differences between the proposed system results and total station measurements for indoors experiments

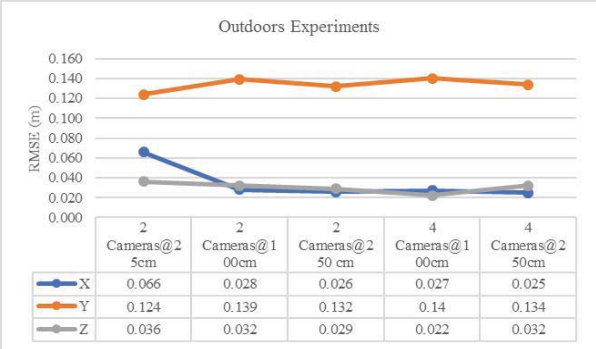

Figure 9. RMSE for differences between the proposed system results and total station measurements for outdoors experiments

The covariance matrices for least squares solutions were computed to determine the precision of image space resection and object space intersection results. Then, the standard deviations are deduced from the covariance matrices. As per, the system workflow, the least squares adjustment was repeated more than once during the experiments. Consequently, the overall relative precision was computed over all the entire system operation by averaging the standard deviations withdrawn from the covariance matrices. Table 3 shows the overall relative precision for the image space resection results for the indoors set of experiments for the five configurations. Whereas, table 4 represents the overall relative precision for the object space coordinates for the indoor set of experiments for the five configurations.

Config.	σ_{X_p}	σ_{Y_p}	σ_{Z_p}	σ_ω	σ_φ	σ_κ
Config. 1	8 mm	5 mm	8 mm	0.42”	0.38”	0.22”
Config. 2	9 mm	4 mm	8 mm	0.41”	0.37”	0.21”
Config. 3	9 mm	6 mm	9 mm	0.42”	0.39”	0.22”
Config. 4	9 mm	4 mm	8 mm	0.43”	0.37”	0.22”
Config. 5	9 mm	6 mm	9 mm	0.44”	0.39”	0.22”

Table 3. Overall relative precision for the image space resection results for the indoors experiments

Config.	σ_X	σ_Y	σ_Z
Config. 1	34 mm	132 mm	53 mm
Config. 2	11 mm	39 mm	17 mm
Config. 3	6 mm	15 mm	7 mm
Config. 4	9 mm	30 mm	13 mm
Config. 5	4 mm	13 mm	6 mm

Table 4. Overall relative precision for the object space coordinates for the indoors experiments

On the other hand, table 5 shows the overall relative precision for the image space resection results for the outdoors set of experiments for the five configurations. Whereas, table 6 represents the overall relative precision for the object space coordinates for the outdoor set of experiments for the five configurations.

Config.	σ_{X_p}	σ_{Y_p}	σ_{Z_p}	σ_ω	σ_φ	σ_κ
Config. 1	29 mm	17 mm	29 mm	1.60”	1.35”	0.65”
Config. 2	36 mm	20 mm	34 mm	1.66”	1.51”	0.72”
Config. 3	37 mm	22 mm	37 mm	1.70”	1.55”	0.85”
Config. 4	42 mm	22 mm	41 mm	1.79”	1.68”	0.77”
Config. 5	37 mm	22 mm	37 mm	1.70”	1.56”	0.85”

Table 5. Overall relative precision for the image space resection results for the outdoors experiments

Config.	σ_X	σ_Y	σ_Z
Config. 1	122 mm	454 mm	217 mm
Config. 2	45 mm	16 mm	72 mm
Config. 3	23 mm	61 mm	31 mm
Config. 4	42 mm	165 mm	69 mm
Config. 5	19 mm	56 mm	27 mm

Table 6. Overall relative precision for the object space coordinates for the outdoors experiments

6. CONCLUSION

In this paper, a low-cost image-based mobile mapping system was developed and validated. The total cost of the system was nearly 650 U.S. dollars. The system consists of a set of digital non-metric consumer grade cameras, that can be used to generate maps of scales 1:2500 or smaller.

Generally, the results show that RMSE using four cameras system with 250 cm baseline provided less values than RMSE obtained from dual cameras system configuration. Quad cameras system configuration provided higher redundancy for observations used to determine all unknown parameters required for mapping and tracking processes.

However, for outdoors experiments RMSE gave higher values than indoors experiments. Indoors experiments were performed within controlled environment eliminating many factors that would have reduced precision of system as imaging mode, and accuracy of image space coordinates determination.

In general, the system met its design objectives, aside from some discrepancies. However, the system was found to drift after first 50 m of operation from initial position to reach RMSE of ± 35 cm. Consequently, the proposed system requires a consistent update of position along its motion trajectory.

REFERENCES

Durrant-Whyte, H., and Bailey, T., 2006. “Simultaneous Localization and Mapping: Part I.” IEEE Robotics and Automation 99-108.

Egels, Y., and Kasser, M. 2003. Digital Photogrammetry. CRC Press.

El-Sheimy, N., and Hassan, T. 2007. “Mobile Mapping Systems - The New Trend in Mapping and GIS Applications.” Ontario Professional Surveyor Magazine, 14-19.

Felicitas, L., and Forstner, W., 1995. Matching Techniques. Bonn: Institut fur Photogrammetrie, Universitat Bonn.

Fraser, C. S., and Al-Ajlouni, S., 2006. “Zoom-Dependent Camera Calibration in Close-Range Photogrammetry.” Photogrammetric Engineering and Remote Sensing (American Society of Photogrammetry and Remote Sensing) 1017-1026.

Fuentes-Pacheco, J., Rulz-Ascencio, J., and Manuel Rendon-Mancha, J., 2012. “Visual simultaneous localization and mapping: a survey.” Springer Science 55-80.

Gruen, A., 1997. “Fundamentals of videogrammetry - A review.” Human Movement Science 155-187.

Krishnan, A., and J. Kollipara. 2014. “Intelligent Indoor Mobile Robot Navigation Using Stereo Vision.” Signal & Image Processing : An International Journal (SIPIJ) 5 (4): 45-53.

Kwiatek, K., and Tokarczyk R., 2014. “Photogrammetric Applications Of Immersive Video Cameras.” ISPRS Technical Commission V Symposium. Riva del Garda, Italy. 211-218.

Lemus, R., S. Diaz, C. Gutiérrez, D. Rodríguez, and F. Escobar. 2014. “SLAM-R Algorithm of Simultaneous Localization and Mapping Using RFID for Obstacle Location and Recognition.” Journal of Applied Research and Technology 551-559.

Li, R., 1997. “Mobile Mapping: An Emerging Technology for Spatial Data Acquisition.” Photogrammetric Engineering & Remote Sensing 63 (9): 1085-1092.

Luhmann, Thomas, Robson, S., Kyle, S., and Boehm, J., 2013. Close-Range Photogrammetry and 3D Imaging. London: Walter de Gruyter.

Mc Glone, J. C., Mikhail, E. M., Bethel J. S., and Mullen R., 2004. Manual for Photogrammetry. American Society of Photogrammetry and Remote Sensing.

Mikhail, E., and Graci G., 1981. Analysis and adjustment of survey measurements. New York: Van Notstr and Reinhold company.

Mikhail, E., and Ackermann, F. 1982. Observations and Least Squares. University Press of America.

Mortenson, M. 2007. Geometric Transformations for 3D Modeling. Michigan: Industrial Press.

Schenk, T., 2005. “Introduction to Photogrammetry.” Department of Civil and Environmental Engineering and Geodetic Science, The Ohio State University, Columbus, 54-55.

Siciliano, B., and Khatib, O., 2008. Springer Handbook of Robotics. Heidelbeerg: Springer.

Low-Cost GNSS/MEMS Sensors integrated Vision System for Motion and Position Estimation of a bicycle

H.W. Chang [a]*

[a] Dept. of Geomatics Engineering, National Cheng Kung University, Tainan, Taiwan – hwchang@mail.ncku.edu.tw[b] Dept. of

KEY WORDS: MEMS, Bicycle, Kalman Filter, CDR, Optical flow

ABSTRACT:

In the past decade, the low-cost sensors such as inertial sensors, Global Navigation Satellite System (GNSS) and camera are commonly embedded in modern smartphone. These Micro Electro-Mechanical Systems (MEMS) based sensors have covered various measurements that enable the new application for smartphone. The possibility of using smartphone to navigate with significant accuracy has blooming rapidly as well as complementary application like gaming. Beside navigation purpose, camera in the smartphone has been used as event data recorder or frequently used for capturing images. Inspired by these new applications, this research tends to extend Cycle Dead Reckoning (CDR) algorithm with vision feedback. CDR is an algorithm that integrates GNSS/MEMS sensors to derive speed model based on pedalling frequency. Its major contribution is when the system lost the satellite signal, it continuously monitoring pedalling motion in order to derive stable speed compared to INS. In comparison to traditional GNSS/MEMS integration, CDR has the advantage of lower complexity while the rider is pedalling under GNSS denied environment. However, CDR cannot work in some scenario such as downhill sliding or idling or inaccurate transformation matrix between sensors frame to platform. To reach the objective of accurate and continuous positioning and integrate response events, this paper applies fast optical flow estimation to obtain misalignment for the use of CDR.

1. INTRODUCTION

With the Micro-Electric Mechanical System (MEMS) techniques, equipment is no long cumbersome and expensive. MEMS-based sensors are widely used in many products such as phones, watches, glasses, shoes, tablets, belts or other wearable devices. These common embedded sensors include inertial sensors for angular rate and acceleration, barometer for pressure measurement, magnetometer for magnetic field measurements, GNSS for receiving wireless communication for positioning, etc. The advantages of using MEMS-sensors eliminate the need of always continuous wireless signal connection and wired data communication which increases the portability and seamless functions in many different applications. Thanks to the continuous evolution of motion sensors (accelerometer and gyroscopes), human motion can now be assessed outside a laboratory simply and apply easily to different daily commute. The measurements provided by these motion sensors include raw acceleration, angular rate, height, and heading. Motion sensors are self-contained and do not rely on the transmission or reception of signals, thereby minimizing problems such as, signal blockage, attenuation, jamming, and multipath characteristic of synthetic environments. In addition, MEMS-based sensors have been widely applied for orientation tracking (Eisenman, Miluzzo et al. 2007, Sadi and Klukas 2013), and human body's upper limb motion (Chang, Georgy et al. 2013).

With the evolution of motion sensors, human motion can now be easily assessed. No sophisticated setup is needed. This assessment can be done with a set of sensors, such as accelerometers, gyroscopes, barometers, and magnetometers. With the recent advancements in Micro-Electro-Mechanical Systems (MEMS), MEMS-based sensors can be easily incorporated into small portable devices. MEMS-based sensors are ideal for use in sport applications to record and monitor human motion because of their low cost, light weight, small size, and low power consumption.

Cycling is considered a means of transportation in some countries, while it is a popular form of recreation in a lot of other countries. Cycling also has other general fitness, military and sport applications, among others. The capability to obtain a meaningful navigation solution for cycling applications using a portable device in any orientation and without any constraints is beneficial for both normal consumers and athletes. Enabling cycling navigation on freely-used portable devices, although it is a hard problem, will consequently enable many applications.

The Global Navigation Satellite System (GNSS) has been the most common technique used to provide position and velocity information. It can be found in many commercial cycling navigators, such as in the Edge from Garmin. However, GNSS requires a direct line of sight to four or more satellites to estimate a position, which becomes an issue when the line of sight is obscured. Other wireless positioning techniques have been proposed as integrated technologies with GNSS to position the user while indoors or in urban areas, where GNSS is obstructed or unavailable. These include WLAN (IEEE 802.11), Bluetooth (IEEE 802.15) and others. Usually these supplementary wireless positioning techniques require extra cost due to initial installment and maintenance of infrastructure. Besides the unfathomable cost to install and maintain such infrastructure in all buildings, receiving wireless signals continuously at all times in all places is also completely

* Corresponding author

unrealistic. In addition, communicating with wireless positioning techniques for positioning could potentially expose personal information. Consumers value their privacy, which might reduce the desire of using such an application. Therefore, it is important to use other techniques to provide viable navigation solutions in all environments.

For a long time, the common technique for solving this problem is to augment GNSS with complementary sensors. The complementary and autonomous sensors include inertial navigation systems (INS), odometers, magnetometers and barometers, etc. In order to achieve a continuous and uninterrupted navigation solution, navigation algorithms should be able to work in many different common scenarios, such as driving (in-vehicle navigation), walking (pedestrian navigation) and riding bicycle (cycling navigation). All of the aforementioned scenarios are typical to a daily commute. For the past decades, the most mature navigation algorithms were designed for in-vehicle navigation using heavy, expensive and complex devices; see for example (Chiang and Chang 2010) (Niu, Nasser et al. 2007, Syed, Noureldin et al. 2010). After several years of development, new navigation algorithms designed for pedestrian navigation have been proposed and improved significantly (Harle 2013). With the advanced sensors and techniques mentioned previously, consumers and mainstream users can expect to easily mount a personal navigation device (PND), which could be their smartphone, to a vehicle, bicycle, or to their own body (Chang, Georgy et al. 2012)

In order to mitigate position errors accumulated during GNSS outages, Cycling Dead Reckoning (CDR) was proposed by the authors (Chang, Georgy et al. 2013). CDR highly outperforms traditional INS in cycling applications using portable devices, the same way Pedestrian Dead Reckoning (PDR) highly outperforms INS in walking applications. The proposed CDR relies on detecting pedaling cycles using gyroscope readings and the derived pitch and roll. The periodic cycling motion causes sinusoidal signals in pitch and/or roll values. Pedaling cycles are detected and pedaling frequency is calculated. With the reference speed and position (from GNSS or others), the models connect the pedaling frequency to the forward speed, and the detected cycles to the travelled distance. Misalignment derived from optical flow is then used to transfer forward speed and travelled distance into velocity and position. The details of these methods and routines will be described in the methodology section. The results section will then demonstrate the possibility of using optical flow to estimate misalignment and compare the position performance with different misalignment estimation. Finally, the conclusion section will summarize the proposed navigation solution.

1. METHODOLOGY

A typical GNSS/ inertial sensor integration, aided by other MEMS-based magnetometers and a barometer, is proposed as the core scheme. An overview of the proposed cycling navigator is illustrated in Figure 1. Three different cases are considered in the proposed system: 1) when GNSS signals are available, the system updates state vectors with GNSS position and velocity updates, magnetometer and barometer updates, as well as Non-Holonomic Constraint (NHC) updates using the estimated transformation matrix between the sensor frame and the bicycle's frame. This GNSS position and velocity information is also fed to the CDR for the training phase if pedaling motion is detected, as well as road slope information within a certain threshold. If the non-pedaling motion is detected, no training takes place; 2) during GNSS outages or degradation and when pedaling motion is detected, the proposed system applies the detected pedaling cycles and frequency to the CDR to generate position and velocity updates, and then feeds these updates to the integrated navigation solution; 3) during GNSS outages or degradation and when no pedaling is detected, the proposed scheme will not apply CDR, but will use the integrated navigation solution with NHC and other possible updates, such as with the magnetometer and barometer. The following paragraphs introduce coordinate frames relationships and the required matrix to integrate multiple sensors. Then it describes the use of the algorithm of GNSS/INS which can provide the attitude solution needed for the consequent algorithms. The next subsection describes the pedaling/non-pedaling algorithm, followed by the training and utilization phases of CDR. Finally is the innovative part of using optical flow to estimate misalignment.

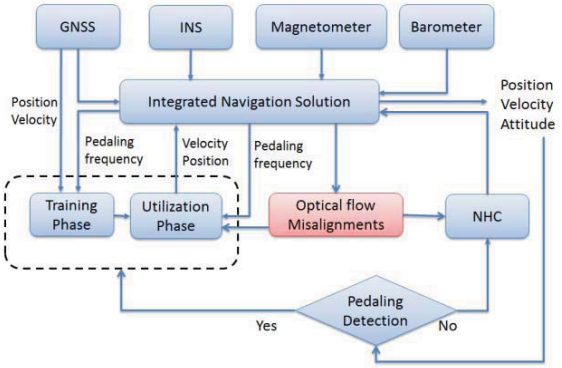

Figure 1. Block diagram of the overall system.

1.1 Illustrations of the coordinates

Motion constraints are coming from the knowledge of common law of specific motion in the platform. Therefore, the constraints are given in the platform frame. Traditional systems (such as vehicle navigation) with tethered sensors easily use constraints because of the non-varying misalignment between frames. The misalignment between the sensors frame (b –frame) and the platform or vehicle frame (v –frame) raises the need to form a transformation matrix (here after, defined as C_b^v). In traditional application with mounting misalignment, C_b^v is fixed. However, for portable application the phone can be carried anywhere on a human or bicycle such as on chest, arm, belt, thigh or lower leg. In this case, C_b^v is a time-varying matrix which must be estimated before employing motion constraints and updates. Figure 2 shows the definitions of the four frames used in this paper. As shown in this figure, the x-axis in v-frame represents the forward direction; the z-axis in v-frame represents the downward direction; and the y-axis represents a complete right-handed system. The l-frame chosen in this paper is North-East-Down (NED) frame, which means the x-axis points geodetic north, the z-axis is orthogonal to the reference ellipsoid and points down to the earth, and the y-axis represents a complete right-handed system. The image frame of x-axis coincides with the y-axis in b frame and y-axis in image frame coincides with the opposite direction of x-axis in b frame.

A misalignment angle is defined as the angle given by the b-frame less the angle given by the v-frame. To be more specific, please refer to (Chang, Georgy et al. 2015). In figure 3, it depicts the heading misalignment used in this paper. The roll and pitch values given in the b-frame are provided by inertial sensors while heading values can be provided either by the

gyroscope with given initial heading or by magnetometer. The original work in estimating this heading misalignment is by an algorithm that checks the raw data of acceleration with the roll and pitch values within each pedaling cycle. And therefore, it has two disadvantages: the estimated heading misalignment rate depends on the cycling rate; without pedaling the relationship used in the previous work will stop functioning.

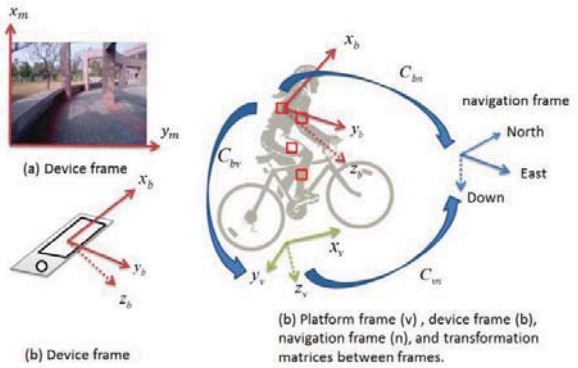

Figure 2. Definitions of each corrdinate frames and transformation matrices

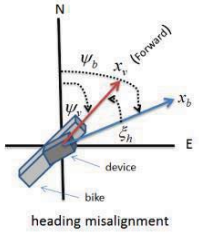

Figure 3. Heading misalignment

1.2 GNSS/INS integration

Assume the accelerometer and the gyroscope are lying perfectly on a horizontal plane, and the measured acceleration represents the specific force applied on the sensor itself. Then an object's position and velocity can be estimated by integrations. However, in the real world, the sensors seldom lie perfectly along a horizontal plane. Theoretically, any static object on earth suffers gravitational force and earth rotational rate. Therefore, the readings from the gyroscope are important to derive the transformation matrix between the sensors frame (b –frame) and navigation or local level frame (l–frame). With this matrix, the gravitational component and the earth rotation rate can be deprived and the target's acceleration remains. The mathematical equation of this procedure is defined as mechanization (El-Sheimy 2006). A simple form of the mechanization equation in the local level frame can be expressed as follows:

$$\begin{bmatrix} \dot{r}^l \\ \dot{v}^l \\ \dot{C}_b^l \end{bmatrix} = \begin{bmatrix} D^{-1}v^l \\ C_b^l f^b - 2(\Omega_{ie}^l + \Omega_{el}^l)v^l + g^l \\ C_b^l(\Omega_{ib}^b + \Omega_{il}^b) \end{bmatrix} \quad (1)$$

where r^l is the position vector, v^l is the velocity vector, C_b^l is the transformation matrix from the b-frame to l-frame, g^l is the gravity vector in l-frame, $\Omega_{ib}^b, \Omega_{il}^b$ are the skew-symmetric matrices of the angular velocity vectors $\omega_{ib}^b, \omega_{il}^b$ respectively, D^{-1} is a 3x3 matrix as a functions of the user's latitude and ellipsoidal height.

EKF is a process of obtaining a set of values for a set of parameters from a set of observations. EKF consists of two parts: (1) prediction that uses the system model to predict the solution in the next epoch; and (2) Updates that fuse the new observation to the modified predicted solution. Typically, GNSS/INS integration uses high data rate sensor readings in the system model to calculate how the state vector changes over time and uses low data rate observations to update the current state vector. In this paper, four types of observation are used in the update stage: (1) position and velocity updates from GNSS; (2) height updates from the barometer; (3) heading updates from the magnetometer; and (4) motion constraints from the position domain. With the additional velocity measurement given in bicycle-frame and estimated velocity, the following linearized velocity observation model is used:

$$\begin{aligned} \delta z_v &= \hat{v}^v - \tilde{v}^v = v^v - \begin{bmatrix} V_{f,j} \\ 0 \\ 0 \end{bmatrix} \\ &= C_b^v C_n^b \delta v_{IMU}^n - C_b^v C_n^b (v_{IMU}^n \times)\delta\psi - e_v \end{aligned} \quad (2)$$

where $\hat{v}^v$ is the predicted velocity from the integrated navigation solution given in v-frame, $\tilde{v}^v$ is the measurement velocity given in v-frame, δv_{IMU}^n is the velocity error of the inertial sensors given in n-frame, $v_{IMU}^n \times$ is the skew-symmetric form of velocity vector, e_v is the velocity error in meters/second, $\delta\Psi$ is the attitude errors; $V_{f,j}$ is the forward speed derived from the chosen speed model; and C_n^b is the estimated transformation matrix between n-frame and b-frame.

$$\begin{aligned} \Delta P_f &= C_p \times \hat{s} \\ E_{k+1} &= \Delta P_f \sin(A_z) + E_k \\ N_{k+1} &= \Delta P_f \cos(A_z) + N_k \end{aligned} \quad (3)$$

where C_p is the number of detected cycles; A_z is the azimuth (heading) of the platform (i.e. bicycle), which is derived from the portable device heading and the heading misalignment; and E_k, N_k are the derived east and north position at time k. For a complete detailed equation of the EKF loop, see (Gelb 1999).

1.3 Pedaling/Non-pedaling algorithm

The pedaling detection algorithm uses Fast Fourier Transform (FFT) and autocorrelation to detect possible frequency of the attitude signal. Peak detection is applied to detect peaks in the attitude signal according to the given threshold of slope. The average time interval between peaks will be used to double check the pedaling frequency detected by FFT or autocorrelation. If the time interval between peaks and the amplitude at the peaks are consistent, the forward speed, pedaling frequency and heading rate are recorded for each complete cycle. Finally, a validation process is applied to prevent irregular motion. It checks the current and previous speeds, frequencies and heading rates between two detected sequential cycles, if they are within reasonable ranges, the conditions are satisfied and pedaling cycles are detected. The measurements from accelerometers and gyroscopes within each detected cycle are then used to calculate the 3D misalignments.

1.4 Optical flow estimation to heading misalignment

Vision based module that determines the device heading misalignment was proposed by (Kazemipur 2015). However, optical flow is not a new technique. Optical flow has been used extensively for obstacle avoidance, terrain following, visual servo control and localization (Herissé, Hamel et al. 2012). The idea is based on the apparent motion of brightness patterns within a sequence of images. In order to maintain this assumption of consistency of brightness patterns and accelerate the process for real-time application, it is important to do the following four pre-processing: (1) size reduction from 1080x1920 pixels to 108x192 (factor of 10%) at frame rate 30 fps. (2) grayscale conversion (3) histogram equalization and (4) image smoothing. Because of the limitation of the content, complete equations of these pro-processing please refer to (Kazemipur 2015).

Formally, brightness constancy is the assumption that a pixel at location (x,y,t) with intensity I(x,y,t) will have moved by Δx and Δy in the interval between images Δt (Farnebäck 2000).

$$\mathrm{I}(\mathrm{x},\mathrm{y},\mathrm{t}) = \mathrm{I}(\mathrm{x}+\Delta\mathrm{x},\mathrm{y}+\Delta\mathrm{y},\mathrm{t}+\Delta\mathrm{t}) \tag{4}$$

Assuming the movement is not too big that the Equation (4) can be expanded using a first-order approximation of Taylor series:

$$\mathrm{I}(\mathrm{x}+\Delta\mathrm{x},\mathrm{y}+\Delta\mathrm{y},\mathrm{t}+\Delta\mathrm{t}) = \mathrm{I}(\mathrm{x},\mathrm{y},\mathrm{t}) + \frac{\delta I}{\delta x}\Delta x + \frac{\delta I}{\delta y}\Delta y + \frac{\delta I}{\delta t}\Delta t \tag{5}$$

where $(\frac{\delta \mathrm{I}}{\delta \mathrm{x}}, \frac{\delta I}{\delta y})$ is the spatial derivative of the image intensities and $\frac{\delta \mathrm{I}}{\delta \mathrm{t}}$ is the temporal derivative. The spatial derivative can be obtained by convolving the image with a selective mask such as Sobel filter and aggregating the result across the image (Ying-Dong, Cheng-Song et al. 2005) and the temporal derivative can be obtained by convolving two sequent images. Obviously when the Equation (5) is satisfied, it yields:

$$\frac{\delta I}{\delta x}\Delta x + \frac{\delta I}{\delta y}\Delta y + \frac{\delta I}{\delta t}\Delta t = 0 \tag{6}$$

Dividing each term by the time interval Δt:

$$\frac{\delta I}{\delta x}\mu_{\mathrm{x}} + \frac{\delta I}{\delta y}\mu_{\mathrm{y}} + \frac{\delta I}{\delta t} = 0 \tag{7}$$

Where the $\mu_{\mathrm{x}}\ and\ \mu_y$ are the x and y components of the velocity and referred to as the optical flow. In order to solve this equation which has two unknown and one condition, many methods have been proposed such as Horn-Schunck method (Horn and Schunck 1981) and Lucas-Kanade method (Lucas and Kanade 1981). Here in this paper, the conjugate gradient is applied to solve large linear systems instead of Gauss-Seidel. The advantage of this method is that it does not try to solve equation Ax=b which contains large matrix, it only need to write a function that consists of filtering and weighting to apply A to x (Liu, Freeman et al. 2008). In the experiment, it shows the better immunity to vibration and bigger movement. The results will be shown in the result section.

1.5 CDR training and utilization

CDR is trained one time and usually finished within few minutes under open sky and good GNSS environment. The idea is to build the relationship between pedaling frequency and forward speed, as well as detected cycles and travelled distance. Without changing the gear, the pedaling frequency affects forward speed linearly. After the CDR module training is complete, it predicts the forward speed from pedaling frequency and predicts the travelled distance from the detected cycles. (No need to have GNSS) Equation (8) shows the trained speed model.

$$\mathrm{V_k} = \mathrm{a} \times \mathrm{f_k} + \mathrm{b} \tag{8}$$

where slope *a* and offset *b* are estimated during GNSS availability, $\mathrm{f_k}$ is the detected pedaling frequency at time *k,* and $\mathrm{V_k}$ is the forward speed derived from GNSS during the training phase or the predicted forward speed with given pedaling frequency during the utilization phase.

The travelled distance (*s*) during each complete cycle is theoretically constant (at a certain gear ratio), and therefore this value is calculated by averaging the distance travelled, which is calculated from the GNSS positions provided by several detected cycles to remove blunders. By knowing the exact beginning time and ending time for each cycle, the travelled distance s of i cycle is defined as:

$$\mathrm{s_i} = \widehat{\mathrm{V}}_{\mathrm{i}} \times \Delta\mathrm{t} \tag{9}$$

where $\widehat{\mathrm{V}}_{\mathrm{i}}$is the mean value of horizontal forward speed derived from the reference system during the i cycle; Δt is the time spent for each cycle. Given sufficient training pairs at the single gear selection, the mean value of *s* is defined as reference travelled distance ($\widehat{\mathrm{S}}$). Equation (8) and (9) are then feed into EKF by using Equation (2) and (3).

2. RESULTS

To evaluate the performance of the proposed methods, experiments were performed with smartphone. The device information is shown in Table 1. The palnned route of this experiment is shown in Figure 4.

Sony Xperia Z3	Information
Dimension	146×72×7.3 mm
Weight	152 g
CPU	Quad-core 2.5 GHz
GPU	Adreno 330
Camera	20.7MP,f/2.0,25mm
GNSS	A-GPS,GLONASS,BDS

Table 1. related information of Sony Xpera Z3

Figure 4. planned route of this experiment

A device that contains an accelerometer triad, a gyroscope triad, a 3D magnetometer, and a barometer was used to collect the experimental data. The first task is to see the accuracy and image processing speed of heading misalignment estimation. Therefore the phone is carried in hand to rotate the device with expected angle. For having the reference heading misalignment, currently this is the way to have the coarse expected values. The second task is the use of heading misalignment for the update using NHC and CDR.

2.1 Estimation of misalignment

After the dual-channel (μ_x, μ_y) flow map F has been obtained, the single channel matrices $\mu_{x_k}(x,y) and\ \mu_{y_k}(x,y)$ are derived by splitting F. Then the misalignment is derived by the following equations:

$$\theta_k = \tan^{-1}\left(\sum_{j=0}^{N_y-1}\sum_{i=0}^{N_x-1}\mu_{y_k}(i,j), \sum_{j=0}^{N_y-1}\sum_{i=0}^{N_x-1}\mu_{x_k}(i,j)\right) \quad (10)$$

Figure 5 shows the results from one of the video with different designed of heading misalignments. At a device angle of zero degrees from 0 to 8s, a strong flow in the positive x-direction is observed with minor oscillations occurring in the y-direction. Therefore, the misalignments are close to expected angle zero. However, the fluctuation is observed according the steps motions. In the (Kazemipur 2015), the results also have these and even stronger fluctuation. This can be mitigated by smoothing the results like in this reference. Rotating the device at 8 to 12 s to -90 degree orientation resulted in a strong flow in the y-direction with a reduced flow in x-direction. It is noticed that during the rotation (around 8s), the estimation is not accurate because of the extremely large movements of the pixels. Finally the device is rotated again to -50 degree. In this figure, the blue line represents the forward half part of image which has no relative moving objects. In another words, the image objects move because of the movement of camera. The red line however, could have catch the user's feet in some images. It shows the effects of having relative moving objects will degrade the heading misalignment estimation.

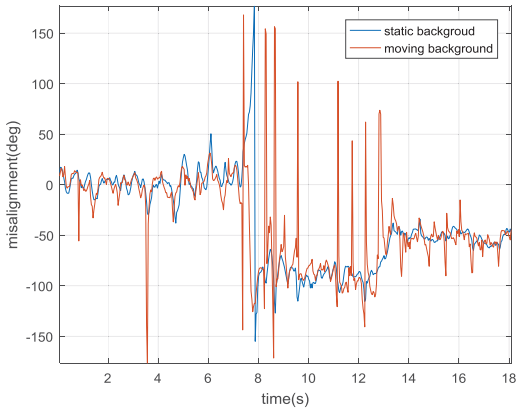

Figure 5. Heading misalignment by optical flow.

2.2 Trajectory of the bike

Figure 6 shows the results of the trajectory. As shown in this figure, the integrated GNSS/CDR/Vision shows an acceptable result in blue line while the estimation from GNSS/MEMS inertial sensors give an unreasonable result (not shown in this figure because it will make the major part becomes too small) easily due to the accumulated error speed of inertial systems errors is too fast.

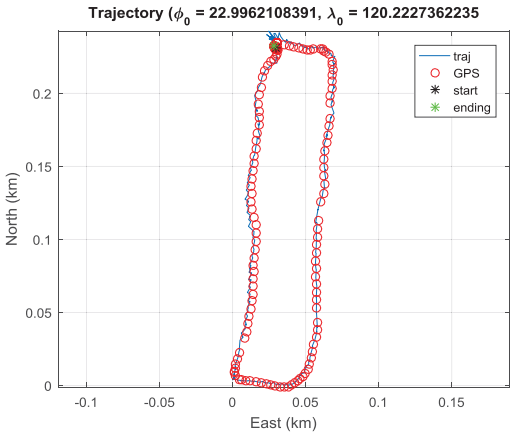

Figure 6. Trajectory result

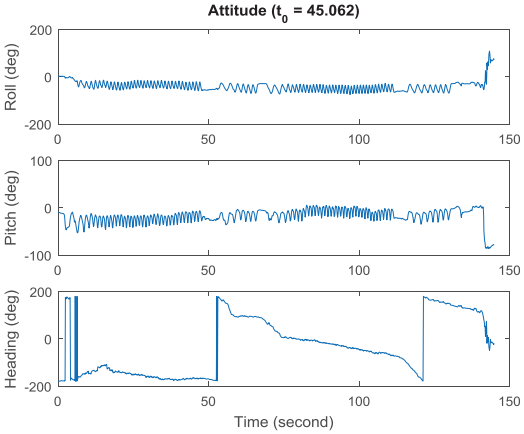

Figure 7. Attitude estimation

In the Figure 7, the roll and pitch have caught the pedalling motion because the sensors are in the pockets. It is worth mention that for low cost inertial sensors (typically found in smartphone) to estimate full navigation solution (position, velocity and attitude) is a very challenging task especially when the devices are suffering significant motions. In this test, both position and attitude are good enough to give readable results. Currently the misalignment using optical flow was implemented on MATLAB with average 0.4s in finishing one process. This could be easily increased by using GPU or others.

3. CONCLUSION AND FUTURE WORK

This paper has shown the continuous work on the development of CDR used in low-cost multiple sensor integration. The proposed heading misalignment estimation by optical flow can be used for vehicle, pedestrian walking motion or cycling when the camera catches images. Considering the failure rate of feature detection based computer vison, the optical flow method is chosen to increase the successful rate of estimation. However, it is also possible to use Visual Odometer to estimate the heading misalignment. Another potential method is the use of deep learning such as (Fischer, Dosovitskiy et al. 2015). It is important to know that in order to increase the effectiveness of

NHC, the time-vary heading misalignment is needed in high data rate.

ACKNOWLEDGEMENTS

The author would acknowledge the financial support by the Ministry of Science and Technology, ROC (Taiwan) (MOST 105-2119-M-006-019-MY2)

REFERENCES

Chang, H.-W., J. Georgy and N. El-Sheimy (2012). Low Cost Multi-Sensors Navigation Solution for Sport Performance Assessment. ION GNSS 2012, Nashville, Tennessee, USA.

Chang, H.-W., J. Georgy and N. El-Sheimy (2013). "Cycling Derived Models for Enhancing Navigation Performance of a Low Cost Multi-Sensors System." Journal of Aeronautics, Astronautics and Aviation **45**(3): 179-186.

Chang, H. W., J. Georgy and N. El-Sheimy (2015). "Improved Cycling Navigation Using Inertial Sensors Measurements From Portable Devices With Arbitrary Orientation." IEEE Transactions on Instrumentation and Measurement **64**(7): 2012-2019.

Chiang, K.-W. and H.-W. Chang (2010). "Intelligent Sensor Positioning and Orientation Through Constructive Neural Network-Embedded INS/GPS Integration Algorithms." Sensors **10**(10): 9252-9285.

Eisenman, S. B., E. Miluzzo, N. D. Lane, R. A. Peterson, G.-S. Ahn and A. T. Campbell (2007). "BikeNet: A mobile sensing system for cyclist experience mapping." ACM SenSys.: 87-101.

El-Sheimy, N. (2006). Inertial Techniques and INS/DGPS Integration. ENGO 623-course notes. Calgary, Canada, Department of Geomatics Engineering, University of Calgary.

Farnebäck, G. (2000). Orientation Estimation Based on Weighted Projection onto Quadratic Polynomials. VMV.

Fischer, P., A. Dosovitskiy, E. Ilg, P. Häusser, C. Hazırbaş, V. Golkov, P. van der Smagt, D. Cremers and T. Brox (2015). "Flownet: Learning optical flow with convolutional networks." arXiv preprint arXiv:1504.06852.

Gelb, A. (1999). Applied optimal estimation, MIT Press.

Harle, R. (2013). "A survey of indoor inertial positioning systems for pedestrians." IEEE communications surveys and tutorials **15**(3): 1281-1293.

Herissé, B., T. Hamel, R. Mahony and F.-X. Russotto (2012). "Landing a VTOL unmanned aerial vehicle on a moving platform using optical flow." IEEE Transactions on Robotics **28**(1): 77-89.

Horn, B. K. and B. G. Schunck (1981). "Determining optical flow." Artificial intelligence **17**(1-3): 185-203.

Kazemipur, B. (2015). Computer Vision Aiding Smartphone Sensors for Indoor Location Applications, University of Calgary.

Liu, C., W. T. Freeman, E. H. Adelson and Y. Weiss (2008). Human-assisted motion annotation. Computer Vision and Pattern Recognition, 2008. CVPR 2008. IEEE Conference on, IEEE.

Lucas, B. D. and T. Kanade (1981). "An iterative image registration technique with an application to stereo vision."

Niu, X., S. Nasser, C. Goodall and N. El-Sheimy (2007). "A universal approach for processing any MEMS inertial sensor configuration for land-vehicle navigation." Journal of Navigation **60**(02): 233-245.

Sadi, F. and R. Klukas (2013). "New jump trajectory determination method using low-cost MEMS sensor fusion and augmented observations for GPS/INS integration." GPS Solutions **17**(2): 139-152.

Syed, Z., A. Noureldin and N. El-Sheimy (2010). Positioning Platform for Low-cost, Accurate, Infrastructure-free Machine Control. ION GNSS, Oregon, Portland.

Ying-Dong, Q., C. Cheng-Song, C. San-Ben and L. Jin-Quan (2005). "A fast subpixel edge detection method using Sobel–Zernike moments operator." Image and Vision Computing **23**(1): 11-17.

ACCELERATING THE CONVERGENCE PERIOD OF GPS/GLONASS PRECISE POINT POSITIONING USING PSEUDORANGE MULTIPATH AND NOISE MITIGATION

M.Abou-Galala[a*], Mosbeh R.Kaloop[a**], Mostafa Rabah[b] and Zaki M.Zidan[a]

[a] Department of Public Works Engineering, Mansoura University, Mansoura 35516, Egypt
[b] Department of Civil Engineering, Benha University, Benha, Egypt
(*mabougalala@yahoo.com, **mosbeh@mans.edu.eg)

KEY WORDS: Precise Point Positioning, GPS, GLONASS, TEQC, Multipath, Convergence Period.

ABSTRACT:

A major limitation of precise point positioning (PPP) is that it needs a long convergence period to obtain the steady-state float ambiguities. This slow convergence is largely caused by the slow change of satellite geometry and the remaining un-modeled errors. In contrast, with combining GPS and GLONASS observations, the more visible satellites can improve the poor satellite geometry distribution, and then a reduction in the convergence period can be achieved. By mitigating the multipath and noise in pseudoranges, the float ambiguity estimates can be more accurate rapidly, and therefore the PPP convergence period can be reduced. This study introduces the pseudorange multipath and noise mitigation to a combined GPS/GLONASS PPP model, aiming to shorten the PPP convergence period. TEQC multipath linear combination or observable is used to compute the pseudorange multipath and noise corrections. Pseudorange multipath and noise are mitigated using two methods: firstly, direct multipath observable corrections in the PPP functional model; and secondly, weights derived from the multipath observable in the PPP stochastic model. 7-day data sets from 108 globally distributed IGS stations were utilized. The results indicated that combining GLONASS observations with GPS-only PPP can reduce the convergence period by 32 % in case of equal- weighted pseudoranges for each system. In addition, the weights derived from TEQC multipath observable can reduce the convergence period of combined GPS/GLONASS-PPP by 25 %.

1. INTRODUCTION

Within the last 15 years, Precise Point Positioning (PPP) has received increasing attentions from the GNSS scholars until it recently becomes the preferred technique in a wide range of the scientific and commercial applications. The PPP is an elegant positioning method that can achieve sub-centimetre horizontal and few centimetres vertical accuracy with a single static dual-frequency GNSS receiver along with precise IGS satellite orbit and clock corrections; and modelling of some special errors (Zumberge et al. 1997; Kouba and Héroux 2001; Seepersad and Bisnath, 2014).

Although PPP is an easy, cost-effective and high-accuracy positioning method, it still suffers a long convergence period which prevents the use of PPP in the high-accuracy real-time positioning applications. The convergence period can be defined as how long the solution took for the coordinates or the ambiguities reach a specific accuracy or a steady state, then no leaving it. The sources of this long convergence period are the slow change of satellite geometry and imprecise noisy code measurements (Geng et al. 2011). First, slow changes of poor satellite geometry result in a strong correlation between the inaccurate ambiguities and position estimates (Li and Shen, 2010), which in turn lengthens the convergence period. Second, imprecise noisy code measurements are used in initialization of the ambiguity values, which will be consequently far from the accurate ambiguity values and consequently a long period is required to obtain the accurate values.

For reducing the convergence period, many efforts have been made through some ways such as: modeling or mitigating the unmanaged PPP biases, ambiguity resolution and combining two or more satellite systems together. El-sobeiey and El-rabbany (2012) designed a rigorous model for the second-order ionospheric effect in order to shorten the PPP convergence period. They concluded that the convergence period was reduced by 15% in case of the second-order ionospheric effect was accounted for. Li and Zhang (2014) utilized GPS and GLONASS PPP with fixed GPS ambiguities and float GLONASS ambiguities. Their results showed that the convergence period was shortened by 40%. Lou et al. (2015) combined the GPS, GLONASS, BeiDou and Galileo observations for improving the accuracy and convergence of PPP. They found that the convergence period improvement was more than 60 % for both single- and dual-frequency PPP. Li et al. (2015) investigated the GPS, GLONASS, BeiDou, and Galileo data for the real-time PPP and found that the convergence period were improved by 70 % to about 11 min. Geng and Shi (2016) resolved undifferenced ambiguities for both GPS and GLONASS simultaneously by estimating accurate ionosphere-relevant fractional cycle biases (FCBs) from a dense network for reducing the real-time PPP initialization period. The initialization period was reduced from over 30 min to 17 min and 50 % of initialization periods were less than 5 min.

Exiting techniques for multipath mitigation and detection can be categorized into three main branches: antenna-based techniques, receiver signal filtering techniques and observation data processing techniques (Dai et al. 2014; Moradi et al. 2015). Firstly, antenna-based techniques comprise using a choke-ring antenna or ground plane (Tranquilla et al., 1994); using a right-hand circularly polarized (RHCP) antenna; using multi-antenna arrays (Ray et al., 1999); and selecting the antenna location for an environment without reflective objects. Secondly, receiver signal filtering techniques include using a narrow correlator (Van Dierendonck et al., 1992); using a strobe correlator (Townsend et al., 1995); and using a vision correlator (Fenton and Jones, 2005). Thirdly, observation data processing techniques involve the multipath linear combination (Moradi et al. 2015; Wang et al. 2015; Seepersad and Bisnath,

2015); using the wavelet transform (Satirapod and Rizos 2005); sidereal filtering inside the observation domain (Dong et al. 2016; Fuhrmann et al., 2015); sidereal filtering inside the coordinate domain (Larson et al., 2007); estimating multipath by the ray tracing (Lau and Cross, 2007); and weighting schemes depending on the elevation angle (Collins and Langley, 1999) or the signal-to-noise ratio (Bilich and Larson, 2007).

Therefore, the main aim of this paper is to reduce the PPP convergence period that is important for applying the PPP in the commercial GNSS applications. In addition, the reduction of GPS/GLONASS PPP convergence period is done by using TEQC multipath linear combination or observable to mitigate the pseudorange multipath and noise in the functional and stochastic PPP model. Also, a proposed weighting scheme based on TEQC multipath corrections is implemented here. This paper is organized as follows: first, the combined GPS/GLONASS PPP model and the two proposed methods for multipath mitigation are described. Then, the data collection and experimental setup for this study are illustrated. After that, the results and analysis of the performance of the combined PPP model and the two methods in reducing the PPP convergence period are presented and discussed. Finally, the conclusions are given.

2. METHODS

2.1 Combined GPS/GLONASS PPP Model

The basic undifferenced pseudorange and carrier phase between a (GPS or GLONASS) satellite s and a receiver r can be expressed as follows (Cai and Gao, 2013; Li and Zhang, 2014):

$$P_{r,j}^{s,G} = \rho_r^s + c(dt_{r,j}^G - dt^{s,G}) + T^{s,G} + I_{r,j}^{s,G} + B_{r,j}^G - B_j^{s,G} + e_{r,j}^{s,G} \quad (1)$$

$$\phi_{r,j}^{s,G} = \rho_r^s + c(dt_{r,j}^G - dt^{s,G}) + T^{s,G} - I_{r,j}^{s,G} + \lambda_j(N_{r,j}^{s,G} + b_{r,j}^G - b_j^{s,G}) + \varepsilon_{r,j}^{s,G} \quad (2)$$

$$P_{r,j}^{s,R} = \rho_r^s + c(dt_{r,j}^R - dt^{s,R}) + T^{s,R} + I_{r,j}^{s,R} + B_{r,j}^R - B_j^{s,R} + e_{r,j}^{s,R} \quad (3)$$

$$\phi_{r,j}^{s,R} = \rho_r^s + c(dt_{r,j}^R - dt^{s,R}) + T^{s,R} - I_{r,j}^{s,R} + \lambda_j(N_{r,j}^{s,R} + b_{r,j}^R - b_j^{s,R}) + \varepsilon_{r,j}^{s,R} \quad (4)$$

Where superscripts G and R refer to the GPS satellite and the GLONASS satellite, respectively; the subscript j stands for the carrier frequency; ρ is the true geometric range; c is the speed of light; dt_r and dt^s are the clock biases of receiver and satellite, respectively; $\boldsymbol{T}$ is the slant frequency-independent tropospheric delay; $\boldsymbol{I}_j$ is the slant ionospheric effect on the j frequency; $B_{r,j}$ and B_j^s are the pseudorange hardware delay biases of receiver and satellite at the j frequency, respectively; λ_j is the carrier phase wavelength at the j frequency; $\boldsymbol{N}$ is the carrier phase ambiguity term; $b_{r,j}$ and b_j^s are the receiver and satellite uncalibrated phase delay (Ge et al,. 2008) at the j frequency; e is the pseudorange multipath and noise; ε is the carrier phase multipath and noise.

For PPP functional model, Ionosphere-free linear combination is used due to its ability of eliminating the first-order ionospheric effects. Considering that relativistic effects, phase wind-up effect, earth tide displacements, and satellite/receiver phase center offset are accounted for. In addition, precise combined GPS/GLONASS satellite orbit and clock information are used, the PPP functional model can be written as follows (Cai and Gao, 2013; Li and Zhang, 2014):

$$P_{if}^{s,G} = \rho_r^s + c(dt_r^G) + T^{s,G} + B_{r,if}^G - B_{if}^{s,G} + e_{if}^{s,G} \quad (5)$$

$$\phi_{if}^{s,G} = \rho_r^s + c(dt_r^G) + T^{s,G} + \lambda_j(N_{if}^{s,G} + b_{r,if}^G - b_{if}^{s,G}) + \varepsilon_{if}^{s,G} \quad (6)$$

$$P_{if}^{s,R} = \rho_r^s + c(dt_r^R) + T^{s,R} + B_{r,if}^R - B_{if}^{s,R} + e_{if}^{s,R} \quad (7)$$

$$\phi_{if}^{s,R} = \rho_r^s + c(dt_r^R) + T^{s,R} + \lambda_j(N_{if}^{s,R} + b_{r,if}^R - b_{if}^{s,R}) + \varepsilon_{if}^{s,R} \quad (8)$$

Where P_{if} and ϕ_{if} are the pseudorange and carrier phase ionosphere-free linear observables, respectively. In this combined PPP model, the unknowns are the receiver coordinates, the GPS receiver clock offset, the GLONASS receiver clock offset, the wet part of zenith tropospheric delay and the float GPS/GLONASS ambiguities. Owing to the limited accuracy of GLONASS satellite orbit and clock corrections and the ignored pseudorange hardware delays biases, the weights of GLONASS pseudoranges are assigned to be half of the weights of GPS pseudoranges in order to reduce the impact of the larger GLONASS pseudorange residuals on the positional estimates (Cai and Gao, 2013).

2.2 GPS/GLONASS Multipath Linear Combination

Dual-frequency pseudorange and carrier phase measurements are sufficient to build the multipath linear combination in order to compute GPS/GLONASS pseudorange multipath and noise corrections. The multipath linear combination or observable for frequency i equals (Estey and Meertens 1999; Xia et al. 1999; Wang et al. 2015):

$$MP_i = P_i - \frac{f_i^2 + f_j^2}{f_i^2 - f_j^2}\lambda_i\varphi_i + \frac{2f_j^2}{f_i^2 - f_j^2}\lambda_j\varphi_j \quad (9)$$

Where f is the carrier frequency; the subscripts ($i, j = 1,2, i \neq j$) refer to the different frequencies. The multipath linear combination contains the pseudorange multipath and noise, the constant ambiguity term and the hardware delays provided that carrier phase observations are free of cycle slips. Pseudorange multipath and noise are isolated by removing the constant ambiguity and the hardware delays which can be considered as constant during one day through a zero-mean process. The zero-mean process for a series of multipath linear combinations can be expressed as:

$$mp_i = MP_i - m \quad (10)$$

Where *mp* is the isolated pseudorange multipath and noise correction; *MP* is the multipath linear combination; *m* is the mean of the series of multipath linear combinations during the specified duration. Figure. 1 shows the multipath observable *mp1* for GPS satellite G07 and the multipath observable *mp1* for GLONASS satellite R11 at the station JPLM (Pasadena, United States) on DOY 213 in 2016. For the first method, TEQC software is used to calculate the multipath and noise corrections (or the multipath observable) for GPS/GLONASS RINEX data (Estey and Meertens 1999). Then, these corrections are utilized in the functional model to make the computed ranges precise and less noisy in the range domain. Consequently, the ambiguities will reach the accurate values at earlier period.

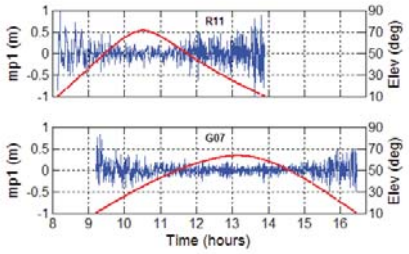

Figure 1. The multipath observable mp1 for G07 (at the below) and for R11 (at the top) at station JPLM in USA on DOY 219 in 2016.

2.3 Multipath-Dependent Stochastic Modeling

Stochastic models can be used to mitigate biases that are difficultly modelled or corrected in the functional model. The widely used stochastic model in GNSS data processing is the weighting scheme based on the satellite elevation angle. The simple assumption for the elevation-based stochastic model is that as the angle decreases, the noise level of un-modeled errors and imperfections in the functional model will increase, so the weight will decrease. The elevation stochastic model can be expressed as in equation (11). But, the elevation stochastic model has approximate weights that do not reflect the realistic characteristics of pseudorange multipath and noise. On the other hand, a realistic stochastic model can be established by multipath corrections that are calculated by the multipath linear combination. Thus, the second method proposed is the multipath-based stochastic model which can be used to mitigate the pseudorange multipath and noise.

$$\mathrm{SUW_Elev} = \sin(Elev) \qquad (11)$$

In this method, after computing the multipath observable, the moving variance algorithm with a window length of 5 epochs is applied to compute the variance of this multipath observable at every epoch. Then, these variances are normalized and converted to weights that are used in the stochastic model in order to assign higher weights to the less multipath and noisy pseudoranges and lower weights to the more multipath and noisy pseudoranges. Also, in this method, the pseudorange multipath and noise are not mitigated in the functional model, but is mitigated only in the stochastic model. The multipath-based sigma of unit weight of the pseudorange ($\mathrm{SUW_MP_i}$) on the *i* frequency is illustrated in equation (12) (Seepersad and Bisnath, 2015). The sigma of unit weight related to the pseudorange ionosphere-free observable is obtained by the average of the weights on the two frequencies.

$$\mathrm{SUW_MP_i} = (\tanh(\mathrm{WeightMP_i}/100) + \sin(Elev)) \qquad (12)$$

Figure.2 illustrates the comparison between the elevation-based and multipath-based stochastic models at the site JPLM (Pasadena, United States), for G07 and R11, on DOY 213 of 2016. Figure.2.a, 2.b and 2.c show the multipath-based sigma of unit weight; the elevation-based sigma of unit weight; and the multipath observable and the elevation angle, respectively, for the satellite G07. Figure.2.d, 2.e and 2.f show the same items for the satellite R11. The formula of the elevation stochastic model is simple to apply but not realistic, while the formula of the multipath stochastic model can reflect the realistic quality of the observations. In addition, Figure.3 illustrates the difference between the multipath and elevation weights for the pseudorange ionosphere-free observables for G07 and R11, at site JPLM, on DOY 213 in 2016.

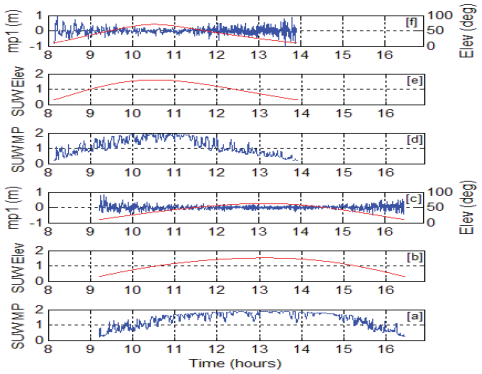

Figure 2. Comparison of stochastic models for pseudoranges related to G07 and R11 at site JPLM on DOY 213 of 2016.

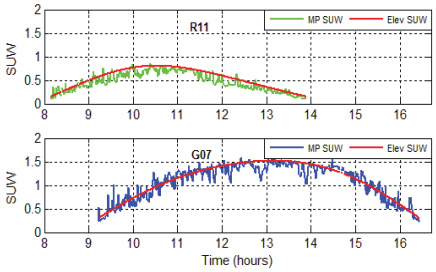

Figure 3. Multipath-based and elevation-based weighting function related to pseudorange observations of G07 and R11 at site JPLM on DOY 213 of 2016.

3. DATA COLLECTION AND EXPERIMENTAL SETUP

In this study, daily GPS/GLONASS observations from 108 globally distributed IGS stations on DOYs from 213 to 219 in 2016 with a sampling interval of 30 second were selected as illustrated in Figure. 4 in order to test the methods presented in this paper. Each daily data set is processed with an hourly initialization in order to increase the convergence tests to about 17700. MANS-PPP software (Abou-Galala, 2016), was designed with MATLAB language and based on the FORTRAN source code of the on-line Canadian spatial reference service precise point positioning (CSRS-PPP), is used as the used PPP processing engine in this study.

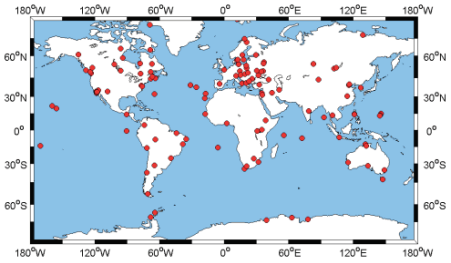

Figure 4. Distribution of the selected 108 IGS stations.

Table 1 summarized the GPS/GLONASS PPP processing strategy, error corrections and estimated parameters. The convergence period is computed as the time length that the solution or 3D position error needs to reach a specific accuracy and remains stable under it. The 3D position error is defined as the difference distance between the accepted "true" position and the output "biased" position. The accepted position was taken from the IGS accumulative weekly SINEX solutions. In this study, the data sets were only processed in the static mode.

Item	Models
Satellites	GPS+GLONASS; about 56 satellites
Estimator	LSQ in the sequential mode
Observations	Undifferenced phase and code observations
observable	Ionosphere-free linear combination
Signal selection	GPS: L1/L2; GLONASS: L1/L2
Sampling rate	30 s
Elevation cutoff	10 deg
Phase-windup effect	Modeled (Wu et al. 1993)
Tropospheric delay	Initial model (Saastamoinen model) + random-walk process
Ionospheric delay	Eliminated by ionosphere-free combination
Receiver clock	Estimated, white noise (one for each system)
Station displacement	Solid Earth tide, pole tide, IERS Convention 2003 (McCarthy and Petit 2003)
Satellite antenna phase center	GPS and GLONASS PCO/PCV corrected with igs08.atx
Receiver antenna phase center	igs08.atx
Terrestrial frame	ITRF2008 (Altamimi et al. 2011)
Station coordinate	Estimated
Phase ambiguities	Estimated as constant and float for each arc

Table 1. GPS+GLONASS PPP processing strategy, error corrections and estimated parameters.

4. RESULTS AND DISCUSSIONS

4.1 Combined GPS/GLONASS PPP

To illustrate the performance of combining GPS and GLONASS systems in improving the PPP convergence, Figure. 5 shows the convergence of combined GPS/GLONASS PPP solution against the GPS-only PPP solution at the site VIS0 (Visby, Sweden) on DOY 215 in 2016. A 3D position accuracy level of 30 cm was selected to examine the PPP convergence period by this technique. The GPS/GLONASS PPP solution converged at 22 minutes, while the GPS PPP solution converged at 32.5 minutes. The GPS/GLONASS PPP solution had an initial 3D error of 438 cm, while the GPS PPP solution had an initial 3D error of 334 cm. For the convergence stability, an rms error of the GPS/GLONASS PPP was 120 cm, while the GPS PPP had an rms error of 125 cm. Figure. 6 illustrates the convergence period of GPS PPP and GPS/GLONASS PPP on each day for the all data sets at the 95% confidence level. On all days, combined GPS/GLONASS PPP solution has shorter convergence period than GPS PPP solution. Also, there is a large similarity between the convergence periods of the Combined GPS/GLONASS PPP solution. For GPS PPP solution, there is a little dissimilarity between the convergence periods.

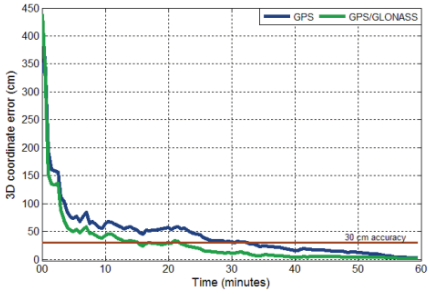

Figure 5. The convergence performance using the combined GPS/GLONASS PPP against the GPS PPP at station VIS0 on DOY 215 of a year 2016.

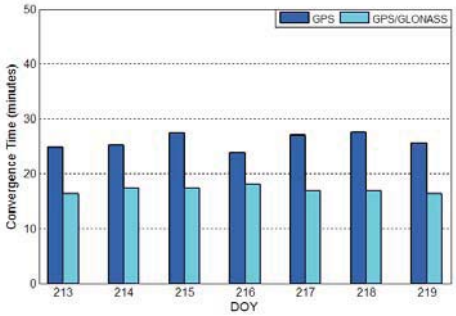

Figure 6. The daily convergence period of GPS PPP and combined GPS/GLONASS at the 95% confidence level.

In order to evaluate the performance of this combined PPP model in improving the convergence period, the combined GPS/GLONASS PPP model was examined in contrast to the GPS PPP model with using an identical weighting scheme for GPS pseudoranges and the half of that weighting scheme for GLONASS pseudoranges. Figure. 7 presents the distribution of convergence periods by the GPS PPP and Figure. 8 presents the distribution of convergence periods by the combined GPS/GLONASS PPP. The distribution of GPS PPP convergence periods had a mean of 10 minutes and a standard deviation of 7.4 minutes, while the distribution of GPS/GLONASS PPP had a mean of 6.7 minutes and a standard deviation of 5 minutes.

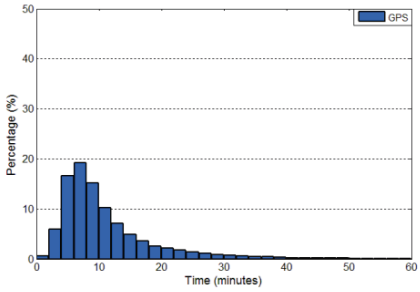

Figure 7. Distribution of the GPS PPP convergence periods

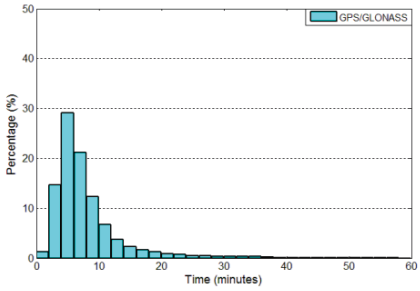

Figure 8. Distribution of the combined GPS/GLONASS PPP convergence periods

In Figure. 7 and 8, the 95% confidence intervals of GPS PPP convergence periods were 2 to 32 minutes, while the 95% confidence intervals of GPS/GLONASS PPP convergence periods were 1.5 to 22 minutes. In addition, 3.5% and 2.4% of the convergence periods are more than three times of the standard deviations for GPS PPP and GPS/GLONASS PPP solutions, respectively. For the GPS PPP, the rejected solutions are caused by poor satellite geometry or bad quality of the observations. The rejected solutions were reduced in case of the GPS/GLONASS PPP, because combining observations from GPS and GLONASS satellites can improve the poor satellite geometry. Figure. 9 presents the distribution of the difference in convergence period between GPS-PPP and GPS/GLONASS PPP solutions. The majority of the convergence periods (66 %) were reduced by the combined GPS/GLONASS PPP. Thus, these reductions in convergence period assure that combining GLONASS and GPS satellites can improve the geometric satellite distribution, which in turn can greatly reduce the PPP convergence period. However, 16 % of the convergence periods were increased. This little negative effect may be a result of the low-quality observations of additional GLONASS satellites (Tolman et al. 2010).

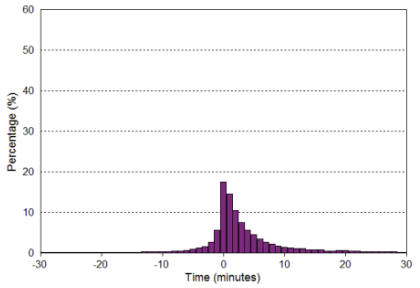

Figure 9. Distribution of the difference in convergence period between GPS-PPP and GPS/GLONASS PPP solutions

Moreover, the solutions are divided into three groups [G1, G2 and G3] according to the geographic latitude, in order to analyze the convergence performance of the combined GPS/GLONASS PPP through different latitudes. Table 2 represents the latitude limits for each group; the convergence periods of the GPS PPP and the GPS/GLONASS PPP solutions; and the reduction ratio of the convergence period for each group. The number of stations in G1, G2 and G3 are 11, 60 and 34, respectively.

	Limits	Convergence period (minutes)		Reduction
		GPS-PPP	GPS/GLONASS PPP	
G1	10°S - 10°N	26.50	23.90	10 %
G2	10°-50°S & 10°-50°N	27.50	17.30	37 %
G3	50°-90°S & 50°-90°N	21.30	13.90	35 %

Table 2. The convergence performance of the combined GPS/GLONASS PPP in the low, mid and high latitude areas.

Both GPS PPP and combined GPS/GLONASS PPP solutions have shorter convergence period in the areas with higher latitude. Also, the combined GPS/GLONASS PPP reduced the convergence period by 37% and 35% in the mid latitude and high latitude areas, respectively.

4.2 GPS/GLONASS Multipath Linear Combination

In this section, at the site VIS0 for the DOY 215, The GPS/GLONASS PPP solution using the multipath observable was tested. In a similar way, a 3D position accuracy level of 30 cm was set to examine the PPP convergence performance, illustrated in Figure. 10.

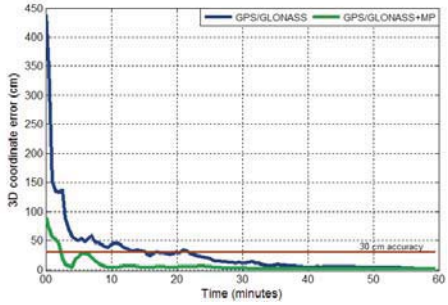

Figure 10. The convergence performance using TEQC multipath linear combination at station VIS0 on DOY 215 of a year 2016.

A 3-minute convergence was achieved by The GPS/GLONASS PPP solution using the multipath observable, while the GPS/GLONASS PPP solution has a 22-minute convergence. The GPS/GLONASS PPP+MP has an initial 3D error of 90 cm, while the GPS/GLONASS PPP has an initial 3D error of 438 cm. For the convergence stability, the multipath observable technique greatly reduced the rms error from 120 cm to 29 cm. In addition, Figure. 11 shows the distribution of the convergence periods of combined GPS/GLONASS PPP augmented by the multipath observable. A mean of 6.8 minutes and a standard deviation of 5.3 minutes are the statistical information of this distribution. Also, the 95% confidence intervals of the convergence periods range from 1.5 to 23

minutes. Illustrated in Figure. 12 is the distribution of the difference in convergence period between GPS/GLONASS PPP enhanced by the multipath corrections and GPS/GLONASS PPP solutions in case of equally weighted pseudoranges for each solutions.

The multipath observable technique improves only 24 % of the convergence periods, while 22 % were deteriorated. By TEQC multipath observable, accurate pseudorange multipath and noise corrections can be estimated, starting from the first epoch, if the carrier phase observations are free of cycle slips. Little improvements were seen by the multipath observable, this may be due to the unsuccessful cycle-slip detection and repair in some cases. This limitation prevents the precise removal of the ambiguity terms; consequently multipath corrections are not accurate and biased.

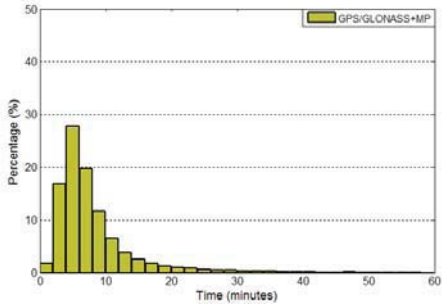

Figure 11. Distribution of convergence periods of the combined GPS/GLONASS PPP enhanced by the multipath linear combination

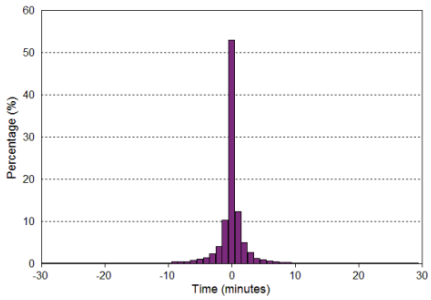

Figure 12. Distribution of the improved convergence period for the GPS/GLONASS multipath linear combination

4.3 Multipath-Dependent Stochastic Modeling

Moreover, at the site VIS0 on the DOY 215, the multipath weights and the elevation weights were tested in order to examine the convergence period of GPS/GLONASS PPP solution to a 30 cm 3D position accuracy level, illustrated in Figure. 13. The GPS/GLONASS PPP solution enhanced by the multipath weights had a convergence period of 5 minutes, while The GPS/GLONASS PPP solution enhanced by the elevation weights had a convergence period of 6 minutes. The multipath weights solution had an initial 3D error of 377 cm, while the elevation weights solution had an initial 3D error of 346 cm. For the convergence stability, the 3D error rms of the multipath weights was 82 cm, while the 3D error rms of the elevation weights was 93 cm. Figure. 14 shows the distribution of the convergence periods of combined GPS/GLONASS PPP augmented by the multipath weights. A mean of 5.4 minutes and a standard deviation of 3.9 minutes are the statistical information of this distribution. Also, the 95% confidence intervals of the convergence periods range from 1 to 16.50 minutes. Figure. 15 illustrates the distribution of the difference in convergence period between GPS/GLONASS PPP enhanced by the multipath weights and GPS/GLONASS PPP solutions with identical weights for pseudoranges.

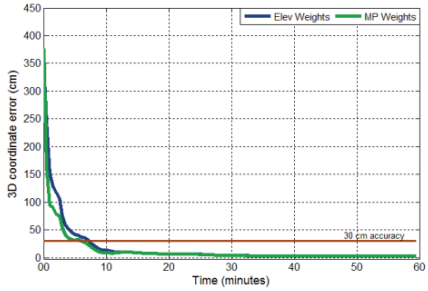

Figure 13. The convergence performance using the multipath stochastic model against the elevation stochastic model at station VIS0 on DOY 215 of a year 2016.

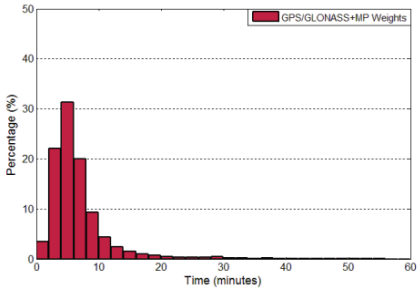

Figure 14. Distribution of convergence periods of the combined GPS/GLONASS PPP enhanced by the multipath stochastic model

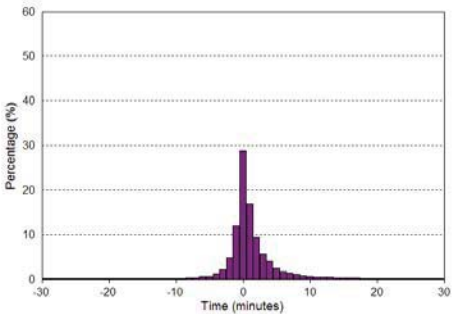

Figure 15. Distribution of the improved convergence period by the multipath stochastic model

The multipath weights reduced 48 % of the convergence periods, while 23 % of them were increased. It is noted that the multipath weights has double improvements of the multipath observable inside the functional model. This is because the multipath weights in the stochastic modelling are not affected by cycle slips as the multipath observable mitigation inside the functional modelling. The elevation weights were also analyzed for improving the GPS/GLONASS PPP convergence period for comparing its performance with the performance of the multipath weights. For statistical information, the convergence periods have a mean of 5.4 minutes and a standard of 3.9 minutes. Also, the elevation weights reduced 46 % of the periods and had deteriorations of 22%. In addition, table 3 illustrates the summary of the differences between the two models.

	Multipath weights	Elevation weights
Reality	Near realistic	Approximate
Extra data	Yes	No
Computation	Complex	Easy

Table 3. The differences between the two types of weights.

5. CONCLUSION:

A major limitation of precise point positioning (PPP) is that it needs a long convergence period to obtain the steady-state float ambiguities. This slow convergence is largely caused by the slow change of satellite geometry and the remaining un-modeled errors. With combining GPS and GLONASS observations, the more visible satellites can improve the poor satellite geometry distribution, and then a reduction in the convergence period will be achieved. By mitigating the multipath and noise in pseudoranges, the float ambiguity estimates will be more accurate rapidly, and therefore the PPP convergence period will be reduced.

In this study, GPS/GLONASS observations from 108 globally distributed IGS stations on DOYs from 213 to 219 in 2016, are used. The two proposed methods are executed inside the combined GPS/GLONASS PPP processing engine in order to examine them in reducing the PPP convergence period to a predefined three-dimensional positioning accuracy of 30 cm. The reductions of both methods are calculated relative to the standard GPS/GLONASS PPP solution that assigns equal weights to the pseudoranges in each system and ignores the pseudorange multipath and noise. Since the weighting scheme based on the sine function of the satellite elevation is widely used in most of GNSS processing softwares, the proposed multipath weights method is compared to the elevation weights. It is obvious that combining observations from the two satellite constellations can improve the performance of PPP and shorten its convergence period. The results have showed that the direct mitigation method of the TEQC multipath observable has a limitation. This limitation is that multipath observable corrections have a high sensitivity to undetected cycle slips during their computation inside TEQC software. Also, the results have demonstrated that the proposed multipath weights can mitigate the pseudorange multipath and noise, which in turn can reduce the PPP convergence period.

For the combined GPS/GLONASS PPP, The relationship between the performance of PPP convergence and the geographic latitude was also studied. Results show that the convergence period improvement in the mid- and high latitude areas is larger than that in the low-latitude areas. Both GPS PPP and combined GPS/GLONASS PPP solutions have shorter convergence period in the high latitude areas.

ACKNOWLEDGEMENTS

This work was supported by Mansoura University Research Grant. The authors gratefully acknowledge these supports.

REFERENCES

Abou-Galala, M., 2016. Enhancing Convergence Time for Precise Point Positioning Through Multipath Observable. MSc Thesis, Public Works and Civil Engineering Department, Mansoura University, Mansoura, Egypt.

Altamimi, Z., X. Collilieux, and L. Métivier, 2011. ITRF2008: an improved solution of the international terrestrial reference frame. J Geod, 85(8), pp. 457–473. doi:10.1007/s00190-011-0444-4

Bilich, A. and K.M. Larson, 2007. Mapping the GPS multipath environment using the signal-to-noise ratio (SNR). Radio Sci, 42(6), RS6003

Cai, C. and Y. Gao, 2013. Modeling and assessment of combined GPS/GLONASS precise point positioning. GPS Solut, 17(2), pp. 223–236. doi: 10.1007/s10291-012-0273-9

Collins, J.P. and R.B. Langley, 1999. Contract Report No.DAAH04-96-C-0086/TCN98151 for the United States Army Corps of Engineers Topographic Engineering Center "Possible weighting schemes for GPS carrier phase observations in the presence of multipath", University of New Brunswick, Fredericton, New Brunswick, Canada, http://gge.unb.ca/Personnel/Langley /Langley.html

Dai, W., D. Huang, and C. Cai, 2014. Multipath mitigation via component analysis methods for GPS dynamic deformation monitoring. GPS Solut, 18(3), pp. 417–428. doi:10.1007/s10291-013-0341-9

Dong, D., M. Wang, W. Chen, Z. Zeng, L. Song, Q. Zhang, M. Cai, Y. Cheng, and J. Lv, 2016. Mitigation of multipath effect in GNSS short baseline positioning by the multipath hemispherical map. J Geod, 90(3), pp. 255–262. doi:10.1007/s00190-015-0870-9

Elsobeiey, M., El-Rabbany, A., 2012. On modelling of second-order ionospheric delay for GPS precise point positioning. J Navig, 65(1), pp. 59–72

Estey L.H. and C.M. Meertens, 1999. TEQC: the multi-purpose toolkit for GPS/GLONASS data. GPS Solut, 3(1), pp.42–49. doi:10.1007/PL00012778

Fenton, P. C. and J. Jones, 2005. "The Theory and Performance of NovAtelInc.'s. Vision Correlation". ION GNSS 2005, Long Beach, CA, USA

Fuhrmann, T., X. Luo, A. Knoepfler, and M. Mayer, 2015. Generating statistically robust multipath stacking maps using congruent cells. GPS Solut, 19(1), pp. 83–92. doi:10.1007/s10291-014-0367-7

Ge, M., G. Gendt, M. Rothacher, C. Shi, and J. Liu, 2008. Resolution of GPS carrier-phase ambiguities in precise point positioning (PPP) with daily observations. J Geod, 82(7), pp. 389–399. doi:10.1007/s00190-007-0187-4

Geng, J. and C. Shi, 2016. Rapid initialization of real-time PPP by resolving undifferenced GPS and GLONASS ambiguities simultaneously. J Geod, doi: 10.1007/s00190-016-0969-7

Geng, J., F.N. Teferle, X. Meng, and A.H. Dodson, 2011. Towards PPP-RTK: Ambiguity resolution in real-time precise point positioning. Adv Space Res, 47(10):1664–1673

Kouba J. and P. Heroux, 2001. Precise Point Positioning using IGS orbit and clock products. GPS Solut, 5(2):12–28

Larson, K.M., A. Bilich, and P. Axelrad, 2007. Improving the precision of high-rate GPS. J Geophys Res 112, B05422. doi:10.1029/2006JB004367

Lau, L. and P. Cross, 2007. Development and testing of a new ray-tracing approach to GNSS carrier-phase multipath modelling. J Geod, 81(11), pp. 713–732. doi:10.1007/s00190-007-0139-z

Li, B. and Y. Shen, 2010, Global navigation satellite system ambiguity resolution with constraints from normal equations. J Surv Eng-ASCE, 136(2), pp. 63-71.

Li, P. and X. Zhang, 2014. Integrating GPS and GLONASS to accelerate convergence and initialization times of precise point positioning. GPS Solut, 18(3), pp. 461-471. doi: 10.1007/s10291-013-0345-5

Li, X., M. Ge, X. Dai, X. Ren, M. Fritsche, R. Wang, J. Wickert, and H. Schuh, 2015. Accuracy and reliability of multi-GNSS real-time precise positioning: GPS, GLONASS, BeiDou, and Galileo. J Geod, 89(6), pp. 607–635. doi: 10.1007/s00190-015-0802-8

Lou, Y., F. Zheng, S. Gu, C. Wang, H. Guo, and Y. Feng, 2015. Multi-GNSS precise point positioning with raw single-frequency and dual-frequency measurement models. GPS Solut, 20(4), pp. 849–862 doi: 10.1007/s10291-015-0495-8

McCarthy, D. and G. Petit, 2003. IERS conventions, IERS technical note no. 32, Publisher of the Federal Agency for Cartography and Geodesy: Frankfurt am Main, Germany

Moradi, R., W. Schuster, S. Feng, A. Jokinen, and W. Ochieng, 2015. The carrier-multipath observable: a new carrier-phase multipath mitigation technique. GPS Solut, 19(1), pp. 73–82. doi: 10.1007/s10291-014-0366-8

Ray, J.K., M.E. Cannon, and P. Fenton, 1999. Code Range and Carrier Phase Multipath Mitigation Using SNR, Range and Phase Measurements in a Multi-Antenna System. ION GPS 1999 Nashville, USA.

Satirapod, C. and C. Rizos, 2005. Multipath mitigation by wavelet analysis for GPS base station applications. Surv Rev, 38(295), pp. 2–10

Seepersad G. and S. Bisnath, 2014. Challenges in assessing PPP performance. J Applied Geodesy, 8(3), pp. 205–222

Seepersad G, Bisnath S (2015) Reduction of PPP convergence period through pseudorange multipath and noise mitigation. GPS Solut, (2015) 19(3), pp. 369–379, doi: 10.1007/s10291-014-0395-3

Tolman, B.W., A. Kerkhoff, D. Rainwater, D. Munton, and J. Banks, 2010. Absolute precise kinematic positioning with GPS and GLONASS, Proceedings ION-GNSS-2010, Institute of Navigation, Portland, Oregon, pp. 2565–2576

Townsend, B., P. Fenton, K. van Dierendonck, and R.D.J. van Nee, 1995. L1 Carrier Phase Multipath Error Reduction Using MEDLL Technology. ION GPS 1995, Palm Spring, pp. 1539-1544.

Tranquilla, J.M., J.P. Carr, and H.M. Al-Rizzo, 1994. Analysis of a choke ring ground plane for multipath control in Global Positioning System (GPS) applications. IEEE Transactions on Antennas and Propagation, 42 (7), pp. 905-911.

Van Dierendonck, A.J., P. Fenton, and T. Ford, 1992. Theory and Performance of Narrow Correlator Technology in GPS Receiver. J Navig, 39(3), pp. 265-283

Wang G., K. de Jong, Q. Zhao, Z. Hu, and J. Guo, 2015. Multipath analysis of code measurements for BeiDou geostationary satellites. GPS Solut, 19(1), pp. 129–139. doi: 10.1007/s10291-014-0374-8

Wu, J.T., S.C. Wu, G.A. Hajj, W.I. Bertiger, and S.M. Lichten, 1993. Effects of antenna orientation on GPS carrier phase. Manuscr Geod, 18:91–98

Xia, L., J. Liu, S. Zhang, and Y. Deng, 1999. Analysis on code multipath mitigation by phase-aided smoothing. Geo-spatial Inf Sci, 2(1) pp. 73–77

Zumberge J., M. Heflin, D. Jefferson, M. Watkins, and F. Webb, 1997. Precise point positioning for the efficient and robust analysis of GPS data from large networks. J Geophys Res, 102(B3), pp. 5005–5017

ROAD TEST RESULTS AND ANALYSIS ON INTEGRATING VISUAL ODOMETRY WITH CAR MOTION SENSORS FOR POSITIONING AND NAVIGATION

Muhammed Tahsin Rahman[a,*], Tashfeen B. Karamat[b], Sidney Givigi[c], Aboelmagd Noureldin[c]

[a] Queen's University, Kingston, ON, Canada - muhammed.rahman@queensu.ca
[b] Royal Military College, Kingston, ON, Canada - tashfeen.karamat@queensu.ca
[c] Royal Military College, Kingston, ON, Canada - (sidney.givigi, aboelmagd.noureldin)@rmc.ca

KEY WORDS: Visual Odometry, INS, GPS, GNSS, Integration, Kalman Filter, Sensor Fusion

ABSTRACT:

The global navigation satellite system (GNSS) provides absolute positioning information with consistent level of accuracy over long periods of time. However, the system fails to provide reliable positioning estimates when the signals coming from the satellites are blocked or experience other sources of interference such as multipath, jamming, etc. To ensure a reliable navigation solution during such periods of signal outage, GNSS is commonly integrated with an inertial navigation system (INS). The major drawback of the INS appears during extended GNSS outages, where the gyroscope drift errors become significant, leading to an unusable position estimate. To improve the overall system accuracy, visual odometry (VO) is increasingly being used as an aid to traditional GNSS/INS systems. This paper presents results of the combined GNSS/INS/VO solution during outages up to 10 minutes long, and shows how the proposed integration significantly outperforms the conventional GNSS/INS solution.

1. INTRODUCTION

1.1 Background

The global navigation satellite system (GNSS) is the solution of choice for navigating in outdoor environments. Signals from a satellite constellation (such as GPS) are processed by a receiver, and absolute position and velocity estimates are calculated based on these signals. Meter level accuracy is common using such a system (Noureldin et al., 2013). The system, however, is highly susceptible to signal blockage, interference, and multipath errors. To ensure a reliable solution during such adverse conditions of signal outage, GNSS is commonly integrated with an inertial navigation system (INS), which has good short term accuracy and does not rely on any external sources for determining position, velocity and attitude. Therefore, the integration of these two systems allows for a more accurate navigation solution, which is usable even over short periods of GNSS signal outage.

The main issue arises when these outages extend over long periods of time; such situations occur in urban canyons, forests, indoors, and underwater to name a few. In such situations, extreme outages can range from 5-10 minutes. During such outages, when there is no GNSS signal to reset errors in the INS, the overall solution becomes unusable. Furthermore, current autonomous land vehicles and other Intelligent Transportation System (ITS) applications require sub-meter level accuracy 95% of the time. This has not yet been achieved using commercial grade INS systems, and using more accurate INS hardware is prohibitive due to their higher cost, larger physical dimensions and higher power requirements.

Algorithms such as the 3D reduced inertial sensor system (3D-RISS) (Atia et al., 2014; Cossaboom et al., 2012) have been developed that aim to minimize the use of gyroscopes while implementing mechanization. Such techniques, when integrated with GNSS using the extended Kalman filter (EKF), provide a much improved solution due to the lower number of sensors that drift (only 1 gyroscope instead of 3). However, with lower cost inertial sensors and high frequency of outages, such algorithms are still limited in their navigation estimate.

Recently, a growing body of research is targeting the use of image sequences to localize a vehicle. This technique, known as visual odometry (VO) (Nister et al., 2004), provides an additional source of information and can be fused with other systems to make use of the advantages inherent in each system.

1.2 Motivation

Land vehicles are now equipped with cameras utilized for forward collision, blind spot display, and lane departure warning systems. The availability of these technologies provides an attractive opportunity to further increase the navigation accuracy through the use of VO techniques.

Visual systems rely on environmental cues to estimate the relative rotation and translation of a vehicle with respect to some initial states. Inherently, like the INS, VO is a dead reckoning system. However, given that the scene in front of the video recording camera is relatively static, the attitude and position estimate from the visual system do not experience large amounts of drift. On the other hand, gross errors in feature detection from the video frames lead to sudden bursts of error, which are then exacerbated as the trajectory continues. These aspects of VO are complimentary to the INS, which provides a consistently smooth solution that has more severe time-based drift. The proposed algorithm seeks to take advantage of these complimentary characteristics.

The ultimate goal of this paper is to develop and present results of an integrated multi-sensor system consisting of GNSS fused with both inertial and vision systems. Such integration offers seamless positioning for land vehicles in all environments, especially during longer outages where traditional GNSS/INS systems exhibit large errors in positioning estimates.

*Corresponding author

1.3 Objectives

This paper presents new experimental results over long trajectories, where the proposed multi-sensor fusion algorithm greatly enhances the accuracy of the overall navigation solution. Integrating GPS, INS, and VO takes advantage of each system's complimentary characteristics and hence overcomes several limitations inherent in each system. The objectives of this paper are as follows:

1. Provide an overview of the INS and VO systems used
2. Describe the experimental setup
3. Present and discuss the results

2. SYSTEM OVERVIEW

2.1 3D Reduced Inertial Sensor System (3D-RISS)

The sensors used in 3D-RISS are:

1. Forward accelerometer: f_y
2. Transversal accelerometer: f_x
3. Up-facing gyroscope: ω_z
4. Odometer: v_{od} differentiated to give a_{od}

Using the above sensors, a complete navigation solution is found. Figure 1 provides a block diagram representation of the mechanization algorithm and indicates the sensors used to compute each state. These are detailed in equations 1 to 9.

$$p = \sin^{-1}\left(\frac{f_y - a_{od}}{g}\right) \tag{1}$$

$$r = -\sin^{-1}\left(\frac{f_x + v_{od}\omega_z}{g\cos p}\right) \tag{2}$$

$$\dot{A} = -\left(\omega_z - \omega^{ie}\sin\varphi - \frac{v_e \tan\varphi}{R_N + h}\right) \tag{3}$$

$$v_e = v_{od}\sin A\cos p \tag{4}$$

$$v_n = v_{od}\cos A\cos p \tag{5}$$

$$v_u = v_{od}\sin p \tag{6}$$

$$\dot{h} = v_u \tag{7}$$

$$\dot{\varphi} = \frac{v_n}{R_M + h} \tag{8}$$

$$\dot{\lambda} = \frac{v_e}{(R_M + h)\cos\varphi} \tag{9}$$

where
p = Pitch
r = Roll
A = Azimuth
v_e = Velocity East
v_n = Velocity North
v_u = Velocity Up
h = Height
φ = Latitude
λ = Longitude
g = acceleration due to gravity
ω^{ie} = Earth's rate of rotation
R_N = Normal radius of curvature of the Earth
R_M = Meridian radius of curvature of the Earth

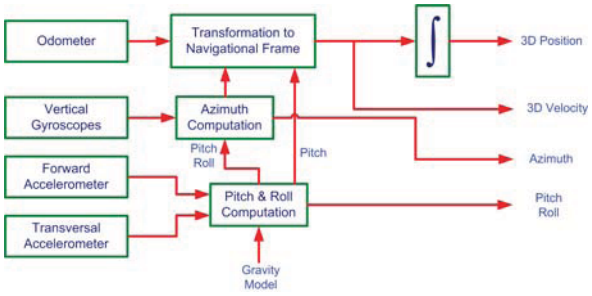

Figure 1. 3D-RISS mechanization block diagram with state computation using relevant sensors (Noureldin et al., 2013)

The 3D-RISS mechanization outperforms traditional systems that use 3-axis accelerometers and 3-axis gyroscopes for their mechanization (Iqbal et al., 2008). The main reasons for this improvement are due to the utilization of the car odometer, which has scale factor errors that can be compensated for in the EKF with GPS updates, and the presence of fewer gyroscopes. A more detailed study of the subject can be found in (Noureldin et al., 2013).

2.2 Visual Odometry (VO)

Feature Detection, Description and Tracking The first step of a VO scheme is to detect significant points -also known as keypoints- in an image, run feature descriptor algorithms on those points and then match or track them in subsequent image(s). Several detection and description algorithms exist (Fraundorfer and Scaramuzza, 2012). The choice of algorithms employed depends largely on the computational restraints, the motion baseline, and the environment (Gauglitz et al., 2011). For our system, we used a Shi-Tomasi corner detector with a Kanade-Lucas-Tomasi (KLT) tracker, due to the relatively short baseline (at a frame rate of 5Hz) and the urban environment, which is rich in corners.

Motion Estimation The keypoints in both frames are related through the epipolar constraint, $\acute{p}^T E p = 0$ (Hartley and Zisserman, 2000), where $\acute{p}$ represents the keypoints in the second frame, E represents the *essential matrix*, and p represents the corresponding keypoints in the first frame. It is important to note that keypoints here are normalized, i.e. $p = K^{-1} \cdot [x, y, 1]^T$, where x and y represent the pixel locations of a keypoint and K represents the camera calibration matrix. The points used, $\acute{p}$ and p, should be projected to the unit sphere. The minimum number of points required to solve for the *essential matrix* is 5 (Nistér, 2004). Once an estimate of the *essential matrix* has been found, the incremental translation and rotation between the frames is given by $E = [t]_x R$, where $[t]_x$ is the skew-symmetric matrix of the translation vector t, and R is the rotation matrix. Decomposing E leads to 4 possible solutions of t and R. The cheirality constraint (Nistér, 2004) can be used to determine the correct solution.

Other works are present in the literature that aim to reduce the minimum number of points required for calculating E. For instance, non-holonomic constraints can be exploited such that only 1 point is needed (Scaramuzza, 2011). However, for the algorithm to produce accurate results the camera must be placed close to the back wheel axis, limiting the size of the vehicle that can be used. For our experimental setup, a longer vehicle as shown in Figure 2, the algorithm gives inaccurate results.

RANSAC A major motivation for reducing the minimum number of points required to solve for E is to reduce the computational time in the outlier removal stage. Erroneous matches, deemed outliers, cause significant errors in the VO solution, and -given the dead-reckoning nature of the system- these errors are quickly compounded. Random Sample Consensus (RANSAC) (Fischler and Bolles, 1981) is the most commonly used scheme to remove outliers. A summary of the paradigm is as follows: A minimum set of keypoints are first used to instantiate a model - the hypothesis-, against which other keypoints are checked. Once a suitable consensus set of keypoints has been reached, the entire consensus set is used to estimate E. As the minimal set increases, so too does the computational complexity of the algorithm. For example, with 20 keypoints the 5-point algorithm can generate a total of 15504 possible solutions, while the 1-point algorithm can generate only 20.

To reduce the computational complexity of the RANSAC algorithm several improvements have been suggested. For example, preemptive RANSAC (Nister, 2003) (and its subsequent improvement (Gomes-Neto and Carvalho, 2014)) aims to score the observations against the hypotheses, the score representing the log-likelihood of the observation given that the hypothesis accurately represents the motion model. Other schemes, such as (Cheng and Lai, 2009) and (Songmin Jia and Xu, 2016) suggest novel methods for building on the original RANSAC scheme to improve accuracy and computational efficiency. It should be noted that these schemes aim to maximize the probability of a correct set of keypoints with minimal computations rather than finding the absolute best set.

2.3 System Integration

The two systems mentioned above are loosely coupled with GPS. The individual solutions, 3D-RISS mechanization and VO, are computed and then fused using an extended Kalman filter (EKF). The error states are computed by the filter with measurement updates coming from GPS, when available. Once estimated, these errors are subtracted from the dead-reckoning solution and then subsequently reset in the next iteration. More details of the derivation of the error states are presented in (Noureldin et al., 2013). It is important to note that the stochastic errors of the inertial sensors were modeled using first order Gauss-Markov models. Furthermore, the CarChip speed sensor from the car's OBD II port was a control input for the system model rather than a measurement update. Measurement updates from GPS consisted of latitude, longitude, height, East velocity, North velocity, and Up velocity.

3. EXPERIMENTAL ANALYSIS

3.1 Experimental Setup

The experimental setup is shown in Figure 2, where a long land vehicle was equipped with all the required sensors. The developed GPS/INS/VO integration was evaluated using the following:

1. Novatel OEM4 GPS Receiver
2. MEMS Grade Crossbow IMU (model IMU300CC-100)
3. CarChip connected to the OBD II interface for recording the car's forward speed
4. MiVue 388 Dash Cam, shown in Figure 3

Figure 2. Land vehicle used in the extended trajectory

Figure 3. Cameras placed on the car. Although 2 cameras were setup only 1 was used in the algorithm

The algorithm integrated the data from the above sensors using the GPS/INS/VO algorithm and compared the results to a reference solution. Also, the classic GPS/INS algorithm was implemented using the same sensors (except for the camera). This ensured that the only difference between the proposed method and the already established algorithm was the incorporation of VO.

The Novatel solution, consisting of the OEM4 GPS receiver integrated with a tactical-grade SPAN-CPT IMU was used as the reference. Table 1 provides a comparison of the IMUs between the experimental trials and the reference. Since we are primarily concerned with the algorithm performance during outages the GPS receiver used was the same for the experimental trial and the reference.

Specifications	**Crossbow MEMS-IMU**	**Novatel Span-CPT**
Update Rate	100 Hz	100 Hz
Gyroscopes		
Bias	$< \pm 2$ deg/s	$< \pm 20$ deg/hr
Scale Factor	$< 1\%$	$< 0.15\%$
Angle Random Walk	2.22 deg/$\sqrt{hr}$	0.0667 deg/$\sqrt{hr}$
Accelerometers		
Bias	$< \pm 30$mg	$< \pm 50$mg
Scale Factor	$< 1\%$	$< 0.4\%$
Range	± 2g	± 10g

Table 1. Comparison of experimental and reference IMU

3.2 Experimental Results

The trajectory analyzed was performed in downtown Kingston and lasted for 48 minutes. Throughout the trajectory, 7 outages of varying lengths were simulated in post-processing. The outages were introduced under a variety of conditions: during sharp turns, straight line segments, different speeds, and complete stops. There were always enough features to implement VO. Figure 4 shows the entire trajectory with the outage locations marked.

Figure 4. Complete Kingston trajectory. Red portions indicate presence of GPS signal while cyan portions indicate GPS outages. The GPS outages have been numbered.

			GPS/INS		GPS/INS/VO	
Outage	Duration	Avg. Speed (km/h)	RMS Error (m)	Max Error (m)	RMS Error (m)	Max Error (m)
1	5 mins	29.8	61.6	102.6	18.1	40.8
2	10 mins	34.8	203.6	425.3	43.5	81.4
3	2 mins	24.4	23.6	32.7	14.1	22.2
4	2 mins	16.0	41.1	68.1	11.0	16.8
5	5 mins	42.7	168.8	376.5	17.7	38.8
6	1 min	49.2	20.3	29.6	10.9	17.6
7	1.5 mins	42.0	9.4	19.0	4.1	10.5

The proposed GPS/INS/VO algorithm was implemented alongside the traditional GPS/INS algorithm, and both were compared to the reference Novatel solution. In both cases (GPS/INS/VO and GPS/INS) the INS mechanization was done using 3D-RISS on the Crossbow IMU and the GPS receiver used was the Novatel OEM4. Since we are mainly concerned with land vehicle navigation in urban environments, the metrics that we use to quantify accuracy are the 2D RMS error and the 2D maximum error between the solution and the reference.

When considering the entire trajectory without any simulated outages the RMS error was the same for both the proposed and the classical methods (1.12m). This indicates that when GPS was available it dominated the solution. On the other hand, when the GPS signal was not available -in the case of outages- the solutions had vastly differing accuracies. Figure 5 displays the RMS position errors for the GPS/INS and the GPS/INS/VO solutions. Figure 6 displays the maximum position error for both solutions.

The vast improvement of the addition of VO is clearly seen in the case of outages. In the most extreme case, when the outage reaches 10 minutes, the RMS error drops from 203.6m without VO to 43.5m with VO. This is a 78.6% improvement in the solution. Figure 7 compares visually what this outage looks like. In all such comparisons, the red track represents the Novatel solution, the green track represents the GPS/INS/VO solution and the blue track represents the GPS/INS solution. It can be seen that even if map matching techniques were to be used to try and correct the GPS/INS solution, erroneous conclusions could be drawn, since the solution drifts to a completely different road. In the case of GPS/INS/VO, however, this is not the case. Although the error is still relatively large, the solution remains usable. The same can be seen in Figure 8, where the outage involves portions of the trajectory that has several more turns. The turns introduce scale factor errors to the gyroscope measurements (Noureldin et

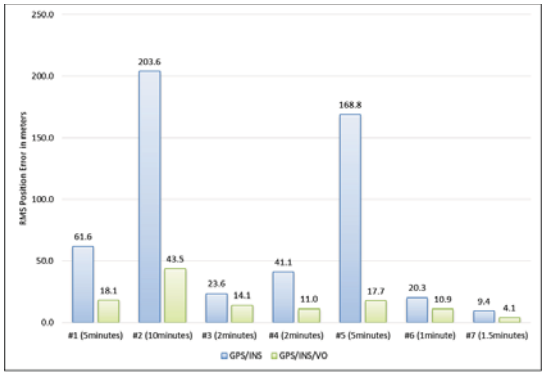

Figure 5. Comparison of the RMS position errors between the original GPS/INS and the proposed GPS/INS/VO integration.

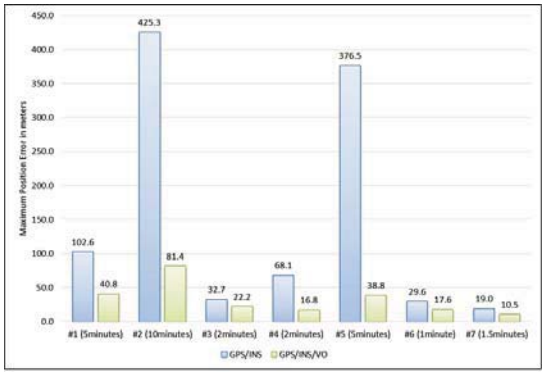

Figure 6. Comparison of the maximum position errors for both solutions. The errors are with respect to the Novatel solution

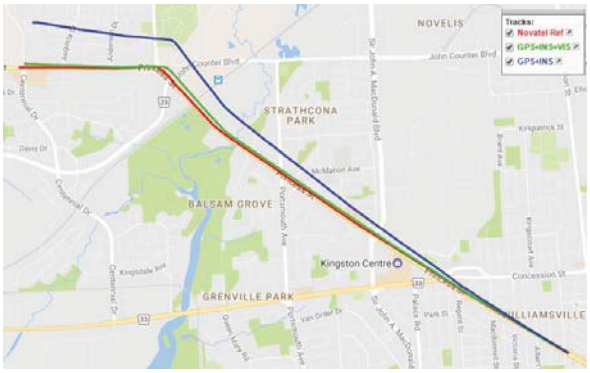

Figure 7. Outage 2: A 10 minute outage with one significant turn at a moderate average velocity

al., 2013), which would cause greater errors in the mechanization. As was the case with the 10 minute outage, the solution is greatly improved with the addition of VO.

The different solutions during outage 6 are shown in Figure 9, that considers a straight line segment at greater velocity. It can be seen from the mechanization equations presented in section 2.1 that greater velocities modulate the errors in position. Therefore, although the outage is relatively short, only 1 minute, the errors are still significant. The solution with the inclusion of VO, while still being cogent, is not as pronounced as in the previous cases. This can be attributed to 2 major factors. Firstly, gyroscope drift is mainly time based, and a shorter trajectory would mean that the EKF bias estimate did not suffer significantly. Secondly, higher velocities mean that the baseline distance between successive frames captured by the camera is large. A VO system's accuracy depends on a relatively short baseline distance. Furthermore, to improve on computational efficiency, we used a feature tracking algorithm rather than a feature matching one. This means that feature matches in successive frames were established by a localized search around the keypoint being considered. Larger baseline distances move each keypoint a greater distance away from where it was in the previous frame, leading to a lower number of established matches. And a lower number of matches reduces the noise cancellation properties of the VO solution, leading to lower accuracy in the final solution.

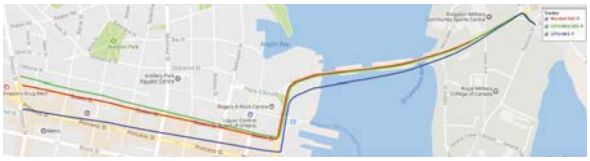

Figure 8. Outage 1: A 5 minute outage with 2 significant turns and a moderate average velocity

Figure 9. Outage 6: A 1 minute outage of a straight line segment at relatively higher average velocity

4. CONCLUSION

In this paper some fundamental concepts of 3D-RISS mechanization and VO were reviewed. Further, results of their loosely coupled integration together with GPS were presented, showing how the integration improves the navigation accuracy during extended outages. The GPS/INS/VO solution was compared to the original GPS/INS solution during several outages, ranging from 1 minute to 10 minutes. In the most extreme case, adding VO improved the solution by 78.6%.

Future work in the area of multi-sensor fusion algorithms involving the INS and VO would be to implement visual-inertial odometry (VIO) solutions, utlizing the advantages of 3D-RISS over full 6 degrees of freedom IMUs. Furthermore, the drift of 3D-RISS is mainly restrained to the heading angle, which could provide insight into developing tightly coupled integration schemes involving VO and pseudo range measurements of GPS.

References

Atia, M. M., Karamat, T. and Noureldin, A., 2014. An enhanced 3d multi-sensor integrated navigation system for land-vehicles. *Journal of Navigation* 67(04), pp. 651–671.

Cheng, C.-M. and Lai, S.-H., 2009. A consensus sampling technique for fast and robust model fitting. *Pattern Recognition* 42(7), pp. 1318 – 1329.

Cossaboom, M., Georgy, J., Karamat, T. and Noureldin, A., 2012. Augmented kalman filter and map matching for 3d riss/gps integration for land vehicles. *International Journal of Navigation and Observation*.

Fischler, M. A. and Bolles, R. C., 1981. Random sample consensus: A paradigm for model fitting with applications to image analysis and automated cartography. *Commun. ACM* 24(6), pp. 381–395.

Fraundorfer, F. and Scaramuzza, D., 2012. Visual odometry : Part ii: Matching, robustness, optimization, and applications. *IEEE Robotics Automation Magazine* 19(2), pp. 78–90.

Gauglitz, S., Höllerer, T. and Turk, M., 2011. Evaluation of interest point detectors and feature descriptors for visual tracking. *International Journal of Computer Vision* 94(3), pp. 335.

Gomes-Neto, S. and Carvalho, B. M., 2014. Generalized preemptive ransac making preemptive ransac feasible even in low resources devices. In: *2014 International Conference on Computer Vision Theory and Applications (VISAPP)*, Vol. 3, pp. 406–415.

Hartley, R. I. and Zisserman, A., 2000. *Multiple View Geometry in Computer Vision*. Cambridge University Press, ISBN: 0521623049.

Iqbal, U., Okou, A. F. and Noureldin, A., 2008. An integrated reduced inertial sensor system - riss / gps for land vehicle. In: *2008 IEEE/ION Position, Location and Navigation Symposium*, pp. 1014–1021.

Nister, 2003. Preemptive ransac for live structure and motion estimation. In: *Proceedings Ninth IEEE International Conference on Computer Vision*, pp. 199–206 vol.1.

Nistér, D., 2004. An efficient solution to the five-point relative pose problem. *IEEE Trans. Pattern Anal. Mach. Intell.* 26(6), pp. 756–777.

Nister, D., Naroditsky, O. and Bergen, J., 2004. Visual odometry. In: *Proceedings of the 2004 IEEE Computer Society Conference on Computer Vision and Pattern Recognition, 2004. CVPR 2004.*, Vol. 1, pp. I–652–I–659 Vol.1.

Noureldin, A., Karamat, T. B. and Georgy, J., 2013. *Fundamentals of Inertial Navigation, Satellite-Based Positioning and their Integration*. Springer.

Scaramuzza, D., 2011. 1-point-ransac structure from motion for vehicle-mounted cameras by exploiting non-holonomic constraints. *International Journal of Computer Vision* 95(1), pp. 74–85.

Songmin Jia, Ke Wang, X. L. and Xu, T., 2016. A novel improved probability-guided RANSAC algorithm for robot 3D map building. *Journal of Sensors*.

LOW COST STRUCTURES OSCILLATION MONITORING USING TERRESTRIAL PHOTOGRAMMETRY

O. A. El-Kadi [a*], A.Y. El Shazly [b,]

[a] Dept. of Geomatics Engineering, Cairo University, Egypt – o.elkadi@aucegypt.edu
[b] Dept. of Geomatics Engineering, Cairo University, Egypt – Adel_shazly@hotmail.com

KEY WORDS: Terrestrial photogrammetry, Structural health monitoring, OpenCV, Automation, deformation monitoring ,Image geometric correction, Image processing.

ABSTRACT:

Slender structures oscillate due to dynamic loading encountered by wind and earth quakes, the oscillation amplitude yet depends on the structure's natural frequency and the form of loading wave. Monitoring of such oscillation is a raising concern for the benefit of structural health monitoring of historical structures and sensitive facilities. Moreover, the analyzed measurements can be implemented in further structural dynamic analysis for repair and remodelling purpose. Tri-axial accelometers combined with different sensors and\or high frequency GPS receivers are commonly suggest system for this task, while some recent researches suggested the use of infrared holography.
In this research, an approach using terrestrial photogrammetry is introduced, by using non-metric on shelf cameras. The large zoom capacities offered by low cost in market bridge type cameras allows the camera sensor to capture small sampling area at far distance which is mandatory for precise monitoring of structures. Moreover, offered high video sampling rate allows monitoring at adequate frequencies approaching 60 to 120Hz.
The proposed monitoring approach doesn't require a pre-camera calibration which ease its application using high rage of offered optical zoom according to site condition; several tests for oscillation and deformation are performed and analysed to examine accuracy and reliability of the proposed monitoring approach. Structural tests for full scaled specimens subjected to cyclic loading are monitored and planned to be used for the validation of the proposed monitoring approach.
The proposed monitoring system allows low cost and reliable oscillation monitoring for different structures, with sub-millimetre accuracy and adequate frequency, which ease the implementation of this system for real-time monitoring of historical slender structures and for various oscillation monitoring applications.

1. INTRODUCTION

The problem solving using simple approach is always recommended, as using simple mathematical models reduces computing requirements and eases the process of results judgment. Yet it is very difficult to simplify a photogrammetric problem in a simple form due to the influence of various non-linear factors affecting the image formation.
Moreover, the concept of low cost technique is commonly correlated, nowadays to a robust solution that can be solved without the need of complex setup procedure.
For example, in case of ortho-photo, where the image plane is parallel to the object surface the principle of similarity is valid all over the image as:

$$P = L'_1 / L_1 = L'_2/L_2 \qquad (1)$$

Where
P = The image spatial resolution (image scaling)
L' = The object measurement in pixels
L = The actual size of the object

Accordingly, if the problem can be simplified to be ortho-photo with minimal lens distortion effect, the modelling procedures can be much simplified.

2. PROBLEM DEFINITION AND METHODOLOGY

2.1 Problem definition

One of the main challenges facing oscillation monitoring of slender structures is the relative position of a stable monitoring platform adequate for monitoring purposes.
The monitoring station position is commonly at far distance apart and its relative position varies according to the structure type and the surroundings, which requires a camera with a suitable optical zoom, to achieve the required position for structure health monitoring and structural dynamic testing applications.

2.2 Methodology

An on-shelf camera of bridge type can be used for this purpose as such camera models have optical zoom that achieves 85X, with some adequate optical sensors of about 16 to 18 mega pixels.
The high variation of the camera to object position compiled with the variation of optical zoom, difficilitated the use of pre-calibrated camera.
As a result, the work flow is reversed by linearization of first video frame, by applying fourth degree two-dimensional

polynomial transformation, to allow on spot projection of skewed object plan and minimize the effect of radial and tangential lens distortion.

A regular chess board pattern target was used as per Zang (1998); the equal spaced pattern is used as control points for the sake of the polynomial projection, which in this case requires a minimum of 30 points.

The estimated polynomial coefficients are then applied to project the successive video frames, while a detected intermediate point in the chess board is used for the oscillation monitoring, to avoid the distortion that may be residual at the outer projected zone, using Harris corner detector. Chris Harris (1998).

Figure 1. Target attached to a test setup configuration

A python script was developed to allow changing the video to sequence of frames and detect the chess board pattern points, preform the projection, and calculate the movement between the frames sequence with respect to the initial frame in the sequence.

NUMPY and CSIPY libraries were used for array, math, and linear algebra computations, while OpenCV and SCIKIT-image libraries were used for image processing.

3. DEVELOPING OF PHOTOGRAMMETRIC MODEL

The photogrammetric model used is based on the projection of the initial Depiction in the sequence, remains constant and the oscillation captured is perpendicular to the camera frame.

The maximum displacement is assumed to be smaller than half the target width, to ensure that the tracked points are all occupied in the projected area

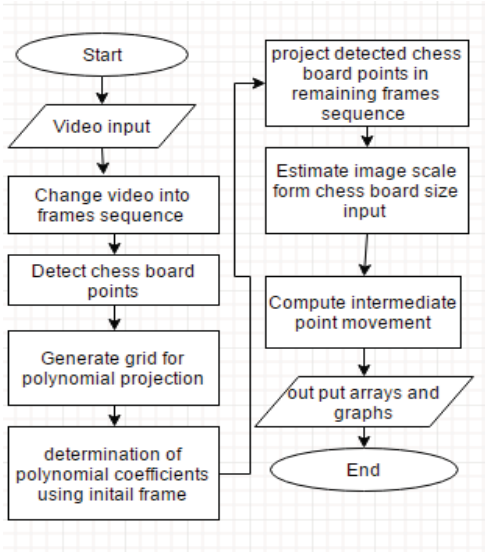

Figure 2. Flow chart for the python script

Polynomial function from 4th degree is used to minimize the effect of radial and tangential distortion as:

$$U = a_1 x^4 + a_2 y^4 + a_3 x^4y^4 + a_4 x^3 + a_5 y^3 + \ldots\ldots \quad (2)$$
$$V = b_1 x^4 + b_2 y^4 + b_3 x^4y^4 + b_4 x^3 + b_5 y^3 + \ldots\ldots$$

Where U, V = image coordinates
x, y = image coordinates
a_n, b_n = object coordinates

The stated polynomial function has 30 coefficients to be estimated, least squares can be applied where:

$$\mathbf{A} = \begin{bmatrix} 1 & u_1 & v_1 & \cdots \\ 1 & u_2 & v_2 & \cdots \\ \vdots & \vdots & \vdots & \ddots \\ 1 & u_K & v_K & \cdots \end{bmatrix}, \mathbf{a} = \begin{bmatrix} a_0 \\ a_1 \\ \vdots \\ a_{N-1} \end{bmatrix}, \mathbf{b} = \begin{bmatrix} b_0 \\ b_1 \\ \vdots \\ b_{N-1} \end{bmatrix}, \mathbf{x} = \begin{bmatrix} x_1 \\ x_2 \\ \vdots \\ x_K \end{bmatrix}, \mathbf{y} = \begin{bmatrix} y_1 \\ y_2 \\ \vdots \\ y_K \end{bmatrix}$$

$$\mathbf{a} = (\mathbf{A}^T\mathbf{A})^{-1}\mathbf{A}^T\mathbf{x}, \quad b = (\mathbf{A}^T\mathbf{A})^{-1}\mathbf{A}^T y \quad (3)$$

While object grid is calculated based on the average chess box size in the image, then linear scaling is performed for pixel to mm conversion.

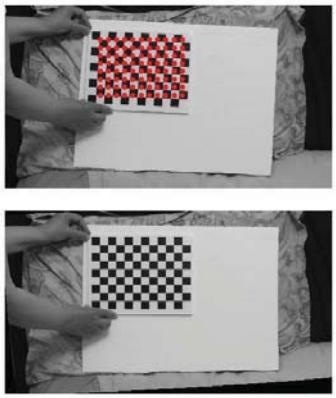

Figure 3. a) grid for polynomial projection b) projected image

The high order polynomial projection showed a good response to highly skewed images, where it approximates 2 steps of projective transform and undistorting the image using lenses tangential and radial coefficients.

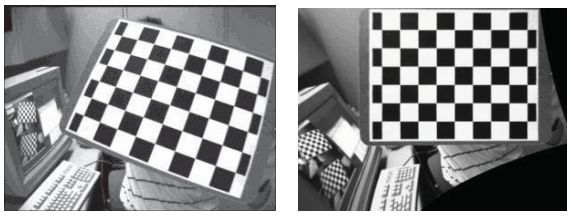

Figure 4. a) input skewed image, b) projected image

Sub pixel refinement algorithm for corner detection based on gradient direction and neighbourhood search is implemented from OpenCV library to increase detection accuracy and reduce the effect of image noise.

4. RESULTS AND ANALYSIS

4.1 Test on a predefined grid movement

As per the photogrammetric model description where target grid is projected orthogonal to camera, the detected motion is then projected, which leads to detection of in plane motion relative to target face. The approach applied hereby neglects the off-plane oscillation effect.
This test is based on grid pattern movement in X direction, Y direction, XY direction and random pattern, the video is captured in 30 fps settings. Which was found to be 29fps from captured video properties.

4.1.1 Movement in x-direction: 8 marks at 20mm intervals was marked on a white board, a video is captured using camera mounted over tripod, while the target is attached on a board and moved by hand from initial mark in x direction to last mark and back, to have a movement of about 160mm in X direction, the recorded video had a length of 59 seconds, and decomposed in to 1770 frame.

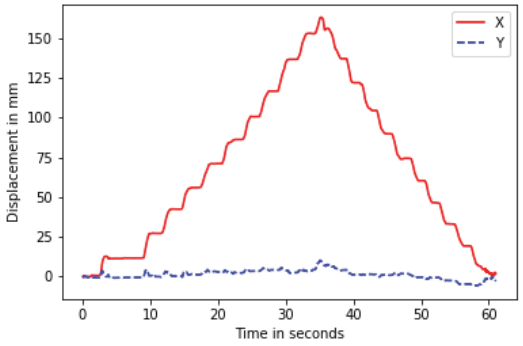

Figure 5 Detected oscillation in x direction

4.1.2 Movement in Y-direction: 4 marks at 20mm intervals was marked on a white board, a video is captured for 25 while moving the board from initial position to 4th mark and back, the 754 frames of 1920 x 1080 pixels' size needed about 70 seconds for analysis using a modern business edition Laptop of 16 GB ram and i7 processor.

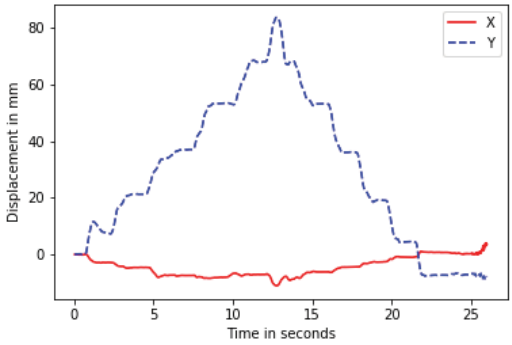

Figure 6 Detected oscillation in x direction

4.1.3 Movement in XY-direction: As previous setups a video is capture, while is moved on diagonal direction of about 40 degrees from y axis. To avoid coincided x and y graph representation.

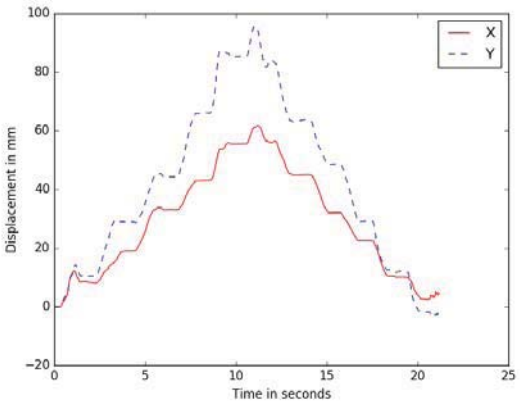

Figure 7 Detected oscillation in XY direction

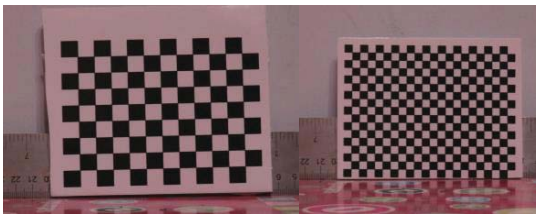

Figure 8 Different configurations used to test accuracy of detected deformations

4.2 Test by linear scale using small displacement and still frames

This test is performed to examine the accuracy of measured deformations. Still images of 4608 x 3456 and 1920 x 1080 pixels' size were used.
Next shown graph is for 20mm chessboard grid which is moved along x direction with small displacements that varied form sub-millimetre to 10 mm as follows (0.5,1,2,3,4,5,10,15,20 and 30mm) while detected x displacement in frames were as following:
(0.57, 1.1 ,2.19, 3.38 ,4.06, 5.05, 10.13, 15.62, 20.32, 30.27)

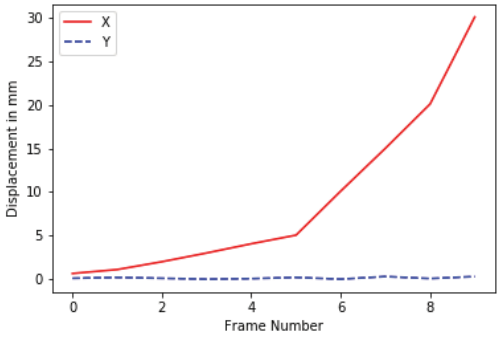

Figure 9 Detected Displacements in X direction

While theoretically if the chessboard of 240 mm width is covering 50% of frame width of 1920 pixels, then accuracy of 0.25mm is expected, hand placement of chessboard and manual reading of 0.5mm and 1mm ruler scale can produce an error of about 1mm.

5. CONCLOSION AND RECOMMENDATIONS

The analysis performed on both video and still images using suggested polynomial projection approach showed a precise deformation and oscillation monitoring results, and a high monitoring rate of about 30hz was captured.
While using hand controlled motion results human errors. The ongoing analysis of setup shown in Figure 1 where a dynamic actuator is used to simulate oscillation of structures can give better analysis and conclusions. However, the used python script is under development to overcome memory over flow, resulting from large frame number extracted from test videos (about 17000 frame) and to allow matching of measured and input waves start.
Monitored point is selected to be in the mid of chessboard, at which minimal distortion effect occurs. Accordingly, the maximum measured drift shouldn't exceed half of target dimension.
The proposed monitoring approach allowed robust use of camera optical zoom, while the camera is focused and set on manual focus during monitoring to avoid any change in frames properties due to focal length variation.

ACKNOWLEDGEMENTS

The Author would like to acknowledge the support of Z.Zayed and A. Madbouly for their help in different test setups and the construction engineering department at the American University in Cairo for allowing the use of structural lab facilities for the sake of this research.

REFERENCES

Zhang, Z., 1998. A Flexible New Technique for Camera Calibration. Technical Report MSR-TR-98-71, Microsoft Research.

Harris, C. and Stephens, M., 1988, A COMBINED CORNER AND EDGE DETECTOR. AVC 1988 doi:10.5244/C.2.23

Suliman, C. et al., 2009. SINGLE CAMERA CALIBRATION IN 3D VISION. THE ANNALS OF "DUNAREA DE JOS" UNIVERISTY OF GALATI FASCICLE III,2009, Vol.32, No.2, ISSN 1221-454X.

Temiz, M. and Kulur, S., 2008. RECTFICATION OF DIGITAL CLOSE RANGE IMAGES: SENSOR MODELS, GEOMETRIC IMAGE TRANSFORMATION AND RESAMPLING. The International Archives of the photogrammetry, Remote Sensing, and Spatial Information Sciences. Vol XXXVII. Part B5. Beijing 2008.

Escalera, A. and Armingol, J., 2010. Automatic Chessboard Detection for Interinsic and Exterinsic Camera Parameter Calibration. Sensors 2010,10,2044; doi:10.3390/s100302027.

OpenCv.org, OpenCV 2.4.13.2 documentation, Feature Detection., http://docs.opencv.org/2.4/modules/imgproc/doc/feature_detection.html?highlight=cornersubpix#cornersubpix (Jan, 2016)

3D RECONSTRUCTION WITH 2D TILTING LIDAR USING VISION ONLY POSITIONING METHOD

C. Joly[a], B. Ricaud[b], A. de La Fortelle[a]

[a] Mines ParisTech, PSL Research University, Center for Robotics, 60 bd Saint Michel 75006 Paris - cyril.joly@mines-paristech.fr,arnaud.de_la_fortelle@mines-paristech.fr.
[b] Nexter Systems, 11 alle des Marronniers, 78000 Versailles - b.ricaud@nexter-group.fr

KEY WORDS: Non-urban 3D reconstruction, Tilting LiDAR, Image processing, Stereo images, ADAS

ABSTRACT:

This paper presents the first step of a system which will provide assistance to drivers for piloting in rough environments, such as off-road or post-crisis environment. The purpose of the approach is to inform the driver where the dangers are and how to avoid them. To achieve it, we implemented an algorithm making 3D reconstruction of the surrounding of the vehicle. Our approach uses sensors fusion of LiDAR and stereoscopic cameras and works in two simple steps in order to reach real-time requirement. First, a visual odometry approach using the cameras is used to compute the motion of the vehicle, then the previous result is used to compute the 3D coordinates of the points provided by the LiDAR. The use of the visual odometry approach helps to avoid heavy point cloud matching algorithm. Moreover, in order to limit the cost of the solution, the 3D point cloud is created using a 2D LiDAR tilting with a servomotor to obtain a cheap 3D LiDAR scanner.
Previous work showed that the approach was interesting but the stereoscopic visual odometry algorithm was not efficient enough. This paper focus on the visual odometry improvement. By using a first step of monocular image processing based on a fast template matching methods, we can have a good approximate estimation of the rotation. This approximation is used as a new input of the visual odometry algorithm which is now initialized close to the good solution and can converge much more faster. This results in a dramatic improvement in the 3D point cloud and the trajectory computed, by dividing by more than 4 the drift error.

1. INTRODUCTION AND RELATED WORK

1.1 Context

Driving a big vehicle in rough environments such as off-road or post-crisis areas can be very difficult and stressful. However, this is a typical situation that drivers of military vehicles have to deal with. Accidents with such vehicles occur quite often; this is why it looks necessary to provide some systems, called ADAS (Advanced Driver Assistance Systems) to help the driver. A very classic one is the video feedback. In some armored vehicles which do not have any glass, it is the only feedback of the scene. In these cases, the loss of depth information and the poor vision angles make accidents easy to occur, leading to casualties even if there is no enemy on the field. To solve this problem, one way is to make vehicle autonomous. However, army is not ready to accept such strategic vehicle to be autonomous. Thus, this research aims at defining and setting up a driving assistance for remote or indirect driving which is able to be used in rough or unstructured environment. In order to achieve this goal, we chose to implement a 3D reconstruction algorithm that is capable to detect negative (under the ground) and positive (on the ground) obstacles and to display it on the screen. This paper focuses on the reconstruction algorithm and presents an affordable way to get the 3D map of the surrounding of the vehicle. It has to be done by using affordable sensors and real time algorithm.

1.2 Related work

In order to detect hazard on the road, we are interested in having a map of the surrounding of the vehicle: this is the field of mobile mapping. Mobile mapping is a very active topic of research, mostly because it is typically a mandatory information for robots and vehicle automation. Moreover, the Simulatenaous Localization and Mapping (SLAM) approaches (Smith and Cheeseman, 1986) emphasize the necessity of mobile mapping. Today, there are many sensors available, like LiDAR (Light Detection And Ranging), that can be 2D or 3D, cameras (monocular or stereoscopic) or even depth-cameras ("RGB-D" sensors, like Kinect or time of flight cameras).

We can roughly separate mapping technologies into three categories that will be discussed according to the application of obstacle detection for military purpose:

1. Accurate offline mobile mapping systems, like (Paparoditis et al., n.d.) that computes dense 3D point clouds with Velodyne (3D LiDAR) sensors. They are really useful for offline mapping purpose and can provide a very accurate solution. Most of the time, this kind of system uses RTK-GPS with high grade IMU in order to compute the position of the vehicle to a centimeter accuracy which allows to have a very accurate positioning of the different 3D scans. However, the technology embedded in these systems can not work in real time and use very expensive sensors that is not compatible with our application. Moreover, the use of GPS is not suitable for military purpose.
2. Online mapping methods based on SLAM approach (Durrant-Whyte and Bailey, 2006). It means that the same sensor is used to compute both the map of the environment and the trajectory. The literature in this field is very important and many solutions are now available. However, SLAM methods needs to maintain a complex map with many correlations, which make the computational burden important. This is not suitable for military vehicle where the computational resources are limited.

3. Online positioning and mapping in two different steps. Here, two different modalities are used to sense the environment and have the position of the vehicle. It helps to provide fast solution without having to manage correlation process like in SLAM that use the same sensor to optimize the positioning and the map. This is the approach we used in our previous work (Ricaud et al., 2015): positioning was done thanks to visual odometry and mapping was done with a LiDAR.

In our previous work (Ricaud et al., 2015), the 3D reconstruction was made with a "cheap" 2D LiDAR tilting on a servomotor in order to bring 3D information. In order to help in positioning the different scans, we used LibViso2 (Geiger et al., 2011), a visual odometry using stereo images. The 3D map was made by the laser impacts and their positioning was done thanks to the ego motion computed by the visual odometry algorithm. Although the results showed a good proof of concept, an important lack of precision in the odometry method lead to an inaccurate 3D reconstruction. One of the causes was the computation speed which appeared too slow to enable a precise estimation and a vicious circle appeared: because the environment was "difficult" for LibViso2 algorithm, it took long time to converge, thus more time separates the following set of images, leading to more difficulty time to converge... This paper proposes to enhance the methodology in (Ricaud et al., 2015) in order to solve the previous problem.

1.3 Paper organization

The paper is organized as follows. The global framework is described in section 2. Some reminders about the military context are also provided. Both hardware and software aspects will be discussed. Section 3 is dedicated to the major contribution of this paper which results in the optimisation of LibViso2 that is needed to maintain the 3D local map consistent. This optimization is based on a rough computation of the ego-motion of the vehicle. Finally, results and some perspectives are given in sections 4 and 5.

2. GLOBAL FRAMEWORK

This section describes the global framework of the tilting LiDAR approach. First, some reminder about our application are provided. Then, the hardware setup is presented. Finally, the software framework is presented, with a special focus about the improvement that were added comparing to (Ricaud et al., 2015).

2.1 Constraints due to the application

Unstructured environment and military application constrained the system by several criteria:

- The purpose of the system is to provide a local map of the dangerous areas surrounding the vehicle. Thus, there is no need to store a complete map and the full trajectory of the vehicle with respect to it.
- Environment can hide negative obstacles which are difficult to detect without help of depth sensor (Cappalunga et al., 2010). Because cameras are very sensitive to the conditions of illumination, depth cameras are not suitable for outdoor application (Piatti and Ditag, 2010). Thus we prefered to focus on LiDAR technology for sensing the environment,

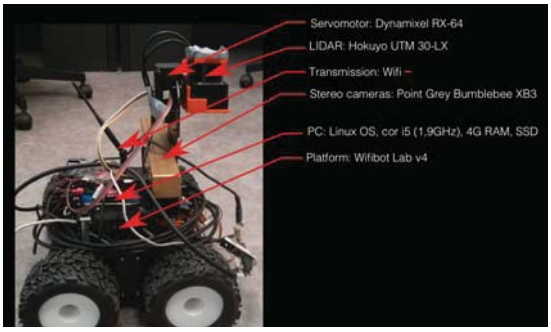

Figure 1. Experimental testbed

- Military prerogatives lead our system definition to avoid GPS technologies to be independent of GPS outages (that can be decided by another government).
- In our application the system suffers from a lot of vibrations, so, IMU seemed not to be the best option for motion estimation (Braman and Grossman, 2006). Moreover, the same limitation occurs with odometry: wheels can be affected by very large errors in rough environment.
- The last constraint was cost. It makes 3D LIDAR such as Velodyne unaffordable for our application.

Finally, we decided to design a system which merges vision and LiDAR data as (Malartre et al., 2010) did for off-road SLAM. In our application, vision sensor handles odometry and a 2D LiDAR that rotates thanks to a small motor for reconstructing the environment. Making the LiDAR rotating allows to have 3D information. The reason of using some visual odometry information is explained in the section that describes the software architecture (2.3)

In the following, the system is described more in details. However, it was not possible to build it directly on a vehicle. To this reason, a small robot was used as a proof of concept. The following description deals with this special hardware.

2.2 Hardware setup

The hardware setup (Fig. 1) is made of 3 parts that are described in the following paragraphs:

1. A mobile pltaform
2. The "Tilting LiDAR", made from a classical 2D LiDAR and a servomotor
3. A stereoscopic camera

2.2.1 Mobile platform To perform our test, the Wifibot platform was used[1]. It is a small robot that has four motorized wheels with tires, equipped of brushless motors and hall encoders. It is completely opened (all source codes are provided), and modular. It was also equipped with a I5 1.9Ghz Processor, 4Go RAM and a SSD, which means that even complex algorithms could be ruined on it.

[1] http://www.wifibot.com

2.2.2 Tilting LiDAR Classical 2D LiDAR are made of one emitter of light (generally infrared) and one receiver, both of them rotate around a known axis. It computes a distance by measuring the time that the light takes to come back to the receiver. Thanks to the rotation, it can provide a 2D scan of the environment. Our method proposes to use this kind of LiDAR by making the sensor itself rotating (around an axis that is perpendicular to the "normal" rotation axis).

For our experiments, an Hokuyo UTM-30LX is used. It acquires data at 40 Hz with an angular resolution of 0.25 between two points on its original rotating axis. This angular resolution implies a step between points of 4 cm at 10 m and 13 cm at 30 m; at close range step is close to zero centimeter. This LiDAR is then assembled on a servomotor (Bioloid RX64), that can give its current angle through a serial connexion.

To create a 3D acquisition with the 2D LiDAR and the servomotor there are 2 possibilities that differ by the axis of rotation. Assuming that the nominal position of the LiDAR has its normal axis of rotation aligned with the vertical (in green on Fig. 4), the two possibilities for rotating the sensor are longitudinal or lateral axis can be used. In (Ricaud et al., 2015), we showed that longitudinal axis was the best solution for our application. The next paragraphs briefly remind the reasons.

Lateral axis (in red on Fig. 3): When acquisition is done with rotation of the lateral axis, scans are acquired along the movement. Flaws of this method are that there is not a view of the close and the far environment at any time, and there is a large disparity in scans density between close and far acquisitions. Actually, the further the acquisitions are, the larger are the steps between scans (see Fig. 2). The second point is an issue concerning obstacles. Actually, with the steps between scans, obstacles can be missed or difficult to detect if they are in a big step. This method was not suitable for our approach but is compatible with stationary approaches like (Espino et al., 2011).

Longitudinal axis (in blue on Fig. 3): The other type of approach is done with rotation around the longitudinal axis. This approach is also used by (Larson and Trivedi, 2011, Zhang and Singh, 2014) in their algorithms. In this case, all the scans give a partial estimation of the road in front of the vehicle up to 30 m. Then, scans density is dispatched along lateral axis with a high density in width of the vehicle (which interests us) and low density on far lateral environment (see Fig. 2). The lateral steps between scans are from 4 cm (close to the robot) to 40 cm (at 10 m on the side). On the longitudinal axis steps are from zero centimeter to 13 cm at 30 m. Figure 4 and Table 1 show more in details these properties.

Finally, in order to compute 3D scans, we retrieve normal 2D scans and the most recent servomotor angle. Then, we compute the 3D coordinates of the orignal points in the robot frame. With this tilting LiDAR approach, it is very easy to get a 3D map of the surrounding of the robot when it is static. **However, during motion, it is more complicated because the servomotor cannot be used too fast: about 90 deg/s (otherwise, it may move too fast during a normal scan). Thus, it takes 2 seconds to do a complete acquisition**. As a consequence, the motion of the robot cannot be neglected (Fig 4). This is why visual odometry is used (section 2.3).

2.2.3 Stereoscopic cameras Finally, the system has stereoscopic cameras. This sensor is used to compute visual odometry.

Points density at:	$\leq$ 1m	10m	30m
Longitudinal axis	$\approx$ 0cm	4cm	13cm
Lateral axis	4cm	40cm	1.2m

Table 1. Points density according to the LiDAR axis of rotation

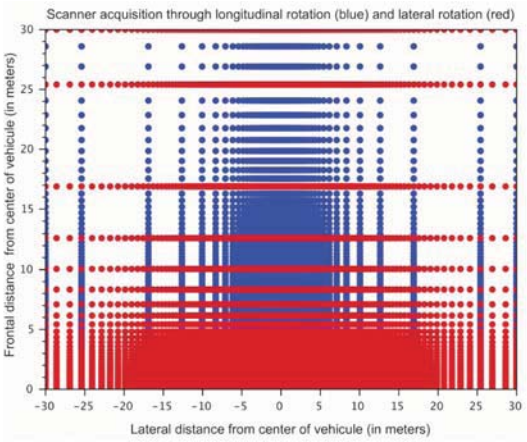

Figure 2. Simulation of point cloud without any obstacle (all the impact points are on the ground) according to the strategies of LiDAR rotation: lateral axis (red) and longitudinal axis (blue).

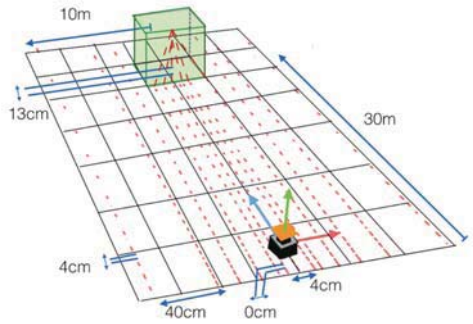

Figure 3. Example of a static acquisition with longitudinal rotation

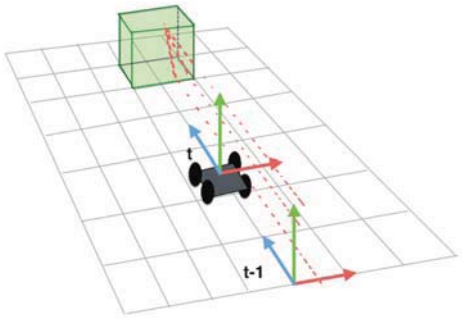

Figure 4. 3D acquisition during motion with longitudinal rotation of the LiDAR

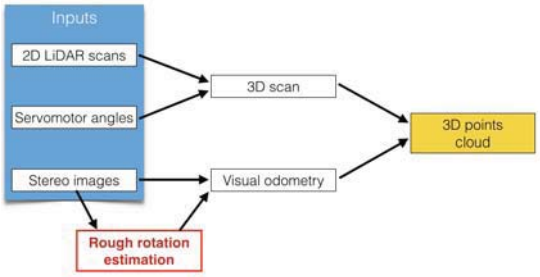

Figure 5. Global framework of the reconstruction algorithm

Contrary to monocular odometry, stereoscopic odometry allows to compute the scale factor of the trajectory, which is mandatory in our case. The cameras system is a Point Grey *Bumblebee XB3*. It is made of 3 cameras but only two of them are used (this allows to chose between 2 different baselines). For our tests, we used the baseline of 12cm.

2.3 Software architecture

2.3.1 Acquisition, synchronisation and processing All the data are captured with ROS. A special driver as been developed in order to integrate the servomotor angles readings. This allows us to save Rosbag files with all the data and to "play" them at a different moment. During the test of the algorithms, real time condition are simulated: it means the Rosbag file is played at the normal speed. If the algorithm cannot process all the data, a part of it has to be ignored.

2.3.2 Algorithm Global architecture of the algorithm is described on Fig 5. It is based on the fact that we have to take into account the robot motion in order to provide a good 3D reconstruction. Thus, if we consider the current point cloud at time step $t-1$ (which correspond to a 2D scan with a known servomotor position), the motion between time steps $t-1$ and t has to be taken into account in order to add the points acquired at time t (Fig. 4). This is done by LibViso2 algorithm which provides odometry information with scale factor using only the stereo cameras (Geiger et al., 2011). More details about the choice of this algorithm can be found in (Ricaud et al., 2015).

It appeared in (Ricaud et al., 2015) that although Libviso2 worked very fine in urban area, it had some problems to deal with our data and provided a poor odometry accuracy, thus leading to a bad point cloud. We realized that this is due to the time needed for convergence. Indeed, Libviso2 is an iterative algorithm: to compute the relative motion (rotation and translation) between $t-1$ and t, it starts from identity matrix (which means *no motion*) and then try to converge to the good solution step by step. The red box on Fig 5 is to speed up the convergence: the idea is to find a way to have an approximate solution that provides a better initialization than the identity matrix. Moreover, we have to compute this approximation very fast; otherwise it is useless. The next section describes in detail this process and the assumption that were made to make it as fast as possible.

3. ODOMETRY IMPROVEMENT

3.1 Hypotheses and framework

When computing its solution, LibViso2 computes a 6 degrees of freedom motion which represents the motion between time steps $t-1$ and t. It can be represented with a translation vector $\mathbf{t}$ and a rotation matrix $\mathbf{R}$. Let $\mathbf{x} = [x_c\ y_c\ z_c]^T$ the coordinate of a 3D point in the camera frame at time $t-1$, and $\mathbf{x}' = [x'_c\ y'_c\ z'_c]^T$ its coordinates in the camera frame at t. We have:

$$\mathbf{x}' = \mathbf{R}^T(\mathbf{x} - \mathbf{t}) \tag{1}$$

LibViso2 tries to estimate both $\mathbf{R}$ and $\mathbf{t}$ in an iterative process that starts from $\hat{\mathbf{R}}_0 = \mathbf{I}$ (identity matrix) and $\hat{\mathbf{t}}_0 = \mathbf{0}$. It appeared that the algorithm waste a lot of iterations in finding the rotation parameters. **Thus, we decided to find an acceptable estimation of this matrix in an efficient way**.

In order to solve this problem, we propose to use the following hypotheses:

- Only the rotation part is estimated. Thus, $\mathbf{t}$ is assumed to be zero in (1). This is equivalent of saying that all the distances of the points in the images are much bigger than the translation of the cameras: $||\mathbf{x}|| \gg ||\mathbf{t}||$. In practice, this assumption is not so bad because the motion between 2 time steps remains small (odometry computation as to be done at more than 10Hz).
- It is assumed that the rotation matrix is due to yaw and pitch angles. Roll angle is neglected comparing to the others.
- Finally, the two angles considered are assumed to be close to zero (small motion hypothesis) which allows to linearize easily the equations (typically: $\cos\alpha \approx 1$ and $\sin\alpha \approx \alpha$).

Although the previous hypotheses are very restrictive (especially the cancelation of translation and roll angle), we except to compute a "not too bad" rotation matrix able to initialize LibViso2 in a good way. In order to do this, the following method is used. It is based on a monocular only estimation:

1. First, N points are randomly selected in one image at time step $t-1$ and their corresponding points in the image at t (paragraph 3.2). To do this, a template matching method is used. This results in N couples of images coordinates representing the pixels motion between the two time steps,
2. Then, the previous couples are used to compute N different rotation matrices (paragraph 3.3). Because of the previous assumptions, only 2 degrees of freedom have to be estimated. This results that only one pixel displacement is enough to estimate the parameters. Thus, N estimations of the rotation can be independently computed.
3. Finally, because of the previous assumption, some of the previous estimation may be inconsistent. The last step consist in finding the outliers in the previous result and compute the final solution thanks to least squares minimization (paragraph 3.4).

3.2 Template matching

The aim of this first part is to find correspondances between images at $t-1$ and t in a fast way. To limit the computational burden, we decide to not use interest points and descriptor like SIFT, SURF... In each image of the stereo camera, we chose $N = 10$ points randomly and store a small area of a template around this point. Then, we find in the corresponding image at

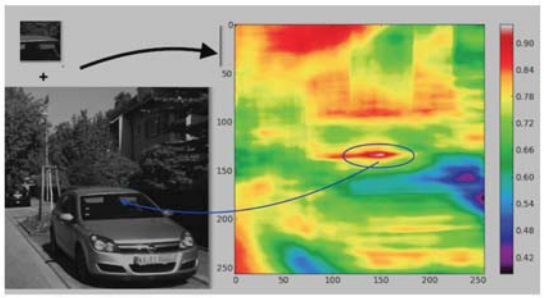

Figure 6. Example of template matching

time t the position of the new template, with template cross correlation matching (Lewis, 1995, Briechle and Hanebeck, 2001). The following lines describe the method.

Let I be a greyscale image of size $M_x \times M_y$ and $I(u,v)$ the intensity value at pixel coordinates (u,v). We define T a subset of I of size $N_x \times N_y$ that we call template. For a new image I', we look for the new position of T. To measure the similarity T with a subset of I' shifted of (u,v), the normalized cross-correlation coefficient $\gamma(u,v)$ is computed:

$$\gamma(u,v) = \frac{\sum_{(x,y)\in D}\left(I'(x,y)-\bar{I}_{u,v}\right)\left(T(x-u,y-v)-\bar{T}\right)}{\sqrt{\sum_{(x,y)\in D}\left(I'(x,y)-\bar{I}_{u,v}\right)^2 \sum_{(x,y)\in D}\left(T(x-u,y-v)-\bar{T}\right)^2}} \quad (2)$$

where $D = \{u \dots N_x - u - 1\} \times \{v \dots Ny - v - 1\}$. Moreover, $\bar{I}_{u,v}$ and $\bar{T}$ are defined by:

$$\begin{cases} \bar{I}_{u,v} &= \dfrac{1}{N_x N_y} \displaystyle\sum_{(x,y)\in D} I'(x,y) \\ \bar{T} &= \dfrac{1}{N_x N_y} \displaystyle\sum_{x=0}^{N_x-1}\sum_{y=0}^{N_y-1} T(x,y) \end{cases} \quad (3)$$

In (2) the numerator is the correlation of T in the subset of I' shifted of (u,v). If this subset and T are very similar, each product will be positive and the sum will be high. If there is no correlation, the global sum will be close to zero. Moreover, the denominator of (2) is the product of the standard deviations of T and the subset of I' that is considered. It makes the similarity measure robust to change in brightness and contrast (Briechle and Hanebeck, 2001).

Finally, the best position of T in the image I' is given by finding the maximum value of γ:

$$(u', v') = \arg\max_{(u,v)} \gamma(u,v) \quad (4)$$

Fig. 6 shows an example of template matching. Left part shows a full image with a small template on the top. Right part shows the evaluation of γ as a function of the pixel coordinates. In practice, we do not evaluated on the $M_x \times M_y$ possible coordinates. In order to optimize the computational cost, γ is evaluated in a small box centered on the initial position of the template (this strategy is relevant because we do not expect strong motion between two images).

Finally, for each template T_i ($i \in \{1 \dots N\}$) of coordinates (u_i, v_i) in image I, we associate its position (u'_i, v'_i) in the image I'. The difference between these coordinates will be used to compute the rotation matrix $\mathbf{R}$. The next paragraph describes the mathematical aspects of this estimation.

3.3 Rotation estimation with one template matching

This paragraph describes the computation of the rotation matrix with the template coordinates. First, some reminder about the pinhole camera are provided. Then, we show how to use this projection model to compute an approximation of the yaw and pitch angles thanks to the result of only one template matching.

3.3.1 Pinhole camera model This paragraph provides a brief reminder of the pinhole camera model, i.e. how to convert 3D coordinates into images coordinates. Let $\mathbf{x} = [x_c\ y_c\ z_c]^T$ be the coordinates of a 3D point in the camera frame. $\mathbf{z}$ axis is in the direction of the optical axis. The first step is to project $\mathbf{x}$ on the plane $z = 1$. The corresponding point is called $\mathbf{m}$:

$$\mathbf{m} = \begin{bmatrix} \frac{x_c}{z_c} \\ \frac{y_c}{z_c} \\ 1 \end{bmatrix} \quad (5)$$

Finally, the pixel coordinates $\mathbf{p} = [u\ v\ 1]^T$ are given by:

$$\mathbf{p} = \underbrace{\begin{bmatrix} f_x & s & c_u \\ 0 & f_y & c_v \\ 0 & 0 & 1 \end{bmatrix}}_{\mathbf{K}} \mathbf{m} \quad (6)$$

where $\mathbf{K}$ is the intrinsic calibration matrix of the camera (assumed to be known). It depends on the optical parameters and the sensor. f_x and f_y are the focal distances, s the skew factor and (c_u, c_v) the coordinates of the optical axis in the image.

In order to simplify the presentation of the method, we take $f_x = f_y = f$ and $s = 0$ in the following developments. They can be adapted without major difficulty with a more general calibration matrix.

3.3.2 Computation of the rotation matrix According to the previous hypotheses, the rotation matrix is represented with the yaw (ψ) and pitch (ϕ) angles.

$$\mathbf{R} = \begin{bmatrix} \cos\psi & 0 & \sin\psi \\ 0 & 1 & 0 \\ -\sin\psi & 0 & \cos\psi \end{bmatrix} \cdot \begin{bmatrix} 1 & 0 & 0 \\ 0 & \cos\phi & -\sin\phi \\ 0 & \sin\phi & \cos\phi \end{bmatrix} \quad (7)$$

Taking into account that ψ and ϕ are small angles, (7) can be simplified:

$$\mathbf{R} \approx \mathbf{I} + \begin{bmatrix} 0 & 0 & \psi \\ 0 & 0 & 0 \\ -\psi & 0 & 0 \end{bmatrix} + \begin{bmatrix} 0 & 0 & 0 \\ 0 & 0 & -\phi \\ 0 & \phi & 0 \end{bmatrix} \quad (8)$$

In the following, these notations are used:

- (u_i, v_i) and (u'_i, v'_i) are the coordinates of the template i in images at time steps $t-1$ and t,
- $\mathbf{x_i} = [x_i\ y_i\ z_i]^T$ and $\mathbf{x'_i} = [x'_i\ y'_i\ z'_i]^T$ are the 3D corresponding coordinates in the camera frame (at time steps $t-1$ and t)

First, we can see that using (5-6) leads to:

$$\left\{ \begin{array}{rcl} \frac{x_i}{z_i} & = & \frac{u_i - c_u}{f} \\ \frac{y_i}{z_i} & = & \frac{v_i - c_v}{f} \end{array} \right. \text{ and } \left\{ \begin{array}{rcl} \frac{x'_i}{z'_i} & = & \frac{u'_i - c_u}{f} \\ \frac{y'_i}{z'_i} & = & \frac{v'_i - c_v}{f} \end{array} \right. \quad (9)$$

In order to find an expression of ψ and ϕ, we propose to compute $\mathbf{x}$ as a function of $\mathbf{x}'$ and then to apply the pinhole model. Taking into account (1) and (8), we have:

$$\mathbf{x} = \begin{bmatrix} x_i \\ y_i \\ z_i \end{bmatrix} = \begin{bmatrix} x'_i + \psi.z'_i \\ y'_i - \phi.z'_i \\ z'_i - \psi.x'_i + \phi.y'_i \end{bmatrix} \quad (10)$$

Applying the pinhole projection model to the new expression of $\mathbf{x}$ leads to:

$$\left\{ \begin{array}{rcl} \frac{u_i - c_u}{f} & = & \frac{x'_i + \psi.z'_i}{z'_i - \psi.x'_i + \phi.y'_i} \\ \frac{v_i - c_v}{f} & = & \frac{y'_i - \phi.z'_i}{z'_c - \psi.x'_i + \phi.y'_i} \end{array} \right. \quad (11)$$

Then, (12) can be simplified by dividing all the numerators and denominators by z'_i, and then applying (9):

$$\left\{ \begin{array}{rcl} \frac{u_i - c_u}{f} & = & \frac{u'_i - c_u + \psi.f}{f - \psi.(u'_i - c_u) + \phi.(v'_i - c_v)} \\ \frac{v_i - c_v}{f} & = & \frac{v'_i - c_u - \phi.f}{f - \psi.(u'_i - c_u) + \phi.(v'_i - c_v)} \end{array} \right. \quad (12)$$

For simplifying the notation, we define $U_i = \frac{u_i - c_u}{f}$, $V_i = \frac{v_i - c_v}{f}$, $U'_i = \frac{u'_i - c_u}{f}$ and $V'_i = \frac{v'_i - c_v}{f}$. Finally, multiplying the two equations in (12) by $(f - \psi.(u'_i - c_u) + \phi.(v'_i - c_v))$ leads to:

$$\underbrace{\begin{bmatrix} 1 + U_i.U'_i & -U_i.V'_i \\ V_i.U'_i & -1 - V_i.V'_i \end{bmatrix}}_{\mathbf{A}_i} \underbrace{\begin{bmatrix} \psi \\ \phi \end{bmatrix}}_{\mathbf{X}} = \underbrace{\begin{bmatrix} U_i - U'_i \\ V_i - V'_i \end{bmatrix}}_{\mathbf{B}_i} \quad (13)$$

Thus, (13) shows that it is possible to compute the two angles **for each template matching solution** by inverting a simple 2×2 system:

$$\mathbf{X} = \mathbf{A}_i^{-1} \mathbf{B}_i \quad (14)$$

This computation has to be done N times, but is really fast (only a very small system to inverse).

3.4 Outlier rejection and final solution

In the previous paragraph, we showed that it is possible to compute a solution for each template matching. This section focuses on the way to make the fusion of all the solutions.

First, we should remind that these solutions are computed thanks to strong hypotheses which can be violated if the points associated to the template are too close to the camera. Moreover, some template matching can also be inconsistent and should not be taken into account for the computation of the solution. To these reasons, a methodology to reject outliers is proposed:

1. First, a solution is computed for each template. This provides a set of (ψ_i, ϕ_i) ($i \in \{1 \dots N\}$).
2. Then, the median value for ψ and ϕ is computed. The median is an interesting statistic indicator because it is robust to outliers.
3. Finally, we define as inliers the solutions that have ψ_i and ϕ_i inside an interval centered on the median value.

This strategy can be seen as a simplified version of RANSAC algorithm (Fischler and Bolles, 1981). In order to save computational time, we take advantage of the fact that one template matching can provide one solution. Thus, we can directly compare the N solutions except of computing several solutions with a subset of templates.

Finally, the value for $\mathbf{X} = [\psi \ \phi]^T$ is computed by the least squares optimization of the following overdetermined system:

$$\underbrace{\begin{bmatrix} \mathbf{A}_1 \\ \vdots \\ \mathbf{A}_M \end{bmatrix}}_{\mathbf{A}} \cdot \mathbf{X} = \underbrace{\begin{bmatrix} \mathbf{B}_1 \\ \vdots \\ \mathbf{B}_M \end{bmatrix}}_{\mathbf{B}} \quad (15)$$

where $\mathbf{A}$ and $\mathbf{B}$ are made only with the inliers $\mathbf{A}_i$ and $\mathbf{B}_i$ defined in (13). The solution is thus given by:

$$\mathbf{X} = \begin{bmatrix} \psi \\ \phi \end{bmatrix} = \left(\mathbf{A}^T \cdot \mathbf{A} \right)^{-1} \mathbf{A}^T \mathbf{B} \quad (16)$$

Finally, the solution of (16) is used in (7) to compute and approximated rotation matrix which will be used as an initial value for LibViso2.

4. EXPERIMENTAL RESULTS

Our new solution was evaluated with real data. First, the experimental setup and the metric that will be used for evaluation are presented. Then, results are shown with a discussion.

4.1 Experimental setup and evaluation metrics

The algorithm was evaluated with real data acquired while the robot was driven in a small garden. The test area is about 40 meters wide and 30 meters long, composed of herbs, little rocks; for the little robot that we used, the area cannot be exactly considered as plane. During our tests, tracking system to have the ground truth of the robot trajectory was not available (because of outdoor situation). So, we put manually several landmarks that helps us to define a reference trajectory. However, only the starting and end points were known accurately. Moreover, an acquisition with a FARO 3D LiDAR scanner was realized in our testing area (Fig. 7). This scanner is a very accurate static station with high resolution. The coordinates of the landmarks were extracted from this point cloud.

The algorithm was tested in two situations: at low speed (1m/s) and high speed (5m/s). Low speed trajectory was about 40 meters long and high speed trajectory was about 24.5 meters.

Although the solution is not supposed to compute a complete trajectory and map, we use the global trajectory as a benchmark. Two metrics were used:

1. Trajectory error: the computed trajectories are compared to the reference one. More attention is given to the final error since it gives a good idea about the short term drift.
2. Point cloud error: the point cloud generated thanks to our algorithm is compared to the ground truth provided by the FARO scanner.

Trajectory error	in meter	in %
LibViso2 only		
Over 40m at 1m/s	3.25m	8.05 %
Over 24.5 at 5m/s	16m	66.3%
LibViso2 with rotation initialization		
Over 40m at 1m/s	1m	3 %
Over 24.5 at 5m/s	5m	20%

Table 2. Trajectory errors

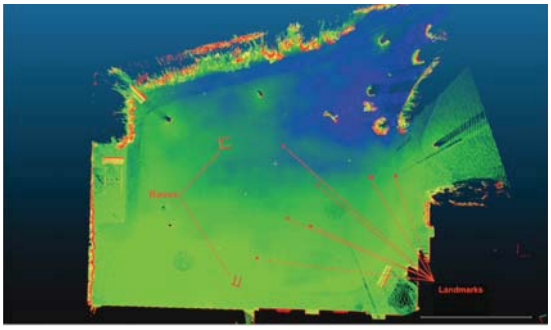

Figure 7. Reference scan of the area

In all the cases, the results provided by our algorithm are compared to the one provided by the original framework without rotation initialization for LibViso2.

4.2 Results

Low speed tests show a final 3% error on trajectory estimation (see table 2). As Fig. 8 shows, the trajectory is close to the reference and optimization made with rotation estimation allowed a noticeable gain (from 8% of final error to 3%). This result shows that the short term drift is very small, even in sharp turns: thus 3D reconstruction of the surrounding may not be impacted. This result is confirmed by the quality of the 3D reconstruction (Fig 10) which shows a dramatic improvement between original algorithm and our new algorithm. In (Ricaud et al., 2015), conclusion was that the reconstructed data were not accurate enough for obstacles detection and localization. Now, the surrounding point cloud is accurate enough to be segmented in a good way.

However, high speed tests show a final 20% error on trajectory (see table 2 and Fig. 9). In this case the system was not close enough to the reference trajectory, thus showing an important short term error. Thus, the consistency of the point cloud is not good enough to perform obstacle detection. Nevertheless, the solution is still better than the original one with LibViso2 only (from 66% to 20% on the final error).

Finally, the number of iterations needed for LibViso2 is also studied. Results are shown on Fig 11. It appeared that the proposed initialization step is really effective for improving the convergence time of the visual odometry algorithm. The number of iterations needed is almost always 4 only. Without rotation initialization, there were several peaks at more than 7 iterations, up to 13. These peaks were clearly removed by our method.

4.3 Discussion

Results at low speed are satisfying. In the perimeter of our application, it means that our system is able create a 3D reconstruction of environment which can be used to detect hazard without using

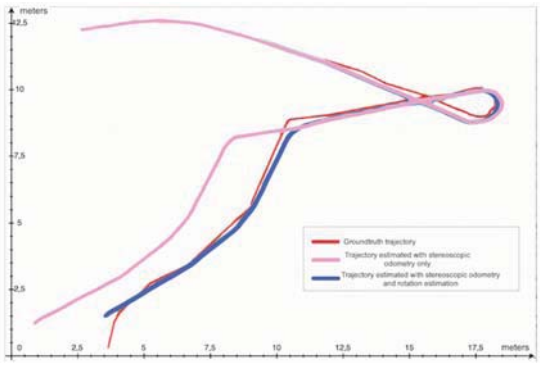

Figure 8. Trajectories at low speed — Red: reference trajectory, Purple: solution with LibViso2 only, Blue: solution with rotation initialization

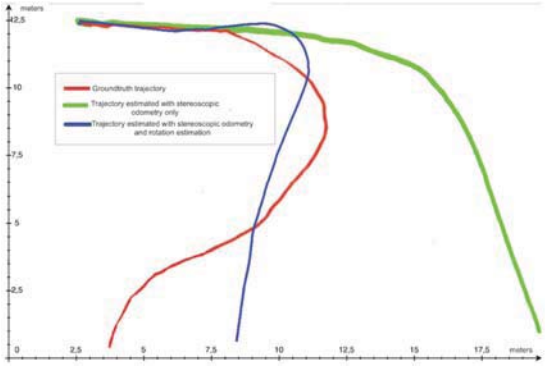

Figure 9. Trajectories at high speed — Red: reference trajectory, Green: solution with LibViso2 only, Blue: solution with rotation initialization

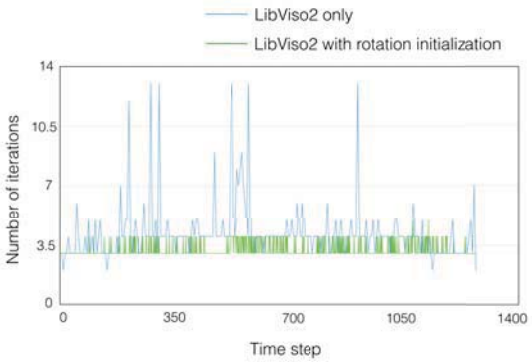

Figure 11. Number of iterations needed for LibViso2

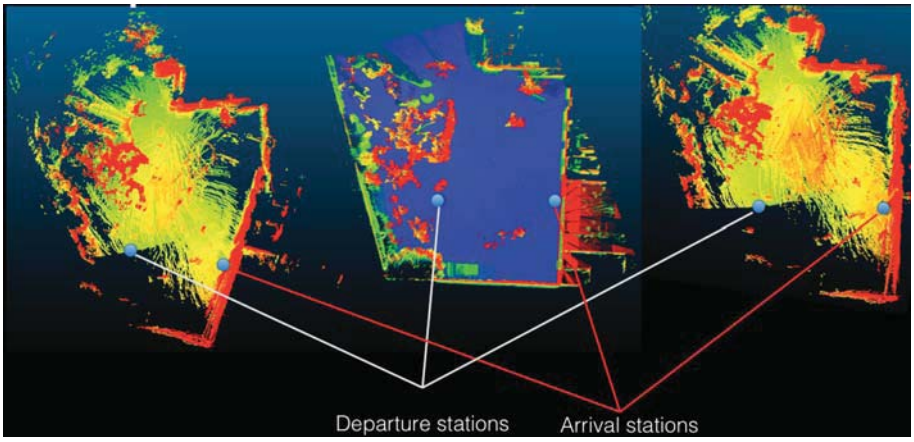

Figure 10. Point cloud at low speed — Left: solution with LibViso2 only, Middle: ground truth, Right: solution with rotation initialization

global positioning system. This was not the case with the previous version. However, it appeared that the algorithm does not compute reconstruction near enough to detect negative obstacles (holes...) but it is really effective for positive obstacles detection. On the other side, the algorithm needs to be improved for higher speed case.

5. CONCLUSION AND PERSPECTIVES

In this article we presented a system for 3D reconstruction in unstructured environment designed for a future hazard detection system for military vehicles. Description of hardware and software setup was provided to understand the concept in details. Then, an optimisation of a the framework of (Ricaud et al., 2015) was proposed; it consisted in computed a rough estimation of the rotation matrix to initialize the visual odometry algorithm. Results with real data acquired by a small robot showed that our optimization brings an important gain for trajectory estimation and 3D reconstruction. They showed that the method proposed is suitable for low speed driving, but still suffers of inconstancies at high speed. Thus, this validated the proof of concept.

Future work will focus on optimizing the method for high speed driving. Next, some test with real military vehicles have to be done to confirm the validity of this proof of concept.

ACKNOWLEDGMENT

This work was supported by the French armored vehicle manufacturer Nexter Systems.

REFERENCES

Braman, T. and Grossman, O., 2006. Designing vibration and shock isolation systems for micro electrical machined based inertial measurement units. In: *2006 IEEE/ION Position, Location, And Navigation Symposium*, pp. 400–404.

Briechle, K. and Hanebeck, U. D., 2001. Template matching using fast normalized cross correlation.

Cappalunga, A., Cattani, S., Broggi, A., McDaniel, M. S. and Dutta, S., 2010. Real time 3d terrain elevation mapping using ants optimization algorithm and stereo vision. In: *2010 IEEE Intelligent Vehicles Symposium*, pp. 902–909.

Durrant-Whyte, H. and Bailey, T., 2006. Simultaneous localisation and mapping (slam): Part i the essential algorithms. *IEEE ROBOTICS AND AUTOMATION MAGAZINE* 2, pp. 2006.

Espino, J. C., Steux, B. and Hamzaoui, O. E., 2011. Safe navigating system for indoor environments. In: *The 5th International Conference on Automation, Robotics and Applications*, pp. 419–423.

Fischler, M. A. and Bolles, R. C., 1981. Random sample consensus: A paradigm for model fitting with applications to image analysis and automated cartography. *Commun. ACM* 24(6), pp. 381–395.

Geiger, A., Ziegler, J. and Stiller, C., 2011. Stereoscan: Dense 3d reconstruction in real-time. In: *2011 IEEE Intelligent Vehicles Symposium (IV)*, pp. 963–968.

Larson, J. and Trivedi, M., 2011. Lidar based off-road negative obstacle detection and analysis. In: *2011 14th International IEEE Conference on Intelligent Transportation Systems (ITSC)*, pp. 192–197.

Lewis, J., 1995. Fast normalized cross-correlation. In: *Vision interface*, Vol. 10number 1, pp. 120–123.

Malartre, F., Delmas, P., Chapuis, R. and Debain, C., 2010. Real-time dense digital elevation map estimation using laserscanner and camera slam process. In: *2010 11th International Conference on Control Automation Robotics Vision*, pp. 1212–1218.

Paparoditis, N., Papelard, J.-P., Cannelle, B., Devaux, A., Soheilian, B., David, N. and Houzay, E., n.d. Stereopolis ii: A multi-purpose and multi-sensor 3d mobile mapping system for street visualisation and 3d metrology.

Piatti, D. and Ditag, A., 2010. Time-of-flight cameras: tests, calibration and multi-frame registration for automatic 3d object reconstruction. pp. 2008–2010.

Ricaud, B., Joly, C. and de La Fortelle, A., 2015. Non urban driver assistance with 2d tilting laser reconstruction. In: *Mobile Mapping Technology Proceedings*.

Smith, R. C. and Cheeseman, P., 1986. On the representation and estimation of spatial uncertainly. *Int. J. Rob. Res.* 5(4), pp. 56–68.

Zhang, J. and Singh, S., 2014. Loam: Lidar odometry and mapping in real-time. In: *Robotics: Science and Systems Conference*.

A NEW PLATFORM FOR ACTIVITY TRACKING IN SMART HEALTH SENSOR MONITORING SYSTEMS

Alaa Hussien, Sherine Youssef, Cherine Fathy
Computer Department College of Engineering, Arab Academy for Science and Technology (AAST), Alexandria, Egypt. allaa.hussien@student.aast.edu, sherin@aast.edu, cherine fathy@ieee.org

KEY WORDS: Neuropathy, Myopathy, muscle activity, disorder tracking, ALS, MUAP, EMG

ABSTRACT:
Healthcare improvement and monitoring has become the primary focus of studies and researches nowadays especially with the evolution of Internet of Things. A Health monitoring sensor network system is presented in this paper to track the patient's Electromyography Signal Remotely for Neuromuscular disorders diagnosis and treatment. In this paper, a new model is introduced for muscle activity disorder tracking through analyzing of Electromyogram signals (EMG). The proposed model integrates wavelet packet transform with candidate selection of Motor unit action potential (MUAP) for efficient feature extraction. A multi-class disorder discrimination of EMG signals is designed for various disorders identification such as Myopathy and Amyotrophic Lateral Sclerosis (ALS). Experiments have been conducted on large dataset of EMG signals to demonstrate the performance and robustness of the proposed model in terms of sensitivity, accuracy, and specificity. The proposed model outperforms existing models. Experimental results indicate up to 5.76 % improvement in terms of accuracy in case of multi-classification.

INTRODUCTION/SIGNIFICANCE OF THIS WORK:
IoT provides the devices the ability to share information directly with each other which makes it possible to collect, analyze and record new data streams faster and more accurately. Our concern in this paper is focused though on health care integrated with Internet of Things since its considered to be one of the most attractive and essential application areas for the IoT. A network of devices or sensors are connected together to record, collect and investigate vital and biomedical data about the patient [1]. An Electromyogram (EMG) signal is a biomedical signal that is concerned with the electrical activity of the muscle during voluntary contraction. Each muscle consists of muscle fibers which are connected to a motor neuron that transfers signals from the brain or spinal cord to the muscle. A single motor neuron and a set of muscle fibers connected to it are called motor unit (MU). Neuromuscular disorders are divided into motor neuron disorder and musculoskeletal disorder. Other names for them are Neuropathy and Myopathy respectively. The first one is caused due to the destruction or death of motor neurons. On the other hand, Myopathy is the damage of muscle fibers which causes muscle dysfunction.

METHODOLOGY:

1) *EMG Signal Decomposition*

Full decomposition is made to detect all the active motor units within the EMG signal [2].

2) *Choose Candidate MUAP*

When raw EMG signal is decomposed, a multiple temporal patterns of MUAP are extracted. In

this proposed model, not all MUAPs extracted from EMG signal by decomposition are used. It was proved in [1] that choosing only one MUAP and analyzing it by extracting discriminative features from it, is computationally more efficient than analyzing all the extracted MUAPs. The MUAP with higher peak to peak is chosen to be used for features extraction.

3) *Wavelet Packet Transform*

In our proposed method, wavelet packet-based feature level and the node, feature extraction phase is used next.

4) *Feature Extraction*

Selecting the appropriate feature leads to high classification accuracy. we only chose the most effective features to differentiate easily between MUAP classes, which are Standard Deviation of the coefficients of WPT, Autocorrelation, Skewness and RMS.

5) *Classification*

Classification phase begins by applying the extracted wavelet packet-based features as an input to the classifier [3]. A trainly models built to discriminate between three classes subjects: Normal class, Myopathy class and Neuropathy class. In this paper, and to test the performance of our approach, our model was tested on K-Nearest Neighbour (KNN) classifiers at K= 5.

6) *Decision sent over Network*

After the decision is made in the classification phase, the decision is then transferred across the network. Using mobile applications, personal devices, the doctors will be able to remotely track the patient's health and specify the right treatment across every stage of healing.

EXPERIMENTS AND CONCLUSION:

For comparison purpose, our approach was also employed on a public dataset [4] by running 10-fold cross validation which proved how our approach is computationally efficient in classifying between Normal, Neuropathy and Myopathy cases. Table I shows total accuracy results comparing our work with previous studies that used cross validation and the same dataset as well.

Table I: Comparison of proposed model with previous work

Paper	Accuracy
N.Guler et al,2005 [12]	85.4%
C.Katsis et al ,2007 [13]	88.70%
R.Istenic et al,2010 [14]	69.43%
S.Kocer et al,2010 [15]	90.00%
A.Goen et al,2013 [4]	91.20%
Proposed Model	95. 50%

Performance Evaluation in presence of noise

Like any other signal, EMG signal is affected by the physiological and environmental

surroundings. To evaluate the robustness of our approach, two types of noise are introduced: Movement artefact and Cross Contamination artefact[5].

1) Movement Artefact

It occurs when the sensor or the cable connecting the electrode to the amplifier moves causing motion artefacts. In brief, when the muscle contracts, skin and electrodes move with respect to one another. The frequency range of the motion artefact is usually between 1-10 Hz and has amplitude just like the EMG signal. To simulate such artefact, a periodic sinusoidal with 10 Hz was created and added on the EMG signal. Accuracy was calculated again after adding motion artefact and the results were really satisfactory as it was approximately equal 93% .

2) Cross Contamination Artefact

EMG signal might not all be resulting from the required muscle; some may be resulting from the neighboring muscles. These signals are called "Cross Talk" signals which may superimpose the EMG signal and distorts the amplitude of the signal. A sinusoidal periodic signal with 16 and 56 Hz were created and added on the EMG signal to test the robustness of the model. 97% and 93% of accuracy was earned after feeding the signals to our model.

REFERENCES:

[1] A. B. M. S. U. Doulah1, S.A.N. Fattah1, W. Zhu2, M. O.Ahmad2, DCT domain feature extraction scheme based on motor unit action potential of EMG signal for neuromuscular disease classification. Published in Healthcare Technology Letters on 17th March 2014.

[2] McGill KC, Lateva ZC, Marateb HR. EMGLAB: an interactive EMG decomposition program. J Neurosci Methods 149(2):121-133, 2005. [The software is available at http://www.emglab.net]

[3] N. F. Güler and S. Koçer, "Classification of EMG signals using PCA and FFT," Journal of Medical Systems, vol. 29, no. 3, pp. 241-250, June 2005.

[4] Nikolic M. Detailed Analysis of Clinical Electromyography Signals EMG Decomposition, Findings and Firing Pattern Analysis in Controls and Patients with Myopathy and Amytrophic Lateral Sclerosis. PhD Thesis, Faculty of Health Science, University of Copenhagen, 2001. [The data are available as dataset N2001 at http://www.emglab.net]

[5] C. D. Katsis, T. P. Exarchos, C. Papaloukas, Y. Goletsis, D. I. Fotiadis, and I. Sarmas, "A two-stage method for MUAP classification based on EMG decomposition," Computers in Biology and Medicine, vol. 37, no. 9, pp. 1232-1240, 2007.

TUNING OF THE ERROR COVARIANCE PARAMETERS IN EKF-BASED INS/GPS SYSTEMS: A PRACTICAL APPROACH

Mostafa Mahmoud[a,*], Islam Alaa[b], Amr Wassal[a], Aboelmagd Noureldin[c], Amr ElDieb[b]

[a] Computer Engineering Department, Cairo University, Cairo University Road, Giza 12613, Egypt - mostafa_mahmoud_mohamed@cu.edu.eg ,wassal@eng.cu.edu.eg
[b] Systems Design Group, Si-Ware Systems, 3 Khaled Ibn Al-Waleed Street, Heliopolis, Cairo 11361, Egypt - (islam.alaa, amr.eldieb)@si-ware.com
[c] Department of Electrical and Computer Engineering, RMC / Queens University, Kingston, Ontario, Canada - aboelmagd.noureldin@rmc.ca

KEY WORDS: Extended Kalman Filter (EKF), Inertial Navigation Systems (INS), Micro-Electro-Mechanical-System (MEMS), Global Positioning Systems (GPS), Root Mean Square Error (RMSE)

ABSTRACT:

The low cost, small size and low power consumption micro-electro-mechanical-system (MEMS) inertial sensors enabled the use of inertial navigation systems (INS) in many consumer applications. This was not possible in the past with high end INS due to cost and size constraints. However, MEMS inertial sensors suffer from bias drift, which is stochastic in nature and significantly influence the long-term positioning accuracy. The long-term position drift is mainly due to the inherent mathematical integration of the inertial sensor biases resulting in heavily degraded positioning over a short period of continuous use. On the other hand, Global Positioning Systems (GPS) offer position, velocity and timing information with consistent level of positioning accuracy, albeit suffering from the problem of signal outage due to losing direct line-of-sight with sufficient number of GPS satellites in both indoor and some outdoor conditions or due to multi-path effects. The INS can provide reliable navigation information for the short-term hat can bridge GPS outages. In addition, INS provides information about the attitude and heading angles of the moving platform. Therefore, due to the complementary nature of the INS and the GPS information, they are usually fused together to generate more robust and reliable navigation information. This fusion can be done with different techniques, such as Kalman filters, which used in our work. In this paper, different tuning methodologies for similar systems in the literature are reviewed qualitatively in brief. Consequently, the methodology for the tuning of the error covariance matrices R, Q, and P in EKF-based INS/GPS systems used is described. The results of the tuning of the EKF-based INS/GPS system is presented for two different datasets. The first dataset is acquired using a high-end tactical-grade SPAN unit featuring Novatel HG1700 IMU module. The second dataset is acquired from a MEMS-based SCC1300-D04 IMU unit from VTI. A comparative study of the performance of the proposed approach using the two datasets utilizing the tuning methodology described is discussed in this paper against a reference ground-truth dataset for the same trajectories.

1. INTRODUCTION

Reliable and precise positioning and navigation systems play a vital role in many civilian applications including smart driving, unmanned aerial vehicles (UAVs) control, transportation tracking and monitoring among many others. The emerging technologies of the low-cost MEMS-based inertial sensors (i.e. 3-axis gyroscopes and accelerometers) permitted the design and implementation of cost-efficient inertial navigation systems (INS). However, such systems are not reliable on the long run as their accuracy is degraded while operation due to the bias drift in MEMS-based sensors. On the other hand, the Global Positioning System (GPS) can provide positioning and navigation information with bounded error characteristics. Therefore, it is thought that, the fusion between INS and GPS can achieve better performance in both short run and long run conditions. Several attempts were done to efficiently fuse INS and GPS together in a single navigation system using different fusion techniques. However, Extended Kalman Filter (EKF) was the most common method that is usually used for integration. In this paper, the INS/GPS integration using an EKF is presented, the tuning of the EKF as well as the results of fusion and tuning are illustrated using two different data sets against ground truth trajectories.

*Corresponding author

The remainder of this paper is organized as follows. INS/GPS integration is explained in section 2. Section 3 explained the tuning methodology in detail. The simulation and experimental tests are presented in section 4 followed by the concluding remarks in section 5.

2. INS/GPS INTEGRATION

The block diagram of the integration between the INS and the GPS is shown in Figure 1. Raw sensor data are mechanized in order to generate the INS navigation information (i.e. attitude, velocity, and position) and is then fused with the GPS inside an EKF. Consequently, The output of the fusion is fed-back to the system to enhance the system performance.

2.1 Navigation System Model

The following equation represent the system model for the INS mechanization used in the INS/GPS integration which yields the attitude, velocity and position realized in the local level frame.

$$\begin{bmatrix} \dot{r}^l \\ \dot{V}^l \\ \dot{R}_b^l \end{bmatrix} = \begin{bmatrix} D^{-1}V^l \\ R_b^l f_b - (2\Omega_{ie}^l + \Omega_{el}^l)V^l + g^l \\ R_b^l(\Omega_{ib}^b - \Omega_{il}^b) \end{bmatrix} \quad (1)$$

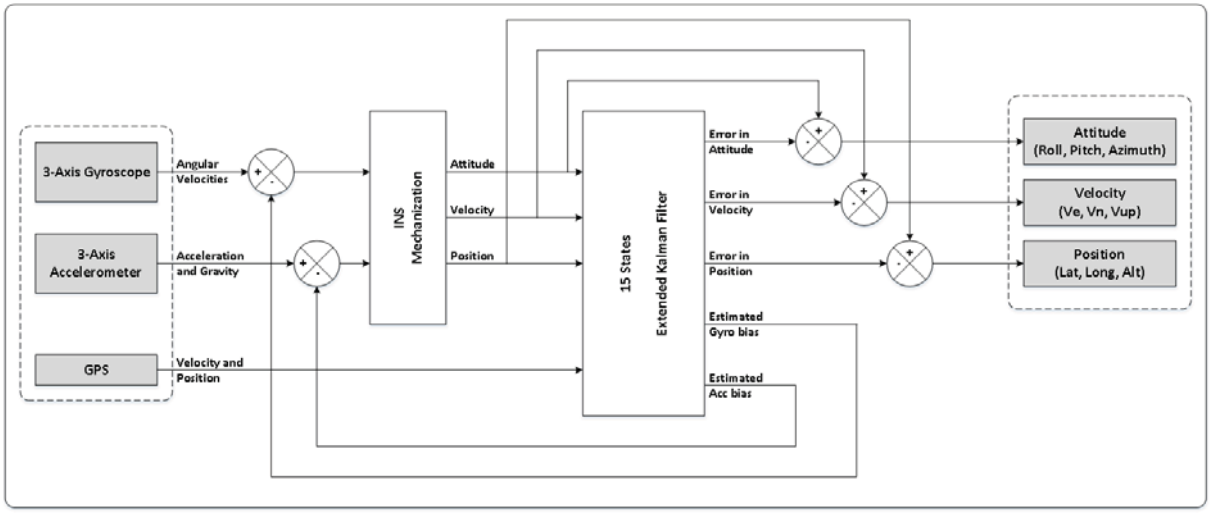

Figure 1. INS/GPS integration

Where:

- $\dot{r}^l$: is the time rate of change of the position.
- $\dot{V}^l$: is the time rate of change of velocity.
- $\dot{R}_b^l$: is the time rate of change of rotational matrix from body frame to local level frame.
- R_b^l : is the rotation matrix from body frame to local level frame.
- f_b : is the acceleration in the body frame.
- g^l : is the earth gravity vector in the local level frame.
- Ω_{ie}^l : is the skew symmetric matrix of earth rotation about its spin axis.
- Ω_{el}^l : is the skew symmetric matrix of orientation change of local level frame with respect to the earth.
- Ω_{ib}^b : is the skew symmetric matrix of the measurements of angular velocities.
- Ω_{il}^b : is the skew symmetric matrix of the compensation term used to account for the earth rotation rate and orientation change of the local-level.

The mentioned nine navigational states (attitude, velocity, and position) suffer from a severe drifting effect after a very short period of time due to the numerical integration of the stochastic bias in inertial sensors which amends the integration with a GPS to optimally estimate the stochastic biases and correct the error in the navigation states.

2.2 INS/GPS Fusion Using an Extended Kalman Filter

Extended Kalman Filter (EKF) is the conventional estimation tool that is used to fuse data from INS and GPS systems together to achieve continuous, accurate and reliable positioning and navigation solution. This method requires the knowledge of the error covariance of the different information sources present in the system to estimate the navigation state. The error covariance matrices present in the system are the Q matrix which defines the error covariance of the driving information source (the INS in this case), the R matrix which defines the error covariance of the aiding information source (the GPS in this case), and the P matrix which defines the error covariance of the system states. The performance of the EKF-based INS/GPS systems depends heavily on the initial values of different error covariance matrices that are present in the filter. These initial values affect both the accuracy of the estimated states, and the filter convergence time. The R and Q matrices determine the weight by which each source, the driving source and the aiding source, of information in the system contributes to the final estimated state. Proper choice of the values inside the R and Q matrices will result in better accuracy in the estimated navigation state. On the other hand, the initial values of the elements of the P matrix affect directly the filter convergence time, which, together with the previously mentioned matrices, define the overall system performance (Quinchia et al., 2013). The following equations summarize the kalman filter operation, derivation details can be found in (Noureldin et al., 2013)

EKF starts by the $Prediction$ step that includes projecting the state ahead, and projecting the error covariance ahead. The $Prediction$ step is illustrated in the following equations:

$$\hat{x}_k = A\hat{x}_{k-1} \tag{2}$$

$$P_k^- = AP_{k-1}A^T + Q \tag{3}$$

After that, the filter proceeds to the $Correction$ step, in which the kalman gain is computer, the estimates are updated by the measurement, and the error covariance gets updated. The $Correction$ step is illustrated in the following equations:

$$K_k = P_k^- H^T (HP_k^- H^T + R)^{-1} \tag{4}$$

$$\hat{x}_k = \hat{x}_k^- + K_k(z_k - H\hat{x}_k^-) \tag{5}$$

$$P_k = (I - K_k H)P_k^- \tag{6}$$

2.3 Feedback and State Correction

The EKF-based INS/GPS system estimates the error in attitude, velocity, and position. It also estimates the stochastic part of the sensor bias for the 3-axis gyroscope and the 3-axis accelerometer. These estimated errors in the navigation state are then subtracted

from the INS results in order to produced the corrected navigation states. Moreover, the estimated stochastic sensors' bias values are fed-back to the sensors to be subtracted from the raw sensors' quantities. The fed-back sensor biases help the INS to limit the drift in a real-time manner.

3. KALMAN FILTER TUNING

The estimation of the error covariance parameters in EKF-based systems is usually performed offline before the system final deployment. The definition of these parameters is dependent on the filter state definition, and whether EKF will be used to estimate the full navigation state or the error in it. Subsequently, the values resulting from the error covariance parameters estimation is used as a starting point, and will need further manual fine tuning in order to achieve the best achievable performance from the EKF. This iterative process of manual fine tuning of the EKF is usually judged by the system convergence time, the existence of divergence intervals in the state error covariance matrix, and the final estimated state accuracy. However, different attempts were undertaken in order to tackle the problem of tuning Kalman Filters and its derivatives in an efficient way. The main objective of all these attempts was either to estimate the initial values of different covariance matrices P_0, R, and Q, or to adaptively change their values during operation to account for any dynamic changes in the inputs characteristics. In (Powell, 2002) formulated the tuning problem as a numerical optimization problem, and solved it using the Downhill Simplex Algorithm. While in (Bolognani et al., 2003) a method for proper choice of the covariance matrices in EKF based on a self-tuning procedure was presented. The method is based on a complete normalization of the EKF representation to allow the self-tuning procedure to fit in a wide range of filter configurations. The objective of this proposal was to find a method for tuning for mass-produced products that includes EKF as a building block inside it without the need to tune each part at its own in order to compensate for manufacturing uncertainties. The paper discussed the method and reported its performance in an AC motor drives-related application. In addition to that, (Loebis et al., 2004) discussed the use of fuzzy logic techniques for the estimation of the initial error covariance parameters in two proposed kalman filters. The filters are used for the navigation of an autonomous underwater vehicle. Means of cost function for adaptive tuning of the kalman filter covariance was also mentioned in (Basil et al., 2004). Furthermore, (Macias and Exposito, 2006) proposed a method for the self-tuning of kalman filters to track the harmonic random changes. The method proposes an adaptive procedure for the estimation of the driving source covariance matrix as well as the state covariance matrix every time epoch. The method was tested against sudden input changes to show their performance in such conditions. A significant improvement in the kalman filter performance was shown in (Akesson et al., 2007) by the proposal of a tool for kalman filter tuning. This tool is based on the generalization of the autocovariance least-squares method to systems with mutually correlated noise characteristics. Moreover, (Åkesson et al., 2008) a method for estimating the noise covariance from process data is proposed based on the linear relation between the covariance and the autocovariance and formulating the problem as a least-squares problem. Besides that, (Shu et al., 2013) discussed the tuning and steady-state performance of a third-order integrated random walk model in details and was compared with a first-order auto-regressive model. The results showed that a well-tuned third-order integrated random walk model-based KF outperform the other method. Finally, (Matisko and Havlena, 2013) presented a method for the tuning of the error covariance matrices using bayesian approach and monte Carlo simulations is presented and compared with other methods in the literature.

3.1 Utilized Tuning Methodology

1. P_0 **Matrix** represents the error in the kalman state. The initial values are defined as the error in the error state and are defined as the average between the ground truth S_{ref} and the corrected INS data S_{INS} by the estimated error E_{est} from EKF as illustrated in (7).

$$P_0(i,j) = \begin{cases} avg((S_{ref} - S_{INS}) - E_{est}), & \text{if } i = j \\ 0, & \text{otherwise} \end{cases} \quad (7)$$

It is assumed that the navigation states' error characteristics are independent from each other and completely decoupled. Consequently, and as noted from the previous equation, only diagonal elements has covariance values and off-diagonal elements are all set to zeros to satisfy this assumption. Moreover, Experiments shown that setting the P_0 matrix to zeros or values very close to zeros affects the convergence time negatively. Finally, The P_0 matrix is only initialized and then gets updated automatically by the EKF equations.

2. R **Matrix** represents the error covariance in the aiding sensors (i.e. the GPS in our case). Usually, GPS modules provide the error variance or standard deviation information for both position and velocity. These received variance values can be used directly in the R matrix. They represent the confidence in the received GPS readings and are affected by outage and interference conditions. At each epoch, new values are received and fed to the R matrix.

3. Q **Matrix** represents the error in the driving sensors (i.e. INS in our case). The initial values are defined as the error between the ground truth S_{ref} and the uncorrected INS data S_{INS} as illustrated in (8).

$$Q(i,j) = \begin{cases} avg((S_{ref} - S_{INS})), & \text{if } i = j \\ 0, & \text{otherwise} \end{cases} \quad (8)$$

Similar to the P_0 matrix, it is assumed that the navigation states' error characteristics in the standalone INS are independent from each other and completely decoupled. Consequently, and as noted from the previous equation, only diagonal elements has covariance values and off-diagonal elements are all set to zeros to satisfy this assumption. Finally, The Q matrix is only initialized and is not changed during operation, as the error reliability of the INS is not likely to change during operation in our case.

4. Error Covariance Fine Tuning is performed after the final offline definition of different error covariance matrices. An iterative process of manual fine tuning of the EKF is initialed and is usually judged by the system convergence time, the existence of divergence intervals in the state error covariance matrix, and the final estimated state accuracy.

4. SIMULATION AND EXPERIMENTAL RESULTS

The results of the tuning of the EKF-based INS/GPS system are presented for two different datasets. The first dataset is acquired using a high-end tactical-grade SPAN unit featuring Novatel HG1700 IMU module. The second dataset is acquired from

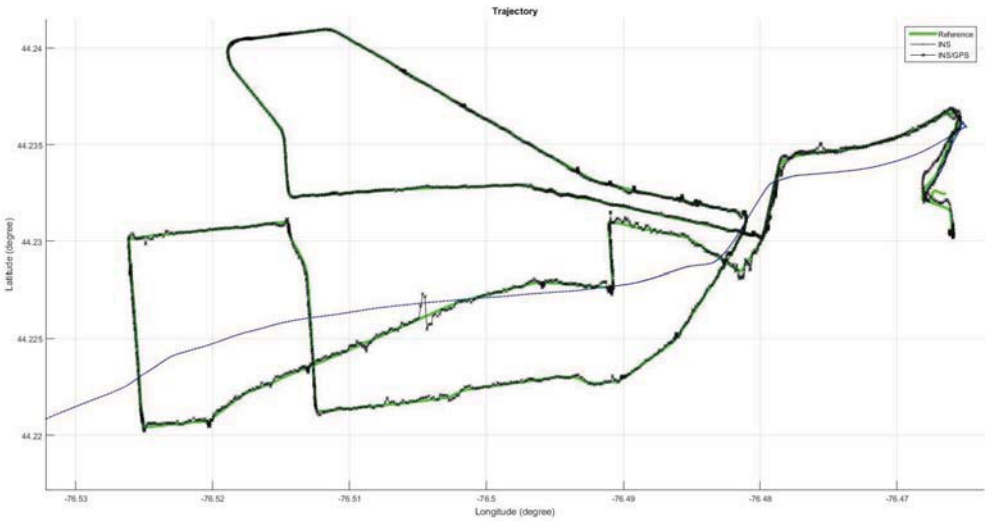

Figure 2. Novatel HG1700 Trajectory Results

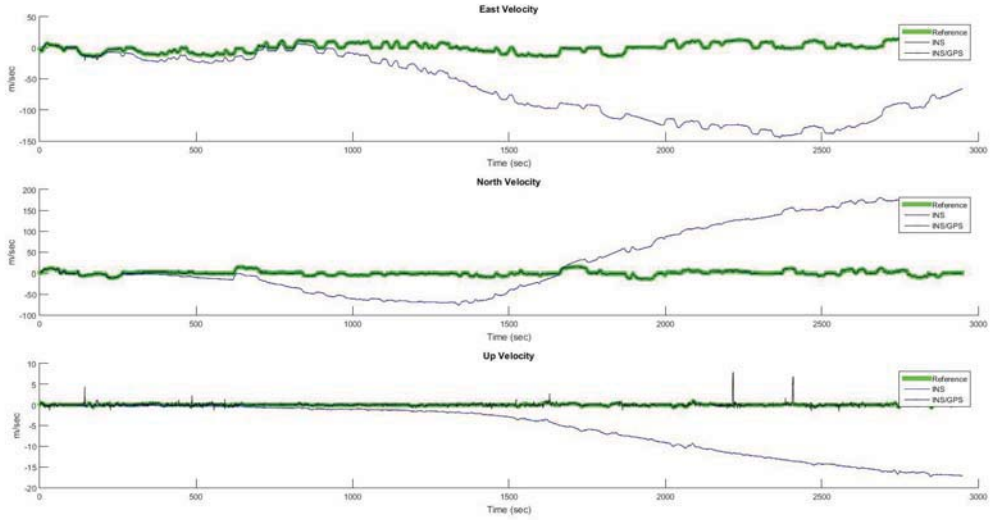

Figure 3. Novatel HG1700 Velocity Results

a MEMS-based SCC1300-D04 IMU unit from VTI. Figure 2 shows the trajectory produced by the standalone INS vs. the INS/GPS integration against the reference trajectory of the high-end tactical-grade SPAN unit. In addition to that, Figure 3 and Figure 4 show the accuracy of the the velocity and attitude of the system for both the standalone INS and the integrated INS/GPS system against the same reference trajectory. A large drift in position, velocity, and attitude can be observed in the INS-standalone system results. While, this drift was bounded and eliminated after the integration with the GPS. Analytically, The maximum root mean square error (RMSE) values of different navigation states are presented in Table 1

Table 1. Comparison between the maximum RMSE in standalone INS and integrated INS/GPS

	$RMSE_{INS}$	$RMSE_{INS/GPS}$
Position	42363.7 m	2.8515 m
Velocity	60.2683 m/sec	0.2424 m/sec
Attitude	1.795°	0.8517°

Figure 5 shows the trajectory produced by the standalone INS vs. the INS/GPS integration against the reference trajectory MEMS-based SCC1300-D04 IMU unit from VTI. It shows that the tuned EKF-based INS/GPS yields a more robust and reliable navigation information than the standalone INS.

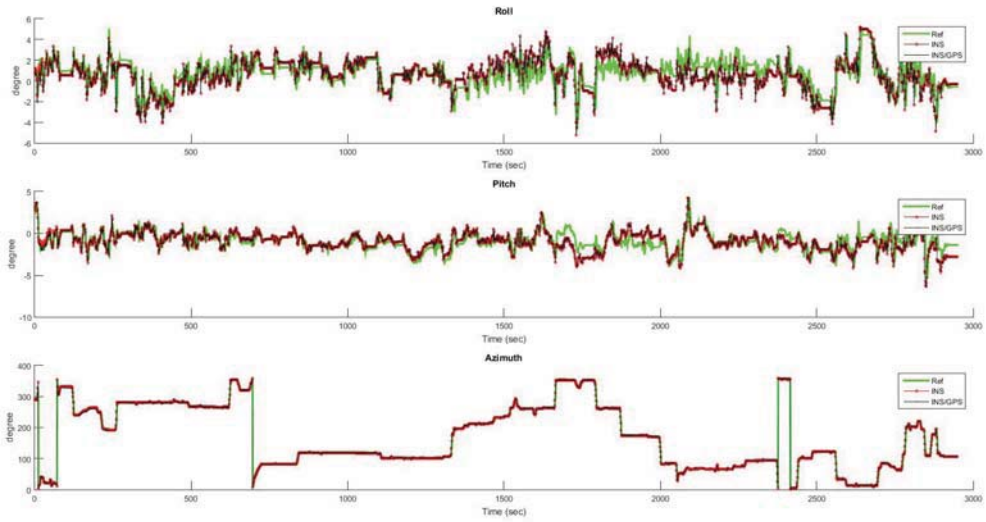

Figure 4. Novatel HG1700 Attitude Results

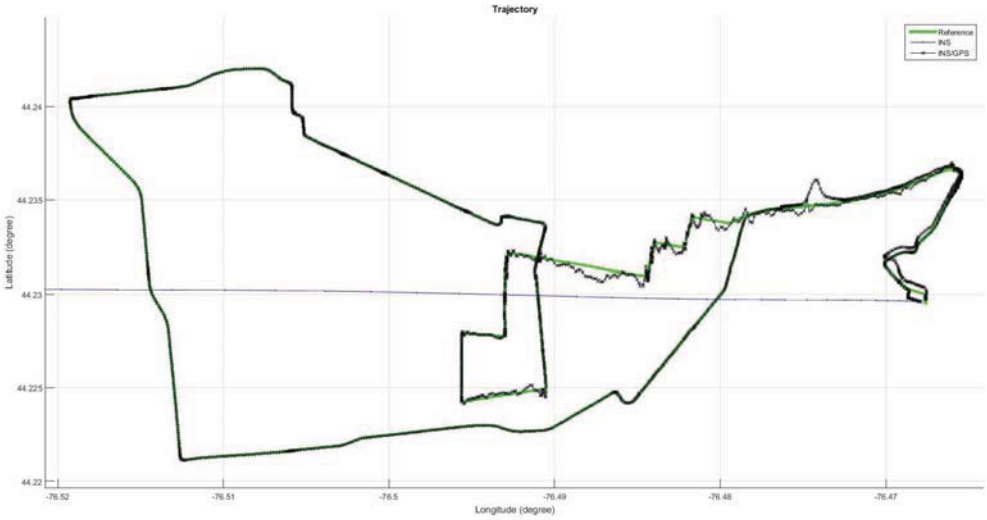

Figure 5. VTI SCC1300-D04 Trajectory Results

5. CONCLUSION

Standalone INS navigation systems are essential to be used because of their ability to provide continuous navigation information regardless of the environment conditions. On the other hand, the GPS navigation capabilities are affected by different environmental aspects such as the outage and signal interference among many others. However, it can provide a good navigation accuracy on the long term. Obviously, INS and GPS are complementary in nature and fusing them will yield a stable navigation solution both on the short term and on the long term. The integration accuracy and yielded performance depends heavily on the quality of the tuning of different error covariance parameters presented in the system. In this paper, the integration between the INS and GPS using an EKF was presented. Different tuning methodologies were reviewed qualitatively and in brief. A tuning methodology for the error covariance matrices was presented and applied on two datasets taken from a high-end tactical-grade SPAN unit featuring Novatel HG1700 IMU module and a MEMS-based SCC1300-D04 IMU unit from VTI. The results presented show how the tuned EKF achieved a better performance than each system alone (i.e. INS and GPS) in terms of the accuracy and the fast convergence.

ACKNOWLEDGEMENT

This work was partially supported by a Collaborative Funded Project (CFP) grant, number **PDP2014.R16.2**, from ITIDA's Information Technology Academia Collaboration (ITAC) program.

The authors appreciate this generous support and acknowledge it.

REFERENCES

Åkesson, B. M., Jørgensen, J. B., Poulsen, N. K. and Jørgensen, S. B., 2008. A generalized autocovariance least-squares method for kalman filter tuning. *Journal of Process Control* 18(7-8), pp. 769–779.

Akesson, B. M., Jorgensen, J., Poulsen, N. K. and Jorgensen, S. B., 2007. A tool for kalman filter tuning. *Computer Aided Chemical Engineering* 24, pp. 859.

Basil, H., Anathasayanam, M. and Puri, S., 2004. Adaptive kalman filter tuning in integration of low-cost mems-ins/gps. In: *AIAA Guidance, Navigation, and Control Conference and Exhibit*, p. 5122.

Bolognani, S., Tubiana, L. and Zigliotto, M., 2003. Extended kalman filter tuning in sensorless PMSM drives. *IEEE Transactions on Industry Applications* 39(6), pp. 1741–1747.

Loebis, D., Sutton, R., Chudley, J. and Naeem, W., 2004. Adaptive tuning of a kalman filter via fuzzy logic for an intelligent auv navigation system. *Control engineering practice* 12(12), pp. 1531–1539.

Macias, J. R. and Exposito, A. G., 2006. Self-tuning of kalman filters for harmonic computation. *IEEE Transactions on Power Delivery* 21(1), pp. 501–503.

Matisko, P. and Havlena, V., 2013. Noise covariance estimation for kalman filter tuning using bayesian approach and monte carlo. *International Journal of Adaptive Control and Signal Processing* 27(11), pp. 957–973.

Noureldin, A., Karamat, T. B. and Georgy, J., 2013. *Fundamentals of Inertial Navigation, Satellite-based Positioning and their Integration*. Springer Nature.

Powell, T. D., 2002. Automated tuning of an extended kalman filter using the downhill simplex algorithm. *Journal of Guidance, Control, and Dynamics* 25(5), pp. 901–908.

Quinchia, A., Falco, G., Falletti, E., Dovis, F. and Ferrer, C., 2013. A comparison between different error modeling of MEMS applied to GPS/INS integrated systems. *Sensors* 13(8), pp. 9549–9588.

Shu, H., Simon, E. P. and Ros, L., 2013. Third-order kalman filter: Tuning and steady-state performance. *IEEE Signal Processing Letters* 20(11), pp. 1082–1085.

Revised March 2017

Mobile-based Remotely Veichle Tracking System

Essam A. Hamied
Information & Documentation Center
Arab Academy for Science and Technology
Alexandria, Egypt
essamabdelhamied@aast.edu

Sherin M.Youssef
Department of computer Engineering
Arab Academy for Science and Technology
Alexandria, Egypt
sherin@aast.edu

***Abstract*— Vehicle tracking is monitoring the location of a truck, car or any moving vehicle using the GPS system. The paper introduces a model for the development of remotely vehicle tracking system which integrates GPS tracking and Google Maps. It also remotely monitors the dynamic changes of vehicle sensors changes. This tracking system can inform you the location and route travelled by vehicle, and that information can be observed from any other remote location. It also includes the web application that provides you exact location of target. This system enables us to track target in any weather conditions. This system uses GPS and 3G technologies. The developed system can robustly track vehicles and moving trucks on google maps with high accuracy**

I. INTRODUCTION

In today's world, the use of Mobiles is of increasingly in use while compared to the use and adoption of Internet. The technological improvements in the recent times have made Mobile Phones very handy and compact. The earlier Mobile Phones so called "Hand Phone" was of size equal to that of a landline and the only difference was that it was wireless. Now we have "Smart Phones" that are the size of our palm. Mobile Computing plays a vital role in today's modern world. Mobile Computing has paved a path for the various modern techniques. Mobile Computing involves mobile communication, mobile hardware, and mobile software. Communication issues include ad-hoc and infrastructure networks as well as communication properties, protocols, data formats and concrete technologies [7].

Today Mobile Computing is so widely used that it has penetrated in all aspects of our lives. Mobile Computing is an active area of research. Most applications available to users today are targeted at teenagers and yuppies and are mostly infotainment applications. For example, music downloader, friend locators and news updates are some of the various applications available. It will take a few more years before which. The Mobile Applications developed today contains flaws that will have to be rectified and be provided with further advancements that help's the applications to be more efficient. The global position system (GPS) has become a common functionality in handheld devices, and therefore, several location-tracking applications have been developed, including continuous location-tracking of elders and children for safety reasons or to prevent them from being lost car monitoring and tracking, and intelligent transportation systems.

GPS tracking uses elements of both time and location to provide data points for the user. GPS, or Global Positioning System, is a satellite navigation system that receives data via satellites in space. GPS tracking can be used to track vehicles, equipment, mobile phones, people, animals, and more. A common use for GPS is for the user to set and receive live step-by-step directions. The GPS signal is transmitted from a device (either stand alone or a mobile phone) and the time and location data is sent to the satellite. The GPS tracking information is processed and then sent to a data center for storage. In the case of GPS tracking, the data is sent to servers and then translated into meaningful and money-saving reports [8].

GPS vehicle tracking can be an important money-saving tool for your small- or medium-sized business. If you have a fleet of vehicles, GPS tracking may be able to help your fleet reduce idle times, improve routing operations, and better customer service. As a result, you may be able to lower overhead business costs and increase your bottom line. GPS tracking for your fleet vehicles allows you to run a smarter business overall [9].

Recently, Google has developed the Android platform, which is an open system, offering high flexibility on development. Due to this, it is very useful to develop a GPS navigation system on the Android platform with combing many Google resources. With Google Maps' free navigation functionality, people may prefer the costless service from Google over that of paid services. GPS does not need the support of any kind of internet network to provide information accurately, but if combined with any network it, the accuracy of the system could be enhanced in a much better way.

II. LITERATURE SURVEYING

Real-time tracking and management of vehicles has been a field of interest for many researchers and a lot of research work has been done for tracking system. Recently the various anti-theft modules like steering wheel locked equipment, network tracking system and traditional electronic alarm are developed along with client identification and real time performance monitoring.

The paper presented by El-Medany, W.; Al-Omary et al describes a real time tracking system that provides accurate localizations of the tracked vehicle with low cost. GM862 cellular quad band module is used for implementation. A monitoring server and a graphical user interface on a website is

also developed using Microsoft SQL Server 2003 and ASP.net to view the proper location of a vehicle on a specific map. The paper also provides information regarding the vehicle status such as speed, mileage [1].

Hu Jian-ming; Li Jie; Li Guang-Hui describes an automobile anti-theft system using GSM and GPS module. The system is developed using high speed mixed type single-chip C8051F120 and stolen automobile is detected by the use of vibration sensor. The system remains in contact with automobile owner through the GSM module, for the safety and reliability of automobile [2].

Fleischer, P.B.; Nelson et al describes development and deployment of GPS (Global Positioning System)/GSM (Global System for Mobile Communications) based Vehicle Tracking and Alert System. This system allows inter-city transport companies to track their vehicles in real-time and provides security from armed robbery and accident occurrences [3].

Le-Tien, T.; Vu Phung describes a system based on the Global Positioning System (GPS) and Global System for Mobile Communication (GSM). It describes the practical model for routing and tracking with mobile vehicle in a large area outdoor environment. The system includes the Compass sensor-YAS529 of Yamaha Company and Accelerator sensor-KXSC72050 of Koinix Company to acquire moving direction of a vehicle. The system will acquire positions of the vehicle via GPS receiver and then sends the data to supervised center by the SMS (Short Message Services) or GPRS (General Package Radio Service) service. The supervised center comprises of a development kit that supports GSM techniques-WMP100 of the Wavecom Company. Finally, the position of the mobile vehicle will be displayed on Google Map [4].

Chew et al. in 2006, proposed A Hybrid Mobile-based Patient Location Tracking System for Personal Healthcare Applications. [5] They proposed a crossbreed portable based area system using the worldwide situating framework (GPS) and cell convenient framework establishment is used to give the range after fitness using modem. Lenain et al., in 2006 proposed Mobile robot control in vicinity of sliding which is an Application to agrarian vehicle way tracking [6].

Varandas et al., in 2010 proposed an mtracker which is a Mobile Tracking Application for Pervasive Environment created for cellular telephones. Through the known geographic position, this requisition empowers the client to track a cell phone and send cautions on the off chance that it is out of the span around an investment point, long ago characterized by the provision chairman. Donko et al., in 2012 proposed Implementation of tracking mobile application and analysis of spatial data. This model presents utilization of existing aspects of global navigation and global position system (GPS), and visualization of Earth using satellite images, in order to gather and store particular data.

III. THE PROPOSED MOBILE BASED VEHICLE TRACKING

A. Mobile Based Tracking

Portable Mobile-based Vehicle Tracking (MVT) framework is a constant versatile application for Android clients. This framework permits clients to view the greater part of the enrolled transport course maps, with current transport areas and transport stops on Google Map. Client can begin review of numerous transport courses at the same time. This likewise incorporates a transport following gimmick for both the learners and staff all-inclusive school and school transports furthermore Community Service courses and comparative applications. This portable website offers the same level of correctness on transport areas as the full offered transport locator on the site however in an organization intended for cell phones.

B. Objectives of MVT

Our main objective is to design and implement an android-based mobile application to tracker the navigation of a vehicle for the purpose of tracking and navigation control. Micro-controller technology will be used during the project and a mobile software will be developed to remotely control the Vehicle via wireless communication. Eclipse software will be used to build the mobile application as it is considered one of the most efficient soft wares based on java programming.

The objectives exploring the proposed Mobile-based Vehicle Tracking system are:

- Introducing the vehicle auto tracker system using the GPS for position information and information transmission respectively.
- Locating the vehicle position in Google maps through track request and providing all transmitted information to the end user in addition to the location of the vehicle on the maps.
- Transmission of vehicle's location and other information to the monitoring station which is the tracking server after specified interval of time.
- Main contribution of the project is to provide effective vehicle location information by updating timely through the feedback mechanism collected from the users.

The features provide the following advantages:

- GPS car tracker provides tracking updates every 2 minutes so you never lose track of your car.
- Car tracking device uses Google maps, monitor car move on a map in real time
- Get alerted when your car moves between different zones.
- Mobile alert notification in case of emergency
- Traffic bottle neck alerts
- Electronic profile for vehicle sensing changes.

C. Architecture of Mobile based Vehicle Tracking

The architecture of the system is as shown in figure. This basically consists of two applications, first web based and second one android app. The web based application provides the registration process for vehicles and mobile app is used in tracking the vehicle.

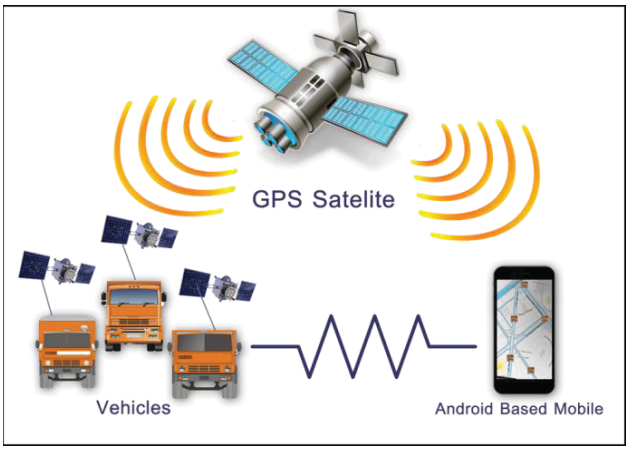

Figure 1: Mobile-based Vehicle System Architecture

Figure 2: Mobile-based application

D. GPS Technology

The Global Positioning System (GPS) will be the main completely practical Global Navigation System (GNSS). The GPS utilizes a heavenly body of between 24 and 32 Medium Earth Orbit satellites that transmit exact microwave indicates that empower GPS collectors to focus their area, speed, course, and time. A GPS collector gets the indicators from no less than three satellites to compute separation and utilizes a triangulation method to figure its two measurement (scope and longitude) position or in any event four satellites to register its three measurement (scope, longitude and height) position. Android gadgets utilize the same worldwide situating engineering as Google Maps and most outsider GPS instruments do. This permits clients to find themselves on a guide, discover and explore to goals through definite bearings, and inquiry maps utilizing various diverse strategies. GPS tracking devices collect information on how drivers behave in the field and transmit this data to a computer or mobile device, ready to be accessed at any time and from any location.

E. 3G/3.5G Technology

3G, short for third generation, is the third generation of wireless mobile telecommunications technology. This is based on a set of standards used for mobile devices and mobile telecommunications use services and networks that comply with the International Mobile Telecommunications-2000 (IMT-2000) specifications by the International Telecommunication Union. 3G finds application in wireless voice telephony, mobile Internet access, fixed wireless Internet access, video calls and mobile TV.

3G telecommunication networks support services that provide an information transfer rate of at least 200 kbit/s. Later 3G releases, often denoted 3.5G and 3.75G, also provide mobile broadband access of several Mbit/s to smartphones and mobile modems in laptop computers. This ensures it can be applied to wireless voice telephony, mobile Internet access, fixed wireless Internet access, video calls and mobile TV technologies.

This system of correspondence permits a way to be built between two gadgets. Once the two gadgets are joined, a steady stream of advanced information is relayed. GSM systems comprise of three real frameworks.

The Switching System: The SS systems have five databases in it which perform crucial operation, each database performing a unique task. It performs the major call processing and subscriber related functions.

The Base Station System (BSS): The BSS are basically the outdoor units consisting of iron rods of high lengths. BSS are responsible for connecting subscribers (MS) to mobile networks making the entire process of communication through Radio transmission.

Mobile Station (Subscriber): It also has a mobile unit and a smart card which is referred as Subscriber Identity Module (SIM) card. This card fitted with the GSM Modem and gives the user more personal mobility.

The bandwidth and location information available to 3G devices gives rise to applications not previously available to mobile phone users. Some of the applications are:

- Global Positioning System (GPS)
- Location-based services
- Mobile TV
- Telemedicine
- Video Conferencing
- Video on demand

F. ULTRASONIC SENSOR

Ultrasonic sensors (also known as transceivers when they both send and receive, but more generally called transducers) work on a principle similar to radar or sonar which evaluate attributes of a target by interpreting the echoes from radio or sound waves respectively.

This technology can be used for measuring wind speed and direction (anemometer), tank or channel level, and speed through air or water. For measuring speed or direction, a device uses multiple detectors and calculates the speed from the relative distances to particulates in the air or water. To measure tank or channel level, the sensor measures the distance to the surface of the fluid. Further applications include: humidifiers, sonar, medical ultrasonography, burglar alarms and non-destructive testing.

Systems typically use a transducer which generates sound waves in the ultrasonic range, above 18,000 hertz, by turning electrical energy into sound, then upon receiving the echo turn the sound waves into electrical energy which can be measured and displayed.

The technology is limited by the shapes of surfaces and the density or consistency of the material. Foam, in particular, can distort surface level readings.

Figure 3: Ultrasonic Sensor Module

IV. RESULTS AND DISCUSSION

Coordinated Vehicle Tracking is planned which is a transport following framework utilized for following and situating of any wandering vehicle by utilizing Global Positioning System (GPS) and Global framework for portable correspondence (GSM).

The current outline is an android provision, which will ceaselessly screen a moving vehicle and report the status of the vehicle on interest. A GSM in the versatile is utilized to send the position (Latitude and Longitude) of the vehicle from a remote spot. The GPS will ceaselessly give the information i.e. the scope and longitude demonstrating the position of the vehicle. The GPS gives numerous parameters as the yield, however just the obliged information turning out and sent to the portable at the other end from where the position of the vehicle is requested and these subtle elements are put away in the database. It is conceivable to make three things by utilizing this outline. First one is it can track the position of vehicle continuously and sends it through GSM. Second one is it is possible to organize vehicles by sending feedback from the mobile application. Third one is related to accident detection, when accident occurs then this can be informed easily.

Two applications are basically designed for user interface purpose. First one is the Asp.net web application that is used by the Admin and also acts as the middleware to android app to connect and store data in database.

We find results of the MVT as shown in the following table 1.

Table 1: Results of comparing systems

Feature	Comparable Systems		
	Mobile Based Vehicle Tracking (MVT)	***Automated Systems Using GPS Modem***	***Manual Systems***
Accuracy	95%	40%	50%
Server Usage	25%	25%	0%
Maps Display	Yes	Yes	No
Data Managment	80%	20%	0%
Access Speed	85%	40%	20%
Interactive	85%	40%	20%
Feedback	85%	0%	30%

REFERENCES

[1] El-Medany,W.;Al-Omary,A.;Al-Hakim,R.;Al-Irhayim,S.;Nusaif,M.,"A Cost Effective Real-Time Tracking System Prototype Using Integrated GPS/GPRS Module," Wireless and Mobile Communications (ICWMC), 2010 6th International Conference on,vol.,no.,pp.521,525,20-25Sept.2010

[2] Hu Jian-ming; Li Jie; Li Guang-Hui, "Automobile Anti-theft System Based on GSM and GPS Module," Intelligent Networks and Intelligent Systems (ICINIS), 2012 Fifth International Conference on , vol., no., pp.199,201, 1-3 Nov. 2012

[3] Fleischer, P.B.; Nelson, A.Y.; Sowah, R.A.; Bremang, A., "Design and development of GPS/GSM based vehicle tracking and alert system for commercial inter-city buses," Adaptive Science & Technology (ICAST), 2012 IEEE 4th International Conference on , vol., no., pp.1,6, 25-27 Oct. 2012

[4] Le-Tien, T.; Vu Phung-The, "Routing and Tracking System for Mobile Vehicles in Large Area," Electronic Design, Test and Application, 2010. DELTA '10. Fifth IEEE International Symposium on ,vol., no., pp.297,300, 13-15 Jan. 2010

[5] S.H. Chew, P.A. Chong, E. Gunawan, K.W. Goh, Y. Kim and C.B. Soh, "A hybrid mobile-based patient location trackingsystem for personal healthcare applications", 28th Annual International Conference Ofthe IEEE, 2006.

[6] R. Lenain, B. Thuilot, C. Cariou and P. Martinet, "Mobile robot control in presence of sliding:application to agricultural vehicle path tracking", 45th IEEE Conference on Digital Object Identifier, 2006.

[7] Bashir, F., Porikli, F.: Performance evaluation of object detection and tracking systems. In: IEEE Int. W. on Performance Evaluation of Tracking and Surveillance, PETS 2006 (2006)

[8] Buch, N., Orwell, J., Velastin, S.A.: Detection and classification of vehicles for urban traffic scenes. In: International Conference on Visual Information Engineering, VIE 2008, July 2008, pp. 182–187. IET (2008)

[9] Arthur Thompson and Wayne Goodridge, “Bus Coming: Description and Evaluation of Bus Tracking System for Rural Areas”, International Journal of Innovative Science, Engineering & Technology, Vol. 1 Issue 5, July 2014

PRELIMINARY STUDY OF A TIME DEPENDENT MODEL FOR EXTERIOR ORIENTATION OF HYPERSPECTRAL IMAGE CUBES

A. Berveglieri [a] and A. M. G. Tommaselli [b]

Univ Estadual Paulista – UNESP, Faculty of Science and Technology, Presidente Prudente, Brazil,
Department of Cartography
[a] adilsonberveg@gmail.com, [b] tomaseli@fct.unesp.br

KEY WORDS: Hyperspectral Image, Multi-band, Polynomial model, FPI camera

ABSTRACT:

A preliminary study on the orientation of hyperspectral image cubes acquired with frame type camera is presented in this paper. Since the spectral bands are not recorded at the same instant by the camera, each band is acquired at a distinct position and attitude during the flight. The proposed technique uses time dependent polynomials (with 18 parameters) to describe the platform trajectory during each hypercube acquisition (provided that the acquisition time is known). A set of hyperspectral images with direct georeferencing data was collected using a Rikola camera boarded on an unmanned aerial vehicle (UAV). The experiments used four hypercubes with 10 selected spectral bands of a sensor. Due to the high number of images that a hyperspectral survey can produce, the experiments also took into account the feasibility of using few bands to determine the polynomial parameters, which were used to estimate the exterior orientation parameters (EOPs) of each band. The polynomial parameter estimation was performed by bundle adjustment using integrated sensor orientation (ISO), and the accuracy assessment was based on analysis of checkpoints. The results indicated an accuracy of 1.5 ground sample distance (GSD) in planimetry and 2.3 GSD in height, which were close to the results achieved when all bands were individually oriented in the bundle adjustment.

1. INTRODUCTION

Remote sensing studies in small areas have achieved improvements with the introduction of lightweight sensors boarded on unmanned aerial vehicles (UAVs). The use of hyperspectral framing cameras enables data acquisition with high temporal and spatial resolution. Additionally, more complete investigations can be performed based on analysis of this kind of image. Hyperspectral data are useful for several remote sensing applications that need detailed spectral characteristics, e.g., geology, environmental monitoring, precision agriculture, forest or tree health measurements (Goetz, 2009; Honkavaara et al., 2013).

Several hyperspectral sensing technologies that collect 2D frame images with tuneable filters have been introduced in the market (Aasen et al., 2015; Gupta et al., 2008; Hagen and Kudenov, 2013; Lapray et al., 2014). Hyperspectral sensors based on tuneable filters can capture 2D spatial images, and the spectral dimension is collected as a function of time. Unlike pushbroom sensors, framing cameras record 2D spatial information, and 3D data can be derived by stereo-matching to complement hyperspectral data. Since an object can be imaged from different viewpoints, stereoscopic measurements and analysis of multidirectional reflectivity characteristics (Honkavaara et al., 2013) can be performed. The hyperspectral frame cube or hypercube can be generated simultaneously if all bands are collected at the same instant (Aasen et al., 2015) or based on band co-registration if the band acquisition is unsynchronised (Honkavaara et al., 2013).

When accurate 3D data are required, the determination of exterior orientation parameters (EOPs) is essential to describe the position and attitude of UAV platforms. EOPs can be determined directly by a GPS/inertial system, indirectly by bundle block adjustment, or still by integrated sensor orientation (ISO), this last being a combination of the two previous techniques. Due to the instability of UAV platforms and of camera interior orientation parameters, EOPs should be corrected to improve their accuracy with well-known photogrammetric procedures being adopted to solve this task.

An example of 2D hyperspectral camera is the Rikola model, which was adopted for this study. This camera captures image cubes formed by a set of spectral bands with a frame geometry. The embedded technology is based on a tuneable Fabry-Perot Interferometer (FPI), which is installed inside the lens system. However, one major problem is that the Rikola camera can acquire hypercubes up to 50 bands, which would make unfeasible the image orientation separately for each band, that is, up to 50 sets of interior orientation parameters (IOPs) and more 6 EOPs per band (300 parameters). Considering that, it is crucial to develop rigorous and efficient techniques to cope with this type of images.

Thus, this study investigates a time dependent technique for simultaneous image orientation including all bands by using a time dependent polynomial to describe EOP variations. The procedure should be performed because the spectral bands are not recorded at the same instant, which results in differences in the positions and attitude of the image bands acquired during the aerial survey. The time interval between bands (e.g., Rikola model 2015(Rikola Ltd, 2015)) is accurately known and spectral bands are grabbed in a sequence following the platform movement. Thus, a hardware solution with event logging directly implemented in the Rikola camera enables to record the GPS time of each spectral band, since the camera sends a pulse for each band. Such pulses are received by the GPS/inertial system and the time of each event is saved on raw file for post-processing. Even if time tagging is not used, the time

differences are known from the factory settings with high accuracy.

The approach proposed in this paper uses a time dependent polynomial function to model the platform trajectory (position and attitude changes) during the cube acquisition to replace the set of 300 EOPs (for instance, when using 50 bands) for each cube. Consequently, from the image orientation of a spectral band, other bands can have their EOPs estimated by polynomials, provided that the acquisition time is known.

To apply the proposed approach, the polynomial parameters were estimated using an adapted bundle adjustment but considering few bands. The accuracy of the image orientation using polynomial parameters was assessed based on checkpoints. A comparison of accuracy was also performed considering results obtained with few bands and with all bands of a sensor. The preliminary trials showed that the results were close to each other, indicating that the time dependent polynomial model can be used to estimate the EOPs in a sequence of spectral bands, without requiring a bundle adjustment for each band.

2. BACKGROUND

2.1 FPI camera

VTT Technical Research Centre of Finland and Rikola Ltd (2015) have developed a lightweight hyperspectral based on a FPI technology (Saari et al., 2009) that can be carried by UAVs (see the model used in Figure 1(a)).

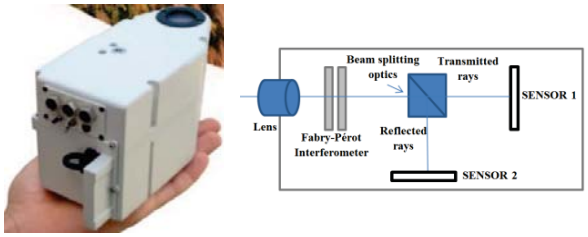

(a) (b)

Figure 1. (a) Rikola camera. (b) Diagram representing the internal system. Source: Oliveira et. al (2016.)

The camera internal system is composed of a FPI and piezoelectric actuators. As depicted in Figure 1(b), two partially reflective surfaces form the FPI, which are installed parallel to each other and separated by a gap. The light rays passing through the FPI undergo multiple reflections. The length of the optical path between the gap generates the wavelengths that are transmitted by the interferometer. Thus, the spectral bands are a function of the interferometer air gap. Using several air gap values of the FPI, a set of wavelengths [500-900 nm] can be produced using two CMOS sensors redirected by a beam splitting device (Oliveira et. al, 2016).

The FPI camera can be used with different configurations depending on the application and on the adopted camera model. Table 1 presents the main technical details of the camera used for this study. The hyperspectral images are collected as data cubes with a number of predefined bands.

In this type of camera, the spectral bands are not recorded at the same instant, generating differences in the EOPs of the image bands acquired during the aerial survey. For a configuration with 50 bands, the time interval from band to band is approximately 22 ms, and image bands are grabbed sequentially while the platform is moving, as depicted in Figure 2.

Camera model	Rikola FPI2015
Nominal focal length	9 mm
Pixel size	5.5 µm
Image dimension	1017 × 648
Sensors	CMOS
Spectral resolution	10 nm, FWHM
Weight	< 700 g

Table 1. Technical details. FWHM (full width at half maximum).

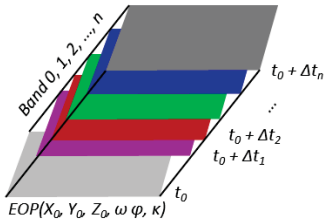

Figure 2. Image band displacements in the hypercube during the aerial survey.

2.2 Polynomial models

The EOPs, as depicted in Figure 2, vary continously as a function of time and, therefore, they can be modelled by polynomials representing a uniformly variable motion. A set of second-order polynomials is presented in Eq. (1) to model the position (X, Y, Z) and attitude (ω, φ, κ) of each spectral band in the hypercube.

$$\begin{aligned} X &= X_0 + a_1 t + b_1 t^2 \\ Y &= Y_0 + a_2 t + b_2 t^2 \\ Z &= Z_0 + a_3 t + b_3 t^2 \\ \omega &= \omega_0 + a_4 t + b_4 t^2 \\ \varphi &= \varphi_0 + a_5 t + b_5 t^2 \\ \kappa &= \kappa_0 + a_6 t + b_6 t^2 \end{aligned} \quad (1)$$

This set of polynomials is composed of eighteen parameters, in which each component a_i represents a platform speed and b_i indicate a acceleration. The time interval t of each band with respect to a reference band can be given by a sequence delay calculator provided by the camera manufacturer (Rikola Ltd.) or by a time stamp tagged in the GNSS receiver. Having time of each band EOPs can be interpolated from GPS/inertial data or estimated by bundle adjustment. In any case, estimating individual sets of EOPs for each band is time consuming.

3. EXPERIMENTAL RESULTS

3.1 Camera calibration

As mentioned in the previous section, Rikola camera works with a configurable number of spectral bands. Table 2 shows the wavelength (λ) of the configured 25 bands considering the two sensors. However, for the trials in this study, only the ten bands from sensor 2 were used to assess the polynomial model with bundle adjustment.

The interior orientation parameters (IOPs) of the Rikola camera were estimated in a terrestrial calibration field. This field is

composed of coded targets with Aruco form (Garrido-Jurado et al., 2014), which are automatically identified and recognized in the images, as presented by (Tommaselli et al., 2014). A set of twelve hyperspectral images were taken for camera calibration, and four examples are showed in Figure 3. Complete details about Rikola camera calibration in test field are commented by (Oliveira et al., 2016).

Sensor 2			Sensor 1	
Spectral band	λ (nm)		Spectral band	λ (nm)
1	506.22		11	650.96
2	519.94		12	659.72
3	535.09		13	669.75
4	550.39		14	679.84
5	565.10		15	690.28
6	580.16		16	700.28
7	591.90		17	710.06
8	609.00		18	720.17
9	620.22		19	729.57
10	628.73		20	740.42
			21	750.16
			22	769.89
			23	780.49
			24	790.30
			25	819.66

Table 2. Spectral bands configured in the Rikola camera.

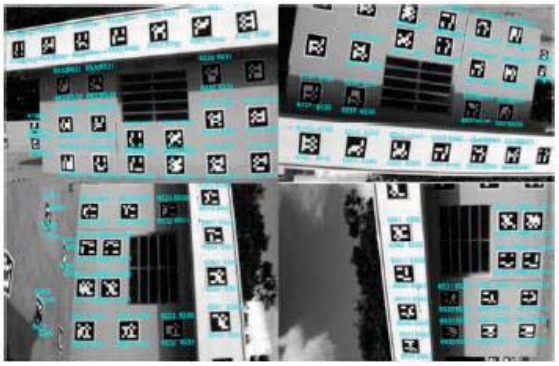

Figure 3. Examples of hyperspectral images used in the camera calibration.

Only the first spectral band (506.22 nm) of the sensor 2 was used to estimate the focal length (f), principal point (x_0, y_0) and lens distortions (K_1, K_2, K_3, P_1, P_2). These IOPs were estimated using self-calibrating bundle adjustment with constraints imposed to the ground coordinates, as proposed by (Kenefick et al., 1972). The mathematical model was based on collinearity equations with addition parameters of the Conrady-Brown model (Fryer and Brown, 1986). Table 3 displays the values estimated for the IOPs of the sensor 2.

Parameter	Value	Standard deviation
f (mm)	8.63948802	0.00152412 (±0.28 pixels)
x_0 (mm)	-0.01559536	0.00195755 (±0.36 pixels)
y_0 (mm)	-0.27827994	0.00139124 (±0.25 pixels)
K_1 (mm^{-2})	-0.00406824	0.00003643
K_2 (mm^{-4})	-0.00003113	0.00000765
K_3 (mm^{-6})	0.00000128	0.00000050
P_1 (mm^{-1})	-0.00000390	0.00000363
P_2 (mm^{-1})	0.00001722	0.00000453
a posteriori sigma	0.32	(*a priori sigma* = 1)

Table 3. IOPs estimated by camera self-calibrating.

3.2 Aerial image acquisition

A UAV platform with integrated sensors was assembled to collect hyperspectral images with direct georeferencing data, as shown in Figure 4. The Rikola camera was connected to the IMU (Inertial Navigation System Novatel IGM-S1) to record the GPS instant of each spectral band acquisition, since the camera sent one pulse per band. Thus, the pulses were received by the GPS of the IMU and the instants were recorded in the raw GPS data file for post-processing.

Hyperspectral aerial images were acquired at a flying height of 160 m with flight speed of 4 m/s over an area with GCPs and checkpoints. This flight configuration yielded an image overlap of 80% and also generated images with ground sample distance (GSD) of 11 cm.

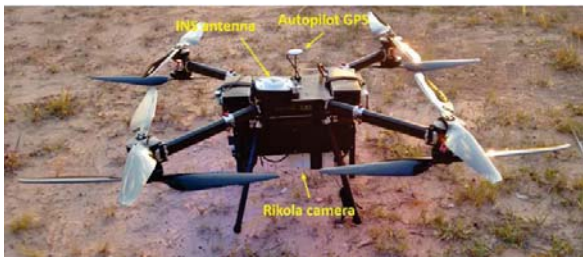

Figure 4. UAV platform with the hyperspectral camera integrated to the GPS/IMU system.

Four hyperspectral image cubes were selected to be used with the time dependent polynomial model. Figure 5 displays the block geometry. As the sensor 2 is composed of ten bands, all were used in the bundle adjustment with the polynomial model. Thus, four hypercubes with 10 spectral bands each were considered, achieving a number of 40 images. Image coordinates of five GCPs and three checkpoints were manually measured over all images. In addition, six tie points were extracted automatically to improve and ensure the image block geometry.

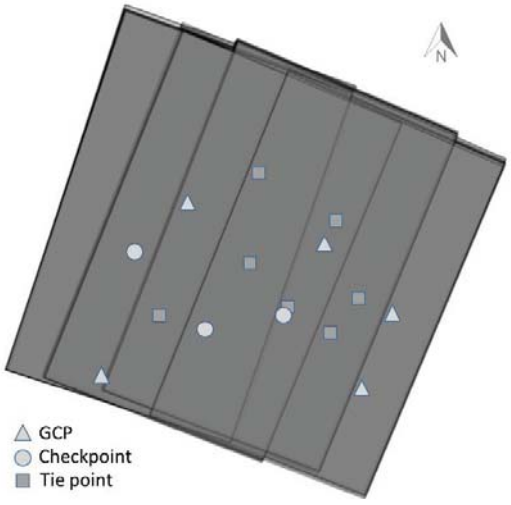

Figure 5. Hyperspectral aerial image block with the GCPs, checkpoints and tie points.

3.3 Bundle adjustment

To perform the bundle adjustment, the photogrammetric block was configured using direct georeferencing data as initial approximations for the EOPs, i.e., weighted constraints of 20 cm in (X_0, Y_0, Z_0) and 1° in (ω, φ, κ). A standard deviation of 1 pixel was assigned to the image coordinates due to the image blurring, whereas a standard deviation of 5 cm was used in the object coordinates based on the post-processing accuracy. The previously calibrated IOPs were configured as fixed in the adjustment procedure.

The time dependent polynomial model was implemented and added to an in-house developed software called triangulation with multiple sensors - TMS (Marcato Junior and Tommaselli, 2013). Thus, this software was used to perform the bundle adjustment. Three groups of bundle adjustment trials were conducted for purposes of analysis and comparison of results. The first one considered a bundle adjustment (with integrated sensor orientation) to estimate the EOPs of the ten individual bands of the four hypercubes (total = 40 images). The other two groups were formed with a minimum of bands, i.e, with four (1^{st}, 4^{th}, 7^{th}, 10^{th}) bands (4 bands × 4 cubes = 16 images) and with three (1^{st}, 5^{th}, 10^{th}) bands (summing up to 12 images).

The objective of this study was to assess the accuracy of this approach and the optimum number of bands to be used to estimate the polynomials. A comparison can be made to check the polynomial parameters and the quality of the EOPs when using a minimal number of bands. This is important because the bundle adjustment of all bands in a large hyperspectral block may be unfeasible, since large hyperspectral blocks would result in thousands of images.

3.4 Results

The three groups of experiments were performed with the configuration described in section 3.3 and block geometry shown in Figure 5. Data provided by direct georeferencing were used as initial values for the EOPs in the bundle adjustment along with the GCPs collected in field.

Table 4 presents the estimated values of the polynomial parameters (a_i and b_i) separated by hypercubes and number of bands. The bundle adjustment with 10 bands was used as a reference for comparison and it was observed that the differences in a_i and b_i are larger when using three bands than when using four bands, as expected.

The flight speed in XY represented by a_1 and a_2 varied around 4 m/s, and angular accelerations were detected by the parameters b_4, b_5 and b_6 due to variations in the platform movement.

Table 5 shows the resulting RMSE in the GCPs with the bundle adjustment of each group. As it can be seen, when four and three bands in each cube were used, smaller errors (~13 cm, 20 cm, 7 cm in XYZ) were obtained in the comparison with 10 bands for each cube.

N. of cubes	N. of bands each	X(m)	Y(m)	Z(m)
4	10	0.16	0.22	0.09
4	4	0.13	0.21	0.07
4	3	0.13	0.20	0.07

Table 5. RMSE of the GCPs in the object space using the polynomial models.

With respect to the accuracy of the bundle adjustment, Table 6 presents the resulting RMSE in three checkpoints (see Figure 5) in the object space. The bundle adjustment with 10 bands obtained an error of 16 cm in planimetry and 25 cm in height, which in the comparison with the image GSD represent approximately 1.5 GSD and 2.3 GSD, respectively.

N. of cubes	N. of bands each	X(m)	Y(m)	Z(m)
4	10	0.16	0.16	0.25
4	4	0.21	0.15	0.23
4	3	0.15	0.13	0.35

Table 6. RMSE of the checkpoints in the object space using the polynomial models.

Since this bundle adjustment considered all bands, such results were used as a reference to verify the errors of the other groups. As it can be seen in Table 6, using four bands generated errors of 21 cm and 15 cm in XY, respectively, and 23 cm in height. Although smaller planimetric errors have been obtained by using three bands, the discrepancy in Z was much greater, with a difference of 1 GSD approximately.

Cube	N. of bands	a1	a2	a3	a4	a5	a6	b1	b2	b3	b4	b5	b6
1	10	3.92	3.89	-0.22	-0.73	1.20	-3.77	-0.02	-0.03	-0.08	-4.01	2.67	2.31
2		3.76	4.02	-0.63	-4.01	1.94	0.37	-0.05	-0.01	-0.21	0.65	-3.29	-0.43
3		4.29	3.95	0.04	1.64	-0.39	-0.64	0.06	-0.02	0.01	-12.10	3.40	2.29
4		4.20	3.92	0.16	-3.36	0.25	0.98	0.05	-0.02	0.04	-1.02	3.56	-1.57
1	4	3.97	3.97	-0.03	-0.83	0.98	-5.10	-0.01	-0.01	-0.03	-3.54	2.54	6.72
2		3.92	4.00	-0.30	-4.18	1.88	0.40	-0.02	-0.01	-0.12	1.41	-2.80	-0.12
3		4.17	3.92	-0.07	1.26	-0.32	-0.24	0.04	-0.03	-0.04	-10.78	2.63	1.47
4		4.10	3.98	0.19	-3.42	0.09	1.09	0.02	-0.01	0.08	-1.36	4.59	-1.72
1	3	3.99	3.98	-0.05	-1.35	1.40	-4.94	0.00	-0.01	-0.01	-1.93	0.91	5.08
2		3.93	4.00	-0.30	-4.20	2.07	0.35	-0.02	0.00	-0.09	1.55	-3.46	0.12
3		4.14	3.92	-0.13	2.42	-0.93	-0.91	0.04	-0.03	-0.03	-15.06	4.26	3.53
4		4.10	3.98	0.18	-2.88	0.05	1.73	0.02	-0.01	0.05	-3.76	4.88	-4.25

Table 4. Polynomial parameters estimated by bundle adjustment.

When comparing the results of using four or three bands with those with 10 bands, the results were more consistent when using four bands. In this case, the largest difference was obtained in X-coordinate (21 cm – 16 cm = 5 cm), which is a difference equivalent to 1/2 GSD.

In general, the polynomial models using a minimum of bands showed that can estimate the EOPs of all bands of a hypercube with an accuracy close to that obtained when using all bands.

4. CONCLUSIONS

This study presented a preliminary experiment on the hyperspectral frame image orientation using time dependent polynomial models. The main objective was to assess a type of polynomial model for image orientation of hypercubes. The purpose was also to verify the optimum number of image bands to estimate the polynomial model to replace an individual bundle adjustment with all bands. This is important because the image orientation with all bands is a time-consuming task and unfeasible for large image blocks.

The experiment with bundle adjustment considering three and four bands showed that the polynomial models were able to estimate EOPs for all bands of the hypercubes. The results obtained with fewer bands were close to those when all bands were used. Based on the preliminary results, the use of four bands can be recommended to determine the EOPs of all bands in a hypercube. Such results indicated an accuracy around 1.5 GSD in planimetry and 2.3 GSD in height.

It is important note that the calibrated IOPs were used as absolute constraints in the experiments, and an assessment on the IOPs should still be performed to verify their stability. Temperature variation, UAV platform movement and vibrations and the particular feature of the interferometer can contribute to the instability of the hyperspectral sensor during the image acquisition. Then, an on-the-job calibration must be performed to analyse the technique. However, this procedure requires a block geometry with cross flight strips, which was not used in this study. In future works, such procedure will be studied, as well as a bundle adjustment with more hypercubes, including the two sensors of the hyperspectral camera.

ACKNOWLEDGEMENTS

The authors would like to thank the São Paulo Research Foundation (FAPESP) [grants 2013/50426-4 and 2014/05533-7] for financial support and Nuvem UAV Company for providing aerial images.

REFERENCES

Aasen, H., Burkart, A., Bolten, A. and Bareth, G., 2015. Generating 3D hyperspectral information with lightweight UAV snapshot cameras for vegetation monitoring: from camera calibration to quality assurance. *ISPRS Journal of Photogrammetry and Remote Sensing*, 108, 245–259.

Fryer, J.G. and Brown, D.C., 1986. Lens distortion for close-range photogrammetry. *Photogrammetry Engineering & Remote Sensing*, 52(1), pp. 51–58.

Garrido-Jurado, S., Muñoz-Salinas, R., Madrid-Cuevas, F.J. and Marín-Jiménez, M.J., 2014. Automatic generation and detection of highly reliable fiducial markers under occlusion. *Pattern Recognition*, 47(6), pp. 2280–2292.

Goetz, A.F.H., 2009. Three decades of hyperspectral remote sensing of the earth: a personal view. *Remote Sensing of Environment*. 113(1), pp. S5–S16.

Gupta, N., Ashe, P.R. and Tan, S., 2008. A miniature snapshot multispectral imager. In: *Infrared Technology and Applications XXXVI*. Presented at the SPIE, p. 76602G.

Hagen, N.A. and Kudenov, M.W., 2013. Review of snapshot spectral imaging technologies. *Optical Engineering,* 52(9), pp. 1–23.

Honkavaara, E., Saari, H., Kaivosoja, J., Pölönen, I., Hakala, T., Litkey, P., Mäkynen, J. and Pesonen, L., 2013. Processing and assessment of spectrometric, stereoscopic imagery collected using a lightweight UAV spectral camera for precision agriculture. *Remote Sensing*, 5(10), pp. 5006–5039.

Kenefick, J.F., Gyer, M.S. and Harp, B.F., 1972. Analytical self-calibration. *Photogrammetric Engineering*, 38, pp. 1117–1126.

Lapray, P.J., Wang, X., Thomas, J.B. and Gouton, P., 2014. Multispectral filter arrays: recent advances and practical implementation. *Sensors*, 14(11), pp. 21626–21659.

Marcato Junior, J., Tommaselli, A.M.G., 2013. Exterior orientation of CBERS-2B imagery using multi-feature control and orbital data. *ISPRS Journal of Photogrammetry and Remote Sensing*, 79, pp. 219–225.

Oliveira, R.A., Tommaselli, A.M.G. and Honkavaara, E., 2016. Geometric calibration of a hyperspectral frame camera. *Photogrammetric Record*, 31(155), pp. 325–347.

Rikola Ltd, 2015. . Hyperspectral Camera. URL (accessed 17 Jan 2017).

Saari, H., Aallos, V.-V., Akujärvi, A., Antila, T., Holmlund, C., Kantojärvi, U. and Mäkynen, J., 2009. Novel miniaturized hyperspectral sensor for UAV and space applications. *SPIE* 7474.

Tommaselli, A.M.G., Marcato Junior, J., Moraes, M.V.A., Silva, S.L.A. and Artero, A.O., 2014. Calibration of panoramic cameras with coded targets and a 3D calibration field. In: *The International Archives of the Photogrammetry, Remote Sensing and Spatial Information Sciences*. Vol. XL-3/W1, pp. 137–142.

A COOPERATIVE LOCALIZATION SYSTEM FOR UNMANNED AERIAL VEHICLES: PROTOTYPE DEVELOPMENT AND ANALYSIS

S. Goel [a,b,*], A. Kealy [a], B. Lohani [b], G. Retscher [c]

[a] Dept. of Infrastructure Engineering, The University of Melbourne, Australia - goel.salilg@gmail.com, akealy@unimelb.edu.au
[b] Dept. of Civil Engineering, Indian Institute of Technology Kanpur, India - blohani@iitk.ac.in
[c] Dept. of Geodesy and Geoinformation, TU Wien, Vienna, Austria - guenther.retscher@geo.tuwien.ac.at

KEY WORDS: Cooperative Localization, Unmanned Aerial Vehicle, Ultra-Wide Band Sensor, P2I Localization

ABSTRACT:

Cooperative localization (CL) has long been studied especially in the domain of wireless sensor networks and has been found to provide superior localization accuracy under certain conditions but has been limited to static networks. It has been demonstrated that cooperative localization can prove to be especially helpful in GNSS challenging environments where some nodes of a cooperative network may not have access to GNSS. Further, using numerical simulations it has been demonstrated that information sharing in a cooperative network helps all the nodes and can improve the localization accuracy even in GNSS available environments. With this motivation, this paper explains the development of a cooperative localization system for UAVs developed at The University of Melbourne, Australia. This paper provides details of the mathematical framework implemented in the developed system and includes details of the mechanism involved for integrating several sensors and components for developing the complete system. The developed system integrates low cost GNSS, MEMS Inertial sensors, Ultra-Wide Band sensor and raspberry pi with UAVs to develop a cooperative swarm capable of operating in partially GNSS denied environments. Specifically, this prototype pertains to Peer to Infrastructure (P2I) localization strategy in which a swarm of UAVs rely on static nodes for localization. The mathematical framework and the developed prototype is validated using multiple real world experiments. Experimental results indicate that navigation level accuracies (~4 m) can be achieved in GNSS challenging environments using the developed cooperative network.

1. INTRODUCTION

Over the past five years, Unmanned Aerial Vehicles (UAVs) have attracted hobbyists, researchers and people from industry. While hobbyists have primarily been interested in developing UAVs for general recreational activities, the focus of academia and industry has shifted from developing conventional UAVs to exploring their potential and capabilities in different applications. Some of the proposed applications of UAVs include mapping, surveillance, search and rescue operations, dealing with emergency scenarios with applications in healthcare and disaster management. Undeniably, UAVs have the capability to solve a number of challenging problems, some of which have been highlighted in the above-mentioned applications. However, a swarm of UAVs operating cooperatively can achieve much more than a single UAV. A swarm of UAVs is generally faster, more efficient as well as robust than a single UAV. For example, in applications such as search and rescue operation or mapping an unknown environment, a swarm of cooperating UAVs can cover a larger amount of area in a short amount of time. It is primarily because of this reason that a lot of research is now being directed towards developing cooperative swarm networks. One of the major requirements in operation of a UAV or a cooperative swarm network is precise and robust localization of all the dynamic nodes. The existing cooperative networks make use of Global Navigation Satellite Systems (GNSS) for localization. Therefore, such networks perform well in open environments where GNSS signal is easily accessible but fail to operate in GNSS challenging environments such as urban canyons, forests, tunnels etc. It has been demonstrated through numerous simulation studies (Goel et al. 2016b, Li and Nashashibi 2013, Goel et al. 2016c, Goel et al. 2016d) and some experimental tests (Goel et. al 2016a) that all nodes in a cooperative network may be localized by information sharing in GNSS challenging environments. Cooperative localization (CL) makes use of GNSS that is available to some nodes in the network as well as some relative measurement among the nodes to localize the nodes without GNSS. Although the primary focus of CL has been to aid nodes without GNSS access, it has been demonstrated that in the cases of full GNSS availability such as in open environments, CL may even improve the localization accuracy of all the participating nodes. This is possible through sharing of some relative information among the nodes. This relative information can either be relative range, range angle, relative position etc. The relative information, information from other on-board sensors and information transmitted by other nodes about their states is then fused together using an appropriate estimation algorithm such as Extended Kalman Filter (EKF) (Bailey et. al 2011, Goel et. al. 2016b), Unscented Kalman Filter (UKF) (Shi et. al 2010), Covariance intersection filter (Carrillo-Arce et. al 2013, Li and Nashashibi 2013, Wanasinghe et. al 2014) or Belief Propagation (BP) (Chen et. al 2013, Savic and Zazo 2013, Wan et. al 2014) etc. This estimation is generally performed through a suitable estimation architecture such as centralized or distributed. A centralized architecture employs a central server that can either be located on one of the UAVs or may be installed in a secure location inside a building. All the UAVs are required to be in constant communication with the server and any loss in communication with the server may result in the failure of the UAV. The UAVs send all relevant information to the server, where it is processed and information such as state and associated covariance is transmitted back to the corresponding nodes. It is evident that a

* Corresponding author

centralized architecture requires a robust communication network and possibly a larger communication bandwidth to operate. In a distributed architecture, each UAV (or node) performs the processing locally using the on-board processor rather than relying on a central server as in a centralized architecture. Therefore, the communication load in a distributed architecture is relative lesser and any loss in communication to other nodes will not cause a node (or UAV) to fail, as is the case in a centralized architecture.

Another important component of a cooperative localization system is the kind of available communication architecture. In general, two different architectures are available: Peer to Infrastructure (P2I), and Peer to Peer (P2P). A P2I architecture refers to communication between a Peer (i.e. a dynamic node such as UAV) and Infrastructure (traffic lights, buildings etc.) while in a P2P architecture the dynamic nodes mostly communicate with their peers (i.e. other nodes). In cases when infrastructure is available, nodes may or may not communicate with them. Hence P2I system is applicable where sufficient infrastructure is already available such as in complex urban environments while a P2P system can be typically deployed anywhere.

A key component in a cooperative localization system is the estimation architecture and the algorithm adopted in that architecture. Two kinds of estimation architectures are generally available: Centralized and distributed (Goel et. al 2016c). Due to the inherent configuration of a Peer to Infrastructure localization system, a distributed estimation architecture can be readily employed. A distributed architecture is generally preferred over a centralized architecture since a distributed system is scalable and more robust than a centralized architecture. A comparative analysis of the two estimation architectures is presented in Goel et. al (2016d). Although algorithms such as BP and CIF are mathematically sound, we restrict ourselves to simpler estimation algorithms such as EKF due to lower computation resources available on the UAV. Use of these simpler algorithms will allow us to perform on board computations and thus allow the system to be used in applications that require results in real time.
The proposed cooperative localization system brings together low cost GNSS, MEMS inertial sensors and Ultra-Wide Band (UWB) radio sensor. The UWB radio serves the purpose of measuring relative range between the two nodes of a cooperative system as well as communication of relevant information between the nodes. This paper focuses on development of a P2I cooperative localization system for UAVs using low cost sensors such as GNSS, Inertial Measurement Unit (IMU) and UWB sensor and analysis and evaluation of the developed prototype.

2. EXTENDED KALMAN FILTER FOR COOPERATIVE LOCALIZATION

The kinematic model for a dynamic node (UAV) in a cooperative network is described by equations (1)-(3). These equations are expressed in Earth Centred Earth Fixed (ECEF) frame but can also be expressed in a local frame such as North East Down (NED) or any other desired frame.

$$\dot{r}^e = v^e \tag{1}$$

$$\dot{v}^e = R_b^e f_b - 2\Omega_{ie}^e v^e + g^e \tag{2}$$

$$\dot{\alpha}^e = R_{\alpha^e}\omega_{ib} \tag{3}$$

Where $\dot{x}$ denotes rate of change of a quantity x with time. In the above equations, the position, velocity, and attitude of a UAV is denoted by r^e, v^e and α^e, respectively. The observations from inertial sensors such as accelerations recorded by the accelerometer and angular rates recorded by gyroscopes in the IMU body frame (denoted by b) are denoted by f_b and ω_{ib}, respectively. The notations Ω_{ie}^e and g^e denote skew symmetric matrix of angular velocity of ECEF frame with respect to inertial frame and gravity vector in ECEF frame, respectively. The rotations matrix R_b^e transforms from IMU body to ECEF frame and matrix R_{α^e} is given as follows,

$$R_{\alpha^e} = \begin{bmatrix} 1 & \sin\phi\tan\theta & \cos\phi\tan\theta \\ 0 & \cos\phi & -\sin\phi \\ 0 & \sin\phi\sec\theta & \cos\phi\sec\theta \end{bmatrix}$$

Where ϕ and θ denote roll and pitch angles, respectively and form a part of the attitude vector along with the yaw angle. An important component of modelling dynamic model which includes inertial observations is to include the model for the biases inherent in the inertial sensors. Additionally, biases are present in the clock of GPS receiver installed on the UAV. This bias is referred to as 'receiver clock bias' and is also modelled using a random walk model as demonstrated by Goel et. al (2016a) and Goel et. al (2016b). This paper uses Extended Kalman Filter (EKF) for fusion of information from inertial sensors, GNSS and Ultra Wide Band (UWB). A detailed derivation of the mathematical framework for cooperative localization including the associated matrices is given by Goel et. al (2016a) and Goel et. al (2016b). The general measurement model in a cooperative localization system is given as,

$$Z_k^i = h\left(r_k^i, r_k^j\right) + v_k^i \tag{4}$$

Where Z_k^i denotes the measurement vector and includes GNSS pseudoranges from the satellites as well as relative range measurements to the fixed infrastructure. The measurement function is denoted by $h\left(r_k^i, r_k^j\right)$. The measurement function changes according to the kind of measurement available. For example, when GNSS pseudoranges are available, measurement function is given by equation (5).

$$\rho_p = \sqrt{\left(x_k^i - x_k^p\right)^2 + \left(y_k^i - y_k^p\right)^2 + \left(z_k^i - z_k^p\right)^2} + \left(c_b\right) + e_{\rho_p} \tag{5}$$

Where satellite coordinates at instant k are denoted by $\left(x_k^p, y_k^p, z_k^p\right)$. For the case when relative range measurements to the fixed infrastructure are available, measurement function is given by equation (6).

$$d_k^{ij} = \sqrt{\left(x_k^i - x_k^j\right)^2 + \left(y_k^i - y_k^j\right)^2 + \left(z_k^i - z_k^j\right)^2} + e_k^{ij} \tag{6}$$

The above measurement functions are used to develop the complete measurement model. The measurement matrix for this cooperative localization is given as follows,

$$H_k = \begin{bmatrix} \frac{\partial \rho_1}{\partial r} & 0_{1x3} & 0_{1x3} & 0_{1x3} & 0_{1x3} & 1 \\ . & . & . & . & . & . \\ \frac{\partial \rho_{p-1}}{\partial r} & 0_{1x3} & 0_{1x3} & 0_{1x3} & 0_{1x3} & 1 \\ \frac{\partial \rho_p}{\partial r} & 0_{1x3} & 0_{1x3} & 0_{1x3} & 0_{1x3} & 1 \\ . & . & . & . & . & . \\ . & . & . & . & . & . \\ \frac{\partial d^{1i}}{\partial r} & 0_{1x3} & 0_{1x3} & 0_{1x3} & 0_{1x3} & 0 \\ . & . & . & . & . & . \\ \frac{\partial d^{ij}}{\partial r} & 0_{1x3} & 0_{1x3} & 0_{1x3} & 0_{1x3} & 0 \end{bmatrix} \quad (7)$$

Where ρ_p denotes the pseduorange measurement from the p^{th} satellite. In the cases when GNSS measurement is not available, all the rows corresponding to pseudoranges are removed from the measurement vector. Thus standard EKF equations can be used for cooperative UAV localization. This is advantageous for the system as this reduces the computational complexity during processing and allows real time implementation of the above filter. This completes the mathematical framework for cooperative localization. The next section presents the details of the cooperative localization prototype.

3. COOPERATIVE UAV LOCALIZATION PROTOTYPE

This section provides details of a single UAV prototype that forms a part of a cooperative network. The developed UAV brings together GNSS, Inertial sensors including accelerometer and gyroscope and UWB radio. The UWB is used to measure relative ranges between the UAVs and the fixed infrastructure. The same UWB can also be used for transmission of information such as position of fixed infrastructure to the UAV. The UAV used in this research is a 4 arm octocopter. The developed prototype is shown in Figure 1.

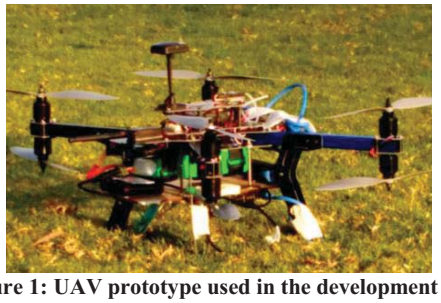

Figure 1: UAV prototype used in the development of a cooperative localization system.

An octocopter such as the one shown in above figure is preferred over a quadcopter due to the redundancy and additional stability offered by the octocopter. The redundancy offered due to the use of eight rotors is useful when any of the rotors fail mid-flight during a mission. Further, the use of 8 rotors ensures increased stability in challenging flying conditions such as flying in windy regions. A block diagram showing the integration architecture in a UAV prototype is shown in Figure 2.

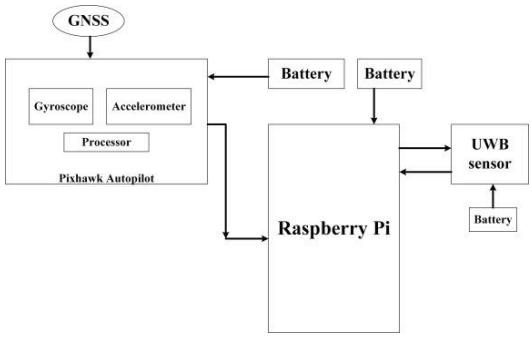

Figure 2: Block diagram showing the integration of sensors and other components on the developed UAV (after Goel et. al 2017).

The Raspberry Pi and Pixhawk autopilot together act as the brain of a UAV. Raspberry Pi is particularly responsible for controlling the sensors (especially UWB) on-board UAV while Pixhawk is responsible for ensuring a stable flight. The time stamping of all the data is performed by the Rapsberry Pi. Further, Raspberry Pi ensures communication of relevant information with the fixed infrastructure through UWB. It is to be noted that this communication can also be performed using standard Wi-Fi. The GNSS and Inertial sensor data is stored on the Pixhawk while UWB data is stored on the Raspberry Pi. The UWB data is time synchronized according to the GNSS time tag via the on-board Raspberry Pi. Some of the details of the sensors including their cost are listed in Table 1. From this table, it is evident that all the sensors are low cost, light weight and have a small form factor. This makes them ideal for a UAV based application. One of the objectives of this research is to evaluate the performance of low cost cooperative UAV localization system which is discussed in the next section.

Table 1: Details of sensors onboard a UAV.

Sensor	Dimensions	Weight	Cost
P410 UWB	76mm x 80mm x 26mm	58 g	$100
Pixhawk Autopilot	81.5mmx 50mm x 15.5mm	38 g	$200
uBlox GPS	38mm x 38mm x 8.5mm	16.8 g	$140

One of the requirements for a P2I cooperative UAV localization system is precise knowledge of states of the static nodes. In this paper, this state is determined apriori using conventional surveying methods using GNSS and network RTK to establish the states of static nodes. These static nodes are occupied by UWB radio that allows communication between static and dynamic nodes. A network adjustment using a standard GPS post processing software is performed to establish the precise coordinates of these static nodes. The computed coordinates are stored in the memory of the Raspberry Pi on-board the UAV and can be recalled when communicated with the corresponding static node. In the next section, the performance of this localization system is evaluated in real world conditions and analysed under different conditions.

4. RESULTS AND DISCUSSION

Cooperative P2I localization system for UAVs have been well studied using numerical simulations. A detailed analysis of this system using simulations is given in Goel et. al (2016b) and Goel et. al (2016d). This paper focuses on experimental

evaluation of this P2I cooperative localization system. A preliminary evaluation of this system is presented in Goel et. al (2016a). The experimental performance evaluation was done using multiple series of experiments. In this paper, two such experiments are presented and discussed. The experimental setup for the first experiment is shown in Figure 3.

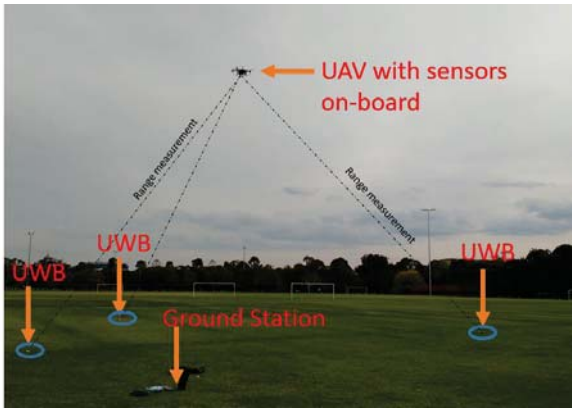

Figure 3: Experimental setup for evaluation of a Cooperative P2I localization system.

In this setup, a network of infrastructure points consisting of fixed UWB radios is setup. A total of five UWB radios were setup on the ground in this experiment. The precise coordinates of these points were obtained through a dual frequency GNSS receiver using standard GNSS RTK (Real Time Kinematic) processing techniques. The UAV is flying according to a pre-specified flight plan while it is communicating with the infrastructure based UWBs. This paper assumes that this UAV is flying in GNSS denied environments and thus only relies on communication with infrastructure nodes and the on-board inertial sensors for localization. The plan view of the trajectory followed by the UAV is shown in Figure 4.

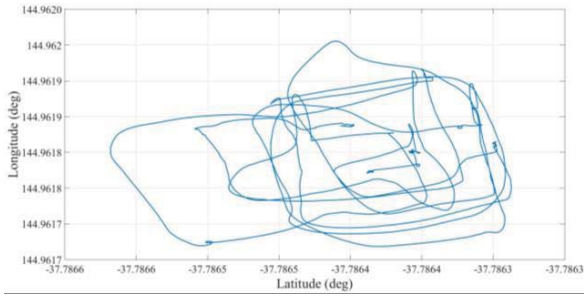

Figure 4: Plan view of the trajectory followed by the UAV.

A plot of velocity of UAV along three directions is shown in Figure 5. The UAV is flying at a height of about 12m above the ground and at speeds up to 4-5 m/s as can be seen in Figure 5. The dynamic nature of the UAV in flight is evident in Figure 4 and Figure 5. The UWB data from two infrastructure points and availability of UWB measurements is shown in Figure 6 and Figure 7, respectively. Although five UWBs were installed at fixed locations, only four were operational as can be seen in Figure 7. This is due to malfunctioning of one of the UAVs during the mission causing it to stop communicating with the UAV. Hence, the UAV had to rely on the other four static nodes for localization.

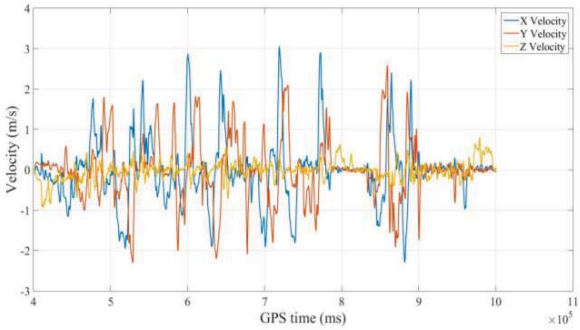

Figure 5: Plot of UAV velocity during cooperative P2I localization experiment.

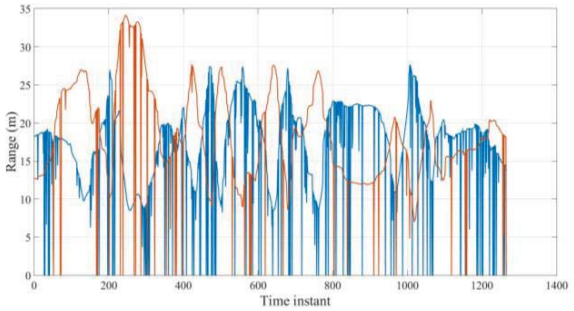

Figure 6: Relative range from UWB installed at two of infrastructure points.

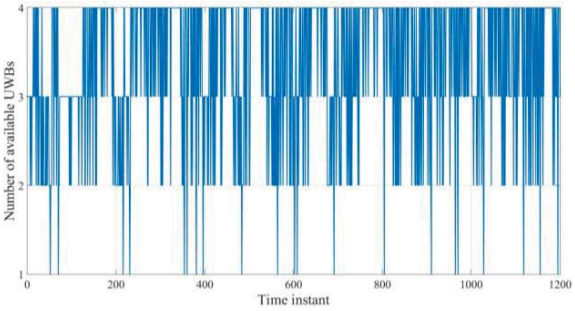

Figure 7: Availability of UWB measurements with time as the UAV is moving around.

The variation in the range measurement recorded by the UWBs is typically 10-35 m. A few sudden drops in range measurements can be seen in Figure 6. This is due to problems in communication with the fixed UWB points. The performance of the localization system in terms of localization accuracy is depicted in Figure 8 to Figure 10. The localization accuracy is affected by the number of available UWBs. It is evident from these figures that localization accuracy stabilizes to around 7 m when range measurements from 4 UWBs are available simultaneously. When less than 3 UWBs are available for an extended period of time, localization error grows due to errors in inertial observations. However, this error returns to around 6-7 m when more than 3 UWB measurements become available. A CDF plot of localization error is shown in Figure 10. It is evident from this figure that more than 95% of the time, the error in position is less than 10m. This is despite the fact that communication in network was inconsistent and kept breaking at irregular intervals.

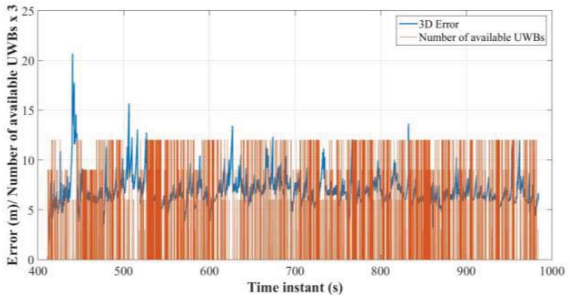

Figure 8: Plot of error in 3D position with time. The number of available UWBs are also shown in the same image.

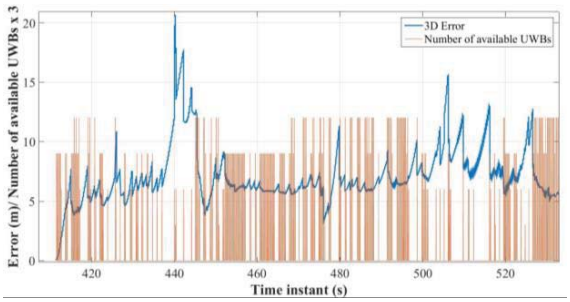

Figure 9: An enlarged version of Figure 8.

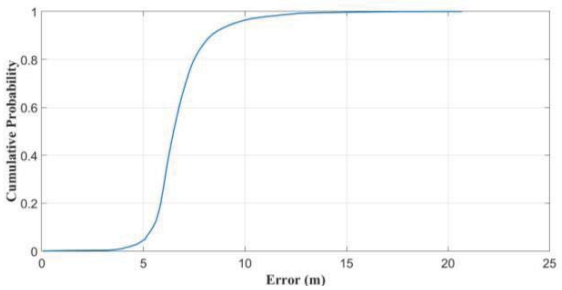

Figure 10: CDF plot of error in 3D position of UAV.

Thus, the initial experiments demonstrated that about 6-7m accuracy in position is achievable in GNSS denied environments. In the second experiment, we increase the number of UWB infrastructure nodes. This second experiment serves two purposes. The first objective is to ensure the repeatability of the experiment and the second objective is to study the effect of increase in infrastructure nodes on localization accuracy. The second experiment follows almost the same trajectory as in the first experiment as shown in Figure 4 but utilizes more static nodes in the system. The velocity profile of the UAV in the second experiment is similar to the first experiment as shown in Figure 5. In the second experiment, about 12 UWB infrastructure nodes are used. This ensures that despite communication problems, more than 4 UWB infrastructure nodes are able to communicate with the UAV at any given time. Figure 11 shows UWB measurements from two of the infrastructure nodes and Figure 12 shows the number of communicating UWB nodes available at any given time instant. The variation in the range measurements is about 10-35 m. Due to the increased number of UWBs in the second experiment, a large number of UWBs (up to 11) are available for communication at any time instant. A majority of the time only 9 UWBs are available for communication. This is beneficial for cooperative localization as higher number of communicating nodes are expected to improve the localization accuracy.

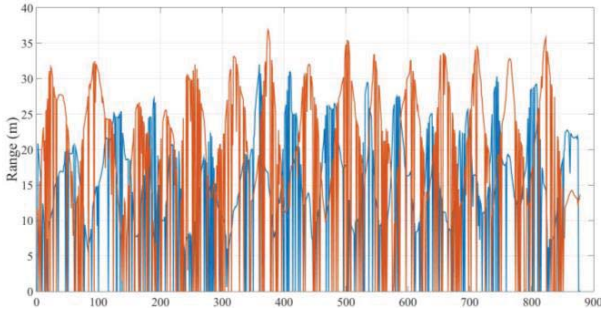

Figure 11: Relative range measurements from two UWBs in the second experiment.

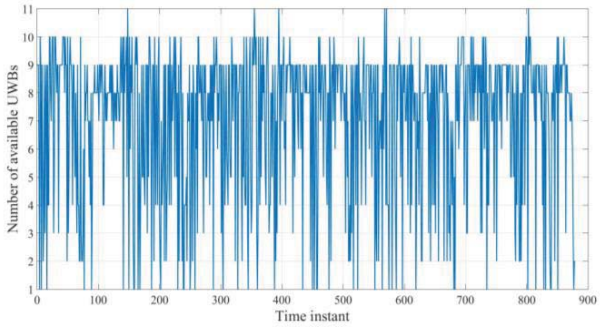

Figure 12: A plot of number of communicating UWBs in the second experiment.

The localization error of the UAV in the second cooperative P2I localization experiment is shown in Figure 13 along with the number of UWBs available (shown in orange colour). Since the number of UWBs has been increased to about 12, a good number of UWBs (greater than 4) are available for a majority of the time. Around time instant 400, the number of communicating nodes decreases to less than 3 for some time. This causes the localization error to grow up to 50 m. However, when the number of communicating nodes increase, the error decreases to around 4 m. Two zoomed views of Figure 13 are shown in Figure 14 and Figure 15. The variation of localization error is visible more clearly in these figures.

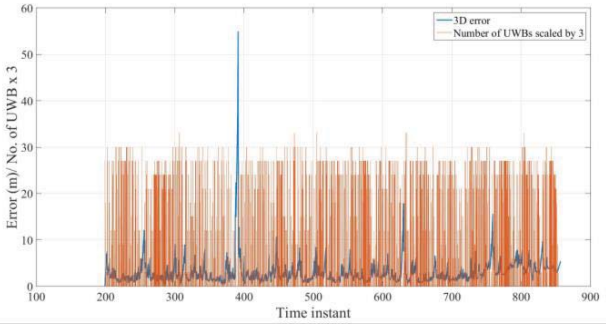

Figure 13: Plot of 3D error in UAV localization in the second cooperative localization experiment.

The histogram and CDF plot of the localization error is shown in Figure 16 and Figure 17. Compared to the first experiment when only 4 UWB nodes were available during the experiment, the localization accuracy has improved quite significantly in this experiment. For more than 95% of the time, the localization error is less than or equal to 5 m, as compared to 10 m in the previous case. This demonstrates the effect of increasing the number of communicating nodes as well as network

connectivity in a cooperative network on the localization accuracy. It is expected that any further improvement in either network connectivity or number of communicating nodes will result in a corresponding improvement in the accuracy.

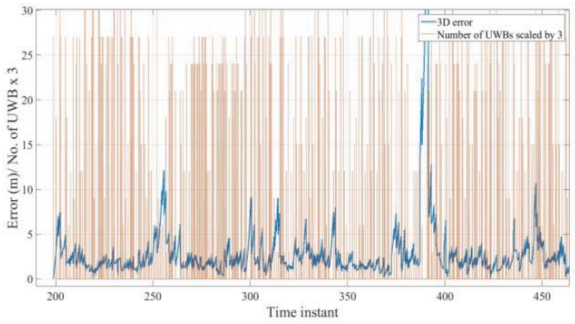

Figure 14: Zoomed view of Figure 13.

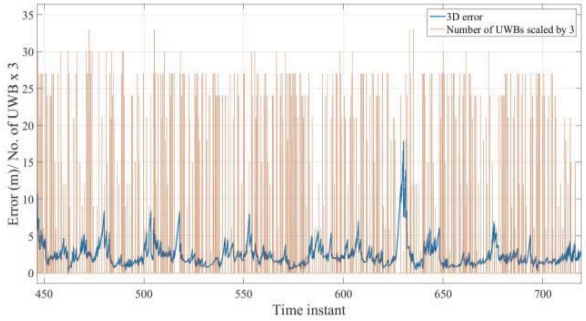

Figure 15: Zoomed view of Figure 13.

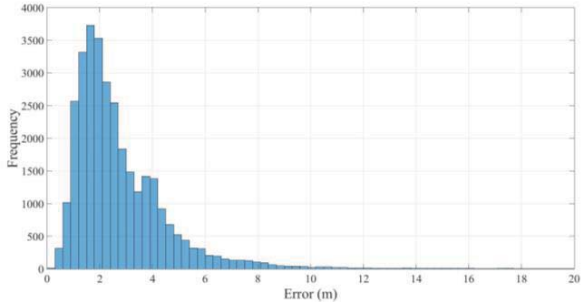

Figure 16: A histogram plot of error in 3D location of UAV.

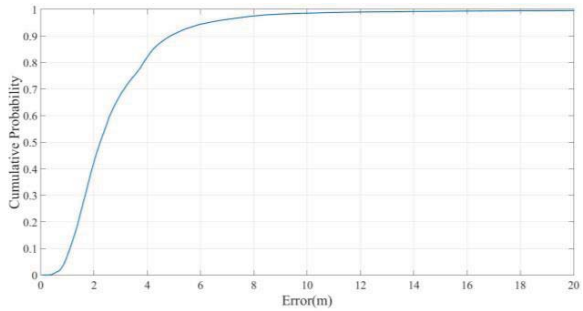

Figure 17: A CDF plot of error in 3D location of UAV.

Thus, the performance analysis of the developed cooperative P2I localization system for UAVs is performed using extensive experimentation. The results of two of these experiments are presented in this paper. Through these experiments, it has been demonstrated that under good communication conditions, localization accuracy of about 4-5 m can be expected using low cost sensors under GNSS denied conditions. In the presence of GNSS, the localization accuracy is further expected to be improved with the aid of cooperative localization. One of the major challenges faced in this system is to maintain a consistent communication between the static nodes and dynamic UAV. Although increasing the number of static nodes has ensured that more nodes are available during localization, it has not eliminated the original problem of inconsistent communication. This problem can potentially be removed by the use of better and possibly more expensive UWB sensors. The next section presents the conclusions of this paper and discusses some ideas for the future work.

5. CONCLUSIONS AND FUTURE WORK

A cooperative Peer to Infrastructure localization system for UAVs was developed and demonstrated in this paper. This system was developed using low cost sensors such as GNSS, Inertial and UWB sensor. Although various simulation studies have shown the usability of such a system, the performance of this system has not been evaluated in a real world scenario. This paper developed a prototype of a cooperative localization system and analysed its performance in real world scenarios. Through multiple experiments, it was demonstrated that localization accuracy of about 4-5 m is achievable under good communication conditions. Addition of a GNSS to this system is expected to further improve the localization accuracy. The major challenge in the existing system is maintaining a consistent communication with the fixed infrastructure nodes. It has been demonstrated through experiments that quality of the communication link has a direct impact on the localization accuracy of the system. Nevertheless, a navigation level localization accuracy is still achievable using low cost sensors even in cases when communication link is not perfect. Such a system can be used in GNSS denied or GNSS challenging environments for applications such as search and rescue missions, situational awareness, disaster management, assisted guidance and navigation, etc.

The future work will focus on further improvement of this system by addition of better quality sensors. Also, other dynamic UAVs will also be added to the existing system to develop a full cooperative P2I and P2P localization system. The analysis of a P2P localization system is currently being performed and some of the preliminary results have been in presented in Goel et. al (2017).

ACKNOWLEDGEMENTS

The authors would like to thank Dr. Charles Toth, Ohio State University, USA for providing the UWB sensors for experimentation.

REFERENCES

Bailey, T., Bryson, M., Mu, H., Vial, J., McCalman, L., Durrant Whyte, H. (2011) Decentralised cooperative localization for heterogeneous teams of mobile robots, in Proc. of the IEEE International Conference on Robotics and Automation, Shanghai, China, pp. 2859-2865

Shi, X., Tiesheng, W., Huang, B., Zhao, C., (2010). Cooperative multi-robot localization based on distributed UKF. Proceedings - 2010 3rd IEEE International Conference on

Computer Science and Information Technology, ICCSIT 2010, 6, pp.590–593.

Goel, S., Kealy, A., Retscher, G., and Lohani, B., 2016a. Cooperative P2I Localization using UWB and Wi-Fi, Proceedings of International Global Navigation Satellite System (IGNSS) Symposium, December 6-8, Sydney, Australia.

Li, H., Nashashibi, F. (2013). Cooperative multi-vehicle localization using split covariance intersection filter. IEEE Intelligent Transportation Systems Magazine, 5(2), pp.33–44.

Wanasinghe, T.R., Mann, G.K.I., Gosine, R.G. (2014). Decentralized Cooperative Localization for Heterogeneous Multi-robot System Using Split Covariance Intersection Filter. In 2014 Canadian Conference on Computer and Robot Vision. IEEE, pp. 167–174.

Goel, S., Kealy, A., and Lohani, B. 2016b. Cooperative UAS localization using low cost sensors. ISPRS Annals of Photogrammetry and Remote Sensing, III-1, 183-190.

Carrillo-Arce, L.C., Nerurkar, E. D., Gordillo, J. L., Roumeliotis, S. I. (2013). Decentralized multi-robot cooperative localization using covariance intersection. In 2013 IEEE/RSJ International Conference on Intelligent Robots and Systems. IEEE, pp. 1412–1417.

Chen, X., Gao, W., Wang, J. (2013). Robust all-source positioning of UAVs based on belief propagation. EURASIP Journal on Advances in Signal Processing, 2013(1), p.150.

Savic, V., Zazo, S. (2013). Cooperative localization in mobile networks using nonparametric variants of belief propagation. Ad Hoc Networks, 11(1), pp.138–150.

Wan, J., Zhong, L., Zhang, F. (2014). Cooperative Localization of Multi-UAVs via Dynamic Nonparametric Belief Propagation under GPS Signal Loss Condition. International Journal of Distributed Sensor Networks, 2014, pp.1–10.

Goel, S., Kealy, A., and Lohani, B. 2016c. Infrastructure vs Peer to Peer Cooperative Positioning, Proceedings of ION GNSS+, September 12-16, Portland, Oregon, USA.

Goel, S., Kealy, A., and Lohani, B. 2016d. Cooperative localization of Unmanned Aerial Vehicles using GNSS, MEMS Inertial and UWB sensors, Journal of Surveying Engineering. (Accepted, in Press).

Goel, S., Kealy, A., and Lohani, B., 2017. A Distributed Cooperative UAV Swarm Localization System: Development and Analysis, Proceedings of ION GNSS+, September 25-29, Portland, Oregon, USA. (Accepted).

AN IMPROVED MODEL FOR MULTI-CONSTELLATIONS GNSS SINGLE FREQUENCY PRECISE POINT POSITIONING

Mahmoud Abd Rabbou[1] and Adel El-Shazly[2]
Faculty of Engineering, Cairo University, Egypt; mahmoud.abdelrahman@cu.edu.eg[1]
Faculty of Engineering, Cairo University, Egypt; adel_shazly@hotmail.com[2]

KEY WORDS: Single frequency PPP, BSSD, Quasi-Phase, GPS, GNSS, GLONASS, Galileo, Beidou.

ABSTRACT:

We develop a new single frequency PPP model, which uses constrained between- satellite-single-difference ionosphere-free (BSSD IF) quasi-phase with quad GNSS single frequency observations. To overcome of the limitations of poor satellite geometry, especially in urban areas, multi-constellation GNSS observations such as Galileo and BeiDou observations are added to the GPS and GLONASS observations to enhance the satellite geometry and increasing of the measurement redundancy. Furthermore, to completely remove the receiver code biases, loosely-coupled satellite single difference technique is applied on the multi-constellation GNSS single frequency observations. In addition, to overcome the limitation of the ionospheric impact which represent the main source of error in single frequency PPP, ionosphere-free GNSS code and phase observations, which is known as a quasi-phase observations model is employed. To overcome the rank deficiency problem due to the existence of ambiguity parameters, additional observations are added to constrain the ambiguity parameters working as a priori observations which are selected as the half of code and phase difference. The developed model is compared with the traditional undifferenced with ionospheric error corrected by the final Global Ionospheric model (GIM). It is shown that using of BSSDIF-PPP technique enhances the positioning accuracy by 35%, 30%, 34% 30% and 29% compared with the GIM based PPP model for the GPS only, GPS/GLONASS, GPS/Galileo, GPS/BeiDou and GNSS combinations, respectively after one hour of GNSS data processing.. However, after six hours of GNSS data processing comparable positioning accuracy can be obtained from all developed single frequency models.

1. INTRODUCTION

Commonly, precise point positioning (PPP) uses dual-frequency GPS/GLONASS observations and can obtain positioning accuracy comparable to that of differential positioning in both static and kinematic modes. However, PPP is featured with a relatively long convergence time to achieve sub-decimeter positioning accuracy, which is mainly attributed to the un-calibrated receiver biases and poor satellite geometry. In addition, dual-frequency GNSS systems are expensive and may not provide a cost-effective solution in many instances. The use of low-cost single-frequency GNSS receivers, on the other hand, is limited by the effect of ionospheric delay. As a result, to obtain a cost effective precise PPP solution, a new single frequency PPP model should be developed taking into consideration the current limitations of PPP techniques.

The significance of using multi-constellation GNSS is mainly noticed in challenging environment, such as urban areas, where the signals are either partially blocked by urban obstacles or contaminated by multipath interference. In addition, measurements from multiple GNSS constellations not only improve the satellite geometry, but also increase the redundancy, which in turn improve the positioning accuracy and convergence time. However, the additional GNSS observations introduce additional biases such as inter-system biases, which can be treated as additional unknowns in the estimation filter. The drawback of this strategy is that the number of unknowns will be increased by one for each GNSS system added. The minimum number of satellites for the basic combined GNSS positioning solution will be (3+j), where j is the number of systems used representing the additional receiver clock unknowns to the filter. For GNSS applications in dense areas, increasing the number of unknowns might be critical in obtaining a good solution. In addition, further un-calibrated GNSS biases such as receiver and satellites differential code biases will be added, which, unless properly handled, degrade the positioning accuracy. The contribution of the additional observations from a particular constellation to the existing GPS observations is mainly based on the number of satellites from that constellation and the satellite geometry enhancement. A minimum of two visible satellites is required from a particular constellation to contribute to the positioning solution considering the additional receiver clock unknown term added for each constellation. Due to the relatively large number of visible GLONASS satellites at present, the additional GLONASS observations improve the PPP positioning accuracy and convergence time (Cai and Gao 2007, Choy et al. 2013 and Abd Rabbou and El-Rabbany 2015). On the other hand, the contribution of adding Galileo observations to those of GPS can be considered marginal due to the limited number of Galileo satellites (e.g., Píriz et al. 2008; Montenbruck et al. 2011; Steigenberger et al. 2011; Abd Rabbou and El-Rabbany 2015).

This research aims to develop a single frequency PPP model, which combines the observations of all current GNSS constellations, including GPS, GLONASS, Galileo and Beidou. The developed model uses constrained between satellite single difference quasi-phase GNSS observations. The developed model is compared with the traditional undifferenced and BSSD models with ionospheric error corrected by the final Global Ionospheric model (GIM) and the undifferenced quasi-phase GNSS observation model. The final precise products of the International GNSS Service multi-GNSS experiment (IGS-MEGX) network are used to account for the GNSS satellite orbit and clock errors (Montenbruck et al., 2014). The ionospheric delay is largely corrected through the IGS global ionosphere maps (GIM) model (Schaer et al., 1998). The hydrostatic and wet components of the tropospheric zenith path delay are modelled through the UNB3 model. All remaining errors and biases are accounted for using existing models as shown in Kouba (2009).

2. SINGLE FREQUNECY BSSD IF PPP MODEL

The basic GNSS observation equations for single-frequency pseudorange and carrier-phase observations of a particular constellation can be written as:

$$P=\rho + cdt_r - cdt^s + T + I + c(d_r - d^s) + d_m + e \quad (1)$$

$$\Phi=\rho + cdt_r - cdt^s + T - I + c(\delta_r - \delta^s) + \delta_m + \lambda(N + \varphi_r - \varphi^s) + \varepsilon \quad (2)$$

where P is GNSS pseudorange measurement in meters; Φ is the GNSS carrier phase measurement in meters; ρ is the true geometric range in meters from the antenna phase center of the receiver at reception time to the antenna phase center of the satellite at transmission time; dt_r and dt^s are the clock errors for receiver and satellite, respectively; d_r and d^s are frequency-dependent code hardware delay for receiver and satellite, respectively in seconds; δ_r and δ^s are frequency-dependent carrier phase hardware delay for receiver and satellite, respectively in seconds; e, ε are relevant system noise and un-modeled residual errors in meters; N is the integer ambiguity parameters in cycles; φ_r and φ^s are the initial phase biases at the receiver and the satellite, respectively in cycles; λ is the wavelengths of the carrier frequency in meters; c is the speed of light in vacuum in meter/second; T is the tropospheric delay component in meters; I is the ionospheric delay component in meters; $d_m$and δ_m are the multipath interference component for code and phase, respectively in meters.

Current GNSS receivers take the GPS time system as a reference, which introduces an inter-system bias (ISB) when combining the observations of GPS and other GNSS system. In addition, the IGS-MGEX satellite clock corrections, which are used in this research, are referred to the GPS time and include the ionosphere-free linear combinations of the satellite code hardware delays of the various GNSS systems (Steigenberger et al. 2014). As such, using Equations 1 and 2 and considering the multi-GNSS observations, including GPS and the other GNSS systems (Subscripted by J), the mathematical model for single frequency GNSS PPP can be written as (Abd Rabbou and El-Rabbany, 2015):

$$P_G=\rho_G + c(dt_r + d_G) - c\bar{dt}_G^s - c(B_G^s) + T_G + I_G + e_G \quad (3)$$

$$P_J=\rho_J + c(dt_r + d_G) - c\bar{dt}_J^s - c(B_J^s) + c[ISB_J] + T_J + I_J + e_J \quad (4)$$

$$\Phi_G=\rho_G + c(dt_r + d_G) - c\bar{dt}_G^s - c(B_G^s) + T_G - I_G + [\lambda\bar{N}_G + c(\delta_G - d_G) - c(\delta_G^s - d_G^s)] + \varepsilon_G \quad (5)$$

$$\Phi_J=\rho_J + c(dt_r + d_G) - c\bar{dt}_J^s - c(B_J^s) + c[ISB_J] + T_J - I_J + [\lambda\bar{N}_J + c(\delta_J - d_J) - c(\delta_J^s - d_J^s)] + \varepsilon_J \quad (6)$$

Where $d\bar{t}^s$ is the satellite clock error lumped with the ionosphere-free differential code bias, which can be obtained from the IGS-MGEX*; B* is a bias term representing the combined effect of differential code bias of the satellite*; ISB* is the inter-system bias. In our single-frequency GNSS model (Equation 3 to 6), the GPS receiver hardware delay d_G is lumped to the receiver clock error and the combined receiver clock bias is considered as a single unknown in our estimation filter.

Considering the opposite ionospheric impact in both code and phase measurements, the ionospheric error can be effectively removed by taking the average of the code and phase observations which is known as the quasi-phase observation (Yunck, 1993). The mathematical equations of the single frequency ionosphere-free observation can be written as

$$\bar{\Phi}_G=\frac{\Phi_G + P_G}{2}=\rho_G + c(dt_r + d_G) - c\bar{dt}_G^s - c(B_G^s) + T_G + \frac{[\lambda\bar{N}_G + c(\delta_G - d_G) - c(\delta_G^s - d_G^s)]}{2} + \bar{\varepsilon}_G \quad (7)$$

$$\bar{\Phi}_J=\frac{\Phi_J + P_J}{2}=\rho_J + c(dt_r + d_J) - c\bar{dt}_J^s - c(B_J^s) + T_J + c[ISB_J] + \frac{[\lambda\bar{N}_J + c(\delta_J - d_J) - c(\delta_J^s - d_J^s)]}{2} + \bar{\varepsilon}_J \quad (8)$$

where $\hat{\Phi}_G$ and $\hat{\Phi}_J$ are the quasi-phase observations for GPS and other GNSS observations. According to Equations (7) and (8), we can note that the ionospheric effect is totally removed. In addition, due to the small phase measurements noise which can be neglected, the noise characteristics of the quasi-phase $\hat{\varepsilon}_G$ and $\hat{\varepsilon}_J$, are mainly contributed by half of the code measurements noise, e_G and e_J, respectively.

However, the mathematical model for the ionosphere-free described in Equations (8) and (9) presents a singularity model. To overcome the rank deficiency problem, additional observations should be added to constrain the ambiguity parameters working as a priori observations. Commonly, the code observations are used as a priori observations (Andrei et al, 2009 and Choy, 2013). In current research, the a priori observation is selected as the half of code and phase difference as follows,

$$\hat{\Phi}_G=\frac{\Phi_G - P_G}{2}=\frac{[\lambda\bar{N}_G + c(\delta_G - d_G) - c(\delta_G^s - d_G^s)]}{2} - I_G + \hat{\varepsilon}_G \quad (9)$$

$$\hat{\Phi}_J=\frac{\Phi_J - P_J}{2}=\frac{[\lambda\bar{N}_J + c(\delta_J - d_J) - c(\delta_J^s - d_J^s)]}{2} - I_J + \hat{\varepsilon}_J \quad (10)$$

However, as can be seen from Equations 9 and 10, the ionospheric parameters are affecting the constrained equations. This can be overcome by correcting these observations using the existing ionospheric models such as the GIM model or can totally ignoring the ionospheric range delay with assuming higher observation uncertainty. In this research, the second option is employed.

To completely remove the receiver biases and ionospheric error from the single-frequency observations, the ionosphere-free code and phase combinations described in Equations 7 to 10 can be applied on the satellite single difference observations. The mathematical for BSSD quasi-phase observation can be written as follows

$$\bar{\Phi}^{ij}_{gnss} = \frac{\Phi^{ij}_{gnss} + P^{ij}_{gnss}}{2} = \Delta\rho^{ij}_{gnss} - c\,d\bar{t}^{ij}_{gnss} - c(B^{ij}_{gnss}) + \Delta T^{ij}_{gnss} + \frac{\Delta[\lambda\bar{N} - c(\delta^s_J - d^s_J)]^{ij}_{gnss}}{2} + \bar{\varepsilon}^{ij}_{gnss} \quad (11)$$

The a priori observation is selected as the half of the BSSD code and phase difference as follows

$$\hat{\Phi}^{ij}_{gnss} = \frac{\Phi^{ij}_{gnss} - P^{ij}_{gnss}}{2} = \frac{\Delta[\lambda\bar{N} - c(\delta^s_J - d^s_J)]^{ij}_{gnss}}{2} - \Delta I^{ij}_{gnss} + \hat{\varepsilon}^{ij}_{gnss} \quad (12)$$

where the IGS GIM model is used for correcting the ionospheric term

3. GNSS DATA PROCESSING

The extended Kalman filter (EKF) is employed to estimate the unknown parameters, as detailed in Jekeli (2001). For the BSSD IF single frequency PPP techniques, the estimation state vector consists of the three GNSS receiver coordinates, namely latitude, longitude, and altitude, the wet tropospheric unknown and the float ambiguity parameters. The complete state vector for the BSSD IF model can be written as:

$$\delta x = [\delta\phi, \delta\lambda, \delta h, \Delta T_w, A_{1i}, .. A_{ni}] \quad (13)$$

where $\delta\phi$, $\delta\lambda$ and δh are the positioning errors in latitude, longitude and altitude T_w is the wet tropospheric component ; A is the float ambiguity term as described in Equations 11 and 12. For the standard single frequency GNSS PPP model, the GNSS observations are assumed to be uncorrelated and followed the Gaussian distribution with zero mean. As a result, the variance-covariance matrix takes the form of a diagonal matrix with a 100 times ratio between the GNSS code and phase observation precision. The GPS and GLONASS code and phase observation precision is set to be 0.5 and 0.005 m, respectively. According to Steigenberger et al, (2015), the clock and orbital products for Galileo and BeiDou are less accurate compared with GPS clock and orbital products. As a result, the Galileo and BeiDou code and phase observations are weighted by ¼ with a precision taken as 1 and 0.01 m, respectively. For the ionosphere-free model, the quasi-phase observables are assumed linearly correlated with the ambiguity-constrained observables and the precision of both observables are taken as ½ of the code precision (Choy et al., 2013).

To verify the performance of our single frequency GNSS PPP models, data sets from eleven globally distributed IGS-MGEX stations are processed. The datasets collected at the selected stations on seven consecutive days, i.e. April 1–7, 2014, are used for numerical analysis. The selected stations are occupied by different types of GNSS receivers. Single-frequency observations from GPS L1, GLONASS G1, Galileo E1and BeiDou B1 signals are adopted in this study. The BeiDou and Galileo antenna offsets recommended by the MGEX project are used to correct the PCOs of BeiDou and Galileo satellites (Rizos et al., 2013). Six-hour position solutions are analysed to represent the PPP performance in a short observation time. For the seven-day datasets, each day is divided into four sessions. Each session is processed separately so that a total of 308 sets of results are obtained to derive a statistical estimate on the positioning accuracy.

4. GNSS DATA ANALYSIS AND RESULTS

To evaluate the performance of different GNSS combinations namely GPS only, GPS/GLONASS, GPS/Galileo, GPS/BieDou and GPS/GLONASS/Galielo/BeiDou (GNSS), the positioning results with time for BRST at April 1, 2014, are shown herein as an example. Figures 1 shows the positioning errors with time for the various GNSS constellation combinations at stations BRST. All PPP solutions are referenced to the GNSS station coordinates published by Center for Orbit Determination in Europe (CODE, 2015). It can be seen that the major contribution to the PPP solution enhancement is due to the additional GLONASS observations. This is due to the good availability of GLONASS compared with the other constellation, which significantly affects the overall satellite geometry. On the other hand, because of their limited number of visible satellites, the addition of Galileo and BeiDou systems has a marginal effect on the positioning accuracy, in comparison with the GPS-only solution. In contrast, comparable results are obtained with the GPS/GLONASS and the all-constellation GNSS solutions. It can be also seen that the ionosphere-free single frequency PPP model gives significant positioning accuracy enhancement compared with the undifferenced GIM based technique.

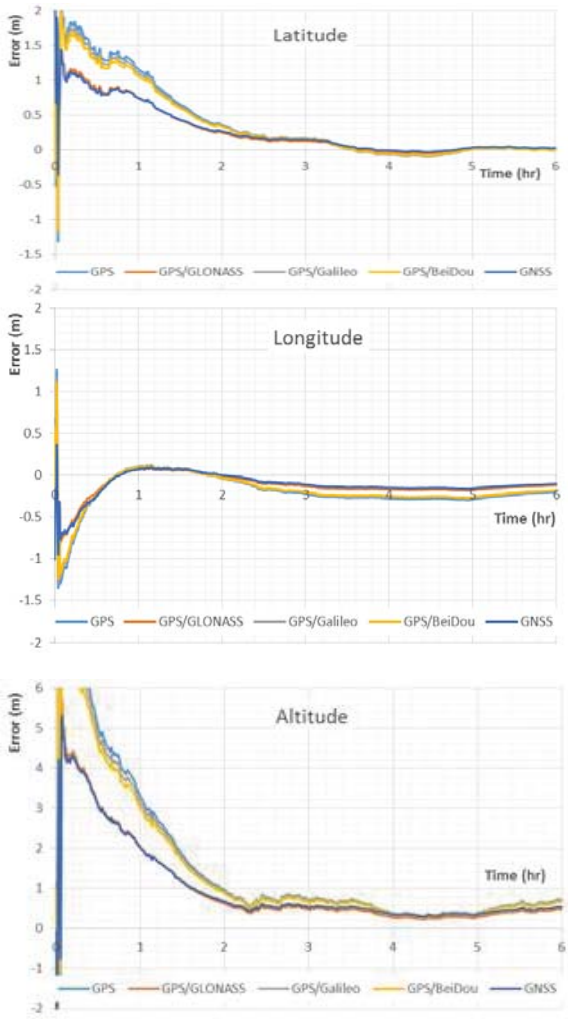

Figure 1. The positioning errors using the Single frequency GNSS PPP model for the different GNSS combinations

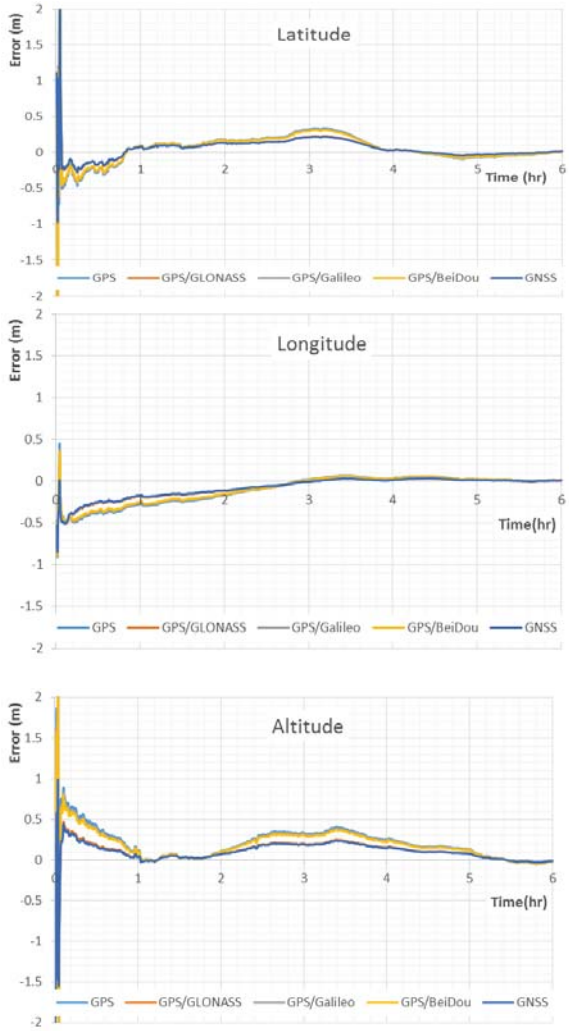

Figure 2. The positioning errors using the BSSD IF Single frequency GNSS PPP model for the different GNSS combinations

Table 1 summarize the 3D average positioning errors for the four developed single frequency PPP models after 2h of data processing. For GPS only, it can be seen that the 3D positioning accuracy is enhanced by 13 cm compared with the GIM based technique when the IF- PPP is used. Furthermore, using the BSSD and BSSD-IF techniques improve the positioning accuracy by 5cm and 2 cm compared with the GIM and IF single frequency PPP techniques, respectively. Comparable results are obtained for both the GPS/Galileo and GPS/BeiDou combinations. For the GPS/GLONASS combination solution, the 3D positioning mean is enhanced by 6 cm when the IF-PPP technique is used compared with the GIM based model. Further improvement can be noticed when BSSD techniques are used in comparison with the undifferenced techniques.

Table 1. the 3D average positioning errors in meter for the four single-frequency PPP developed models after 2 hours of data processing

GNSS Combination	*GPS*	*GPS/GLONASS*	*GPS/Galileo*	*GPS/BiDou*	GNSS
Standard PPP	0.48	0.27	0.45	0.39	0.22
IF-PPP	0.35	0.21	0.32	0.32	0.2
BSSD- PPP	0.43	0.24	0.4	0.35	0.21
BSSD-IF-PPP	0.32	0.17	0.3	0.26	0.21

Figure 3 shows the mean of positioning errors after one hours of data processing. It can be seen that using the IF-PPP technique enhanced the positioning accuracy by 25%, 20%, 24% 20% and 19% compared with the GIM based PPP model for the GPS only, GPS/GLONASS, GPS/Galileo, GPS/BeiDou and GNSS combinations, respectively. Furthermore, an average of 15% positioning accuracy enhancement can be obtained when the BSSD techniques are used compared with the undifferenced techniques.

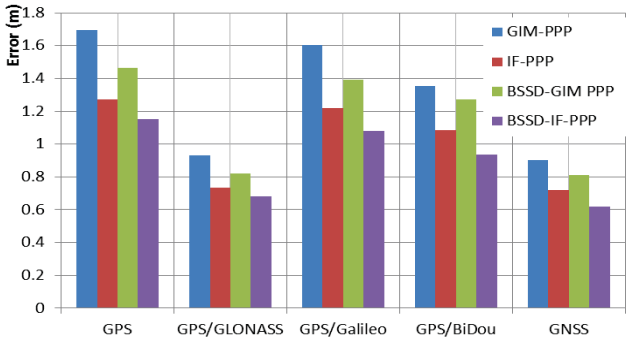

Figure. 3. The mean positioning accuracy after one hour for the different GNSS combinations

5. CONCLUSION

We developed PPP models, which combines single frequency observations of multi-constellation GNSS systems, including GPS, GLONASS, Galileo and BeiDou. Four Single Frequency GNSS PPP models are developed, namely; the undifferenced single frequency GNSS PPP model and the final IGS GIM model was used to account for the ionospheric delay , the undifferenced ionosphere-free (IF) code and phase model known as quasi-phase model, the between-satellite-single-difference model (BSSD) and the between-satellite-single-difference ionosphere-free (BSSDIF) model. The IGS-MGEX final precise products were used to account for the orbital and clock errors, respectively. The contribution of the additional GNSS observations to the PPP solution was assessed through comparison with the traditional GPS-only counterpart. It was shown that the contribution of the additional GLONASS and BeiDou observations with good satellite availability is significant. It was also shown that the using of IF-PPP model significantly enhanced the positioning accuracy compared with the GIM based PPP. After two hours of data processing, the 3D positioning accuracy was enhanced by 13 cm compared with the GIM based technique when the IF- PPP is used and comparable results are obtained from both the GPS/Galileo and GPS/BeiDou combinations. For the GPS/GLONASS combination solution, the 3D positioning mean was enhanced by 6 cm when the IF-PPP technique is used compared with the GIM based model. Further improvement can be noticed when

BSSD techniques are used in comparison with the undifferenced techniques.

6. REFERENCES

Abd Rabbou, M. and El-Rabbany, A. (2015) PPP Accuracy Enhancement Using GPS/GLONASS Observations in Kinematic Mode. Positioning, 6, 1-6. http://dx.doi.org/10.4236/pos.2015.61001

Abd Rabbou, M., El-Rabbany, A, (2015), Precise Point Positioning using Multi-Constellation GNSS Observations for Kinematic Applications, Journal of applied Geodesy, DOI: I10.1515/jag-2014-0021.

Cai C, Gao Y (2007). Precise point positioning using combined GPS and GLONASS observations. Positioning, 1(11).

Cai C, Gao Y (2008) Estimation of GPS-GLONASS System Time Difference with Application to PPP. Proceedings of the 21st International Technical Meeting of the Satellite Division of The Institute of Navigation Savannah, GA, September 2008, pp. 2880-2887.

Choy S, Zhang S, Lahaye F, Héroux P (2013) A comparison between GPS-only and combined GPS+ GLONASS Precise Point Positioning. Journal of Spatial Science, 58(2), 169-190.

CODE, (2015) Center for Orbit Determination in Europe, ftp://ftp.unibe.ch/aiub.

El-Rahman, M. A., & El-Rabbany, A. (2013). Performance Evaluation of USTEC Product for Single-Frequency Precise Point Positioning. GEOMATICA, 67(4), 253-257.

El-Rahman, M. A., & El-Rabbany, A. (2013). Performance Evaluation of USTEC Product for Single-Frequency Precise Point Positioning. GEOMATICA, 67(4), 253-257.

Jekeli C (2001) Inertial navigation systems with geodetic applications. Walter de Gruyter.

Kouba J (2009) A guide to using International GNSS Service (IGS) products. International GNSS.

Leandro R F, Langley R B, and Santos M C (2008) UNB3m_pack: a neutral atmosphere delay package for radiometric space techniques. GPS Solutions, 12(1), 65-70.

Montenbruck O, Hauschild A, Hessels U (2011) Characterization of GPS/GIOVE sensor stations in the CONGO network. GPS Solutions, 15(3), 193–205.

Montenbruck O, Steigenberger P, Khachikyan R, Weber G, Langley R B, Mervart L, Hugentobler U (2014) IGS-MGEX: Preparing the Ground for Multi-Constellation GNSS Science, Inside GNSS, 9(1), 42-49.

PheltsR.E.,RangeBiasesonModernizedGNSSCodes,Proceedings ofEuropeanNavigationConferenceGNSS/TimeNav, Geneva,Switzerland.http://waas.stanford.edu/~wwu/papers/ gps/PDF/PheltsENC07.pdf,2007.

Píriz R, García Á M, Tobías G, Fernández V, Tavella P, Sesia I, Hahn J (2008) GNSS interoperability: offset between reference time scales and timing biases. Metrologia, 45(6), S87.

Schaer, S., Gurtner, W., & Feltens, J. (1998, February). IONEX: The ionosphere map exchange format version 1. In Proceedings of the IGS AC workshop, Darmstadt, Germany (Vol. 9, No. 11).

Steigenberger P, Hugentobler U, Loyer S, Perosanz F, Prang L, Dach R, Uhlemann M, Gendt G, Montenbruck O (2014) Galileo Orbit and Clock Quality of the IGS Multi-GNSS Experiment, Advances in Space Research, doi: 10.1016/j.asr.2014.06.030.

Steigenberger P, Hugentobler U, Montenbruck O, Hauschild A (2011) Precise orbit determination of GIOVE-B based on the CONGO network. Journal of Geodesy, 85(6), 357-365.

ACUURACY ASSESSMENT OF DIFFERENT ALGORITHMS USED FOR DERIVING BATHYMERTY FROM LANDSAT 8 SATELLITE IMAGES, APPLIED IN EGYPT, CASE STUDY (SOMA BAY, RED SEA)

SALEH, E. A [a], El-Shazly, A.H.[b], El-Ghazaly,M.S. [c], Ahmed,K.M[d]

[a] Faculty of Engineering, Cairo University–eng.eslamali@gmail.com
[b] Faculty of Engineering, Cairo University- adel_shazly@hotmail.com
[c] Faculty of Engineering, Cairo University–globalgb@globalgeobits.com
[d] Faculty of Engineering, Cairo University- kamal@eng.cu.edu.eg

Commission VI, WG VI/4

KEY WORDS: Satellite-derived bathymetry – Landsat 8- Ratio Model - Sun glint Removal –linear model

ABSTRACT:

Remotely sensed data, especially satellite images of multispectral bands, are regarded as an effective tool for gathering bathymetric information, which is useful for different marine application. The objective of this paper is to evaluate the performance of two water depth extraction models for the generation of reliable depths from freely available Landsat 8 multispectral satellite images in Egypt. The models used for derived bathymetry in Soma bay- Egypt were : Lyzenga linear transform, and Ratio algorithm. After the images were pre-processed, six ratios and three linear combinations were calculated and input to the ratio and Linear transform models respectively. The two models were calibrated and validated using data generated by a Single beam echo sounder (SEBS) integrated with a DGPS instrument. The results showed that both models when applied to Landsat 8 images, provided depth accuracies that are suitable for preliminary design for marine applications such as shore protection. In addition, the most suitable band ratios and combinations were demonstrated.

1. INTRODUCTION

Extracting bathymetric information is vital for several marine applications and costal monitoring. Examples of such applications are: producing nautical charts, marine planning, dredging of channels, predicting channel erosion, and decomposition, sediment transportation, and finally shore line change detection. Ship based techniques such as single beam echo sounder (SEBS), and Multi beam echo sounder, as well as airborne LIDAR bathymetry (ALB) are traditional techniques used for extracting bathymetric information. Such techniques provide reliable water depths at a relatively high cost. The disadvantage of the traditional methods is the difficulty to reach certain areas such as shallow and remote areas. Extracting depths from remotely sensed images provided a solution that is can be more cost effective, less time consuming, and more frequent. The theoretical principles behind satellite-derived bathymetry (SDB) are the fact that the different ranges of light wavelengths are affected in different ways by the water column. Among the different bands in a satellite image, the blue and green bands have the largest penetration depths through a water column. Several methods were developed for SDB that are either analytical or empirical. Analytical models rely on measured factors, such as attenuation and backscattering, to derive the depth of water, while the empirical models rely on the relationship between pixel values and field measured depths. An early attempt to derive an empirical model was performed by (Lyzenga 1978), which was updated on 1981 and 1985. Lyzenga assumed that the reflectance recorded by the sensor is linearly proportion with the bottom reflectance, and is exponentially proportion with water depth. In his early work, Lyzenga used the reflectance from a single band, he then proposed that using more than one band will lead to better results. Stumpf et al. (2003) proposed an empirical model based on establishing relation between the ratio of reflectance between two bands and the control depths. The ratio algorithm by (Stumpf et al., 2003) proposed its benefit in deep water(>25m), and in the shallow areas especially these areas where sea grass grow at the bottom. Regardless of the model employed, several sources of images were experimented to derive depth from reflectance such as aerial images (Lyzenga 1978), Landsat images (Lyzenga 1981; Spitzer and Drink 1983; Philopt1989), IKONOS (Stumpf et al., 2003; Su et al., 2003), Quick Bird (Conger et al., 2006; Lyons et al., 2011), and World view (Bramante et al., 2010). The purpose of this paper is to compare two algorithms, namely (Lyzenga 1985) and (Stumpf et al., 2003), and evaluate their performance for generating depths in soma bay , Egypt using freely available multiband satellite images.

2. DATA DESCRIPTION

2.1 Study Area:

The study area is Soma bay – Egypt as shown in (fig. 1). Soma Bay is a coastal resort on the Red Sea in Egypt where the depth ranges between one and fifteen meters, 45 km south of Hurghada International Airport. The bay is about 5 km long and 2 km wide. The geographic coordinates of the study area are :(596927.387E m, 2970257.77N m) & (59904.239E m, 2969208.91N m).

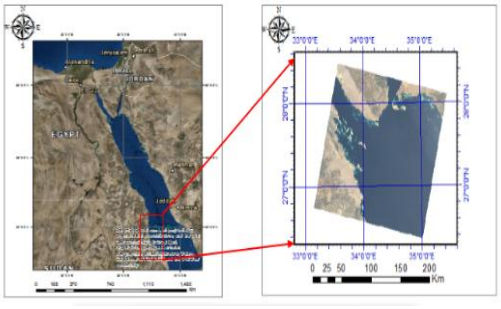

Figure 1. Study Area.

2.2 Satellite images

Landsat 8 satellite images is employed for deriving bathymetric information in this research. The images include the coastal-blue band, which is instrumental for marine applications. In addition, they are multispectral-bands images which are available for free. The images include 11 bands of an average spatial resolution that ranges between 15 and 100 meters .The spatial resolution for bands 1 to 7 and band 9 is 30 m, for band 8 (panchromatic) is 15 m, and for bands 10, and 11 is 100 m. The temporal resolution is 16 days, and the ground coverage of one scene is 170 km in north –south direction by 183 km in the east-west direction. The date of the satellite scene used is June 2015, which is the closest to the date of the bathymetric survey used for calibration. The attributes of the scene used is summarized in table 1.

LANDSAT_SCENE_ID	"LC81740412015191LGN00"
Path –Row	174 - 41
Projection	UTM
Datum	WGS 84
Zone	36 N
DATE_ACQUIRED	2015-07-10
Cloud cover	0.77%
Coverage	
X min X max	513600 m – 741300 m
Y min –Y max	2918100 m -3150600 m

Table 1. Attributes of Landsat 8 scene.

2.3 Calibration Points

For model calibration, a set of data gathered by a single beam echo sounder equipped with a DGPS instrument. The bathymetry included 12 scan lines that were perpendicular to the shoreline every about 100, and three cross lines that were parallel to the shoreline. The points along each scan line were about 2m apart. The horizontal accuracy of the survey was better than 5 cm, a standard deviation of 15 cm. The points were processed and georeferenced to the world wide projection system UTM-zone 36 N, the depths varied between 2 and 15 m.

3. BACKGROUND

3.1 Radiometric Calibration of Image

Landsat 8 images are provided in the form of digital values (DN). Radiometric calibration is utilized to convert these non-physical values to radiance or surface reflectance using the rescaling coefficients provided in the associated metadata file (MTL). Spectral radiance rescaling is archived by applying equation (1) (Survey, 2005).

$$L_\lambda = M_l * Q_n + A_l \quad (1)$$

Where, L_λ =Radiance measured in (W/m^2 Srad µm)
Q_n= Quantized digital number.
M_l=Multiplicative rescaling coefficients.
A_l= Additive rescaling coefficients.

3.2 Atmospheric Correction

The effect of haze and atmospheric scattering must be removed before applying bathymetric models. The method used in this research to correct for atmospheric effect is Dark object subtraction (DOS), as introduced by (Chaves 1988). DOS is a popular method for atmospheric correction, which was used by several researchers such as (Benny and Dawson 1983, Green et al., 2000). The method is based on subtracting the lowest digital number DN throughout the scene from DN of the remaining pixels. Afterwards, the following equations (2) through (5) are used consequentially to convert DNs to surface reflectance:

$$L_{Min} = M_l * Q_n min + A_l \quad (2)$$

Where L_{min} =Minimum radiance value for each pixel.
Q_{nmin} = Darkest pixel (lowest) digital number.
M_l=Multiplicative rescaling coefficients.
A_l= Additive rescaling coefficients.

(Pacheco et al., 2015) in his pervious work cosider the fact that Some pixels are truly dark by its nature according to (Chavez, 1996) and need to be removed from the set of minimum radiance as computed by equation (2). Therefore a 1% reflectance value is assumed for those pixels. This reflectance value is converted to radiance through equation (3)

$$L_{Haze1\%} = \frac{.01 * E_{sun\lambda} * \cos_{\theta s} * TAU_v * TAUz}{\pi * d^2} \quad (3)$$

Where $L_{haze1\%}$ = targets assumed to be truly dark and the reflectance assumed to be =.01
d= earth sun distance in astronomical units (provided in the MTL files).
θs = Solar Zenith angle. (Provided in the MTL files)
TAUv, TAUz =Transmission coefficients for sun-to earth, and earth -to- satellite (for (Dos) method, of TAUv, TAUz =1)

Then, path radiance (Lp) is computed using equation (4):

$$L_p = L_{Min} - L_{Haze1\%} \quad (4)$$

Finally, surface reflectance of a pixel is computed as given in equation (5) (Survey, 2005)

$$\rho = \frac{L_p * \pi * d^2}{E_{sun\lambda} * \cos_{\theta s} * TAU_v * TAUz} \quad (5)$$

Where ρ = surface reflectance value for each pixel.

3.2 Sun Glint Removal

Sun glint removal is an essential process in extracting water depth from satellite images. According to (Kay et al., 2009) "One of the greatest confounding factors limiting the quantity and accuracy of remotely sensed data from water bodies is sun glint, the specular reflection of directly transmitted sunlight from the upper side of the air-water interface". In general, proposed deglinting models were categorized into two main categories (Kay et al., 2009). The first category was proposed for low resolution ocean imagery of 100–1000 m, while the second category was proposed

for high resolution images <10 m. Sun glint is removed from the visible bands of high resolution images using the NIR-Band, this is based on the assumption that the water leaving-radiance for the NIR band is very small (Hedley et al., 2009). Hochberg et al. (2003) proposed that glint removal can be removed using two pixels only, while Hedley et al. (2009) proposed that glint removal can be removed using a set of pixels over deep water. In either model, the deglinting is achieved using equation (6) (Doxani et al., 2012):

$$\rho_i' = \rho_i - S * (R_{NIR} - Min_{NIR}) \quad (6)$$

Where $\rho i'$ = the pixel values after removing sun glint (for visible bands)
ρi = pixel value before correction.
S = slope of the linear regression obtained between the NIR values and the corresponding visible bands.
Min_{NIR} = the lowest pixel value in the NIR band for the selected sample.
R_{NIR} = the pixel value in the NIR band.

3.4 Linear Transform Model

Early attempts for water depth extraction were introduced by (Lyzenga 1978), who introduced the liner transform model according to the following equation (7).

$$R_w = (A_d - R_w) * e^{-gz} + R_\infty \quad (7)$$

Where R_w =Water reflectance.
A_d= Bottom albedo.
g=attenuation of light through water column.
Z= estimated water depth.
R_∞= reflectance of pixels over optically deep water.

The linear transform model assumes that the light attenuation is exponentially related to two main components namely: Water column, and bottom reflectance. The equation is further simplified to calculate the depth of water by equation (8)

$$Z = \frac{1}{g}\left[\frac{ln\left((A_d - R_w)\right)}{ln(R_w - R\infty)}\right] \quad (8)$$

The linear transform model as presented in equation (8) employs a single band. It assumes that the water column for the whole scene is homogenous, and that the bottom formation is uniform (Lyzenga, 1978). Later, Lyzenga (1985) further developed the model, as described in equation (9), to include two bands to overcome the possible changes in bottom reflectance.

$$Z = a_0 + a_1 * X_1 + a_2 * X_2 \quad (9)$$

Where X_1 = Ln (R_{w1}-R_∞)
X_2= Ln (R_{w1}-R_∞)
R_∞ = deep water pixel value.
a_0, a_1, a_2 = Coefficients resulted from multiple linear regression.

Lyzenga et al. (2006) proposed to use more than two bands leads to better accuracies, as the influence of bottom type variation had reduced. The linear transform is describes according to equation (10):

$$Z = a_0 + \sum_{i=1}^{n} a_i * X_i \quad (10)$$

Where X_i = Ln (R_{wi}-R_∞)
a_0= intercept of multiple regression.
a_i = constant of each band used in the model.

3.5 Ratio Model

(Stumpf et al., 2003) proposed the ratio model, which is based on the later version of the linear transform model. The ratio model is based on the assumptions that the light attenuates exponentially with water depth, and that the penetration of light through water varies according to each band characteristics. The fact that some bands have higher absorption capabilities, while others have higher penetration capabilities motivated (Stumpf et al., 2003) to establish a ratio between two bands that increases with depth as given in equation (11).

$$Z = m_1\left[\frac{ln\,(n * R_w(\lambda_i)}{ln\,(n * R_w(\lambda_i)}\right] - m_0 \quad (11)$$

Where m_1= constant to calculate the absolute depth
m_0= offset for zero depth
n=constant to ensure that algorithm values remain positive (1000)
$R_w(\lambda_i)$ = Reflectance of band i

(Stumpf et al., 2003) the proposed ratio model to avoid the short comings that surfaced when the linear model was applied in shallow water with grass. The ratio model minimized the errors resulting from the variation of bottom soil types, and in addition improved the estimation of deep water (>25m) depth.

4. METHDOLOGY

4.1 Pre –Processing of Images

The raw data was downloaded from the USGS website: https://earthexplorer.usgs.gov. Images selected were the nearest in date to the scan with minimal cloud coverage. The radiometric calibration of the image was calculated using the coefficients provided in the Meta Data File. The DN of raw data were converted to spectral radiance, then the image was atmospherically corrected using the DOS method. The lowest significant pixel value for each band was determined by drawing histograms of DNs and selecting the lowest DN of frequency around 1000. Sun glint was removed using the technique introduced by (Hedley et al., 2009). Even though the literature classifies the most suitable sun glint removal techniques according to resolution, (Hochberg et al., 2003) suggested that the method proposed by (Hedley et al., 2009) can be used if NIR bands are involved, regardless of image resolution. The glint removal was done according to equation (6), mentioned above. In this method, a sample of about 10,000 pixel over the deep water is selected for the deglinting process. The correlation between the NIR

bands (5 and 6) and the four visible bands (1, 2, 3, and 4) was examined to determine which NIR band to be used. All visible bands recorded high correlation values with band 5. In addition, the image was classified using Normalized Difference Water Index (NDWI) to mask the non-water bodies in the water.

4.2 Model Calibration

The models were then calibrated using a scan that employed a single beam echo sounder integrated with DGPS. For the ratio model (Stumpf et al., 2003), six different ratios were investigated namely: (costal/blue)[C/B], (costal/green)[C/G], (costal/ red)[C/R], (Blue/green)[B/G], and (green /Red)[G/R]. For the linear transform model (Lyzenga 1985), three different linear combinations were investigated namely: (costal, green, blue)[C-B-G], (costal, green, red)[C-B-R], and (costal, blue, green, red)[C-B-G-R].

The calibration process is done by matching pixel values with the corresponding depths measured in the field. Model calibration was implemented with and without gridding of scan points. At first, scan points were gridded using the inverse distance method to calculate interpolated depths at grid corners, where pixel values were also recorded. The coefficients of the linear model, as presented in equation (10), were calculated by applying linear regression between depths and pixel values, while the corresponding coefficients of the ratio model, as presented in equation (11), were calculated by applying multiple linear regression. The coefficients of both models are shown in tables 2 and 3.

	B/R	B/G	C/B	C/G	C/R	G/R
m_1	25.61	85.86	369.05	80.278	27.711	15.600
m_0	25.49	82.40	353.07	74.484	27.207	12.373

Table 2.Coefficients of the ratio model at different combinations; gridded data.

	[C-B-G]	[C-B-R]	[C-B-G-R]
a_0	0.465	6.316	-0.842
a_1	5.431	55.947	-11.513
a_2	7.780	-51.803	26.862
a_3	-15.763	-5.539	-21.133
a_4	0.000	0.000	2.722

Table 3. Coefficients of linear transform model at different combinations; gridded data.

Even though the reflectance value associated with a pixel is representative of the entire pixel, the scan values within a pixel might not effectively represent the average depth within that pixel. An example of this situation is when the scan line passes near, and parallel to, the edge of the pixel. Therefore the analysis was repeated without gridding and considering only the scan points that are within 25 m from the centre of the pixel. Tables 4, and 5 show the coefficients of both the ratio model and the linear model respectively.

	B/R	B/G	C/B	C/G	C/R	G/R
m_1	32.896	92.182	779.73	88.963	34.411	29.712
m_0	34.547	88.493	752.03	82.703	35.287	29.330

Table 4.Coefficients of the different ratios, non-gridded data

	[C-B-G]	[C-B-R]	[C-B-G-R]
a_0	2.087	8.578	0.584
a_1	16.560	65.059	-7.002
a_2	-2.545	-59.529	23.585
a_3	-16.430	-5.814	-23.813
a_4	0.000	0.000	3.999

Table 5. Coefficients of the linear transform model; non gridded data models

5. RESULTS

5.1 Correlation

The same trend of correlation between water depth and pixel values was recorded when gridded (case A) and non-gridded (case B) data was used. When the ratio model was implemented, higher correlation coefficients were observed at the [C/G], and [B/G] ratios in both cases (A) and (B). On the other hand, when the linear model was implemented, higher correlation coefficients were observed at the [C-B-G], and [C-B-G-R] combinations in both cases. (Fig. 2 and 3) show the correlation coefficients for both cases and for different ratios and combinations.

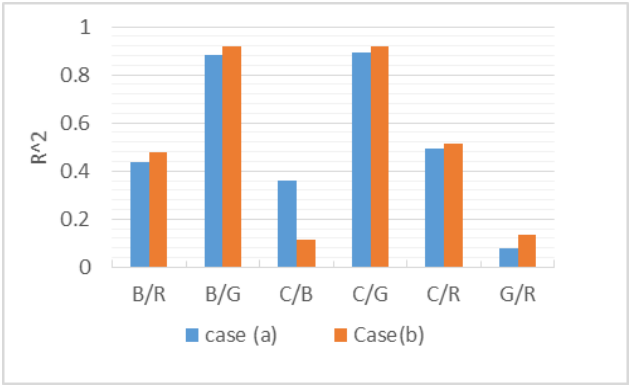

Figure 2. Correlation coefficients for different ratios.

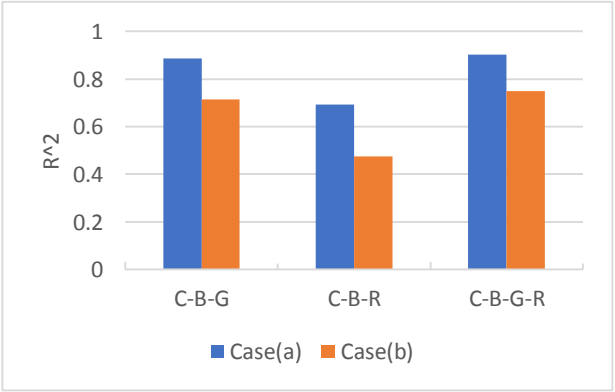

Figure 3. Correlation coefficients for Linear Combinations

5.2 Model Validation

5.2.1 Ratio Model Validation: The same trend was recorded when the predicted depths were compared to the actual depths. In both cases (A) and (B), gridded or non-gridded data, the [B/G] and the [C/G] ratios performed better than the remainder of the ratios as shown in (fig. 4 through 6). Whereas, the non-gridded data were more reliable in the prediction process than the gridded data, especially when the maximum absolute difference is considered.

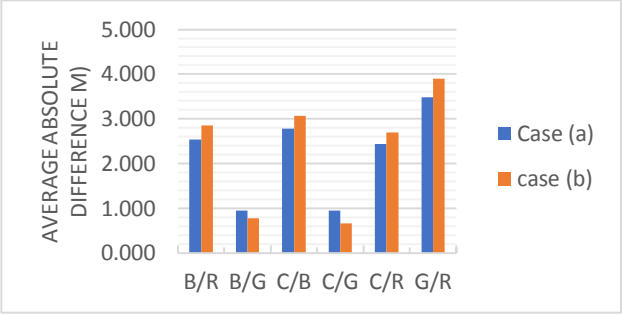

Figure 4. Average absolute difference (m)

As shown in (fig. 5), replacing the blue band with the coastal band did not significantly improve the accuracy of the predicted depths. This conclusion can also be noticed in tables (8) and (9).

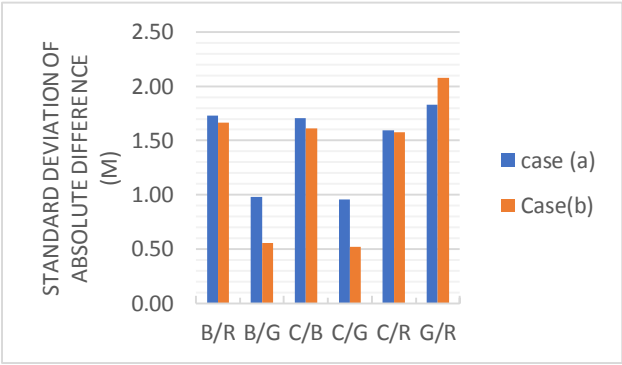

Figure 5. Standard deviation of absolute difference (m)

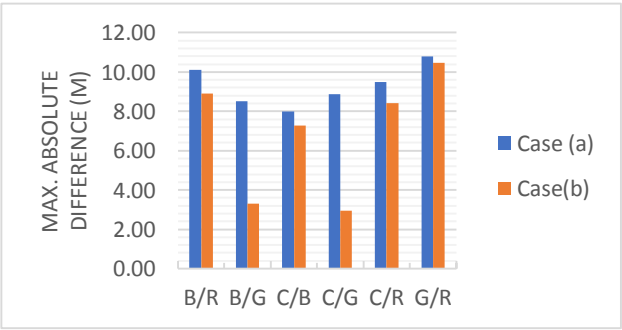

Figure 6. Max. absolute difference (m)

Tables 6 through 8 show the 1518 tested points distributed by difference ranges. As illustrated in table 6, that the difference between the actual and predicted values were less than 3 meters at 99.7% and 100% of the tested points in the [B/G] and the [C/G] ratios respectively.

Diff. ranges	Blue/Green[B/G]		Costal/Green[C/G]	
	points	Cum.%	points	Cum.%
0-.5	504	33.20	695	45.78
.5-1	627	74.50	464	76.35
1-1.5	253	91.17	249	92.75
1.5-2	67	95.59	74	97.63
2-2.5	47	98.68	18	98.81
2.5-3	16	99.74	18	100.00
>3	4	100.0	0	100.00
total	1518		1518	

Table 6.Frequency of absolute differences for (blue /green) and (costal/green)

Abs. differences ranges \ depth range	0_6	6_9	9_12	12_15	>15
0-.5	81	178	241	4	0
.5-1	5	142	469	11	0
1-1.5	7	40	184	22	0
1.5-2	6	28	9	24	0
2-2.5	3	17	4	23	0
2.5-3	0	4	0	8	4
>3	0	4	0	0	0
Points number	102	413	907	92	4

Table 7. Frequency of absolute difference for each depth Range for (blue/green) ratio.

Abs. differences ranges \ depth range	0_6	6_9	9_12	12_15	>15
0-.5	54	243	379	19	0
.5-1	39	83	328	14	0
1-1.5	6	34	168	41	0
1.5-2	3	34	24	13	0
2-2.5	0	5	4	5	4
2.5-3	0	14	4	0	0
>3	0	0	0	0	0
Points number	102	413	907	92	4

Table 8. Frequency of absolute difference for each depth Range for (Costal/green) ratio.

5.2.2 Linear Model Validation: The same trend continued when the predicted depths were compared to the actual depths when the linear model was applied. In both cases, gridded or non-gridded data, the [C-B-G] and the [C-B-G-R] combinations performed better than the [C-B-R] combination as shown in (fig. 7 through 9). The non-gridded data were more reliable in the prediction process than the gridded data, especially when the maximum absolute difference is considered.

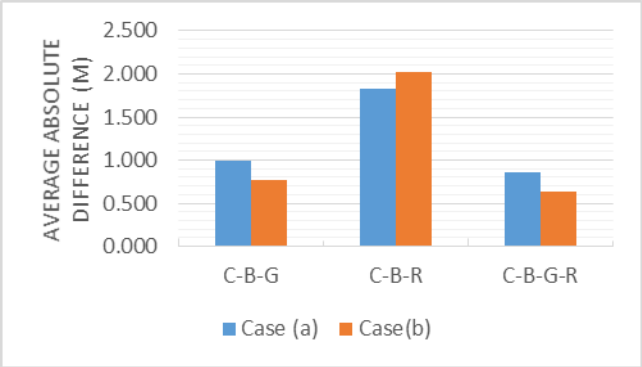

Figure 7. Average absolute difference (m)

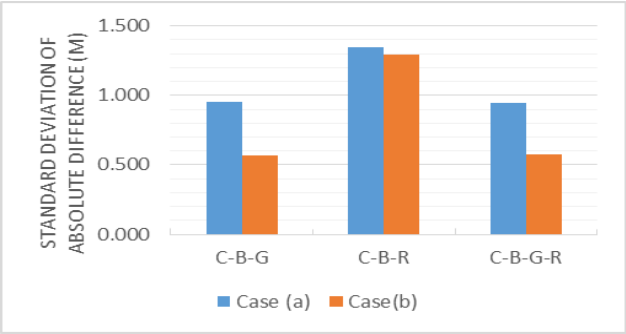

Figure 8. Standard deviation of absolute difference (m)

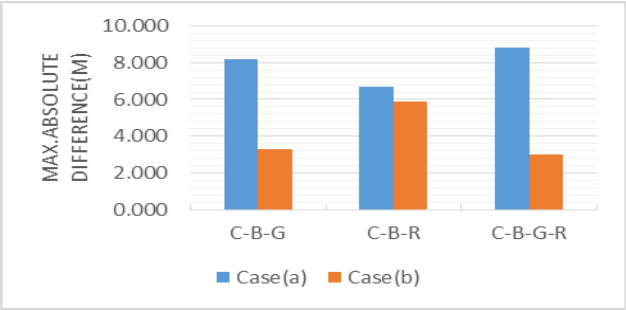

Figure 9. Max. absolute difference (m)

Tables 9 through 12 show the 1518 tested points distributed by difference ranges. Table 9 shows that the difference between the actual and predicted values were less than (3 m) at (99.74%) and (99.93%) of the tested points in the[C-B-G] and the [C-B-G-R] ratios respectively.

Diff. ranges	[C-B-G]		[C-B-G-R]	
	points	Cum.%	points	Cum.%
0-.5	611	40.25%	793	52.24%
.5-1	423	68.12%	399	78.52%
1-1.5	319	89.13%	167	89.53%
1.5-2	0	89.13%	0	89.53%
2-2.5	129	97.63%	114	97.04%
2.5-3	32	99.74%	44	99.93%
>3	4	100.00%	1	100.00%
total	1518		1518	

Table 9. Frequency of absolute differences for (costal-blue-green) and (costal-blue-green-Red)

Abs. differences ranges \ depth range	0_6	6_9	9_12	12_15	>15
0-.5	13	229	362	7	0
.5-1	28	97	276	22	0
1-1.5	26	52	226	15	0
1.5-2	35	20	37	37	0
2-2.5	0	9	6	7	1
2.5-3	0	2	0	4	3
>3	0	4	0	0	0
Points number	102	413	907	92	4

Table 10.Frequency of absolute difference for each depth Range for (costal-blue-green) combination.

Abs. differences ranges \ depth range	0_6	6_9	9_12	12_15	>15
0-.5	42	96	42	0	0
.5-1	28	105	70	2	0
1-1.5	32	114	87	2	0
1.5-2	0	61	141	5	0
2-2.5	0	24	118	15	0
2.5-3	0	10	138	12	0
>3	0	3	311	56	4
Points number	102	413	907	92	4

Table 11. Frequency of absolute difference for each depth Range for (costal-blue- Red) combination.

Abs. differences ranges \ depth range	0_6	6_9	9_12	12_15	>15
0-.5	9	150	614	20	0
.5-1	16	125	217	41	0
1-1.5	20	83	45	19	0
1.5-2	39	37	23	11	4
2-2.5	18	6	4	1	0
2.5-3	0	11	4	0	0
>3	0	1	0	0	0
Points number	102	413	907	92	4

Table 12. Frequency of absolute difference for each depth Range for (costal-blue-green-Red) combination.

The results showed that both combination [C-B-G] and [C-B-G-R] acts almost similar. Both models had about (97%) of differences less than (2 m). the [C-B-R] combination showed relatively good estimation up to 9 meter depth, for depths greater than (9 m), more than (33%) of points recorded error exceeded 3m. Over all, third combination recorded good estimation of depths with max difference about (3 m) occurred in one location.

And for greater depths (12-15m), differences limited by (3m) difference value.

6. CONCLUSION

The potential of using Landsat 8 as a tool for extracting water depths in Egypt was investigated through this paper. Landsat 8 was chosen for the analysis as a free source of images that contains the coastal band. Two traditional models were used for water depth prediction based on pixel values; namely the linear and the ratio models. After pre-processing the image, the models were calibrated and validated using scanned points of a single beam echo sounder equipped with a DGPS instrument. The calibration processes was performed in two cases: (A) with gridded points and (B) with non-gridded points. The results suggests that using non-gridded data provides a more reliable representation of the data for depth prediction. For the ratio model, using the ratio between each of the costal or the blue band and the green band tends to improve the correlation between measured and predicted depths. When both ratios were used (Costal /green or blue /green) the lowest RMSE, and absolute differences were recorded. However, using the ratio model, the coastal band did not significantly affect the accuracy of the results. In this case older Landsat images, such as Landsat 7, remain reliable for depth prediction. Consequently, images that are closer in date to available scans may be obtained. In general, applying linear transform model, the more bands used, the better the results. However, the costal–blue-green and the costal-blue-green–red combinations resulted in almost similar results. To conclude, even though the resolution of Landsat 8 images is not fine enough for detailed engineering design, this paper shows that depths can be extracted from Landsat 8 images at values of maximum error less than 3 m and standard deviation less than 1m. This freely available data may be considered suitable for certain marine applications, such: preliminary design of marine projects and shoreline protection. In this case, the use of the ratio model with either the [C/G] or the [B/g] ratio is recommended. The ratio model was found to be faster than the linear model as it requires the computations of less coefficients.

7. REFERENCES

Bramante J., Raju D. K. and S.T. Min, 2010. Derivation of bathymetry from multispectral imagery in the highly turbid waters of Singapore's south islands. A comparative study.

Chaves, P.S. (1988): An improved dark-object subtraction technique for atmospheric scattering correction of multi spectral data, Remote Sensing Environ. , 24 (3), 459-479

Conger, C. L., Hochberg, E. J., Fletcher, C. H., and M. J. Atkinson, 2006. De correlating remote sensing color bands from bathymetry in optically shallow waters. IEEE Trans. on Geoscience and Remote Sensing, 44, pp.1655–1660.

Doxani, G., Papadopoulou, M., Lafazani, P., Pikridas, C., 2012. Shallow-water bathymetry over variable bottom types using multispectral Worldview-2 image. Xxxix Isprs XXXIX, 159–164.

Green E., Mumby P., Edwards A. and C. Clark, 2000. Remote Sensing handbook for Tropical Coastal Management. Coastal Management Sourcebooks series, UNESCO Pub., Chapt. 8

Hedley J.D., Harborne A.R. and P.J. Mumby, 2005. Simple and robust removal of sun glint for mapping shallow-water benthos. Int. J. Remote Sensing, 26 (10) pp. 2107-2112.

Hochberg, E.J., Andrefouet S. and M.R. Tyler, 2003. Sea su-rface correction of high spatial resolution Ikonos images to improve bottom mapping in near-shore environments, IEEE Trans. Geoscience and Remote Sensing,41(7), pp.17241729.

Kay S., Hedley J.D. and S. Lavender, 2009. Sun glint correction of high and low spatial resolution images of aquatic scenes: a review of methods for visible and near-infrared band wavelengths. Remote Sens., 1, pp. 697-730

Lyzenga D., 1978. Passive remote sensing techniques for mapping water depth and bottom features. Applied Optics 17(3), pp. 379-383.

Lyzenga D., 1981. Remote sensing of bottom reflectance and after attenuation parameters in shallow water using aircraft and Landsat data. Int. J. Remote Sensing, 2(1), pp. 71-82.

Lyzenga D., 1985. Shallow-water bathymetry using combined lidar and passive multispectral scanner data. Int. J. Remote Sensing, 6(1), pp. 115-125.

Lyzenga D., Malinas N. and F. Tanis, 2006. Multispectral bathymetry using a simple physically based algorithm. *IEEE Trans. Geoscience and Remote Sensing*, 44(8), pp. 2251-2259.

Pacheco, A., Horta, J., Loureiro, C., Ferreira, 2015. Retrieval of nearshore bathymetry from Landsat 8 images: A tool for coastal monitoring in shallow waters. Remote Sens. Environ. 159, 102–116. doi:10.1016/j.rse.2014.12.004.

Philpot, W.D., 1989. Bathymetric mapping with passive multispectral imagery. Applied Optics. 28, pp.1569–1578

Stumpf R., Holderied K. and M. Sinclair, 2003. Determination of water depth with high-resolution satellite imagery over Variable bottom types. Limnol. Oceanogr, 48, pp.547-556.

Survey, U.S.G., 2005. Landsat 8 (L8) Data Users Handbook. America (NY). 8, 1993–1993.

`

SEPARABILITY ANALYSIS FOR MULTIPLE SIMULTANEOUS FAULTS IN GNSS AND GNSS/INS INTEGRATION SYSTEMS

A .Almagbile [a*] and J. Wang [b]

[a] Dept. of Geography-Yarmouk University-Irbid-Jordan, a.magbile@yu.edu.jo
[b] School of Civil & Environmental Engineering, University of New South Wales, Sydney-Australia, jinling.wang@unsw.edu.jo

KEY WORDS: Separability Measure, Multiple Faults, Reliability, GNSS, GNSS/INS

ABSTRACT

Multiple fault detection and exclusion (FDE) in either GNSS or GNSS/INS integration systems has already been investigated through using various (FDE) algorithms. This due to the fact that when sensor failures or faulty measurements are occurred in any navigation time the navigation solution is hardly performed. Thus it is necessary to check the integrity and reliability of the navigation solution particularly for safety or liability-critical applications. This paper implements fault tests statistics for detecting and identifying multiple faults cases in integrated GNSS/INS systems. More specifically, it presents separability measures when two and three faults occur in the integration through using maximum and global correlation between fault tests statistics. The results show that when two or three faults were injected in the observations, other pure observations are flagged as faulty observations due to the high correlation between them and the faulty measurements. This means that separating the faulty measurements is difficult particularly when the number of observations is insufficient to perform the fault test. In other words, the system needs to be fused with other GNSS systems (e.g., GLONASS) in order to increase the number of observations and hence improve the robustness of navigation.

1. INTRODUCTION

One of the popular methods that have been used for detecting and excluding (FDE) fault/outlier in either GNSS or GNSS/INS systems is Receiver autonomous integrity monitoring (RAIM). This method has widely been used for checking the integrity of navigation through providing a warning message to the user when the system must not be used for navigation. Another statistical-based approach which has extensively been used for detecting and excluding fault in many GNSS applications is Detection, Identification and Adaptation (DIA) method (Teunissen and Salzmann, 1989; Wang et al, 1997). The principle of DIA method depends on three consecutive steps namely detection, identification and adaptation. In detection step, a global model test is employed to check whether the system includes faults or not. If the system is contaminated by faults, identification (local test) step is used to identify the faulty observations in order to be excluded. The role of adaptation step which is also known as outlier separability comes to eliminate the faults from the model (Gillissen and Elema, 1996). Both RAIM and DIA are limited to detect and exclude single fault at a time. However, this is not always the case due to the fact that the navigation system may include multiple simultaneous faults particularly when two or more GNSS systems are fused together.

Early studies that dealt with quality control for GNSS or GNSS/INS integration assumed that the system includes single fault at a time. These studies such as Sturza (1989) presented a fault detection algorithm based on hypothesis testing in parity space while Magrabi and Gibbens (2000) adapted the parity space Fault Detection and Diagnosis methods using fully multiple decentralized filters running at a time. Teunissen (1990) investigated quality control of integrated navigation systems using innovation and recursive filtering. An innovation based autonomous integrity monitoring extrapolation (AIME) was presented by Diesel and King (1995). Brenner (1995) used Kalman filter to test the performance of integrity monitoring.

In some cases, the navigation system may encounter with multiple simultaneous faults. The source of these faults can be originated to the GNSS system fusion. For instance, when two GNSS systems (GPS/GLONASS) are integrated, there is an increase probability of occurrence of multiple faults in the system. This is due to the fact that each system may include at least one fault. As a result of that, several investigations (e.g., Kok, 1984; Wang and Chen, 1999; Knight et al, 2010) have been developed to detect and exclude multiple faults in either GNSS or GNSS/INS systems. These studies have been directed toward extending previous FDE methods or developing new statistical approaches in order to improve the integrity of navigation system.

Regarding fault separability/exclusion in either GNSS or GNSS/INS systems, many studies have focused on exclusion single fault in the system. Fault separability includes testing the ability of the system to separate between "good" measurement and the contaminated one. The ability of the system can be examined through the correlation coefficient between fault tests statistics. The higher the correlation between tests statistics, the less likely the system can separate the fault. In other words, due to the high correlation between fault tests statistics, several alternative hypotheses occur (Yang et al, 2013). Förstner (1983) developed a mathematical approach of correlation coefficient in order to evaluate the capability of the system to separate the null hypothesis from the alternative hypothesis. Hewitson (2003);

*Corresponding author

Hewitson and Wang (2006); Wang and Knight (2012) employed correlation coefficient between fault test under the presence of single fault in integrated multiple GNSS systems (GPS/GLONASS and GPS/GLONASS/GALILLEO). While Almagbile and Wang (2011), Almagbile et al (2011) evaluated outlier separability measures in integrated GPS/INS systems under different number of visible satellites, satellites geometry and the number of system states models.

For separability of multiple faults, multi-dimensional correlation coefficient between faults tests statistics is employed. Therefore, two-dimensional separation is conducted. In the first dimension, the separation is achieved between the null hypothesis and the alternative hypotheses. The second dimension is performed to separate between the true and the false alternative hypotheses. The true alternative hypotheses occur when the system is really contaminated by faults while false alternative hypotheses appear when the correlation between faulty observations and other pure measurements is high. In this case some observations are flagged as faulty observations wrongly.

Very few studies investigated multiple faults separation measure in GNSS and GNSS/INS systems. Förstner (1983) extended the correlation coefficient form single fault case to multi-dimensional correlation between multiple faults detection statistics. Li (1986) introduced the global correlation coefficients between multiple fault detection statistics. Recent studies (Wang et al, 2012 and 2013, Alqurashi and Wang, 2014) examined maximum and global correlation in GNSS and GNSS/INS integration. However, the results of all of these studies were based on simulation studies and never considered real GNSS or INS observations. Therefore, real GNSS and INS observations and integration is needed in order to gain more insights into multiple fault separability.

In this paper, time-differenced carrier phase observations were fused with INS through using Kalman filter. Then multi-dimensional correlation coefficients between multiple faults statistics were employed to separate between the null and the alternative hypotheses. The structure of the paper is as follows: Section 2 provides the quality control of GNSS and integrated GNSS/INS systems including statistical procedures for detection and identification multiple faults. Section 3 analyse multi-dimensional correlation coefficients approaches. Section 4 provides tests and results followed by concluding remarks in Section 5.

2. QUALITY CONTROL OF GNSS AND GNSS/INS SYSTEMS

Least squares procedures are utilized to perform the mathematical and stochastic model of multi GNSS systems. GNSS/INS however, Kalman filtering is converted to least squares in order to acquire the benefit of snapshot approach (Sorenson, 1970; Salzmann, 1993; Wang et al, 1997, 2008). In Kalman filter as least squares, the observation vector is formed through integrating the predicted states $\bar{x}_k$ and the measurement model z_k in one vector. By this way, optimal estimate of the state parameters can be obtained.

Mathematically, the discrete time of the system state and measurement model of the Kalman filtering can be written as follow:

$$x_k = \Phi_{k-1} x_{k-1} + w_k \tag{1}$$

$$z_k = H_k x_k + v_k \tag{2}$$

Where x_k is $(n \times 1)$ state vector, Φ_k is $(n \times n)$ transition matrix, z_k is $(r \times 1)$ observation vector, H_k is $(r \times n)$ observation matrix. The variables w_k and v_k are uncorrelated white noise errors with covariance matrices Q_k and R_k respectively. Then equation (1) and (2) can be integrated as follows:

$$l_k = \begin{bmatrix} z_k \\ \bar{x}_k \end{bmatrix}, A_k = \begin{bmatrix} H_k \\ E \end{bmatrix}, v_k = \begin{bmatrix} v_{zk} \\ v_{\bar{x}k} \end{bmatrix} \tag{3}$$

$$l_k = A_k x_k + v_k \tag{4}$$

Where E is the $(m \times m)$ identity matrix. The corresponding variance- covariance matrix Cl_k which is derived from the measurement noise covariance matrix R_k and the predicted states covariance matrix $\bar{P}_k$ of Kalman filtering can be written as (Wang et al, 1997):

$$C_{lk} = \begin{bmatrix} R_k & 0 \\ 0 & \bar{P}_k \end{bmatrix} = P^{-1} \tag{5}$$

where P is the weight matrix. The optimal estimate of the state parameters $\hat{x}_k$ and error covariance matrix $Q_{\hat{x}\bar{k}}$ can be written as:

$$\hat{x}_k = (A_k^T P A_k)^{-1} A_k^T P l_k \tag{6}$$

$$Q_{\hat{x}\bar{k}} = (A_k^T P A_k)^{-1} \tag{7}$$

The Kalman filter residuals v_k and cofactor Q_{vk} can be written as:

$$v_k = \begin{bmatrix} v_{zk} \\ v_{\bar{x}k} \end{bmatrix} = A_k \hat{x}_k - l_k \tag{8}$$

$$Q_{vk} = Cl_k - A_k Q_{\hat{x}\bar{k}} A_k^T \tag{9}$$

The symbol *k* is used as a notation for the current epoch and it will be ignored throughout this paper for simplification. After performing the KF as least squares, detection, identification and adaptation (DIA) approach can then be used in integrated navigation systems.

2.1 Detection and identification of multiple faults

This step comes after employing the global test to identify which measurements are contaminated by outliers. Multiple

fault tests can be written as follows (Wang and Chen, 1999; Knight et al, 2010):

$$w_i^{\theta} = \frac{l^T PQ_v PH_i (H_i^T PQ_v PH_i)^{-1} H_i^T PQ_v Pl}{\sigma_0^2} \quad (10)$$

Where H_i is an n by θ matrix, with rank θ, (n is the number of observations, while θ represents the number of faults), containing zeros with a one in each column corresponding to fault. Fault test based on (10) can be applied for different number of faults such as one, two or three faults. The procedure is to apply (10) for single fault and remove the outlier if exist, then to two outliers, three. In this study we consider two faults exist in the measurements. In this case θ is equal to 2 and th H_i matrix takes the following form:

$$H = \begin{bmatrix} 0 & 0 & . & i & 0 & n \\ 0 & 0 & 0 & . & j & n \end{bmatrix}^T \quad (11)$$

The w_i^{θ} is also $_{(n\times\theta)}$ matrix corresponding to the $_{H_i}$ matrix. When the w_i^{θ} exceeds the predefined critical value, the null hypothesis will be rejected because one or more faults are existing in the observations.

Since the alternative hypothesis is accepted, the fault test statistics become non-central Chi-square distribution and then the non-centrality parameter can be written as (Baarda, 1968; Wang and Chen, 1999):

$$\lambda = \frac{z^T H^T PQ_v PHz}{\sigma_0^2} \quad (12)$$

Where z is the true outlier vector, if the outlier identification is possible, the largest w_i^{θ} test is corresponding to the true outlier vector.

2.2 Reliability measures

In order to evaluate the system ability for detecting faults in the model, internal reliability measures which include minimal detection bias (MDB) and also known as marginally detectable error (MDE) is used. With given a certain probabilities of Type I error α and Type II errors β, For multiple faults (θ =2 or more) MDB can be computed through determining the multiple correlation coefficients. Multiple correlation coefficients are equivalent to the correlation coefficients between two single fault test statistics. Multiple correlation coefficients p_{ij}^{θ} and MDB for multiple faults can then be written as (Knight et al., 2010, Almagbile et al, 2011):

$$P_{ij}^{\theta} = \sqrt{\frac{h_i^T PQ_v PH_j (H_j^T PQ_v PH_j)^{-1} H_j^T PQ_v Ph_i}{h_i^T PQ_v Ph_i}} \quad (13)$$

With bounds of P_{ij}^{θ} are: $0 \le P_{ij}^{\theta} \le 1$,

The $_{h_i}$ vector containing zeros with a one in each column corresponding to fault.

And MDB for multiple faults $\nabla_0 S_i^{\theta}$ can be written as (Knight et al, 2010):

$$\nabla_0 S_i^{\theta} = \sqrt{\frac{\lambda\sigma_0^2}{h_i^T PQ_v Ph_i (1 - P_{ij}^{\theta})}} \quad (14)$$

2.3 Separability measures

For Multiple faults case, the separability measures are employed to discriminate between several true and false alternative hypotheses. For instance, when two faults exist in the observations then two true alternative hypotheses should be accepted. However due to the correlation coefficients between faults tests statistics, more than two alternative hypotheses may occur, therefore some pure observations are also flagged as faulty observations wrongly.

According to the theory there are three types of errors namely type I error (α), type II error (β) and type III error (γ). Type I error occurs in case of accepting the null hypothesis H_0 while the alternative hypothesis $_{H_{a1}}$ is true. On the other hand, if accepting $_{H_{a1}}$ while $_{H_0}$ is true, type II error will appear. Type III error occurs in case of separating between two alternative hypotheses $_{H_{a1}}$ and $_{H_{a2}}$. It is the probability of choosing $_{H_{a2}}$ though $_{H_{a1}}$ is true and vice versa (förstner, 1983).

Mathematically, maximum and global correlation can be written as follows (förstner, 1983; Deren, 1986, Wang et al, 2012):

$$P_{w_1^{\theta}, w_2^{\theta}} = H_1^{\theta} PQ_v PH_2^{\theta} \quad (15)$$

where H_1^{θ} and H_2^{θ} is the same as in equation (14), $P_{w_1^{\theta}, w_2^{\theta}}$ represents the correlation between two fault tests w_1^{θ} and w_2^{θ} equation (20) can be expanded as follows:

$$P_{w_1^{\theta}, w_1^{\theta}} = H_1^{\theta} PQ_v PH_1^{\theta} \quad (16)$$

$$P_{w_2^{\theta}, w_2^{\theta}} = H_2^{\theta} PQ_v PH_2^{\theta} \quad (17)$$

$$P_{w_1^{\theta}, w_2^{\theta}} = H_1^{\theta} PQ_v PH_2^{\theta} \quad (18)$$

$$P_{w_2^{\theta}, w_1^{\theta}} = H_2^{\theta} PQ_v PH_1^{\theta} \quad (19)$$

When multiplying all equations together, matrix M can be created:

$$M_{w_1^{\theta}, w_2^{\theta}} = (P_{w_1^{\theta}, w_1^{\theta}})^{-1} (P_{w_1^{\theta}, w_2^{\theta}}) (P_{w_2^{\theta}, w_2^{\theta}})^{-1} (P_{w_2^{\theta}, w_1^{\theta}}) \quad (20)$$

The rank of matrix M is the same as the number of faults to be detected. Thus if the number of faults is 2 then M is (2x2). Finally, the maximum eigenvalue of matrix M is represent the correlation coefficient between multiple faults statistics (Wang et al, 2012).

$$(Q_{w_1^\theta, w_2^\theta})\max = \sqrt{\lambda \max (M_{w_1^\theta, w_2^\theta})} \quad (21)$$

The global correlation coefficients can also be computed as follows (e.g., Li, 1986, Wang et al, 2012):

$$(Q_{w_1^\theta, w_2^\theta})_{Global} = \frac{tr(M_{w_1^\theta, w_2^\theta})}{\sqrt{rank_{w_1^\theta} . rank_{w_2^\theta}}} \quad (22)$$

Where $rank_{w_1^\theta} . rank_{w_2^\theta}$ are the rank of tests w_1^θ and w_2^θ, respectively.

3. TEST AND RESULTS

3.1 Test

In this paper, real dataset have been used for GNSS/INS integration. Only GPS among other GNSS systems has been used and integrated with INS. The data have been collected using Leica 530 GPS receivers and one **BEI C-MIGITSII (DQI-NP)** INS unit. . In our tests, the GPS base station was located on the top of Electrical Engineering, UNSW and another one along with **DQI-NP** was set on the top of a land–based vehicle**.** Figure 1 shows vehicle trajectory of the moving receiver. The number of visible satellites was fluctuated around 6 to 8 satellites over the navigation time. GPS observations were used to update 24 error states with 3 states for each of position, velocity, attitude, acceleration biases, acceleration scale factor, gyro biases, gravity, and lever arm.

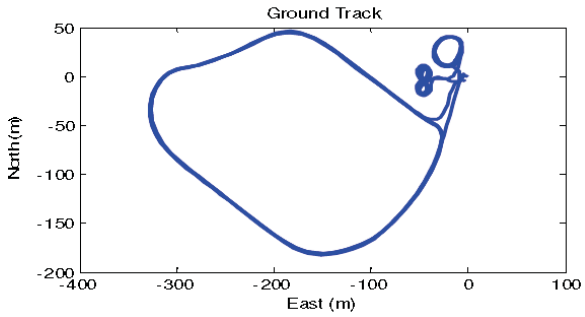

Figure 1. vehicle trajectory

The integration of GPS with INS has been performed using carrier phase through using dual rate Kalman filter (Han and Wang, 2011). In normal situation, carrier phase observations need mathematical procedures to fix the ambiguity before using them in any applications. In this paper however, carrier phase ambiguity has been solved using time-differenced carrier phase procedure. Then they integrated with INS using high rate Kalman filter. Since time-differenced carrier phase are only relative measurements because they retrieved from consecutive epochs, the position error of the integrated system will cumulate with time. In order to deal with such problem, pseudorange observations have been used in specific navigation time to control the accumulation of system error (Han and Wang, 2011).

In order to evaluate the performance of the fault detection test statistics in integrated GPS/INS systems, multiple faults were injected (simulated) in GPS observations at different locations and navigation time. Then multiple fault detection test was implemented to check the performance of fault test for truly separate the contaminated measurement from other pure measurements.

3.2 Results analysis

3.2.1 Two faults case: In this scenario, epoch 100 among the total epochs 649 were selected in order to implement faults separability test. It has been found that the number of visible satellites in this epoch was 7 satellites. Thus, two faults of 5 and 6 cm were injected in observations 3 and 5 respectively. It has been shown that the values of fault test statistics for all measurements combinations before injection the faults do not exceed the critical value (13.82). This means that there was no fault was found in this epoch. This situation can be seen in figure 2 (upper). In case of simulated faults however, the situation has been illustrated in figure 2 (bottom). As normal situation, the value of fault test for measurements combinations (3,5) was the highest (around 100 cm) among other measurements combinations. In addition, it can also be seen that all measurements combinations that include either 3 or 5 (faulty observations) exceed the critical value. An instance of this is the measurements combinations (1,3), (1,5), (2,3) and (4,5) which have at least one faulty observation exceed the critical value.

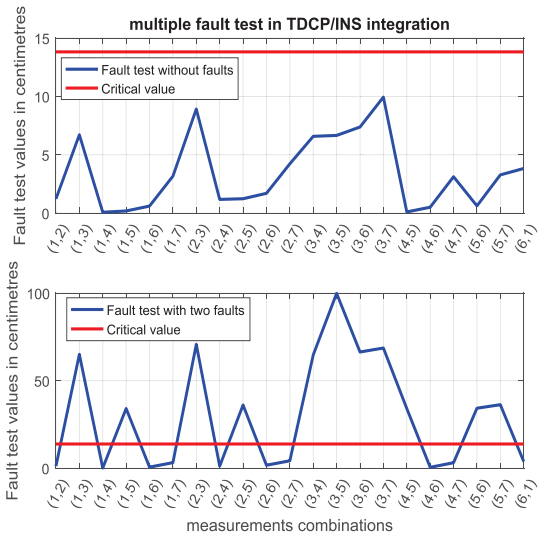

Figure 2. fault test for two faults in measurements 3 and 5 in TDCP/INS system

The MDBs for two fault case is presented in figure 3. It can be seen that the values of MDBs are very small. This is due to the fact that the accuracy of TDCP/INS is very high. One can see that the values of MDBs are fluctuated around 0.04 centimetres.

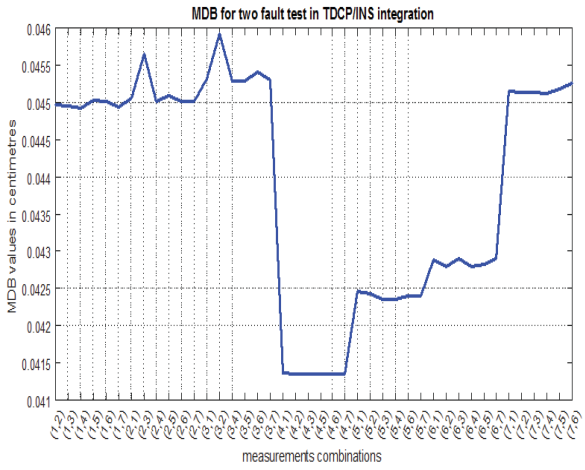

Figure 3. MDBs for two faults in TDCP/INS systems

Figure 4 illustrate the variations of the maximum and global correlation coefficients between the faulty measurement pair (3, 5) and all other measurement pairs. It can be noticed that the maximum correlation between the faulty measurements and some pairs is one whereas the values of the global correlation for all pairs do not exceed 0.8 except for pair (3,5). This is because this pair represents the correlation between themselves. Moreover, one can see that when measurements combinations have at least one common observation, the values of correlation become high. This situation can be seen in both maximum and global correlation. For example, the correlation between the combinations (3,5) and (1,3), (1,5), (2,3), (5,6), (5,7) is one and 0.7 in maximum and global correlation respectively. However, when measurements combination do not include either 3 or 5, the correlation becomes very low as in (1,2), (1,6),(4,6) and (6,1).

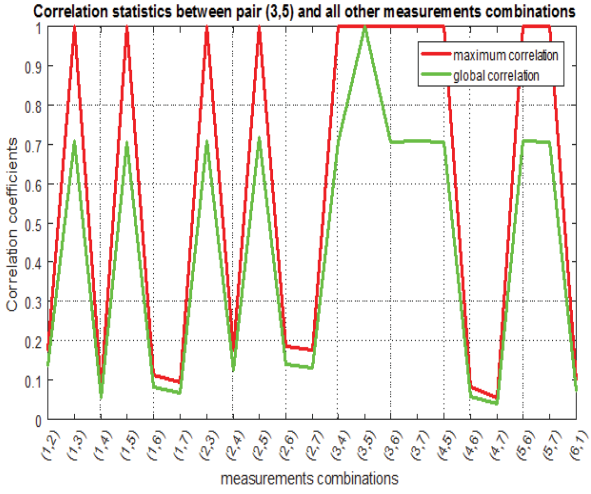

Figure 4. maximum and global correlation between measurements combinations (3,5)(faulty measurements) and all other measurements combinations.

3.2.2 Three faults case: In this scenario, three faults were injected in observations 2, 3 and 5 with fault size of 8, 5 and 6 centimetres respectively. Then fault test were implemented for identifying the faulty observations among all other observations. One might see that the values of fault test when it is implemented without injection faults (figure 5, upper) is higher comparing with those presented in two fault scenario. Furthermore, it can be seen when three faults were simulated in three observations, the values of fault test for almost all measurement combination exceed the critical value (17). As normal situation, the highest value is for the combination (2,3,5) because those observations include the faults. In addition, as mentioned in the previous scenario, the combinations that include at least on of the fault observations have high values. Whereas, the combinations such as (1,4,6), (1,4,7) and (4,6,7) are the lowest because neither of them includes faulty observations (figure 5, bottom).

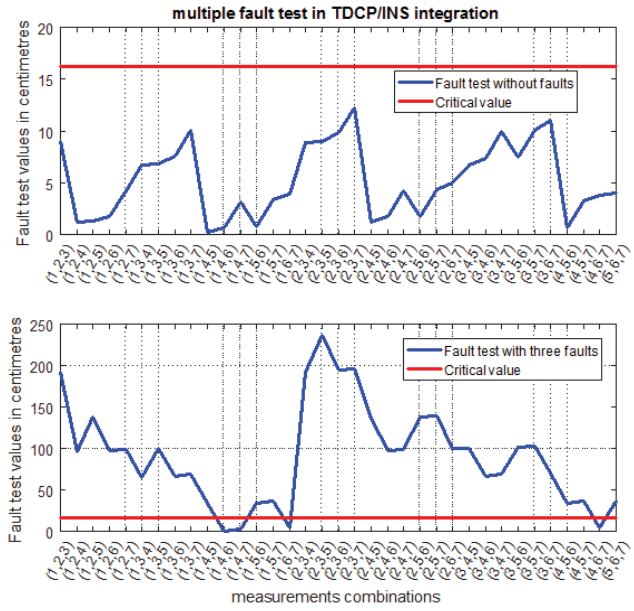

Figure 5. fault test for three faults in measurements 2, 3 and 5 in TDCP/INS system

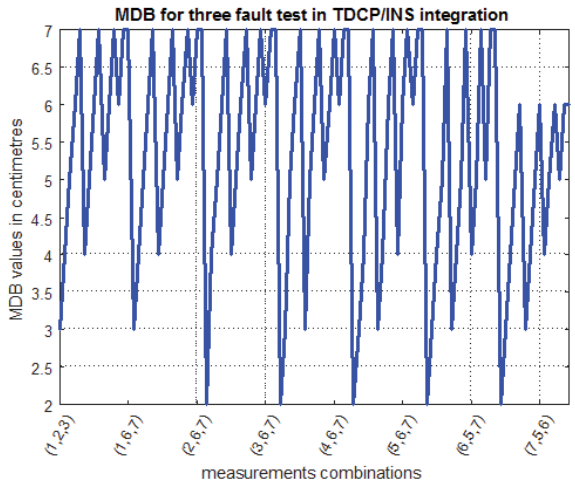

Figure 6. MDBs for three faults in TDCP/INS systems

Figure 6 represents the MDBs for three fault case. As can be seen the values of MDBs are all higher comparing with those presented in the previous section. The range of MDBs values is between 2 and 7 cm.

Maximum and global correlation is shown in figure 6. It is clear that almost all the combinations are highly correlated with combination (2,3,5). However, very few combinations have low correlation with the faulty observations. This is due to the fact that those observations do not share any observation with the faulty one.

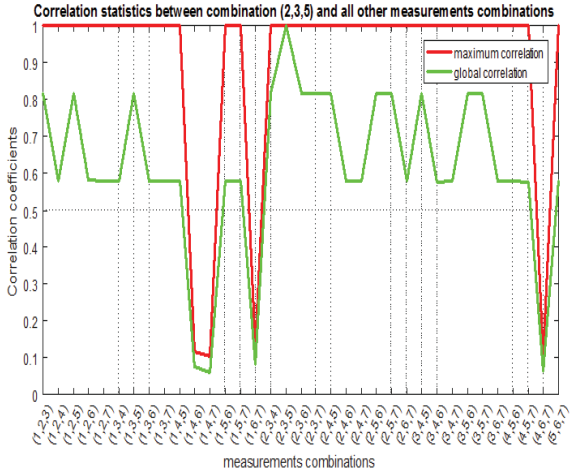

Figure 7. maximum and global correlation between measurements combinations (2,3,5)(faulty measurements) and all other measurements combinations.

As can be seen in Table 1 which illustrates the situation of fault test for three faults case the number of influenced measurements is very high. This is due to the high correlation between the faulty observations and all other observations. It is clear that when a combination includes one faulty observation, the value of fault test is less than the combination that includes two or three faulty observations. An instance of this is the combination (1,2,3) which includes two faulty observation (2 and 3), the values of fault test is 192. Whereas the combination (1,2,6) includes one faulty observation (2) and thus the fault test value is around 97.

One can note that the navigation solution cannot be performed when the number of visible satellites is seven with two or three faulty satellites. It has been found that very few combinations such as (1,4,6), (1,4,7) and (4,6,7) can be used to perform the navigation solution. However, this number of observations (satellites) is insufficient for navigation. In order to overcome this problem, other GNSS systems (e.g., GLONASS, GALILLEO and BEIDOU) can be fused with GPS to improve the number of constellations.

4. CONCLUDING REMARKS

This paper has implemented fault test statistics for two and three faults case in TDCP/INS integration system. Reliability and separability measures where used for identifying the faulty observations. Through numerical analysis it has been found that when two faults were simulated in the observations, the number of influenced observations increased due to the fact that the correlation between fault tests is high. This has been found in maximum and global correlation. In case of three fault scenario, the situation becomes more complex due to increase the number of influenced observations.

It has also found that when the number of satellites is seven with two or three faulty satellites, the navigation solution cannot be performed. This is due to the fact that the number of un contaminated satellites is less than four. Thus, satellites redundancy can be improved when two or more of GNSS constellations (e.g., GLONASS) are integrated with GPS. More thoroughly investigations about multiple faults separability in different cases of satellites redundancy and geometry are needed.

Table 1. fault test statistics for three fault case (faults of 8,6 and 5 cm in observations 2,5 and 3 respectively)

Measurements combinations			W (without faults)	W (with faults)	difference	Faulty measurements	Influenced measurements
1	2	3	9.013	192	183	2 and 3	1
1	2	4	1.224	96	94.8	2	1 and 4
1	2	5	1.291	138	136	2 and 5	1
1	2	6	1.768	96.7	94.9	2	1 and 6
1	2	7	4.256	98.6	94.3	2	1 and 7
1	3	4	6.716	65.1	58.3	3	1 and 4
1	3	5	6.809	99.9	93.1	3 and 5	1
1	3	6	7.564	66.8	59.3	3	1 and 6
1	3	7	10.04	68.9	58.9	3	1 and 7
1	4	5	0.186	34.1	33.9	5	
1	4	6	0.606	0.61	0	nill	nill
1	4	7	3.168	3.17	0	nill	nill
1	5	6	0.739	34.3	33.5	5	1 and 6
1	5	7	3.337	36.3	33	5	1 and 7
1	6	7	3.901	3.9	0	nill	nill
2	3	4	8.922	192	183	2 and 3	4
2	3	5	8.953	236	227	2,3 and 5	2,3,and 5
2	3	6	9.791	195	185	2 and 3	6
2	3	7	12.21	196	183	2 and 3	7
2	4	5	1.238	137	136	2 and 5	4
2	4	6	1.699	96.7	95	2	4 and 6
2	4	7	4.23	98.6	94.3	2	4 and 7
2	5	6	1.774	138	136	2 and 5	6
2	5	7	4.339	139	135	2 and 5	7
2	6	7	4.956	99.5	94.5	2	6 and 7
3	4	5	6.66	99.9	93.2	3 and 5	4
3	4	6	7.379	66.4	59	3	4 and 6
3	4	7	9.944	68.6	58.7	3	4 and 7
3	5	6	7.48	101	93.5	3 and 5	6
3	5	7	10.08	103	92.7	3 and 5	7
3	6	7	11.02	70.7	59.7	3	6 and 7
4	5	6	0.623	34.3	33.7	5	4 and 6
4	5	7	3.278	36.3	33	5	4 and 7
4	6	7	3.827	3.83	0	nill	nill
5	6	7	4.016	36.6	32.6	5	6 and 7

REFERENCES

Almagbile A. and Wang J. (2011) Analysis of outlier separability in integrated GPS/INS systems. *IGNSS symp*. Sydney Australia 15-17 November.

Almagbile A., Wang J., Ding W. & Knight N. (2011) Sensitivity analysis of multiple fault test and reliability measures in integrated GPS/INS systems. *Archives of Photogrammetry, Cartography and Remote Sensing (APCRS)*, 22, 25-37.

Alqurashi. M and Wang. J. (2015) Performance Analysis of Fault Detection and Identification for Multiple Faults in GNSS and GNSS/INS Integration, Journal of Applied Geodesy, 9 (1), pp. 35–48

Baarda W. (1968) A testing procedure for sse in geodetic networks, *Netherlands Geodetic Commission, New Series*

Brenner M. (1995) Integrated GPS/Inertial Fault Detection Availability, *9th International Technical Meeting of the Satellite Division of the Institute of Navigation*, Kansas City, USA, 1949-1958.

Diesel J. and King J. (1995) Integration of Navigation Systems for Fault Detection, Exclusion and Integrity Determination – Without WAAS, ION National Technical Meeting, California, USA, 683-692.

Förstner W. (1983) Reliability and discernibility of extended Gauss-Markov models, *Deutsche Geodätische Kommission (DGK)*, Report A, 98, 79-103.

Gillissen and Elema (1996) Test results of DIA: A real-time adaptive integrity monitoring procedure used in an integrated navigation system, *International Hydrographic Review,* Monaco, Vol. LXXIII, No. 1

Han, S. and Wang, J. (2012) Integrated GPS/INS Navigation System with Dual-Rate Kalman Filter, *GPS Solution*, Vol. 16, No. 3, pp. 389-404

Hewitson S. and Wang J. (2006) GNSS Receiver Autonomous Integrity Monitoring (RAIM) performance analysis, *GPS Solutions*, 10(3), pp. 155-170.

Knight N., Wang, J. and Rizos C. (2010) Generalized measures of reliability for multiple outliers, *Journal of Geodesy*, 84(4), pp. 625-635.

Kok J. (1984) On data snooping and multiple outlier testing. *NOAA Technical Report*, NOS NGS.30,USA. Department of Commerece Rockvillle, Maryland.

Li D.(1986) Trennbarkeit und Zuverlässigkeit bei zwei verschiedenen Alternativhypothesen im Gauß-Markov-Mödell. Z.f.Verm,Wesen 111, pp. 114-128.

Magrabi, S. M., & Gibbens, P. W. (2000). Decentralised fault detection and diagnosis in navigation systems for unmanned aerial vehicles. *In Position Location and Navigation Symposium*, IEEE 2000: pp. 363-370.

Salzmann M. (1993) Least squares Filtering and Testing for Geodetic Navigation Applications, *Netherlands Geodetic Commission, publications on Geodesy, New Series*, Delft, The Netherlands, No. 37,

Sorenson H. W. (1970) Least Squares Estimation: from Gauss to Kalman, *IEEE Spectrum 7*, pp. 63-68.

Sturza M. A. (1989) ***Navigation System Integrity Monitoring Using Redundant Measurements,*** Navigation: Journal of the Institute of Navigation, 35(4), pp. 69-87.

Teunissen, P.J.G. and Salzmann, (1989) A Recursive Slippage Test for Use in State-Space, Filtering, Journal of Geodesy, Vol. 14, pp. 383-390

Teunissen P. J. G. (1990) Quality control in integrated navigation systems, *Proc IEEE PLANS'90*, Las Vegas, U.S.A., pp. 158-165

Wang J., Stewart M. and Tsakiri M. (1997) On quality control in hydrographic GPS surveying, *Third Australian Hydrographic Symposium*, 30 November- 3December, Fremantle, Western Australia, 1-10.

Wang J. and Chen Y. (1999) Outlier detection and reliability measures for singular adjustment models. *Geomat Res Aust. 71*, pp. 57-72

Wang J., Lee H.K., Hewitson S. and Lee H.-K. (2003) ***Influence of Dynamics and Trajectory on Integrated GPS/INS Navigation Performance.*** Journal of Global Positioning Systems, 2(2), pp. 109-116.

Wang J., Xu C. and Wang J.A. (2008) Applications of robust Kalman filtering schemes in GNSS navigation. *Int. Symp. on GPS/GNSS*, Yokohama, Japan, 25-28 November, pp. 308-316.

Wang J. and Knight N. (2012) New Outlier Separability Test and Its Application in GNSS Positioning. *Journal of Global Positioning Systems*, 11(1), pp. 46-57.

Wang, J., Almagbile, A., Wu, Y., & Tsujii, T. (2012) Correlation Analysis for Fault Detection Statistics in Integrated GNSS/INS Systems. *Journal of Global Positioning Systems, 11*(2), pp. 89-99.

Wang. J., Wu. Y., Alqurashi. M and (2013) Separability Analysis for Multiple Faults in GNSS/INS Integration, International Global Navigation Satellite Systems Society *IGNSS Symposium, Gold Coast, Qld Australia 16-18 July, 2013*

Yang, L.,Wang, J., Knight, N. L., & Shen, Y. (2013). Outlier separability analysis with a multiple alternative hypotheses test. *J Geod*, 87, pp. 591–604

PERFORMANCE ANALYSIS OF REAL-TIME PRECISE POINT POSITIONING IN EGYPT.

Ahmed Mansour[a], Mahmoud Abd Rabbou[b], Adel El Shazly[c]

[a] Faculty of Engineering, Cairo University, Egypt - ahmed.mansour.abdalla@cu.edu.eg
[b] Faculty of Engineering, Cairo University, Egypt - mahmoud.abdelrahman@cu.edu.eg
[c] Faculty of Engineering, Cairo University, Egypt - adel_shazly@hotmail.com

Commission VI, WG VI/4

KEY WORDS: Real-Time Service (IGS RTS), Precise Point Positioning, RT-PPP, RTK.

ABSTRACT:

Recently, the International GNSS Service (IGS) has confirmed the availability of open access real-time (RT) GNSS precise orbital and clock products. Until a recent time, GNSS users were able to use the IGS orbit and clock precise corrections only for Precise Point Positioning (PPP) in post processing mode, which confining the accessibility of using PPP to be employed in wide range of real-time navigation applications. However, with the availability of real-time precise products, precise real-time navigation applications can be feasible through PPP with only one receiver reducing the cost and complexity of current navigation techniques. In Egypt, for precise real-time navigation, a real-time kinematic technique with minimum two GNSS receivers are commonly employed to reach to centimetre- level accuracy for surveying applications. However, recently, commercial organizations started to present its GNSS correction services in the Egyptian market through global GNSS virtual network in real time mode using only one user receiver. The providers of the commercial products have claimed to reach to decimetre- level accuracy (5 cm) however; the main limitation of such networks is the low resolution of the global stations used in corrections estimation in addition to the cost of the service. In contrast, the RT-IGS services are free and available online with high resolution of the IGS global stations employed in GNSS corrections estimation. As a result, in this research, we study the performance of RT-PPP comparing its accuracy with respect to the post-processing based PPP and relative positioning system.

1. INTRODUCTION

Real-time kinematic RTK positioning techniques deserved the merit of being the most domination technique for real-time application in both of precise positioning and navigation communities for a long time, exceed to three decades. As the performance of RTK is incomparable in achieving centimetre-level accuracy in precise applications and machine automation. To develop the effectiveness and the efficiency of RTK technique and increase its benefits to RTK users Many private companies have implemented permanently and continuously operating reference stations (CORS) networks. However, Construction of the infrastructure of these networks required an expensive investment which represented in satisfying several factors such as density, quality, functionality, integrity and robustness of CORs (Choy et al., 2016).

The limitations and drawbacks that expose all DGNSS techniques due to the cost and complexity of existing one or more reference GNSS receivers situated at known coordinates base stations and baseline length restrictions provide the PPP techniques the opportunity to play the role of the best alternative for carrier phase-based relative GNSS techniques. However, the significant limitation challenged PPP technique which represented in the long convergence times (20 minutes or more) required for the ambiguity float solution to converge to ensure centimetre-level positioning accuracy (Rizos et al., 2012). Without the needs of reference stations, PPP technique overcomes the baseline range limitation and depending on the precise GNSS products provided, for example, by the International GNSS Service IGS. PPP confined in post-processing missions due to the delay in the availability of satellite orbital and clock correction product. The IGS products latency which related to its accuracy reach to 18 days for final products with 2.5 cm orbit error and less than 0.1 ns satellite clock error (Tomasz, 2015).

IGS to support its superiority in both of post and real-time processing missions launched IGS real-time service IGS RTS. on April 1, 2013, IGS has confirmed the availability of open access real-time products (Elsobeiey and Al-Harbi, 2016), which offered to the PPP users free and easily access through registration to have the advantage of obtaining corrections streams in real-time that enable RT-PPP and related application required time synchronization. RTS provide PPP users with a reliable and diverse real-time GNSS combination products for GPS and under experiment for GLONASS till now.

This paper is an endeavour to present in detail and sufficient results in both static and kinematic modes that require real-time data processing as well provide the potential accuracy comparisons could be made between real-time, post processing PPP and relative techniques (RTK) in order to focus on the performance of real-time PPP technique by using the IGS real-time service (RTS) for applications that require an accurate real-time solution. As still till now there are a limited number of papers presenting sufficient field test results and performance while practicing RT-PPP using RTS products. In the first section, a summary of the post-processing and product characteristics and availability and real-time service RTS product types and description of each combination was provided. The second section describes the mathematical models used in PPP technique and the errors that need to be applied in Post-processing PPP and RTK and considered in RT-PPP. the results of static and kinematic solution are presented in the fourth section. The last

section summarises this study and contains the conclusion of the performance of real-time PPP technique.

2. PRECISE POINT POSITIONING PRODUCT

2.1 Post Processing PPP Product

The satellite orbit and clock errors corrected in PPP technique algorithms using precise satellite orbit and clock corrections products which available as (sp3 and clk) files through the internet for post-processing applications and classified according to its availability to IGS final rapid and ultra-rapid products that provide the estimated satellite orbit and clock corrections with corresponding latency in the availability reach to (18 days, 41 hours and 9 hours respectively). Table 1 lists the availability and accuracy of IGS products according to IGS products description http://igs.org/products.

Product type	Accuracy		Latency
	Orbits	clock	
Ultra-rapid (predicted)	5 cm	1.5 ns SDev	Real-time
Ultra-rapid (estimated)	3 cm	50 PS SDev	3-9 hours
Rapid (estimated)	2.5 cm	25 PS SDev	17-41 hours
Final (estimated)	2.5 cm	20 PS SDev	12-18 days

Table 1. IGS precise products availability and accuracy

2.2 Real-time PPP RTS Product

Real-time service is formed through corporations with Natural Resources Canada (NRCan), the German Federal Agency for Cartography and Geodesy (BKG), and the European Space Agency's Space Operations Centre in Darmstadt, Germany (ESA/ESOC). its infrastructure is based on 160 station operators, multiple data centres, and 10 analysis centres around the world. Now, the RTS streams contain not only GNSS satellite orbit and satellite clock corrections in real-time to correct the broadcast ephemeris, but also GNSS observations streams from globally distributed high- quality GNSS receivers. As well broadcast ephemeris can be obtained in real-time with a high repetition rate through two streams one of them for GPS, GLONASS and Galileo satellites are produced using BKG's NTRIP Client (BNC) software (RTCM3EPH) and the other one for GPS only (RTCM3EPH01) (Hadas and Bosy, 2015). The RTS products are broadcasted as RTCM state-space representation (SSR) correction streams over the Internet using the Networked Transport of RTCM via Internet Protocol (NTRIP).

The RTS products are referenced with respect to the International Terrestrial Reference Frame 2008 (ITRF2008) (Elsobeiey and Al-Harbi, 2016). Orbit corrections are provided as along track, cross-track and radial offsets to the Broadcast Ephemeris in an Earth-cantered and Earth-fixed reference frame (Krzan and Przestrzelski, 2016). Some latency accompanies real-time products due to the time spent on transmit the data, process observations, update the correction stream and, in case of the combined product and to combine solutions from each Analysis Center (AC) (Hadas and Bosy, 2015).

Type	Description	Orbit Ref. Point
IGS01, IGC01	Single-epoch combination solution All epochs are independent of each other, Because of no filters are applied.	APC (IGS01) CM (IGC01)
IGS02	This is a Kalman filter combination solution. The mean satellite position is computed from all AC	APC
IGS03	Same approach as IGS02, it also includes GLONASS corrections	APC

Table 2. RTS combinations Streams

3. MATHEMATICAL MODEL

Dual-frequency receivers are used for the ionosphere-free linear combination can be formed to remove the first order ionosphere effect as differencing techniques are not used in PPP algorithms and no relative ionospheric measurement delays can be significantly mitigated (Rizos et al., 2012). Satellite orbit and clock errors in equation (1) and (2) can be removed using precise orbit and clock products. The general ionosphere-free equations for pseudorange and carrier-phase can be written as (Rabbou, 2016):

$$P_3 = \frac{f_1^2 P_1 - f_2^2 P_2}{f_1^2 - f_2^2} = \rho_s + c(dt_r - dt^s) + T + c(Ad_{r1} - Bd_{r2}) + c(Ad^{s1} - Bd^{s2}) + e \quad (1)$$

$$\phi_3 = \frac{f_1^2 \phi_1 - f_2^2 \phi_2}{f_1^2 - f_2^2} = \rho_s + c(dt_r - dt^s) + T + c(A\delta_{r1} - B\delta_{r2}) + c(A\delta^{s1} - B\delta^{s2}) + (\overline{\lambda N}) + \varepsilon \quad (2)$$

where P_1 and P_2 are GNSS pseudorange measurements on L_1 and L_2 , respectively;
ϕ_1 and ϕ_2 are the GNSS carrier phase measurements on L_1 and L_2 , respectively;
T is the tropospheric delay component;
d_r and d^s are frequency-dependent code hardware delay for receiver and satellite, respectively;
δ_r and δ^s are frequency-dependent carrier phase hardware delay for receiver and satellite, respectively;
e, ε are relevant system noise and un-modelled residual errors;
$\overline{\lambda N}$ is the ambiguity term for phase measurements (this term is not integer).
A and B are frequency dependent factors:
$A = \frac{f_1^2}{f_1^2 - f_2^2}$ and $B = \frac{f_2^2}{f_1^2 - f_2^2}$;

There are several methods and models were applied to mitigate the effect of tropospheric delay in GNSS positioning techniques. The impact of troposphere as a non-dispersive medium cannot be overcome by the observation combination of L1 and L2 data (Krzan and Przestrzelski, 2016), correction of tropospheric delay is included in the processing of data using real-time PPP software as the BNC program using the Saastamoinen model. BNC estimates the tropospheric delay per equation as:

$$d_{dry} = (0.0022768 \pm 5.10^{-7}) \frac{P_0}{g(\emptyset, H)} \quad (3)$$

$$T(z) = T_{apr(z)} + \frac{dT}{cos(z)} \quad (4)$$

where $T_{apr(z)}$ = The a-priori tropospheric delay derived from Saastamoinen model.

Table 3. Errors needed to be applied in Post-processing PPP and RTK and considered in RT-PPP (BNC)

Correction Type	Post-processing PPP	(RT-PPP) Considered in BNC	Relative GNSS (RTK)
Satellite Specific Errors			
Precise satellite clock corrections	✓	✓	
Satellite antenna phase centre offset	✓	✓	✓
Satellite antenna phase centre variations	✓		✓
Precise satellite orbits	✓	✓	
Group delay differential	✓		
Relativity term	✓		
Satellite antenna phase wind-up error	✓		
Receiver Specific Errors			
Receiver antenna phase centre offset	✓	✓	✓
Receiver antenna phase centre variations	✓	✓	✓
Receiver antenna phase wind-up	✓		
Geophysical Models			
Solid earth tide displacements	✓		
ocean loading	✓		
Polar tides	✓		
Plate tectonic motion	✓		
Atmospheric Modelling			
Tropospheric delay	✓	✓	✓
Ionospheric delay	✓	✓	✓

Also, several corrections applied to PPP account for reaching centimetre- level accuracy such as phase wind-up corrections, satellite antenna phase centre corrections, solid earth tide corrections and ocean loading corrections which are required for enhancement PPP solutions, However, the pervious corrections could be applied as optional or not considered for relative techniques. In addition, it important to understand that some of these corrections are not included in the processing of data using real-time PPP software as the BNC program. Table 3 lists the errors which required to be corrected in the case of PPP compared to relative positioning techniques (Rizos et al., 2012) and the corrections take in the considerations or included in the processing of data using real-time BNC software.

4. FIELD SYSTEM TEST

The purpose of this paper is to analyse the performance of real-time PPP technique by using the IGS real-time service (RTS) for static and kinematic applications that require an accurate positioning. A Real vehicular test was conducted in April 2016 to evaluate the performance of the real-time kinematic PPP. The vehicular test was carried out along railway track from Bani Suif to Assuit, which represent challenging situations for satellite navigation with actual frequent partial GNSS outages of several seconds. The Leica GX1230 receiver was used to collect the data used in this work. The GNSS data was limited to the GPS and GLONASS code and phase observation was collected at a 1 Hz rate. Carrier phase-based relative GNSS positioning solution is used as a reference. To create this reference solution, other Leica GX1230 receiver was set up at nearby stations with maximum baselines 30 km for every setup with precisely known coordinates determined using static GNSS processing. In this research, three sets of kinematic GNSS data were used in the evaluation with approximate 60 km distance for each set of data. Figure 1 shows one of the Railway Trajectories extended totally to about 32 km of collected kinematic data. Each set of GNSS

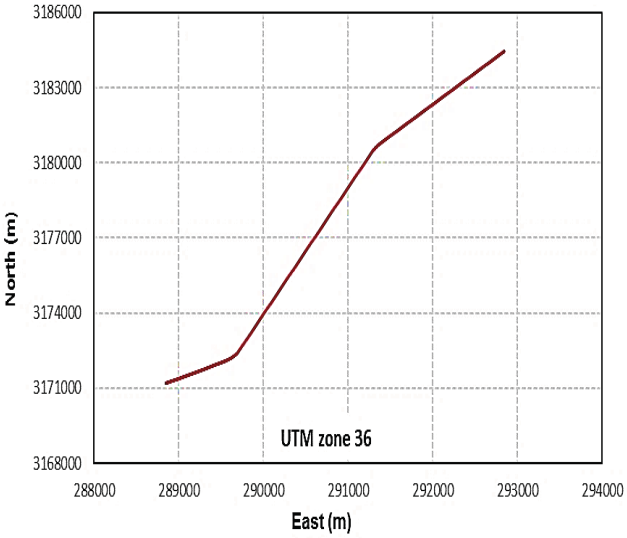

Figure 1. Railway Trajectory

data includes approximate 45 mins of a static data before moving to consider the convergence time of PPP. In addition, GNSS data that was observed from five reference solutions used in the evaluation of the static performance of RT-PPP each setup spent more than 2 hours' observation interval.

5. GNSS DATA PROCESSING

The collected GNSS data was processed instantaneously in real-time (for executing RT-PPP technique) using the open source BNC software produced under General Public License (GPL) and available online at http://igs.bkg.bund.de/ntrip/download.

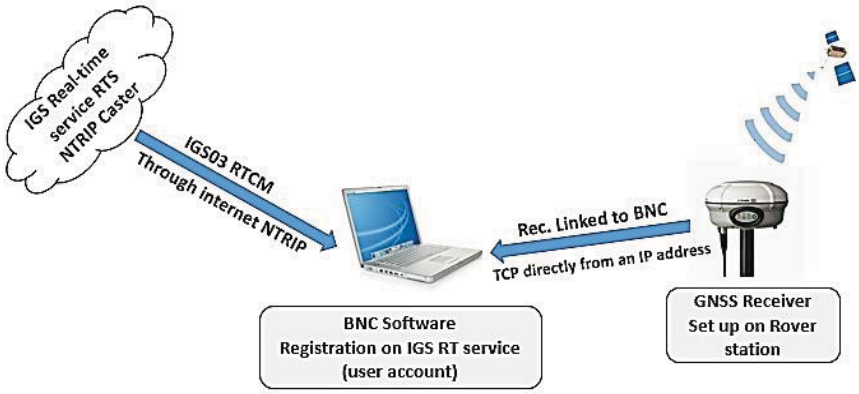

Figure 2. RT-PPP Technique Components

Streaming real-time GNSS data and corrections over the Internet has been one of the major duties of BNC as Open Source real-time software (Georg Weber, 2016). also, BNC was designed for the other purposes represented in receiving real-time GNSS data streams available through NTRIP transport protocol or directly from a GNSS receiver via TCP directly from an IP address without using NTRIP transport protocol which was implemented in this test. furthermore, generating orbit and clock corrections to Broadcast Ephemeris to support the implementation of real-time Precise Point Positioning RT-PPP techniques to determine GNSS positions in static and kinematic modes. Figure shows the RT-PPP technique components. Both IGS02 and IGS03 RTS streams which are based on Kalman filter estimation are used for orbital and clock corrections for GPS and GPS/ GLONASS combinations, respectively. The RTS corrections streams are linked directly to the BNC software and the rover GNSS receiver attached to the railway vehicular in real time mode. The undifferenced ionosphere-free linear combination of GPS and GLONASS code and phase observations is considered as the processing GNSS data. The tropospheric error is estimated as an additional unknown with a priori values derived from Saastamoinen model. Also, all sets of raw static and kinematic observation data were submitted to online post-processing PPP application for GNSS data the Canadian Spatial Reference System (CSRS-PPP).

6. RESULTS

6.1 Static RT PPP results

Figs. 3 and 4 show the real-time PPP solution errors in easting, northing and up direction for base stations FA and MA obtained by using IGS03 RTS streams based on Kalman filter estimation for orbital and clock corrections for GPS and GLONASS combinations. Solution spent near to 30 minutes as convergence time needed for the ambiguity float solution to converge to reach centimetre level positioning accuracy. Final PPP solution was received after 12 days from online submitting the observation data to CSRS-PPP post-processing service using until final IGS sp3&clk product became available. As expected, final PPP solution needed about or less than 20 minutes' convergence time less than RT PPP required. However, it can be noticed that the RT PPP solution accuracy is comparable to final PPP accuracy. fig.5 clarifies the difference between RT PPP and final PPP as well table 4 that lists root mean square error values in east, north, up, 2D and 3D directions for two techniques.

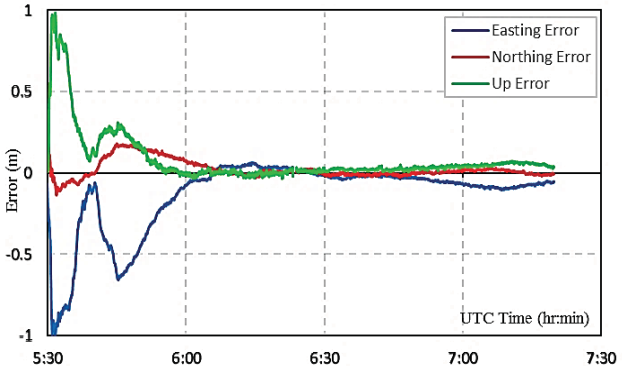

Figure 3. Real-time PPP solution errors in easting, northing and up direction for base station (FA)

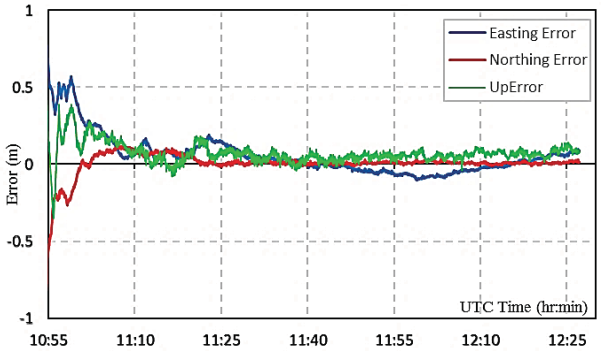

Figure 4. Real-time PPP solution errors in easting, northing and up direction for base station (MA)

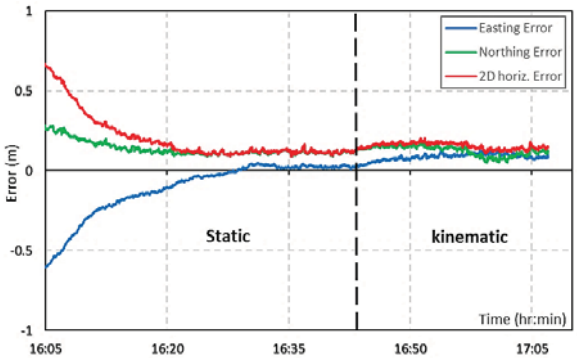

Figure 6. kinematic Real-time PPP solution errors in easting, northing, up and 2D direction for the trajectory

Table 3. Comparison between Real-time PPP and Final PPP solution

Station	Real-time PPP RMS (m)					Final PPP RMS (m)				
	East	North	Up	2D	3D	East	North	Up	2D	3D
St. (FA1)	0.08	0.09	0.30	0.12	0.32	0.05	0.03	0.12	0.05	0.13
St. (MA)	0.07	0.04	0.08	0.08	0.11	0.04	0.06	0.05	0.07	0.09
St. (FA2)	0.16	0.05	0.08	0.17	0.18	0.03	0.01	0.03	0.03	0.04

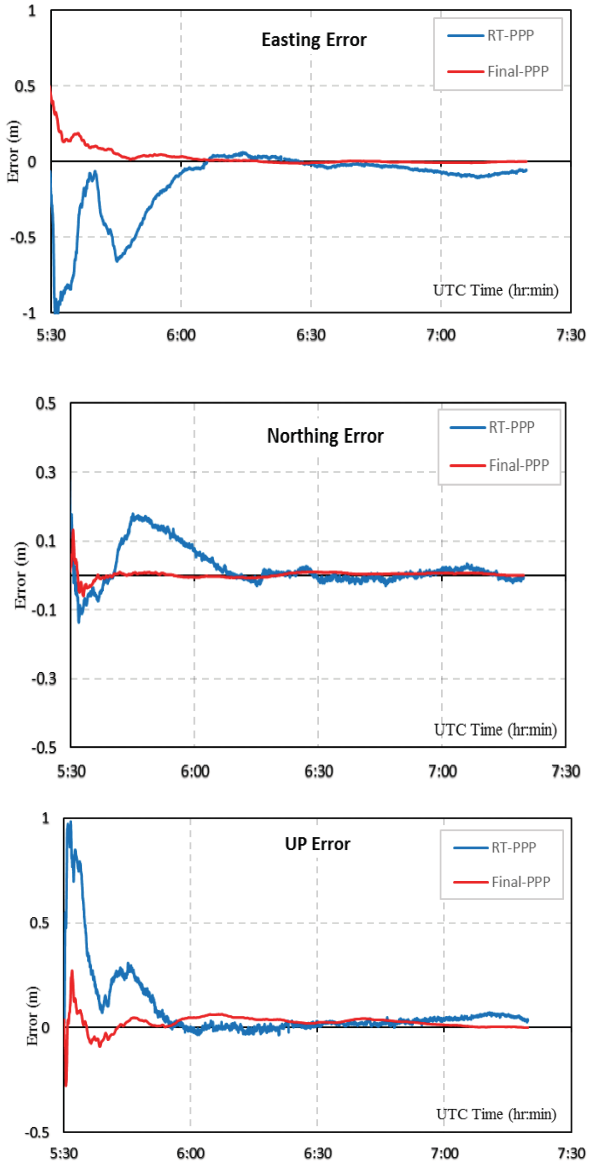

Figure 5. The difference between real-time IGS RTS PPP and post processing final PPP for base station (FA)

6.2 Kinematic RT PPP results

The results are plotted on figure 6 for one of trajectories test present the easting, northing and 2D errors calculated from the difference between IGS-RTS PPP solution and RTk solution as the RTK result considered as the reference solution in kinematic part., it shows that the solution converged after 25 minutes. The real-time processing and frequently updated of solution errors values plotted also on charts made the monitoring of solution convergence easiest and efficient to make the decision to start moving in kinematic application after reaching centimetre level positioning accuracy.

Figure 6 presents the comparison between the IGS-RTS PPP solution and ultra-rapid, final post processing PPP solution considering only the results after convergence in easting, northing and up directions. The RT PPP solution estimated with error values around 5 cm and less than 10 cm in east and north direction and near 20 cm in up direction.

6.3 Multi-Constellation RT PPP results

The real-time service pursued to support RTS product which confining to GPS and GLONASS correction with other GNSS system correction products. By using several open source tools such as BNC and with the availability of real-time Galileo orbits graciously provided by German Aerospace Center/ Munich Technical University DLR/TUM, the Centre national d'études spatiales CNES real-time analysis center now extend RTS users with State Space Representation for Galileo. Galileo real-time correction as a new product are obtainable via the CLK93 stream accompanied by 5-10 cm estimated user range error. As well, Now, CLK93 stream contains Beidou real-time corrections product, the credit of the availability of Beidou product comes back to the use of the extrapolated multi-constellation orbits recently provided by German Research Centre for Geosciences GFZ. the CNES real-time analysis center now provides State Space Representation for Beidou https://igscb.jpl.nasa.gov/ . table 4 lists the RTCM messages contained in CLK93 stream.

Orbits, Clocks& Code biases	interval	RTCM message
GPS	5 sec	1060, 1059
GLONASS	5 sec	1066, 1065
Galileo	5 sec	1243, 1242
Beidou	5 sec	1261

Table 4. The CLK93 stream description

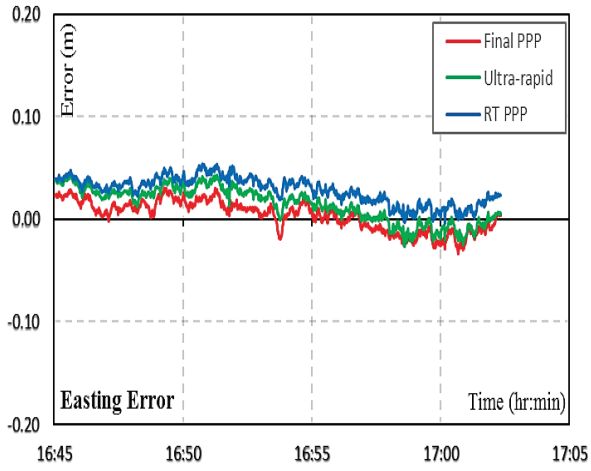

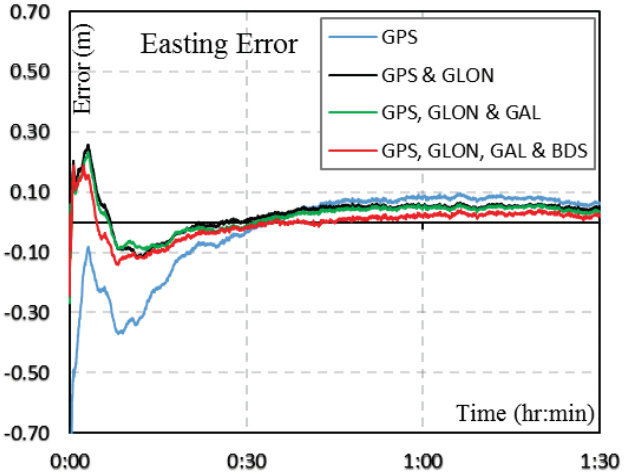

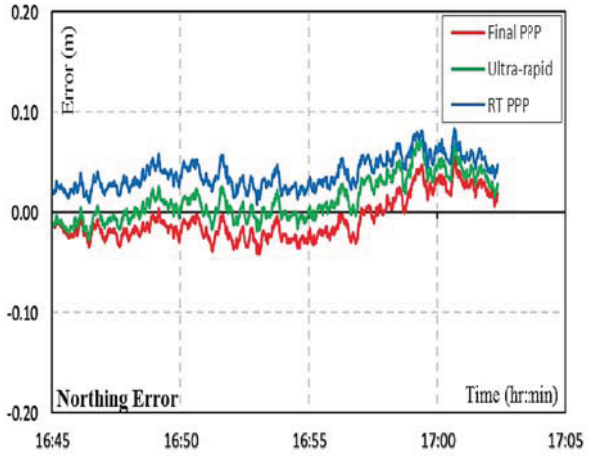

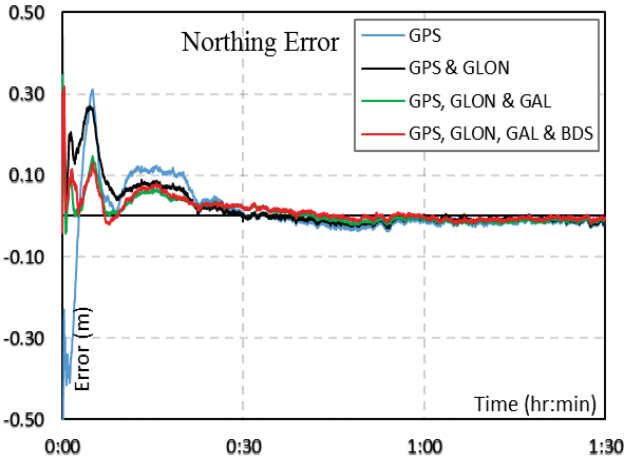

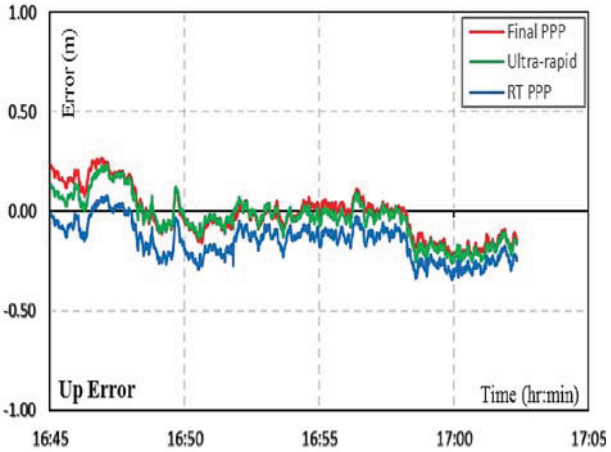

Figure 7. The difference between the real-time GPS/GLONASS RT PPP solution, ultra-rapid, final post processing PPP solution and RTk solution in moving part

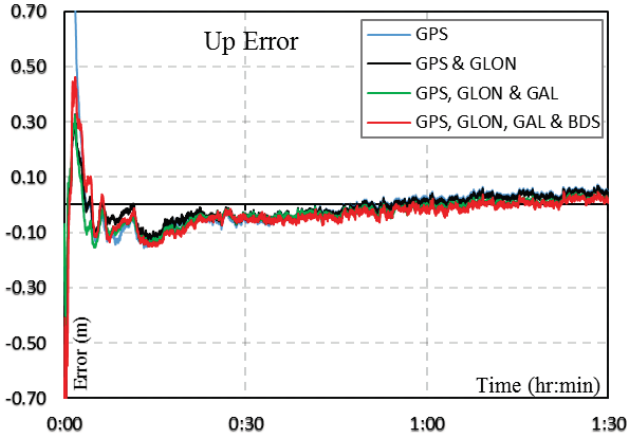

Figure 8. Multi-Constellation RT PPP results for GMSD IGS station

Table 5 Comparison between RT PPP RMS (cm) using GNSS Multi-Constellation systems after solution convergence

RMS in (Cm)	GPS	GPS & GLONASS	GPS, GLONASS & GALILEO	GPS, GLONASS, GALILEO &BDS
Easting	6.1	3.9	3.5	1.9
Northing	2.1	1.8	1.6	1.5
Up	4.9	4.5	2.8	3.0

To evaluate the involvement of the other GNSS real-time correction products, GNSS data from IGS station namely, GMSD was collected in February 2017 using TRIMBLE NETR9 Receiver with TRM59800.00 + SCIS antenna observed GPS, GLONASS, Galileo, Beidou and QZSS systems. figure 9 plots the number of satellites that processed in each system. The input data are GNSS code and carrier-phase measurements. The CLK93 precise orbit and clock real-time stream products are employed to account for orbital and clock errors and synchronized with IGS GNSS observation data using different GNSS systems combinations. table 8 shows the positioning errors in east, north and up direction for GPS only, (GPS&GLONASS), (GPS, GLONASS& Galileo) and (GPS, GLONASS, Galileo& BDS). As can be noticed that, the significant effect on positioning accuracy come back to the combination of GPS and GLONASS, the solution accuracy just keep enhancement after adding Galileo and Beidou with marginal effect compared with GPS and GLONASS that showed in figure 10.

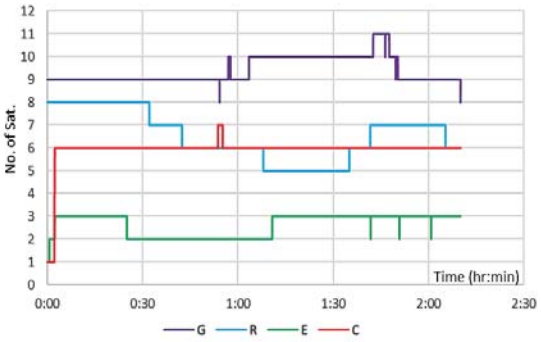

Figure 9. The GNSS satellite availability for GMSD station

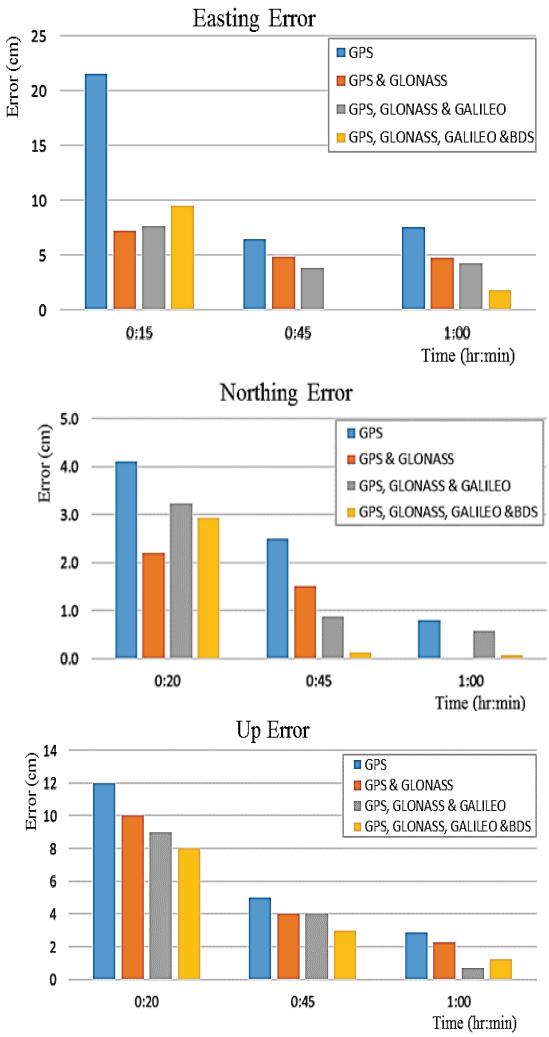

Figure 10. The positioning accuracy for different GNSS combinations for station GMSD

7. CONCLUSION

This paper investigated the performance of real-time PPP technique in detail in both static and kinematic modes that require real-time data processing through using several types of RTS streams product such as IGS02, IGS03 and CLK93 to present the contribution of real-time products available now for GPS GLONASS, Galileo and Beidou system moreover, provided the potential accuracy comparisons could be made between real-time, post processing PPP and relative techniques (RTK).

The results estimated from RTS products showed that the RT PPP solution reach centimetre level positioning accuracy which predispose this technique for use in several areas in both of static and kinematic modes particularly in areas where there are lack of continuously operating reference stations (CORS), Steadily, the significant limitation expose the PPP represents in convergence time essential to reach this accuracy. Nevertheless, the results offered in this article indicate the great potential of RT PPP positioning technique, along with its further development. It will be possible to apply it in several applications as mobile mapping application using RTS corrections for enhanced its positioning accuracy.

REFERENCES

Choy, S., Bisnath, S., Rizos, C., 2016. Uncovering common misconceptions in GNSS Precise Point Positioning and its future prospect. GPS Solut. 21, 1–10. doi:10.1007/s10291-016-0545-x

Elsobeiey, M., Al-Harbi, S., 2016. Performance of real-time Precise Point Positioning using IGS real-time service. GPS Solut. 20, 565–571. doi:10.1007/s10291-015-0467-z

Georg Weber, 2016. BKG Ntrip Client (BNC) Software Version 2.12.

Hadas, T., Bosy, J., 2015. IGS RTS precise orbits and clocks verification and quality degradation over time 2001, 93–

105. doi:10.1007/s10291-014-0369-5
Krzan, G., Przestrzelski, P., 2016. Gps/glonass precise point positioning with igs real-time service products. Acta Geodyn. Geomater. 13, 69–81. doi:10.13168/AGG.2015.0047
Rabbou, M.A., 2016. Positioning Technique Using Multi-Constellation GNSS : GPS , GLONASS , Galileo and BeiDou Multiple Ambiguity Datum Precise Point Positioning Technique Using Multi-Constellation GNSS : GPS , GLONASS , Galileo and BeiDou. doi:10.4236/pos.2015.63004
Rizos, C., Janssen, V., Roberts, C., Grinter, T., 2012. Precise Point Positioning: Is the Era of Differential GNSS Positioning Drawing to an End? FIG Work. Week 2012 1–17. doi:http://www.gmat.unsw.edu.au/snap/publications/rizos_etal2012a.pdf
Tomasz, H., 2015. GNSS-Warp Software for Real-Time Precise Point Positioning. Artif. Satell. 50, 59–76. doi:10.1515/arsa-2015-0005

MAPPING AND ANALYSIS OF TERRAIN GEOMORPHOLOGY USING SIMULATED AIRBORNE LiDAR DATA CAPTURE OF LOW POINT CLOUD DENSITIES

Fahmy F. F. Asal [a]

[a] Civil Engineering Department, Faculty of Engineering, Menoufia University, Shebin El-Kom, Egypt; fahmy_asal@hotmail.com

Keywords: Geomorphology, Mapping, Terrain analysis, DTM/DEM/DSM, Airborne LiDAR, Point cloud density, Visual analysis.

ABSTRACT

Terrain geomorphology studies require acquisition of extensive high-resolution topographic data for extraction of different earth's surface parameters. Airborne Light Detection and Ranging (LiDAR) has been one of the most important and efficient technologies that can capture very dense and very accurate digital elevation data for extended areas in relatively short times that can be utilized in terrain geomorphic analysis. However, processing of very high density LiDAR data could lead to serious time and memory consumption problems. Reductions in LiDAR data are expected to lower data acquisition and data processing costs; but this might affect feature recognitions from the generated maps. This research aimed to evaluate the effects of reductions in LiDAR data on mapping and analysis of terrain geomorphology in addition to answer the question to what extent LiDAR data can be reduced without smoothing fine terrain geomorphology details. Last returns of raw LiDAR dataset acquired at bare lands for Gilmer County, USA between March and April 2004 has been used in this analysis. Reductions have been performed randomly on the raw LiDAR dataset at different percentages to simulate LiDAR data acquisitions of lower data volumes. Topographic maps in addition to Digital Terrain Models (DTMs) have been created from the lower volume datasets and have been visually and statistically analyzed. Also, 3D views have been created for the produced DTMs for much clearer visual analysis of different terrain geomorphology elements under reductions of LiDAR data volumes. From the analysis it can be recommended that any reductions in the volumes of the LiDAR data might lead to smoothing of fine terrain details. However, the smoothing effect is very limited till reductions of the LiDAR data volume down to 75%. On the other hand more reductions in the data volume down to 50% have produced decrease by about 7% in the standard deviation of the DTM elevations, with more losses in terrain details but the 3D view of the corresponding DTM is still not that bad that makes it could be suitable for some applications. With greater reductions in the LiDAR data volume down to 25%, the standard deviation of the DTM elevations has decreased by about 19% with poor representation of different terrain details in addition to clear degradations of the DTM 3D view.

1. INTRODUCTION

Geomorphology is an earth science that concerns with studying the topography of the earth's surface including terrain shapes and irregularities in addition to the spatial distribution of the landscape elements (Liu et al., 2012, Podobnikar. 2005, Kaya, 2000). Terrain shapes and types vary considerably with different types of landscapes across the earth's surface starting from mountainous terrains with rough textures to flat plains with smooth textures (Liu et al., 2012). Geomorphological analysis also known as, geomorphometry, terrain morphometry, terrain analysis and land surface analysis constitutes a science of qualitative and quantitative analysis of the earth's surface (Podobnikar, 2010). Terrain geomorphology analysis provides valuable approaches for interpretation of complex geomorphologies such as mountainous streambeds in addition to mapping and classification of water channel geomorphologies. Real field observations have to be exploited in such analysis for characterization of topography and geomorphology of the terrain and assessment of the changes caused by natural phenomena such as large and surge floods. Quantitative studies of terrain geomorphology usually require acquisition of extensive high-resolution topographic data for the extraction of the earth's surface parameters which constitute the backbone of any terrain geomorphological analysis through exploitation of the main products of the topographic data namely; the Digital Terrain Models (DTMs) as inputs (Liu et al., 2012). Digital terrain models created from remote sensing data very often contain errors and outliers due to the sensor physical limitations and the low contrast of the terrain textures (Chen et al. 2016). In this context, it is important to note that qualitative and quantitative terrain geomorphology analysis may include visual interpretation of the landscape, accuracy analysis of mapping different geomorphology feature elements, slope mapping analysis, contourline mapping, hillshade view analysis, surface roughness extraction and analysis, surface curvature analysis, in addition to extraction and analysis of features such as landslide scarp and streamline beds. Also, in digital terrain analysis, geomorphological feature lines are important terrain formations, since they accurately describe changes in the surface; smoothness and continuity(Chen et al., 2015). High-resolution topographic data provides great potential for quantitative analysis of the earth's surface through improving interpretation of the different terrain geomorphic features where the these features can be identified precisely from high-resolution and high quality DTMs (Trevisani et al., 2010). Traditional engineering surveying techniques such as spirit leveling, precise leveling,, total station observations, analytical aerial photogrammetry and RTK GPS can provide very high quality and very high accuracy digital elevation data that can be exploited in creation of high quality DTMs, However, these methods demand intense labors and long times which makes them very costly. Digital image matching techniques using digital aerial photography, Synthetic Aperture Radar (SAR) technologies and stereo high resolution satellite images can provide dense digital elevation data in short times with reasonable costs but the qualities are still not that high enough for accurate terrain analysis. Airborne Light Detection And Ranging (LiDAR) has been one of the most important and efficient technologies that can capture very dense and very accurate digital elevation data for extended areas in relatively short times that can be utilized in construction of high accuracy and high quality DTMs; necessary for reliable terrain geomorphic analysis. The availability of LiDAR data has opened a new era of landscape analysis where improvements in

the data resolution makes it possible to accurately model microtopography over extended large areas; however, when comparing the point cloud data density and processing costs against the obtained accuracy this might be too costly (Brubaker et al. 2013). However, this has opened a new era for accurate and reliable terrain geomorphology analysis where airborne LiDAR data have been widely applied in many geomorphological fields such as: studying landslides, sediment dynamics and flood modeling. Additionally, airborne LiDAR data can be exploited in geomorphological mapping of the gravel-bed rivers, tidal channels and river valley environments. Furthermore, LiDAR data can be used in evaluation of river bank erosion and long-term changes caused by fluvial and debris-flow activity, assessment of the slopes in headwater channels, hillslope to valley transition and delineation of the water surface (Trevisani. et al., 2010). However, processing of such very high density LiDAR data that is usually called as point cloud data could leads to serious time and memory consumption problems (Chu et al., 2014). Reductions in high point cloud densities of airborne LiDAR data are expected to lower data acquisition and data processing costs; however this could affect mapping of terrain geomorphology and feature recognitions from the generated DTMs.

Trevisani et al., 2009 analyzed and interpolated airborne LiDAR topographic dataset by the use of geostatistical techniques in order to examine the geomorphology of a scree slope area in the Eastern Italian Alps. They analyzed the digital terrain models generated from airborne LiDAR-using variogram maps as spatial continuity indexes for evaluation of the reproduction of spatial variability of topography and for the characterization and comparison of different morphological features occurring in the study site. They recommend that variogram maps efficiently synthesize the spatial variability of topography in a local search window, representing suitable "fingerprints" of surface morphology.

Trevisani et al., 2010 analyzed airborne LiDAR data for studying geomorphology of the channel bed of Rio Cordon that is characterized by alternating step pools, cascades in addition to rapids with steps. They applied three geomorphometric indices namely; a slope index computed on the whole width of the channel bed, directional variograms computed along the flow direction and perpendicular to it, and local anomalies, calculated as the difference between directional variograms at different spatial scales. They recommended that directional variograms in the flow direction and local anomalies have proven to be effective at recognizing morphologic units, such as steps, pools and clusters of large boulders. Moreover, at the spatial scale of channel reaches, the applied indices demonstrated satisfactory capability to outline patterns associated with boulder cascades and rapids with steps, however, they did not clearly differentiate between morphologies with less marked morphological differences, such as step pools and cascades (Trevisani et al., 2010).

Werbrouck et al. 2011 discussed generation of high precision DTM from high density airborne LiDAR data for landscape archaeological studies. Their objective was creation of detailed topographical surfaces free of artificial features and topographical artifacts in addition to visualizing natural and current topography through implementation of true ground points only. They employed semi-automatic removal of ground features and artifacts basing on topographical vector data, visual interpretations and slope analysis where they constructed two surface models; a TIN (Triangulated Irregular Network) model and a grid model, DTM. Both datasets were used as images that were interpreted using ancillary data from historical sources.

Liu et al. 2012 analyzed multi-temporal LiDAR data of high accuracy and high resolution through the use of a geomorphometric model for extracting landslides where two sets of LiDAR data were acquired before and after heavy rainfall. They extracted Geomorphometric parameters including slope, curvature, OHM, OHM roughness, and topographic wetness index using stencils of landslide polygons overlaid on respective thematic maps derived from LiDAR DTM and the determined the ranges of every parameter from the statistics of the landslide area. The ranges of the parameters of land- slides were optimized for the model by the statistics of the landslide area. They recommended that the overall accuracy predicted by their model was 64.9% (Liu et al. 2012).

Migoń et al. 2013 reviewed recent advances in the use of high-resolution airborne LiDAR data in landform mapping and interpretation in the mountainous terrain of the Sudetes (SW Poland), They recommend that the use of LiDAR data has allowed reevaluation of landforms known before, and discovery of surface features such as glacial and per glacial landforms in the Karkonosze, morphological signatures of mass movements in the Stołowe Mountains, fluvial features and morphotectonic analysis in the Izerskie Mountains. Also, they indicated that although LiDAR immensely increases the scope for landform recognition and mapping in addition to image interpretation this should be verified in the field. Additionally, they concluded that although LiDAR DTMs can show even landforms 1.0 to 2.0 m in length, thresholds of sizes 4.0 to 6.0 m look to be more realistic unless surface features are linear and continue over long distances.

Brubaker et al. 2013 employed two LiDAR datasets of different point cloud densities of 0.714 and 10.28 pts/m^2 in creation of DTMs of 1.0 m grid cells then, they compared the roughness between both different dataset DTMs using the standard deviation of slope, standard deviation of curvature, a pit fill index, and the difference between a smoothed splined surface and the original DTM. They recommend that lowland areas tended to have the highest roughness values for all methods, with other areas showing distinctive patterns of roughness values across metrics but their study results suggest that the high-resolution LiDAR data did not improve the roughness modeling in comparison with the coarser statewide LiDAR. They concluded that LiDAR data resolution may not be as important as the algorithm and the methodology exploited in generating LiDAR DTMs for roughness modeling purposes.

Chu et al. 2014 state that recognition of geomorphic features from high-resolution LiDAR DTM constitutes the first key step for landslide risk assessment. They studied the effect of LiDAR sample sizes and interpolation methods on the identification of the landslide scarps hidden in the forest. They recommended that LiDAR sample size affects visual identification of landslide scarps in addition, LiDAR data point density data controls the level of detail in the LiDAR DTMs.

Tomljenovic and Rousell, 2014 state that airborne laser scanning has become a new method for collection of accurate spatial data in the form of point clouds that can be as dense as 200 points per square metres (pts/m^2). They evaluated the influence of the spatial point density on the obtained results from a pre-developed object-based rule set which incorporates formalized knowledge for extraction of 2D building outlines where they used point cloud datasets with varying densities (18,

16, 9, 7, 5, 2, 1 and 0.5 pts/m^2) in their analysis. Their results indicated that using higher density point clouds increases the level of classification completeness and correctness.

Chen et al. 2015 carried out a study in which they proposed a method called thin plate spline-based feature-preserving method for LiDAR data reductions. This method is based on selections of numbers of significant terrain points and extraction of geomorphological features from the raw dataset for preserving the original accuracy of the generated DTMs as possible, while maximally keeping terrain features. They made applications on four sites with different topographies including; flat, undulating, hilly and mountainous terrains for the analysis of the effects of the application of the thin plate spline-based feature-preserving for LiDAR data reductions on the generated DTMs. Additionally, they compared the results from these methods with those of the thin plate spline based algorithm without features and two classical data selection methods including maximum z-tolerance and the random method. They recommended that thin plate spline-based feature-preserving and thin plate spline based algorithm without features methods are more accurate than the classical methods in terms of the error ranges and root mean square errors with better ability of preserving geomorphological features, especially for the mountainous terrains.

This research aimed to evaluate the effects of reductions in airborne LiDAR point cloud data densities on mapping and analysis of terrain geomorphology since these reductions could lower data acquisition and data processing costs. It also aimed to answer the question to what extent LiDAR data can be reduced without neglecting fine and important details in mapping terrain geomorphology. Last returns of raw LiDAR dataset acquired at bare lands for Gilmer County, USA between March and April 2004 and downloaded from the county website has been used in this analysis. Reductions have been performed randomly on the raw LiDAR data at different percentages to simulate lower density LiDAR data acquisitions. Creation of subsets from the original raw LiDAR data have been performed using ArcGIS geostatistical analyst extension where new data files of 75%, 60%, 50% and 25% of the original data have been created. The created different volume data subset files have been subjected to visual and statistical analysis in order to assess how much efficient is ArcGIS geostatistical analyst in preserving the visual statistical properties of the original data after any subset operation. Topographic maps have been created from the original raw LiDAR data and from the subsets of data where contourline intervals have been chosen as 1.0 metres. Moreover, Digital Terrain Models (DTMs) have been created from the original raw LiDAR data and from the subset LiDAR data files using ArcGIS 9.3 where the Inverse Distance Weighting (IDW) with the power of four and grid resolution of 0.50 meters have been used for all the generated DTMs. Furthermore, 3D views for terrain geomorphology have been produced using the ArcGIS 9.3 ArcSeen extension. Qualitative and quantitative analysis of the topographic maps and digital terrain models have been performed in addition, visual analysis of the terrain geomorphology elements at 2D and 3D has been undertaken.

2. CREATION AND ANALYSIS OF SIMULATED LOWER DENSITY LiDAR DATASETS

Figure 1 shows a sample of raw LiDAR data which constitutes last returns acquired at bare lands for Gilmer County, USA between March and April 2004 that has been downloaded from the county website. The sample data constitutes a complete LiDAR tile of filename 000010_lst that covers an area of dimensions 1,000 metres by 1,000 metres with 424320 LiDAR data measurements, giving LiDAR point cloud density of 0.42432 points per a squared metre (pts/m^2), which refer to one LiDAR measurement for every 2.3567 squared metres. Reductions of the data have been carried out using ArcGIS 9.3 geostatistical analyst extension using a black box random model to simulate LiDAR data acquisitions of lower point cloud density. Four sets of lower data volumes of 75%, 60%,50% and 25% of the original data have been created to simulate LiDAR data capture of 0.31824, 0.254592, 0.21216, 0.10608 pts/m^2 respectively. Also, visual analysis of the figures 1, 2, 3, and 4 shows that the ArcGIS 9.3 geostatistical analyst extension has kept the same relative degree of contrasts in tones and textures within the four figures.

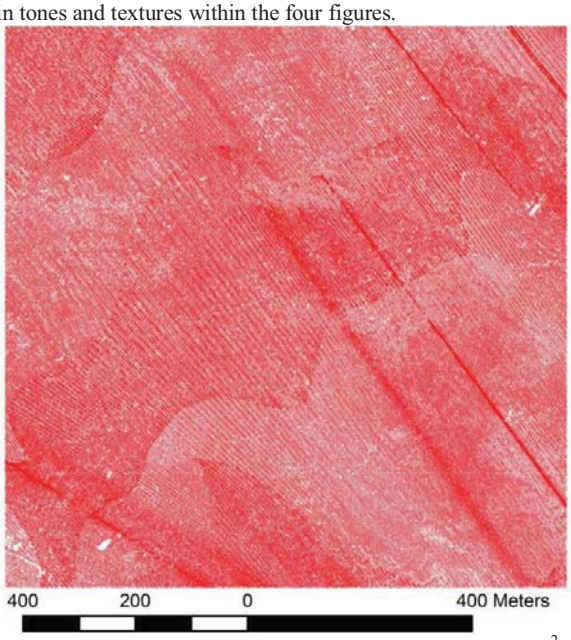

Figure 1. The original raw LiDAR data of 0.0.424320pts/m^2 point cloud density (100% of the original data).

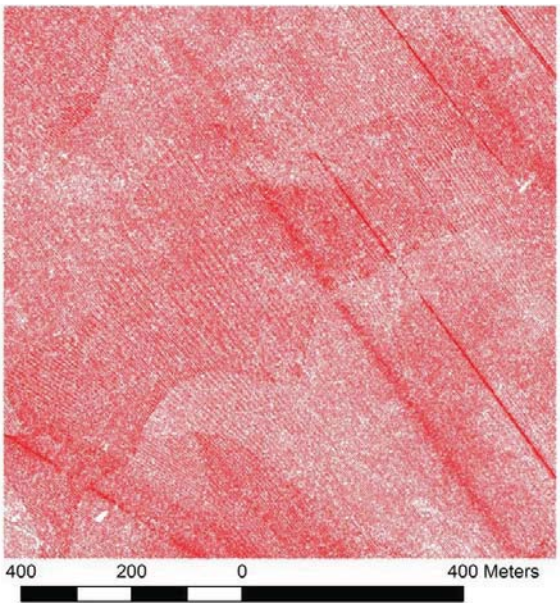

Figure 2. Simulated raw LiDAR data capture at 0.318240 pts/m^2 point cloud density (75% of the original data).

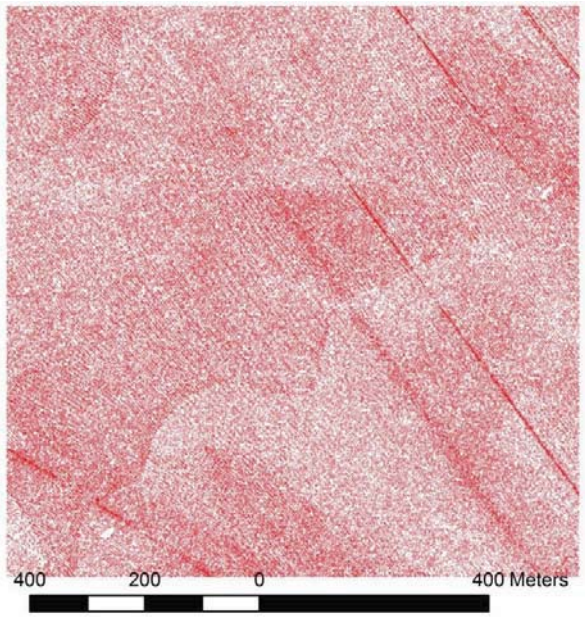

Figure 3. Simulated raw LiDAR data capture at 0.21216 pts/m^2 point cloud density (50% of the original data).

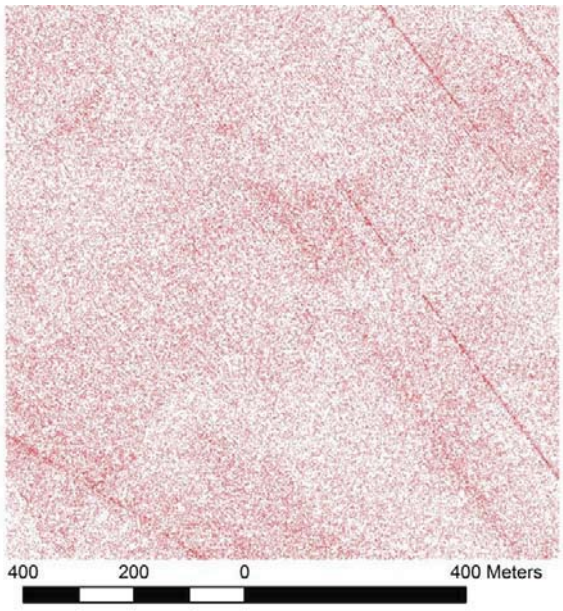

Figure 4. Simulated raw LiDAR data capture at 0.106080 pts/m^2 point cloud density (25% of the original data).

Table 1 depicts the statistical properties of these files besides the statistical properties of original data file. Also. figures 2, 3 and 4 show simulated raw LiDAR data capture of 0.318240, 0.21216 and 0.10608 pts/m^2 respectively. The statistical properties of the different simulated sets of data are recorded in table1 as have been calculated using ArcGIS geostatistical analyst extension. The analysis aimed to show how coincidence of the statistical properties of the simulated low volume LiDAR data capture with their correspondings of the original raw LiDAR data file. From the analysis it can be seen that ArcGIS geostatistical analyst has produced subset files of statistical properties that are almost coincident with the corresponding values of the original raw LiDAR data. This applies for the maximum, the minimum, mean, the range and the standard deviation of the elevations which is an indication of the efficiency of the ArcGIS geostatistical analyst and superiority of its subset random model.

Statist. Quant.	100% of raw data	75%of raw data	60% of raw data	50%of raw data	25% of raw data
No. of points	424320	318240	254592	212160	106080
Density (pts/m^2)	0.424	0.318	0.255	0.212	0.106
Min. elev.(m)	289.94	289.94	290.01	289.94	290.38
Max. elev.(m)	390.49	390.49	390.49	390.49	390.39
Mean elev.(m)	345.19	345.19	345.223	345.2	345.19
Range elev.(m)	100.55	100.55	100.48	100.55	99.93
Std. Dev.(m)	20.77	20.773	19.278	20.764	20.76

Table 1. Statistical analysis of the original LiDAR data and the created subsets of the original data to simulate lower volume LiDAR data acquisitions.

3. TOPOGRAPHIC MAPPING OF TERRAIN GEOMORPHOLOGY FROM SIMULATED LiDAR DATA CAPTURE AT LOWER DATA DENSITIES

Figure 5 presents a topographic map generated from the original raw LiDAR data. Also, figures 6, 7 and 8 depict topographic maps generated from three simulated LiDAR data captured at lower data volumes of 75%, 50% and 25% of the original raw LiDAR data. Visual analysis of the topographic maps shows great similarity between figure 6, the topographic map generated from 75% of the original data and figure 5, the topographic map generated from 100% of the original raw LiDAR data. This appears in similar shapes of the contourline, similar concentrations and similar colours of the contourline concentrations referring to similarity in surface slopes and steepness and consequently similarity in mapping geomorphology elements in the two topographic maps.

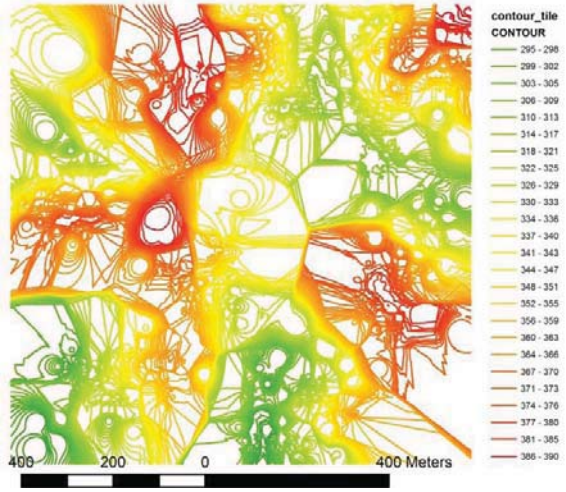

Figure 5. Topographic map generated from the original raw LiDAR data of 0.0.42432 pts/m^2 point cloud density (100% of the original data).

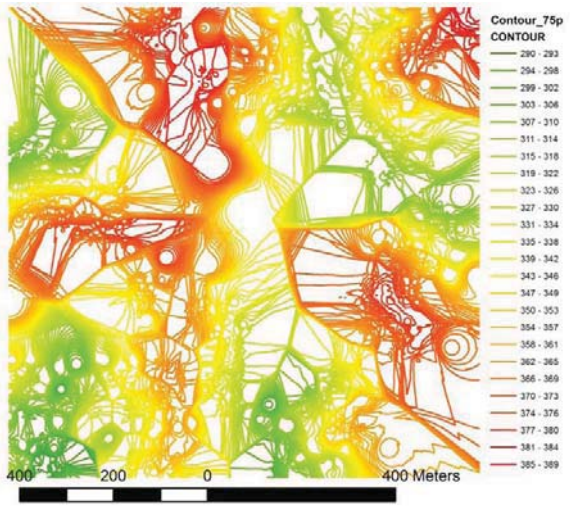

Figure 6. Topographic map generated from simulated raw LiDAR data capture at 0.318240 pts/m^2 point cloud density (75% of the original data).

When comparing figure 7, the topographic map generated from simulated raw LiDAR data of 50% of the original data with the topographic map generated from the original raw LiDAR, figure 5, differences appear in the rounded shapes of the contourlines at the lower right corner of figure 7 addition to difference in the contourline concentrations with clearer differences in the colours of these concentrations. Wider differences appear in figure 8, which is a topographic map generated from simulated raw LiDAR data captured 25% of the original data where greater differences can be seen in the shape and concentrations of the contour lines with changes in the colours of the contourline concentrations. Also, figure 8 depicts coarse tones and course textures reflecting smoothing of main elements of the terrain geomorphology due to losses of significant percentages of the original data.

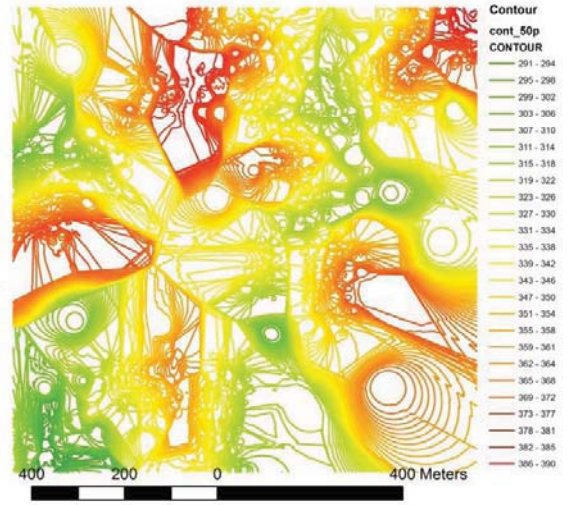

Figure 7. Topographic map generated from simulated raw LiDAR data capture at 0.21216 pts/m^2 point cloud density (50% of the original data).

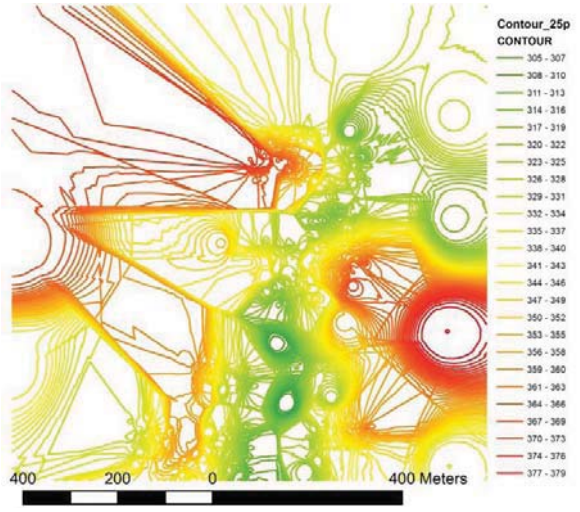

Figure 8. Topographic map generated from simulated raw LiDAR data capture at 0.10608 pts/m^2 point cloud density (25% of the original data).

Table 2 depicts the statistical properties of the four topographic map, figures, 5, 6, 7 and 8. From table 2 the values of the min., the max. the mean and the ranges of the contourlines in addition to the standard deviation of the contourlines elevations in the topographic map from 75% of the data are almost the same values of topographic map from the original raw LiDAR data which indicates that omitting of 25% of the data did not leave much effects on the statistical properties of the generated topographic maps. Also, reductions in the data volumes down to 50% have recorded decreases on the standard deviation of the contourline elevations by about 7%. However, with more reductions in the data volume down to 25% has left clearer effects on the statistical properties of the generated topographic maps, where the standard deviation has decreased by 29%. This refers to greater smoothing and approximating of the terrain geomorphology element has to be expected when omitting more than 75% of the original data.

Statist. Quant.	Cont. from 100% of raw data	Cont. from 75% of raw data	Cont. from 60% of raw data	Cont. from 50% of raw data	Cont. from 25% of raw data
No. of Cont.	1042	1066	912	1092	540
Min. cont.	295	290	293	291	305
Max. cont.	390	389	384	390	379
Mean cont.	342.5	341.923	342.58	343.23	336.27
Range cont.	95	99	91	99	74
Std. Dev.(m)	23.5	23.762	20.655	21.873	16.69

Table 2. Statistical analysis of the topographic maps generated from the original raw LiDAR data and from simulated raw LiDAR data capture at low data volumes.

4. DIGITAL TERRAIN MODELLNG OF TERRAIN GEOMORPHOLOGY FROM SIMULATED LiDAR DATA CAPTURE AT LOWER DATA DENSITIES

Digital Terrain Models (DTMs) have been created from the original raw LiDAR data and from the simulated lower volume LiDAR data. Four DTMs, presented in figures 9, 10, 11 and 12 have been generated from datasets of 100%, 75%, 60%, 50% data 25% of the original data respectively. The Inverse Distance Weighting (IDW) method of interpolation with power of four and grid cell sizes of 0.5 metres by 0.5 metres have been exploited in creation of the DTMs from the raw LiDAR data of different data volumes. Also, table 3 depicts the statistical analysis results of the generated DTMs.

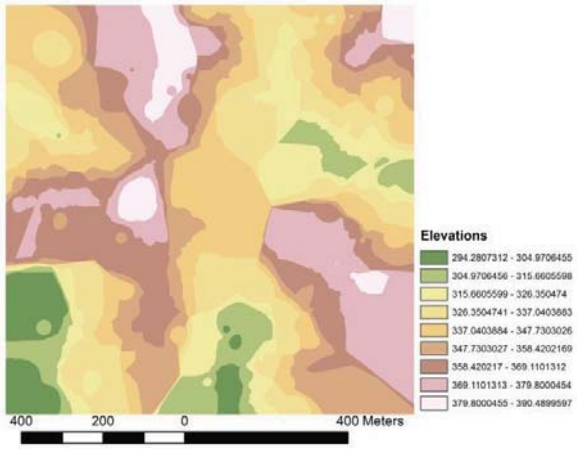

Figure 9. Digital terrain model generated from the original raw LiDAR data of 0.0.424320pts/m^2 point cloud density.

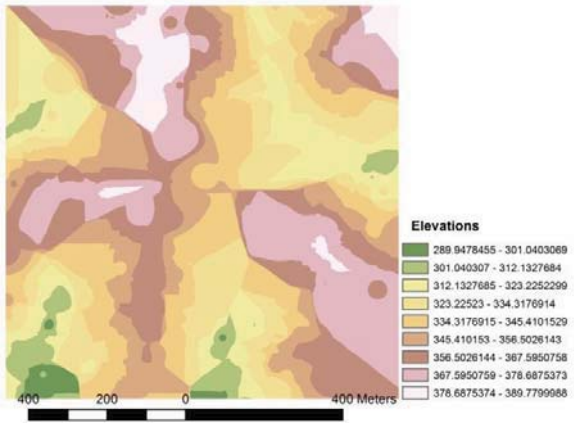

Figure 10. Digital terrain model generated from simulated raw LiDAR data capture at 0.318240 pts/m^2 point cloud density (75% of the original data).

The elements of the digital image interpretation have been exploited for visual analysis of the DTMs generated from LiDAR datasets of different volumes. The elements of the digital image interpretation include the shape, size, 2D locations of the colour patches in addition to changes in the tones/colours within the DTMs. Also, the texture which expresses the arrangements and repetitions of the tones that could be smooth, intermediate or rough textures constitutes one of the main digital image interpretation elements that have been evaluated here. Additionally, the patterns which express the arrangements of the spatial objects on the ground are other important criteria of the elements of the digital image interpretation (Jensen, 2000, Lillesand and Keifer, 2000, Jensen, 2005).

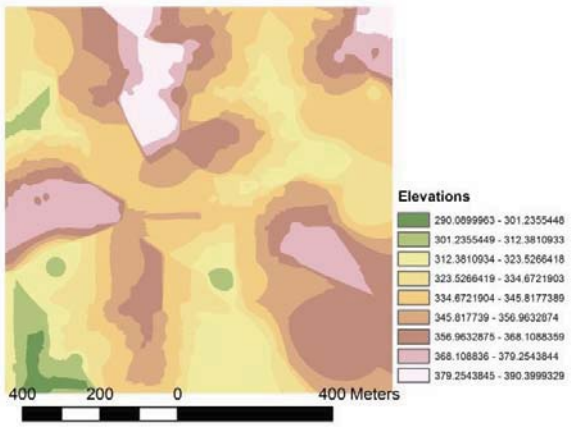

Figure 11. Digital terrain model generated from simulated raw LiDAR data capture at 0.21216pts/m^2 point cloud density (50% of the original data).

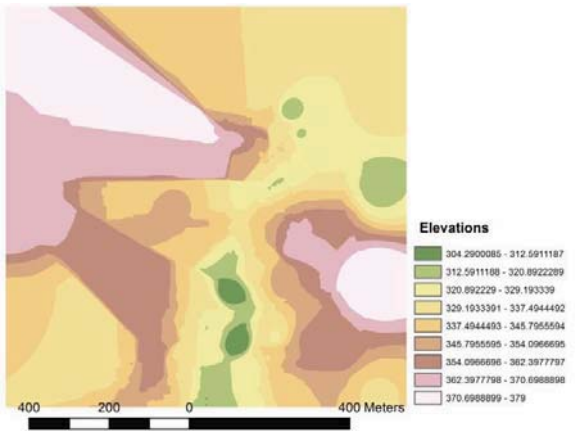

Figure 12. Digital terrain model generated from simulated raw LiDAR data capture at 0.10608 pts/m^2 point cloud density (25% of the original data).

Little differences can be visually interpretable between figure 9, the DTM generated from the original LiDAR dataset and figure 10 which is a DTM generated from 75% of the original data. The differences are very clear in the sizes of the colour patches and changes in the tones. Also, the DTM from 75% of the data is less structured compared to the original LiDAR data DTM. This refers to smoothing of very fine elements of the terrain geomorphology. The differences are wider when comparing figure 11 which is a DTM from 50% of the data and the original data DTM figure 9 where smoothing of the tones and textures in figure 11 is clearer. When comparing figure 12, the DTM from 25% of the data with figure 9, the original data DTM, it can be found that there are much clearer effects of smoothing and approximating of terrain geomorphology elements where very big colour patches of extended areas dominate the DTM from 25% of the original data giving highly smoother tones and much coarser textures which refers to very

highly smoothed DTMs have to be expected when omitting 75% of the data.

Statist. Quant.	DTM from 100% of data	DTM from 75% of data	DTM from 60% of data	DTM from 50%of data	DTM from 25% of data
No. of points	424320	318240	254592	212160	106080
Density (pts/m^2)	0.424	0.318	0.255	0.212	0.106
Min. elev.(m)	294.281	289.948	292.702	290.09	304.29
Max. elev.(m)	390.49	389.78	384.03	390.4	379
Mean elev.(m)	345.319	346.343	343.806	344.598	347.43
Range elev.(m)	96.209	99.832	91.328	100.31	74.71
Std. Dev.(m)	20.709	21.191	19.278	19.240	16.763

Table 3. Statistical analysis results of DTMs generated from the original LiDAR data and from reduced volume LiDAR data to simulate LiDAR data acquisitions of lower point densities.

When looking at table 3, that presents the statistical analysis results of DTMs generated from the original raw LiDAR data and from the reduced volume LiDAR data, it can be noticed that the statistical quantities including the min., the max., the mean and the ranges of the elevations in addition to the standard deviation of the DTM elevations record small changes in values with the reductions of data volumes down to 75% and 60% of the original data, however the changes in those statistical quantities are widen with more reductions in the volumes of the LiDAR data down to 50%. In this context, reductions down to 50% of the data have produced decreases in the standard deviations of the DTM by about 7% of the standard deviation of the DTM from the original data. However, more reductions in the volumes of the LiDAR data down to 25% of the original data have produced considerable decreases in the statistical quantities of the DTM. For example, reductions in the volumes of LiDAR data down to 25% of original data have produced 22% decrease in the range of the elevations in the DTM and 19% in the standard deviations of the DTM elevations which means high degree of terrain geomorphology smoothing.

5. 3D VISUALIZATION OF THE DTMs CREATED FROM SIMULATED LiDAR DATA CAPTURE AT LOWER DATA DENSITIES

3D visual analysis has been undertaken so that the changes in terrain geomorphology elements due to omitting parts of the original LiDAR data can be 3D viewed and become more interpretable. As followed in the visual analysis of the digital terrain models the elements of the digital image interpretation have been employed in this analysis but in three dimensional. Clear differences in the 3D views can be interpreted between figure 13; the 3D view for the DTM from the original LiDAR data and figures 14 which is a 3D view for the DTM generated from reduced LiDAR data volume down to 75% of the original data. This appears in smoothing the tops of the hills and less corrugations in figure 14 which refers to disappearing of fine elements of the terrain geomorphology. The same can said on figure 15 which is 3D view from a DTM of reduced LiDAR data volumes down to 50%. However, the degree of terrain smoothing of fine geomorphology elements is higher.

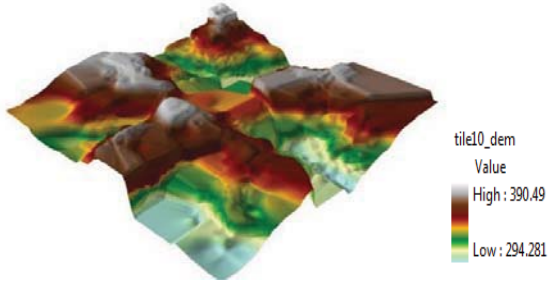

Figure 13. 3D view of digital terrain model generated from the original LiDAR data of 0.0.424320 pts/m^2 point cloud density.

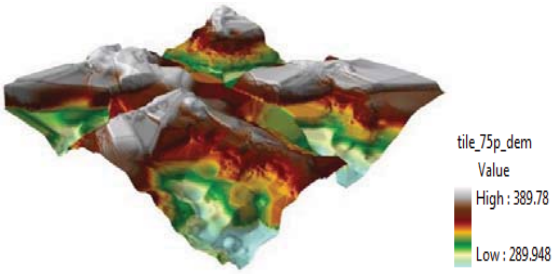

Figure 14. 3D view of digital terrain model generated from simulated raw LiDAR data capture at 0.318240 pts/m^2 point cloud density (75% of the original data).

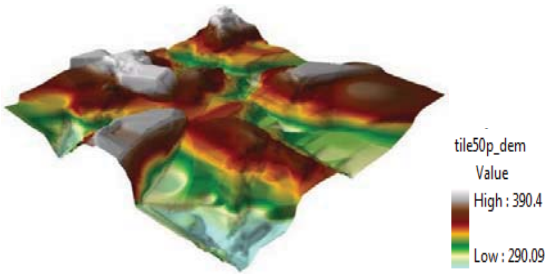

Figure 15. 3D view of a digital terrain model generated from simulated raw LiDAR data capture at 0.21216 pts/m^2 point cloud density (50% of the original data).

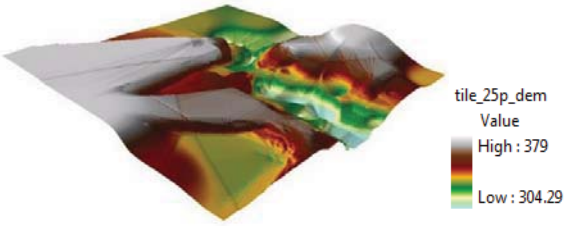

Figure 16. 3D view of a digital terrain model generated from simulated raw LiDAR data capture at 0.10608 pts/m^2 point cloud density (25% of the original data).

When comparing figure 16 which is a 3D view of the DTM generated from only 25% of the original data with the 3D from the original data DTM in figure 13 it can be seen that the terrain geomorphology has been largely smoothed and approximated resulting in disappearance of main terrain elements such as the

tops of the hills and smoothing of the valleys between the different hills. Also, degradations of the terrain elevations are very high in figure 16. It can be recommended that reductions in LiDAR data volumes produces smoothing of fine terrain geomorphology elements till reductions down to 75% of the data, however this can be bearable for some applications. On the other hand more reductions down to 50% results in bigger losses of terrain geomorphology element but the 3D view is still not that bad. With reductions down to 25% of the original data, poor representation of the terrain geomorphology with smoothing and disappearing of main elements of the terrain geomorphology have resulted where inaccurate outcomes have to be expected with the involvements of these low volumes of data in different applications .

6. DISCUSSIONS

Airborne LiDAR data have been widely applied in many terrain geomorphology fields such as: studying landslides, sediment dynamics and flood modeling as it usually enjoys high density and high accuracy where this data can be acquired in relatively short times compared to other engineering surveying and remote sensing techniques. However, processing of very high density LiDAR data could lead to serious time and memory consumption problems (Chu et al., 2014). Reductions in high point cloud densities of airborne LiDAR data are expected to lower data acquisition and data processing costs; however this could affect mapping of terrain geomorphology and feature recognitions from the generated DTMs. As this research concerns with studying the effects of reductions in LiDAR data volumes on mapping terrain geomorphology, reductions of the test data have been undertaken using the geostatistical analyst extension working under ArcGIS 9.3, where four reduced datasets files of data volumes of 75%, 60%, 50% and 25% of the original data have been created using black box random functions. Visual and statistical analysis of the produced data set file has shown that ArcGIS geostatistical analyst has produced subset files of statistical properties that are almost identical to those of the original raw LiDAR data which assures the efficiency of the ArcGIS geostatistical analyst in creating subsets of data.

Topographic maps have been created from the original raw LiDAR data and from the produced subsets of data where the contourline intervals have been chosen equal to 1.0 metres. Additionally, Digital Terrain Models (DTMs) have been created from the original raw LiDAR data and from the subset LiDAR data files using ArcGIS 9.3 3D analyst where the Inverse Distance Weighting (IDW) with the power of four and grid resolution of 0.50 metres by 0.5 meters have been unified for all the generated DTMs. Furthermore 3D views for terrain geomorphology have been created using the ArcGIS 9.3 ArcSeen extension. Qualitative and quantitative analysis of the topographic maps and digital terrain models have been performed; in addition visual analysis of the terrain geomorphology elements at 2D and 3D has been undertaken.

Visual analysis of the topographic maps has shown great similarity between the topographic map generated from 75% of the original data and the topographic map generated from 100% of the original raw LiDAR data referring to no much effect on the topography with reductions in the data volume down to 75% of the original data. When comparing the topographic map generated from simulated raw LiDAR of 50% of the original data with the topographic map generated from the original raw LiDAR clearer differences appear in the rounded shapes of the contourlines at the lower right of topographic map from 50% of the data. Additionally, differences in the contourline concentrations with clearer differences in the colours of the these concentrations are observables. However, wider differences appear in the topographic map generated from simulated raw LiDAR data capture of only 25% of the original data where greater differences in the contourline shapes and concentrations can be observed with much coarser tones and textures reflecting disappearance of main elements of terrain geomorphology due to big omissions of great parts of the original data.

Visual and statistical analyses of the digital terrain models created from the simulated raw LiDAR data captures of lower point cloud densities has provided additional understanding of how reductions of the data volumes could affect mapping of terrain geomorphology elements. Differences can be visually interpretable between the DTM generated from the original LiDAR dataset and the DTMs generated from 75% of the original data but these differences are very small. The differences are wider when comparing the DTM from 50% of the data with the original data DTM where smoothing of the tones and textures in the DTM are clear. When comparing the DTM from 25% of the data with the original data DTM, wider smoothing and approximating of terrain geomorphology are very much clearer as very big patches of similar colour areas dominate the DTM giving much smoother tones and textures. The statistical analysis of the DTM from different simulated datasets has shown small effect on the statistical quantities of the DTMs till reductions down to 60% of the original data. On the other hand reductions down to 50% of the data have produced decreases in the standard deviation of the DTM elevation by about 7%. Alternatively, reductions in the volumes of LiDAR data down to 25% of original data have produced 22% decrease in the range of elevations in the DTM in addition to 19% in the standard deviations in the DTM elevations which means high degree smoothing for terrain geomorphology elements.

Visual analysis of the 3D views of the generated DTMs has given clearer understanding of the changes in mapping of terrain geomorphology elements due to omitting parts of the LiDAR data. Clear differences in 3D views between the 3D view for the DTM from the original data and the 3D view for the DTM generated from reduced volumes of LiDAR down to 75% of the original data are interpretable. This appears in smoothing tops of the hills and less corrugated surface which refers to disappearance of fine elements of the terrain geomorphology. The same can said on the 3D view from a DTM of reduced LiDAR data volumes down to 50%, but the degree of terrain smoothing and neglecting of fine terrain geomorphology elements is higher. When comparing the 3D view of the DTM generated from only 25% of the data with the original data DTM it can be seen that the terrain geomorphology has been smoothed and approximated with disappearance of main and important elements of the topography with poor representation of the terrain.

7. CONCLUSIONS

This research aimed to evaluate the effects of reductions in airborne LiDAR point cloud data densities on mapping and analysis of terrain geomorphology since these reductions could lower data acquisition and data processing costs. It also aimed to answer the question to what extent LiDAR data can be reduced without neglecting fine and important details in mapping terrain geomorphology. Last returns of raw LiDAR dataset acquired at bare lands for Gilmer County, USA between

March and April 2004 has been used in this analysis. Reductions have been performed randomly on the raw LiDAR data at different percentages to simulate LiDAR data acquisitions of lower densities where the produced lower volume datasets have been visually and statistically analyzed and compared against the original dataset. Topographic maps have been created from the original raw LiDAR data in addition to the lower volume subsets of data where visual and statistical analysis of these maps has been undertaken. Also, Digital Terrain Models (DTMs) have been created from the original raw LiDAR data and from the reduced volume LiDAR data where they have been subjected to visual and statistical analysis. Moreover, 3D views have been generated for the obtained DTMs for much clearer visual analysis of the terrain geomorphology elements. From the analysis it can be recommended that any reductions in the volumes of LiDAR data might lead to disappearance of fine details of the terrain geomorphology. For some applications disappearance of very fine details in the terrain geomorphology might not be that important where the data volume can be reduced down to 75% without noticeable effects on the outcomes from the applications. On the other hand, more reductions down to 50% have produced decrease in the standard deviation of the DTM elevations by only 7% but with more losses in bigger size terrain geomorphology element, however, the 3D view is still not that bad that it can be suitable for different applications. With more reductions down to 25% of data volume the standard deviation of the DTM elevations has decreased by 19% with poor representation of the terrain geomorphology due to smoothing and disappearance of main details of the terrain geomorphology where inaccurate outcomes have to be expected when incorporating such low volumes of LiDAR data in different applications.

REFERENCES

Chen, C., Liu, F., Li, Y., Yan, C. Liu, G., 2016. A robust interpolation method for constructing digital elevation models from remote sensing data. Geomorphology 268 (2016) 275–287 Elsevier B.V.

Chen, C. Yanyan Li, Y., Changqing Yan, C., Dai , H. and Liu, G., 2015, A Thin Plate Spline-Based Feature-Preserving Method for Reducing Elevation Points Derived from LiDAR. Remote Sens. 2015, 7, 11344-11371; doi:10.3390/rs70911344.

Chu, H.-J., Wang, C.-K., Huang, M.-L., Lee, C.-C., Chun- Yu Liu &Lin, C.-C., 2014. Effect of point density and interpolation of LiDAR-derived high- resolution DEMs on landscape scarp identification, GIScience & Remote Sensing, 51:6, 731-747, DOI: 10.1080/15481603.2014.980086.

Jensen, J. 2005. *Introductory Digital Image Processing – a Remote Sensing Perspective*. Third Edition. Pearson Prentice Hall, Upper Saddle River, New Jersey, 07458. USA.

Jensen, J. 2005. *Introductory Digital Image Processing – a Remote Sensing Perspective*. Third Edition. Pearson Prentice Hall, Upper Saddle River, New Jersey, 07458. USA.

Jensen, J. 2000. *Remote Sensing of the Environment: An Earth Resource Perspective*. Pearson Prentice Hall, Upper Saddle River, New Jersey 07458.

Kaya, S. 2000. Determination of Geomorphological Characteristics around of the Isiklar Mountain by Using Remote Sensed Data and DEM. International Archives of Photogrammetry and Remote Sensing. Vol. XXXIII, Part B7 Amsterdam 2000.

Kristen, M. Brubaker, Wayne, L. Myers, P. J. Drohan, D., Miller, A. and Elizabeth, Boyer., W, 2013. The Use of LiDAR Terrain Data in Characterizing Surface Roughness and Microtopography. Hindawi Publishing Corporation Applied and Environmental Soil Science, Volume 2013, Article ID 891534, 13 pages http://dx.doi.org/10.1155/2013/891534.

Lillesand, T. M. and Keifer, R. W. 2000. *Remote Sensing and Image Interpretation*. Fourth Edition, John Wiley & Sons, Inc.

Liu, J.-K.. Hsiao, K.-H. and Peter Shih, P. T.-Y., 2012. A Geomorphological Model for Landslide Detection Using Airborne LiDAR Data. Journal of Marine Science and Technology, Vol. 20, No. 6, pp. 629-638 (2012) DOI: 10.6119/JMST-012-0412-1.

Migoń, P., Kasprzak, Andrzej, M., Traczyk., 2013. How high-resolution DEM based on airborne LiDAR helped to reinterpret landforms – examples from the Sudetes, SW Poland. Landform Analysis, Vol. 22, 89–101, 2013, doi: http://dx.doi.org/10.12657/landfana.022.007.

Podobnikar, T., 2010. Geomorphic Analysis of the low quality digital elevation model. 13th AGILE International Conference on Geographic Information Science 2010 Guimarães, Portugal.

Podobnikar, T., 2005. Production of integrated digital terrain model from multiple datasets of different quality. International journal of geographical information science, Taylor & Frances, 19/1, 69–89.

Tomljenovic, I. and Rousell, A., 2014. Influence of point cloud density on the results of automated ObjectBased building extraction from ALS data. Proceedings of the AGILE'2014, International Conference on Geographic Information Science, Castellón, June, 3-6, 2014. ISBN: 978-90-816960-4-3.

Trevisani, S., Cavalli, M., and Marchi, L., 2010. Reading the bed morphology of a mountain stream: a geomorphometric study on high-resolution topographic data. Hydrol. Earth Syst. Sci., 14, 393–405, 2010. www.hydrol-earth-syst-sci.net/14/393/2010/.

Trevisani, S., Cavalli, M., and Marchi., L. 2009. Variogram maps from LiDAR data as fingerprints of surface morphology on scree slopes. Nat. Hazards Earth Syst. Sci., 9, 129–133, 2009 www.nat-hazards-earth-syst-sci.net/9/129/2009/

Werbrouck, I.; Antrop, M.; Eetvelde, V.; Stal, C.; Maeyer, P.; Bats, M.; Bourgeois, J.; Court-Picon, M.; Crombé, P.; De Reu, J.; De Smedt, P.; Finke, P.A.; Van Meirvenne, M.; Verniers, J.; Zwertvaegher, A. 2011. Digital elevation model generation for historical landscape analysis based on LiDAR data, a case study in Flanders (Belgium). Expert Systems with Applications, Vol. 38 (7), p. 8173-8185. doi: 10/1016/j.eswa.2010.12.162.

COMPARISON OF AIRBORNE LIDAR SYSTEM CALIBRATION ALGORITHMS

M. Miller[a], A. Habib[a]

[a]Digital Photogrammetry Research Group
Lyles School of Civil Engineering
Purdue University, 550 Stadium Mall Dr., West Lafayette, IN 47907, USA
-(mill1154, ahabib)@purdue.edu

KEY WORDS: Airborne LiDAR, system calibration, systematic errors, mounting parameters

ABSTRACT:

With light detection and ranging (LiDAR) systems being a crucial technology for on the fly mapping and spatial analysis, the user community needs to have standardized LiDAR system calibration procedures that are robust for the wide range of users and scenarios. This study compares three existing approaches for airborne LiDAR system calibration; namely, Simplified, Quasi-Rigorous, and Rigorous LiDAR calibrations. In lieu of using expensive control surfaces for LiDAR system calibration, these methods compare overlapping LiDAR strips and they differ based on the level of detail needed. Two of them have certain assumptions on the data that pertain to characteristics like flight geometry. This study further characterizes these algorithms by observing the calibration outcome when the data collection deviates from the specific assumptions. It was observed that when deviating from the assumptions, some of the biases are estimated correctly but some of them differ from their true value. Even though all biases are not estimated correctly, a significant increase in accuracy is obtainable.

1. INTRODUCTION

A LiDAR system refers to the laser-ranging unit as well as the integrated direct geo-referencing system. The direct geo-reference system is comprised of a Global Navigation Satellite System (GNSS) and an Inertial Navigation System (INS). In addition to each component of the LiDAR system having many advances in the past decade, the airborne platforms have had significant advances. Together, these advances have accelerated the growing use and application of LiDAR systems because they are more accurate, readily available, and not as costly. With the large user community and its continual increase, development of standard operating procedures for LiDAR system modeling and calibration will ensure that the systems consistently meet industry standards. A reliable mathematical model relates all system parameters and system measurements from each component in order to calculate each point's ground coordinates. In addition to that, the appropriate model should include parameters that account for systematic errors within the LiDAR system. Quality assurance (QA) and quality control (QC) procedures are needed to maintain quality throughout all preparation, collection, and data delivery steps. The prominent QA procedure is calibration, which is needed to accurately decouple and estimate system parameters. This minimizes the impact of systematic errors on the resulting point cloud.

Often times, LiDAR system calibration is done by the data provider and is considered a trade secret, while quality control(QC), is traditionally done by the end user and is done in order to prove the completeness and correctness of the LiDAR product (Bang et al., 2010). The end user does not always have access to the raw measurements of the LiDAR system, which has resulted in the development of many heuristic approaches to calibration that don't require them. Since these heuristic approaches often degrade (or have the potential to degrade) the homogeneity of the point clouds, this study focuses on some specific system calibration approaches that have been developed to address the absence of raw measurements, while preserving the rigor of calibration by securing the use of the sensor model. The three LiDAR calibration methods used in this study are named the Simplified, the Quasi-Rigorous, and the Rigorous. The three methods each have certain assumptions with respect to the collection and system that conclusively define the data required for each calibration. The Simplified only requires point clouds while the other two require additional information such as the integrated GNSS/INS positions and orientations, and the LiDAR unit measurements. Because the Simplified calibration has the most assumptions it requires the least amount of input information, while the Rigorous approach has no assumptions yet requires the most information. The details of these calibrations can be found in Habib et al. (2010) and Kersting (2011). This research will investigate the impact on parameter estimation after violating these assumptions. The background information for understanding these calibration methods are presented in section 2, derivations of the calibration procedures will be covered in section 3, and the results and conclusions will be covered in sections 4 and 5, respectfully.

2. LIDAR SYSTEM CALIBRATION BACKGROUND

2.1. LiDAR Point Positioning Equation

The common approach to determine the coordinate values of each LiDAR pulse involves many coordinate systems which are shown in Figure 1 and are well documented in Kersting (2011), and Shan and Toth (2009). The notation of spatial offsets and rotations are detailed below.

a) $\boldsymbol{r}_{\boldsymbol{a}}^{\boldsymbol{b}}$ denotes the spatial offset between point $\boldsymbol{a}$ and a coordinate system associated with point $\boldsymbol{b}$

b) $\boldsymbol{R}_{\boldsymbol{a}}^{\boldsymbol{b}}$ denotes the rotation matrix to apply in order to get from coordinate system $\boldsymbol{a}$ to coordinate system $\boldsymbol{b}$

In the *laser beam* coordinate system ($\boldsymbol{lb}$), the coordinates of object point $\boldsymbol{l}$ are represented by Eq. (1), if the z-axis positive direction is in the same direction or opposite direction of the laser beam the top

and bottom sign is used repsectively. In the LiDAR unit coordinate system (***lu***), the coordinates of point ***l*** are defined by Eq. (2). In the inertial Measurement Unit (IMU) body frame (***b***), the coordiantes of point ***l*** are defined by Eq. (3). In the mapping reference frame (***m***), the coordiantes of point ***l*** are defined by Eq. (4).

$$r_l^{lb} = \begin{bmatrix} 0 \\ 0 \\ \pm\rho(t) \end{bmatrix} \quad (1)$$

$$r_l^{lu} = R_{lb}^{lu}(t)\, r_l^{lb}(t) \quad (2)$$

$$r_l^{b} = r_{lu}^{b} + R_{lu}^{b} R_{lb}^{lu}(t) r_l^{lb}(t) \quad (3)$$

$$r_l^{m} = r_b^{m}(t) + R_b^{m}(t) r_{lu}^{b} + R_b^{m}(t) R_{lu}^{b} R_{lb}^{lu}(t) r_l^{lb}(t) \quad (4)$$

Note that this LiDAR point-positioning equation does not have redundancy for deriving the ground coordinates. It is a summation of system parameters and direct measurements. This characteristic plays a major role in the evaluation of the positional quality of LiDAR point clouds (Habib et al., 2009).

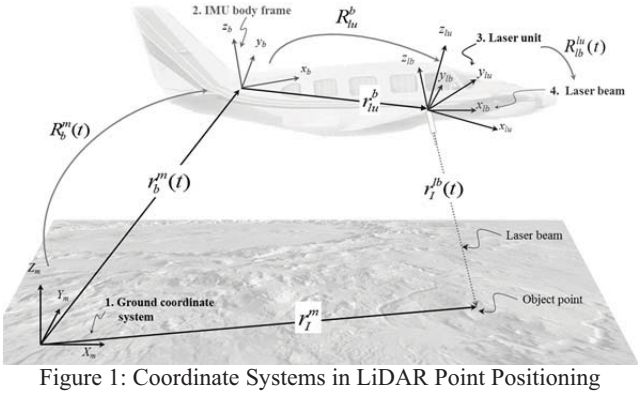

Figure 1: Coordinate Systems in LiDAR Point Positioning Equation (Habib et al., 2009)

2.2. Theoretical Basis of LiDAR System Calibration

The calibration process provides the values of the system parameters by modeling the scanning, ranging, and positioning process, which allows for reconstructing the point cloud as close as possible to the true representation. There are two different sets of system parameters. The first consists of the parameters within the LiDAR unit and are referred to as *internal characteristics.* They include the range (ρ) offset: $\Delta\rho$, and the scan angle (β) scale factor: $\boldsymbol{S}$. The internal characteristics are well documented in (Baltsavias, 1999) and (Schenk, 2001). The second set of system parameters is referred to as the *mounting parameters*. They include the lever arm (r_{lu}^{b}) components: $[\Delta X \quad \Delta Y \quad \Delta Z]^T$, and the boresight ($R_b^m$) components: $[\Delta\omega \quad \Delta\boldsymbol{\varphi} \quad \Delta\kappa]^T$. This concept is analogous to the system calibration process in photogrammetry where we find the interior orientation parameters (IOPs) and the mounting parameters, the IOPs concept of the camera is similar to that of the internal characteristics of a LiDAR unit. The calibration uses the initial values of the system parameters but then strategically determines their refined values by comparing overlapping strips and control information.

2.3. Data Collection for LiDAR System Calibration

The calibration process is carried out by detecting and minimizing discrepancies that inhibit the compatibility of overlapping point clouds, or of point clouds and control information. In order to determine the optimal and minimal flight configuration that maximizes the visibility of discrepancies, the impact of the biases should be determined. The impacts have been mathematically derived in previous research (Habib et al., 2009), and are shown in Table *1*. They are based on the following assumptions: **a)** The IMU body frame is aligned with its $\boldsymbol{x_b}$, $\boldsymbol{y_b}$, and $\boldsymbol{z_b}$ axes pointing in starboard, flight, and up directions, respectively, **b)** The airborne platform is flying with a constant heading along the South-to-North and North-to-South directions. These flight lines will be denoted as *forward* and *backward,* **c)** The IMU body frame and the laser unit coordinate systems are almost parallel to each other with small boresight angles ($\boldsymbol{\Delta\omega, \Delta\varphi, \Delta\kappa}$). **d)** We are dealing with a linear scanner that maps a flat terrain across the flight direction. If there is double signage on a term in Table *1* or any following equation, the top sign represents the forward flight and the bottom sign represents the backward flight.

Table 1: Effects of Biases on Each Component of the Reconstructed Coordinate (Habib et al., 2009)

	$\boldsymbol{\delta X_m}$	$\boldsymbol{\delta Y_m}$	$\boldsymbol{\delta Z_m}$
$\boldsymbol{\delta\Delta X}$	$\pm\delta\Delta X$	0	0
$\boldsymbol{\delta\Delta Y}$	0	$\pm\delta\Delta Y$	0
$\boldsymbol{\delta\Delta Z}$	0	0	$\delta\Delta Z$
$\boldsymbol{\delta\Delta\omega}$	0	$\mp z\delta\Delta\omega$	0
$\boldsymbol{\delta\Delta\varphi}$	$\pm z\delta\Delta\varphi$	0	$-x\delta\Delta\varphi$
$\boldsymbol{\delta\Delta\kappa}$	0	$\pm x\delta\Delta\kappa$	0
$\boldsymbol{\delta\Delta\rho}$	$\mp\sin(S\beta)\,\delta\Delta\rho$	0	$-\cos(S\beta)\,\delta\Delta\rho$
$\boldsymbol{\delta S}$	$\pm z\beta\delta S$	0	$-x\beta\delta S$

If a term from Table 1 has the double signage, $\pm$ or $\mp$, it is *flying direction dependent*. The only time this is not true is when a term includes, $\pm$ or $\mp$, in addition to the lateral distance, x, the scan angle, β, or the sine of the scan angle, $\sin(\beta)$. For example, a term with $\pm x$ is not flying direction dependent because the sign of x also changes for forward and backward flights, thus negating the flying direction dependence. If a term has x or $\boldsymbol{\beta}$ in it, then it is *scan angle dependent*, and if a term has z in it then it is *flying height dependent*. It can be concluded from this table that in order to estimate all of the biases there should be three total strip-pairs. The phrase, *strip-pair*, is used to denote two overlapping flight strips that we have chosen to compare. The first two strip-pairs should have a forward and backward flight with almost 100% overlap, but the two strip-pairs should be at different flying heights. The third strip-pair should be two parallel flight lines of the same direction with about 50% overlap (Bang et al., 2010). The effect that the heading bias, $\boldsymbol{\delta\Delta\kappa}$, has on the object space coordinates is detectable with the pair going in the same direction. The bias in the leverarn in the along the flight direction, $\boldsymbol{\delta\Delta Y}$, and the bias in the pitch, $\boldsymbol{\delta\Delta\omega}$, are highly correlated and must be decoupled by using two flying heights (Habib et al., 2010). The $\boldsymbol{Z}$ component of the lever-arm is usually very good, but it is coupled with the bias in the range measurement. The Quasi-rigorous and Rigorous calibration methods are able to determine the bias in the range measurement because it can only be determined through the use of external control and the current implementation of the

Simplified method does not allow the use of control (Habib et al., 2010).

These calibration methods entail a matching procedure which is based on using distinct points as conjugate features. However, it is not guaranteed that the same exact point will occur in overlapping strips because LiDAR data is irregular. Other research has used higher level features, such as planes or lines as conjugates (Vosselman, 2002), but with that approach the mathematical relationship between the features and the system parameters to be estimated is lost (Skaloud,and Lichti, 2006). Since using points as conjugates is the only way to preserve the crucial relationship between the features and the sensor model, conjugate points are heuristically approached with a procedure called iterative closest patch (ICPatch). ICPatch performs the matching procedure by comparing discrete points in one scan and triangular irregular networks (TIN) in the other scan and is well documented in Habib et al. (2009) and Bang (2010).

3. CALIBRATION ALGORITHM METHODOLOGY

The following calibration derivations show how assumptions are used when there is a full or partial unavailability of raw measurements. The *raw measurements* being referred to here, consist of the position and orientation of the IMU body frame interpolated at the time of the individual laser pulses, $\boldsymbol{r_b^m(t)}$ and $\boldsymbol{R_b^m(t)}$, respectively, as well as the ranges and mirror angles needed to define $\boldsymbol{r_I^{lu}(t)}$.

3.1. Rigorous Calibration Procedure

The calibration mathematical model follows upon the established theoretical basis of comparing overlapping point clouds, and control information. The point-positioning equation (4) is represented in a symbolic form in Eq. (5). The system parameters are represented as $\boldsymbol{x}$ and the system measurements are represented as $\boldsymbol{y}$**.** The noise that is contaminating the system measurements is $\boldsymbol{e}$, and $\boldsymbol{\Sigma}$ represents the variance-covariance matrix of that noise vector. The two flight lines within a strip-pair are denoted by subscripts $\boldsymbol{A}$ and $\boldsymbol{B}$. Eq. (6) represents the mathematical relationship between conjugate points. It states that conjugate points should have identical coordinates after removing the noise impact ($\boldsymbol{e_A}$ and $\boldsymbol{e_B}$), and using the true values of system parameters $\boldsymbol{x}$. In order to be used in a Least Squares Adjustment, that equation must be linearized, which is shown on the right side of Eq. (7). The terms, $\boldsymbol{f_A}$ and $\boldsymbol{f_B}$, are the predicted point cloud coordinates reconstructed with the noise-contaminated measurements and the approximate values for the system parameters, for flight lines $\boldsymbol{A}$ and $\boldsymbol{B}$, respectively. These are the coordinates of the initial point cloud before calibration. The Jacobian matrices in Eq. (7), $\boldsymbol{J_{x_A}}$ and $\boldsymbol{J_{x_B}}$, are relative to the system parameters, and, $\boldsymbol{J_{y_A}}$ and $\boldsymbol{J_{y_B}}$, are relative to system measurements. The Jacobian matrices are evaluated using the available measurements and the approximate system parameter values. The theoretical basis of the proposed LiDAR calibration algorithm here is that we compare the point clouds and use the discrepancies to estimate the unknown system parameters. Therefore, we take the predicted coordinates, $\boldsymbol{f_A}$ and $\boldsymbol{f_B}$, and put them on the left side leaving the values to be estimated on the right side. This leads to the final representation of the calibration math model, Eq. (8). Note that these calibration algorithms also carry the uncertainty values, so that the uncertainty of the estimated system parameters can be stochastically determined through error propagation.

$$r_I^m = f(y - e, x)\ \&\ e \sim (0, \Sigma) \tag{5}$$

$$r_{I_A}^m - r_{I_B}^m = f(y_A - e_A, x) - f(y_B - e_B, x) = 0 \tag{6}$$

$$r_{I_A}^m - r_{I_B}^m \approx f_A - f_B + J_{x_A}\delta x - J_{y_A}e_A - J_{x_B}\delta x + J_{y_B}e_B \tag{7}$$

$$f_A - f_B = \left(J_{x_B} - J_{x_A}\right)\delta x + \left(J_{y_A}e_A - J_{y_B}e_B\right)$$
$$\left(J_{y_A}e_A - J_{y_B}e_B\right) \sim (0, J_{y_A}\Sigma_A J_{y_A}^T + J_{y_B}\Sigma_B J_{y_B}^T) \tag{8}$$

Control surfaces are not largely needed for these calibration procedures, but as stated before in section 2.3, control information in the $\boldsymbol{Z}$ direction is necessary if either the lever arm bias in the $\boldsymbol{Z}$ direction or the range bias need to be detected and estimated. Eq. (9) through Eq. (11) parallels the sequence of Eq. (6) thorough Eq. (8), except that the conjugate point is now a control point instead of a point from flight line $\boldsymbol{B}$. The noise-free control point is represented as $\boldsymbol{r_{I_C}^m}$, and the noise-contaminated control point is represented as $\boldsymbol{r_{I_{C_o}}^m}$. The noise contaminating the control point is represented as $\boldsymbol{e_C}$, and its variance-covariance matrix is represented as $\boldsymbol{\Sigma_C}$. Equations (8) and (11) are simultaneously used in a Least Squares Adjustment to solve for the unknown system parameters.

$$r_{I_A}^m - r_{I_C}^m = f(y_A - e_A, x) - \left(r_{I_{C_o}}^m - e_C\right) = 0\ \&\ e_C \sim (0, \Sigma_C) \tag{9}$$

$$r_{I_A}^m - r_{I_C}^m \approx f_A - r_{I_{C_o}}^m + J_{x_A}\delta x - J_{y_A}e_A + e_C \tag{10}$$

$$f_A - r_{I_{C_o}}^m = -J_{x_A}\delta x + \left(J_{y_A}e_A - e_C\right)$$
$$\left(J_{y_A}e_A - e_C\right) \sim (0, J_{y_A}\Sigma_A J_{y_A}^T + \Sigma_C) \tag{11}$$

3.2. Quasi-Rigorous Calibration Procedure

The Quasi-Rigorous (QR) calibration is developed assuming we have the time-tagged point clouds and time-tagged position information of the trajectory. This excludes the raw measurements, $\boldsymbol{R_b^m(t)}$, and $\boldsymbol{r_I^{lu}(t)}$. The calibration will be very similar to the procedure outlined in the Rigorous derivation, but the missing raw measurements will need to be synthesized using the given point cloud and trajectory positions. In order to effectively synthesize the measurements, the data should follow certain assumptions. Such as, the IMU body frame is aligned with its $\boldsymbol{x_b}$, $\boldsymbol{y_b}$, and $\boldsymbol{z_b}$ axes pointing in starboard, flight, and up directions, respectively. The IMU body frame and the LiDAR unit coordinate system are almost parallel to each other with small boresight angles $\boldsymbol{(\Delta\omega, \Delta\varphi, \Delta\kappa)}$ describing their rotational relationship, thus simplifying the rotation matrix through the algebraic small angle approximation. We are dealing with a linear, vertical scanner that maps the terrain across the flight direction. Therefore, the coordinates of a given point $\boldsymbol{I}$ relative to the LiDAR unit coordinate system $\boldsymbol{r_I^{lu}(t)}$ can be represented by the lateral and vertical distances between the flight trajectory and the point in question, $\boldsymbol{x(t)}$ and $\boldsymbol{z(t)}$, respectively.

These assumptions simplify the LiDAR point-positioning equation (4) into Eq. (12).

$$r_I^m = r_b^m(t) + \begin{bmatrix} \cos(\kappa) & -\sin(\kappa) & 0 \\ \sin(\kappa) & \cos(\kappa) & 0 \\ 0 & 0 & 1 \end{bmatrix} \begin{bmatrix} \Delta x \\ \Delta y \\ \Delta z \end{bmatrix} + \begin{bmatrix} \cos(\kappa) & -\sin(\kappa) & 0 \\ \sin(\kappa) & \cos(\kappa) & 0 \\ 0 & 0 & 1 \end{bmatrix} \begin{bmatrix} 1 & -\Delta\kappa & \Delta\varphi \\ \Delta\kappa & 1 & -\Delta\omega \\ -\Delta\varphi & \Delta\omega & 1 \end{bmatrix} \begin{bmatrix} x(t) \\ 0 \\ z(t) \end{bmatrix} \quad (12)$$

This calibration is based on biased time-tagged point cloud coordinates (i.e., they have been derived through inaccurate/biased system parameters) as opposed to the Rigorous where it is based on the raw measurements and system parameters. Once the impact from the biases is accounted for, the discrepancy equations can be formed in the same manner they were for the Rigorous calibration (but there is no linearization step). The discrepancy equations can be evaluated using the raw measurements synthesized from the time-tagged point clouds and system trajectory. The synthesized raw measurements should be derived according to the steps outlined in the research of Habib et al.(2010) and Bang (2010).

3.3. Simplified Calibration Procedure

The Simplified calibration can be used when the system raw measurements are fully unavailable. The Simplified calibration is markedly different from the other two because instead of iterating on the system parameter estimation, there is a direct estimation via a linear relationship. The linear relationship relates the magnitudes and the directions of the observed discrepancies to the nature of the biases. However, such a mathematical relationship can only be derived by imposing specific assumptions on the data. The Simplified calibration holds all the same assumptions as the Quasi-Rigorous and more. The additional assumptions state that the terrain variation should be much smaller when compared with the flying height above ground, and the flight lines should be parallel. In addition to those assumptions the XY-axes of the mapping reference frame should be defined at the average terrain elevation, and should be defined such that the Y-axis is half-way between the flight lines in question. The Y-axis should also be aligned along the flight direction, ensuring that the strips are flown in the South-to-North and North-to-South directions. These reference frame manipulations and the two assumptions specific to this calibration allow the flying height above ground, $\boldsymbol{z(t)}$, to be assumed as a constant, and denoted as $\boldsymbol{z}$. With these assumptions, the LiDAR point-positioning equation, Eq. (4), simplifies into Eq. (13).

$$r_I^m = r_b^m(t) + \begin{bmatrix} \pm\Delta x \\ \pm\Delta y \\ \Delta z \end{bmatrix} + \begin{bmatrix} \pm x(t) \pm z\,\Delta\varphi \\ \pm x(t)\,\Delta\kappa \mp z\,\Delta\omega \\ z - x(t)\,\Delta\varphi \end{bmatrix} \quad (13)$$

After accounting for the impact of the biases, two cases of the discrepancy equation can be developed. The current implementation of the Simplified calibration does not incorporate control and therefore does not have a discrepancy equation for that scenario, as the other calibrations do. The Simplified calibration performs a series of substitutions with the discrepancy equations to define a relationship that does not require the system raw measurements. The series of substitutions uses the term, $\boldsymbol{D}$, the lateral distance between the two flight lines in question. This is possible because of the assumptions and reference frame manipulations mentioned above. The steps used to reformulate the discrepancy equations are detailed in Habib et al.(2010) and Bang (2010). From these steps, it can be observed that flight lines of the same direction result in a constant shift in **X**, **Y**, and **Z**, and a rotation around the Y-axis of the pre-defined mapping frame. These shifts and the rotation are related to the biases according to Eq. (14). The variables $\boldsymbol{H}$ and $\boldsymbol{\beta_T}$ are the flying height and the maximum scan angle, respectively.

$$\begin{bmatrix} X_T \\ Y_T \\ Z_T \\ \varphi \end{bmatrix} = \begin{bmatrix} -D/H\delta\Delta\rho - \mathrm{H}\beta_\mathrm{T}\delta S \\ -D\delta\Delta\kappa \\ D\delta\Delta\varphi \\ 2\beta_T\delta S \end{bmatrix} \quad (14)$$

The steps also reveal the observation that flight lines going in opposite directions introduce a constant shift in **X** and **Y**, as well as a rotation around the Y-axis of the pre-defined mapping frame. These shifts and the rotation are related to the biases according to Eq. (15).

$$\begin{bmatrix} X_T \\ Y_T \\ \varphi \end{bmatrix} = \begin{bmatrix} 2\delta\Delta x - 2H\delta\Delta\varphi \mp D/H\delta\Delta\rho \mp H\beta_T\delta S \\ 2\delta\Delta\mathrm{Y} + 2\mathrm{H}\delta\Delta\omega \mp D\delta\Delta\kappa \\ 2\delta\Delta\varphi \pm 2\beta_T\delta S \end{bmatrix} \quad (15)$$

Thus, the Simplified calibration procedure relates the detected discrepancy between overlapping strips, which can be modeled by three shifts and a rotation angle across the Y-axis of the mapping reference frame, to the biases in the system parameters.

4. RESULTS

The goal of these tests is to investigate the impact on system parameter estimations after violating the calibration assumptions. The incorporation of control is not an outlined assumption, but a test was included to see how the impact of the number of control points affects the bias estimations. Some of the assumptions outlined in the derivations are not included in this study because if they are not followed, then the data can simply be mathematically manipulated in order that the assumption is met.

The point clouds used in these tests are generated by simulating flights over a USGS generated Digital Elevation Model (DEM), which does not have any man-made objects such as buildings with gable roofs. The DEM height ranges from 0m to 100m, with a standard deviation of 18.2m. The figure below shows the result of two flight lines flown over the DEM (the headings of the flight lines in this simulation happen to differ by 30 degrees). It would be optimal to perform these tests on real data, but the simulated data is adequate enough in order to have a grasp on the impact each test has.

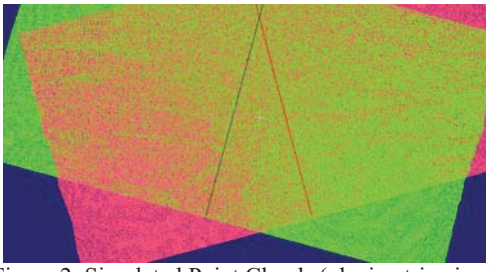

Figure 2: Simulated Point Clouds (planimetric view)

For the simulation, the user defines the LiDAR unit specifications and the uncertainty of each measurement in the system. For the specifications, the pulse rate was set at 33.3 kHz, the scan rate was set at 40 (scans/sec), and the laser angle at 30 degrees. The uncertainty values are in Table *2*, which are used to generate random noise for each linear and angular measurement per pulse.

Table 2: Uncertainty of the LiDAR System Components Used in these Experiments

Uncertainty of LiDAR System Components	
GNSS – X, Y, Z (m)	0.05, 0.05, 0.10
INS - ω, φ, κ (")	9, 9, 18
Mirror Angle Encoder (")	3
Range (m)	0.02

Table *3* represents the expected accuracy of the adjusted coordinates, computed by taking the root mean squared error (RMSE) between the true coordinates and the coordinates with noise. If we were using non-simulated data these values would not be available, and the results would be compared to the results from rigorous error propagation in Table *4* (which are very similar to the values in Table *3*). The estimated parameters from the calibration should be compared with the simulated parameters, which are shown on the left side of result tables. An RMSE analysis was done on the coordinates before calibration and after calibration, Which compares the RMSE of the biased and true coordinates with the RMSE of the adjusted and true coordinates. The RMSE after calibration will be compared to the values from Table *3*. The biased coordinates are contaminated with noise and biases, as is the case in a real world scenario. The true coordinates have no noise and no biases, and the adjusted coordinates are the result of adjusting the biased coordinates with the calibration results. It is worth noting that the Simplified and Quasi-Rigorous calibrations use biased coordinates in their respective discrepancy equations (derived above), whereas the Rigorous discrepancy equations use the system parameters and measurements.

Table 3: Expected Accuracy of Calibrated LiDAR Coordinates

Expected Accuracy of Calibrations (RMSE of Noisy & Error Free Coordinates)	
X	0.096
Y	0.100
Z	0.105

Table 4: Error Propagation at Various Scan Angles

Uncertainty of LiDAR Coordinates			
uncertainty (m)	0° scan angle	15° scan angle	30° scan angle
sigma X	0.112	0.110	0.101
Sigma Y	0.108	0.116	0.136
Sigma Z	0.102	0.105	0.113

4.1. Deviating From the Parallel Flight Lines Assumption

The Simplified calibration requires that the flight lines be parallel to each other in order for the point positioning equation used within the calibration to be valid. Four different tests were done with varying levels of deviation from parallel. Their results are listed in the columns of Table *5*.

Table 5: Simplified Calibration Results with Parallel and Non-Parallel Flight Lines

		Simplified Calibration Results			
		0° Deviation	**10° Deviation**	**20° Deviation**	**30° Deviation**
Simulated Biases					
δΔX (m) :	0.200	0.205	**0.237**	**0.259**	**0.282**
δΔY (m):	0.200	0.189	0.188	0.186	0.197
δΔω ("):	36.000	37.013	36.364	36.692	35.688
δΔφ ("):	36.000	35.993	34.704	33.053	31.300
δΔκ ("):	36.000	34.653	37.735	45.743	**51.379**
δS:	0.00100	0.00096	**0.00080**	**0.00073**	**0.00055**

For the case where there is no deviation in Table *5*, it is observed the estimated biases are very close to the simulated biases and the RMSE values after calibration in Table *6* meet the expected RMSE of 10cm (Table *3*). The comparison between the before and after calibration RMSE values shows an 84%, 82%, and 60% increase in accuracy for the **X**, **Y**, and **Z** coordinate, respectively. By inspecting the after calibration RMSE in Table *6* we can see that as the flight lines are deviated further and further from parallel the ***X*** coordinate accuracy consistently falls. This is due to the bias estimations in the leverarn in the across flight direction, $\boldsymbol{\delta\Delta x}$, and in the scan angle scale factor bias, $\boldsymbol{\delta S}$, degrading as the flight lines are deviated. The scan angle scale factor bias additionally affects the **Z** coordinate, which is also degrading in accuracy with the deviating flight lines. The estimation of the bias in the heading, $\boldsymbol{\delta\Delta\kappa}$, starts to degrade after the 20 degree deviation, and its affect on the **Y** coordinate accuracy is observable in the 30 degrees deviation. When comparing the RMSE before and after calibration, we can see that even when some of the estimated biases differ from their simulated value, there are still significant accuracy increases after the calibration. At the various deviations, the **X** coordinate accuracy increases by 70%-50% percent, the **Y** by 80%, and the **Z** by 60% to 40%.

Table 6: RMSE Analysis of Simplified Calibration Results with Parallel and Non-Parallel Flight Lines

		RMSE Before and After Simplified Calibration			
		0° Deviation	**10° Deviation**	**20° Deviation**	**30° Deviation**
coordinate		**Before Calibration: Difference of Biased & True Coordinates**			
X	RMSE	0.575	0.521	0.511	0.458
	($\bar{x}$,σ)	(-8.2e-02,5.7e-01)	(-6.7e-02,5.2e-01)	(-7.1e-02,5.1e-01)	(-6.4e-02,4.5e-01)
Y	RMSE	0.565	0.505	0.503	0.516
	($\bar{x}$, σ)	(5.2e-01,2.1e-01)	(1.7e-01,4.8e-01)	(1.9e-01,4.7e-01)	(2.0e-01,4.8e-01)
Z	RMSE	0.26	0.254	0.255	0.231
	($\bar{x}$, σ)	(1.6e-01,2.0e-01)	(1.5e-01,2.0e-01)	(1.5e-01,2.1e-01)	(1.3e-01,1.9e-01)
coordinate		**After Calibration: Difference of Adjusted & True Coordinates**			
X	RMSE	0.093	0.144	0.174	0.239
	($\bar{x}$, σ)	(8.1e-04,9.3e-02)	(-1.7e-02,1.4e-01)	(-4.1e-02,1.7e-01)	(-7.4e-02,2.3e-01)
Y	RMSE	0.099	0.101	0.106	0.121
	($\bar{x}$, σ)	(8.6e-04,9.9e-02)	(-2.4e-05,1.0e-01)	(-6.4e-03,1.1e-01)	(-2.2e-02,1.2e-01)
Z	RMSE	0.105	0.114	0.118	0.133
	($\bar{x}$, σ)	(-1.0e-04,1.0e-01)	(-3.1e-02,1.1e-01)	(-3.8e-02,1.1e-01)	(-5.6e-02,1.2e-01)

4.2. Deviating from the Terrain Relief Assumption

The Simplified calibration requires the terrain relief to be relatively low with respect to the flying height in order for the point positioning equation to be valid. The two calibrations below show how the bias estimations change when we deviate from the low terrain relief assumption.

Table 7: Simplified Calibration Results Before and After Deviating From the Terrain Relief Assumption

		Simplified Calibration Results	
		100m Range Terrain Relief	**300m Range Terrain Relief**
Simulated Biases		**Estimated Biases**	
δΔX (m) :	0.200	0.205	0.230
δΔY (m):	0.200	0.189	**0.116**
δΔω (''):	36.000	37.013	43.869
δΔφ (''):	36.000	35.993	37.437
δΔκ (''):	36.000	34.653	**24.910**
δS:	0.00100	0.00096	**0.00132**

Table 8: RMSE Analysis of Simplified Calibration Results Before and After Deviating From the Terrain Relief Assumption

		RMSE Before & After Simplified Calibration	
		100m Range Terrain Relief	**300m Range Terrain Relief**
coordinate		**Before Calibration: Difference of Biased & True Coordinates**	
X	RMSE	0.575	0.336
	($\bar{x}$, σ)	(-8.2e-02,5.7e-01)	(-1.1e-01,3.2e-01)
Y	RMSE	0.565	0.453
	($\bar{x}$, σ)	(5.2e-01,2.1e-01)	(1.8e-01,4.2e-01)
Z	RMSE	0.26	0.177
	($\bar{x}$, σ)	(1.6e-01,2.0e-01)	(6.7e-02,1.6e-01)
coordinate		**After Calibration: Difference of Adjusted & True Coordinates**	
X	RMSE	0.093	0.131
	($\bar{x}$, σ)	(8.1e-04,9.3e-02)	(-3.3e-02,1.3e-01)
Y	RMSE	0.099	0.094
	($\bar{x}$, σ)	(8.6e-04,9.9e-02)	(5.3e-03,9.3e-02)
Z	RMSE	0.105	0.108
	($\bar{x}$, σ)	(-1.0e-04,1.0e-01)	(1.8e-02,1.1e-01)

The calibration and RMSE results for the *100m range Terrain* results are the same as the *0° Deviation* scenario from the previous section and are shown again in Table *7* for a side by side comparison to the new results. When the terrain releif is not releatively low compared to the flying height, as is the case in the 300m range scenario, it is observed that the leverarm bias in the flight direction, $\boldsymbol{\delta\Delta y}$, the bias in the heading, $\boldsymbol{\delta\Delta\kappa}$, and the bias in the scan angle scale factor, $\boldsymbol{\delta S}$, estimations are significantly different than their simulated values. The leverarm bias in the across flight direction, $\boldsymbol{\delta\Delta x}$, is also affected by this high variation in terrain height. In *Table 8,* the after calibration RMSE of the **X** coordinate increased due to the inaccurate bias estimations in the leverarm bias in the across flight direction, $\boldsymbol{\delta\Delta x}$, and the scan angle scale factor bias, $\boldsymbol{\delta S}$. Therefore, it does not meet the expected value of 10cm from Table *3*. The inaccurate bias estimations in the leverarm in the flight direction, $\boldsymbol{\delta\Delta y}$, and the heading bias, $\boldsymbol{\delta\Delta\kappa}$, both affect the **Y** coordinate accuracy, but a decreased accuracy is not observed for **Y** in Table *8* because their impacts have canceled each other out. In conclusion, even though the terrain relief assumption is not followed, the comparison of the RMSE values for before and after the calibration reduces by 61%, 80%, and 39% for the **X**, **Y**, and **Z** coordinates, respectively.

4.3. Deviating From the Vertical Scanner Assumption

The Simplified and the Quasi-Rigorous calibrations require the scanner to be vertical in order for the point positioning equation used within the calibration to be valid. Meaning, the pitch and roll of the platform should be approximately zero. The calibrations have been run with two different scenarios to show how the bias estimations change when we deviate from this assumption. The first calibration is done with a vertical scanner and the second is done with the platform pitch and roll at 8 degrees. The calibration and RMSE results for the *Vertical Scanner* are the same as the *0° Deviation* scenario and are shown again for a side by side comparison to the new results.

Table 9: Simplified Calibration Results Before and After Deviating From the Vertical Scanner Assumption

	Simplified Calibration Results		
		Vertical Scanner	Non-Vertical Scanner
Simeanlated Biases		**Estimated Biases**	
δΔX (m) :	0.200	0.205	0.197
δΔY (m):	0.200	0.189	**0.144**
δΔω (''):	36.000	37.013	40.289
δΔφ (''):	36.000	35.993	**2.785**
δΔκ (''):	36.000	34.653	33.539
δS:	0.00100	0.00096	0.00098

Table 10: RMSE Analysis of Simplified Calibration Results Before and After Deviating From the Vertical Scanner Assumption

		RMSE Before & After Simplified Calibration	
		Vertical Scanner	Non-Vertical Scanner
coordinate		**Before Calibration: Difference of Biased & True Coordinates**	
X	RMSE	0.575	0.478
	($\bar{x}$, σ)	(-8.2e-02,5.7e-01)	(-1.4e-02,4.8e-01)
Y	RMSE	0.565	0.492
	($\bar{x}$, σ)	(5.2e-01,2.1e-01)	(1.7e-01,4.6e-01)
Z	RMSE	0.26	0.286
	($\bar{x}$, σ)	(1.6e-01,2.0e-01)	(2.0e-01,2.1e-01)
coordinate		**After Calibration: Difference of Adjusted & True Coordinates**	
X	RMSE	0.093	0.283
	($\bar{x}$, σ)	(8.1e-04,9.3e-02)	(-1.0e-01,2.7e-01)
Y	RMSE	0.099	0.101
	($\bar{x}$, σ)	(8.6e-04,9.9e-02)	(1.5e-03,1.0e-01)
Z	RMSE	0.105	0.133
	($\bar{x}$, σ)	(-1.0e-04,1.0e-01)	(2.7e-02,1.3e-01)

When the scanner is set in a non-vertical orientation, it is observed that the leverarm bias in the flight direction, $\boldsymbol{\delta\Delta y}$, and the bias in the roll, $\boldsymbol{\delta\Delta\phi}$, are significantly different than their simulated values. In Table *10*, the after calibration RMSE value for the **X** and **Z** coordinates increased due to the inaccurate bias estimations in the roll, $\boldsymbol{\delta\Delta\phi}$. Therefore, they do not meet the expected value of 10cm from Table *3*. The inaccurate bias estimation of the leverarm in the flight direction, $\boldsymbol{\delta\Delta y}$, impacts the **Y** coordinate, but that impact is canceled out by the impacts from the slightly degraded estimations in the pitch bias, **δΔω**, and the heading bias, **δΔκ**. The calibration reduced the RMSE values by 41%, 80%, and 53% for the **X**, **Y**, and **Z** coordinates, respectively, when compared to the before calibration RMSE values. Although this scenario violated the assumptions there is still a significant increase in the accuracy.

Table 11: Quasi-Rigorous Calibration Results Before and After Deviating From the Vertical Scanner Assumption

	Quasi-Rigorous Calibration Results		
		Quasi-Rig	Quasi-Rig
Simeanlated Biases		**Estimated Biases**	
δΔX (m) :	0.200	0.201	0.182
δΔY (m):	0.200	0.198	**0.157**
δΔω (''):	36.000	35.959	40.139
δΔφ (''):	36.000	36.120	**3.666**
δΔκ (''):	36.000	35.946	30.273
δS:	0.00100	0.00100	0.00100

Table 12: RMSE Analysis of Quasi-Rigorous Calibration Results Before and After Deviating From the Vertical Scanner Assumption

		RMSE Before & After Quasi-Rigorous Calibration	
		Vertical Scanner	Non-Vertical Scanner
coordinate		**Before Calibration: Difference of Biased & True Coordinates**	
X	RMSE	0.575	0.478
	($\bar{x}$, σ)	(-8.2e-02,5.7e-01)	(-1.4e-02,4.8e-01)
Y	RMSE	0.565	0.492
	($\bar{x}$, σ)	(5.2e-01,2.1e-01)	(1.7e-01,4.6e-01)
Z	RMSE	0.26	0.286
	($\bar{x}$, σ)	(1.6e-01,2.0e-01)	(2.0e-01,2.1e-01)
coordinate		**After Calibration: Difference of Adjusted & True Coordinates**	
X	RMSE	0.093	0.261
	($\bar{x}$, σ)	(8.1e-04,9.3e-02)	(-9.1e-02,2.4e-01)
Y	RMSE	0.099	0.102
	($\bar{x}$, σ)	(8.6e-04,9.9e-02)	(9.9e-05,1.0e-01)
Z	RMSE	0.105	0.131
	($\bar{x}$, σ)	(-1.0e-04,1.0e-01)	(2.6e-02,1.3e-01)

When the scanner is non-vertical for the Quasi-Rigorous calibration, the results are quire similar to the Simplified non-vertical scenario. The **X** and **Z** coordinate accuracies lowered due to the inaccurate bias estimations in the roll, $\boldsymbol{\delta\Delta\phi}$, and therefore do not meet there expected accuracy of 10cm. The inaccurate bias estimations in the leverarm in the flight direction, $\boldsymbol{\delta\Delta y}$, impacts the **Y** coordinate, but that impact is canceled out by the impacts from the slightly degraded estimations in the pitch bias, **δΔω**, and the heading bias, **δΔκ**. Even thought the assumption was not followed, the calibration reduced the RMSE values by 45%, 80%, and 55% for the **X**, **Y**, and **Z** coordinates, respectively, when compared to the before calibration RMSE values.

4.4. Investigating the Number of Control Points

The Quasi-rigorous and Rigorous calibrations have the option to incorporate vertical control which is needed to estimate the bias in the range measurement. The calibrations below compare the results that had 10 control points versus results that had 100 control points. *Table 13* shows that the Quasi-Rigorous calibration is not significantly different between the case with 10 control points and the case with 100 control points. Similarly, it can be observed from the calibration results in *Table 15* that the Rigorous calibration is not sensitive to the amount of control either.

Table 13: Quasi-Rigorous Calibration Results While Varying the Number of Control Points

	Quasi-Rigorous Calibration Results		
		15 Control Points	100 Control Points
Simulated Biases		**Estimated Biases**	
δΔX (m) :	0.200	0.205	0.211
δΔY (m):	0.200	0.196	0.194
δΔω (''):	36.000	36.888	37.095
δΔφ (''):	36.000	36.423	36.498
δΔκ (''):	36.000	34.703	35.425
dS:	0.00100	0.00099	0.00100
δΔρ (m):	0.300	0.314	0.305

Table 14: Quasi-Rigorous Calibration Results While Varying the Number of Control Points

		RMSE Before & After Quasi-Rigorous Calibration	
		15 Control Points	**100 Control Points**
coordinate		**Before Calibration: Difference of Biased & True Coordinates**	
X	RMSE	0.597	0.598
	($\bar{x}$, σ)	(-4.4e-02,5.9e-01)	(-4.5e-02,5.9e-01)
Y	RMSE	0.498	0.496
	($\bar{x}$, σ)	(1.8e-01,4.7e-01)	(1.8e-01,4.6e-01)
Z	RMSE	0.246	0.239
	($\bar{x}$, σ)	(-1.6e-01,1.9e-01)	(-1.5e-01,1.9e-01)
coordinate		**After Calibration: Difference of Adjusted & True Coordinates**	
X	RMSE	0.092	0.092
	($\bar{x}$, σ)	(-9.5e-05,9.2e-02)	(2.1e-04,9.2e-02)
Y	RMSE	0.099	0.100
	($\bar{x}$, σ)	(-1.4e-03,1.0e-01)	(-1.4e-03,1.0e-01)
Z	RMSE	0.107	0.105
	($\bar{x}$, σ)	(2.3e-02,1.0e-01)	(1.2e-02,1.0e-01)

Table 15: Rigorous Calibration Results While Varying the Number of Control Points

Rigorous Calibration Results			
		15 Control Points	**100 Control Points**
Simulated Biases		**Estimated Biases**	
δΔX (m) :	0.200	0.198	0.195
δΔY (m):	0.200	0.205	0.196
δΔω ("):	36.000	35.084	36.654
δΔφ ("):	36.000	35.817	35.941
δΔκ ("):	36.000	37.136	37.136
dS:	0.00100	0.00101	0.00100
δΔρ (m):	0.300	0.296	0.308

Table 16: Rigorous Calibration Results While Varying the Number of Control Points

		RMSE Before & After Rigorous Calibration	
		15 Control Points	**100 Control Points**
coordinate		**Before Calibration: Difference of Biased & True Coordinates**	
X	RMSE	0.595	0.597
	($\bar{x}$, σ)	(-4.5e-02,5.9e-01)	(-4.5e-02,5.9e-01)
Y	RMSE	0.496	0.496
	($\bar{x}$, σ)	(1.7e-01,4.6e-01)	(1.7e-01,4.6e-01)
Z	RMSE	0.233	0.236
	($\bar{x}$, σ)	(-1.4e-01,1.9e-01)	(-1.4e-01,1.9e-01)
coordinate		**After Calibration: Difference of Adjusted & True Coordinates**	
X	RMSE	0.092	0.092
	($\bar{x}$, σ)	(4.8e-04,9.2e-02)	(5.6e-04,9.2e-02)
Y	RMSE	0.100	0.100
	($\bar{x}$, σ)	(3.8e-04,1.0e-01)	(4.7e-04,1.0e-01)
Z	RMSE	0.107	0.105
	($\bar{x}$, σ)	(-4.8e-04,1.0e-01)	(-8.7e-04,1.0e-01)

Both the RMSE results after calibration from the Quasi-Rigorous and Rigorous meet the expected accuracy of 10cm. When comparing the before RMSE with the after RMSE in Table *14* for the Quasi-Rigorous and Table *16* for the Rigorous, the RMSE values decreased by 85%, 80%, and 60% for the **X**, **Y**, and **Z** coordinates, respectively, after both calibrations.

5. CONCLUSIONS AND FUTURE WORK

The patterns revealed through this series of tests help to characterize the Simplified, Quasi-Rigorous, and Rigorous calibrations. Inspecting which biases are, or are not, effected when we deviate from the assumptions guides the process of understanding which coordinates are effected. The bias estimations with the non-parallel flight lines, high terrain relief, and non-vertical scanner are expected to degrade because their respective calibration math model and algorithm does not account for these deviations. Even though they do not account for any of the deviations tested here, the after calibration RMSE still significantly increased by 40-80% when compared to the before calibration RMSE, depending of the test and coordinate. To expand upon this suite of calibration methods, a new calibration will be developed that has all the capabilities of the Quasi-Rigorous method but does not require the time-tagged trajectory like the Quasi-Rigorous method does. Other future work includes developing standard operating procedures for a stability analysis of LiDAR system calibration methods in order to determine how long the calibrated system parameters last before a new calibration should be done.

REFERENCES

Baltsavias, E., 1999. Airborne laser scanning: existing systems and firms and other resources, *ISPRS Journal of Photogrammetry and Remote Sensing*, 54(2-3):164–198.

Bang, K., 2010. *Alternative Methodologies for LiDAR System Calibration,* Ph.D. dissertation, Department of Geomatics Engineering, University of Calgary, Canada, 160 p.

Habib, A. F., Bang, K.I., Kersting, A., and Lee D.C., 2009. Error budget of LiDAR systems and quality control of the derived data, *Photogrammetric Engineering and Remote Sensing*, Vol. 75, No. 9, pp. 1093-1108.

Habib, A. F., Bang, K.I., Kersting, A., and Lee D.C., 2009. Alternative Methodologies for LiDAR System Calibration, *Remote Sensing*, 2(3), pp. 1093-1108.

Kersting, A., 2011. *Quality Assurance of Multi-Sensor Systems,* Ph.D. dissertation, Department of Geomatics Engineering, University of Calgary, Canada, 265 p.

Schenk, T., 2001. *Modelling and Analyzing Systematic Errors in Airborne Laser Scanners*, Technical Notes in Photogrammetry, Vol. 19, The Ohio State University, Columbus, US.

Shan, J. and Toth, C. K., 2009. *Topographic Laser Ranging and Scanning*, CRC Press, Boca Raton, US, 590p.

Skaloud, J. and Lichti, D., 2006. Rigorous approach to boresight self-calibration in airborne laser scanning, *ISPRS Journal of Photogrammetry and Remote Sensing*, Vol. 61, No. 6, pp. 47-59.

Vosselman, G., 2002. Strip offset estimation using linear features, *3rd International Workshop on Mapping Geo-Surfical Processes using Laser Altimetry*, [CDROM]. 7-9 May, Columbus Ohio, US.

ON THE DEVELOPMENT OF A REGIONAL IONOSPHERIC CORRECTION MODEL FOR LOW-COST SINGLE FREQUENCY GNSS USERS

Mohamed Abdelazeem[a,*], Rahmi N. Çelik[b], Ahmed El-Rabbany[c]

[a] Civil Engineering Department, Aswan University, Egypt- m.abdelazeem@aswu.edu.eg
[b] Geomatics Engineering Department, Istanbul Technical University, Turkey- celikn@itu.edu.tr
[c] Civil Engineering Department, Ryerson University, Toronto, Canada- rabbany@ryerson.ca

KEY WORDS: Ionosphere modeling, single-frequency PPP, Total electron content, Differential code bias

ABSTRACT:

Modeling the ionosphere vertical total electron content (VTEC) and its spatiotemporal characteristics are crucial for low-cost single-frequency precise point positioning (PPP) users. This, however, requires that the differential code bias (DCB) for both of the satellite and the receiver be rigorously accounted for. For this purpose, an ionospheric model using GNSS observations from a regional network is developed. The proposed model has a spatial and temporal resolutions of 1º×1º and 15 minutes, respectively. The GNSS observations are processed using the Bernese 5.2 software package in order to extract the geometry-free linear combination of the smoothed code observations. The spherical harmonic expansion function is used for modeling the VTEC and the receiver/satellite DCBs. To validate the developed model, the VTEC values are estimated and compared with the final international GNSS service-global ionospheric map (IGS-GIM) counterparts over three different days. Additionally, the satellite and the receiver DCB values are determined and compared with the IGS-GIM counterparts. The findings reveal that the estimated VTEC and DCBs are comparable to the IGS-GIM counterparts.

1. INTRODUCTION

Ionospheric delay is currently the dominant error source for low-cost single-frequency precise point positioning (PPP) users. Therefore, the availability of a precise ionospheric correction model is crucial for precise positioning applications. A number of models have been developed in order to account for the vertical total electron content (VTEC) and its spatiotemporal characteristics, including the widely used International GNSS Service Global Ionospheric Maps (IGS-GIMs). Unfortunately, however, the IGS-GIM model has a limited spatiotemporal resolution, which may not be adequate for single-frequency PPP applications.

To precisely estimate the VTEC, the differential code bias (DCB) for the both of the satellite and the receiver must be accounted for. Differential code bias is the difference in code hardware delays at two different frequencies. The receiver DCB values are not stable over one day, while the satellite DCBs are stable (Schaer, 1999).

A number of ionospheric delay correction models have been developed by a number of researchers (e.g., Tu et al. 2013; Durmaz and Karslioglu 2015; Hoque and Jakowski, 2015; Kao et al. 2015; Li et al. 2015; Rovira-Garcia et al., 2015; Xi et al. 2015; Abdelazeem et al. 2016a, 2016b). Durmaz and Karslioglu (2015) developed a regional model for VTEC, satellite and receiver DCB using the multivariate adaptive regression B-splines (SP-BMARS) method. To examine their proposed model, the VETC values were computed and compared with the center for orbit determination in Europe global ionospheric maps (CODE-GIMs) counterparts. In addition, the satellite and receiver DCBs were estimated and compared with the CODE counterparts. The results demonstrated that their model showed good agreement with the CODE counterparts.

This study aims to develop a regional vertical total electron content, satellite and receiver differential code biases estimation model over Europe. The developed model has a spatial and temporal resolutions of 1º×1º and 15 minutes, respectively. GNSS observations from 60 reference stations are processed using the Bernese 5.2 software package in order to extract the VTEC, satellite and receiver DCB values. The VTEC values obtained through the proposed model are compared with the IGS-GIMs counterparts in three different days in order to represent the ionosphere seasonal variation. Moreover, the satellite and the receiver DCBs are computed and compared with the IGS-GIMs counterparts. It is shown that our developed model has a good agreement with the IGS-GIMs counterparts.

2. IONOSPHERIC MODEL DEVELOPMENT

The basic GNSS code observation equations can be written as follows (Kleusberg and Teunissen, 1998):

$$P_1 = \rho_r^s + c(dt_r - dt^s) + I_{r,1}^s + T_r^s + c\left(d_{r,1} + d_1^s\right) + \varepsilon_{p,1} \qquad (1)$$

$$P_2 = \rho_r^s + c(dt_r - dt^s) + I_{r,2}^s + T_r^s + c\left(d_{r,2} + d_2^s\right) + \varepsilon_{p,2} \qquad (2)$$

where P_1 and P_2 are the pseudorange measurements on L_1 and L_2, respectively; ρ_r^s is the satellite-receiver true geometric range; c is the speed of light in vacuum; dt_r and dt^s are the receiver and satellite clock errors, respectively; $I_{r,1}^s$ and $I_{r,2}^s$ are the ionospheric delay on L_1 and L_2, respectively; T_r^s is the tropospheric delay; d_r and d^s are the code hardware delay for the receiver and the satellite, respectively; ε_p is the code unmodeled errors, including noise and multipath.

To remove the geometrical term, tropospheric delay, receiver and satellite clock errors, the geometry-free linear combinations of code observations are used. It can be obtained by subtracting the simultaneous un-differenced code as follows (Dach et al., 2015):

$$P_4 = \tilde{P_1} - \tilde{P_2} = MF \times K \times VTEC + c(DCB^s + DCB_r) \quad (3)$$

where P_4 is the geometry-free linear combination of the smoothed code observations; $\tilde{P_1}$ and $\tilde{P_2}$ are the smoothed code observations on L_1 and L_2, respectively; MF is the ionospheric mapping function; K is frequency-dependent factor; $VTEC$ is the ionosphere vertical total electron content; DCB^s and DCB_r are the differential code biases for the satellite and the receiver, respectively.

The frequency-dependent factor can be expressed as follows:

$$K = \frac{40.3(f_1^2 - f_2^2)}{(f_1^2 f_2^2)} \quad (4)$$

where $f_1$and f_2 are the carrier phase frequencies on L_1 and L_2 signals. The mathematical expression for the ionospheric mapping function can be written as follows (Dach et al., 2015):

$$MF = \left[cos\left(arcsin\left(\frac{R}{R+H}sin(z)\right)\right)\right]^{-1} \quad (5)$$

where z is the satellite's zenith distance at receiver; R is the mean radius of the Earth, and H is the effective height of ionosphere thin shell layer. This effective height corresponds to the maximum electron density at the F_2 peak, which ranges from 350 km to 450 km.

In order to model the VTEC on a regional scale, the spherical harmonic expansion function is used depending upon the geographic latitude (β) and the sun-fixed (s) longitude of the ionosphere pierce point (IPP), respectively (Schaer, 1999):

$$E(\beta, s) = \sum_{n=0}^{n_{max}} \sum_{m=0}^{n} \bar{P}_{nm}(\sin\beta)\,(a_{nm}\cos ms + b_{nm}\sin ms) \quad (6)$$

where n_{max} is the maximum degree of the spherical harmonic expansion; $\bar{P}_{nm}$ are normalized associated Legendre functions of degree n and order m; a_{nm} and b_{nm} are the unknown coefficients of spherical harmonics.

Substituting Equations 4, 5 and 6 into Equation 3, the ionospheric spherical harmonic model can be expressed as:

$$\sum_{n=0}^{n_{max}} \sum_{m=0}^{n} \bar{P}_{nm}(sin\,\beta)\,(a_{nm}\,cos\,ms + b_{nm}\,sin\,ms) = \left(\frac{f_1^2 f_2^2}{40.3(f_1^2 - f_2^2)}\right) * cos\left(arcsin\left(\frac{R}{R+H}sin(\alpha z)\right)\right) * [P_4 - c(DCB^s + DCB_r)\,] \quad (7)$$

where a_{nm}, b_{nm}, DCB^s and DCB_r are the unknowns parameters to be estimated.

In order to separate the DCBs of the satellites and receivers, an additional constraint must be used. It assumes that the sum of the satellite differential code biases is zero as follows (Dach et al., 2015).

$$\sum_{s=1}^{s=max} DCB^s = 0 \quad (8)$$

3. METHODOLOGY

In order to develop the proposed ionospheric delay correction model, a regional network consisting of 60 IGS and EUREF reference stations in Europe has been used (Figure 1). As shown in Figure 1 that the station distribution is homogenous and represents different latitudes in order to reflect different ionospheric characteristics. GNSS observations for three different days (day 150, 220 and 360 in year 2013) have been downloaded (IGS, 2017) to reflect the ionospheric seasonal variations in May, August and December, respectively. The geomagnetic and solar activities indices for the three days under consideration are given in Table 1 (OMNIWeb, 2017). It is shown that the geomagnetic activity is quiet, while is the solar activity is medium in the three examined days.

Each observation file has a 24-hour time span and a 30-second time interval. An elevation cut-off angle of 15º has been used. The Bernese 5.2 software package has been used in order to process the observation files. To extract the VTEC, the satellite and the receiver DCBs, the IGS final satellite orbit, satellite clock and earth orientation parameters have been used (IGS, 2017) and then have been converted into the Bernese formats. The un-differenced code observations have been smoothed. In the parameters estimation process, the effective height has been selected to be 450 km. In addition, a maximum degree and order equal to 6 of the spherical harmonic expansion have been selected with a 15-minute interval. A group of 49 coefficients of the spherical harmonic model has been obtained each time epoch. The spatial and temporal resolution of the extracted VTEC map is 1º×1º and 15 minutes, respectively.

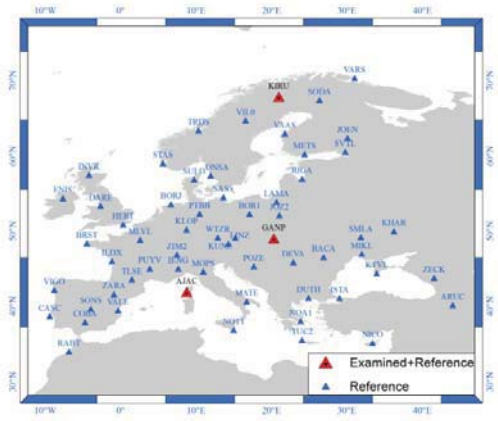

Figure 1. Distribution of reference and examined stations

Table 1. $F_{10.7}$ and A_P indices for the examined days (OMNIWeb, 2017)

DOY	A_p-index	$F_{10.7}$ -index
150	2	106.9
220	3	107.3
360	2	120.6

4. RESULTS AND ANALYSIS

In order to evaluate the proposed model, the satellite differential code biases are estimated. Thereafter, the estimated satellite DCBs are compared with the IGS-GIMs counterparts for the three days under consideration. Figure 2 shows the standard

deviation (STD) for the differences. It is shown that the estimated satellite DCB values are closer to the IGS-GIMs counterparts with STD values less than 0.6 ns.

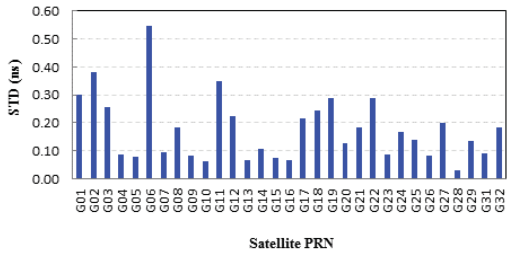

Figure 2. STD for the estimated satellite DCB compared with the IGS-GIM.

Moreover, the receiver DCBs for three stations are computed. The examined stations are located at different latitude with different receiver types (Table 2). The estimated receiver DCBs are compared with the IGS-GIMs counterparts.

Table 2. Examined stations characteristics

Station	Latitude	Longitude	Receiver type
AJAC	41.9275º	8.7626º	LEICA GR25
GANP	49.0347º	20.3229º	TRIMBLE NETR9
KIRU	67.8574º	20.9684º	SEPT POLARX4

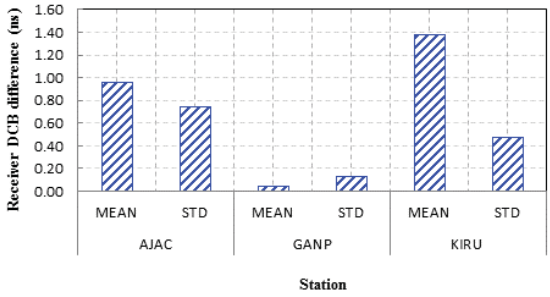

Figure 3. Differences of the estimated receiver DCB

Figure 3 illustrates the mean and STD values for the differences between the estimated receiver DCBs and the IGS-GIMs counterparts. As shown in Figure 3, the estimated receiver DCB have good agreement with the IGS-GIMs counterparts with mean difference values less than 1.4 ns and STD values less than 0.8 ns.

To further assess the developed model, the vertical total electron values over the three examined stations are computed. Then, the estimated values are compared with the IGS-GIMs counterparts for the three days under consideration. For illustration purposes, only the VTEC profiles for stations AJAC, GANP and KIRU, respectively on DOY 220 are given in Figure 4.

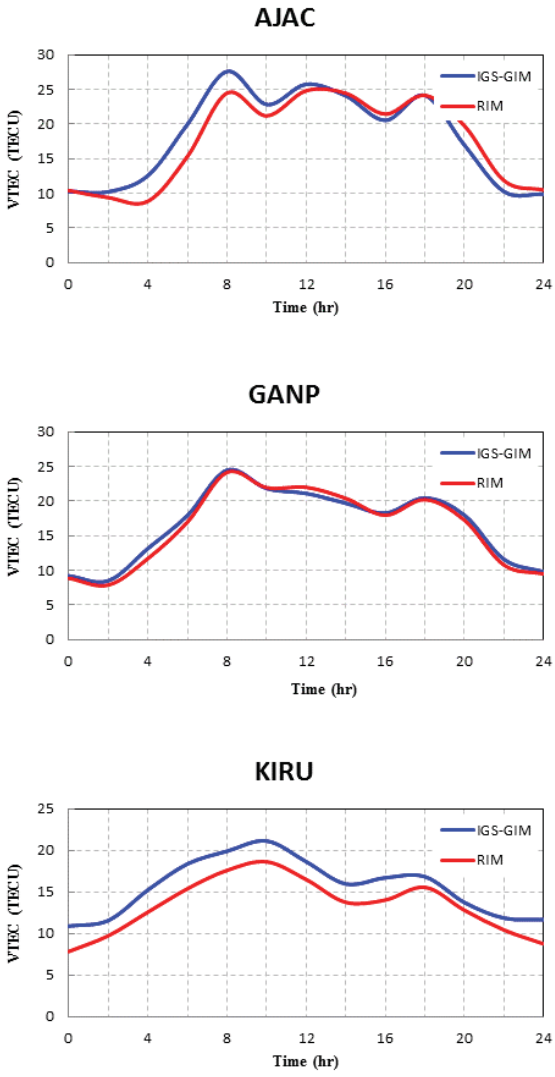

Figure 4. VTEC profiles at stations AJAC, GANP and KIRU, respectively on DOY 220.

It is shown that the estimated VTEC values are closer to the IGS-GIMs counterparts at station GANP. Also, the differences at stations AJAC and KIRU are slightly large. This can be attributed to the station location, as station AJAC is located at the border of our model. In addition, station KIRU is located at a high latitude.

The distribution of the vertical total electron content at stations AJAC, GANP and KIRU are shown in Figure 5. Also, the mean and STD values are computed and given in Figure 5.

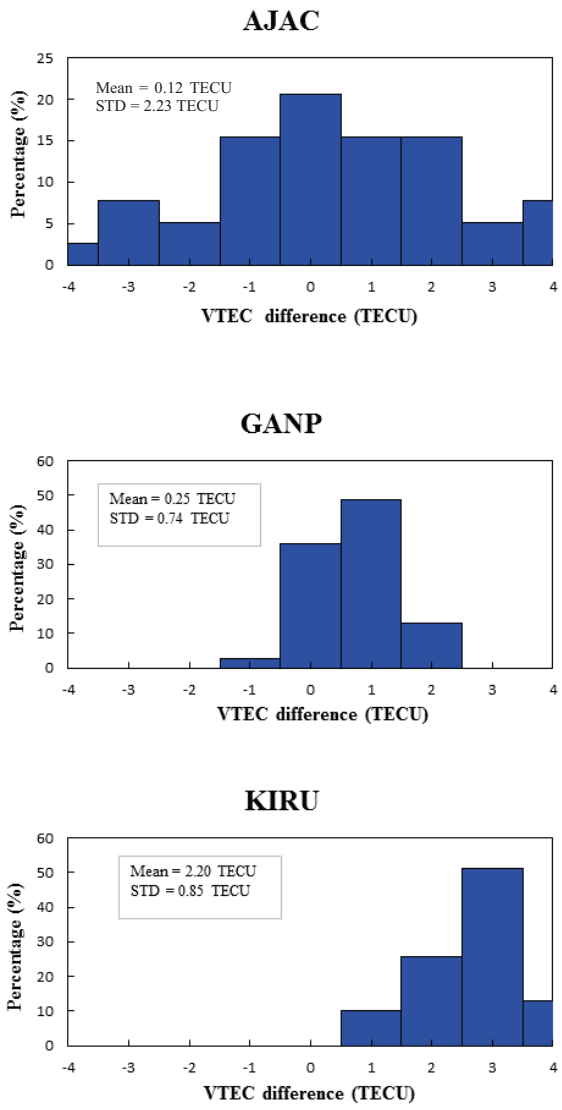

Figure 5. Distributions of VTEC differences at stations AJAC, GANP and KIRU, respectively.

As shown in Figure 5, the difference between the estimated VTECs and the IGS-GIMs is a function of the station location. This is particularly true for station AJAC, which is located at the border of the developed model.

5. CONCLUSION

In this study, a regional ionospheric correction model for low-cost single frequency GNSS users in Europe has been developed. GNSS observations from a regional network have been processed using the Bernese 5.2 software package. The spherical harmonic expansion function has been used to model the VTEC and the satellite and receiver DCBs. The vertical total electron contents have been estimated at a 1º×1º and a 15-minute spatial and temporal resolutions, respectively. To assess the developed model, the satellite DCBs have been estimated. In addition, the receiver DCBs for three different stations located at different latitudes, which are occupied by different receiver types, have been computed. It has been shown that the estimated DCBs agree with those of the final IGS-GIMs with a standard deviation less than 0.8 ns. As well, the values of the estimated VTEC were comparable to the final IGS-GIM counterparts.

REFERENCES

Abdelazeem, M., Çelik, R. N. and El-Rabbany, A., 2016a. An enhanced real-time regional ionospheric model using IGS real-time service (IGS-RTS) products. *Journal of Navigation*, 69, 521-530.

Abdelazeem, M., Çelik, R. N. and El-Rabbany, A., 2016b. An improved regional ionospheric model for single-frequency GNSS users. *Survey Review*, doi: 10.1080/00396265.2016.1138581.

Dach, R., Lutz, S., Walser, P. and Fridez, P., 2015. Bernese GNSS Software Version 5.2. Astronomical Institute, University of Berne (AIUB).

Durmaz, M. and Karslioglu, M. O., 2015. Regional vertical total electron content (VTEC) modeling together with satellite and receiver differential code biases (DCBs) using semi-parametric multivariate adaptive regression B-splines (SP-BMARS). *Journal of Geodesy*, 89, 347-360.

Hoque, M. M. and Jakowski, N., 2015. An alternative ionospheric correction model for global navigation satellite systems. *Journal of Geodesy*, 89, 391-406.

International GNSS Service, IGS, 2017. ftp://cddis.gsfc.nasa.gov/. Accessed on March 1st, 2017.

Kao, S.-P., Chen, Y.-C., Ning, F.-S. and Tu, Y.-M., 2015. An LS-MARS method for modeling regional 3D ionospheric electron density based on GPS data and IRI. *Advances in Space Research*, 55, 2256-2267.

Kleusberg, A. and Teunissen, P.J.G., 1998. GPS for Geodesy. Springer-Verlag, Berlin.

Li, Z., Yuan, Y., Wang, N., Hernandez-Pajares, M. and Huo, X. 2015. SHPTS: towards a new method for generating precise global ionospheric TEC map based on spherical harmonic and generalized trigonometric series functions. Journal of Geodesy, 89, 331-345.

OMNIWeb,2017. http://omniweb.gsfc.nasa.gov/form/ dx1.html. Accessed on March 1st, 2017.

Rovira-Garcia, A., Juan, JM., Sanz, J. and Gonzalez-Casado, G. 2015. A worldwide ionospheric model for fast precise point positioning. *IEEE Transactions on Geoscience and Remote Sensing* 53, 4596-4604.

Schaer, S. 1999. Mapping and predicting the earth's ionosphere using the global positioning system. PhD Thesis. University of Bern, Switzerland.

Tu, R., Zhang, H., Ge, M. and Huang, G., 2013. A real-time ionospheric model based on GNSS precise point positioning. *Advances in Space Research*, 52, 1125–34.

Xi, G., Zhu, F., Gan, Y. and Jin, B. 2014. Research on the regional short-term ionospheric delay modeling and forecasting methodology for mid-latitude area. *GPS Solutions*, 19, 457-465.

Segmentation-based Classification of Point Cloud Data

Y.J. Lin [a, *], A. Habib [a]

[a] Digital Photogrammetry Research Group
Lyles School of Civil Engineering
Purdue University, 550 Stadium Mall Dr., West Lafayette, IN 47907, USA
- (lin599, ahabib)@purdue.edu

KEY WORDS: Segmentation, Classification, Ground, Building, Pole-like feature, Vegetation

ABSTRACT:

Point cloud modeling and interpretation have been an essential task for many applications such as digital building model generation, urban planning, and as-built documentation of industrial sites. Non-structured point clouds, which do not possess any semantic information, need to undergo a sequence of data processing steps to derive the necessary information for 3D modeling and interpretation. For feature extraction and object modeling, segmentation is an important step to categorize the constituents of a point cloud into subgroups that share similar characteristics. For point cloud interpretation and object recognition, classification plays an important role in providing high-level of contextual information.
In this paper, we introduce a segmentation-based point cloud classification strategy that partitions a point cloud into ground, building, pole-like features, vegetation, and unknown regions. For deriving the classification geometric attributes, the point cloud is partitioned through a simultaneous multi-class region-growing segmentation procedure, where planar, linear/cylindrical, and rough segments are identified. Then, the segmentation results are refined through a quality control procedure. The geometric attributes of segments can provide useful information for a list of classifiers. The paper demonstrates the feasibility of the proposed method through the classification results from a real dataset.

1. INTRODUCTION

With the development of new and innovative techniques for 3D data collection and processing, ways of describing and modeling 3D environment have undergone dramatic changes in recent years. In the past few decades, optical imagery from outer space satellites to the ubiquitous cameras and laser scanners that can acquire or derive point clouds are used to reconstruct our surroundings. However, raw 3D point cloud data is discrete and unstructured without semantic information. Therefore, point clouds must be processed to extract useful information for further applications, such as digital building model generation, urban planning (Gonzalez-Aguilera, et al. 2013), cultural heritage documentation (Alshawabkeh and Haala, 2004), and change detection. Object modeling and interpretation are the major research areas that deal with describing 3D environments. Due to the complex nature of the real world, automatic feature extraction and classification of objects from non-semantic and unstructured point cloud is a critical issue. Therefore, in this paper, we propose a method to partition point cloud and augment the derived segments with high-level contextual information such as ground, building, pole-like feature, and vegetation.

For extracting features and modeling objects, segmentation is an important technique to categorize point cloud into subgroups that share similar characteristics. Segmentation approaches can be generally classified as being either spatial or parameter domain. For the spatial-domain approach (e.g., region-growing based segmentation), a point cloud is segmented into subgroups according to the spatial proximity and similarity of local attributes. The local neighborhood could be derived through three different approaches, digital surface model (DSM), triangulated irregular network (TIN), and point cluster (Rottensteiner and Briese, 2002; Vosselman et al., 2004; Rabbani et al., 2006). Yang and Dong (2013) derived geometric attributes from point cluster and classified points into planar, linear, and spherical categories using Support Vector Machine (SVM). Then, region growing is applied according to the attribute similarities of each point such as principal direction, normal vector, and intensity. The spatial domain region growing methods are usually preferred due to their computational efficiency. However, their performance is quite sensitive to noise level within the point cloud in question as well as the selected seed-points/regions (Wang and Shan, 2009; Awwad et al., 2010; Lari and Habib, 2014).

On the other hand, for the parameter domain approach, every point is associated with a feature vector according to certain defined attributes. The feature vectors are incorporated into parameter domain and then, peak-detection techniques are applied for extracting the points with similar features as segments. Sampath and Shan (2010) derived the surface normal through Voronoi neighborhood and then, the surface normal of all planar points are clustered through the fuzzy k-means method. Lari and Habib (2014) introduced an approach to classify individual points as either belonging to planar or linear/cylindrical local neighborhoods using Principal Component Analysis (PCA). Then, the attributes are transformed into a parameter-domain where the peak is determined through octree-based peak detection approach. Parameter-domain segmentation techniques do not depend on seed points. However, the identification of peaks in the

* Corresponding author

constructed attribute space is a time-consuming process, whose complexity depends on the dimensionality of the involved feature vector (Wang and Shan, 2009).

For object interpretation and recognition from a point cloud, classification plays an important role in providing high-level contextual information. Classification approaches can be categorized into classifier-based and supervised-based classification. Both classification approaches require feature attributes related to classified targets (e.g., area and shape). The classifier-based classification can be used for general category classification (e.g., ground, non-ground classification (Meng et al., 2010)) based on some criteria and thresholds without training data. Chang et al. (2008) utilized the fact that sudden elevation changes, which usually correspond to non-ground objects, to separate ground and non-ground points. Carlberg et al. (2009) used 3D shape analysis and region growing to identify planar and rough regions and proposed a list of classifiers to identify water, ground, roof, and tree features from airborne LiDAR Data. Moussa and El-Sheimy (2010) used area growing technique to extract patches based on neighborhood height similarity. The extracted patches are classified according to their area into buildings, vegetation, and ground. Lafarge and Mallet (2012) used geometric attributes (e.g., non-planarity, elevation, scatter, and regular grouping) to classify point cloud into buildings, vegetation, ground, and clutter. Then, building points are used for modeling. Cabo et al. (2014) simplified the point cloud through voxel-based structure, and utilized the pole-like characteristics, planimetric voxel size, and spatial relationship, to extract pole-like features.

On the other hand, supervised-based classification categorizes data based on its similarity to the training data using decision tree. This approach can classify data into more categories (e.g., tree species classification) but training data is required. Samadzadegan and Ramzi (2010) proposed a classifier fusion system scheme based on SVM for classification of LiDAR data into building, tree, and ground with the help of training data. Shapovalov and Velizhev (2011) trained non-associative Markov Network in a principled manner using a structured SVM to classify point cloud into ground, buildings, cars, trees, and vehicles. Weinmann et al. (2014) defined twenty-one geometric 3D and 2D feature characteristics to categorize point cloud into wires, poles/trunks, façades, ground, and vegetation through a supervised-based classification.

In this paper, we propose a segmentation-based point cloud classification strategy that classifies a given point cloud into ground, buildings, pole-like features, vegetation, and unknown categories. A multi-class simultaneous region-growing segmentation is applied to extract the segments and their geometric information (e.g., planar, linear/cylindrical, and rough) for the classification. The geometric features of segments can provide useful information for the classifier. The feasibility of the proposed classification strategy is demonstrated through classification results from a real dataset. Based on the obtained results, the paper finally makes some conclusions and recommendations for future work.

2. METHODOLOGY OF SEGMENTATION AND CLASSIFICATION

This section provides the methodology for classifying derived segments according to their geometric attributes. First, a given point cloud is partitioned into planar, linear/cylindrical, and rough segments through multi-class simultaneous segmentation. Then, the derived segments are improved and validated through a quality control procedure and then, are categorized into ground, buildings, pole-like features, vegetation, and unknown regions through a sequence of classifiers. The flowchart of the proposed methodology is shown in Figure 1.

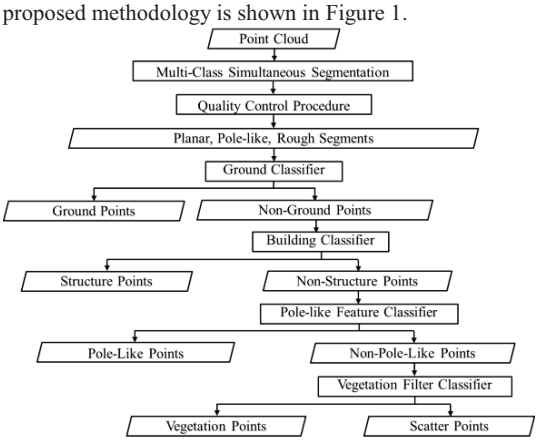

Figure 1. Flowchart of the proposed segmentation and classification

2.1 Multi-Class Simultaneous Segmentation

The multi-class simultaneous segmentation (Habib and Lin, 2016) is applied to a given point cloud for grouping points that share similar characteristics and deriving geometric attribute for each subgroup. Through this segmentation, we simultaneously extract planar, linear/cylindrical, and rough segments.

First, a set of seed points is established based on a random selection of pre-specified percentage of points. A local neighborhood for each seed point (seed region) is established. For each seed region, we perform a PCA to decide whether such seed region belongs to planar, linear/cylindrical, or rough feature. For seed regions that have been classified as planar or linear/cylindrical, we perform a least-squares adjustment procedure to determine the parameters of the best-fitting plane or line/cylinder through their constituents. Then, the seed regions are sorted according to the a-posteriori variance factor of the fitted surface. One should note that such a-posteriori variance factor is an indication of the normal distances between the points within the seed region and the best-fitted model. The region growing segmentation process then proceeds starting from the seed region with the lowest a-posteriori variance factor to generate planar and linear/cylindrical segments. For the remaining non-segmented points, we apply a distance-based grouping to form rough segments. In this way, we can derive planar, linear/cylindrical, and rough segments. In order to provide the complete segments for the following analysis, an over-segmentation correction strategy is applied on planar and pole-like features.

2.2 Segmentation Quality Control Procedure

For evaluating and improving the segmentation results, we implement two quality control procedures including 1) mitigation of interclass competition for neighboring points (Habib and Lin, 2016) and 2) over-segmentation mitigation (Lari and Habib, 2013).

To implement the first quality control, we consider possible invasion scenarios among segments (i.e., planar, linear/cylindrical, and rough) that belong to different segment classes (e.g., part of a linear segment derived in an earlier stage

could invade a neighboring planar one. The points in other segment classes will be added to segments of the class in question according to the normal distances from these points to segment surface. Then for the second quality control, planar and linear/cylindrical segments are checked to identify over-segmentation instances. The direction of adjacent segments in the same segment class is compared to check for over-segmentation. When neighboring segments have similar directions, they would be recognized as the same segment and merged.

2.3 Ground Classifier

Ground/non-ground classification is applied through the heuristic classification technique proposed by Lari and Habib (2012). This approach considers physical properties of the derived planar segments (i.e., area and slope) and discontinuity measure (i.e., height difference to planimetric distance ratio (ΔH/D)) between adjacent planar segments. The classification process starts with the identification of non-ground segments. First, slope and area are checked to discriminate non-ground segments. A planar segment with a steep slope is identified as non-ground objects when its area is less than a pre-defined threshold (TH1). Then, the segments which are significantly higher than their adjacent segments are marked as non-ground segments. To identify those higher segments, the discontinuity measure (i.e. height difference to planimetric distance ratio (ΔH/D) between the nearest boundary points) is estimated for all boundary points. A segment is classified as non-ground segment when the discontinuity measure is larger than a pre-defined threshold (TH2). For the remaining segments, when their height is at the same height or slightly higher than their non-ground adjacent segments, those segments are classified as non-ground segments. After determining non-ground segments, a ground segment can be decided when it is relatively large and lower than its adjacent segments.

2.4 Building Classifier

Most of buildings are comprised of of planes. Therefore, we firstly focus on planar segments with large area as potential candidates for a building class. However, some structures (e.g., windows, eaves, and door frames) close to a building could be classified as small-area planar segments and other non-planar segments (i.e., pole-like and rough segments). Those structures should be recognized as part of the building. In order to identify those structures, a connectivity analysis between building planar segments and non-building ones is applied.

For building classifier, we assume that all the ground segments have been identified. The remaining planar segments with larger area than a predefined threshold (TH3) are identified as a building class. Then, we examine the height difference from ground of the horizontal planar segments to avoid adding the near ground ones. One should note that most vertical planar regions in the real world are man-made structures. However, horizontal ones could be a higher grass area that are not classified into ground segments. After identifying large planar segments as a building class, the connectivity analysis is applied to recognize other segments that could belong to the buildings. In the connectivity analysis, we examine whether a non-building segment is close to a building segment and could be augmented to the building class. First, the distance between every point in a non-building segment to nearby building planar points is checked. When the majority of the constituents of the segment in question are close to a building planar segment, it will be recognized as part of a building and incorporated into the building category. In this process, three thresholds, percentage (TH4) of neighboring points that are within a distance (TH5) to building planar segments and the corresponding average normal distance (TH6), are used to decide whether the segments belong to the building class or not. For example, in Figure 2, the points of a non-building segment within a pre-defined distance (TH5) to a building planar segment are marked in red and the rest is marked in green. When the percentage of red points to the whole points is larger than a pre-defined percentage (TH4) and the average normal distance from the non-building segment to the building planar segment is smaller than a pre-defined threshold (TH6), the segment in question is recognized as part of the building and classified into building category. Therefore, the segment in Figure 2a is recognized as building class but the one Figure 2b is not.

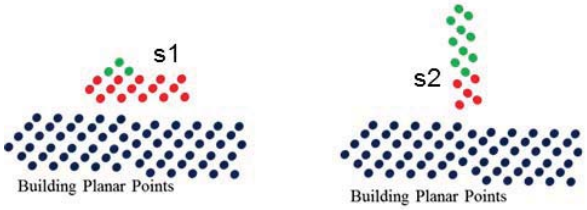

Figure 2. (a) A segment S1 is classified as building class (b) while the segment s2 is not classified as building class

2.5 Pole-like feature Classifier

In our approach, we identify the pole-like feature (e.g., light pole) from linear/cylindrical segments. However, the linear/cylindrical segments could come from tree branches, trunks, light poles, and fences. For detecting a pole-like feature from linear/cylindrical segments, we utilize the following characteristics: (1) axis direction, (2) the height difference (TH7) between the segment to ground, and (3) isolation measures/descriptors.

For the first characteristic, the pole-like feature should have a vertical axis. Therefore, axis directions of all the linear/cylindrical segments are examined whether they are close to the direction vector (0, 0, 1). For the second characteristic, a pole-like feature should connect to the ground. Hence, the height difference of the lowest point of a segment to ground should be less than a pre-defined value (TH7). Finally, the pole-like feature should be isolated. More specifically, a pole-like feature should not connect to other segments except at its two ends (i.e., bottom and top of a pole-like feature). Since the bottom of a light pole could connect to a base or ground and the top of a light pole could be clustered into other segments due to the shape of light pole. For the isolation measure, we define a buffer around a segment for checking whether it is connected to other segments, as shown in Figure 3. If a linear/cylindrical segment complies with the above three characteristics, it will be classified as being part of the pole-like feature class.

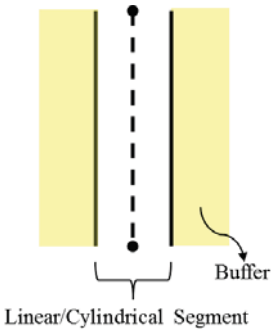

Figure 3. The isolation measure for a pole-like feature

2.6 Vegetation Classifier

The components of vegetation (e.g., tree) could be all types of segments (i.e., planar, linear/cylindrical, and rough). A tree could be comprised of many linear/cylindrical and some rough segments. However, if we only examine a linear/cylindrical segment, it could be difficult to identify whether it belongs to vegetation or unknown classes. Therefore, a grouping method is applied first. The grouping method starts from a rough segment and clusters neighboring segments which include planar, linear/cylindrical, and rough until there is no neighboring segments can be grouped. Then, the grouping method will be applied again to another rough segment until every unclassified rough region has been assigned to a group. After such grouping process, the height difference between the lowest point of a group and the ground segments should be less than a pre-defined threshold (TH7) and the height difference within a group should be large than a threshold (TH8). For the remaining segments, which have not been classified as vegetation, they will be categorized as unknown class.

3. EXPERIMENTAL RESULTS

For demonstrating the feasibility of the proposed classification strategy, a real dataset collected by a terrestrial laser scanner, Leica HDS 3000, is used. The covered area includes ground, buildings, light poles, and trees. Through this dataset, we can evaluate the performance of the approach in classifying a given point cloud into ground, buildings, pole-like features, vegetation, and unknown categories. Figure 4 shows a perspective view of the dataset, where the assigned color is based on the height of the different points. Table1 lists the processing thresholds used for this dataset.

Figure 4. Perspective view of the dataset

Table 1. Classification thresholds

Thresholds	Meaning	Value
Ground Classifier		
TH_1	Area	1,500m^2
TH_2	Discontinuity (Height difference/ Planimetric distance)	1m/2m
Building Classifier		
TH_3	Area	5m^2
TH_4	Percentage	60 %
TH_5	Distance	0.7m
TH_6	Average normal distance	0.7m
Pole-like Feature Classifier		
TH_7	Height difference to ground	1m
Vegetation Classifier		
TH_7	Height difference to ground	1m
TH_8	Height difference within a group	3m

Figure 5 illustrates the segmentation results from the multi-class segmentation procedure. Figure 6 shows the type of segments from the segmentation results. In Figure 6, planar segments are shown in blue, linear/cylindrical segments are shown in green, and rough segments are shown in red. Most building and ground points are grouped into planar segments. For pole-like features, they are grouped into linear/cylindrical segments. The vegetation (e.g., tree) includes planar, linear/cylindrical, and rough segments. In Figure 7, the final classification results with detailed views are shown. Through qualitative evaluation, one can see that buildings and structures close to building (e.g., windows and door frames) have been classified as a building class. Pole-like features have been successfully identified. Trees including leaves, branches, and trunks are also classified into vegetation category. However, some details could be wrongly identified such as the fence near the tree structure could be recognized as tree.

Figure 5. Segmentation results

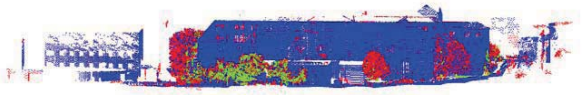

Figure 6. Segment type (blue: planar, green: linear/cylindrical, red: rough)

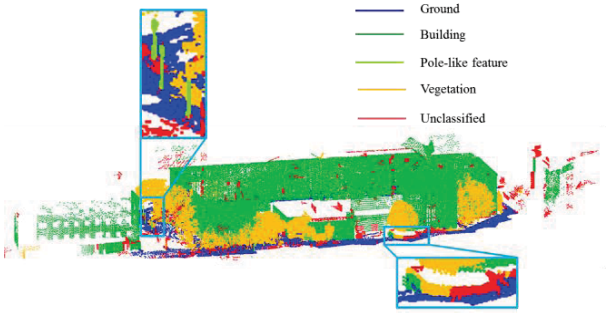

Figure 7. Classification results

4. CONCLUSIONS AND RECOMMENDATIONS FOR FUTURE WORK

In this paper, we proposed a method of combining point cloud segmentation and classification. A given point cloud is first segmented through a region growing based multi-class segmentation into planar, linear/cylindrical, and rough segments. The segmentation results are then used to provide reliable geometric attributes for the classification. The proposed classifiers can provide high-contextual information to the derived segments and catalog them into ground, buildings, pole-

like features, vegetation, and unknown class. We demonstrated the feasibility of the proposed method using a real dataset and evaluated the segmentation and classification results. Future work will test more datasets and focus on the identification of more classes (e.g., bushes and fences). Moreover, different scenario will be considered such as classification of point cloud data along transportation corridors. In such a method, we will consider more spatial relationship between segments (e.g., topology) within the classification process.

REFERENCES

Alshawabkeh, Y., Haala, N., 2004. Integration of digital photogrammetry and laser scanning for heritage documentation. International Archives of Photogrammetry and Remote Sensing, 35, B5.

Awwad, T. M., Zhu, Q., Du, Z., Zhang, Y., 2010. An improved segmentation approach for planar surfaces from unstructured 3D point clouds. The Photogrammetric Record, 25(129), 5-23.

Carlberg, M., Gao, P., Chen, G., Zakhor, A., 2009. Classifying urban landscape in aerial LiDAR using 3D shape analysis. In Image Processing (ICIP), 2009 16th IEEE International Conference on, pp. 1701-1704.

Chang, Y., Habib, A., Lee, D., Yom, J., 2008. Automatic classification of lidar data into ground and non-ground points. International archives of Photogrammetry and Remote Sensing, 37, pp. 463-468.

Cabo, C., Ordoñez, C., García-Cortés, S., Martínez, J., 2014. An algorithm for automatic detection of pole-like street furniture objects from Mobile Laser Scanner point clouds. ISPRS Journal of Photogrammetry and Remote Sensing, 87, pp. 47-56.

Gonzalez-Aguilera, D., Crespo-Matellan, E., Hernandez-Lopez, D., Rodriguez-Gonzalvez, P., 2013. Automated urban analysis based on LiDAR-derived building models. Geoscience and Remote Sensing, IEEE Transactions on, 51(3), pp. 1844-1851.

Haala, N., 2013. The landscape of dense image matching algorithms. In Proceedings of Photogrammetric Week 2013, Stuttgart, Germany, pp. 271–284.

Lari, Z., Habib, A., 2014. An adaptive approach for the segmentation and extraction of planar and linear/cylindrical features from laser scanning data. ISPRS Journal of Photogrammetry and Remote Sensing, 93, pp. 192-212.

Lafarge, F., Mallet, C., 2012. Creating large-scale city models from 3D-point clouds: a robust approach with hybrid representation. International journal of computer vision, 99(1), pp. 69-85.

Rabbani, T., Van Den Heuvel, F., Vosselmann, G., 2006. Segmentation of point clouds using smoothness constraint. International Archives of Photogrammetry Remote Sensing and Spatial Information Sciences, 36(5), pp. 248-253.

Rottensteiner, F., Briese, C., 2002. A new method for building extraction in urban areas from high-resolution LIDAR data. International Archives of Photogrammetry Remote Sensing and Spatial Information Sciences, 34(3/A), pp. 295-301.

Meng, X., Currit, N., Zhao, K., 2010. Ground filtering algorithms for airborne LiDAR data: A review of critical issues. Remote Sensing, 2(3), pp. 833-860.

Moussa, A., El-Sheimy, N., 2010. Automatic classification and 3D modeling of LiDAR data. In Proceedings of the ISPRS Commission III symposium-PCV 2010.

Samadzadegan, F., Bigdeli, B., Ramzi, P., 2010. Classification of LiDAR data based on multi-class SVM. Int. Arch. Photogrammetry, Remote Sens. Spatial Inf. Sci, pp. 1-6.

Shapovalov, R., Velizhev, A., 2011. Cutting-plane training of non-associative markov network for 3d point cloud segmentation. In 3D Imaging, Modeling, Processing, Visualization and Transmission (3DIMPVT), 2011 International Conference on, pp. 1-8.

Sampath, A., Shan, J., 2010. Segmentation and reconstruction of polyhedral building roofs from aerial lidar point clouds. IEEE Transactions on geoscience and remote sensing, 48(3), pp. 1554-1567.

Wang, J., & Shan, J., 2009. Segmentation of LiDAR point clouds for building extraction. In American Society for Photogramm. Remote Sens. Annual Conference, Baltimore, MD, pp. 9-13.

Weinmann, M., Jutzi, B., & Mallet, C., 2014. Semantic 3D scene interpretation: a framework combining optimal neighborhood size selection with relevant features. ISPRS Annals of the Photogrammetry, Remote Sensing and Spatial Information Sciences, 3, pp. 181-188.

Vosselman, G., Gorte, B. G., Sithole, G., Rabbani, T., 2004. Recognising structure in laser scanner point clouds. International archives of photogrammetry, remote sensing and spatial information sciences, 46(8), pp. 33-38.

Yang, B., & Dong, Z., 2013. A shape-based segmentation method for mobile laser scanning point clouds. ISPRS Journal of Photogrammetry and Remote Sensing, 81, pp. 19-30.

A Structure-from-Motion Approach Using UAV-based Imagery for Precision Agriculture Applications

F. He [a, *], W. Xiong [a], A. Habib [a]

[a] Digital Photogrammetry Research Group
Lyles School of Civil Engineering
Purdue University, 550 Stadium Mall Dr., West Lafayette, IN 47907, USA
– (he270, xiong43, ahabib)@purdue.edu

KEY WORDS: Structure from Motion, UAVs mapping, Bundle Adjustment, Precision Agriculture

ABSTRACT:

Nowadays, thanks to recent advances in sensor calibration and automated triangulation, accurate mapping using low-cost Unmanned Airborne Vehicles (UAVs) with RGB frame camera is gaining significant attention from researchers in the mapping and plant science fields. However, due to the fact that the crop fields usually have poor and/or repetitive textures, 3D image-based reconstruction using UAV images acquired for precision agriculture applications remains to be a challenging task. In this paper, a three-step Structure from Motion (SfM)-based procedure is proposed for accurate 3D reconstruction using UAV-based images. In the first step of the proposed procedure, two approaches, which take advantage of prior information regarding the flight trajectory, are proposed for reliable relative orientation in the presence of a high percentage of outliers. Then, image orientation recovery and sparse point cloud generation are simultaneously achieved through an image augmentation process. Finally, a global bundle adjustment involving Ground Control Points (GCPs) and check points is carried out to refine the estimated image EOPs relative to the mapping reference frame. In order to evaluate the feasibility of the proposed procedure, two real datasets, which are acquired with different configurations over a test agriculture field, are utilized. In addition, a comparative performance analysis between the proposed procedure and the Pix4D software is performed. The derived experimental results demonstrate that the proposed procedure is capable of providing accurate UAV-based 3D reconstruction for precision agriculture applications. It also presents superior performance when compared to the Pix4D software.

1. INTRODUCTION

In conventional photogrammetric mapping, large-area 3D reconstruction has been established using manned-airborne data acquisition platforms. Such image-based 3D reconstruction requires the knowledge of the Interior Orientation Parameters (IOPs) of the utilized camera, Exterior Orientation Parameters (EOPs) of the involved images, and corresponding points/features in the set of overlapping images. The IOPs can be derived from a camera calibration process. The EOPs of the involved imagery can be either derived through an indirect geo-referencing procedure using tie and control points or a direct geo-referencing process through the implementation of a GNSS/INS unit on-board the mapping platform. While the latter approach has the practical convenience of simplifying the geo-referencing process, it requires significant initial investment for the acquisition of a high-end GNSS/INS Position and Orientation System (POS) – especially, when seeking high level of reconstruction accuracy.

Instead of using conventional manned-photogrammetric data acquisition platforms, low-cost UAVs have recently emerged as a promising geospatial data acquisition system to satisfy the needs of wide range of applications (Tao and Li, 2007). Compared to manned-airborne systems, UAVs are more advantageous for small area mapping since they can be quickly deployed and flown at lower elevation resulting in more cost-effective 3D mapping at higher resolution. In the existing body of literature, SfM approaches and dense image matching techniques have been investigated. SfM automates the process of EOP recovery. Dense image matching, on the other hand, provides feature correspondences among overlapping images at the pixel level. In addition, thanks to recent advances in both low-cost direct geo-referencing systems as well as imaging sensors operating at different portions of the electromagnetic spectrum, utilizing UAVs, which are equipped with directly geo-referenced RGB-frame cameras, for precision agriculture has become an important application that is gaining significant attention from researchers in both mapping and plant science fields (Habib et al., 2016). It is worth mentioning that, although current commercial software (e.g., Pix4D and PhotoScan) can automate the process of image-based 3D reconstruction, utilization of such software for precision agriculture applications remains to be a challenging task. This is mainly due to the fact that agriculture fields usually contain poor and/or repetitive textures, which can severely impact the relative orientation recovery for UAV-based images. Therefore, this paper aims at proposing a transparent SfM-based system, which can be augmented with different user-defined constraints, for precision agriculture applications. To be more specific, this research will be focusing on the following issues:

1. Automated relative orientation recovery of UAV-based images in the presence of prior information regarding the flight trajectory,
2. Sparse image-based point cloud generation from multiple images acquired from low-cost Large-field-of-view (LFOV) cameras onboard UAV platforms,
3. Accuracy analysis of the derived 3D reconstruction through check point analysis, and
4. Comparison of the proposed approach against available commercial software, such as Pix4D.

* Corresponding author.

To address these issues, the utilized methodology is introduced in the next section. Afterwards, experimental results with real datasets are discussed. Finally, drawn conclusions as well as recommendations for future work are presented.

2. METHODOLOGY

In this section, the proposed SfM procedure for UAV-based 3D reconstruction while using a low-cost LFOV camera is introduced. Figure 1 illustrates the workflow of the proposed procedure. This procedure includes three steps. In the first step, the relative orientation parameters relating stereo-images are directly derived from conjugate point features. In the second step, the initial recovery of image EOPs is achieved. Specifically, a local coordinate frame is initially established, and then the EOPs of the remaining images are sequentially recovered in an incremental image augmentation process. Finally, in the third step, a global bundle adjustment, which integrates both Ground Control Points (GCPs) and Check Points, is carried out for indirect geo-referencing and accuracy analysis.

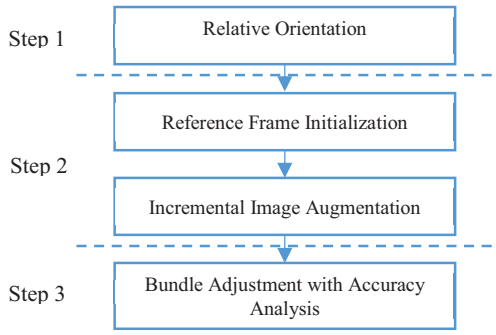

Figure 1. The proposed workflow for the SfM-based 3D reconstruction

2.1 Relative Orientation

In the past few decades, recovery of the Relative Orientation Parameters (ROPs) relating overlapping images has been investigated within both the photogrammetric and computer vision research communities (Habib and Kelley, 2001; Heipke, 1997; Zhang et al., 2011). In general scenarios, the IOPs of the utilized camera are usually assumed to be known. For a given stereo-pair, ROP estimation involves the derivation of five parameters, which include three rotation angles and two translation parameters (i.e., an arbitrary scale is assumed for the ROP estimation procedure). The most well-known approach for ROP recovery is based on the co-planarity constraint (Mikhail et al., 2001), where a least-squares adjustment is solved while using a minimum of five conjugate points. However, due to the nonlinear nature of the co-planarity model, approximate values for the unknowns, which are refined through an iterative process, have to be available. Establishing good-quality approximations can be challenging for situations where the mapping platform exhibits excessive maneuvers between the data acquisition epochs (e.g., close range mapping applications). To address such a challenge, several closed-form solutions, which do not require approximations, for ROP recovery have been developed, such as the eight-point and the five-point algorithms (Hartley, 1997; Longuet-Higgins, 1987; Nistér, 2004). Although such closed-form solutions have been widely used in various applications, mitigating the impact of outliers in automatically matched points remains to be a challenging task. In order to deal with UA-based images acquired for precision agriculture applications, two approaches are proposed to derive reliable estimation of ROPs in the presence of high percentage of matching outliers. The proposed approaches have following characteristics:

1. Both proposed approaches take advantage of prior information regarding the flight trajectory, which can be derived from the designed mission plan and/or geo-referencing information from an onboard GNSS/INS unit.

2. The first approach is based on a two-point closed-form solution. It assumes that the UAV is moving at constant flying height while operating a nadir-looking (i.e., we are dealing with vertical images that are captured from the same flying height). Starting from such assumptions, the nine elements of the Essential Matrix, which contains all information regarding the ROPs relating two overlapping images, can be reduced to four with an additional constraint among them. Meanwhile, considering the fact that the relative orientation can be only established up to an arbitrary scale, the four elements of the Essential Matrix can be derived using a minimum of two point correspondences. In addition, this approach can be incorporated within a RANSAC framework for outlier removal among the initial conjugate point pairs.

3. The second approach is an iterative five-point approach. It starts with a linearization process of the co-planarity constraint starting from prior information regarding the ROPs relating the stereo-pair in question to derive a set of linear equations in the unknown corrections to the approximate ROP values. A minimum of five conjugate pairs are required to derive an estimate of the ROPs through an iterative procedure until a convergence criterion is achieved. In this approach, a built-in outlier removal process is adopted within the iterative procedure by imposing constraints on the normalized image coordinates according to epipolar geometry.

4. In practice, due to wind conditions and the light-weight of UAVs, the acquired UAV images are expected to show significant deviations from the assumption of the proposed two-point approach (i.e., the images are acquired with the camera's optical axis pointing in the vertical direction and at the same flying height). Therefore, a hybrid approach that starts with the two-point approach and uses the estimated initial values for the iterative five-point approach can be adopted when dealing with stereo-images that exhibit significant variations from the designed flight plan.

2.2 Initial Recovery of Image EOPs

Once the ROPs of all possible stereo-pairs are estimated, an incremental approach, which is developed by He and Habib (2014), is adopted for the initial recovery of the image EOPs. This incremental approach is initiated by defining a local coordinate frame. Then, all the images are sequentially augmented into a final image block.

The local coordinate system is established using an image triplet that satisfies both a large number of corresponding points and good compatibility configuration. The first condition can be easily satisfied by maximizing the total number of corresponding points within the image triplet. The second condition is evaluated through a method referred to as compatibility analysis, which was developed by He and Habib (2014).

Once the local coordinate frame is established, the remaining images are sequentially augmented into the final image block or

trajectory. The proposed approach utilizes a geometric structure, which is referred to as the reverse tree structure for the augmented images (Martinec and Pajdla, 2007), as the basis for the EOP recovery. In this research, the proposed reverse tree-structure-based approach incorporates a linear approach for the estimation of the image EOPs (He and Habib, 2014). In order to reduce the effects of error propagation, at each step of the image incremental augmentation, only the image that exhibits the highest compatibility with the previously referenced imagery is selected and referenced into the pre-defined local coordinate system.

2.3 Global Bundle Adjustment

Since the derived sparse point cloud from the SfM approach is only defined in an arbitrary local coordinate system, an absolute orientation process has to be applied for defining the derived point cloud as well as the estimated image EOPs relative to the mapping reference frame. In this research, correspondences between the GCPs and the derived sparse point cloud are first manually identified. Then, a 3D similarity transformation process is performed to evaluate approximate parameters (i.e., scale factor, three translation parameters, and three rotation angles) relating the two involved coordinate systems.

Now that the 3D similarity transformation has been applied, the accuracy analysis of the derived UAV-based 3D reconstruction results can be conducted through a global bundle adjustment integrating the GCPs and check points. In the implemented bundle adjustment process, GCPs are established for absolute orientation/datumn definition, and check points are established for accuracy evaluation. In this research, besides the derived conjugate points from the SfM approach, tie points corresponding GCPs and check points are manually identified. Then, these image measurements are integrated into the bundle adjustment for a global refinement. Finally, the residuals at each check point are computed. Figure 2 illustrates the inputs and outputs of the global bundle adjustment process.

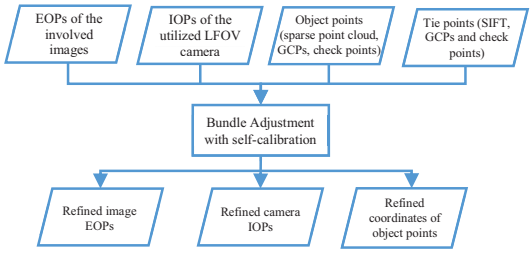

Figure 2. The proposed global bundle adjustment process for accuracy analysis

3. EXPERIMENTAL RESULTS

The main objective of the experimental results is illustrating the feasibility of the proposed SfM-based procedure, which aims at 3D reconstruction using UAV-based images for precision agriculture applications. Therefore, we conduct several experimental tests using real image datasets.

3.1 Dataset Description

The test site involved in the experiments covers an agriculture field at Purdue Agronomy Center for Research and Education (ACRE) in Wester Lafayette, United States. Two real datasets are acquired by a multi-rotor DJI Phantom2 UAV with GoPro Hero 3+ Camera over the test site. The internal characteristics of the GoPro camera has been estimated through a calibration procedure similar to the one proposed by He and Habib, (2015). One should note that, for the utilized UAV platform, the GoPro camera is mounted on a gimbal to ensure that images are acquired with the camera's optical axis pointing in the nadir direction. The main characteristics of the two real datasets are described as below.

Dataset 1 is comprised of 569 images that are captured from a flying height of approximately 15 meters with the utilized multi-rotor UAV moving at a speed of roughly 8 m/s (See Figure 3(a) for sample image). The overlap and side lap percentages for the acquired images are approximately 60%.
Dataset 2 includes 1,191 images acquired with a 5 m/s speed of the same UAV platform at a flying height of almost 15 meters (See Figure 3(b) for sample image). The overlap and side lap ratio among the acquired images are almost 80%.

(a) (b)

Figure 3. (a) A sample image from real dataset 1, and (b) a sample image from real dataset 2

In order to evaluate the derived 3D reconstruction results from the two real datasets, 10 GCPs and 18 check points are established. Both GCPs and check points are surveyed by an RTK GPS with an approximate accuracy of $\pm 2\,cm$. The configuration of the utilized GCPs and check points are shown in Figure 4.

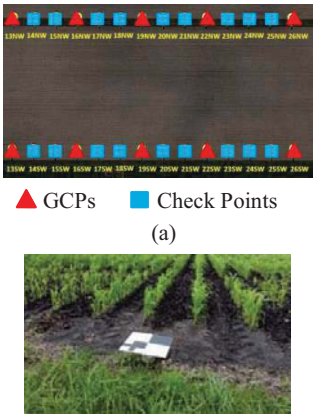

(a)

(b)

Figure 4. (a) Configuration of the GCPs and check points, and (b) a sample image of the targets established for both GCPs and check points in the test field

3.2 Accuracy Analysis

For each real dataset, by applying the proposed SfM-based procedure, the EOPs of involved images are recovered, and a sparse point cloud is simultaneously generated. Figure 5 illustrates the generated sparse point cloud as well as the positions and orientation of all involved images for the two real datasets. Afterwards, a 3D similarity transformation process is

applied using at least three GCPs with good spatial distribution for deriving initial values of EOP and ground coordinates relative to the reference frame. Finally, the global bundle adjustment with GCPs and check points is carried out to refine the derived image EOPs, object coordinates, and camera IOPs. One should note that, since the number of derived tie points can vary a lot from different approaches (e.g., the proposed SfM-based procedure usually provides hundreds of thousands of tie points, while only hundreds of tie points can be identified for the GCPs and check points), distinct variances are considered for different types of tie points in the global bundle adjustment. More specifically, in this research, the standard deviation of SfM-based tie points is set to 7 pixel; the standard deviation of tie points corresponding to the GCPs and check points are set to 0.5 pixel.

Once the global bundle adjustment process is completed, the derived square root of a posteriori variance (σ_0) can be computed. In this research, the derived σ_0 values from the two real datasets (0.00137 mm and 0.00128 mm, respectively) are all smaller than one pixel size (0.00155 mm), which indicates a good precision of the derived UAV-based 3D reconstruction. In the meantime, in order evaluate the accuracy of the derived 3D reconstruction results in the mapping coordinate system, the root-mean-square error (RMSE) for the check points is investigated. The derived RMSE values are presented in Table 1, where one can observe that, for both real datasets, the RMSE values for X and Y coordinates are 0.01 m, while the RMSE value for Z coordinate is 0.04 m. Such results indicate that the UAV-based 3D reconstruction achieves a good accuracy in the object space.

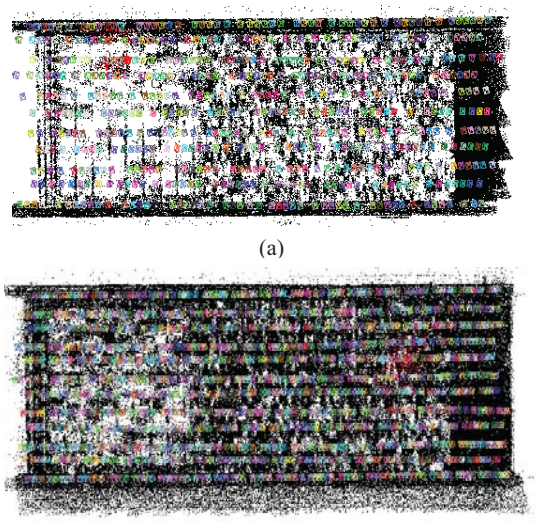

(a)

(b)

Figure 5. Reconstructed sparse point cloud and positions and orientation of all involved experimental images from (a) real dataset 1 and (b) real dataset 2.

	Real Dataset 1	Real Dataset 2
RMSE_X (m)	0.01	0.01
RMSE_Y (m)	0.01	0.01
RMSE_Z (m)	0.04	0.04
Total_RMSE (m)	0.02	0.02

Table 1. The derived RMSE values at check points from real datasets 1 and 2

3.3 Comparison with Pix4D

The objective of the last stage of the experimental results is a comparative performance analysis between the proposed SfM-based procedure and the Pix4D software. Therefore, qualitative and quantitative evaluation methodologies need to be established. In this research, the quantitative analysis is performed by comparing the number of images, whose EOPs have been successfully recovered from the proposed procedure and the Pix4D software. Table 2 reports the number of estimated image EOPs from the real datasets. One can observe that the proposed SfM-based procedure provides EOP estimation for all images (569, and 1,191 images, respectively) from the two real datasets, while only 487 out of 569 and 1100 out of 1191 image EOPs are recovered from Pix4D. Such result demonstrates that the proposed SfM-based procedure is capable of providing more reliable EOP estimation when dealing with UAV images acquired over an agricultural field. In the meantime, the qualitative evaluation is conducted by evaluating the RGB-based orthophoto mosaic of the entire test field using the two real datasets. In this research, a DEM is initially interpolated from the sparse point cloud that is derived from either the proposed SfM procedure or Pix4D. Then, the DEM together with the bundle adjustment-based EOPs and the GoPro IOPs are used to generate the RGB-based orthophoto. Figure 6 illustrates the cropped RGB-based orthophotos that are respectively generated from the proposed SfM-based procedure and Pix4D. Through closer visual inspection on the derived orthophotos, one can observe obvious gaps and discrepancies in the RGB-based orthophoto generated by the Pix4D software (See Figures 6b and 6d). The orthophoto generated from the proposed procedure, on the other hand, shows good quality (See Figures 6a and 6b). Such results also indicate that, compared to Pix4D, the proposed procedure has superior performance when dealing with sets of agricultural field images acquired by the utilized UAV platform.

	Total Number of Images	Number of Images (The Proposed Procedure)	Number of Images (Pix4D)
Real Dataset 1	569	569	487
Real Dataset 2	1,191	1,191	1,100

Table 2. Number of recovered image EOPs for datasets 1 and 2

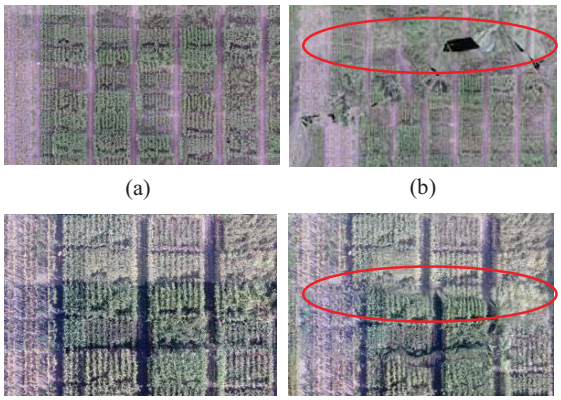

(a) (b)

(c) (d)

Figure 6. (a) and (b) are cropped from RGB-orthophotos generated from real dataset 1 using the proposed procedure and Pix4D; (c) and (d) are cropped from RGB-orthophotos generated from real dataset 2 using the proposed procedure and Pix4D.

4. CONCLUSIONS AND RECOMMENDATIONS FOR FUTURE WORK

In this paper, we proposed a fully automated procedure for UAV-based 3D reconstruction, which can be used for precision agriculture applications. Then, accuracy analysis is performed on the derived point clouds. Besides, a comparative performance analysis between the proposed procedure and Pix4D is carried out. For the experimental tests, two real datasets acquired by a DJI Phantom 2 UAV with a GoPro Hero 3+ camera are utilize. The derived experimental results from accuracy analysis using GCPs and check points indicate that the 3D reconstruction can be achieved with a good level accuracy. In addition, by comparing the derived results from the proposed procedure and Pix4D, we can draw the conclusion that the proposed procedure has better performance when dealing with UAV images acquired for precision agriculture applications.

It is important to note that, in this research, we only tested our proposed procedure on one low-cost UAV platform. For future work, more tests will be carried out on images acquired from different UAV platforms with different flight configurations. Besides, automated identification of GCPs and check points will be investigated as well.

ACKNOWLEDGEMENT

The information, data, or work presented herein was funded in part by the Advanced Research Projects Agency-Energy (ARPA-E), U.S. Department of Energy, under Award Number DE-AR0000593. The views and opinions of authors expressed herein do not necessarily state or reflect those of the United States Government or any agency thereof.

REFERENCES

Habib, A., Kelley, D., 2001. Automatic relative orientation of large scale imagery over urban areas using modified iterated Hough transform. ISPRS J. Photogramm. Remote Sens. 56, 29–41.

Habib, A., Xiong, W., He, F., Yang, H.L., Crawford, M., 2016. Improving Orthorectification of UAV-Based Push-Broom Scanner Imagery Using Derived Orthophotos From Frame Cameras. IEEE J. Sel. Top. Appl. Earth Obs. Remote Sens. 1–15.

Hartley, R.I., 1997. In defense of the eight-point algorithm. Pattern Anal. Mach. Intell. IEEE Trans. On 19, 580–593.

He, F., Habib, A., 2015. Target-based and Feature-based Calibration of Low-cost Digital Cameras with Large Field-of-view, in: ASPRS 2015 Annual Conference, Tampa, Florida.

He, F., Habib, A., 2014. Linear approach for initial recovery of the exterior orientation parameters of randomly captured images by low-cost mobile mapping systems. Int. Arch. Photogramm. Remote Sens. Spat. Inf. Sci. 40, 149.

Heipke, C., 1997. Automation of interior, relative, and absolute orientation. ISPRS J. Photogramm. Remote Sens. 52, 1–19.

Longuet-Higgins, H.C., 1987. A computer algorithm for reconstructing a scene from two projections. Read. Comput. Vis. Issues Probl. Princ. Paradig. MA Fisch. O Firschein Eds 61–62.

Martinec, D., Pajdla, T., 2007. Robust rotation and translation estimation in multiview reconstruction, in: Computer Vision and Pattern Recognition, 2007. CVPR'07. IEEE Conference on. IEEE, pp. 1–8.

Mikhail, E.M., Bethel, J.S., McGlone, J.C., 2001. Introduction to modern photogrammetry. John Wiley & Sons Inc.

Nistér, D., 2004. An efficient solution to the five-point relative pose problem. Pattern Anal. Mach. Intell. IEEE Trans. On 26, 756–770.

Tao, C.V., Li, J., 2007. Advances in mobile mapping technology. CRC Press.

Zhang, Y., Huang, X., Hu, X., Wan, F., Lin, L., 2011. Direct relative orientation with four independent constraints. ISPRS J. Photogramm. Remote Sens. 66, 809–817.

INDOOR SURVEYING WITH LOW COST UWB DEVICES

Andrea Masiero [a,*], Francesca Fissore [a], Alberto Guarnieri [a], Antonio Vettore [a]

[a] Interdepartmental Research Center of Geomatics (CIRGEO), University of Padua,
Viale dell'Università 16, Legnaro (PD) 35020, Italy
masiero@dei.unipd.it
(francesca.fissore, alberto.guarnieri, antonio.vettore)@unipd.it

KEY WORDS: UWB, Mobile Mapping, Indoor Positioning

ABSTRACT:
This paper compares the problem of providing indoor survey of a mediaeval bastion in Padua, Italy. Terrestrial laser scanning (TLS) survey is considered in order to provide a state of the art reconstruction of the bastion. Then, photogrammetric survey is considered as well. Control points are typically used to avoid deformations and ensure correct scaling of the reconstruction. However, other external instruments shall be used (total station, GNSS receiver if outdoors) in order to have information about control point positions. This work is part of a project aiming at the development of a system exploiting only ultra-wide band (UWB) devices to provide correct scaling of the reconstruction. In particular, low cost Pozyx UWB system is used in this work to estimate camera positions during image acquisitions. Comparing camera positions obtained from UWB measurements with those obtained from photogrammetric reconstruction allows to estimate the scaling factor for a metric reconstruction. Compared with the TLS survey, the considered photogrammetric indoor reconstruction of the bastion results in a RMSE of 21.9cm, average error 13.4cm, and standard deviation 13.5cm. Excluding left extreme part of the bastion, where the presence of several poles make reconstruction harder, (RMSE) fitting error is 17.3cm, average error 11.5cm, and standard deviation 9.5cm.

INTRODUCTION:
Current surveying methods typically use GNSS as positioning technique: when positioning is performed outdoors, in good satellite signal reception conditions, this method allows accurate performance, which can be useful in a wide range of applications and environments. However GNSS positioning provides unreliable results when being used in other working conditions: indoors and in certain outdoor environments (e.g. close to high buildings or mountains, in forests) its use is often impracticable or not sufficiently accurate.
Positioning in such working conditions, challenging for GNSS, can be achieved by using inertial measurements provided by the Inertial Measurement Unit (IMU): integration of acceleration, gyroscope and magnetometer measurements provide estimate of position changes (it is worth to notice that GNSS enables geo-referencing). Unfortunately, IMU measurements are typically quite noisy, and their estimated positions typically quickly drift from the correct trajectory unless periodically corrected by means of different measurements, e.g. in recent works IMU measurements have been integrated with vision, WiFi (received signal strength, fingerprinting),

geometric constraints on the environment [1,2].

This paper considers another method for positioning in environments challenging for GNSS: positioning based on the use of Ultra-Wideband (UWB) devices. More specifically, device position is obtained by means of range measurements, which can be directly derived by the times of flight of Ultra-Wideband (UWB) radio signals (as usual when dealing with range based positioning, four measurements from known positions (provided by devices not lying on a plane) are needed in order to enable 3D positioning, whereas three are enough for positioning on a planar surface (2D positioning)).

Similarly to IMU positioning, UWB allow to obtain position estimated with respect to a local coordinate system, however it has the advantage of not requiring external measurements to reduce any drift.

First, this work investigates the characteristic of systematic and random errors for Pozyx devices [3], i.e. a set of low cost UWB devices: random noise is shown to be quite small (3 centimetres, approximately) hence potentially allowing positioning with an accuracy level of few centimetres. Systematic error has been previously modelled as a constant time lag (e.g. due to device synchronization) [4] and as a polynomial term, as a function of distance [5,6]. Actually, according to our experiments, systematic errors of the considered low cost UWB devices are significantly anisotropic, i.e. when aiming at fully exploiting the positioning potentiality of the UWB signals, dependence on the orientation of the device di be tracked and on its direction (angle) with respect to the other UWB antennas is typically not negligible.

Taking into account of the above observations, a complete calibration of the UWB systematic error might be quite complicated for a simple user of the positioning system. Motivated by this consideration, this paper aims at (partially) compensate the UWB systematic error while not requiring complicated calibration procedures to the user: the system should be as simple as possible for the user.

Hence, the tracking system provide estimates of the range measurement errors due to systematic errors in order to reduce their effect on the positioning performance. Furthermore, off-line optimization of the trajectory and of the systematic errors is considered in order to further reduce the positioning errors.

Comparison of the positioning results are made considering several techniques: Extended Kalman filter, Maximum Likelihood, other linear approximations of the system. Different configurations of the UWB network are also considered in order to reduce the positioning errors: analysis of the obtained results is provided in accordance with the spatial distribution of the systematic error previously estimated.

Despite being cheaper than other UWB products on the market, thanks to the proposed error compensation (which reduces up to 30% of the positioning error in our experiments) the obtained results are good (despite not at the same level of high-end devices, e.g. shorter maximum range) and allow to clearly improve positioning with respect to using just inertial sensors (i.e. IMU).

The proposed positioning system, integrated with a photogrammetric reconstruction system, is tested on a case study in Padua (Italy), indoor surveying of the “Impossibile” bastion, along the walls of Padua, where GNSS is clearly not available. The reconstructed point cloud is compared with the 3D model obtained by means of terrestrial laser scanning technique.

OBJECTIVES:

The objective of this paper is the analysis of the performance of a mobile mapping solution based on the use of photogrammetry and low cost UWB devices. The considered UWB devices are Pozyx low cost indoor navigation solution. This goal is achieved through using map information to re-correct MEMS-based inertial sensors results using a two-layer structure PF/KF algorithm. Also, to balance between the estimation accuracy and the computational speed, three PFs, including SIS PF, APF, and BPF are designed and implemented in this paper.

UWB POSITIONING SYSTEM :

Pozyx is a low cost UWB positioning system recently developed by Pozyx Lab [3] (first devices have been shipped in 2016). Two types of Pozyx devices can be distinguished, anchors and tag. Anchors are assumed to be in a fixed and known position during all the navigation, whereas tag can move in the environment. Goal of the system is that of providing estimates of tag position based on range measurements of the distances between tag and anchors. Interestingly, Pozyx devices are provided of an auto-detecting procedure that allows them to detect and synchronize with each other. Once turned on, tag and anchors starts to communicate and to provide range measurements. Code executed by the tag can be easily personalized. In particular, in our case tag was used just to collect range measurements. Nevertheless, it is worth to notice that Pozyx system is already provided of a positioning functionality, which can be used to estimate tag position in real time on the tag itself. However, this functionality has not been used in our experiments in order to save computational power, and hence allowing a higher frequency for range collection.

Figure 1. UWB Pozyx device powered by a standard external battery.

Pozyx devices are quite small (maximum side size is 6cm) and lightweight (≈12g), hence particularly well suited for mobile mapping applications. Thanks to their low power consumption they can be conveniently powered with standard external batteries via a specific USB cable (see Fig. 1). Certain nominal characteristics of interest of Pozyx system are reported in the following table:

	Nominal values
Range accuracy	10 cm
Maximum range	100 m
Maximum update rate	80 Hz

Table 1. Pozyx nominal characteristics.

However, it is worth to notice that actual values for the parameters reported above depend on several factors (e.g. environment and system settings). In particular, some experimental results aiming at checking real performance of the system are reported in the following.

Fig. 2(a) shows the histogram of UWB ranging errors obtained comparing ground truth distance between a Pozyx anchor with the tag along a track of 40 check points. During the track relative distance and orientation between tag and anchor changed extensively. Error distribution is approximately normal with mean quite close to zero (0.7 cm) and standard deviation 16 cm. Similar results can be obtained also for the other Pozyx devices. In particular, average error becomes closer to zero when averaging errors from more devices. The obtained accuracy is quite close to the nominal one, but higher.

Fig. 2(b) shows ranging error values obtained varying the distance from tag and anchor from 2 m to 40 m. Values shown in the figure are the averages of 1000 time samples, whereas bars corresponds to $(-\sigma,+\sigma)$ interval centered on the average error value. Error behavior with respect

to different values of the distance is quite irregular.

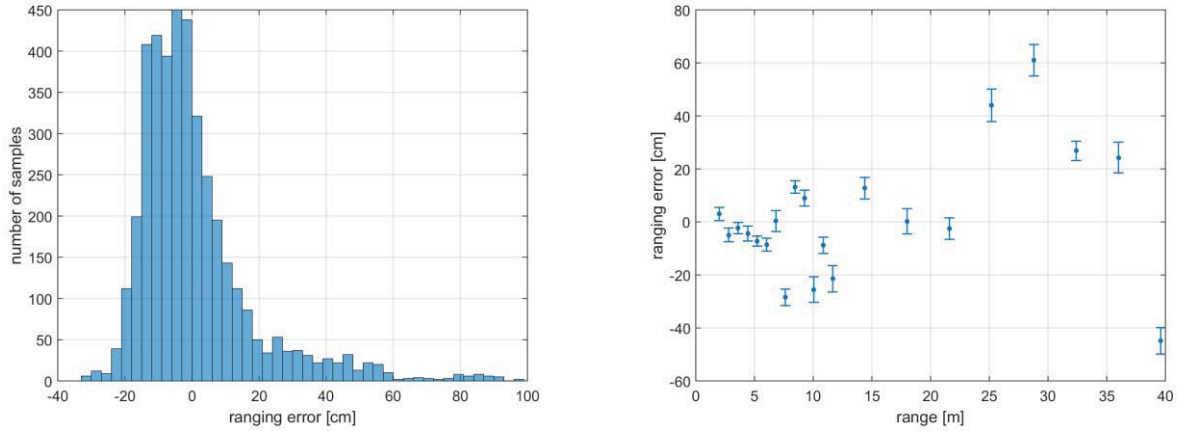

(a) (b)

Figure 2. (a) UWB ranging error distribution. (b) Ranging error varying distance.

Maximum range depends on the working conditions, but according to our experiments it is hard to reach values close to the nominal maximum range. Measurement update frequency can also change depending on the range value (the larger the value the lower the update frequency).

Anchor positions are assumed to be known to be able to solve the positioning problem. Range measurements can be combined by using an Extended Kalman Filter (EKF) in order to obtain estimates of the tag position.
In particular, in the case study considered in this work, four anchors were distributed as shown in Fig. 3 on the ground inside of the Impossibile bastion. Anchor positions have been measured by means of a Leica TCR 702 Total Station. However, it is worth to notice that the use of a total station might be difficult in certain environments/operating conditions. The validation of results that can be obtained by using alternative options in order to obtain estimates of anchor positions (e.g. self-positioning of anchors by means of their own measurements, native functionality included in the Pozyx system) is foreseen in our future investigations.

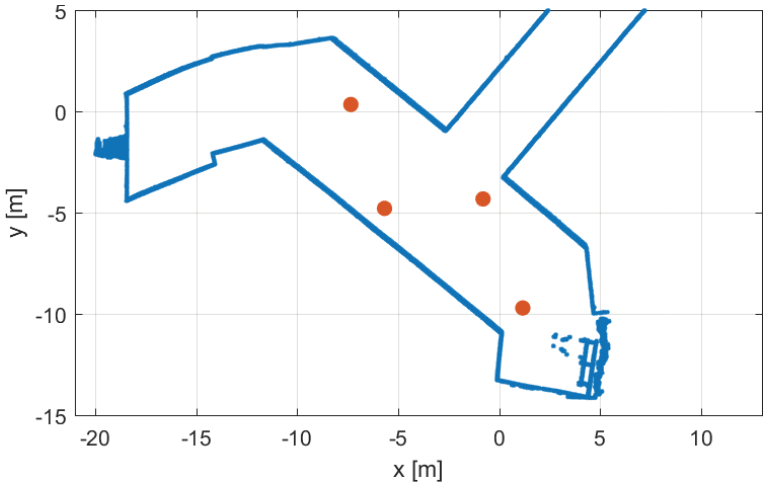

Figure 3. Positions of UWB anchors (red spots) in the considered case study.

Tag has been attached to the camera used for photogrammetric reconstruction. Tag has been moved at approximately constant altitude during the survey. In particular, its altitude with respect to the approximately planar surface where anchors were positioned was fixed at a constant value (h=1.5 m) during image acquisitions in order to obtain best positioning results from the four anchors used during data collection in the bastion. Consequently, EKF has been formulated in order to track the tag position on a planar surface at constant altitude.

Tag dynamic is modeled as follows:

$$\begin{bmatrix} x_{t+1} \\ \dot{x}_{t+1} \end{bmatrix} = \begin{bmatrix} 1 & T \\ 0 & 1 \end{bmatrix} \begin{bmatrix} x_t \\ \dot{x}_t \end{bmatrix} + w_t$$

where x_t is the 2D position at time t of the tag on the planar surface at constant altitude, T is the time period between the two estimates, and w_t is the model noise.

Measurement equation for anchor i is:

$$y_{t,i} = \sqrt{(x_{t,u} - q_{i,u})^2 + (x_{t,v} - q_{i,v})^2 + h^2} + z_t$$

where $y_{t,i}$ is the measurement of anchor i at time t, q_i is the position of anchor i, and z_t is the measurement noise.

Integration of EKF based on UWB measurements with a previously developed pedestrian dead reckoning-like approach for indoor navigation [7] will also be considered in the future.

PHOTOGRAMMETRIC RECONSTRUCTION:

Images of the bastion have been taken by using a Canon G7X camera (20.2 MPix), with settings fixed at constant values (1/60s shutter speed, f/1.8 aperture, 8.8mm focal length, i.e. 35mm equivalent: 24mm). 335 images have been collected varying camera position and orientation in the bastion.

Agisoft PhotoScan has been used in order to obtain a self-calibrated reconstruction of the bastion.

Estimate of reconstruction scale has been obtained by computing the best (in least squares sense) rigid transformation (rotation, translation and scale) between the camera positions provided by PhotoScan and the corresponding ones estimated with the Pozyx system. In this process the same weight have been given to all positions estimated by the UWB system. However, positions far from UWB are clearly affected by a higher estimation error with respect to those surrounded by anchors. Introducing different weights depending on the considered position might improve scale estimation performance.

During each image acquisition camera has been firmly held for 2-3 seconds. Manual synchronization between camera and UWB measurements has been initially set taking into account of measurements provided by the inertial measurement unit (approximately still when taking images). Then, synchronization has been refined inserting it in the least squares minimization process previously considered for the scale estimation.

3D REFERENCE MODEL – TLS SURVEY:

In order to provide a 3D reference dataset for the assessment of the UWB-based photogrammetric reconstruction system, the interior of the "Impossible bastion" was fully surveyed with a Leica ScanStation C10 terrestrial laser scanner (TLS). Based on TOF measuring principle, this scanning system combines all-in-one portability with the ability of performing total station-like surveys (traverse and resection). The laser features full 360º × 270º field-of-view thanks to the adoption of Smart X-Mirror design, low beam divergence (<6 mm @ 50 m), high accuracy (6 mm @ 50 m), long range (300 m @90% reflectivity), dual-axis compensator and high scan speed (50k pts/sec). In addition, the total station-like interface and on-board graphic colour touch screen display allow users onsite data viewing. Moreover, this scanner also has internal memory storage of 80 Gigabytes which is ideal for large area surveying.

Data Collection

The laser survey of the fortification was carried out by using the traversing method. This surveying procedure allows the user to take advantage of the Leica C10 built-in dual-axis compensator to use conventional surveying techniques to perform a traverse, and establishing relationships between successive scanner positions within a known or assumed coordinate system. Because the dual-axis compensator automatically corrects scan data for vertical, the traverse procedure does not require as many targets as regular target-based registration.

An open traverse consisting of 9 laser stations was set up to completely cover the study area.

On each station the laser scanner was set on a tripod and then carefully leveled and plumbed directly over the top of the traverse mark on the ground. Levelling of the instrument is required in order to enable automatic registration of acquired scans and to minimize measurement errors. After setting out the TLS, bearing and coordinates of the back station were set in order to define the fore station. Position of back and fore stations were measured by the laser scanner using proper Leica target poles (Fig. 4), whose sizes are automatically stored in the laser firmware.

Figure 4: Setup of the Leica C10 over a traverse mark and target pole over the back target.

In order to meet the requirement of a clear line of sight between each target station (back and fore) and the laser station, scanner positions were carefully designed by taking into account the inner geometry of the fortification.
From each laser station a set of scans were acquired with an average spatial resolution of about 1 cm at a distance of 10 m. Following a few initial tests, this value was deemed the most suited to generate a 3D model with good level of detail for subsequent analyses.

Data processing

The raw data collected with the ScanSation C10 were then imported in Leica Cyclone software for processing. Firstly, the sequence of the scan stations was assembled in the Cyclone Traverse Editor in order to build the traverse. To this aim, instrument and target heights were entered for each scanner position. After verification and validation, the traverse could be carried out. Following this step, a registration process was applied in order to transform all the individual scans into a single dataset using 6 parameters of a rigid-body transformation [8]. However with traversing, some initial constraints between laser stations could be generated and used to strength the alignment among the scans, giving a very geometrically accurate 3D model. Indeed, at the end of traverse processing, the laser stations and associated point clouds were defined in a common reference frame. This way scans acquired from different locations resulted to be already spatially "close" each other. In addition, the information about instrument levelling, stored at each scanner position within the scans, allowed to remove a degree of freedom in the computing of the spatial transformation parameters between laser stations. Thus, by exploiting both these kind of spatial information, scan alignment could be automatically performed. However, since the generation of a laser traverse is always affected by residual errors, the registration results achieved this way needed to be furtherly refined. To this aim, an iterative global alignment process, based on the well known ICP (Iterative Closest Point) algorithm, was applied to all the pre-registered scans [9,10]. After the refinement step, the average residual alignment error was reduced to few millimeters (Fig. 5), and a global point cloud of about 27 mil of points was obtained (Fig. 6). As such large amount of points was mainly due to the high degree of overlap between adjacent scans, the global cloud was properly decimated in CloudCompare software,

setting an average point spacing of 1 cm. A final point cloud of ca 3.8 mil of points was then generated.

Constraint ID	ScanWorld	ScanWorld	Type	Error Vector
Cloud/Mes...	100: Stazione ...	300: Stazione ...	Cloud: Cloud/Mesh - Cloud...	aligned [0.003 m]
Cloud/Mes...	200: Stazione ...	400: Stazione ...	Cloud: Cloud/Mesh - Cloud...	aligned [0.003 m]
Cloud/Mes...	200: Stazione ...	100: Stazione ...	Cloud: Cloud/Mesh - Cloud...	aligned [0.003 m]
Cloud/Mes...	200: Stazione ...	300: Stazione ...	Cloud: Cloud/Mesh - Cloud...	aligned [0.003 m]
Cloud/Mes...	400: Stazione ...	500: Stazione ...	Cloud: Cloud/Mesh - Cloud...	aligned [0.003 m]
Cloud/Mes...	400: Stazione ...	300: Stazione ...	Cloud: Cloud/Mesh - Cloud...	aligned [0.003 m]
Cloud/Mes...	500: Stazione ...	600: Stazione ...	Cloud: Cloud/Mesh - Cloud...	aligned [0.004 m]
Cloud/Mes...	600: Stazione ...	700: Stazione ...	Cloud: Cloud/Mesh - Cloud...	aligned [0.008 m]
Cloud/Mes...	300: Stazione ...	800: Stazione ...	Cloud: Cloud/Mesh - Cloud...	aligned [0.006 m]
Cloud/Mes...	800: Stazione ...	900: Stazione ...	Cloud: Cloud/Mesh - Cloud...	aligned [0.007 m]

Figure 5: Results of the registration refinement.

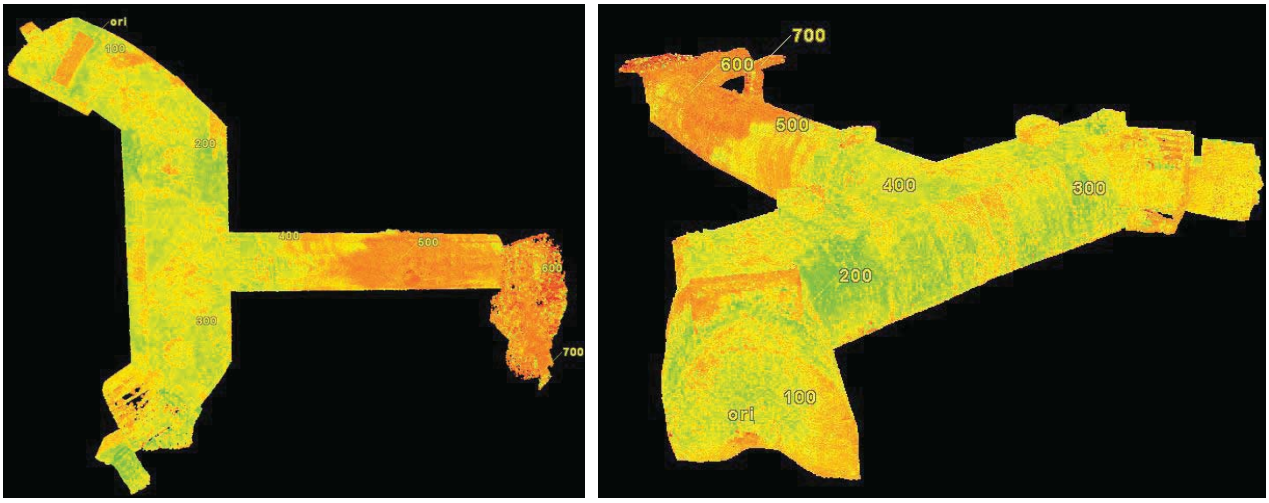

(a) (b)

Figure 6: Top view (a) and perspective view (b) of the decimated 3D model of "Impossible" bastion derived from TLS measurements. Intensity data are mapped onto the model with false color scale. Numbers denote traverse stations.

RESULTS:

Agisoft PhotoScan provided a reconstruction of 221 million points. Scaling factor has been estimated by comparing camera positions in the photogrammetric reconstruction and in the UWB positioning. Resulting estimated scale factor is 2.35, approximately.

Registration between TLS and photogrammetric reconstruction has been done with ICP algorithm. Resulting (RMSE) fitting error is 21.9cm, average error 13.4cm, and standard deviation 13.5cm. Fig. 7 shows how errors values are distributed over the bastion.

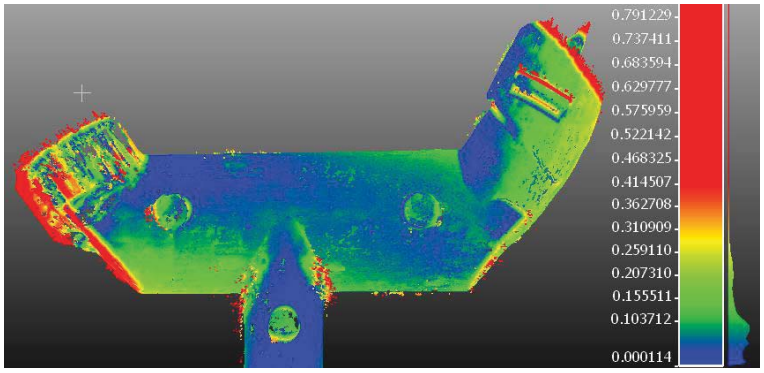

Figure 7: Error map for scale = 2.35. Figure was obtained from CloudCompare. Red values corresponds to higher error values. Values are saturated at 41cm (red values start approximately at 33cm, as shown in the color bar on the right).

As shown in Fig. 7, most critical areas are those at the two (left and right) extremes of the bastion. Main reason for this is the error in the estimated scaling factor between PhotoScan and metric reconstruction. This is confirmed by Fig. 8, which shows the error map when considering scale factor = 2.27. This scale factor value has been experimentally derived in order to obtain best fit between PhotoScan and TLS reconstruction. It is quite apparent that scaling factor used in Fig. 8 allows to obtain a better fitting than in Fig. 7. RMSE fitting error in this case is 12.3cm, average error 3.6cm, and standard deviation 7.8cm.

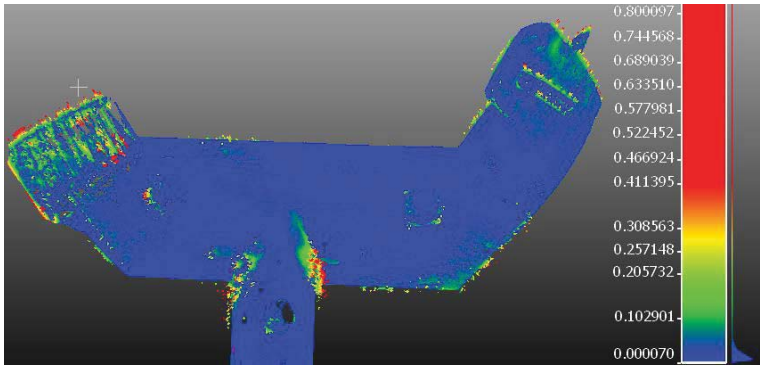

Figure 8: Error map for scale = 2.27. Figure was obtained from CloudCompare. Red values corresponds to higher error values. Values are saturated at 41cm (red values start approximately at 33cm, as shown in the color bar on the right).

It is worth to notice that some error peaks are still present in fig. 8, mostly due to reconstruction noise. Actually, a critical part in this reconstruction is given by the top left extreme part of the bastion in Fig. 8: this area is intrinsically quite complex to reconstruct, as visible in Fig. 9.

Figure 9: Left extreme part of the bastion.

Indeed, excluding the area shown in Fig. 9 from the validation, resulting (RMSE) fitting error is 17.3cm, average error 11.5cm, and standard deviation 9.5cm when considering scaling factor 2.35. When considering scaling factor 2.27, RMSE is 8.4cm, average error 2.4cm, and standard deviation 3.1cm.

CONCLUSIONS AND FUTURE WORKS:

This paper compared indoor surveys of a mediaeval bastion in Padua done by means of (i) TLS and (ii) photogrammetric reconstruction, where metric scale in the latter is provided by a UWB based positioning system. The rationale of the latter is basically that of developing a low cost system for indoor surveys. Metric scale in this case is obtained by comparing camera positions in the structure from motion reconstruction (obtained by Agisoft PhotoScan) with those obtained by the considered UWB system. Pozyx UWB devices provided range measurements, which were processed off-line. Tag Pozyx device was attached to the camera during image acquisitions. Camera altitude was approximately constant during the survey, hence its altitude was set to a known constant value in the positioning algorithm in order to obtain best 2D positioning performance. Scaling factor estimated with this method 2.35 is only quite close to the best fitting one (e.g. 2.27). Improving positioning method, for instance introducing different weights for the UWB estimates, might allow to obtain better estimates of the scaling factor.

Error on the scale causes a RMSE on the overall reconstruction of 21.9cm, whereas the use of scale factor 2.27 leads to 12.3cm RMSE. Area shown in Fig. 9 is that causing most of the largest errors. Excluding that from the validation RMSE reduces to 17.3cm with scaling factor 2.35 (and 8.4cm with scaling factor 2.27). Applying some more smoothing to the photogrammetric reconstruction might probably allow to reduce the presence of certain isolated large errors due to large values of reconstruction noise.

Future investigations will also dedicated to self-positioning of UWB devices, which actually can be of major interest in real applications. Furthermore, comparison with results obtained with Leica Pegasus backpack mobile mapping system will also be investigated.

REFERENCES:

1. Saeedi, S., Moussa, A., El-Sheimy, N., 2014, Context-Aware Personal Navigation Using Embedded Sensor Fusion in Smartphones. Sensors, 14, pp. 5742–5767.
2. Widyawan, 2012, Virtual lifeline: Multimodal sensor data fusion for robust navigation in unknown environments, Pervasive Mob. Comput., 2012, 8, pp. 388–401.
3. Pozyx Lab, Pozyx positioning system, https://www.pozyx.io/
4. Hol, J, 2011, Sensor Fusion and Calibration of Inertial Sensors, Vision, Ultra-Wideband and GPS. Ph.D. Thesis, The Institute of Technology, Linköping University, Linköping, Sweden.
5. Dierenbach, K., Ostrowski, S., Jozkow, G., Toth, C.K., Grejner-Brzezinska, D.A., Koppanyi, Z., 2015, UWB for Navigation in GNSS Compromised Environments, Proceedings of the 28th International Technical Meeting of The Satellite Division of the Institute of Navigation (ION GNSS+ 2015), pp. 2380-2389.
6. Toth, C., Jozkow, G., Ostrowski, S., Grejner-Brzezinska, D.A., 2015, Positioning Slow Moving Platforms by UWB technology in GPS-Challenged Areas, The 9th International Symposium on Mobile Mapping Technology, MMT 2015.
7. Masiero, A., Guarnieri, A., Pirotti, F., Vettore, A., 2014, A particle filter for smartphone-based indoor pedestrian navigation. Micromachines 5(4), pp. 1012-1033.
8. Reshetyuk, Y., 2009, Self-Calibration and Direct Georeferencing in Terrestrial Laser Scanning, Stockholm Royal Institute of Technology.
9. Besl, P. J., McKay, N. D., 1992. A method for registration of 3-D shapes. IEEE Transactions on Pattern Analisys and Machine Intelligence, 4(2): 239–256.
10. Chen, Y., Medioni, G, 1992. Object modelling by registration of multiple range images. Image and Vision Computing, 10(3):145–155.

Alternative Approaches for Feature-Based Down-sampling of Irregular Point Clouds for Fine Registration

F. He [a,*], Y. J. Lin[a], W. Xiong[a], A. Habib[a]

[a] Digital Photogrammetry Research Group
Lyles School of Civil Engineering
Purdue University, 550 Stadium Mall Dr., West Lafayette, IN 47907, USA
– (he270, lin599, xiong43, ahabib) @purdue.edu

KEY WORDS: Point Cloud Registration, Down-sampling, Local Point Density, Planar Features, Gaussian Sphere

ABSTRACT:

Due to the varying nature of acquired/derived 3D data from active/passive sensors, the fine registration of point clouds with non-uniform point density remains to be a challenging task. To address this challenge, two down-sampling procedures, which aim at improving the efficiency and accuracy of the ICPatch-based fine registration, are introduced in this paper. Specifically, the first approach is based on an adaptive down-sampling strategy to remove redundant points in areas with high point density while keeping points in lower density regions. The second procedure starts with the derivation of surface normal for the constituents of a given point cloud using their local neighborhoods. The derived surface normals are represented on a Gaussian Sphere. Then, a down-sampling procedure is achieved by removing points from detected peaks in the Gaussian Sphere. Experimental results from both simulated and real datasets are conducted to verify the feasibility of the proposed down-sampling procedures in providing reliable transformation parameters in the presence of random noise in the acquired point clouds. In addition, the derived experimental results also demonstrate that the implemented down-sampling can exceed the performance of some conventional fine registration approaches, which utilize either the original or uniformly down-sampled points, in terms of providing smaller RMSE values and faster convergence rate.

1. INTRODUCTION

Accurate three dimensional modelling of objects has become an important task for various applications, such as industrial site modelling, 3D documentation of historical monuments, urban planning, and several civilian and military applications. Currently, 3D reconstruction/representation of objects can be achieved through either active or passive remote sensing systems. Active sensors, such as laser scanners, directly provide precise and dense point cloud, which is properly scaled, along the scanned objects. In spite of the high point density of laser scanning data, break-lines are not usually well defined by such data. The derived laser-based point cloud usually lacks spectral information (especially when dealing with data collected by laser scanners onboard mobile platforms). On the other hand, passive sensors such as digital frame cameras can be incorporated for 3D reconstruction while providing spectral attributes for the derived coordinates. Such semantic attributes would allow for the derivation of better and more reliable information pertaining to the reconstructed objects. However, the main challenge in deriving 3D information from passive sensors is feature matching in overlapping imagery (i.e., the automated identification of conjugate features in the involved images). Considering the complementary characteristics of derived 3D data from active and passive sensors, the geospatial research community has advocated the integration of point clouds from these data acquisition modalities (González-Aguilera et al., 2009). One should note that effective integration of such derived data depends on their alignment relative to a common reference frame, which is known as the registration problem.

The registration of 3D point clouds involves the estimation of the 3D Helmert transformation parameters (i.e., scale factor, three translations, and three rotation angles) relating the reference frames of the different point clouds. Depending on the accuracy of estimated transformation parameters, current registration procedures can be categorized into either coarse or fine registration techniques (Matabosch et al., 2005). Coarse registration is usually used to establish rough alignment between the involved point clouds (He and Habib, 2016). Fine registration, on the other hand, starts from coarsely-aligned point clouds to achieve more precise alignment of the involved datasets. The most commonly used approach for fine registration is the Iterative Closest Point (ICP), where the transformation parameters are iteratively refined by generating pairs of corresponding points and minimizing point-to-point distances (Besl and McKay, 1992; Chen and Medioni, 1991). Due to the irregular nature of point clouds, point-to-point correspondence cannot be always assumed. Therefore, different variants of the ICP have been introduced. For example, the Iterative Closest Patch (ICPatch) utilizes points in one point cloud and triangular patches in another point cloud as the registration primitives (Habib et al., 2010a). Instead of minimizing the point-to-point distance, the ICPatch approach is implemented by minimizing the sum of the squared normal distances between conjugate point-patch pairs. Although current ICP and its variants (e.g., ICPatch) have demonstrated their feasibility in providing reliable point clouds registration, they do not consider the varying characteristics of 3D point clouds arising from active and passive sensors onboard various platforms. For example, the point density acquired from airborne laser scanners (ALS) is usually in the range from 1 to 40 pts/m2 (Hyyppä et al., 2009), which is much lower than that for a terrestrial laser scanner (TLS) and mobile terrestrial laser scanner (MTLS) data. In practice, such varying nature might lead to unreliable estimation of the transformation parameters. The potential challenges associated with the ICP-based registration for 3D point clouds derived from active and passive sensors can be summarized as follows:

1. The derived image-based/laser-based point clouds usually include excessive number of points. Therefore, for these

* Corresponding author. This is useful to know for communication with the appropriate person in cases with more than one author.

datasets, the conventional ICP-based registration, which utilizes the entirety of the available points, is usually very time-consuming. For example, there are usually thousands of points acquired along a given planar feature within a high point density area. However, only a few of them are required to represent a reliable planar surface, whereas the remaining points are redundant.

2. Due to the nature of the utilized sensors, the acquired point clouds usually do not have a uniform point density. For example, the point cloud acquired by a TLS usually have a higher point density close to the scanner. Such variations in point density will negatively impact the quality of the registration procedure as they might lead to over-weighting for points in high density areas.

The existing body of literature has demonstrated that point cloud down-sampling will have a significant impact on improving the efficiency and accuracy of the fine registration. Turk and Levoy (1994) proposed a simple down-sampling strategy for the ICP, where the involved point clouds is randomly down-sampled. In each iteration of the ICP, a set of random points are utilized. However, such simple down-sampling strategy does not consider the local surface characteristics or the local point density variation within the involved point clouds, and it only improves the efficiency of the registration by reducing the number of utilized points. Weik (1997) investigated the utilization of points with high intensity gradient to improve the accuracy of the ICP-based registration. However, in his work, color or intensity information is required. A most recent down-sampling strategy for the ICP is proposed by Rusinkiewicz and Levoy (2001). In their work, a normal space, which is based on the surface normal of each point, is first generated. Then, points are selected in the normal space to make sure variation among normal vectors is as large as possible. However, some "unreliable" points, such as points from trees and other vegetation, may be utilized for the estimation of transformation parameters. This would lead to an unstable alignment of the point clouds.

Therefore, this research is dedicated to addressing the above-mentioned challenges for point cloud fine registration – namely, the excessive number of points, and the varying point density - by presenting two alternative approaches. Different from current point cloud down-sampling techniques (e.g., random-based down-sampling), the introduced approaches consider the physical characteristics of the encompassing surfaces and the distribution of point clouds in 3D. More specifically, the first approach is based on an adaptive down-sampling strategy to remove redundant points in areas with high point density while keeping points in lower density regions. The second procedure starts with deriving surface normal, which can be presented on a Gaussian Sphere, of a given point cloud using their local neighborhoods. Then, down-sampling is achieved by removing points from peaks detected in the Gaussian sphere. It is worth mentioning that in the proposed two approaches, only points from planar regions will be identified and utilized for the fine registration. The motivation behind using planar points is that rough/linear points may have negative impacts on the fine registration as either point-to-point or point-to-patch correspondences cannot be assumed. Finally, a comparative analysis, which comments on the computational efficiency and the registration quality, will be carried out in this research to evaluate the performance of the two proposed approaches.

In the remainder of this paper, the details of the two introduced approaches for point cloud fine registration are first introduced. Afterwards, a comparative analysis, which comments on the computational efficiency and the registration quality, is conducted on both simulated and real datasets. Finally, drawn conclusions and recommendations for future work are introduced.

2. SPATIAL INFORMATION-BASED DOWN-SAMPLING METHODOLOGIES

In this research, a fully automated workflow, which incorporates the two proposed down-sampling approaches, is implemented for improving the fine registration relating two point clouds (i.e., the ***aligned*** and ***reference*** point clouds). As shown in Figure 1, the proposed workflow includes three steps. In the first step, the ***aligned*** point cloud is initially classified as planar, linear/cylindrical, and rough points based on their local neighborhoods. Then, the two proposed approaches are conducted on points from planar regions to reduce the data size. Finally, the down-sampled planar points are introduced to an Iterative Closest Patch (ICPatch) algorithm for fine registration (Habib et al., 2010b).

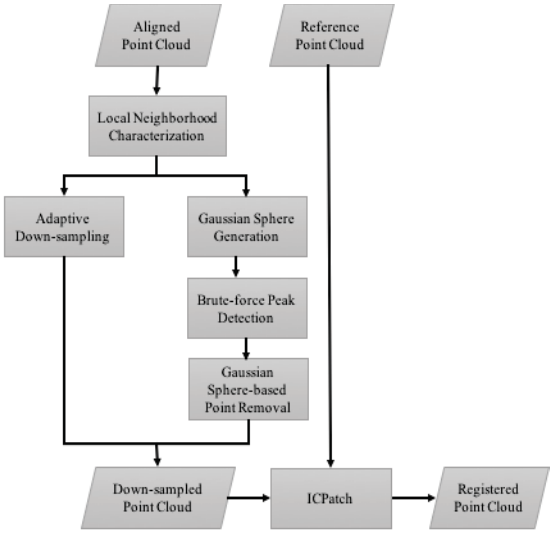

Figure 1. Workflow of the proposed methodologies

2.1 Localization Neighborhood Characterization

Since the proposed down-sampling procedures are only applied on points within planar regions, a local neighborhood characterization is initially implemented for identifying the points that belong to planar, linear and cylindrical, and rough features. The local neighborhood characterization can be achieved through an eigenvalue analysis for a given point $\boldsymbol{P_o}$ using its $\boldsymbol{n}$ nearest neighbors. The eigenvectors represent the orientation of the neighborhood in the 3D space, while the eigenvalues define the extent of the neighborhood along the directions of their corresponding eigenvectors. For a planar neighborhood, one of the eigenvalues will be quite small when compared to the other two (See Figure 2). Once the local planar neighborhood is classified, the local point density of the identified planar point can be derived. The mathematical model for the local point density estimation is presented as Equation 1.

$$LPD\left(\frac{pnts}{m^2}\right) = \frac{n+1}{\pi r_n^2} \quad (1)$$

Where,

$\boldsymbol{n}$ is the number of points within the local neighborhood, and

$\boldsymbol{r_n}$ is the distance between the point $\boldsymbol{P_0}$ and its $\boldsymbol{n}^{th}$ farthest neighbor.

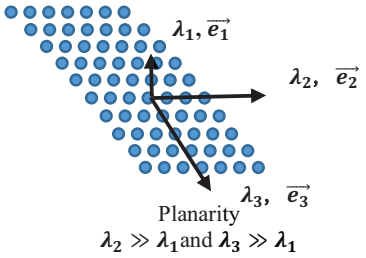

Figure 2. Eigenvalue analysis of a planar neighborhood

2.2 Point Cloud Down-Sampling

Now that the local neighborhood characterization is completed, the two proposed approaches can be adopted to reduce the number of points along planar surfaces. In this research, the first approach is based on an adaptive down-sampling procedure (Al-Durgham,2014; Lin,2016). The second approach, on the other hand, is achieved by removing points from detected peaks in a Gaussian Sphere, which is generated from the surface normal derived from the local neighborhood characterization process.

2.2.1 Adaptive Down-Sampling

The conceptual basis of the adaptive down-sampling is to achieve a desired point density through the probability-based test in Equation 2.

$$\delta = \frac{t}{d_i} = \begin{cases} \geq r, & maintain \\ else, & eliminate \end{cases} \quad (2)$$

Where,
t is the desired point density in pts/m^2,
d_i is the local point density within the ith point local neighborhood in pts/m^2, and
r is a random number that is picked from a uniform distribution in the range [0, 1].
According to Equation 2, when the local point density (d_i) of a point is below a desired point density (t), the point will be maintained in the down-sampled point cloud since the test value (δ) will be larger than 1. On the other hand, Since the range for the random number (r) generated using a uniform distribution in the range of [0, 1], when the local point density is larger than the desired point density, the point has a probability of (1 - δ) to be removed. Interest readers can refer to Lin (2016) for more details.

2.2.2 Gaussian Sphere-Based Down-Sampling

Alternatively, motivated by the fact that points within the same planar region have similar surface normals, the second approach starts with the derivation of surface normal for the constituents of a given point cloud. In this research, the surface normal of points along planar surfaces are derived through the local neighborhood characterization, which has been introduced in Section 2.1. Then, the derived surface normals for all those points that are classified as planar features are represented on a Gaussian Sphere. Afterwards, the down-sampling is achieved by removing points from detected peaks in the Gaussian Sphere. Due to the utilization of the Gaussian Sphere, this approach will be denoted here forth as the "Gaussian Sphere-based Down-sampling". In the remainder part of this section, the Gaussian Sphere-based approach is introduced through three steps, which can be summarized as: Gaussian Sphere generation, brute force-based peak detection, and Gaussian Sphere-based point removal.

Gaussian Sphere Generation: With the purpose of down-sampling points that have similar surface normal, a representation that groups points into a different domain is required. Gaussian sphere, also known as the Extended Gaussian Image (EGI) is a mapping of the surface normals of a specific object onto a sphere of unitary radius to represent the orientation attribute (Horn, 1984). For any point cloud data, the EGI could be established by projecting the surface normal estimated for the constituents of a point cloud to a specific sphere. Figure 3 shows a sample Gaussian sphere created from a point cloud dataset.

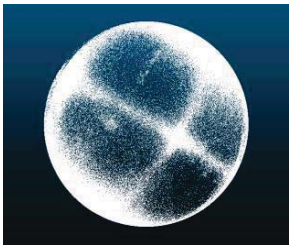

Figure 3. A sample image of a Gaussian Sphere

A practical approach to generate the Gaussian Sphere starts with normalization of the surface normal for each point into a unit vector. Then, these unit vectors are represented in the 3D space using a sphere with unit radius. It is important to note that, since points with similar surface normal are mapped onto the same location on the Gaussian Sphere, planar regions sharing similar direction but spatially disconnected contribute to a common peak. Therefore, the number of points within the planar regions can be reduced by down-sampling each corresponding peak on the derived Gaussian Sphere.

Brute Force-based Peak Detection: In order to remove redundant points from each peak on the Gaussian Sphere, the identification of existing concentration areas on the Gaussian Sphere is required. A brute-force peak detection approach, which traverses the Gaussian Sphere point cloud (Lari and Habib, 2014), is adopted in this research. More specifically, this approach starts with constructing a KD-tree structure for all derived surface normals, which can be represented on the Gaussian Sphere. As shown in Figure 4, a threshold of 5° solid angle is then pre-defined to determine the search radius for peak detection. Afterwards, each of the involved points is traversed to retrieve the one with the maximum number of neighboring points within the pre-defined search radius on the Gaussian Sphere for peak detection. Once a peak is identified, the detected point as well as all points fallen into its neighborhood as determined by the 5° solid angle are eliminated from the KD-tree structure. Such peak detection and elimination process will be repeated until the largest number of points within a given neighborhood is smaller than a predefined threshold.

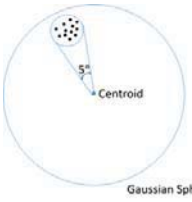

Figure 4. A 5° solid angle on Gaussian Sphere is predefined to determine the search radius for peak detection

Gaussian Sphere-based Point Removal: Before applying the down-sampling process, one should note that a single peak detected on the Gaussian Sphere may correspond to several spatially-disconnected planar regions. In order to identify these spatially-disconnected planar regions, the proposed point removal strategy starts with a Euclidean distance-based connected component approach, which aims at grouping points into several disconnected planar surfaces based on point-to-point Euclidean distances. As shown in Figure 5, points $\boldsymbol{i}$ and $\boldsymbol{j}$ are grouped into the same planar surface $\boldsymbol{P}$ as the distance $\boldsymbol{d_{ij}}$, which denotes the distance between the two given points (i.e., $\boldsymbol{i}$ and $\boldsymbol{j}$), is less than a pre-defined threshold $\boldsymbol{d}$. On the other hand, point $\boldsymbol{k}$ cannot be grouped into $\boldsymbol{P}$ since the distance $\boldsymbol{d_{ik}}$ exceeds the threshold. Now that the connected component procedure is completed, a reduction percentage is applied on each group to remove redundant points and maintain a maximum number of points for each of the detected peaks on the Gaussian Sphere. Different from the adaptive down-sampling approach, the Gaussian Sphere-based point removal does not rely on the estimated local point density.

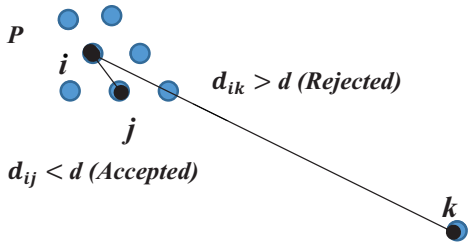

Figure 5. Sample image to demonstrate Euclidean distance-based connected component

2.3 ICPatch Registration

Once the down-sampling procedure is finalized, the ICPatch approach is implemented for the precise alignment of the involved point clouds. In this research, the ICPatch registration is performed between the ***aligned*** point cloud, which has been down-sampled through the introduced approaces, and the ***reference*** data. Instead of point-to-point correspondence, the geometric primitives chosen for the ICPatch registration are points and triangular patches (Habib et al., 2010). Therefore, for any two overlapping surfaces, one of the point clouds is kept as is, and the other one is converted to a set of triangular patches. Conventionally, a Triangulated Irregular Network (TIN) is usually utilized for the patch generation. However, the generation of TIN can be only adopted in 2D space. Therefore, in this research, instead of using the TIN to define the patches, the point-to-patch correspondences are established by searching for the three closest points of each query point. Then, the co-planarity constraint is implemented using all derived point-to-patch correspondences to solve for the transformation parameters between the two involved point clouds. In this research, query points are selected in the ***aligned*** point cloud, and the corresponding patches are defined in the ***reference*** data.

3. EXPERIMENTAL RESULTS

Experimental results from simulated and real datasets have been conducted to investigate the feasibility of the two proposed down-sampling procedures in providing reliable transformation parameters for the fine registration of 3D point clouds.

3.1 Simulated Dataset

There are two objectives for the experimental testing with simulated dataset. The first objective is to evaluate the impact on the estimated transformation parameters when adding noise with different magnitude to the simulated point cloud. In this research, the ability of the tested approaches to deal with introduced noise is evaluated by gradually increasing the noise level to a standard deviation of ± 0.05 m. Only the two proposed approaches are tested for the first objective. The second objective, on the other hand, is to evaluate the performance of the implemented down-sampling procedures against two commonly adopted strategies for the ICPatch registration, including using: 1) all possible points and 2) a set of randomly down-sampled points. More specifically, for the simulated dataset, a set of five planes with different orientation have been generated (See Figure 6). The ground coverage of the simulated dataset is 20 m by 20 m, and the height range is 25 m. The maximum point density of the simulated planes is 1600 pts/m^2, while the minimum point density is 25 pts/m^2. Then, a set of pre-defined 3D-Helmert transformation parameters, Table 1, is applied to the simulated points to generate another point cloud established in a different coordinate system. In this research, the point cloud, which is transformed to a different coordinate system, is utilized as the ***reference***, while the original simulated points are considered as the ***aligned*** dataset. Figure 6 illustrates both the ***reference*** and ***aligned*** point clouds.

$T_X\ (m)$	$T_Y\ (m)$	$T_Z\ (m)$	s	$\omega°$	$\phi°$	$\kappa°$
-0.15	-0.38	0.27	1.0	3.5	-2.8	1.6

Table 1. The 3D-Helmert transformation parameters relating the coordinate systems of the simulated ***reference*** and ***aligned*** datasets

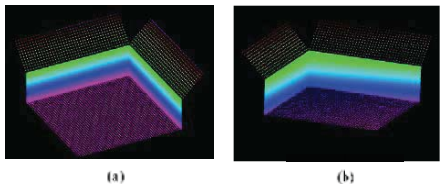

Figure 6. The (a) ***reference***, and (b) ***aligned*** point clouds for the simulated datasets

3.1.1 Simulated Dataset Results

Table 2 illustrates the absolute rotation and translation differences between the estimated and true transformation parameters at each given noise level using the two proposed approaches. In order to compare these two approaches with the other two commonly adopted strategies (i.e., using a set of randomly selected points or all possible points), the convergence of each estimated transformation parameter as well as the derived RMSE values (i.e., the RMSE of point-to-patch normal distances in ICPatch) for each conducted tests are illustrated in Figure 7. It is worth noting that this comparison is only conducted on the simulated dataset with a ± 0.05 m noise level. One should also note that since the number of points may have significant impact on the fine registration, in this research, the number of points derived from the adaptive down-sampling is used as the reference number. Then, the reduction percentage of Gaussian Sphere-based and random down-sampling is accordingly adjusted to ensure a compatible number of query points for the ICPatch registration. In this experimental test, the desired local point

density for the ***aligned*** point cloud is set to 20 pts/m2. Table 3 presents the number of points utilized in each of the conducted tests. To be specific, the total number of points in the ***aligned*** dataset is reported in Column 2. Since both adaptive and Gaussian Sphere-based down-sampling are conducted on points along planar surfaces, the number of planar point features, which are derived from the local neighborhood characterization process, is presented in Column 3. The number of points utilized for ICPatch is illustrated in Column 4.

Noise (m)	$\Delta T_x\ (m)$	$\Delta T_y\ (m)$	$\Delta T_z\ (m)$	$\Delta\omega$ (°)	$\Delta\phi$ (°)	$\Delta\kappa$ (°)
Adaptive Down-sampling						
0.01	0.002	0.001	0.002	0.002	0.003	0.001
0.02	0.001	0.002	0.002	0.004	0.005	0.002
0.03	0.001	0.010	0.012	0.011	0.002	0.010
0.04	0.011	0.001	0.014	0.010	0.008	0.019
0.05	0.003	0.022	0.006	0.005	0.019	0.011
Gaussian Sphere-based Down-sampling						
0.01	0.004	0.003	0.001	0.002	0.001	0.001
0.02	0.007	0.010	0.002	0.003	0.006	0.004
0.03	0.009	0.011	0.011	0.007	0.003	0.007
0.04	0.009	0.004	0.006	0.012	0.016	0.028
0.05	0.004	0.025	0.007	0.011	0.027	0.031

Table 2. Absolute rotation and translation differences for various noise values using the adaptive and Gaussian Sphere-based down-sampling

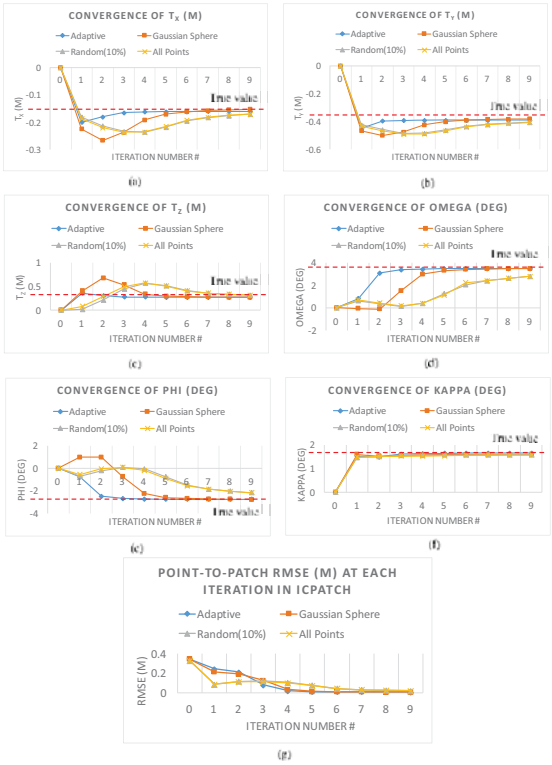

Figure 7. (a) – (f) Estimated transformation parameters, and (g) RMSE values of point-to-patch normal distance at each ICPatch iteration in the four conducted tests: 1. adaptive downsampling, 2. Gaussian Sphere-based down-sampling, 3. random down-sampling, and 4. using all points.

	Number of points in the ***aligned*** dataset	Number of planar point features	Number of down-sampled points for ICPatch
Adaptive	10,709	99,977	3,944
Gaussian Sphere	10,709	99,977	3,944
Random	10,709	N/A	3,944
All Points	10,709	N/A	10,709

Table 3. The number of points utilized in the four conducted tests: 1. adaptive down-sampling, 2. Gaussian Sphere-based down-sampling, 3. random down-sampling, and 4. using all points.

Closer inspection of the derived results in Tables 2 and 3, and Figure 7 reveals the following:

1. For simulated dataset with gradually increasing the noise level to a standard deviation of ± 0.05 m, the maximum absolute rotation and translation errors derived from the two proposed down-sampling procedures are 0.019° and 0.031° , and 0.0022 m and 0.0025 m, respectively (highlighted in Table 2). This result indicates that both the adaptive and Gaussian Sphere-based down-sampling provide accurate estimate for the transformation parameters.
2. Compared to the two commonly adopted strategies – random down-sampling or using all points, the two implemented procedures have much faster convergence rate. This result demonstrates that the two implemented down-sampling approaches can be more efficient for the fine registration.
3. The ICPatch registration using either a set of randomly selected or all possible points demonstrate a similar performance in terms of their convergence rate. This is due to the fact that the random down-sampling does not change the distribution of the utilized point clouds (i.e., after applying the random down-sampling, there are more points in the high point density area while less points in the low point density regions).
4. In spite of the comparable RMSE values of the point-to-patch normal distance, the proposed adaptive down-sampling demonstrates better convergence rate on both estimated translation and rotation parameters when comparing to the Gaussian Sphere-based approach. This result indicates that the proposed adaptive down-sampling can be more helpful for the fine registration since it requires less iterations to converge.

3.2 Real Dataset

One real dataset, which is acquired at the vicinity of a building, is utilized for the experimental test. For this real dataset, two point clouds with a total number of 66,541 (***reference*** dataset) and 143,779 (***aligned*** dataset) points are acquired by a Leica HDS 3000 static laser scanner. Similar to the experimental tests for the simulated dataset, both the two proposed approaches and the two commonly adopted strategies are conducted on the real dataset. For the adaptive down-sampling approach, the desired local point density is set to 20 pts/m^2. In this experimental test, a total number of 23,059 points are maintained in the ***aligned*** dataset after conducting the adaptive down-sampling. Then, the reduction percentages for the Gaussian Sphere-based and random down-sampling are accordingly adjusted to ensure a compatible number of points used in the ICPatch registration. Figure 8 illustrates the two utilized real laser point clouds.

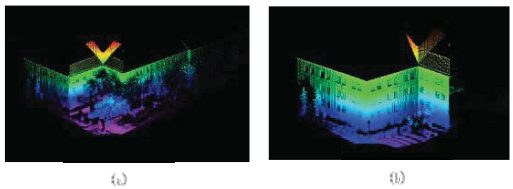

Figure 8. The (a) ***Reference***, and (b) ***aligned*** point clouds for the real dataset

3.2.1 Real Dataset Results

The experimental results derived from the real dataset is presented in Table 4. To be specific, columns 2, 3, and 4 of the table show the number of points utilized in each of the conducted test. Besides, the derived RMSE values of the point-to-patch normal distance and the total execution time for each of the conducted tests are reported in Columns 5 and 6 of Table 4, respectively.

Looking into these results, one can note that, for this real dataset, the random down-sampling has the largest RMSE value of 0.071 m, while the adaptive down-sampling demonstrates the smallest RMSE value of 0.044 m. Compared to the adaptive down-sampling, the Gaussian Sphere-based down-sampling has a similar performance in terms of the derived RMSE value. However, it takes the longest time to complete the whole procedure since we use a brute-force approach for the peak detection, which is quite inefficient and time-consuming. Considering both the execution time and the derived RMSE values, one can conclude that the adaptive down-sampling is the best option for this real dataset since it is capable of providing a small RMSE value while completing the whole procedure within a relative short execution time.

	Adaptive	Gaussian Sphere	Random	All Points
Number of points in the ***aligned*** dataset	143,799	143,799	143,799	143,799
Number of planar point features	12,7862	12,7862	N/A	N/A
Number of down-sampled points for ICPatch	23,059	23,059	23,059	143,799
RMSE (m)	0.044	0.048	0.071	0.060
Execution time (sec)	113.27	895.61	34.52	193.56

Table 4. The experimental results of the four tests 1. adaptive down-sampling, 2. Gaussian Sphere down-sampling, 3. random down-sampling, and 4. using all points for the real dataset

4. CONCLUSIONS AND RECOMMENDATIONS FOR FUTURE WORK

In this research, we introduced two down-sampling procedures for the registration of 3D point clouds with non-uniform point density. The first procedure utilizes an adaptive down-sampling strategy to remove redundant points in areas with high point density while keeping the points in lower density regions. The second procedure starts with the derivation of surface normal for each point. Then, the surface normal are projected on a Gaussian sphere. Afterwards, down-sampling is achieved through removing points from peaks detected in the Gaussian sphere. Experimental results have shown that both adaptive and Gaussian Sphere-based down-sampling procedures are capable of providing reliable estimate of the transformation parameters in the presence of random noise in the utilized point clouds. It is worth mentioning that for the Gaussian Sphere-based down-sampling procedure, the peaks are detected through a brute-force approach with a fixed search radius. This implementation can be time-consuming and inefficient. Therefore, our future work will focus on the improvement of peak detection in the Gaussian Sphere. Rather than adopting the brute-force strategy for peak detection, a more efficient search strategy will be used. Then, the utilization of an adaptive search radius, which can be derived while considering the local noise level, will be investigated.

REFERENCES

Al-Durgham, K., 2014. Geometric Features Extraction and Automated Registration of Static Laser Scans Using Linear Features.

Al-Durgham, M. M., 2014. The Registration and Segmentation of Heterogeneous Laser Scanning Data. University of Toronto.

Besl, P.J., McKay, N.D., 1992. Method for registration of 3-D shapes, in: Robotics-DL Tentative. International Society for Optics and Photonics, pp. 586–606.

Chen, Y., Medioni, G., 1991. Object modeling by registration of multiple range images, in: Robotics and Automation, 1991. Proceedings., 1991 IEEE International Conference on. IEEE, pp. 2724–2729.

González-Aguilera, D., Rodríguez-Gonzálvez, P., Gómez-Lahoz, J., 2009. An automatic procedure for co-registration of terrestrial laser scanners and digital cameras. ISPRS J. Photogramm. Remote Sens. 64, 308–316.

Habib, A.F., Detchev, I., Bang, K., 2010a. A comparative analysis of two approaches for multiple-surface registration of irregular point clouds. Int Arch Photogramm Remote Sens Spat Inf Sci 38.

Habib, A.F., Detchev, I., Bang, K., 2010b. A comparative analysis of two approaches for multiple-surface registration of irregular point clouds. Int Arch Photogramm Remote Sens Spat Inf Sci 38.

He, F., Habib, A.F., 2016. A Closed-form Solution for Coarse Registration of Point Clouds Using Linear Features. Journal of Surveying Engineering, 142(3), 04016006.

Horn, B.K., 1984. Extended gaussian images. Proc. IEEE 72, 1671–1686.

Hyyppä, J., Wagner, W., Hollaus, M., Hyyppä, H., 2009. Airborne laser scanning. SAGE Handb. Remote Sens. SAGE 199–211.

Lari, Z., Habib, A., 2014. An adaptive approach for the segmentation and extraction of planar and linear/cylindrical features from laser scanning data. ISPRS J. Photogramm. Remote Sens. 93, 192–212.

Lin, Y.-J., Ronald R, B., Habib, A., 2016. Planar-Based Adaptive Down-Sampling of Point Clouds. Photogramm. Eng. Remote Sens. 82, 955–966.

Matabosch, C., Salvi, J., Fofi, D., Meriaudeau, F., 2005. Range image registration for industrial inspection. Mach. Vis. Appl. Ind. Insp. XIII 5679, 216–227.

Rusinkiewicz, S., Levoy, M., 2001. Efficient variants of the ICP algorithm, in: 3-D Digital Imaging and Modeling, 2001. Proceedings. Third International Conference on. IEEE, pp. 145–152.

Turk, G., Levoy, M., 1994. Zippered polygon meshes from range images, in: Proceedings of the 21st Annual Conference on Computer Graphics and Interactive Techniques. ACM, pp. 311–318.

Weik, S., 1997. Registration of 3-D partial surface models using luminance and depth information, in: 3-D Digital Imaging and Modeling, 1997. Proceedings., International Conference on Recent Advances in. IEEE, pp. 93–100.

MONITORING IONOSPHERIC PERTURBATIONS OVER EGYPT BASED ON NATIONAL GNSS NETWORK

Mahmoud Abd Rabbou[1] and Adel El-Shazly[2]
Faculty of Engineering, Cairo University, Egypt; mahmoud.abdelrahman@cu.edu.eg[1]
Faculty of Engineering, Cairo University, Egypt; adel_shazly@hotmail.com[2]

KEY WORDS: GNSS, Regional Ionosphere modelling, GIM, IGS

ABSTRACT:

Ionospheric impact has the ability to cause severe propagation errors in modern radio communication systems such as aircraft communications and Global Navigation Satellite Systems (GNSS). As a result, real time detection of ionospheric effects is helpful to estimate the potential degradation of the performance of these systems. Globally, the International GNSS Service (IGS) provides Global Ionospheric Maps (GIM). However, the accuracy of these maps is affected by the global IGS GNSS stations distribution and network resolution. Unfortunately, currently, there are no IGS stations in Egypt, with low IGS GNSS network resolution in the Middle Eastern region, which in role is affecting the accuracy of IGS ionospheric estimation for Egypt region. Advances in Egyptian space physics research and related disciplines require better spatial and time resolution ionospheric information than the products provided by GIM. Global navigation satellite systems (GNSS) have been widely used to monitor variations in the earth's ionosphere by estimating total electron content (TEC) using dual-frequency observations. This research is targeting to develop a national near real-time ionospheric mapping based on a well national distributed GNSS network. The study objective is to develop a national GNSS-based, bias-free ionospheric TEC mapping methodology for Egypt, which would provide a better resolution in time and space than is currently available by IGS Global Ionospheric Maps (GIM) due to the unavailability of International GNSS Service (IGS) GPS receivers in Egypt. Adjusted spherical harmonic (ASHA) model will be developed for ionospheric total electron content (TEC) estimation. Slant TEC values along the GNSS signal paths are quantified from a network of GNSS receivers and converted to vertical TEC by means of the single layer mapping function. The model coefficients and GNSS differential biases are estimated from vertical TEC at the ionospheric pierce points and used to interpolate TEC at any location within the Egypt region.

1. INTRODUCTION

The ionosphere determination is an attractive field of scientific research today due to its general high impact on human, environment and technology. The ionosphere significantly affects terrestrial-based radio communication and attenuates high frequency wave propagating through it. Its effect on radio waves of astronomical origin in the bandwidth 70 MHz to 20 GHz,includes phase jitter, phase delay, refraction, scintillation and attenuation. Currently, wide range of tools is used to study the ionosphere and it's attributed physical and chemical processes (Hernández-Pajares et al. 2009). Global Navigation Satellite System (GNSS) represents a major tool to study the atmosphere layers especially the ionosphere(Amerian et al.2013 , Wu et al.2014, Tang et al.2014, Abdelazeem et al., Kao et al.2015, Li et al.201 , Zhang et al.2015, Xi et al.2015, Yang and Gao 2015, Durmaz and Karslioglu 2015). GNSS is a satellite-based navigation system which is used to detect the position and time in the three dimension earth and space. The advent of GNSS has led to technical revolutions in navigation as well as in fields related to surveying. Apart from surveying and navigation interest, GNSS has great importance in scientific applications. The GNSS satellites transmit signals that propagate through the ionosphere that exists at about 60 –1500 km above the Earth's surface (Hargreaves, 1992). The free electrons populating in this region of the atmosphere affects the propagation of the signals by changing their velocity and direction of travel. Ionosphere is highly seasonal (time) and geographical (space) variable with certain solar-related disturbances. Ionospheric range delay is a major error source in GNSS positioning and navigation, as a result, the ionosphere research attracts significant attention from the GNSS community.

The total electron content (TEC) represents the major parameter of the ionosphere that produces most of the effects of the radio signals. The GNSS ionospheric delay is proportional to the amount of TEC along the path from the GNSS satellite to a receiver. TEC is the integral of electron density in a 1 m2 column along the signal transmission through the ionospheric path. For ionosphere researchers, TEC describes the background state of the ionosphere. For these reasons, there are a number of GNSS networks whose main task is to provide measurements to allow assimilation of TEC maps. There are four prominent IGS Ionosphere Associate Analysis Centers (IAACs) that have been generated global TEC maps for over one decade. They are the Center for Orbit Determination in Europe (CODE), European Space Operations Center of ESA (ESOC), Jet Propulsion Laboratory (JPL), and Technical University of Catalonia (UPC). However, global TEC maps have limited precision and resolution which are often inadequate to describe detailed features of local ionosphere. There is the need for regional ionosphere models to provide high precision ionosphere delay correction. The existing regional ionosphere model typically relies on modeling of measurements from a dense local GNSS network in order to achieve high precision.

This research is targeting to establish a national ionospheric model for Egypt to provide high precision ionosphere delay correction. A Spherical Harmonic Model will be used in establishing the national ionospheric model. The spherical harmonics expansion up to degree and order 15. The proposed ionosphere maps will be generated on a daily basis using data from about 30 national dual frequency based GNSS stations along Nile valley and its Delta. The Targeting temporal resolution is two-hours and spatial resolution of 0.5° and 0.5° in longitude and latitude, respectively. Instrumental biases for all GPS satellites and ground stations will be estimated as constant values for each day.

2. IONOSPHERIC PROPAGATION EFFECTS

The propagation of a radio wave through the ionospheric plasma is described by the refractive index of the ionosphere. The refractive index mainly depends on the electron density, the strength and direction of the geomagnetic field in relation to the ray path. Thus, the spatial distribution of the electron density along the ray path and corresponding geomagnetic field relationships determine the ionospheric impact on the electromagnetic wave.

The phase refractive index n_p can be derived from the Appleton – Hartree formula as (Bassiri & Hajj, 1993)

$$n_p = 1 - \frac{f_p^2}{2f^2} \pm \frac{f_p^2 f_g \cos\Theta}{2f^3} - \frac{f_p^2}{4f^4}\left[\frac{f_p^2}{2} + f_g^2(1+\cos^2\Theta)\right]$$
$$f_p^2 = \frac{n_e e^2}{4\pi\varepsilon_0 m}$$
$$f_g = \frac{eB}{2\pi m} \quad (1)$$

where f is the signal frequency; f_p and f_g are the plasma and gyro frequencies, respectively; ε_0 is the free space permittivity; B is the geomagnetic induction; Θ is the angle between the wave propagation direction and the geomagnetic field vector B; e, n_e, m are the electron charge, density and mass, respectively. Equation (1) indicates that the phase ionospheric index is less than unity which means that the phase velocity is greater than the speed of light in a vacuum which is called phase advance impact. As a result, through the ionospheric layer, the integration of electrons n_e along the path of the receiver-satellite gives a distance less than the real range. In contrast with the phase ionospheric refraction index, which is affecting the GNSS carrier-phase observation with advanced impact, the group ionospheric fraction index is affecting the GNSS pseudorange observations which can describe as

$$n_g = 1 + \frac{f_p^2}{2f^2} \mp \frac{f_p^2 f_g \cos\Theta}{2f^3} + \frac{f_p^2}{4f^4}\left[\frac{f_p^2}{2} + f_g^2(1+\cos^2\Theta)\right] \quad (2)$$

As can be seen from Equation (2), the group ionospheric refraction index is larger than the unity which is leading to group velocity less that the speed of light in a vacuum which is called group delay impact. In other words, when the signal pass through the ionospheric layer, the integration of electrons n_e along the path of the receiver-satellite gives a distance more than the real range. Commonly, the higher order terms of the ionospheric refractions are neglected which represent less than 0.1% of the total ionospheric effect. Therefore, Equation (1) and (2) can be simplified to

$$n_p = 1 - \frac{f_p^2}{2f^2} = 1 - \frac{40.3}{f^2} N_e \quad (3)$$

$$n_g = 1 + \frac{f_p^2}{2f^2} = 1 + \frac{40.3}{f^2} N_e \quad (4)$$

Where N_e is the electron density in the ionosphere, which is changed with the height having a maximum of $N_e \sim 10^{11} - 10^{12} e/m^3$. According to its definition, the ionosphere delay/advance is the integration of electrons along the signal path

$$I = \int (n-1)dl \quad (5)$$

$$I_p = \frac{40.3}{f^2}\int N_e dl \quad (6)$$

$$I_g = -\frac{40.3}{f^2}\int N_e dl \quad (7)$$

Where I_p and I_g are the first order phase advance and code delay ionospheric impact on GNSS signals , respectively. The integral part is defined as the slant total electron content STEC

$$STEC = \int N_e dl \quad (8)$$

Commonly, the STEC is given as TEC units $1\ TEC = 10^{16} e/m^3$. Finally the ionospheric effect on GNSS signal can be written as

$$I = \frac{40.3 * 10^{16}}{f^2} STEC \quad (9)$$

where I is the ionospher delay in meters and f is the signal frequency in HZ.

3. GNSS MATHEMATICAL MODEL

The basic GNSS observation equations for GNSS pseudorange and carrier-phase observations of a particular constellation can be written as:

$$P = \rho + cdt_r - cdt^s + T + I + c(d_r - d^s) + d_m + e \quad (10)$$

$$\Phi = \rho + cdt_r - cdt^s + T - I + c(\delta_r - \delta^s) + \delta_m + \lambda(N + \varphi_r - \varphi^s) + \varepsilon \quad (11)$$

Where P is GNSS pseudorange measurement in meters; Φ is the GNSS carrier phase measurement in meters; ρ is the true

geometric range in meters from the antenna phase center of the receiver at reception time to the antenna phase center of the satellite at transmission time; dt_r and dt^s are the clock errors for receiver and satellite, respectively; d_r and d^s are frequency-dependent code hardware delay for receiver and satellite, respectively in seconds; δ_r and δ^s are frequency-dependent carrier phase hardware delay for receiver and satellite, respectively in seconds; e, ε are relevant system noise and un-modeled residual errors in meters; N is the integer ambiguity parameters in cycles; φ_r and φ^s are the initial phase biases at the receiver and the satellite, respectively in cycles; λ is the wavelengths of the carrier frequency in meters; c is the speed of light in vacuum in meter/second; T is the tropospheric delay component in meters; I is the ionospheric delay component in meters; $d_m$and δ_m are the multipath interference component for code and phase, respectively in meters.

The mathematical equations of dual frequencies observations with concentrated independent frequency based errors and neglecting the phase receiver and satellite hardware delays, can be written as

$$P_1=\rho^* +I_1+B_{r1}-B^{s1}+e_1 \quad (12)$$

$$P_2=\rho^* +\frac{f_1^2}{f_2^2} I_1+B_{r1}-B^{s1}+e_2 \quad (13)$$

$$\Phi_1=\rho^* -I_1+\lambda N_1+\varepsilon_1 \quad (14)$$

$$\Phi_2=\rho^* -\frac{f_1^2}{f_2^2} I_1+\lambda N_2+\varepsilon_2 \quad (15)$$

where ρ^* is the geometric range lumped with the frequency independent errors, namely receiver and satellite clocks and troposphere error. As can be seen, a dual-frequency GPS receiver can measure the difference in ionospheric delays between the L1 and L2 of the GPS frequencies, which are generally assumed to travel along the same path through the ionosphere. Thus, the ionospheric delay can be obtained from a linear combination called geometry free as follows

$$P_4=P_1-P_2=(1-\frac{f_1^2}{f_2^2})I_1+DCB_r-DCB^s \quad (16)$$

$$\Phi_4=\Phi_1-\Phi_2=(1-\frac{f_1^2}{f_2^2})I_1+\lambda N_{12} \quad (17)$$

Where $P_4$and Φ_4 are the geometry free linear combination for pseudorange and phase measurements, respectively; DCB_r and DCB^s are the receiver and satellite differential code biases, respectively. As can be seen from Equation (16) that the ionospheric delay is biased by the satellite and receiver differential code biases and featured with high noise level. In contrast, due to the small values of the phase biases and noise level, the phase based geometry-free present smoother ionospheric delay. However, phase based ionospheric delay is biased by the ambiguity parameters λN_{12}. To overcome these limitations, a phase based smoothing process can be applied to code measurements to remove the noise and time-vary code biases from the pseudorange based geometry free. Then, the smoothed pseudorange geometry-free can be used to estimate the ionospheric delay along with the constant code biases, using the adjusted spherical harmonic (ASHA) model.

4. ADJUSTED SPHERICAL HARMONIC MODEL

The slant total electron content (STEC) is estimated from GNSS dual-frequency observations considering smoothed pseudorange based geometry-free P_{4s} as follow

$$P_{4s}=40.3*10^{16}(\frac{1}{f_1^2}-\frac{1}{f_2^2})STEC+DCB_r-DCB^s \quad (18)$$

$$STEC=-\frac{f_1^2 f_2^2}{40.3*10^{16}(f_1^2-f_2^2)}(P_{4s}-DCB_r+DCB^s) \quad (19)$$

Commonly, the ionosphere is assumed to be concentrated in a thin layer at altitude H, as a result, the STEC can be translated into the vertical total electron content (VTEC) using the modified single-layer model (MSLM) as used in CODE VTEC products by defining a mapping function (MF)

$$VTEC = MF(v)\,STEC \quad (20)$$

$$MF(v) = cos[arcsin(\frac{R}{R+H}sin(\alpha v))] \quad (21)$$

where v is the satellite elevation angle, R is the earth's radius, and H is the attitude of the ionosphere thin layer (normally the approximate peak height of the F2 layer). R is set to 6,371 km. H and α can be set by users. Commonly, they are defaulted as H = 506.7 km and a = 0.9782, which are consistent with the values used by the CODE group. An ionospheric spherical harmonic function can be applied to simulate the VTEC as E(φ, η) which can be expressed as follows (Schaer 1999):

$$VTEC = E(\varphi,\eta) = \sum_{n=0}^{n_{max}}\sum_{m=0}^{n} P_{mn}(sin\varphi)\,(a_{nm}\,cos\,m\eta + b_{mn}\,sin\,m\eta) \quad (22)$$

where ϕ is the geocentric latitude of the ionosphere pierce point (IPP), η = λ - λ0 is the sun-fixed longitude of the IPP: λ and λ0 are the longitude of the IPP and the apparent solar time, respectively, a_{mn} and b_{mn} are the regional ionosphere model coefficients, P_{mn} are normalized Legendre polynomials. Substituting Equation (19) and (20) into Equation (22), the following expression can be obtained:

$$VTEC = \sum_{n=0}^{n_{max}}\sum_{m=0}^{n} P_{mn}(sin\varphi)\,(a_{nm}\,cos\,m\eta + b_{mn}\,sin\,m\eta) = cos[arcsin(\frac{R}{R+H}sin(\alpha v))][-\frac{f_1^2 f_2^2}{40.3*10^{16}(f_1^2-f_2^2)}(P_{4s}-DCB_r+DCB^s)] \quad (23)$$

where a_{mn}, b_{mn}, DCB_r and DCB^s are the estimated unknown parameters. The order of spherical harmonics expansion depends on the areas. Commonly, for the regional, 8-15th order are sufficient. The set of the ionosphere coefficients will be assumed every 2 h to be consistent with GIM model, for one GPS station, there are more than 20,000 measurements every day (epoch time 30 sec). Thus, the number of observations is much more than the number of unknown parameters. According to the theory described above, the DCB and ionosphere coefficients can be estimated from GPS dual frequency observations by the least squares (LS) method. However, due to the singularity of Equation (23), additional constrain should be added to separate the satellite and receiver differential code biases. Traditionally, the sum of all GNSS satellite DCB values is assumed to be zero. Under this constraint condition, Equation (13) reaches full rank and the DCBs of the satellites and receivers can be separated.

5. GNSS DATA PROCESSING

Egypt established a continuous operating reference stations network (CORS) along Nile valley and its Delta to mainly overcome the problems of GPS campaign and guarantee that the surveying works all over the country to be unified in the same datum. The CORS stations cover the country from Mediterranean Sea at the North to Aswan at the South and it consists of 40 stations as shown in Figure 1. The continuous operating reference stations network (CORS) consists of 40 stations spaced by distances that range from 50 km to 70 km. The stations are equipped with dual frequency GNSS receivers (Trimble Net R5). The GPS/GLONASS rinex observations of 35 stations are collected and processed by our developed MATLAB software.

Figure 1. Egyptian GNSS CORS network

MATLAB software called EGY_ION is developed to model the mathematical equations presented in the previous Section. The software is include five main functions: a MATLAB function reading the GNSS RINEX files to exclude the GNSS observations, a MATLAB function navigation messages to exclude the satellite coordinates in real time, a Matlab function to apply the geometry free linear combinations for pseudorange and phase observations, a MATLAB function to apply a phase based smoothing for the pseudorange geometry free linear combination observations, a MATLAB function for the least square estimator for Equation (24), in addition to other secondary calculation functions. Figure (2) shows the flow chart for the proposed software.

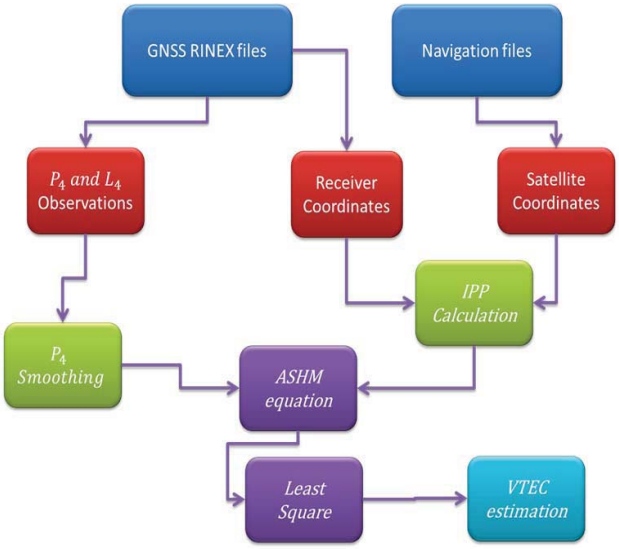

Figure 2 EGY_ION flow chart

6. IONOSPHERE DATA RESULTS

As the positioning accuracy of single frequency precise point positioning (SFPPP) attribute mainly to the ionospheric error affecting the GNSS signals, the performance of the developed Egyptian ionospheric map (EIM) can be verified through the positioning accuracy of SFPPP for number of controlling stations which are not included in the national network used in ionospheric estimation. Five GPS/.GLONASS stations are selected to investigate the performance of the developed ionospheric model in comparison with the Klobuchar and GIM models. The results show that the positioning accuracy of SFPPP based on EIM achieves centimetre-level accuracy in contrast with SFPPP based on GIM and Klobuchar with decimetre to meter-level accuracy which attributes to the improvement in the national TEC values estimated. Figure 3 and 4 show the SFPPP positioning accuracy for Stations at Alexandria and Cairo, respectively.

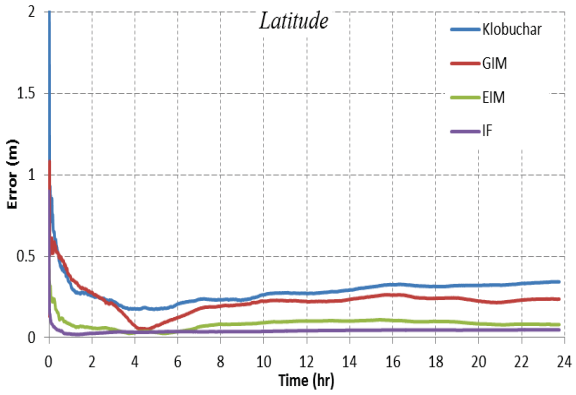

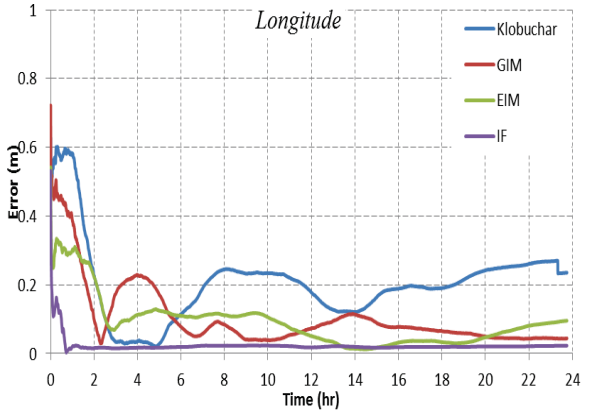

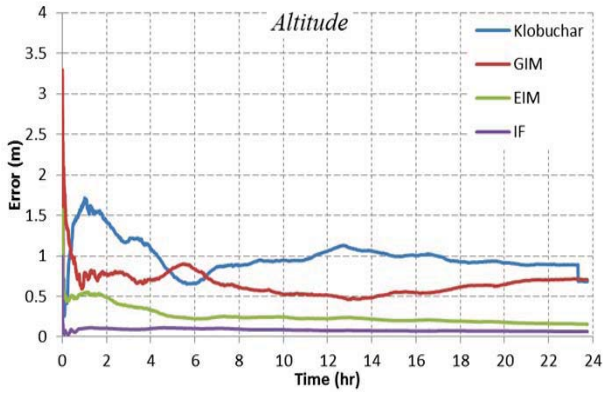

Figure 3. the single frequency Position accuracy for different ionospheric models for Station at ALEX

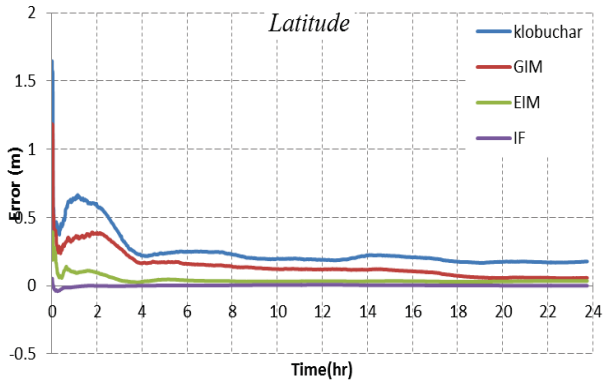

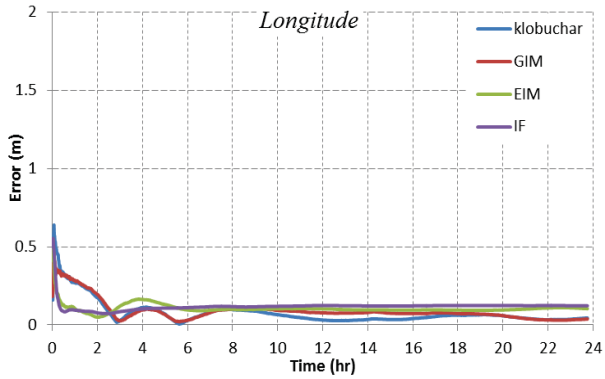

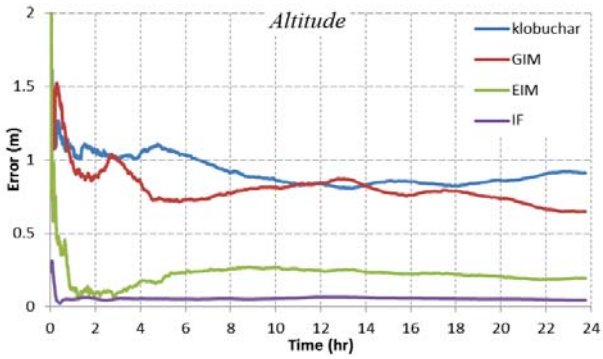

Figure 4. the single frequency Position accuracy for different ionospheric models for Station CAIRO

Figure 5 shows the root mean square error (RMSE) for latitude, longitude and altitude of Klobuchar, GIM and the proposed EIM models in comparison with the ionosphere free mode. As can be seen that the use of EIM model improves the positioning accuracy to centimetre -level and speeded up the convergence time in comparison with the Klobuchar and GIM models. For latitude, the EIM model enhances the positioning accuracy by 65 % after 30 mins of GNSS data processing compared with the GIM based positioning accuracy. While the positioning accuracy enhanced by 70% after one hour of data processing in comparison with GIM. In addition, for longitude, the positioning accuracy enhanced by 40% after 30 mins while the enhancement reaches to 55% after one hour of GNSS data processing. Moreover, for altitude, the positioning accuracy is improved by 60 % and 75 % after 30 and 60 mins of GNSS data processing, respectively.

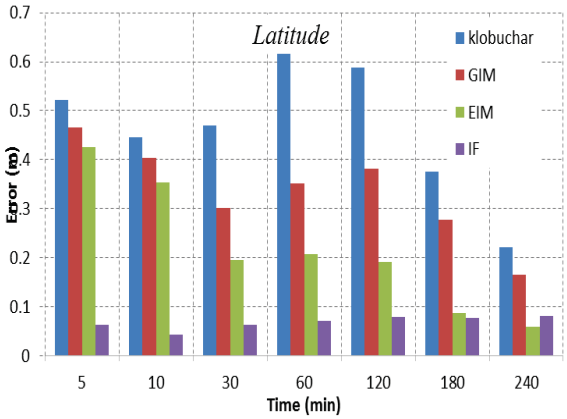

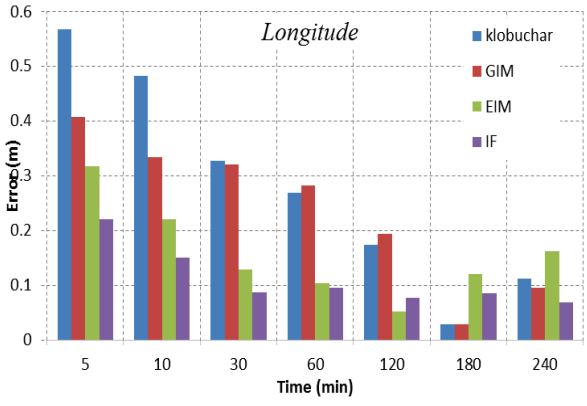

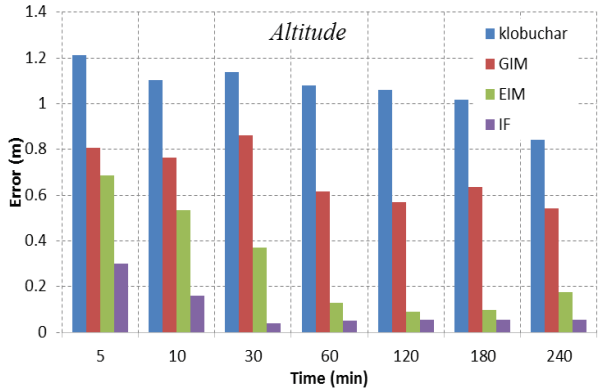

Figure 5. the RMSE for latitude, longitude and altitude of Klobuchar, GIM and EIM models

7. CONCLUSION

In this research, we developed Egyptian ionospheric maps (EIM) based on national GNSS network. Adjusted spherical harmonic (ASHA) model was developed for ionospheric total electron content (TEC) estimation. The slant TEC values along the GNSS signal paths were quantified from a network of GNSS receivers and converted to vertical TEC by means of the single layer mapping function. MATLAB software called EGY_ION was developed to model the mathematical modelling used to process GPS/GLONASS geometry-free observations from the national GNSS network. The performance of the developed Egyptian ionospheric map (EIM) WAS verified through the positioning accuracy of SFPPP for number of controlling stations which are not included in the national network used in ionospheric estimation. Five GPS/.GLONASS stations are selected to investigate the performance of the developed ionospheric model in comparison with the Klobuchar and GIM models. The positioning accuracy of SFPPP based on EIM achieves centimetre-level accuracy in contrast with SFPPP based on GIM and Klobuchar with decimetre to meter-level accuracy which attributes to the improvement in the national TEC values estimated. In addition, the EIM model the convergence time in comparison with the Klobuchar and GIM models.

8. REFERENCES

Abdelazeem, M., Çelik, R.N., and El-Rabbany, A., 2016. An enhanced real-time regional ionospheric model using IGS real-time service (IGS-RTS) products. Journal of Navigation, 69, 521–530.

Amerian, Y., Hossainali, M.M., and Voosoghi, B., 2013a. Regional improvement of IRI extracted ionospheric electron density by compactly supported base functions using GPS observations. Journal of Atmospheric and Solar-Terrestrial Physics , 92, 23–30.

Bassiri, S., and G. A. Hajj (1993), Higher-order ionospheric effects on the GPS observables and means of modeling them, Manuscr. Geod.,18, 280–289.

Durmaz, M. and Karslioglu, M.O., 2015 . Regional vertical total electron content (VTEC) modeling together with satellite and receiver differential code biases (DCBs) using semi-parametric multivariate adaptive regression B-splines (SP-BMARS). Journal of Geodesy , 89, 347–360.

Hargreaves, J.K., 1992. The solar-terrestrial environment, Cambridge atmospheric and space science series, Cambridge University Press.

Hernández-Pajares, M., et al., 2009. The IGS VTEC maps: a reliable source of ionospheric information since 1998. Journal of Geodesy, 83, 263–275.

Kao, S.-P., et al. ,2015 . An LS-MARS method for modeling regional 3D ionospheric electron density based on GPS data and IRI. Advances in Space Research , 55, 2256–2267.

Li, Z., et al., 2015. SHPTS: towards a new method for generating precise global ionospheric TEC map based on spherical harmonic and generalized trigonometric series functions. Journal of Geodesy, 89, 331–345.

Tang, W., Jin, L., and Xu, K., 2014 . Performance analysis of ionosphere monitoring with BeiDou CORS observational data. Journal of Navigation , 67, 511–522.

Wu, X., et al. , 2014 . Evaluation of COMPASS ionospheric grid. GPS Solutions , 18, 639–649.

Yang, H. and Gao, Y., 2015 . Regional TEC modelling based on combined GPS/BeiDou. International technical meeting of the satellite division of the institute of navigation, ION GNSS+, 2015, September 14-18, Tampa, Folrida.

Zhang, R., et al. , 2015. Modeling regional ionospheric delay with ground-based BeiDou and GPS observations in China. GPS Solutions, 19, 649–658.

Comparative Analysis of Image and LiDAR-Based Elevation Maps from a UAV Platform for Agriculture Management

Fangning He[a,*], Magdy Elbahnasawy[a], Tamer Shamseldin[a], A. Habib [a]

[a] Digital Photogrammetry Research Group
Lyles School of Civil Engineering
Purdue University, 550 Stadium Mall Dr., West Lafayette, IN 47907, USA
– (he270, melbahn, tshamsel, ahabib)@purdue.edu

KEY WORDS: UAV, 3D Reconstruction, Image, LiDAR, Precision Agriculture.

ABSTRACT:

Low-cost unmanned airborne vehicles (UAVs) have recently emerged as a promising platform for remote-sensing data acquisition to satisfy the needs of various applications. To date, utilization of UAVs, which are equipped with RGB-frame cameras and geo-referenced laser scanners, for precision agriculture and high throughput phenotyping has gained significant attention from researchers in both mapping and plant science fields. Although, several research efforts have been exerted towards both image-based and LiDAR-based 3D reconstruction with UAV platforms, unfortunately, almost no research has been conducted on a quantitative comparison of these approaches for precision agriculture applications. In this paper, we introduce two approaches for image-based and LiDAR-based Digital Surface Models (DSMs) generation using a multi-rotor UAV platform. Then, a comparative analysis is performed on the DSMs that are derived from real dataset acquired over an agriculture field. The experimental results demonstrate the feasibility of the proposed approaches in providing reliable 3D reconstruction for precision agriculture applications.

1. INTRODUCTION

Nowadays, due to the global challenge of ensuring crop yield for food and fuel generation, precision agriculture, which aims at optimizing crop yield while preserving resources, has gained tremendous interest from researchers in plant science as well as other fields (Habib et al., 2017). Among various applications, high throughput phenotyping is an important precision agricultural approach that combines methodologies and protocols to quantify plant growth, structure, and composition at multiple scales over the growing season (Fiorani and Schurr, 2013). Traditional phenotyping is based on destructive and labor/time-consuming approaches that are mainly conducted in a controlled environment with limited coverage such as greenhouses. In order to alleviate these disadvantages, many research efforts have been conducted on remote sensing-based phenotyping, as it is nondestructive and noninvasive while being capable of providing abundant and diversified information (Araus and Cairns, 2014). To date, with the ever-increasing technological developments in Mobile Mapping Systems (MMS), several platforms, such as mobile sensor systems onboard tractors, tethered balloons, and manned aircrafts, have become attractive options (Busemeyer et al., 2013; Deery et al., 2014). However, some financial and technical constraints (e.g., the initial investment, mobilization cost, and the required technical expertise of end users) prevent the widespread adoption of such human-operated systems. Alternatively, unmanned airborne vehicles (UAVs) have recently emerged as a promising platform for remote-sensing data acquisition to satisfy the needs of various applications. Compared to those human-operated mobile mapping systems, advantages of UAV-based platforms include low cost, ease of storage and deployment, ability to fly lower and collect high-resolution data, and filling an important gap between wheel-based and manned airborne platforms (He and Habib, 2016). Among the possible MMS platforms, UAVs are now becoming competitive platforms for remote sensing-based phenotyping (Habib et al., 2016; Honkavaara et al., 2013; Ribera et al., 2016; Zhang and Kovacs, 2012).

From a mapping point of view, current UAV-based 3D mapping can be achieved through either active or passive remote sensing systems. Active sensors, such as laser scanners, directly provide precise and dense point clouds along the mapped objects. Although, several consumer-grade direct geo-referencing units have been introduced to the market, significant initial investment for the acquisition of a high-end GNSS/INS Position and Orientation System (POS) is still required, especially when seeking high level of reconstruction accuracy. Derived point clouds from active sensors usually lack spectral information, which are needed for the derivation of better and more reliable interpretation to the reconstructed objects. On the other hand, passive sensors, which commonly utilize digital line/frame imaging sensors, can be incorporated for 3D reconstruction while providing spectral attributes for the derived elevation information. However, automated identification of conjugate features in overlapping images, which is commonly known as the matching problem, remains to be a challenging task. For agricultural applications, the matching problem is further complicated by repetitive patterns and/or lack of unique texture within the covered area.

Although, several research efforts (He and Habib, 2016; Wallace et al., 2014, 2012) have been exerted towards UAV-based 3D reconstruction using different remote sensing modalities (i.e., active and passive sensors), it is worth noting that almost no research has been conducted on quantitative comparing of these approaches when dealing with a multi-rotor UAV platform (e.g., DJI S1000+) for precision agriculture applications. Therefore, this paper aims at providing a comparative analysis of the derived Digital Surface Models (DSMs) from a UAV platform, which is equipped with a SONY Alpha 7R digital camera and a Velodyne VLP16 laser scanner aided by the Applanix APX-15 UAV GNSS/Inertial OEM unit. To be more specific, this paper will be focusing on the following issues:

1. Automated image-based DSM generation using UAV-based imagery, which is acquired over agriculture field with repetitive patterns and insufficient texture,

2. Automated laser-based DSM generation using a direct geo-referencing process with consumer-grade GNSS/INS unit, and
3. Comparison of image-based and laser-based DSMs.

To address these issues, the utilized system configuration is introduced in the next section. Then, the proposed methodology for image-based and LiDAR-based DSM generation is explained. Afterwards, the experimental results derived from real datasets are discussed. Finally, drawn conclusions and recommendations for future work are presented.

2. SYSTEM CONFIGURATION

In this section, we investigate the specifications of each individual component of the utilized UAV platform, which ensures that the system will be capable of satisfying the needs of precision agriculture applications. To be specific, this system includes a direct geo-referencing (DG) or navigation unit based on an integrated IMU and GNSS receiver board, one active optical imaging unit and one passive imaging unit. All these components are rigidly fixed within the UAV platform as shown in Figure 1.

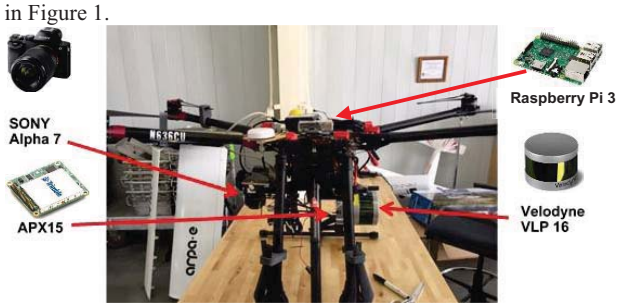

Figure 1. Current UAV-based mapping system configuration

2.1 Platform Selection

For precision agriculture application, we want to maximize the flight duration and minimize the payload. Also, since we will use both LiDAR and cameras on the same system, a multi rotor drone UAV will be more suitable than a fixed-wing UAV. Price wise, the cheaper UAV is, of course, the better.

Considering the DJI S1000+ as the UAV platform, it is designed for professional aerial mapping applications, as well as providing some advantages such as safety, stability and ease of use. It is a vertical take-off and landing UAV that weighs approximately 4.4 Kg without batteries and its maximum takeoff weight is 11 Kg. It can fly for 15 minutes with takeoff payload of 9.5 Kg, which means that this time increases as the weight decreases. The S1000+ will allow to have around 4 to 5 Kg payload of sensors/equipment to be installed on the mapping system (DJI, 2017). The specification of the DJI S1000+ UAV is presented in Table 1.

	Specifications
Weight	4.4 kg
Take-off Weight	6 kg 11 kg
Stator Size	41 x 14 mm
Power Requirements	Lithium-Polymer (LiPo): - Maximum: 4000 W - Hovering: 1500 W at 9.5 kg take-off weight

Table 1. DJI S1000+ UAV Specifications

2.2 Navigation Unit

Generally, the manipulation of the collected optical data requires the geo-referencing of the mapping platform, which means the determination of the position and the orientation of the individual sensors relative to a user-defined coordinate system (Chiang et al., 2012). It is worth noting that the geo-referencing of a mobile LiDAR system has to be established using on an integrated GNSS/INS system, which is known as direct georeferencing (Chiang et al., 2015). On the other hand, the geo-referencing of passive-sensors (i.e., RGB frame camera) can be achieved through either an indirect or direct geo-referencing. The main advantages of direct geo-referencing include reducing or even eliminating the ground control requirement, which is quite useful in mapping remote and inaccessible areas, as well as reducing the cost of the overall mapping process (establishing ground control is the most expensive mapping task next to the deployment of the data acquisition platform). Therefore, the incorporation of GNSS/INS position and orientation system has become the default for the majority of UAV-based mapping platforms. For this research, the Applanix APX-15 UAV is considered due to its low weight, compact size, and precise, robust positioning and orientation information. Regarding the post-processing mode, the unit estimates pitch and roll with 0.025 degree and heading (yaw) with 0.08 degree of accuracy and the position accuracy is 0.02-0.05 meter. The position, roll, pitch, and heading output can be extended up to 100 Hz as illustrated in Table 2 (Applanix, 2017).

	Specifications
Weight	60 grams
Size	67 L x 60 W x 15 H mm (nominal)
Power	8-32 V DC
Position Accuracy (post processing)	0.02 - 0.05 (m)
Velocity Accuracy (post processing)	0.015 (m/sec)
Roll & Pitch Accuracy (post processing)	0.025 (deg)
Heading Accuracy (post processing)	0.080 (deg)
IMU data rate	200 Hz
GNSS data rate	5 Hz

Table 2. APX-15 Specifications

2.3 Active Sensor

In this research, a Velodyne VLP-16 is used for the selected UAV platform. Axes definitions and specifications of the Velodyne VLP 16 are shown in Figure 2 and Table 3, respectively.

Velodyne VLP-16 is a small LiDAR unit, it has 16 lasers beams, which are aligned over the range of +15.00 degrees to -15.00 degrees that provides the vertical field of view (ω), and it delivers a 360-degree horizontal field of view (α). The VLP-16 does not have visible rotating parts. The VLP-16 generates a point cloud of up to 300,000 points per second with a range of 100 meters and typical accuracy of +/- 3 cm at 5-20 Hz (Velodyne LiDAR, 2017).

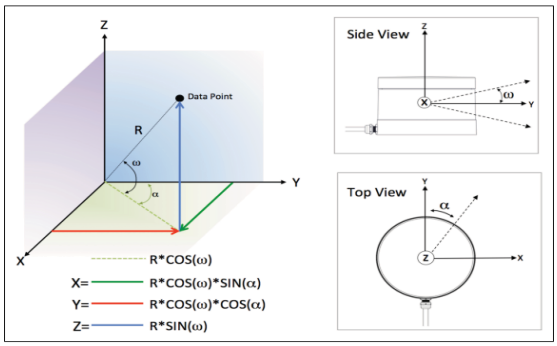

Figure 2. Velodyne VLP16 axes (spherical to XYZ)

	Specifications
Weight	830 grams
Number of channels	16
Horizontal Field of View (FOV)	360°
Vertical Field of View (FOV)	30°
Angular resolution (horizontal/azimuth)	0.1° -0.4°
Rotational speed	5-20 rotations per second (adjustable)
Returns range of	up to 100 meters
Modes of operation	Single and Dual return modes (strongest/last)
3D LiDAR data point generated	Single return mode: ~300,000 points per second Dual return mode : ~600,000 points per second

Table 3: Velodyne VLP16 Specifications

2.4 Passive Sensor

For the camera, there are a variety of selections, either high-end industrial cameras or commercial cameras. For the high-end cameras, they have many wiring controls for both triggering and strobe signals, however, in terms of the price, they are expensive. These controls enable the camera to have an accurate time tagged images and there are no synchronization problems. On the other hand, for the commercial cameras, there are no such controls either for triggering or strobes, which will cause synchronization issues. For the current platform, a commercial camera, Sony alpha 7R, which is 35mm full frame and 36.4 Mega Pixels size, is used to minimize the overall cost of the system. The synchronization issues are addressed through alternative solutions for the triggering and strobe signals. The specifications of the Sony alpha 7R camera are shown in Table 4.

	Specifications
Weight	465 grams
Size	127 x 94 x 48 mm
Sensor	36.3 megapixel
Continuous shooting	4 fps
Flash x-sync	1/160 sec
Approximate Pixel Pitch	4.88 microns
Sensor size:	861.6mm2 (35.90mm x 24.00mm)

Table 3: Sony Alpha 7R Specifications

2.5 Data Storage Media

Unlike the Sony alpha 7R camera, which has a built-in memory card for storing images, VLP16 LiDAR has about 8 megabits/second data rate and it needs an appropriate media for storing the collected data in a given mission. Mini computers are investigated for this purpose but its weight is about 500 gm, which means almost 10% of the UAV payload is used. Alternatively, Raspberry Pi 3 with 1.2 GHz 64-bit quad-core ARMv8 CPU is used with around 50 gm weight. This choice saved around 90% of the weight compared with other selection. Besides, its smaller dimensions make it easier to select its installation spot on the UAV.

3. METHODOLOGY

In this section, the proposed methodology for image-based and LiDAR-based DSM generation is presented. Specifically, the image-based approach is first introduced. Then, the LiDAR-based approach is discussed.

3.1 Image-based DSM generation

As shown in Figure 3, the proposed methodology for image-based DSM generation can be summarized as three steps:

1- The image-based DSM generation starts with the Structure from Motion (SfM) approach, which has been developed by He and Habib (2014), for automated aerial triangulation of the captured image frames. Similar to most SfM-based approaches, the proposed procedure includes three steps. In the first step, the relative orientation parameters (ROPs) relating stereo-images are derived from conjugate point features. In this research, considering the fact that UAV-based imagery acquired for precision agriculture applications usually contain repetitive patterns and/or lack of unique texture within the covered area, two approaches are proposed for reliable estimation of ROPs. Different from the conventional methods, whether it is based on a non-linear (Mikhail et al., 2001) or closed-form solution (Nistér, 2004), the proposed approaches take advantage of prior information regarding the flight trajectory, and is capable of dealing with overlapping images in the presence of high percentage of matching outliers. Interested readers can refer to He and Habib (2016) for more information about the two proposed approaches. Once the ROPs of all possible stereo-pairs are estimated, an incremental approach is adopted for the initial recovery of the image EOPs. Specifically, the incremental approach is initiated by defining a local coordinate frame. Then, all images are sequentially augmented into a final image block. Once the initial approximate EOPs are estimated, a feature tracking procedure, which aims at identifying conjugate point features from multiple overlapping images, is adopted. Finally, a bundle adjustment process, which utilizes the estimated image EOPs as well as the tracked tie points, is conducted to refine the derived image EOPs as well as coordinates of 3D object points.

2- Since the derived image EOPs and the sparse point cloud are only defined in an arbitrary local coordinate system, an absolute orientation process has to be conducted to establish the transformation from the local frame to the mapping coordinate system. In this research, in order to estimate the 3D similarity transformation parameters (i.e., scale factor, three translation parameters, and three rotation angles) relating local and mapping coordinate systems, tie points corresponding to the GCPs are first manually identified. Then, the 3D coordinates of tie points, which are defined in the local coordinate system, are computed through a spatial intersection. Afterwards, the transformation parameters are estimated using the GCPs and their corresponding local coordinates. Finally, the set of estimated parameters are used to transform the derived image EOPs as well as 3D object coordinates from the local coordinate system to the mapping

frame. Now that the 3D similarity transformation has been applied, an indirect geo-referencing process, which utilizes a global bundle adjustment, is conducted to refine the derived geo-referencing parameters. One should note that, in this implemented bundle adjustment process, GCPs are used for datum definition.

3- Given the geo-referenced EOPs, image-based dense point cloud can be generated through dense image matching techniques. Among different approaches, the semi-global matching (SGM) algorithm (Hirschmuller, 2005), which minimizes the image matching costs along several one-dimensional path directions through the image, has recently emerged as a promising technique for image-based dense reconstruction. To date, several research efforts (Gerke, 2009; Hirschmüller and Bucher, 2010) have demonstrated that the SGM is capable of offering a good matching accuracy for various applications. The SGM is originally established on normalized image stereo-pairs, where the stereo images are re-sampled in a way that the epipolar lines are parallel to the x-axis of the image. Although the utilization of such normalized stereo images is sufficient for some computer vision applications, where stereo-cameras are used for data acquisition, it may significantly increase the computational expense for most mapping applications, which mainly deal with sets of overlapping images. In order to overcome this limitation, an object space-based approach is proposed in this research. To be more specific, the proposed approach has several characteristics:

- Rather than generating normalized image stereo-pairs, the proposed approach is performed on a dense voxel established in the object space. Based on such configuration, it is not necessary to derive the matching cost in image space. Instead, the matching cost can be directly formulated on each voxel using all images, which could be more advantageous for mapping applications.
- The semi-global optimization can be conducted in the voxel space with 16 paths, which leads to the direct derivation of image-based dense point cloud.
- The sparse point cloud derived from the bundle adjustment process can be used to facilitate the image-based point cloud generation procedure. Specifically, the utilization of the prior knowledge regarding the reconstructed objects is capable of reducing the search range in the voxel space, which results in improvement of reconstruction accuracy as well as decrease of processing time. Finally, a regular DSM can be generated based on the derived image-based dense point cloud.

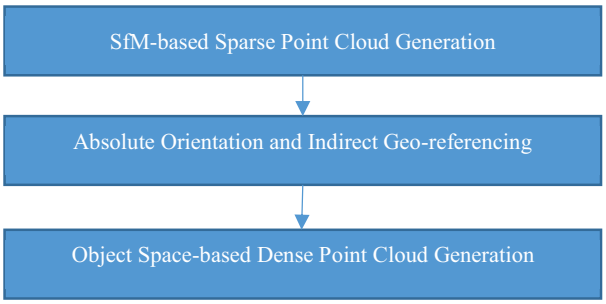

Figure 3. Proposed work flow for image-based DSM generation

3.2 LiDAR-based DSM generation

Improvements of the direct geo-referencing technology led to a positive impact on the adoption of LiDAR systems for the acquisition of dense and accurate surface models for precision agriculture applications. In general, a UAV-based LiDAR system requires two main components: an integrated GNSS/INS to provide position and orient information, and a laser scanner to provide the range/distance from the laser-beam firing point to its footprint. Usually, GNSS and INS are integrated in one GNSS/INS module known as DG unit. With the utilization of DG unit, LiDAR systems can directly provide an accurate DSM with a dense set of irregular points, surpassing the quality of those derived from other techniques, such as manual photogrammetric DSM generation, radar interferometry, and contour interpolation.

For this research, the integrated GNSS/INS (APX-15) unit supplies sequentially precise time pulses, known as pulse-per-second (PPS) signals to LiDAR (VLP16), which is responsible for triggering the active sensor (laser scanner unit) every second. Synchronization to GNSS pulse-per-second (PPS) signals gives the capability of determining the exact firing time of each laser beam, and should be received by the interface box of the active sensor. In addition, the integrated GNSS/INS unit provides a navigation message in NMEA format ($GNRMC message), which includes information regarding position, rotation, and GNSS time (Velodyne LiDAR, 2017). This navigation message is recorded over a dedicated RS-232 serial port and is received by the laser scanner via the interface box in the form of serial data, which should be at 9600 baud rate.

An illustration of the different coordinate systems of a GNSS/INS-assisted mobile LiDAR unit is represented in Figure 4. As shown in the figure, the coordinates of a given point ***I*** relative to the mapping reference frame can be derived through a vector summation process as can be seen in Equation 1.

$$r_I^m = r_b^m(t) + R_b^m(t) r_{lu}^b + R_b^m(t) R_{lu}^b R_{lb}^{lu}(t) r_I^{lb}(t) \qquad (1)$$

In this equation, $r_b^m(t)$ and $R_b^m(t)$ are the position and the orientation of the IMU body frame relative to the mapping reference frame, and they are derived through the GNSS/INS integration process. r_{lu}^b and R_{lu}^b are the lever arm vector and boresight matrix, which relate the LiDAR unit coordinate system and IMU body frame. One should note that both r_{lu}^b and R_{lu}^b are time independent since the IMU and LiDAR units are rigidly fixed onboard the platform. They can be derived through a calibration process. $r_I^{lb}(t)$ is the range between the laser beam firing point and point ***I***. $R_{lb}^{lu}(t)$ defines the rotation between the laser beam and the laser unit coordinate systems. Both $r_I^{lb}(t)$ and $R_{lb}^{lu}(t)$ are obtained from the LiDAR unit measurements.

Given the LiDAR equation, one can conclude that the accuracy of the LiDAR point cloud depends on the quality of the measurements from the individual system components and their spatial relationship as defined by the mounting parameters. Even though the measurements of the individual system components (GNSS, INS and LiDAR) are quite precise, serious errors can result from inaccurate estimation of the mounting parameters. Therefore, precise LiDAR system calibration is necessary to ensure the accuracy of the point cloud generation process. In this research, since the data acquisition is conducted over an agricultural field, almost no suitable features can be utilized for the calibration.

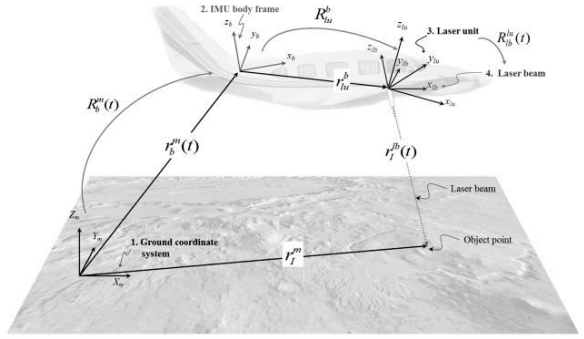

Figure 4. Coordinate Systems and Vector Summation in LiDAR Equation (Habib, 2016)

In order to overcome such challenge, a novel calibration board design, which could be easily deployed and setup within indoor and outdoor environments as well as giving the ability to facilitate the identification of conjugate planar features, is proposed. To be more efficient, the calibration boards are combined with high reflective surfaces (stop signs) with known dimension, which increase the speed of the automation process of target detection. The new calibration boards are shown in Figure 5. In this research, calibration is done at the beginning of the data collection process, keeping the same system configuration and conditions, and at the end of the data collection to ensure the system calibration stability and robustness. The proposed calibration mainly depends on extracting planar features from the new calibration boards with reflective surfaces.

Figure 5. Calibration boards with reflective surface for aerial system

4. EXPERIMENTAL RESULTS

In this section, the comparative analysis is conducted on image-based and LiDAR-based DSMs that are derived from real datasets using the proposed methodology.

4.1 Dataset Description

The test site involved in the experiments covers an agriculture field at Purdue University's Agronomy Center for Research and Education (ACRE) in Wester Lafayette, United States. The main characteristics of the acquired image and laser datasets are described as below.

The **Image Dataset** is comprised of 639 images that are captured from thirteen flight lines with approximate 60% overlap and side lap (See Figure 6 (a) and (b) for sample images). The flying height of the utilized DJI S1000+ UAV is approximate 40 meters and the flying speed is roughly 8 m/s. Moreover, 10 GCPs and 26 check points are established. Both GCPs and check points are surveyed by an RTK GPS with an approximate accuracy of $\pm 2\ cm$. Then, the root-mean-square-error (RMSE) for the check points is evaluated after conducting the bundle adjustment as described in Section 3.1. For this experimental dataset, the RMSE values for the X, Y, and Z coordinates are 0.03 m, 0.03m, and 0.04 m, respectively, which indicates a good accuracy of the image-based 3D reconstruction.

Due to the limited battery endurance, the **LiDAR Dataset** is acquired on the same day in a separate mission with eight flight lines. The flying height of the UAV platform is approximate 45 meters and the flying speed is 5 m/s. A total number of 25 million laser points is acquired over the involved test site (See Figure 6 (c) for a sample area of the reconstructed laser points).

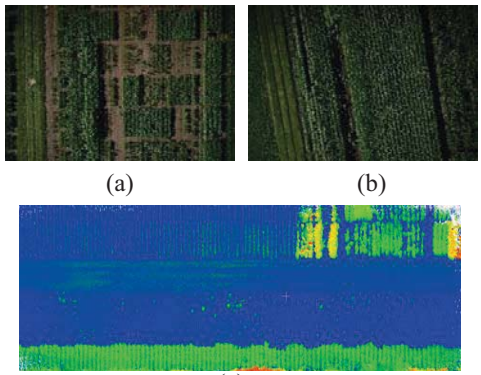

(a) (b)

(c)

Figure 6. (a) and (b) two sample images from the image dataset, and (c) a sample area from the laser dataset (laser points are colorized based on elevation)

4.2 Accuracy Analysis

Now that the image-based and LiDAR-based point clouds are generated, the DSMs are interpolated at four-centimeter Ground Sampling Distance (GSD). For qualitative evaluation of the derived DSMs, six spatially-distributed profiles are generated across the whole field. The width of each profile is 12 centimeters. Figure 7 illustrates the image-based and LiDAR-based profiles. Looking into these profile figures, it is evident that the two DSMs are capable of providing comparable height reconstruction in the selected areas. Moreover, one can also observe that some points from the LiDAR-based DSM are below the image-based DSM. This is mainly because the laser beam can penetrate through the gaps between the leaves while the image-based reconstruction can only define the top of the canopy.

For the quantitative evaluation, both correlation analysis and statistical calculations (e.g., RMSE) are conducted to examine the similarity between the image-based and LiDAR-based heights within the same profiles. The formula for computing the RMSE value is presented in Equation 2.

$$RMSE = \sqrt{\frac{\sum_{i=1}^{n}(Z_{x,y}^{image} - Z_{x,y}^{LiDAR})^2}{n}} \quad (2)$$

Where, $Z_{x,y}^{image}$ and $Z_{x,y}^{LiDAR}$ are the Z values extracted from the same location (x, y) in the image-based and LiDAR-based DSMs. The derived correlation and RMSE values are reported in Table 5. From such results, one can conclude the following:

• The minimum correlation between the image-based and LiDAR-based height estimation is 0.75, which indicates good positive correlations between the DSMs that are derived from the two different approaches.

• Another observation to note is that the derived RMSE values range from 0.36 m to 0.49 m. As it has been explained earlier, this is mainly because the laser beam is able to penetrate through the gaps between the leaves, which results in the points reconstructed underneath the canopy layer.

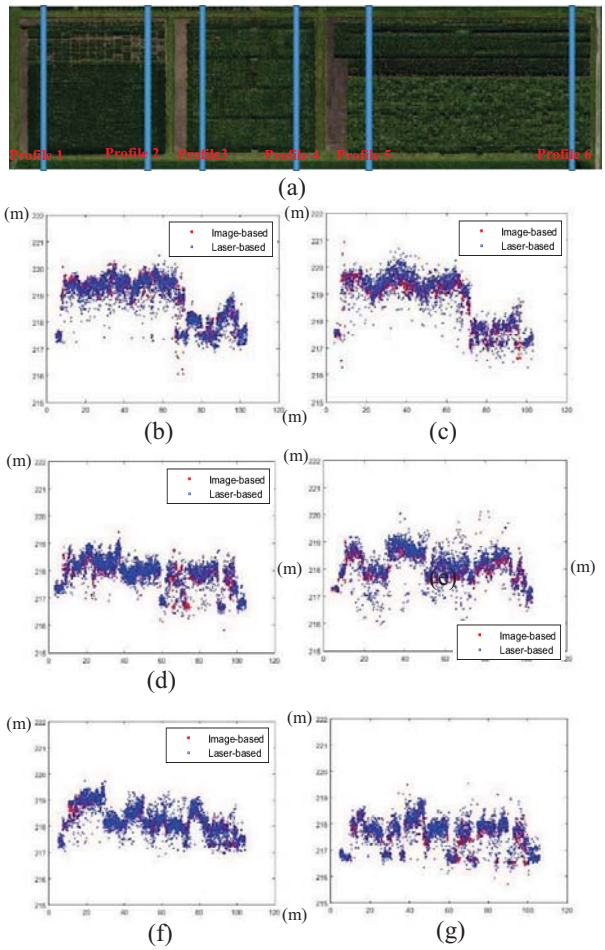

Figure 7. (a) Locations of selected profiles, and (b) to (g) cross section of profiles 1 to 6 (the image-based DSM is shown in red, and the laser-based DSM is visualized in blue).

Profile	Correlation (R)	RMSE (m)
1	0.85	0.49
2	0.84	0.48
3	0.76	0.36
4	0.75	0.37
5	0.76	0.42
6	0.77	0.37
Overall	0.86	0.39

Table 5. Correlation (*R*) and RMSE calculation between the image-based and laser-based DSMs

5. CONCLUSIONS AND RECOMMENDATIONS FOR FUTURE WORK

In this paper, we investigated the performance of both image-based and LiDAR-based 3D reconstruction from a UAV platform for precision agriculture applications. Then, a comparative analysis was performed on the derived image-based and LiDAR-based DSMs. For the experimental test, a DJI S1000+ multi-rotor UAV with a SONY Alpha 7R digital camera and a Velodyne VLP16 laser scanner is utilized. By performing both qualitative and quantitative evaluation, we can draw the conclusion that the proposed image-based and LiDAR-based approaches are capable of providing comparable 3D reconstruction for precision agriculture applications.

It is worth noting that current image-based DSM generation is achieved through an indirect geo-referencing procedure, which is quite inefficient and time-consuming. In order to alleviate such problem, the GPS-assisted triangulation and direct geo-referencing, which utilizes the consumer-grade GNSS/INS unit onboard the UAV platform, will be investigated for the image-based DSM generation. In addition, considering the fact that high throughput phenotyping aims at accurate estimation of important phenotypic traits, such as height, canopy closure and leaf structure, the feasibility of using remote sensing-based (i.e., image-based and LiDAR-based) techniques for plant traits estimation will be studied for future work.

ACKNOWLEDGEMENT

The information, data, or work presented herein was funded in part by the Advanced Research Projects Agency-Energy (ARPA-E), U.S. Department of Energy, under Award Number DE-AR0000593. The views and opinions of authors expressed herein do not necessarily state or reflect those of the United States Government or any agency thereof.

REFERENCES

Applanix, 2017. APX-15 UAV - Applanix [WWW Document]. APX15UAVApplanix.URLhttps://www.applanix.com/downloads/products/specs/APX15_DS_NEW_0408_YW.pdf (accessed 3.9.17).

Araus, J.L., Cairns, J.E., 2014. Field high-throughput phenotyping: the new crop breeding frontier. Trends Plant Sci. 19, 52–61.

Busemeyer, L., Mentrup, D., Möller, K., Wunder, E., Alheit, K., Hahn, V., Maurer, H.P., Reif, J.C., Würschum, T., Müller, J., others, 2013. Breedvision—A multi-sensor platform for non-destructive field-based phenotyping in plant breeding. Sensors 13, 2830–2847.

Chiang, K.-W., Tsai, M.-L., Chu, C.-H., 2012. The Development of an UAV Borne Direct Georeferenced Photogrammetric Platform for Ground Control Point Free Applications. Sensors 12, 9161–9180. doi:10.3390/s120709161.

Chiang, K.-W., Tsai, M.-L., Naser, E.-S., Habib, A., Chu, C.-H., 2015. New Calibration Method Using Low Cost MEM IMUs to Verify the Performance of UAV-Borne MMS Payloads. Sensors 15, 6560–6585. doi:10.3390/s150306560.

DJI, 2017. Spreading Wings S1000+ [WWW Document]. URL http://www.dji.com/spreading-wings-s1000-plus (accessed 3.9.17).

Fiorani, F., Schurr, U., 2013. Future scenarios for plant phenotyping. Annu. Rev. Plant Biol. 64, 267–291.

Gerke, M., 2009. Dense matching in high resolution oblique airborne images. Int Arch Photogramm Remote Sens Spat Inf Sci 38, W4.

Habib, A., 2017. Photogrammetric & LiDAR Georeferencing [WWWDocument].URLhttps://engineering.purdue.edu/CE/Aca

demics/Groups/Geomatics/DPRG/Slides_Laser_2017/CH_2 (accessed 3.9.17).

Habib, A., Han, Y., Xiong, W., He, F., Zhang, Z., Crawford, M., 2016. Automated Ortho-Rectification of UAV-Based Hyperspectral Data over an Agricultural Field Using Frame RGB Imagery. Remote Sens. 8, 796.

Habib, A., Xiong, W., He, F., Yang, H.L., Crawford, M., 2017. Improving Orthorectification of UAV-Based Push-Broom Scanner Imagery Using Derived Orthophotos From Frame Cameras. IEEE J. Sel. Top. Appl. Earth Obs. Remote Sens. 10, 262–276.

He, F., Habib, A., 2016. Automated Relative Orientation of UAV-Based Imagery in the Presence of Prior Information for the Flight Trajectory. Photogramm. Eng. Remote Sens. 82, 879–891.

He, F., Habib, A., 2014. Linear approach for initial recovery of the exterior orientation parameters of randomly captured images by low-cost mobile mapping systems. Int. Arch. Photogramm. Remote Sens. Spat. Inf. Sci. 40, 149.

Hirschmuller, H., 2005. Accurate and efficient stereo processing by semi-global matching and mutual information, in: Computer Vision and Pattern Recognition, 2005. CVPR 2005. IEEE Computer Society Conference on. IEEE, pp. 807–814.

Hirschmüller, H., Bucher, T., 2010. Evaluation of digital surface models by semi-global matching.

Honkavaara, E., Saari, H., Kaivosoja, J., Pölönen, I., Hakala, T., Litkey, P., Mäkynen, J., Pesonen, L., 2013. Processing and assessment of spectrometric, stereoscopic imagery collected using a lightweight UAV spectral camera for precision agriculture. Remote Sens. 5, 5006–5039.

Mikhail, E.M., Bethel, J.S., McGlone, J.C., 2001. Introduction to modern photogrammetry. N. Y.

Nistér, D., 2004. An efficient solution to the five-point relative pose problem. IEEE Trans. Pattern Anal. Mach. Intell. 26, 756–770.

Ribera, J., He, F., Chen, Y., Habib, A.F., Delp, E.J., 2016. Estimating Phenotypic Traits From UAV Based RGB Imagery, in: Proceedings of the ACM SIGKDD Conference on Knowledge Discovery and Data Mining, Workshop on Data Science for Food, Energy, and Water. San Francisco.

Velodyne LiDAR, 2017. VLP-16 Users Manual [WWW Document]. URL http://velodynelidar.com/docs/manuals/VLP-16%20User%20Manual%20and%20Programming%20Guide%2063-9243%20Rev%20A.pdf (accessed 3.9.17).

Wallace, L., Lucieer, A., Watson, C.S., 2014. Evaluating tree detection and segmentation routines on very high resolution UAV LiDAR data. IEEE Trans. Geosci. Remote Sens. 52, 7619–7628.

Wallace, L., Lucieer, A., Watson, C., Turner, D., 2012. Development of a UAV-LiDAR system with application to forest inventory. Remote Sens. 4, 1519–1543.

Zhang, C., Kovacs, J.M., 2012. The application of small unmanned aerial systems for precision agriculture: a review. Precis. Agric. 13, 693–712.

COMBINED PIXEL/OBJECT BASED BUILDING EXTRACTION TECHNIQUE FROM HIGH RESOLUTION REMOTE SENSING SATELLITE IMAGES

Mahmoud A. Shawky [a], Ahmed S. Elsharkawy [b], Essam Hamza [a], Hassan Elhifnawy [b]
[a] Electric and Computer Engineering Department, Aircraft Armament (A/CA), Military Technical College, Cairo, Egypt, abdellam30@yahoo.com, hamzaesam@gmail.com
[b] Civil Engineering Department, Military Technical College, Cairo, Egypt, hassanelhifnawy@gmail.com, ahmadshawky007@gmail.com

Commission VI, WG VI/4

KEY WORDS: pixel based, object based, Normalized Difference Building Index (NDBI).

ABSTRACT:

In recent years, satellite imaging sensors provide images with not only colour bands with spectra in visible spectral zone but also with bands in different invisible zones. These bands give dense information about different features in addition to texture information from colour bands. These advantages of satellite images are a motivation of this research to get maximum benefits of different bands to extract buildings from an urban area.
The research paper investigated a new building representation value based on just two colour bands (yellow and green) from high resolution World View 2 (WV2) satellite image. This representation is considered as building Normalized Difference Building Index (NDBI). The building index is used to detect pixels that represent buildings. Edge detection technique is applied on image of detecting building pixels to obtain the preliminary building boundaries. Morphological operations are applied on the image of building boundaries to get most probable building boundaries and represent them as polygons.
Building extraction is applied on the same image using commercial techniques included in the most famous image processing software which is ERDAS IMAGINE to produce an image of extracted building. This image is used in assessing the results of the investigated technique to get its efficiency against commercial software results.
This research investigated a new building extraction technique from high resolution remote sensing satellite image through MATLAB environment. The investigated technique is automated, fast and gives excellent results in case of red roof top and brightens surfaces of buildings.

1. INTRODUCTION

In recent years, object oriented in optical remote sensing images is one of the fundamental keys in the field of aerial and satellite image analysis. It received significant attentions for many applications as, feature extraction from high resolution satellite imagery. There are many researches introduced feature extraction techniques based on different algorithms as template matching-based object detection methods, knowledge-based object detection methods, object-based image analysis (OBIA)-based object detection methods and machine learning-based object detection methods(Cheng et. al., 2016). A satellite image has three or more spectral bands. The selection of spectral bands for extracting specific features depends on available data and the interaction among spectral bands and the required features (Lu, D. and Q. Weng, 2007). Spectral and spatial resolution of the new satellite World View-2 (WV2) are influenced on the quality of the mapping urban features and distinguishing detailed land cover (Elsharkawy et. al., 2012).WV2 satellite image contains new four spectral bands, Coastal blue, Yellow, Red edge and NIR-2, that are used in distinguishing features of land cover increasing the overall accuracy of feature extraction applications (Salehi et. al., 2012). Mahmoud et. al. (2016) illustrated that Investigated the optimum bands for urban area classification and define features from multi-spectral images based on available data is important factors to minimize the processing time , the cost and obtained better results. Muller et. al. (2016) demonstrated that Water Research Commission (WRC) was derived the use of very high resolution(VHR) satellite imagery from theWorldView2 (WV2) sensor for the detection of salt accumulation in irrigated areas can be executed by using 10 vegetation indices so WV2 is provided spectral and spatial factors for Concluding indices to detecting special objects . Elsharkawy et al, (2011) executed in the research that improvement separation and detecting four mainly classes of land cover (vegetation, water, shadow, and man-made objects.) by careful study of the spectral profiles of the 8-bands of the WorldView-2 data was provided spectral characteristics such as NDVI and band rationing. which will lead to the contribution of the new bands into enhancement classification of urban area(Elsharkawy et. al., 2011) . Li, X., et al, (2013)derived combined of object based and pixel-based classification provides a new way to classify land-cover types, especially mixed land-cover types, using satellite images where Object-oriented classification deals with objects delineated by a segmentation and edge detection algorithm and in other side Shackelford et al, (2003)are provided that pixel based is used to identify the digital number or pixel value of each class in the imagery by comparing the n-dimensional data vector for each pixel with the prototype vector for each class and utilizes both spectral and spatial information to discriminate between spectrally similar Road and Building classes. Using combination between object based and pixel based are improved classification and extraction objects from high resolution satellite images and increase overall accuracy compared when using one of them only(Salah and M.,2014). the new bands in the WV-2 imagery is one of the important key in the separation between confusing classes such as between water and shadows, and the separation between bare soils and asphalt roads in addition to The Integrated band ratio and edge detection techniques like curvelet transform increased detection of building rather than using the combination of band ratio only (Elsharkawy et. al., 2012). Man-made objects available in very high resolution (VHR) satellite images where buildings and

roads are the two most important object classes of an urban area and extracting information belonging to these two classes could be very useful for a number of applications, e.g. urban area monitoring/detection, change detection, estimation of human population, transportation, and telecommunication so a very large number of researchers have been involved for the detection of buildings and road using associated characteristics of each class like shadow ,solar illumination and spectral information for automated distinguishing them from an urban area(Ok. and A.O, 2013).Baltsavias et al (1997) demonstrated that utilizing multiple images and accurate reference data based on criteria such as completeness, geometric accuracy and shape similarity enhancement results and increased accuracy of the estimated and extraction building .Radiometric, geometric, edge detection and shadow criteria approaches are very important factors to perform the building extraction (Attarzadeh et. al., 2012 .Crommelinck et al., (2016) derived that Pixel-based approaches are often used to extract low-level features, which are extracted directly from the original, possibly noisy pixels do not consider information about spatial relationships. Object-based approaches are used to extract high-level features, which define shapes in images that are detected invariant of scale, illumination, orientation and translation. High-level features are mostly extracted based on the information provided by low-level features to improvement results. WV2 is the first commercial high-resolution satellite to provide 8 spectral sensors in the visible to near-infrared range. This research paper investigates the minimum spectral bands that can be used for building extraction from WV2 satellite images. The proposed building extraction technique minimizes the use of all spectral bands of WV2 satellite image that tends to minimize the image production and computational costs.

2. AREA OF STUDY

The available data of an image of residential areas was provided by Digital Globe, http://www.digitalglobe.com from (WV2) satellite sensor .The image was captured on October 9th, 2011 which is land cover area in a residential area of Presidio of San Francisco, California of area equals to 24.5 hectares approximately. The area of study is an urban area contains different features, buildings, roads, vegetation areas and. The projection of this image is UTM, with datum of WGS84 zone 10N. The area of study is bounded by coordinates as upper left corner coordinates are (lat 37° 48\ 14.4427\\ N, lon 122o 28\ 32.1099\\ W) and lower right corner coordinates of the image are (lat 37° 47\ 59.4439\\ N, lon 122° 28\ 11.1731\\ W)

3. RESEARCH ALGORITHM AND METHODOLOGIES

The proposed algorithm begins with a data fusion between original high resolution panchromatic image 0,5m and the low resolution multispectral imagery 2m to generate 8-spectral bands with a resolution of 0.50 m by "HP Resolution Merge techniques". The process involves a convolution using a High Pass Filter (HPF) on the high resolution data, then combining this with the lower resolution multispectral data. The result of these techniques provides excellent details and a realistic representation of original multispectral scene colours. The approach includes four main stages: pixel based classification process, object based extraction process, morphological operation and detecting buildings based on statistical analysis as shown in figure(1)

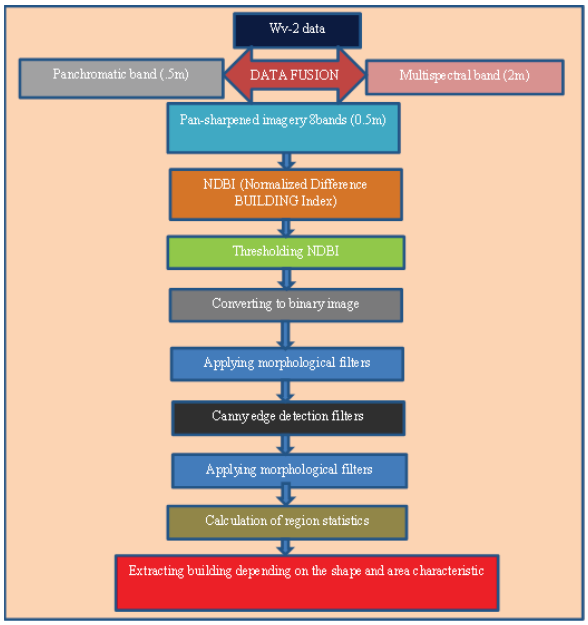

Figure 1. The proposed algorithm of research algorithm

The proposed building extraction technique is built based on different methods. Pixel based classification method is applied to detect pixels that representing building candidates. Object based classification is used to detect edges of extracted building pixels and identifying building candidates based on area thresholding. Statistical analysis is applied on building candidates, pixels and boundaries to extract final buildings from the area of study

3.1Pixel Based Classification: Pixel-based Classification method is used to classify pixels in the area of study. Normalized Difference Building Index (NDBI) is calculated from Green (G) band and Yellow (Y) band according equation (1) to detect building pixels. This equation developed by taking random points in study area for roof of building and uses the Spectral Profile to visualize the reflectance spectrum of a single pixel through many bands using points. A careful study of spectral profile allowed estimating of the chemical composition of the material in the spectral bands and selecting yellow and green bands which contain high spectral information about t building class to generate NDBI. Then selecting suitable thresholding value which is from 0.3 to 0.9 by visualization colour map of NDBI WV-2 satellite image to extract pixels for red roof and brighten surfaces of building

$$\mathrm{NDBI} = \frac{(Y-G)}{(Y+G)} \qquad (1)$$

Where Y= Yellow (Y) band
G= Green (G) band

3.2Object Based Classification: Object based classification of area of study is based on detecting edges of existing features. The edge detection in an identification of locations of local change in the image intensity. It is, usually associated with a discontinuity in either the image intensity or the first derivative of the image intensity (Gonzalez, 2008). an edge detection algorithm extracts the main properties from an image which are building edges for the current of interest. Edge detection is a filter, but it differs from usual filters in its

accordance with actual spatial patterns, and other advantages are also gained. The common types of techniques can be grouped into two categories, Laplacian and gradient. The Laplacian technique seeks for zero crossings in the second derivative of the image to find edges and the gradient technique detects the edges by detecting the maximum and minimum in the first derivative of the image (Canny et. al., 1986; Chen et. al., 2012). So there are various type of filters which are mainly gradient based as Roberts, Sobel and Prewitt edge detection operators, Canny edge detection technique is based on Laplacian edge detector and Canny. Canny edge detection algorithm is more costly in comparing to Sobel, Prewitt and Robert's operator. Even though, the canny edge detection algorithm has a better performance under the noisy conditions in image (Shrivakshan et. al., 2012). To get the benefits of canny edge detection technique it is used to identify the feature boundaries in this research

3.2.1Canny edge detection: Canny is used to find optimal edge as a set of characteristic that maximize the probability of detecting true edges while minimizing the probability of false edges in addition to find the zero-crossings of the second directional derivative of a smoothed image were a reasonable measurement of true edges (Bhadauria et. al., 2013).Canny edge detection technique is performed according to the following Steps as in figure (2):

-Step1: image convolution by Gaussian filter to smooth image

-Step 2: Compute the gradient magnitude and orientation using finite difference approximations for the partial derivatives by applying mask in figure (3).

-Step 3: Apply non maxima suppression to the gradient magnitude, Use the double thresholding algorithm to detect and link edges

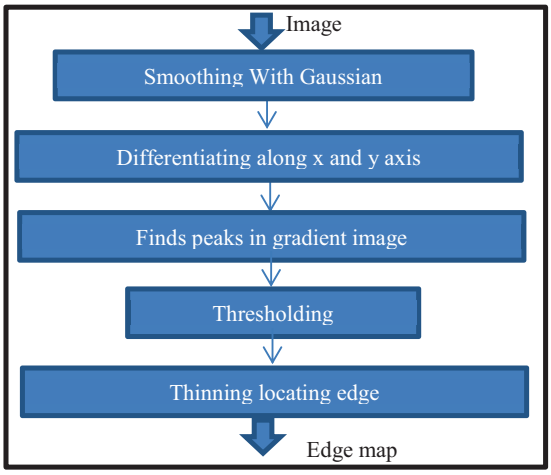

Figure 2. Canny Edge Detector

-1	0	1
-2	0	2
-1	0	1

-1	2	1
0	0	0
-1	-2	-1

Figure 3. Kernel of the canny mask

3.3Morphological filter: Morphological operation is utilized for extracting main component of images that are provided more benefits in the description of region shape such as object boundaries also useful in representation. Morphological operation is used in pre-processing and post processing such as thinning, pruning, filling, erosion and dilates. Erosion and dilation are fundamentals operation in morphological processing that is used in enhancing the object boundaries as needed (Gonzalez, 2008) Morphological operation is such as Erosion, dilation and filling used in this research to eliminate the undesired pixels and a filling operation applied to generate the parcels that represent preliminary building candidates.

3.4detecting buildings based on statistical analysis: The final step involves calculation of statistics for the enclosed boundaries which measures a set of properties for each connected component (object) in such as area, ratio between major and minor axis and extent.in the research roof of buildings based on shape and area characteristics candidates from parcels and edges such as area which is represented the actual number of pixels in the region for roof of buildings ,ratio of major/minor is specified the lengths (in pixels) of the major axis and minor axis of roofs and extent specifies the ratio of pixels in the boundaries of building to pixels in the total bounding box or computed as the area divided by the area of the bounding box of buildings.so this sets were taken in consideration to extract roof of buildings as much as possible.

3.5Object Oriented for Building Extraction: Object-Oriented Image Classification method is a useful and important method to extract and classify objects from high resolution satellite images which enables the software to simulate human visual processing by interpolating data not just on a pixel by pixel basis but also by searching for object-based measures such as texture, shadow, shape, size. The model parameters are defined by using the robust extraction imagine objective tool which extract the characteristics of different features. Such as buildings and trees. These enable to generate vectors from remotely sensed imagery and geospatial data which can be used in a GIS with minimal post processing (Chepkocheiet. al., 2011; Karagiannis et. al., 2012)

IMAGINE Objective has possessed of seven levels. Each level has one or more operators which are utilized depending on the level. The order of each level in IMAGINE Objective performs in specific and unchangeable step , but the order of the operators inside each level can be modified by the operator The following procedure describes the seven levels with operators for each level to develop model for extracting roof of building step-by-step as shown in figure(6) (Chepkocheiet. al., 2011; Karagiannis et. al., 2012; Imagine Objective Users Guide, 2010) :

1) Raster Pixel Processor (RPP)

level is used to Classify roof of building and non-roof building pixels from the original image This level was performed with the Single Feature Probability(SFP) technique which applied by taking area of interest from building pixels as training and non-roof building pixels as background then classifying the image. This step will create a probability image with pixel values indicating the high probability of being building pixel and Lower probability values are assigned to pixels are similar to other in the background training samples.

2) Raster Object Creators (ROC)

ROC Level generates sets of objects and groups of pixels from remotely sensed imagery. Segmentation operator is a way of partitioning raster images into segments based on pixel values

and locations. Pixels that are spatially connected and have similar values are grouped in a single segment. The result is a thematic image where pixel values represent number of class raster objects. The Pixel Probability Layer (RPP) is used to compute the pixel probability zonal mean of each segment and that zonal mean is used as the value of the segments pixel probability attribute.

3) Raster Object Operator (ROO)
ROO level allow the operator to use the raster objects generated by the Raster Object Creator. ROO may perform a variety of process on the raster objects including thinning or shrinking and eliminating. Probability filter is applied to remove all raster objects whose zonal probability mean less than the specified Minimum probability value and remaining objects with higher probability.
4) Raster to Vector Conversion (RVC)
RVC Level converts groups of raster objects to groups of vector objects. The generated groups of vector objects may be either polygons or polylines trace operators. Polygon trace is a raster to vector converter that traces the outlines and boundaries of raster objects and converts them to vector objects and shapefile (.shp) is produced from this step.

5) Vector Object Operators (VOO)
VOO Level may perform a variety of process on the vector objects including: splitting vector objects into multiple new vector objects, merging multiple input vector objects into a single vector object, reshaping the existing Vector Objects, eliminating undesired vector objects that do not match some criteria. Generalize filter remove noise, undesired pixels and improves the performance of processing.

6) Vector Object Processor (VOP)
VOP Level performs classification on vector objects which are used by an object classifier. The object classifier depends mainly on the spatial properties and geometry features by measuring size and shape property of the building. There are different types of operators which measure statistic property of vector objects this performed classification on the building vector objects from VOO by specifying area operator which computed the area of each polygon shape of roof buildings in the input vector file. The output vector object has an area attribute containing the result of this required area of roof buildings.

7) Vector clean up Operators (VCO)
VCO Level clean up the group of vector objects to produce a nice final output. Some vector cleanup operators will use the probability attribute generated by the in VOP the operation such as splitting vector objects into multiple new vector objects ,merging multiple input vector objects into a single vector object, reshaping the existing vector objects, eliminating undesired vector objects that do not match some criteria, matching vector objects to a template or fitting them to a fixed shape or shape type such as an orthogonal polygon At the last level the buildings were smoothed using smooth filter based on smooths polygon objects in a vector layer.

4. DISCUSSION AND RESULT

Figure (4) shows the input image of area of study with RGB color channels. The two bands yellow and Green are extracted for all image pixels, NDBI is calculated for all image pixels and represented as one channel image shown in figure (5) Then selecting suitable thresholding value which is from 0.3 to 0.9 by visualization color map of NDBI WV-2 satellite image as shown in figure (6) to extract pixels for red roof and brighten surfaces of building.

Figure 4. WV-2 satellite image of Presidio of San Francisco

Figure 5. NDBI was applied on area of study

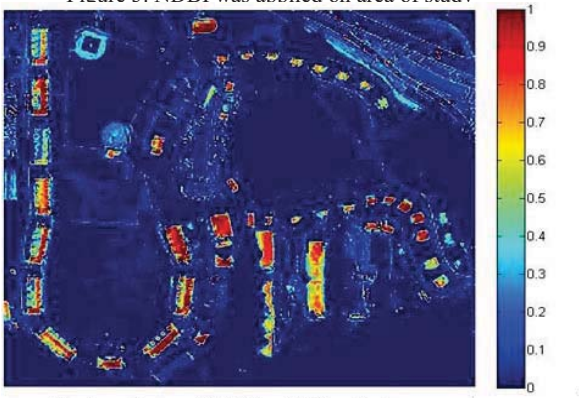

Figure 6. Color map of NDBI from WV-2 satellite image

Morphological operation will be used to remove undesired noised pixels and improve output after selecting thresholding from NDBI operation as shown in figure (7).canny edge detection finding edges in an images and contour boundaries of buildings roofs as in figure (8).

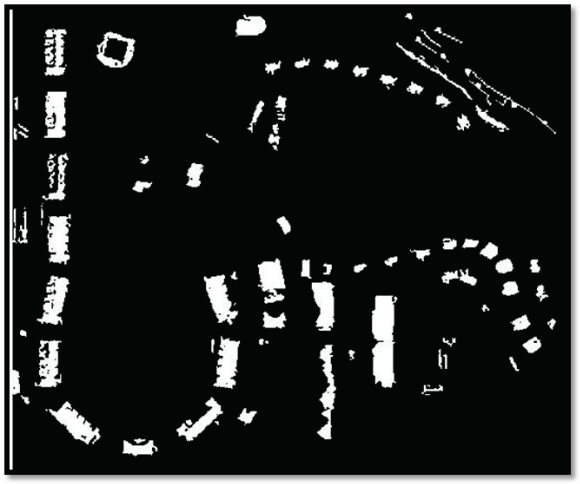

Figure 7. Applying morphological operation to eliminate undesired pixels

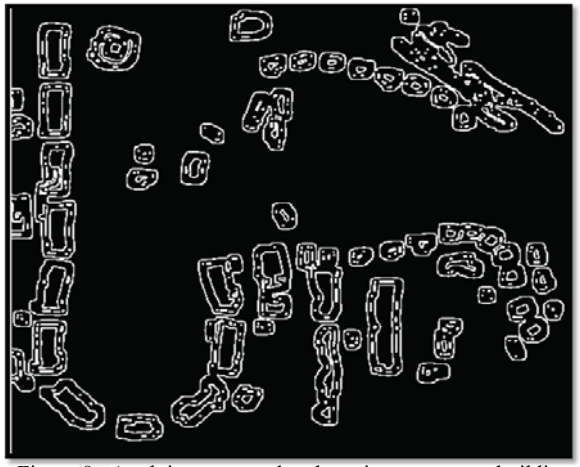

Figure 8. Applying canny edge detection to contour building boundaries

Labeling result as in figure (9) to study and evaluate feature geometry such as area and extent to extract building only as much as possible. Finally result of the proposed algorithm after overlying in original image as shown in figure (10)

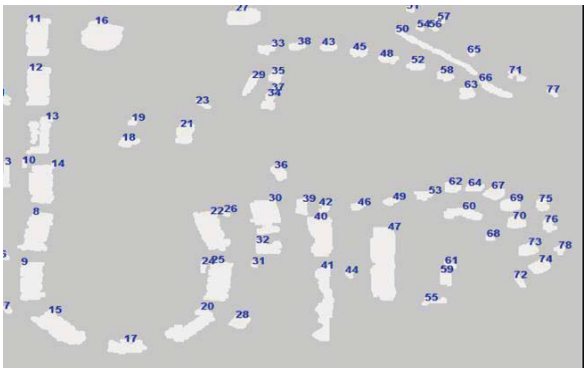

Figure 9. Labeling image to define geometry of objects

Figure 10. Overlay candidate pixel result on original image

At imagine objective Figure (11) shows the output image of area of study with RGB color channels at RRP level and segmented image at ROC level as in figure (12) then using probability filter operator at ROO level to extract segmented roof of building as shown in figure (15). Finally, VCO level shows the final output result of the imagine objective as shown in figure (13).

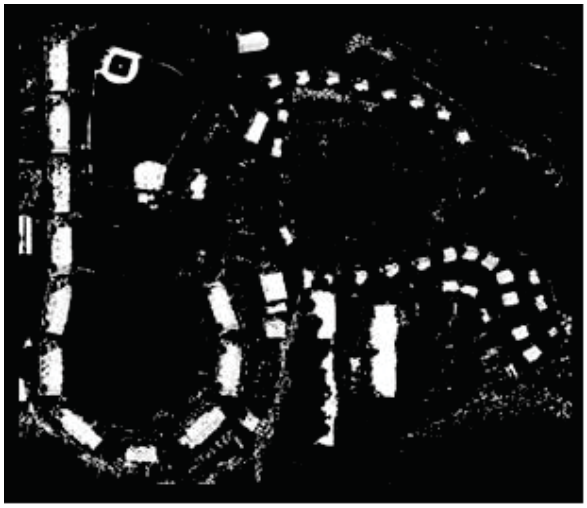

Figure11. Raster Pixel Processor (RPP) Classify roof of building

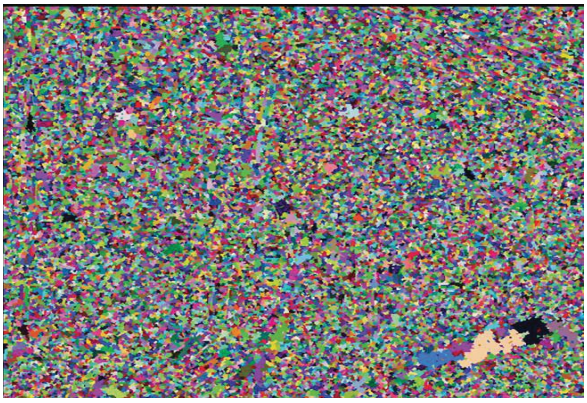

Figure 12. Raster Object Creators (ROC) Segmentation techniques

Figure 13. Raster Object Operator (ROO) was executed By probability filter

Figure 14. Vector clean up Operators (VCO) using Smooth filter

5. ASSESSMENT OF THE PROPOSED TECHNIQUE

The ground truth is generated manually to detect buildings from the image of area of study. Figure (15) shows a ground truth vector layer of extracted buildings that contains56 buildings in the area of study. The proposed technique succeeded in extracting 56 buildings from the area of study as shown in figure(10) and objective imagine succeeded in extracting 55 buildings from the area of study in figure(20). So, the proposed technique is acceptable for building extraction applications from multispectral remote sensing images with successful percentages equal to 100%.

Assessment the result of the feature extraction models for red roof buildings by calculating some of indicators from results in figure (16) and figure (17) .these indicators define the capability of the model to extract polygons comparing with ground truth. Indicators are applied in equation (2), (3) and (4) to calculate completeness, correctness and overall quality of the model (Karagiannis et. al., 2012; Agouris et. al., 2004) the omission and commission errors of the procedure are calculated. The omission error was computed by dividing the number of polygons that were not detected by the model (False Negatives) with correct number of polygons that have appeared by the test data (photo-interpretation, ground truth). The commission error was computed by dividing the incorrectly detected polygons (False Positives) with the correct number of polygons (photo-interpretation, ground truth). Indicators were calculated from final results of two algorithms.

$$\text{Completeness} = \frac{TP}{TP+FN} \quad (2)$$

$$\text{Correctness} = \frac{TP}{TP+FP} \quad (3)$$

$$\text{Quality} = \frac{TP}{TP+FP+FN} \quad (4)$$

Where TP = True Positives (TP) are objects (correctly extracted pixels) that are correctly detected by model.

FP = False Positives (FP) are the incorrectly polygons that have been detected by the model as buildings.

FN= False Negatives (FN) are the correctly polygons that mistakenly have not been detected by the model.

The methods of the achievement of the assessment using five comparisons were calculated for the extraction model of imagine objective and the proposed algorithm. Finally, the results were imported into the calculation of the indicators and errors that mentioned. Table 1 shows the final accuracy of the procedure.

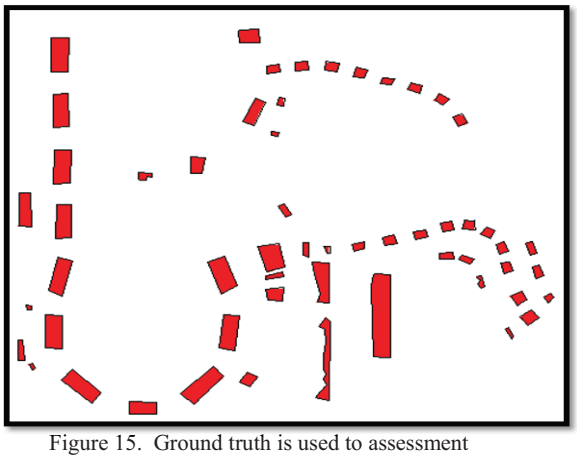

Figure 15. Ground truth is used to assessment

Figure 16. Overlay vector layer of proposed algorithm on original images

Figure 17. Overlay vector layer of imagine objective on original images

Indicators	Type of algorithm	
	Proposed algorithm	Imagine objective
	%	%
Omission errors	0	1.7
Commission errors	17.8	1.0
Completeness index	100	98
Correctness index	84.8	90
Quality index (%)	84.8	88.7

Table 1.Assessment results of the feature extraction techniques

CONCULSION

In the present study, feature extraction of building in suburban area in high resolution satellite images was discussed using the MATLAB software, ERDAS Imagine Objective. To sum up, at the end of the whole process we can conclude the following, by using NDBI which generated only from two bands yellow and green combined with object based technique all buildings in area of study were detected and completeness result was equal to 100% .on the other side imagine objective was executed by using 8 bands of wv2 satellite images and the completeness result was equal to 98%. The investigated technique is automated and gives excellent results in case of red roof top buildings.

6.REFERENCES

Cheng, G. and J. Han, A survey on object detection in optical remote sensing images. *ISPRS Journal of Photogrammetry and Remote Sensing,* 2016. 117: p. 11-28.

Lu, D. and Q. Weng, A survey of image classification methods and techniques for improving classification performance. *International journal of Remote sensing*, 2007. 28(5): p. 823-870.

Elsharkawy, A., M. Elhabiby, and N. El-Sheimy. Improvement in the Detection of Land Cover Classes Using the WorldView-2 Imagery. in *ASPRS, International Scientific Conference*. 2012.

Salehi, B., Y. Zhang, and M. Zhong. The effect of four new multispectral bands of WorldView2 on improving urban land cover classification. *ASPRS 2012 Annual Conference*. 2012.

Mahmoud A. Shawky, et al., Investigation of Optimum Spectral Bands forUrban Area Classification from World View2(WV2) Satellite Image. *International Journal of Innovative Research in Computerand Communication Engineering*, 2016. 4(9): p. 15701- 15707.

Muller, S.J. and A. van Niekerk, Identification of WorldView-2 spectral and spatial factors in detecting salt accumulation in cultivated fields. *Geoderma*, 2016. 273: p. 1-11.

Elsharkawy, A. A modified parallelepiped-like method for supervised classification for high resolution satellite imagery. in *CGU Annual Scientific Meeting*, Banff, Calgary. 2011.

Li, X., et al., A hybrid method combining pixel-based and object-oriented methods and its application in Hungary using Chinese HJ-1 satellite images. *International Journal of Remote Sensing*, 2013. 34(13): p. 4655-4668.

Shackelford, A.K. and C.H. Davis, A combined fuzzy pixel-based and object-based approach for classification of high-resolution multispectral data over urban areas. *IEEE Transactions on GeoScience and Remote sensing*, 2003. 41(10): p. 2354-2363.

Salah, M., Combining Pixel-Based and Object-Oriented Support Vector Machines using Bayesian Probability Theory. *ISPRS Annals of the Photogrammetry, Remote Sensing and Spatial Information Sciences,* 2014. 2(7): p. 67.

Elsharkawy, A., M. Elhabiby, and N. El-Sheimy, New Combined Pixel/Object-Based Technique for Efficient Urban Classification Using Worldview-2 Data. *International Archives of the Photogrammetry, Remote Sensing and Spatial Information Sciences*, 2012. 39: p. B7.

Ok, A.O., Automated Extraction of Buildings and Roads in a Graph Partitioning Framework. *ISPRS Annals of*

Photogrammetry, Remote Sensing and Spatial Information Sciences, 2013. 1(3): p. 79-84.

Baltsavias, E. and O. Henricsson, Automatic Extraction of Man-Made Objects from Aerial and Space Images (II). 1997: *Springer Science & Business Media*.

Attarzadeh, R. and M. Momeni, Object-Based Building Extraction from High Resolution Satellite Imagery. *ISPRS-International Archives of the Photogrammetry, Remote Sensing and Spatial Information Sciences,* 2012. 1: p. 57-60.

Crommelinck, S., et al., Review of Automatic Feature Extraction from High-Resolution Optical Sensor Data for UAV-Based Cadastral Mapping. *Remote Sensing*, 2016. 8(8): p. 689.

Gonzalez, R.C. and R.E. Woods, Digital image processing. 2008, Prentice hall Upper Saddle River, NJ, USA:.

Canny, J., A computational approach to edge detection. *IEEE Transactions on pattern analysis and machine intelligence, 1986(6): p. 679-698.*

Chen, L., I.W. Tsang, and D. Xu, Laplacian embedded regression for scalable manifold regularization. *IEEE transactions on neural networks and learning systems*, 2012. 23(6): p. 902-915.

Shrivakshan, G. and C. Chandrasekar, A comparison of various edge detection techniques used in image processing. *IJCSI International Journal of Computer Science Issues*, 2012. 9(5): p. 272-276.

Bhadauria, A., H. Bhadauria, and A. Kumar, Building extraction from satellite images. *IOSR Journal of Computer Engineering,* 2013. 12(2): p. 76-81.

Chepkochei, L.C. Object-oriented image classification of individual trees using Erdas Imagine objective: case study of Wanjohi area, Lake Naivasha Basin, Kenya. in Proceedings, *Kenya Geothermal Conference*. 2011.

Karagiannis, G. and D. Argialas, Semi-automatic object-based building change detection in suburban areas from Quickbird imagery using the ERDAS Imagine Objective software. Advances in Geosciences, 2012: p. 594-607.

Imagine Objective Users Guide, L.G. 2010.

Agouris, P., P. Doucette, and A. Stefanidis, Automation and digital photogrammetric workstations. *Manual of Photogrammetr*y, 2004: p. 949-981.

COOPERATIVE LOCALIZATION IN INDOOR ENVIRONMENTS USING CONSTRAINED DIFFERENTIAL WI-FI AND UWB MEASUREMENTS

G: Retscher [a, *], A. Kealy [b], V. Gikas [c], H. Hofer [a], A. Ettlinger [a], F. Obex [d]

[a] Dept. of Geodesy and Geoinformation, TU Wien – Vienna University of Technology, Gusshausstrasse 27-29, 1040 Vienna, Austria - guenther.retscher@geo.tuwien.ac.at - h.hannes@gmx.at - andreas.ettlinger@geo.tuwien.ac.at
[b] Dept. of Infrastructure Engineering, The University of Melbourne, Building 173, Parkville Victoria 3052, Australia - a.kealy@unimelb.edu.au idowman@ge.ucl.ac.uk
[c] Laboratory of Geodesy, School of Rural and Surveying Engineering, National Technical University of Athens, 9 H. Polytechniou Str., Zographos, 15780, Athens, Greece - vgikas@central.ntua.gr
[d] Freelancer, Vienna, Austria - obex@chello.at -

KEY WORDS: Cooperative positioning, Indoor positioning, Wi-Fi, RSS measurements, Differential technique, Reference stations

ABSTRACT:

To locate a group of mobile smartphone users within a neighbourhood Cooperative Positioning (CP) can be applied whereby the user localization is performed using its own measurements plus any additional information coming from neighbouring users in the form of inter-nodal ranges or other means. In this study, Wi-Fi and UWB are employed to form a networked solution. Two new differential Wi-Fi positioning approaches based either on the Differential GPS (DGPS) or Very Long Baseline Interferometry (VLBI) operational principle are developed for (tri)lateration. By the use of reference station observations the received signal strength (RSS) measurements of the access points is corrected to reduce short- and long-time variations of the RSS at the user side. Static and kinematic tests using six users carrying different smartphones were conducted in an indoor lab in the practical evaluation. Five Raspberry Pi's served as reference stations and access points together with another three additional Wi-Fi routers. One user enabled the hotspot function on his mobile device so that the other users could measure the RSS to derive inter-nodal ranges for the cooperative positioning solution. Additional five UWB units were carried by the users serving as either a reference for the derivation of the inter-nodal ranges or in order to be integrated into the overall positioning solution. Ground truth for these experiments was measured using a robotic total station. It is proven that both DWi-Fi approaches outperform conventional RSS lateration and the integration with UWB further strengthens the CP solution.

1. STUDY OBJECTIVES

Nowadays, most personal mobility scenarios require the localization of a group of end users or individuals within a group or neighbourhood. Not rarely, this is the case in adverse operating conditions, such as in large inter-modal transit stations where only limited positioning information is available (Retscher and Obex, 2015). A solution to this problem is referred to as Cooperative Positioning (CP). In CP, end user localization is performed using its own measurement data plus any additional information coming from neighbouring users in the form of inter-nodal ranges or other means (see e.g. Kealy et al., 2015). In this study, absolute indoor localization of a user group is enabled with novel differential Wi-Fi (Wireless Fidelity, a.k.a. Wireless Local Networks WLAN) positioning approaches. Furthermore, the use of Ultra Wide Band (UWB) and its combination with Wi-Fi for localization of the user group is investigated to form a networked solution.

2. WI-FI POSITIONING

Wi-Fi positioning is generally based on the measurement of the received signal strength (RSS) to the surrounding wireless access points. This appraoch was first introduced by Bahl and Padmanabhan (2005) for location fingerprinting. In this work (tri)lateration is employed for user localization. The derivation of ranges between the user and the access points is prone to large short- and long-time variations of the measured RSS. Thus, two differential approaches termed DWi-Fi have been developed to overcome this drawback. They are either derived from the well-known DGPS or VLBI positioning principles. Then, the spatial and temporal variations of the Wi-Fi RSS can be taken into account if differential corrections from reference stations in the area of interest are applied (see Retscher and Tatschl, 2016).

A low-cost implementation of these reference stations is realized using a number of Raspberry Pi units, which serve simultaneously as both access points and reference stations – emitting and scanning Wi-Fi signals. A Raspberry Pi is a low-cost credit card sized computer. An USB Wi-Fi adapter with a rod areal antenna is plugged into each Raspberry Pi and the internal Wi-Fi card is used in addition. The employed hardware is depicted in Figure 1.Using these devices the RSS scans are recorded together with the MAC addresses of the Wi-Fi access points continuously.

Furthermore, Wi-Fi signals of all available access points in the area of interest are measured and integrated into the positioning solution.

* Corresponding author

Figure 1. Raspberry Pi unit including an internal Wi-Fi card and an external USB Wi-Fi adapter with a rod areal antenna

Using a network of Raspberry Pi's in the area of interest it is then possible to deduce the differential corrections. These corrections are then applied to the current RSS scans from the mobile user on his smartphone.

For the data collection a smartphone application (Android App) was used which was developed by Hofer (Hofer and Retscher, 2016), which is able to scan the Wi-Fi signals and record the RSS of the smartphone users continuously. The so-called Combined Positioning System App CPS is able to record RSS values and the smartphones' orientation on selected locations with the 'CPS Kompass WiFi-Scanner'. Along a trajectory the 'CPS Sensor-WiFi-Recorder' can be used to record RSS values continuously together with the smartphone inertial sensor data, i.e., the accelerations from the accelerometer, direction of movement from a combination of the magnetometer and gyroscope and the altitude with the barometric pressure sensor. Figure 2 shows the user interface of the App.

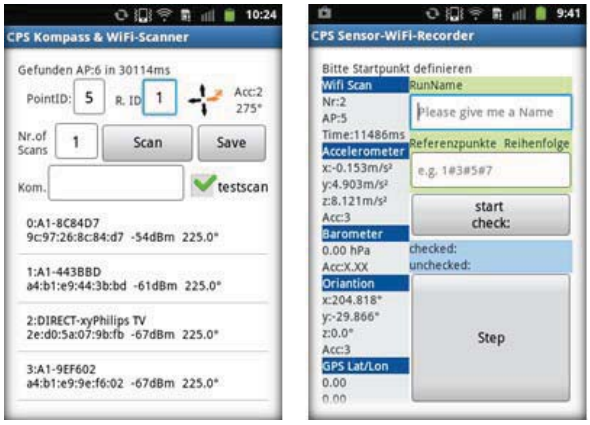

Figure 2. Data acquisition CPS App user interface (CPS Kompass & WiFi-Scanner on the left and CPS Sensor-WiFi-Recorder on the right)

3. PRACTICAL EVALUATION

In the practical evaluation, static and kinematic tests using six App users carrying different smartphones were conducted in an indoor lab with a size of approximately 400m^2. Five Raspberry Pi's served as reference stations as well as access points. Three additional Wi-Fi routers were deployed in the indoor lab to cover the whole area. In the test scenarios, one of the six users enabled the hotspot function on his smartphone so that the other five users can measure the RSS. Then inter-nodal ranges between all users were derived from the RSS measurements. Thus, a CP positioning solution was calculated for the whole user group. In another experiment, five UWB units were carried by the mobile users serving as either a reference for the derivation of the inter-nodal ranges or in order to be integrated into the overall positioning solution. Ground truth for these experiments was measured using a robotic total station.

4. CONCLUSION

Based on these tests, it was proved that both DWi-Fi approaches outperform standard RSS lateration as positioning accuracies can be increased significantly. A CP solution is obtained due to the additional derivation of the inter-nodal ranges between the users. In addition, the integration with UWB further strengthens the CP solution. The inertial sensors in the smartphones were also recorded with the App. This information can be used for dead reckoning purposes while its integration in the overall positioning solution could further benefit continuous cooperative localization of the user group.

REFERENCES

Bahl, P., Padmanabhan, V. N., 2005. RADAR: An In-Building RF-Based User Location and Tracking System. In: Omar A. M. Aly, A. S. Omar (eds.): *2nd Workshop on Positioning, Navigation and Communication*, Ultra-wideband Expert Talk (UET'05), Magdeburg, Germany, pp. 775–784.

Hofer, H, Retscher, G., 2016. Combined Out- and Indoor Navigation with Smart Phones Using Intelligent Check Points. In: *13th International Symposium on Location-Based Services LBS 2016*, Vienna, Austria, pp. 82-90.

Kealy, A., Retscher, G., Toth, C., Hasnur-Rabiain, A., Gikas, V., Grejner-Brzezinska, D. A., Danezis, C., Moore, T., 2015. Collaborative Navigation as a Solution for PNT Applications in GNSS Challenged Environments – Report on Field Trials of a Joint FIG/IAG Working Group. Journal of Applied Geodesy, 9(4), ISSN 1862-9016, DOI 10.1515/jag-2015-0014, pp. 244-263.

Retscher, G., Obex, F., 2015. InKoPoMoVer – Cooperative Positioning for Real-time User Assistance and Guidance at Multi-modal Public Transit Junctions. Journal of Applied Geodesy, 9(3), ISSN 1862-9016, DOI 10.1515/jag-2015-0006, pp. 198-206.

Retscher, G., Tatschl, T., 2016. Indoor Positioning Using Wi-Fi Lateration – Comparison of Two Common Range Conversion Models with Two Novel Differential Approaches. IEEE Xplore, *2016 4th International Conference on Ubiquitous Positioning, Indoor Navigation and Location Based Services (UPINLBS)*, Shanghai, China, 10 pgs.

Change Detection Analysis of Urban Land Cover Changes Using SPOT5 of Arar City, Saudi Arabia

Saleh Mesbah[1], Khaled Mahar[2] and Sultan Al-Adham Alenezi[2]
[1]Remote Sensing & Spatial Studies Unit, College of Engineering and Technology, Arab Academy for Science, Technology & Maritime Transport, Alexandria, Egypt. saleh.mesbah@aast.edu
[2]College of Computing and Information Technology, Arab Academy for Science, Technology & Maritime Transport, Alexandria, Egypt. sultan.alenezi85@gmail.com khmahar@aast.edu

Abstract: Urban land cover/use mapping has received an increasing amount of attention from urban planners and scientists with its various benefits regarding urban development and environmental quality. Remote sensing becomes an important source of data for urban land use/land cover mapping and environmental monitoring. Recent advances in satellite imaging technology have provided rich data for urban land use/land cover mapping from high resolutions to moderate resolutions for detailed mapping with high accuracy. This study aims to use remotely sensing data to identify urban land cover changes in Arar city, Saudi Arabia. This paper describes the use of SPOT5 images in particular, to extract the urban land cover changes in Arar city. Hybrid classification techniques are used and carried out to extract four urban land covers: urban areas, vegetated areas, vacant land and hilly areas. Results indicate that the study area has undergone significant changes. Urban land cover in the study area increased during the period from 2002 to 2012. This study uses the success of remote sensing technique for mapping and monitoring urban extension and its dynamic changes in Arar city.

Keywords: Urban land cover; SPOT5; change detection; Urban planning; Arar City.

I. INTRODUCTION

The majority of the world's population now resides in urban environments and information on the internal composition and dynamics of these environments is essential to enable preservation of certain standards of living.[1] The availability of urban land cover data is critical to policy makers, particularly for planners, because of their ability to monitor the impact of planning policies, the direction of urban growth and the development progress. Urban land cover continually changes over time and space, and local government must be able to update their databases to reflect current land use. However, conventional methods of obtaining urban land cover data require a great deal of time, effort and money to meet fast growing cities.

Remote sensing can provide an important source of data for urban land use/land cover mapping and environmental monitoring.[2] Urban land cover/use mapping has received an increasing amount of attention from urban planners and scientists with its various benefits regarding urban beauty and environmental quality (Chen et al., 2007). Thus, various techniques have been applied for mapping urban land cover. According to McDermid et al. (2005) [3], image classification, per-pixel models, and spatial pattern analysis techniques are effective tools for extracting information, but scientists and resource managers require guidance for their effective application.

Recent advances in satellite imaging technology have provided rich data for urban land use/land cover mapping from high resolutions (e.g. QuickBird, IKONOS and SPOT5) to moderate resolutions (e.g. ASTER, IRS and LANDSAT). Considering these data, the detailed mapping of urban land use/land cover should be possible with high accuracy potential.

This study aims to examine how remote sensing data can be helpful for extracting urban land cover changes in Arar city, Saudi Arabia.

II. RELATED WORK

The rate at which the world has been urbanizing in the last 100 years has been brisk. Currently, the majority of the world population lives in urban areas.[1] For the preservation of the urban environments and to ensure those living in those areas enjoy certain standards of living, collecting information on the internal composition and dynamics of these areas is very important. Policy makers and planners rely on urban land and cover data which influences growth in urban areas. Often, the changes in land use in urban environments happen very quickly and authorities have to constantly update their databases to capture current land use. Obtaining these data is, however, expensive and time consuming if done in conventional way.

Collecting data on urban land use/land cover mapping can be done through the use of remote sensing.[2] The benefits of land cover mapping have led to increasing attention and adoption by planners and scientists (Chen et al. 2007). According to McDermid et al. (2005) [3] extracting information is done through image classification, per-pixel mode, and spatial pattern technique. The users of these techniques, who may be managers or scientists, require training on how to use them effectively.

The most widely used technique of extracting information in remote sensing is image classification.[3] Under

this technique, data are grouped by category or by fuzzy decision rules. A number of image classification processes can be employed these include sub-pixel, per-pixel, supervised or unsupervised, parametric or non-parametric, and hard or soft (Chen et al. 2007)

Thanks to satellite imaging technology, planners can access rich data for urban planning at high or low resolution. Urban authorities can, therefore, map land use in their jurisdictions with a high degree of accuracy.

Efforts towards environmental protection and sustainable development have relied on remote sensing technology to map land use in urban areas that are developing rapidly. Specifically, SPOT HRV that employs cover frequency method are based on remote sensing.[4] A two-stage classification procedure, the SPOT High Resolution Visible (HRV), has normally been adopted in studies that have been done the past. The procedure has been used in the extraction of land use data in rural-urban fringe environments. During the first stage, SPOT HRV data, using the supervised maximum-likelihood classification (MLC), is categorized into 12 land cover types. The second stage entails the extraction of cover frequencies by the user. This is done by using the process of moving a pixel window over the land cover map that was developed during stage one.

Jensen et al. (2001) used a neural network image interpretation system to map land use from data collected using remote sensors [5]. He reports that he started by taking the remote sensing imagery and placing it in classes based on either land use or cover types. Later, he segmented rural land cover information in a homogeneous polygons geographic information system (GIS) format. The result was digitized. Jensen's work proved that inexperienced image interpreters could gain hands-on on experience through working on image interpretation prototypes.

Other than remote sensing, land use can be mapped using multi-temporal Landsat Thematic Mapper (TM) data. According to the work of Yuan et al. (2005), by using this method, he achieved 94% overall seven-class classification accuracies in the four years that he used TM [6]. The maps used were generated by post-classification change detection methods. Overall, this technique proved to be accurate and economical in both mapping and analyzing land use patterns and changes and the results generated would be useful in assisting policy decisions with reference to land management.

Chen et al. (2007) reported that an object-oriented approach to mapping urban land cover with ASTER imagery has been tested in the city of Beijing, China. Using ASTER data, scientists used an object oriented classification to generate land use maps for the city. The test with the use of this method in Beijing demonstrated that an accuracy of 85% can be attained with a kappa index of 0.81.

III. THE STUDY AREA

The city of Arar is founded in 1951 (1375 AH), after the construction of the Aramco oil pipeline (Tapline) was completed. It was initially an oil pumping station with a health center and worker housing. Workers at Arar were primarily from the regions of Al-Ahsa, Ha'il, Yanbu Al Wajh. Arar got its name from the original oil field that existed before the town, "Field RR", one of many in the country, where it was known by the locals as "R.R." which later became 'Ar'ar.The name Arar means juniper in Arabic.[7] Arar is located in the north of Saudi Arabia, at Latitude: 30° 54' 21 N, Longitude: 41° 8' 20 E, in the heart of a vast rocky limestone plain. It lies about 1100 km northwest of Riyadh, and about 60 km from the Iraqi border [7].

Arar's climate is continental, with hot summers, and cold winters with temperatures below freezing. Winds generally blow from the east or west, rarely from the south. It is noteworthy that the rainfall in the region has declined gradually over recent years. It is also noted that snow is not uncommon, falling on average every two to three years [7].

Fig 1: A general geographic location map of Arar [7]

IV. ANALYSIS

The data used through this study are collected from different sources. It consists of SPOT5 satellite images acquired in 2002 and 2012. Data used also include field survey measurements for collecting in situ data about land cover classes description used in both images classification and accuracy assessment and to define ground control points (GCPs) for geo-referencing processes.

4.1. Post Classification Technique

The methodology adopted in this study follows two different paths. The first involves digital image processing and analysis of satellite data to produce land cover thematic map. The second deals with change detection analysis of the multi-date satellite images. The first path consists of visual data preparation and interpretation. The image preprocessing phase involves sub-area creation, and geometric correction. This phase also involves both unsupervised and supervised classification; and classification accuracy assessment. Post-processing prepares the output of the final maps resulted from classification process. The processing of the temporal satellite images started with the most recent available images covering the region: SPOT 5 of year 2012, then the older one: SPOT 5 of year 2002.

The images are processed and analyzed using ERDAS Imagine 10 There are two broad approaches for classifying the land surface into different land cover types using multi-band remotely sensed data: unsupervised and supervised classification [8]. In unsupervised classification, classes are selected based on statistical clustering algorithms, whereas in supervised classification the user guides the selection of classes by identifying areas of known land cover type (training data) and using these to characterize the classes produced in the classification.

Supervised classification is performed using the hybrid classification technique (Bourne and Graves, 2001). For the purposes of classification, a number of ground truth points are selected that are within continuous areas of each land cover category. About 25% of the identified training pixels are used for accuracy assessment and the remainders are used for classification. Figures 2 and 3 represent false color composite images for the years 2002 and 2012, respectively.

The hybrid classification technique involves performing an unsupervised classification using the ISODATA algorithm to identify 100 spectral signatures, which while large in number seems to be necessary due to the nature of the study area. Information classes are assigned to these signatures using ground truth data. These signatures are analyzed to identify spectrally distinct signatures. A signature is merged, deleted or retained; depending on the number of other signatures that are close to this signature and the level of accuracy needed. This process is performed until 15 distinct signatures remained. These signatures are used as input for a maximum likelihood supervised classification which produced a supervised classification image. This result is applied to remove small patches comprising few pixels from the classified image. The resulted supervised classification images of both dates are illustrated in Figures 4 and 5.

4.2. Classification Accuracy Assessment

The pre-selected training areas prepared during field trips were used to compute the classification accuracy. Error matrices as cross-tabulations of the mapped class versus the reference class were used to assess classification accuracy. Overall accuracy, user's and producer's accuracies were then derived from the error matrices. In addition, to assess how well the Landsat classifications fit to other land cover inventories, the results of SPOT classifications for years 2002, and 2012 were compared to the field inventory that contains all information about the dominant land covers and the main land uses in the area during those specific dates. The overall accuracy calculated for both years 2002 and 2012 were about 93.35% and 97.5%, respectively, and that are considered to be acceptable values. The producer's and user's accuracy are summarized in Table 1.

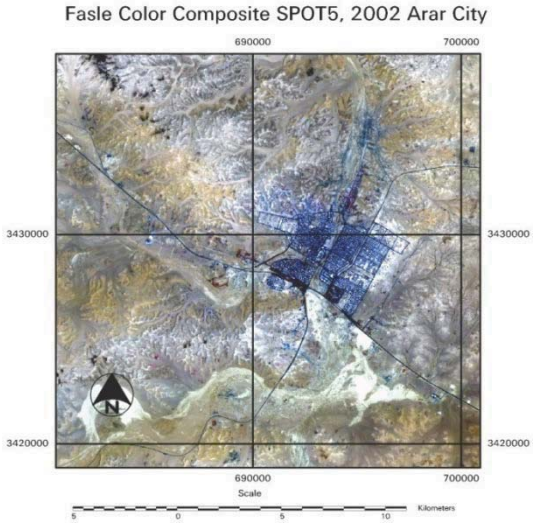

Fig 2: False color composite spot5 (2002) of arar city.

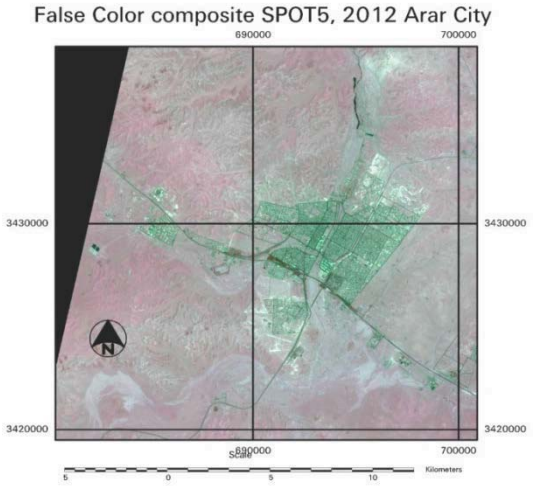

Fig 3: False color composite spot5 (2012) of arar city

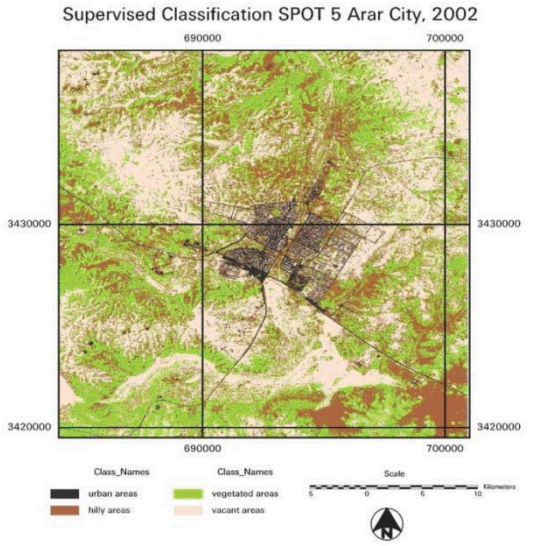

Fig 4: Supervised classification of spot5 (2002)

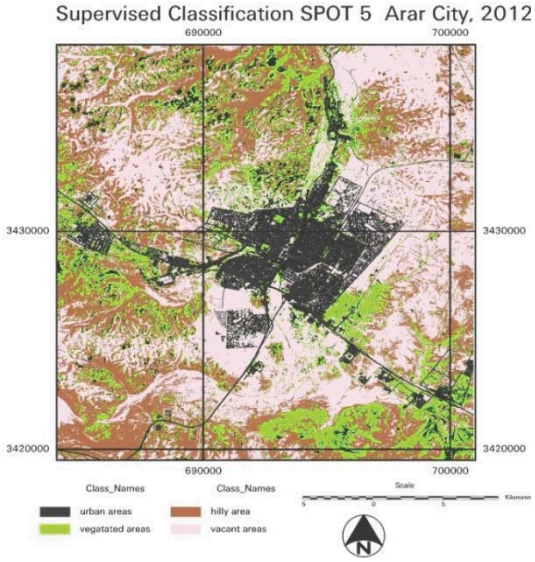

Fig 5: Supervised classifications of spot5 (2012).

Table (1): A summary of classification accuracy.

Years	2002		2 0 12	
Land cover class	Producer's	User's	Producer's	User's
Urban Area	96.4	96.2	98.6	95.8
Hilly area	92.3	94.1	96.8	96.7
Vegetated areas	91.8	88.4	98.2	89.6
Vacant areas	92.9	91.9	96.4	95.2
Overall Accuracy	93.35		97.5	

4.3 Change Detection Analysis:

Changes occurring on the Earth's surface can generally be attributed to either natural or anthropogenic forces. Natural changes relate to both seasonal and annual variations in climatic conditions, and are often reflected by variations in natural land cover. The change detection procedures assume that a change in surface cover or surface material will produce a corresponding change in the reflectance of the study area. A significant component of change detection methods using remote sensing is related to the characterization of natural ecosystem structure and function at synoptic scales. As these methods mature, there is an increased need for remote sensing data and associated analysis techniques in detecting and monitoring change, particularly for resource management and planning. With the parallel expansion of computer processing capabilities and software, specifically developed to handle image and spatially explicit data, (i.e. image analysis systems and geographic information systems); spatial data products have become more widely accepted outside the remote sensing community.

One of the major applications of remotely-sensed data is change detection, because of repetitive coverage at short intervals. There are several ways to carry change detection analysis using satellite images as follow:

(i) Techniques for image enhancement, such as image differencing and rationing, which represent the simplest change detection procedure. The results of these enhancements have not been entirely satisfactory because they provide the analyst with little information regarding the nature of change.

(ii) Techniques for data compression, such as principal components analysis (PCT) of the multi-temporal satellite image data. PCA is effective in enhancing the regions with the localized changes. Principal components transformation requires no a priori information and thus can be applied in a less direct fashion rather other techniques.

(iii) Techniques of classification of multi-temporal date. Classification techniques have been applied at promising levels of accuracy, but with some precautions because results using classification approaches are tend to compound any mis-classification and mis-registration errors that may be present in individual classifications, it this technique needs a high level or accuracy in all steps.

A new modified approach extracted from the multi-temporal date technique has been raised lately. This is perhaps the most common approach to change detection and has been successfully used by El-Hattab (2002)[9] to monitor land use changes in northwestern coastal zone of Egypt.

As for our case study, following the supervised classification of both images from the individual years, a multi-date post-classification comparison change detection algorithm is used to determine changes in land cover during the period of 2002-2012. The post-classification approach provides "from–to" change information where the kind of landscape transformations that have occurred can be easily calculated and mapped with high accuracy.

In order to visualize the changes occurred in urban in the period between year 2002 and year 2012 for each separate land cover, a simple technique was used (El-Hattab, 2002) [9]. This technique can be summarized as follows:

1. For urban land cover class, a re-coding process to be applied on the basis of giving that class a value " 2 " for the older date (year 2002) and value " 3 " in newer one (year 2012), while giving other classes and background a value " 1 " for both years.
2. By multiplying the two re-coded images, a change detection image for that land cover class is created. This image has four main classes:
   (i) Lost areas from 2002 to 2012, which have a value "2" (i.e. 2*1);
   (ii) No changes areas, which has a value "6" (i.e. 2*3);
   (iii) Gained areas from 2002 to 2012, which has a value "3" (i.e. 3*1);
   (iv) Other classes and background, which have a value "1" (i.e. 1*1).

All previous steps are repeated to create a final change image for urban land cover class, representing areas of change (either positive or negative) and no change. The final change detection resulted image of urban land cover classes show high positively changes as illustrated in Figure 5. Table 2 summarizes all the statistics obtained during change detection

analysis of urban land cover class for Arar city from 2002 to 2012.

Table (2): A summary of the statistics obtained during change detection analysis of the urban land cover classes.

Land Cover Class	Year 2002 (Spatial Resolution 2.5 m)			Year 2012 (Spatial Resolution 2.5 m)			Change	
	Pixels	*Area (Km^2)*	*Area %*	Pixels	*Area (Km^2)*	*Area %*	*Area (Km^2)*	*Area %*
Deep Water	498079	*6.723*	*18.97 %*	2008665	*14.37*	25.13 %	7.647	6.16%

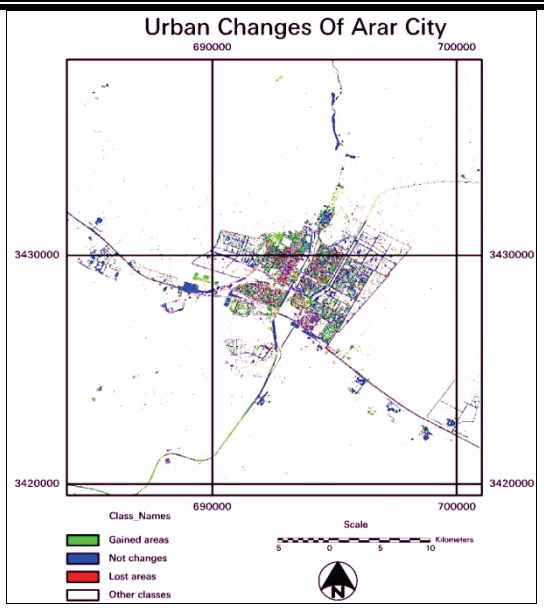

Fig 6: Change detection of urban land cover classes of Arar city, Saudi Arabia.

V. INTERPRETATION AND DISCUSSION

This research considered the performance of SPOT5 data for mapping areas of urban areas in Arar city. Using multi-temporal satellite image data potentially enables the mapping of changes of urban areas, rather than using limited ground measurements.

Change detection techniques give a powerful tool for clarifying urban areas; also change detection techniques can give a quantitative view for the conversion of classes, which give an opportunity to calculate the extension of urban areas.

Rapid development in a city like Arar poses several challenges including problems associated with urbanization for urban managers and policy makers. Meeting these challenges requires access to timely and reliable information. This paper has shown that remote sensing can provide timely and relevant urban land cover data that are often difficult to obtain using traditional data-gathering methods.

The traditional supervised maximum likelihood classification method, available in most image processing software, when applied to a SPOT5 image the results become acceptable for urban land cover information.

VI. CONCLUSION

The Maximum Likelihood supervised classification and the Post-classification change detection technique are used in this study for monitoring the Land Use and the Land Cover (LULC) changes within the Arar city during the past 10 years within the periods 2002-2012. The study area was classified into four land cover classes; urban area, Agriculture, hilly area, and vacant area.

The study proved that there was a trend of change (increasing urban areas) in the urban areas within the Arar city.

Remote sensing is capable of extracting urban land cover information and changes in Arar city, Saudi Arabia. Urban land cover information represented a tremendous potential capability in urban planning at Arar city. Land use planning, community facilities planning, transport planning, and environmental planning all can benefit from this information.

REFERENCES

1) Phinn S., Stanford M., Scarth P., et al., "Monitoring the composition of urban environments based on vegetation-impervious surface-soil (VIS) model by subpixel analysis techniques", International Journal of Remote Sensing, vol. 23, no. 20, pp. 4131 – 4153, 2002.
2) Zhang Q., Wang J., Peng X., et al., "Urban built-up land change detection with road density and spectral information from multi-temporal Landsat TM data", *International Journal of Remote Sensing*, vol. 23, no. 15, pp. 3057 – 3078, 2002.
3) McDermid GJ., Franklin SE., LeDrew EF., "Remote sensing for large-area habitat mapping". *Progress in Physical Geography*, vol. 29 no. 4, pp. 449-474, 2005.
4) Gong P., Howarth PJ., "Land-use classification of spot HRV data using a cover-frequency method", *International Journal of Remote Sensing*, vol.13, no 8, pp.1459-1471, 1992.
5) Jensen JR., Qiu F., Patterson K., "A neural network image interpretation system to extract rural and urban land use and land cover information from remote sensor data", *Geocarto International*, vol. 16 no. 1, pp. 21-30, 2001.
6) Yuan F., Sawaya KE., Loeffelholz BC., et al., "Land cover classification and change analysis of the Twin Cities (Minnesota) Metropolitan Area by multitemporal Landsat remote sensing", *Remote Sensing of Environment,* vol. 98, no. 2-3, pp. 317-328, 2005.
7) Municipality of Jeddah. 2004, Jeddah Structure Plan. Jeddah Municipality, Saudi Arabia.
8) Lillesand MT., Kiefer WK., *Remote sensing and image interpretation,* John Wiley and Sons, New York, 2000.
9) El-Hattab MM., "Environmental Decision Support System for a Coastal Area, Based on Remote Sensing and Geographic Information Systems", Ph.D. thesis, *Institute of Graduate Studies and Research, Alexandria University,* 2002.
10) Chen, Y., P. Shi, et al. P. Shi, T. Fung, J. Wang and X. Li, 2007, Object-oriented classification for urban land cover mapping with ASTER imagery. International Journal of Remote Sensing, 28(20), 4645 - 4651.
11) Bourne, S.G. and Graves, M.R. (2001). *Classification of Land-Cover Types for the Fort Benning Ecoregion Using Enhanced Thematic Mapper Data*: Engineer Research and Development Center, Vicksburg MS Environmnetal Lab. ADA395102.

EXTRACTION OF FAÇADE ELEMENTS BASED ON WAVELET ANALYSIS USING POINT CLOUDS

Bisheng Yang [a,*], Fuxun Liang [a,*],Zhen Dong[a]

[a] State Key Laboratory of Information Engineering in Surveying, Mapping and Remote Sensing,
Wuhan University, Wuhan, China, 430079
(bshyang, liangfuxun)@whu.edu.cn

KEY WORDS: Façade Reconstruction, Wavelet Analysis, Distribution Histogram

ABSTRACT:

Extraction of façade elements (e.g. walls, windows, air-conditions) is a prerequisite for the reconstruction of building façade. This paper proposes a method for automatic extraction of façade elements using TLS point clouds. Generally, the method is achieved by decomposing the façade into rectangular cells and recombining them as building elements. We first perform a Haar wavelet analysis of distribution histograms (density distribution and depth distribution) to get splitting lines, and divide the facade into rectangular cells according to the splitting lines. Then the cells belonging to walls are detected by a region growing algorithm, and the left cells are sorted into extrusions or intrusions respectively according to the pre-defined rules. With neighboring cells of the same kind merged, boundary regularization can be carried out finally. Experiment results demonstrate that the proposed method performs well in extracting façade elements and is robust to occlusion and density variation, with the accuracy of element boundaries at the centimeter level.

INTRODUCTION:

The reconstruction of cities is a topic of significant intellectual and commercial interest. Point clouds have been widely used for city reconstruction (Musialski 2013). There are some effective methods for extracting building façade from point clouds (Yang 2015). While automatically transforming façade point clouds into facade elements remains a challenge due to the diversity of façade structures, non-uniform density of points, missing parts and having a rather large amount of noise and outliers in the dataset.

Several studies have put efforts on this issue. Pu and Vosselman (2009) did works on individual object extraction from laser data, in which they used the holes in dataset as a clue to detect windows. The method is not applicable in scenes where the windows are covered by curtains. Recently, Zolanvari and Laefer (2016) proposed a Slicing Method for curved façade and window extraction from point clouds, which is quite computationally-efficient but without a consideration of occlusion.

Another commonly considered strategy is cell decomposition. The cell decomposition technic is first introduced by Becker and Haala (2009) to find clues of splitting lines in point clouds, and they used a derivation tree to describe the dataset as sequences of wall and windows. Yousefzadeh (2014) described an automatic data-driven method which starts from raw laser data and ends with object extraction. They used a cellular representation of point clouds.

Inspired by them, the strategy of cell decomposition is also used in our work. The objective of this paper is to provide a solution which automatically extracts the facade elements accurately and efficiently. The proposed method is achieved by decomposing the façade into rectangular cells and recombining them as facade elements, where the Haar wavelet analysis is used to discover local changes in density and depth for cell decomposition. This wavelet analysis based method achieves improvements in these aspects: i) reduce the sensitivity to the lack of data caused by occlusions; ii) increase the accuracy in boundary regularization.

2. METHODOLOGY:

The depth information, which is the distance of points to the preference plane, has been given much attention in past research works. While the point density, which describes the amount of points in a specified space size, is mostly considered as an interference in data processing, because it could be a challenge to select thresholds suitable for scenes with varying point densities. The density variation is determined by many factors, including the distance and angle between the point and the scanner, occlusions, local structure changes and so on. In this paper, with a process of cell decomposition, we try to deduce the semantic structures on façade using information of both depth and point density. The proposed method consists of three steps: preprocessing, façade cell decomposition and element extraction. The workflow of the proposed method is shown in Fig 1.

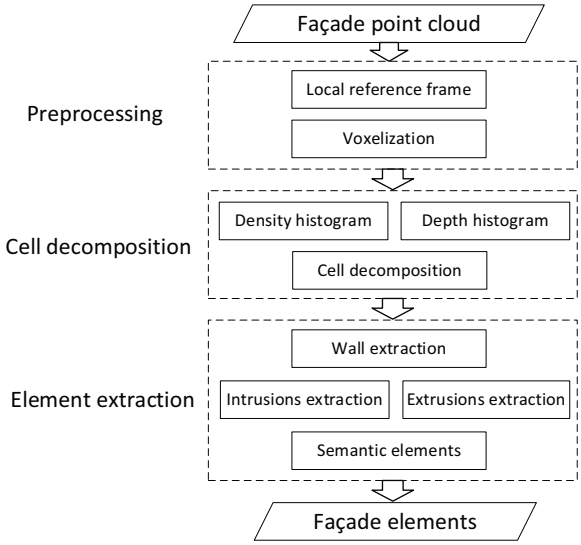

Fig.1.Workflow of the proposed method

2.1 Preprocessing

2.1.1 Local reference frame: For the sakes of computing efficiency and further processing, we first establish a local reference frame (LRF) for the façade point cloud. The axes of the LRF is determined by performing a Principal Component Analysis (PCA). Specifically, a covariance matrix C is constructed using all the points as follows:

$$\mathrm{C} = \frac{1}{N}\sum_{i=1}^{N}(P_i - \overline{P})(P_i - \overline{P})^T \qquad (1)$$

where N is the number of points, $P_i = (x_i, y_i, z_i)$ is the coordinate of the i th point in the point cloud , and $\overline{P}$ represents the coordinate of the center point. Then the eigenvalues $\{\lambda_1, \lambda_2, \lambda_3\}$ in the order of decreasing magnitude and the corresponding eigenvectors $\{e_1, e_2, e_3\}$ are computed by performing an eigenvalue decomposition on C. e_3 is the estimated normal vector of façade and defined as X axis. And with the vertical direction as Z axis, the Y axis can be decided as a right-hand coordinate system.

The classical PCA is vulnerable to noises, and to overcome this limitation, a Robust PCA proposed by Candes (2011) is finally used in this paper. The Robust PCA divides the data matrix into two parts: one low rank component which contains the real information and one sparse matrix mainly corresponding to the noise, thus to reduce the impact of noise in the point cloud.

The origin $O = \{x_0, y_0, z_0\}$ is then chosen by setting the smallest values projected on the three directions so that there will be no negative values in coordinates after transforming the point cloud to the LRF, like shown in Fig 2.

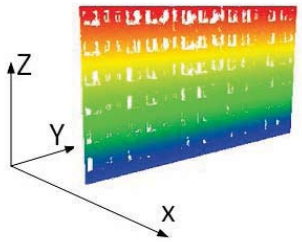

Fig.2.The Local Reference Frame

2.1.2 Voxelization: In the voxelization step, the bounding box of point cloud in LRF is separated into a series of cube voxels $\mathrm{V} = \{\mathrm{v}_{\mathrm{ijk}}, \mathrm{i} \in \mathrm{N}_x, \mathrm{j} \in \mathrm{N}_y, \mathrm{k} \in \mathrm{N}_z\}$ according to a predefined voxel size, where N_x , N_y , N_z represents the total voxel numbers along to X, Y, Z axes, and $\mathrm{v}_{\mathrm{ijk}}$ is a voxel. By selecting only one point in each voxel, the point cloud is simplified in order to accelerate the following computations. The density variation caused by distance to the scanner as mentioned before can also be decreased in this phase (Fig 3). To avoid an over simplification which may lead to a loss of useful structure information, the voxel size should be set neither too large nor too small. In the experiments, we set 0.05 m as the voxel size.

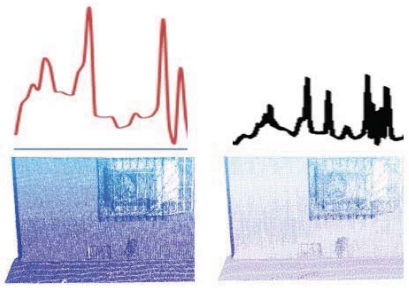

Fig.3.The point density histogram before and after simplification

2.2 Cell Decomposition

2.2.1 Generation of histograms: The voxels are then used to generate the histograms. To be specific, we obtain the Y-density distribution histogram Y_{dens} and Z- density distribution histogram Z_{dens} by counting the number of filled voxels belonging to the same row or column respectively:

$$Y_{dens} = \{y^1_{dens}, y^2_{dens}, \ldots, y^{N_y}_{dens}\} \quad ,$$

$$y^j_{dens} = \sum_{i,k} v_{ijk}, v_{ijk} \neq \phi \qquad (2)$$

$$Z_{dens} = \{Z^1_{dens}, Z^2_{dens}, \ldots, Z^{Nz}_{dens}\},$$

$$Z^k_{dens} = \sum_{i,j} v_{ijk}, v_{ijk} \neq \phi \qquad (3)$$

And the the Y- depth distribution histogram and Z- depth

distribution histogram are obtained by calculating the average depth of points belonging to the same row or column respectively:

$$Y_{depth} = \{y^{1}_{depth}, y^{2}_{depth}, \ldots, y^{N_y}_{depth}\},$$
$$y^{j}_{depth} = \sum_{j} d_j \Big/ y^{j}_{dens} \quad (4)$$
$$Z_{depth} = \{z^{1}_{depth}, z^{2}_{depth}, \ldots, z^{N_y}_{depth}\},$$
$$z^{k}_{depth} = \sum_{k} d_k \Big/ z^{k}_{dens} \quad (5)$$

where the d_j and d_k actually equals to the x coordinate of the voxel.

While the X- density distribution histogram is computed in the same way as the Y- density distribution histogram, and the location that has the largest density is considered as the 'temporary wall plane'.

2.2.2 Haar wavelet analysis: In this section, the splitting lines is acquired according to the result of wavelet analysis of distribution histograms, where Haar Wavelet is chosen as the wavelet basis. The Haar wavelet basis function describes a discrete change in different scales, thus it is suitable to detect the significant local changes in discrete signal. The Discrete wavelet transform (DWT) decomposes the original signal into the detail items and the approximate items. After a DWT analysis, the possible changes in original signals caused by the structure change are magnified in the detail of the 1st scale, like shown in Fig 4. These locations can then be used to acquire splitting lines.

Firstly, the peaks in 1st detail is detected, and those that are too close are merged, with only the larger peak left. Then the peaks extracted from density histograms and depth histograms need to be merged together according to the same rule. Finally we can have the splitting lines on both Y axis and Z axis.

2.2.3 Cell feature: According to the locations of splitting lines, the façade can then be re-separated again into small cells, which are made up of some neighboring voxels between the adjacent splitting lines. Successively, the cell features including the cell normal vector, the curvature and the cell depth are calculated. The cell normal vector and curvature are estimated by the PCA using all points belonging to the cell, and the cell depth is a mean value of all depth of points in this cell.

2.3 Element Extraction

2.3.1 Wall extraction

With all the cell features calculated, a region growing algorithm is used to extract the cells that belong to the wall. The region growing algorithm first find a seed, and then search neighbors of the seed and pick the satisfied ones out as wall cell and add it to the seed list. When the neighbors of the current seed are all checked, this seed is pushed out and the top one on the seed list is then selected as the current one, as a loop. If all the neighbors have been traversed or all the seeds are pushed out, the loop of region growing is finished.

The seed cell here is first set with the constraint conditions:

1) The curvature is smaller than 0.01, which indicates that the cell tend to be a plane in general;
2) The angle between the cell normal and the X axis is smaller than 5°;
3) The depth to the temporary wall plane is smaller than 0.1 m.

The growing constraint conditions are as follows:

1) The angle between the current cell and the seed cell is smaller than 5°;
2) The depth difference between the current cell and the seed cell is smaller than 0.05 m.

2.3.2 Element extraction: After wall extraction, the left cells are mainly those of façade elements. According to the cell features, the cells are sorted into extrusions (balconies, porches and air-conditions) and intrusions (windows). Respectively, the extrusions are structures with complete planes, while the windows are always incomplete with holes and noise. By merging the neighboring cells that belong to the extrusions and intrusions respectively, an element is roughly extracted.

Due to the complex conditions in point cloud, the rough extraction result may contain mistakes and need to be further refined, with an assumption that boundaries of elements are supposed to be straight lines.

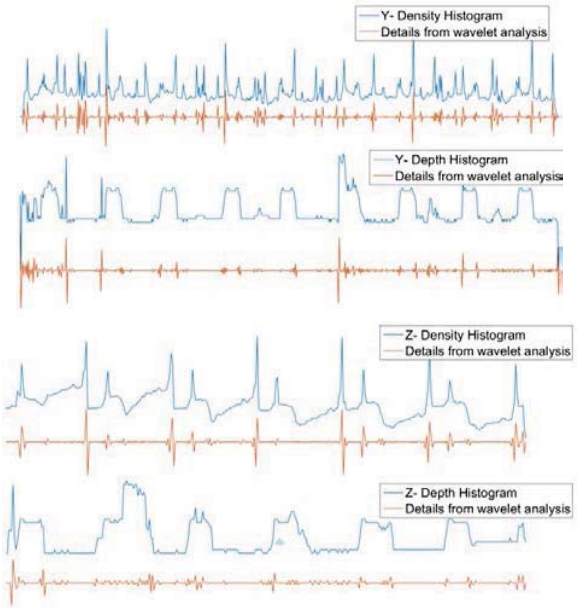

Fig.4.Ddensity histograms and the corresponding results of wavelet analysis

3. EXPERIMENTS

The test data is collected at Wuhan University by a RIEGL VZ-400 laser scanner system, and used to validate the proposed method. The data is scanned from a dormitory, with windows and air-conditions distributed on the façade. As a fusion result of three stations, the second data contains some holes, and has a large density variation. The façade elements include windows and air-conditions.

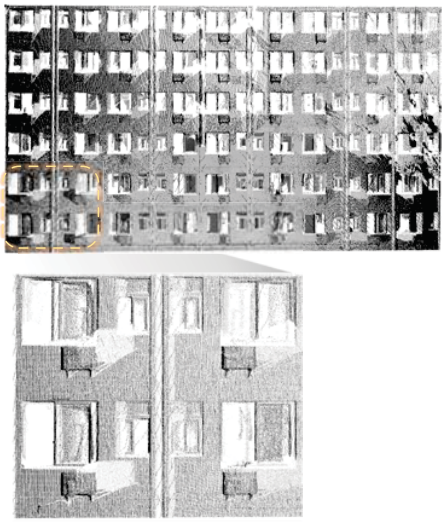

(a) Test data colored by intensity

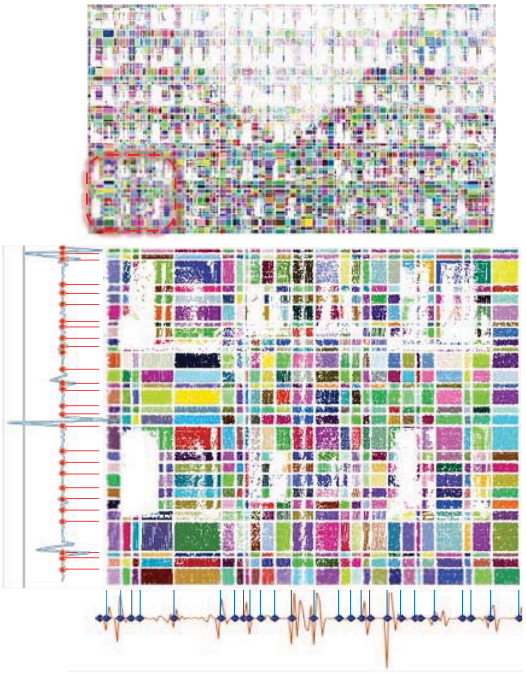

(b) Results of cell decomposition with splitting lines

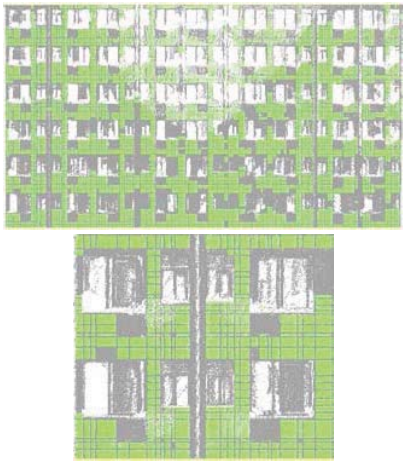

(c) the wall cells extraction result

(d) Extraction results. Red rectangles represent extracted windows, and blue rectangles represent extracted air-conditions.

Fig.5.Data and the experiment results

The experiment result shown in Fig.5 is satisfactory. Fig 5(a) illustrates the raw data, and (b) results of cell decomposition, (c) the wall cells extraction result and (d) the final result. Façade elements including windows and air-conditions are extracted accurately and completely. And the accuracy of boundaries is ensured at a centimeter level, which is sufficient for modeling. Though there are some mistakes in initial extraction result, the obvious repeatability in structure is used for the final correct results.

4. CONCLU SION

This paper proposed a wavelet analysis based method to automatically extract façade elements from the point cloud. Generally, the method is achieved by decomposing the façade into rectangular cells and recombining them as building elements. We first perform a Haar wavelet analysis of

distribution histograms (density distribution and depth distribution) to get splitting lines, and divide the facade into rectangular cells according to the splitting lines. Then the cells belonging to walls are detected by a region growing algorithm, and the left cells are sorted into extrusions or intrusions respectively according to the pre-defined rules. With neighboring cells of the same kind merged, boundary regularization can be carried out finally. The method was evaluated using two façades. Experiments demonstrate that the proposed method performs well in different kinds of facades and it also shows a robustness to occlusion and density variation. Future work will try to explore the method in other applications like holes recovery and data compression.

Reference:

Becker, Susanne and Haala, Norbert. Grammar Supported Facade Reconstruction from Mobile LIDAR Mapping [C]. In Proc. CMRT XXXVIII, Part 3/W4; Paris, France: Int. Arch. Photogramm., Remote Sens. Spatial Inf. Sci. 2009, 229–34.

Candès E J, Li X, Ma Y, et al. Robust principal component analysis?[J]. Journal of the ACM (JACM), 2011, 58(3): 11.

Friedman S, Stamos I. Online detection of repeated structures in point clouds of urban scenes for compression and registration[J]. International journal of computer vision, 2013, 102(1-3): 112-128.

Musialski P, Wonka P, Aliaga D G, et al. A survey of urban reconstruction [C]. Computer graphics forum. 2013, 32(6): 146-177.

Pu, Shi and Vosselman, George. Knowledge based reconstruction of building models from terrestrial laser scanning data [J]. ISPRS Journal of Photogrammetry and Remote Sensing. 2009, 64 (6), 575-84.

Schmittwilken J, Plümer L. Model-based reconstruction and classification of facade parts in 3D point clouds[J]. International Archives of the Photogrammetry, Remote Sensing and Spatial Information Sciences, 2010, 38(1): 269-274.

Wang R, Ferrie F P, Macfarlane J. A method for detecting windows from mobile LiDAR data[J]. Photogrammetric Engineering & Remote Sensing, 2012, 78(11): 1129-1140.

Yang B, Dong Z, Zhao G, et al. Hierarchical extraction of urban objects from mobile laser scanning data [J]. ISPRS Journal of Photogrammetry and Remote Sensing, 2015, 99: 45-57.

Yousefzadeh M, Leurink F H M. A general data-driven algorithm for façade structure modeling using ground based laser data [J]. The International Archives of Photogrammetry, Remote Sensing and Spatial Information Sciences, 2014, 40(3): 381.

Zolanvari, SM Iman and Debra F. Laefer. Slicing Method for curved façade and window extraction from point clouds [J]. ISPRS Journal of Photogrammetry and Remote Sensing, 2016, 119: 334-346.

DYNAMIC VARIATION EFFECTS ON THE STOCHASTIC PERFORMANCE OF SMARTPHONE SENSORS USING ALLAN VARIANCE AND GENERALIZED METHOD OF WAVELET MOMENTS

A. Radi [a, *], Y. Li [a], N. El-Sheimy [a], A. Sesay [b]

[a] Dept. of Geomatic Engineering, University of Calgary, Calgary, Canada – ahmed.elboraee@ucalgary.ca, liyou331@gmail.com, elsheimy@ucalgary.ca
[b] Dept. of Electrical Engineering, University of Calgary, Calgary, Canada – sesay@ucalgary.ca

KEY WORDS: Stochastic Modeling, Errors, Inertial Sensors Calibration, IMU, Allan Variance, Generalized Method of Wavelet Moments

ABSTRACT:

This paper aims at studying the behaviour of inertial sensors errors related to Micro-Electromechanical Systems (MEMS) based Inertial Measurement Units (IMUs) mounted on two different smartphones when measured in static and dynamic conditions. The error processes were estimated using two different methods, Allan Variance (AV) and the Generalized Method of Wavelets Moments (GMWM). The developed model parameters related to laboratory dynamic environment are compared to those obtained under static conditions. A contamination test was applied to all data sets to distinguish between clean and corrupted ones using Confidence Interval (CI) investigation. Finally, an attempted is presented to find the link between the error model parameters and the augmented dynamic of the platform under test

1. INTRODUCTION

1.1 General Introduction

Global Navigation Satellite System (GNSS) is known to be an accurate positioning system for different applications to reach accurate localization in outdoor environments. A major demerit of GNSS in general, is the performance degradation when Radio Frequency (RF) signals are not available, i.e. loss of line of sight with the satellites being tracked, over short time period (Jensen, 2010). On the other hand, Inertial Navigation Systems (INS), classified as a dead reckoning navigation systems, provide high frequency precise short term positioning information. Nevertheless, a major drawback is referred to inertial sensors' errors that growth with time and lead to accuracy degradation of position with respect to time (El-Sheimy, 2014).

The integration of both systems, known as INS/GNSS, provides an accurate, reliable and complementary system with better performance in comparison to stand-alone one. In order to improve the integrated navigation performance especially during GNSS outage, accurate calibration of the IMU sensors should be performed (Park, 2005). Such errors are known to have two parts, deterministic and stochastic. The deterministic part, for instance sensor bias and scale factor, could be eliminated by laboratory calibration where sensor errors could be determined by comparing the sensor outputs with a known reference inputs (Li et al., 2015). Such part is beyond the scope of this paper. On the other hand, stochastic errors require correct modelling and estimation which is considered to be a nontrivial task especially for low-cost MEMS inertial sensors. MEMS based inertial sensors are being used lately instead of traditional bulky ones due to its small size light weight and low power consumption (Woodman, 2007). Generally, the components of inertial sensors' stochastic error model may contain one ore more random latent process (e.g White Noise (WN), correlated noise and Random Walk (RW)). Few researches investigated the behaviour of stochastic characteristics during different environmental conditions such as temperature variation (Aggarwal et al., 2006, El-Diasty et al., 2007) and (Radi, 2017) and dynamics of the platform on which sensors are mounted (Wis and Colomina, 2010, Stebler et al., 2014a, Stebler et al., 2015).

1.2 Objective

The dynamic dependent error analysis for low-cost MEMS IMUs mounted on smartphones is the main area of interest in this paper. To be specific, the objective of this paper can be summarized as follow:

First, reveal the stochastic characteristics of MEMS sensors and their changes according to the dynamic conditions using reference signals provided in laboratory environment using a single axis turn table. The state-of-art navigation filters contain residual deterministic sensor errors (e.g., gyro and accelerometer biases and scale factors) in the state vector, and estimate them in real time. However, stochastic errors are commonly modelled by using relatively simple stochastic processes such as 1st order Gauss-Markov processes, random walks, and random constants. The stochastic parameters, which compose the navigation system noise Q, are commonly set according to the RW in the datasheet, or set based on the stochastic modelling result under static conditions. Through this research, we will analyse whether we need to use more complex stochastic models, and choose different parameter setting according to platform dynamics changes.

Second, expose the link between the inertial sensor errors and platform dynamics using a suitable observation technique to see how the dynamics has an influence on the errors of the IMU under test.

Finally, investigate on the pros and cons of the most widely used AV method in identifying low-cost MEMS sensor error sources

* Corresponding author

and computing the error parameters quantification under various laboratory dynamic conditions. With the development of modern estimation theory and methods, maybe we can use more advanced method to provide more accurate identification or computation results.

2. METHODOLOGY

2.1 Inertial Sensors' Stochastic Processes

The main random processes related to inertial sensors are briefly defined in this section as follow:

Quantized Noise (QN): The small difference between the real amplitude of the point under sampling and the bit resolution of the Analog-to-Digital Converter (ADC) is called a quantization error (Savage, 2002).

White Noise (WN): The random amount added to the actual signal and with a long term average equal to zero is defined as white noise (Engineers, 1999). This noise term is often known as Angular/Velocity Random Walk (A/VRW) for gyros and accelerometers, respectively.

Bias Instability (BI): Also know as flicker noise and generally this type of noise is related to the instability of the bias offset for a sensor output measured in ideal environment (Engineers, 1999).

Random Walk (RW): A random process that can be considered as one of the exponentially correlated noise cases with a very long correlation time (Abdel-Hamid, 2006). This noise term is often known as Rate/Acceleration Random Walk (R/AccRW) for gyros and accelerometers, respectively.

Drift Ramp (DR): A very low frequency noise process that is often called Drift Rate/Acceleration Ramp (DR/AccR) for gyros and accelerometers, respectively.

Gauss Markov (GM): If a stationary Gaussian process has an exponentially correlation time, it is called a Gauss-Markov process as defined in (Nassar, 2005). Sometimes it is used as an approximation for BI noise term (Guerrier et al., 2016).

2.2 Allan Variance

AV is a method of representing Root-Mean Square (RMS) random drift error as a function of averaging times (Allan, 1966). Originally, it was developed to study the frequency stability in clocks, oscillators and amplifiers in mid-1960 by David Allan. Later on, it was used to identify different latent random processes hidden in different measurements (Zhang et al., 2008). It is simple to compute, much better than having a single RMS drift number to apply to a system error analysis, and also simple to understand (El-Sheimy et al., 2008).

The procedure in this paper is as follows: The characteristic curve is first obtained by applying the AV algorithm to the entire data. The curve is then measured to determine the types and magnitudes of certain random errors possibly residing in the data according to its slope. Finally, the random errors are identified and modelled.

In this paper this operation is being carried out within laboratory environment for static data, then repeated for various dynamic conditions through a single axis turn table. Detailed AV mathematical calculation steps could be highlighted in (Hou, 2005) and (Niu et al., 2014).

2.3 Generalized Method of Wavelet Moments

GMWM is an estimation method based on the idea of Generalized Method of Moments (GMM) estimators (Vaccaro and Zaki, 2012). The GMWM makes use of the relation between the Wavelet Variance (WV) and the parameters of a latent process, estimating the latter by minimizing the distance between the empirical and model-based WV (Guerrier et al., 2013). It is also important to mention that this method could also be based on the AV since the Haar WV is simply twice the AV with additional benefits (Guerrier and Molinari, 2016). The standard WV is being calculated to obtain the characteristic curve. Robust WV is also computed, compared to the standard calculated WV to check the existence of any outliers in the data (Guerrier and Molinari, 2016). The next step is the estimation of the model parameters, more than one model could be estimated and ranked using Wavelet Information Criteria (WIC) to determine which model is the best (Guerrier et al., 2015). A full theoretical flowchart for the GMWM calculation steps could be illustrated in Figure.1. More mathematical details about the GMWM could be found in (Guerrier et al., 2013) and (Stebler et al., 2014b).

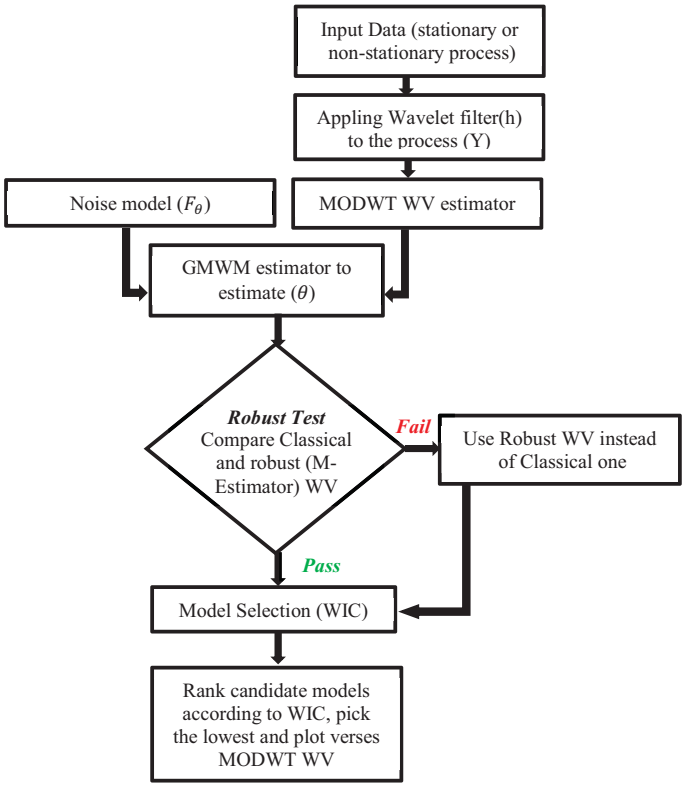

Figure 1. GMWM Estimator Flowchart (Radi, 2017)

3. EXPERIMENTS AND RESULTS

3.1 Static Data

The data were collected at the PLAN Group Inertial Lab at the University of Calgary using the SmartMotor Series 4 Single Axis Positioning and Rate Table (Figure 2) which has a rate accuracy of 0.02% (Over 1 revolution).

The data was collected in two different modes, the first one is the static mode and the second is the dynamic one. Static data sets were collected first at room temperature using MEMS-based

IMUs mounted on two different smartphones, namely Samsung S4 and iPhone 5S.

Regarding the IMU models inside the smartphones, iPhone 5S equipped with a 3D accelerometer (Bosch Sensortec BMA220, Gerlingen, Germany) and an integrated 3D gyroscope (ST-Microelectronics, L3G4200DH, Geneva, Switzerland). On the other hand, Samsung S4 has an InvenSense MPU-6500 inertial module which is a 6-axis motion tracking device that combines a 3-axis gyroscope, 3-axis accelerometer, and a Digital Motion Processor (DMP) all in a small 3x3x0.9 mm package.

The IMUs static data were sampled at 20 and 100 Hz for the Samsung S4 and iPhone 5S respectively for almost (15 mins) at room temperature and were saved and extracted from the phones for post-processing. The choice for such data length will be illustrated later.

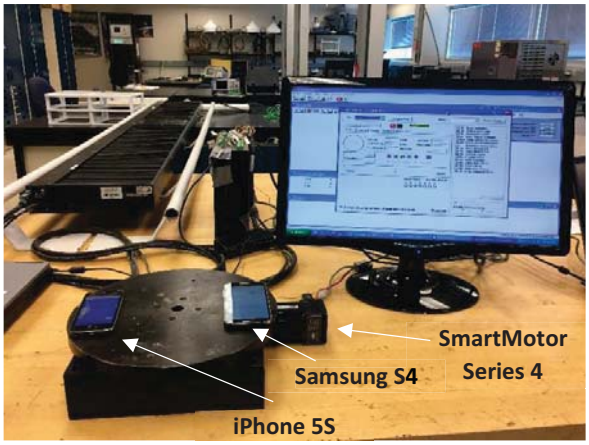

Figure 2. SmartMotor Series 4 Single Axis Positioning and Rate Table

The performance of each of the MEMS inertial sensors is predicted and estimated using AV and GMWM to study the noise characteristics and to identify the sensors' stochastic model parameters.

This operation is repeated for the two aforementioned smartphone in the two different modes. Figures 3 and 4 show the AV plot for Samsung S4 and iPhone 5S Z-Gyro measurements while Table 1 lists the identified error coefficients after AV analysis for Z-Gyros.

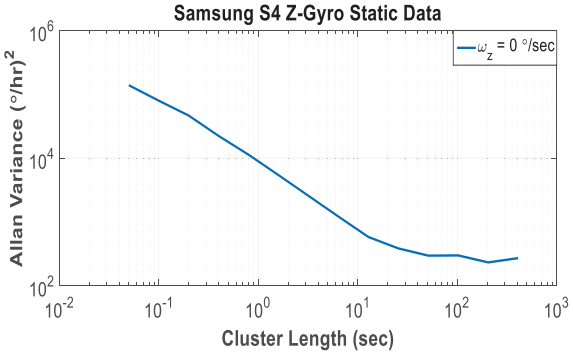

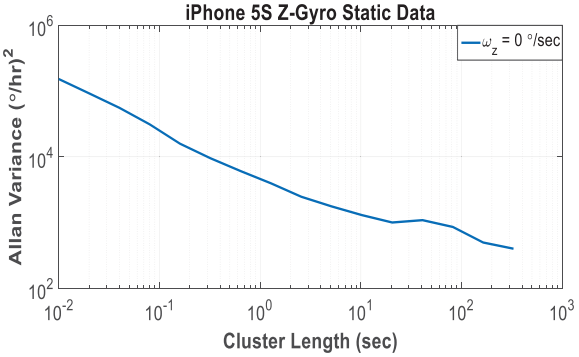

Figure 3, 4. Allan Variance for Samsung S4 and iPhone 5S Z-Gyros Measurements (Static Mode)

Exp. No.	Noise Coefficient	ARW N $\boldsymbol{deg/\sqrt{h}}$
Samsung S4 Z-Gyro		
0	$\omega_z = 0°/s$	1.5511
iPhone 5S Z-Gyro		
0	$\omega_z = 0°/s$	1.0978

Table 1. Identified Error Coefficients after AV Analysis for Samsung S4 and iPhone 5S Z-Gyros (Static Mode)

From Table 1, it is clear that the ARW is the dominant noise parameter that could be observed for both Samsung S4 and iPhone 5s gyros as it is considered to be high frequency noise term. Other low frequency noise terms such as correlated noise require long-term data in order to be observable.

3.2 Dynamic Data

After performing the AV analysis on the static data, additional analysis is needed to see how the inertial sensors' noise parameters change with dynamics. Different quantities could be used to define the meaning of "dynamics". Such quantities could be summarized as linear velocity (v), linear acceleration $(\dot{v})$, linear jerk $(\ddot{v})$, angular velocity (ω), angular acceleration $(\dot{\omega})$ and angular jerk $(\ddot{\omega})$ (Kane and Levinson, 1985). In this paper, we are interested in investigating the effect of angular velocity (ω) and angular acceleration $(\dot{\omega})$ on stochastic model parameters of MEMS inertial sensors mounted on the aforementioned smart-phones. Using the SmartMotor Series 4 Single Axis Positioning and Rate Table commands, it is possible to let the turntable rotate with, for example, constant angular velocity (defined as reference signal) and collect data measurements from the smart-phones' IMUs fixed on the turntable (defined as measured signal). The sensor error signal (defined as residual signal) is simply the difference between the measured signal and the reference one. The next step will be to study the relation between residual signal and the applied platform dynamics.

3.2.1 Constant angular velocity and angular acceleration:

In order to study the effect of the applied angular velocity and angular acceleration, different angular velocities' and accelerations' commands were sent to the SmartMotor turntable via SmartMotor Terminal Window.

First, such commands allow the turn table to rotate with five constant (fixed) angular velocities, that represent the mentioned reference signal, for 15 minutes. The angular velocity values are (9, 18, 36, 72 and 120 deg/sec). Thus, the performed test covers

the ordinary operational angular velocity of smartphones. Second, starting from initial angular velocity equals to zero ($\omega_{z_0} = 0$) and making use of the SmartMotor turntable, different angular acceleration values were applied, specifically 1 and 2 deg/sec^2.

It is important to mention that both static and dynamic data (used for angular velocity investigation) have equal data length and collected at the same lab. Thus, the only factor to be changed is the applied dynamic quantity. Consequently, fair judgment could be obtained. At each angular velocity/acceleration value, the data was collected twice for both smartphones. The main reason for that is to make sure that the performance of each sensor is almost the same when repeating the same test. In other words, to ensure the repeatability factor for inertial sensors under test.

For angular acceleration experiments, data length will be shorter than angular velocity measurement. The main reason for that is that the SmartMotor turntable used for reference signal has a maximum angular velocity "threshold" that could not be run over. Such a limit allows the collection of data with length 225 and 155 sec for $\dot{\omega}$ equals to 1 and 2 deg/sec^2, respectively.

The performance of each of the MEMS inertial sensors is estimated at different angular velocity/acceleration value using AV and GMWM to study the noise characteristics and to identify the sensors' stochastic model parameters. This operation is repeated for the two aforementioned smartphones. Figure. 5, 6 shows the signal measured by the Z-gyro for Samsung S4 and iPhone 5S, respectively, after applying different angular velocity (ω_z) using the turntable.

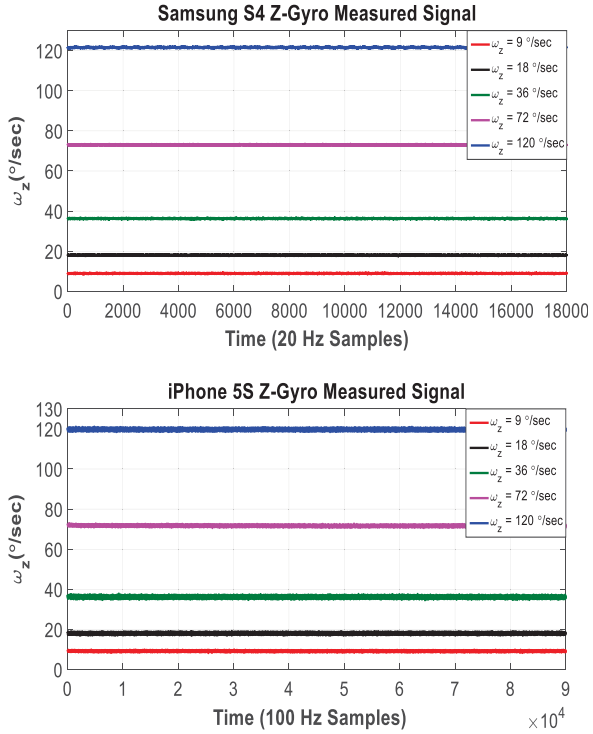

Figure 5, 6: Measured Signal for Samsung S4 Z-Gyro and iPhone 5S Z-Gyro (Applied Angular Velocity for 15 minutes)

It is clear that each data set was collected under fixed value of angular velocity/acceleration, the reason for that is referred to the tools used for the data analysis, AV and GMWM. To be more specific, these tools require situational environment for the stochastic behaviour (Wis and Colomina, 2010) which could be obtained under fixed values of dynamic quantity for each experiment, for instance fixed angular velocity/acceleration. Also, Figure 7 highlights the signal measured by the Z-gyro for Samsung S4 after applying angular acceleration ($\dot{\omega}_z$) using the turntable. Figure 7 illustrates both sensor measured signal and reference signal designated in blue and red colors, respectively. It is clear how the gyro output (measured angular velocity) forms a triangular or trapezoidal motion profile due to the applied ascending angular acceleration.

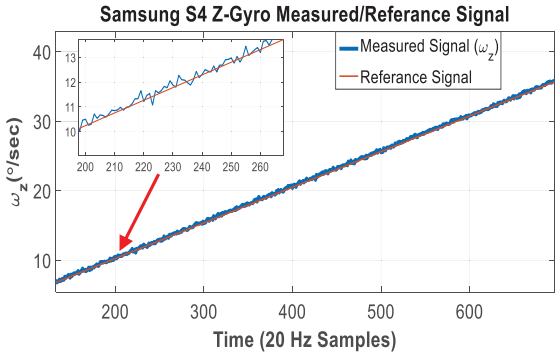

Figure 7: Measured Signal for Samsung S4 Z-Gyro (Applied Angular Acceleration for 225 Second)

To get the residual signal in each experiment, the reference signal value is being subtracted from the measured Z-gyro signal illustrated in Figure 5, 6 and 7. Figure 8 gives an example to the residual signal for the Samsung S4 Z-Gyro measurements after applying 9 deg/sec constant angular velocity.

3.2.2 Allan Variance Analysis: Figures 9 and 10 show the AV for Samsung S4 and iPhone 5S Z-Gyro measurements while Table 2 lists the identified error coefficients after AV analysis for Z-Gyros.

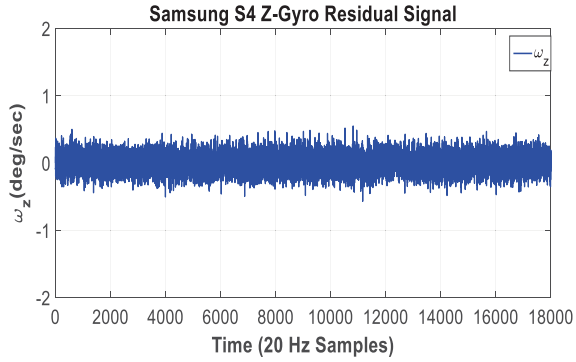

Figure 8: Residual signal for Samsung S4 Z-Gyro Measurements (Dynamic Mode with applied 9 deg/sec)

Table 2 shows the direct effect of changing dynamics on the estimated stochastic model parameters' values of gyros mounted on both smart phones under test. Such an effect leads to the importance of having a dynamic dependence stochastic model for the aforementioned sensors.

Regarding the 15 minutes data sets, the practical reason for choosing it is that many applications care about only the short-term performance (as in long-term the INS errors can be corrected through the use of other techniques). For such data sets, which are considered to be "short" data, it is clear that the ARW is the dominant noise parameter that could be observed which is similar to the AV analysis performed for static data sets.

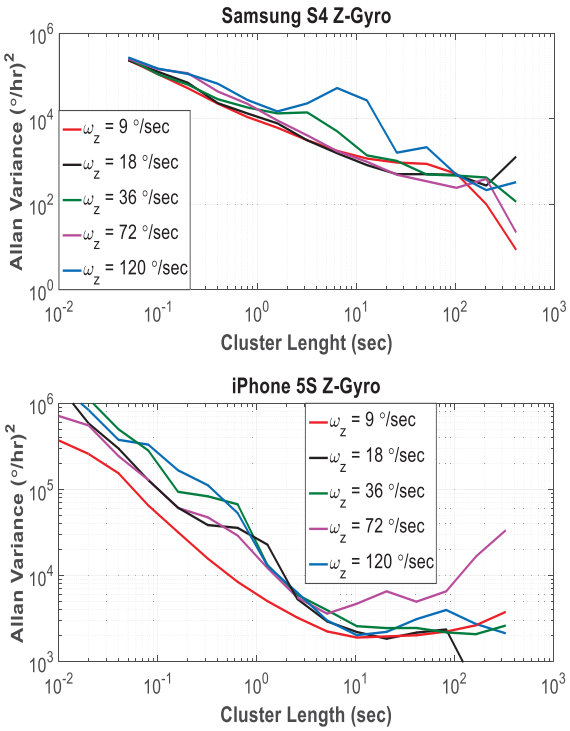

Figure 9, 10: Allan Variance for Samsung S4 Z-Gyro and iPhone 5S Z-Gyro Measurements

Exp. No.	Noise Coefficient	ARW N $deg/\sqrt{h}$	BI B deg/h	RRW K $deg/h^{3/2}$
Samsung S4 Z-Gyro				
1	$\omega_z = 9°/s$	1.6087	…	…
2	$\omega_z = 18°/s$	1.7695	33.2482	…
3	$\omega_z = 36°/s$	1.8353	…	…
4	$\omega_z = 72°/s$	2.0574	23.8295	…
5	$\omega_z = 120°/s$	2.5242	…	…
6	$\dot{\omega}_z = 1°/s^2$	2.5656	…	…
7	$\dot{\omega}_z = 2°/s^2$	2.4189	…	…
iPhone 5S Z-Gyro				
1	$\omega_z = 9°/s$	1.1788	66.3658	…
2	$\omega_z = 18°/s$	1.702	…	…
3	$\omega_z = 36°/s$	2.4233	…	…
4	$\omega_z = 72°/s$	1.6711	90.1593	17.2218
5	$\omega_z = 120°/s$	2.5048	68.5729	…
6	$\dot{\omega}_z = 1°/s^2$	3.4811	…	…
7	$\dot{\omega}_z = 2°/s^2$	3.0855	…	…

Increased, Decreased

Table 2. Identified Error Coefficients after AV Analysis for Samsung S4 and iPhone 5S Z-Gyro Measurements

Other noise parameters such as correlated noise and drift ramp need large amount of data in order to be observable (Stebler et al., 2015). Consequently, Table 2 clarifies how the ARW is the dominant noise term for short cluster length. However, increasing the angular velocity value always affect ARW value for both Samsung S4 and iPhone 5S gyros. Specifically, the change of Samsung S4 ARW parameter reached over 62 % with angular velocity changes from static condition to 120 deg/sec. Moreover, the change of the iPhone 5S gyro ARW parameter is clearly more obvious as it reached to 128 % for the same range of angular velocity change. This analysis illustrates how the ARW parameter related to the iPhone 5S gyro is more sensitive to the measured angular velocity value than the Samsung S4 one. Other stochastic noise parameters, such as BI, could hardly be detected as illustrated in Table 2.

Regarding the angular acceleration, only ARW noise term could be detected for both Samsung S4 and iPhone 5S gyros. The reason for that is having a short data length due to the previously mentioned limitation of the turntable usage. Results from Experiments 6 and 7 shows that applying angular acceleration always increases the ARW value of the gyro under test for both smartphones when compared to static data (Experiment 0). For more numerical details, ARW value growth to 65% and 56% for the Samsung S4 Z-Gyro and to 217% and 181% for the iPhone 5S one. It is clear that the angular acceleration effect on the white noise value is larger than the angular velocity effect on the same stochastic parameter even for a shorter time. Though, increasing the angular acceleration value showed a reversal effect on the Samsung S4/iPhone 5S gyros compared to increasing the angular velocity.

Table 2 shows how the change of ARW parameter for the Samsung S4 Z-Gyro reduced by almost 6 % with angular acceleration changes from 1 to 2 deg/sec^2. Taking into consideration that we only used two sets of data for such analysis, this could be considered a low percentage compared to the angular velocity effect. In addition to that, similar behaviour was detected for the iPhone 5S Z-Gyro where the change of its ARW parameter is slightly more obvious as it decreased to 13 % of its value for the same range of angular acceleration increasing. However, using short data with only two angular acceleration values might be the reason of having a contradiction between angular velocity and angular acceleration effects, with respect to ARW behaviour. Consequently, longer data is highly recommended with more angular acceleration values in order to fairly judge the angular acceleration effect on ARW noise parameter. Also longer data could allow low frequency noise parameters, for instance correlated noise and DRR, to appear.

3.2.3 GMWM Analysis: Now we will use different technique, GMWM, which was proposed lately to estimate the so-called latent or composite process. When using AV method, in order to attain an accurate noise model for any measured signal, it should be guaranteed that the data under test is "clean". In other word, free of contaminations, outliers or any extreme observations that might be hidden inside the data. Broadly, this is not an easy task to perform. However, GMWM offers a way to go through that by simply replacing the estimated WV with the robust M-estimator proposed by (Guerrier and Molinari, 2016) which has well defined asymptotic properties as well as better finite sample performance compared to existing estimators. When comparing both the robust and the classical WV to do such a "contamination test", if there is significant difference over the initial scales such as one WV lying outside of the other's Confidence Interval (CI), then it is generally better to use the robust version as this means that the contamination test fails. Otherwise, the classical WV would be appropriate for such data with an indication of having an outliers' free data set (Balamuta et al., 2016b).

As a next step, Figure 11 shows how the contamination test was applied on Samsung S4 Z-gyro residual signal obtained from rotating the SmartMotor turn table with angular velocity value equals to 9 deg/sec. It is obvious that both classical and robust WVs are lying inside each other's confidence of interval. Consequently, such data is clean which means that we can use the classical WV for model parameters estimation.

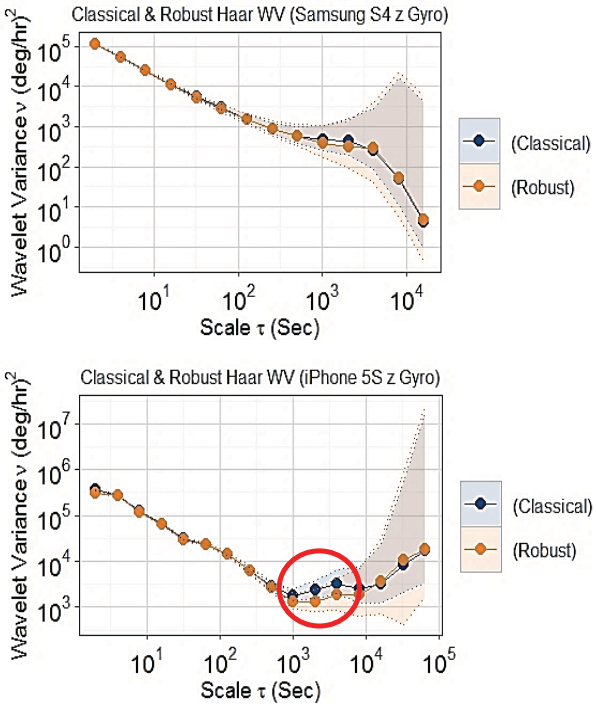

Figure 11, 12: Comparison between Classical and Robust WV for Samsung S4 Z-Gyro and iPhone 5S Z-Gyro (Dynamic Mode with applied 9 and 72 deg/sec)

On the other hand, Figure 12 shows how the contamination test fails with Experiment 4 (where 72 deg/sec angular velocity applied) for iPhone 5S Z-Gyro data set. This could be designated by the red circle area where the robust WV lies outside the CI of the classical one. Considering the fact that iPhone data set for Experiment 4 contains outliers, and referring to Table 2, it is noticeable that the ARW value of this specific data set does not follow the general attitude as other data sets. Moreover, the appearance of RRW noise parameter only in this data set is another clue that match the idea of how such data is contaminated. As a conclusion, we will not depend on the AV analysis for data collected using iPhone regarding Experiment 4. After the contamination test, it is important to identify the most accurate noise model for each data set individually. Based on the length of data sets, a set of nine candidate models were constructed for the Samsung S4 and iPhone 5S Z-gyros at each data set just to demonstrate the concept of modelling selection. Candidate models are illustrated in Table 3 with their related model parameters.

Model Number	Model Parameters
Model # 1	WN
Model # 2	WN+GM
Model # 3	WN+GM+RW
Model # 4	WN+GM+DR
Model # 5	WN+GM+RW+DR
Model # 6	WN+2*GM
Model # 7	WN+2*GM+RW
Model # 8	WN+2*GM+DR
Model # 9	WN+2*GM+RW+DR

Table 3. Candidate Models for Samsung S4 and iPhone 5S Z-Gyro Measurements

The main outcome of model selection process is to find the model that describes the latent stochastic processes of the inertial sensor data set under test (Guerrier et al., 2015). Generally, more than one model, among a list of candidate models, could describe such behaviour. To ensure maximum accuracy, GWMW provides the ability to select the best model based on WIC which illustrate generally how well the estimated model can predict the values of the WV issued from another realization of the same process (Balamuta et al., 2016a).

The mentioned criteria is based on two terms, the first term is called the "Objective Function" which is related to the goodness-of-fitness of each candidate model (Balamuta et al., 2016b). This term usually decreases as the number of model parameters is increased to reach a better fitting with the observed signal WV. The second term is called the "Optimism" which represents the complexity of the model. Consequently, its value increases with increasing the number of model parameters as a penalty for overfitting (Balamuta et al., 2016b).

The sum of both aforementioned terms gives the so called Wavelet Information Criteria which could be considered as a way to judge how adequate the selected stochastic model is suitable for the data under test (Balamuta et al., 2016a). Calculating the WIC for each model listed in Table 2, the model ranking operation was performed and the best model would be the one with smallest WIC value.

Based on the proposed criteria, the estimated parameters of the error models are calculated for the Samsung S4 Z-Gyro and iPhone 5S Z-Gyro under different angular velocity/acceleration values. Figure 13 shows the comparison between empirical and implied "estimated" WVs for the two aforementioned gyros at some selected values of ω_z. Equivalent results are highlighted in Table 4 which shows the influence of dynamics changing on the model parameters for both Samsung S4 and iPhone 5S Z-Gyros.

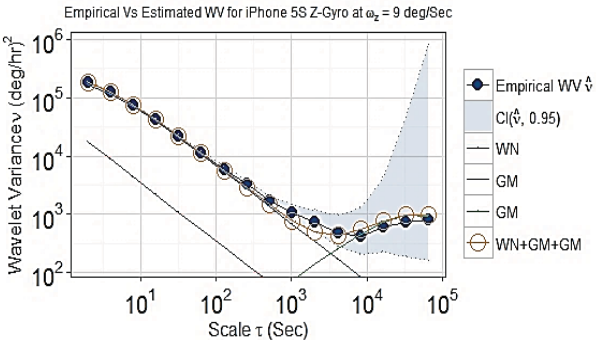

Figure 13: Empirical Compared to Estimated WV for iPhone 5S Z-Gyro (Dynamic Mode with applied 9 deg/sec)

Regarding both sensors under test, Table 4 highlights how the gyro noise model structure did not change due to changing a certain applied dynamics value. To be more specific, a model composed of only white noise was detected to be the best fit model for all values of angular velocities/acceleration related to Samsung S4 Z-Gyro. Also, for angular velocity effect, a white noise random process added to two 1st order Gauss Markov processes was selected for all error measurement regarding iPhone 5S Z-Gyro.

Exp. No.	Noise Coefficient	WN(ARW) N $deg/\sqrt{h}$	GM1 β_1, σ^2_{GM1} $1/s, deg/\sqrt{h}$	GM2 β_2, σ^2_{GM2} $1/s, deg/\sqrt{h}$
Samsung S4 Z-Gyro				
0	$\omega_z = 0°/s$	6.4222	…	…
1	$\omega_z = 9°/s$	7.7647	…	…
2	$\omega_z = 18°/s$	8.054	…	…
3	$\omega_z = 36°/s$	8.2101	…	…
4	$\omega_z = 72°/s$	8.7495	…	…
5	$\omega_z = 120°/s$	9.0579	…	…
6	$\dot{\omega}_z = 1°/s^2$	10.0156	…	…
7	$\dot{\omega}_z = 2°/s^2$	9.7023	…	…
iPhone 5S Z-Gyro				
0	$\omega_z = 0°/s$	1.0692	1.7101, 7.049	9.7259e-3, 1.0601
1	$\omega_z = 9°/s$	2.1993	1.812, 10.9602	1.5432e-2, 0.9763
2	$\omega_z = 18°/s$	6.8632	6.9739, 17.709	7.2487e-2, 1.7943
3	$\omega_z = 36°/s$	2.967	1.8926, 18.4464	1.4675e-2, 1.149188
4 †	$\omega_z = 72°/s$	…	…	…
5	$\omega_z = 120°/s$	11.6178	0.16507, 0.3293	1.6252e-2, 1.26445
6	$\dot{\omega}_z = 1°/s^2$	5.4455	1.4157, 24.854	…
7	$\dot{\omega}_z = 2°/s^2$	2.8367	1.4488, 23.8911	…

Increased, Decreased, † Contaminated dataset

Table 4: Identified Error Coefficients after GMWM Analysis for Samsung S4 Z-Gyro and iPhone 5S Z-Gyro and Measurements

The direct effect of changing the applied dynamics was reflected in the magnitude of the aforementioned noise parameters. Such magnitudes could be analyzed as follow:

Compared to static data results, raising the angular velocity value mostly affect ARW value to be increased for both Samsung S4 and iPhone 5S gyros with a maximum increasing percentage reached 41 % and 986 % respectively. Such behaviour was repeated in case of angular acceleration increasing. For more numerical details, ARW value growth to 55% and 51% for the Samsung S4 Z-Gyro and to 409% and 165% for the iPhone 5S one.

Regarding correlated noise processes, a combination of two 1st order GM processes could be observed under all angular velocity points but with different response according to applied angular velocity value. Specifically, according to Samsung S4 Z-Gyro, both variances of the GM1(σ^2_{GM1}) and GM2 (σ^2_{GM2}) mostly increase with raising the angular velocity with a maximum change reached over 161 % for σ^2_{GM1} and approximately 19 % for σ^2_{GM2}. On the other hand, reciprocal (β_1) of the time constant appeared to have a reversal behaviour as it first increased and then decreases with a maximum degradation percentage reached 90 %. Unfortunately, the attitude of β_2 could not be well detected with dynamic, angular velocity, variation. Due to having shorter data sets for angular acceleration experiments, only one 1st order GM processes could be recognized. Table 4 shows how the values of σ^2_{GM1} and β_1 could hardly be changed according to increasing $\dot{\omega}_z$ from 1 to 2 deg/sec^2.

Based on the proposed contamination test results, data set collected for Experiment 4 (where 72 deg/sec angular velocity applied to iPhone 5S Z-Gyro) is considered to include outliers. As a result, no analysis was performed for such data set in Table 4.

4. CONCLUSION

The dynamic dependent error analysis for low-cost MEMS IMUs mounted on two different smartphones was investigated in this paper. Two different tools named Allan Variance and the Generalized method of Wavelet Moments were used for noise characterisation related to inertial sensors output measurements. The detailed estimation results were highlighted of static and dynamic data sets collected at different applied dynamic quantities, angular velocity and acceleration, using two MEMS-based IMUs, InvenSense MPU-6500 and ST-Microelectronics L3G4200DH, mounted on Samsung S4 and iPhone 5S smartphones respectively. The AV / GMWM characteristic curve was constructed and used to identify the type and level of stochastic noise parameters raising in the output datasets for gyros of both MEMS IMUs. Repeating the same analysis for different applied dynamics allows to identify the general attitude of such parameters as a reflection of platform dynamic variation.

Comparing the two aforementioned methods showed that AV could efficiently detect ARW as well as their general attitude in both static and dynamic modes. As a demerit, AV tool never have the ability to detect any outliers on the data under test which could possibly lead to inaccurate modeling for measured signals. Nevertheless, the GMWM solved that by comparing the classical WV with another robust one using the so called Robust/Contamination Test. Moreover, GMWM could successfully identify correlated noise parameters represented in the sum of one or more 1st order GM process which never could be discriminated using AV. As a conclusion, we need to use more complicated stochastic models, rather than AV ones, putting into consideration the choice of different parameter setting according to platform dynamic variations. Finally, Different candidate models were evaluated by a proposed criteria (WIC) that compromise the goodness of fitness of each model and its related complexity. The model selection results indicated that noise model structure was not affected due to the applied dynamics. Only model parameters' values differ according to dynamic variations. Consequently, augmented stochastic noise model in Kalman Filter will have the same structure with different parameters' magnitudes according to applied dynamics which will be investigated in future publications.

ACKNOWLEDGEMENTS

The data used in this paper were collected at the PLAN Group Lab at the University of Calgary. We would also like to show our gratitude to Dr. Thyagaraja Marathe, Postdoctoral Fellow, Geomatics Engineering Department at the University of Calgary for sharing his experiences regarding operating the SmartMotor Series 4 Single Axis Positioning and Rate Table in this research.

REFERENCES

Abdel-Hamid, W.,2006. Accuracy enhancement of integrated MEMS-IMU/GPS systems for land vehicular navigation applications: *Library and Archives Canada= Bibliothèque et Archives Canada*.

Aggarwal, P., Syed, Z., Niu, X., & El-Sheimy, N., 2006. Cost-effective testing and calibration of low cost MEMS sensors for integrated positioning, navigation and mapping systems. *Paper presented at the Proceedings of XXIII FIG Congress*, Munich, Germany.

Allan, D. W., 1966. Statistics of atomic frequency standards. *Proceedings of the IEEE*, 54(2), 221-230.

Balamuta, J., Guerrier, S., Molinari, R., & Yang, W., 2016. A Computationally Efficient Framework for Automatic Inertial Sensor Calibration. *arXiv preprint arXiv*:1603.05297.

Balamuta, J., Molinari, R., Guerrier, S., & Yang, W., 2016. The gmwm R package: a comprehensive tool for time series analysis from state-space models to robustness. *arXiv preprint arXiv*:1607.04543.

El-Diasty, M., El-Rabbany, A., & Pagiatakis, S., 2007. Temperature variation effects on stochastic characteristics for low-cost MEMS-based inertial sensor error. *Measurement Science and Technology*, 18(11), 3321.

El-Sheimy, N., 2014. *Lecture note 623–Inertial Techniques and INS/DGPS Integration.* In: Department of Geomatics Engineering, University of Calgary.

El-Sheimy, N., Hou, H., & Niu, X., 2008. Analysis and modeling of inertial sensors using Allan variance. *IEEE Transactions on instrumentation and measurement*, 57(1), 140-149.

Engineers, I. o. E. a. E., 1999. *IEEE Standard Specification Format Guide and Test Procedure for Linear, Single-axis*, Nongyroscopic Accelerometers: IEEE.

Guerrier, S., & Molinari, R., 2016. Wavelet variance for random fields: an m-estimation framework. *arXiv preprint arXiv*:1607.05858.

Guerrier, S., Molinari, R., & Skaloud, J., 2015. Automatic identification and calibration of stochastic parameters in inertial sensors. *Navigation*, 62(4), 265-272.

Guerrier, S., Molinari, R., & Stebler, Y., 2016. Theoretical Limitations of Allan Variance-based Regression for Time Series Model Estimation. *IEEE Signal Processing Letters*, 23(5), 597-601.

Guerrier, S., Skaloud, J., Stebler, Y., & Victoria-Feser, M.-P., 2013. Wavelet-variance-based estimation for composite stochastic processes. *Journal of the American Statistical Association*, 108(503), 1021-1030.

Hou, H., 2005. Modeling inertial sensors errors using Allan variance: *Library and Archives Canada= Bibliothèque et Archives Canada*.

Jensen, A. B., 2010. "GNSS Satellite Orbits", Technical University of Denmark.

Kane, T. R., & Levinson, D. A., 1985. "Dynamics, theory and applications". McGraw Hill.

Li, Y., Georgy, J., Niu, X., Li, Q., & El-Sheimy, N., 2015. Autonomous calibration of MEMS gyros in consumer portable devices. *IEEE Sensors Journal*, 15(7), 4062-4072.

Nassar, S., 2005. Improving the inertial navigation system (INS) error model for INS and INS/DGPS applications: *National Library of Canada= Bibliothèque nationale du Canada*.

Niu, X., Chen, Q., Zhang, Q., Zhang, H., Niu, J., Chen, K., . . . Liu, J., 2014. Using Allan variance to analyze the error characteristics of GNSS positioning. *GPS solutions*, 18(2), 231-242.

Park, M., 2005. Error analysis and stochastic modeling of MEMS-base inertial sensors for land vehicle navigation applications: *Library and Archives Canada= Bibliothèque et Archives Canada*.

Radi, A., Li, Y., & El-Sheimy., 2017. Temperature Variation Effect on The Stochastic Performance of Smartphone Sensors Using Allan Variance and Generalized Method of Wavelet Moments. In: *The Institute of Navigation International Technical Meeting*, California, USA.

Savage, P. G., 2002. Analytical modeling of sensor quantization in strapdown inertial navigation error equations. *Journal of Guidance, Control, and Dynamics*, 25(5), 833-842.

Stebler, Y., Guerrier, S., & Skaloud, J., 2015. An approach for observing and modeling errors in MEMS-based inertial sensors under vehicle dynamic. *IEEE Transactions on Instrumentation and Measurement*, 64(11), 2926-2936.

Stebler, Y., Guerrier, S., Skaloud, J., Molinari, R., & Victoria-Feser, M.-P., 2014. Study of MEMS-based inertial sensors operating in dynamic conditions. *Paper presented at the 2014 IEEE/ION Position, Location and Navigation Symposium-PLANS 2014*.

Stebler, Y., Guerrier, S., Skaloud, J., & Victoria-Feser, M.-P., 2014. Generalized method of wavelet moments for inertial navigation filter design. *IEEE Transactions on Aerospace and Electronic Systems,* 50(3), 2269-2283.

Vaccaro, R. J., & Zaki, A. S., 2012. Statistical modeling of rate gyros. *IEEE Transactions on Instrumentation and Measurement*, 61(3), 673-684.

Wis, M., & Colomina, I., 2010. Dynamic dependency of inertial sensor errors and its application to INS/GNSS navigation. *Proc. NAVITEC Congr*, 1-7.

Woodman, O. J., 2007. "An introduction to inertial navigation", University of Cambridge, Computer Laboratory, Tech. Rep. UCAMCL-TR-696, 14, 15.

Zhang, X., Li, Y., Mumford, P., & Rizos, C., 2008. Allan variance analysis on error characters of MEMS inertial sensors for an FPGA-based GPS/INS system. *Paper presented at the Proceedings of the International Symposium on GPS/GNNS*

Automatic Panoramic Sequence and Mobile LiDAR Registration via Similarity Measurements

Jianping Li[a,*], Xianghong Zou[a], Bisheng Yang[a,*],Ronggang Huang[a]

[a]State Key Laboratory of Information Engineering in Surveying, Mapping and Remote Sensing,Wuhan University, Wuhan, China – (lijianping, bshyang)@whu.edu.cn

KEY WORDS: LiDAR, Panoramic Sequence, Registration, MMS

ABSTRACT:

The paper presents a method to register panorama sequence with laser scanning data accurately. And the calibration of relative orientation between panorama and IMU is not required. Firstly, fusion of panorama structure from motion (SFM) and GPS is launched to obtain a good initial exterior orientation parameters (EoPs) of panorama. Secondly, the sequence of panoramic images could be entirely registered to point clouds via the mutual information. In this way, the proposed method could overcome the instability in the registration of a single panoramic image and point clouds.

1. Introduction

Image-to-range registration is prerequisite for many applications due to the fact that the additional color information offered by the camera gives the mobile mapping system a much richer view of the world [1]. The registered images are critical not only for texture-mapping 3D models of large-scale scenes, but also for applications such as point cloud classification using the color information [2]. The problem of image-to-range can be solved by estimating the relative camera pose with respect to the range sensor. Existing methods can be divided into three major categories: multi-view based matching, structural features based matching and mutual information based matching.

Multi-view-based matching relies on the 3D points from structure-from motion, and converts the 2D-3D registration problem to 3D-3D registration problem. L. Liu present a general framework to align 3D points from structure-from motion with range data [3]. Multi-view-based method requires a high degree of image overlap. However the MMS can hardly achieve the overlap requirements, otherwise it will cause a lot of data redundancy. Structural feature based methods depend on the 3D points recovered from 2D images. L. Liu matched structural features in both 2D and 3D space to estimate the relative camera pose [4]. However, due to the differences between camera and range sensor in terms of sensing characteristics, such as imaging spectrum and resolution, it is challenging to find reliable correspondence between features extracted from 2D-image and 3D-range scans. Mutual Information based matching was initially developed for the registration of multi-modal medical images. A. Mastin introduced MI into the registration of 2D-3D urban sensing data [5]. An extension of MI, NMI was introduced by R. Wang [6]. Compared with MI-based registration, NMI shows more robust

performance in registering ground image and laser scanning. However, the mutual information of the single panoramic image and the point cloud intensity is less stable, and the registration may fail.

Our research is motivated by the fact that there are considerable misalignment between the panoramic images and laser scanning data on mobile mapping system according to direct geo-reference data [7], especially when the relative position between panoramic and laser scanning sensor is not calibrated. Moreover the mutual information of the panoramic image and the point cloud intensity is less stable. If the relative pose of each panorama in the sequence is obtained, and the mutual information of each panoramic image in the whole sequence between the intensity of the point cloud will be calculated, which can provide a registration with higher robustness. To summarize, the contributions of this paper are listed below:

1. A method for calculating the initial panoramic pose of panoramic image sequence combined with GPS is proposed. So the calibration of relative orientation between panorama and IMU is not required.
2. A more efficient and robust matching method than the single panoramic image matching is proposed.

2. Methodology

The registration method proposed in this paper is divided into two main steps： i) Coarse registration based on GPS aided SFM; ii) Fine registration based on mutual information between sequence panorama and range data. Firstly, fusion of panorama structure from motion (SFM) and GPS is launched to obtain a good initial exterior orientation parameters (EoPs) of panorama. And then, the sequence of panoramic images could be entirely registered to point clouds via the mutual information. The details of the workflow are shown in Fig.1.

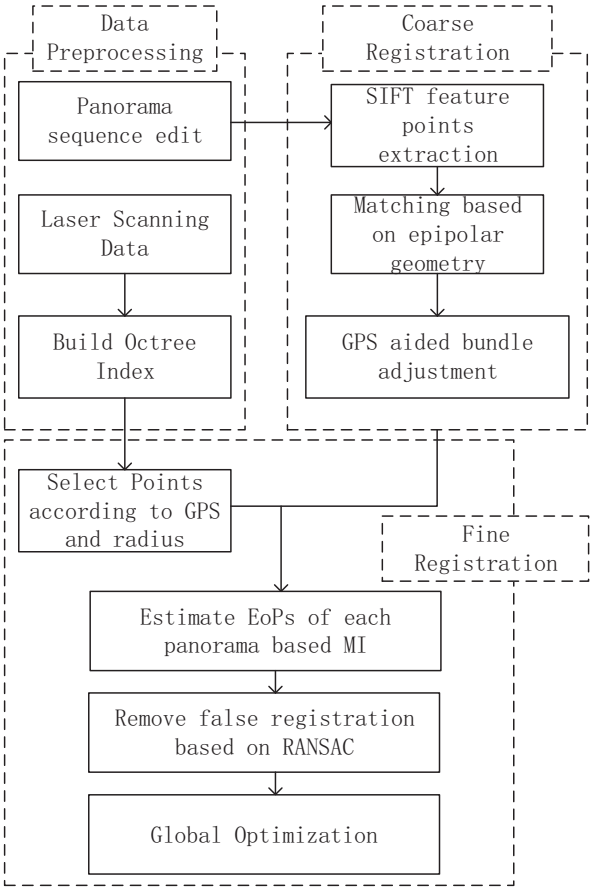

Fig.1.Workflow of the proposed method

2.1 Coarse registration

The process of coarse registration is as follows: (1) Feature points extraction of each panoramic image based on SIFT (2) Match based on epipolar geometry (3) GPS aided panorama SFM.

The epipolar geometry for panoramic camera has been already presented in [8].Then the relative pose of each panorama is determined with the 5-point algorithm or 8-point algorithm[9]. To get the absolute EoPs of panorama, take the GPS positions as the initial centers of the panorama images in incremental SFM process. After all the panorama images are added into the SFM system, the re-projection error of each feature points and distance between estimated exposure centers and GPS positions are considered into the bundle adjustment. Then a good initial EoPs of panorama sequence can be obtained.

2.2 Fine registration

The fine registration process is as follow: (1)Traverse each panorama in the sequence, set 20m as radius and the GPS position of panorama as center, points in the sphere are selected from the point cloud index. The selected points will be used to calculate the mutual information. (2) Estimate the EoPs of each panorama based on [5]. Because of the MI is not stable for all the images, RANSAC is used for removing bad estimations in the panoramic image set. (3)Let the right estimation as the key frame, the bundle adjustment is utilized again. This time, the EoPs of the key frames are set as

fixed values which are obtained by the MI based algorithm. And the fine EoPs of remaining panorama can be obtained.

3. Experiments and analysis

Experimental data is collected from Optech LYNX Mobile Mapper in Wuhan University. The mobile mapping system is composed of a 360° LiDAR sensor, six high-resolution cameras, a Ladybug 3 camera. Experimental point cloud data volume is 12.6G, in order to retrieve point cloud data efficiently, an octree index is constructed for point cloud data[10]. A total of 19 panorama images were recorded in the experiment area. The GPS position of each exposure was recorded in each panoramic image, and the exposure position was obtained from the original GPS data plus the MMS original calibration value. Secondly, it is necessary to remove the same part of the panorama image that is blocked by its own body, to avoid affecting the matching of the feature points and the mutual information calculation.

The spherical camera model is used to perform feature points matching and geometrical filtering. The matching results of two adjacent panoramas are shown in Fig.2.

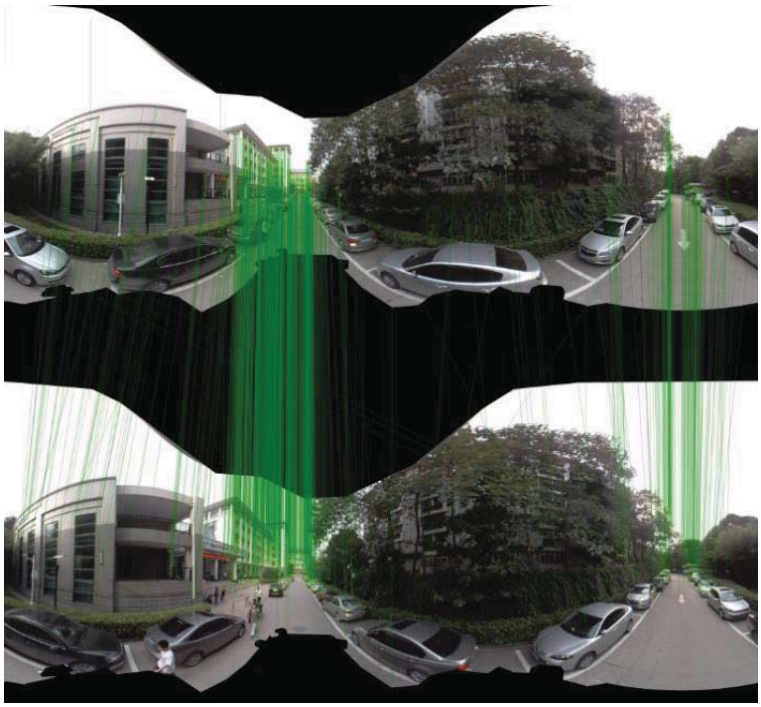

Fig.2. Feature points matching and geometrical filtering. The green lines matches the feature points of two adjacent panoramic images.

GPS positions of panoramic images are taken as the initial center of the exposure centers, and GPS aided bundle adjustment is utilized. The result of the coarse registration is shown in Fig.3.

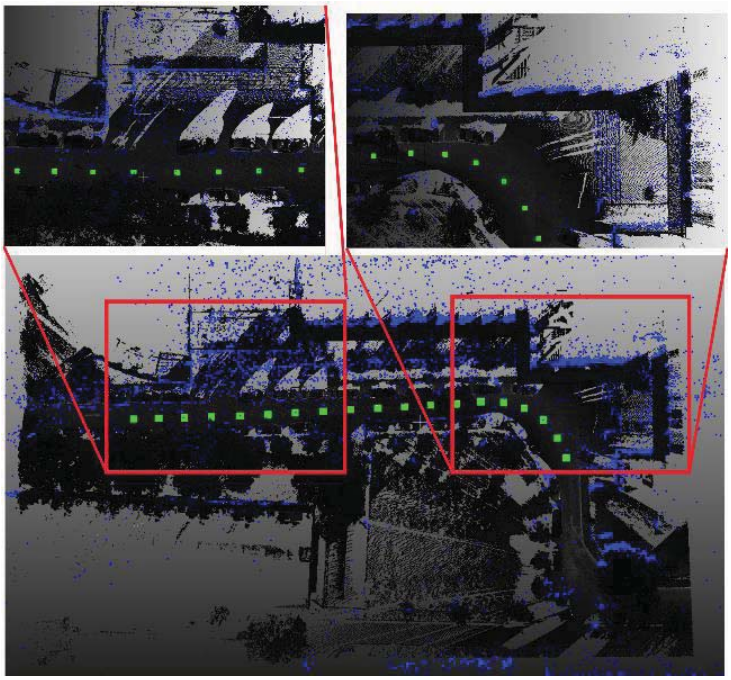

Fig.3.Result of coarse registration. Blue points are feature points from SFM,Green points are poses of panoramics, black points are lidar data.

The coarse registration result is taken as the initial EoPs of the panoramic images, and the matching result is shown in Fig.4. The final registration results are obtained by finding the maximum mutual information of single panorama image and global optimization. One of the final registration results is shown in Fig.4. And the colored point cloud is shown in Fig.5.

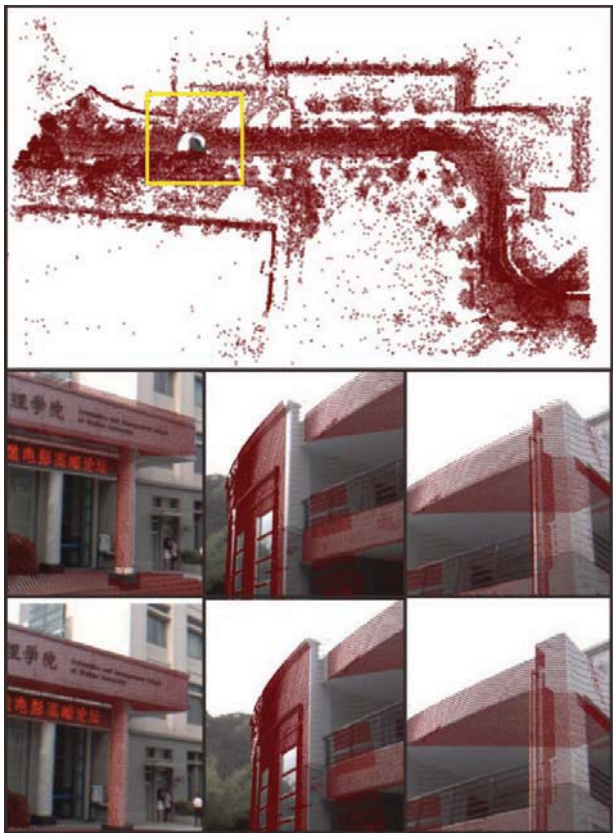

Fig.4 Coarse and fine registration result of one sample panorama. The first row show the position of the sample panorama in the LiDAR point cloud. The second row show the coarse registration result of the sample. The third row show the fine registration of the sample.

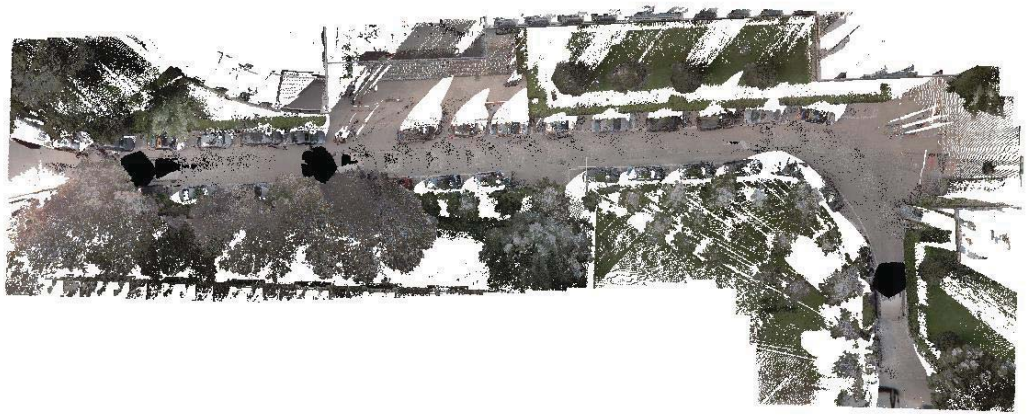

Fig.5 Colored point cloud of study area

To evaluate the accuracy of the proposed method, corners picked up manually are back-projected onto the panoramic image. The manually selected corners should be easily recognizable in the panoramas well as in the point cloud, ie. building corners, wheel centers of vehicle. An example of selected points on panorama is shown in Fig.6.The back-projection error of the corresponding points is taken as the evaluation standard as shown in Table.1.

Fig.6 Example of selected corner points on panorama.

Table.1
Performance of the proposed method

Proposed coarse Registration			Proposed Fine Registration		
Error (pixel)			Error (pixel)		
Average	Max	RMSE	Average	Max	RMSE
18.50	26.80	5.01	3.13	3.79	0.40

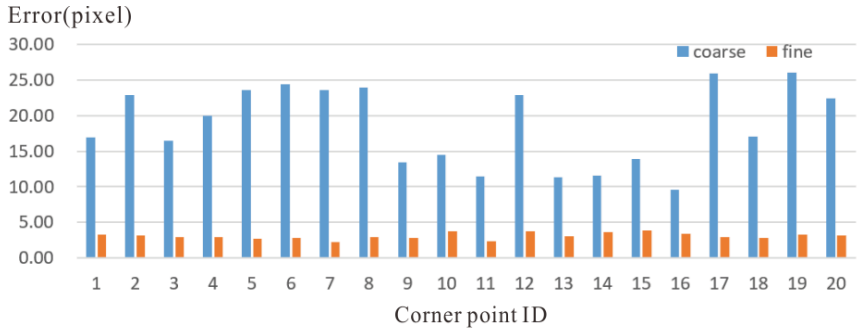

Fig.7 Distribution of back-projection errors for study area

4. Conclusion

In this paper, for the purpose of laser point cloud and panoramic image registration, we propose a robust 2D-panoramic sequence to 3D-range registration method that can work with the panoramic sequence collected by MMS. The relative position relation of panorama sequence is determined firstly, which avoids duplication of single image registration and improves robustness. Using sequent images as a whole to compute mutual information with range data improves the mutual information registration robustness.

REFERENCES:

[1] B. Yang and Z. Dong, "A shape-based segmentation method for mobile laser scanning point clouds," *ISPRS Journal of Photogrammetry and Remote Sensing,* vol. 81, pp. 19-30, 7// 2013.

[2] S. Barnea and S. Filin, "Segmentation of terrestrial laser scanning data using geometry and image information," *ISPRS Journal of Photogrammetry and Remote Sensing,* vol. 76, pp. 33-48, 2// 2013.

[3] L. Lingyun, I. Stamos, Y. Gene, G. Wolberg, and S. Zokai, "Multiview Geometry for Texture Mapping 2D Images Onto 3D Range Data," in *2006 IEEE Computer Society Conference on*

Computer Vision and Pattern Recognition (CVPR'06), 2006, pp. 2293-2300.

[4] L. Liu and I. Stamos, "Automatic 3D to 2D registration for the photorealistic rendering of urban scenes," in *2005 IEEE Computer Society Conference on Computer Vision and Pattern Recognition (CVPR'05)*, 2005, pp. 137-143 vol. 2.

[5] A. Mastin, J. Kepner, and J. Fisher, "Automatic registration of LIDAR and optical images of urban scenes," in *Computer Vision and Pattern Recognition, 2009. CVPR 2009. IEEE Conference on*, 2009, pp. 2639-2646.

[6] R. Wang, F. P. Ferrie, and J. Macfarlane, "Automatic registration of mobile LiDAR and spherical panoramas," in *2012 IEEE Computer Society Conference on Computer Vision and Pattern Recognition Workshops*, 2012, pp. 33-40.

[7] T. Cui, S. Ji, J. Shan, J. Gong, and K. Liu, "Line-based registration of panoramic images and LiDAR point clouds for mobile mapping

" *Sensors (Switzerland),* vol. 17, 2017.

[8] A. Pagani and D. Stricker, "Structure from Motion using full spherical panoramic cameras," in *Computer Vision Workshops (ICCV Workshops), 2011 IEEE International Conference on*, 2011, pp. 375-382.

[9] R. Hartley and A. Zisserman, *Multiple view geometry in computer vision*: Cambridge university press, 2003.

[10] A.-V. Vo, L. Truong-Hong, D. F. Laefer, and M. Bertolotto, "Octree-based region growing for point cloud segmentation," *ISPRS Journal of Photogrammetry and Remote Sensing,* vol. 104, pp. 88-100, 2015.

INAVSET: A BENCHMARK OF INDOOR NAVIGATION USING SMARTPHONES

Liu Kun, Pei Ling *, Deng Zhantao, Qian Jiuchao, Liu Peilin,Yu Wenxian

Shanghai Jiao Tong University, Shanghai Key Laboratory of Navigation and Location-based Services,
School of Electronic information and Electrical Engineering, Shanghai, China -
liukunlove@yeah.net, ling.pei@sjtu.edu.cn, hit_zhantaodeng@126.com
(jcqian,liupeilin,wxyu)@sjtu.edu.cn

KEY WORDS: Benchmark, Indoor Navigation, Smartphone, Calibration, Dataset

ABSTRACT:

Location Based Service (LBS) has played a more and more important role in military and government industries, emergency services, and the commercial sector. Nowadays the growing popularity of smartphones is undoubtedly the main carrier of location-based services in personal applications. The powerful context-sensing ability makes smartphone a potential promise for the use of indoor localization. And with the booming of wireless communication and sensing technologies, indoor positioning is attracting more and more attentions from both academies and industries.

Although there are many papers in the literature trying to solve the indoor localization problem using a variety of methods, there still exists a significant drawback in the field that is the lack of a common dataset for the purpose of comparison. Therefore, an all-in-one dataset is very necessary for both research and product development purposes. Under these conditions, iNavSet[1], which has been improved by our team over the past several years, aims at collecting and sharing state-of-the-art multi-sensor data such as acceleration, gyroscope, and magnetometer data in a specific area. With the advent of depth sensors, our dataset also includes depth data. In addition, the data for images and videos are included in our dataset for visual navigation. The dataset is used to assess different algorithms and methodologies for indoor positioning. The accuracy of these algorithms can be compared with real data. As ground truth, Vicon and HAIP system were acquired to measure real coordinates.

1. INTRODUCTION

Location Based Service (LBS) has played a more and more important role in military and government industries, emergency services, and the commercial sector. Unfortunately, the Global Navigation Satellite System which is dominant in outdoor localization can hardly provide indoor localization due to high signal attenuation and severe multipath effect. Nowadays truly ubiquitous smartphones are undoubtedly the main carrier for personal location based services.

As the indoor environment is complex and changeable, the main challenges that indoor positioning faces include the following:

(1) Indoor signal may experience a serious multipath interference due to the reflection caused by furniture and walls.

(2) Many ranging techniques are based on the line-of-sight (LoS) condition, but it is usually difficult to meet due to the occlusion in the indoor environment;

(3) The high density of indoor obstacle will lead to the rapid signal attenuation and scattering;

(4) The indoor environment will change rapidly in the transient because of pedestrian movement and the switch of the doors and windows;

(5) Indoor location has high requisition for accuracy than outdoor ones;

Currently the popular indoor location methods are generally the following: the use of the earth magnetic field for indoor localization (Inderst et al., 2015); WLAN fingerprint positioning (He et al., 2014); pedestrian dead reckoning (PDR) using high-precision inertial sensors and an emerging technology (Chernoguz et al., 2013) called Simultaneous Localization and Mapping (SLAM). Although there are so many papers and literature trying to solve the indoor positioning issues using above methods, there still exists one significant drawback in these field that is the lack of a common dataset for comparison of methods. Usually, each researcher has his or her own data for testing. Under these conditions, it is not possible to compare different methods since the particularities of each experiment are hardly reproducible. For example, in photogrammetry, there are many detailed and specific dataset like the Middlebury test on dense image matching, the KITTI suite for mobile robotics and autonomous driving research (Geiger et al., 2013), the image matching benchmark promoted by EuroSDR (Haala, 2014) and the ISPRS WGIII/4 test (Nex et al., 2015)on urban object detection and 3D building reconstruction and so on. Prior to this, the dataset associated with indoor positioning exist but not detailed. For instance, there is an available database for comparing WLAN fingerprint-based indoor localization methods called UJIIndoorLoc (Torres-Sospedra et al., 2014) and in the magnetic field-based indoor localization field, a database called UJIIndoorLoc-Mag (Torres-Sospedra et al., 2015) also exists.

Compared to geomagnetic positioning and WLAN fingerprint positioning, fusion navigation is increasingly popular. It has high positioning accuracy and adaptability and other characteristics. Therefore, this paper is devoted to the establishment of such a dataset: it contains the raw data for most smartphone sensors including accelerometers, gyroscopes, magnetometers, linear accelerometers, barometers and ambient light sensor. And, it also includes WLAN and Bluetooth-related information (Pei et al., 2012). In particular, the smart devices used in this article are Google's Project Tango which have a depth sensor that can record depth information and a motion tracking sensor that can record the pose information of the

[1] iNavSet:Navigation Dataset, https://drive.google.com/open?id=0B6z7kjxTgTAgR0FScGZJeFRSR2s

device. Finally, it includes visual data that can be used for later validation of the SLAM algorithm.

2. TEST PLATFORM

This section provides additional information about the recording platform and sensor setup we have used to record this dataset. Our recording platform is a Google project tango, which makes it easy to see the items beyond our real world. The device is equipped with Nvidia quad-core Tegra K1 processor, running Android 4.4 and we use the following sensors:
(1) Inertial Navigation System (GPS/IMU)
(2) RGB camera
(3) Motion track camera
(4) Depth camera

Figure 1. Platform device - Google Project Tango

Figure 1 is the data acquisition platform that we use. We listed the main sensor parameters of the device as shown in Table 2.

Sensor type	Parameter		
	Manufacturers	Power(W)	Resolution
Accelerometer	Bsquare	0.25	0.0098
Magnetometer	Bsquare	0.6	0.152
Gyroscope	Bsquare	6.5	1.0E-9
Barometer	Bsquare	0.6	0.01
Light Sensor	Capella Microsystems	1670	307
Gravity Sensor	AOSP	/	/
Linear Acceleration Sensor	AOSP	/	/

Table 2. The relevant sensor parameters of the platform

3. TEST ENVIRONMENT

As the indoor environment rich and varied, different environments have different effects on the experiment. In general, this test environment is divided into open spaces, semi-open spaces and indoor-outdoor buffer areas. More specifically, from the view of the indoor physical signal distribution, the situation may become richer. For example, in an open area, we can distinguish strong magnetic field environment and weak magnetic field environment according to the electromagnetic field. The following criteria are the basis for dividing the indoor environment into different categories:
(1) The number of nearby WLAN hotspots
(2) The number of nearby electromagnetic equipment devices (such as computers, televisions, printers, air conditioning, etc.);
(3) The number of nearby solid obstructions, such as desks, chairs, flower pots and so on;
(4) The strength of GPS signals in nearby areas;
(5) The number of pedestrians in nearby areas;
Please note that these division criteria are not unique and that the division criteria will become more complicated for more complex indoor environments.

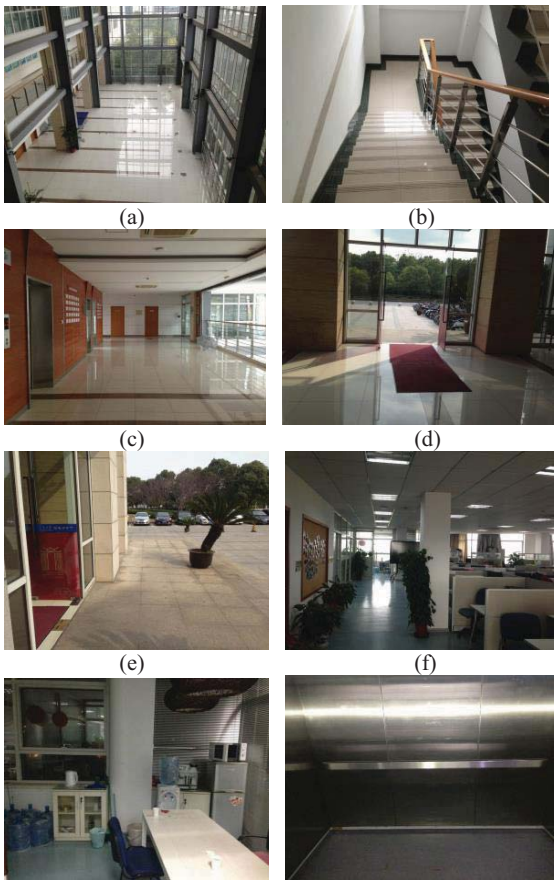

Figure 3. Test environment (Microelectronics building, Shanghai Jiao Tong University): a) hall, b) stairs, c) corridor indoor, d) indoor-outdoor buffer area, e) corridor outdoor, f) office, g) tea room h) elevator

3.1 Stairs & Hall

Stairs or hall as shown in Fig. 3a and Fig. 3b are open areas, where there is almost no interference with electromagnetic equipment. So the use of geomagnetic positioning in this region will be a good choice. In this area, we can test the vertical positioning ability and floor recognition ability.

3.2 Corridor & Meeting room

These areas belong to semi-open space and they generally don't have a lot of electromagnetic interference. But there will be WLAN hotspots in the nearby. It is worth noting that there are two types of corridor, the first is completely indoors ones, surrounded by windows and doors and the other is closed to the windows.

3.3 Office

Fig. 3f shows us a typical laboratory environment where there are a variety of disturbances in the whole area. For example, the presence of a large number of pedestrians is interfering with the RF signal; the received signal strength of WLAN hotspots is influenced duo to a large number of desks and other electronic equipment; a large number of computers and servers that cause electromagnetic interference and so on. Even there is a lot of GPS signal interference in the area near the windows.

3.4 Elevator

The elevator (Fig. 3h) is one of the main places where magnetic values is transformed all the time. It also belongs to an open space. Here we can identify the floor using the barometric data.

3.5 Tea room

As is shown in Fig. 3g, the area has a wealth of electromagnetic interference. Refrigerators, microwave ovens, etc. will have an unpredictable impact on our data.

3.6 Indoor and outdoor buffer area

Fig. 3d and Fig. 3e are typical indoor and outdoor buffer area environments. The GPS signal strength in these areas is generally high. So in these environments, we can use the indoor positioning together with global navigation satellite system (GNSS) to achieve fusion positioning.

4. TEST CASES

There are many ways pedestrians walk. The result of the different walking mode positioning will be different. In this article, test cases covers static test, moving test and stereo test. From the trajectory point of view, the moving test can be divided into straight line, broken line, circle, random walking, and so on. From the motion point of view, the test cases include stationary, walking, fast walking, running, going up stairs, going down stairs, using elevator, and so on. The other major issue that has to be considered is the fact that users carry smartphones in a variety of ways (Kunze et al., 2009). With regard to the smartphone carrying mode, we will consider the modes including phoning, texting, pocket, swing, in-bag and so on.

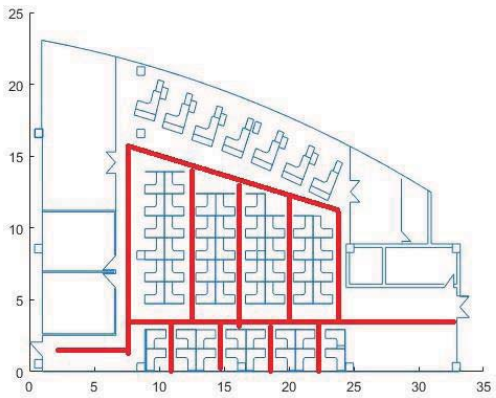

Figure 4. Two-dimensional plane model of the main laboratory

Fig. 4 is a map of our main laboratory, in which the red line represents the area through which pedestrians can pass. Most of our data will come from these regions. The entire laboratory covers an area of over 600 square meters so that it can provide enough samples. Here we briefly explain several different motion patterns and the corresponding test requirements.

4.1 Static testing

The purpose of static testing is to evaluate the positioning of stationary objects at a specific location. Test requirements are as follows:
(1) The number of samples to be measured is not less than 10.
(2) Need to combine the corresponding timestamp.
(3) The corresponding real position of the object needs to be combined.
(4) Select a clean test environment (no electromagnetic interference, pedestrian interference, walls and other occlusion of the environment, the proposed first floor lobby), and select a number of test points in the region, as shown in Fig.5.

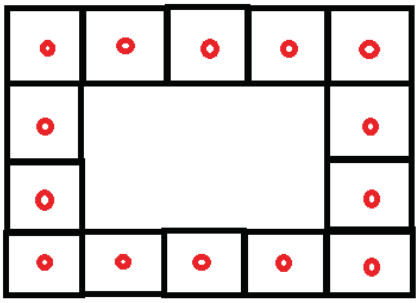
Figure 5. Static test points distribution diagram

4.2 Dynamic testing

In order to make the final positioning more accurate, we divided the movement model as detailed as possible into the following five categories:
(1) Linear motion
Linear motion's requirements are as follows: The movement speed is 1.0M / s; The test consists of eight motion directions, as shown in Fig. 6; The number of output data points recorded in each direction of motion is not less than two (ie, at least two positioning results are output during each uninterrupted movement.) The motion distance provided by the site must satisfy at least two positioning data; Need to combine the corresponding timestamp. The corresponding real position of the object needs to be combined.

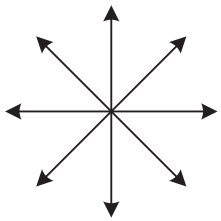
Figure 6. Linear motion diagram

(2) Linear re-entrant motion

Linear re-entrant motion's requirements are as follow: The movement speed is 1.0M / s; the test consists of four motion directions, the route is shown in Fig. 7; each test needs to undergo at least 2 re-entry, as shown in Fig. 8: A -> B -> A -> B.

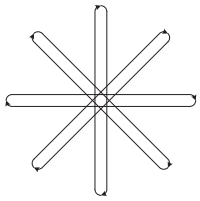

Figure 7. Linear re-entrant motion diagram

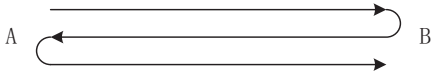

Figure 8. Linear re-entrant motion diagram

(3) Straight - line angular motion
Straight - line angular motion's requirements are as follows: The movement speed is 1.0M / s; the test process is carried out around a square path, and the travel consists of two moving directions. The course is shown in Fig.9; At least two positioning data are output during each edge movement, and the total amount of data recorded in each movement direction of the rectangle is not less than 50. (The motion distance provided by the site shall satisfy at least 2 positioning data when moving along each edge, otherwise the indicator can't be tested).

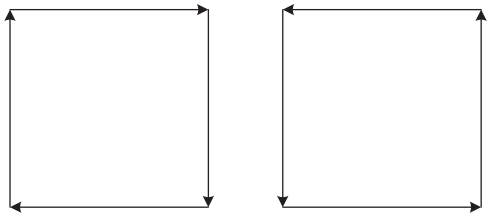

Figure 9. Straight - line angular motion diagram

(4) Circular motion
Circular motion's requirements are as follow: The movement speed is 1.0M / s; The test includes two movement directions, the routes are shown in Figure 10; At least 8 positioning data points are output every week along the circle (the motion distance provided by the site must meet this condition, otherwise the indicator can't be tested); The total amount of data recorded in each movement direction of the circle is not less than 50.

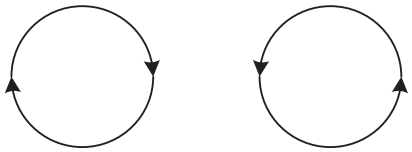

Figure 10. Circular motion diagram

(5) Free - track motion

Free - track motion's requirements are as follow: The movement speed is 1.0M / s; Movement can be done in any direction.

4.3 Stereo adaptability testing

The test is able to identify the vertical position. It can be divided into the following two categories: static floor identification and dynamic floor identification.
(1) Static floor identification: It requires a record of at least 20 measurements per floor.
(2) Dynamic floor identification: It requires a record of at least 20 measurements per floor; it needs to test the ability to identify the floor in the case of rise and fall processing.

5. CALIBRATION METHODS

This is a critical step to generate the ground truth associating with the test dataset. In the iNavSet, we provide three types of calibration methods. In our laboratory, we have already setup a motion capture system namely Vicon[2] which can calibrate a moving object with accuracy up to sub-millimeter level in a limited space. Furthermore, in a four-floor office building, we have set up the high accuracy indoor positioning system namely HAIP made by NOKIA which can provide the accuracy with 0.3 meters. In the 600 square meters semi-open space, we placed many marks which have been carefully calibrated using laser measure beforehand. The Vicon and HAIP systems can provide the 100Hz and 10Hz calibration without intervention. Before introducing the calibration method, we first need to introduce the various reference coordinate systems we use.

5.1 Test coordinate systems

Figure 11. The plane diagram of the third floor.

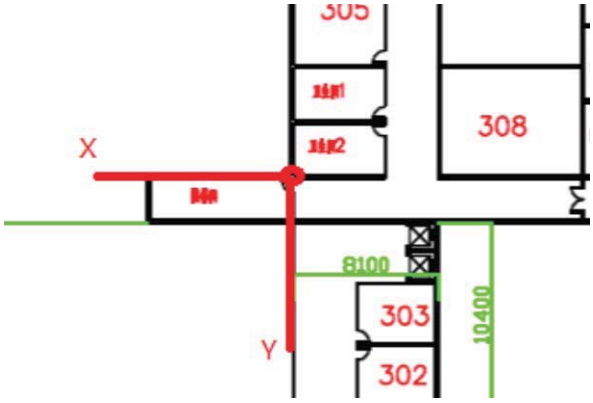

Figure 12. A more clear plane diagram where shows the axes of x and y apparently

[2] https://www.vicon.com/

As long as it is related to the positioning or navigation problems, the coordinate system must be a very important concept. So, here we give the reference coordinate system referenced by our dataset. As shown in Figure 11, this is the plane diagram of our entire third floor, the main source of our data. A red dot in the figure represents the position of the zero point. Figure 12 shows the position of the initial point and the direction of the three reference axes x, y, z more clearly.

5.2 Vicon system

Oxford Metrics Limited is one of the world's leading providers of optical motion capture systems. In the 1970s, Oxford Metrics Limited served the UK Navy in the research and production of remote sensing and control technology. Into the 80's they will own in the military field of high-tech, gradually used for civilian areas, in the medical, sports, engineering, biology and many other areas of manufacturing for motion capture Motion Capture system. At the end of the 1980s, OML applied Motion Capture technology to the animation field of film and television. With its outstanding performance and the best price-performance ratio, OML won the conviction and favour of foreign production companies, and now it has become the world's most notably motion capture system.

Figure 13. Vicon three-dimensional motion analysis system

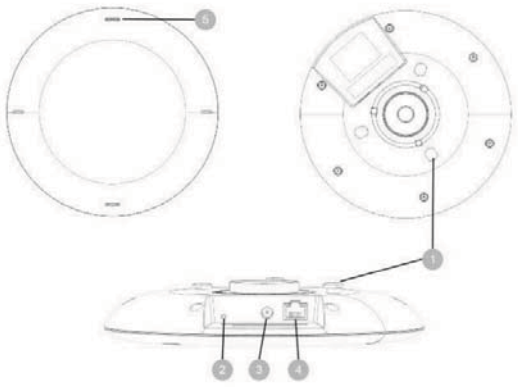

Figure 14. HAIP analysis system

5.3 HAIP system

HAIP's indoor precision positioning solution uses Bluetooth-based triangulation technology, in addition to using the phone's Bluetooth module, the need to deploy Bluetooth base stations, up to sub-meter positioning accuracy.

According to Nokia, the installation of multiple positioning devices within the building to form a set of indoor positioning system, the phone will be able to receive the signal from the system used to determine their location. The advantage of this positioning system is that it uses 2.4GHz frequency, and Bluetooth, WiFi is the same frequency, so existing mobile phones do not need to add an additional antenna, it is fully compatible with the market of mobile phones, Users only need to install a new location software development on the phone. More importantly, this short-range positioning signal is able to control power consumption at a very low level, the required energy is one-tenth of receiving normal GPS signal.

5.4 Marks in laboratory

There are a lot of stickers on the floor in our main lab. They are divided into red and black ones as shown in Fig.15. As we can see in Fig. 15a, the coordinates of these marks have been measured by laser before. The distance between two adjacent marks may also be different. Fig. 15b shows the distribution of all marks in the whole laboratory. There is a total of 48 markers, of course, the real coordinates of these marks will be given in our dataset.

(a)

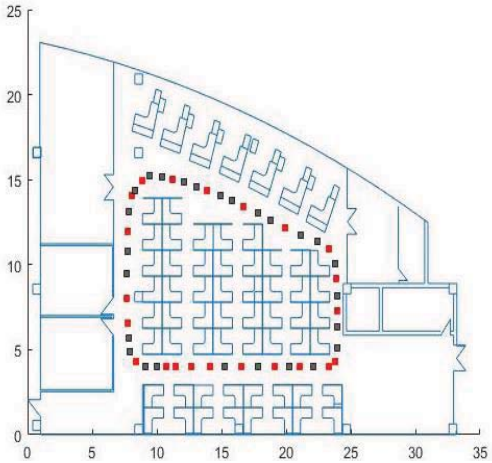

(b)

Figure 15. Marks in laboratory: a) the marks in the real scene, b) full lab labels

6. DATASET DESCRIPTION

In the iNavSet, we collect all data which are possible for positioning. For instance, the depth value from depth sensor, the pose of the device including orientation and rotation data, the IMU data from accelerometers and gyroscope,, the data of RF signals from WIFI, Bluetooth, Cellular network, environmental features from barometers and ambient light sensor, the visual data from RGB camera.

6.1 The pose data

The pose data record the state of the device at a certain time, it contains the following 7 numeric elements:
W The quaternion W-value
X The quaternion X-value
Y The quaternion Y-value
Z The quaternion Z-value
x The x coordinate value of the device
y The y coordinate value of the device
z The z coordinate value of the device

As an example, Table 16 shows an extract of one record recorded in December 1, 2016. Due to the length of this record, only 4 poses of the device at different moments are listed.

timestamps / values	8134.794	8134.854	8134.919	8134.949
W	0.052682	0.044852	0.03835	0.02390
X	-0.03741	-0.04010	-0.03870	-0.03378
Y	0.556812	0.557779	0.560213	0.564122
Z	0.828121	0.827805	0.826554	0.824652
x	-0.01062	-0.01118	-0.01166	-0.0120
y	0.12365	0.139262	0.156691	0.16524
z	-0.03887	-0.04477	-0.051683	-0.05557

Table 16. An example of one device's pose data

6.2 The sensor data

As mentioned above, we have collected a large number of IMU data in each specific experimental environment. Our data has been stored as a simple text file as follows:

Ts_1 Mx_1 My_1 Mz_1 Ax_1 Ay_1 Az_1 … $Gyox_1$ $Groy_1$ $Gyoz_1$
…
Ts_n Mx_n My_n Mz_n Ax_n Ay_n Az_n … $Gyox_n$ $Groy_n$ $Gyoz_n$

Where n is the number of samples collected in a specific environment. Mx represents the component value of magnetometer in the horizontal direction, Similarly, My represents the value of the y direction and Mz represents the value of the vertical direction. In addition to magnetometer, our dataset also includes real-time data from accelerometers (A), gyroscopes (Gyo), linear accelerometers (LA), gravity (Gra), ambient light (AL), barometers (B) and so on.
Table 17 shows the sensor data as an example, Due to the limitations of the article, only the values of the magnetometer in all directions are given here. These fragments are extracted from the entire dataset, and specific data can be found in our dataset.

Timestamps	M		
	Mx	My	Mz
1487817503769	-88.750	31.945	-40.753
1487817503811	-87.6875	31.13	-40.555
1487817503865	-87.687	31.130	-40.555
…			
1487817504393	-89.5	32.141	-41.605

Table 17. Example of sensor data extracted from dataset

6.3 The visual data

This is a feature of our dataset. Introducing the visual part on the basis of traditional inertial positioning will make indoor positioning more accurate. These original images or videos can be used for different visual algorithms.

6.4 The WLAN data

The WLAN data records all the original data of the hotspot devices around the whole building. Table 18 shows us an example that extracts from a dataset. Not difficult to find, there are several parameters that we must be treated rigorously.
(1)**RSSI** The most important information for WLAN fingerprinting comparison purposes are the WAPs detected and their RSSI level values.
(2)**MAC** The physical address of each hotspot.
(3)**Building ID & Floor ID** An integer value that corresponds to the building or the specific floor where the data was taken. The number 0 of Building ID corresponds to the school's microelectronics building while the number 1 corresponds to the other buildings. The number 1 corresponds to the first floor and similarly, the number 2, 3, 4 represents the second floor, the third floor and the fourth floor. Table 19 shows the Building ID for each building of the school.

Building ID	Real Building
0	Microelectronics Building
1	Others

Table 19. Relation between buildingID and the real building.

(4)**Environment** As we have mentioned before, data collection in a variety of different environments. Table 20 provides a detailed description of the specific environment in which each number corresponds.

ID	Environment
1	Hall
2	Stairs
3	Elevator
4	Corridor
5	Buffer Area
6	Pantry
7	Laboratory
8	Meeting room

Table 20. Relation between environment ID and the real environment.

(5)**Pose** In the course of the experiment, users have a variety of ways to carry intelligent devices, such as in his hand, on his pocket, answer the phone, etc. Table 21 lists the various carrying modes. Here the static and movement are relative to the

	Building ID	Floor ID	Environment	pose	RSSI ID_1	RSSI ID_2	RSSI ID_3	…	RSSI ID_n	MAC	Ground Truth	Calibration Method
1	0	1	1	1	0	0	0		0	*	(0,0,0)	3
2	1	2	2	2	-97	-97	-97		-97	*	(14,3.2,0)	3
3	0	3	2	3	0	0	0		0	*	(14,9.3,0)	3
4	1	1	3	2	0	0	0		0	*	(14,12,0)	3
…										*	(3.6,8.2,0)	
n	1	4	4	4	-67	-67	-67		-67	*	(4.3,17,0)	3

Table 18. Examples extracted from dataset, recorded on December 4th, 2016

person. For example, when users edit text messages, in fact, the device is in a relatively static state.

Pose ID	Mode
1	Answer the phone
2	Texting (static)
3	On pocket
4	In hand (moving)

Table 21. Relation between pose ID and the mode that tester holds the device.

(6)**Ground Truth** The measured value at each moment needs to have a real value corresponding to it, namely, the ground truth. Because the ultimate goal is to achieve positioning, all the truth values are in the form of coordinates. We use two different methods to represent all truth values. The first one is represented by (x, y, z) coordinates, and the reference frame is world's reference frame; the other one is represented by (Latitude, Longitude, Altitude) whose system is geographic coordinate system.

(7)**Calibration Method** As described above, there are three calibration methods available. These three methods correspond to serial numbers 1, 2 and 3 respectively. For example, the calibration method in the last column of Table 18 is numbered 3, indicating the use of a manual assisted calibration method. The specific correspondence between the ID and the calibration method is shown in Table 22.

ID	Calibration Methods
1	Vicon Calibration
2	HAIP Calibration
3	Manual Assisted Calibration

Table 22. Relation between calibration ID and the specific methods

7. CONCLUSIONS

In this paper, a comprehensive and integrated dataset, iNavSet, has been proposed to compare different positioning algorithms. First, at the beginning of the article, the test platform and all the test environments involved have been described in detail. Second, most of the circumstances in which pedestrians walk in the indoor environment have been already considered, which is the highlight of the article. In order to overcome the occasional and other human disturbance, pedestrian movement in every environment was repeated several times. In addition, three calibration methods for measuring the true position were also listed. Therefore, the samples obtained from iNavset could be considered objective and realistic.

In order to verify the validity of iNavSet, some of the data extracted from it was employed in our indoor positioning algorithm. The results are similar to those of many positioning algorithms and the maximum error is around 1.2 meters. Figure 22 reflects this result intuitively to us where the blue line indicates the pedestrian's trajectory from the algorithm and the red scatter plot represents the real position coordinates.

Some information in the iNavSet, such as MAC Address of WLAN hotspots, may be anonymized due to privacy reasons.

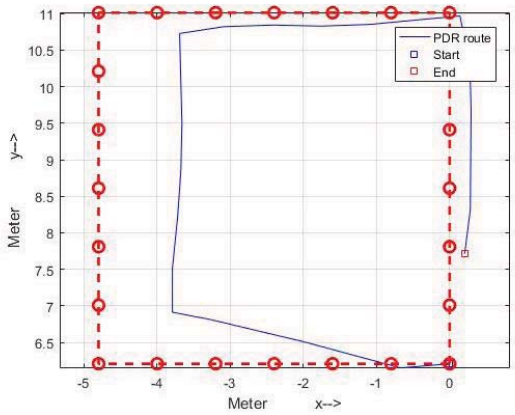

Figure 23.The comparison result of the trajectory obtained both from algorithm and ground truth

REFERENCE

Chernoguz, N., & Kagan, A. (2013). Pedestrian navigation system and method. *US*, *US8355888*.

Gruen, A., Remondino, F. and Zhang, L., 2005. The Bamiyan project: multi-resolution image-based modelling. In: Recording, Modeling and Visualization of Cultural Heritage, Taylor & Francis / Balkema, ISBN 0 415 39208 Xpp, pp. 45-54

Haala, N., 2014. Dense Image Matching Final Report. EuroSDR Publication Series, Official Publication No. 64, pp. 115-145.

He, X., Badiei, S., Aloi, D., & Li, J. (2014). WiFi iLocate: WiFi based indoor localization for smartphone. *Wireless Telecommunications Symposium* (pp.1-7). IEEE.

Inderst, F., & Santoni, F. P. M. (2015). 3D pedestrian dead reckoning and activity classification using waist-mounted inertial measurement unit.*International Conference on Indoor Positioning and Indoor Navigation*(pp.1-9). IEEE.

Kunze, K., Lukowicz, P., Partridge, K., & Begole, B. (2009). Which Way Am I Facing: Inferring Horizontal Device Orientation from an Accelerometer Signal. *International Symposium on Wearable Computers*(pp.149-150). IEEE Computer Society.

Nex, F., Gerke, M., Remondino, F., Przybilla, H. J., Bäumker, M., & Zurhorst, A. (2015). Isprs Benchmark for Multi-Platform Photogrammetry. PIA15+HRIGI15 – Joint ISPRS conference (Vol.II-3/W4).

Pei, L., Liu, J., Guinness, R., & Chen, Y. (2012). The evaluation of WiFi positioning in a Bluetooth and WiFi coexistence environment. (Vol.7, pp.1-6). IEEE.

Torres-Sospedra, J., Montoliu, R., Martinez-Uso, A., & Avariento, J. P. 2014. UJIIndoorLoc: A new multi-building and multi-floor database for WLAN fingerprint-based indoor localization problems. *International Conference on Indoor Positioning and Indoor Navigation* (pp.261-270).

Torres-Sospedra, J., Rambla, D., Montoliu, R., & Belmonte, O. (2015). UJIIndoorLoc-Mag: A new database for magnetic field-based localization problems. International Conference on Indoor Positioning and Indoor Navigation (pp.1-10). IEEE.

Three Levels Security Model for Secure Cloud Storage

Sheren A. El-Booz, Gamal Attiya and Nawal El-Fishawy

Computer Science and Engineering Dept.,
Faculty of Electronic Engineering, Menoufia University, Egypt
{eng.sheren1975@gmail.com, gamal.attiya@yahoo.com, nelfishawy@hotmail.com}

KEY WORDS: Cloud Computing, Privacy Preserving, Public Auditability, Third Party Auditor, One Time Password, Advanced Encryption Standard, Automatic Blocker Protocol.

ABSTRACT

The rapid growth in cloud computing field increases security service requirements. Many security techniques have been developed to improve data confidentiality and integrity on the cloud storage servers. In spite of these efforts, several organizations still suffer from some security breaches as Email spoofing, and data phishing. This paper tackles the security breaches problem and presents a three levels security model to ensure security of outsourced data on cloud data centers. The proposed system combines Time-based One Time Password (TOTP), Automatic Protocol Blocker (APB), and the Advanced Encryption Standard (AES). The proposed system is deployed in the real Amazon Web Services (AWS) cloud and the system performance is monitored by using the Cloud Watch service. The experimental results proved that the proposed system is efficiently secure and running normally on Elastic Beanstalk service. In addition, the proposed system does not influence the memory or CPU performance and does not make any overhead or complexity in the communication.

1. INTRODUCTION

Cloud computing has become the new evolution of distributed/utility computing field in which dynamically scalable and often virtualized resources are provided as a service over the Internet. It defined as Internet-based computing as it provides shared processing resources (e.g., networks, servers, storage, applications, and services) and data to computers and other devices on demand through the Internet. The National Institute of Standard and Technology (NIST) define cloud as a model for enabling ubiquitous, on-demand access to a shared pool of configurable computing resources, which can be rapidly provisioned and released with minimal management effort [1]. Cloud computing and related storages provide users and enterprises with various capabilities to store and process their data in data centers that may be located far from the user, ranging in distance from a city to the world.

Recently, several industries are turning to cloud technology as an efficient way to improve quality of services due to its capabilities to reduce overhead costs, downtime, and automate infrastructure deployment. Cloud computing allows companies to avoid upfront infrastructure costs (e.g., purchasing servers) and enables organizations to focus on their core businesses instead of spending time and money on computer infrastructure. As well, it allows enterprises to get their applications up and running faster, with improved manageability and less maintenance and enables Information Technology (IT) teams to more rapidly adjust resources to meet fluctuating and unpredictable business demand [2]. However, as with every new important phenomenon, there are issues that limit its widespread adoption. One of the major problems that arise with cloud data storage is security [3]. As data is stored in geographically distributed data centers, how users will get the confirmation about storing data. Moreover, the users of cloud must be able to use the cloud storage as the local storage, without worrying about the need to verify the data integrity and data consistency. Therefore, to ensure the correctness and integrity of users' data in the cloud, an effective and flexible data (storage) security model is required.

Many experts consider security in a cloud environment to be much tighter than in a traditional environment. The administrators and engineering who run cloud environments do not have to be generalists as is usually the case in traditional environments. They focus on securing environment or data. Recently, several researchers have been conducted with the aid of Third Party Auditor (TPA) to verify the data stored in the cloud storages and be sure that it is not tampered [4, 5]. The TPA can perform the auditing on behalf of a user and provide the audit report to the user. Using the TPA who have the expertise to audit data outsourced to the cloud storage servers is one of the safeguards that the data owners takes to ensure the protection of their outsourced data on cloud storage. This technique is also useful for Cloud Service Providers (CSP) to achieve its reputation by getting higher reliability, consistency and data integrity ratings or certificates from TPA to improve their business on commercial point of view. Other researchers enhance cloud security by using Automatic Protocol Blocker (APB) [6] or using Advanced Encryption Standard (AES) [7]. Nevertheless, in spite of these efforts, there are several organizations still suffer from some security breaches. For example, the Dropbox security breach, and iCloud 2014 leak [8].

This paper presents a new three levels security model to ensure security of outsourced data stored in cloud data centers. The proposed model combines Time-based One Time Password (TOTP), Automatic Protocol Blocker (APB), and the Advanced Encryption Standard (AES). The proposed model is deployed in real Amazon Web Services (AWS) cloud and the system performance is monitored by using the Cloud Watch service. The experimental results proved that the proposed system is efficiently secure and running normally on Elastic Beanstalk service without affecting functionality and performance of both the memory and CPU. It guarantees three primitives: integrity, confidentiality, and authentication. In addition, the proposed system does not make any overhead or complexity in the communication.

The rest of the paper is organized as follows. Section 2 introduces the security problem and challenges. Section 3

presents a simple survey of the related work. Section 4 describes the proposed methodology while Section 5 presents the simulation results and the experimental results when deploying the model on Amazon Beanstalk. Finally, Section 6 lists the concluding remarks.

2. SECURITY PROPLEM AND CHALLENGS

As the development of cloud computing, security issue has become a top priority, as shown in Figure 1 [9]. Briefly, for cloud computing, organizations' data are stored in geographically distributed large data centres. There may be a possibility that information belonging to different customers resides on same data server. Therefore, information leakage may arise by mistake when information for one customer is given to other [2]. Also, because the service provider can access the data that is in the cloud at any time, it could accidentally or deliberately alter or even delete information [10]. Additionally, hackers are spending substantial time and effort looking for ways to penetrate the cloud. Because data from hundreds or thousands of companies are stored on large cloud servers, hackers can gain control of huge stores of information through a single attack. For example, Dropbox had been breached in October 2014, having over 7 million of its users' passwords stolen by hackers. By having these passwords, they are able to read private data as well as have this data be indexed by search engines (making the information public) [8]. This delivers great incentive to public cloud computing service providers to prioritize building and maintaining strong management of secure services. Therefore, an effective and flexible data (storage) security model is required to ensure the correctness and integrity of users' data in the cloud.

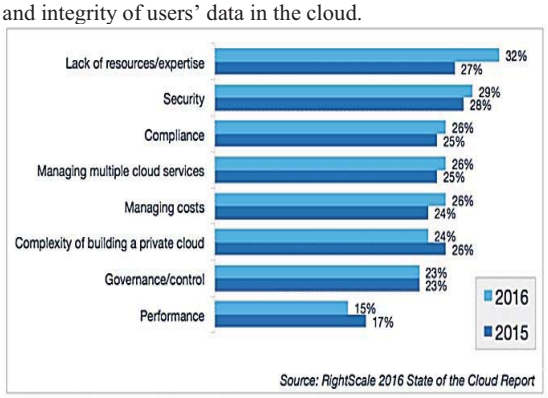

Figure 1. Cloud Challenges 2016 vs. 2015 [9]

3. RELATED WORK

Recently, several researchers are concerned with cloud security and challenges. They do their utmost to guarantee the power full and secure model for the users to ensure their data secrecy on the cloud. In [11], a public auditability model is proposed to improve data integrity on the cloud. The model is developed based on a combination between BLS–based homomorphic authenticator and MHT. This combination would support public auditability for fully dynamic data. In [12], a public auditability system called Provable Data Possession (PDP) is presented for ensuring possession of files on untrusted storages. This model employee the RSA–based homomorphic authenticators for data auditing. By using this model, public auditing is achieved, but it only supports static data. The authors improved their work by considering dynamic version of the PDP model. However, the system puts a priori restrict bound the number of queries and does not support fully dynamic data operations. That is it only allow basic block operations with limited functionality, and block insertions cannot be supported. In [13], the authors extend the work in [12] to fully support provable updates to the stored data files using rank-based authenticated skip lists. The scheme is considered a fully dynamic version of the PDP solution. To support updates, especially for block insertion, the extended PDP eliminates the index information in the tag computation in the PDP model and employ authenticated skip list data structure to authenticate the tag information of challenges or updated blocks first before the verification procedure. However, the efficiency of the extended PDP scheme remains unclear.

In [14], a new scheme called Proof of Retrievability (PoR) is proposed. Here, both spot-checking and error correcting codes are used to ensure both possession and retrievability of data files on the cloud storage system. However, the queries number a client can perform is also a fixed priori, and the introduction of precomputed sentinels prevents the development of realizing dynamic data updates. An improved PoR scheme is designed in [15] by using publicly verifiable homomorphic authenticators built from BLS signatures. Although the enhancement achieves the purpose, still, the authors only consider static data files.

In [16], the authors introduce a new concept of Third Party Auditor (TPA) to reduce online burden and keeps data integrity and privacy preserve. An improved technique of verifying data integrity on cloud by utilizing the concept of TPA is introduced in [17-19]. The authors approved that involving the TPA may associate additional risk to the confidentiality of data. Therefore, a new scheme is developed in [20] using Homomorphism Authenticators by Sphere Shaped Marker (HASSM) mechanism to authenticate and provide the cloud data accessing ability to the end users. Sphere Shaped Marker signature is used to audit the data without downloading the files. Nevertheless, the computational cost is reduced largely using the HASSM mechanism, as the file downloading is avoided during the verification.

4. PROPOSED METHODOLOGY

In [21], we have developed a secure cloud storage system combining the TOTP and the ABP. In this system, each data owner may rent a TPA for auditing process. For more authorization, the system used the ABP to fully protect the storage system from unauthorized TPA and used the TOTP for cloud users' verification to secure the cloud storage system against pre-activated users' accounts. Although the system combined two security levels, it suffers from the Man-In-The-Middle Attack (an attack over data transmission) that may tamper the metadata and keys through transmission. That is, after implementing the proposed system [21] in real cloud [24], we found that the data is hacked during transmission because the hackers deduced the generated keys.

In this section, we enhance the system proposed in [21] by adding a third level of security to ensure security of outsourced data in cloud data centers and overcome the Man-In-The-Middle Attack problem. The enhanced secure cloud storage system combines the TOTP [22], the APB [23] and the AES [7]. These three levels security enhances the authentication level of cloud security. In the enhanced system, the data owner (organization admin) controls all the privileges in system to be sure that who can access the outsourced data on cloud storage servers. User authentication is verified by using two-factor authentication:

the first is exercised with a username and password while the second is caused by the implementation of the TOTP. The ABP is used to fully protect the storage system from unauthorized TPA. Additionally, to increase security and overcome the Man-In-The-Middle Attack, the proposed model uses the AES to encrypt the generated keys between data owners and cloud server provider (CSP). Figure 2 shows the general framework of the proposed system while Figure 3 illustrates the phases where the three security levels are implemented in the proposed system.

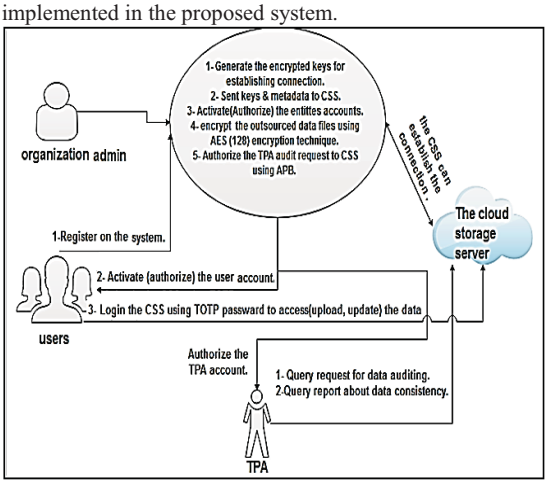

Figure 2. Enhanced Secure Cloud Storage System

The enhanced system has three phases:

• **Setup phase**: initializes the connection between the data owner (organization admin) and the cloud storage servers and generates the keys for all the system and metadata. In addition, the keys are encrypted by using the AES encryption technique for more secrecy on our system.

• **Data Access Phase**: the users can register in system, then login the system using two-factor authentication: a username and password, and the TOTP (a password token/code generated between the data owner and cloud server for one session and one period activation of user account). Before outsourcing data files, the data owner must encrypt their data by the AES to ensure data integrity.

• **Data Audit Phase**: the TPA, who rented by the organization admin, can login the system for an audit process upon the data owner need. The data owner first sends the keys and metadata to the TPA for auditing process. Then, the TPA sends audit request to the CSP, this audit request authorized with the ABP. If data owner doesn't authorize that process by activating the TPA account, then the TPA can't access system. Otherwise, the TPA can access the system and have the consistency query report form the service provider. Finally, the TPA sends the data report to data owner, as shown in Figure 2.

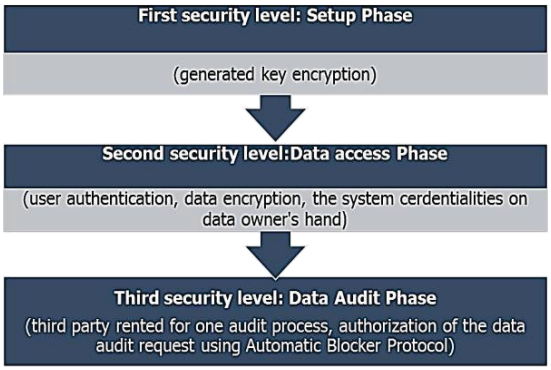

Figure 3. Security Levels of the Enhanced System

5. PERFORMANCE EVALUATION

This section presents the performance evaluation of the proposed model by using two scenarios. In the first scenario, the system performance is evaluated by simulation while in the second scenario, the system is implemented in real Amazon cloud and the performance is monitored by the cloud watch service.

5. 1 Simulation Results

The proposed system is implemented using Java enterprise edition web application running on apache tomcat server. The experiments are performed on traditional laptop Intel core™ 17-3517U CPU 240 GHZ, 4 GB RAM and 64 operating system. To evaluate the enhanced system, it should be tested against hacking the user credential ties, the TPA auditing credential ties, and hacking the data transmitted between the cloud entities.

The proposed system is evaluated using penetration test program called (Open Web Application Security Project (OWASP)) [27, 28]. The OWASP is an online community dedicated to web application security. This program has 10 tests, which are used to examine any web application security level. OWASP top 10 tests are: 1-Injection, 2– Broken Authentication and Session Management, 3- Cross-Site Scripting (XSS), 4- Insecure Direct Object References, 5- Security Misconfiguration, 6- Sensitive Data Exposure, 7- Missing Function Level Access Control, 8- Cross-Site Request Forgery (CSRF), 9- Using Components with Known Vulnerabilities, and 10– Invalidated Redirects and Forwards. In our system evaluation we used the most 5 tests that examine privacy preserving in our system. These tests include:

• **Test 1: SQL injection**. All the individuals (external users, internal users, and administrators).

•**Test 2: Broken Authentication and Session Management**. Anonymous attackers attempt stealing the users' accounts or spoofing their passwords, the generated TOTP for each user to be authenticated, generated for one session. And APB authorizes the TPA queries to CSP. Our provided solution to overcome that weakness.

• **Test 3**: **Sensitive Data Exposure**. Who can access our data is the important and dangerous issue in securing data, so we assume that organization admin is the only one who allows all interpreters in the system to access the data, and encrypting data using AES encryption technique before be outsourced to CSP.

• **Test 4: Cross-Site Request Forgery (CSRF**). The requests between interpreters mustn't hacked, so more

precautions are taken into account as (TOTP user login in system).

Test 5: Invalidated Redirects and Forwards. Examines the web application against HTTP sessions, if the sessions redirected in a true manner or not to assure the tokens between the interpreters and the server.

Table 1 presents the simulation results of different tests. It shows a comparative study between results obtained by applying the enhanced system, the proposed system [21] and the most recent existing system [25]. From the table, the test results of the recent privacy preserving system indicate that these systems have some vulnerability. However, the enhanced three level secure system increases the data confidentiality and availability. From Table 1, adding the AES for the key encryption in the enhanced system, could prevent the SQL injection. This proposal prevent the Man-In-The-Middle Attack that considered as a very dangerous attack where the attacker can tamper with the SQL data base and can access the system with these information. These results demonstrate the effectiveness and efficiency of the enhanced system when auditing shared data integrity. It guarantees three primitives, integrity, confidentiality and authentication. Table 2 summarizes how the enhanced system and other cloud storage system may overcome the security issues.

Table 1. Simulation Results

Penetrate Test	Recent system [25]		Proposed system [21]		Enhanced System	
	Result	Hacking	Result	Hacking	Result	Hacking
Test 1: SQL injection	**Intact:** No SQL injection	3 hours	**Intact:** No SQL injection	1 day	**Intact:** No SQL injection	3 days
Test 2: Broken Authentication	**Not Intact:** the authentication is broken due to the usage of static password	2 days	**Intact:** the users authentication not broken due to the user's login with TOTP	3 days	**Intact:** the users authentication not broken due to the user's login with TOTP	3 days
Test 3: sensitive data exposure	**Not Intact:** the outsourced data encrypted using DES encryption tech.	3 days	**Intact:** the outsourced data encrypted using AES (256 key length) encryption techno.	5 days	**Intact:** the outsourced data encrypted using AES (256 key length) encryption techno.	5 days
Test 4: CSRF	**Not Intact:** the hacked accounts	1 day	**Intact:** the accounts are secure due to TOTP valid for only one time and one session.	5 days	**Intact:** the accounts are secure due to TOTP valid for only one time and one session.	5 days
Test 5: invalid directs and forwards	**Not Intact:** the sessions managed using HTTP.	1 day	**Intact:** the sessions managed using HTTPS.	3 days	**Intact:** the sessions managed using HTTPS.	3 days

Table 2. Overcoming the security challenges by different systems.

Security Issue	Related Works [25]	Enhanced System
1- Authentication	1-The users use Email & static password to login the system.	1-The users can login the system using Email and password with a TOTP code.
2- Authorization	1- Any registered users can login the system. 2-The TPA rented upon agree between CSP and the data owner, so the deal between TPA&CSP appear.	1-Only the activated users 'accounts can login the system. 2-The data owner is the only one that can rent TPA and authorize him.
3- Data Integrity	The data query reports may lose due to the contract between CSP and TPA.	The data audit query is authorized with the APB.
4- Data confidentiality	The data encrypted by the DES.	1-The data encrypted by the AES that is low time consuming in encryption and decryption. 2- The keys are encrypted by the AES for guarantee the data confidentiality.
5- Data Privacy & Availability	1- Any registered users can access the data files. 2- The system credentials are on the CSP hands based on the SLA.	1- Only activated users' accounts with the TOTP can login the system. 2- The system credentials are on the data owners 'hand.so the CSP deal with the TPA not exists. 3- The TPA audit requests are authorized by the APB. Therefore, the CSP can't hide the data losses.

The second evaluation is done to teste the influence of the enhanced system on both the memory and CPU performance when uploading data files of different sizes from different users on the server. Figure 4 shows the CPU utilization when uploading data files of different sizes from 10 users onto the storage server by using the proposed system [21] and the enhance system while Figure 5 shows the memory usage. From Figures. 4 and 5, the enhanced system slightly increases the CPU utilization and memory usage. Figures. 6 and 7 show the CPU utilization and the memory usage at different number of users. From the Figures, the CPU utilization and the memory usage increase as the number of users increases. In addition, the enhanced system slightly increases the CPU utilization and memory usage comparing with the proposed system [21].

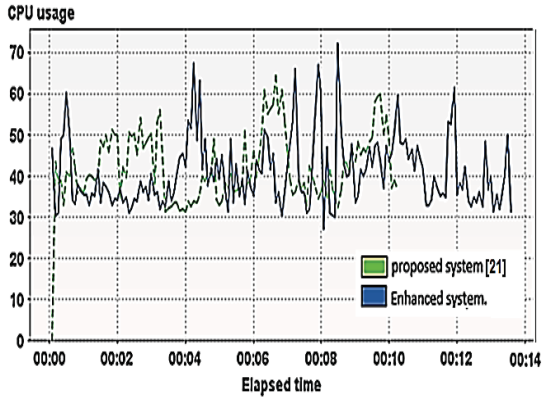

Figure 4. CPU usage by different systems at 10 users

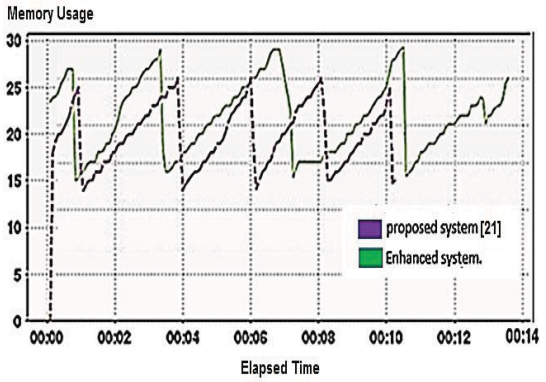

Figure 5. Memory usage by different systems at 10 users

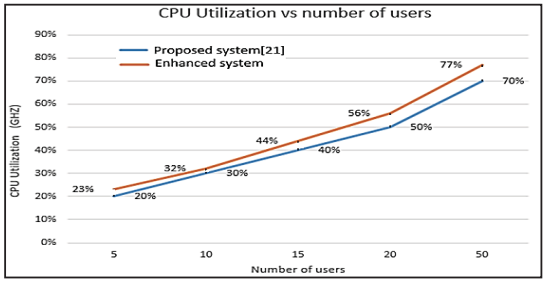

Figure 6. CPU Utilization at different number of users

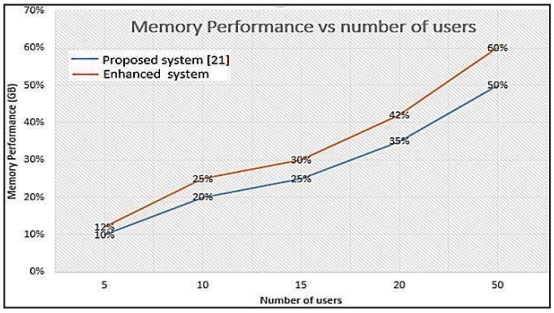

Figure 7. Memory Performance at different number of users

From the above simulation results, the enhanced system ensures security of outsourced data stored in cloud data centers with minimum influence on the functionality and performance of both the memory and CPU.

5.2 Experimental Results (AMAZON ELASTIC BEANSTALK Service)

To test the enhanced system in real environment, the proposed model is deployed in real Amazon Web Services (AWS) cloud and the system performance is monitored by using the Cloud Watch service [24]. Amazon is the most popular and reliable cloud storage service provider for web services. It provides scalable and inexpensive cloud services; Elastic Compute Cloud (EC2), Elastic Beanstalk, Simple Storage Services (S3), Cloud Watch… etc. The Elastic Beanstalk is Platform as a Service (PAAS) allowing users to create their applications or upload them to a definable set of AWS. These services including EC2 (computes the capacity of the cloud), Cloud Watch (monitoring of the resources and applications on cloud), and cloud load balancer (handles the details of your hosting environment such as capacity provisioning, load balancing, auto scaling, and application health monitoring) [24].

Deploying the proposed system on the Amazon Elastic Beanstalk service:

1. Register and have an account using the management console, as shown in Figure. 8, to use the Amazon Web Services (AWS) [26].
2. Choose the services that you want. Here, we suppose to use the Elastic Beanstalk service is a cloud deployment service that automate the web application. It supports web apps written with (PHP, JAVA, Ruby, Python, etc.) as shown in Figure. 9.
3. Deploy the proposed system on 64 bit Amazon Linux 2016.03 v2.1.1 running Tomcat 8 Java 8 platform on 8GB memory storage and on T1.Micro instances at a variant zones.
4. Use the Elastic Compute service to handle with the instances that we use, to run our system on them as shown in Figure. 10, they work efficiently on the instances.
5. Handle the data in the web application. We used AWS S3 (Simple Storage Service) that can used to restore and save any amount of data files, as shown in Figure 11.

6. Use Cloud Watch monitoring service of the AWS to show the performance of the web application, CPU utilization and time consumed for web app data files load.
7. By monitoring the performance of the systems using Cloud Watch service, the enhanced system improve the secrecy of the storage cloud system and doesn't increase the overhead in the CPU utilization comparing with the proposed system [21], as shown in Figures 12, 13.

Figure 8. Amazon Web Services (AWS) account sign in [26]

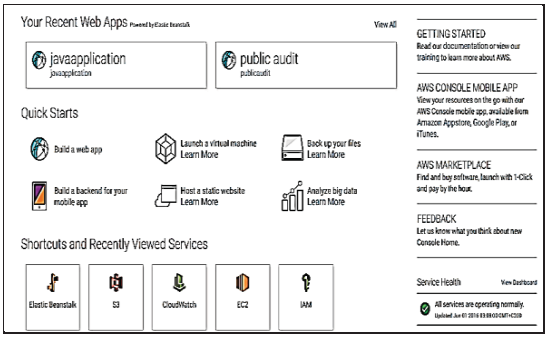

Figure 9. AWS web services & my applications

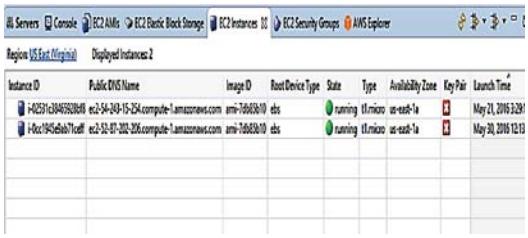

Figure 10. Elastic Computing Instances

Figure 11. AWS S3 services

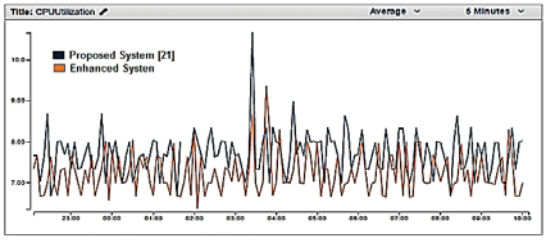

Figure 12. Cloud Watch monitoring of CPU Utilization in 5minutes

6. CONCLUSION

This paper tackled the privacy preserving public auditing and presented a novel three levels security model to ensure security of outsourced data in cloud data centers. The proposed model combined three efficient techniques; Time-based One Time Password (TOTP), Automatic Blocker Protocol (ABP), and Advanced Encryption Standard (AES). The proposed model is evaluated by both simulation and real experiments. Where, proposed model is deployed in real Amazon Web Services (AWS) cloud and the system performance is monitored by using the Cloud Watch service. The experimental results proved that the proposed system is running normally on Elastic Beanstalk service without affecting functionality and performance of both the memory and CPU. The results also demonstrated the effectiveness and efficiency of the proposed system when auditing shared data integrity. It guarantees three primitives: integrity, confidentiality and authentication. In addition, the proposed system does not make any overhead or complexity in the communication.

REFERENCES

[1] P. Mell and T. Grance, 2009 "*The NIST Definition of Cloud Computing*," National Institute of Standards and Technology, Information Technology Laboratory,. http://www.nist.gov/itl/cloud/

[2] https://en.wikipedia.org/wiki/Cloud_computing. Retrieved 01-09-2016.

[3] R. Kalaichelvi Chandrahasan, S Shanmuga Priya and L. Arockiam, 2012 "*Research Challenges and Security Issues in Cloud Computing*", International Journal of Computational,3(3).

[4] Abhishek Mohta, Ravi Kant Sahu,Lalit Kumar Awasthi, ,2012 "*Robust Data Security for Cloud while using Third Party Auditor*" International Journal of Advanced Research in Computer Science and Software Engineering Research Paper,2(2).

[5] V. Ashish Bhagat and Ravi Kant Sahu, 2013 "*Using Third Party Auditor for Cloud Data Security: A Review*" International Journal of Advanced Research in Computer Science and Software Engineering Research, 3(3).

[6] Rohini Kadlag and Rohit Devika, 2014 "A Survey on Automatic Protocol Blocker for Privacy-Preserving Public Auditing in Cloud Computing,"

International Journal of Innovative Technology and Exploring Engineering,3(12).

[7] Vishal R. Pancholi and Bhadresh P. Patel, 2016 "Enhancement of Cloud Computing Security with Secure Data Storage using AES," International Journal for Innovative Research in Science & Technology, 2(9).

[8] Hector Salcedo, "Google Drive, Dropbox, Box and iCloud Reach the Top 5 Cloud Storage Security Breaches List," Posted Nov 20, 2014. https://psg.hitachi-solutions.com/credeon/blog/google-drive-dropbox-box-and-icloud-reach-the-top-5-cloud-storage-security-breaches-list. Retrieved 09-06-2016.

[9] http://www.rightscale.com/blog/cloud-industry-insights/cloud-computing-trends-2016-state-cloud-survey. Retrieved 01-09-2016.

[10] Mark D. Ryan, 2011 "*Cloud Computing Privacy Concerns on Our Doorstep*," Communications of the ACM, 54, pp 36-38.

[11] C. Wang, Q. Wang, K. Ren, and W. Lou, 2013 "*Privacy-Preserving Public Auditing for Secure Cloud Storage*," IEEE Transactions on Computers, 62(2), pp. 1-12.

[12] G. Ateniese, R. D. Pietro, L. v. Mancini, and G. Tsudik, 2008, "*Scalable and Efficient Provable Data Possession*", Proceedings of the 4th International Conference on Security and Privacy in Communication Networks, pp. 1–10,.

[13] C. Erway, A. Kupcu, C. Papamanthou, and R. Tamassia, ,2009, "*Dynamic Provable Data Possession*", Proceedings of the 16th ACM conference on Computer and communications security (CCS), pp. 213-222.

[14] A. Juels, J. Burton, and S. Kaliski, 2007 "*Proofs of Retrievaliability for Large Files*", Proceedings of the 14th ACM Conference on Computer and Communications Security (ccs), pp. 584-597.

[15] H. Shecham, and B. Wates, 2008 "Compact Proofs of Retrievliablilty", Advances in Cryptology-ASIACRYPT, 5350, pp. 90–107.

[16] M. Venkatesh, M. R. Sumalatha and C. SelvaKumar, 2012, "*Improving public Auditability data possession in data storage security for cloud Computing*", Proceedings of the International Conference on Recent Trends in Information Technology, pp. 463-467.

[17] S. Bhagyashri and Y. B. Gurave. 2014, "*A Survey on Privacy Preserving Techniques for Secure Cloud Storage,"* International Journal of Computer Science and Mobile Computing, 3(2), pp. 675-680.

[18] B. Banu Priya, V. Sobhana, and Mishmala Sushith, 2015,"*Concise Survey on Privacy Preserving Techniques in Cloud*", International Advanced Research Journal in Science, Engineering and Technology,2(2).

[19] T. Paigude, T. A. Chavan, 2013 "*A survey on Privacy Preserving Public Auditing for Data Storage Security,"* International Journal of Computer Trends and Technology (IJCTT), 4(3), pp. 412-418.

[20] Sathiya MoorthySrinivasan,and Chnrasekar, 2014, "*Providing dynamic Audit services using Homomorphism Athenticators in Cloud Infrastructure"*, Journal of Theoretical and Applied Information Technology,67(3).

[21] Sheren A. El-Booz, Gamal Attiya and Nawal El-Fishawy,2015, "*A Secure Cloud Storage System Combining Time-based One Time Password and Automatic Blocker Protocol*", Proceedings of the 11th International Computer Engineering Conference, Cairo University, pp. 208-216, 29-30 December 2015. IEEE Explore, pp. 188-194, 978-1-5090-0275,.

[22] M. Raihi, S. Machani, M. Pei, and J. Rydell,2011 "*TOTP: Time-Based OneTime Password Algorithm," Request for Comments (RFC) 6238* .

[23] K. Kiran, K. Padmaj, and P. Radha,2012, "*Automatic Protocol Blocker for Privacy-Preserving Public Auditing in Cloud Computing*", International Journal of Computer Science And Technology (IJCST),3(1).

[24] www.aws.amazon.com. Retrieved 30/5/2016.

[25] Salve Bhagyashri1, Y.B.Gurav and P.G Scholar, 2014,"*Privacy-Preserving Public Auditing for Secure Cloud Storage*," IOSR Journal of Computer Engineering (IOSR-JCE), 16(4), pp. 33-38.

[26] www.aws.amazon.com/account. Retrieved 6-3-2016.

[27] www.owasp.org/index.php/Top_10. Retrieved April 2015.

[28] OWASP TESTING GUIDE, V4.0. www.owasp.org. Retrieved April 2015.

NOVEL HIGHLTY ISOLATED TRIPLEXER ANTENNA TO INTEGRATE AVIATION AND RADIO NAVIGATION SATELLITE SERVICES INCLUDING GPS, GLONASS, GALILEO, BEIDOW AND SAR WITH DIFFERENT COMMUNICATIONS APPLICATIONS

Mohamed A. H. Oweis, W. Swelam, Mohamed H. A. Abd El Azeem

Dept. of Electronics and Communications Engineering, Arab Academy for Science, Technology and Maritime Transport (AASTMT), Cairo, Egypt (mahassanv, wswelam)@gmail.com, mhabdazeem@aast.edu

KEY WORDS: Antenna, Triplexer, GPS, Aviation, Satellite Applications, Navigation

ABSTRACT:

This Novel Paper intends to propose a new concept of covering and integrating different satellite applications with single antenna system. This will enhance the capabilities of the navigation satellite systems by adding the ability to make use of the S-microwave frequency band communications applications such as (Mobile Satellite Services (MSS), Public Protection and Disaster Relief Services (PPDR) and Mobile to Satellite Services) on the same antenna added to both the lower and upper L-microwave frequency band where both the Aviation Radio Navigation Service (ARNS) and Radio Navigation Satellite Service (RNSS) including the GPS, Glonass, Galileo, BeiDou and SAR lies on the RF spectrum. The proposed approach is a highly isolated triplexer single antenna implemented on a two-layer printed circuit board. The triplexer antenna is designed and manufactured with a three different resonance frequencies separated to cover multiple separated satellite communication applications. The propounded design comprises of rectangular three-port antenna mounted on Rogers RO4350B two-layer substrate fed by microstrip transmission line and coplanar wave-guide (CPW). The overall antenna's dimensions are 80.5 x 77 mm2. The presented antenna design has been simulated and optimized using finite integration technique (FIT) with the commercial CST studio. The obtained results show port isolation -20dB in average with good impedance matching between -18 and -36dB at each port of the operating frequencies. The achieved directivity is 3.3, 4.5 and 6.2 dBi at 1.5, 2.5, and 3.6 GHz with 97%, 90% and 66% high efficiency respectively.

1. INTRODUCTION

The satellite communication industry is in continuous development from legacy satellites to modernized satellites which requires intensive research and enhancement of each component with focus on the RF components. Broadening the applications that could be covered within the same antenna system directly enhances the satellite overall capabilities. The legacy satellites are usually equipped with multiple transceivers for different purposes. The industry researchers continuously investigating a method to significantly reduce the size and weight of multiplexers-diplexers, triplexers, and quadplexers—for multi-carrier radio frequency (RF) signal transmission to significantly reduce GPS satellite's launch weight and cost to orbit. Thus, equipping the GPS satellite RF system with triple- or multiband antenna system will increase the overall satellite performance, since it is quite complicated to integrate the antenna elements in a limited compact space with isolation controlled. In previous studies, the followed different techniques to maintain good isolation between different transceivers which summed up as follows: (i) using decoupling and matching network [1-2]. Consequently, the circuit size will increase in contradiction with the obliged limited space. (ii) Development of multiband antennas with common structure as monopole, slotted antennas [3-4]. Achieving single input configuration of these multiband antennas whenever used with multiple transceivers is difficult and requires adding filters to facilitate the connectivity, which will add extra elements [5]. Therefore, many researchers approached the insertion of the filters and antennas termed as antenna triplexer –duplexer. Defected ground structure (DGS) commonly used approach [6-8]. This helped minimizing the required space and enhanced isolation. Nevertheless, there is scarcely published highly isolated frequency triplexer-antenna as demonstrated in [9]. To the best of authors' knowledge, antenna-triplexer intended to be used in GPS III satellites [10]. Based on aforementioned approaches, a competent integrated triplexer antenna is proposed in this work, which is capable of achieving multi-band operations highly isolated, supporting triple band operated simultaneously, with no need to terminate any of the ports and extra filtering structure can be reduced to preserve the compactness when necessary. This will help the modernized GPS satellite systems enhancement.

2. ANTENNA DESGN, CONFIGURATION AND CHARACTERIZATION

The proposed triplexer antenna has a three-port configuration as depicted in Fig.1 consists of a rectangular loop as the radiating element and two rectangular slots, forming two-layered design where port-2 & port-3 lie on the front layer and port-1 on the back layer. The radiating element is excited at port-1 via a coplanar waveguide (**CPW**) feed line. Moreover, two microstrip feed lines are optimised carefully for port-2 & port-3 excitation which are considered as indirect feeding. In

order to secure good isolation as targeted between the three-ports, the microstrip feed lines are on the top layer whilst the rectangular and the **CPW** feed lines are placed at the bottom layer. Therefore, two transitions will exist namely; the microstrip-to-**CPW** transition and microstrip-to-slot transition.

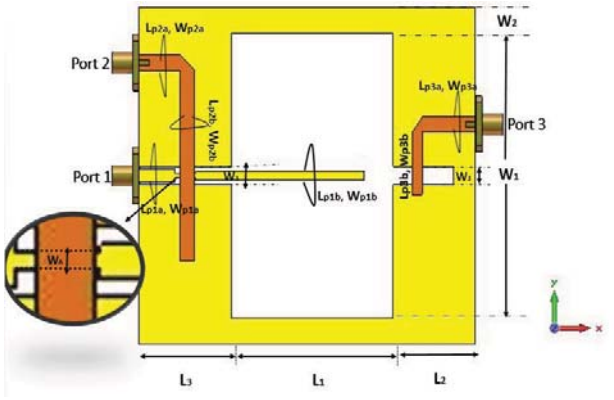

Fig. 1: Geometry of the proposed antenna-triplexer.

The presented antenna is designed and fabricated on a Rogers RO4350B substrate with relative permittivity (ε_r) 3.48, height (**h**) 1.524 mm, tangential loss (**δ**) 0.0037 and conductor thickness (**t**) 0.035 mm [11]. The design is simulated and fabricated with 50 Ohms SMA connectors on the three-ports. Table 1 shows the details of the antenna optimised parameters.

Para meter	Value (mm)	Param eter	Value (mm)	Para meter	Value (mm)
L1	38.9	L_{p3b}	14.3	W_{p2a}	3.5
L2	19.6	L_{p3a}	12.6	W_{p2b}	3.5
L3	22	W1	65	W_{p1b}	2
L_{p1a}	8.5	W2	6	W_{p3b}	2.4
L_{p2b}	43.5	W3	4	W_{P3a}	3.5
L_{p2a}	9.8	W_A	0.8		
L_{p1b}	40.5	W_{P1a}	4.9		

Table 1: Dimensions distribution of the proposed antenna.

Adjustment of the operating frequency centre f1 at port-1 can be achieved by properly tuning the length of Lp1b. Enhancement of the impedance matching is obtained by slightly increasing the width of Wp1b. Note that, optimising the matching by Wp1b will affect the operating centre frequency f2. Since increasing the width will shrink the slot that is excited by the feed line of port- 2, therefore, the operating frequency f2 should be readjusted after finishing port 1 optimization as they represent a transition loop. The constriction in the centre line WA of the co-planar feed line of port 1 is very sensitive element to changes and carefully optimized to achieve better matching results. Optimizing the operating frequency f2 can be done by tuning Lp2b and the matching can be optimized by L3. Decreasing L3 will enhance the matching for f2 but this will increase L1 that subsequently will affect f1 because it will enlarge the perimeter of the rectangular loop that is around one wavelength of the lowest operating frequency f1. Therefore, ports 1 and 2 must be optimized carefully as illustrated earlier in order to achieve the best performance. Port 3 can be optimized individually. The length of the microstrip feed line Lp3b greatly shifts the operating frequency f3. The length and width W3 of the corresponding slot enhance the matching. Adjusting the operating frequency f3 to be at the middle between f1 and f2 greatly enhances the isolation between ports since port 3 is placed at the opposite side of the other two ports.

3. RESULTS AND DISCUSSION

As a fruitful result of the above mentioned design hierarchy with intensive optimization of the crucial parameters, the required performance is achieved; the effective antenna area occupies merely 80.5x77 mm^2. The simulated s-parameters are illustrated in Fig. 2 showing multiband resonance at triple frequency bands 1.5, 3.6 and 2.5 GHz operating at port 1, 2, 3 respectively. Fig. 3 shows high isolation between the three operating frequencies nearly -19dB. The associated bandwidths that are recorded under -10dB reflection coefficient for the three operating frequencies are 710, 300 and 400 MHz respectively. The targeted frequency range scope of the designed and fabricated triplexer-antenna to cover both L-band and S-band satellite frequency bands ranges from 1-2 GHz and 2-4 GHz respectively, which allows covering and integrating different satellite applications with a single antenna system. This will enhance the capabilities of the navigation satellite systems which operate within L- microwave frequency band at 1.57 GHz by adding the ability to make use of the S-microwave frequency band communications applications, such as Mobile Satellite Services (**MSS**), Public Protection and Disaster Relief Services (**PPDR),** on the same antenna added to both the lower and upper L-microwave frequency band where both the Aviation Radio Navigation Service (**ARNS**) and Radio Navigation Satellite Service (**RNSS**), including the GPS, Glonass, Galileo, BeiDou and SAR, lie on the same spectrum. Moreover, the key achievement of the proposed validated design is that the overall isolation between the three operation frequencies is better than -20dB due to different excitation modes of the circuit itself. The excitation direction is constructive where desired and destructive where unneeded, which enables multiband operating frequencies with neither adding filtering components nor terminating any of the three ports. The simulated directivity versus theta variations in Fig. 4 is showing a directive pattern toward each resonating centre frequency. Total efficiency in Fig. 5 shows higher efficiency, more than 90%, for port 1 and port 3 operating frequencies and lower efficiency, 65%, for port 2 operating frequency due to better matching for port 1 and port 3 in comparison with

port 2 operating frequency. The farfield directivity shows directive radiation with main lobe magnitude 3.37, 6.31 and 4.55 dBi with total efficiencies at the triple band centre frequencies about 97%, 66% and 90% respectively. The simulated surface current distribution is shown in Fig. 6 at each port. Once port-1 is fed via the SMA-connector, the CPW feed line generates multi-mode excitation. Fig. 6(a) shows the current flows from port-1 towards the CPW feed line, which leads to electric field induction from the rectangular loop arms, in parallel; the microstrip-to-CPW transition produces an odd-mode excitation. The feeding from port-2 leads to coupling that occurs from the microstrip line to the CPW feed line which supports the excitation at port-1 and shows a clear excitation along the microstrip line as illustrated in Fig. 6(b). Port 3 uses a microstrip-to-slot transition which produces a bi-directional excitation mode, the current is concentrated along the microstrip feed line and across the slot in the opposite plane as shown in Fig. 6(c). Furthermore, a minimal current is transferred to the opposite ports 1 & 2 which results in good isolation.

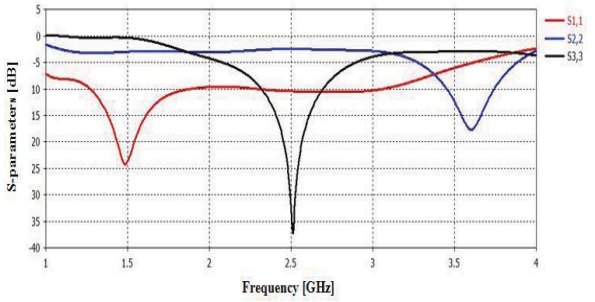

Fig. 2: Simulated S-parameters of the proposed antenna.

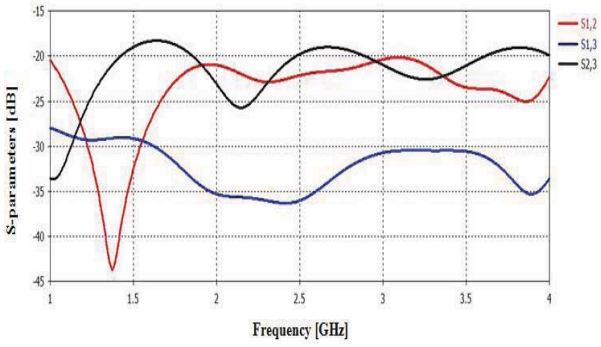

Fig. 3: Simulated isolation of the proposed antenna.

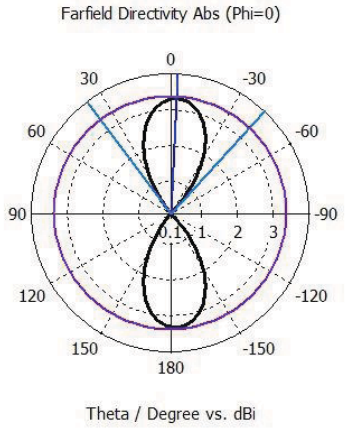

(a)

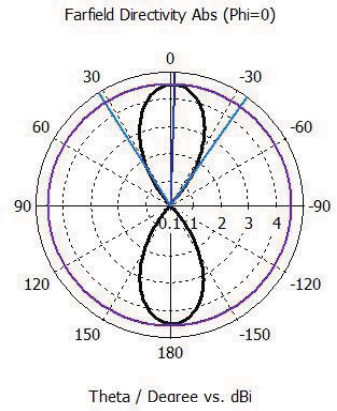

(b)

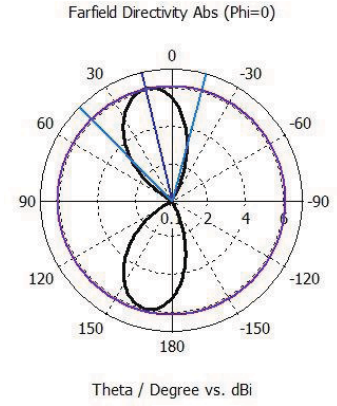

(c)

Fig. 4: The simulated directivity in dBi versus Theta in degree. (a) Port-1, (b) Port-2, (c) Port-3.

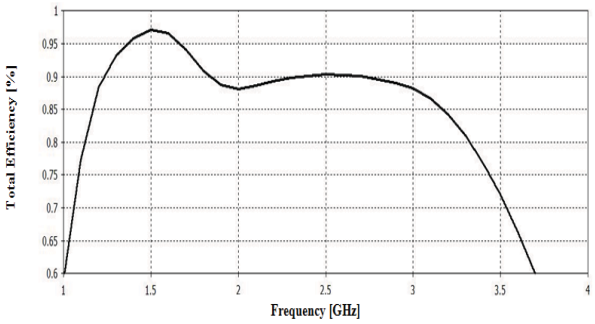

Fig. 5: Total efficiency of the proposed antenna.

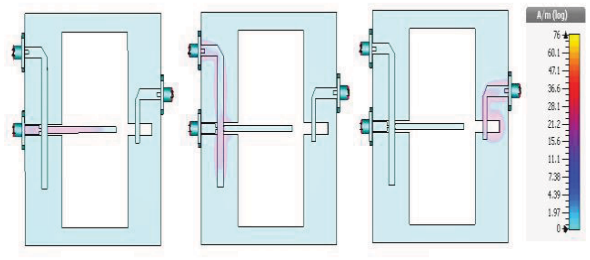

(a) (b) (c)

Fig. 6: Current distribution through. (a) Port-1, (b) Port-2, (c) Port-3.

4. FABRICATION AND MEASUREMENT

Three-port triplexer antenna is fabricated on Rogers RO4350B substrate with overall dimensions of 80.5 x 77 mm^2. The fabricated triplexer-antenna is shown in Fig.7. Laboratory chemical etching manufacturing process has been used for fabrication. The measured and simulated results of s-parameters (S11, S22, and S33) are illustrated in Fig. 8 while insertion loss (S12, S13, S23) versus frequency is illustrated in Fig. 9. Tracing the measured results from the fabricated antenna is showing a similar behaviour and trend of the reflection coefficient and isolation simulated results. The little difference between simulated and measured s-parameters is due to the connection loss between printed circuit board and SMA connectors, soldering process and tester connection attenuation. The presented triplexer antenna design is well validated with the fabrication measurements for covering the desired bands with high isolation between the three ports.

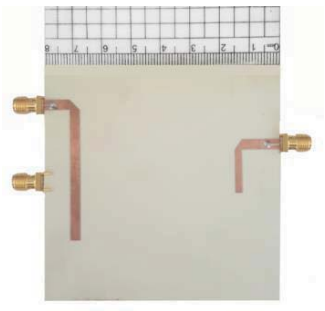

(a)

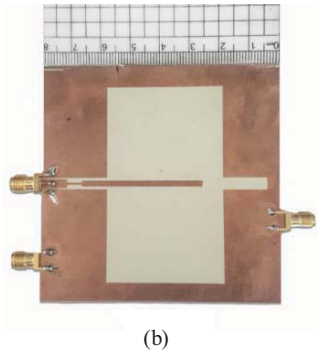

(b)

Fig. 7: Fabricated triplexer-antenna. (a) Front Layer, (b) Back Layer

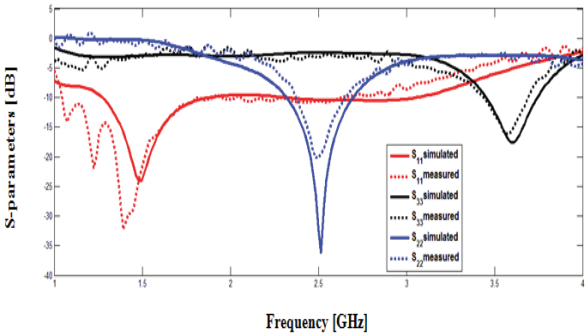

Fig. 8: Comparison of simulated and measured S-parameters.

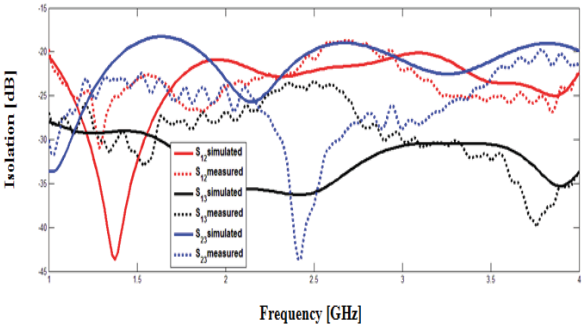

Fig. 9: Comparison between simulated and measured isolation.

5. CONCLUSION

A highly isolated triplexer-antenna has been reported. The design has an excellent isolation better than -20 dB, covering triple microwave frequency bands resonating from separate three ports 1, 2, 3 at centre frequencies 1.5, 3.6, 2.5 with operating bandwidth 710, 300 and 400 MHz and good directivity achieved 3.3, 4.5 and 6.2 dBi respectively. Furthermore, the antenna design has combined the privilege of simplicity and compact size which eases the integration with the satellite systems. The triplexer antenna optimised design is well fabricated using chemical etching process; fabricated measured s-parameters and insertion losses showed similar

behaviour in comparison with the commercial CST microwave studio simulated antenna design results. The measured good three-port isolation is achieved via orthogonal intrinsically even, odd and bi-directional excitation modes. As a result, triplexer antenna design is validated which would allow the industry to consider the proposed design in the fore mentioned applications.

REFERENCES

1.Addaci, R., A. Diallo, C. Luxey, P. L. Thuc, and R. Staraj, "Dual-band WLAN diversity antenna system with high port-to-port isolation," IEEE Antennas Wireless Propag. Lett.,Vol. 11, 244-247, 2012.

2. Yu, Y., Y. Jiang, W. Feng, S. Mbayo, and S. Chen "Compact multiport array with reduced mutual coupling," Progress In Electromagnetics Research Letters, Vol. 39, 161-168, 2013.

3. J. Anguera, A. Andujar, and C. Garcia, "Multiband and small coplanar antenna system for wireless handheld devices," IEEE Trans. Antennas Propag., vol. 61, no. 7, pp. 3782–3789, Jul. 2013.

4. Swelam, W., "Triple-band T-shape microstrip patch antenna with slotted ground plane for PCS, UMTS and bluetooth communication systems," Proc. IEEE AP-S Int. Symp., 1-4, Jul. 2010.

5.H. Liu, W. Xu, Z. Zhang, and X. Guan, "Compact diplexer using slotline stepped impedance resonator," IEEE Microw. Wireless Compon. Lett., vol. 23, no. 2, pp. 75–77, Feb. 2013.

6.Y. Hao and C. G. Paini, "Isolation enhancement of anisotropic UC-PBG microstrip diplexer patch antenna," IEEE Antennas Wireless Propag. Lett., vol. 1, pp. 135–137, 2002.

7.Y. Chung, S.-S. Jeon, D. Ahn, J.-I. Choi, and T. Itoh, "High isolation dual-polarized patch antenna using integrated defected ground structure," IEEE Microw. Wireless Compon. Lett., vol. 14, no. 1, pp. 4–6, Jan. 2004.

8. Mahmoud, S., W. Swelam, and M. Hassan, "Parametric study of slotted ground microstrip patch antenna," IOSR Journal of Electronics and Communication Engineering (IOSR-JECE), Vol. 11, No. 1, 01, 08, Ver. III, Jan.-Feb. 2016.

9. Cheong, P., K.-F. Chang, W.-W. Choi, and K.-W. Tam, "A highly integrated antenna-triplexer with simultaneous three-port isolations based on multi-mode excitation," IEEE Trans. Antennas Propag., Vol. 63, No. 1, 363,368, Jan. 2015.

10. www.gps.gov

EVALUATION OF DISTINCTIVE FEATURES FOR LAND/WATER CLASSIFICATION FROM MULTISPECTRAL AIRBORNE LIDAR DATA AT LAKE ONTARIO

S. Morsy *, A. Shaker, A. El-Rabbany

[a] Department of Civil Engineering, Ryerson University, 350 Victoria St, Toronto, ON M5B 2K3, Canada - (salem.morsy, ahmed.shaker, rabbany)@ryerson.ca

Commission I, WG I/7

KEY WORDS: LiDAR, Multispectral, Classification, Roughness, Point Density, Intensity Density

ABSTRACT:

Land/Water classification is very crucial for coastal zones management, flood monitoring, water resources assessment, and surface water area estimation. Over the past decades, remotely sensed data have been employed in land/water classification. Recently, multispectral airborne LiDAR sensors, which acquire a diverse spectral reflectance values (i.e., intensity) from different objects on the surface of the Earth, have been developed. In this research, six distinctive features, based on the geometric and radiometric attributes of multispectral LiDAR point clouds, are extracted and assessed for land/water classification. The six features can be categorized as following: a) two elevation-based features, namely elevation difference (ΔZ) and Roughness (R); b) two intensity-based features, namely intensity coefficient of variation (ICOV) and intensity density (ID); and c) two geometry-based features, namely point density (PD) and multiple returns (MR). A study area located at Lake Ontario in Scarborough, Ontario, Canada was tested to evaluate the performance of the six features for land/water classification. The LiDAR data were collected by the world's first multispectral airborne LiDAR sensor "Optech Titan" at three wavelengths (1.550, 1.064, and 0.532 μm). The land/water boundary was digitized from an aerial image, captured simultaneously during the survey mission, in order to validate the land/water classification results. Generally, the achieved results from the elevation-based features provide higher overall accuracy (more than 81%) than the geometry-based and the intensity-based features.

1. INTRODUCTION

Airborne Light Detection And Ranging (LiDAR) is widely used in remote sensing applications. LiDAR elevation and intensity data, collected using single wavelength airborne LiDAR systems, have been utilized for land/water classification (Höfle et al., 2009). Brzank et al. (2008) delineated the land/water boundaries in the Wadden Sea with the assumption of that the water bodies exhibit low elevation and low intensity. However, this is not always the case for inland water areas, which might exhibit high elevation. Schmidt et al. (2012) introduced a point-wise supervised classification using LiDAR data collected at the Wadden Sea based on conditional random fields. The maximum completeness and correctness of the classified water points were 82.4% and 66.3%, respectively. Smeeckaert et al., (2013) used a set of features, extracted from 3D LiDAR points, to train a Support Vector Machine (SVM) algorithm to classify water areas. The previous studies relied on prior knowledge of land/water interface to aid in the supervised classification process and used LiDAR data collected at single wavelength.

Recently, Teledyne Optech has launched the world's first airborne multispectral LiDAR sensor "Optech Titan". This sensor collects LiDAR data in three channels C1, C2, and C3 at wavelengths of mid-infrared (MIR): 1.550 μm, near-infrared (NIR): 1.064 μm, and green: 0.532 μm, respectively. The data are acquired at pulse repetition frequencies (PRF) range from 50 to 300 kHz/channel, with maximum combined channels PRF of 900 kHz. The sensor's scan frequency and scan angle is up to 210 Hz and ±30°, respectively. The typical altitude ranges from 300 to 2000 m above ground level (AGL) in all channels for topographic applications, and from 300 to 600 m AGL in C3 for bathymetric applications. Combining the multispectral LiDAR data collected in the three channels facilitates new applications for LiDAR such as land/water classification.

Over the past year, a few studies have been reported on the use of the Optech Titan multispectral LiDAR data for land cover classification. Wichmann et al. (2015) analysed the spectral patterns of different land covers and showed that the intensity values could be potentially used in land cover classification. Morsy et al. (2016a) created three intensity bands and a digital surface model (DSM) from LiDAR data. The maximum likelihood classifier was then applied to different band combinations. A dataset of an urban area was classified into six classes, namely buildings, trees, roads, grass, soil, and wetland. An overall accuracy of 65.5% was achieved using the combined three-intensity bands, and improved to 72.5% by incorporating the DSM.

In addition, investigations were conducted to explore the use of the Optech Titan data in one specific application, for example, tree species classification (Yu et al., 2016), vegetation mapping (Nabucet et al., 2016), or road mapping (Karila et al., 2017). Fernandez-Diaz et al. (2016) presented an overview on the use of the multispectral Titan data in different applications, such as ground cover classification, measuring water depths in shallow water areas, and forestry mapping. However, nothing was reported on land/water classification.

* Corresponding author

In our previous work, we investigated the use of three Normalized Difference Water Indices (NDWIs) in land/water classification (Morsy et al., 2016b). The intensity data collected by the Optech Titan at the three channels were employed to form $NDWI_{G\text{-}NIR}$, $NDWI_{G\text{-}MIR}$, and $NDWI_{NIR\text{-}MIR}$ as follows:

$$NDWI_{G-NIR} = \frac{G - NIR}{G + NIR} \quad (1)$$

$$NDWI_{G-MIR} = \frac{G - MIR}{G + MIR} \quad (2)$$

$$NDWI_{NIR-MIR} = \frac{NIR - MIR}{NIR + MIR} \quad (3)$$

where *MIR*, *NIR,* and *G* are the intensity values from the MIR, NIR, and green wavelengths, respectively.

The results showed that the NDWIs could not be directly used for land/water classification. This is due to that the water body and vegetation areas exhibit a close range of intensity values at the three wavelengths (Morsy et al., 2016b). As a result, the water points were misclassified as vegetation points.

This paper aims to evaluate a set of point features, extracted from multispectral LiDAR data, in land/water classification. In this study, two elevation-based features, two intensity-based features, and two geometry-based features are extracted and evaluated for this application.

2. STUDY AREA AND DATASET

The land/water classification was tested on a study area covering part of Lake Ontario, located in Scarborough, Ontario, Canada, and other land objects, such as roads, grass, and tress, shown in Figure 1. The multispectral LiDAR data were acquired using the Optech Titan sensor on September 3rd, 2014. The data specifications are provided in Table 1. A subset with a dimension of 400 m by 200 m was clipped to be tested. Figure 2 shows the LiDAR point clouds.

Figure 1. Google image showing the study area

Parameter	Specification
Wavelength	Channel 1 = 1.550 µm Channel 2 = 1.064 µm Channel 3 = 0.532 µm
Altitude	420 m
Scan Angle	±15°
PRF	200 kHz/channel; 600 kHz total
Scan Frequency	200 Hz
Number of returns	Up to 4 returns
Number of points	Channel 1 = 971,482 Channel 2 = 1,123,409 Channel 3 = 1,403,382

Table 1. LiDAR data specifications

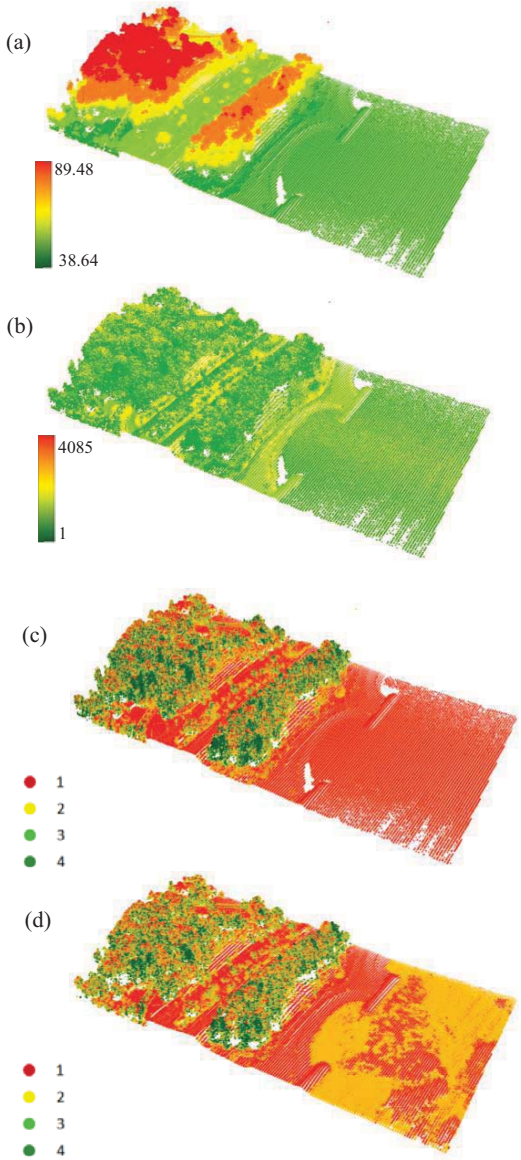

Figure 1. LiDAR point clouds from C2 colorized by: (a) elevation, (b) intensity, and (c) number of returns, and from C3 colorized by: (d) number of returns

3. METHODOLOGY

The overall workflow of this study is shown in Figure 4. Six point features were extracted from the LiDAR data. These features are divided into three categories, namely elevation-, intensity-, and geometry-based features. For each point, the features were extracted from the neighbouring LiDAR points within a circle with radius *r* equals to double average point spacing (i.e., 0.5 m) in order to preserve the land water boundary at high resolution. The water points were classified

based on the following assumptions. First, the water points are assumed to have the lowest intensity values in the scene. Second, the intensity variation is higher in water bodies than land areas due to the wavy effect and different scan angles. Third, the MIR and NIR wavelengths are usually used to acquire LiDAR data from the water surface, while the green wavelength is used to acquire LiDAR data from the water surface and bottom due to its ability in penetrating water bodies. These characteristics increase the usefulness of LiDAR data in land/water classification, when the green channel is combined with MIR or NIR channel. A threshold value was then applied to each extracted feature in order to classify all water and land points. The details of those point features are presented in the following subsections.

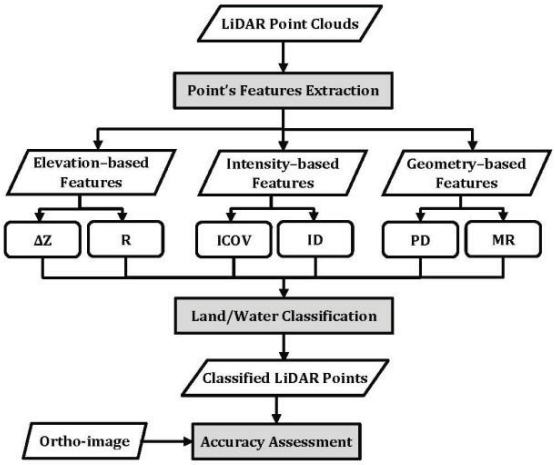

Figure 3. The overall workflow

3.1 Elevation-based Features

Assuming a LiDAR point p_i and a point of its neighbouring points is j, where $j = 1, 2, 3, \ldots, n$, and n is the total number of neighbouring points of p_i.

3.1.1 Elevation Difference (ΔZ): Within the searching circle, the ΔZ between the maximum and the minimum elevation was calculated. The water surface was assumed to be horizontal in C1 and C2, and hence the $\Delta Z^{C1 \text{ or } C2}$ was considered minimal. In contrary, in C3, the water body should have sufficient water depth and can be controlled by the maximum detectable water depth by the sensor. The land or water point was then classified based on thresholds values $H_{thresh1}$ and $H_{thresh2}$ as follows:

$$\begin{cases} p_i \text{ is a water point, if } \Delta Z_{p_i}^{C1 \text{ or } C2} \le H_{thresh1} \\ \qquad\qquad \& \; H_{thresh1} < \Delta Z_{p_i}^{C3} \le H_{thresh2} \\ p_i \text{ is a land point, otherwise} \end{cases} \quad (4)$$

3.1.2 Roughness (R): The roughness is the standard deviation of the elevation, which can be calculated from Equation (5), where Z is the point's elevation.

$$R_{p_i}^{C1 \text{ or } C2 \text{ or } C3} = \frac{1}{n-1}\sum_{j=1}^{n}(Z_j - \overline{Z})^2 \quad (5)$$

The R was assumed to be increased for water body in C3 (R^{C3}) rather than C1 (R^{C1}) or C2 (R^{C2}). Based on that, a threshold value R_{thresh} was selected to classify land and water points as follows:

$$\begin{cases} p_i \text{ is a water point, if } R_{p_i}^{C1 \text{ or } C2} \le R_{thresh} \\ \qquad\qquad \& \; R_{p_i}^{C3} > R_{thresh} \\ p_i \text{ is a land point, otherwise} \end{cases} \quad (6)$$

3.2 Intensity-based Features

Intensity coefficient of Variation (ICOV): The water body exhibits relatively high intensity variation. This is because the wavy effect and that the data were collected at different scan angles. This characteristic was used as such the $ICOV$ was increased in water body rather than land areas. For each LiDAR point in any channel, the $ICOV^{C1 \text{ or } C2 \text{ or } C3}$ can be calculated from:

$$ICOV_{p_i}^{C1 \text{ or } C2 \text{ or } C3} = \frac{\frac{1}{n-1}\sum_{j=1}^{n}(I_j - \overline{I})^2}{\frac{1}{n}\sum_{j=1}^{n} I_j} \quad (7)$$

where I is the LiDAR point's intensity value. A threshold value $ICOV_{thresh}$ was then applied to classify LiDAR points as follows:

$$\begin{cases} p_i \text{ is a water point, if } ICOV_{p_i}^{C1 \text{ or } C2 \text{ or } C3} \ge ICOV_{thresh} \\ p_i \text{ is a land point, otherwise} \end{cases} \quad (8)$$

3.2.1 Intensity Density (ID): The intensity density is defined as the percentage of points, which have intensity values less than threshold value I_{thresh}. For each point, $ID^{C1 \text{ or } C2 \text{ or } C3}$ can be calculated form:

$$ID_{p_i}^{C1 \text{ or } C2 \text{ or } C3} = \frac{no.\ of \text{ points } with\ I \le I_{thresh}^{C1 \text{ or } C2 \text{ or } C3}}{n} \cdot 100 \quad (9)$$

The water points were assumed to have ID less than certain percentage ID_{thresh} as follows:

$$\begin{cases} p_i \text{ is a water point, if } ID_{p_i}^{C1 \text{ or } C2 \text{ or } C3} \ge ID_{thresh} \\ p_i \text{ is a land point, otherwise} \end{cases} \quad (10)$$

3.3 Geometry-based Features

3.3.1 Point Density (PD): The point density was calculated for each LiDAR point. In water body, the PD was assumed to be increased in C3 (PD^{C3}) rather than C1 (PD^{C1}) or C2 (PD^{C2}). So that, a threshold value PD_{thresh} was selected to classify land and water points as follows:

$$\begin{cases} p_i \text{ is a water point, if } PD_{p_i}^{C1 \text{ or } C2} \le PD_{thresh} \\ \qquad\qquad \& \; PD_{p_i}^{C3} > PD_{thresh} \\ p_i \text{ is a land point, otherwise} \end{cases} \quad (11)$$

3.3.2 Multiple Returns (MR): A double returns are recorded from the water body in C3, while single returns are recorded in C1 or C2. Based on these characteristics, the water and land points can be classified.

3.4 Accuracy Assessment

The land/water boundary was digitized from an aerial image, captured during the survey mission. Table 2 provides the number of water and land points in each channel. The classification results were evaluated through the completeness and correctness (Heipke et al., 1997) as follows:

$$Completeness\ (\%) = \frac{TP}{TP + FN} \cdot 100 \quad (12)$$

$$Correctness\ (\%) = \frac{TP}{TP + FP} \cdot 100 \quad (13)$$

where TP: is the true positive, representing the point which was classified as water in the classification process and reference data; FN: is the false negative representing the point which was classified as land in the classification process and as water in the reference data; and FP: is the false positive, representing the point which was classified as water in the classification process and as land in the reference data.

Channel	Water	Land
C1	137,383	834,099
C2	192,294	931,115
C3	518,803	884,579

Table 2. LiDAR reference points

4. RESULTS AND DISCUSSIONS

In this section, the classified LiDAR points using the six point features are presented. The threshold values were selected by experiments to minimize the type I (FP) and II (FN) errors.

4.1 Elevation-based Features Results

To preserve the horizontal water surface in C1 or C2, the $H_{thresh1}$ was set to 0.5 m. The maximum recorded water depth in C3, $H_{thresh2}$, was set to 10 m. The R_{thresh}, which controlled the R of LiDAR water point's elevation with respect to its neighbouring points, was selected to be less than or equal 0.1 m in C1 and C2 and greater than 0.1 m in C3. The classified LiDAR points based on the ΔZ and R features are shown in Figure 4. Table 3 summarizes the accuracy measures of the classified LiDAR points using the ΔZ and R features.

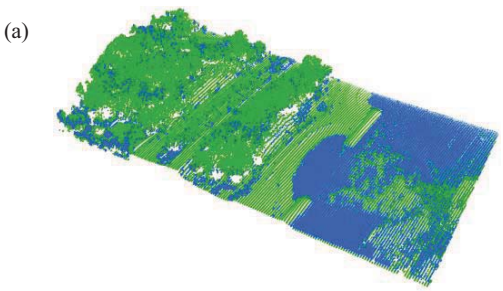

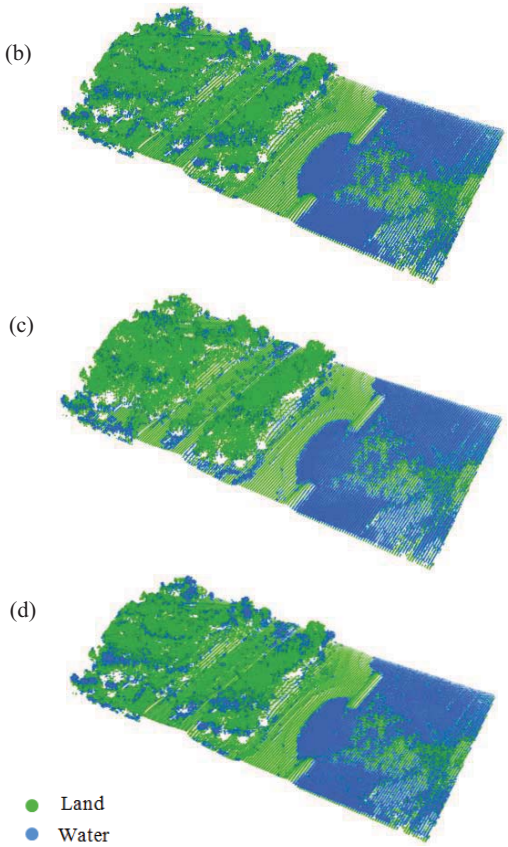

Figure 4. Classified LiDAR points based on: (a) ΔZ (C1C3), (b) ΔZ (C2C3), (c) R (C1C3), and (d) R (C2C3)

Feature	Completeness (%)		Correctness (%)	
	Water	Land	Water	Land
ΔZ (C1C3)	**78.3**	**85.0**	**75.4**	**87.0**
ΔZ (C2C3)	78.2	81.1	70.8	86.4
***R* (C1C3)**	**80.9**	**84.5**	**75.4**	**88.3**
***R* (C2C3)**	79.6	78.2	68.2	86.7

Table 3. Completeness and correctness using ΔZ and R

Since the tested data representing a coastal area, the water bodies could be assumed that they occupy the lower elevation in the scene. As a result, a threshold value could be directly applied to the elevation attribute in order to detect all water points. However, this is not always the case for inland water areas, where the water bodies do not necessarily occupy lower elevation. Therefore, ΔZ and R features were expected to be able to classify water areas. The overall accuracy obtained from ΔZ feature is 82.5% and 80.0% by combining C1 with C3 and C2 with C3, respectively. An overall accuracy of 83.2% and 78.7% is obtained from R feature by combining C1 with C3 and C2 with C3, respectively. These features show the capability of combining the data from multi-channel, however the misclassification was occurred due to that the searching radius for neighbouring points was too small to ensure sufficient number of points. That requires a larger searching radius (Morsy et al., 2017).

4.2 Intensity-based Features Results

Based on the relatively high variation of intensity values in the water body in all channels, water points were classified if they have *ICOV* greater than $ICOV_{thresh}$. The $ICOV_{thresh}$ was selected to be 1 for C1 and C2, while 0.5 was selected for C3. As aforementioned, the ID is the percentage of LiDAR points that have intensity values below a I_{thresh}. Since the water points were assumed to have the lowest intensity values in the scene, the higher *ID* represents water points. The minimum ID_{thresh} percentage was selected to be 70% for all channels, and the I_{thresh} was selected to be 200, 300, and 50 for C1, C2, and C3 channels, respectively. Figure 5 shows the classified LiDAR points using the *ICOV* and *ID* features from the three channels. The completeness and correctness of the classified points are provided in Table 4.

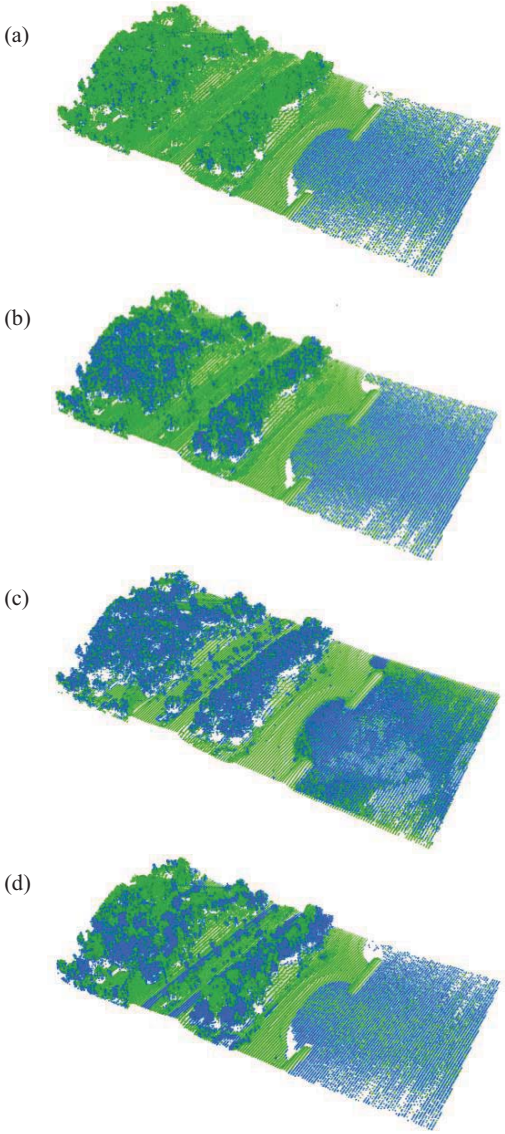

Figure 5. Classified LiDAR points based on: (a) ICOV (C1), (b) ICOV (C2), (c) ICOV (C3), (d) ID (C1), (e) ID (C2), and (f) ID (C3)

Feature	Completeness (%)		Correctness (%)	
	Water	Land	Water	Land
***ICOV* (C1)**	**75.1**	**91.4**	**58.8**	**95.7**
***ICOV* (C2)**	72.0	70.5	33.5	92.4
***ICOV* (C3)**	54.9	48.8	38.6	64.8
***ID* (C1)**	69.2	**60.3**	22.3	**92.2**
***ID* (C2)**	77.6	53.6	25.7	92.0
***ID* (C3)**	**84.3**	56.9	**53.4**	86.1

Table 4. Completeness and correctness using ICOV and ID

The overall accuracy obtained from *ICOV* feature using C1 is (89.0%) higher than C2 (70.8%) and C3 (67.6%). This is because some vegetation areas (i.e., trees) in C2 (Figure 5b) have a relatively high intensity variation that increased the *ICOV*, and hence the vegetation was misclassified as water. In C3 (Figure 5c), similarly as C2 and in addition, the edges of the water body have a low intensity variation that decreased the *ICOV*, and hence the water points at the edges were misclassified as land. For *ID* feature, the overall accuracy measures are relatively low (61.6%, 57.7%, and 67.1% using C1, C2, and C3, respectively). This is because the water points were assumed to have the lowest intensity values in the scene, but the vegetation points also have low intensity values and close to the intensity values of the water points in all channels as reported in (Morsy et al., 2016b). Therefore, the vegetation points were misclassified as water points.

4.3 Geometry-based Features Results

The land/water classification using geometry-based features relies on the returns from the water bottom. Therefore, the combination of C1/C2 with C3 was conducted. The PD_{thresh} was set to 10 points/m^2 when C1 was combined C3, while 12 points/m^2 was selected in case of using C2 with C3. For *MR* feature, if a LiDAR point has double returns in C3 and a single return either in C1 or C2, this point was classified as water; otherwise, it was classified as land. Figure 6 shows the classified LiDAR points using *PD* and *MR* features. Table 5 provides the accuracy measures of the classified points.

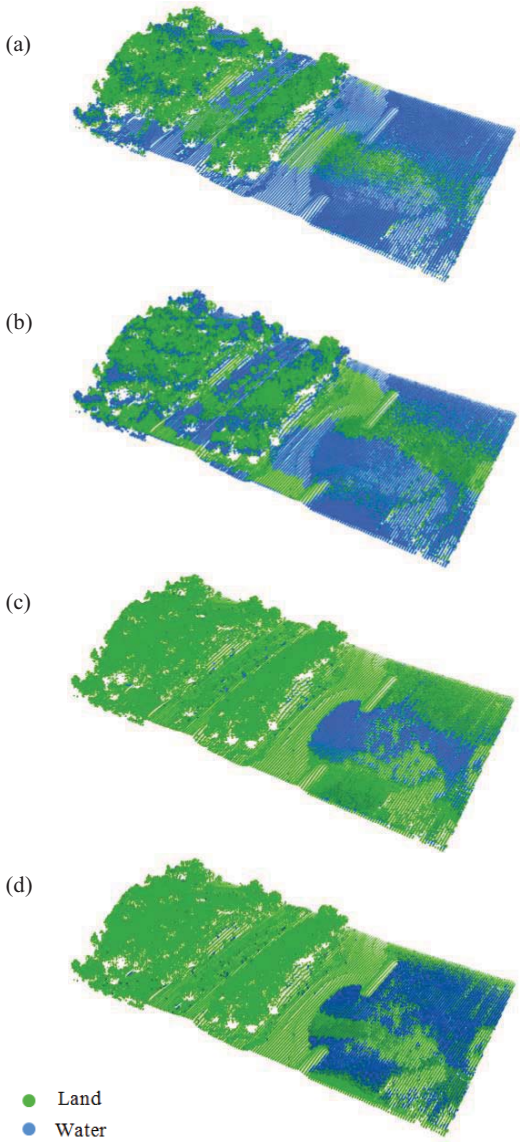

Figure 6. Classified LiDAR points based on: (a) PD (C1C3), (b) PD (C2C3), (c) MR (C1C3), and (d) MR (C2C3)

Feature	Completeness (%)		Correctness (%)	
	Water	Land	Water	Land
***PD* (C1C3)**	**82.4**	**61.5**	**55.6**	**85.6**
***PD* (C2C3)**	77.0	61.4	53.9	82.0
***MR* (C1C3)**	39.5	98.5	93.9	73.5
***MR* (C2C3)**	**53.4**	**98.5**	**95.4**	**78.3**

Table 5. Completeness and correctness using PD and MR

An overall accuracy of 69.2% and 67.2% was achieved using *PD* feature when C1 or C2 was combined with C3, respectively. The *MR* feature achieved an overall accuracy of 76.7% and 81.8% when C1 or C2 was combined with C3, respectively. There are two reasons for points' misclassification. First, some water points have single returns in C3, as shown in Figure 1d, from the water surface or bottom. Second, the selected searching radius was too small, and hence many of LiDAR points did not have neighbouring points. Therefore, larger searching radius should be used (Morsy et al., 2017). However, the use of *MR* feature shows promising results and the classification accuracy could be increased once the all points of the water body have double returns in C3.

5. CONCLUSIONS

In this research, multispectral airborne LiDAR data were explored for land/water classification at Lake Ontario. The multispectral airborne Optech Titan sensor was used to collect the LiDAR data over Lake Ontario at three wavelengths, namely MIR (1.550 μm), NIR (1.064 μm), and green (0.532 μm). Six LiDAR point features based on elevation, intensity, and geometry were extracted and evaluated for land/water classification. The elevation-based features results demonstrated the highest overall classification accuracy of 81.2% in average, while the intensity-based features results showed relatively low accuracies with an average of 66.2%. The geometry-based features results demonstrated an average overall classification accuracy of 73.8%. The elevation-based feature, ΔZ and, the geometry-based feature *MR* are automatically extracted for each LiDAR point. Consequently, the automation of the whole land/water classification process will be further investigated.

ACKNOWLEDGEMENTS

This research work is supported by Discovery and CRD Grants from the Natural Sciences and Engineering Research Council of Canada (NSERC) and the Ontario Trillium Scholarship (OTS). The authors would like to thank Dr. Paul E. LaRocque from Teledyne Optech for providing the LiDAR data from the world's first commercial multispectral airborne LiDAR system, the Optech Titan.

REFERENCES

Brzank, A., Heipke, C., Goepfert, J. and Soergel, U., 2008. Aspects of generating precise digital terrain models in the Wadden Sea from LiDAR–water classification and structure line extraction. *ISPRS Journal of Photogrammetry and Remote Sensing*, *63*(5), pp.510-528.

Fernandez-Diaz, J.C., Carter, W.E., Glennie, C., Shrestha, R.L., Pan, Z., Ekhtari, N., Singhania, A., Hauser, D. and Sartori, M., 2016. Capability Assessment and Performance Metrics for the Titan Multispectral Mapping LiDAR. *Remote Sensing*, *8*(11), p.936.

Heipke, C., Mayer, H., Wiedemann, C. and Jamet, O., 1997. Evaluation of automatic road extraction. *International Archives of Photogrammetry and Remote Sensing*, *32*(3 SECT 4W2), pp.151-160.

Höfle, B., Vetter, M., Pfeifer, N., Mandlburger, G. and Stötter, J., 2009. Water surface mapping from airborne laser scanning using signal intensity and elevation data. *Earth Surface Processes and Landforms*, *34*(12), pp.1635-1649.

Karila, K., Matikainen, L., Puttonen, E. and Hyyppä, J., 2017. Feasibility of Multispectral Airborne Laser Scanning Data for Road Mapping. *IEEE Geoscience and Remote Sensing Letters, 99*. (Accessed online: February 27, 2017).

Morsy, S., Shaker, A. and El-Rabbany, A., Forthcoming. Using multispectral airborne LiDAR data for land/water discrimination: a case study at Lake Ontario. *International Journal of Digital Earth*.

Morsy, S., Shaker, A. and El-Rabbany, A., 2016. Potential use of multispectral airborne LiDAR data in land cover classification. *Proceedings of the Asian conference on Remote Sensing (ACRS), Colombo, Sri Lanka*.

Morsy, S., Shaker, A., El-Rabbany, A. and LaRocque, P.E., 2016. Airborne multispectral LiDAR data for land-cover classification and land/water mapping using different spectral indexes. *ISPRS Annals of the Photogrammetry, Remote Sensing and Spatial Information Sciences*, *3*(3), pp.217-224.

Nabucet, J., Hubert-Moy, L., Corpetti, T., Launeau, P., Lague, D., Michon, C. and Quenol, H., 2016, October. Evaluation of bispectral LiDAR data for urban vegetation mapping. In *SPIE Remote Sensing*. International Society for Optics and Photonics.

Schmidt, A., Rottensteiner, F. and Soergel, U., 2012. Classification of airborne laser scanning data in Wadden sea areas using conditional random fields. *International Archives of the Photogrammetry, Remote Sensing and Spatial Information Sciences*, *39*, p.B3.

Smeeckaert, J., Mallet, C., David, N., Chehata, N. and Ferraz, A., 2013. Large-scale classification of water areas using airborne topographic LiDAR data. *Remote Sensing of Environment*, *138*, pp.134-148.

Wichmann, V., Bremer, M., Lindenberger, J., Rutzinger, M., Georges, C. and Petrini-Monteferri, F., 2015. Evaluating the potential of multispectral airborne LiDAR for topographic mapping and land cover classification. *ISPRS Annals of the Photogrammetry, Remote Sensing and Spatial Information Sciences*, *1*, pp.113-119.

Yu, X., Hyyppä, J., Litkey, P., Kaartinen, H., Vastaranta, M. and Holopainen, M., 2017. Single-Sensor Solution to Tree Species Classification Using Multispectral Airborne Laser Scanning. *Remote Sensing*, *9*(2), p.108.

A NOVEL APPROACH FOR STEP DETECTION USING A FREE-MOVING HANDHELD DEVICE

M. Khedr [a,b] *, N. El-Sheimy [a]

[a] Dept. of Geomatics Engineering, University of Calgary, 2500 University Dr NW, Calgary, AB, Canada, T2N1N4 – (maan.khedr, elsheimy)@ucalgary.ca
[b] Department of Computer Engineering, Arab Academy for Science and Technology, Alexandria, Egypt

KEY WORDS: Step Detection, Smartphones, Non-constrained, Inertial Navigation System, IMU, Sensor Fusion, Pedestrian Dead Reckoning

ABSTRACT:

Pedestrian navigation is one of the most challenging problems in navigation. this is due to the high dynamics of pedestrian motion, especially when using a non-constrained navigation device such as smartphones. This paper proposes a method for step detection of a pedestrian as part of a Pedestrian Dead Reckoning (PDR) solution. The method makes use of both gyroscope and accelerometer data to detect the pedestrian step under non-constrained free-motion use of the navigation device (smartphone, handheld device) without the need to classify the type of motion and use case of the device. The accelerometer and gyroscope data are filtered based on the most recent steps duration adaptively, after which the acceleration norm is analysed for peak/valley detection with an adaptive time filtering for removal of false peaks and valleys. Further verification of detected peaks and valleys is applied in case of the presence of dominant angular motion through coinciding peak filtering between the acceleration norm and the angular velocity over the dominant axis of motion. Finally, a step is verified through displacement thresholding to validate if a step was taken or if the patterns only existed due to hand motion. From the experimental results, it can be seen that the step detection algorithm performs with a minimum of 98.8% in cases of consistent device pose and 97.4% in cases of device pose change during motion without abrupt state transition.

1. INTRODUCTION

Recent advances in Micro-Electro-Mechanical Systems (MEMS) technology has made it feasible to manufacture Inertial Measurement Units (IMU) sensors that are low cost, and low on power consumption on chip while being of light weight (Davidson, Vazquez, and Piche 2009; El-Sheimy and Niu 2007). Most of the smart devices the pedestrians use these days are equipped with such technology. The presence of these sensors at the disposal of the user made it very appealing to be used for various applications such as: activity and health monitoring (Huang et al. 2010), gaming and personal navigation (Qian et al. 2015), and emergency services (Renaudin et al. 2007).

The market for Location Based Services (LBS) is ever growing with increasing demand for more accurate services. The primary source for tracking users' location is the Global Navigation Satellite Systems (GNSS). GNSS systems are always undergoing modernizations that increase their coverage and accuracy. However, GNSS can provide reliable positioning and navigation information in most cases, it suffers from degraded service in environments where the satellite signals are blocked, attenuated, or reflected (Misra and Enge 2010). Such environments include urban canyons and indoors, where most of our day-to-day activities take place.

Although many techniques have been developed to try to overcome the drawbacks of GNSS, it remains an open issue to navigate, and locate a pedestrian in environments where the signals are not that reliable or even denied. For this particular reason, Inertial Navigation Systems (INS) are becoming a very hot topic for pedestrian navigation in particular as they do not rely on external signals for the navigation and localization process.

An IMU is a group of sensors that can sense the motion of the user. Although IMUs have been utilized for navigation long ago (Wrigley 1977), GNSS systems took over as the dominant navigation concept over the past few decades. Recent advances in INS (Tazartes 2014) made them appealing again for the use as an aiding for the GNSS in case of an outage or unreliable signal, while also they can be very useful for the case of pedestrian navigation. This integration can provide a continuous navigation solution that works under varying conditions.

MEMS IMU are low-grade sensors that are also referred to as commercial-grade. In (Noureldin, Karamat, and Georgy 2013) a comparison of the different types and grade of IMU is presented. The comparison shows the relatively high errors of the commercial-grade IMUs in comparison to the higher more expensive counterparts. (Shin and El-Sheimy, 2002) , provides a performance comparison between the different underlying technologies used in IMU sensors. The performance charts show that MEMS technology suffers from the highest error budget in terms of Parts Per Million (PPT). But on the other hand it is not practical for pedestrians to use high-grade IMUs for navigation as they tend to be expensive, large, heavy, and require higher power sources, also they cannot be installed on smartphones.

With the high error magnitude and noise of MEMS IMU comes a limitation to their reliability over time. The use of conventional Dead Reckoning (DR) methods tend to drift quickly over short time span, yielding wrong navigational information.

Methods for correction have been proposed and used to enhance the performance of such system such as: Zero Velocity Update (ZUPT) (Abdulrahim et al. 2014), Zero Angular Rate Update (ZARU) (Groves 2013), Magnetic Angular Rate Update (MARU) (Zampella et al. 2012), and Heuristic Drift Reduction (HDR) (Personnel and Systems 2009). The problem with these techniques is the requirement of certain conditions to be met before they can be applied, which in most cases does not hold with handheld devices.

A modified form of DR is Pedestrian Dead Reckoning (PDR), which exploits information about the human motion, namely the Gait Cycle (GC) (Rose and Gamble 2006) to limit the drifting of the solution. PDR is composed of three main algorithms, step detection, step length estimation, and alignment, where the user location is obtained through the accumulation of steps, given a step length and the direction of each step (Ojeda and Borenstein 2007b). Hence, step detection is a crucial task of PDR.

In order to use a non-constrained device for PDR navigation, a robust step detection technique is needed to detect the steps taken by the user under varying motion conditions and speeds regardless of the use case and motion of the navigation device itself. The use of acceleration data by itself is not sufficient to fully describe the pedestrian motion. The forces exerted by the pedestrian during motion are not fully linear components, and hence part of the motion information lies within the gyroscope measurements.

The remainder of this paper is organized as follows: section 2 presents the related work and state-0f-the-art techniques for step detection. Section 3 discusses the proposed methodology for the step detection. Section 4 presents the experimental setup for testing the hypothesis. Section 5 shows the results of the algorithm. Finally, section 6 draws conclusions from the presented results.

2. RELATED WORK

This section presents some of the existing techniques for step detection and counting. The techniques presented can be categorized into two categories: Foot-mounted, and Handheld devices.

2.1 Foot-mounted step detection approaches

Multiple approaches rely on the use of an IMU strapped down to the foot of the user. Such an approach relishes the benefits of closely capturing the characteristics of the GC and the underlying kinetics of it. For example, during the stance phase, such an approach utilizes the fact that it is known that the IMU should be stationary, meaning that the expected measurements from the accelerometer and the gyroscope are that of gravity vector and zero respectively, hence it can be easier to detect the stance phase from the sensor measurements. Furthermore, the accurate detection of the stance phase would enable the use of correction methods for compensating for the drift in the measurements.

For the case of foot-mounted sensors, the detection process relies on the use of thresholds for detecting the stance phase in most cases, or the use of GC state transition modelling.

(Ojeda and Borenstein 2007a) proposes a threshold-based approach that relies on the use of gyroscope measurements for the detection of the stance phase. The stance is detected when the gyroscope measurements fall within a predefined threshold. A more reliable approach presented in (Jimenez et al. 2010) where multiple threshold-based constrains are defined for both accelerometer and gyroscope measurements, where three threshold checks are carried out and a step is identified when all three conditions are met. (Foxlin 2005) also uses thresholds for acceleration measurements to identify a stance, but it also incorporates a validation step through defining a minimum time span for the stance.

Threshold-based detection can suffer from degraded performance especially in fast walking and running modes. This is due to the fact that the stance period gets diminished and might pass undetected. To overcome this limitation, multiple researches proposed the use classifiers and state transitions to model the transition between the four phases of the GC so as to get higher detection rates.

(Pappas et al. 2001) defines a Finite State Machine (FSM) that describes the possible transitions from each of the four phases of the GC with a probability transition matrix. By using the probability transition matrix and the processing the measurements of the accelerometer and the gyroscope, the phase is detected. Similarly in (Yun et al. 2007), a state transition is defined. The update in this approach is the use of a tri-axial gyroscope instead of only a single axis gyroscope.

(Young and Sangkyung 2009) propose an FSM that is based on the assumption that the GC is a Hidden Markov Model (HMM). The measurements from the gyroscope and the force resistors installed on the sole of the shoe are used for the phase classification along with the probability transition matrix. This work was modified in (Park and Suh 2010) to replace the force resistors by accelerometer and redefining the probability transition matrix.

A Bayesian Network (BN) was proposed in (Xu et al. 2015). The aim of the network is to distinguish the stance phase only using a set of three threshold-based constraints for the accelerometer and gyroscope measurement, and a predefined GC phase threshold defined by kinesiology.

A different approach was presented in (Norrdine, Kasmi, and Blankenbach 2016) that proposes the use of a magnetometer on one shoe while placing a permanent magnet on the other. The algorithm detects the steps through the processing of the magnetometer measurements, which are no longer the magnetic north but the proximity of the magnet on the other shoe.

For the use of threshold-based detection and state transitions, a predictable pattern should exist. This hypothesis holds for tethered sensors in most cases such as the foot-mounted case, but in the case of a free-moving handheld device there are no predictable outcome at a given time and hence researchers resort to other methods as will be presented in the next subsection.

2.2 Handheld devices

In case of untethered-handheld devices, there is no detectable zero velocity region for the stance phase of the GC as the human upper body half is in continuous motion unlike the foot. Moreover, the free motion of the device makes it harder to detect patterns in the signals as the patterns keep changing as the device's placement and use changes. Based on that, methods for step detection rely on peak extraction. Peaks in accelerations usually represent a heal strike and can be identified as the beginning of a step and the ned of the previous. Regular peak detection techniques

usually rely on classifiers to determine the use of the handheld device – smartphone – to adaptively adjust the step detection thresholds.

The most dominant feature in the accelerations that can be used for step detection is the presence of peak values at heal strike. (Huang et al. 2010) relies on the detection of peaks step detection. The proposed algorithm requires a training phase to estimate the user dependant thresholds for step detection before it can be used for navigational purposes. This is inconvenient as the parameters estimated will work for one user but is not guaranteed to work for others, while another limitation is that it only works in compassing mode.

(Susi, Renaudin, and Lachapelle 2013) proposes the use of a classifier to identify the type of motion the device is experiencing. Once the device use case is identified, a decision of using either the accelerometer or the gyroscope measurements is made based on the class of motion identified. The steps are then detected through peak extraction technique. The classifier proposed is a supervised classifier, which mean a training phase was required to obtain the thresholds for the decision making in the classifier.

Another approach that uses a classifier was presented in (Xiao et al. 2015). The classifier classifies the motion type into one of two classes through the use a periodicity detection algorithm. After which, peaks are extracted to represent candidate steps that are then filtered for removal of false steps. The validation of candidate steps is through the integration of the measurements during the step duration to check if significant displacement

occurs, while also a turn detection algorithm is employed to eliminate false steps during turns.

The problem with peak detection is that false peaks can occur due to the free-motion of the smartphone.(Lee, Choi, and Lee 2015) propose an adaptive filtering method for eliminating false peaks. Unlike most approaches, the presented work uses the norm of the acceleration measurements from the accelerometer and not only vertical acceleration analysis for the step detection. the process starts by extracting pairs of peak/valley. Each peak and valley being detected is a candidate until verified through magnitude and temporal filtering. Upon the verification of a peak/valley pair, a step is identified.

(Kammoun, Pothin, and Cousin 2015) uses a different approach of classification by employing a fuzzy-logic classifier. Features from a Band-Pass filtered acceleration norm are extracted and evaluated with a membership function. The output of the classifier is then processed through a set of rules for defuzzification to make a decision regarding a step being detected.

Other methods for step detection that rely on other sensors have been suggested such as the work presented in (Ozcan and Velipasalar 2015). In this work the authors propose the use of the camera in the smartphone for step detection. the limitation for this kind of approach is that the smartphone motion is restrained as in order to count the steps, the smartphone has to be held in a position that captures the foot motion.

Foot-mounted step detection techniques have been extensively studied and have been shown to provide high accuracy, yet the problem remains that it requires specialized equipment that the user will use solely for the purpose of navigation while those sensors are most likely available in his handheld device. The other trend in the research is the use of the smartphone, while trying to estimate the pose of the device in order to adaptively change the step detection criteria.

The fact that a user might change the pace of walking at any time while also the device pose might change, imposes a great challenge. The attempt of separation of the two phenomena so as to estimate a device pose and correspondingly adapt the step detection technique imposes higher complexity and introduces possible error due to wrong pose estimation. The authors in this paper argue that the step detection decision should be based on features that are dependent of the device pose and use case to work in a unified manner.

3. PROPOSED METHODOLOGY

In this section, a novel step detection algorithm is proposed that is independent from the smartphone use case and does not require a classifier to adaptively tune the parameters for the step detection. As a first step, the algorithm mainly works on analysing features of the norm of acceleration and angular velocities. This approach is to avoid errors introduced in the Local Level Frame (LLF) measurements by accumulated errors from device orientation tracking.

From studying the norm of the accelerations in the case of a fixed device pose – compassing mode – to obtain the pattern of accelerations exerted by the walking motion, it was concluded that the acceleration norm has the following properties:

The acceleration norm has a sinusoidal pattern where each pair of peak/valley represent a step. Figure 1 shows an example of regular walking pattern with peaks and valleys detected by the proposed algorithm.

The magnitude difference between the peak/valley pair is inversely proportional to the step duration and proportional to the motion pace. Figure 2 and Figure 3 elaborates the change in magnitude in correspondence to pace variation with time.

The use of net force acceleration norm – uncompensated for gravity component – as shown in Figure 4 , magnifies the pattern in the signal around the peaks and valleys while also smoothing it around the gravity shift component. This is due to the combined factor from both linear acceleration and gravity as presented in equation (1).

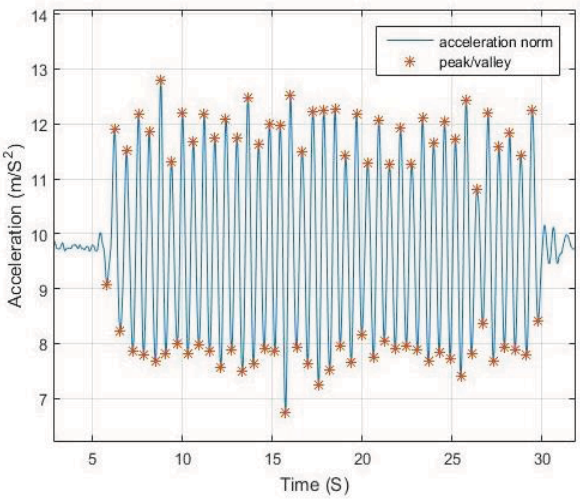

Figure 1 Walking sinusoidal pattern

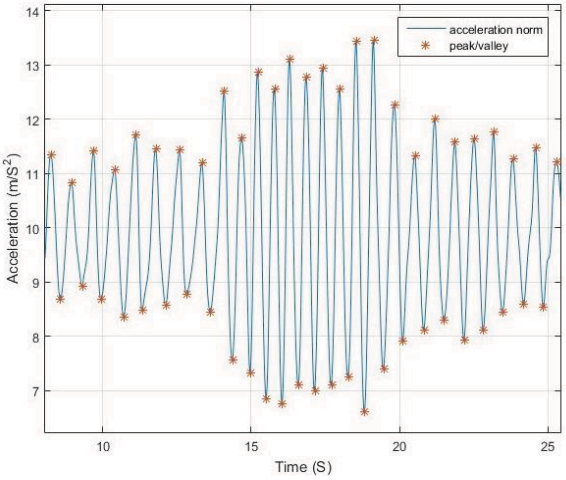

Figure 2 Walking with varying pace

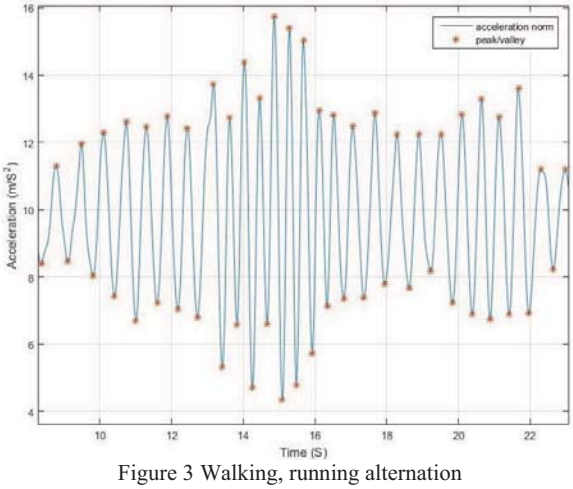

Figure 3 Walking, running alternation

$$F_{net}^2 = F_{acc}^2 + g^2 - 2 * F_{acc} * g * \cos(\emptyset) \quad (1)$$

$$a_{norm} = \sqrt[2]{{a_x}^2 + {a_y}^2 + {a_z}^2} \quad (2)$$

Where: F_{net} = net force magnitude
F_{acc} = linear acceleration vector norm
g = gravity norm
$\emptyset$ = the angle between gravity and linear acceleration
a_x, a_y, a_z= accelerations in the body frame

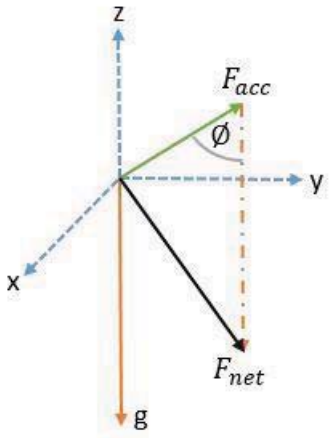

Figure 4 Forces applying to the accelerometer and their equivalent

Based on these findings, the algorithm proposed applies a peak/valley pair detection with time filtering based on the peak-to-valley magnitude. Verification of peaks and valleys for cases of high device motion is also applied through further investigating the dominant axis of angular rotation, where a peak/valley extraction is also applied conditionally to the state of repetitive-high-variance patterns. The peaks of the angular velocity should coincide within a threshold from the peak of the acceleration.
Figure 5 illustrates the block diagram for the proposed algorithm that will be discussed in the following subsections.

3.1 Pre-processing

The norm of the acceleration and angular velocity measurements are low-pass filtered as an initial step in preparation for step detection. the low pass filter is set to a frequency that represents the pace of the user and is adaptive.
The frequency of motion of the user varies depending on the state whether it is walking or running with different paces. From the collected data of varying walking and running speeds, the frequency of motion was found to be less than 5 Hz which is to be used as an initial cut-off frequency for the filtering process.
During the motion of the pedestrian the cut-off frequency is updated based on the most recent step duration. a Butterworth filter of order 3 was selected for the filtering process. The low order of the filter gives it a high response time and low lag that makes it fitting for real-time processing.

3.2 Peak/valley detection

For the extraction of peaks and valleys, a moving window of 3 measurements is used. As presented in equation 3, the candidate peak and valley are detected as the maximum in the middle of the window or a minimum respectively.

$$\begin{matrix} peak, & a_{n-1} < a_n > a_{n+1} \\ valley, & a_{n-1} > a_n < a_{n+1} \end{matrix} \quad (3)$$

Where: a= acceleration norm

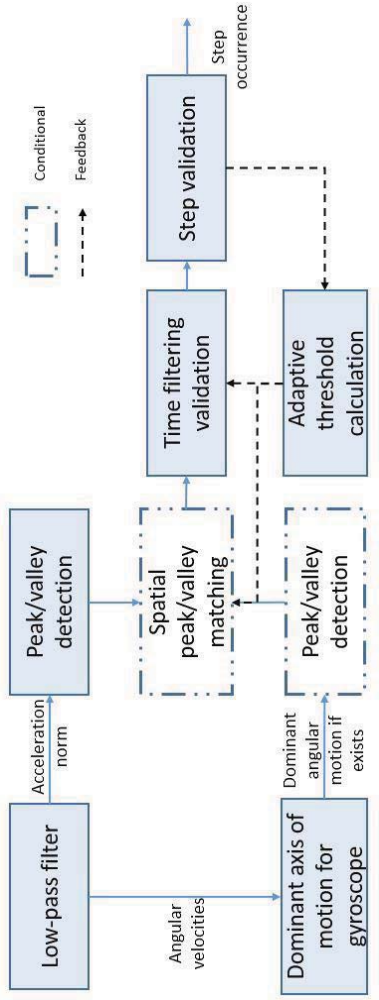

Figure 5 Proposed algorithm block diagram

For the use of the angular velocity, the variance of the measurements over the previous peak/valley period for each axis is computed to obtain the dominant axis of rotation. The peak/valley will be extracted from the dominant axis of rotation and should be in the vicinity of the peak/valley detected from the accelerations.

3.3 Peak/valley validation

For validating a recently detected peak or valley, a time threshold is used, the time difference between the peak and valley should be around half the time span of the step. As the current step pace is unknown, the previous step is used. In regular motion a transition state occurs between walking and running, and vice versa, meaning the user increases/decreases speed over few steps to reach the target speed. This means that the time span of the current step is related to the previous step. Based on that assumption the time filtering between a peak and valley is based on the previous valley to peak duration with a threshold to accommodate for changing pace.

$$\Delta t = t_{(p|v)_{n-1}} - t_{(p|v)_{n-2}} \quad (4)$$

$$th_t = 0.5 * \Delta t \quad (5)$$

$$\Delta t - th_t < t_{(p|v)_n} - t_{(p|v)_{n-1}} < \Delta t + th_t \quad (6)$$

Where $t_{(p|v)}$= time of peak or valley
Δt= time interval between peak and valley
th_t= time threshold

If a double peak or valley occurs concurrently within a short time period, a decision has to be made which of them is to be considered the actual peak. This can occur due to perturbations in the measurements induced by the free-motion of the device. In case of peaks, the maximum of the two concurrent peaks will be used as the peak, while in case of valleys it will be the minimum of the two valleys.

During motion, analysis of the gyroscope measurements is applied. For each of the gyroscope axes, the variance and periodicity of the measurements is computed, where if any of the axis exhibits high variance it indicates a swinging motion. In such event peaks and valleys of the dominant axis of motion for the angular velocity are extracted, where each peak and valley in the gyroscope measurement should coincide with a peak in the acceleration norm. a window of measurements is utilized where a peak from the acceleration should coincide with a peak/valley from the dominant axis of motion from the angular velocity as shown in Figure 6.

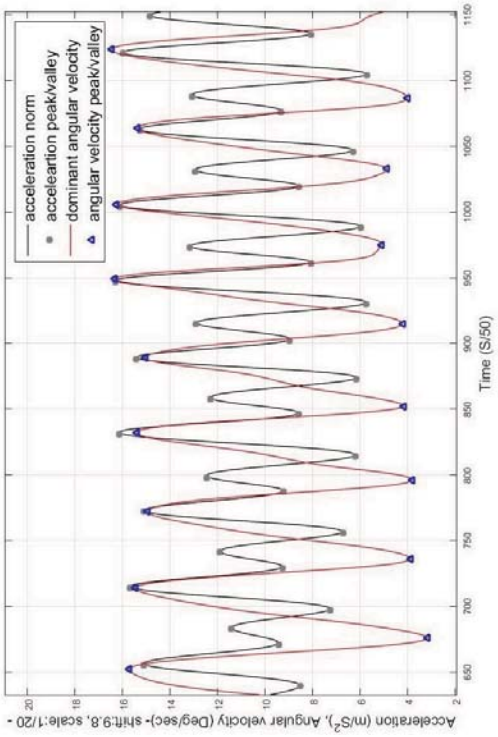

Figure 6 Acceleration norm and dominant angular velocity measurements during swinging motion

3.4 Step validation

A step is validated through the double integration of the acceleration measurements during the step window. If the displacement accumulated through the detected step window is found to be significant based on an adaptive threshold test, a step is counted. The threshold for the displacement changes corresponding to the duration of the step and the peak-to-valley magnitude to account for short steps.

```
Algorithm
Low-pass filter measurements
State ← Detect candidate
If state = peak
    If previous_state=valley && time_since_valley>th1
        If dominant_angular_motion
            If angular_peak_time within peak_window
                Valid peak detected
            Endif
        Else
            Valid peak detected
        Endif
    Elseif previous_state=peak && time_since_peak<th2
        If current_peak>previous_peak
            If dominant_angular_motion
                If angular_peak_time within peak_window
                    Update peak
                Endif
            Else
                Update peak
            Endif
        Endif
    Elseif
Elseif state = valley
    If previous_state=valley && time_since_valley>th1
        If dominant_angular_motion
            If angular_peak_time within peak_window
                Valid peak detected
            Endif
        Else
            Valid peak detected
        Endif
    Elseif previous_state=peak && time_since_peak<th2
        If current_peak>previous_peak
            If dominant_angular_motion
                If angular_peak_time within peak_window
                    Update peak
                Endif
            Else
                Update peak
            Endif
        Endif
    Elseif
Endif
If accumulated_displacement> th_distance
    Stepcount++
Else
    Discard step
Endif
```

4. EXPERIMENTAL SETUP

For testing the proposed algorithm, data sets have been collected using two smartphones, the Iphone6 and HTC one m9.

A description of the data sets collected and used for testing is presented in Table 1.

The collected data was used for testing without calibration and compensation for systematic errors. This is due to the fact the measurements are used on an epoch-by-epoch basis and hence no accumulated error is introduced into the system.

The data was collected by five test subjects, each performing tests for all device poses presented in the table for the three step modes. Furthermore, all tests carried were of real case motion and not through the use of a treadmill, where the use of treadmills

for data collection used in some of the research limits and restrains the motion speed of the test subject. Also in case of change of step mode from walking to running, the treadmill acceleration pattern removes the factor of user dependent transition between states.

Datasets			
Device pose	**Step mode**		
	walking	Running	Combined
Compassing	5 (100 steps)	5 (100 steps)	5 (100 steps)
Dangling	5 (100 steps)	5 (100 steps)	5 (100 steps)
Texting	5 (100 steps)	5 (100 steps)	5 (100 steps)
Phoning	5 (100 steps)	5 (100 steps)	5 (100 steps)
Pocket	5 (100 steps)	5 (100 steps)	5 (100 steps)
Free-motion	5 (100 steps)	5 (100 steps)	5 (100 steps)

Table 1 Collected Dataset

5. RESULTS

The proposed step detection algorithm was implemented on Matlab for evaluation and verification. Although the results that will be presented are not the result of a real- time processing of the data, but the Matlab code was developed so as to process the data as a data stream without the use of any information regarding the full dataset to be an imitation of a real-time scenario.

The adaptive filtering method employed by the algorithm minimizes problem arising from either over-filtering or under-filtering the signals. For example, if the motion pace is high while the cut-off frequency is significantly lower, this will cause loss of motion information, while on the other hand if the pace is slow but the cut-off frequency is significantly higher, motion noise remains dominant in the signal causing the presence of consecutive peaks and valleys in a short period of time. In Figure 7 a comparison between using a constant cut-off frequency for the low-pass filter with an adaptive cut-off frequency is presented. As shown in the regions encircled, using a high cut-off frequency to accommodate for high step frequency results in fluctuations that can be considered as faulty steps unless temporally filtered. Using an adaptive cut-off frequency minimizes the possibility of occurrence of such cases, which reduces the possibility of over counting steps.

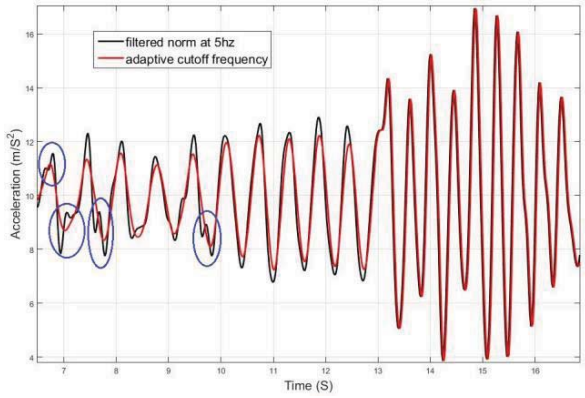

Figure 7 Constant cut-off frequency vs adaptive filtering

Although the adaptive filtering removes most of the fluctuations, the possibility that fluctuations in the measurements would happen still exist, hence the need for the time filtering module.

Results from the step detection algorithm for the datasets collected are presented in Table 2. For each device pose, three step modes were tested with a total of 500 steps for each. A single step miss of extra step count represents an 0.02% accuracy loss.

Detection accuracy (%)			
Device pose	**Step mode**		
	walking	Running	Combined
Compassing	99.8	99.8	99.8
Dangling	99.4	99.2	99.2
Texting	99.6	99.4	99.2
Phoning	99.6	99.6	99.4
Pocket	100	99.8	99.6
Free-motion	99.0	98.4	98.0

Table 2 Step Detection accuracy

For the case of non-varying device pose, results for step mode of walking yield the highest accuracy. In case of transition between step modes, the accuracy of detection is slightly effected due to the abrupt change in step frequency, while in case of smooth transition from walking to running and vice versa the adaptive filtering can cope with the transition. Results show an average accuracy of detection of 99.68%, 99.55% and 99.45% for walking, running, and combined step modes respectively.

For the case of changing device pose while maintaining step mode, the performance of the algorithm slightly degrades due to the presence of hidden steps during transition. In specific transition from dangling to any state and vice versa has the greatest impact as during the transition the dominant peaks are corresponding to the forward motion of the arm coinciding with the opposite leg step. For elaboration in case of holding the phone in the right hand, the peak for the left foot stepping forward is dominant while as the arm swings back with the right foot moving forward the corresponding peak is diminished as can be seen from Figure 6. During the transition to dangling or the other way round, a step can pattern might fully get suppressed.

Results for the case of changing device pose show an accuracy of 99%, 98.4%, and 98% for step modes of walking, running, and combined states respectively, while the minimum accuracy for a single test was 97.4% in the case of combined step mode with changing device pose.

6. CONCLUSIONS

A novel step detection algorithm was presented in this paper. The proposed algorithm is developed as part of a PDR system for pedestrian navigation using smartphones. The algorithm does not require training or prior knowledge of device pose and does not attempt to classify the type of motion and device pose for successfully detecting steps.

For the step detection, the algorithm uses the acceleration norm after low-pass filtering based on an adaptive cut-off frequency. This filtering process minimizes wrong peak/valley detection which makes the algorithm suitable for different step modes regardless of the device pose. The algorithm also uses angular velocity measurements from the dominant axis of motion to verify the peaks and valleys detected from the accelerations, while also eliminating most of the remaining false peaks and valleys using time filtering.

The experimental results show high accuracy of step detection, especially in the case of a fixed device pose with an average accuracy of 99.6% and a minimum of 98.8% in the case of combined step mode while swinging the phone. In the case of varying device pose, an average accuracy of 98.4% was achieved, with a minimum accuracy of 97.4%.

the proposed algorithm performance is only slightly affected by the transitions between certain device poses and can be used as part of different application that require a high accuracy step detection whether those applications are for health monitoring, navigation, or gamming.

ACKNOWLEDGEMENTS

This work was supported by Professor Naser El-Sheimy funds, from NSERC and Canada Research Chairs programs, as part of a research on robust PDR system for mobile navigation.

REFERENCES

Abdulrahim, Khairi, Terry Moore, Chris Hide, and Chris Hill. 2014. "Understanding the Performance of Zero Velocity Updates in MEMS-Based Pedestrian Navigation." *International Journal of Advancements in Technology* 5(2).

Davidson, Pavel, Manuel A. Vazquez, and Robert Piche. 2009. "Uninterrupted Portable Car Navigation System Using GPS, Map and Inertial Sensors Data." Pp. 836–40 in *2009 IEEE 13th International Symposium on Consumer Electronics*. IEEE.

El-Sheimy, Naser and Xiaoji Niu. 2007. "The Promise of MEMS to the Navigation Community." *Inside GNSS* 2(2):46–56.

Foxlin, Eric. 2005. "Pedestrian Tracking with Shoe-Mounted Inertial Sensors." *IEEE Computer Graphics and Applications* 25(6):38–46.

Groves, Paul D. 2013. *Principles of GNSS, Inertial, and Multisensor Integrated Navigation Systems (2)*. Norwood, US: Artech House.

Huang, Yan et al. 2010. "Activity Monitoring Using an Intelligent Mobile Phone - A Validation Study." P. 1 in *Proceedings of the 3rd International Conference on PErvasive Technologies Related to Assistive Environments - PETRA '10*. New York, New York, USA: ACM Press.

Jimenez, A. R., F. Seco, J. C. Prieto, and J. Guevara. 2010. "Indoor Pedestrian Navigation Using an INS/EKF Framework for Yaw Drift Reduction and a Foot-Mounted IMU." in *Proceedings of the 2010 7th Workshop on Positioning, Navigation and Communication, WPNC'10*.

Kammoun, Soufien, Jean Baptiste Pothin, and Jean Christophe Cousin. 2015. "An Efficient Fuzzy Logic Step Detection Algorithm for Unconstrained Smartphones." in *IEEE International Symposium on Personal, Indoor and Mobile Radio Communications, PIMRC*.

Lee, Hwan Hee, Suji Choi, and Myeong Jin Lee. 2015. "Step Detection Robust against the Dynamics of Smartphones." *Sensors (Switzerland)*.

Misra, Pratap. and Per. Enge. 2010. *Global Positioning System : Signals, Measurements, and Performance*. Ganga-Jamuna Press.

Norrdine, Abdelmoumen, Zakaria Kasmi, and J??rg Blankenbach. 2016. "Step Detection for ZUPT-Aided Inertial Pedestrian Navigation System Using Foot-Mounted Permanent Magnet." *IEEE Sensors Journal* 16(17):6766–73.

Noureldin, Aboelmagd, Tashfeen B. Karamat, and Jacques Georgy. 2013. *Fundamentals of Inertial Navigation, Satellite-Based Positioning and Their Integration*. Springer.

Ojeda, Lauro and Johann Borenstein. 2007a. "Non-GPS Navigation for Security Personnel and First Responders." *Journal of Navigation* 60(3):391–407.

Ojeda, Lauro and Johann Borenstein. 2007b. "Personal Dead-Reckoning System for GPS-Denied Environments." Pp. 1–6 in *2007 IEEE International Workshop on Safety, Security and Rescue Robotics*. IEEE.

Ozcan, Koray and Senem Velipasalar. 2015. "Robust and Reliable Step Counting by Mobile Phone Cameras." *Proceedings of the 9th International Conference on Distributed Smart Cameras* 164–69.

Pappas, Ion P. I., Milos R. Popovic, Thierry Keller, Volker Dietz, and Manfred Morari. 2001. "A Reliable Gait Phase Detection System." *IEEE Transactions on Neural Systems and Rehabilitation Engineering* 9(2):113–25.

Park, Sang Kyeong and Young Soo Suh. 2010. "A Zero Velocity Detection Algorithm Using Inertial Sensors for Pedestrian Navigation Systems." *Sensors (Basel, Switzerland)* 10(10):9163–78.

Personnel, For and Tracking Systems. 2009. "Heuristic Reduction of Gyro Drift." *Journal of Navigation* 62(1):41–58.

Qian, Wei-Xing, Qing-Hua Zeng, Jun-Wei Wan, and Zhi Xiong. 2015. "Pedestrian Navigation Method Based on Kinematic Mechanism of Human Lower Limb." *Zhongguo Guanxing Jishu Xuebao/Journal of Chinese Inertial Technology* 23(1):24–28.

Renaudin, Valérie, Okan Yalak, Phillip Tomé, and Bertrand Merminod. 2007. "Indoor Navigation of Emergency Agents." *European Journal of Navigation Science* 5(3).

Rose, Jessica. and James Gibson. Gamble. 2006. *Human Walking*. Lippincott Williams & Wilkins.

Shin, E. H. and N. El-Sheimy. 2002. "A New Calibration Method for Strapdown Inertial Navigation Systems." *Zeitschrift Für Vermessungswesen* 127(1):41–50.

Susi, Melania, Valérie Renaudin, and Gérard Lachapelle. 2013. "Motion Mode Recognition and Step Detection Algorithms for Mobile Phone Users." *Sensors (Switzerland)* 13(2):1539–62.

Tazartes, Daniel. 2014. "An Historical Perspective on Inertial Navigation Systems." Pp. 1–5 in *2014 International Symposium on Inertial Sensors and Systems (ISISS)*. IEEE.

Wrigley, W. 1977. "HISTORY OF INERTIAL NAVIGATION." *NAVIGATION, Journal of the Institute of Navigation* 24(1):1–6.

Xiao, Zhuoling, Hongkai Wen, Andrew Markham, and Niki Trigoni. 2015. "Robust Pedestrian Dead Reckoning (R-PDR) for Arbitrary Mobile Device Placement." *IPIN 2014 - 2014 International Conference on Indoor Positioning and Indoor Navigation* (October):187–96.

Xu, Zhengyi, Jianming Wei, Bo Zhang, and Weijun Yang. 2015. "A Robust Method to Detect Zero Velocity for Improved 3d Personal Navigation Using Inertial Sensors." *Sensors (Switzerland)* 15(4):7708–27.

Young, Soo Suh and Park Sangkyung. 2009. "Pedestrian Inertial Navigation with Gait Phase Detection Assisted Zero Velocity Updating." Pp. 336–41 in *ICARA 2009 - Proceedings of the 4th International Conference on Autonomous Robots and Agents*.

Yun, Xiaoping, Eric R. Bachmann, Hyatt Moore, and James Calusdian. 2007. “Self-Contained Position Tracking of Human Movement Using Small Inertial/Magnetic Sensor Modules.” Pp. 2526–33 in *Proceedings 2007 IEEE International Conference on Robotics and Automation*. IEEE.

Zampella, Francisco, Mohammed Khider, Patrick Robertson, and Antonio Jim??nez. 2012. “Unscented Kalman Filter and Magnetic Angular Rate Update (MARU) for an Improved Pedestrian Dead-Reckoning.” *Record - IEEE PLANS, Position Location and Navigation Symposium* 129–39.

LOW-COST UAV IMAGERY SYSTEM FOR SITE-SPECIFIC WEED MANAGEMENT

M. Hassanein [a, *], N. El-Sheimy [a]

[a] Department of Geomatics Engineering, University of Calgary, Calgary, Alberta, Canada - (mohamed.hassanein2, elsheimy)@ucalgary.ca

Commission VI, WG VI/4

KEY WORDS: UAV, Weed Detection, Image Binarization, SSWM, Precision Agriculture

ABSTRACT:

This paper introduces a new weed patches detection approach which uses RGB images acquired from a low-cost imagery sensor installed on an Unmanned Aerial Vehicle (UAV). The detection of weed patches is considered as an important step in Site-Specific Weed Management (SSWM) process, which is an important management system for agriculture economic development and environmental protection. The proposed approach includes image binarization system using the Hue, Saturation, and Value (HSV) color space to convert RGB images to binary images with enhanced abilities to detect vegetation parts in the image. Following the binarization step, the proposed approach creates a suitable grid to divide the binary image into zones where weed patches can be detected by computing the vegetation density of each zone. The zone which has a high vegetation percentage will be considered as a weed patch. The achieved results of using the proposed weed detection approach shows high potential of detecting weed patches in the agriculture field from images acquired at high flying altitude using consumer grade cameras. Such weed detection methodology is providing an important step to reduce the needed number of images to cover the agriculture field and therefore speed-up the weed management process. Moreover, providing an efficient weed detection approach with a low-cost UAV imagery system, increases the potential of adopting the use of these systems by the farmers.

1. INTRODUCTION

Agriculture is an important source of livelihood in all parts of the world. The importance of agriculture includes supplying clothing, medicine and employment opportunities along with providing environmental and natural resources preservation. To improve such advantages of agriculture it was important to transform the agriculture industry to be a knowledge-based industry which uses technologies that can facilitate the increase of the agriculture production while preserving the impact of these technologies on the environment (Zhang and Kovacs, 2012). Since 1990s the application of different technologies as GNSS and Remote Sensing showed substantial contributions in smart farming or more inclusively Precision Agriculture (PA).

PA involve advanced technologies to perform better management of farm inputs such as fertilizers, chemical herbicides, seeds, water, etc., with the main aim to use the right activities at the right place and time (Mulla, 2012). Conventional management systems used for agriculture industry aims to perform uniform application of agriculture inputs, while PA management system aims to perform a customized use for agriculture inputs based on the needs of each part of the field.

Weed management is considered as one of the most important agriculture activities that PA management systems can provide different advantages economically and environmentally. A weed is defined as an unwanted plant that grows in the agriculture field. The presence of these weeds in the agriculture field mainly affect the agriculture production as weeds compete the crop plants for the available living resources as water, fertilizers, direct sunlight and growth space (Ajinkya Paikekari et al., 2016). Due to such competition, along with applying different management systems for delivering the exact needs to the crop plants, it is possible to have unhealthy crops which will affect the production of the agriculture field. Therefore, it is important for farmers to remove weeds from the agriculture field using a weed management procedure.

Generally, the most common approach for weed management depends on spraying a uniform distribution of chemical treatments as herbicides over the whole agriculture field to kill weed plants in the field, even though that weeds can't cover the whole agriculture field. Using such uniform management is considered as uneconomic use of herbicides along with its dangerous effects on the environment. Due to such concerns, it is important to develop a PA management system for weed management which is the Site-Specific Weed Management (SSWM) (Peña Barragán et al., 2012). The use of SSWM aims to detect weed plants or spots in the field and use herbicides to kill these weed plants. In this case, the SSWM involves providing herbicides sprayer systems with a full map of the crop field, showing the spots or the patches of the weeds, where these type of maps are named as the weed maps (Shaw, 2005).

A weed map can be generated using different types of Remote Sensing systems such as the aerial or terrestrial systems. The use of aerial Remote Sensing systems for weed management is implemented through spectral imagery analysis techniques along with using the vegetation indices to detect weed spots (Lamb and Brown, 2001). In the early growth season, using such spectral analysis approaches for weed detection suffers from some limitations. First, the insufficient spatial resolution of the images for discrimination between bare soil and seedling crops and weeds is considered a main limitation. Second, the weed and crop plants have a similar spectral reflectance (Price, 1994), so the use of spectral imagery analysis is limited to discriminate between crop and weed plants. Third, the reflectance of the bare soil on the crop field interferes the detection procedures which also limits the use of spectral analysis techniques.

In the last decade, UAV platforms underwent tremendous developments especially regarding the payload and battery life of

* Corresponding author

the platforms. Such developments offered a suitable solution for using Remote Sensing technology for different PA activities as crop health monitoring (Laliberte et al., 2010; Lelong et al., 2008) and weed management (Peña, 2015; Peña et al., 2015; Zhang and Kovacs, 2012). The major advantage of using UAV platforms for Remote Sensing systems is the provision of higher spatial resolution due to low flying height. To overcome the limitations of spectral analysis techniques for weed detection within imagery data in the early growth season, UAV-borne imaging systems are used to provide ultra-high spatial resolution data. The high spatial resolution of the acquired imagery data from UAV is crucial to discriminate between small weed and crop seedling at early growth season using different image processing or spatial analysis techniques. Different researches reported the ability of using UAV-based Remote Sensing systems to introduce good potential for SSWM application (Göktogan et al., 2012; A. Paikekari et al., 2016; Peña Barragán et al., 2015, 2012; Peña and Gutiérrez, 2012).

Generally, the proposed approaches for weed detection using UAV imagery systems aim to detect crop rows as an initial step, so the remaining parts of the acquired image of the field will consist of weed plants and bare-soil. Then, using a suitable vegetation index, such as the Normalized Difference of Vegetation Index (NDVI), it is possible to discriminate between weeds and bare-soil. For example, Peña Barragán et al. (2012) used a UAV-borne imaging system for weed detection using the crop row detection. The research aimed to detect crop rows in the first step, followed by classifying the in-between rows objects into plants or bare soil using the NDVI to detect weed plants. The authors developed an Object Based Image Analysis (OBIA) procedure for automatic detection of crop rows and identification of weeds between these rows. The achieved results showed the ability to detect crop rows with accuracy 95% along with weed detection of accuracy 90%.

For the same purpose of weed detection from UAV-based Remote Sensing imagery data, Peña & Gutiérrez (2015) proposed another weed detection approach, which also depends on crop row detection to detect weeds. The authors detect crop rows using Hough Transform as these rows take the shape of lines. The proposed research used two different types of imaging sensors, visible light and multi-spectral (six bands) cameras, onboard a UAV platform at two different flying heights (30 and 100m) to study the effect of changing the used sensor and the flying height on the weed detection accuracy. As the proposed approach tested two types of imagery sensors, different vegetation indices were used to suit each sensor. For the visible light sensor image, the Excess Green Vegetation Index (ExG) where used to discriminate plants from bare soil, while the NDVI was used for the multi-spectral sensor images for the same purpose. The achieved results showed the potential of such approach with a mean absolute error changing from 0.032 to 0.252 meters. The main conclusion from the proposed research was that the best results were achieved for 30 meters of flying height with the use of multi-spectral sensor showed better results than other cases.

Later, Peña Barragán et al. (2015) performed a detailed study for using a UAV system for weed detection. The used UAV was operated on different flying heights of 40, 60, 80, and 100 meters with a visible-light camera and a multi-spectral camera. The authors used a similar OBIA image analysis technique, which was introduced by the same authors (Peña Barragán et al., 2012). The achieved results suggested to use multi-spectral camera to collect imagery data with flying height of 40 meters to reach an accuracy of 91 % for weed detection. The main limitations of these techniques are mainly the need to use multispectral imagery sensors and to use low flying altitude to reach high weed detection accuracy.

This paper aims to develop an efficient approach to detect weed patches using low-cost UAV imagery systems. There are two main targets of the proposed approach. First, enhance the ability to detect weed patches form higher flight altitude to reduce the needed number of images to cover the agriculture field. Second, enhance the speed of weed detection by avoiding the need for crop rows detection which is considered as a major initial step for any weed detection approach (Peña and Gutiérrez, 2012; Tellaeche et al., 2008).

The proposed approach aims to detect weed patches from images acquired using a consumer grade RGB camera from higher flying altitude than 40 meters, recommended by different weed detection approaches (Peña Barragán et al., 2015). The proposed approach depends on detecting the weed patches instead of individual weed plants as they have higher effect on agriculture production. Moreover, increasing the ability of using low-cost RGB sensor to reduce the cost of using such UAV imagery, should increase the famers interest of using such systems for weed management agriculture applications.

The paper is organized as follows: Section 2 describes the proposed weed detection process including the image binarization and the grid system detector. Section 3 covers the performance of the proposed weed detection approach. Finally, in section 4 the conclusions are presented.

2. THE WEED DETECTION PROCESS

This paper aims to develop a weed patch detection approach for SSWM application. The proposed technique is targeting the detection of weed patches from RGB images acquired by consumer grade camera mounted on UAV platform. The use of UAV for different PA activities as weed management, showed high advantages for increasing the agriculture production in the recent years, mainly due to the high delivered spatial resolution images. Generally, as showed, the current available approaches for weed detection and management using UAV platforms, depend on using multi-spectral cameras to acquire the field's images. The main advantage of these multi-spectral images is the ability to detect vegetation objects using vegetation indices as (NDVI). The need to develop weed detection approach from RGB images is mainly motivated by the need to reduce the cost of the UAV imagery system. Also, the proposed approach through this paper has another important objective by detecting weed patches from images acquired at higher flight altitude compared to other previous approaches.

Moreover, the proposed weed detection approach is targeting the detection of weed patches in the agriculture field instead of detecting each weed plant. Generally, there are three major types of weed distribution in the agriculture fields, as shown in figure (1). First, the regular weed distribution is where the weeds density is distributed equally on the agriculture field. Second, the random distribution where the weeds are distributed with equal density, but with unequal spacing on the field. Third, which is the most common distribution, the patchy weed distribution is where the weeds are concentrated in some spots in the field. The detection of weed patches is more valuable than the detection of individual weed plants. This is mainly due to the higher effect of weed patch compared to the individual weed plant. Also, with adopting the weed patch detection is providing a faster weed detection approach compared to detecting each weed plant in the agriculture field.

The proposed weed patch detection approach goes through two major steps. First, an image binarization process is used to convert the acquired RGB colour image into a vegetation binary image where the vegetation objects in the RGB image are represented as white pixels while the remaining objects are represented in black pixels. The use of such approach aims to

discriminate the vegetation objects as crop and weed plants from the remaining parts of the agriculture image as the bare soil. The second step of the weed patch detection is the use of a grid of zones, where the zones that contain high percentage of vegetation presence will be detected and considered as weed patches. Figure (2), is showing a general flow chart of the proposed approach.

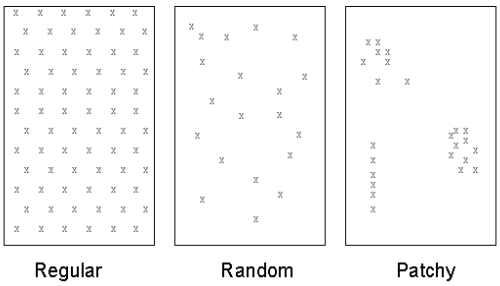

Figure 1. Weed distribution cases in the agriculture field (Wiles et al., 1992).

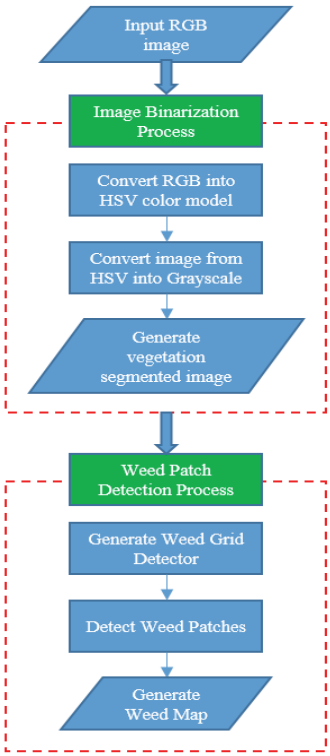

Figure 2. flowchart of the weed detection approach.

2.1 Image Binarization Process

The use of UAV imagery system for weed management application and other PA activities mainly depends on using the machine vision, computer vision, or image processing methods due to the delivered high spatial resolution images. The main issue related with the use of these methods is the image segmentation. For different PA activities as weed management and crop monitoring, an automatic segmentation of vegetation objects from the acquired images of the field is considered as an important step (Guijarro et al., 2011). The process of segmenting the crop canopy in images is named as image binarization which aims to convert the input RGB image into binary (black and white) image. The delivered binary image is providing an important representation of vegetation objects, as the vegetation objects (weeds and crops) are represented with white color while the remaining parts are represented with black color. As there are two main components in the agriculture field, the bare soil and the vegetation objects, the discrimination between these two components can enhance the efficiency of PA activities as weed management and crop monitoring (Comba et al., 2015; Tang et al., 2016; Tellaeche et al., 2008).

There are several strategies that have been used for RGB image segmentation for detecting the vegetation objects. These strategies are based on different approaches. First, the visible spectral index approaches depend on using different indices as the excess green index (ExG) or the excess red index (ExR). The main limitation of these approaches is the need to fix a suitable threshold for the final segmentation. Other approaches for image segmentation are based on using a specific threshold as Otsu's method (Otsu, 1979). These approaches are generally targeted to solve a two classes segmentation problem. The basic steps for these approaches depends on converting the RGB image into grayscale image and then compute the suitable threshold to generate the binary image or the two segments image. The main limitation for such specific based approaches is that they are based on a major assumption that the image objects can be clustered into two main parts which are vegetation and non-vegetation based on a specific color threshold as non-vegetation objects are always darker than vegetation objects, which might be affected due to illumination and lightning conditions. The third type of image segmentation approaches used for such vegetation object segmentation is based on supervised and unsupervised learning approaches. For example, Meyer et al. (2004) used unsupervised approaches as fuzzy clustering for segmenting regions of interest. While, Tian and Slaughter (1998) developed a plants detection approach using supervised learning process.

As most of these approaches from the three strategies are highly affected with the illumination conditions, which is an important factor affecting the UAV acquired images for any agriculture field, the adopted image segmentation technique depends on using HSV color space to deal with the illumination variability. To generate a vegetation binary image from a color RGB image, the adopted technique depends on two main steps. First, the acquired image color space is converted from RGB color space into HSV color space. Following, a specific threshold is used to segment the vegetation object in the HSV image. The following parts is providing full description for these two steps.

2.1.1 Converting the image color space: A color space or a color model of an image is the use of a coordinate system to describe colours in the image. For example, one of the most common used color models is the RGB, where all objects in the image have a color representation based on using three main colours which are the red (R), green (G), and blue (B). The main limitation of discriminating the green color objects (vegetation objects) from the RGB color space image is the high correlation between the three color channels used to generate the color for these objects. Also, as the RGB images for the agriculture field is easily affected by lightness condition due to cloud coverage and imaging time, the segmentation precision could by highly affected if the RGB images were used directly for the vegetation segmentation process (Tang et al., 2016). So, it is important to convert the acquired RGB image into different color space to have higher ability to detect objects with green color.

The HSV color model uses the hue, saturation, and value parameters to represent RGB color model in a cylindrical coordinate system, as shown in figure (3). The hue or the H parameter represents the angle around the central vertical axis.

The saturation or the S parameter represents the distance along the horizontal axis of the cylinder. Finally, the value or the V parameter represents the distance along the vertical axis. Any color in the HSV is represented based on the following. The H parameter is the color grade, so any color has an independent representation. The hue (H) or the angular dimension starts with the red at 0^0, then reaches the primary green at 120^0, following reaches the primary blue at 240^0, and finally goes back to red at 360^0. On the other hand, the saturation (S) parameter represents the vibrancy of the color, while the value (V) parameter represents the brightness of the color.

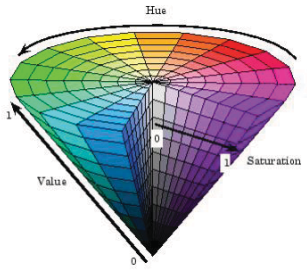

Figure 3. HSV color model (Riaz et al., 2008)

Using such color representation enhances the ability to detect colours for different computer vision applications especially as the H component is not affected in different light conditions. So, it can be used to discriminate objects based on their color even at different illumination conditions (Tang et al., 2016). Due to such advantages that can be provided from using HSV color model, the first step of the used image binarization process is the converting of the image color model from RGB into HSV using the following procedure (Park et al., 1999). First, the R, G, and B values are normalized as:

$$R' = R/255 \quad (1)$$

$$G' = G/255 \quad (2)$$

$$B' = B/255 \quad (3)$$

Then, the maximum (M) and the minimum (m) of the normalized R, G, and B is detected along with the difference between the maximum and minimum values as C.

$$M = \max(R', G', B') \quad (4)$$

$$m = \min(R', G', B') \quad (5)$$

$$C = M - m \quad (6)$$

Using the previous values the H, S, and V parameters can be computed using the following equations.

$$H = \begin{cases} 0^0 & if\ C = 0 \\ 60^0 * \left(\frac{G' - B'}{C}\ mod 6\right) & if\ M = R' \\ 60^0 * \left(\frac{B' - R'}{C} + 2\right) & if\ M = G' \\ 60^0 * \left(\frac{R' - G'}{C} + 4\right) & if\ M = B' \end{cases} \quad (7)$$

$$S = \begin{cases} 0 & if\ M = 0 \\ \frac{C}{M} & if\ M \neq 0 \end{cases} \quad (8)$$

$$V = M \quad (9)$$

2.1.2 Image segmentation: Following the construction of the HSV image the second step of image binarization or the vegetation objects segmentation starts. To perform the image segmentation, the HSV image is binarized through using a suitable threshold to detect the green objects only. As the HSV color model enhance the ability to detect color green through using the suitable H value which represents the green color. As mentioned, the H parameter is an angular representation for the color, so with using the H value as the threshold the green color can be detected. Using the H values for the different colours, the H value for green color is ranging between 60^0 and 180^0, where the primary green is at H equal to 120^0. So, the followed sequence to reach the segmented image was by converting the HSV image into gray scale image in the first step, where it is important to note that the H parameter is the controlled in the converting process as the other two channels (S and V) values are ranging between 0 and 1. The second step is to use a suitable threshold to detect the green illumination within the gray scale image.

2.2 Weed Patch Detection

The proposed approach for weed patch detection depends on creating a grid of zones, as shown in figure (4). The generated grid main objective is to divide the images field into zones. So, with analysing the vegetation intensity at each zone, the weed patches could be detected. To generate the weed grid detector, it is important to select a reasonable grid zone window size (I_w). Another important issue to detect the weed patches is selecting the suitable intensity of vegetation objects in the grid zone to be considered as weed patch. In the following parts, these two important issues will be discussed.

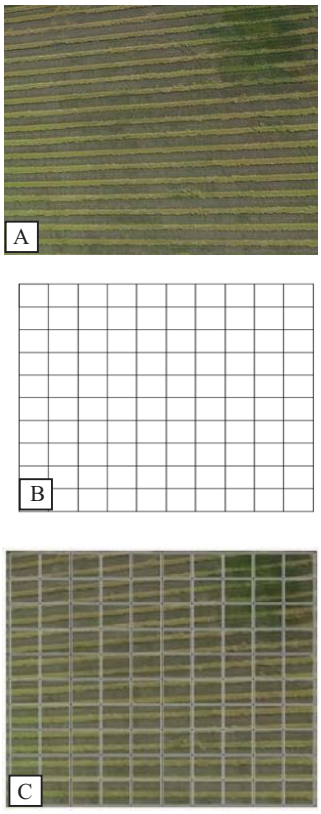

Figure 4. (A): agriculture field infected with weed patch, (B): Weed detector grid, (C): agriculture field divided zones.

2.2.1 Grid detector window size (I_w): The suitable grid detector window size is effected with different factors as the flying altitude, the crop row width, and the crop and weed type. So, to achieve an efficient weed detector approach, it is important to develop an algorithm to automatically detect the suitable grid window size despite the mentioned factors. The proposed method to detect the grid window size goes through the following steps, as shown in figure (5).

First, the inputted binary image longest side length is used to create a group of grids where each grid has a different window size (I_w). The largest successful grid window size is selected, as shown in figure (5). Following, the grid window size is reduced by 20% and check for a successful detection. If the detector grid is successful, the reduction of window size continuous until it failed. The smallest successful window size is considered as the suitable window grid size (I_w).

There are two important conditions for considering the window grid size a successful detector, beside detecting weed patches:

- Some of the detected weed patches must belong to the detected weed patch with the with the previous successful window.
- Excluding the detected weed patches within the detected weed zones acquired by the previous grid, the remaining weed patches shouldn't exceed 10% of the remaining image.

After selecting the suitable window size, the detected weed zones using the selected grid goes through a final condition to remove blunders zones to finally produce the weed map. The condition is accepting the detected weed zones which has detected neighbour zones within at least two different orientation.

2.2.2 Weed Patch Detector: Another important issue related to detecting weed patches is selecting the suitable ratio of vegetation density in the grid zone to be selected as weed patch. After testing different ratios, the 90% ratio showed the most suitable results. It is important to state that selecting the suitable grid window size (I_w) has higher effect than selecting the suitable vegetation intensity ratio.

3. RESULTS AND ANALYSIS

For testing the proposed approach, the following sections provide description the imagery data along with the achieved results for each step of the proposed weed detection approach.

3.1 Image Acquisition

To test the proposed approach, an RGB consumer grade camera of model Canon PowerShot SX260 HS was used on fixed wing UAV from AgEagle for aerial systems, as shown in figure (6). The UAV imagery system was used to collect images for an agriculture field in the southern part of Alberta, Canada. The used image for testing the weed detection approach was acquired for an agriculture field planted in rows from 120 meters flying altitude.

Figure 6. AgEagle fixed wing UAV on the left, Canon PowerShot SX260 HS camera on the right.

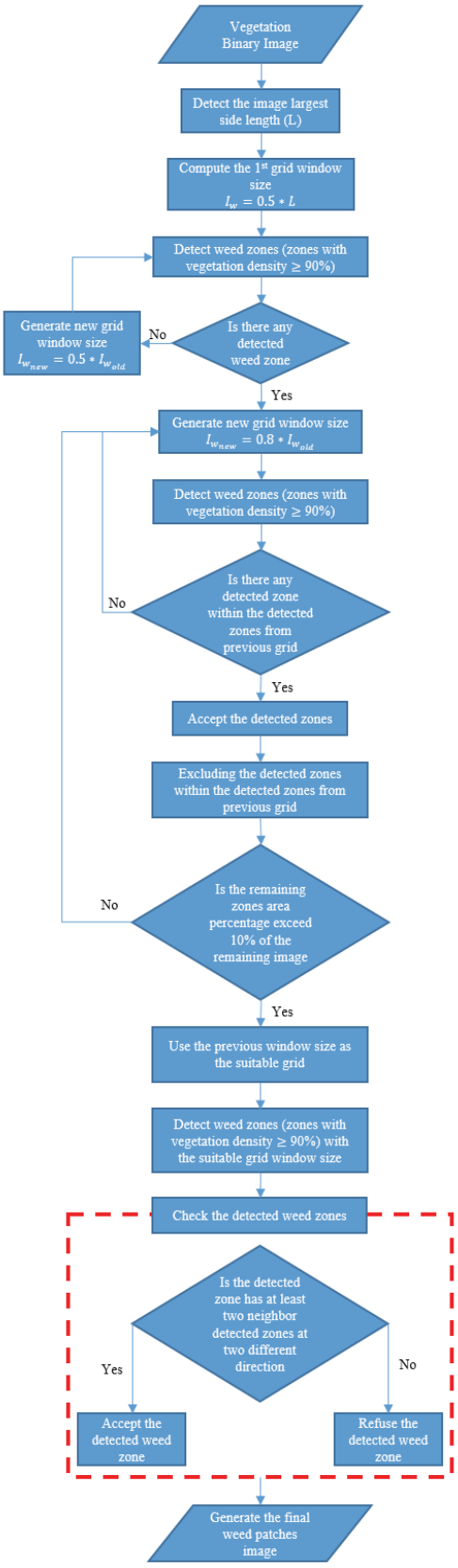

Figure 5. Flowchart of detecting the suitable window size for efficient weed patch detection.

3.2 Image Binarization

Following the mentioned flow chart in figure (2), the image binarization or the vegetation segmentation step starts with converting the acquired image color space from the RGB into HSV. Then, the binarization step is performed through converting the HSV image into grayscale image by normalizing the H channel. Following, with testing different thresholds values, the binary segmented image is generated. Figure (7) shows the different acquired images for the image binarization process.

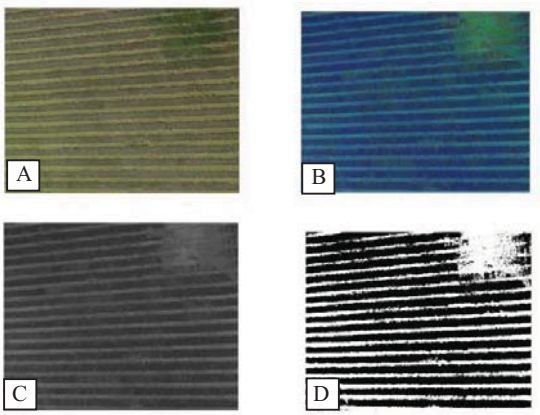

Figure 7. The generated images at different stages of the agriculture field through the binarization process; (A): RGB color model, (B): HSV color model, (C): Grayscale image, (D): vegetation binary image

3.3 Weed Patch Detection

The second step of the proposed weed detection approach is the construction of the grid detectors and the detection of weed patches. To test this step, the acquired binary image is rotated into different rotations to test the change of crop rows rotation effect on the proposed approach accuracy.

Following the presented flow chart in figure (5), for each image, the longest side length is selected to be used to create the grid detector window size (l_w). The proposed methodology of selecting the suitable window size, starts with testing different window size to detect the largest window size that can detect weed patch. The initial window size is equal to 50% of the selected side length. Then, the grid is used to detect zones that has a vegetation intensity ratio exceed 90%. later, the window grid size is reduced till detecting the smallest successful window size that can achieve the two major conditions. First, the grid can detect weed patches that belong to the largest weed patch detected by previous successful window grid detector. Second, the detected weed patches area doesn't exceed 10% of the image after removing the detected weed patches within border and the previous weed patch. The smallest accepted window size is considered as the suitable window size for the weed patch grid detector. Figure (8) is showing the detected weed patches for different window sizes.

As shown in figure (8), the smallest successful window size is 50 for the case shown in figure (8.G) as the case of window size of 40 as shown in figure (8.H) failed with the second condition due to the high percentage of detected weed zones which might be crop rows. The final step is using the detected weed patches with the selected window grid size as the generated weed patch map after removing the blunder detected zones, as shown in figure (9). Figure (10) shows the different achieved results using the proposed approach for different rotated images.

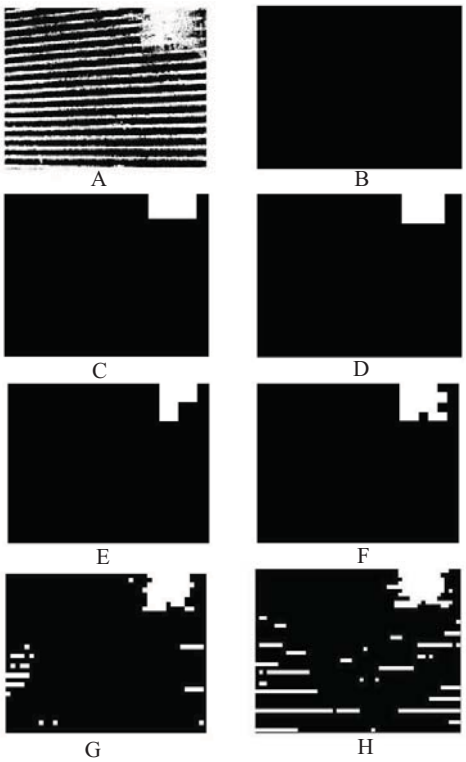

Figure 8. (A): the initial binary image, (B) – (H): detected weed zones for different window sizes (500, 250, 200, 150, 100, 50, 40).

Figure 9. The final weed map

4. CONCLUSION

The weed detection is considered as an important part for SSWM application which is a main activity of the modern agriculture development or the precision agriculture. This paper is introducing a different track for weed management based on detecting weed patch instead of detecting the individual weed plant. Also, the proposed approach is targeting reducing the complexity of the weed detection process by avoiding detecting crop rows. The ability of the proposed approach to detect the same weed patch location within the different rotated images, as shown in figure (10), validate the ability of the proposed approach to detect weed patches with different crop row orientations.

It is important to note that the achieved results proved the ability of the proposed approach to detect weed patches using RGB images acquired from consumer grade imagery sensors. Such ability reduces the cost of using UAV imagery system for weed management. Moreover, the proposed approach successfully detected weed patches from images acquired from the maximum allowed flying altitude which is 120 meters. The importance of achieving such objective. Such advantage contributes in reducing the required number of images needed to cover large agriculture

filed, so reduce the amount of collected data and speed up the process of generating weed maps for the whole field.

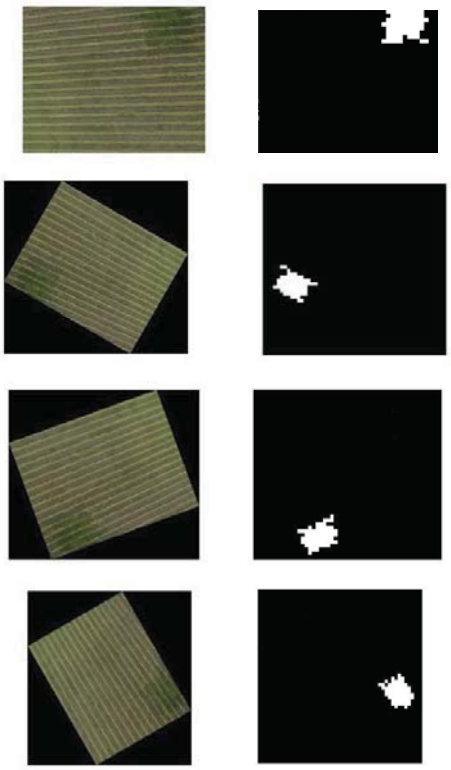

Figure 10. Detected weed patches for different cases of rotated crop rows.

ACKNOWLEDGEMENTS

This work was supported by Dr. Naser El-Sheimy research funds from NSERC and Canada Research Chairs programs. Also, the authors would like to thank Acuvec Geospatial Inc. for their generous support to provide the required imagery data to test the proposed approach.

REFERENCES

Comba, L., Gay, P., Primicerio, J., Ricauda, D., 2015. Vineyard detection from unmanned aerial systems images. Comput. Electron. Agric. 114, 78–87.

Göktogan, A.H., Reid, A., Bryson, M., Hung, C., Sukkarieh, S., 2012. The System Perspective of Using UAVs in Weed Surveillance and Management. Isr.Uc.Pt.

Guijarro, M., Pajares, G., Riomoros, I., Herrera, P.J., Burgos-artizzu, X.P., Ribeiro, A., 2011. Automatic segmentation of relevant textures in agricultural images. Comput. Electron. Agric. 75, 75–83.

Laliberte, A.S., Herrick, J.E., Rango, A., Winters, C., 2010. Acquisition , Or thorectification , and Object-based Classification of Unmanned Aerial Vehicle (UA V) Imager y for Rangeland Monitoring 76, 661–672.

Lamb, D.W., Brown, R.B., 2001. Remote-Sensing and Mapping of Weeds in Crops. J. Agric. Eng. Res. 78, 117–125.

Lelong, C.C.D., Burger, P., Jubelin, G., Roux, B., Labbé, S., Baret, F., 2008. Assessment of Unmanned Aerial Vehicles Imagery for Quantitative Monitoring of Wheat Crop in Small Plots 3557–3585.

Meyer, G.E., Neto, J.C., Jones, D.D., Hindman, T.W., 2004. Intensified fuzzy clusters for classifying plant, soil, and residue regions of interest from color images. Comput. Electron. Agric. 42, 161–180.

Mulla, D.J., 2012. Special Issue : Sensing in Agriculture Review Twenty five years of remote sensing in precision agriculture : Key advances and remaining knowledge gaps 5. Biosyst. Eng. 114, 358–371.

Otsu, N., 1979. A threshold selection method from gray-level histograms. IEEE Trans. Syst. Man. Cybern. 9, 62–66.

Paikekari, A., Ghule, V., Meshram, R., 2016. WEED DETECTION USING IMAGE PROCESSING 1220–1222.

Paikekari, A., Ghule, V., Meshram, R., Raskar, V.B., 2016. Weed Detection Using Image Processing. Int. Res. J. Eng. Technol. 3.

Park, D.S., Park, J.S., Kim, T.Y., Han, J.H., 1999. Image indexing using weighted color histogram. Proc. 10th Int. Conf. Image Anal. Process. 909–914.

Peña Barragán, J.M., Kelly, M., Castro, A.I.D., López Granados, F., 2012. Object-Based Approach for Crop Row Characterization in Uav Images for Site-Specific Weed Management. Procedings 4th GEOBIA 426–430.

Peña Barragán, J.M., Torres-Sánchez, J., Serrano Pérez, A., Castro, A.I.D., López Granados, F., 2015. Quantifying efficacy and limits of unmanned aerial vehicle (UAV) technology for weed seedling detection as affected by sensor resolution. Sensors (Basel). 15, 5609–5626.

Peña, J.M., 2015. An automatic object-based method for optimal thresholding in UAV images : Application for vegetation detection in herbaceous crops 114, 43–52.

Peña, J.M., Gutiérrez, P.A., 2015. a Weed Monitoring System Using Uav-Imagery and the Hough Transform. Actas la Soc. Española Malherbologia 1, 233–239.

Peña, J.M., Gutiérrez, P.A., 2012. A Weed Monitoring System Using Uav-Imagery And The Hough Transform, 233–239.

Peña, J.M., Torres-sánchez, J., Serrano-pérez, A., Castro, A.I. De, López-granados, F., 2015. Quantifying Efficacy and Limits of Unmanned Aerial Vehicle (UAV) Technology for Weed Seedling Detection as Affected by Sensor Resolution 3, 5609–5626.

Price, J.C., 1994. How unique are spectral signatures? Remote Sens. Environ. 49, 181–186.

Riaz, M., Kang, G.K.G., Kim, Y.K.Y., Pan, S.P.S., Park, J.P.J., 2008. Efficient Image Retrieval Using Adaptive Segmentation of HSV Color Space. 2008 Int. Conf. Comput. Sci. Its Appl. 491–496.

Shaw, D.R., 2005. Translation of remote sensing data into weed management decisions. Weed Sci. 53, 264–273.

Tang, J.L., Chen, X.Q., Miao, R.H., Wang, D., 2016. Weed detection using image processing under different illumination for site-specific areas spraying. Comput. Electron. Agric. 122, 103–111.

Tellaeche, A., Burgos-artizzu, X.P., Pajares, G., Ribeiro, A., 2008. A vision-based method for weeds identification through the Bayesian decision theory 41, 521–530.

Tian, L.F., Slaughter, D.C., 1998. Environmentally adaptive segmentation algorithm for outdoor image segmentation. Comput. Electron. Agric. 21, 153–168.

Wiles, L.J., Wilkerson, G.G., Gold, H.J., 1992. Value of information about weed distribution for improving postemergence control decisions. Crop Prot. 11, 547–554.

Zhang, C., Kovacs, J.M., 2012. The application of small unmanned aerial systems for precision agriculture : a review 693–712.

REMOTE HEALTHCARE MONITORING SYSTEM THROUGH MOBILE APPLICATION

Nancy S. El-Gamil [a, *], Alaa M. Adel El-Shazli [a, *], Sherin M. Youssef [a, *]

[a] Department of Computer Engineering, Arab Academy for Science and Technology, Alexandria, Egypt - nancyelgamil@gmail.com, alaa.alshazli@live.com, sherin@aast.edu, sherin.youssef@gmail.com

KEY WORDS: E-Health Care, Electrocardiogram (ECG), Mobile E-Health monitoring, QRS complex, Arduino, Wavelet.

ABSTRACT:

The eHealth monitoring, or remote electronic health monitoring, is a technology to enable monitoring of patients outside of clinical settings, which may increase access to care and decrease healthcare delivery costs. Incorporating eHealth monitoring systems in diagnosis and regular check-ups can significantly improve an individual's quality of life. It allows patients to maintain independence, prevent complications, and minimize personal costs. In addition, patients and their family members feel comfort knowing that they are being monitored and will be supported if a problem arises. The research starts with a study of the technology of mobile applications, with emphasis on the analysis of different mobile platforms and mobile software developing tools. The objective of the paper is to design and implement a remote mobile health care monitoring system. The designed E-health system will be able to monitor and track Pulse and oxygen in blood, Body temperature, and cardiac status through Electrocardiogram sensor (ECG), Glucose and airflow breathing state. A signed interface will be implemented to transfer and visualize the sensor readings to the device. A mobile application will be designed to process, monitor, and visualize this medical information. A data visualization GUI will be designed for Android devices. Different modules have been designed and implemented using Eclipse IDE to access mobile resources. The system will also be capable of remotely analysis ECG signals. These ECG signals maybe normal and abnormal. The hardware design includes an Arduino ADK board, which has a host interface to connect with Android based devices.

1. INTRODUCTION

Mobile applications are applications or services that can be pushed to smartphones, tablet computers and other mobile devices or downloaded and installed locally to help users by connecting them to Internet services. The popularity of mobile applications has continued to rise, as their usage has become increasingly prevalent across mobile phone users. Mobile applications allow a user to customize a phone to their specific set of wants and needs. It's easy to find and install, and once you start using them, will become a necessary part of your mobile life. Most recently, there has emerged significant interest in healthcare applications to be developed for smart phones.

Considerable efforts have been made to the development of remote control systems for human health. Remote healthcare monitoring may include monitoring and tracking user's Pulse and oxygen in blood, Body temperature, and cardiac status through Electrocardiogram sensor (ECG), Glucose and airflow breathing state.

Rural and remote areas also share common traits such as generally older populations, higher levels of health risks and higher rates of disease, chronic disease and injury. People living in these areas generally have less access to health services with shortages of almost all health professions and health-related infrastructure. Remote healthcare monitoring for the elderly and disabled can provide increased quality of life for people who might be living in rural areas and find it too difficult to leave their homes for regular check-ups, and for the ones who have difficulty in any physical activity such as leaving bed or walking. It can also provide a remote interface with the doctor's mobile, via mobile application, to provide control and monitoring via a smart phone or web browser. The patient can regularly get his checks done at home and even send them to his doctor through the mobile app, and on the other hand, the doctor can check all the readings and provide the patient with the most suitable medicine, and treatment. This paper will describe the approach, which is implemented to control various health problems with Android smart phone.

2. OBJECTIVES

The objective of the paper is to design and implement a mobile healthcare monitoring system. The designed E-health system will be able to monitor and track patients and athletes' medical status using a various number of sensors including a pulse-oximeter to measure pulse and oxygen in the blood, body temperature sensor, electrocardiogram sensor (ECG) to track cardiac status, a GSR sensor to measure skin response and an airflow and breathing sensor to check the breathing state. A signed interface will be implemented to transfer and visualize the sensor readings to the device. A mobile application will be designed to process, monitor, and visualize this medical information. A data visualization GUI will be designed for Android devices. Different modules have been designed and implemented using Eclipse IDE to access mobile resources. The system will also be capable of remotely analysis ECG signals. These ECG signals maybe normal and abnormal. Patient will then be able to send the result to the professionals for consultancy. The hardware design of the system includes an Arduino ADK board, which has a host interface to connect with Android based devices.

* Corresponding author
* Corresponding author
* Corresponding author

3. METHODOLOGY

In summary, in our developed paper, a number of different medical health sensors will be used, such as: pulse-oximeter, ECG, airflow/breathing, temperature, GSR and Glucometer.
Moreover, Arduino technology will be used to integrate the mentioned sensors.
The system is implemented as a mobile application to which the results and readings will be sent from the Arduino wirelessly via Bluetooth. Throughout the lifecycle, two different scenarios have been explored. First scenario involved connecting a Pulse Sensor to Arduino and interfacing it to display readings in two different ways, once using the Arduino USB cable and once using Bluetooth.
The second scenario incorporated an Arduino compatible eHealth monitoring kit and wirelessly, as in Figure 1, interfacing it with an Android powered mobile device via Bluetooth. The phases included introduction to the medical sensors and their readings.

Figure 1. Model Diagram

3.1 Medical Sensors

In this system, the following sensors will be used:

1. Pulse and Oxygen in Blood.
2. ElectroCardioGram.
3. Airflow and Breathing.
4. Body Temperature.
5. Galvanic Skin Response.
6. Glucometer.

3.1.1 Pulse and Oxygen in Blood: Pulse and Oxygen in Blood is one of the sensors that were connected to the eHealth kit. Pulse oximetry a non-invasive method of indicating the arterial oxygen saturation of functional haemoglobin. Oxygen saturation is defined as the measurement of the amount of oxygen dissolved in blood, based on the detection of haemoglobin and deoxyhaemoglobin.
A pulse oximeter sensor is useful in any setting where a patient's oxygenation is unstable, including intensive care, operating rooms, recovery rooms, emergency and hospital ward settings, pilots in unpressurized aircraft, for assessment of any patient's oxygenation, and determining the effectiveness of or need for supplementary oxygen.
Acceptable normal ranges for patients are from 95 to 99 percent. The sensor needs to be connected to the Arduino, without using external/internal battery.

Figure 2. Pulse and Oxygen Sensor

3.1.2 ElectroCardioGram: ElectroCardioGram (ECG) is a diagnostic tool that is routinely used to assess the electrical and muscular functions of the heart. The ECG has grown to be one of the most commonly used medical sensors in modern medicine.
We can detect the following on the ECG:
1. The orientation of the heart (how it is placed) in the chest cavity.
2. Evidence of increased thickness (hypertrophy) of the heart muscle.
3. Evidence of damage to the various parts of the heart muscle.
4. Evidence of acutely impaired blood flow to the heart muscle.
5. Patterns of abnormal electric activity that may predispose the patient to abnormal cardiac rhythm disturbances.

Figure 3. ElectroCardioGram Sensor

3.1.3 Airflow (Breathing): Abnormal respiratory rates and changes in respiratory rate are a broad indicator of major physiological instability, and in many cases, respiratory rate is one of the earliest indicators of this instability. Therefore, it is critical to monitor respiratory rate as an indicator of patient status. Airflow sensor can provide an early warning of hypoxemia.
The nasal / mouth airflow sensor is a device used to measure the breathing rate in a patient in need of respiratory help or person. This device consists of a flexible thread, which fits behind the ears, and a set of two prongs, which are placed in the nostrils to measure breathing.

Figure 4. Airflow Sensor

3.1.4 Body Temperature: Body temperature depends upon the place in the body at which the measurement is made, and the time of day and level of activity of the person. Different parts of the body have different temperatures.
The commonly accepted average core body temperature is 37.0°C (98.6°F). In healthy adults, body temperature fluctuates about 0.5°C (0.9°F) throughout the day, with lower temperatures in the morning and higher temperatures in the late afternoon and evening, as the body's needs and activities change.
It is of great medical importance to measure body temperature. The reason is that a number of diseases are accompanied by characteristic changes in body temperature. Likewise, the course of certain diseases can be monitored by measuring body temperature, and the efficiency of a treatment initiated can be evaluated by the physician.

Temperature ranges are as follows:

Hypothermia < 35.0 °C (95.0 °F)
Normal 36.5–37.5 °C (97.7–99.5 °F)
Fever or Hyperthermia > 37.5–38.3 °C (99.5–100.9 °F)
Hyperpyrexia > 40.0–41.5 °C (104–106.7 °F)

Figure 5. Body Temperature Sensor

3.1.5 Galvanic Skin Response: Skin conductance, also known as galvanic skin response (GSR) is a method of measuring the electrical conductance of the skin, which varies with its moisture level. This is of interest because the sweat glands are controlled by the sympathetic nervous system, so moments of strong emotion, change the electrical resistance of the skin.

Figure 6. Galvanic Skin Response Sensor

3.1.6 Glucometer: Glucometer is a medical device for determining the approximate concentration of glucose in the blood. A small drop of blood, obtained by pricking the skin with a lancet, is placed on a disposable test strip that the meter reads and uses to calculate the blood glucose level. The meter then displays the level in mg/dl or mmol/l.

Figure 7. Glucometer Sensor

3.2 Arduino eHealth Shield

There are many different types of Arduino, each of which has a different application to the others. Furthermore, there are a variety of different shields that can be used to enhance or add more features to the Arduino board being used.
The e-Health Sensor Shield allows Arduino users to perform biometric and medical applications where body monitoring is needed by using different sensors: pulse and oxygen in blood, electrocardiogram, airflow, body temperature, galvanic skin response and glucometer. This information can be used to monitor in real time the state of a patient or to get sensitive data in order to be subsequently analysed for medical diagnosis.
To illustrate the establishment of connections to and from the Arduino board: First, the data was transmitted from the Arduino to a computer using the USB cable. Then, a Bluetooth connection was established between the Arduino and a computer. Finally, by the end of the development period, it was possible to connect the Arduino to an Android powered mobile device and display sensor results, this was done by wirelessly by connecting them using Bluetooth technology.
The final output is a fully functional Android compatible mobile application that displays sensor readings and plots graphs if required.

Figure 8. eHealth Shield

After Finishing the first Phase which consist of the study of the Arduino board, how to control the sensors, and how to get the readings sent to the mobile through the Arduino board. The second phase start, the second phase consist of the interface and mobile Application, where the mobile application is implemented with the interface and the connection between the Arduino board and the mobile application.
This remote monitoring system includes a classifying stage, which is mainly responsible for classifying the readings of the sensors for the patient as a healthy or an unhealthy patient. If there is any abnormal reading, the patient is notified as being unhealthy, and advised to send results to the doctor for consultancy and follow ups.
The system is not only capable of remotely analysis ECG signals but also give the patient the ability to send the result to the professionals for consultancy.

3.3 Analysis of ECG signals

The importance of ECG analysis comes from the fact that it can discover many cardiac diseases such as ventricular fibrillation, arrhythmia, atria abnormality, and cardiac infraction.
Electrocardiogram signal is one of the most important biological signals used to diagnose heart diseases.
Fundamentally an ECG signal is simply a representation of the electrical activity of the heart muscle from different angles as it changes with time. Electrodes are placed on different parts of a patient's limbs and chest to record the signal. It is a graphical record of the direction and magnitude of the electrical activity that is generated by depolarization and repolarization of the atria and ventricles. ECG varies from person to person due to the difference in position, size, anatomy of the heart, age, relatively body weight, chest configuration and various other factors. In this paper we used pre-recorded data of the PTB Diagnostic ECG Database.

Examples of ECG signal are shown in Figure 9.

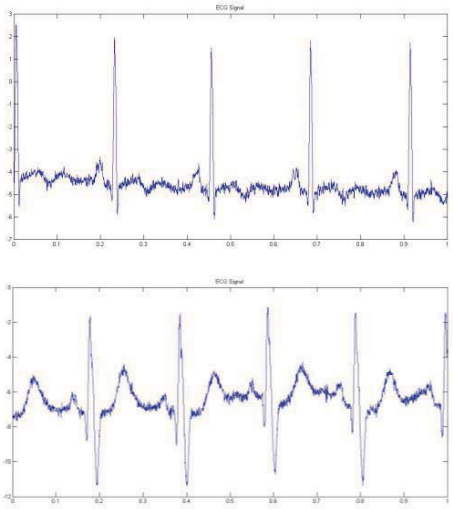

Figure 9. ECG Signal

A brief overview of this electrical activity follows.
The ECG is characterized by a recurrent wave sequence of P, QRS, and T wave associated with each beat as in Figure 10.

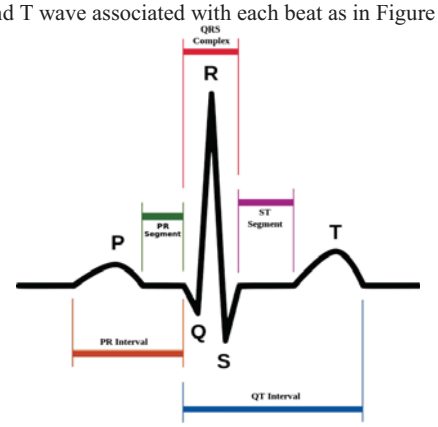

Figure 10. ECG waves

The shape of ECG conveys very useful hidden information in its structure. The amplitude and duration of each wave in ECG signals are often used for the manual analysis.
ECG signal should be processed to extract important information. Structure of ECG signal processing as shown in Figure 11.

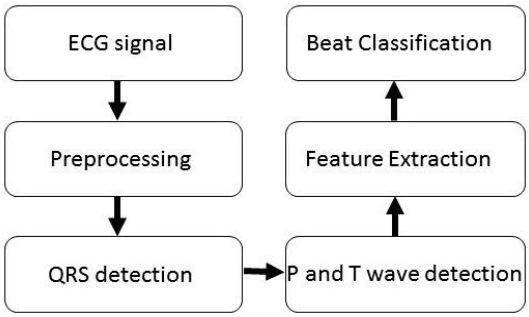

Figure 11. Structure of ECG signal

(a) Pre-processing

The Pre-processing of an ECG signal is performed for the removal of noise associated with the ECG signal.
ECG signal mainly contains noises of different types such as Powerline Interference, Baseline Wandering and Muscle Noise.
Artefacts are the noise induced to ECG signals that result from movements of electrodes. One of the common problems in ECG signal processing is baseline wander removal which is a common noise in ECG signal.
Baseline wander is a low-frequency component present in the ECG system. This is due to offset voltages in the electrodes, respiration, and body movement. This can cause problems in the analysis of the ECG waveform. We subtract base and divide by gain which come from the info file. This file gives various information regarding the ECG signal.
In this paper, we used MATLAB to remove baseline in order to obtain good ECG signal noise free.

(b) QRS Detection

The QRS complex is a name for the combination of three of the graphical deflections seen on a typical ECG signal. It is the most striking waveform within the ECG, caused by ventricular depolarization of the human heart. It is seen as three closely related waves on the ECG (Q, R and S wave).
The normal duration (interval) of the QRS complex is between 0.08 and 0.10 seconds. A QRS duration of greater than 0.12 seconds is considered abnormal. The detection of a QRS complex seems not to be a very difficult problem. However, in case of noisy signal not every QRS complex contains a Q wave, an R wave, and an S wave.

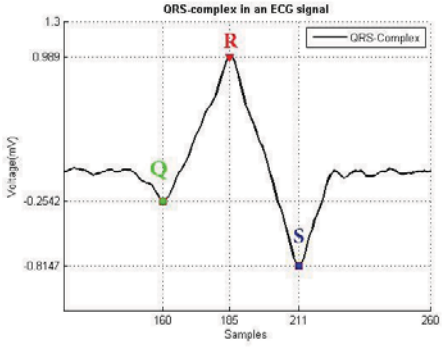

Figure 12. QRS complex

(c) P and T wave Detection

Detection of P and T waves is an important part in the analysis and interpretation of ECG.
The P-waves represent atrial depolarization. In sinus rhythm, there should be a P-wave preceding each QRS complex.
The normal duration (interval) of the P wave is less than 0.12 seconds.
The T-wave represents the voltage repolarization influence after ventricular depolarization. Repolarization is lower than depolarization, and as a result the T wave is more spread out and has a lower amplitude (height) than the QRS wave. It is after ST segment having the same direction with QRS complex, whose width is about 0.05-0.25 seconds.

(d) Feature Extraction

The purpose of the Feature Extraction process is to select and retain relevant information from original signal. The Feature Extraction stage extracts diagnostic information from the ECG signal.

In this paper, we used Wavelet Transform to extract features.

The discrete wavelet transform has a huge number of applications in science, engineering, mathematics, and computer science. It is a time-scale representation that has been used in signal compression and the detection of ECG characteristic points also.

The Wavelet transformation is a linear operation that decomposes the signal into a number of scales related to frequency components and analyses each scale with a certain resolution.

The advantages of wavelet methods are possibility of receiving good quality signal for beat to beat analysis and possibility of having high quality signal. It is also able to decompose signals at various resolutions, which allows accurate feature extraction from ECG signal.

And we also detected the average difference between R peaks.

Here is example for Wavelet packet decomposition of ECG signal as in figure 13.

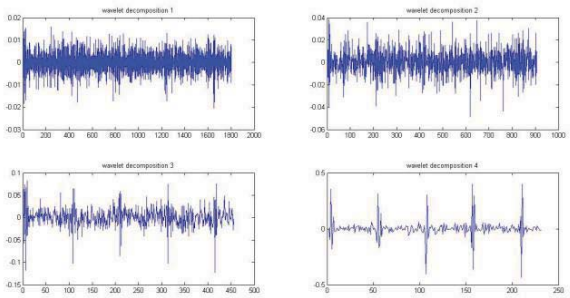

Figure 13. WPD

(e) Beat Classification

ECG beat classification plays an important role in the timely diagnosis of the critical heart condition.

Beats were classified into two different classes as normal beats and abnormal beats.

ECG signals can be used as a diagnostic tool to determine abnormalities in cardiac function or it can be visualize the effects of cardiac tissue damage. Abnormalities in the QRS complex indicate problems in the ventricles or ventricular conduction. In normal ECG, T wave is of positive amplitude but in abnormal ECG, the T wave can be inverted having negative amplitude.

There are various abnormal ECG signals as follows:

Sinus bradycardia

Bradycardia is a term to describe the heart beating more slowly than normal. Sinus bradycardia can occur in well-conditioned athletes and during sleep relaxation. In the case of athletes, the heart muscle is tremendously strong and efficient at pumping blood, therefore, less contraction needed. During deep relaxation, the body is at rest and requires less oxygen consumption than during normal activity which allows the heart rate to slow. However, sinus bradycardia can also occur as a result of heart disease or as a reaction to medication and when there is a normal upright P wave in lead II (sinus P wave) preceding every QRS complex. A sinus rhythm of less than 60 beats per minute is called sinus bradycardia. This may be a consequence of increased vagal or parasympathetic tone.

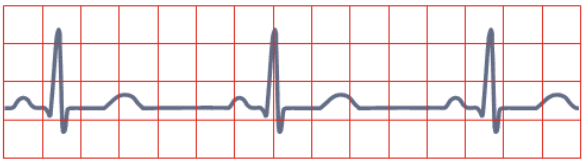

Figure 14. Sinus bradycardia

Sinus tachycardia

Excessive heart rate above 100 beats per minute (BPM) which originates from the SA node. Causes include stress, fright, illness and exercise. It is essential to identify one P for each QRS. It may be difficult to differentiate a sinus tachyarrhythmia from an atrial tachyarrhythmia

A sinus rhythm of higher than 100/min is called sinus tachycardia. It occurs most often as a physiological response to physical exercise or psychical stress, but may also result from congestive heart failure.

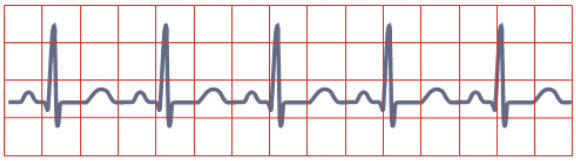

Figure 15. Sinus tachycardia

Junctional rhythm

If the heart rate is slow (40-55/min), the QRS-complex is normal, the P-waves are possibly not seen, then the origin of the cardiac rhythm is in the AV node. Because the origin is in the junction between atria and ventricles, this is called junctional rhythm. Therefore, the activation of the atria occurs retrograde (i.e., in the opposite direction). Depending on whether the AV-nodal impulse reaches the atria before, simultaneously, or after the ventricles, an opposite polarity P-wave will be produced before, during, or after the QRS-complex, respectively. In the second case the P-wave will be superimposed on the QRS-complex and will not be seen.

Figure 16. Junctional rhythm

4. EXPERIMENTS AND CONCLUSION

In this paper, a practical mobile-based E-Health monitoring system has been introduced. Experiments have been carried out through the Arduino controlled eHealth Mini Lab. The proposed platform is shown to tackle many of the challenges of health care. The introduced model handle the features of remotely monitoring, mobility, and access as a helping tool for earlier medical disease detection. The tracked medical status

includes Pulse and Oxygen in Blood, ElectroCardioGram, Airflow and Breathing, Body Temperature, Galvanic Skin Response and Glucometer. Additionally, an effective GUI mobile interface that has been designed and implemented to track the medical readings and acquired real-time medical signals on Android powered mobile devices. It is also applied for remotely diagnosis of radiological patterns. It shown to be robust and support special needs and elder people. The use of mobile applications to track health is becoming more widespread. Number of different sensors and Arduino technology are used, along with production of a fully functional product.

Different kinds of medical sensors are interfaced with mobile software kits using tools, like Eclipse IDE to produce this remote healthcare monitoring system.

The paper has emphasized the benefits of mobile healthcare monitoring, which include being able to track your health from the convenience of your home, sending the results to a doctor and not having to worry about transportation, distance or traffic to and from the clinic or hospital.

The paper also detect QRS complex and P and T wave from the original ECG signal. Then classify the signal to normal and abnormal beats.

REFERENCES

Fatos Xhafa, Philip moore, 2015. Advanced Technological Solutions for E-Health and Dementia Patient monitoring. ISSN 2327-9354.

Khan Md Ashikul Alam, 2014. Automated Synthesized Health Monitoring System, Anglia Ruskin University.

Fuchao Zhou, 2011. Mobile personal health care system for patients with diabetes, Iowa State University.

Katz., R., Mesfin, 2012. Lessons from a community-based mHealth diabetes self-management program: "it's not just about the cell phone", Suppl 1:67-72.

"Rural and remote health", 2017, https://www.healthdirect.gov.au/rural-and-remote-health.

"Understanding an electrocardiogram signal", 2017, http://geekymedics.com/understanding-an-ecg/.

Goldberger AL, Amaral LAN, Glass L, Hausdorff JM, Ivanov PCh, Mark RG, Mietus JE, Moody GB, Peng C-K, Stanley HE. PhysioBank, PhysioToolkit, and PhysioNet: Components of a New Research Resource for Complex Physiologic Signals. Circulation 101(23):e215-e220 [Circulation Electronic Pages; http://circ.ahajournals.org/content/101/23/e215.full]; 2000 (June 13). PMID: 10851218; doi: 10.1161/01.CIR.101.23.e215.

P.sasikala, Dr.r.s.d. WahidaBanu, 2011, Extraction of P wave and T wave in Electrocardiogram using Wavelet Transform, (IJCSIT) International Journal of Computer Science and Information Technologies.

P. Sasikala, 2010, Robust R Peak and QRS detection in Electrocardiogram using Wavelet Transform, (IJACSA) International Journal of Advanced Computer Science and Applications.

Wikipedia, "QRS complex", 2017. https://en.wikipedia.org/wiki/QRS_complex.

"The Basis of ECG Diagnosis", 2017. http://www.bem.fi/book/19/19.htm.

Jaakko Malimivuo, Robert Plonsey, 1995. Bioelectromagnetism. Oxford University Press, New York.

C. Saritha, V. Sukanya, Y. Narasimha Murthy, 2008, ECG Signal Analysis Using Wavelet Transform, Bulg. J. Phys.

FEASIBILITY STUDY OF A BACKPACK MOBILE TERRESTRIAL SYSTEM WITH A LOW COST OMNIDIRECTIONAL CAMERA

M. B. Campos [a], A. M. G. Tommaselli [a], E. Honkavaara [b.]

[a] São Paulo State University (UNESP), Presidente Prudente, Brazil
mariana.bcampos@gmail.com, tomaseli@fct.unesp.br
[b] Finnish Geospatial Research Institute (FGI), Helsinki, Finnish - eija.honkavaara@nls.fi

Commission VI, WG VI/4

KEY WORDS: poly-dioptric solutions, personal mobile mapping, 360° view cameras, mobile terrestrial systems

ABSTRACT:

Recently, a diversity of miniaturized and low cost sensors has entered in the market. Commercial GNSS receivers and IMU can be purchased for less than US$ 100 while, some models of omnidirectional cameras can be purchased by more or less than 500 dollars. Therefore, low-cost mobile mapping approaches can be developed integrating these systems. Most of these sensors were not developed for high accuracy metric purposes. However, good practices in data acquisition and rigorous methods of data processing can enable satisfactory results for a range of mapping applications. Looking to this background, the main objective of this paper is to present low cost Personal Mobile Terrestrial System (PMTS) approach composed by an omnidirectional camera with off-the-shelf navigation systems. PMTS evaluation was performed, analysing system feasibility and possible applications with centimetric accuracy.

1. INTRODUCTION

The main objective in this paper was to study an accurate, economic, viable and fast method to acquire indirect data with a ground view in difficult access places. Traditionally, terrestrial survey has applied static approaches. Inspired by surveying techniques, the sensors, which can be an optical camera or a laser scanner, are placed on a tripod to capture a limited scene, then tripod and sensor are moved to a new position or station to repeat the process until the entire area has been covered. Sometimes, this process can be time consuming and costly. Therefore, aiming a faster acquisition, Mobile Terrestrial Mapping System (MTMS) began to be developed and earned attention for a set of applications in indoor, urban, heritage and forest environments.

Mobile mapping systems are composed by navigation and remote sensors integrated in a common moving platform (Schuwarz and El-Sheimy, 2004), providing efficient, cost-effective, and complete data collection, considering the dynamic displacement of the sensors. Different types of platforms can be used in terrestrial mapping such as cars (Kukko *et al*, 2012), ground robots (Klingensmith *et al*, 2016), small Unmanned Aerial Vehicles (Shen *et al*, 2012), boats (Moraes *et al*, 2016), and a person (Kukko *et al* 2012; Corso *et al* 2013; Liang *et al* 2014; Lauterbach *et al*, 2015; Forsman *et al.*,2016). Personal Mobile Terrestrial System (PMTS) consist of a set of sensors that are carried by a human operator, for instance in a backpack, to acquire measurements of the environment while walking. Backpack platform provides mobility in environments where wheeled vehicles cannot be used, such as gravel roads, narrow passages, some cultural heritage locations, indoor buildings and forests.

Regarding forest mapping, the usage of PMTS has emerged in recent years. Kukko *et al*. (2012) introduced a backpack personal system composed by a MLS (FARO photon 120) and a NovAtel SPAN GPS-IMU for forest monitoring in Finland, obtaining a 3D point cloud accuracy range between 2- 5 centimetres. However, this PMTS has some disadvantages, such as two operators needs and system weight (approximately 30 kg), limiting its operability. The system proposed by Kukko *et al* (2012) was improved by Liang *et al* (2014), which showed a 10kg PMTS developed with a Global Navigation Satellite System (GNSS) receiver (NovAtel Flexpak6), an IMU (NovAtel UIMU-LCI) and FARO Focus3D 120 laser scanner. This acquisition system was either applied for forest purposes, estimating tree diameter at breast height with centimetre accuracy. An approach with digital cameras was presented by Forsman *et al.* (2016). In this work a multi-camera system in a backpack structure to estimate tree attributes in low density forest plots based on terrestrial photogrammetric techniques. This system was composed by five synchronized cameras: three Canon EOS 7D with wide angle lens and two Canon EOS 40D with Canon zoom lenses, in which DBH was obtained with an RMSE of 3.9 cm. In the same year, also aiming DBH estimation, Berveglieri *et al.* (2016) proposed an automatic technique to measure tree stem using vertical terrestrial images collected with a fisheye lenses camera in a tripod with a telescopic pole.

Despite of previous studies, these related works showed the relevance of researches involving PMTS with backpack platforms in forest applications. The most of PMTS uses mobile laser scanner solutions. This is a good alternative since MLS provide fast data acquisition, dense surface coverage, high relative accuracy and real time point cloud visualization. However, Mobile laser scanners are still a high-cost and heavy. MLS produce a huge amount of data, which could be a further problem for data processing and long-term storage. Furthermore, these sensors depend of an accurate inertial data for all instances, which can be unfeasible in a dynamic mapping inside a dense forest, for instance.

The optical approaches proposed by Forsman *et al.* (2016) and Berveglieri *et al.* (2016) obtained an accuracy in the tree parameters estimation compatible with MLS's backpacks and manual techniques. Nonetheless, some optical systems have some limitations such as the system weight and the implementation as single station at the centre of the plot, in which only a limited area of the plot is imaged. Omnidirectional systems, on the other hand, are lighter and outperform previous

sensors such lasers scanners and stereo cameras, in terms of the amount of usable information around the sensor for a fast environment mapping. Therefore, these systems can be an alternative to improve the limitations in the methods proposed by these authors.

In this regard, a new approach of PMTS with a backpacked omnidirectional system is presented in this paper. The omnidirectional system combines two fisheye lenses, with 180° horizontal field of view each, in a single camera structure, providing 360° imaging coverage (poly-dioptric solutions). The navigation system was developed combining low cost sensors such as a MPU 6050 inertial measurement unit with an Ublox NEO-6M GPS receiver integrated in an Arduino microprocessor. The description of this new PMTS is presented in Section 2. Experiments and results with this system are discussed in Section 3.

2. 360° BACKPACK MOBILE IMAGING SYTEM

The main subject of Section 2 is the development of the PMTS, which involves Sensor choice, settings and integration. Therefore, Section 2.1 describe system configuration, while, Section 2.2 discuss data integration procedure.

The mobile terrestrial system proposed in this research is a PMTS composed by a low cost omnidirectional camera and a navigation system carried by a backpack platform (Figure 1.a). Backpack was equipped with a rigid structure in "T" design. Omnidirectional system (Figure 1.b) was positioned in the top of this structure with the GNSS receiver and antenna, while, inertial navigation system, Arduino microprocessor and SD (Secured Digital) card (Figure 1.c) were placed below.

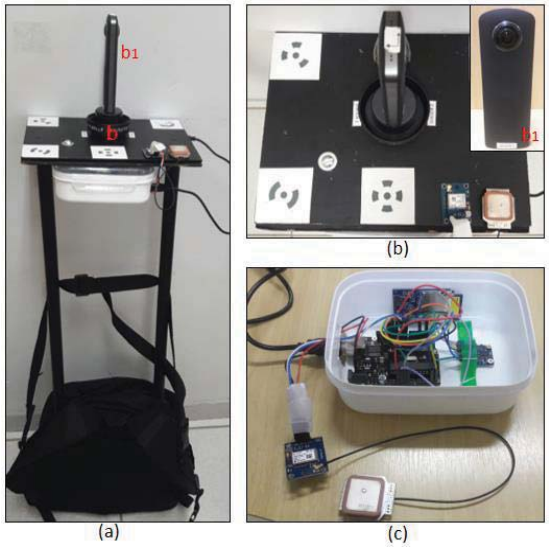

Figure 1. Backpack mobile terrestrial system with omnidirectional camera.

2.1 PMTS features

The omnidirectional system (Ricoh Theta S) is a poly-dioptric solution composed by two digital cameras with 180 degrees' fisheye lenses specially arranged in back-to-back position to cover a 360° field of view. Ricoh Theta S provides a still image, composed by images from both cameras acquired at the same instant. The processed image is generated internally spending 8 seconds. This image delay hinders an acceptable dynamic acquisition of images, which could not provide suitable images base length. Furthermore, Ricoh introduces tilt corrections and stitching which make difficult proper calibration. Therefore, dual-fisheye video was used to acquire omnidirectional data, since it's provides dense and continue frames acquisition. Also, dual-fisheye video is stored in the camera without any internal process. Video can be converted in frames for each camera separately with 960 x 1080 pixels image size and 0.005 mm pixel size.

An omnidirectional system calibration was done with dual-fisheye video frames, considering an independent bundle adjustment for each sensor. The unified approach to least squares adjustment was applied (Mikhail and Ackerman, 1976). Ricoh Theta S fisheye lenses follow Equidistant projection. Therefore, equidistant projection function with a distortion model for fisheye lenses was implemented in the in-the-house software CMC (Calibration Multi Cameras, Marcato Junior *et al*, 2015). Table 1 shows the Interior Orientation Parameters (IOP) estimated for both cameras and respective standard deviations. The set of IOP employed was focal length (f), principal point coordinates (x_0, y_0) symmetric radial distortion coefficients, k1, k2 and k3 and decentering distortion coefficients, p1 and p2 (Conrady, 1919; Brown, 1971).

IOP	Camera 1	Camera 2
$f(mm)$	1.4310 ± 0.0012	1.4303 ± 0.0019
$x_0(mm)$	-0.0016 ± 0.0010	0.0042 ± 0.0014
$y_0(mm)$	0.3013 ± 0.0011	0.2942 ± 0.0015
$k_1(mm^{-2})$	-0.0185 ± 0.0007	-0.0162 ± 0.0013
$k_2(mm^{-4})$	7.49E-3 ± 0.0004	6.21E-3 ± 0.0006
$k_3(mm^{-6})$	-1.39E-3 ± 0.0001	-1.18E-3 ± 8.56E-5
$p_1(mm^{-1})$	-2.43E-4 ± 6.71E-5	-7.44E-4 ± 9.58E-5
$p_2(mm^{-1})$	8.79E-4 ± 7.49E-5	-1.95E-4 ± 1.12E-4

Table 1. IOP and standard deviations for camera 1 and camera 2 that composes Ricoh Theta S omnidirectional system.

The inertial measurement unit used, named as MPU 6050, is a combination of MEMS (MicroElectroMechanical Systems). This IMU consists of an accelerometer and a gyroscope with three axes (six degrees of freedom - 6DoF), integrated in a GY-521 electronic board. MPU 6050 provides accelerations and gravity data for X, Y and Z axis, using a 16-bit digital analogic converter. Therefore, yaw, pitch and roll angles can be estimated. An application using MPU 6050 in a vehicle platform is presented in Masino et al, (2016).

Ublox NEO-6M is a low-cost single frequency GPS receiver with low power consumption. This device is made with an internal GPS active antenna designed for tracking the L-band signals in the frequency of 1575 MHz. The processed data is delivered in the NMEA (National Marine Electronics Association) protocol, providing position, velocity and time (PVT) data computed by the receiver and detailed information on satellites tracked. Alternatively, raw GPS observations can be accessed by sending specific messages from RTKlib (Takasu and Yasuda, 2009), which brings to the user many options for obtaining coordinates, aiming a low cost mobile mapping solution. Another models from Ublox, such as NEO-6T and NEO-6P, also provide GPS Raw data output.

MPU 6050 and Ublox NEO-6M were integrated in an Arduino microprocessor (BlackBoard). Arduino is powered by a small external 5V battery, requiring low-energy supply. A SD card adapter for Arduino is also used for recording sensors data. This

section summarizes all devices configurations that compose the PMTS proposed. Table 2 presents dimensions (width, length and height) and approximated cost (US$) of each PMTS component. Given system description, Section 2.2 discusses data integration process.

Device	Dimensions (W, L, H)	Cost*
Ricoh Theta S	44 x 23 x 130 mm	$350
MPU 6050	20 x 16 x 1 mm	$49
GPS receiver	25 x 35 x 1 mm	$6
GPS Antenna	34.4 x 29 x 8.9 mm	$10
Arduino	53 x 68 x 1 mm	$25
SD card board	31 x 51 x 1 mm	$5
PMTS	----------	**$445**

*Prices based on Amazon.com and official sellers without taxes.

Table 2. PMTS devices dimensions and cost.

2.2 Data integration from PMTS sensors

PMTS provide omnidirectional images, GPS position and IMU orientation angles, requiring time synchronization and estimation of position and angle offsets between each measurement unit. This section describes the procedures from acquisition to postprocessing for data integration.

Coordinated Universal Time (UTC) obtained from Ublox NEO-6M (hhmmsscc) was used to synchronize sensor's data acquisition in order to enable the extraction of corresponding attitude and position of the camera for each time that images were acquired. An Arduino script was developed to integrate the navigation sensors. MPU 6050 and Ublox NEO-6M were set for a baud rate of 9600. GPS receiver was configured with a data collection rate of 1 second, while IMU data collection rate was ten times higher than GPS receiver (10 Hz). Then, both sensors are initialized. In case of signal or connection loss, sensors initialize function is restarted. The main loop was developed to collect GPS and IMU raw data, convert IMU raw data in yaw, pitch and roll angles and record both in a SD card. Recording data in a SD card was done using an Arduino library. Since IMU collection rate is overdone, a restriction to reduce the amount of data was added. IMU data was only recorded when GPS data is recorded, in other words, data is inscribed in the SD card with 1 second.

Ricoh Theta S records 29 dual-fisheye video frames per second for each camera. Omnidirectional system clock is Local Time (LT). Frame videos can be roughly synchronized by converting LT to UTC. For double check, a small led, whose light pulse is synchronized with GPS recording, appears in each dual-fisheye video frames, aiming a further visual check. This synchronization is performed with an average accuracy of 0.04 seconds. Usually, a person walks at an average speed of 1.4 meters/s resulting in 5 cm synchronization error in object space, at the most, which is acceptable.

Physical misalignments between sensors need to be determined in order to relate the direct positioning and orientation measurements and the camera EOPs. This involves the estimation of linear and angular parameters between sensors. Several methods have been proposed to estimate the system calibration parameter with direct and indirect measurements approaches. PMTS calibration consists of two main steps. First, estimation of the calibration parameters between cameras in the omnidirectional system and then the calibration parameters between cameras and navigation system sensors.

Considering that Ricoh Theta S is a dual system, linear offsets (lever-arm) and three-angular offset (boresights) between cameras projection centre need to be estimated. The relation between these cameras can be considered stable, because they are mounted in the same structure. Therefore, angles of relative orientation ($\Delta\omega$, $\Delta\phi$, $\Delta\kappa$), the distance (D) between both perspective center (X_0, Y_0, Z_0) of cameras and base elements (B_x, B_y, B_z) can be calculated as a function of the EOP of each camera station. EOPs were obtained in the camera calibration process described in Section 2.1. The relative orientation matrix composed by $\Delta\omega$, $\Delta\phi$, $\Delta\kappa$ rotations is obtained considering the rotation matrix of sensor 1 and the rotation matrix of sensor 2.

Estimated $\Delta\omega$ and $\Delta\phi$ were less than 1', while, Bx and By are inferior to 1 mm, which can be considered insignificant compared to PMTS accuracy level. As already mentioned, Ricoh Theta S cameras are arranged in back-to-back position, resulting in a $\Delta\kappa$ close to 180 degrees (179.67° ± 1') and a Bz of -1.83 cm estimated with a standard deviation of 1mm, which can be considered compatible with D (0.0184 m ± 1 mm).

Lever-arm between each camera projection centre and GPS antenna phase centre, and, boresight between IMU and cameras need to be estimated. Since calibration parameters between cameras are known, the lever-arm and the boresight can be calculated for camera 1 and extended to camera 2, considering the relative orientation between them. Considering centimetre accuracy expected for PMTS data, lever-arm between each camera projection centre and GPS antenna phase centre was previously measured in laboratory using a calliper with 0.05 mm accuracy. Table 3 shows the lever-arms between GPS receiver antenna and Ricoh Theta S ($\Delta\rho x$, $\Delta\rho y$, $\Delta\rho z$) for Cameras 1 and 2.

Boresight angles are difficult to measure in laboratory with a suitable accuracy, therefore they are usually estimated in an indirect process. In preliminary experiments, MPU 6050 presented a considerable instability during the survey, in which noises are probably higher than the influence of boresight angles correction. Therefore, in this first experiments, boresight between IMU and cameras will be neglected.

Calibration Parameters	Camera 1	Camera 2
$\Delta\rho x$ *(mm)*	101.4 ± 0.05	83 ± 0.05
$\Delta\rho y$ *(mm)*	85.05 ± 0.05	85.05 ± 0.05
$\Delta\rho_z$ *(mm)*	138 ± 0.05	138 ± 0.05

Table 3. Lever-arms for PMTS system.

3. EXPERIMENTS AND PRELIMINARY RESULTS

Section 3 describes experiments and preliminary results with PMTS. Experiment I (Section 3.1) consisted of assessment of the navigation system positional accuracy. An accurate initial position supports a more reliable photogrammetric process, for instance, in image matching and bundle adjustment procedures. Then, considering the data obtained with this PMTS a dense point cloud was generated in Experiment II (Section 3.2) and compared to manual DBH observations to estimate product accuracy.

3.1 Navigation System assessment

Absolute positional accuracy can be assessed considering how close the measured value is to a reference value. To acquire reference positioning data, a Topcon HIPER SR (L1/L2) GNSS receiver was installed in the backpack platform to acquire simultaneously the same trajectory data as Ublox, as depicted in

Figure 2. The offsets between Topcon HIPER SR and Ublox NEO-6M were estimated with a 0.05 mm accuracy calliper, as presented in Table 4.

Offsets HIPER SR x NEO-6M	$\Delta\rho x$	$\Delta\rho y$	$\Delta\rho z$
Values *(cm)* ± 0.05 *mm*	0.1	14.165	0.3

Table 4. Offsets between Topcon HIPER SR and Ublox NEO-6M antenna phase center.

Figure 2. Experiment I – Data acquisition for navigation system positional accuracy analysis using PMTS with Topcon SR GNSS receiver.

Aiming comparative analysis, both receivers, used as rover, were configured with a data collection rate of 1 Hz. Ublox NEO-6M data was acquired in the NMEA format. Topcon SR data was obtained with a relative positioning in kinematic mode computed with RTKlib, using PPTE station from Brazilian Network for Continuous GNSS Monitoring (RBMC) as base (baseline < 500 m), also with a data collection rate of 1 Hz. Reference data from Topcon HIPER SR was obtained with 87% of the points with ambiguity-fixed solution. The standard deviation of the positioning solution was 8.8 mm in N, 9.2 mm in E and 21.3mm in height.

Trajectories in open (Figure 3) and vegetated (Figure 5) areas inside the campus were chosen to assess both positional accuracy and loss of signal in covered areas. Figure 3 presents the open area trajectory. Red line trajectory represents Ublox NEO-6M data. The reference positional data obtained with Topcon HIPER SR is depicted as blue points. It can be noticed that trajectory format and size is well recorded by Ublox NEO-6M receiver.

Horizontal and vertical accuracies were analyzed by comparing the distance (ΔD) between points coordinates measured, for each 1 second, with Ublox NEO-6M and with Topcon HIPER SR (reference), corrected from offsets (Table 4). Figure 4 shows the resultant distances obtained for each second (UTC) of survey in the trajectory. Horizontal discrepancies were illustrated in blue. Ublox NEO-6M presented good results in horizontal coordinates with an average discrepancy of 30 cm with respect to Topcon SR positional and a standard deviation of 21 cm, illustrated in blue in Figure 4. The biggest problem observed in Ublox NEO-6M positioning was the height estimation. When vertical differences are incorporated in the calculation of ΔD an average discrepancy of 4.3 m with respect to Topcon SR positional with 1 m standard deviation was obtained. Planialtimetric discrepancies are illustrated in green in Figure 4.

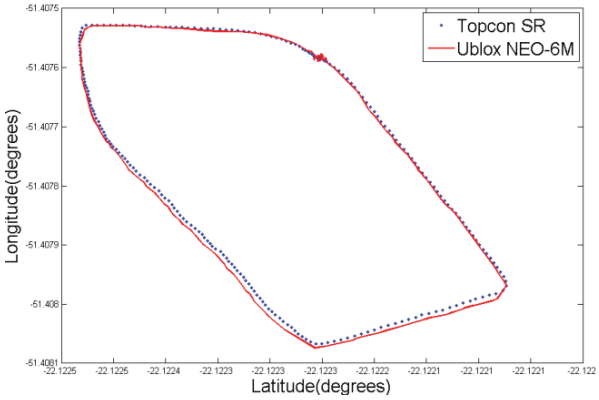

Figure 3. Experiment I –PMTS trajectory in an open area.

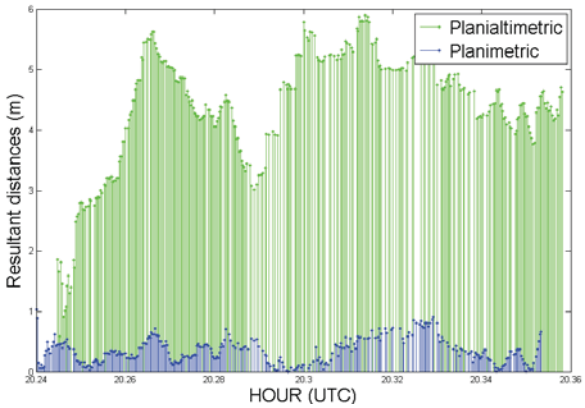

Figure 4. Experiment I – Comparative analyses between Ublox NEO-6M single frequency GPS receiver and the dual frequency GNSS receiver Topcon SR in kinematic positioning.

It is well known that height estimation is a critical issue in GPS positioning because, elevation accuracy significantly decreases due to loss of satellites, multipath errors or poor satellite geometry, and this problem is more critical in single frequency GPS receiver. Considering high ionospheric activity in Brazil, a metric accuracy between 1 and 5 meters, is expected in height estimation using Ublox NEO-6M receiver. This problem can be minimized using a Differential Global Positioning System (DGPS) method which will be assessed in future work.

A second trajectory was assessed simulating forest conditions. As discussed by Naesset *et al*. (2001), most of positioning problems in difficult access places, such as under forest canopies, is the number of available satellites. Figure 5 shows in yellow the trajectory obtained with Ublox NEO-6M receiver data and in blue points the Topcon SR data. A huge loss of signal occurred with Topcon SR receiver in covered areas, in which less than the four-minimum number of satellites were grabbed. On the other hand, with Ublox NEO-6M receiver data it was possible to reproduce the trajectory followed inside the forest area also with centimetric accuracy in planimetry.

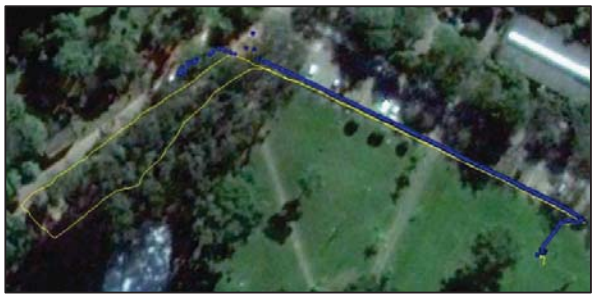

Figure 5. Experiment I –PMTS trajectory in a forest area.

This result can be explained by the Topcon SR filter components which are more rigorous to reject low power signals and non RHCP signals when compared to Ublox NEO-6M, which acquires more signals, even with low quality. Therefore, despite of the inferior quality, low-cost receiver can be a good alternative in covered areas. Ublox NEO-6M coordinates can be used as input data for many photogrammetric process, such as in the reduction of search space for image matching, integrated bundle adjustment approaches and dense image matching, aiming an 3D point cloud. This approach considering inertial navigation data as initial parameters values is well known in photogrammetry as Integrated Sensor Orientation (ISO). For practical purposes, uncorrected systematic errors, which causes a reliability problem, can be mitigated with an ISO approach.

3.2 PMTS Point Cloud

A 3D reconstruction with the SfM-based software Agisoft PhotoScan was performed to assess the PMTS. Dual fisheye video frames were simultaneous acquired. A total of 29 Dual fisheye frames per second were extracted from Ricoh Theta S video. A set of 90 frames in the vegetated area (Figure 6) was selected, aiming to reconstruct the path in this area with GNSS adverse conditions. These frames were selected manually considering UTC time and the small led synchronized with GPS record (led is triggered at each 30 frames). Dual fisheye frames (1920 x 1080 pixels) were converted to single frames corresponding to each camera that composes Ricoh Theta SData from Camera 1 and Camera 2 were processed independently, using PhotoScan. Figure 6 shows an example of omnidirectional image sequence.

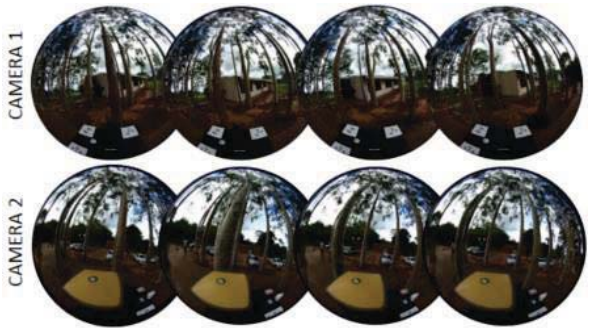

Figure 6. Experiment II – Example of omnidirectional images from PMTS.

A PhotoScan project was created setting the mathematical model (fisheye), initial EOP and system calibration offsets Results obtained with PMTS in Experiment I (camera position and attitude and omnidirectional images) were used as input reference data. 3D cameras coordinates were determined in Universal Transverse Mercator (UTM) projection system. The positional standard deviations applied were 1m in planimetry (N, E) and 5 m in altimetry (H). The offsets presented in Table 3 were also informed. For those positions in which a loss of signal was observed a linear data interpolation in N, E and height was done.

PhotoScan workflow consists of tie points generation, EOP estimation and dense image matching. A manual tie points filtering was performed to exclude wrong matching points. Then, a bundle adjustment was performed to refine camera positions, camera attitudes and camera calibration parameters (calibrated). The optimal bundle adjustment setting was found by extensive experimentation. Finally, with images oriented, a dense 3D cloud was generated. A high-accuracy setting was used in dense image matching. Figure 7 shows the 3D point cloud generated.

Figure 7. Experiment II – 3D point cloud obtained with PMTS data processing in Agisoft PhotoScan Software.

Since the study area has many trees distributed along the trajectory, a possibility is to evaluate PMTS product accuracy comparing tree features such as DBH computed from the generated point cloud with manual measurements. In this regard, DBH were extracted from the point cloud with a semi-automatic method, considering tree features, for instance, using LAStools and FugroViewer free-software. Manual measures were performed using a caliper. A total of seven (7) measurements were performed. The standard deviation of the discrepancies between this seven (7) DBH estimated from 3D point cloud and from manual measures obtained was 1.45 cm. The results presented are compatible with the other techniques of indirect DBH estimation as presented in Section 1, showing a possible PMTS application.

4. CONCLUSIONS

In this paper we presented a low cost and lightweight Personal Mobile Terrestrial System composed by an omnidirectional camera with off-the-shelf navigation systems. The PMTS costs around of 450 US$ and weighs less than 5 kg, which is a great advantage over traditional systems with backpacked LASER scanners.

This optical-based omnidirectional system can be considered an option for mobile mapping over covered areas. However, the omnidirectional system used, Ricoh theta S, has some disadvantages. Regarding the use of still images, the internal resampling process lasting 8 s, makes unfeasible the dynamic sequential acquisition of images in this mode. Therefore dual-fisheye frame video was used. The drawback is the low resolution of the frame video compared to the still image. Nevertheless, this approach can be explored with other omnidirectional system, such as Samsung gear 360, in which raw dual-fisheye images are also available.

Experiment I and II explored the feasibility of the proposed PMTS. Experiment I evaluated a low-cost GPS receiver, which showed the potential of low cost system used as source of initial information for the photogrammetric processing, aiming an ISO approach. The result of an ISO solution using a commercial software presented in Experiment II showed some potential applications of this system, especially when centimetre accuracy is required.

ACKNOWLEDGEMENTS

This work was jointly funded by Fundação de Amparo à Pesquisa do Estado de São Paulo (FAPESP— Grant: 2013/50426-4) and Coordenação de Aperfeiçoamento de Pessoal de Nível Superior (CAPES).

REFERENCES

Berveglieri, A.; Tommaselli, T.; Liang, X.; Honkavaara, E., 2016. Photogrammetric measurement of tree stems from vertical fisheye images. *Scandinavian Journal of Forest Research*, n. just-accepted, p. 1-23.

Brown, D. C., 1971. Close-Range Camera Calibration. *Photogrammetric Engineering*, v. 37, n. 8, p. 855-866.

Conrady, A., 1919. Decentered Lens Systems. *Monthly Notices of the Royal Astronomical Societ*y, v. 79, p. 384–390.

Corso, N; Zakhor, A., 2013 Indoor localization algorithms for an ambulatory human operated 3d mobile mapping system. *Remote Sensing,* v. 5, n. 12, p. 6611-6646.

Forsman, M.; Börlin, N.; Holmgren, J, 2016. Estimation of Tree Stem Attributes Using Terrestrial Photogrammetry with a Camera Rig. *Forests*, v. 7, n. 3, p. 61.

Klingensmith, M.; Sirinivasa, S. S.; Kaess, M. , 2016. Articulated robot motion for simultaneous localization and mapping (arm-slam). *IEEE Robotics and Automation Letters*, v. 1, n. 2, p. 1156-1163.

Kukko, A., Kaartinen, H., Hyyppä, J., Chen, Y., 2012 Multiplatform mobile laser scanning: Usability and performance. *Sensors*, v. 12, n. 9, p. 11712-11733.

Lauterbach, H. A.; Borrmann, D.; Heß, R.; Eck, D.; Schilling, K.; Nüchter, A., 2015. Evaluation of a backpack-mounted 3D mobile scanning system. Remote Sensing, v. 7, n. 10, p. 13753-13781.

Liang; X.; Kukko; A.; Kaartinen; H.; Hyyppä; J.; Yu; X.; Jaakkola; A.; Wang; Y., 2014. Possibilities of a personal laser scanning system for forest mapping and ecosystem services. *Sensors*, v. 14, n. 1, p. 1228-1248.

Marcato Junior, J; Moraes, M.V.A., Tomaselli, A. M. G., 2015 Geometric calibration of a Stereographic fisheye lens camera. *Boletim de Ciências Geodésicas*, Curitiba.

Masino, J.; Frey, M.; Gauterin, F.; Sharma, R., 2016 Development of a highly accurate and low cost measurement device for field operational tests. In: *IEEE International Symposium on Inertial Sensors and Systems*, 2016. p. 74-77.

Mikhail, E. M.; Ackerman, F.,1976. *Observations and Least Squares*. IEP, New York. 497p

Moraes, M. V. A.; Tommaselli, A. M. G.; Santos, L. D., Rubio, M. F; Carvalho, G. J.; Tommaselli, J. T. G., 2016. Monitoring Bank Erosion in Hydroelectric Reservoirs With Mobile Laser Scanning. *IEEE Journal of Selected Topics in Applied Earth Observations and Remote Sensing*, v. 9, n. 12, p.5524-5532.

Naesset, E., 2001 Effects of differential single-and dual-frequency GPS and GLONASS observations on point accuracy under forest canopies. *Photogrammetric Engineering and Remote Sensing*, v. 67, n. 9, p. 1021-1026.

Schwarz, K. P.; El-Sheimy, N., 2004. Mobile mapping systems–state of the art and future trends. *International Archives of Photogrammetry, Remote Sensing and Spatial Information Sciences*, v. 35, n. Part B, p. 10.

Takasu, T; Yasuda, A., 2009. Development of the low-cost RTK-GPS receiver with an open source program package RTKLIB. In: *international symposium on GPS/GNSS*. Jeju, Korea: International Convention Centre. p. 4-6.

GNSS/INS integrated with intelligent vision system for path reconstruction of a bicycle

Tz-Chiau Su [a], Hsiu-Wen Chang [b]

[a] Department of Geomatics, University of National Cheng Kung University, Tainan, Taiwan
a0973131100@gmail.com
[b] Department of Geomatics, University of National Cheng Kung University, Tainan, Taiwan
seawing1984@gmail.com

KEY WORDS: Bicycle, Computer Vision, VO, GNSS, INS, Low Cost Sensor

ABSTRACT:

The technique of positioning and navigation is undoubtedly a popular topic of research in nowadays. GNSS(Global Navigation Satellite System) and INS(Inertial Navigation System) are two main technique in navigation field. They have been used widely in many aspects such as automobiles guidance, pedestrian guidance or indoor navigation. However, these navigation systems also have their own disadvantages respect to others. Conceptually, GNSS will be influenced by type of signal or even no signal in harsh environment. In addition to GNSS, the performance of self-contained INS depends on price and the size. The error will increase rapidly by time when the cheaper one such as MEMS based INS. Therefore, in order to minimize the cost and reach a better precision of navigation solution, this paper aim at recovering path and attitude by means of GNSS/INS combining with vision system. In this research, camera installed in smartphone is used to capture information from successive images and bicycle is chosen to be the carrier in this study. Comparing with automobile, bicycle can twist sideways and generates a significant roll angle change that makes this research more challenging. In addition, rider can easily enter some place without sufficient GNSS signal such as small alley, forest or urban area. The goal is to combine integrated system with intelligent vision system to enable continuous and seamless navigation.

1. INTRODOCTION

The Global Navigation Satellite System(GNSS) is a combination of astronomical and radio navigation that has been used in vary fields such as civil aviation, pedestrian guidance, automobile guidance and surveying. It can provide position and velocity solution that its accuracy varies from meter to centimetre. However, a disadvantage of GNSS is the necessity of good light-of-sight visibility to the satellites. In GNSS signal degraded or even denied environment such as urban area, forest or even indoor, it gives large positioning error or even no solution. On the other hand, as a complementary system, Inertial Navigation System(INS) has the characteristic of self-contained that the performance is not influenced by the environment such as urban and forest. Instead of ranging information from GNSS, INS contains accelerometer and gyroscope that provides specific force and angular rates, respectively. By integration of measurements which are derived from accelerometer and gyroscope, the attitude and position of device will be obtained. The disadvantage of INS is the navigation errors increase with time because of the accumulation of error. To avoid these abovementioned problems in GNSS and INS individually, GNSS/INS integration using well-known Extended Kalman Filter(EKF) which provides optimal results for predicting states like offsets, drifts and scale factors of employed sensors and update states from heterogeneous measurement has become a popular technique. It not only constrains the limit of error but also enlarges the scope of guidance either indoor or outdoor.

Nowadays, smartphone becomes an indispensable product for people that it can be viewed as a large carrier containing a lot of sensors such as camera, Bluetooth, GNSS receiver and so on. Among them, MicroElectroMechanical Systems(MEMS) technology which is characterized by small size, light weight and low cost makes navigation more accessible. Therefore, MEMS-based inertial sensor combined with GNSS has become an important and challenging integration navigation system. Besides smartphone, MEMS-inertial sensor is possibly integrated with other sensor (such as barometer and magnetometers) in small devices, such as watches, shoes, belt, helmet, etc. However, the nature of low cost sensor represents a rapid error accumulation that causes the use in long-term navigation challenging. This is the reason that many researchers endeavour to improve the situation. For instance in this paper, instead of providing the information of navigation by integrating GNSS/IMU measurements, GNSS/INS/Vision will be proven as a favourable alternative.

Even though GNSS/INS integration provide reliable and accurate solutions, it is inevitable to enter a signal degraded environment where GNSS solution becomes unstable. In this case, MEMS-based INS becomes the main provider of navigating information and the drift of trajectory will start to increase quickly. In this research, computer vision system is considered to aid GNSS/INS for recovering trajectory. By means of capturing a sequence of images which has sufficient overlap, the relative pose and translation will be derived based on the characteristic of epipolar constraint. The video sensor is a single moving camera which is calibrated and installed in smartphone. It generates what we call monocular Visual Odometry (VO) that can be used in conjunction with information from other sources such as GNSS, INS, wheel encoder, etc. The difference from stereo scheme is that both the relative motion and 3-D structure must computed from 2-D bearing data causing the absolute scale unknown(Hartley and Zisserman 2003). Because the performance of MEMS-based inertial sensor deteriorates with time rapidly, the accuracy of position decrease when devices move into GNSS hostile environment. In order to enable continuous and seamless navigation, VO is integrated with INS to provide a stable solution of position.

In comparison to a four-wheel vehicle, there are two reasons that bicycle is chosen to be the carrier in this work. First, the dynamics of a two-wheel vehicle features a higher level of complexity given that more degrees of freedom must be taken into account. For example, a bicycle can twist sideways that

generates a significant roll angle change. A slight pitch angle has to be considered as well. Second, it is a continuous research on CDR(Chang, Georgy et al. 2013) where the frequency of the pedal is used to aided the GNSS/INS integration but lack of the long term reliable performance. By means of computing the travelled distance per peddling cycle, it gives the estimation of the scale required for monocular VO. Finally, all information derived from GNSS, INS, CDR and VO, the integration of KF provide an alternative navigation when GNSS/INS integration cannot recover trajectory well.

2. METHODOLOGY

2.1 Kalman Filter (KF):

As an iterative mathematical process, Kalman Filter(KF) uses a set of equations and consecutive data input to rapidly estimate the true value, position, velocity, etc of the object being measured. The filter is one of the most widely used methods for tracking and estimation due to simplicity, optimality, tractability and robustness. For this reason, KF becomes a popular estimation technique for GNSS/INS integration. The KF estimates a process by using a form of feedback control which means that it estimates the process state based on the priori knowledge of the motion and then obtains feedback from measurements. Therefore, the equations of KF are divided into two parts that contains time update equations (or to say predictor equations) and measurement update (or to say correct equations) equations. In this research, the time update equation and measurement update equation are nonlinear, that is, an updated filter called extended Kalman Filter (EKF) is used. Generally, data derived from INS such as acceleration and angle rate are used in the time update equations for prediction of next step. On the other hand, other position derived from GNSS or VO will be view as measurements and utilized to correct current state vector. By combining these two parts, extended Kalman filter benefits GNSS/INS/VO integration. As shown in Figure1, the state vector is calculated and predicted by INS at “time update”. The “measurement update” correct the estimation at corresponding time when the measurements given from GNSS.

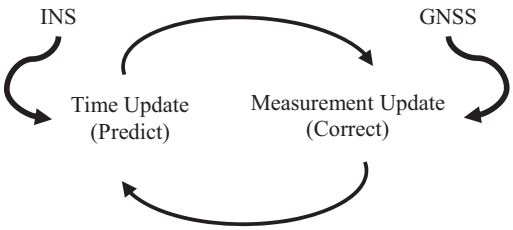

Figure 1. The EKF cycle

2.2 Visual Odometry (VO):

In recent years, camera has become cheaper and the power of computer processor increased dramatically. Hence, high-resolution images can be processed much faster and approaching to near real time on standard hardware that encourages many researchers to focus on computer vision. An important application of computer vision is to autonomous navigation of vehicles and robots. Visual odometry is an implementation of computer vision that estimates the egomotion of an agent using only the input of a single or multiple cameras attached to it. Monocular VO is defined when the implementation involves only one camera and stereo VO involves at least two cameras. Most of research done in VO has been produced using stereo camera for refraining from scale problem. In this research, however, the camera installed in smartphone is expected. Monocular VO naturally becomes an optimal alternative. The difference from the stereo scheme is that in the monocular VO, both the relative motion and 3-D structure must be computed from 2-D bearing data and the absolute scale is unknown. The VO pipeline is shown in Figure 2 and a detailed description follows.

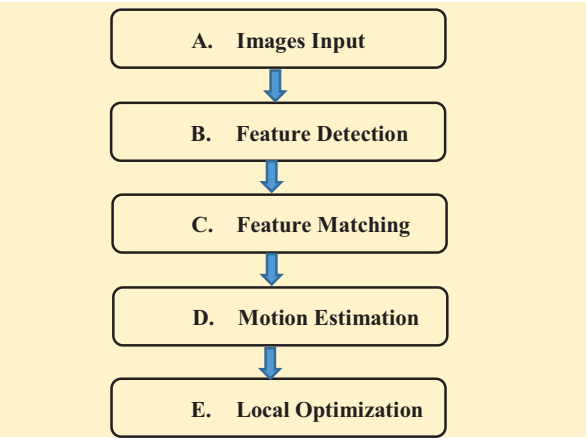

Figure 2. A simple flow chart shows the process of VO

A. Images Input

When a sequence of images collected, image undistortion is an important pre-processing before starting the VO. Distortion happens when lines that are straight in the real world becomes curved in the images. This step compensates for this lens distortion and provides the intrinsic and extrinsic parameters of the camera system. In this research, camera installed in smartphone was calibrated by the popular method uses a planar checkboard-like pattern. Several images of the board shown at different positions and orientations by ensuring that the field of view of camera filled as much as possible is necessary. The intrinsic and extrinsic parameters are calculated through a least square minimization method. Moreover, the camera frame is defined referring to INS frame. Because the distance between camera and IMU is close enough to be neglected, the relation of these two frames depend only on a rotational matrix which is described in Sec. 3 in detail.

B. Feature Detection

The task of finding point correspondence between two or more images contains same scene or object is part of many computer vision applications. In this step, the image turned into grey level for the searched of salient keypoints that are likely to match well in other images. When it comes to feature detection, different kinds of detector have been proposed. Some of them are utilized for corners detection, and some of them belong to blobs detection. Speeded Up Robust Features (SURF) is one kind of blobs detection and it is adopted in this research. Compared to other algorithms of feature detection, SURF features its efficiency and repeatability. Nonetheless, the most important is that the property of blobs detection allows large change in scale and viewpoint. Based on these characteristics, it becomes a stable and reliable feature detector for images taken from a single camera of smartphone mounted on a bicycle(Bay, Ess et al. 2008).

C. Feature Matching

Feature matching follows the step of feature detection searches for corresponding features in other images. The simplest way for matching features between two images is to compare all feature descriptors in the first image to all other feature descriptor in the second image. (The descriptor aims at providing a unique and robust description for an image feature, for example, intensity

distribution of the pixels within the neighbourhood of the point of interest can be described by a descriptor.) Because of the nature of error accumulation, it will be ineffective if VO takes all consecutive images for motion estimation. A better method is to select the key-frame among all images. On the one hand using less images can reduce the error accumulation and on the other hand key-frame selection allows to process in real-time.

Matched points are usually contaminated by outliers due to wrong data association. There are many reasons for outlier exist such as image noise, occlusions, blur, changes in viewpoint, etc. To acquire an accurately motion estimation, Outlier removal is an indispensable task in VO. An ideal and common algorithm for outlier rejection is random sample consensus(RANSAC) (Fischler and Bolles 1981) that is to compute model hypotheses from randomly sampled sets of data points and then verify theses hypotheses on the other data points. When a hypothesis selected shows the highest consensus with other data, it will be selected as a solution. Because of the characteristic of random process, RANSAC may derive a different solution on different runs. However, the sufficient iterations give a stable solution of this algorithm but consume much time. Therefore, how to balance computational time and stability of solution in RANSAC depends on experimental setting.

D. Motion Estimation

As a core computation step, the transformation between the current image and previous image is computed from a set of corresponding matching points that the outliers have been removed. The geometric relation between two images of a calibrated camera within enough overlap can be described by the so-called essential matrix E (Longuet-Higgins 1987). According to the basic projection principle, the relation between 3-D points and camera can be written as:

$$\begin{aligned} x_t &\sim KX_t \\ x_{t+1} &\sim K'X_{t+1} \end{aligned} \tag{1}$$

where X_t, X_{t+1} are the 3-D points coordinate of image taken in previous and current camera, and x_t, x_{t+1} are the corresponding image coordinate. K, K' represent the projection relationship between 3-D world and image consist of intrinsic parameters. The relationship of camera between previous step and current step can be described by a rotational matrix and a translational vector:

$$X_{t+1} = RX_t + t \tag{2}$$

where R is the rotational matrix and t is the translational vector. Combining (1) and (2), the new form can be derived as:

$$K'[RX_t + t] \sim x_{t+1} \tag{3}$$

where symbol "$\sim$" denotes the equivalence is valid up to a multiplicative scalar. Because of inverse matrix of K' exist which is represented as K'^{-1}, multiply by K'^{-1} in (3) and the function will become:

$$RX_t + t \sim K'^{-1} x_{t+1} \tag{4}$$

Then the next step is to do cross product operation with translational vector t on both sides of (4):

$$[t]_\times RX_t = [t]_\times K'^{-1} x_{t+1} \tag{5}$$

And then, do dot product operation with $K'^{-1} x_{t+1}$ on both sides of (5) and according to the rule of cross product and dot product $a \cdot (b \times a) = 0$, we can get:

$$x_{t+1}{}^T K'^{-T} [t]_\times RX_t = 0 \tag{6}$$

Combining (1) and (6), it will become:

$$x_{t+1}{}^T K'^{-T} [t]_\times RK'^{-1} x_t = 0 \tag{7}$$

Finally, let $E = K'^{-T}[t]_\times RK^{-1}$, the relation between the corresponding matched points in current and previous image can be treated as a well-known epipolar constrain(Longuet-Higgins 1987):

$$x_{t+1}{}^T E x_t = 0, \tag{8}$$

In order to solve the essential matrix, this research adopts a simple and straightforward eight-point algorithm that each feature match gives a constraint of the following form:

$$\begin{bmatrix} uu' & u'v & u' & uv' & vv' & v' & u & v & 1 \end{bmatrix} E = 0, \tag{9}$$

Where E = $[k_1\ k_2\ k_3\ k_4\ k_5\ k_6\ k_7\ k_8\ k_9]^T$ and (u, v), (u', v') is the corresponding image coordinate in two camera frame.

This is a homogeneous linear equation that can be solved when the number of matched points is equal to eight. To improve the robustness of solution, least square method based on more than eight matched points is used to forms as overdetermined linear system. Because essential matrix contains rotation and translation information, extracting rotation matrix and translation matrix from essential matrix by singular value decomposition(SVD) can build the transformation matrix. Ultimately, concatenating all the transformations will recover the motion trajectory of camera.

E. Local Optimazation

Windowed bundle adjustment not only refines the camera parameters but also refine the 3-D landmarks simultaneously. By selecting the size of window (in this research, the window size is set to five), window bundle adjustment will perform a parameter optimization of camera pose and 3-D landmark for image frames included in this window(Triggs, McLauchlan et al. 1999). More formally, the goal of bundle adjustment is to minimize the image reprojection error that the function is shown below:

$$\arg\min_{X^i, C_k} \sum_{i,k} \left\| p_k^i - g(X^i, C_k) \right\|^2 \tag{10}$$

where p_k^i represents ith image point of the 3-D landmark X^i measured in kth image and $g(X^i, C_k)$ represents the image projection according to the current camera pose C_k.

Bundle adjustment is known to significantly reduce the drift and improve the accuracy of trajectory. The larger window size is selected, the lower computational efficiency it is. For considering the ability of implementing VO in real time, therefore, the window size of bundle adjustment used in this experiment is equal to five.

2.3 Scale Problem:

To recover the trajectory of an image sequence, the different transformation have to be concatenated. In monocular VO, however, absolute scale is unknown because it only has the bearing information. In normal circumstance, absolute scale can be derived by GNSS. A simple way is to take advantage of time and frequency synchronization between VO and GNSS for implement a GNSS/VO integration. However, the goal of this research is to recover the trajectory using VO in GNSS-denied environment that ensure the trajectory will not be interrupted or error accumulate too fast by INS or CDR. In this case, therefore, the behaviour of pedals of bicycle will be modelled like CDR. The frequency of pedal is an index to compute the totally distance. At the first, the travelled distance of bike's wheel per one loop is measured. Then, by having the reference velocity from good GNSS, the relationship of pedalling frequency and forward speed is established. The problem here is how to determine the number of revolutions. An idea is to detect the state of accelerometer included in IMU. To implement this idea, an additional inertial sensor (or can be other possible motion sensors setup on the bicycle directly) is placed in pocket of pants for detection. When a human is riding a bike, the behaviour of pedalling is recorded. Taking the information of average acceleration in three axes, the trend is shown in Figure 3. The one complete pedalling motion is recorded by total acceleration and behaves like a sine wave contains with noise. According to different frequency of pedalling motion when rider rides in different circumstance, the amplitudes varies. Therefore, in order to detect one complete of pedalling, an adaptive threshold is set as the red line shown in figure 3. When the blue line has a high peak that is higher than high threshold and then goes down when the low peak is lower than low threshold, this phenomenon will be determined as one turn of pedal. Waves don't have a peak over the threshold and don't have a sequential low peak is treated as vibration or noises. Since the acceleration has suffered the high noise, a low pass filter could be further applied and additional threshold can be set according to the time interval between each complete cycle. The concept based on the fact that the continuous motion of human changes step by step. Without the shifting of gears, time required to finish each pedalling cycle should has similar value. For further information, refer to (Chang, Georgy et al. 2014).Although this method may have a quickly error accumulation, the error is located in an acceptable interval when the traveling distance is less than 200 meters.

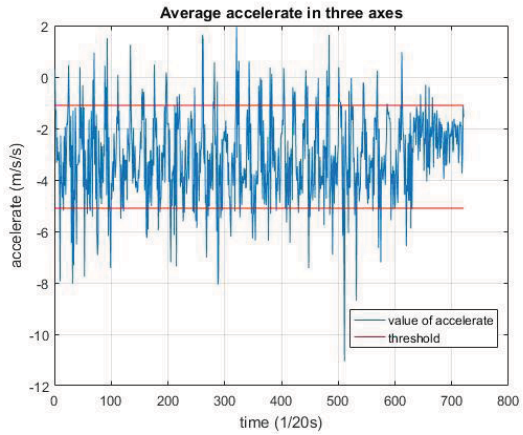

Figure 3. Average accelerate of IMU in smartphone

3. EXPERIMENTAL OPERATION

3.1 Experiments:

The experimental platform is based on a smartphone (Sony Xperia Z3) mounted on a bicycle where it contains basic sensors including GNSS receiver, IMU, camera, barometer and magnetometer. The related information of this type of smartphone is shown in Table 1. The camera installed in smartphone has been set to acquires low resolution of video at 640 × 480 pixels at frequency of 29 Hz. This is designed to accelerate the speed of calculation.

Sony Xperia Z3	Information
Dimension	146×72×7.3 mm
Weight	152 g
CPU	Quad-core 2.5 GHz
GPU	Adreno 330
Camera	20.7MP,f/2.0,25mm
GNSS	A-GPS,GLONASS,BDS

Table 1. related information of Sony Xpera Z3

Figure 4 shows the device mounted on the bicycle. Data were acquired from the camera of smartphone. At the beginning, a reasonable initial state should be determined. The initial position is provided by GNSS that the coordinate system is global. In order to reduce the complexity of attitude among bicycle, smartphone and IMU, the camera lens is be set toward forward as possible as it can that the directional problem between bicycle and camera can be solved which shown in Figure 5.

Figure 4. experimental bicycle and smartphone

Figure 5. smartphone mounted on the head of bicycle

Then, it is important to match camera coordinate system and IMU coordinate system. Both of them and their three axes are shown in Figure 6. Z axis in camera frame is coincide with direction of lens. IMU frame also has this property that z axis is point to back of the smartphone. That is, by rotating the z axis will make two frame become consistent. The following shows the rotation function.

$$C_c^l = R_1(\alpha)R_2(\beta)R_3(\gamma + 270^o) \tag{11}$$

where C_c^l = rotation from camera frame "c" to IMU frame "l". R_1, R_2, R_3 = rotation matrix related three Axes

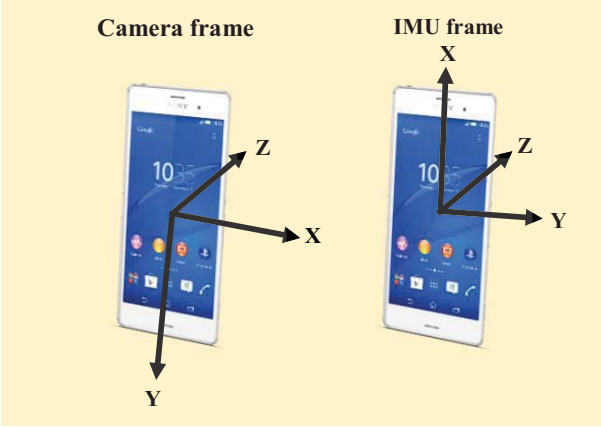

Figure 6. smartphone on left is located in camera frame and smartphone on right is located in IMU frame

The dataset was obtained in National Cheng Kong University in Taiwan during February 2017. The area of this place about $10000m^2$ that lendth is about 230 meters and width is about 40 meters. And this place is surrounded by many large building which taller than 20 meters. Therefore, it is possible that GNSS receives weak signals and has worse geometry. Figure 7 shows this place and the blue line represents the planned route.

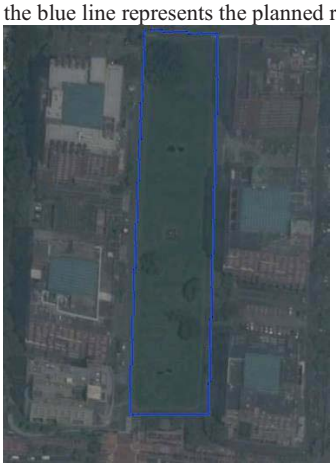

Figure 7. planned route of this experiment

4. RESULT

In this section, two experiments are carried out. The purpose of the first experiment is to test the performance with the stand alone GNSS and VO/INS integration. For the first part, Figure 8 shows the comparison of trajectory between GNSS only method and VO/INS integration method. The blue line represents GNSS method and red line represents integration method of INS and VO when the rider started from the bottom right and rode counter clockwise back to the same location as starting location. The related information is shown in table 2 that the planned route has total distance about 540 meters. Because of the synchronization of frequency, some statistics can be calculated conveniently. The maximum difference of these two routes is 12 meters that we can see an apparent displacement located at lower left of this figure. Red line suffers from a severe lateral movement due to an irregular motion of bicycle handle bar. As we know, the body frame of bicycle is not equal to the camera frame because of the different motion behaviour. The attitude of camera installed in smartphone mounted on the front of bicycle is mainly influenced by handle bar. That is, an intensely tremor will cause a large change of the geometry among several consecutive images which is the reason of error up to 12 meters. Therefore, it is important to keep a stable ride for motion estimation using camera. Another reason cause a weird movement is the quality of images. The camera installed in smartphone cannot be as stable as an independent monocular camera that there are many blurred images interspersed in a set of consecutive images. Therefore, in order to mitigate this problem as much as possible, a specific number of matched image candidates will be determined and the unsuitable images which have insufficient or no matched points will be discarded.

The absolute mean in table 2 shows an average of difference between GNSS trajectory and VO/INS trajectory. And the misclosure is the displacement between start point and end point based on VO/INS method. A misclosure ratio is computed by the value of misclosure divides totally distance and represents in percentage. Root-mean-square (RMSE) is an index presents how close the measurements to the mean value. In this experiment, the solution of GNSS is viewed as the mean value and the RMSE is 8.21 meters. Generally, solution of GNSS installed in smartphone cannot give a really good result. It contains about 5-10 meters error related to the solution derived from high-quality precision instruments. That is, although the value of RMSE seems to be large, it includes a comprehensive error produced from both method.

In the second experiment the simulated GNSS outage is intended to be added. At the beginning of this experiment, GNSS/INS integration is used to calculate the trajectory. In the middle of this route, the information of GNSS is excluded deliberately. In general, a moderate threshold for switching to another system can be set easily. For example, when the number of received satellites is lower than a certain threshold for a while, VO will start to collect data to bridge the solution or to maintain the solution accuracy of INS. And when the sufficient number of received satellites has recovered to a stable range, the GNSS solution will be used again. The position solution of interrupted point of GNSS is taken as the initial position of VO. Figure 9 shows the result of experiment that the blue line is the trajectory derived from GNSS only and the red line is the solution of VO/INS integration when GNSS stops working. The start-end point locates at the upper left of figure. The misclosure at the end of red line is about 9.23 meters. Figure 10 shows the result on Google earth that blue dots is the trajectory of GNSS only and the red dots is the trajectory of VO/INS integration. In VO/INS integration part, in order to refrain from insufficient matching point on corresponding matched images, the speed of bicycle is not too high for ensuring the quality of geometry. Therefore, it's apparently that the dots are concentrated before and after the corner. When the bicycle passes through the corner and enter the straight way, the speed of bicycle will increase and the dots become sparse.

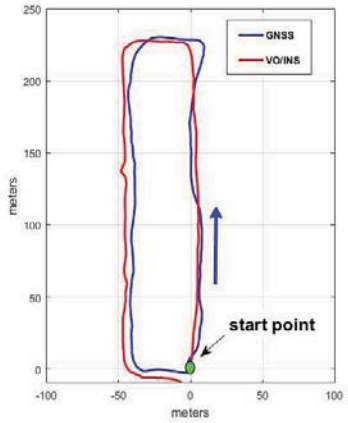

Figure 8. trajectory comparison

Totally distance	540 m
Maximum error	12 m
Absolute mean	6 m
Misclosure	5.35 m
RMSE	8.21 m

Table 2. statistics of experiment

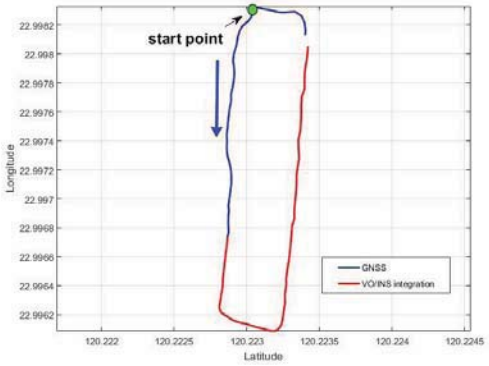

Figure 9. trajectory connection between using only GNSS and VO/INS integration in global frame

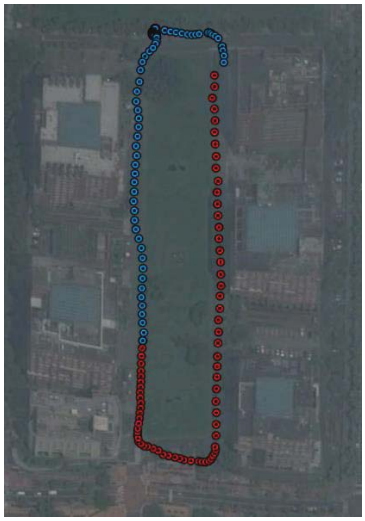

Figure10. trajectory connection on GOOGLE earth

5. CONCLUSION AND FUTURE WORK

This paper emphasizes on low cost sensor such as MEMS-based accelerometer and gyroscopes that can aids VO for trajectory reconstruction. The result shows a reasonable solution that VO/INS integration can indeed recover the trajectory and the end position of this trajectory produced by VO/INS is very close to GNSS trajectory. Because of the poor result when this research uses INS installed in smartphone only, it is not suitable to take MENS-based INS as the main sensor for navigation. This research uses VO to be the main tool of navigation and makes INS as auxiliary tool to provide a reasonable scale estimation needed in VO for navigation. And this paper finally validate that the trajectory can be recovered even if using low cost sensor and low resolution of images on a smartphone when GNSS cannot give a good solution or not exist.

In this research, many steps have not been optimal including the calculating efficiency, accuracy of algorithm, stability and convenience. In the future, an improved algorithm of VO and other integration will be presented. For example, the eight-point algorithm for motion estimation can be replace by 5-point algorithm which is more popular in VO filed. Nonetheless, a neural network method will be adopted to detect the attitude of camera for promoting the computational efficiency. And the trajectory will be better when the smoothing and nonholonomic constrain are used. After improvement, it is worth to consider a longer distance up to several kilometres for testing. Or the bicycle can be ridden to more complicated environment such entering underpass from outside.

ACKNOWLEDGEMENTS

The authors would acknowledge the financial support by the Ministry of Science and Technology, ROC(Taiwan) (MOST 105-2119-M-006-019-MY2)

REFERENCES

Angrisano, A. (2010). GNSS/INS integration methods. *Dottorato di ricerca (PhD) in Scienze Geodetiche e Topografiche Thesis, Universita'degli Studi di Napoli PARTHENOPE, Naple*.

Welch, G., & Bishop, G. (1995). An introduction to the Kalman filter.

Hewitson, S., & Wang, J. (2010). Extended receiver autonomous integrity monitoring (e raim) for gnss/ins integration. *Journal of Surveying Engineering*, *136*(1), 13-22.

Julier, S. J., & Uhlmann, J. K. (1997, July). New extension of the Kalman filter to nonlinear systems. In *AeroSense'97* (pp. 182-193). International Society for Optics and Photonics.

Bay, H., Tuytelaars, T., & Van Gool, L. (2006, May). Surf: Speeded up robust features. In *European conference on computer vision* (pp. 404-417). Springer Berlin Heidelberg.

Bay, H., Ess, A., Tuytelaars, T., & Van Gool, L. (2008). Speeded-up robust features (SURF). *Computer vision and image understanding*, *110*(3), 346-359.

Chang, Hsiu-Wen, Georgy, Jacques, El-Sheimy, Naser, "A Low Cost Multi-Sensors Navigation Solution for Sport Performance Assessment," *Proceedings of the 25th International Technical*

Meeting of The Satellite Division of the Institute of Navigation (ION GNSS 2012), Nashville, TN, September 2012, pp. 3791-3798.

Scaramuzza, D., & Fraundorfer, F. (2011). Visual odometry [tutorial]. *IEEE robotics & automation magazine*, *18*(4), 80-92.

Fraundorfer, F., & Scaramuzza, D. (2012). Visual odometry: Part II: Matching, robustness, optimization, and applications. *IEEE Robotics & Automation Magazine*, *19*(2), 78-90.

Tardif, J. P., George, M., Laverne, M., Kelly, A., & Stentz, A. (2010, October). A new approach to vision-aided inertial navigation. In *Intelligent Robots and Systems (IROS), 2010 IEEE/RSJ International Conference on* (pp. 4161-4168). IEEE.

Kazemipur, B. (2015). *Computer Vision Aiding Smartphone Sensors for Indoor Location Applications* (Doctoral dissertation, University of Calgary).

Guarnieri, A., Pirotti, F., & Vettore, A. (2013). Low-cost MEMS sensors and vision system for motion and position estimation of a scooter. *Sensors*, *13*(2), 1510-1522.

Chang, H.-W., J. Georgy and N. El-Sheimy (2013). Monitoring Cycling Performance Using a Low Cost Multi-Sensors Navigation Solution. The International Symposium on Mobile Mapping Technology. Tainan, Taiwan.

Chang, H.-W., J. Georgy and N. El-Sheimy (2014). "Cycling dead reckoning for enhanced portable device navigation on multi-gear bicycles." GPS Solutions: 1-11.

Fischler, M. A. and R. C. Bolles (1981). "Random sample consensus: a paradigm for model fitting with applications to image analysis and automated cartography." Communications of the ACM 24(6): 381-395.

Hartley, R. and A. Zisserman (2003). Multiple view geometry in computer vision, Cambridge university press.

Longuet-Higgins, H. C. (1987). "A computer algorithm for reconstructing a scene from two projections." Readings in Computer Vision: Issues, Problems, Principles, and Paradigms, MA Fischler and O. Firschein, eds: 61-62.

Bay, H., A. Ess, T. Tuytelaars and L. Van Gool (2008). "Speeded-up robust features (SURF)." Computer vision and image understanding **110**(3): 346-359.

Chang, H.-W., J. Georgy and N. El-Sheimy (2013). Monitoring Cycling Performance Using a Low Cost Multi-Sensors Navigation Solution. The International Symposium on Mobile Mapping Technology. Tainan, Taiwan.

Chang, H.-W., J. Georgy and N. El-Sheimy (2014). "Cycling dead reckoning for enhanced portable device navigation on multi-gear bicycles." GPS Solutions: 1-11.

Fischler, M. A. and R. C. Bolles (1981). "Random sample consensus: a paradigm for model fitting with applications to image analysis and automated cartography." Communications of the ACM **24**(6): 381-395.

Hartley, R. and A. Zisserman (2003). Multiple view geometry in computer vision, Cambridge university press.

Longuet-Higgins, H. C. (1987). "A computer algorithm for reconstructing a scene from two projections." Readings in Computer Vision: Issues, Problems, Principles, and Paradigms, MA Fischler and O. Firschein, eds: 61-62.

Triggs, B., P. F. McLauchlan, R. I. Hartley and A. W. Fitzgibbon (1999). Bundle adjustment—a modern synthesis. International workshop on vision algorithms, Springer.

VISUAL SURVEILLANCE SYSTEMS FOR TRACKING MULTIPLE MOVING OBJECTS BAYESIAN ALGORITHM

Essam. M. Hassane [a], Sherin. M. Youssef [b], Hany. H. Mahmoud [c]

[a] Information & Documentation Center, Arab Academy for Science &Technology, Alexandria, Egypt - essamabdelhamied@aast.edu
[b] Dept. of computer Engineering, Arab Academy for Science &Technology, Alexandria, Egypt - sherin@aast.edu
[c] Dept. of computer Engineering, Arab Academy for Science &Technology, Alexandria, Egypt – hany.said.1980@ieee.org

KEY WORDS: Bayesian Algorithm, detecting objects, tracking moving objects, tracking system

ABSTRACT:

A new method is proposed for detecting and tracking multiple moving objects. The method is based on Bayesian approach to find correspondences between moving objects over frames. By using colour values and position information of the moving objects as observations, probabilistically assign tracks to those objects. Allow for tracks to be lost and then recovered when they resurface. The probabilistic assignment method, along with the ability to recover lost tracks, adds robustness to the tracking system. Present results that show that the Bayesian method performs well in difficult tracking cases and compare the probabilistic results to a Euclidean distance based method.

I. INTRODUCTION

Automated video surveillance is an important research area in the commercial sector [1, 2]. The ability to track a particular object or objects in successive frames is an important step in object tracking and classification applications. In many tracking applications, whether in the visible or non-visible spectrum, multiple target objects are to be analyzed at each time step. Finding reliable correspondences between objects in one time step to objects in the next is a nontrivial task given the non-deterministic nature of the subjects, their motion, and the image capture process itself. It can be a difficult task in some cases, especially in the presence of noisy measurements from the sensors, occlusion from objects in the field of view, and changes in orientation and direction of movement of the objects. Technology has reached a stage where mounting cameras to capture video imagery is cheap, but finding available human resources to sit and watch that imagery is expensive. Surveillance cameras are already prevalent in commercial establishments, with camera output being recorded to taps that are either rewritten periodically or stored in video archives. After a crime occurs, a store is robbed or a car is stolen, investigators can go back after the fact to see what happened, but of course by then it is too late. While options are still open for avoiding the crime. Keeping track of people, vehicles, and their interactions in an urban or battlefield environment is a difficult task [3, 4, 5].

In the work discussed in this paper, track the issue of real-time multiple object correspondence in outdoor stationary camera scenes. The detection of moving pixels using subtraction from a moving average background model. The moving pixels are clustered into regions, which refer to as blobs, so that pixels belonging to a single object are grouped together. Once moving regions have been identified, the next task is to generate tracks of these objects over successive frames. This is essentially a correspondence task, the goal of which is to find a match for each blobs in the previous frame to one of the blobs in the current frame. Bayesian inference based on the color and position information of the moving objects. When the information from a frame does not support the presence of an object, allow for the corresponding track to be declared 'lost'. If the object resurfaces in subsequent frames, the system reassigns the track to the object. Thus, the Bayesian method is able to handle occlusion, disappearance of objects, sudden changes in object velocity, and changes in object color profile and size.

This paper is organized as follows. Section II illustrates the proposed motion detection and object tracking phases. Experimental results and analysis of applying DWT, Bayesian algorithm are presented in section III. Finally, conclusions are driven in section IV.

II. MOTION DETECTION AND OBJECT TRACKING

A. Discrete Wavelet Transform

Wavelet transform provides a special basis that a signal can express features easily and efficiently. Localization in both frequency and time/spatial domains is the greatest advantage of discrete wavelet transform (DWT) over Fourier transform based methods. The spatial localization indicates that after the wavelet transform takes place, the coefficients in a certain position at the wavelet sub-images correspond to the details of different frequencies in the corresponding spatial location [6, 7].

Two-dimensional DWT can be used to decompose an image into four sub-images. Filters are applied in one dimension first, vertically or horizontally and then in the other dimension as shown in Fig. 1. The wavelet transform connotes hierarchical features, and an image example Fig. 2a can be decomposed into four sub-images. The four sub-images that the wavelet transform preserves not only the frequency features but also spatial features as shown in Fig. 2b. An original image can be decomposed into four different bands (LL, HL, LH, HH) by using the discrete wavelet transform. These sub-bands contain different frequency characteristics after filtering. The high-pass filter extracts the high frequency part and the low-pass filter gives the low frequency information representing the most energy of an image [8, 9, 10]. Fig. 2c shows the Sub-bands of third-level DWT. In this paper, only the low frequency part is used for processing due to the consideration of low computing cost and noise reduction issue. The proposed method decreases the computing cost by using two-level DWT.

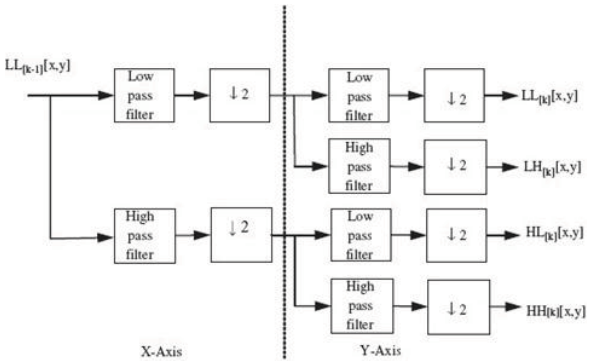

Fig. 1 The structure of a forward two-dimensional DWT

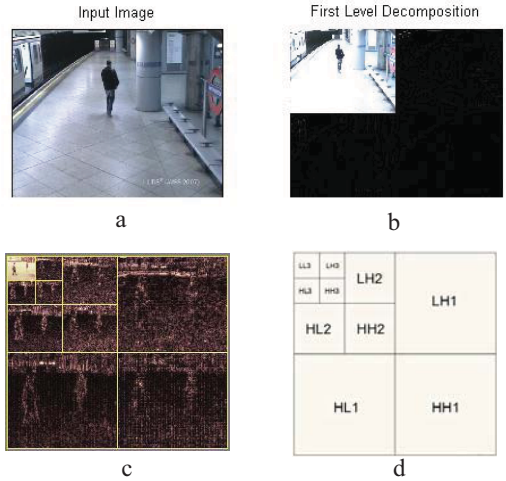

Fig. 2 Original Image, First-level transform, Third-level transform, Sub-band of third-level DWT

B. Background Subtraction

Background subtraction is widely used as the basis for moving object extraction from image sequences. The background image is subtracted from the interesting frame image.

Let D (x, y) be the difference image obtained by computing the absolute values of the difference between the background and the current frame image and then thresholding by a given threshold value T in Eq.1;

$$D(x,y) = \begin{cases} 1 \; IF \; LL_{[3]n}(x,y) \\ 0 \; otherwise \end{cases} \quad (1)$$

Where $LL_n(x, y)$ is the low frequency sub-image of third level DWT of current frame, LL (x, y) is the low frequency sub image of third level DWT of background frame and n is the frame number.

C. Motion Segmentation

In the work discussed in this paper use a moving average model where the average intensity value for each pixel over a window of N frames where N = 150 is regarded as the background model. Moving objects do not contribute much to the average intensity value [10]; thus, the model becomes a reasonable estimate of the background. If $I^k(y,x)$ is the intensity level at coordinates $Y = y$ (column) and $X = x$ (row) of the K^{th} frame in the sequence $bg^k(y,x)$ is the average background model value at (y, x) for frame k, then

Equation (2)

$$bg^k(y,x) = \frac{1}{N}\left(\sum_{j=k-(N/2)}^{k+(\frac{n}{2})} I^j(y,x) \right)$$

The segmented output is:

$$seg^k(y,x) = 1 \text{ , if } \left| bg^k(y,x) - bg^k(y,x) \right| > \text{T}$$
$$= 0 \quad otherwise$$

Where T is a predetermined threshold, typically 10.

Following segmentation, region growing is used to locate each moving object. An envelope is established around each object of interest by use of morphological erosion and dilation filters. Additional noise is filtered by ignoring blobs less than S pixels (typically 20) in size.

D. Change Detection and Sequence Tester

A new change detector is used to detect the changes in a video sequence and divide the sequence into scenes to be encoded independently. A further enhancement is done using a sequence tester to test each scene for high activity. (Due to motion) and decide whether or not another reference frame (key frame) is needed. Simulation results prove the enhanced performance of the suggested. The mechanism proposed here, is based on segmenting the video into scenes using a change detector. For each scene, one or more key frames are chosen.

A scene is a sequence of shots that belong together semantically. There are two kinds of shot boundaries in videos: Abrupt shot changes called "cuts", and, Gradual transitions between two different shots. The proposed scene cut detector is simple and fast. The objective of the detector is to divide the whole video into independent sequences to be encoded separately. This is done in 2 steps. Firstly, the video as a whole is used to get the global cuts, thus dividing the video into sequences this is done by the change detector (CD). Secondly, each sequence is further investigated to ensure that there is no high level of changes between the frames that may cause artifacts in the decoded video. The results are efficient since it keeps complexity low and the presence of this module in the code improves efficiency.

Change Detector (CD)

The detector uses the normalized sum of absolute difference between each two successive frames on a pixel-by-pixel basis. If the normalized difference (normalized_diff) is high, then an abrupt cut is present. It can be described in the following rules:

If (normalized_diff is low) then (cut_type is continuous)

If (normalized_diff is mid) then (cut_type is gradual change)

If (normalized_diff is high) then (cut_type is abrupt change)

Using the change detector algorithm (CD), it was efficient enough to detect abrupt cuts and help divide the video file into sequences. But in the case of long scenes where motion occurs, the high level of changes between frames must be considered. This is because the detector depends on differencing frames. For each scene, a key frame is chosen and all the other frames are differenced from it. When long scenes with high level of changes between frames especially with respect to the key frame, the encoded frame carries a lot of information that may be lost due to lousy encoding and decoding so another key frame must be used according to Fig 3.

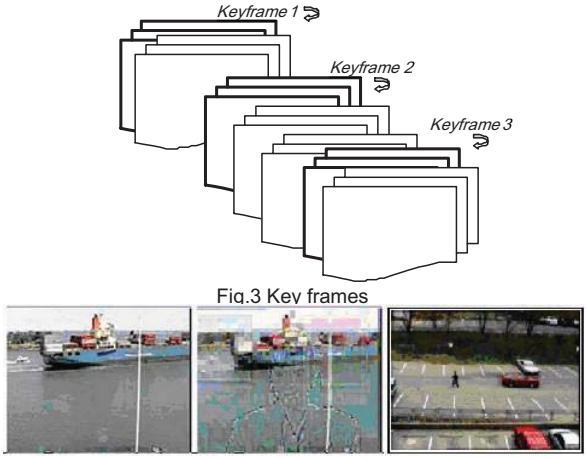

Fig.3 Key frames

For each scene, a key frame is chosen and all the other frames are differenced from it. The change detector algorithm is used to determine the gradual change and abrupt change.

E. Object Tracking

We perform object tracking by determination correspondences between blob in the previous bod and blobs in the current frame. In the case of a noiseless environment and perfect segmentation of blobs, the task is straightforward because a one-to-one correspondence can be usually being found for a blob in two successive frames. In reality, however, there is often a great deal of uncertainty in the final segmentation. Failure to detect small yet valid blobs due to their size, occlusion of valid blobs by other objects in the scene, change in object orientation, entry (or exit) of objects in the scene, and camera jitter are the main reasons for uncertainty. These factors make correspondence a difficult problem to solve, particularly for videos that are shot outdoors. Our goal is to develop a correspondence scheme that is robust to these sources of uncertainty.

F. General tracking approach

For each motion blob in the first frame, a new track is created. In subsequent frames, matching blobs are sought for each track in the previous frame. Matched tracks are updated with position and color information from the matching blob. We allow tracks to be declared 'lost' if any of the factors mentioned above causes the algorithm to fail to detect a suitable match for a track. The track is not deleted but is 'kept alive' for a few frames in hopes that a match will be found. A track is deleted only if a suitable match is not found for L (typically 5) consecutive frames. If there is any blob in the new frame that cannot be matched to an existing track, then a new track is generated. A list of currently 'active' tracks is maintained for each time step/frame.

G. The correspondence algorithm

Commonly, a distance-based match matrix is used to solve the correspondence problem. To facilitate track correspondence, we designed a Bayesian inference method to find matching blobs in consecutive frames. We also calculate the probability that a track is 'lost' in the current frame. The basic idea behind our approach is that given an object (blob) in the current frame, there is some probability that a blob of similar color and position will be observed in the next frame. Using Bayes' formula, we can find the probability of a blob belonging to a track from the previous frame, given the blob's color and position observations.

The sub-problem can be formulated thus:

If $T^{k-1} = \{t_1^{k-1}, t_2^{k-1}, \dots, t_{u^{k-1}}^{k-1}\}$ is the set of tracks in frame (k-1) and $O^k = \{o_1^k, o_2^k, \dots, o_{v^k}^k\}$ is the set of moving blobs in frame k. Here, t_j^{k-1} is the j[th] track,$u^{k-1}1$ is the total number of tracks in frame (k-1),o_i^k is the i[th] blob found in frame k and v^k is the total number of moving blobs in frame k.

In other words, what is the probability of assignment of track t_j^{k-1} to blob o_i^k for all j and i? An increase in the probability of assignment of track t_j^{k-1} to a blob O_i^k should automatically reduce the probability of assignment of track t_j^{k-1} to other blobs O_m^k where m ≠ i. If no suitable match for t_j^{k-1} is found, then the probability that it is 'lost' should be made high.

By looking at the observations for all elements $t_j^{k-1} \in T^{k-1}$ we update a belief matrix which contains the probability of match for each track to each candidate blob.

III. RESULTS

In this section, we did several experiments to prove the feasibility of the proposed tracking and identification method. We used an entry-level video camera and capture card to capture test sequences in different campus, and simulated several cases of condition for moving objects, such as single object indoors, single object in outdoor environment with static background, single object in outdoor environment with varied background, and multiple objects outdoors. All the test sequences are stored in Microsoft AVI format with raw data of resolution 320 X 240 and frame rate of 30 frames/s. Several experiments have been carried out to simulate several cases of condition for moving objects, such as single object indoors, single object in outdoor environment with static background and single object in outdoor environment with varied background.

Figure 4 shows an example of the experimental results of tracking single object indoors. The reason why we use discrete wavelet transform is its noise resistant ability.

A. Tracking single objects

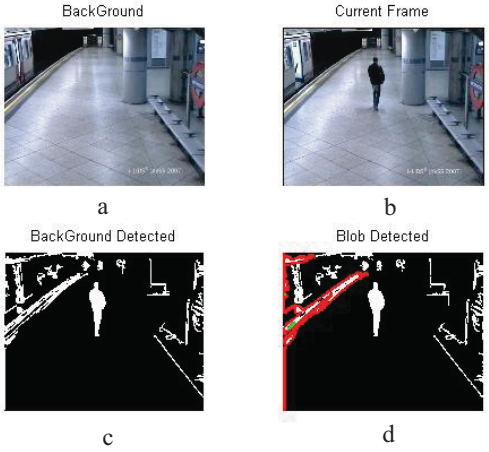

Fig. 4 Tracking a single object in indoor environment with static background

B. Tracking multiple objects

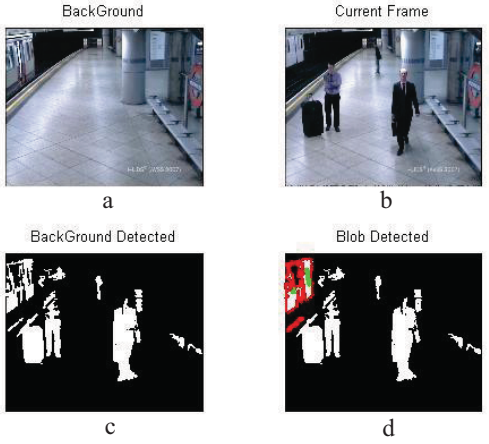

Fig. 5 Tracking a multi objects in indoor environment with static background

In order to test the proposed tracking and identification method for multiple objects, we capture eight video sequences outdoors with multiple moving objects crossed each other for the experiments. In sequence 1, there are three persons in the test video stream, and they enter into the surveillance system in crossed manner. Figs. 5a, 5b, and 5c show how these three persons move in the video sequence. At first, the man who wears red clothes enters the scene from the right side, and then the man who wears gray clothes enters the scene from the left side. They walk to each other and overlap in the middle of the scene.

C. Comparison with other Methods for Object Detection

The object detection algorithm is compared with two background-based object detection algorithms. One of the algorithms uses an adaptive MOG model [11], the other uses nonparametric background subtraction (NPB) [12].

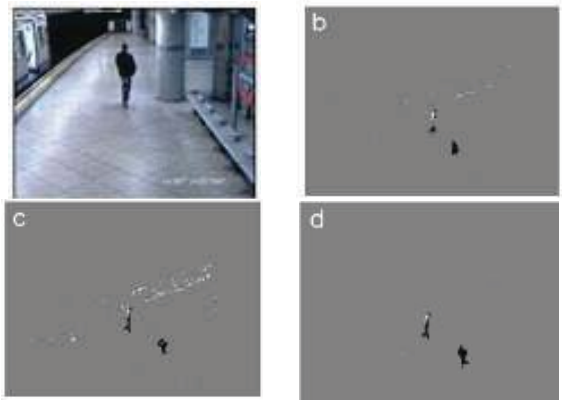

Fig.6 Comparisons of three object detection algorithms: (a) original image #110 in sequence, (b) result of MOG, (c) result of NPB, and (d) result of the proposed algorithm

Fig. 6(a) is the original image. This image is low contrast and there are some distractors such as the light from the windows and the tree. Fig. 6(b) shows the detection results obtained from the MOG algorithm. The two objects are detected but not very well even though the parameters in the MOG algorithm are carefully chosen, especially the threshold T and standard deviation. Fig. 6(c) shows the detection result using NPB. The results are better than those obtained from the MOG algorithm. Most of the pixels associated with the two objects are found. This algorithm is affected by high gray level gradients. For example, there are some false detections near the windows. Fig. 6(d) shows the detection results obtained using the proposed algorithm. It can be seen that the new algorithm performs better than MOG and NPB with more accurate detections and fewer false alarms. The algorithm was tested in more cluttered night-time scenes. The camera is wide view; the objects have low contrast and a small apparent size. Most of the current algorithms, including NPB, fail to detect the objects.

Table 1 Comparison of the Normalized Jaccard coefficient between the new algorithm and the MOG-, NPB-based algorithms on different sequences of frames.

Video sample no.	MOG	NPB	The proposed method
"Two persons"	78.65%	85%	98%
"Traffic sequence"	55.71%	63.98%	97%
"Persons at a Distance"	Less than 10%	Low than 10%	94%
"Zooming camera Sequence"	Less than 10%	Low than 10%	96%

D. Evaluation of the Experiments

Comparisons are carried out between the proposed algorithm and both the MOG- and NBP-based algorithms. The performances of the three algorithms are measured using the Jaccard coefficient [13,14], J defined by

J = TP/ (TP + FP + FN) %

Where TP (true positives) is the number of moving objects correctly detected, FP (false positives) is the number of false detections of moving objects and FN (false negatives) is the number of missed detections of moving objects. The ground truth is obtained manually in each frame of the sequence.

Table 1 gives the values of normalized Jaccard (NJ) coefficient in Table 1, J is used to describe the detection accuracy of single frame and NJ gives the detection accuracy for the whole sequence. For the sequence "two persons", the MOG and NBP algorithms both succeed to some extent. The NPB algorithm detects low contrast objects better than the MOG algorithm but it has too many false alarms.

The proposed algorithm achieves the best (97%). For the sequence "traffic sequence", the MOG and NBP algorithms do not work well because of the light reflections.

The new algorithm gives satisfactory results (97%). For the two sequences "persons at a distance" and "zooming camera sequence", it is very difficult to detect objects using the MOG and NBP algorithms because of the low contrast and the zooming camera. The NJ score is so low that it is ignored in Table 1. The proposed algorithm works relatively well on the two sequences (94% and 96%).

IV. Conclusions and Future Work

While Bayesian reasoning and networks have been used by many researchers in video surveillance, this paper describes a direct way of using Bayesian inference for solving the correspondence problem in tracking. It is direct in the sense that the color and position of the new blobs are the observations, while the assignment of blobs to known tracks is the hypothesis.

With the provision for allowing tracks to be declared as lost, we add robustness to the system and can pick up tracks of objects which may have disappeared momentarily due to occlusion or other reasons.

Though we currently work in RGB space, the method may be easily expanded to other observation spaces such as HSV. It could also be adapted through experimentation to IR imagery using intensity rather than color and adding object size as an observation for finding correspondence. In hyper spectral data, Principal Components Analysis could be done to choose the best bands, and the PDF's of these bands would be used in place of RGB PDF's for the Bayesian inference. The Bayesian correspondence method is a generic approach and not specific to color video data. We plan to adapt it to other imaging modalities in the future.

CONCLUSIONS AND FUTURE WORK

While Bayesian reasoning and networks have been used by many researchers in video surveillance, this paper describes a direct way of using Bayesian inference for solving the correspondence problem in tracking. It is direct in the sense that the color and position of the new blobs are the observations, while the assignment of blobs to known tracks is the hypothesis.

With the provision for allowing tracks to be declared as lost, we add robustness to the system and can pick up tracks of objects which may have disappeared momentarily due to occlusion or other reasons.

Though we currently work in RGB space, the method may be easily expanded to other observation spaces such as HSV. It could also be adapted through experimentation to IR imagery using intensity rather than color and adding object size as an observation for finding correspondence. In hyper spectral data, Principal Components Analysis could be done to choose the best bands, and the PDF's of these bands would be used in place of RGB PDF's for the Bayesian inference. The Bayesian correspondence method is a generic approach and not specific to color video data. We plan to adapt it to other imaging modalities in the future.

ACKNOWLEDGEMENTS

All praises be to Allah (SWT) for blessing me with opportunities abound and showering upon me his mercy and guidance all through the life. I pray that He continues the same for the rest of my life.

I am writing these acknowledgments at the end of my paper study journey. I would like to thank all those whom I owe them a lot. I am grateful to Prof. Dr. Sherin Youssef who always taught me a lot. I would like to express my gratitude and sincere thanks for her supervision of this paper. I am also grateful to Dr. Hany Hanafy for his valuable comments on my progress, and for the constructive criticism at different stages of my study, teaching me the professional way of thinking and helping me in the final appearance of this work. Their honest and precise review was helpful to trace points of weakness in the paper and strengthen them.

Many thanks to my parents and my sisters for their help and support during my study. I also thank my dearest Dr. Eman Kamel for the generous support, constant help providing me with necessary references.

Moreover, I must never forget to thank Dr. Mahmoud Farouk, Eng. Tarek Ragy for always being there when I needed help and support. at all the important stages in my education, in the most crucial of times, I can remember their presences by my side.

My deep respect and gratitude to Eman Abd El-latif for guiding me early in life and encouragement during my work. I greatly appreciate care and dedication in constructively criticizing my work.

I would like to specially thank Eng. Dahlia Gamal, Eng. Hashem Fekry without whom I would not have had this achievement without their great efforts to encourage and develop my passion for learning. I deeply appreciate your belief in me. You are the source of my inspiration. Please accept my heart-felt gratitude.

Finally, I would like to thank all my friends for helping me and would also like to thank all those who have directly or indirectly contributed to the success of my work.

REFERENCES

[1] Guohui Li, Jun Zhang, Hongwen Lin , D. Tu, and Maojun Zhang, " A moving object detection approach using integrated background template for smart video sensor," in Proceedings of the 21st IEEE Instrumentation and Measurement Technology Conference, IMTC 04, May 2004, vol. 1, pp. 462- 466.

[2] C. Stauffer and W. E. L. Grimson, "Learning patterns of activity using real-time tracking," IEEE Trans. on Pattern Analysis and Machine Intelligence, vol. 22, no. 8, pp. 747- 757, Aug. 2000.

[3] J. L. Barron, D. J. Fleet, and S. Beauchemin, "Performance of optical flow techniques," International Journal of Computer Vision, vol. 12, no. 1, pp. 43–77, 1994.

[4] B. K. P. Horn and B. G. Schunck, "Determining optical flow," Artificial Intelligence, 17, pp. 185-203, 1981.

[5] Wang, J. Y. A. and Adelson, E. H., "Spatio-temporal segmentation of videodata" , in Proceedings of SPIE on Image and Video Processing II, 2182, pp. 120- 131, San Jose, Feb. 1994.

[6] R.E. Kalman, "A new approach to linear filtering and prediction problems," Trans. American Society of Mechanical Engineers, Journal of Basic Engineering, vol. 82, pp. 35– 45, 1960.

[7] Y. Bar-Shalom and T. E. Fortmann, Tracking and Data Association. Academic Press, 1988.

[8] M. Isard and A. Blake, "Condensation - conditional density propagation for visual tracking," International Journal of Computer Vision, vol. 29, no. 1, pp. 5–28, 1998.

[9] C. Rasmussen and G. D. Hager, "Probabilistic Data Association Methods for Tracking Complex Visual Objects," IEEE Trans. on Pattern Analysis and Machine Intelligence, vol. 23, no. 6, pp. 560-576, Jun. 2001.

[10] S. Intille, J. Davis, and A. Bobick, "Real-time closedworld tracking," IEEE CVPR, pp. 697-703, 1997.

[11] C. Stauffer, W.E.L. Grimson, "Adaptive background mixture models for real-time tracking," CVPR, 1999, pp. 252–260.

[12] S. J. McKenna,Y. Raja, S. Gong, "Tracking color objects using adaptive mixture models," Image Vision Comput. 17 (3) (1999) 225–231.

[13] L. Wang, W. Hu, T. Tan, "Recent developments in human motion analysis," Pattern Recognition 36 (3) (2003) 585–601.

[14] P. Sneath, R. Sokal, The Principle and Practice of Numerical Classification, W.H. Freeman, New York, 1973.

DEVELOPING A NEW TECHNUQUE FOR DETECTING TWO CRITICAL-NODES IN ADHOC NETWORKS

Ibrahim S. Fayed[a], *Mokhtar A. A. Mohamed*[b], *Gamal Attiya*[c] *and Nawal A. El-Fishawy*[d]

Department of Computer Science & Engineering, Faculty of Electronic Engineering Menoufia University, Egypt
[a]*ibrahim_fayed@outlook.com,* [b]*moukhtar_ahmed@yahoo.com,* [c]*gamal.attiya@yahoo.com,* [d]*nelfishawy@hotmail.com*

KEY WORDS: Ad hoc networks, critical nodes, localized algorithms.

ABSTRACT:

Recently, one of the important requirements, in ad hoc networks, is to avoid partitioning problem due to dynamic movement of special node(s) called "Critical Node(s)". Critical node refers to the node that its removal from the network will break it into many partitions. Many researches presented different algorithms to detect such critical node(s) in any ad hoc network. These researches did not take the situation if two nodes together can cause also network separation if both of them are moved or removed at the same time. This paper introduces a new technique called "Two Critical-Nodes Detection Algorithm (TCNDA)" to determine individual critical node(s) and also to determine each two node pair(s) which are critical together.

1. INTRODUCTION

The area of Ad hoc networks is very active nowadays due to its infrastructure-less nature, simplicity of deployment in areas where infrastructure hard to established, mobility and self-configurable nature make it suitable for huge range of applications. These applications include military and battlefield scenarios and disaster situations where no infrastructure is present, search and rescue jobs, transmission of road and weather conditions, taxi cab network and inter-vehicle networks and educations operation by establish virtual classrooms and ad hoc communications through meetings or lectures (I. Ahmad, 2016), (M. Rath, 2016), (S. Kaur, 2016).

Ad hoc network is a group of wireless mobile nodes creating a temporary network without any fixed infrastructure and no need to centralized administration. Nodes in ad hoc network communicate with each other in a peer-to-peer style where any two nodes are near enough to each other are assumed to have a direct radio link. The maximum distance enough to establish the direct radio link to other node is called the node's transmission range. Each node plays two important roles: host and router to forward the packets of other nodes .To accomplish a connected ad hoc network; there must be a direct path of multi-hop path from a node to every other node (M. Jain, 2015).

In any network, critical node represent the node which its removal from the network will break the network into many partitions. As shown in Figure.1, both node (1) and (2) are critical nodes. Nodes inside each partition are capable of communicate with each other but nodes in other partitions are inaccessible. There are many applications of detection of critical node. The applications involve situations where the aim is to either protect the connectivity of nodes in a network by securing the most critical nodes or attacking the most critical nodes in order to have minimum connections between all pairs of nodes in the network (M. Edalatmanesh, 2013).

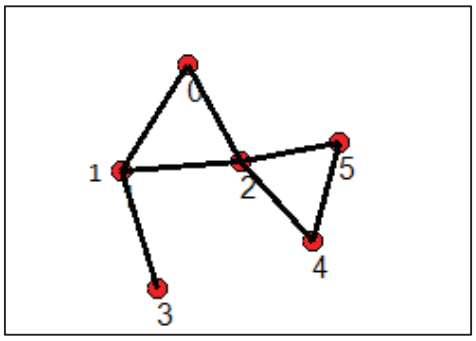

Figure. 1: An example of a small network

Some of ad hoc network applications are very critical from being separated such as communication between members of a rescue team or between soldiers in a battle field. In such situations, human life may be depending on the availability of this communication network. So the detection of critical node is very important as first step to take care of it to avoid its failure or removal.

This paper provides a literature review of the most recent methods that concern with the detection of critical node in ad hoc networks. Then, it presents novel algorithm for detection of critical nodes in Ad-hoc networks. The proposed approach is called Two Critical Nodes Detection Algorithm (TCNDA). This approach enable each node to determine if it's local critical or there are another node from its k-hop neighbours and both of them together are critical. Finally, the proposed approach is evaluated and the effectiveness of TCNDA in determining the criticality of the node is validated through simulation experiments. Simulation results demonstrate that the performance of TCNDA with local k-hop information is quite competitive compared to centralized algorithm with global network information.

The rest of this paper is organized as follows. Section 2 introduces some of related work. Section 3 presents the TCNDA algorithm while Section 4 describes the performance evaluation of proposed algorithms. Finally, concluding remarks are listed in Section 5.

2. RELATED WORK

The algorithms concern with the detection of critical node can be classified into centralized and distributed based on the way of execution. Centralized algorithms (M. Duque-Anton, 2000), (D. Goyal, 2002) required a node to have global information about the all network topology. In (M. Duque-Anton, 2000), Duque-Anton et al. used depth first search (DFS) In order to detect the critical nodes, the rest-connectivity value was introduced, which defined as the number of node pairs which got disconnected when the separation element is removed from the graph. In (D. Goyal, 2002) they extend the depth first search (DFS) used in (M. Duque-Anton, 2000) to detect the links what they name as critical links. Critical links can be defined in several ways. One possible definition is that a link AB is critical if both nodes A and B are critical nodes. But, two critical nodes may have another alternate path between them. So a better way to define critical link is that the link connecting two critical nodes so that, when this link is removed from the graph, the graph becomes disconnected. However Centralized algorithms required keeping global information about topology which involves very communication overhead and thus may not be suitable in ad hoc network.

Oppositely, distributed algorithms don't need network keeping global information at any node and can be used for ad hoc network. For example DDFS (Distributed Depth-First Search) which has been discussed in (S. Xiong, 2010) implements DFS in the graph in a distributed manner. But they show by experiments that the time delay of DDFS is much higher and it is more sensitive than the other algorithms to failures of links and nodes. X. Liu et al. (X. Liu, 2009) presented a distributed mechanism to detect cut vertices in overlay networks called CAM (Connection Adjacency Matrix). In CAM, every cut candidate sends a component probe message to each neighbor, which contains timestamp, a TTL threshold indicating the expiration time of the message. Every node when receives a new message, it updates its local knowledge and make a choice to forward the message or to return arrival message. Each candidate updates its CAM graph based on the returned arrival messages. The candidate node is a cut vertex if its CAM graph has more than one component. However experiments and results in (S. Xiong, 2010) shows that CAM takes too large communication cost, which is not suitable for ad hoc networks. Xiong et al. (S. Xiong, 2010) presented a distributed algorithm called CVD (Cut Vertex Detection) to detect cut vertices. CVD travels through the nodes of a network in parallel and colors the edges based on the interval-coded spanning tree. Then it decides the cut vertices by counting the edge colors.Sheng et al. (M. Sheng, 2006) presented a distributed algorithm called DMCC (Detection algorithm based on Midpoint Coverage Circle). DMCC constructs an area (Midpoint Coverage Circle) with node n as the center to detect whether node n is a critical node in the sub-graph G*. if node i is detected as a critical node in G*, it should find all possible global paths of node i neighbors by using RREQ (Route Request) and RREP (Route Reply) to make a decision if it is a global critical or not. If the node is non-critical in G* there is no need to check in the global. So this will reduces communication overhead and will increases speed.

Both Jorgic et al. (M. Jorgic, 2004) and Imran et al. (M. Imran , 2013) show how to find a critical node in k-hop information, and present the accuracy of k-hop critical nodes by comparing it with the global critical node. These algorithms only determine one critical node when removed the network is separated into groups and don't take the situation if two nodes together are removed the network separated. However, our proposed TCNDA algorithm determines the critical nodes and two nodes together as critical in K-hop information by making updating of LASCNN algorithm descried in (M. Imran , 2013).

3. PROPOSED ALGORITHM

The TCNDA determine the critical nodes and two nodes together as critical using local information. Local information is dependent on k-hop notation, two nodes are *k*-hop neighbours if the shortest path between them has *k* or less hops. If node has information about itself only we say it has 0-hop information, but if node has information about direct neighbours only then it has 1-hop information, also if it has information about the neighbours of its direct neighbours then it has 2-hop information and so on.

3.1 Builds k-hop connection list :

Nodes collect their local information of k-hop neighbours after discovering each other by sending "hello" messages to its neighbours containing the information of their (k-1)-hop neighbours. The1-hop information is a list of direct neighbours with their geographic positions. The 2-hop information is gotten by spreading lists of 1-hop neighbours and so on. Using the k-hop information nodes establish a k-hop connection list. For example, a 1-hop connection list of node (1) for the network Fig.1 is shown in Table 1 where each row is a connection between two nodes.

Table 1: 1-hop connection list of node (1).

1-hop connection list	
1 < > 0	direct neighbours
1 < > 2	direct neighbours
1 < > 3	direct neighbours
0 < > 2	determined by positions

A 1-hop connection list holds the direct neighbours of a node in the form of a pair. the connection between the neighbours are determine by calculation of distance between them using their geographic positions and compare it with the radio range of the node, usually this radio range are constant for all nodes. For example, node (1) can determine the connection between its 1-hop neighbors Node (0) and node (2) based on their position. Similarly by collection the 1-hop connection list of the 1-hop neighbors without duplication, 2-hop connection list can be established. Also the established 2-hop connection list will contain the connections between 1-hop neighbors and between a1-hop and 2-hop neighbors, but connection between 2-hop neighbors can be determined based on the distance between the nodes like in constructing the 1-hop connection list. If we will have 2-hop connection list there is no need to determine the connection between 1-hop neighbors when build the 1-hop connection list because it will be involved in 2-hop connection list .In the same way if we work in k-hop connection list it will have the connection between (k-1)-hop and k-hop and we need to determine the connection between k-hop neighbors only and

no need to determine it in any other steps. Table2 shows a 2-hop connection list of node (1).

Table 2: 2-hop connection list of node (1).

2-hop connection list
1 < > 0
1 < > 2
1 < > 3
0 < > 2
2 < > 5
2 < > 4
4 < > 5

Keeping the connection list updated is very important because topology of ad hoc network continuously changes due to network dynamics. Nodes in ad hoc networks always exchange update messages to display any changes in topology and share the criticality of nodes. Once a node receiving an update message it forwards the message to (k-1)-hop neighbours.so every node will update its connection list based on these massages.

3.2 Detection phase:

After each node builds its k-hop connection list it will process it to decide whether it is critical node or not. If it is not critical, it will decide whether there is another node connected with it and both of them together are critical.

First step in detection phase is check the number of connection in the connection list, if the number of connection is one connection only, then the node is leaf node and the remove of it from the network will not disconnect other node, so it will be not critical and there is no chance to be critical together with other node for example node (3) in Figure 1 is leaf node. On the other hand if the number of connections is more than one, the node create a list of neighbours nodes which are connected without it called connected-neighbours list and it will be empty in the first iteration. After that the node start processing its connection list one by one, if the connection has the node tested itself then ignore the connection and go to the next connection. If the connected- neighbours list is empty then add the two nodes of the connection into the connected-neighbours list. Otherwise, if the connection has a common node with the connected-neighbours the other node will be added into the connected-neighbours. After processing all connection in the connection list we check the size of the connected-neighbours list, if the size is increase from the last iteration then repeat the iteration. In this manner, the connected-neighbours list will has all the connected neighbours without the node. If the size of the connected-neighbours list is equal to the number of k-hop neighbors of the node, node is not critical. But if the size is less then node is critical.

For example if we test node (9) in figure 2, TCNDA algorithm needs four iterations to build node (9) connected-neighbours list as shown in table 3 (column 3). At the beginnig connected-neighbours list is empty. At first itration, TCNDA will ignore connections (9 < > 6) and (9 < > 0) because these connections have node (9) itself. Then, TCNDAwill go through the other rest connections to process them one by one. Because connected-neighbours list is empty until now,both nodes (6) and (7) will be added to it due to processing connection (6 < > 7) . No nodes will be added after processing connections (0 < > 1) ,(0 < > 3) and (0 < > 2) because node (6) and (7) are not common with these connections . After that, node (3) and (1) will be add after processing connections (3 < > 7) and (1 < > 7) because node 7 is common in them. In this moment iteration 1 is finished by existence of node 6,7,3,1 in connected-neighbours list of tested node (9). At second iteration, node (0) will be added when processing connection (0 < > 1) because now node (1) is common in this connection. Similarly, node (2) will be added to this list during processing of connection (0 < > 2) in the third iteration. Finally at fourth iteration, there are no nodes that will be added, so process of building node (9) connected-neighbours list is complete. We should notice that number of iteration will be changed according to the tested node. As shown in table 3. We can see the size of the node (9) connected-neighbours list is equal to the number of k-hop neighbors. So node (9) is not critical alone.

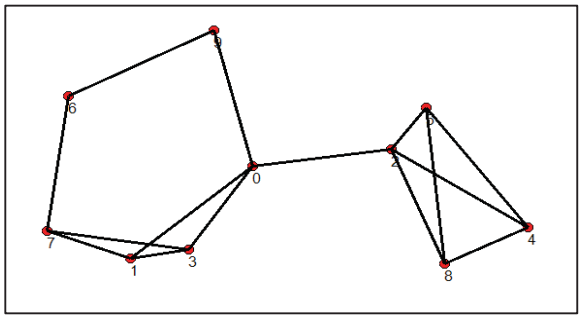

(a) Network before detection

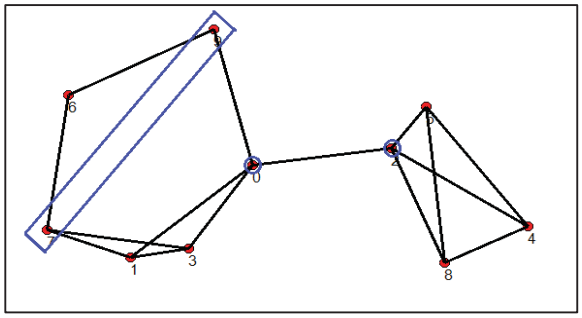

(b) Network after detection

Figure 2: example of network and the detection of criticality using TCNDA.

If the node is not critical then we will test every node in k-hop neighbors to see if there is another node with the node we test and both of them together are critical. If the node is leaf node or critical node ignore it, on the other side we will process the connection list one by one, if the connection has the node itself or the node tested in this then ignore the connection and go to the next connection. And continue like before until connected-neighbours list filled. If the size of the connected-neighbours list is equal to the number of (k-hop neighbors of the node -1), the node and the tested node together are not critical. But if the size is less, then the node and the tested node together are critical. If both of nodes together are critical, both nodes send a confirmation message to the other node to ask if it also see the same thing. The confirming message increases the accuracy, because this allows the node to know if there is alternative path out of its local k-information.

Table 3: node (9) lists for 2-hop.

2-hop neighbours	2-hop connection list of node(9)	connected-neighbours list to test criticality of					
		node (9)	node (9) and node (6)	node (9) and node (7)	node (9) and node (1)	node (9) and node (3)	node (9) and node (2)
6	9 < > 6	6	0	0	6	6	6
0	9 < > 0	7	1	1	7	7	7
7	6 < > 7	3	3	3	3	1	3
3	0 < > 1	1	2	2	0	0	1
1	0 < > 3	0	7		2	2	0
2	0 < > 2	2					
	3 < > 7						
	1 < > 7						

```
1.  If Connection List Size = 1 then
2.      node N is not critical
3.  else if Connection List Size > 1 then
4.      lContinue = true
5.      While (lContinue == True)
6.          lContinue = false
7.          For each connection in the connections List
8.              If connection don't contain N then
9.                  If connected-neighbours list size = 0 then
10.                   Add the pair of current connection into the connected-neighbours list
11.                   lContinue = true
12.                 Else
13.                     If any node from the pair of connection exist in connected-neighbours list then
14.                         If the other node not exist in connected-neighbours list then
15.                             Add the other node to connected-neighbours list
16.                             lContinue = true
17.                         End if
18.                     End if
19.                 End if
20.             End if
21.         End for
22.     End while
23.     If connected-neighbours size < number of k-hop neighbors then
24.         Node N is critical
25.     Else
26.         Node N is not critical
27.         Clear items in connected-neighbours list
28.         For each node M  in  k-hop neighbors
29.             If m is not ( leaf node or critical node ) then
30.                 lContinue == True
31.                 While (lContinue == True)
32.                     lContinue = false
33.                     For each connection in the connections List
34.                         If connection don't contain N or M then
35.                             If connected-neighbours list size = 0 then
36.                                 Add the pair of current connection into the connected-neighbours list
37.                                 lContinue = true
38.                             Else
39.                                 If any node from the pair of connection exist in connected-neighbours list then
40.                                     If the other node not exist in connected-neighbours list then
41.                                         Add the other node to connected-neighbours list
42.                                         lContinue = true
43.                                     End if
44.                                 End if
45.                             End if
46.                         End if
47.                     End for
48.                 End while
49.             End if
50.             If connected-neighbours size < number of k-hop neighbors -1 then
51.                 Send confirm message to node  m if received yes Add node M to critical together list
52.             End if
53.         End for
54.     End if
55. End if
```

Figure 3: Pseudo code of the proposed TCNDA of each node N in the network

For example, after node (9) process its connection list of 2-hop and generate connected-neighbours list, and the size of the connected-neighbours list indicates that node (9) is not critical alone. Then node (9) will test every node in its 2-hop neighbours except the critical node already like node(0) and generate the connected-neighbours list to test criticality of node(9) and the tested node together. If the size of the connected-neighbours list is less than the number of 2-hop neighbours -1then node (9) and the tested node together are critical. From table 3 we can see node (9) are critical with node (7).

TCNDA identify the k-hop criticality of the node from the first time after build the connection list. But if the node is not critical we can't determine if there is another node from its direct neighbours both of them together are critical from the first time. Because, it's dependent of the criticality of the direct neighbours, If the node is leaf or critical don't take it into account. So this part is determined after each node shares its criticality. Obviously, if a node identified by TCNDA as k-hop not critical it will be globally not critical and determine noncritical node is very important in recovery algorithms, but if a node identified by TCNDA as k-hop critical or two noncritical nodes together are critical it may be not globally critical because it is possible to exist alternative paths in the network out of the range of the k-hop. Taking into account no critical point is lost this kind of localized algorithms is suitable and helpful. Figure 3 shows the pseudo code of the proposed TCNDA.

4. RESULTS AND ANALYSIS

The accuracy of the proposed localized algorithm is proved by comparing the results with the equivalent globalized algorithm which are perfectly accurate through simulation experiments. A simulator coded in C# is developed to validate the performance of proposed algorithm. The algorithms presented in (Furuzan, 2007), (Ibrahim, 2016) are used to generate random connected topologies with specified radio range (R) OR average number of neighbors for each node (D). The experiments are accomplished in area (A) with dimensions equal to 800×800 m. The radio range (R) of the nodes and the number of nodes is changed among 10, 30, 50, 70, 90 and 110.Also, the average number of neighbors for each node (D) is changed among (3 to 9). For each experiment, the average value of the results is taken after executing each algorithm 10 times.

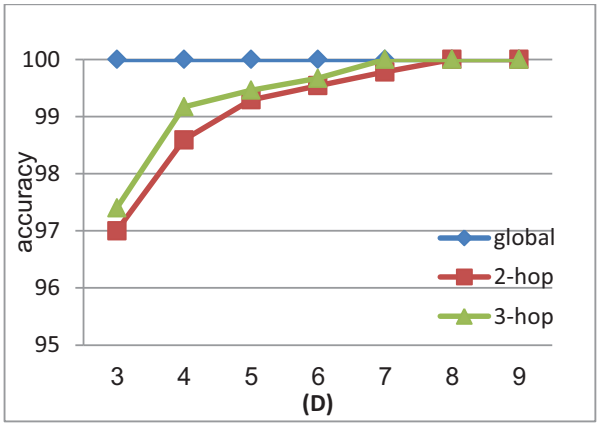

A

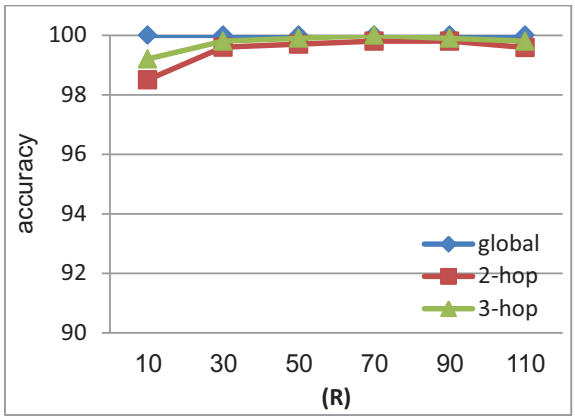

B

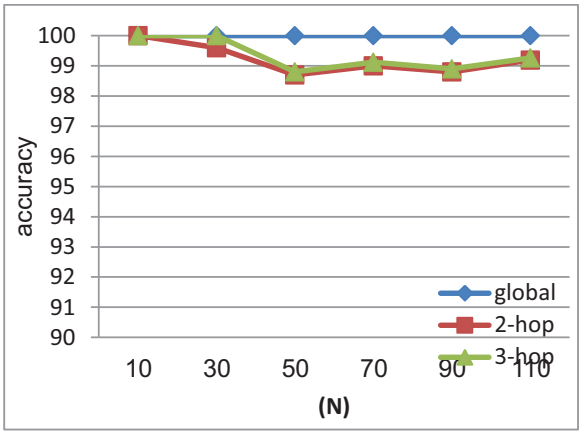

C

Figure 4: the accuracy of detection of critical pairs when changing in d (A), when changing in radio range (B) and when changing in number of nodes (C).

Figure 4 shows the accuracy of detection of critical pairs when n=50 and d vary between (3 to 9) in (A), when n=50 and R vary between (10 to 110) in (B) and when d=4 and N vary between (10 to 110) in (C). The performance of TCNDA in detection of critical pairs with local information is very competitive compared with the global information that can exactly detect all critical pairs. The accuracy of TCNDA in our experiment for 2-hop and 3-hop local information is generally over 96% and the main reason for this high accuracy comparing to the accuracy of the detection of one critical node presented in (M. Imran , 2013) is the confirming message which node sent to other node when it detect its critical with it, Because this allow the node to know if there is alternative path out of its local k-information. So the error of determining pair of nodes as local critical which are indeed not is decreased.

Table 4 shows the number of critical nodes and number of second critical nodes which are not critical alone but critical with other node two together, the number of nodes used in experiments is 30 and the radio range is 50. The table shows that when the number of critical nodes is increase the number of 2nd critical nodes is decrease. Some pairs detected by local information not detected by the global information and this is understandable because alternative paths may be exist but the local information of both nodes create the pair critical not

contain this alternative paths. Also Some pairs detected by global information not detected by the local information because the node may be local critical and not global critical so the node not calculated as second local critical but its already detected as local critical so this error is acceptable in most scenarios.

Table 4: the number of critical nodes and 2nd critical nodes when n=30 and R=50.

	Global critical	2-hop critical	3-hop critical	Global 2nd critical	2-hop 2nd critical	3-hop 2nd critical
1	12	20	17	8	0	4
2	17	17	17	0	0	0
3	14	17	14	3	2	3
4	12	21	12	9	0	9
5	13	22	19	9	0	3
6	15	19	15	4	0	4
7	13	18	13	9	4	9
8	16	16	16	2	2	2
9	18	18	18	0	0	0
10	16	16	16	3	3	3

5. CONCLUSION

In this paper, TCNDA algorithm is developed for detection of critical node in ad hoc networks. It is localized and distributed algorithm. This algorithm enable each node to determine if it's local critical or there are another node from its k-hop neighbours and both of them together are critical. TCNDA is evaluated and the effectiveness of it in determining the criticality of the node is validated through simulation experiments. Simulation results demonstrate that the performance of TCNDA with local k-hop information is quite competitive compared to centralized algorithm with global network information.

REFERENCES

I. Ahmad, U. Ashraf, and A. Ghafoor, 2016. “A comparative QoS survey of mobile ad hoc network routing protocols,” Journal of the Chinese Institute of Engineers, vol. 39, no. 5, pp. 585–592.

M. Rath, B. K. Pattanayak, and B. Pati, 2016. “Energy Efficient MANET Protocol Using Cross Layer Design for Military Applications,” Defence Science Journal Def. Sc. Jl., vol. 66, no. 2, p. 146.

S. Kaur, S. Kaur, and C. Sharma, 2013. “An Overview of Mobile Ad hoc Network: Application, Challenges and Comparison of Routing Protocols,” IOSR-JCE IOSR Journal of Computer Engineering, vol. 11, no. 5, pp. 7–11.

M. Jain and S. Chand, 2015. “Issues and Challenges in Node Connectivity in Mobile Ad Hoc Networks: A Holistic Review,” Wireless Engineering and Technology WET, vol. 07, no. 01, pp. 24–35.

M. Edalatmanesh, 2013." Heuristics for the Critical Node Detection Problem in Large Complex Networks",PhD thesis, Faculty of Mathematics and Science, Brock University, St. Catharines, Ontario.

M. Duque-Anton, F. Bruyaux, and P. Semal, 2000. “Measuring the Survivability of a Network: Connectivity and Rest-Connectivity,” Eur. Trans. Telecomm. European Transactions on Telecommunications, vol. 11, no. 2, pp. 149–159.

D. Goyal and J. J. Caffery, 2002. "Partitioning Avoidance in Mobile Ad Hoc Networks Using Network Survivability Concepts," in the Proceedings of the 7th International Symposium on Computers and Communications (ISCC'02), Giardini Naxos, Italy, pp. 553 – 558.

S. Xiong and J. Li, 2010. "An Efficient Algorithm for Cut Vertex Detection in Wireless Sensor Networks," in the proceedings of the 2010 IEEE 30th International Conference on Distributed Computing Systems (ICDCS) Genova, Italy, pp. 368-377.

X. Liu, L. Xiao, A. Kreling, and Y. Liu, 2006. "Optimizing overlay topology by reducing cut vertices," in in the Proceedings of the 2006 international workshop on Network and operating systems support for digital audio and video, Rhode Island, USA.

M. Sheng, J. Li, and Y. Shi, 2006 “Critical Node Detection in Mobile Ad Hoc Network”, the 20th International Conference on Advanced Information Networking and Applications (AINA’06).

M. Jorgic, I. Stojmenovic, M. Hauspie and D. Simplot-Ryl, 2004. “Localized Algorithms for Detection of Critical Nodes and Links for Connectivity in Ad hoc Networks”, in: "Proc. 3rd IFIP Mediterranean Ad Hoc Networking Workshop (MED-HOC-NET 2004), Bodrum, Turkey".

M. Imran, M. A. Alnuem, M. S. Fayed, and A. Alamri, 2013 .“Localized Algorithm for Segregation of Critical/Non-critical Nodes in Mobile Ad Hoc and Sensor Networks,” Procedia Computer Science, vol. 19, pp. 1167–1172, 2013.

Furuzan Atay, and Ivan Stojmenovic, 2007. "Generating Random Graphs for Wireless Actuator Networks." IEEE International Symposium on a World of Wireless, Mobile and Multimedia Networks.

Ibrahim S. Fayed, Mokhtar A. A. Mohamed, Gamal Attiya and Nawal A. El-Fishawy, 2016. " Two Efficient Approaches for Generating Topologies of Ad-hoc Networks", in proc. of 1st internationsl conference on Advanced Technology and Applied Sciences (ICaTAS), Kuala Lumpur, MALAYSIA.

Positioning Accuracy Improvement Using Low-Cost Inertial Sensors

Abdalla Eldesoky [a], Ahmed M.Kamel [b], M. Elhabiby [c], Hadia Elhennawy [a]

[a] Dept. of Comm. Ain Shams University, Cairo, Egypt (a_dosoky123@yahoo.com , Hadia.elhennawy@eng.edu.eg), [b] Dept. of R&D. Military Technical College, Cairo, Egypt a.kamel@mtc.edu.eg,[c] Dept. of Public Works, Ain Shams University, Cairo, Egypt elhabiby@meng-tech.com

KEY WORDS: MEMS, Inertial Sensors, Deterministic Errors, Random Errors, Calibration, Mechanization

ABSTRACT:

Low cost Micro Electrical Mechanical Systems (MEMS) inertial sensors are well known for their degraded performance if used in a self-contained navigation system due to large number of errors that affect the sensor's output. In this paper, an evaluation of navigation performance improvement technique through experimental work for such sensors is introduced. The metric used in this work to evaluate the performance, is the position error calculated using a MEMS based inertial navigation system (INS) integrated with slow 1 Hz updates of position and velocity from global positioning system (GPS) receiver. For such evaluation, it is required to calculate the deterministic errors for gyroscopes and accelerometers that comprise the IMU, and to estimate the random errors using Allan variance technique for different bandwidths. To achieve this goal, a precise deterministic calibration process and random noise model of a chosen MEMS IMU is applied. The calibrated data then is used with the GPS/INS integration system model, the test results show that the error in position is reduced when the calibration procedure is applied correctly to remove different types of errors. The estimated noise errors are compensated when used to feed the sensors fusion algorithm, Kalman Filter (KF) in this work, which led to improve the positioning accuracy.

1. INTRODUCTION

An Inertial Navigation Systems (INS) is used as a primary mean of navigation in mostly all of the guided, unmanned, and autonomous systems. For long-time, the inertial measuring units (IMUs) used in onboard navigation systems were heavy and expensive. Recently, (MEMS) with advantages of low-cost, small-size, light-weight and low power consumption are widely used to comprise inertial navigation systems [2, 8, 16]. The requirements of any used INS are to provide high accuracy information about the position, velocity and attitude over a certain period of time. The problem of using (MEMS) is that their accuracy degrades rapidly with time. To provide accurate estimation of navigation information, the errors from the MEMS IMU must be appropriately treated in order to turn the observations into useful data for object position determination. The errors of inertial sensors are classified into deterministic errors and random stochastic errors [12, 14, 15].The selected IMU sensor's assembly used in this work is MPU-6050 from InvenSense® [11]. This IMU combines a 3-axis gyroscopes triad (gyros), 3-axis accelerometers triad. Deterministic errors such as bias and scale factor are calculated using high accurate turntable for gyros and fixed position for accelerometer. On other hand, the random errors such as velocity/Angular random walk (V/ARW), bias instability, rate random walk, etc. are estimated using different modeling techniques. One of common method used to estimate the stochastic errors is *Allan Variance* (AV) which is used in this research [3, 4, 6, 9].Outputs of the MEMS IMU which are the rotation rates measured by 3-axis gyroscopes and the specific forces measured by 3-axis accelerometers are used in GPS/INS loosely coupled integration model to optimally estimate the attitude, the velocity and the position of the vehicle [1, 13].

The objective of this work is to evaluate and validate the performance improvement of the selected low-cost MEMS inertial sensor by applying calibration and noise estimation techniques, that helps in virtually upgrade the sensor performance to mimic higher grade ones in terms of navigation states estimation. In the next section, the calculation of the deterministic errors is discussed, section (3) presents the random errors, section (4) describes the GPS/INS integration system model, and section (5) reports the experimental work and results. Conclusions and future work are drawn in section (6).

2. CALCULATION OF THE DETERMINISTIC ERRORS

Calibration of the inertial sensors plays an important role in the ultimate accuracy of MEMS IMU. An accurate turntable is used to introduce reference rotation rates for the 3-axis gyroscope calibration. On other hand fixed static position tests are used to collect the six-position raw data of 3-axis accelerometer calibration. Among different types of deterministic errors this work focuses on scale factor and bias as presented in the following subsections.

2.1 Gyroscope calibration

The following model represents the single-axis gyroscope measurement of the angular rate [13].

$$\tilde{w}_{ib}^{b} = w_{ib}^{b} + b_g + S_g w_{ib}^{b} + N_g w_{ib}^{b} + \varepsilon_g , \qquad (1)$$

where $\tilde{w}_{ib}^{b}$ is the gyroscope measurement vector.

w_{ib}^{b} is the true angular rate velocity vector.

b_g is the gyroscope instrument bias vector.

S_g is the matrix of the gyroscope scale factor error.

N_g is the matrix representing non-orthogonality of the gyro triad.

ε_g is a vector representing the accelerometer sensor noise.

For the 3-axis gyroscope to be calibrated, a reference rotation rate of the turntable is changed in a wide range of reference rates through fixed span steps (in this case from 6 (deg/sec) to -6 (deg/sec) with step two degrees). At each step, the rotation speed is kept constant for a certain period of time that allows the sensor outputs to stabilize for every IMU axis and the gyroscope

raw data are collected. The collected data is plotted against the reference data and curve fitted to a first order equation in the form of $y = ax + b$ to get the slope of the line represents the (scale factor) and the shifted value represents the (bias) as shown in the figure (1), from the equation (1) the corrected measured angular rate $w^{b}_{corrected}$ for every gyroscope driven as follows:

$$w^{b}_{corrected} = \frac{(\tilde{w}^{b}_{ib} - b_g)}{(1 + sf_g)}, \quad (2)$$

where sf_g is the scalar scale factor of gyro

Figure 1. The slope and shift of the measured data

2.2 Accelerometer calibration

The actual measurement can be modeled by the following equation [13].

$$\tilde{f}^{b} = f^{b} + b_a + S_{a1} f + S_{a2} f^{2} + N_a f + \delta g + \varepsilon_a, \quad (3)$$

where $\tilde{f}^{b}$ is the accelerometer measurement vector.

f^{b} is the true specific force vector.

b_a is the accelerometer instrument bias vector.

S_{a1} is the matrix of the linear scale factor error.

S_{a2} is the matrix of the non-linear scale factor error.

N_a is the matrix representing non-orthogonal of the accelerometer triad

δg is the deviation from the theoretical gravity value.

ε_a is a vector representing the accelerometer sensor noise

For each accelerometer to be calibrated, the sensitive axis is directed to be in the level plane pointing to up direction in the fixed static position and its output raw data was collected for long period of time, the average of the collected data gives f_{up}, then the unit platform was rotated 180°, so the accelerometer sensitive axis was pointing down, and the output raw data was again collected for the same time and averaged to obtain f_d finally, the mean values of the collected data for up and down positions were calculated for 3axis-accelerometer (bias and scale factor) calculation, as shown in figure (2) and equations (4-8).

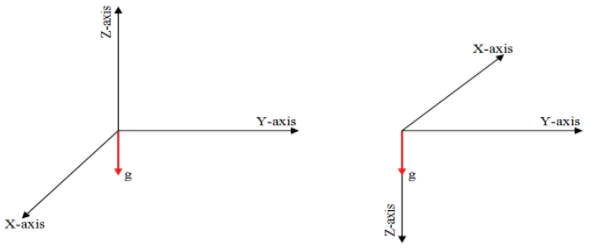

Figure 2. The sensitive axis upward on the left and downward on the right

$$\tilde{f}^{b}_{up} = b_a + (1 + sf_a) g, \quad (4)$$

where sf_a is the scalar scale factor of accelerometer.

$$\tilde{f}^{b}_{d} = b_a - (1 + sf_a) g. \quad (5)$$

By adding equations (4), (5), the bias is calculated

$$b_a = \frac{\tilde{f}^{b}_{up} + \tilde{f}^{b}_{d}}{2}, \quad (6)$$

and by subtracting equations (4), (5), the scale factor is obtained

$$sf_a = \frac{\tilde{f}^{b}_{up} - \tilde{f}^{b}_{d} - 2g}{2g}, \quad (7)$$

where g is the earth gravity.

From the equation (3) the corrected measured specific force $f^{b}_{corrected}$ for every accelerometer will be

$$f^{b}_{corrected} = \frac{(\tilde{f}^{b} - b_a)}{(1 + sf_a)}. \quad (8)$$

3. RANDOM ERRORS

The errors generated by noise sources which are statically independent, there are many approaches for modeling noise developed. The power spectral density (PSD) is a frequency-domain approach which gives a complete analysis of the error sources but the results are difficult to extract [10], for time-domain approach, the Allan variance technique is a straight forward method, it is simple and efficient procedure for verifying and modeling random errors by representing the root mean square random drift error as function of averaging time.

3.1 Allan variance

Assume N samples of data from an inertial sensor (accelerometer or gyroscope) with a sample time of τ_0 form a groups of data points with duration $\tau_0, 2\tau_0, \ldots\ldots, n\tau_0$, with $n \prec (N-1)/2$, each member of the group is called a cluster [7, 17]. Associated with each cluster is a time T, such as $T = n\tau_0$. If the instantaneous output of the sensor is Ω_s and its integration is the angle for example, so Allan variance $\sigma^2_{\Omega}(\tau)$ is described as follows:

$$\vartheta(t) = \int^{t} \Omega_s(t')dt', \quad (9)$$

$$\bar{\Omega}_k(\tau) = \frac{\vartheta(t_k + \tau) - \vartheta(t_k)}{\tau}, \quad (10)$$

$$\sigma^2_{\Omega} = \langle \frac{1}{2} (\bar{\Omega}_{k+1} - \bar{\Omega}_k)^2 \rangle, \quad (11)$$

where τ is an averaging time, and operator $\langle \ldots \rangle$ is defined as an infinite time averaging:

$$\langle f(t) \rangle = \lim_{T \to \infty} \frac{1}{T} \int_{-T/2}^{T/2} f(t) dt. \quad (12)$$

For finite number of samples N, the Allan variance σ_Ω^2 can be estimated as:

$$\sigma_\Omega^2(\tau) \cong \frac{1}{2(K-1)} \sum_{K=1}^{K-1} (\bar{w}_{k+1}(M) - \bar{w}_k(M))^2, \quad (13)$$

where M means number of samples in one cluster, $K = N/M$ is the number of clusters, and $\bar{w}_k(M)$ is average in cluster K. There is a unique relationship that exists between PSD and A is expressed as

$$\sigma_\Omega^2(\tau) = 4 \int_0^\infty S_\Omega(f) \frac{\sin^4(\pi f \tau)}{(\pi f \tau)^2} df. \quad (14)$$

The output of MEMS sensors is affected by several types of noise. Allan's definition and results are related to different noise terms such as A/VRW, bias instability, rate random walk, quantization noise, and rate ramp. If the noise sources are statically independent, then the computed AV is the sum of the squares of each error type

$$\sigma^2(\tau) = \sigma_{arw}^2(\tau) + \sigma_b^2(\tau) + \sigma_{rw}^2(\tau) + \ldots. \quad (15)$$

It is normally plotted as the square root of the AV, $\sigma(\tau)$ versus τ, on a log-log plot to provide a direct indication of the types of random processes. The relationships of various random noise sources and slope of root Allan variance plot as shown in figure (3).

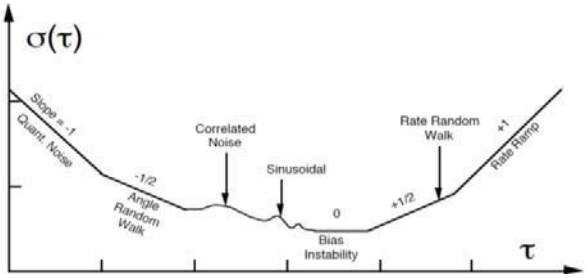

Figure 3. Sample plot of AV analysis results, (after [7])

3.2 Noise source analysis

The relationship of various noise sources and Allan variance is shown in Table (1)

Noise type	Parameter of interest	Root Allan variance	Slope of root Allan
Quantization	Q	$\sigma_Q(\tau) = \frac{\sqrt{3}Q_z}{\tau}$	-1
Angular random walk	N	$\sigma_{Arw}(\tau) = \frac{N}{\sqrt{\tau}}$	-1/2
Bias instability	B	$\sigma_b(\tau) = 0.664B$	0
Rate random walk	K	$\sigma_{rrw}(\tau) = K\sqrt{\tau/3}$	+1/2
Rate ramp	R	$\sigma_{rr}(\tau) = \frac{R\tau}{\sqrt{2}}$	+1

Table 1. The relationship of various noise sources and Allan variance [7]

4. GPS/INS INTEGRATION SYSTEM MODEL

4.1 Mechanization model in local level frame (LLF)

Mechanization is the process of calculating the position, velocity and attitude of the vehicle from the raw data of the IMU outputs which include rotation rates measured by the gyroscopes triad and specific forces measured by the accelerometer triad, all of which are with respect to the inertial frame as, shown in figure (4) [1-13].

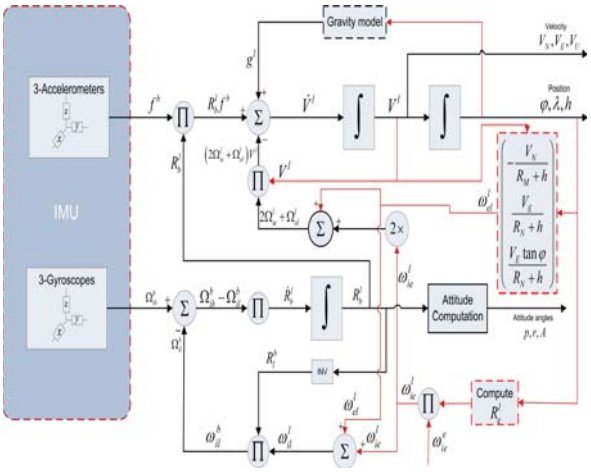

Figure 4. Mechanization diagram of an INS in the local level frame (after [5])

In this figure, the accelerometers measure the acceleration in the body frame and have to be transformed into a universal navigation frame to get useful information. This is done by constructing a transformation matrix using the attitude angles obtained from integrating the gyro rates. The projected accelerations are then purified from the external effects of gravity and Coriolis motion to get pure implication of the body motion. The accelerations are then integrated to obtain velocity and position as described in [1, 13].

4.2 Loosely coupled GPS/INS integration

IN this integration, the GPS and INS operate independently and provide separate navigation solutions. To improve the solution the position and/or velocity from GPS is fed to optimal estimator, usually a kalman filter. The INS solution is also supplied to the filter which takes the difference between the two, and based upon the error models, estimates the INS errors, as shown in figure (5).

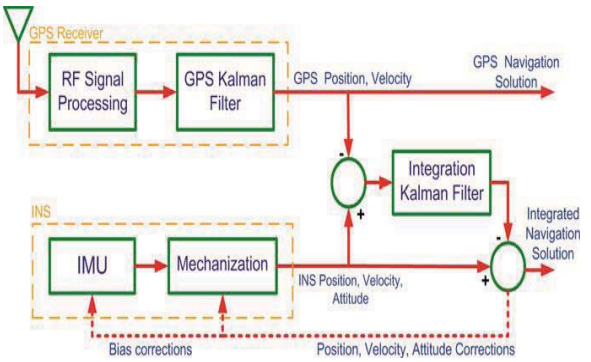

Figure 5. A block diagram of a loosely coupled INS/GPS integration(after [13])

The propagation model of discrete form of Extended Kalman Filter (EKF) is given by [13]

$$\delta X_k = (I + F\Delta t)\delta X_{k-1} + G\Delta t w_{k-1}. \quad (16)$$

The state vector includes error components of position, velocity, attitude, gyroscope drifts and accelerometer biases as

$$\delta X^{l}_{15\times1} = \left[\delta r^{l}_{3\times1} \quad \delta V^{l}_{3\times1} \quad \delta\varepsilon^{l}_{3\times1} \quad \delta\omega^{l}_{3\times1} \quad \delta f^{l}_{3\times1}\right]^T, \quad (17)$$

where F is the (15x15) dynamic matrix contains the INS error models for the states, G is noise distribution matrix and W is unit-variance white Gaussian noise matrix.

5. EXPERIMENTAL WORK AND RESULTS

5.1 Gyroscope deterministic errors

By applying the procedure in section II (A) on IMU MPU6050, the results of the bias and the scale factor for the 3-axis gyroscope as shown in Table (2) and figure (6) in which there is some discontinuity in the steps because the turn table must stop after each rate and enter the new rate value.

5.2 Accelerometer deterministic errors

By applying the procedure in section II(B) on the selected IMU MPU6050, the obtained results of the calculated bias and the scale factor for the 3-axis accelerometer as shown in Table (3) and figure (7) in which smoothing filter is applied on the measured and corrected data for demonstration purposes.

Noise type	G.X	G.Y	G.Z
Bias(deg./sec)	-2.7347	0.66529	-1.0604
Scale factor	0.0099	0.0022	-.00851

Table 2. Bias and scale factor of 3-axis gyroscope

Noise type	A.X	A.Y	A.Z
Bias(mg)	2.6	12.5	-49.4
Scale factor	-0.0055	0.0048	0.0094

Table 3. Bias and scale factor of 3-axis accelerometer

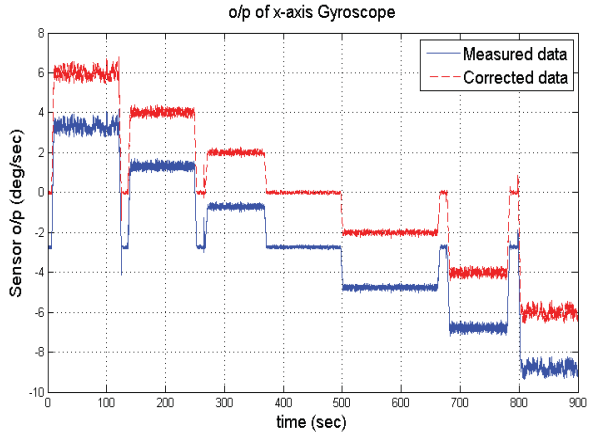

Figure 6. A comparison data before and after calibration for x-axis gyroscope

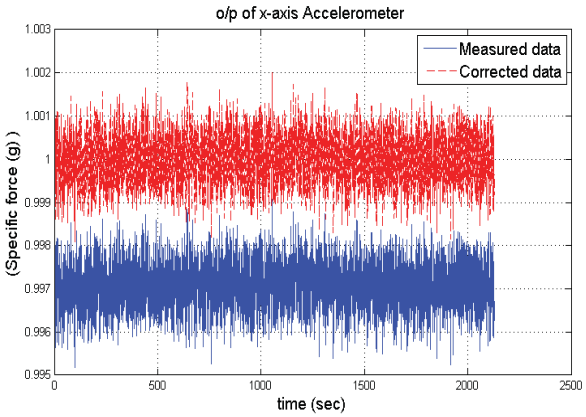

Figure 7. A comparison data before and after calibration for x-axis accelerometer

5.3 Allan Variance Results

A five hours static data is collected from IMU MPU6050 under the same environmental conditions for different bandwidths considering the Nyquist theorem. The Allan variance curves of 3-axis gyroscope as shown in figure (8) and figure (9), with sampling rate 100Hz, and for bandwidths 21(Hz) and 44 (Hz) respectively. The Allan variance curves of 3-axis accelerometer as shown in figure (10) and figure (11), with sampling rate 100Hz, and for bandwidths 21(Hz) and 44 (Hz) respectively. Noise errors are shown in Tables (4) and (5), relative to the table (1)

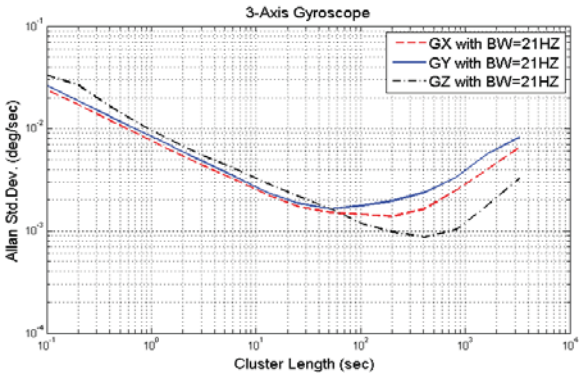

Figure 8. AV curve with 100Hz sample rate and BW=21Hz for 3-axis gyroscope

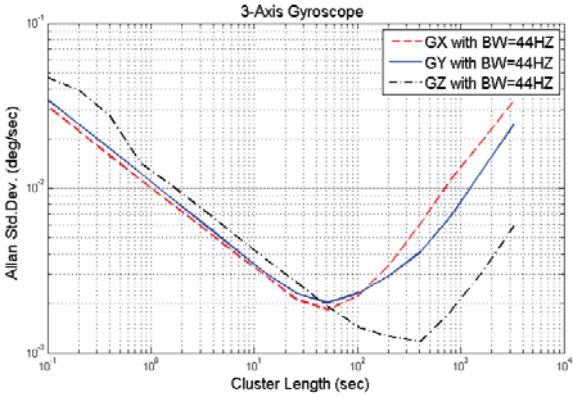

Figure 9. AV curve with 100Hz sample rate and BW=44Hz for 3-axis gyroscope

Noise type	BW	G.X	G.Y	G.Z
Angular random walk($\deg/\sqrt{h}$)	21Hz	0.45	0.504	0.57
Rate random walk $\deg/h^{3/2}$		33.69	44.28	14.67
Angular random walk($\deg/\sqrt{h}$)	44Hz	0.6	0.72	0.84
Rate random walk $\deg/h^{3/2}$		92.88	75.6	9.29

Table 4. Noise errors of 3-axis gyroscope

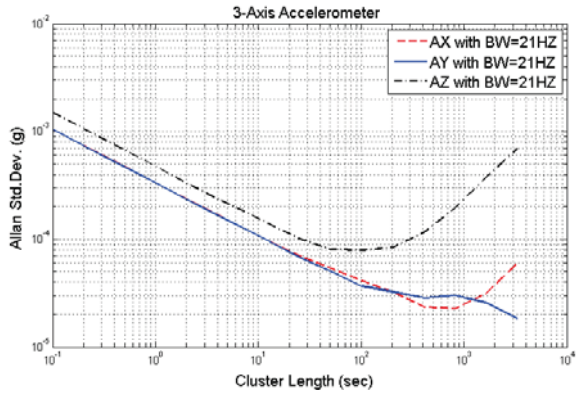

Figure 10. AV curve with 100Hz sample rate and BW=21Hz for 3-accelerometer

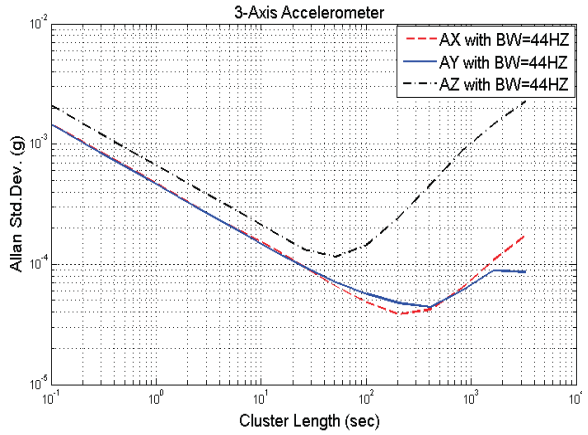

Figure 11. AV curve with 100Hz sample rate and BW=44Hz for 3-axis accelerometer

Noise type	BW	A.X	A.Y	A.Z
Velocity random walk(mg)	21Hz	0.34	0.36	0.48
Rate random walk $mg/\sqrt{\sec}$		0.0014	—	0.01
Velocity random walk(mg)	44Hz	0.48	0.47	0.63
Rate random walk $mg/\sqrt{\sec}$		0.0039	0.004	0.0083

Table 5. Noise Errors of 3-Axis Accelerometer

5.4 Vehicle navigation test

5.4.1 Test environment: By applying the procedure in section (4), a car-navigation test was carried out in fifth settlement near the ring road. By using IMU MPU6050 and GPS SKM53 module from Skylab fixed on the car as shown figure (12) During the data acquisition, raw data from IMU and GPS measurement were recorded at 17.5Hz and 1Hz, respectively and there were about 7~10 visible satellites with car velocity 40 km in average. Figure (13) shows the reference trajectory of the experiment relative to GPS data that is a bolded red line and the navigation trajectory is relative to the arrows. The total navigation time is 513 sec. Initial alignment is held at the beginning in static mode form 240 sec., after that, the car had traveled for 273 sec.

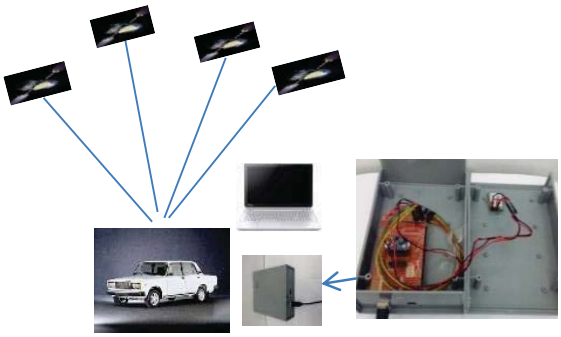

Figure 12. Car-navigation systems structure

Figure 13. Reference trajectory

5.4.2 Navigation results during GPS 1sec. update rate The performance of GPS/INS integration system is improved after deterministic calibration, it is found that the quantitative position errors such as, the mean, standard deviation, maximum error and Horizontal Error (HE), is decreased after correction as shown in table (6) and figure (13). The HE is reduced by 9.68%.In figure (14) the 3D velocity in East, North and Up directions are depicted. It is clear that there is reduction in errors after using calibrated data. Figure (15) shows the attitude errors before and after calibration. In this figure the roll, pith and azimuth are quickly changing in phase for the raw data due to un-calibrated gyro drift. This phenomena is clearly reduced after calibration and the attitude angles have minor variations. Figure (16) and figure (17) show the navigation result in East/North and the Total velocity relative to GPS reference velocity before and after calibration.

		Position errors (m) for 1sec. GPS update rate			
		Mean	Std.	Max. Error	Horizontal Error
Raw data	East	3.987	4.45	25.56	***43.235***
	North	10.71	8.36	34.87	
Calibrated data	East	3.565	4.01	22.22	***39.05***
	North	10.37	8.01	32.11	

Table 6. Position errors during navigation in case of 1sec. GPS update rate

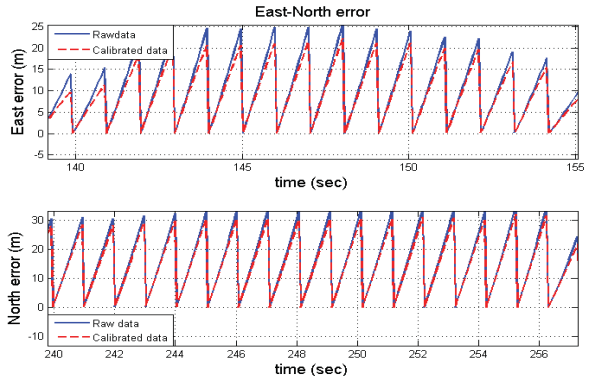

Figure 13. Position errors in East/North for GPS/INS integrated system before and after calibration for 1sec. GPS update rate .

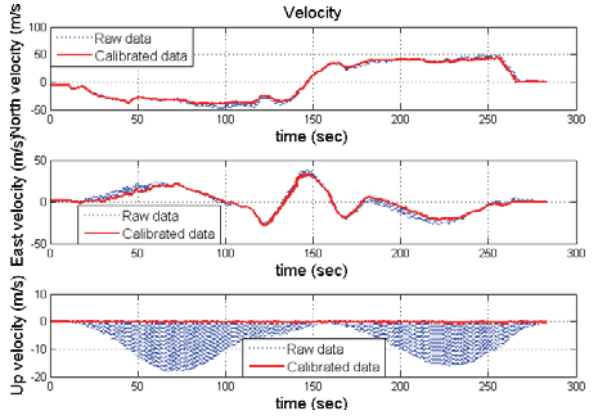

Figure 14. Velocity errors in East, North and Up for GPS/INS integrated system before and after calibration for 1sec. GPS update rate

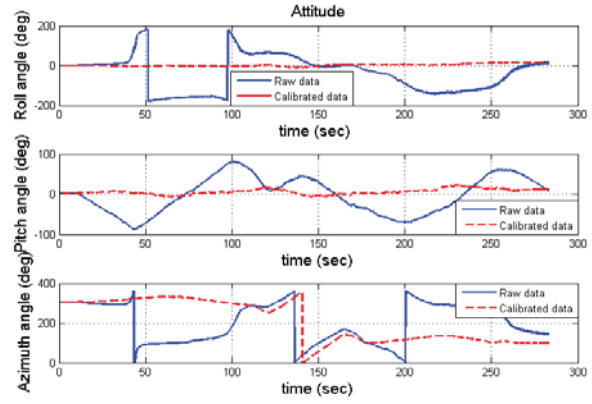

Figure 15. Attitude errors in Roll, Pitch and Azimuth for GPS/INS integrated system before and after calibration for 1sec. GPS update rate

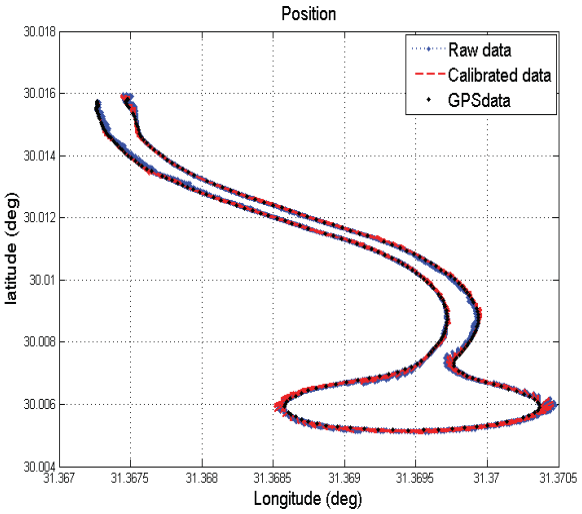

Figure 16. Navigation result in East/North for GPS/INS integrated system before and after calibration for 1sec. GPS update rate

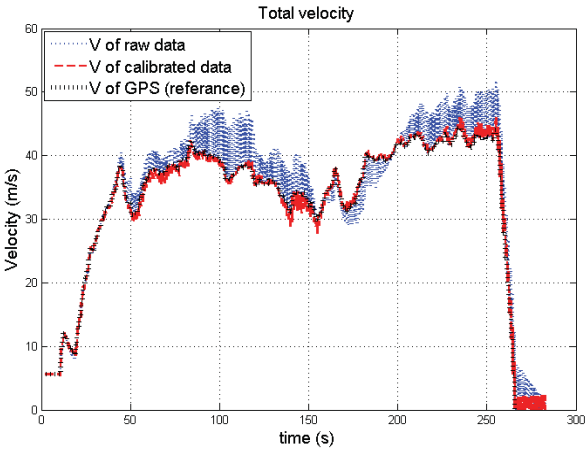

Figure 17. Total velocity for GPS/INS integrated system before, after calibration and GPS reference velocity for 1sec. GPS update rate

5.4.3 Navigation results during 10 sec GPS outage In this section the performance of GPS/INS integration system is improved after deterministic calibration as discussed in (5.4.1) but the HE is reduced by 69.499% as shown in table (7) and figures (18-22).

		Position errors (m) for 10sec GPS outage			
		Mean	Std.	Max. Error	Horizontal Error
Raw data	East	11.27	46.3	478.4	***537.67***
	North	15.06	26.6	245.4	
Calibrated data	East	5.1	2.07	80.82	***163.997***
	North	13.5	19.0	142.7	

Table 7. Position errors during navigation in case of 10sec. GPS outage

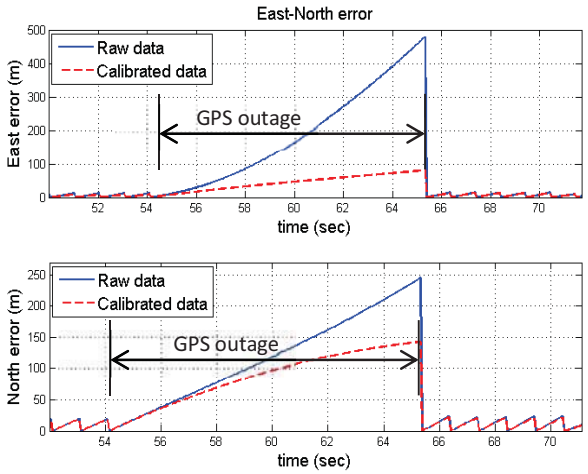

Figure 18. Position errors in East/North for GPS/INS integrated system before and after calibration for 10sec. GPS outage

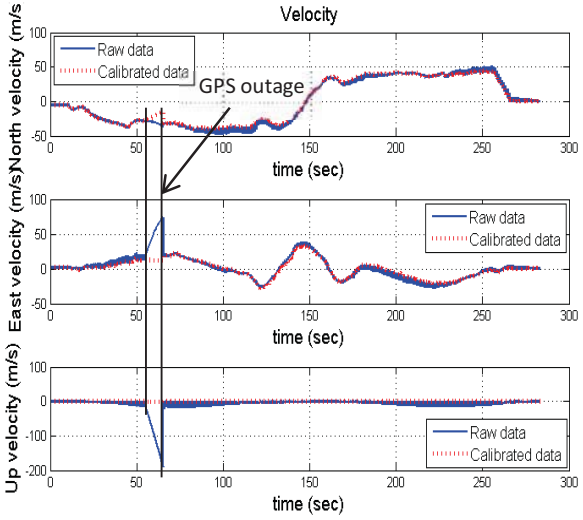

Figure 19. Velocity errors in East, North and Up for GPS/INS integrated system before and after calibration for 10sec. GPS outage

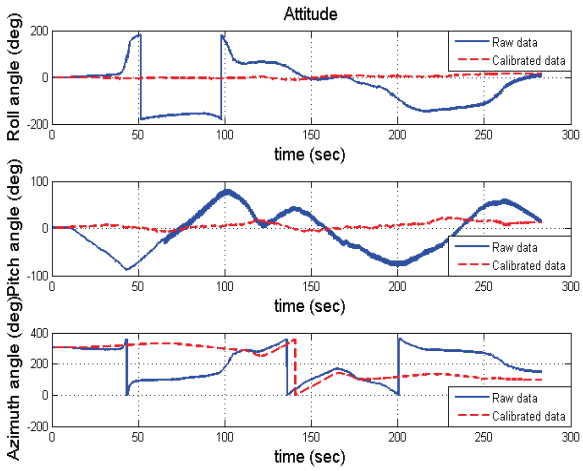

Figure 20. Attitude errors in Roll, Pitch and Azimuth for GPS/INS integrated system before and after calibration for 10sec. GPS outage

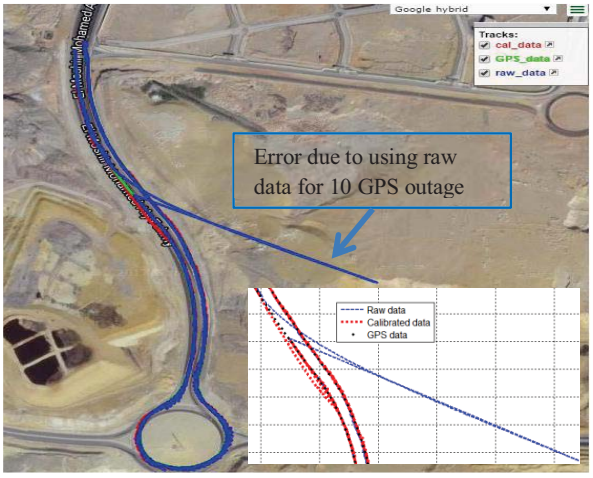

Figure 21. Navigation result in Lat/Lon for GPS/INS integrated system before and after calibration for 10sec. GPS outage

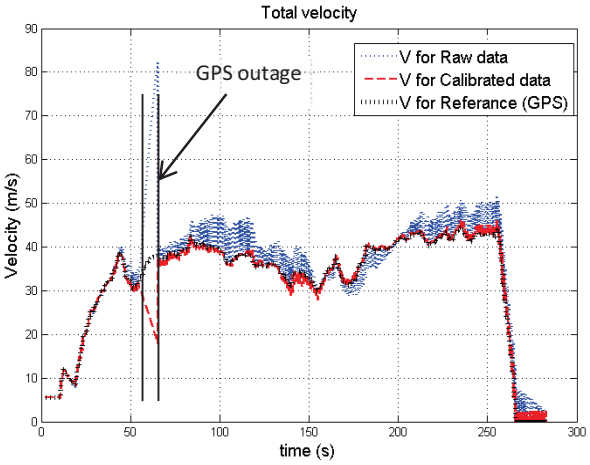

Figure 22. Total velocity for GPS/INS integrated system before, after calibration and GPS reference velocity for 10sec. GPS outage

5.5 Random Noise Modeling

The estimated noise errors such as angular random walk and rate random walk obtained from AV characteristic curves model in (5.3) can be compensated by using the propagation model of discrete (EKF) that discussed in (4.2) and equations (16) and (17) with G and W matrices as follow [9]:

$$G_{15x12} = \begin{bmatrix} 0_{3x3} & 0_{3x3} & 0_{3x3} & 0_{3x3} \\ 0_{3x3} & R_b^l & 0_{3x3} & 0_{3x3} \\ -R_b^l & 0_{3x3} & 0_{3x3} & 0_{3x3} \\ 0_{3x3} & 0_{3x3} & I_{3x3} & 0_{3x3} \\ 0_{3x3} & 0_{3x3} & 0_{3x3} & I_{3x3} \end{bmatrix}. \qquad (18)$$

$$W_{12x1} = \begin{bmatrix} W_{Hg} & W_{Ha} & W_{Rg} & W_{Ra} \end{bmatrix}^T, \qquad (19)$$

where W_{Hg} and W_{Ha} are gyro, accelerometer random walk noise. W_{Rg} and W_{Ra} are gyro, accelerometer rate random walk noise.

The obtained results from AV procedure are substituted in equation (19) and the GPS/INS integration drill is recalculated to obtain a better performance of the system.

V. CONCULSIONS AND FUTURE WORK

This work provides some methods for calculation of deterministic and stochastic estimation error parameters separately. Deterministic errors such as scale factor and bias are calculated, GPS/INS integration system model is implemented and test results shows that the horizontal error improved after the correction of deterministic calibration with position error reduction 9.68% during 1 sec. GPS update rate, and 69.499% during 10 sec. GPS outage. AV characteristic curves of inertial sensor are obtained from which the different types and value of error parameters are presented for different bandwidths, as long as signal sample rate approximately reach three to five times of the sensor bandwidth. AV error parameters will be substituted to GPS/INS integration system to obtain a better performance of the system.

REFERENCES

[1] Aggarwal P.,*MEMS-based Integrated Navigation GNSS technology and applications*,Artech House, 2010.

[2] El-Sheimy N., ENGO 623 Lecture notes: *Inertial Techniques and INS/DGPS Integration*,Calgary University, 2007.

[3] EI-Sheimy N., Hou H., Niu X.,*"Analysis and Modeling of Inertial Sensors Using Allan Variance"* , IEEE Transaction on instrumentation and measurement, vol. 57, No.1, 2008.

[4] EIdesoky A., Kamel A., Elhabiby M., *Elhennawy H. "Performance Enhancement of Low-Cost MEMS Inertial Sensors Using Extensive Calibration Technique"*, 34th National Radio Science Conference, 2017.

[5] Hassabla A., Kamel A.,*"Estimation Techniques for Low-Cost Inertial Navigation Systems"*, Msc., Military Technical College, 2015.

[6] Hou H., *"Modeling Inertial Sensors Errors Using Allan Variance"* ,Msc., Calgary University, 2004.

[7] IEEE Std 952™-1997, *IEEE Standard specification format guide and test procedure for single-axis interferometric fiber optic gyros*, 2008.

[8] KVH Industries Inc,*Guide to Comparing Gyro and IMU Technologies MEMS and FOGs*, 2014.

[9] Kim H., Lee J. G., Park C. G., *"Performance improvement of GPS/INS integrated system using Allan Variance analysis",* The 2004 International Symposium on GNSS/GPS, 2004.

[10] Marinov M., Petrov Z.,*"Allan Variance Analysis on Error Charactrs of Low-Cost MEMS Accelerometer MMA8451Q"*,International Conference of Scientific Paper, 2014.

[11] *MPU-6050 Product Specification*.https://www.invensense.com/products/motion-tracking/6-axis/mpu-6050/

[12] NARANJO C. C. M.,*"Analysis and Modeling of MEMS Based Inertial Sensors"*,Master ,School of Electrical Engineering, Kungliga Tekniska Hgskolan: Stockholm, 2008.

[13] Noureldin A., Karamat T. B., Georgy J. , *Fundamentals of Inertial Navigation, Satellite-based Positioning and their Integration*, Springer , 2012.

[14] Robin L., Perlumutter M., *"IMU & High Performance Inertial MEMS"*,Yole Development,France, 2011.

[15] Shin E. H., *"Estimation Techniques for Low Cost Inertial Navigation",* PHD,in Geomatics Engineering, Calgary, 2005.

[16] Sofian M., Hazry D., Zul A., *"Study of Inertial Measurement Unit Sensor", Proceeding of the International Conference on Man-Machine Systems* (ICoMMS), 2009.

[17] Yuksel Y., Notes on *"Stochastic Errors of MEMS Inertial Units"*, Calgary University, 2012.

FILTER ARCHITECTURES FOR INDOOR LOCALIZATION USING GAUSSIAN PROCESS ON SMARTPHONES

M. Sakr [a, *], N. El-Sheimy [a]

[a] Dept. of Geomatics Engineering, University of Calgary, Calgary, AB, Canada - (mostafa.sakr2, elsheimy)@ucalgary.ca

Commission I, WG I/6

KEY WORDS: Gaussian Process, Indoor Positioning, Filtering, Wi-Fi Fingerprinting, Received Signal Strength Indicator (RSSI)

ABSTRACT:

The realization of the full potential of location based services (LBS) and the real-time location systems (RTLS) is hinged on the availability of accurate and efficient localization algorithms – which exploit the multitude of sensors integrated into handheld and mobile devices, along with the different environmental features of the users' surroundings. The widespread presence of Wi-Fi access points (AP) is a prominent example of such environmental features. These devices are ubiquitous in today's indoor environments; such as residential and professional buildings, airports, hospitals, shopping malls, schools, universities, etc. The abundance of Wi-Fi technology makes it a practical candidate for aiding for indoor localization algorithms. One technique for localization using Wi-Fi signals is fingerprinting of the Wi-Fi received signal strength indicator (RSSI), modeled by Gaussian Process (GP) models. This paper proposes and evaluates different filter architectures to utilize the Wi-Fi RSSI information, along with data from consumer grade inertial measurement unit (IMU) used in smartphones. The proposed localization filters are composed of two parts: the motion model and the measurement update parts. The first part of the paper will compare two kinematic models to capture the motion of the mobile user. The second part will compare different update algorithms to utilize the measured Wi-Fi RSSI values. The performance of the different filters will be compared in terms of the localization errors, run-time, and convergence characteristics of each of the filters.

1. INTRODUCTION

The market for location based services (LBS) and the real-time location systems (RTLS) is expected to grow to US$ 77.84 billion, by 2021 (Markets and Markets, 2017). The application spectrum of these technologies is very broad; including advertising, navigation, tourism, local search, and location based health information and others. There are a lot of factors driving this growth; the proliferation of connected gadgets and appliances in every aspect of life, such as smartphones, wearable devices, in addition to the growth of the internet-of-things (IoT). Consequently, indoor localization continues to be a very active research area, especially in the recent few years, with more emphasis on increasing accuracy, availability, and reliability of the indoor localization solutions, while at the same time addressing the practical aspects of the solutions; such as simplifying the system deployment effort, and decreasing the cost and time required for system training, and map building. To cope with the remarkable advances in this field, many excellent review and survey papers were published to cover the latest developments regarding the different aspects of the indoor navigation and positioning problem (Correa et al., 2014; Fischer and Gellersen, 2010; Harle, 2013; He and Chan, 2016; Hossain and Soh, 2015; Liu et al., 2007; Shang et al., 2015; Yang et al., 2015).

Indoor positioning and localization depended originally on dead-reckoning techniques, using low-cost inertial measurement units (IMUs). However, the positioning solution can drift with time, when using IMUs only. Several aiding techniques, such as fingerprinting or map matching, can be used in conjunction with the inertial solution to limit this drift and enhance the accuracy of the positioning solution. Wi-Fi RSSI signal is one of the most commonly used signals for indoor positioning because of the ubiquity of wireless networks. Wi-Fi RSSI fingerprinting can be divided into two phase: the offline pre-surveying phase, and the online positioning phase (Li, 2016; Zhuang, 2015). The Wi-Fi fingerprint database or map is built in the offline stage. Then, during the online stage, the user captures Wi-Fi RSSI values from different access points, and uses the pre-built map to determine its location. Gaussian Process (GP) can be used to model the Wi-Fi RSSI values over a continuous range (Ferris et al., 2006), using training data – i.e. a trace of Wi-Fi signal strength annotated by the location. More precisely, the GP provides an estimate of the likelihood of the RSSI values conditioned on a new position and the original training data. However, evaluating the likelihood function using GP is computationally demanding, as it involves calculating the inverse of a $N \times N$ matrix, which has complexity in order of $\mathcal{O}(N^3)$, where N is the number of training points (Rasmussen and Williams, 2006).

The main objective of this paper is to investigate different filter architectures for indoor localization using Wi-Fi received signal strength indicator (RSSI), represented using Gaussian Process models, and to evaluate their relative accuracy and run-time. The computational complexity of evaluating the GP can limit its applicability for smartphone positioning application. In order to assess the complexity of using the GP for indoor localization, different filter architectures are implemented and their positioning performance and computational complexity are evaluated. Any navigation filter architecture can be divided into two main components: the kinematic model (for state update), and the measurement update stage. Two different kinematic models are discussed, with 2-D and 3-D state vectors. The measurement update stage is realized using the Extended Kalman Filter (EKF), or the Unscented Kalman Filter (UKF). Additionally, in order to reduce the computational burden of the

* Corresponding author

evaluating GP, the effect of using reduced versions of the GP training data set will be investigated.

Three evaluation criteria are used to compare the different architectures. First, the positioning accuracy of the proposed filters will be evaluated against a reference trajectory. This will be done by comparing the position estimate with the ground-truth reference trajectory. The computation complexity of the different filter architectures will be evaluated, using the simulation run-time, and compared to a reference filter. Finally, the convergence behavior of the different architectures will be discussed.

The next section introduces the Gaussian Process model and discusses the model training and hyperparameters calculation. This section also introduces two different kinematic models that could be used to update the state of the system in absence of external measurements updates. Section 3 introduces the different filter architectures used in this paper. The simulation environment and the results are presented in Section 4. Finally, the conclusions of this paper are presented in Section 5.

2. BACKGROUND

2.1 Gaussian Process Regression

The Gaussian Process (GP) model is a non-parametric model (Rasmussen and Williams, 2006), in which the predicted output of the model – also called the target value – is a function of the training dataset. This contrasts with parametric models, in which the output is a function of the model parameters; for example: a Gaussian model is parametrized by the mean and variance of the distribution. In the case of GP used to model spatial data, the training dataset is composed of tuples, each contains the observed target value and its corresponding position.
More specifically, the GP determines the likelihood of the signal strength conditioned by a new position and training data:

$$p(\, y_*|x_*,\, \mathbf{X}, \mathbf{Y}) \tag{1}$$

where y_* is the estimated target value, i.e. Wi-Fi RSSI value, at position x_*,
$\mathbf{X}, \mathbf{Y}$ are the training dataset.

The training data could be represented as a set of tuples, D, using the elements of the $\mathbf{X}, \mathbf{Y}$ vectors:

$$D = \{(x_1, y_1), (x_2, y_2), \dots, (x_n, y_n)\} \tag{2}$$

where x_i is the horizontal position of the training data, i.e. $x_i \in \mathbb{R}^2$,
y_i is the RSSI value, measured at point x_i.

The following lines show how to evaluate the likelihood function in Equation 1 using GP. The RSSI value can be modeled as the noisy output of a latent function $f(x_i)$, such that:

$$y_i = f(x_i) + \varepsilon \tag{3}$$

where $y_i \in \mathbb{R}$ is the RSSI value,
$x_i \in \mathbb{R}^q$, $\mathbf{X} \in \mathbb{R}^{n \times q}$ and $\mathbf{Y} \in \mathbb{R}^n$.

The Gaussian Process defines a distribution over the function $f(x_i)$ in Equation 3, such that:

$$f(x_i) \sim \mathcal{N}\big(\mathrm{m}(x_i), \mathrm{k}(x_i, x_i')\big) \tag{4}$$

where $\mathrm{m}(x_i)$ is the process mean function.

Typically, the mean function is taken to be zero. However, using zero mean function will drive the mean of estimated RSSI likelihood function to zero in regions with no training data available, as shown in the left panel of Figure 1, where the black circles indicates the locations and the values of the training data used to build the RSSI map for a single AP. Although, the variance of the estimated RSSI value in these regions will be large to account for the lack of training data, this behaviour is not what expected from the RSSI signal. It is expected that the RSSI signal decreases as the user moves away from the AP location. One solution to overcome this limitation is to use a non-zero mean function that decreases with increasing the distance between user and the AP location (Atia et al., 2013). However, the locations of the APs are not known in the context of this paper. As an simple alternative, the mean function is considered a constant and it is set to a very low value, resulting in more realistic estimation for regions with no training data, as shown in the right panel in Figure 1.

The covariance between different function values $f(x_p)$ and $f(x_q)$ is described by a kernel function $k(x_p, x_q)$, such as the commonly used kernel Radial Basis Function (RBF), defined as:

$$k(x_p, x_q) = \sigma_f^2 \exp\left(-\frac{1}{2l^2}\left|x_p - x_q\right|^2\right) \tag{5}$$

$$\mathrm{cov}(y_p, y_q) = k(x_p, x_q) + \sigma_n^2 \delta_{pq} \tag{6}$$

where δ_{pq} is a Kronecker delta,
σ_f, l, σ_n are the GP hyperparameters.

Equation 6 can be extended to all N training points:

$$\mathrm{cov}(\mathbf{Y}) = K + \sigma_n^2 I \tag{7}$$

K is $N \times N$, and $K[p, q] = k(x_p, x_q)$, Equation 1 can be rewritten in terms of the mean and variance functions:

$$p(f(x_*)|x_*, \mathbf{X}, \mathbf{Y}) = \mathcal{N}\big(f(x_*); \mu_{x_*}, \sigma_{x_*}^2\big) \tag{8}$$

$$\mu_{x_*} = \mathrm{k}_*^T (K + \sigma_n^2 I)^{-1} \mathbf{Y} \tag{9}$$

$$\sigma_{x_*}^2 = k(x_*, x_*) - \mathrm{k}_*^T (K + \sigma_n^2 I)^{-1} \mathrm{k}_* \tag{10}$$

and k_* is the covariance between x_* and the N training point $\mathbf{X}$. The kernel function is described by a set of hyperparameters, θ, defined by:

$$\theta = \langle \sigma_n, \mathrm{l}, \sigma_f \rangle \tag{11}$$

The term hyperparameters is used to reassert that these are parameters to a non-parametric model (Rasmussen and Williams, 2006). If the training data is available, the value of the hyperparameters can be determined by minimizing the negative-log likelihood function of the training data, given by:

$$\mathcal{L} = -\log p(\mathbf{Y}|\mathbf{X}, \theta) \tag{12}$$

$$\mathcal{L} = \frac{1}{2} y^T (K + \sigma_n^2 I)^{-1} y + \frac{1}{2} \log|K + \sigma_n^2 I| + \frac{n}{2} \log 2\pi \tag{13}$$

This is a non-linear optimization problem, which could be solved using the conjugate gradient descent algorithm (Nocedal and Wright, 2006). In order to do that, the gradient of the cost function, $\mathcal{L}$, w.r.t the hyperparameters, θ, is calculated:

$$\partial\mathcal{L}/\partial\theta_j = \frac{1}{2} \mathrm{trace}\left((K^{-1} - (K^{-1}y)(K^{-1}y)^T)\, \partial K/\partial\theta_j \right) \tag{14}$$

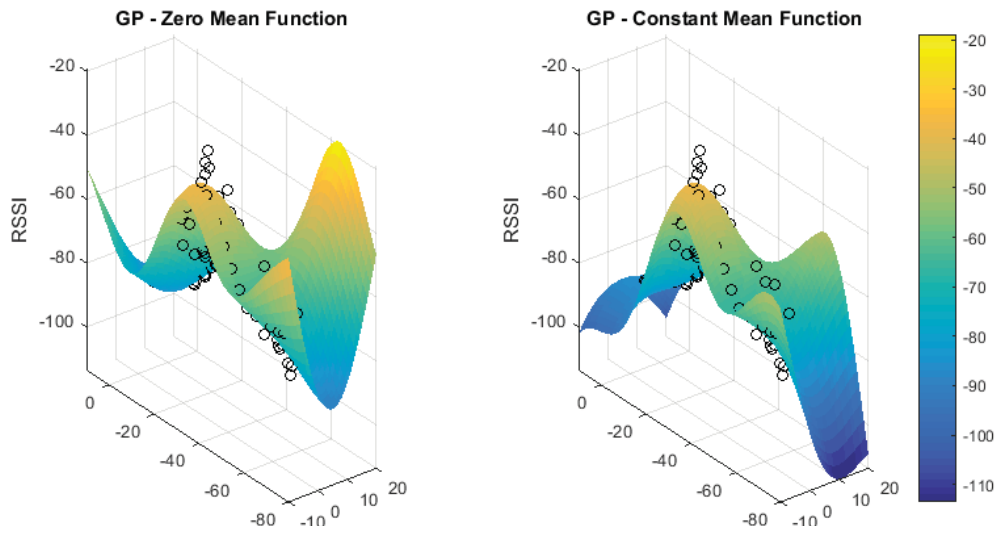

Figure 1. Effect of the GP Mean Function on the Estimated RSSI Value
(left: zero mean function; right: constant mean function)

The derivative w.r.t each of the hyperparameters is given by:

$$\partial K_{[p,q]}/\partial \sigma_f = 2\sigma_f \exp\left(-\frac{1}{2}\left(\left\|x_p - x_q\right\|_2/l\right)^2\right) \quad (15)$$

$$\partial K_{[p,q]}/\partial l = \sigma_f^2 \exp\left(-\frac{1}{2}\left(\left\|x_p - x_q\right\|_2/l\right)^2\right) \times \left(\left\|x_p - x_q\right\|_2^2/l^3\right) \quad (16)$$

$$\partial K_{[p,q]}/\partial \sigma_n = 2\sigma_n \delta_{pq} \quad (17)$$

The result of the optimization process of the GP hyperparameters is used, along with the training data, to model the environmental features across the space. The strength of the GP model is that it provides a value estimate – i.e. mean function – along with an estimate of its accuracy – i.e. the variance function. It is worth noting that although the likelihood calculated by Equation 8 follows a Gaussian distribution, the mean and variance are functions of the training data; they are not simply constants as in regular Gaussian models.

GP models have been used extensively in indoor localization (Aravecchia and Messelodi, 2014; Dashti et al., 2015; Ferris et al., 2006). Additionally, it can be used with simultaneous localization and mapping algorithms to model the Wi-Fi RSSI values (Ferris et al., 2007). Moreover, GP could be used to model other environmental features, such as the magnetic field intensity values (Kemppainen et al., 2015; Vallivaara et al., 2010).

2.2 Kinematic Modeling

This section reviews two different kinematic models that could be used to model the motion of the mobile nodes, which will be used in the time-update section of the localization filters. Two different approaches are presented: the traditional mechanization equations approach and the pedestrian dead-reckoning approach.

2.2.1 Mechanization Equations: These equations are used traditionally for the kinematic modeling of inertial navigation systems (INS) (Naser El-Sheimy, 2016; Noureldin et al., 2013; Titterton and Weston, 2004). In this formulation, the position, velocity, and orientation of the mobile node are represented by the following set of equations:

$$\dot{r}^l = \begin{bmatrix}\dot{\phi}\\ \dot{\lambda}\\ \dot{h}\end{bmatrix} = \begin{bmatrix}0 & \frac{1}{R_M+h} & 0\\ \frac{1}{(R_N+h)\cos\phi} & 0 & 0\\ 0 & 0 & 1\end{bmatrix}\begin{bmatrix}v_e\\ v_n\\ v_u\end{bmatrix} = D^{-1}V^l \quad (18)$$

$$\dot{V}^l = R_b^l f^b - \left(2\Omega_{ie}^l + \Omega_{el}^l\right)V^l + g^l \quad (19)$$

$$\dot{R}_b^l = R_b^l\left(\Omega_{ib}^b - \Omega_{il}^b\right) \quad (20)$$

where ϕ, λ, h are the node coordinates in the earth-centered earth frame,
v_e, v_n, v_u are the velocities in the local-level frame,
R_b^l is the orientation of the node body-frame w.r.t the local-level frame,
R_M, R_N are the two principal radii of curvature of the earth,
g^l is the normal gravity vector,
f^b is the specific force measured in the body frame,
Ω_{ib}^b is the skew-symmetric angular rate measured in the body frame,
Ω_{ie}^l is the earth rotation rate relative to the inertial frame in the local-level frame,
Ω_{el}^l is the local level frame rotation rate relative to the earth frame in the local-level frame.

The error state in the three-dimensional state vector case can be represented by perturbing the system propagation matrix defined by equations (18– 20), and it is given by the following equations (Noureldin et al., 2013):

$$\begin{bmatrix}\delta\dot{\phi}\\ \delta\dot{\lambda}\\ \delta\dot{h}\end{bmatrix} = \begin{bmatrix}0 & \frac{1}{R_M+h} & 0\\ \frac{1}{(R_N+h)\cos\phi} & 0 & 0\\ 0 & 0 & 1\end{bmatrix}\begin{bmatrix}\delta v_e\\ \delta v_n\\ \delta v_u\end{bmatrix} \quad (21)$$

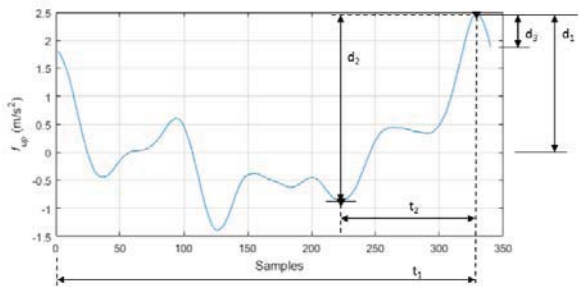

Figure 2. Step Detection

$$\begin{bmatrix}\delta\dot{v}_e\\ \delta\dot{v}_n\\ \delta\dot{v}_u\end{bmatrix}=\begin{bmatrix}0 & f_u & -f_n\\ -f_u & 0 & f_e\\ f_n & -f_e & 0\end{bmatrix}\begin{bmatrix}\delta p\\ \delta r\\ \delta y\end{bmatrix} \quad (22)$$

$$\begin{bmatrix}\delta\dot{p}\\ \delta\dot{r}\\ \delta\dot{y}\end{bmatrix}=\begin{bmatrix}0 & \frac{1}{R_M+h} & 0\\ -\frac{1}{R_N+h} & 0 & 0\\ -\frac{\tan\phi}{R_N+h} & 0 & 0\end{bmatrix}\begin{bmatrix}\delta v_e\\ \delta v_n\\ \delta v_u\end{bmatrix} \quad (23)$$

The state errors are evaluated using measurement update, or using motion constraints (Zhuang et al., 2015).

2.2.2 Pedestrian Dead-Reckoning: Another approach for kinematic modeling is using two-dimensional navigation equations. In this approach the position is not calculated directly by double integration of the acceleration in the motion direction, but it is calculated by accumulating the steps of the mobile node. This technique is called pedestrian dead-reckoning (PDR). Generally, the PDR algorithm is divided into two parts: step detection and position update. The step detection uses the vertical acceleration component and utilizes the following equation (Weinberg, 2002) to calculate the step length:

$$S_{SL}=\sqrt[4]{d_2}\times K \quad (24)$$

where K is a step scaling constant, and d_2 is described in Figure 2, where the y-axis is the magnitude of the vertical acceleration, and the x-axis is the sample number in the processing buffer. A step is detected when all criteria defined in Table 1 are met. These criteria are set to ensure a proper spacing between consecutive peaks, and to ensure the selection of the prominent peak in the current search window.

Step is detected if all following conditions are met	
d_1	> Min. Peak Value
d_2	> Min. Peak Difference
d_3	> Min. Peak Difference
t_1	> Min. Peak Distance
t_2	< Min. Peak Distance

Table 1. Step Detection Criteria

The full state of each node is horizontal position (latitude and longitude) and the orientation of the mobile node (rotation quaternion).

$$x_k=[\phi_k \quad \lambda_k \quad {}^{l}_{b}q_k] \quad (25)$$

The full state propagation equation of the position, in the local-level frame, is given by the following equation.

$$\begin{bmatrix}\phi_{k+1}\\ \lambda_{k+1}\\ {}^{l}_{b}q_{k+1}\end{bmatrix}=\begin{bmatrix}\phi_k+\frac{SL_k\times\cos(A)}{(R_m+h)}\\ \lambda_k+\frac{SL_k\times\sin(A)}{(R_n+h)\times\cos(\phi)}\\ {}^{l}_{b}q_k+\frac{1}{2}\left(\bar{\omega}_\times\times{}^{l}_{b}q_k\times\delta t\right)\end{bmatrix} \quad (26)$$

where SL_k is the step length given by equation (24),
h is the height of the mobile node, which is kept constant,
A is the heading angle,
R_m, R_n are the two principal radii of curvature of the earth.

The error state is modeled as the error in the east and north position and the heading error.

$$\delta x_k=[\delta E_k \quad \delta N_k \quad \delta A_k]^T \quad (27)$$

Linearizing the state propagation model will result in the error state transition matrix:

$$\begin{bmatrix}\delta E_{k+1}\\ \delta N_{k+1}\\ \delta A_{k+1}\end{bmatrix}=\begin{bmatrix}\delta E_k+SL_k\cos(A_k)\,\delta A_k\\ \delta N_k-SL_k\sin(A_k)\,\delta A_k\\ \delta A_k\end{bmatrix} \quad (28)$$

3. FILTER ARCHITECTURES FOR INDOOR LOCALIZATION USING GAUSSIAN PROCESS MODELS

This section describes the different filtering approaches used for indoor localization using RSSI modeled using Gaussian Process models. It gives an brief overview of the filtering algorithm, and shows the detailed measurement update equations for Wi-Fi RSSI updates.

3.1 Extended Kalman Filter

Kalman filter is the optimal filtering algorithm in the case of linear system. However, if the system is non-linear there are several suboptimal approximations to the Kalman filter. One of the simplest approximations is the Extended Kalman filter (EKF) (Gelb et al., 1974; Simon, 2006). In EKF the state estimate probability density function (PDF) is propagated using one point, i.e. the mean of the PDF.

The general form of the system and the measurements equations are given by Equations 29 and 30:

$$x_k=f(x_{k-1},v_k) \quad (29)$$
$$y_k=h(x_k,w_k) \quad (30)$$

where $v_k\sim\mathcal{N}(0,Q_k)$ is the process noise,
$w_k\sim\mathcal{N}(0,R_k)$ is the measurement noise.

EKF Time Update and Measurement Update Algorithm:

1. The non-linear system equation is linearized around the most recent estimate of the state vector ($\hat{x}^+_{k-1}$).

$$F_k = \frac{\partial f}{\partial x}\Big|_{x=\hat{x}_{k-1}^+} \quad (31)$$

$$G_k = \frac{\partial f}{\partial v}\Big|_{x=\hat{x}_{k-1}^+} \quad (32)$$

2. The prior state estimate and prior covariance matrix are calculated using the non-linear system model, and the linearized system model.

$$\hat{x}_k^- = f(\hat{x}_{k-1}) \quad (33)$$

$$P_k^- = F_k P_{k-1}^+ F_k^T + G_k Q_{k-1} G_k^T \quad (34)$$

3. If new measurement is available, the measurement equation is linearized around the prior state estimate.

$$H_k = \frac{\partial h}{\partial x}\Big|_{x=\hat{x}_k^-} \quad (35)$$

$$M_k = \frac{\partial h}{\partial w}\Big|_{x=\hat{x}_k^-} \quad (36)$$

4. The Kalman gain is calculated and the updated state estimate along with the state covariance is calculated according to the following equations.

$$K_k = P_k^- H_k^T \left(H_k P_k^- H_k^T + M_k R_k M_k^T\right)^{-1} \quad (37)$$

$$\hat{x}_k^+ = \hat{x}_k^- + K_k\left(y_k - h(\hat{x}_k^-)\right) \quad (38)$$

$$P_k^+ = (I - K_k H_k) P_k^- \quad (39)$$

- Repeat from step 1.

Remember that the measurement equation for the GP based Wi-Fi estimation is equal to the mean of the likelihood function expression, given by Equation 9. In this case:

$$h(x_k) = \mu_{x_k} \quad (40)$$

The linearization of the measurement equation around x_k is given by the following equations:

$$H_k = \frac{\partial}{\partial x}\left(\mathrm{k}^T (K + \sigma_n^2 I)^{-1}\mathbf{Y}\right)\Big|_{x=\hat{x}_k^-} \quad (41)$$

$$H_k = \left(\frac{\partial}{\partial x}\mathrm{k}\Big|_{x=\hat{x}_k^-}\right)^T \times (K + \sigma_n^2 I)^{-1}\mathbf{Y} \quad (42)$$

$$\frac{\partial}{\partial x}\mathrm{k}\Big|_{x=\hat{x}_k^-} = \frac{1}{l^2}\begin{bmatrix} k_{x,x_0}(x_0 - x) \\ \vdots \\ k_{x,x_m}(x_m - x) \\ \vdots \\ k_{x,x_M}(x_M - x) \end{bmatrix}_{x=\hat{x}_k^-} \quad (43)$$

Note that in the previous equations, K and $\mathbf{Y}$ does not depend on x. They are both function only of the training data.

3.2 Unscented Kalman Filter

The Unscented Kalman Filter (UKF) differs from EKF in the state PDF propagation method. In UKF the state propagation occurs using multiple points, called sigma points, instead of only one point in the EKF case. The estimated state is computed as a weighted sum of these sigma points (Kandepu et al., 2008; Wan and Van Der Merwe, 2000).

In order to reduce the run-time of the UKF, the measurement update is implemented using the UKF algorithm as described in this section, while the state update is done using the linearized version, similar to EKF algorithm. The implemented UKF algorithm, for performing the measurement update against the GP map, is summarized in the following lines:

UKF Measurement Update Algorithm:

1. The state update is performed according to the EKF algorithm, steps 1 – 2.

2. If new measurement is available, calculate sigma points:

$$\chi_{k+1} = \left(-\gamma\sqrt{\hat{P}_{k+1}} \quad 0_{N\times 1} \quad +\gamma\sqrt{\hat{P}_{k+1}}\right) \quad (44)$$

$$\gamma = \sqrt{N + \lambda} \quad (45)$$

$$\lambda = \alpha^2(N + \kappa) - N \quad (46)$$

where N: Number of states,
κ, α are parameters that controls the spread of the sigma points.

3. Evaluate the expected Wi-Fi RSSI value and its variance using the GP model equations, given earlier for each sigma point:

$$Z_{k+1}^{[i]} = h\left(\chi_{k+1}^{[i]}\right) \quad (47)$$

4. Calculate predicted measurement:

$$\hat{z}_{k+1} = \sum_{i=0}^{2n} w_m^{[i]} Z_{k+1}^{[i]} \quad (48)$$

5. Calculate measurement covariance and the measurements and state cross-correlation:

$$P_{k+1}^{zz} = \left(\sum_{i=0}^{2n} w_c^{[i]}\left(Z_{k+1}^{[i]} - \hat{z}_{k+1}\right)\left(Z_{k+1}^{[i]} - \hat{z}_{k+1}\right)^T\right) + R_{k+1} \quad (49)$$

$$\mathrm{P}_{k+1}^{xz} = \sum_{i=0}^{2n} w_c^{[i]}\left(\chi_{k+1}^{[i]}\right)\left(Z_{k+1}^{[i]} - \hat{z}_{k+1}\right)^T \quad (50)$$

6. Evaluate Kalman gain and update the state estimate along with the state covariance:

$$K = P_{k+1}^{xz}(P_{k+1}^{zz})^{-1} \quad (51)$$

$$\hat{x}_{k+1}^+ = \hat{x}_{k+1}^- + K(z_{k+1} - \hat{z}_{k+1}) \quad (52)$$

$$P_{k+1} = \hat{P}_{k+1} - K P_{k+1}^{zz} K^T \quad (53)$$

- Repeat from step 1.

4. EXPERIMENTAL RESULTS

The performance of the different filters is evaluated using data collected by a smartphone, inside one of the buildings at the University of Calgary. The data is collected using a smartphone held horizontally by the user, to maintain the orientation of the smartphone relative to the user. The ground-truth trajectory and the Wi-Fi reference map are recorded and used to evaluate the performance of the proposed filter architectures. The total length of the trajectory is about 270 m, and the duration of the trajectory is about 7 minutes.

The systems models are evaluated first, then the performance of the filters is evaluated according to the localization accuracy, the run-time, and convergence characteristics of the filter.

4.1 System Models Performance

Figure 3 shows a floorplan of the area of interest. It shows also the reference trajectory, the PDR trajectory, and the mechanization trajectory. It is clear that the error from the

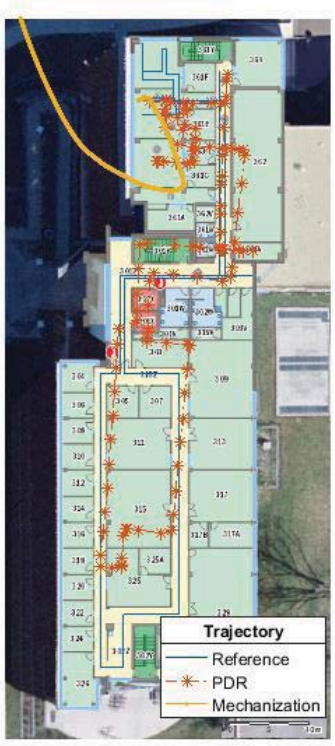

Figure 3. Reference and System Model Trajectories

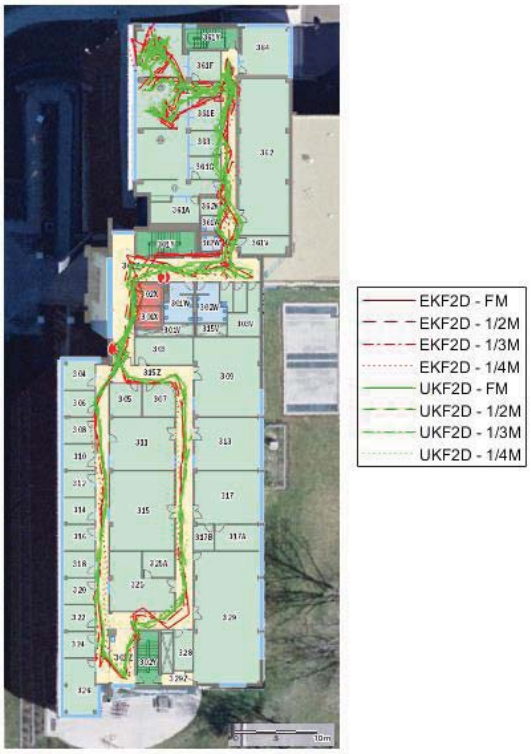

Figure 4. Estimated Trajectories

mechanization equation is increasing with large rate. Additional constraints could be used to enhance the performance of the mechanization equation, including using PDR system models (Zhuang et al., 2015). However, for the rest of this paper, only the PDR system model will be used to evaluate the performance of the different filter architectures.

4.2 Localization Filter Performance

Figure 4 shows the trajectories generated using different filters, with different settings for the Wi-Fi map. This section compares the performance of the EKF, and UKF filters – using a full map, a half-map, a third-map, and a quarter-map. These settings are referred to as FM, 1/2M, 1/3M, and 1/4M respectively. The map reduction is done by dropping a point each two, three or four points from the complete training data set; and since the training data is collected sequentially, dropping points will not result in losing much information from the Wi-Fi map.

The cumulative distribution function (CDF) of the position error is shown in Figure 7. Also, the value of the mean, RMS, and maximum error in position along with the run time of each filter are shown in Figure 6 and in Table 2.

The UKF achieve slightly better positioning errors – between 2.4 to 2.6 m (rms) – relative to the EKF filter – 2.5 m to 2.6 m, while having very similar run times.

The effect of changing the map size is not significant on the positioning accuracy or the total run time. The first observation can be explained by the fact that consecutive training points are correlated, and dropping few of them will not greatly affect the accuracy of the Wi-Fi map. Additionally, decreasing the map size results in decreasing the processing time; however, this decrease is not significant as expected with the $O(N^3)$ complexity. This can be explained by the overhead in the algorithm computation and control code, which dominates the execution time.

4.3 Filter Convergence Characteristics

In all simulations shown earlier the initial state of the different filters was assumed to be known within 1~2 m level of confidence. Figure 5 shows the position error when the initial value is not known. In the EKF and UKF filters this is achieved by setting the initial position to the map middle and increase the initial state covariance matrix.

In this case the EKF, and UKF filters were able to converge eventually, and start following the correct trajectory after few seconds; however, it took them multiple measurements updates to be able to reach the correct estimation. The UKF shows faster convergence time compared to the EKF, where the positioning error dropped faster than the case of the EKF filter.

Filter	Map	Position Error (m)			Time (s)	
		MEAN	*RMS*	*MAX*		
PDR	-	5.7	6.5	12.5	-	-
EKF2D	100%	2.1	2.5	8.0	103	100%
EKF2D	50%	2.1	2.6	8.2	101	98%
EKF2D	33%	2.1	2.6	8.9	100	97%
EKF2D	25%	2.3	2.8	8.8	102	99%
UKF2D	100%	2.1	2.4	6.8	133	129%
UKF2D	50%	2.1	2.4	7.4	124	120%
UKF2D	33%	2.2	2.6	7.1	121	117%
UKF2D	25%	2.2	2.6	8.5	120	116%

Table 2. Position Error and Run-Time

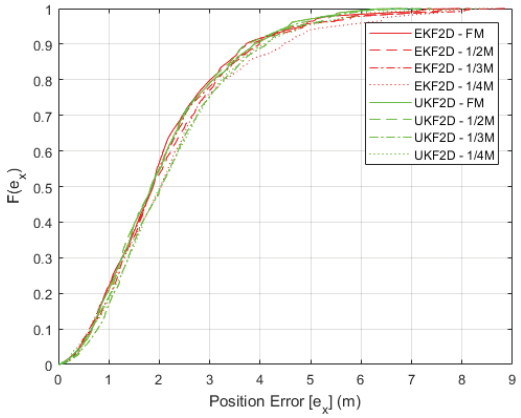

Figure 7. Position Error CDF

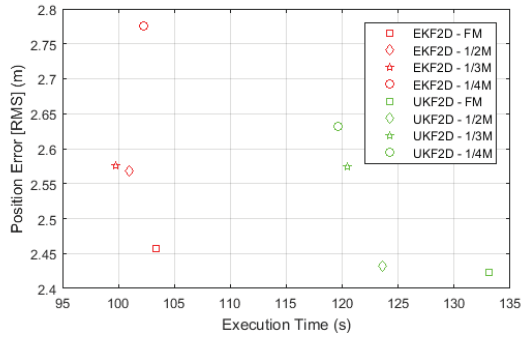

Figure 6. Position Error and Run-Time

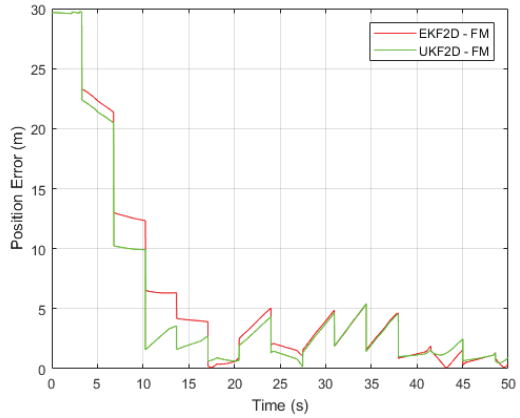

Figure 5. Position Error Convergence

5. CONCLUSIONS

This paper evaluated different localization filter architectures using Wi-Fi RSSI values, represented using Gaussian Process models. The paper examined different kinematics models, and different measurement update approaches. The paper also investigated the effect of reducing the number of the GP training data, and the effects of incorrect or unknown initial values on the performance of different filters. The proposed filters are shown to achieve positioning accuracy of 2.4m, with reasonable execution time.

ACKNOWLEDGEMENTS

This work was supported by Dr. Naser El-Sheimy research funds from NSERC and Canada Research Chairs programs.

REFERENCES

Aravecchia, M., Messelodi, S., 2014. Gaussian process for RSS-based localisation, in: 2014 IEEE 10th International Conference on Wireless and Mobile Computing, Networking and Communications (WiMob). Presented at the 2014 IEEE 10th International Conference on Wireless and Mobile Computing, Networking and Communications (WiMob), pp. 654–659.

Atia, M.M., Noureldin, A., Korenberg, M.J., 2013. Dynamic Online-Calibrated Radio Maps for Indoor Positioning in Wireless Local Area Networks. IEEE Trans. Mob. Comput. 12, pp. 1774–1787.

Correa, A., Barcelo, M., Morell, A., Vicario, J.L., 2014. Enhanced Inertial-Aided Indoor Tracking System for Wireless Sensor Networks: A Review. IEEE Sens. J. 14, pp. 2921–2929.

Dashti, M., Yiu, S., Yousefi, S., Perez-Cruz, F., Claussen, H., 2015. RSSI Localization with Gaussian Processes and Tracking, in: 2015 IEEE Globecom Workshops (GC Wkshps). Presented at the 2015 IEEE Globecom Workshops (GC Wkshps), pp. 1–6.

Ferris, B., Fox, D., Lawrence, N.D., 2007. WiFi-SLAM Using Gaussian Process Latent Variable Models, in: IJCAI. pp. 2480–2485.

Ferris, B., Hähnel, D., Fox, D., 2006. Gaussian Processes for Signal Strength-Based Location Estimation, in: Proc. of Robotics Science and Systems.

Fischer, C., Gellersen, H., 2010. Location and navigation support for emergency responders: A survey. IEEE Pervasive Comput. 9, pp. 38–47.

Gelb, A., Joseph F. Kasper, Jr., Raymond A. Nash, Jr., Charles F. Price, Arthur A. Sutherland, Jr., 1974. Applied optimal estimation. M.I.T. Press, Cambridge, Mass.

Harle, R., 2013. A Survey of Indoor Inertial Positioning Systems for Pedestrians. IEEE Commun. Surv. Tutor. 15, 1281–1293.

He, S., Chan, S.-H.G., 2016. Wi-Fi Fingerprint-Based Indoor Positioning: Recent Advances and Comparisons. IEEE Commun. Surv. Tutor. 18, 466–490.

Hossain, A.K.M.M., Soh, W.-S., 2015. A survey of calibration-free indoor positioning systems. Comput. Commun. 66, pp. 1–13.

Kandepu, R., Foss, B., Imsland, L., 2008. Applying the unscented Kalman filter for nonlinear state estimation. J. Process Control 18, pp. 753–768.

Kemppainen, A., Vallivaara, I., Röning, J., 2015. Magnetic field SLAM exploration: Frequency domain Gaussian processes and informative route planning, in: 2015 European Conference on Mobile Robots (ECMR). Presented at the 2015 European Conference on Mobile Robots (ECMR), pp. 1–7.

Li, Y., 2016. Integration of MEMS Sensors, WiFi, and Magnetic Features for Indoor Pedestrian Navigation with Consumer Portable Devices. PhD diss., University of Calgary.

Liu, H., Darabi, H., Banerjee, P., Liu, J., 2007. Survey of Wireless Indoor Positioning Techniques and Systems. IEEE Trans. Syst. Man Cybern. Part C Appl. Rev. 37, pp. 1067–1080.

Markets and Markets, 2017. Location-Based Services (LBS) Market by Technology & Software - 2021 [WWW Document]. URL http://www.marketsandmarkets.com/Market-Reports/location-based-service-market-96994431.html (accessed 3.13.17).

Naser El-Sheimy, 2016. ENGO 623 - Inertial Surveying and INS/GPS Integration, Course Notes. University of Calgary, Calgary, AB.

Nocedal, J., Wright, S.J., 2006. Numerical optimization, 2nd ed. ed, Springer series in operations research. Springer, New York.

Noureldin, A., Karamat, T.B., Georgy, J., 2013. Fundamentals of Inertial Navigation, Satellite-based Positioning and their Integration. Springer Berlin Heidelberg, Berlin, Heidelberg.

Rasmussen, C.E., Williams, C.K.I., 2006. Gaussian processes for machine learning. MIT Press, Cambridge, Mass.

Shang, J., Hu, X., Gu, F., Wang, D., Yu, S., 2015. Improvement Schemes for Indoor Mobile Location Estimation: A Survey. Math. Probl. Eng. 2015, pp. 1–32.

Simon, D., 2006. Optimal state estimation: Kalman, H [infinity] and nonlinear approaches. Wiley-Interscience, Hoboken, N.J.

Titterton, D.H., Weston, J.L., 2004. Strapdown Inertial Navigation Technology, 2nd ed. Institution of Engineering and Technology.

Vallivaara, I., Haverinen, J., Kemppainen, A., Röning, J., 2010. Simultaneous localization and mapping using ambient magnetic field, in: 2010 IEEE Conference on Multisensor Fusion and Integration for Intelligent Systems (MFI). Presented at the 2010 IEEE Conference on Multisensor Fusion and Integration for Intelligent Systems (MFI), pp. 14–19.

Wan, E.A., Van Der Merwe, R., 2000. The unscented Kalman filter for nonlinear estimation, in: Adaptive Systems for Signal Processing, Communications, and Control Symposium 2000, pp. 153–158.

Weinberg, H., 2002. Using the ADXL202 in pedometer and personal navigation applications. Analog Devices -602 Appl. Note 2, pp. 1–6.

Yang, Z., Wu, C., Zhou, Z., Zhang, X., Wang, X., Liu, Y., 2015. Mobility Increases Localizability: A Survey on Wireless Indoor Localization Using Inertial Sensors. ACM Comput Surv 47, pp. 54:1–54:34.

Zhuang, Y., 2015. Integration of WiFi and MEMS Sensors for Indoor Navigation. PhD diss., University of Calgary.

Zhuang, Y., Lan, H., Li, Y., El-Sheimy, N., 2015. PDR/INS/WiFi Integration Based on Handheld Devices for Indoor Pedestrian Navigation. Micromachines 6, pp. 793–812.

Comparative Analysis of Potential Calibration Alternatives for a Multi-Unit LiDAR System

Yun-Jou Lin *, Radhika Ravi, Tamer Shamseldin, Magdy Elbahnasawy, Darcy Bullock, Ayman Habib
Lyles School of Civil Engineering, Purdue University, 550 Stadium Mall Dr., West Lafayette, IN 47907, USA
- (yjlin, ravi22, tshamsel, melbahn, darcy, ahabib)@ purdue.edu

KEY WORDS: Outdoor Calibration, Multi-Unit LiDAR System, Mounting Parameters, HDL32E, VLP16

ABSTRACT:

Nowadays, mobile mapping systems that can rapidly collect 3D spatial data geo-referenced to a global reference frame have become popular for a variety of applications such as Digital Building Model (DBM) generation, transportation corridor monitoring, telecommunications, precision agriculture, and infrastructure monitoring. To derive point clouds with high positional accuracy from an integrated system of LiDAR sensors and GNSS/INS, calibration of mounting parameters is the foremost and necessary step. This paper proposes a multi-unit LiDAR system calibration procedure that can directly estimate the mounting parameters relating the different laser scanners to the onboard GNSS/INS unit through an outdoor calibration procedure.
The proposed calibration procedure is based on the use of conjugate planar/linear features in overlapping point clouds derived from different drive-runs. In order to increase the efficiency of semi-automatic conjugate feature extraction, specifically designed calibration boards covered by highly reflective surfaces that could be easily deployed and setup within outdoor environments are used in this study. The comparative analysis as well as the performance of the potential system calibration procedures is evaluated using a multi-unit mobile LiDAR system comprised of: 1) a Velodyne HDL-32E laser scanner, 2) a Velodyne VLP-16 laser scanner, and 3) a SPAN CPT direct geo-referencing GNSS/INS unit. The comparative performance of the different calibration alternatives will be evaluated through: 1) a-posteriori variance factor of the least-squares adjustment procedure; 2) quality of fit of the adjusted point clouds to planar surfaces before and after the calibration process. Moreover, this system is going to be used for a lane width evaluation application. A comparison of on-site manually measured lane width and extracted lane width from calibrated point clouds is provided to prove that the proposed procedure can be used in high-accuracy surveying application.

1. INTRODUCTION

LiDAR scanners onboard airborne and terrestrial platforms have been established as a proven technology for the acquisition of dense point clouds with high positional accuracy. The main factors behind the widespread use of LiDAR systems include the ever-continuous improvement in GNSS/INS direct geo-referencing technology as well as enhanced performance and reduced size and cost of laser scanning units. Currently, there are commercially available LiDAR units that are capable of emitting more than a quarter million pulses per second at a cost of less than $10k. Such availability, together with the ever-increasing range of applications – such as Digital Building Model generation, transportation corridor monitoring, telecommunications, precision agriculture, infrastructure monitoring, seamless outdoor-indoor mapping, and power line clearance (Lin et al., 2013; Williams et al., 2013; Weiss and Biber, 2011; Puente et al., 2013) – have led to the development of multi-unit mobile LiDAR systems onboard airborne and terrestrial platforms that are either manned or unmanned. However, the attainment of the full positioning potential of such systems is contingent on an accurate calibration of the mobile mapping unit as a whole. This paper proposes a multi-unit LiDAR system calibration procedure that can directly estimate the mounting parameters relating the different laser scanners to the onboard GNSS/INS unit through an outdoor calibration procedure.

The cost-effective Velodyne laser scanner, which has multi-firing laser beams and can rapidly capture a high volume of data, has been used in many mobile mapping systems and robotics applications (Schwarz, 2010; Choi, 2014; Vallet et al., 2015). Over the past few years, a great deal of research has been studied on modeling the error of Velodyne laser scanners as well as the calibration of integrated LiDAR sensor and GNSS/INS direct geo-referencing units (Atanacio-Jiménez et al., 2011; Glennie et al., 2013). Underwood et al. (2007) calibrated the extrinsic parameters of a SICK LMS-291 and Novatel Synchronized Position Attitude Navigation (SPAN) system by minimizing the error between sensed data and a known structure (i.e., a vertical pole and relatively flat ground). He et al. (2013) used pairwise multi-type 3D geometric features (i.e., point, line, plane) to derive the extrinsic parameters between 2D LiDAR and GNSS/INS. First, the points are segmented into different features and their quality is evaluated to compute weights to be used in the minimization of normal distance between conjugate features. However, when the initial parameters are considerably inaccurate, the segments and derived weights may not be reliable. Chan et al. (2013) introduced an intrinsic parameters calibration for Velodyne HDL-32E based on static stations and also analyzed the temporal stability of range measurements which indicated an approximate warm-up time of 2000 sec for most laser beams. Glennie et al. (2016) performed a geometric calibration with stationary VLP-16 to marginally improve the accuracy of the point clouds by approximately 20%. Moreover, this paper also investigates the range accuracy of VLP-16, which is quoted to have an RMSE value between 22 to 27 mm in the factory supplied calibration certificate. But, it is observed that some of the laser beams have a worse range accuracy than the others. Although many LiDAR system calibration procedures have been developed in the past, outdoor calibration of integrated GNSS/INS and multi-unit 3D laser scanners is still an active area of research.
This paper is focusing on the potential calibration alternatives of a multi-unit LiDAR system onboard a terrestrial mobile mapping vehicle. The focus of the system calibration is to estimate the mounting parameters relating the different system components simultaneously. More specifically, the lever arm and boresight

* Corresponding author. This is useful to know for communication with the appropriate person in cases with more than one author.

angles relating the individual laser scanners and the onboard GNSS/INS unit will be derived. Moreover, this paper provides an iterative calibration procedure that can accurately estimate mounting parameters using initial approximations. The multi-unit mobile LiDAR system used for this research consistes of the following components: 1) a Velodyne HDL-32E laser scanner, 2) a Velodyne VLP-16 laser scanner, and 3) a SPAN CPT direct geo-referencing GNSS/INS unit. The comparative performance of the different calibration alternatives will be evaluated through: 1) a-posteriori variance factor of the least squares adjustment procedure; 2) quality of fit of the adjusted point clouds to planar surfaces before and after the calibration process. Moreover, this mobile system is also adopted for a lane width evaluation application. A comparison of on-site manually measured lane width and extracted lane width from calibrated point clouds is provided to demonstrate the feasibility of proposed strategy.

2. SPECIFICATIONS FOR LiDAR UNITS AND NAVIGATION SYSTEM USED IN THIS RESEARCH

HDL-32E is 149.86 mm high, 85.3 mm in diameter and weighs 1 kg (plus 0.3kg for cabling). It consists of 32 radially-oriented laser rangefinders that are aligned from +10.67˚ to -30.67˚. In total, the vertical Field of View (FOV) is 41.34˚. A 3D Velodyne can rotate the whole unit to achieve a 360˚ horizontal FOV. The reliable return range is approximately from 1 m to 70 m and the point capture rate is around 700,000 points per second (Velodyne (a), 2016).

VLP-16, that has 16 radially-oriented laser rangefinders, is a lite version of HDL-32E. The vertical FOV is from -15˚ to +15 ˚ and the horizontal FOV is 360˚. The effective range is from 1 m to 100 m depending on the application, and the point capture rate is around 300,000 points per second (Velodyne (b), 2016).

The navigation system adopted in this research is SPAN-CPT that combines GNSS and Inertial Measurement Unit (IMU) hardware inside a single enclosure. The GNSS position collection rate is 20 Hz and IMU measurement rate is 100 Hz. The accuracy in position can be less than 2 cm. For the attitude, the accuracy can achieve 0.008˚ and 0.035˚ in the roll/pitch and heading directions, respectively (Novatel, 2014).

3. PROPOSED CALIBRATION PROCEDURE

In this section, we propose a strategy to calibrate the mounting parameters using geometric features (e.g., planar, and linear/cylindrical features). After collecting data from several drive-runs, a 3D point cloud relative to a global reference frame will be derived through a direct geo-referencing system. Then, conjugate features are identified and extracted from the reconstructed point cloud. Finally, an iterative multi-system calibration with weight modification is proposed to derive the mounting parameters based on the minimization of normal distance between conjugate features.

3.1 Conceptual Basis of LiDAR Point Positioning

A typical directly geo-referenced LiDAR system could involve 3 coordinate systems (i.e., mapping frame, IMU body frame, and laser unit frame). A given point, ***I***, acquired from a mobile mapping system can be reconstructed in the mapping coordinate system using Equation 1, which is graphically illustrated in Figure 1. For the laser unit frame, origin is defined at the laser beam firing point and the z-axis is along the axis of horizontal rotation of the laser unit. For a Velodyne system, each laser beam is fired at a fixed vertical angle, $\boldsymbol{\alpha}$, the horizontal angle, $\boldsymbol{\beta}$, is determined based on the rotation of the unit, and the range, $\boldsymbol{\rho}$, is defined by the distance from firing point to its footprint. So, the coordinates of a 3D point relative to the Velodyne laser unit coordinate system, $\boldsymbol{r_l^{lu}(t)}$, is defined by Equation 2. An IMU body frame should be considered when mobile systems are equipped with a GNSS/INS navigation unit. For mobile systems, the lever arm, $\boldsymbol{r_{lu}^b}$, and boresight matrix, $\boldsymbol{R_{lu}^b}$, between laser unit and body frame coordinate systems are time-independent as the laser units are fixed rigidly with respect to the IMU unit. The GNSS/INS integration provides the time-dependent position, $\boldsymbol{r_b^m(t)}$, and rotation, $\boldsymbol{R_b^m(t)}$, relating the mapping frame and IMU body frame coordinate systems, according to the optimized solution from all the available GNSS and inertial measurements.

$$r_l^m = r_b^m(t) + R_b^m(t)\, r_{lu}^b + R_b^m(t)\, R_{lu}^b\, r_l^{lu}(t) \qquad (1)$$

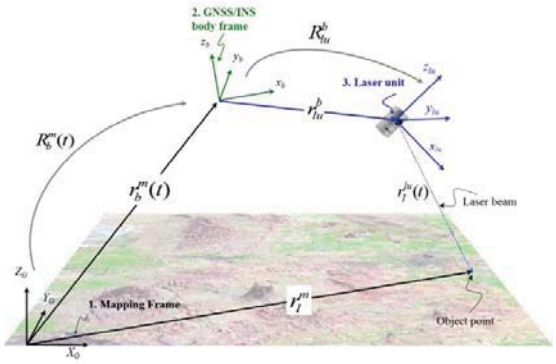

Figure 1. Illustration of point positioning of a directly geo-referenced LiDAR system

$$r_l^{lu}(t) = \begin{pmatrix} x \\ y \\ z \end{pmatrix} = \begin{pmatrix} \rho(t)\cos\beta(t)\cos\alpha(t) \\ \rho(t)\cos\beta(t)\sin\alpha(t) \\ \rho(t)\ \sin\beta(t) \end{pmatrix} \qquad (2)$$

The mathematical formulation for computing the mapping frame coordinates of an object point for 3D point reconstruction from a multi-laser unit system is provided in Equation 3, where a reference sensor and slave sensors are considered. An illustration of such a multi-unit LiDAR system is shown in Figure 2. In Equation 3, the terms r_{lur}^b and R_{lur}^b are the lever arm and boresight matrix, respectively, relating the IMU body frame and the reference laser unit coordinate systems. The extra terms considered in Equation 3, r_{luj}^{lur} and R_{luj}^{lur} are the lever arm and boresight matrix, respectively, rigidly relating the reference sensor, ***lur***, and the slave sensor, ***luj***. One can introduce one or more slave sensors, each one of them rigidly related to the reference sensor by a lever arm and boresight matrix. When a point is acquired by a reference sensor, then r_{luj}^{lur} is zero and R_{luj}^{lur} is an identity matrix. In this scenario, Equation 3 will reduce to Equation 1.

$$r_l^m = r_b^m(t) + R_b^m(t)\, r_{lur}^b + R_b^m(t)\, R_{lur}^b\, r_{luj}^{lur} + R_b^m(t)\, R_{lur}^b\, R_{luj}^{lur}\, r_l^{luj}(t) \qquad (3)$$

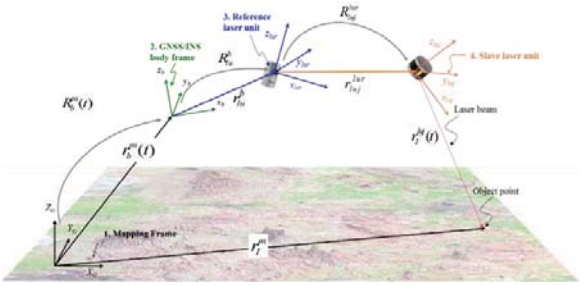

Figure 2. Illustration of point positioning of a directly geo-referenced multi-unit LiDAR system

3.2 Feature Extraction

After reconstructing the point clouds from several drive-runs using the initial estimates for mounting parameters, different types of geometric features (i.e., planar, and linear/cylindrical) can be used as conjugate features for the calibration procedure. However, conjugate point pairs cannot be used since there is no accurate point-to-point correspondence, owing to the irregular distribution of LiDAR points. But, linear/cylindrical and planar features, such as building façade, ground patches, light poles, and lane markers, can be directly extracted from overlapping areas within the drive-runs. However, conjugate feature extraction from several drive-runs could be time-consuming and inefficient, especially when the initial parameters are considerably inaccurate. To facilitate automated identification of conjugate features in such cases, specifically designed calibration boards covered by highly reflective surfaces, that could be easily deployed and setup in outdoor environments, are used in this study, as shown in Figure 3 (a).

The highly reflective boards can be easily identified from intensity data as shown in Figure 3 (b). Firstly, a pre-defined threshold is set to extract the high-intensity points. To avoid the extraction of objects, other than these boards, with high-intensity points, an approximate pre-set region is set as seed points for each board. Then, a distance-based region growing technique is adopted to group the high intensity boards. Other planar features, such as ground patches, can be easily extracted by defining two diagonally opposite corners.

(a)

(b)

Figure 3. (a) Image, and (b) Intensity data of specifically designed highly reflective surfaces from a single drive-run.

3.3 Multi-Sensor System Calibration

In the proposed calibration method, conjugate features are extracted from the point clouds of different sensors and several drive-runs. The mounting parameters of each sensor are derived by minimizing the discrepancies among conjugate features in overlapping drive-runs. The ideal mathematical condition for a conjugate point pair from two overlapping drive-runs is given by Equation 4. However, for non-conjugate points along corresponding planar and linear/cylindrical features, the misclosure vector, $\vec{\boldsymbol{D}}$, would lie along the planar surface or along the linear feature/axis of cylinder, as illustrated in Figure 4. Therefore, a modified weight matrix, $\boldsymbol{P}'$, is introduced to eliminate the non-random component of misclosure vector, $\vec{\boldsymbol{D}}$ (Renaudin et al., 2011) (Equation 5). To derive this matrix, a local coordinate system (UVW) is established first. For linear/cylindrical features, U-axis is aligned along the line/axis of cylinder and V- and W-axes are arbitrarily chosen to satisfy the orthogonality constraint. For planar features, W-axis is aligned along the normal vector of a plane in question, and U- and V-axes are arbitrarily chosen. An illustration of the local coordinate systems for the two types of features is shown in Figure 5. Then, a rotation matrix, R_{XYZ}^{UVW}, is derived according to the components of the vectors, U, V, and W, to relate the local and mapping coordinate systems. This is discussed in more detail later. The weight matrix, P_{XYZ}, in mapping coordinate system is transformed to a weight matrix, P_{UVW}, in the local coordinate system according to the law of error propagation (Equation 6). The weight matrix, P_{UVW}, is modified by assigning a zero weight to the elements corresponding to the misclosure vector direction. More specifically, the misclosure vector can be eliminated by setting a zero weight in the corresponding direction. The misclosure direction of a linear/cylindrical feature is along the U-axis. Therefore, the modified weight matrix, P'_{UVW}, has zero weight in all the elements pertaining to the U-axis (Equation 7). Similarly, the misclosure vector direction of a planar feature is along the U- and V-axes. So, all the elements pertaining to the U- and V-axes are assigned a zero weight (Equation 8). Finally, the modified weight matrix, P'_{XYZ}, in the mapping coordinate system is derived using Equation 9. Finally, the condition given by Equation 4 can be modified to account for non-conjugate points along corresponding features within overlapping drive-runs by applying the obtained modified weight matrix, P'_{XYZ}.

$$r_l^m(\text{drive-run 1}) - r_l^m(\text{drive-run 2}) = 0 \qquad (4)$$

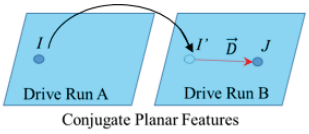

(a)

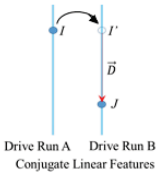

(b)

Figure 4. Discrepancy vector between non-conjugate points along corresponding (a) planar, and (b) linear features

$$P'\vec{D} = P'\begin{bmatrix} d_x \\ d_y \\ d_z \end{bmatrix} = 0 \qquad (5)$$

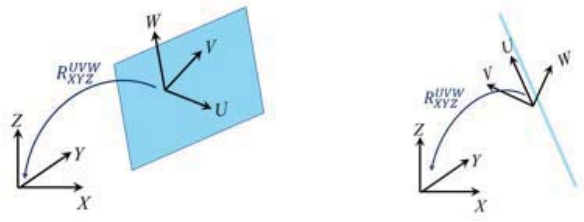

(a) (b)

Figure 5. Illustration of local coordinate systems for (a) planar and (b) linear features

$$P_{UVW} = R^{UVW}_{XYZ}\, P_{XYZ}\, R^{UVW^T}_{XYZ} = \begin{bmatrix} P_U & P_{UV} & P_{UW} \\ P_{VU} & P_V & P_{VW} \\ P_{WU} & P_{WV} & P_W \end{bmatrix} \quad (6)$$

Linear/Cylindrical Feature: $P'_{UVW} = \begin{bmatrix} 0 & 0 & 0 \\ 0 & P_V & P_{VW} \\ 0 & P_{WV} & P_W \end{bmatrix}$ (7)

Planar Feature: $P'_{UVW} = \begin{bmatrix} 0 & 0 & 0 \\ 0 & 0 & 0 \\ 0 & 0 & P_W \end{bmatrix}$ (8)

$$P'_{XYZ} = R^{UVW^T}_{XYZ} P'_{UVW} R^{UVW}_{XYZ} \quad (9)$$

To achieve a higher precision in mounting parameters estimation from the calibration procedure, they need to be decoupled from each other. This decoupling can be achieved using multiple drive-runs. The discrepancies among conjugate features in such drive-runs are then used for estimating the mounting parameters. However, increasing the number of sensors and drive-runs would increase the complexity of extracting conjugate features. For instance, a patch, ***P1***, extracted from different drive-runs (say, drive-run 1 and drive-run 2) and different sensors (say, sensor 1 and sensor 2) will lead to four separate versions for this feature. There will be six possible pairwise combinations for ***P1*** and the conditions to minimize the discrepancies within each of these pairs would no longer be independent. Hence, in this research, one of the versions is selected as reference to be paired with all the other versions of that feature from other sensors and/or drive-runs. The version with maximum number of points belonging to a feature is used as the reference version because this version will be used to derive the modified weight matrix for that feature. So, an increased number of points would increase the redundancy of plane or line/cylinder fitting for the feature, thus resulting in a more accurate estimate of the modified weight matrix. Finally, the mounting parameters for both reference and slave laser units can be derived by minimizing the discrepancies within the conjugate features arising from the above mentioned pairs between the different versions of such features.

However, when the initial estimate of mounting parameters is inaccurate, the estimated modified weight matrix would be imprecise which would affect the accuracy of the derived mounting parameters. Hence, this paper proposes an iterative calibration procedure. Firstly, the discrepancy among extracted features is minimized to derive mounting parameters through the weight modification process. Then, the points along the extracted features are re-generated using the new mounting parameters and the discrepancy among conjugate features is minimized again using a newly defined modified weight matrix. Then, the above steps are repeated until the change in the estimates of the mounting parameters is below a threshold.

4. EXPERIMENTAL RESULTS

4.1 Dataset Description

The data is captured by a designed platform which carries a VLP-16 and an HDL-32E laser scanner together with a SPAN-CPT direct geo-referencing unit, as shown in Figure 6. The five specially designed highly reflective boards are installed, oriented in different directions, in a sufficiently spacious area to drive around them. In this experiment, ten drive-runs, with different directions and lateral distance between them, were made around the five boards at an approximate speed of 4 miles/hr. With ten drive-runs and two laser units, we will have a total of 20 versions for each of the features used for the calibration procedure. The configuration of drive-runs and boards are shown in Figure 7. First, all the points are reconstructed using initial estimates of the mounting parameters, which are obtained from manual measurements/estimates for the lever-arm and boresight angles between SPAN-CPT and reference laser unit, and between the reference and slave laser units. The reconstructed point clouds are used to extract conjugate features. Then, the semi-automatic feature extraction is executed to obtain the points for planar features (i.e., specially designed boards and ground patches) from all the datasets separately, as shown in Figure 8. One should note that the modified weight matrix retains only the discrepancies in the direction normal to the planar surface. Therefore, the geometric direction of extracted features would be critical to conduct a successful calibration. In this experiment, the boards are set up to be perpendicular to each other. These boards, along with the extracted ground patches, ensure enough control along all the directions (i.e., X, Y, Z-directions). Three different test cases are considered for calibration: (1) single sensor calibration for VLP-16, (2) single sensor calibration for HDL-32E, and (3) multi-sensor calibration for VLP-16 and HDL-32E. The quality of the calibration results is then examined by performing a lane width evaluation using the calibrated mobile system consisting of both the VLP-16 and HDL-32E laser scanners.

Figure 6. Mobile Mapping System used in this research

The accuracy of calibration procedure is evaluated by monitoring the a-posteriori variance factor after every iteration of the least squares adjustment procedure and also, the RMSE of the normal distance of points belonging to a planar feature from the best-fitting plane for that feature.

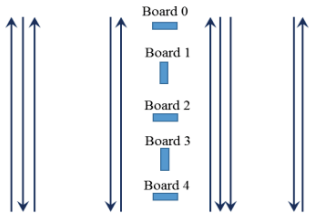

Figure 7. Configuration of drive-runs and calibration boards

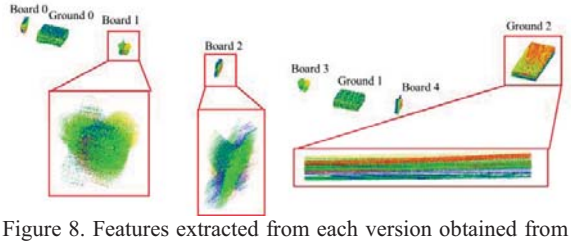

Figure 8. Features extracted from each version obtained from 2 different sensors and 10 different drive-runs (total of 2*10 = 20 different versions)

4.2 Dataset Description

A. Single Sensor Calibration Results

The mounting parameters that are derived in single sensor calibration are the planimetric lever arm components ***(ΔX, ΔY)*** and boresight angles ***(Δω, Δϕ, Δκ)***. The vertical lever arm component (***ΔZ)*** is not adjusted in the calibration procedure. This is because any change in ***ΔZ*** will not introduce discrepancies among the different versions of the same feature captured from different sensors and/or runs. It would only result in a shift of the point cloud in the vertical direction as a whole. So, ***ΔZ*** is manually measured and fixed during the calibration procedure. The initial approximations of the mounting parameters and the final results from the single sensor calibration for VLP-16 as well as HDL-32E sensors are listed in Table 1.

Table 1. Mounting parameters of VLP-16 and HDL-32E before and after single sensor calibration

ΔX (m)	***ΔY*** (m)	***ΔZ*** (m)	***Δω*** (°)	***Δφ*** (°)	***Δκ*** (°)
Initial Mounting Parameter					
VLP16 Mounting Parameters r^b_{VLP16} R^b_{VLP16}					
0.1	0.1	0.28	-10	0	-30
HDL32E Mounting Parameters r^b_{HDL32E} R^b_{HDL32E}					
0.4	0.1	0.3	-5	0	-60
Mounting Parameter After Calibration					
VLP16 Mounting Parameters r^b_{VLP16} R^b_{VLP16}					
0.006	0.189	0.28	-10.620	-1.006	-32.016
HDL32E Mounting Parameters r^b_{HDL32E} R^b_{HDL32E}					
0.475	0.195	0.3	-6.046	-0.064	-58.882

In single sensor calibration, the mounting parameters are derived based on conjugate planar features extracted from a single laser unit. For every iteration, the a-posteriori variance factor ($\hat{\sigma}_o$) of the least-squares adjustment procedure and the RMSE of normal distance of points from best-fitting plane for extracted features are derived to show the improvement. For single sensor calibration of the VLP-16 and HDL-32E scanners, the results are listed in Table 2 and Table 3, respectively.

Table 2. VLP-16 single sensor calibration: A-posteriori variance factor ($\hat{\sigma}_o$) and RMSE of plane fitting

	Number of Points	Before Calibration	Calibration Iteration 1	Calibration Iteration 2	Calibration Iteration 3
$\hat{\sigma}_o$ (m)			0.0470	0.0143	0.0143
Board 0 (m)	12,107	0.119	0.020	0.012	0.012
Board 1 (m)	13,787	0.148	0.143	0.013	0.013
Board 2 (m)	15,686	0.121	0.022	0.010	0.010
Board 3 (m)	13,015	0.130	0.142	0.011	0.011
Board 4 (m)	10,917	0.104	0.018	0.012	0.012
Ground 0 (m)	126,682	0.180	0.018	0.019	0.019
Ground 1 (m)	106,970	0.171	0.025	0.023	0.023
Ground 2 (m)	47,993	0.162	0.023	0.022	0.022

Table 3. HDL-32E single sensor calibration: A-posteriori variance factor ($\hat{\sigma}_o$) and RMSE of plane fitting

	Number of Points	Before Calibration	Calibration Iteration 1	Calibration Iteration 2	Calibration Iteration 3
$\hat{\sigma}_o$ (m)			0.0209	0.0138	0.0137
Board 0 (m)	50,222	0.128	0.019	0.019	0.019
Board 1 (m)	59,224	0.118	0.020	0.020	0.020
Board 2 (m)	70,216	0.125	0.016	0.016	0.016
Board 3 (m)	56,545	0.104	0.021	0.021	0.021
Board 4 (m)	44,469	0.112	0.014	0.014	0.014
Ground 0 (m)	554,942	0.154	0.022	0.021	0.021
Ground 1 (m)	502,867	0.146	0.021	0.020	0.020
Ground 2 (m)	137,191	0.178	0.024	0.023	0.023

It can be seen from the above tables that the RMSE for each feature is consistently improving after every iteration. In single sensor calibration, the accuracy can reach around 2 cm. One should note that the designed boards have a thickness of about 1 cm, so the RMSE will never be less than a centimeter. For VLP-16, the RMSE value is slightly smaller than HDL-32E. One of the possible reasons is that this research does not consider the sensor parameters. When the number of laser beams increases, the number of points would be more but the inconsistency would be more obvious for an object.

B. Multi-sensor Calibration Results

The mounting parameters that are derived in multi-sensor calibration are the planimetric lever arm components ***(ΔX, ΔY)*** and boresight angles ***(Δω, Δϕ, Δκ)*** for all the sensors and the vertical lever arm component (***ΔZ)*** for all but the reference sensor. The ***ΔZ*** value for the reference sensor is not adjusted in the calibration procedure. This is because of the same reason as for the single sensor calibration. Fixing the value of ***ΔZ*** for the reference sensor would establish the datum for the data. So, it is manually measured and fixed during the calibration procedure. The initial approximations of the mounting parameters and the final results from the multi-sensor calibration for VLP-16 as well as HDL-32E sensors are listed in Table 4.

Table 4. Mounting parameters of VLP-16 and HDL-32E before and after multi-sensor calibration

ΔX (m)	***ΔY*** (m)	***ΔZ*** (m)	***Δω*** (°)	***Δφ*** (°)	***Δκ*** (°)
Initial Mounting Parameter					
HDL32E Mounting Parameters r^b_{HDL32E} R^b_{HDL32E}					
0.4	0.1	0.3	-5	0	-60
VLP16 Mounting Parameters r^{HDL32E}_{VLP16} R^{HDL32E}_{VLP16}					
-0.152	-0.259	-0.020	-2.505	-4.329	29.905
Mounting Parameter After Calibration					

HDL32E Mounting Parameters r^{b}_{HDL32E} R^{b}_{HDL32E}					
0.476	0.196	0.3	-6.045	-0.062	-58.881
VLP16 Mounting Parameters r^{HDL32E}_{VLP16} R^{HDL32E}_{VLP16}					
-0.247	-0.399	-0.078	-1.578	-4.327	26.839

In multi-sensor calibration, the HDL-32E and VLP-16 scanners are taken as reference and slave units, respectively. The mounting parameters are derived simultaneously with point pairs from the conjugate features in the HDL-32E and VLP-16 datasets. For the multi-sensor calibration, the a-posteriori variance factor ($\hat{\sigma}_o$) of the least-squares adjustment procedure and the RMSE of normal distance of points from best-fitting plane for extracted features after every iteration are listed in Table 5. Through the qualitative evaluation depicted in Figure 9, one can observe a significant improvement of boards and ground patches after calibration. Moreover, a comparison is provided to assess the quality of single sensor calibration and multi-sensor calibration in Table 6.

Table 5. VLP-16 + HDL-32E multi-sensor calibration: A-posteriori variance factor ($\hat{\sigma}_o$) and RMSE of plane fitting

	Number of Points	Before Calibration	Calibration Iteration 1	Calibration Iteration 2	Calibration Iteration 3
$\hat{\sigma}_o$ (m)			0.0206	0.0134	0.0133
Board 0 (m)	62,329	0.127	0.018	0.018	0.018
Board 1 (m)	73,011	0.126	0.019	0.019	0.019
Board 2 (m)	85,902	0.124	0.015	0.015	0.015
Board 3 (m)	69,560	0.113	0.020	0.020	0.020
Board 4 (m)	55,386	0.114	0.014	0.014	0.014
Ground 0 (m)	681,624	0.164	0.022	0.022	0.022
Ground 1 (m)	609,837	0.156	0.021	0.021	0.021
Ground 2 (m)	185,184	0.212	0.025	0.024	0.024

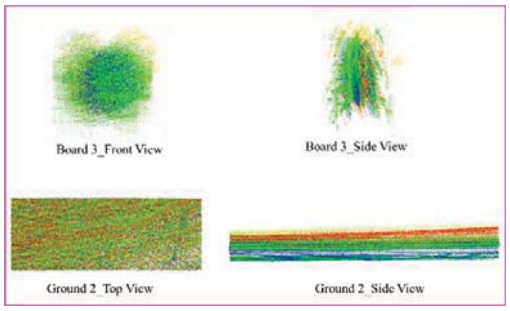

(a)

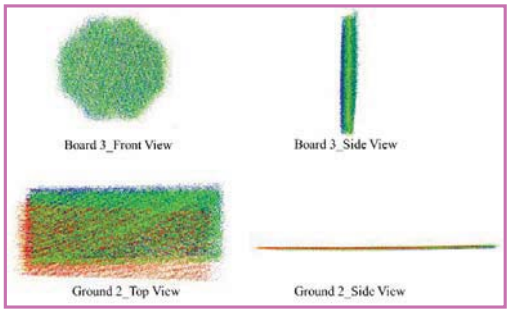

(b)

Figure 9. Qualitative evaluation of some of the extracted boards and ground patches (a) before calibration, and (b) after calibration

Table 6. A comparison of single sensor calibration and multi-sensor calibration

		VLP-16+HDL-32E		VLP-16+HDL-32E	
	Number of Points	Before Single Sensor Calibration	After Single Sensor Calibration	Before Multi Sensor Calibration	After Multi-Sensor Calibration
Board 0 (m)	62,329	0.126	0.018	0.126	0.018
Board 1 (m)	73,011	0.126	0.019	0.126	0.019
Board 2 (m)	85,902	0.124	0.015	0.124	0.015
Board 3 (m)	69,560	0.113	0.019	0.113	0.020
Board 4 (m)	55,386	0.114	0.014	0.114	0.014
Ground 0 (m)	681,624	0.160	0.032	0.160	0.022
Ground 1 (m)	609,837	0.151	0.031	0.151	0.021
Ground 2 (m)	185,184	0.196	0.031	0.196	0.024

From the comparison in Table 6, we can tell that the single-sensor calibration and multi-sensor calibration can reach similar accuracies for the board features but not for ground patches because in case of single-sensor calibration, the Z-value of lever arm will be fixed for both the sensors separately due to which the relative elevation between the two sensors will not be determined. But, in case of multi-sensor calibration, the Z-value of lever arm will be fixed only for one of the sensors which would lead to an accurate estimate for the relative elevation between the two sensors. Hence, the RMSE of ground patches after multi-sensor calibration are all smaller than the ones after single sensor calibration. Another benefit of multi-sensor calibration is that the mounting parameters for all the sensors can be derived simultaneously, but for single sensor calibration, each sensor has to be calibrated separately. So, the number of calibrations depends on the number of sensors.

C. Lane Width Evaluation

One of the applications of point cloud reconstruction is lane width evaluation for road safety inspection. When the lane width is narrow, it is considered less than the standard as it increases the probability of accidents and traffic congestions. So, after the calibration, the data collected for a road is reconstructed using the newly determined mounting parameters. Compared to asphalt, lane markers have higher reflectivity; hence, they can be identified from intensity data in a point cloud and used to determine the lane width. The point clouds from HDL-32E and VLP-16 with digitized lane markers (i.e., red and yellow dots) are shown in Figure 10. The normal distance from the red dots to yellow line (i.e., lane width) is shown in Figure 11. The ground truth of the corresponding area is shown in Figure 12. To evaluate the LiDAR-based lane width, the corresponding value from ground truth is computed by averaging four values, i.e., distance between inner bounds, outer bounds, inner and outer bounds, and outer and inner bounds of yellow and white line, respectively. The comparison of LiDAR-based lane width and its value from ground truth is shown in Figure 13.

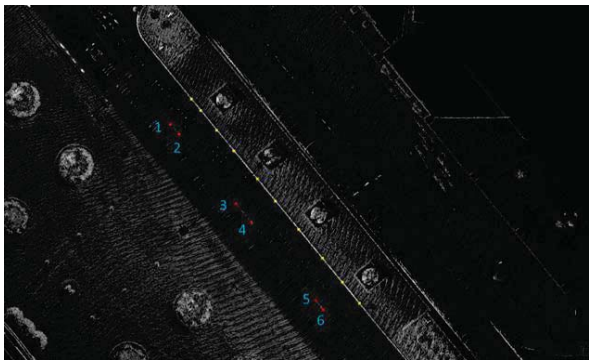

Figure 10. Digitized lane marker based on point clouds from HDL-32E and VLP-16, obtained from a single drive-run

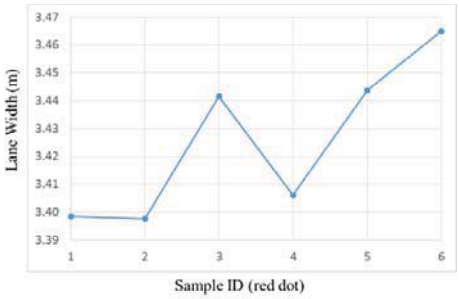

Figure 11. LiDAR-based Lane width obtained using the digitized points

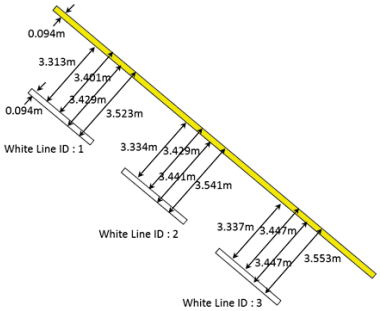

Figure 12. Ground Truth of Lane Width

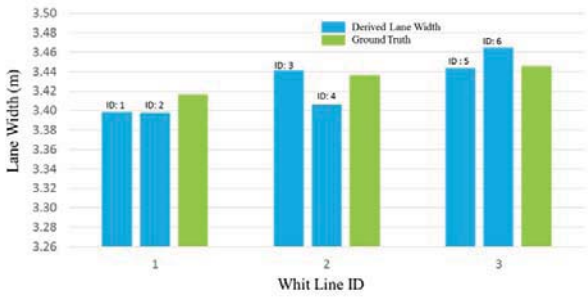

Figure 13. Comparison of LiDAR-based lane width and ground truth lane width

From Figure 13, it is inferred that the difference between the LiDAR-based lane width and ground truth ranges from 0.002 m to 0.030 m and the average is 0.015 m. Considering the random error in ground truth measurements, laser unit measurements, GNSS/INS measurements, and digitization of lane markers, an average bias of 0.015 m is acceptable for this application. From this experiment, it is demonstrated that the proposed calibration procedure can provide highly accurate mounting parameters and the generated point cloud can be used for applications with high accuracy requirements.

5. CONCLUSIONS AND RECOMMENDATIONS FOR FUTURE RESEARCH

In this paper, we provide a multi-sensor LiDAR system calibration method for deriving the mounting parameters simultaneously, instead of performing a separate calibration for each sensor. With the adopted modified weight matrix, the calibration procedure can utilize different types of conjugate features (i.e., planar, linear/cylindrical) at the same time. The proposed iterative calibration method is capable of deriving accurate mounting parameters, even if the initial estimates are considerably inaccurate. Both single unit calibration and multi-unit calibration are conducted using the proposed procedure and both of them can reach an RMSE value of 2 cm for the normal distances of the points from the best-fitting plane/line for the corresponding features. Moreover, this paper uses lane width evaluation to demonstrate that the proposed calibration procedure can derive the mounting parameters accurate enough to be used for an application with a high accuracy requirement. Future work will focus on combining the mounting parameters (i.e., extrinsic parameters) and sensor parameters (i.e., intrinsic parameters) to obtain a comprehensive calibration leading to even more accurate point clouds. Also, using lane markers as calibration primitives will also be investigated.

ACKNOWLEDGMENT

This work was supported in part by the Joint Transportation Research Program – administered by the Indiana Department of Transportation and Purdue University – and the Advanced Research Projects Agency-Energy (ARPA-E), U.S. Department of Energy, under Award Number DE-AR0000593. The implementation of the proposed methodology is supported by Ronald Benziger. The contents of this paper reflect the views of the authors, who are responsible for the facts and the accuracy of the data presented herein, and do not necessarily reflect the official views or policies of the sponsoring organizations.

REFERENCES

Atanacio-Jiménez, G., González-Barbosa, J. J., Hurtado-Ramos, J. B., Ornelas-Rodríguez, F. J., Jiménez-Hernández, H., García-Ramirez, T., & González-Barbosa, R, 2011. LIDAR velodyne HDL-64E calibration using pattern planes. International Journal of Advanced Robotic Systems, 8(5), 59.

Chan, T. O., Lichti, D. D., & Belton, D., 2013. Temporal analysis and automatic calibration of the velodyne HDL-32E LiDAR system. ISPRS Annals of the photogrammetry, remote sensing and spatial information sciences, 2(5/W2), 61-66.

Choi, J., 2014. Hybrid map-based SLAM using a Velodyne laser scanner. In Intelligent Transportation Systems (ITSC), 2014 IEEE 17th International Conference on (pp. 3082-3087). IEEE.

Glennie, C., Brooks, B., Ericksen, T., Hauser, D., Hudnut, K., Foster, J., & Avery, J., 2013. Compact multipurpose mobile laser scanning system—Initial tests and results. Remote Sensing, 5(2), 521-538.

Glennie, C. L., Kusari, A., & Facchin, A., 2016. Calibration and stability analysis of the vlp-16 laser scanner. ISPRS-International Archives of the Photogrammetry, Remote Sensing and Spatial Information Sciences, 3, W4.

He, M., Zhao, H., Davoine, F., Cui, J., & Zha, H., 2013. Pairwise LIDAR calibration using multi-type 3D geometric features in natural scene. In Intelligent Robots and Systems (IROS), 2013 IEEE/RSJ International Conference on (pp. 1828-1835). IEEE.

Lin, H., Gao, J., Zhou, Y., Lu, G., Ye, M., Zhang, C., Liu, L. & Yang, R., 2013. Semantic decomposition and reconstruction of residential scenes from LiDAR data. ACM Transactions on Graphics (TOG), 32(4), 66.

Novatel, 2014. Novatel SPAN-CPT User's Manual, http://www.novatel.com/assets/Documents/Manuals/om-20000122.pdf (Accessed 20 Feb 2017).

Puente, I., González-Jorge, H., Martínez-Sánchez, J., & Arias, P. (2013). Review of mobile mapping and surveying technologies. Measurement, 46(7), 2127-2145.

Schwarz, B., 2010. LIDAR: Mapping the world in 3D. Nature Photonics, 4(7), 429.

Underwood, J., Hill, A., & Scheding, S., 2007. Calibration of range sensor pose on mobile platforms. In Intelligent Robots and Systems, 2007. IROS 2007. IEEE/RSJ International Conference on (pp. 3866-3871). IEEE.

Vallet, B., Xiao, W., & Brédif, M., 2015. Extracting mobile objects in images using a velodyne lidar point cloud. ISPRS Annals of the Photogrammetry, Remote Sensing and Spatial Information Sciences, 2(3), 247.

Velodyne, 2016a. Velodyne HDL-32E User Manual, http://velodynelidar.com/docs/manuals/63-9113%20REV%20K%20MANUAL,USER'S,HDL-32E_Outlined.pdf (Accessed 20 Feb 2017).

Velodyne, 2016b. Velodyne VLP-16 User Manual, http://velodynelidar.com/docs/manuals/63-9243%20Rev%20B%20User%20Manual%20and%20Programming%20Guide,VLP-16.pdf (Accessed 20 Feb 2017).

Williams, K., Olsen, M. J., Roe, G. V., & Glennie, C., 2013. Synthesis of transportation applications of mobile LiDAR. Remote Sensing, 5(9), 4652-4692.

Weiss, U., & Biber, P., 2011. Plant detection and mapping for agricultural robots using a 3D LIDAR sensor. Robotics and autonomous systems, 59(5), 265-273.

CORNER FEATURES AIDED INDOOR SLAM FOR UNMANNED VEHICLES

H. A. Mohamed [a,*], A. M. Moussa [a,b], M. M. Elhabiby [c], N. El-Sheimy [a], Abu B. Sesay [d]

[a] Department of Geomatics Engineering, University of Calgary, Calgary, Alberta, Canada - (haytham.abdalla, amelsaye, elsheimy)@ucalgary.ca
[b] Department of Electrical and Computer Engineering, Port-Said University, Egypt
[c] Public Works Department, Ain Shams University, Cairo, Egypt - mmelhabi@ucalgary.ca
[d] Department of Electrical and Computer Engineering, University of Calgary, Calgary, Alberta, Canada - sesay@ucalgary.ca

KEY WORDS: SLAM, Scan Matching, Hector SLAM, Laser Range Finder, Least Squares, ICP, Corner Registration, Line Extraction, Occupancy Grid

ABSTRACT:

Nowadays, many applications require robots and unmanned ground vehicles (UGVs) to navigate inside unknown environments such as search and rescue operations. Whereas, the vehicle should build a map for the unknown environment while simultaneously estimating its position on the map. Simultaneous Localization And Mapping approach (SLAM) presents a solution for this problem. There are many SLAM methods such as fast SLAM, EKF SLAM, Hector SLAM, and V-SLAM. Hector SLAM is a graph based optimization technique that solves the SLAM problem through nonlinear sparse optimization using occupancy grid, which is a widely used method by mobile robots that utilize laser scan range finders. The occupancy grid presents the environment based on probabilistic approach, where the posterior probability for each cell in the grid is calculated using Bayesian theorem. Ultimately, each cell probability will indicate either the cell is occupied, free, or not visited. However, this method can get trapped in local minima because of the employed gradient ascent. Therefore, the multi-resolution map representation, using multiple occupancy grid maps with different cell sizes, is used to avoid getting trapped in local minima. But, indeed this approach increases the time consumption and the memory requirements of the process. This paper proposes an improved Hector SLAM algorithm where a local scan matching process between successive scan frames is initialized using the detected corners. Thereafter, the iterative closest point (ICP) algorithm is used, as a global scan matching, to adjust the output of the local scan matching with the partially constructed map. This initialization step registers the current point cloud, in the laser scanner frame, to the previous point cloud, in the mapping frame, in order to reduce the process time consumption and decrease the multi-resolution map representation into a single level with small grid cell size. Furthermore, the proposed algorithm is a stand-alone algorithm since it does not require external sources such as odometers for initializing the pose of the vehicle at each scan. The performance and time consumption of the proposed approach are studied and compared with single level and multi-resolution map representations of the Hector SLAM in both static and dynamic environments.

1. INTRODUCTION

Vehicle localization and environmental mapping remain fundamental challenges for operating unmanned vehicles in unknown indoor environments (Santos, 2013) (Arras, 2003). Dynamic environments add more challenges to the UGV (Wolf, 2004). SLAM approach addresses these challenges by incrementally accumulating the current observed portion of the environment with the partial map that has been built, while simultaneously estimating the vehicle's pose. The motivation of using SLAM approach is divided into two different objectives (Siciliano, 2008). One is to maintain an accurate estimation of the vehicle's navigation parameters (Shu, 2013) and the other explores to build an accurate map (Zhao, 2016). According to the motivation, SLAM has been utilized with different sensors such as LIDAR, sonar, RGB camera, and laser range finder.

Typically, Hector SLAM approach can achieve accurate 2D maps of the environments under different scenarios (Kamarudin, 2015). Hector SLAM is a graph based optimization technique that solves scan matching process using Gauss-Newton approach. Consequently, Hector SLAM seeks to estimate the rigid transformation parameters that minimize the alignment error between the current scan and the partially constructed map. Hector SLAM is also defined as graph based because it represents the environments using 2D occupancy grid. The occupancy grid models the surrounding environment based on probabilistic approach (Ozisik, 2008). Thus, the posterior probability for each cell in the grid is calculated from the current sensor's observation and the cell prior probability using Bayesian theorem. Ultimately, each cell probability will indicate either the cell is occupied, free, or not visited.

In some scenarios, Hector SLAM method gets trapped in local minima because of the gradient ascent. Therefore, the multi-resolution map representation, using multiple occupancy grid maps with different cell sizes, is used to avoid getting trapped in local minima (Kohlbrecher, 2011). Whereas, the recommended grid cell size of the low level is half the resolution of the one that is directly above it. Furthermore, the alignment process of each map level is implemented such that the lowest map level is updated using the estimated rigid transformation parameters that is generated from the previous map level. Therefore, this approach increases the time consumption and the memory requirements of the process.

This research paper proposes an improved Hector SLAM algorithm where the scan matching process between successive scan frames is initialized using the detected corners. This initialization step pursues to register the current point cloud, in the laser scanner frame, to the previous point cloud, in the mapping frame, in order to reduce the process time consumption and decrease the required multi-resolution map representation into a single level with small grid cell size. The proposed algorithm is a stand-alone algorithm because it does not require external sources to initialize the pose of the vehicle at each scan. This algorithm utilizes a single low cost 2D laser scan range finder, RPLIDAR 360°, for data collection. It is characterized by approximately low detection range of 6m, max

* Corresponding author

scan rate of 7 Hz, and the angular resolution at the max scan rate is 1.5°.

This research paper is organized as follows: Section 2 describes the overview of the proposed algorithm structure. The used methodology is explained in two phases, where Section 3 illustrates the first phase for local scan matching, while the second phase, the global scan matching, is demonstrated in Section 4. The detection and removal of the dynamic environment is presented and discussed in Section 5. The experimental results are shown in Section 6, and finally the conclusion is presented in Section 7.

2. OVERALL STRUCTURE OF THE PROPOSED ALGORITHM

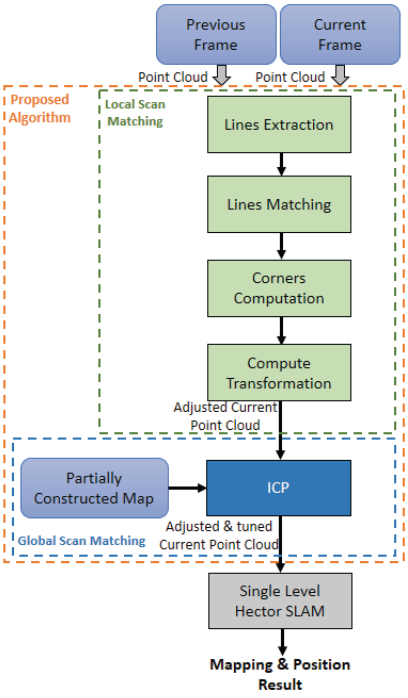

Figure 1. Overall structure of the used algorithm

Figure 1 shows the overall structure of the algorithm used. For every two consecutive scans, the algorithm detects lines, as a preliminary step, from the laser range finder point cloud to exploit the robustness of the line matching compared with the point matching process, and the ability of lines to withstand the perturbation of the moving objects in the dynamic environments (Yin, 2014).

The current detected lines are matched with the previous scan lines after checking mutual compatibility. Corners are being detected, in both scans, from all intersections between the detected lines nevertheless of the physical intersection. Thereafter, the transformation parameters between the successive scans are estimated, in the scanner frame, utilizing the detected corners. This local scan matching yields an adjusted current point cloud which is ready for global scan matching.

Thereafter, iterative closest point (ICP) algorithm (Besl and McKay, 1992) is conducted as a fine-tuning step between the adjusted current point cloud, in the laser scanner frame (l-frame), and the partially constructed map as a global scan matching. The resultant of these two steps is fed to the Hector SLAM. Finally, single level of the Hector SLAM, with small grid cell size such as 5 cm, is adequate for solution convergence instead of multi-level Hector SLAM.

3. LOCAL SCAN MATCHING PHASE

3.1 Line Extraction

Figure 2 shows the detected lines for one scan, in the l-frame, utilizing the line tracking algorithm (LT) and principal component analysis (PCA). The line numbers represent their detection order in the scan, while the red asterisk shows the position of the laser scanner.

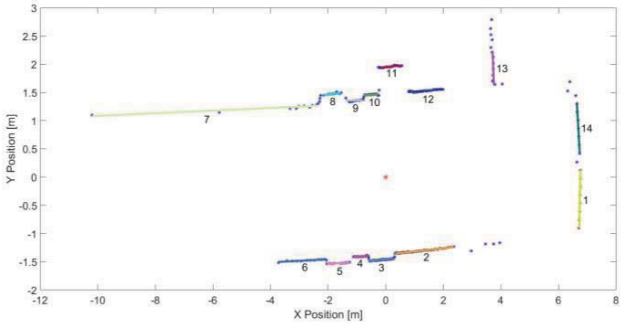

Figure 2. Point cloud data and its extracted lines using line tracking algorithm for one scan in the l-frame

Each point cloud is congregated into groups using the LT algorithm (Muñoz, 2013). Remarkably, the LT algorithm is characterized by simplicity and low time complexity (Borges, 2004), as the time constraint is a critical factor such real-time system. Thereafter, PCA is applied to estimate the fitting line for each group (Jolliffe, 2002). The principal direction of each group is represented by the eigenvector with the highest eigenvalue. While the robustness of each fitted line is represented by the second eigenvector. Short lines which have been detected from small number of points, less than a threshold, are excluded. The probability of line availability and the processing time in different indoor environments have been evaluated in previous work (Mohamed, 2016).

3.2 Line Matching

The aim of this step is to identify matched lines in the current scan within the previous scan lines to facilitate the corner's matching process. The line in the current scan is chosen to be matched with the previous line if all the requirements, described hereafter, have been met.

The inscribed angles between each line of the current scan are calculated with all lines of the previous scan and matching candidate lines are selected according to an angle threshold. Moreover, the orthogonal distances from the origin of the l-frame; the laser scanner position, to all the detected lines are computed in both scans. The projection points of the scanner position onto the detected lines are also calculated. Each line is chosen to be matched when the difference of the orthogonal distance and the Euclidean distance of the projection points are small as possible. Otherwise, there is no matching between the current line with any line in the previous scan.

Figure 3 shows the matched lines, having same colour, between two consecutive scans. Each line is represented by an index

number. The red asterisk represents the position of the laser scanner in the l-frame.

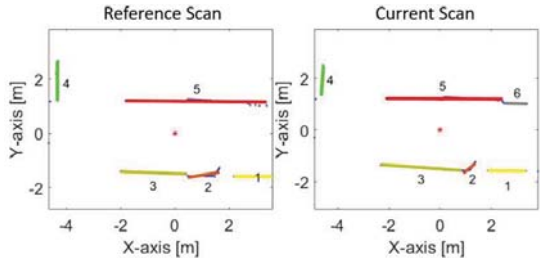

Figure 3. Two successive scans presenting the reference and current scans

3.3 Corners Determination

Thereafter, the corners are calculated from the intersections of all the matched lines in each scan despite of the physical intersection. The uncertainties of the detected corners are calculated from the covariance of the corners (C_c) using the detected lines' variances. The second eigenvalue for each detected line represents the precision of the line. Thus, each matched line is bounded by two deviated lines showing its precision. Consequently, confidence region is constructed around each corner from the intersections of these boundary lines.

Figure 4 shows the confidence ellipse region. The green dashed lines present the boundary lines scaled 25 times for illustration. The red ellipses are the confidence regions. Subsequently, the covariance matrices are employed in the least squares registration step.

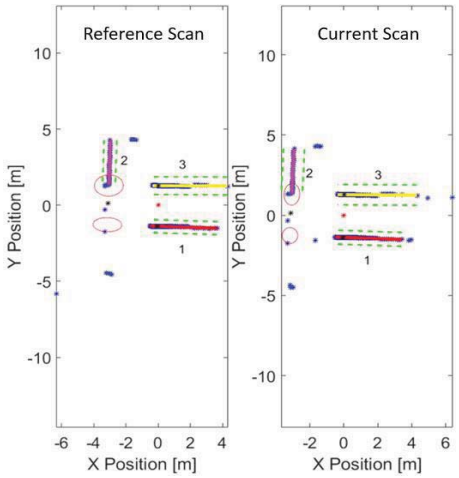

Figure 4. Confidence ellipse region

3.4 Corners Registration

Corners registration is a more cohesive correspondence scheme than the point-to-point scan matching because the probability of the outlier's association is lower. To estimate the local transformation parameters $(\alpha, x_{trans}, y_{trans})$ between the consecutive scans, the weighted least squares method is performed using the detected corners and their variance covariance matrices.

The relation of the consecutive corners can be expressed as (Mohamed, 2016):

$$(T)_{3x3} * (P_c)_{3x2n} = (P_p)_{3x2n} \quad (1)$$

$$\cos(\alpha)\, x_{ci} + \sin(\alpha)\, y_{ci} + x_{trans} = x_{pi} \quad (2)$$

$$-\sin(\alpha)\, x_{ci} + \cos(\alpha)\, y_{ci} + y_{trans} = x_{pi} \quad (3)$$

where T = transformation matrix
P_c = corners points from the current scan
P_p = corners points from the previous scan
n = number of the points in the point cloud
α = rotation angle between the two scans
x_{trans} = translation in the x direction
y_{trans} = translation in the y direction

To minimize the weighted sum of the squares of the residual, Equation (1) is adjusted as given, while (W) is the point's weight matrix:

$$(W)_{2nx2n} * (P_c)_{2nx4} * (x)_{4x1} = (W)_{2nx2n} * (P_p)_{2nx1} \quad (4)$$

$$(x)_{4x1} = \begin{bmatrix} \cos\alpha \\ \sin\alpha \\ x_{trans} \\ y_{trans} \end{bmatrix} \quad (5)$$

$$(P_c)_{2nx4} = \begin{bmatrix} P_{c1x} & P_{c1y} & 1 & 0 \\ P_{c1y} & -P_{c1x} & 0 & 1 \\ \vdots & \vdots & \vdots & \vdots \end{bmatrix} \quad (6)$$

$$(P_p)_{2nx1} = \begin{bmatrix} P_{p1x} \\ P_{p1y} \\ \vdots \end{bmatrix} \quad (7)$$

$$W = C_c^{-1} \quad (8)$$

$$\mathrm{C} = (\mathrm{P_c})^{\mathrm{T}}_{4\mathrm{x}2\mathrm{n}} * (\mathrm{W})_{2\mathrm{nx}2\mathrm{n}} * (\mathrm{P_c})_{2\mathrm{nx}4} \quad (9)$$

$$\mathrm{F} = (\mathrm{P_c})^{\mathrm{T}}_{4\mathrm{x}2\mathrm{n}} * (\mathrm{W})_{2\mathrm{nx}2\mathrm{n}} * (\mathrm{P_p})_{2\mathrm{nx}1} \quad (10)$$

$$\mathrm{C} * (\mathrm{x})_{4\mathrm{x}1} = \mathrm{F} \quad (11)$$

$$(\mathrm{x})_{4\mathrm{x}1} = (\mathrm{C})^{-1} * \mathrm{F} \quad (12)$$

where x = state estimate vector
P_{cix} = current i^{th}corner point in the x direction
P_{ciy} = current i^{th}corner point in the y direction
P_{pix} = previous i^{th}corner point in the x direction
P_{piy} = previous i^{th}corner point in the y direction
W = weight matrix
C_c = covariance matrix of the corners

Ultimately, Equation (13) shows the homogeneous transformation matrix which is calculated from the weighted least square (Aghamohammadi, 2007).

$$T = \begin{bmatrix} \cos\alpha & \sin\alpha & x_{trans} \\ -\sin\alpha & \cos\alpha & y_{trans} \\ 0 & 0 & 1 \end{bmatrix} \quad (13)$$

At the end of this phase, the current point cloud is registered with the previous point cloud in the l-frame. Typically, the current point cloud is adjusted for the global scan matching.

4. GLOBAL SCAN MATCHING PHASE

The last step in the initialization process is accomplished using the ICP algorithm. Although the ICP is susceptible to outlier's association due to fast movement or aggressive manoeuvre, the corner registration aids the ICP algorithm to withstand these situations.

The initialization step prevents the Hector SLAM from getting trapped in local minima. Therefore, the current point cloud is ready to be fed into a single level Hector SALM with small grid cell size instead of multi-level with different grid sizes. Moreover, the initialization step aims to reduce the process time consumption by decreasing the level numbers. After performing the initialization step, Hector SLAM seeks to estimate the rigid transformation, $\varepsilon = (\beta, t_x, t_y)$, that minimizes the total alignment error between the scans and the map (Kohlbrecher, 2011):

$$f(\beta, t_x, t_y) = argmin \sum_{i=1}^{n} [1 - M(S_i(\varepsilon))]^2 \quad (14)$$

where β = rotation angle between the adjusted point cloud and the partially constructed map
t_x = translation in the x direction
t_y = translation in the y direction
$S_i(\varepsilon)$ = point cloud in m − frame as a function of ε
$M(S_i(\varepsilon))$ = map value of the $S_i(\varepsilon)$ $coordinate$
n = number of the points in the point cloud

5. DYNAMIC ENVIRONMENT DETECTION

As mentioned above, the occupancy grid represents the environment based on probabilistic approach. The probability of each cell determines its occupancy status (occupied, free, or not visited). Consequently, the robustness of the cell probabilistic computation method affects the accuracy of the map representation. Therefore, pyramid probabilistic approach is proposed to precisely define the status of the grid cell.

Figure 5 depicts the pyramid probabilistic approach in which the grid cell is divided in the form of pyramid. The max probability is the top of the pyramid and the probability value gradually decreases until reaching the border of the grid cell. Any returned signal on the same cross-section in the cell has the same probability. The probability of each cell is normalized to overcome the distance influence from the objects. This is performed by adding extra layer (cell hit counter) that records all returned signals for each cell. Thus, the probability of the grid cell ranges from 1 to 0.

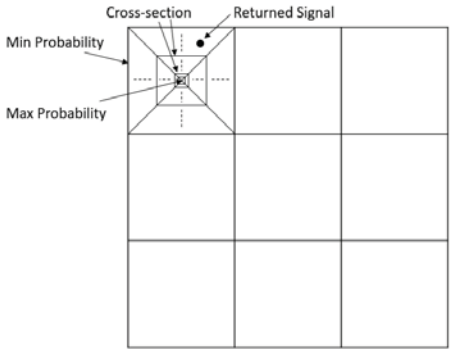

Figure 5. Pyramid probabilistic approach

Since Hector SLAM solves the scan matching process using Gauss-Newton approach by estimating the rigid transformation parameters that minimizes the alignment error between the current scan and the partially constructed map, the dynamic objects significantly affects the accuracy of the map representation as well. Filtering approach is proposed to mitigate this impact of the dynamic objects. The approach depends on adding extra grid layer for the occupancy grid. The layer records the life time for each cell and the counting starts with the first recording of the returned signal. According to the dynamic of the vehicle, the life time threshold is assigned. If the life time of the cell exceeds the life time threshold and the cell hit counter does not exceed a threshold, the cell status is changed from occupied to free due to false occupation caused by moving objects.

6. EXPERIMENTAL RESULTS

The performance and time consumption of the proposed approach are studied and compared with single level and multi-resolution map representation of the Hector SLAM under different conditions in both static and dynamic environments. The recommended grid cell sizes in (Kohlbrecher, 2011) have been used in the presented experiments. These conditions consist of long corridors, aggressive manoeuvres, glass objects, brick walls, and aluminium curtains.

6.1 Static Environment

Figure 6 shows that the Hector SLAM algorithm totally fails to converge and build a map for the first dataset when using single level with grid cell size equal to 5 cm because the algorithm is trapped in local minima. However, it succeeds with higher grid cell size such as 10 cm and more, as shown in Figure 7.

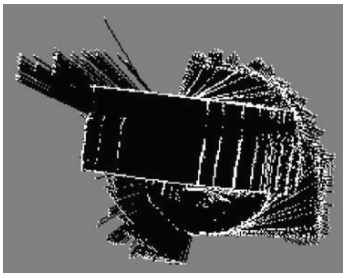

Figure 6. Single level Hector SLAM mapping result using grid cell size 5 cm

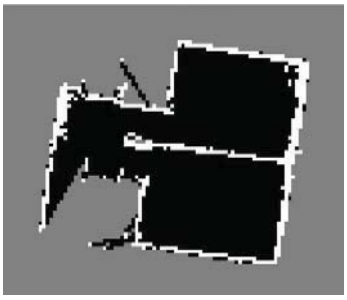

Figure 7. Single level Hector SLAM mapping result using grid cell size 10 cm

Figure 8 and Figure 9 demonstrate the processing time and iteration number of the single level Hector SLAM result using

grid cell size 10 cm. The mean processing time is 0.099 sec while the mean iterations number is 14.66.

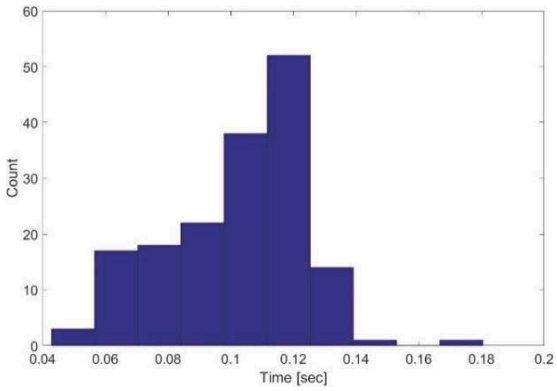

Figure 8. The processing time of the single level Hector SLAM result using 10 cm grid cell size

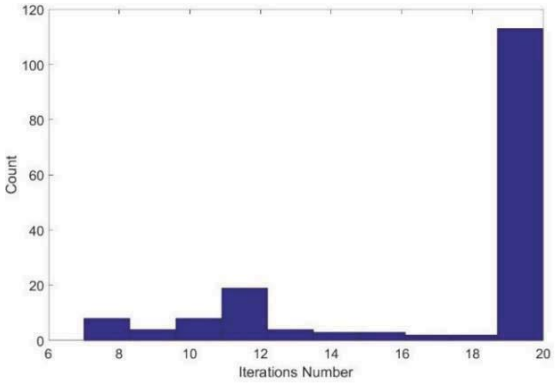

Figure 9. The iterations number of the single level Hector SLAM result using 10 cm grid cell size

Figure 10 shows the mapping result of three levels multi-resolution map representation of the Hector SLAM using grid cell sizes 20, 10, and 5 cm. The mean processing time and number of iterations are 0.19 sec and 38.33 respectively.

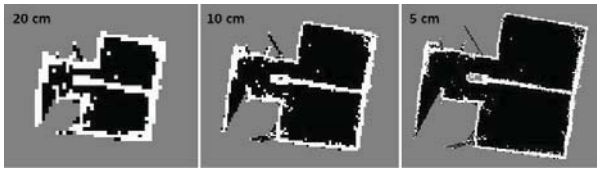

Figure 10. Three levels multi-resolution map representation result using grid cell dimensions 20, 10 and 5 cm

Figure 11 shows the algorithm with single level Hector SLAM mapping and trajectory results using grid cell size 5 cm, the map is displayed in two different representations, occupancy grid map, as shown in sub-figure (a), and point cloud map, as shown in subfigure (b). The red asterisks represent the trajectory of the vehicle. The proposed algorithm succeeds in constructing the map using single level Hector SLAM with approximately small grid cell size.

(a)

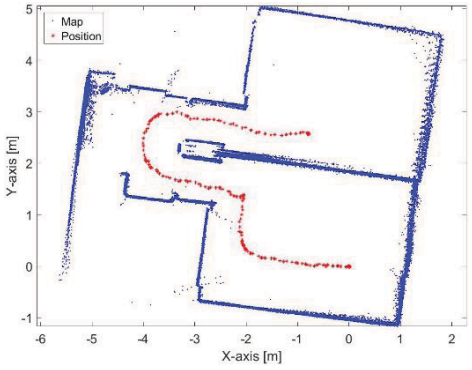

(b)

Figure 11. The proposed algorithm with single level Hector SLAM mapping and trajectory results using grid cell size 5 cm. a) Occupancy grid map b) Point cloud map

Figure 12 and Figure 13 illustrate the result of the processing time and iteration number of the proposed algorithm aiding the single level Hector SLAM using grid cell size 5 cm. The mean processing time is 0.063 sec while the mean iterations number is 11.7.

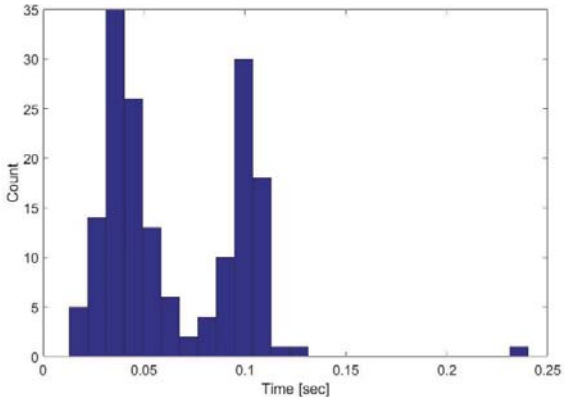

Figure 12. The processing time result of the proposed algorithm using 5 cm grid cell size

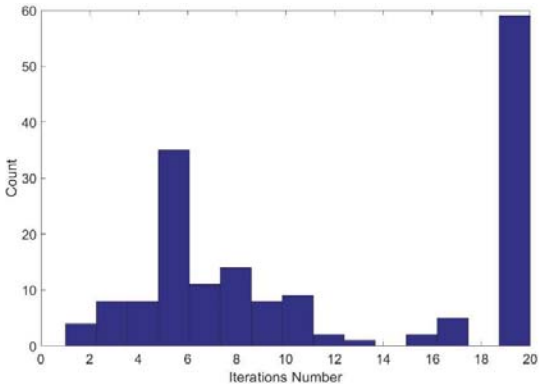

Figure 13. The iterations number result of the proposed algorithm using 5 cm grid cell size

For the second dataset, Hector SLAM using single level fails to converge and build a map for grid cell sizes 20, 10, and 5 cm. Figure 14 shows the mapping result of three levels multi-resolution map representation of the Hector SLAM using grid cell sizes 20, 10, 5 cm. Although, the Hector SLAM algorithm succeeds to converge, but it has a scale problem, as shown clearly in the long vertical corridor. As existence of the noise in the vertical corridor has a significant impact on the convergence result. The mean processing time and number of iterations are 0.39 sec and 47.6 respectively.

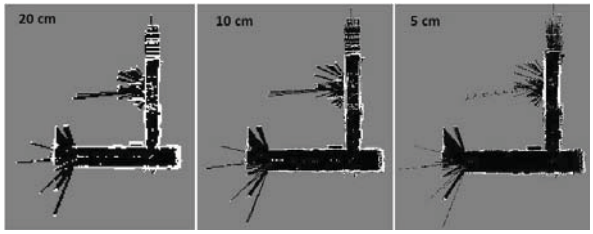

Figure 14. Three levels multi-resolution map representation result using grid cell dimensions 20, 10 and 5 cm

Figure 15 shows the proposed algorithm with single level Hector SLAM mapping and trajectory results using grid cell size 5 cm, the map is displayed in two different representations, occupancy grid map, as shown in sub-figure (a), and point cloud map, as shown in subfigure (b). It is obvious that the vertical corridor has not been affected by the outliers and it slightly overcomes the scale problem as well.

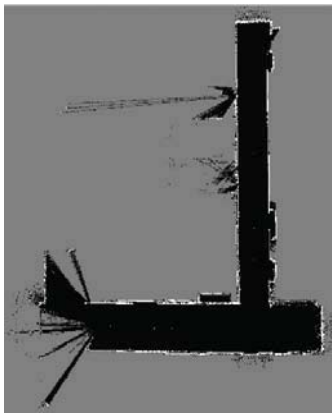

(a)

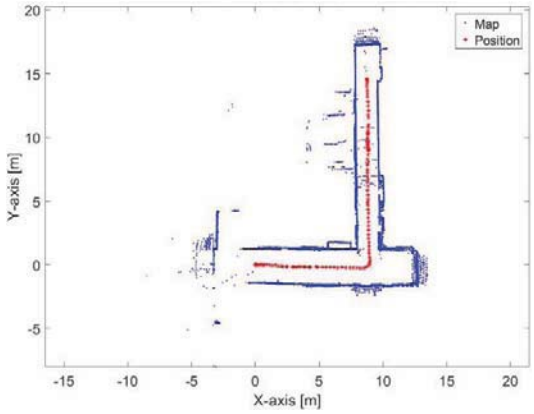

(b)

Figure 15. The proposed algorithm with single level Hector SLAM mapping and trajectory results using grid cell size 5 cm. a) Occupancy grid map b) Point cloud map

Figure 16 and Figure 17 illustrate the result of the processing time and iteration number of the proposed algorithm using grid cell size of 5 cm. The mean processing time is 0.086 sec while the mean iterations number is 15.

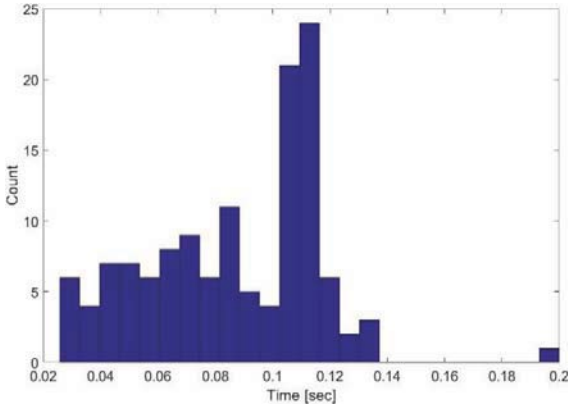

Figure 16. The processing time result of the proposed algorithm using 5 cm grid cell size

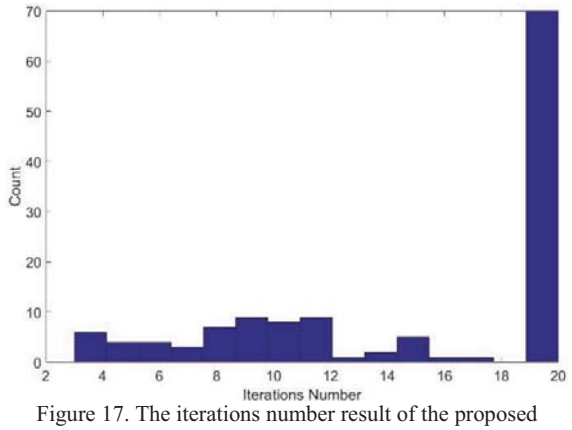

Figure 17. The iterations number result of the proposed algorithm using 5 cm grid cell size

For the third dataset, single level Hector SLAM succeeds to construct a map using 20 cm and higher grid cell size, but fails otherwise. Figure 18 shows the mapping result of three levels multi-resolution map representation of the Hector SLAM using grid cell sizes 20, 10, 5 cm. The mean processing time and

number of iterations are 0.42 sec and 48.27 respectively. The blue arrows exhibit convergence failures in different parts in the map.

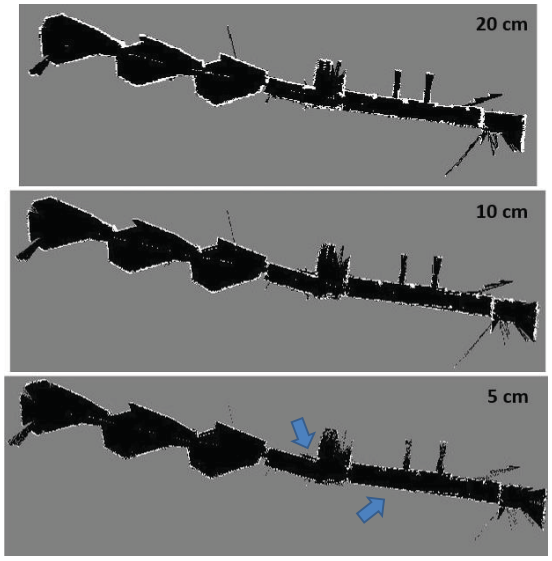

Figure 18. Three levels multi-resolution map representation result using grid cell dimensions 20, 10 and 5 cm

Figure 19 shows the mapping and trajectory results of the proposed algorithm using grid cell size 5 cm. In addition to the processing time reduction, the proposed algorithm avoids the convergence failures exhibited by the three levels Hector SLAM.

(a)

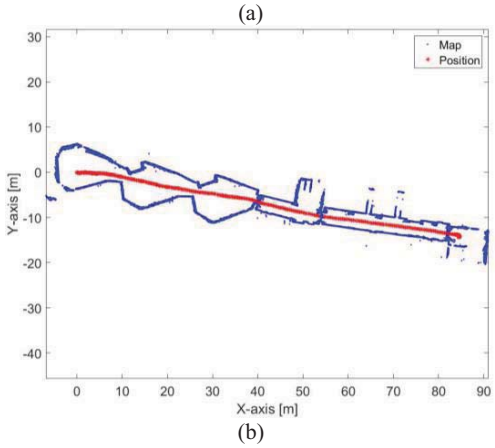

(b)

Figure 19. The proposed algorithm with single level Hector SLAM mapping and trajectory results using grid cell size 5 cm. a) Occupancy grid map b) Point cloud map

Figure 20 and Figure 21 explain the result of the processing time and iteration number of the proposed algorithm with single level Hector SLAM using grid cell size of 5 cm. The mean processing time is 0.078 sec while the mean iterations number is 14.62.

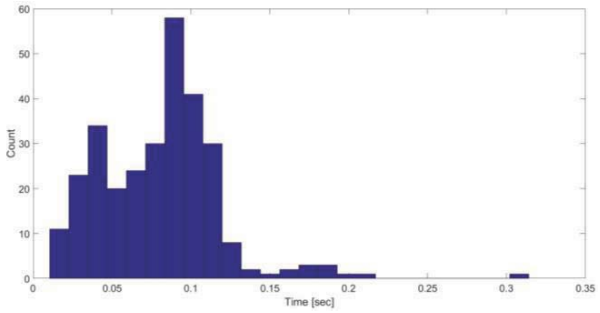

Figure 20. The processing time result of the proposed algorithm with single level Hector SLAM using 5 cm grid cell size

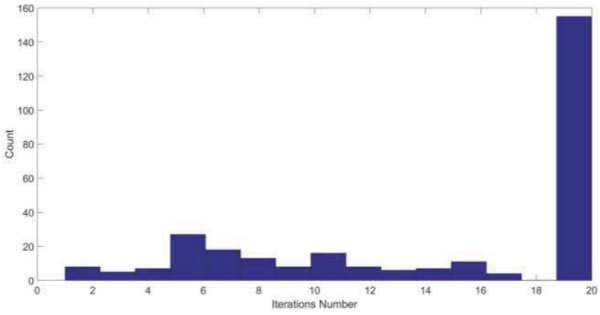

Figure 21. The iterations number result of the proposed algorithm with single level Hector SLAM using 5 cm grid cell size

6.2 Dynamic Environment

Although Hector SLAM uses three levels of multi-resolution map representation, it completely fails to build a map for the dynamic environment dataset, as shown in Figure 22.

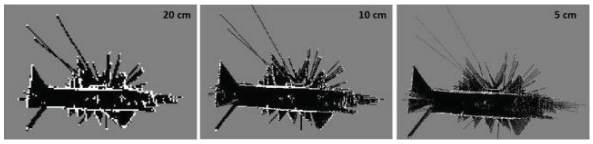

Figure 22. Three levels multi-resolution map representation result using grid cell dimensions 20, 10 and 5 cm

On the other hand, the proposed algorithm succeeds to build a map for the dynamic environment, as shown in Figure 23.

(a)

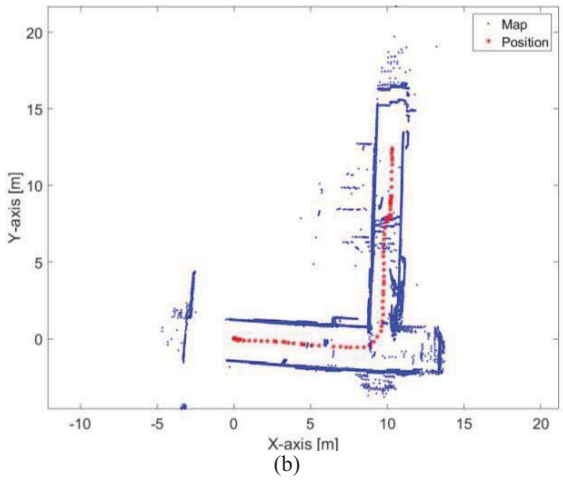

(b)

Figure 23. The proposed algorithm with single level Hector SLAM mapping and trajectory results using grid cell size 5 cm. a) Occupancy grid map b) Point cloud map

Figure 24 and Figure 25 illustrate the result of the processing time and iteration number of the proposed algorithm using grid cell size of 5 cm. The mean processing time is 0.091 sec while the mean iterations number is 14.34.

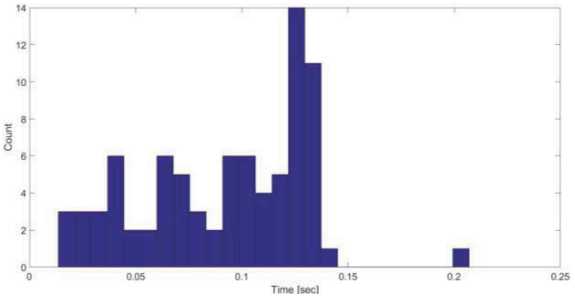

Figure 24. The processing time result of the proposed algorithm using 5 cm grid cell size

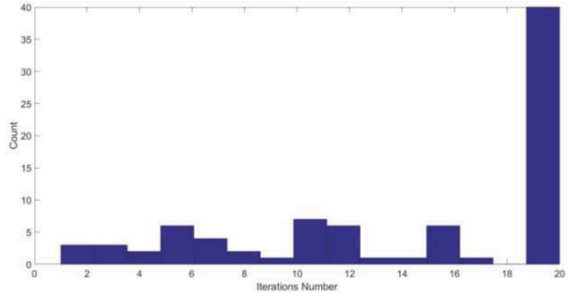

Figure 25. The iterations number result of the proposed algorithm using 5 cm grid cell size

7. CONCLUSION

In conclusion, Hector SLAM is prone to get trapped in local minima due to its gradient ascent approach. Therefore, multiple occupancy grid maps with different cell sizes are used to avoid getting trapped in local minima. Though, this approach increases the time consumption and the memory requirements of the process. The proposed algorithm creates an initialization step to mitigate the time consumption and the memory requirements using corner registration and ICP algorithm.

The algorithm used is compared with the single level and multi-resolution scenarios of the Hector SLAM in static environment. The proposed algorithm aided the single level Hector SLAM, with grid cell size 5 cm, to reduce the convergence time consumption and the iterations number by approximately 36% and 20.2% respectively. It also reduces the convergence time consumption and the iterations number by approximately 72.2% and 68.9% respectively with respect to the three levels multi-resolution Hector SLAM. Furthermore, the proposed algorithm succeeds to help the single level Hector SLAM to converge in the dynamic environment as well, while the multi-resolution map representation of the Hector SLAM completely fails due to the moving objects.

These results indicate the significance of the proposed approach for scan matching through improving matching accuracy and optimizing the processing time, which qualify the approach for real time system implementations.

ACKNOWLEDGEMENTS

This work was supported by Dr. Naser El-Sheimy research funds from NSERC and Canada Research Chairs programs. Thanks also goes to the funding of the first author by the Egyptian government.

REFERENCES

Aghamohammadi, A.A., Taghirad, H.D., Tamjidi, A.H., and Mihankhah, E., 2007. Feature-Based laser scan matching for accurate and high speed mobile robot localization, In: *3rd European Conference on Mobile Robots (ECMR)*, Freiburg, Germany.

Siciliano, B., Khatib, O., 2008. *Springer Handbook of Robotics*. Springer-Verlag Berlin Heidelberg Stürtz GmbH, Würzburg, pp. 871-885.

Wolf, D., and Sukhatme, G.S., 2004. Online simultaneous localization and mapping in dynamic environments, In: *IEEE International Conference on Robotics and Automation (ICRA)*, New Orleans, Louisiana, pp. 1301-1307.

Borges, G.A., and Aldon, M.-J., 2004. Line extraction in 2d range images for mobile robotics. *Journal of Intelligent and Robotic Systems*, 40(3), pp. 267-297.

Mohamed, H.A., Moussa, A.M., Elhabiby, M.M., El-Sheimy, N., and Sesay A.B., 2016. Improved real-time scan matching using corner features, In: *XXIII ISPRS Congress - International Archives of the Photogrammetry, Remote Sensing and Spatial Information Sciences*, Prague, Czech Republic, pp. 533-539.

Jolliffe, I.T., 2002. *Principal Component Analysis 2nd edition*, pp. 1-28.

Yin, J., Carlone, L., Rosa, S., and Bona, B., 2014. Graph-based robust localization and mapping for autonomous mobile robotic navigation, In: *IEEE International Conference on Mechatronics and Automation*, Tianjin, 2014, pp. 1680-1685.

Arras, K.O., 2003. *Feature-Based Robot Navigation in Known and Unknown Environments*. PhD Thesis, the faculty of Science and Technology Engineering, Lausanne federal polytechnic university, Lausanne, Switzerland, pp 1-3.

Kamarudin, K., Mamduh, S.M., Yeon, A.S.A., Visvanathan, R., Shakaff, A.Y.M., Zakaria, A., Kamarudin, L.M., and Rahim, N.A., 2015. Improving performance of 2D SLAM methods by complementing Kinect with laser scanner, In: *IEEE international symposium on robotics and intelligent sensors (IRIS)*, Berjaya Langkawi Resort, Malaysia, pp. 278-283.

Shu, L., Xu, H., and Huang, M., 2013. High speed and accurate laser scan matching using classified features, In: *IEEE International Symposium on Robotics and Sensors Environments (ROSE)*, Washington DC, USA, pp. 61-66.

Zhao, L., Fan, Z., Li, W., Xie, H., and Xiao, Y., 2016. 3D indoor map building with monte Carlo localization in 2D map, In: *International Conference on Industrial Informatics - Computing Technology, Intelligent Technology, Industrial Information Integration (ICIICII)*, Wuhan, pp. 236-240.

Muñoz, L.R., Villanueva, M.G., and Álvarez, C.A.L., 2013. An Extended Line Tracking Algorithm. In: *IEEE International Autumn Meeting on Power, Electronics and Computing (ROPEC)*, Mexico City, Mexico, pp. 1-5.

Santos, J.M., Portugal, D., and Rocha, R.P., 2013. An evaluation of 2D SLAM techniques available in robot operating system, In: *IEEE international Symposium on Safty, Security, and Rescue Robotics (SSRR)*, Linkoping, Sweden.

Ozisik, O., and Yavuz, S., 2008. An occupancy grid based SLAM method, In: *IEEE International Conference on Computational Intelligence for Measurement Systems and Applications*, Istanbul, pp. 117-119.

Besl, P.J., and McKay, N.D., 1992. A method for registration of 3-D shapes, *IEEE Transactions on Pattern Analysis and Machine Intelligence*, 14(2), pp. 239-256.

Kohlbrecher, S., Stryk, O. von, Meyer, J., and Klingauf, U., 2011. A flexible and scalable SLAM system with full 3D motion estimation, In: *IEEE International Symposium on Safety, Security and Rescue Robotics (SSRR)*, Kyoto, pp. 155-160.

PREDICTION OF INERTIAL POSITIONING ERRORS BASED ON GAUSSIAN PROCESS FOR UAVS IN GNSS DENIED ENVIRONMENT

M.M. Mostafa [a, *], A. M. Moussa [a,b],N.El-Sheimy [a] and Abu B. Sesay [c]

[a] Dept. of Geomatics Engineering, University of Calgary, Calgary, Canada - (mostafa.mostafa, amelsaye ,elsheimy)@ucalgary.ca

[b] Department of Electrical Engineering and Computer Engineering, Port-Said University, Egypt

[c] Department of Electrical and Computer Engineering, University of Calgary, Calgary, Canada- (sesay)@ucalgary.ca

KEY WORDS: Gaussian Process Regression, Extended Kalman Filter, Inertial Navigation System

ABSTRACT:

In this paper, a Gaussian Process Regression (GPR) based approach is proposed to improve the positioning reliability and accuracy of the Inertial Navigation System (INS) when the Global Satellite Navigation Systems (GNSS) signal is blocked for short time. The GPR is utilized to model the INS main trend drift errors (due to biases errors) when the GNSS signal is available and to predict these errors during the GNSS signal outage. These predicted errors are used to correct the mechanization output states (velocity and orientation) during this outage period. Three experiments are conducted to evaluate the performance of the proposed method.

1. INTRODUCTION

Recent years have seen an increase in the deployment of autonomous Unmanned Ariel Vehicle (UAV) in many missions such as monitoring of infrastructures (power lines, pipelines, roads), territory surveying and mapping, search and rescue, disaster assessment and management, forest fires and fire-fighting. In order to achieve these missions, an accurate and reliable navigation solution is required. Most of the current autonomous guidance and navigation systems rely on combining both GNSS and INS measurements via a Kalman Filter (KF) for positioning and localization purpose. The GNSS can provide a long-term accuracy with errors limited to a few meters while the INS has the capability of providing a short-term reliable navigation solution. In such challenging tasks and cluttered environments, the GNSS signals can be lost or suffer from the attenuation and multipath effect. During the GNSS signals outage period, the vehicle navigation states are obtained by the INS alone until GNSS signals are reacquired, and hence the navigation solution will deteriorate dramatically due to the drift exhibited by the inertial navigation solution even with short periods of GNSS-outage. Using other aiding sensors or techniques is crucial to limit the accumulated errors associated with INS measurements during the GNSS signal outage. Machine learning approaches can be used to predict the INS errors when the GNSS signal is lost. Then, these predicted errors are employed to compensate the INS mechanization output states to enhance the states accuracy and reliability. Different machine learning algorithms have been utilized to augment the INS during the GNSS signal outage such as neural networks, neuro-fuzzy, Support Vector Machine (SVM) and GPR. An auxiliary fuzzy-based model for predicting the KF positioning error states during GPS signal outages was presented in (Hamid,2007). To develop an appropriate underlying model, intensive data patterns have been collected that covered different vehicle dynamics and motion scenarios to use it through offline training. The difference between KF updated position errors, when GPS is available, and KF predicted one's act as the desired model output during the training process. The time elapsed since losing the GPS signal, accelerometers measurements, gyroscopes measurements and the attitude angles were used as inputs during this stage. Although the test results indicate that the proposed algorithm capable of providing positioning corrections to the INS in standalone mode, it depends mainly on a large amount of offline training data to initialize the desired model. Neuro-fuzzy-based data fusion module for real-time integration of INS and GPS in vehicular navigation has been proposed by (Noureldin, 2007). Results showed that the proposed ANFIS module outperformed previous AI-based data fusion modules with significantly low INS position errors during relatively long GPS outages for both navigational and tactical grades INS.

An enhanced (SVM) based error model was proposed by (Bhatt, 2012). The proposed algorithm was able to overcome other machine learning algorithms problems such as, local minimisation or over-fitting problems. The experimental results demonstrate that, the proposed SVM approach was able to reduce the noise standard deviation by 10–35% for gyroscopes and 61–76% for accelerometers. Moreover, the positional error drifts enhanced by 41% and 80% in comparison to Gauss Markov and neural networks approaches. (Noureldin, 2011) proposed a Delayed Neural Networks (IDNN) approach to model both the INS position and velocity errors based on some past and current epochs of INS position and velocity states, respectively. The proposed algorithm was tested by using dataset that has been collected from different road trajectories by using both navigational and tactical grade INS which were mounted inside land vehicles and integrated with GPS receivers. The results showed that, the prosed algorithm capable of enhancing the positioning accuracy especially for cases of tactical grade INS and long GPS outages.

The GPR has been used to solve different applications problems. For example, the GPR has been trained in (Rasmussen, 2006) to model the robot inverse dynamics. The GPR was used to adequately model the wireless propagation inside complex indoor environments in (Duvallet, 2008).
The GPR based approach was proposed by (M.M. Atia, 2011) to aid the INS during the GPS signal outage for land vehicle. The corrected vehicle velocity and attitude that obtained from the INS output were used as inputs to the GPR during the training

stage and the INS velocity and azimuth deviations from the ground truth (GPS measurements) were used as the desired outputs. When the GPS signal lost, the GPR model is used to predict the INS velocity and azimuth deviations. The predicted INS deviations are used as a virtual update to the KF. A large data set previously collected was used to optimize the hyper-parameters. The proposed technique showed an average position %RMSE reduction of 50% over a large number of experimental runs. The main objective of this paper is to provide a reliable and accurate navigation solution during a short period of GNSS signal outage. This goal is achieved through training a GPR algorithm for a short period in online fashion to correct the mechanization process (velocity and orientation) output states when the GNSS signal is lost.

2. METHODOLOGY

2.1 Training Session

The primary goal of the training session is to generate a nonlinear underlying function that directly maps the inputs to the desired outputs. The training data set is denoted by $= (x_i, \mathrm{w}, y_i)$, where x denotes an input vector of dimension$D$, w denotes the input weights (hyper-parameters) and y denotes the desired output. (GPR) based approach is utilized to achieve this goal and it is used to describe a distribution over functions. It is specified by its mean function $m(\mathrm{x}) = \mathbb{E}[f(\mathrm{x})]$ and the covariance kernel function $k(\mathrm{x}, \mathrm{x}')$ of a real process $f(\mathrm{x})$ as

$$f(x) \sim GP\big(m(x), k(x, x')\big) \tag{1}$$

where $m(\mathrm{x}) = \mathrm{E}[\mathrm{f}(\mathrm{x})]$

The covariance kernel function determines the covariance between output vectors in terms of input vectors and some hyper-parameters. This covariance kernel function can take many forms (Rasmussen, 2006).in this paper the squared exponential covariance function is used as a covariance kernel function to specify the similarity between pairs of random variables as follows:

$$k(\mathrm{x}, \mathrm{x}') = \mathbb{E}\big[\big(f(\mathrm{x}) - m(\mathrm{x})\big)\big(f(\mathrm{x}') - m(\mathrm{x}')\big)\big] \tag{2}$$

The covariance kernel function determines the covariance between output vectors in terms of input vectors and some hyper-parameters. This covariance kernel function can take many forms (Rasmussen, 2006).in this paper the squared exponential covariance function is used as a covariance kernel function to specify the similarity between pairs of random variables as follows

$$cov(f(x), f(x')) = k(x, x') = exp\left(-\frac{1}{2}\frac{|x - x'|^2}{l}\right) \tag{3}$$

where l = length scale

The hyper-parameters are optimized during the training session by maximising the log marginal likelihood of the observations $\{x_i, y_i\}$ conditioned on the hyper-parameters. When the GNSS signal is available, the vehicle orientation and velocity components in the body frame that resulted from the mechanization process after the Extended Kalman Filter (EKF) error states correction are used as inputs to the GPR during the training session. The estimated velocity (in the body frame) and orientation error states that resulted from the GNSS/INS integration in an (EKF) are used as outputs to the GPR during this stage. The used velocity components during the training session are transformed into the body frame to reflect the vehicle dynamics properly. Figure 1 provides an overview of the proposed system during the training session.

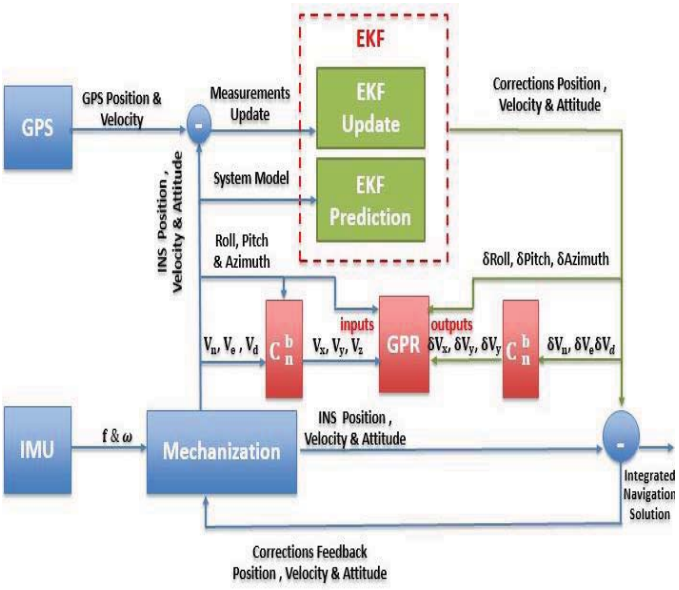

Figure 1. Gaussian Process based approach for inertial drift compensation during the training session

2.2 Prediction Session

Once the GNSS measurements are unavailable, the prediction mode starts to predict the velocity and orientation error states to correct the velocity and orientation drift exhibited by the inertial navigation solution in standalone mode. This error compensation will enhance the 3D position accuracy of the vehicle during the GNSS signal outage. Figure 2 provides an overview of the proposed system during the prediction session.

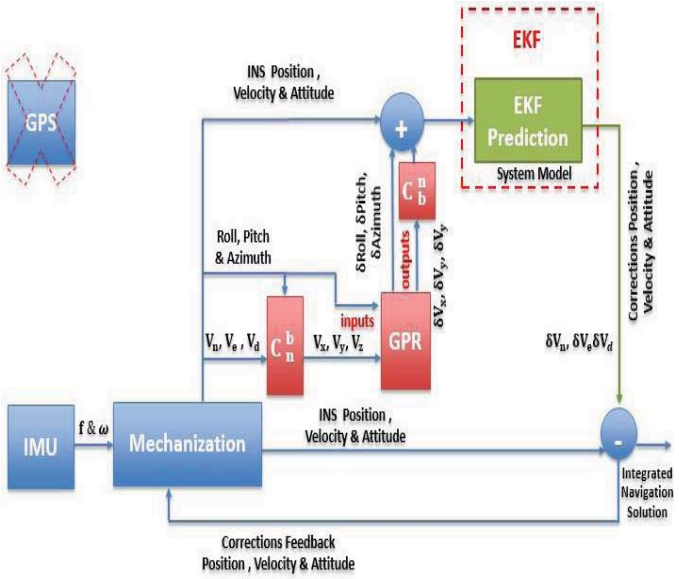

Figure 2 Gaussian Process based approach for inertial drift compensation during the prediction session

Indeed, the prediction process incorporates the knowledge that obtained by the training data $\{(\mathrm{x}_i, f_i | i = 1, \ldots \ldots, n)\}$ and the new inputs (test points x_*) to predict the new outputs values (test

outputs f_*). The joint distribution of the training outputs, f, and the test outputs f_* according to the prior is

$$\begin{bmatrix} f \\ f_* \end{bmatrix} \sim N\left(m(\mathrm{x}), \begin{bmatrix} k(\mathrm{x},\mathrm{x}) & k(\mathrm{x},\mathrm{x}_*) \\ k(\mathrm{x}_*,\mathrm{x}) & k(\mathrm{x}_*,\mathrm{x}_*) \end{bmatrix}\right) \quad (4)$$

where $k(\mathrm{x},\mathrm{x}_*)$ = covariance matrix evaluated at all pairs of training and test points

3. RESULTS

Three experiments are performed in different trajectory parts to evaluate the effectiveness of the proposed algorithm in enhancing the 3D position accuracy during the GNSS signal outage. The UAV flight mission duration is 5.25 minutes. Figure 3 illustrates the three-outage periods along the UAV flight trajectory.

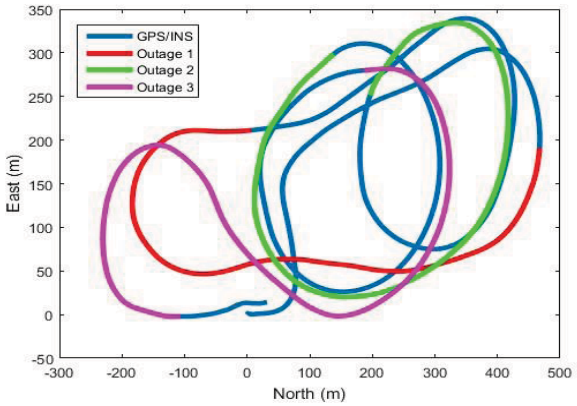

Figure 3. Three-outage periods along the UAV flight trajectory

Figure 4 illustrates the time line for the outage periods along the UAV flight trajectory.

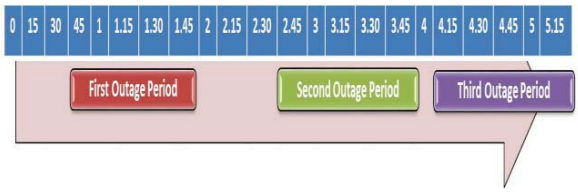

Figure 4. Time line for the outage periods

3.1 First Artificial Outage

The first artificial outage period experiment is performed between 45 second to 1.45 minute after the UAV take off. Figure 5 illustrates a comparison between the estimated 2D flight trajectory outage segments that obtained from the GNSS/INS integration (ground truth segment), INS in standalone mode and INS with GPR correction.

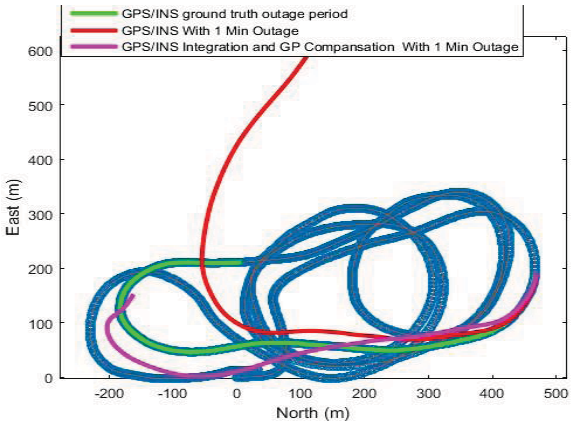

Figure 5. Estimated flight trajectory using INS/GNSS Integration without GNSS outage, INS/GNSS Integration with GNSS outage and INS/GNSS Integration with GNSS outage and GPR correction

Figure 6, 7 and 8 illustrate a comparison between (North, East and Height) position values respectively obtained from (GPR/INS), (INS) during the GNSS outage period with the ground truth-value.

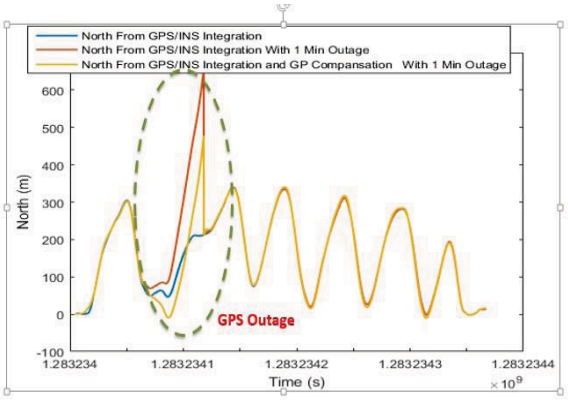

Figure 6. Comparison between (North) values obtained from (INS) and (INS with GPR correction) during the GNSS outage period

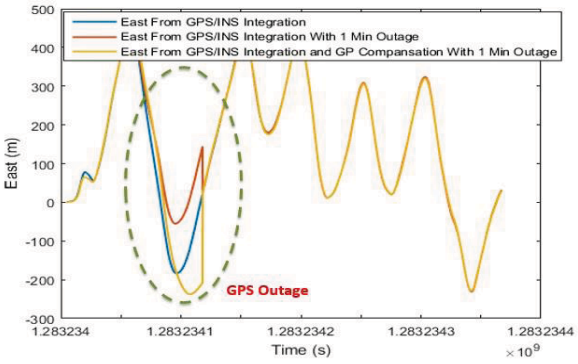

Figure 7. Comparison between (East) values obtained from (INS) and (INS with GPR correction) during the GNSS outage period

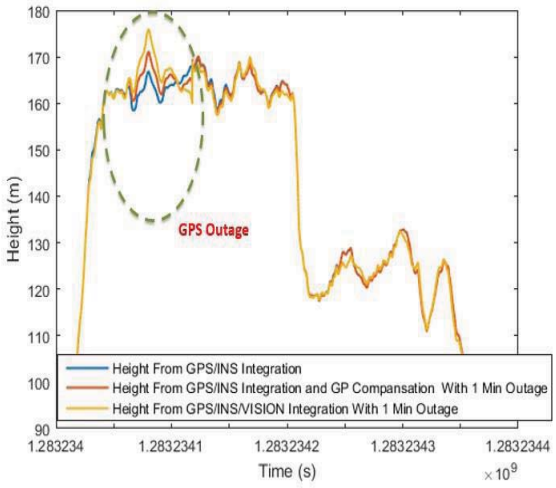

Figure 8. Comparison between (Height) values obtained from (INS) and (INS with GPR correction) during the GNSS outage period

The results indicate that the GPR capable of aiding the INS during a short GNSS signal outage and it demonstrates it is ability to reduce the 3D positioning errors to 49.6% of the INS drift errors in standalone mode even with this small learning period (45sec).

3.2 Second Artificial Outage

The Second artificial outage period experiment is performed between 2.45 min to 3.45 min after the UAV take off. Figure 9 illustrates a comparison between the estimated 2D flight trajectory outage segments obtained from the GNSS/INS integration (ground truth segment), INS in standalone mode and INS with GPR correction. Figures 10, 11 and 12 illustrate a comparison between (North, East and Height) position values respectively that obtained from (GPR/INS), (INS) during the GNSS outage period with the ground truth-value.

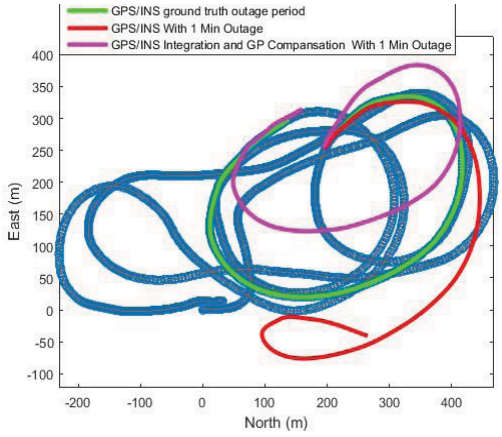

Figure 9. Estimated flight trajectory using INS/GNSS integration without GNSS outage, INS/GNSS integration with GNSS outage and INS/GNSS integration with GNSS outage and GPR correction

The results indicate that the GPR capable of aiding the INS during a short GNSS signal outage and it demonstrates it is ability of reducing the 3D positioning errors to 45.7% of the INS drift errors in standalone mode.

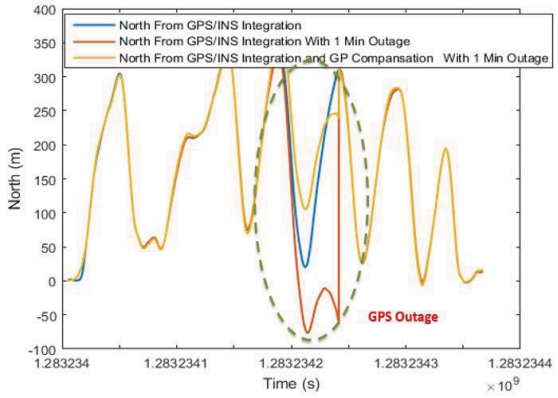

Figure 10. Comparison between (North) values obtained from (INS) and (INS with GPR correction) during the GNSS outage period

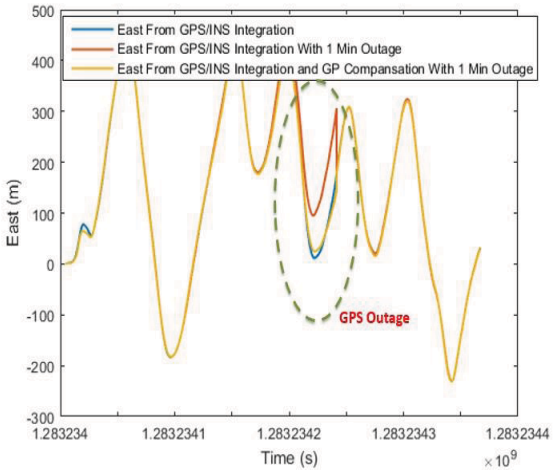

Figure 11. Comparison between (East) values obtained from (INS) and (INS with GPR correction) during the GNSS outage period

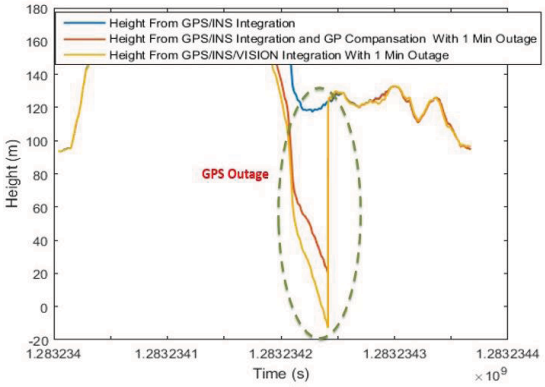

Figure 12. Comparison between (Height) values obtained from (INS) and (INS with GPR correction) during the GNSS outage period

3.3 Third Artificial Outage

The third artificial outage period experiment is performed between 4.15 min to 5.15 min after the UAV take off. Figure 13 illustrates a comparison between the estimated 2D flight trajectory outage segments that obtained from the GNSS/INS integration (ground truth segment), INS in standalone mode and INS with GPR correction. Figures 14, 15 and 16 illustrate a comparison between (North, East and Height) position values respectively that obtained from (GPR/INS), (INS) during the GNSS outage period with the ground truth-value. The results indicate that the GPR capable of aiding the INS during a short GNSS signal outage and it demonstrates it is ability of reducing the 3D positioning errors to 45 % of the INS drift errors in standalone mode.

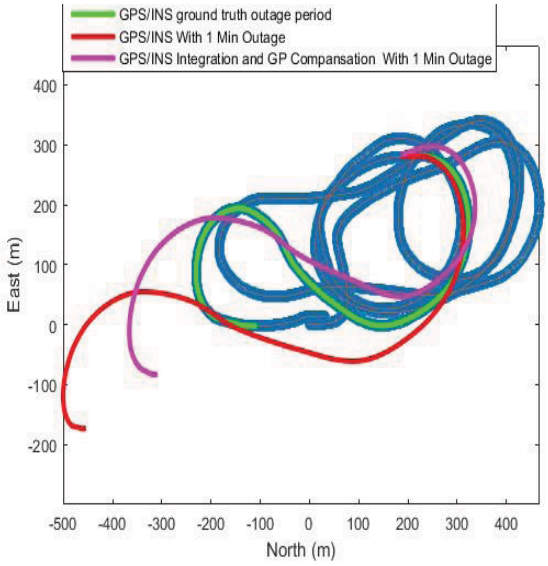

Figure 13. Estimated flight trajectory using INS/GNSS integration without GNSS outage, INS/GNSS integration with GNSS outage and INS/GNSS integration with GNSS outage and GPR correction

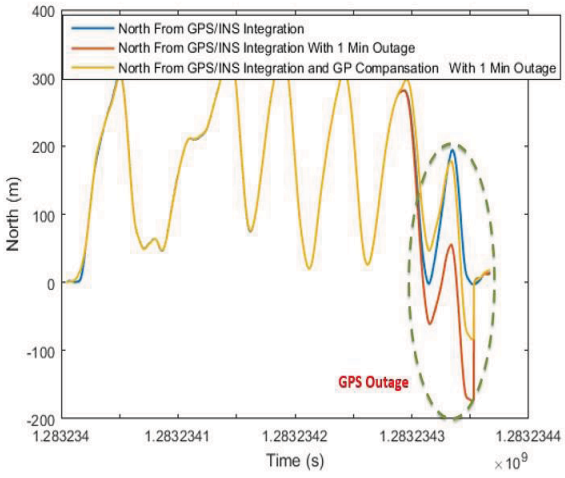

Figure 14. Comparison between (North) values obtained from (INS) and (INS with GPR correction) during the GNSS outage period

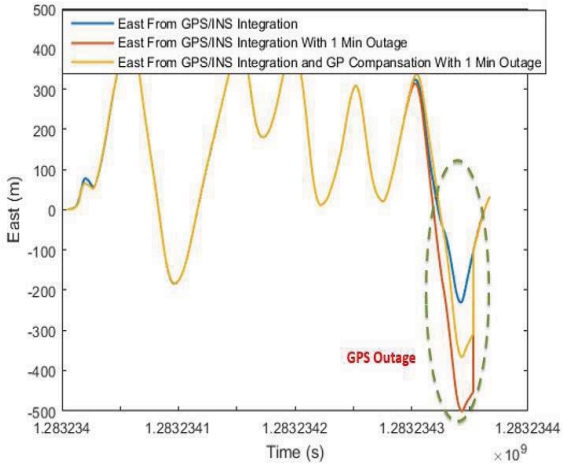

Figure 15. Comparison between (East) values obtained from (INS) and (INS with GPR correction) during the GNSS outage period

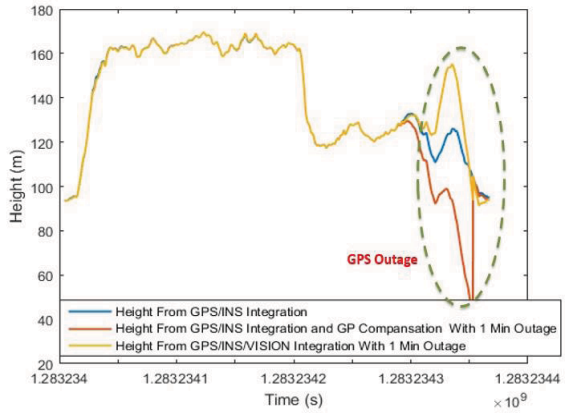

Figure 16. Comparison between (Height) values obtained from (INS) and (INS with GPR correction) during the GNSS outage period

The following table provides a comparison between (RMS Errors) values for the position states that obtained from (INS) and (INS with GPR compensation) during the GNSS outage period with the ground truth-values. The results indicate that the proposed algorithm is outperforming the INS during the GNSS signal outage. Moreover, this technique reduced the average 3D positioning errors to 46.7% of the INS drift errors in standalone mode.

RMS Error (m)	First Outage	Second Outage	Third Outage
INS North Error (m)	66	66.2	46.1
INS&GPR North Error (m)	26.2	28.3	19.6
INS East Error (m)	40	29.3	71.2
INS&GPR East Error (m)	27.9	10.5	32.6
INS Height Error (m)	1.1	23.3	12.1
INS&GPR Height Error (m)	1.9	17.4	6.3
INS 3D position Error (m)	77.2	76.1	85.6
INS&GPR 3D Error (m)	38.3	34.8	38.5
INS&GPR Enhancement %	50.4%	54.3%	55%

Table 1. Comparison between (RMS Errors) values for the position states that obtained from (INS) and (INS with GPR)

In order to assess the GPR ability to model the drift errors, another artificial outage period is performed between min 2.00 to min 3.00 after the UAV take off where an extensive tuning has been performed to remove the bias errors as much as possible during this minute. Figure 17 illustrates a comparison between the estimated 2D flight trajectory outage segments that obtained from the GNSS/INS integration (ground truth segment), INS in standalone mode and INS with GPR correction. Figures 18, 19 and 20 illustrate a comparison between (North, East and Height) position values respectively that obtained from (GPR/INS), (INS) during the GNSS outage period with the ground truth-value. The results indicate that the 3D positioning errors obtained by GPR is worse than the INS in standalone mode by 75.2%. The experiment illustrates the disability of GPR to predict the random noise behavior

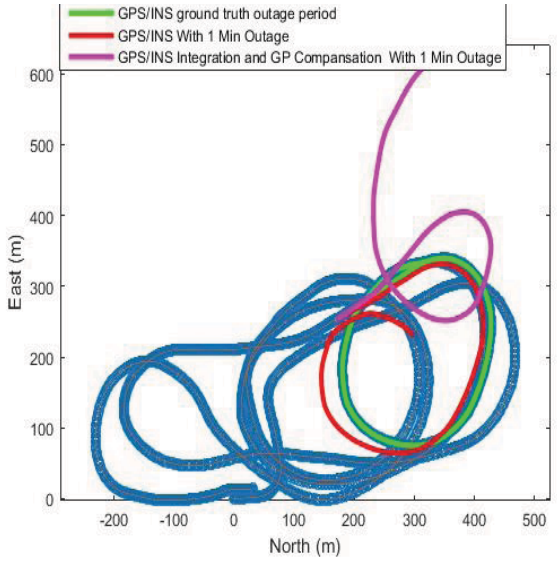

Figure 17. Estimated flight trajectory using INS/GNSS integration without GNSS outage, INS/GNSS integration with GNSS outage and INS/GNSS integration with GNSS outage and GPR correction

.

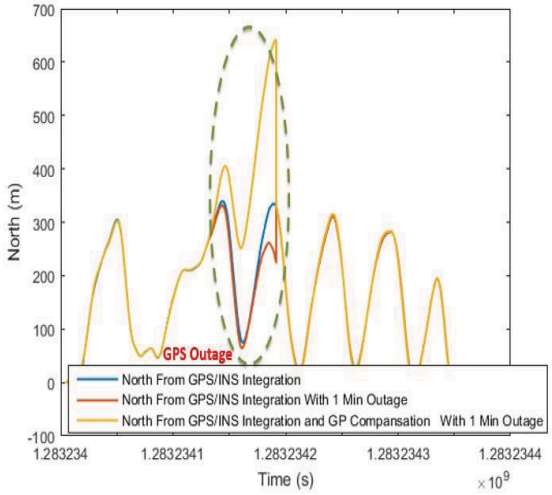

Figure 18. Comparison between (North) values obtained from (INS) and (INS with GPR correction) during the GNSS outage period

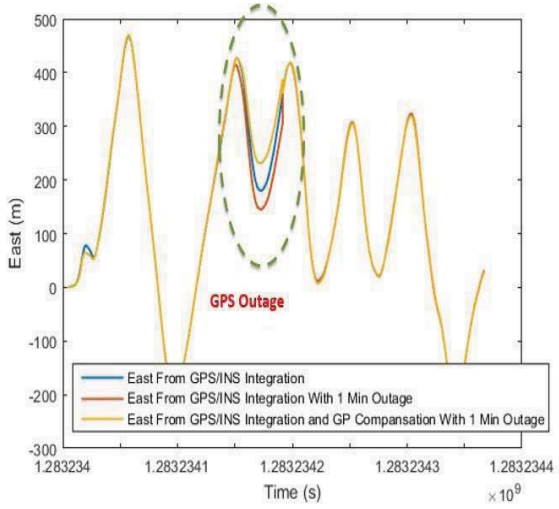

Figure 19. Comparison between (East) values obtained from (INS) and (INS with GPR correction) during the GNSS outage period

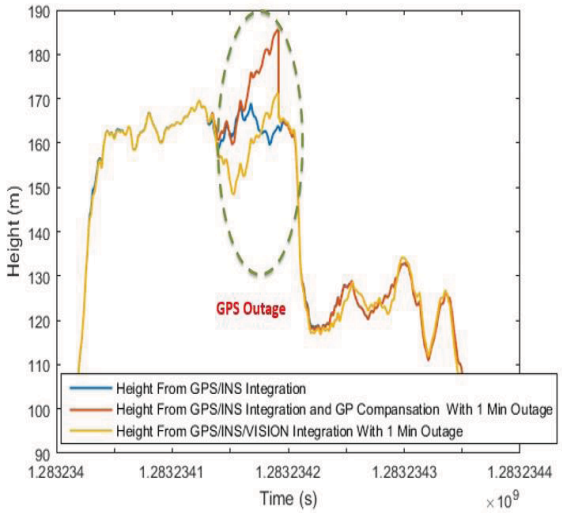

Figure 20. Comparison between (Height) values obtained from (INS) and (INS with GPR correction) during the GNSS outage period

4. CONCLUSION

A GPR based approach is proposed to aid the inertial navigation during GNSS outage periods. The vehicle orientation and velocity components in the body frame that resulted from the mechanization process after the EKF error states correction are used as inputs to the GPR during the learning session. The estimated velocity (in the body frame) and orientation error states that resulted from the GNSS/INS integration in an (EKF) are used as outputs to the GPR during this stage. During the GNSS, signal outage, the predicted velocity and orientation error states from the GPR algorithm are used to compensate the INS mechanization velocity and orientation drift errors. The proposed system is evaluated through three outage periods. An airborne dataset is used to test the proposed approach; this dataset is gathered from a radio-controlled aircraft flown at Kagaru, Queensland, Australia on 31/08/10 (Warren et al. 2014).

The test used the XSens Mti-g INS/GNSS onboard unit to offer the navigation solution with the help of a USB NMEA GNSS.

The experiments results indicate that, the GPR algorithm is able to reduce the average INS 3D positioning errors to 46.7% of the average INS drift errors in standalone mode during the GNSS signal outage even with a short learning period. In addition, the experiments illustrate the ability of GPR to predict only the main trends (due to biases errors) and its failure to predict the random noise behavior.

ACKNOWLEDGEMENTS

This work was supported by Dr. Naser El-Sheimy research funds from NSERC and Canada Research Chairs programs. Thanks also goes to the funding of the first author by the Egyptian government.

REFERENCES

Abdel-Hamid, Walid, Aboelmagd Noureldin, and Naser El-Sheimy. "Adaptive fuzzy prediction of low-cost inertial-based positioning errors." IEEE Transactions on Fuzzy Systems 15.3 (2007): 519-529.

Atia, M. M., A. Noureldin, and M. Korenberg. "Gaussian process regression approach for bridging GPS outages in integrated navigation systems." Electronics letters 47.1 (2011): 52-53. Smith, J., 1987b. Economic printing of color orthophotos. Report KRL-01234, Kennedy Research Laboratories, Arlington, VA, USA.

Bhatt, Deepak, et al. "An enhanced mems error modeling approach based on nu-support vector regression." Sensors 12.7 (2012): 9448-9466.

Duvallet, F., and Tews, A.D.: 'WiFi position estimation in industrial environments using Gaussian processes'. IEEE/RSJ Int. Conf. on Intelligent Robots and Systems, Nice, France, September 2008.

Noureldin, Aboelmagd, Ahmed El-Shafie, and Mohamed Bayoumi. "GPS/INS integration utilizing dynamic neural networks for vehicular navigation." Information Fusion 12.1 (2011): 48-57.

Noureldin, A., A. El-Shafie, and N. El-Sheimy. "Adaptive neuro-fuzzy module for inertial navigation system/global positioning system integration utilising position and velocity updates with real-time cross-validation." IET Radar, Sonar & Navigation 1.5 (2007): 388-396.

Rasmussen, C.E., and Williams, C.: 'Gaussian processes for machine learning' (MIT Press, 2006).

A novel adaptive Kalman filter for MEMS-IMU/Magnetometer fusion

Qifan Zhoua[a,b],*, Hai Zhang, Maan Khedr[b,c], Naser El-Sheimy[b]

[a] School of Automation Science and Electrical Engineering, Beihang University, 100191, Beijing, China- zhanghai@buaa.edu.cn
[b] Dept. of Geomatics Engineering, University of Calgary, Calgary, Alberta, Canada, T2N 1N4,
(qifan.zhou, maan.khedr, elsheimy)@ucalgary.ca
[c] Department of Computer Engineering, Arab Academy for Science and Technology, Alexandria, Egypt

Commission VI, WG VI/4

KEY WORDS: Adaptive Attitude Filter, Redundant Measurement, Kalman Filter, MEMS, Noise Estimation

ABSTRACT:

This paper presents a novel adaptive attitude Kalman filter for MEMS IMU/Magnetometer fusion. The redundant measurement systems based noise estimation theorem is employed to adaptively tune the measurement covariance matrix R in filter and the noise estimation is isolated from the filter prediction and update processes which avoids the negative effect of state estimation error. The proposed algorithm makes use of the short-term accuracy of gyroscope to evaluate the performance of accelerometer derived attitude and the attitude weight derived from different sensors is optimally assigned. Practical experiments are carried out to test the validation of the proposed adaptive attitude filter The achieved results demonstrate that the proposed approach can provide promising orientation solution with fusion of low-cost MEMS IMU and magnetometer.

1. INTRODUCTION

The attitude, which defines the orientation of a coordinate system fixed in body with respect to a reference frame (i.e., local level frame, Earth-Centred, Earth-Fixed), is critical in navigation system. Typically, the gyroscope measurements are processed by an integration algorithm to calculate the attitude of the body frame relative to reference coordinates after the initial alignment process. However, due to the effect of various gyroscope error (i.e. bias, scale factor error, random error), the attitude result will suffer from accumulated error and drift over time. The gyroscope derived orientation cannot provide a long term stable result and can only keep accurate in short term.

In stationary or low dynamic conditions, the specific force vector (i.e., acceleration subtracts gravity) sensed by accelerometers equals to the local gravity acceleration g numerically but is expressed in an opposite direction. In this case, the accelerometer signals can be used to estimate the orientation relative to the horizontal plane. Meanwhile, magnetometers measure the local magnetic field vector to determine the heading relative to the magnetic north. The attitude derived from theses sensors is independent in different time epochs and not impacted by accumulated errors (i.e., the result will not drift). Hence, the gyroscope derived attitude can keep accurate in short term, but will drift over time and diverge eventually; the accelerometer and magnetometer based attitude is positive in restraining drift errors, but is affected by factors such as dynamic condition and local magnetic inference. Aiming to derive a long-term accurate and reliable attitude solution, the attitude filter is designed to optimally fuse the attitude information of different sensors based on the complementary characteristic of inertial sensors and magnetometer

Several studies have been proposed to perform the attitude filter with estimation technology and different system dynamic and measurement models have been developed, such as the linearized Euler angle error equation((Foxlin, 1996), (Setoodeh et al., 2004)), INS Psi-angle error propagation equation((Han and Wang, 2011)), quaternion parameters Choukroun, Bar-Itzhack, and Oshman 2006), Rodrigues parameters attitude update algorithm(Crassidis and Markley, 1996)(Idan, 1996). Additionally, because the IMU may experience different dynamic motions in practical application, the external accelerations will be introduced and cause negative effect on the orientation estimation result. In order to overcome this problem and obtain reliable attitude solution, an adaptive filter is always employed. Wang(Wang et al., 2004), Wei(Li and Wang, 2012) categorized the system dynamic motions into three modes, and designed the measurement variance matrix R tuning strategy and mode switching approach based on the difference between measured accelerations norm and gravity acceleration. Yoo(Yoo et al., 2011) adopted the same strategy and applied it to tune the gain in complementary filter. However, this is a threshold based tuning method, which is sensitive to the chosen value or application, and the threshold selection or designing guide is not discussed. In addition, this method only considers the quantity of the acceleration vector and ignore its direction, so it can introduce large estimation error if the measured specific force equals to g but is not expressed its opposite direction. Hu (Rehbinder and Hu, 2004) used the acceleration norm to evaluate the dynamic condition, and the filter will only use the gyroscope measurement to predict the attitude if the norm is larger than a selected threshold. The research is more concerned with the filter design and stabilization analysis, but stilled suffers from the threshold selection problem. Makni(Makni et al., 2014) employed the residual sequence (Tapley, 1976), which is the innovation sequence adaptive estimation(IAE), to adaptively adjust the R matrix, but the computed R matrix properly loses its positive definite during the online updating process.

Aiming to overcome the aforementioned problems in adaptive attitude filter, a novel redundant measurement systems based noise variance estimation theorem is proposed and proofed, which is also applied to adaptively adjust the contribution of different sensors for the final attitude estimation solution. The proposed theorem makes use of difference operation on measurement system to eliminate the effect of true measurement value and leave only the noise item in the difference sequence.

The advantages of proposed adaptive attitude filter include: 1) the measurement noise item derived by difference operation can best track the actual system dynamic motion and effectively tune the R matrix; 2) using the gyroscope short-term accuracy to evaluate the performance of accelerometer and magnetometer derived attitude.

This paper is organized as follows: Section 2.1 describes the Euler angle based attitude filter design; Section 2,2 introduces the redundant measurement systems based noise estimation theorem; Section 2.3 illustrates the applicability of noise estimation theorem in the attitude filter; Section 3 provides the practical experiment result and Section 4 draws the conclusion.

2. METHODOLOGY

2.1 Euler angle based attitude filter design

The Euler angle update approach is employed to design the attitude filter because this approach is easy to implement, convenient to understand, and has a minimized parameterizing variables number to construct the attitude rotation matrix compared with other attitude representation methods (i.e., DCM, quaternion, Rodrigues parameters). Considering the Euler angles, gyroscope biases, and scale factor errors as system state vector and it consists of three parts.

$$\mathbf{X} = [\mathbf{X}_1 \ \ \mathbf{X}_2 \ \ \mathbf{X}_3]^T \tag{0.1}$$

The $\mathbf{X}_1, \mathbf{X}_2$ and $\mathbf{X}_3$ vectors are defined as:

$$\mathbf{X}_1 = \begin{bmatrix} \theta & \gamma & \varphi \end{bmatrix}^T \quad \mathbf{X}_2 = \begin{bmatrix} b_x & b_y & b_z \end{bmatrix}^T \quad \mathbf{X}_3 = \begin{bmatrix} S_x & S_y & S_z \end{bmatrix}^T \tag{0.2}$$

where x, y and z represent the subscripts for the elements in the b-frame. θ, γ, φ denote pitch, roll and yaw angles. b , S denotes the gyroscope bias and scale factor error. The sensor errors are modelled as the random constants(Maybeck, 1982) and the system dynamic model can be described as:

$$\dot{\mathbf{X}} = f(\mathbf{X}) + \mathbf{G}\mathbf{w}$$
$$\begin{bmatrix} \dot{\mathbf{X}}_1 \\ \dot{\mathbf{X}}_2 \\ \dot{\mathbf{X}}_3 \end{bmatrix} = \begin{bmatrix} \mathbf{A} \\ \mathbf{O}_{3\times3} \\ \mathbf{O}_{3\times3} \end{bmatrix} \begin{bmatrix} \tilde{\boldsymbol{\omega}}_{ib}^b - \mathbf{X}_2 - \mathbf{X}_3 \tilde{\boldsymbol{\omega}}_{ib}^b \\ \mathbf{X}_2 \\ \mathbf{X}_3 \end{bmatrix} + \begin{bmatrix} \mathbf{A} \\ \mathbf{O}_{3\times3} \\ \mathbf{O}_{3\times3} \end{bmatrix} \mathbf{w} \tag{0.3}$$

where, w is the process noise (i.e., the Angular Random Walk (ARW) of gyroscopes). G is the shaping matrix. $\tilde{\boldsymbol{\omega}}_{nb}^b$ denotes the gyroscope measurement which has pre-processed to correct the non-orthogonal error. $\mathbf{O}_{3\times3}$ is a three dimension zeros matrix. Matrix A is expressed as:

$$\mathbf{A} = \begin{bmatrix} \cos\mathbf{X}_1(2) & 0 & \sin\mathbf{X}_1(2) \\ \sin\mathbf{X}_1(2)\tan\mathbf{X}_1(1) & 1 & -\cos\mathbf{X}_1(2)\tan\mathbf{X}_1(1) \\ -\dfrac{\sin\mathbf{X}_1(2)}{\cos\mathbf{X}_1(1)} & 0 & \dfrac{\cos\mathbf{X}_1(2)}{\cos\mathbf{X}_1(1)} \end{bmatrix} \tag{0.4}$$

where, $\mathbf{X}_1(1), \mathbf{X}_1(2), \mathbf{X}_1(3)$ separately denote the three Euler angles, pitch, roll, and yaw in state vector. Although the Euler angle update algorithm will suffer from singular problem and the calculation process discontinue when the pitch angle reaches 90° , an intelligent coordinate switch approach(Qifan and El-Sheimy, 2017) has been proposed to avoid such constrains.

The Euler angles calculated by accelerometers and magnetometers are used as observations. In stationary or low dynamic situation, the specific force measured by accelerometers approximately equals to the local gravity acceleration numerically but is in an opposite direction. Thus, the relationship between accelerometer measurements and Euler angles can be formulated as:

$$\begin{bmatrix} a_x^b \\ a_y^b \\ a_z^b \end{bmatrix} = \mathbf{C}_n^b \begin{bmatrix} 0 \\ 0 \\ g \end{bmatrix} = \begin{bmatrix} -\sin\gamma\cos\theta \cdot g \\ \sin\theta \cdot g \\ \cos\gamma\cos\theta \cdot g \end{bmatrix} \tag{0.5}$$

where (a_x^b, a_y^b, a_z^b) denotes the accelerometer measurement vector in b-frame, g denotes the local gravity value. According to equation (0.5), the pitch and roll angles can be calculated as:

$$\theta_{acc} = \sin^{-1}\left(\frac{a_y^b}{g}\right)$$
$$\gamma_{acc} = \tan^{-1}\left(-\frac{a_x^b}{a_z^b}\right) \tag{0.6}$$

The subscript 'acc' illustrates that the pitch and roll angles are derived through the accelerometer. The azimuth (heading) can be determined by measuring the horizontal component of Earth's magnetic field vector, using a perpendicular pair (or an orthogonal triad) of magnetometers(Caruso, n.d.). A magnetometer triad would measure $m^b = [m_x^b \ m_y^b \ m_z^b]^T$, which is the Earth's magnetic field vector expressed in body frame. If the x-y plane of the body coordinate system is levelled (i.e., is parallel to Earth's local tangent), the magnetometer readings are used to compute heading with respect to magnetic North using the following formula:

$$azimuth = \tan^{-1}\left(\frac{m_{right}}{m_{forward}}\right) = \tan^{-1}\left(\frac{m_x^b}{m_y^b}\right) \tag{0.7}$$

The magnetometer measurement in right and forward directions of the body frame is employed to derive the azimuth. While if the x-y plane is not levelled, we need to map the magnetometer measurement to the locally-level plane through the body-to-locally-level transformation matrix $\mathbf{C}_b^h$ which is calculated by the pitch and roll angles, and then derive the azimuth. This process combines the three following steps:

1) levelling magnetometer measurements to the horizontal plane by using transformation matrix $\mathbf{C}_b^h$;

$$\begin{bmatrix} m_x^h \\ m_y^h \\ m_z^h \end{bmatrix} = \mathbf{C}_b^h \begin{bmatrix} m_x^b \\ m_y^b \\ m_z^b \end{bmatrix} = (\mathbf{C}_3\mathbf{C}_2)^T \begin{bmatrix} m_x^b \\ m_y^b \\ m_z^b \end{bmatrix} = \begin{bmatrix} \cos\gamma & \sin\gamma & -\sin\gamma\cos\theta \\ 0 & \cos\theta & \sin\theta \\ \sin\gamma & -\sin\theta\cos\gamma & \cos\gamma\cos\theta \end{bmatrix}^T \begin{bmatrix} m_x^b \\ m_y^b \\ m_z^b \end{bmatrix} \tag{0.8}$$
$$= \begin{bmatrix} \cos\gamma & 0 & \sin\gamma \\ \sin\gamma\sin\theta & \cos\theta & -\sin\theta\cos\gamma \\ -\sin\gamma\cos\theta & \sin\theta & \cos\gamma\cos\theta \end{bmatrix} \begin{bmatrix} m_x^b \\ m_y^b \\ m_z^b \end{bmatrix}$$

where, (m_x^b, m_y^b, m_z^b) denote the magnetic vector in b-frame, m_x^h, m_y^h , denote the magnetic vector in horizontal plane of n-frame, and m_z^h denotes that in vertical axis of n-frame.

2) calculating the magnetic heading using the horizontal magnetic field components (i.e., the angle between the forward axis and the Earth's magnetic north) according to equation (0.7).

$$\varphi_{mag} = \arctan(\frac{m_x^h}{m_y^h}) = \arctan(\frac{\cos\gamma m_x^b + \sin\gamma m_z^b}{-\sin\gamma\cos\theta m_x^b + \cos\theta m_y^b + \cos\gamma\cos\theta m_z^b}) \quad (0.9)$$

3) computing the geographical heading (i.e., the angle between the forward axis and the Earth's geographic north) by correcting the declination angle to the magnetic heading. The heading calculation is formulated as:

$$\varphi_{geo} = \varphi_{mag} + \varphi_{\text{declination}} \quad (0.10)$$

where φ_{geo} denotes the geographical heading, $\varphi_{\text{declination}}$ denotes the declination. The declination varies with location, and can be obtained from the International Geomagnetic Reference Field (IGRF) model(Finlay et al., 2010).

In this paper, we make use of the orientation results determined by accelerometers and magnetometers as the measurement vector. Combining equation (0.6) and (0.10), the system measurement model is obtained as:

$$\mathbf{Z} = \mathbf{HX} + \mathbf{v} = \begin{bmatrix} 1 & 0 & 0 & \\ 0 & 1 & 0 & \mathbf{O}_{3\times 6} \\ 0 & 0 & 1 & \end{bmatrix}\mathbf{X} + \mathbf{v} \quad (0.11)$$

where, $\mathbf{Z} = \begin{bmatrix} \theta_{acc} & \gamma_{acc} & \varphi_{geo} \end{bmatrix}$ denotes the measurement vector. H denotes the design matrix of observation model and v denotes the measurement noise.

2.2 Redundant measurement systems based noise estimation theorem

We consider that two measurement systems are available for one physical value. Based on this assumption, based on the redundant measurement systems based noise estimation theorem is proposed and the proof is provided.

Theorem:

Assuming that $\mathbf{Z}_1(k)$ and $\mathbf{Z}_2(k)$ are measurements of the value $\mathbf{Z}$ from different systems at time k. The measurements from system 1 and system 2 can be expressed as follows:

$$\begin{aligned} \mathbf{Z}_1(k) &= \mathbf{Z}(k) + \left[\mathbf{f}_1(k) + \mathbf{V}_1(k)\right] \\ \mathbf{Z}_2(k) &= \mathbf{Z}(k) + \left[\mathbf{f}_2(k) + \mathbf{V}_2(k)\right] \end{aligned} \quad (0.12)$$

where $\mathbf{V}_1(k)$ and $\mathbf{V}_2(k)$ are independent and zero mean white noises, $\mathbf{f}_1(k)$ and $\mathbf{f}_2(k)$ are trend items of the measurement errors. If the following conditions are satisfied:

$$\begin{cases} \left|\mathbf{f}_1(k) - \mathbf{f}_1(k-1)\right|^2 \ll E\left(\mathbf{V}_1(k)\mathbf{V}_1(k)^T\right) \\ \left|\mathbf{f}_2(k) - \mathbf{f}_2(k-1)\right|^2 \ll E\left(\mathbf{V}_2(k)\mathbf{V}_2(k)^T\right) \\ E\left(\mathbf{V}_2(k)\mathbf{V}_2(k)^T\right) \ll E\left(\mathbf{V}_1(k)\mathbf{V}_1(k)^T\right) \end{cases} \quad (0.13)$$

The measurement noise variance of system 1 can be estimated as:

$$\mathbf{R}_1 \approx \frac{E\left\{\left[\Delta\mathbf{Z}_1(k) - \Delta\mathbf{Z}_2(k)\right]\left[\Delta\mathbf{Z}_1(k) - \Delta\mathbf{Z}_2(k)\right]^T\right\}}{2} \quad (0.14)$$

where,

$$\begin{cases} \Delta\mathbf{Z}_1(k) = \mathbf{Z}_1(k) - \mathbf{Z}_1(k-1) \\ \Delta\mathbf{Z}_2(k) = \mathbf{Z}_2(k) - \mathbf{Z}_2(k-1) \end{cases} \quad (0.15)$$

Proof of the theorem

The above theorem can be proved as follows.

First, calculating the difference sequence (i.e., the differences between every two adjacent measurements) of the two separate measurement systems:

$$\begin{aligned} \Delta\mathbf{Z}_1(k) &= \mathbf{Z}_1(k) - \mathbf{Z}_1(k-1) = \left[\mathbf{Z}(k) - \mathbf{f}_1(k) - \mathbf{V}_1(k)\right] \\ &\quad - \left[\mathbf{Z}(k-1) - \mathbf{f}_1(k-1) - \mathbf{V}_1(k-1)\right] \\ &= \left[\mathbf{Z}(k) - \mathbf{Z}(k-1)\right] + \left[\mathbf{f}_1(k-1) - \mathbf{f}_1(k)\right] \\ &\quad + \left[\mathbf{V}_1(k-1) - \mathbf{V}_1(k)\right] \end{aligned} \quad (0.16)$$

$$\begin{aligned} \Delta\mathbf{Z}_2(k) &= \mathbf{Z}_2(k) - \mathbf{Z}_2(k-1) = \left[\mathbf{Z}(k) - \mathbf{f}_2(k) - \mathbf{V}_2(k)\right] \\ &\quad - \left[\mathbf{Z}(k-1) - \mathbf{f}_2(k-1) - \mathbf{V}_2(k-1)\right] \\ &= \left[\mathbf{Z}(k) - \mathbf{Z}(k-1)\right] + \left[\mathbf{f}_2(k-1) - \mathbf{f}_2(k)\right] \\ &\quad + \left[\mathbf{V}_2(k-1) - \mathbf{V}_2(k)\right] \end{aligned} \quad (0.17)$$

Then, subtracting the two difference sequences and yield the second order difference sequences, the trend item $\mathbf{f}_1$ and $\mathbf{f}_2$ are extremely small value compared with measurement noise, so they can be safely neglected after subtraction.

$$\begin{aligned} \Delta\mathbf{Z}_1(k) - \Delta\mathbf{Z}_2(k) &= \left[\mathbf{f}_1(k-1) - \mathbf{f}_1(k)\right] - \left[\mathbf{f}_2(k-1) - \mathbf{f}_2(k)\right] \\ &\quad + \left[\mathbf{V}_1(k-1) - \mathbf{V}_1(k)\right] - \left[\mathbf{V}_2(k-1) - \mathbf{V}_2(k)\right] \\ &\approx \left[\mathbf{V}_1(k-1) - \mathbf{V}_1(k)\right] - \left[\mathbf{V}_2(k-1) - \mathbf{V}_2(k)\right] \end{aligned} \quad (0.18)$$

The autocorrelation of the second order difference sequences is:

$$\begin{aligned} &E\left\{\left[\Delta\mathbf{Z}_1 - \Delta\mathbf{Z}_2\right]\left[\Delta\mathbf{Z}_1 - \Delta\mathbf{Z}_2\right]^T\right\} \\ &= E\left(\begin{bmatrix} \left[\left(\mathbf{V}_1(k) - \mathbf{V}_1(k-1)\right) - \left(\mathbf{V}_2(k) - \mathbf{V}_2(k-1)\right)\right]\cdot \\ \left[\left(\mathbf{V}_1(k) - \mathbf{V}_1(k-1)\right) - \left(\mathbf{V}_2(k) - \mathbf{V}_2(k-1)\right)\right]^T \end{bmatrix}\right) \\ &= E\left(\mathbf{V}_1(k)\mathbf{V}_1(k)^T\right) + E\left(\mathbf{V}_1(k-1)\mathbf{V}_1(k-1)^T\right) \\ &+ E\left(\mathbf{V}_1(k-1)\mathbf{V}_1(k)^T\right) + E\left(\mathbf{V}_1(k)\mathbf{V}_1(k-1)^T\right) \\ &+ E\left(\mathbf{V}_1(k-1)\mathbf{V}_2(k-1)^T\right) + E\left(\mathbf{V}_1(k-1)\mathbf{V}_2(k)^T\right) \\ &+ E\left(\mathbf{V}_1(k)\mathbf{V}_2(k-1)^T\right) + E\left(\mathbf{V}_1(k)\mathbf{V}_2(k)^T\right) \\ &+ E\left(\mathbf{V}_2(k)\mathbf{V}_2(k)^T\right) + E\left(\mathbf{V}_2(k-1)\mathbf{V}_2(k-1)^T\right) \\ &+ E\left(\mathbf{V}_2(k-1)\mathbf{V}_2(k)^T\right) + E\left(\mathbf{V}_2(k)\mathbf{V}_2(k-1)^T\right) \\ &+ E\left(\mathbf{V}_2(k-1)\mathbf{V}_1(k-1)^T\right) + E\left(\mathbf{V}_2(k-1)\mathbf{V}_1(k)^T\right) \\ &+ E\left(\mathbf{V}_2(k)\mathbf{V}_1(k-1)^T\right) + E\left(\mathbf{V}_2(k)\mathbf{V}_1(k)^T\right) \end{aligned} \quad (0.19)$$

Due to $\mathbf{V}_1(k)$ and $\mathbf{V}_2(k)$ are uncorrelated, zero mean white noises, we can derive:

$$\begin{aligned} &E\left(\mathbf{V}_1(k-1)\mathbf{V}_1(k)^T\right) = 0, E\left(\mathbf{V}_1(k)\mathbf{V}_2(k)^T\right) = 0, \\ &E\left(\mathbf{V}_2(k-1)\mathbf{V}_2(k)^T\right) = 0 \end{aligned} \quad (0.20)$$

Then equation (0.19) is simplified as:

$$\begin{aligned} &E\left\{\left[\Delta\mathbf{Z}_1 - \Delta\mathbf{Z}_2\right]\left[\Delta\mathbf{Z}_1 - \Delta\mathbf{Z}_2\right]^T\right\} \\ &= E\left(\mathbf{V}_1(k)\mathbf{V}_1(k)^T\right) + E\left(\mathbf{V}_1(k-1)\mathbf{V}_1(k-1)^T\right) \\ &\quad + E\left(\mathbf{V}_2(k)\mathbf{V}_2(k)^T\right) + E\left(\mathbf{V}_2(k-1)\mathbf{V}_2(k-1)^T\right) \end{aligned} \quad (0.21)$$

Because of the equality relationship:

$$E\left(\mathbf{V}_1(k)\mathbf{V}_1(k)^T\right)=E\left(\mathbf{V}_1(k-1)\mathbf{V}_1(k-1)^T\right)$$
$$E\left(\mathbf{V}_2(k)\mathbf{V}_2(k)^T\right)=E\left(\mathbf{V}_2(k-1)\mathbf{V}_2(k-1)^T\right) \quad (0.22)$$

Equation (0.21) becomes:

$$E\left\{\left[\Delta\mathbf{Z}_1-\Delta\mathbf{Z}_2\right]\left[\Delta\mathbf{Z}_1-\Delta\mathbf{Z}_2\right]^T\right\}=$$
$$2E\left(\mathbf{V}_1(k)\mathbf{V}_1(k)^T\right)+2E\left(\mathbf{V}_2(k)\mathbf{V}_2(k)^T\right)=2\mathbf{R}_1+2\mathbf{R}_2 \quad (0.23)$$

When the prerequisite (0.13) is satisfied, the variance of measurement $\mathbf{Z}_1$ can be calculated as:

$$\mathbf{R}_1=E\left[\mathbf{V}_1(k)\mathbf{V}_1(k)^T\right]$$
$$\approx E\left\{\left[\Delta\mathbf{Z}_1(k)-\Delta\mathbf{Z}_2(k)\right]\left[\Delta\mathbf{Z}_1(k)-\Delta\mathbf{Z}_2(k)\right]^T\right\}/2 \quad (0.24)$$

This main concept of this theorem is to make use of the second order difference sequence to eliminate the effect of measurement true value, only leaving the measurement error item in the sequence. This method assumes two measurements system are existing for the measured physical value and adequately utilize mathematical operation, the correlation characteristic between noise and measurement to derive the R matrix estimation.

2.3 The applicability of adaptive noise estimation theorem

The adaptive measurement noise variance matrix R tuning is significant in the attitude filter to best fuse the information from different sensors to acquire a reliable result. While, as analysed in introduction, the drawbacks of current most commonly used scalar based adaptive tuning approach may lead to wrong result or the result suffers from large error. Therefore, we propose to employ the noise estimation theorem in the proposed attitude filter.

This theorem requires that two measurement systems are available for one objective observation. For the attitude filter proposed in this chapter, the attitude can be calculated or derived from two independent systems: the first is from the Euler angle based attitude update algorithm; the second is from the accelerometer and magnetometer measurement formulated in equation (0.6) and (0.9). Hence, the attitude filter satisfies the precondition of the theorem, and we can utilize this approach to adaptively tune the R matrix.

In addition, the gyroscope can keep high accurate in short term. The angle increment of each sample is reliable and suffers from a low error, so the attitude derived from gyroscope integration it considered as system $\mathbf{Z}_2$. The attitude derived from accelerometer and magnetometer is treated as system $\mathbf{Z}_1$. We calculate the first difference sequence of the two systems and can derive:

$$\begin{aligned}\Delta\mathbf{Z}_1&=\mathbf{Z}_1(k)-\mathbf{Z}_1(k-1)=\phi_{acc/mag}(k)-\hat{\phi}(k-1)\\&=\phi(k)+\phi_{sensor\ error}(k)-(\phi(k-1)+\hat{\phi}_{error}(k-1))\\&=(\phi(k)-\phi(k-1))+\phi_{sensor_error}(k)+\hat{\phi}_{error}(k-1)\end{aligned} \quad (0.25)$$

$$\begin{aligned}\Delta\mathbf{Z}_2&=\mathbf{Z}_2(k)-\mathbf{Z}_2(k-1)=\phi_{gyr}(k)-\hat{\phi}(k-1)\\&=(\phi(k-1)+\hat{\phi}_{error}(k-1)+\omega\Delta t+\boldsymbol{\omega}_{error}\Delta t)-(\phi(k-1)+\hat{\phi}_{error}(k-1))\\&=(\phi(k-1)+\boldsymbol{\omega}\Delta t-\phi(k-1))+\boldsymbol{\omega}_{error}\Delta t\\&=(\phi(k)-\phi(k-1))+\boldsymbol{\omega}_{error}\Delta t\end{aligned}$$

where, k denotes the time epoch. Δt denotes the time interval between two epochs. $\phi_{acc/mag}(k)$, $\phi_{gyr}(k)$ denote the attitude derived from different sensors. $\hat{\phi}(k-1)$, $\hat{\phi}_{error}(k-1)$ denotes the filter estimation result and the estimation error. $\phi(k),\phi(k-1)$ denotes the true value of attitude. $\phi_{sensor_error}(k)$ denotes the attitude error caused by accelerometer and magnetometer error or external acceleration. $\boldsymbol{\omega}_{error}$ denotes the measurement error of gyroscope.

The second order difference sequence is calculated as:

$$\begin{aligned}\Delta\mathbf{Z}_1\mathbf{Z}_2&=(\mathbf{Z}_1(k)-\mathbf{Z}_1(k-1))-(\mathbf{Z}_2(k)-\mathbf{Z}_2(k-1))\\&=\phi_{acc/mag}(k)-\hat{\phi}(k-1)-(\phi_{gyr}(k)-\hat{\phi}(k-1))\\&=\phi_{acc/mag}(k)-\phi_{gyr}(k)\\&=\phi_{sensor_error}(k)+\hat{\phi}_{error}(k-1)-\boldsymbol{\omega}_{error}\Delta t\end{aligned} \quad (0.26)$$

As illustrated in above equation, only three error parts are left in the 2nd difference sequence item. Due to the effect of gyroscope error in one sample interval is limited, so the term $\boldsymbol{\omega}_{error}\Delta t$ can be safely neglected. For example, the sensor sampling frequency is assumed as 100Hz, and Δt = 0.01s; then even if the total gyroscope error can achieve up to $20°/s$ which is a very large error, the attitude error involved by gyroscope error is only 0.2°. Moreover, we employ EKF to perform the attitude update procedure due to the nonlinearity of system dynamic model. Because the EKF works in a closed-loop and state vector error $\delta\hat{\mathbf{X}}_{k-1}$ equals to zero; thus, the attitude error $\hat{\phi}_{error}(k-1)$ equals to error and can be safely ignored.

Therefore, equation (0.26) is simplified as:

$$\Delta\mathbf{Z}_1\mathbf{Z}_2\approx\phi_{sensor_error}(k) \quad (0.27)$$

Hence, the 2nd order difference sequence of the attitude calculated from different sensors approximately equals to the attitude error caused by sensor error or external acceleration. This item is considered as measurement error in the measurement model to adjust R matrix, and the adaptive tuning strategy is designed as:

$$\mathbf{R}=\begin{bmatrix}(\theta_{acc}(k)-\theta_{gyr}(k))^2 & 0 & 0\\ 0 & (\gamma_{acc}(k)-\gamma_{gyr}(k))^2 & 0\\ 0 & 0 & (\varphi_{mag}(k)-\varphi_{gyr}(k))^2\end{bmatrix} \quad (0.28)$$

For the proposed R adjustment method, it is derived from the noise estimation theorem described that we use the 2nd difference operation to eliminate the effect of true value leaving only the error item. However, two improvements have been conducted on this theorem: 1) we use the attitude estimation result to replace measurement in (k-1) epoch. But this item disappears during the difference operation, and the estimation error will not affect the R matrix tuning. 2) the measurement noise variance matrix R is statistic illustrated in the theorem, that it calculates the autocorrelation of 2nd difference sequence to derive the R. While we use the 2nd difference result in epoch k to calculate the R(k) instead of employing the statistic. The reason is that the 2nd difference in epoch k exactly reflects the external acceleration or measurement noise, which accords to the dynamic condition of that epoch. In addition, the external acceleration can be treated as measurement noise, and the noise is different and independent in each epoch. Hence, updating R with the information in current epoch is more reasonable.

From another side, due to the short-term accuracy of gyroscope, the attitude variation in a sampling interval estimation by rotation integration is highly reliable and can be considered as the true value, which is expressed as $\Delta\mathbf{Z}_2$ in context. Hence, this item can be used to evaluate the accuracy of attitude variation derived by

acceleration. If their difference $\Delta \mathbf{Z}_1\mathbf{Z}_2$ is small, it means that the acceleration based attitude is reliable and the filter can have more weight on the measurement model. Otherwise, the filter more relies on the system model. This tuning strategy also accords to the attitude filter designing principle, that making use of the complementary of multi sensors to derive a reliable and accurate orientation result.

3. TEST AND RESULT

We perform practical experiments to verify the adaptive filter. In each experiment, we shake the IMU in different directions to introduce the external acceleration. The consumer level IMU MPU-9150 is employed to collected inertial data. The calculated attitude results are compared with commercial Attitude Heading Reference System(AHRS) Xsense Mti for evaluation. In addition, three approaches, including the proposed adaptive filter, standard filter and the scalar based adaptive tuning filter, are employed to derive the orientation for comparison.

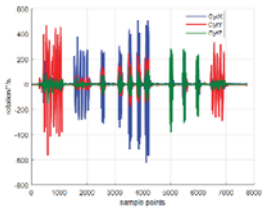

(a) Gyroscope measurement

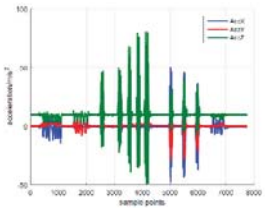

(b) Accelerometer measurement

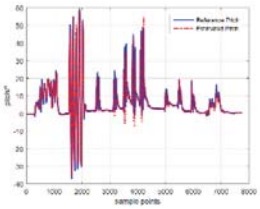

(c) Pitch estimation

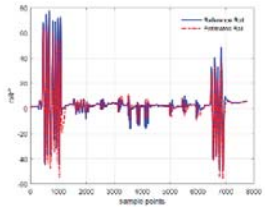

(d) Roll estimation

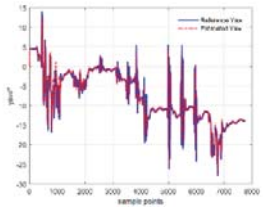

(d)Yaw estimation

Figure 1 Attitude estimation result of practical experiment

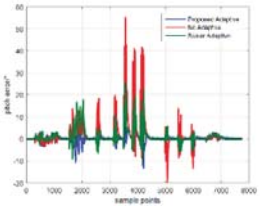

(a)Pitch error

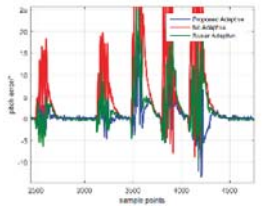

(b) Pitch error in selected period

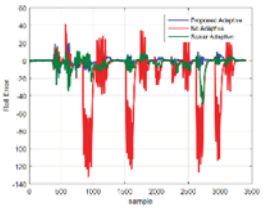

(c) Roll error

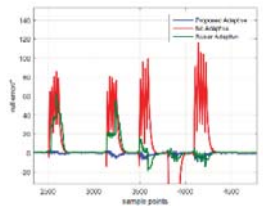

(d) Roll error in selected period

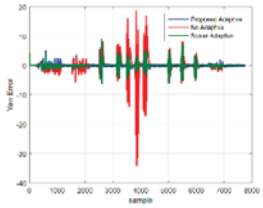

(e) Yaw error

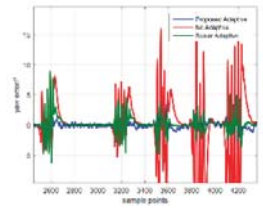

(f) Yaw error in selected period

Figure 2 Attitude comparison of practical experiment

Table 1 Error statistical result of practical experiment

	Proposed Adaptive Filter		Standard Attitude Filter		Scalar Based Attitude Filter	
	Mean	RMS	Mean	RMS	Mean	RMS
Pitch	0.172	2.083	1.982	6.601	1.982	6.60
Roll	1.546	4.603	1.615	19.96	1.615	19.96
Yaw	-0.071	0.758	-0.207	2.97	-0.20	2.97

Figure 1 shows the result of the two experiments. (a)(b) denote the inertial sensor measurement, (c)(d)(e) illustrate the pitch, roll and yaw reference and estimation result of the proposed adaptive filter. The blue and red lines denote the reference value and estimation result. Figure 2 draw the attitude error of three approaches. (a)(c)(e) separately provide the pitch, roll and yaw error; (d)(e)(f) give the attitude error in selected period for better and detailed comparison. The blue, red and yellow line separately denote the proposed adaptive filter, standard filter and the scalar based filter. Table 1 lists the error statistical result of the two practical experiments. A practical issue for the proposed adaptive filter is that we need to multiply a scalar to the R matrix but not directly using the (0.28) in filter. The scalar used in out experiment is 20.

After performing the practical experiment, the orientation estimation result of proposed adaptive filter, standard filter and scalar based adaptive filter have been described in figures and listed in tables. The specific analyses of the three compared methods are summarized in the following.

Standard filter: The result of standard filter suffers from the largest attitude error which can be up to 40 degrees in high dynamic condition. The reason is that the R matrix keeps same during the procedure, so attitude derived from the accelerometer still can have a high contribution for the final solution even it is unreliable.

The scalar based adaptive filter has a much better performance than the standard filter. It makes uses of the scalar, which is the difference of acceleration norm and local gravity acceleration, to adjust the elements of R matrix. This scalar is able to reflect the system dynamic motion and is meaningful in assigning the weight of measurement. However, this approach cannot perform well all the time and have larger attitude error in some periods due to the unsuitable selection of threshold, or improper division of dynamic motion.

The proposed adaptive filter has the best overall performance. This approach effectively employs the short-term accuracy of gyroscope to derive a reliable attitude variation in each sampling interval. Then the attitude variation is used to evaluate the performance of the acceleration derived attitude and correspondingly tune the elements of R matrix. This method utilizes the difference operation to eliminate the effect of true value and only leave the noise item. Hence, this approach has better performance and less attitude error compared with other methods.

4. CONCLUSION

This paper presents a novel redundant based adaptive attitude filter design. The redundant measurement systems based noise estimation theorem is proposed and proofed, and its applicability in the attitude filter is analysed. The measurement error caused by sensor noise or external acceleration is estimated and employed to tune the R matrix online. The experiment result show that the proposed adaptive attitude filter is effectively in providing the system dynamic condition and consequently adjusting the contribution of gyroscope and aiding sensor (i.e. accelerometer, magnetometer) to the final solution. The adaptive filter has achieved a more reliable and accurate orientation estimation result compared with scalar based adaptive filter and standard approach.

REFERENCES

Caruso, M.J., n.d. Applications of Magnetoresistive Sensors in Navigation Systems.

Crassidis, J.L., Markley, F.L., 1996. Attitude estimation using modified Rodrigues parameters.

Finlay, C.C., Maus, S., Beggan, C.D., Bondar, T.N., Chambodut, A., Chernova, T.A., Chulliat, A., Golovkov, V.P., Hamilton, B., Hamoudi, M., 2010. International geomagnetic reference field: the eleventh generation. Geophys. J. Int. 183, 1216–1230.

Foxlin, E., 1996. Inertial head-tracker sensor fusion by a complementary\nseparate-bias Kalman filter. Proc. IEEE 1996 Virtual Real. Annu. Int. Symp. 185–195. doi:10.1109/VRAIS.1996.490527

Han, S., Wang, J., 2011. A Novel Method to Integrate IMU and Magnetometers in Attitude and Heading Reference Systems. J. Navig. 64, 727–738. doi:10.1017/S0373463311000233

Idan, M., 1996. Estimation of Rodrigues parameters from vector observations. IEEE Trans. Aerosp. Electron. Syst. 32, 578–586.

Li, W., Wang, J., 2012. Effective Adaptive Kalman Filter for MEMS-IMU/Magnetometers Integrated Attitude and Heading Reference Systems. J. Navig. 66, 99–113. doi:10.1017/S0373463312000331

Makni, A., Fourati, H., Kibangou, A.Y., 2014. Adaptive Kalman Filter for MEMS-IMU based Attitude Estimation under External Acceleration and Parsimonious use of Gyroscopes 1379–1384.

Maybeck, P.S., 1982. Stochastic models, estimation, and control. Academic press.

Qifan, Z., El-Sheimy, N., 2017. Design, Implementation and Key Issues of Adaptive Tightly Coupled MEMS INS/GPS Integration System. National Library of Canada= Bibliothèque nationale du Canada.

Rehbinder, H., Hu, X., 2004. Drift-free attitude estimation for accelerated rigid bodies. Automatica 40, 653–659. doi:10.1016/j.automatica.2003.11.002

Setoodeh, P., Khayatian, A., Frajah, E., 2004. Attitude estimation by separate-bias Kalman filter-based data fusion. J. Navig. 57, 261–273.

Tapley, B.D., 1976. Adaptive Sequential Estimation with Unknown Noise Statistics 520–523.

Wang, M., Yang, Y., Hatch, R.R., Zhang, Y., 2004. Adaptive filter for a miniature MEMS based attitude and heading reference system, in: Position Location and Navigation Symposium, 2004. PLANS 2004. IEEE, pp. 193–200.

Yoo, T.S., Hong, S.K., Yoon, H.M., Park, S., 2011. Gain-scheduled complementary filter design for a MEMS based attitude and heading reference system. Sensors 11, 3816–3830.

PAVEMENT DEFLECTION ASSESSMENT USING DOPPLER LASERS ON A MOBILE PLATFORM

Michael A. Chapman *[a], Qingquan Li [b], Cao Min [c], Deijin Zhang [d]
[a] Dept. of Civil Engineering, Ryerson University, Toronto, Canada mchapman@ryerson.ca
[b] President, Shenzhen University, Shenzhen, China
[c] Wuhan Wuda Zoyon Science and Technology Co, Wuhan, China 13307100949@189.cn
[d] Wuhan University of Science and Technology Park, Wuhan, China djzhang@whu.edu.cn

KEY WORDS: Deflectometer, Doppler laser, pavement, calibration, mobile

ABSTRACT:

Pavement maintenance represents a significant portion of the budget of transportation agencies. Monitoring pavement health is a critical task that has traditionally been done in a static mode resulting in poor data collection performance. A new mobile system operating at highway travel speeds has been developed. The system incorporates multiple Doppler laser sensors to record the variation of the pavement profile (i.e., deflections) as a loaded vehicle passes along the paved highway corridor. Pavement deflection is a direct indicator of pavement strength which impacts the ability of the load bearing surface to support vehicle loads without deforming to a failure level. The Doppler laser data is processed using the Bernoulli-Euler beam theory related to an elastic foundation support. The computed pavement curvatures are combined to derive a local minimum which reflects the maximum pavement deflection for a given sample interval. The non-destructive nature of the system makes it ideal for pavement health monitoring over extended highway profiles. Such monitoring can take place immediately after construction for contract performance evaluation or after several years of service to indicate the strength of the pavement surface over an extended period of time.
The results of the system calibration and in-field testing are presented to demonstrate the system accuracy and repeatability.
* Corresponding author

1.0 Overview

This paper outlines the development of a system for processing data acquired by a mobile pavement deflectometer that operates at highway traffic speeds. The evaluation of the performance of pavement on modern highways is an important consideration given the number of kilometres of highways and the volume of vehicular traffic that travels these routes daily. In Canada alone, there are hundreds of thousands of kilometres of paved roads and the performance of these roadways affects driver safety and comfort and also impacts the maintenance and rehabilitation budgets of transportation agencies (Statistics Canada, 2008). Over the past few years a more comprehensive approach to evaluating asphalt performance was detailed in the *Mechanistic–Empirical Pavement Design Guide* (MEPDG). This more holistic approach assesses the mechanistic properties of asphalt mixes and their associated binders to calculate the dynamic modulus which is affected by ambient temperatures and traffic loading as well as other factors. In order to effectively collect data for network-based solutions, modern deflectometer instrumentation is necessary (SHRP, 2012). Conventional deflectometers were used in a static mode resulting in very few highway kilometres can be covered daily and, generally, they produced data samples at intervals of 50 to 100 metres and often in only a single lane. Sampling intervals in the range of 20 to 30 centimetres are necessary to give a complete representation of the highway pavement profile. In addition, each lane should be evaluated to determine its performance characteristics. When using a mobile deflectometer, lane closures are not required and, as such, testing personnel and motorist safety is enhanced.

With virtually continuous pavement profile deflection data, the performance of the pavement can be evaluated in a comprehensive network-based manner. Such data can be used to evaluate the performance of new pavement as well as for the determination of the state of existing pavement. By determining the regions of poor performance, preventative measures can be applied to minimize the occurrence of pavement failure such as potholes, cracking and rutting. Furthermore, this will improve the rideability of highways and extend the pavement lifecycles.

Several traffic speed deflectometers (TSD) have been introduced over the past two decades (Rada and Nazarian, 2011). While these systems have shown encouraging results, they have not been able to perform consistently at posted highways speeds and do not give sufficient data quality to fully characterize the loading bearing capacity of pavement. In addition, only a few of the provincial and state transportation agencies in North America have adopted these methodologies for pavement characterization. In Canada, testing is primarily done with static falling weight deflectometers (FWD). Over the past three years, research has been carried out on a new deflectometer system that incorporates four Doppler lasers coupled with a gyroscope and GNSS tracking system. This new system offers the ability to capture pavement deflections through the reconstruction of phase differences of Doppler laser waveforms captured at fixed intervals beneath a mobile platform. The lasers are mounted in a vertical orientation on the bed of the platform and the laser beams are projected towards the pavement. Three of the Doppler lasers are used to define the pavement deflection bowl profile while the fourth Doppler laser is used as a reference source for normalizing the system output. The data is incorporated into the Euler-Bernoulli beam equations as first introduced by Winkler in 1867. Based upon the assumption of a

point load (as introduced through the axels of the mobile platform with a load of 40-100 KN), the maximum deflections can be derived by evaluating the deflection slopes at locations in the deflection profile.

While working with this system over the past three years, various data sets have been assembled along with comparative data derived from traditional and static sensor-based systems. The objective of this paper is to characterize algorithms and procedures for processing the data streams to maximize the reliability of the derived deflections while considering temperature and pavement material effects. Vibrations from vehicular motion over pavement induce high frequency signals in the data. Algorithms have been developed to characterize and, subsequently, minimize the effect of these high frequency artifacts so that the deflection profile is characgterized by a more representative signal. In addition, calibration algorithms and procedures have been developed to optimize the determination of laser orientation angles as well as platform position and orientation. An additional benefit is the generation of reliable data for improving the MEPDG model.

The ultimate goal is to transfer this technology to an operational setting in cooperation with a consortium of companies involved in the transportation sector as well as federal and provincial agencies in North America and elsewhere.

2.0 System Configuration

The mobile Doppler laser deflectometer consists of a platform that is capable of supporting axial loads which can exert a force up to 100 KN. A flatbead transport trailer is ideal for such an application given its rigid structure and axle configuration. Modifications are required to allow the Doppler laser beams to pass through the platform and illuminate the pavement surface with the laser spot (see Figure 1). The lasers must also have sufficient signal strength to generate a useable return signal from standoff distances of up to two (2) metres. Four vibrometers (Doppler lasers) with a vibrometer controller are employed on the current system (see Figure 2). This system configuration accommodates four laser sources and offers a 0.02 μm/s resolution, a maximum velocity of 0.5 m/s and a sample rate up to 350 kHz. Operating ranges up to four (4) metres are achievable with these vibrometers.

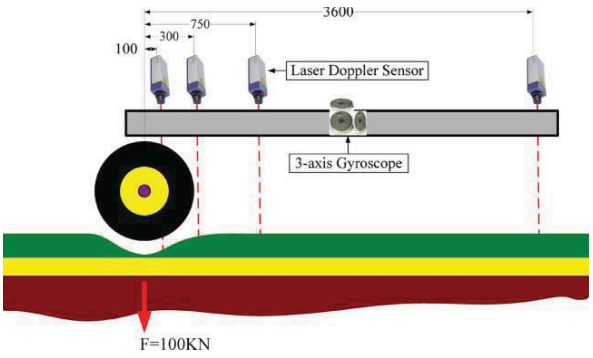

Figure 1 Platform and Doppler Laser Configuration (Li et al, 2013)

In addition, there is a Global Navigation Satellite System (GNSS) and an inertial measurement system (IMU) included in the system for the precise determination of position and orientation information related to the platform at an instant in time. A digital thermometer is also employed to make corrections for temperature variations during data capture.

Figure 2 Laser Vibrometer (www.polytec.com/us/)

The initial system integration has been undertaken and data capture has been achieved. Refinements to data processing and the generation of algorithms for the extraction of pavement parameters are ongoing in order to generate continuous and reliable information. In addition, optimal system parameters such as sampling rates and laser spacing are being optimized for variable velocities and road conditions.

All system outputs are time stamped according to precise GNSS time which permits precise relative information as well as accurate absolute information so that detected deflection can readily be re-occupied for pavement maintenance operations. Precise positioning is critical for a pavement management system so that locations of pavement distress can be readily identified and remedial programs can be carried out in an efficient and cost-effective manner. Vehicle orientations derived from the IMU are also used to normalize the signals from the Doppler lasers so that vehicle slopes and tilts do not introduce any biases which may be misinterpreted as (false) deflections.

3.0 System Calibration

There are three ongoing areas of development, data capture and testing phases. Since the proposed project has multiple components, expertise in algorithm development as well as signal processing and navigation will be required.

3.1 Doppler Laser Array Calibration

The calibration of the system is essential in order to consistently produce reliable pavement deflection information. One aspect of the calibration process is the determination of the optimal Doppler laser position relative to the point where the load is introduced below the axle. Experience with static falling weight deflectometers has shown that several of the sensors should be located within the pavement deflection basin and a reference sensor should be located some distance outside of the deflection basin. It is also recognized that false deflections could be observed simply due to variations in pavement surface smoothness. Sensor positioning is a function of the length of the pavement deflection basin as well as the latency and sample rate of the sensors for a given forward vehicle velocity. With the proposed vibrometers, resolution and sampling rate are of minimal concern since the sensor resolution is sub-micrometer and the sampling rate is sufficient to yield a sub-millimeter data stream

Another aspect of calibration involves the determination of the orientation angles of the Doppler laser with respect to the local vertical direction. There are two components to these misalignment angles: 1) along-axis and 2) cross-axis. Since the system can be subjected to high frequency and amplitude disturbances while operating, periodic calibrations are required so that the data produced is minimally affected by artifacts related to road and vehicle vibrations. A precise determination of misalignment can be achieved if rigorous testing is performed when the system is in static mode. System modifications have

been developed and introduced in order to perform precise misalignment calibrations in a short period with minimal system down time. The proposed strategy involves the use of a calibration platform that is incorporated into the system making it available in the field. Tests have shown the system to be stable after long term use (i.e., several months). A system flow diagram can be seen in Figure 3.

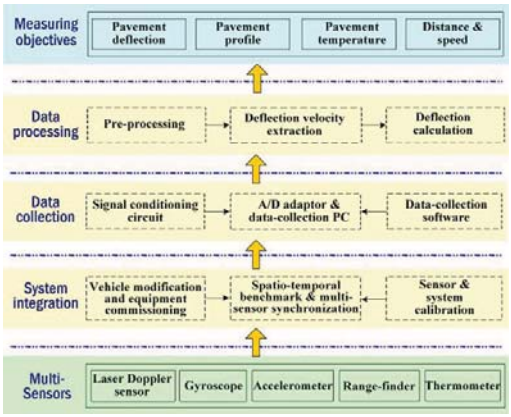

Figure 3 Mobile Deflectometer System Flow

3.2 Data Filtering

The data streams derived from the four Doppler lasers can be generated up 350 kHz and, as such, require sophisticated data handling techniques. It is also important to note that the signal may be contaminated by road and vehicle noise.
The ongoing development has been dedicated to the characterization of the system noise sources. In particular, the road and vehicle may introduce primarily high frequency information which must be filtered so that a cleaner signal is derived for the pavement deflection determination. Signal processing algorithms have been adapted and modified to characterize the spectral signatures that are typically encountered when road and vehicle noise are introduced. These algorithms have been implemented into software in order to filter the noise sources thus minimizing the effect on the longer wavelength signals associated with the pavement deflections (see Figure 4).

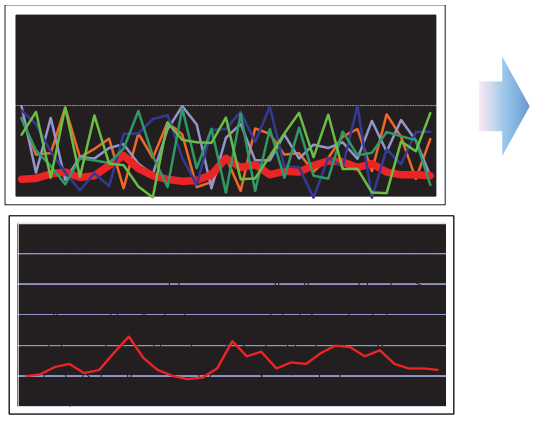
Figure 4 Noise Reduction and Signal Extraction

3.4 Pavement Deflection Extraction

A final aspect of data processing is involved in the application of algorithms and processing strategies for a pavement deflection extraction which will rely on the filtered signals of the four Doppler lasers mounted on a moving vehicle. The time-tagged laser pulses represent the variations in the projection differences which correspond to the deflections of the surfaces (i.e., pavement surfaces) that the laser is scanning. Pavement deflections manifest themselves as pavement basins as the vehicle load is transferred through the tires associated with a given axle (see Figure 1). Pavement deflections have a length/duration and maximum depth. The length and maximum depth of the deflections can be derived from the Doppler laser data. In particular, a Euler-Bernoulli beam equation is used with a point load $\delta(x)$ being introduced at the location (x) of the axle load for a given road stiffness (k) and resulting deflection y(x). Deflection curvature and local minima can be derived when processing the data with the appropriate algorithms and surface elasticity coefficients and beam constant (Grenier et al, 2009 – See Figure 5). Algorithm enhancements have been developed to accommodate deflections measured at highway speeds.

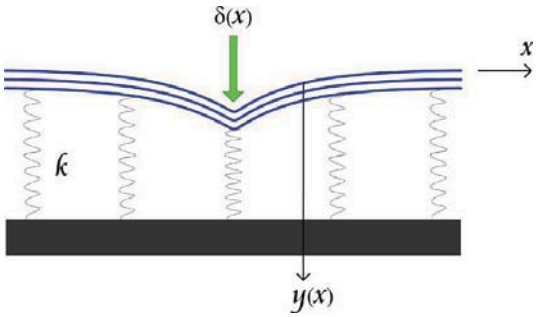

Figure 5 Beam Deflection (Winkler, 1867)

3.5 Future Plans

There ia an ongoing development of the system/process model that handles the high data rates while maintaining data integrity. This system component is also associated with the processing of the data noise which will require the refinement of algorithms and software to effectively minimizes the background noise while maintaining the signal that characterizes the pavement deflections. The system alignment calibration will be streamlined to remove any artifacts induced by the misalignment of the laser axes over short processing times. This alignment issue must be carefully applied for the along-axis direction as well as the cross-axis direction.
The current plan is focussed on the introduction of this pavement measurement technology in the Canadian transportation community so that pavement health can be monitored in a timely and accurate manner. The concept of evaluating new pavement surfaces and introducing pavement repairs prior to pavement failure will offer a cost effective solution which will to lead to an improved rideability of highways with reduced encounters of road deficiencies such as cracks and potholes.

4.0 References

Alshibli, K. A., M. Abu-Farsakh, and E. Seyman (2005) Laboratory Evaluation of the Geogauge and Light Falling

Weight Deflectometer as Construction Control, *J. Mater. Civil Eng.*, Vol. 17, No. 5, pp. 560–569, October.

Andrén , P. (2006) Development and Results of the Swedish Road Deflection Tester, Licentiate thesis, Roy. Inst. Technol., Stockholm, Sweden, pp. 1-103.

Arora, J., S. Nazarian, and V. Tandon (2006) Continuous Deflection Testing of Highways at traffic speeds, Univ. Texas El Paso, El Paso, TX, Tech. Rep. FHWA/TX-06/0-4380-1, 2006.

Baltzer, S., D. Pratt, J. Weligamage, J. Adamsen, and G. Hildebrand (2010) Continuous Bearing Capacity Profile of 18,000 km Australian Road Network in 5 Months, in *Proc. 24th ARRB Conf.–Build. 50 Years Road Transp. Res.*, Melbourne, Australia, pp. 1–11.

Bay, J. A. and K. H. Stokoe (1998) Development of a Rolling Dynamic Deflectometer for Continuous Deflection Testing of Pavements, Univ. Texas, Austin, TX, Tech. Rep. FHWA/TX-99/1422-3F.

Chen, D. H., B. H. Nam, and K. H. Stokoe (2008) Application of Rolling Dynamic Deflectometer to Forensic Studies and Pavement Rehabilitation Projects, *Transp. Res. Rec.*, Vol. 2084, pp. 73–82.

Cheng, P. and B. Oelmann (2010) Joint-angle Measurement using Accelerometers and Gyroscopes—A Survey, *IEEE Trans. Instrum. Meas.*, Vol. 59, No. 2, pp. 404–414, February.

Dahlberg, T. (2006) Track Issues, in *Handbook of Railway Vehicle Dynamics*. New York: Taylor & Francis, Ch. 6, pp. 143–179.

Deblois , K., J. P. Bilodeau, and G. Dore, (2010) Use of Falling Weight Deflectometer Time History Data for the Analysis of Seasonal Variation in Pavement Response, *Can. J. Civil Eng.*, Vol. 37, No. 9, pp. 1224–1231, September.

Diefenderfer, B. K. (2010) Investigation of the Rolling Wheel Deflectometer as a Network-Level Pavement Structural Evaluation Tool, Virginia Transp. Res. Council, Charlottesville, VA, Res. Rep. FHWA/VTRC 10-R.

Elseifi, M. A., A. Abdel-Khalek, K. Gaspard, Z. J. Zhang, and S. Ismail (2011) Evaluation of the Rolling Wheel Deflectometer as a Structural Pavement Assessment Tool in Louisiana, in *Proc. 1st Congr. Transp. Develop. Inst. ASCE*, Chicago, IL, 2011, pp. 628–637.

Ferne, B., P. Langdale, N. Round, and R. Fairclough (2009) Development of the UK Highways Agency Traffic Speed Deflectometer, in *Proc. 8th Int. Conf. Bearing Capacity Roads Railways Airfields*, Champaign, IL, pp. 409–418.

Ferne, B., P. Langdale, N. Round, and R. Fairclough (2009) Development of a Calibration Procedure for the U.K. Highways Agency Traffic-speed Deflectometer, *Transp. Res. Rec.*, Vol. 2093, pp. 111–117.

Gedafa, D. S., M. Hossain, R. W. Miller, and D. Steele (2008) Network Level Pavement Structural Evaluation using Rolling Wheel Deflectometer, in *Proc. 87th Transp. Res. Board Annu. Meeting*, Washington, DC, pp. 1–20.

Gedafa , D. S., M. Hossain, R. Miller, and D. A. Steele (2010) Network Level Testing for Pavement Structural Evaluation using a Rolling Wheel Deflectometer, *J. Test. Eval.*, Vol. 38, No. 4, pp. 439–448, July.

Grenier , S., J.M. Konrad, and D. LeBaeuf (2009) Dynamic simulation of Falling Weight Deflectometer Tests on Flexible Pavements using the Spectral Element Method: Forward Calculations, *Can. J. Civil Eng.*, Vol. 36, No. 6, pp. 944–956, June.

Hadidi, R. and N. Gucunski (2010) Comparative Study of static and Dynamic Falling Weight Deflectometer Back-calculations using Probabilistic Approach, *J. Transp. Eng.*, Vol. 136, No. 3, pp. 196–204, March.

Hildebrand , G., S. Rasmussen, and R. Andrés (1999) Development of a Laser-based High Speed Deflectograph, Danish Road Inst., Roskilde, Denmark, Tech. Rep. 97.

Jenkins, M. (2009) Geometric and Absolute Calibration of the English Highways agency traffic speed Deflectometer, in *Proc. Eur. Conf. Transp. Res. Inst.*, Bron, France, pp. 1–11.

Jitin, A., Tandon V., and Nazarian S. (2006) Continuous Deflection Testing of Highways at Traffic Speeds, Research Report No. FHWA/TX-06/0-4380-1, Center for Transportation Infrastructure Systems,The University of Texas at El Paso, El Paso, TX.

Katicha , S. W., G. W. Flintsch, and B. Ferne (2012) Estimation of Pavement TSD Slope Measurements Repeatability from a Single Measurement Series, in *Proc. 91st Transp. Res. Board Annu. Meeting*, Washington, DC, pp. 1–14.

Krarup , J., S. Rasmussen, L. Aagaard, and P. G. Hjorth (2006) Output from the Greenwood Traffic Speed Deflectometer, in *Proc. 22nd ARRB Conf.—Res. Pract.*, Canberra, Australia, pp. 1–10.

Kim, S. M., J. M. Roesset, and K. H. Stokoe (1999) Numerical Simulation of Rolling Dynamic Deflectometer Tests, *J. Transp. Eng.*,aVol. 125, No. 2, pp. 85–92, March/April.

Kim, J. R., H. B. Kang, D. Kim, D. S. Park, and W. J. Kim (2007) Evaluation of In situ Modulus of Compacted Subgrades using Portable Falling Weight Deflectometer and Plate-bearing Load Test, *J. Mater. Civil Eng.*, Vol. 19, No. 6, pp. 492–499, June.

Lee, J. L. (2006) Improved Rolling Dynamic Deflectometer Testing and Analysis procedures, M.S. thesis, Univ. Texas, Austin, TX, pp. 1-267.

Lee , J. L., B. H. Nam, and K. H. Stokoe (2009) Improved Testing Speed and Rolling Noise Estimation in Rolling Dynamic Deflectometer Testing, in *Proc. GeoHunan Int. Conf. Mater. Des. Construct. Mainten. Test. Pavement*, Changsha, China, pp. 31–36.

Li, Q., Zhou, Q., Mao, Q. and Li, B. (2013) Efficient Calibration of a Laser Dynamic Deflectometer, IEEE Transactions on Instrumentation and Measurement 62(4), 806-813, March.

Lin, D. F., C. C. Liau, and J. D. Lin (2006) Factors Affecting Portable Falling Weight Deflectometer Measurements, *J. Geotech. Geoenviron. Eng.*,Vol. 132, No. 6, pp. 804–808, June.

Nijhof, E., W. Uijttewaal, and R. Heethaar (1994) A Laser-Doppler System for Measuring Distributions of Blood Particles in Narrow Flow Channels, *IEEE Trans. Instrum. Meas.*, Vol. 43, No. 3, pp. 430–435, June.

Nam, B. H. (2011) Transition of the Rolling Dynamic Deflectometer Device from a Screening Tool to an Evaluation Tool for Rigid Airfield Pavement Projects, *Transp. Res. Rec.*, Vol. 2206, pp. 39–51.

Nam, B. H., T. Scullion, and K. H. Stokoe (2011) Rehabilitation Assessment of Jointed Concrete Pavement using the Rolling Dynamic Deflectometer and Ground Penetrating Radar, *J. Test. Eval.*, Vol. 39, No. 3, pp. 346–357, May.

Nam, B. H., J. L. Lee, K. H. Stokoe, D. H. Chen, and J. S. Lee (2011) Application of RDD Continuous Profiling in Maintenance and Rehabilitation of Concrete Pavements, in *Proc. ASCE Geotech.–Emerging Technol. Mater. Des. Rehabil. Inspect. Roadway Pavements*, pp. 125–132, Special Publication 218.

Nazzal, M. D. and L. N. Mohammad (2010) Estimation of Resilient Modulus of Subgrade Soils using Falling Weight Deflectometer, *Transp. Res. Rec.*, Vol. 2186, pp. 1–10.

Ohsumi, A. and N. Nakano (2002) Identification of Physical Parameters of a Flexible Structure from Noisy Measurement Data, *IEEE Trans. Instrum. Meas.*, Vol. 51, No. 5, pp. 923–929, October.

Pratt, D. (2012) Review of the Traffic Speed Deflectograph—Final Project report, Austroads, Sydney, Australia, Tech. Rep., Austroads Publication No. APCR395-12.

Rada, G. R. and Nazarian, S. (2011) The State-of-the-Technology of Moving Pavement Deflection Testing, Final Report, FHWA-DTFH61-08-D-00025, U.S. Department of Transportation, Washington, DC.

Rasmussen, S., J. A. Krarup, and G. Hildebrand (2002) Non-contact Deflection Measurement at High Speed, in *Proc. 6th Int. Conf. Bearing Capacity Roads Railways Airfields*, Lisbon, Portugal, pp. 53–60.

Rasmussen, S., L. Aagaard, S. Baltzer, and J. Krarup (2008) A Comparison of Two Years of Network Level Measurements with the Traffic Speed Deflectometer, in *Proc. Transp. Res. Arena Europe*, Ljubljana, Slovenia, , pp. 1–8.

Ryden , N. and M. A. Mooney (2009) Analysis of Surface Waves from the Light Weight Deflectometer, *Soil Dyn. Earthquake Eng.*, Vol. 29, No. 7, pp. 1134–1142, July.

Simon, L., O. Richoux, A. Degroot, and L. Lionet (2008) Laser Doppler Velocimetry for Joint Measurements of Acoustic and Mean Flow Velocities: LMS-based Algorithm and CRB calculation, *IEEE Trans. Instrum.Meas.*, Vol. 57, No. 7, pp. 1455–1464, July.

Simonin , J. M., D. Lièvre, S. Rasmussen, and G. Hildebrand (2005) Assessment of the Danish High Speed Deflectograph in France, in *Proc. Int. Conf. Bearing Capacity Roads Railways Airfields*, Trondheim, Norway, , pp. 1–10.

Statistics Canada (2008) http://www.statcan.gc.ca/pub/16-002-x/2009001/tbl/transpo/tbl001-eng.htm

Steele, D., J. Hall, R. Stubstad, A. Peekna, and R. Walker (2003) Development of a High-Speed, Rolling-Wheel Deflectometer, pp. 1–14. [http://128.173.204.63/Pavement/fwd/23.pdf].

Strategic Highway Research Program (2012) Assessment of Continuous Pavement Deflection Measuring Technologies, Final Report, Project SHRP2–R06(F), Washington, DC. Systems, *IEEE Trans. Instrum. Meas.*, Vol. 54, No. 6, pp. 2520–2530, December.

Shu, W. (Dec. 2001) Cramér-Rao Bound of Laser Doppler Anemometer, *IEEE Trans. Instrum. Meas.*, Vol. 50, No. 6, pp. 1770–1772.

Tan, C. and S. Park (2005) Design of Accelerometer-based Inertial Navigation

Tertre, A., G. Cascante, and S. L. Tighe (2010) Combining PFWD and Surface Wave Measurements for Evaluation of Longitudinal Joints in Asphalt Pavements, in *Proc. Transp. Res. Board Annu. Meeting*, Washington, DC, pp. 1–18.

Winkler, E., (1867) Die Lehre Von Elasticitaet Und Festigkeit. 1st Edn., H. Dominicus, Prague.

Zhou, F., S. Hu, D. H. Chen, and T. Scullion (2012) RDD Data Interpretation and Its Application on Evaluating Concrete Pavements for Asphalt Overlays, *J. Perform. Construct. Facil.*, Vol. 26, No. 5, pp. 657–667, October.

TIGHTLY COUPLED INTEGRATION OF MULTI-CONSTELLATION GNSS PPP AND MEMS BASED INERTIAL SYSTEM USING NON-LINEAR FILTERING

Mahmoud Abd Rabbou[1] and Ahmed El-Rabbany[2]
Assistant Professor, Department of Civil Engineering (Public works), Cairo University, Cairo, Egypt;
mahmoud.abdelrahman@cu.edu.eg[1]
Professor, Department of Civil Engineering, Ryerson University, Toronto, Canada[2]

KEY WORDS: GNSS, INS, Tightly Coupled, GPS, Galileo, GLONASS, GPS/INS, MEMS

ABSTRACT:

This research develops a low-cost integrated navigation system, which integrates multi-constellation global navigation satellite system (GNSS) precise point positioning (PPP) with a low-cost micro-electro-mechanical sensor (MEMS)-based inertial system for precise applications. between-satellite single-difference (BSSD) ionosphere-free linear combinations of pseudorange and carrier phase measurements from three GNSS constellations, namely GPS, GLONASS and Galileo, are processed. Tightly coupled mechanization is adopted, which is carried out in the raw measurements domain. A number of linear and nonlinear estimation filters, including extended Kalman filter (EKF), unscented Kalman filter (UKF) and particle filter (PF) are developed to merge the corrected GNSS satellite difference observations and inertial measurements and estimate inertial measurements biases and errors. In addition, an improved version of the PF, the unscented particle filter (UPF), which combines the UKF and the PF, is also developed and used in data processing. A tightly coupled GNSS PPP/MEMS-based inertial system is first developed using EKF, which shows that decimeter-level positioning accuracy is achievable. In comparison with the GPS-based integrated system, the multi-constellation GNSS PPP/MEMS-based inertial system improves the latitude, longitude and altitude components precision by 24%, 41% and 41%, respectively. On the other hand, the use of UPF significantly improve the positioning accuracy during the complete GNSS outages, in comparison with the traditional estimation filters. UPF improves the positioning accuracy during the 60-second GNSS outages compared with the EKF by 14%, 13% and 15% in latitude, longitude and altitude, respectively.

1. INTRODUCTION

Global navigation satellite systems (GNSS) provide worldwide positioning, velocity and time synchronization. Traditionally, highly accurate GNSS positioning solution is obtained through carrier-phase observables in differential mode involving two or more receivers. However, the requirement of a base station is usually problematic for some applications. Comparable positioning accuracy, without requiring extra infrastructure, can be achieved through precise point positioning (PPP) technique (Zumberge et al. 1997). PPP uses either un-differenced or between-satellite single difference carrier-frequency and pseudorange observations from a single receiver, in addition to precise orbit and clock products. PPP has been the focus of a number of research groups in the last two decades (see for example, Kouba and Heroux 2001, Gao and Chen, 2004, Collins et al., 2010). To speed up the PPP solution convergence time, a number of PPP ambiguity resolution techniques have been developed (Ge et al, 2008, Geng et al., 2012 and Shi et al., 2014). PPP has been used in a number of applications, including precise surveying, disaster monitoring, off shore exploration, and others (Geng et al., 2013, Xu et al., 2013 and Abd Rabbou and El-Rabbany, 2015).

Unfortunately, GPS often experiences poor satellite visibility or weak constellation geometry in urban areas. This limitation can be overcome through combining multi-constellation GNSS, which is not simply achieved by adding the additional measurements to existing GPS observation models. Inter-system biases exist, which must be taken into account in order to make effective use of the additional GNSS observation. The impact of the additional GNSS observations on the performance of the GPS PPP has been investigated considering only the additional GLONASS observations since a decade due to the unavailability of other GNSS systems (Cai and Gao 2007). After, more researchers have been studied the performance of the combined GPS/GLONASS PPP, which confirms the improvements in the accuracy and convergence time compared with GPS PPP (e.g. Melgard et al 2009, Cai and Gao 2013, Choy et al 2013, Yigit et al 2014, Li and Zhang 2014 and Abd Rabbou and El-Rabbany 2015). With the appearance of other GNSS systems such as the Chinese navigation system BeiDou and the European Galileo system, the combination between these systems and GPS has been studied recently in some research works such as Li et al (2014) and Qu et al (2013) for the combined GPS/BeiDou PPP and Montenbruck et al (2011), Steigenberger et al (2011) and Steigenberger et al (2014) for the combined GPS/Galileo PPP. Furthermore, the performance of the combined four constellation GPS/GLONASS/Galileo/BeiDou PPP has been investigated in recent research work such as Li et al (2015) and Cai et al (2015).

Employing multi-GNSS systems, in contrast to GPS only, decreases the probability of partial GNSS outages due to the availability of a large number of satellites observations. However, GNSS positioning solution may not always be available due to complete GNSS outages in urban canyons. These limitations can be overcome through integrating the GNSS observations with a relatively environment-independent system, the inertial navigation system (INS). On the inertial side, recent advances in micro-electro-mechanical sensors (MEMS) technology enabled the development of a generation of low-cost inertial sensors. MEMS sensors are characterized by their small size, light weight and low cost, in comparison with high-end inertial sensors. However, MEMS sensors have generally poorer performance compared with high-end IMU due to the significantly higher errors and biases affecting these low-cost inertial sensors. Commonly, the extended Kalman filter (EKF) is considered as the estimation filter for GPS/INS integration (e.g., Petovello, 2004, Nassar, 2005 and Abd Rabbou and El-Rabbany, 2014). In EKF, the non-linear system

and observation models are linearized around the updated navigation parameters using the first-order Taylor series expansion, under the assumption that the noise is Gaussian. However, as a result of neglecting higher order terms, EKF might fail to produce a reliable estimation solution, especially during GPS outages. This is particularly the case when low-cost MEMS-based inertial measurement units (IMU) are used.

The unscented Kalman filter (UKF) was introduced by Julier et al. (1995) as a linear regression estimation filter. UKF propagates a deterministically a fixed set of sigma points with appropriate weights through the non-linear motion and observation models to capture the system a posteriori mean and covariance estimates (Bergman 2001). However, similar to EKF, the algorithm is still dealing with the assumption of Gaussian distribution. In contrast to linearization filters, Particle filter (PF) avoids the linearization of the system models. It rather obtains an approximate estimation solution for the nonlinear model. In addition, PF can accommodate non-Gaussian distributions noise(e.g., Yi and Brzezinska 2006; Giremus et al. 2005; Caron et al. 2007; Georgy et al. 2010). The main drawback of the PF, however, is that it is featured by a large computational cost, which represents the main limitation in practical use

To overcome the linearization and computational cost problems, recent research focused on fusing the PF with UKF to form the unscented particle filter (UPF) (Haug, 2005; Simon, 2006). Haug (2005) used UKF to produce a posteriori mean and covariance estimates, which are then employed to produce the PF importance density function for particle generation. Then, the normalized importance weights of the particles are calculated to refine the system posteriori estimates. Although, this technique significantly reduces the number of particles and processing time compared with traditional PF, it confines the PF importance density function to Gaussian distribution. As such, the expected enhancement can be considered limited (Zhou et al. 2010). According to Simon (2006), a bank of EKFs or UKFs can used for each particle combined with the likelihood function to derive the system a posteriori estimates. This technique can significantly reduce the number of needed particles while reserving the non-Gaussian natural of the system noise.

In this research, a UPF is developed, based on the approach proposed by Simon (2006), to merge the multi-constellation GNSS measurements, through un-differenced PPP technique, and the inertial sensor measurements. All of the available GNSS observations, including pseudorange, carrier-phase and corrected Doppler observations, are used. The performance of the developed filter is compared with that of the traditional filters, including the standard EKF, UKF and PF, both when GNSS is available and when a complete GPS outage is encountered.

2. MULTI-CONSTELLATION PPP MODELS

In this study, the between-satellite single differenced ionosphere-free model is considered. Pseudorange and carrier phase observations of three GNSS systems are processed, namely GPS, GLONASS and Galileo. To develop the mathematical equations for BSSD, we refer to the GPS satellite by k, Galileo satellite by h, and GLONASS satellite by n. GPS satellite l is taken as the reference satellite to form BSSD ionosphere-free linear combination (Abd Rabbou and El-Rabbany, 2015)

$$\bar{P}^k_{3G} - \bar{P}^l_{3G} = \sqrt{(x_r - X^k_G)^2 + (y_r - Y^k_G)^2 + (z_r - Z^k_G)^2} - \sqrt{(x_r - X^l_G)^2 + (y_r - Y^l_G)^2 + (z_r - Z^l_G)^2} + (m^k_G - m^k_G)T_w + e^k_G - e^l_G \quad (1)$$

$$\bar{P}^h_{3E} - \bar{P}^l_{3G} = \sqrt{(x_r - X^h_E)^2 + (y_r - Y^h_E)^2 + (z_r - Z^h_E)^2} - \sqrt{(x_r - X^l_G)^2 + (y_r - Y^l_G)^2 + (z_r - Z^l_G)^2} + (m^h_E - m^l_G)T_w + c[ISB_E] + e^h_E - e^l_G \quad (2)$$

$$\bar{P}^n_{3R} - \bar{P}^l_{3G} = \sqrt{(x_r - X^n_R)^2 + (y_r - Y^n_R)^2 + (z_r - Z^n_R)^2} - \sqrt{(x_r - X^l_G)^2 + (y_r - Y^l_G)^2 + (z_r - Z^l_G)^2} + (m^n_R - m^l_G)T_w + c[ISB_R] + e^n_R - e^l_G \quad (3)$$

$$\bar{\Phi}^k_{3G} - \bar{\Phi}^l_{3G} = \sqrt{(x_r - X^k_G)^2 + (y_r - Y^k_G)^2 + (z_r - Z^k_G)^2} - \sqrt{(x_r - X^l_G)^2 + (y_r - Y^l_G)^2 + (z_r - Z^l_G)^2} + (m^k_G - m^k_G)T_w + B^k_G - B^l_G + \varepsilon^k_G - \varepsilon^l_G \quad (4)$$

$$\bar{\Phi}^h_{3E} - \bar{\Phi}^l_{3G} = \sqrt{(x_r - X^h_E)^2 + (y_r - Y^h_E)^2 + (z_r - Z^h_E)^2} - \sqrt{(x_r - X^l_G)^2 + (y_r - Y^l_G)^2 + (z_r - Z^l_G)^2} + (m^h_E - m^l_G)T_w + c[ISB_E] + B^h_E - B^l_G + \varepsilon^h_E - \varepsilon^l_G \quad (5)$$

$$\bar{\Phi}^n_{3R} - \bar{\Phi}^l_{3G} = \sqrt{(x_r - X^n_R)^2 + (y_r - Y^n_R)^2 + (z_r - Z^n_R)^2} - \sqrt{(x_r - X^l_G)^2 + (y_r - Y^l_G)^2 + (z_r - Z^l_G)^2} + (m^n_R - m^l_G)T_w + c[ISB_R] + B^n_R - B^l_G + \varepsilon^n_R - \varepsilon^l_G \quad (6)$$

where $\bar{P}_3$ and $\overline{\Phi_3}$ are the corrected pseudorange and carrier phase measurements, respectively; x_r, y_r and z_r are the receiver unknown coordinates; X^s, Y^s and Z^s are the satellite coordinates computed using the final IGS-MEGX orbital products and corrected for the effect of earth rotation during signal transit; $m^s = \frac{1}{\sin(elevation)}$ is the mapping function for the troposphere wet delay component T_w. ISB_E and ISB_R are the GPS/GLONASS and GPS/Galileo inter-system biases, respectively.

3. GNSS PPP/MEMS MOTION MODEL

Tightly coupled (TC) architecture is implemented in this research, adopting a central filter to process the GNSS raw measurements (pseudorange, carrier-phase and Doppler) and the IMU measurements to produce estimates of the state vector including position, velocity and attitude. The mathematical model of the inertial navigation system is commonly described in the framework of linear dynamic systems. The dynamic behavior of such systems can be described using a state-space representation. For this purpose, a system of non-linear first-order differential equations can be described as (Jekeli 2001):

$$\begin{bmatrix} \dot{r}^n \\ \dot{V}^n \\ \dot{R}_b{}^n \end{bmatrix} = \begin{bmatrix} D \cdot V^n \\ R_b{}^n f^b - (2\Omega^n{}_{ie} + \Omega^n{}_{en}) \cdot V^n + g^n \\ R_b{}^n (\Omega^n{}_{ib} - \Omega^b{}_{in}) \end{bmatrix} \quad (7)$$

where, $\mathbf{r^n}$ is the position vector, latitude, longitude and altitude; $\mathbf{V^n}$ is the velocity vector in the East, North and Up (ENU) reference frame, $\dot{\mathbf{V}}^{\mathbf{n}}$ is the kinematic acceleration vector in the ENU reference frame; $\Omega^{\mathbf{n}}_{\mathbf{en}}.\mathbf{V^n}$ represents the effect of the motion of the ENU frame with respect to the ECEF frame; $2\Omega^{\mathbf{n}}_{\mathbf{ie}}.\mathbf{V^n}$ is the Coriolis acceleration vector; $\mathbf{g^n}$ is the gravity vector, including the gravitation term and the centripetal

term related to the Earth rotation; and f^b is the specific force vector in the body frame, which is measured by the accelerometers. The matrix Ω^n_{ie} is the skew-symmetric matrix of rotation rate vector of the Earth, which can be expressed in the ENU frame as:

$$\Omega^n_{ie} = \begin{bmatrix} 0 & 0 & 0 \\ 0 & \omega \cos\varphi & 0 \\ 0 & 0 & \omega \sin\varphi \end{bmatrix} \tag{8}$$

The matrix Ω^n_{en} is the skew-symmetric matrix of the rotation rate vector of the ENU frame with respect to ECEF frame, expressed in the ENU frame as:

$$\Omega^n_{en} = \begin{bmatrix} \frac{-V_n}{M+h} & 0 & 0 \\ 0 & \frac{V_E}{N+h} & 0 \\ 0 & 0 & \frac{V_E \tan\varphi}{N+h} \end{bmatrix} \tag{9}$$

The matrix Ω^b_{ib} is the skew-symmetric matrix of the rotation rate vector of the body frame with respect to the ECI frame ω^b_{ib}, expressed in the body reference, which is measured by the gyros. The matrix Ω^b_{in} is the skew-symmetric matrix of the rotation rate of the navigation frame with respect to inertial frame ω^b_{in} expressed in the body frame, which is computed combining ω^n_{ie} and ω^n_{en} transforming the result in the body frame as follows:

$$\Omega_{in}{}^{b} = R_n{}^{b} \cdot (\Omega_{ie}{}^{n} + \Omega_{en}{}^{n}) \tag{10}$$

The bias and scale factor drifts are modeled as a first-order Gauss-Markov process, which can be formed as follows:

$$\dot{\delta b}_{ai} = -\frac{1}{\tau_{bai}} \delta b_{ai} + w_{bai} \tag{11}$$

$$\dot{\delta b}_{gi} = -\frac{1}{\tau_{bgi}} \delta b_{gi} + w_{bgi} \tag{12}$$

$$\dot{\delta S}_{ai} = -\frac{1}{\tau_{Sai}} \delta S_{ai} + w_{Sai} \tag{13}$$

$$\dot{\delta S}_{gi} = -\frac{1}{\tau_{Sgi}} \delta S_{gi} + w_{Sgi} \tag{14}$$

where the subscript "i" indicates the axis; τ_a and τ_g are the correlation times for the accelerometers and gyros, respectively; and w_a and w_g are the Gauss-Markov process driving noises, whose spectral densities are q_a and q_g.

With the availability of the IGS MGEX orbital products corrected for the effect of earth rotation during signal transit, the outputs of position and velocity from the INS mechanization are used to predict the pseudorange, phase and Doppler measurements through the non-linear observation equations. The UNB3 tropospheric model, consisting of the Saastamoinen vertical propagation delay model and Niell mapping function, is used to account for the tropospheric error (Leandro et al. 2008). The effects of ocean loading, Earth tide, carrier-phase windup, sagnac, relativity, and satellite antenna phase-center variations are accounted for using existing models (Kouba 2009). Considering the above corrections, the corrected pseudorange, carrier phase and Doppler measurements from GNSS as well as the INS-predicted measurements, are processed by the integration filter to estimate the INS state vector. Finally, the obtained INS state estimates are fed back to the INS mechanization using the closed loop approach. The architecture of the proposed tightly coupled integrated system is shown in Figure 1.

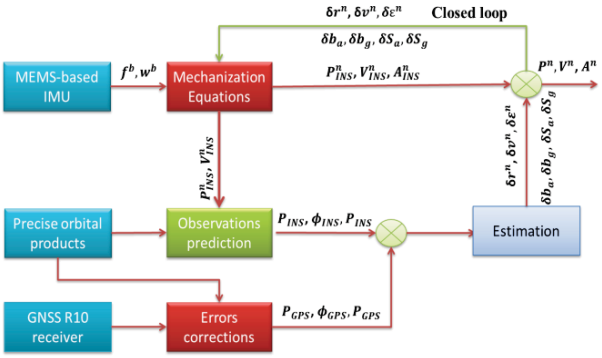

Figure 1 flow chart of the proposed tightly coupled GPS PPP/MEMS integrated system

4. UNSCENTED PARTICLE FILTER

Nonlinear estimation filtering techniques are employed to estimate the state vector of the proposed integrated GPS PPP/MEMS-based inertial system. In this section, the proposed unscented particle filter (UPF) is introduced for the GNSS PPP/MEMS integration.

In UKF, number of points with appropriate weights called sigma points are deterministically selected to simulate the system probability density function under the assumption of Gaussian distribution. According to Bergman (2001), the sigma points can capture the mean and covariance of a random vector up to the third order accuracy. Comparing with the traditional EKF, in which the higher order terms in Tylor expansion series are neglected, the UKF should provide superior performance in simulating the Gaussian distribution and the nonlinearity behaviour of the systems. In contrast with the deterministic sigma points which are simulating Gaussian probability assumption in UKF, PF uses Monte Carlo simulation technique to approximate the non-Gaussian probability distribution through a set of weighted samples called particles around the mean state vector $\bar{x}$ (Doucet et al. 2000). The simulated particles are propagated through the non-linear motion model yielding the prior probabilistic density which works as an importance density function. Then, the observation probability density function which is obtained from passes the predicted particles through the non-linear observation model is used to update the importance density particles. Finally, a resampling step is applied to remove the samples with low weights and the posterior probability is redistributed according to the new selected weights.

In addition to the computational cost of employing the traditional PF due to the large samples needed to fit the posterior probability distribution, the major drawbacks of using the traditional PF, is the use of the prior probabilistic motion density as an importance density function. The motion importance density may fail to move the weighted particles toward the high likelihood regions due to the high drift of low-cost inertial sensors, especially during GPS outages. To

overcome these limitations, bank of UKFs (sigma points generating) is used for each particle to generate the importance density functions. The UKF based importance density is leading to move the particles x^i towards the high likelihood regions by producing new particles $\bar{x}^i$ with included knowledge about the latest observation. The importance sampling step can be modeled as stated in Table 1 (Simon 2006).

Table 1. Unscented particle filter importance sampling implementations

For each particle i=1…N, a set of sigma points are defined for j=1…n as follow:

$$x^{i,j}_{k-1} = x^i_{k-1} + \sqrt{(n+\lambda)P^i_{k-1}},\ w^{i,j} = \frac{1}{2(n+\lambda)}$$

$$x^{i,j+n}_{k-1} = x^i_{k-1} - \sqrt{(n+\lambda)P^i_{k-1}},\ w^{i,j} = \frac{1}{2(n+\lambda)}$$

Sample propagation for each sigma point (time update)

$$z^{i,j}_{k,k-1} = h(x^{i,j}_{k,k-1}),\ \bar{z}^{i,j}_{k,k-1} = \sum_{j=0}^{2n} w^{i,j}\ y^{i,j}_{k,k-1}$$

$$\bar{x}^{i,j}_{k,k-1} = \sum_{j=0}^{2n} w^{i,j}\, x^{i,j}_{k,k-1}$$

$$P^{i,j}_{zk,k-1} = \sum_{j=0}^{2n} w^{i,j}{}_i(\bar{z}^{i,j}_{k,k-1} - z^{i,j}_{k,k-1})(\bar{z}^{i,j}_{k,k-1} - z^{i,j}_{k,k-1})^T$$

$$p^{i,j}_{k,k-1} = \sum_{j=0}^{2n} w^{i,j}(\bar{x}_{k,k-1} - x^i_{k,k-1})(\bar{x}_{k,k-1} - x^i_{k,k-1})^T$$

Sample update for each sigma point (measurement update)

$$K^i{}_k = P^{i,j}_{k,k-1} P^{i,j}_{zk,k-1}{}^T$$

$$\bar{x}^i_k = x^i_{k,k-1} + K_k(z_k - \bar{z}^{i,j}_{k,k-1})$$

$$P^i_k = P^i_{k,k-1} - K_k P^{i,j}_{zk} K_k{}^T$$

$$\bar{x}^i_k \sim q(x_t : x_{0:k-1}, z_{1:k-1})$$

where $\bar{x}_0$ and P_0 are the initial state vector and variance-covariance matrix, respectively; x^i and Z^i are the state and observation vectors for the corresponding sigma points; f and h are the non-linear motion and observation models, respectively; $x_{k,k-1}$, $Z_{k,k-1}$ and $P_{x_{k,k-1}}$ are the time prediction state vector, observation vector and variance-covariance matrix, respectively; x_k, and P_{x_k} are the time update state vector and variance-covariance matrix, respectively.

Tests and Results analysis

A real vehicular test was conducted to evaluate the performance of the developed integrated GNSS-PPP/MEMS-based INS system using UPF. The vehicular test was carried out through downtown Kingston, Ontario, Canada, which was designed to represent challenging situations for real GNSS satellite navigation availability including turns, straight portions, high speed, and slow speeds. The NovAtel SPAN-CPT system and the GNSS Trimble R10 receiver were used to collect the navigation data. The SPAN-CPT system consists of the NovAtel OEM4 receiver and a MEMS-based IMU, which contains three MEMS-based accelerometers and three fiber optic gyros. Carrier phase-based differential GNSS (DGNSS) solution is used as a reference solution. In order to create this reference solution, a GNSS Trimble R7 receiver was setup at a nearby station with precisely known coordinates. The raw dual-frequency GNSS pseudorange, carrier phase and Doppler measurements were collected at a 1 Hz rate, while the IMU raw data was logged at a rate of 100 Hz. The duration of the trajectory test was set for about 55 minutes. During the GNSS availability, two scenarios are considered in this research. The traditional GPS-based integrated system and the developed GNSS-based integrated system including GPS, GLONASS and Galileo, are studied to investigate the contribution of the additional GNSS systems to the positioning accuracy of the integrated system. To investigate the UPF impact on the positioning accuracy of the integrated system during complete GNSS outages, a number of simulated outages are introduced for the trajectory test. Figure 2 shows the GNSS satellite availability during the observation time.

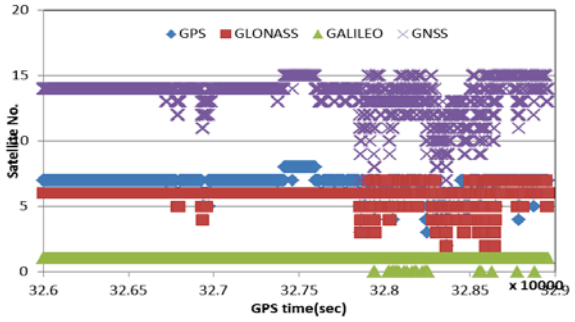

Figure 2. GNSS satellites availability during the trajectory test

Figure 3 shows the positioning accuracy of the developed integrated system when the observations of all GNSS satellites are included in the solution, i.e., no outages are inserted. It can be seen that the addition of GLONASS and Galileo observations enhances the positioning accuracy in comparison with the GPS-only positioning solution.

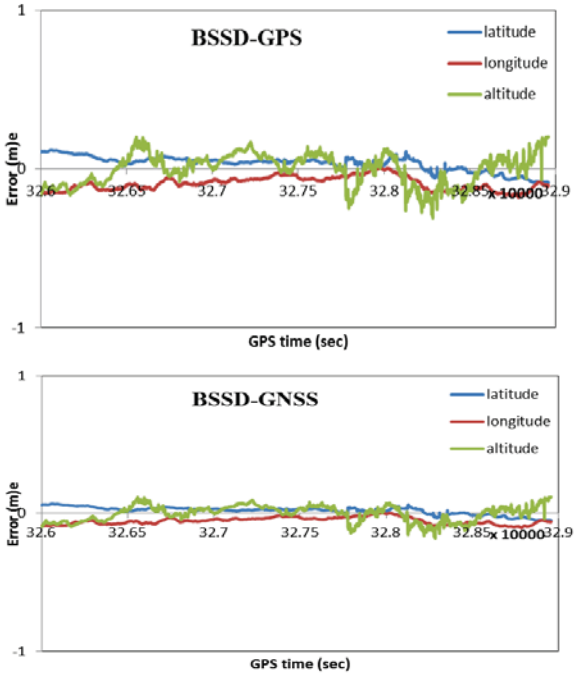

Figure 3. the BSSD PPP positioning accuracy for both GPS only and GNSS (GPS/GLONASS/Galileo)

Table 2 summarizes the statistical characteristics, mainly the root mean square error (RMSE) and the maximum error, for the two PPP integrated system scenarios mentioned above. Comparing the RMSE values for each scenario, it can be seen that the positioning precision is improved by 40%, 41% and 41% for latitude, longitude and altitude in the multi-constellation GNSS PPP solution compared with the GPS-only PPP solution.

Table 2. Statistical analysis of GNSS positioning precision for the first trajectory, with no outages inserted.

PPP techniques	**GPS (BSSD mode)**		
positioning	Latitude	longitude	altitude
RMSE (m)	0.052	0.090	0.082
Maximum error	0.121	0.179	0.306
PPP techniques	GNSS (BSSD mode)		
positioning	Latitude	longitude	altitude
RMSE	0.034	0.059	0.058
Maximum error	0.072	0.106	0.180

To mimic challenging positioning conditions in urban areas, including complete blockage of the GNSS satellites, twelve simulated complete satellite outages of 60s were introduced. Figure 4 shows the positioning errors during the various outages for the developed UPF in comparison with the tradition EKF, UKF and PF estimation filters, referenced to carrier-based DGPS solution with full satellite availability.

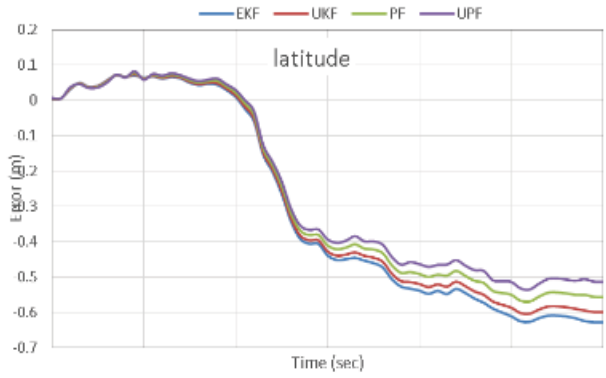

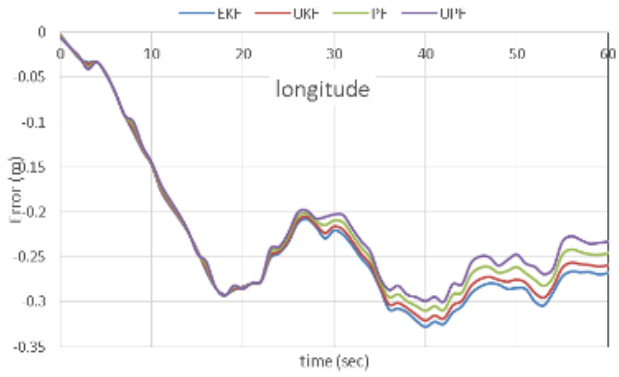

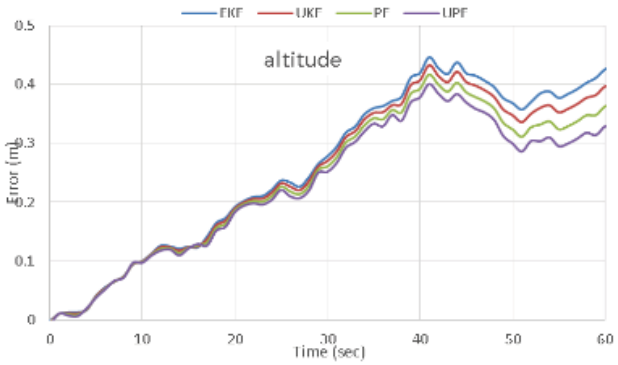

Figure 4. Positioning accuracy during complete GNSS outages for latitude, longitude and altitude

It can be also seen that the UPF slightly enhanced the positioning accuracy during the GNSS outages compared with the tradition estimation filters. However, the non-linear estimation filters failed to present significant improvements in positioning accuracy compared with the traditional EKF. We can note herein that only linear stochastic models are used for all filters to present a unified comparison between the linear and non-linear estimation filters. Further improvements can be detected by using the non-linear estimated filers such as PF and UPF when non-linear stochastic models are considered.

Figure 5 shows the average of maximum positioning errors referenced to the DGPS solution during 60s GNSS outages. It can be notes that the UPF enhances the positioning accuracy during the GPS outages compared with the EKF by 14%, 13% and 15% in latitude, longitude and altitude, respectively. However, compared with PF the improvements are 6%, 5% and 7% in latitude, longitude and altitude, respectively. It can also be seen that both UKF and EKF present comparable positioning accuracy for the three positioning directions.

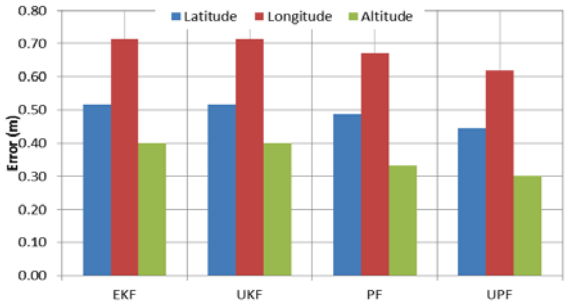

Figure 5 the average of maximum error for different estimation filters during GNSS outages

5. CONCLUSION

We developed a new algorithm for the integration of multi-constellation GNSS PPP, including GPS, GLONASS and Galileo systems, and MEMS-based inertial system. In addition, this paper examined the performance of UPF and compared its results with those of UKF, traditional non-linear PF, and the EKF for tightly-coupled PPP GPS/MEMS-based INS integration. A field trial was conducted to evaluate the performance of the developed system. The positioning results of the integrated system showed that centimeter to decimeter-level accuracy are achievable when the GNSS satellite were available. The addition of GLONASS and Galileo observations enhanced the positioning accuracy in comparison with

standalone GPS-based solution. Comparing the RMSE values for each scenario, it can be seen that the positioning precision is improved by 40%, 41% and 41% for latitude, longitude and altitude in the multi-constellation GNSS PPP solution compared with the GPS-only PPP solution. It has been shown that all estimation filters obtain comparable results in positioning, velocity and attitude, as long as no GPS outages are encountered. However, in comparison with the traditional PF, the use of UPF significantly reduces the number of particles needed to obtain an accurate solution, which speeds up the estimation of navigation parameters. When a complete GPS outage is encountered, the use of UPF enhances the positioning accuracy by up to average 15%, in comparison with other estimation filters.

6. REFERENCE

Abd Rabbou M., El-Rabbany A. (2014), Tightly Coupled Integration of GPS Precise Point Positioning and MEMS-Based Inertial Systems, GPS Solution, http://dx.doi.org/10.1007/s10291-014-0415-3.

Abd Rabbou, M. and El-Rabbany, A. 2015. PPP Accuracy Enhancement Using GPS/GLONASS Observations in Kinematic Mode. Positioning, 6 (1), 1-6.

Abd Rabbou, M., El-Rabbany, A, (2015), Precise Point Positioning using Multi-Constellation GNSS Observations for Kinematic Applications, Journal of applied Geodesy, doi: I10.1515/jag-2014-0021.

Bergman, N. Posterior Cramér-Rao bounds for sequential estimation. In Sequential Monte Carlo methods in practice:2001 (pp. 321-338). Springer New York.

Cai, C. and Gao, Y. 2007. Precise Point Positioning Using Combined GPS and GLONASS Observations. Positioning, 1, 0.

Cai, C. and Gao, Y. 2013. Modeling and assessment of combined GPS/ GLONASS precise point positioning. GPS Solutions. 17 (2), 223–236.

Cai, C., Gao, Y., Pan, L. and Zhu, J. 2015. Precise point positioning with quad-constellations: GPS, BeiDou, GLONASS and Galileo. Advances in Space Research, 56 (1), 133-143.

Caron, F., Davy, M., Duflos, E., & Vanheeghe, P. (2007). Particle filtering for multisensor data fusion with switching observation models: Application to land vehicle positioning. Signal Processing, IEEE Transactions on, 55(6), 2703-2719.

Choy S., Zhang S., Lahaye F. and Héroux P. 2013. A comparison between GPS-only and combined GPS+ GLONASS Precise Point Positioning. Journal of Spatial Science, 58(2), 169-190.

Collins, P., Bisnath, S., Lahaye, F. and Heroux, P. 2010. “Undifferenced GPS ambiguity resolution using the decoupled clock model and ambiguity datum fixing. Navigation, 57(2), 123–135.

Doucet, A., Godsill, S., & Andrieu, C. (2000). On sequential Monte Carlo sampling methods for Bayesian filtering. Statistics and computing, 10(3), 197-208.

Gao, Y., & Chen, K. (2004). Performance analysis of precise point positioning using rea-time orbit and clock products. Positioning, 1(08), 0.

Ge, M., Gendt, G., Rothacher, M., Shi, C., & Liu, J. (2008). Resolution of GPS carrier-phase ambiguities in precise point positioning (PPP) with daily observations. Journal of Geodesy, 82(7), 389-399.

Geng, J., Bock, Y., Melgar, D., Crowell, B. W., & Haase, J. S. (2013). A new seismogeodetic approach applied to GPS and accelerometer observations of the 2012 Brawley seismic swarm: Implications for earthquake early warning. Geochemistry, Geophysics, Geosystems, 14(7), 2124-2142.

Geng, J., Shi, C., Ge, M., Dodson, A. H., Lou, Y., Zhao, Q., & Liu, J. (2012). Improving the estimation of fractional-cycle biases for ambiguity resolution in precise point positioning. Journal of Geodesy, 86(8), 579-589.

Georgy, J., Noureldin, A., Korenberg, M. J., & Bayoumi, M. M. (2010). Low-cost three-dimensional navigation solution for RISS/GPS integration using mixture particle filter. Vehicular Technology, IEEE Transactions on, 59(2), 599-615.

Giremus, A., Tourneret, J. Y., & Djuric, P. M. (2005). An improved regularized particle filter for GPS/INS integration. In Signal Processing Advances in Wireless Communications, 2005 IEEE 6th Workshop on (pp. 1013-1017). IEEE.

Giremus, A.; Tourneret, J. Y.; Djuric, P. M. (2005). An improved regularized particle filter for GPS/INS integration. In Signal Processing Advances in Wireless Communications: 2005, IEEE 6th Workshop on (pp. 1013-1017). IEEE.

Grejner-Brzezinska D A, Da R, and Toth C (1998) GPS error modeling and OTF ambiguity resolution for high-accuracy GPS/INS integrated system. Journal of Geodesy, 72(11), 626-638.

Jekeli, C. (2001). Inertial navigation systems with geodetic applications, Berlin, New York, de Gruyter: ISBN 3-11-015903-1.

Julier, S. J., Uhlmann, J. K., & Durrant-Whyte, H. F. (1995). A new approach for filtering nonlinear systems. In American Control Conference, Proceedings of the 1995 (Vol. 3, pp. 1628-1632). IEEE.

Kouba J (2009) A guide to using International GNSS Service (IGS) products. International GNSS.

Kouba, J., & Héroux, P. (2001). Precise point positioning using IGS orbit and clock products. GPS solutions, 5(2), 12-28.

Leandro R, Santos M C, & Langley R B (2006) UNB neutral atmosphere models: development and performance. Proceedings of ION NTM , 564-573.

Li, M., Qu, L., Zhao, Q., Guo, J., Su, X. and Li, X., 2014a. Precise point positioning with the BeiDou navigation satellite system. Sensors 14 (1), 927–943.

Li, P. and Zhang, X. 2014. Integrating GPS and GLONASS to accelerate convergence and initialization times of precise point positioning. GPS Solutions. 18 (3), 461–471.

Li, T., Wang, J. and Laurichesse, D. 2014b. Modeling and quality control for reliable precise point positioning integer ambiguity resolution with GNSS modernization. GPS Solutions. 18 (3), 429–442.

Li, X., Zhang, X., Ren, X., Fritsche, M., Wickert, J. and Schuh, H. 2015. Precise positioning with current multi-constellation Global Navigation Satellite Systems: GPS, GLONASS, Galileo and BeiDou. Scientific reports, 5.

Melgard, T., Vigen, E., Jong, K.D., Lapucha, D., Visser, H. and Oerpen, O. 2009. G2-the first real-time GPS and GLONASS precise orbit and clock service. In: Proceedings of ION GNSS 2009, September 22–25, Savannah, Georgia, USA, pp. 1885–1891.

Montenbruck, O., Hauschild, A. and Hessels, U. (2011). Characterization of GPS/GIOVE sensor stations in the CONGO network. GPS Solutions, 15(3), 193–205.

Montenbruck, O., Steigenberger, P., Khachikyan, R., Weber, G., Langley, R. B., Mervart, L. and Hugentobler, U. 2014. IGS-MGEX: Preparing the Ground for Multi-Constellation GNSS Science, Inside GNSS, 9(1), 42-49.

Nassar S, and El-Sheimy N (2005) Wavelet analysis for improving INS and INS/DGPS navigation accuracy. Journal of Navigation, 58(01), 119-134.

Petovello, M. G., Cannon, M. E., & Lachapelle, G. (2004). Benefits of Using a Tactical-Grade IMU for High-Accuracy Positioning. Navigation, 51(1), 1-12.

Qu, L., Zhao, Q., Li, M., Guo, J., Su, X. and Liu, J. 2013. Precise point positioning using combined Beidou and GPS observations. In: Proceedings of China Satellite Navigation Conference (CSNC) 2013, May 15–17, Wuhan, China, pp. 241–252.

Ristic, B.; Arulampalam, S.; Gordon, N. Beyond the Kalman filter: Particle filters for tracking applications. Artech House:2004.

Shi, J., & Gao, Y. (2014). A comparison of three PPP integer ambiguity resolution methods. GPS Solutions, 18(4), 519-528.
Simon, D. (2006). Optimal state estimation: Kalman, H infinity, and nonlinear approaches. John Wiley & Sons.
Steigenberger P, Hugentobler, U., Montenbruck, O. and Hauschild, A. 2011. Precise orbit determination of GIOVE-B based on the CONGO network. Journal of Geodesy, 85(6), 357-365.

Steigenberger, P., Hugentobler, U., Loyer, S., Perosanz, F., Prang, L., Dach, R., Uhlemann, M., Gendt, G. and Montenbruck, O. 2014. Galileo Orbit and Clock Quality of the IGS Multi-GNSS Experiment, Advances in Space Research, doi: 10.1016/j.asr.2014.06.030.

Tegedor, J., Øvstedal, O., and Vigen, E. 2014. Precise orbit determination and point positioning using GPS, Glonass, Galileo and BeiDou. Journal of Geodetic Science, 4(1).

Xu, P., Shi, C., Fang, R., Liu, J., Niu, X., Zhang, Q., & Yanagidani, T. (2013). High-rate precise point positioning (PPP) to measure seismic wave motions: an experimental comparison of GPS PPP with inertial measurement units. Journal of Geodesy, 87(4), 361-372.

Yi, Y., Grejner-Brzezinska, D. A. (2006). Tightly-coupled GPS/INS integration using unscented Kalman filter and particle filter. In Proceedings of the 19th International Technical Meeting of the Satellite Division of The Institute of Navigation (ION GNSS 2006) (pp. 2182-2191).

Yigit, C.O., Gikas, V., Alcay, S. and Ceylan, A. 2014. Performance evaluation of short to long term GPS, GLONASS and GPS/GLONASS post-processed PPP. Survey Review. 46 (336), 155–166.

Zhou, J., Knedlik, S., & Loffeld, O. (2010). INS/GPS tightly-coupled integration using adaptive unscented particle filter. Journal of Navigation, 63(03), 491-511.

Zumberge J F, Heflin M B, Jefferson D C, Watkins M M and Webb F H (1997) Precise point positioning for the efficient and robust analysis of GPS data from large networks. Journal of Geophysical Research,102(B3): 5005-5018.

VISION BASED TECHNIQUES FOR BUILDING FAÇADE MONITORING

Andrea Masiero [a,*], Francesca Fissore [a], Antonio Vettore [a]

[a] Interdepartmental Research Center of Geomatics (CIRGEO), University of Padua, Legnaro (PD), Italy
masiero@dei.unipd.it
(francesca.fissore, antonio.vettore)@unipd.it

KEY WORDS: Monitoring, Mobile Mapping, Terrestrial laser scanning, Photogrammetry

ABSTRACT:
The effect of aging, humidity and infiltration and other atmospheric factors causes the need for monitoring building structures and their periodical restoration. Monitoring the status of building façades is a task typically done by a human operator, which has to carefully inspect it in order to determine zones that require restoration or maintenance. Human operator inspection is very reliable when dealing with easily visible parts of the façade (e.g. close to the ground), but it may provide subjective results for parts not so closely visible by the operator. In practice, providing a really accurate estimate of the specific areas that require maintenance and restoration may not be so easy for a human operator (alternatively, it can be a time consuming task if the human operator really aims at carefully inspect all the parts of a large façade).
Motivated by these considerations, in this paper we consider the problem of monitoring the status of the tiles in a University building of the University of Padua. The rationale is that of using geomatics tools, such as photogrammetry and terrestrial laser scanning, in order to develop an easy to use and quite fast method which allows to have reliable estimates of the number of damaged tiles (and identify their position). For what concern photogrammetry, the idea is that of exploiting the ability of UAV to closely reach areas not so easy to reach for human operators in order to have close view images of all the area of interest, which shall be processed to produce 1) a photogrammetric dense cloud reconstruction of the area of interest, 2) a 2D and 3D analysis of images and point cloud in order to identify areas in need of maintenance. In our validation tests, this approach allowed to correctly classify 90.3% of the tiles, whereas the remaining tiles have been distributed among 4% of type I errors (tiles recognized as damaged while being in good conditions), and 5.7% of type II errors (tiles recognized as in good status while being damaged). 4% error on the number of tiles to be restored has been also obtained.
The use of terrestrial laser scanning was investigated as well. However, the results obtained with the considered instrument are unsatisfactory, mostly because of the not sufficient instrument accuracy in distance measurements. The use of different terrestrial laser scanning instrumentation shall be considered in the following development of this work in order to obtain measurements sufficiently accurate to be usable for the considered purpose.

INTRODUCTION:

In the last decades Geomatic techniques have been used for several surveying and monitoring applications, for emergency management, intelligent transportation, infrastructure and building monitoring. In particular, laser scanning and photogrammetry are very frequently chosen among

the different available surveying technologies.
On the one hand, laser scanning technology can be considered as the state of the art of last decade surveying methods (Pirotti 2013, El-Sheimy 2005): high reliability, repeatability and accuracy, typical generation of very dense point clouds, are fundamental factors in order to make terrestrial laser scanning (TLS (Petrie 2009)) an ideal technology for most of terrestrial applications where time acquisition is not a stringent constraint and accessibility to the place of interest is not restricted.
On the other hand, photogrammetric instrumentation is often cheaper, time acquisition is usually shorter than in TLS, generated point cloud can be sufficiently detailed, and accuracy is usually sufficiently good if survey and processing are done by expert personnel (Remondino, 2006). Furthermore, thanks to the recent worldwide spread of drones/unmanned aerial vehicles (UAVs) and good quality cheap digital cameras, the combination of digital photogrammetry and UAVs can be seen as an attractive (quite inexpensive) solution in order to quickly acquire images usable for photogrammetric reconstruction (Chiang 2015, Nex 2014), also in places difficult to reach on the ground (and reachable at much higher cost with other aerial solutions).
Taking into account of the above considerations, in this paper photogrammetry and TLS are considered in order to properly monitoring the status of the façade of a University building in the University of Padua.
Every year a huge amount of money is spent for monitoring, inspection and maintenance of building facades: building materials are subject to deterioration due to several factors, e.g. the influence of natural factors (atmospheric precipitations, sun, wind), infiltrations and aging. Preservation of a good status is mandatory both to avoid issues on other parts of the building and for keeping building appearance similar to the original one.
Human inspection usually play a fundamental role in order to determine required maintenance actions: for instance, to determine which parts have to be restored, refurbished or substituted. However, such decision is typically subjective and sometimes imprecise.
In this paper, the problem of monitoring the status of tiles in a University building is considered: a portion of these tiles have to be periodically substituted because seriously damaged by humidity and infiltrations, however the exact amount of tiles to be substituted per each time is currently estimated very roughly by a human operator.
In order to avoid this subjective and approximate choice, this work compares the use of different surveying methods in order to provide a reliable estimate of the number of damaged tiles: appearance and shape changes shall be used in order to distinguish damaged tiles with respect to the other ones. Unfortunately, this task is quite challenging:
a) shape deformations are visible but typically small (e.g. deformations of few millimeters on the direction orthogonal to the facade plane),
b) appearance changes are usually visible, but they can be influenced by other factors, e.g. color alteration due to external factors, illumination changes.
Photogrammetry and TLS reconstructions are considered in this work to provide 3D reconstructions with the specific goal of providing reliable identification of the deformed and damaged areas. In particular, the final aim of this project is to provide an easy to use tool for

automatically detecting damaged tiles and counting their number.
The considered methodology has been validated on two portions of the University building façade, easily visible by human operators in order to check the tile status, and hence have a reliable ground truth. Being close to the ground images have been collected by a human operator with a consumer camera. However, in order to be effective on all the building façade, the proposed approach has to be applied to images acquired by positions quite close to the building and distributed all over the façade, hence acquired by means of a UAV. At this step of development of the project images acquired by human operator are sufficient in order to validate the system, however acquisition those that shall be the real working conditions of the system is foreseen in the near future (as soon as it will be possible to close the building to student access, for security reasons). Fig. 1 shows the University building façade frequently subject to tile damages due to humidity and infiltrations, whereas Fig. 2(a) and (b) show the two portions considered for the system validation.

(a) (b)

Figure 1. (a) Façade of the University building subject to damages due to humidity, infiltration, aging and atmospheric factors. (b) Zoom on an area of the façade where tiles in good and bad conditions are visible.

(a) (b)

Figure 2. Portions of the façade considered for the system validation, easily visible by human operators which provided ground truth tile classification.

OBJECTIVES:

The goal of this paper is to investigate the use of photogrammetric and terrestrial laser scanning survey methods in order to provide reliable data for a software application able to identify tiles damaged by infiltrations, atmospheric effect and aging. This tool shall be able to locate damaged tiles and provide estimates of their number. This is of great interest for the maintenance of building facades. Indeed, the manual count of the tiles to be substituted at a certain time instant can be long, tedious and the result can be affected by the status of the human operator during such task. Hence, this work aims at providing a semi-automatic procedure for performing this task quickly and with a minimal human interaction.

METHODOLOGY:

The considered method is based on the combined analysis of 2D (i.e. images) and 3D data (i.e. point clouds). The rationale is as follows:

1. First, use 2D information provided by images in order to detect each tile and separate it from the others (image segmentation).
2. Then, use 3D information in the point clouds in order to check the status of each tile (whether it is damaged or not).

2D IMAGE ANALYSIS:

The main goal of 2D image analysis is that of individually identify each tile. This goal is achieved as described in the following.

1. First, in the first considered image a region of containing a tile in good conditions has to be manually selected by an operator. This is a quick and simple interaction, which does not require specific expertise. The considered region is used in order to determine local statistics of good tiles in such image (e.g. average and standard deviation on the three RGB components). The rationale is that being images taken from quite close positions, they consider quite small portions of the façade, hence the aspect of tiles in good conditions in each one of such images is assumed to have similar characteristics in the same image (e.g. RGB components shall assume values in similar intervals of intensities, see for example Fig. 3(a)).
2. Then, a simple threshold method (based on pixel values with respect to the distance from the previously computed average and normalized by the standard deviation) is used in order to make apparent which pixels are probably part of a tile (and in particular part of a tile region in good conditions). Fig. 3(b) shows an example of the results of the thresholding process applied on image in Fig. 3(a). Black pixels (corresponding to a normalized value zero in the image) are those more probably appertaining to a good tile region, whereas white pixels (corresponding to a normalized value one in the image) are those that are

probably not part of a region in bad conditions in a tile. It is worth to notice that the main aim of this step is that of making apparent tile borders, this motivated the choice of a not so stringent threshold, which might not highlight all pixels in a damaged region.

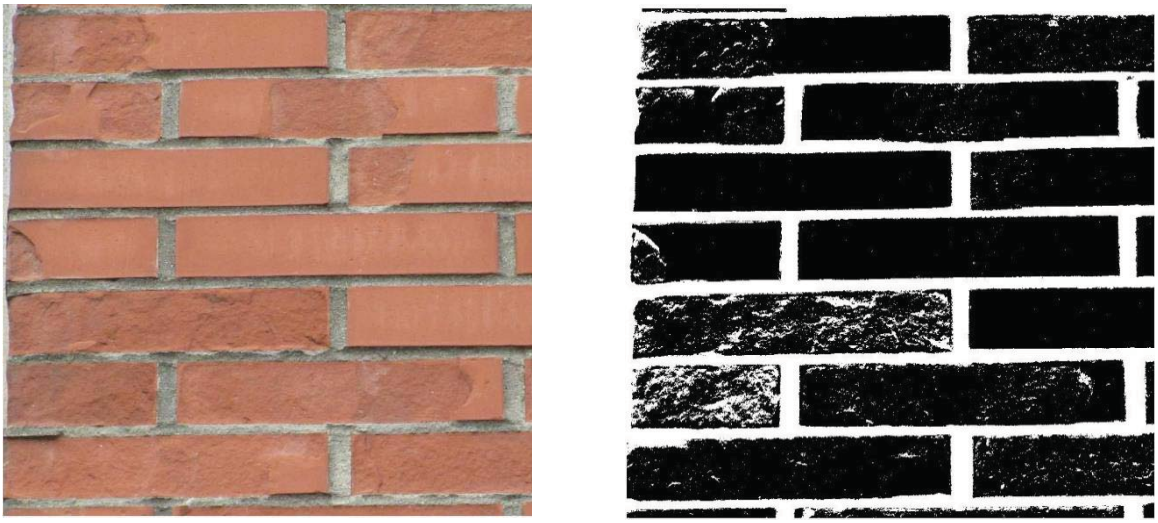

(a) (b)

Figure 3. (a) Image portion showing certain tiles in good and bad conditions. (b) Result of thresholding RGB values of image in (a).

3. Based on the results of step 2, the following procedure is used in order to individually identify each tile in the image:
    - A pixel position is randomly extracted inside of the image, and local maxima and minima of the (discrete) vertical partial derivative of image intensities along the horizontal coordinate of the pixel position are computed.
    - Horizontal axis of the image is assumed to be approximately parallel to the ground (e.g. landscape camera orientation), and hence to the horizontal tile borders. Maxima and minima close to each other, with absolute value higher than three times the standard deviation of the partial derivative over the all line, are matched and considered as hypothetical vertical coordinates of tile borders. When multiple hypothesis can be formulated (multiple local extrema close to each other), the choice that allows to better fit the approximate periodicity of maxima and minima over the image is selected.
    - Each couple of vertical coordinates matched at the previous step approximately identifies a row of tiles in the image. Let I_b be the binary image corresponding to the thresholding process, as in Fig. 3(b). For each tile row, let $f(c)$ be the cost function obtained by summing all values along column c in I_b with vertical coordinates within those of the considered tile row. Then, approximate position of vertical tile borders is determined by searching for large (positive and negative)

variations of *f(c)*. When two consecutive vertical tile borders are matched (left and right), a tile is correspondingly identified. Once a tile is found, a local optimization procedure searches for the best vertical and horizontal border positions corresponding to local extrema of the discrete derivative of *f(c)* (restricted to a neighborhood of the previously estimated horizontal coordinates of the tile) or to local extrema of the counterpart of *f(c)* defined by summing values of I_b along the horizontal direction. These operations are repeated for all tile rows in the image in order to find positions of all tiles. It is worth to notice that in the current implementation of the system tiles are assumed to have rectangular shape, with horizontal borders parallel to the image horizontal axis. Despite this is a quite realistic assumption, a generalization of this segmentation procedure is foreseen in the near future in order to deal with more generic working conditions.

Results of the above procedure for image in Fig. 3(a) are shown in Fig. 4.

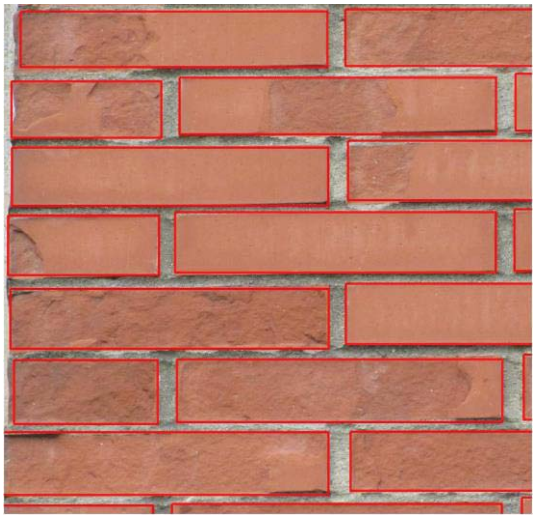

Figure 4. Tiles identified in image of Fig. 3(a).

4. After the first image, the analysis of the following ones takes advantage of previously computed results. The same images are used for photogrammetric reconstruction (see the following section), hence their alignment is exploited in the 2D analysis in order to exploit previous results on new images. More specifically, a quite good approximation of 3D coordinates of already detected tiles can be easily obtained by 1) fitting the region with a plane and 2) considering the intersection of such plane with the ray corresponding to the pixel position (lens distortion can be taken into account as well). Then 3D point is projected onto the new image. Intensity equalization can be done by comparing intensities on regions of already detected tiles. Then, a procedure similar to that previously described can be used in order to detect the remaining tiles.

PHOTOGRAMMETRIC RECONSTRUCTION AND 3D POINT CLOUD ANALYSIS:

A set of 406 images of the portions of the considered University building façade have been collected. Images have been taken by a consumer camera, Canon PowerShot SX210 IS, at maximum resolution (10.5Mpixel, with 16:9 aspect ratio), and allowed the reconstruction of the two validations areas with a total number of more than 80 million of points. Photogrammetric reconstruction has been obtained with Agisoft PhotoScan, which also performed camera self-calibration.

Once obtained the 3D reconstruction the following procedure is adopted in order to analyze the status of each tile.

Tile 3D coordinates are obtained as described in the previous section from the 2D ones. Then, the rationale of the approach is that roughness of damaged tiles should be higher than in that of those in good conditions. In particular, the surface of damaged tiles should be not be as close to be planar to those of good tiles. Fig. 5 and 6 shows two examples of tiles in bad status and their 3D reconstruction (lower intensity values (i.e. darker) in the bottom image are associated to inner tile points with respect to the plane defined by points cloud on the part of the tile in good conditions).

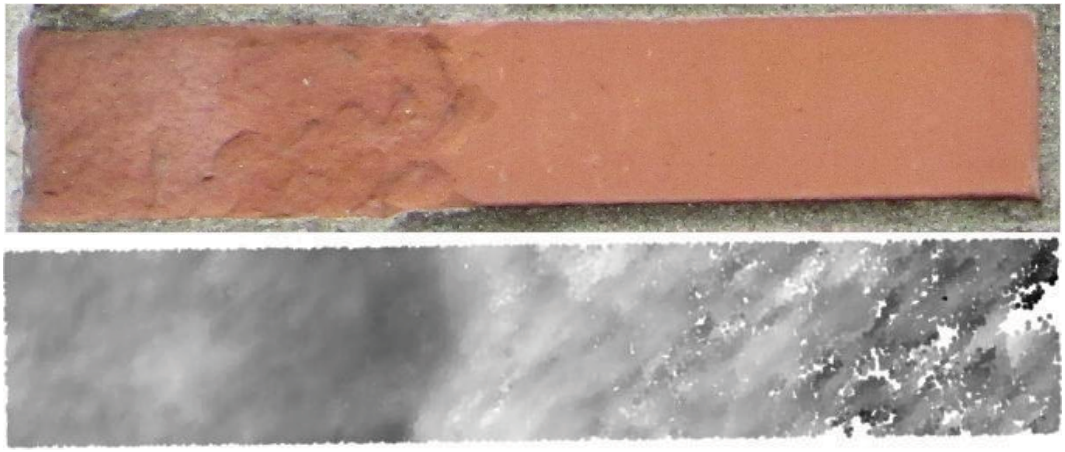

Figure 5. Example of tile in bed conditions (top), and its reconstruction (bottom). Lower intensity values (i.e. darker) in the bottom image are associated to inner tile points with respect to the plane defined by points cloud on the part of the tile in good conditions.

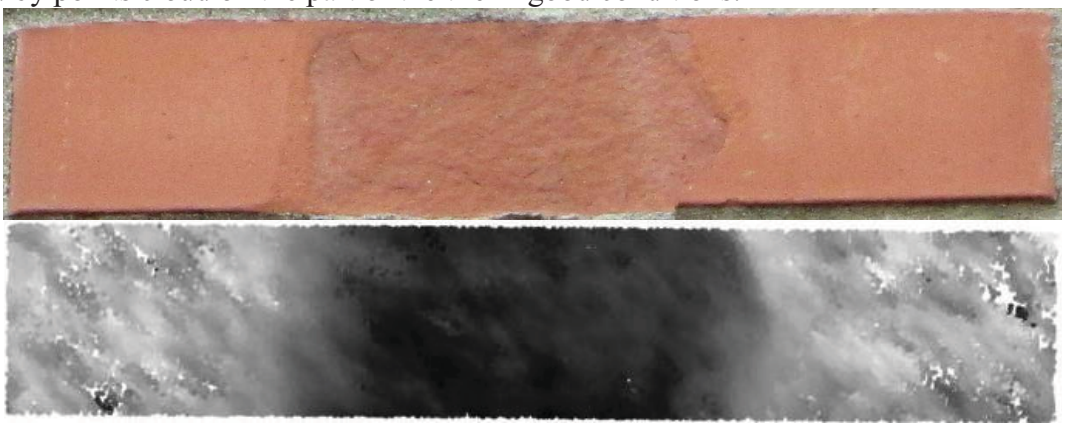

Figure 6. Example of tile in bed conditions (top), and its reconstruction (bottom). Lower intensity values (i.e. darker) in the bottom image are associated to inner tile points with respect to the plane defined by points cloud on the part of the tile in good conditions.

The proposed approach relies on the use of the fitting errors with respect to a planar surface fitted on the tile point cloud. In particular, let us consider tile point profiles associated to the fitting errors, e.g. Fig. 7 (a) and (b) show profiles of the fitting errors associated to tiles in Fig. 5 and 6, respectively.

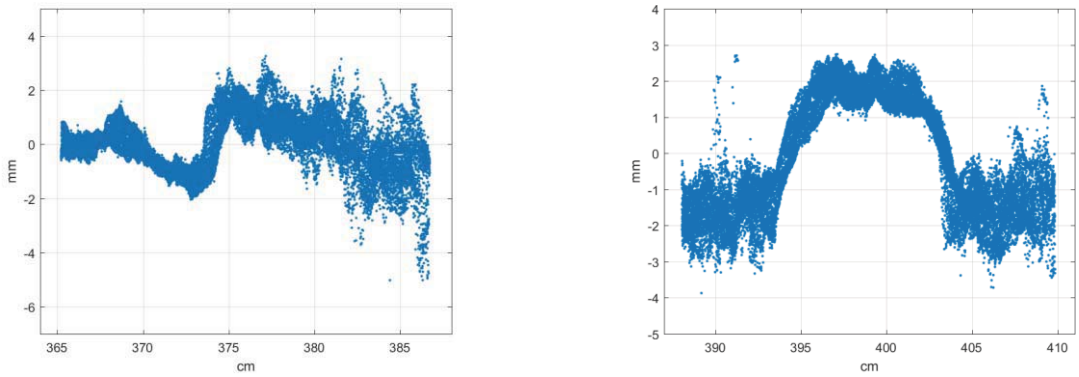

(a) (b)

Figure 7. Fitting error profiles related to tiles shown in Fig. 6 and 7. Horizontal axis correspond to the horizontal axis of the tile. Vertical axis represent coordinate with respect to the orthogonal direction to the façade plane.

Similarly to Fig. 7, Fig. 8 shows also a profile, but related to a tile in good conditions.

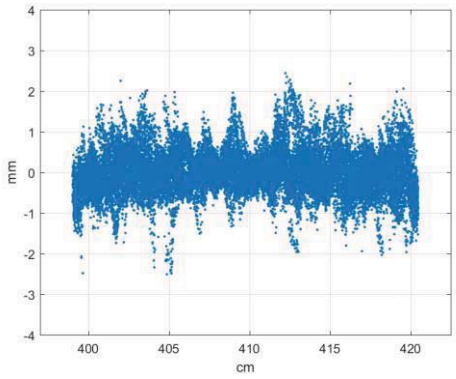

Figure 8. Fitting error profile related to a tile in good conditions. Horizontal axis correspond to the horizontal axis of the tile. Vertical axis represent coordinate with respect to the orthogonal direction to the façade plane.

First, comparing Fig. 7 and 8 it shall be clear that noise in the 3D reconstruction is not so much smaller with respect to tile deformations due to damages (indeed, in certain cases it is not possible to detect such deformations, as shall be shown in the following). Then, as shown in Fig. 8, fitting error distribution in tiles in good conditions is typically quite random, and approximately homogeneously distributed among the tile (i.e. similar characteristics can be seen for each value of the horizontal coordinate in Fig. 8). Differently, fitting errors in Fig. 7 show a clear non-random behavior.
Motivated by the above observation, the following strategy is adopted in order to detect tiles in bad conditions:

1) Fitting errors related to a tile are divided in slices of constant width w (1 cm in our simulations): each tile has dimension $h \times w$, where h is the length of the shorter side of the tile.
2) w has to be set to a value such that each slice contains a sufficiently large number of points. If this assumption is satisfied, then when dealing with tiles in good conditions points in each slice can be considered as random samples taken from the same random distribution.
3) Mean m_i and standard deviation σ_i of the fitting error values are computed for each slice i.
4) According to the above considerations, when considering a tile in good conditions then m_i should be approximately equal to m_j, for all the possible combinations of i and j. Then a simple hypothesis test on the mean of the two populations i and j (for all their possible combinations) is checked:

$$\frac{|m_i - m_j|}{\sqrt{\sigma_i^2 + \sigma_j^2}} > \theta$$

where θ is a design parameter of the procedure ($\theta = 1.5$ in our experiments).
5) Tile is identified as not in good conditions whether the above inequality is satisfied by at least a couple (i,j).

Tiles considered as not completely damaged in the previous case might still be partially damaged. In order to detect this condition it is necessary to detect the presence of slopes on the tile surface. on the tile surface.

TLS 3D POINT CLOUD ANALYSIS:

An approach similar to that presented in the previous section has been investigated also for point clouds deriving by TLS survey. In particular, Leica ScanStation C10 has been used in order to take several acquisitions of the building façade from different distances. Despite in principle an approach similar to that presented above should be effective also with TLS point clouds, in practice at the current state of development of the project, according to our experimental data the use of the considered laser scanner appears to be hardly effective for this task. This is probably mainly due to the not sufficient measurement accuracy (0.4 mm according to Leica ScanStation C10 technical specifications, whereas smaller deformations shall be detected).
Nevertheless, we foresee to overcome this limitation in the near future by using a different TLS, in order to acquire data with a higher level of accuracy.

EXPERIMENTAL RESULTS:

The procedure presented in the previous sections has been validated on the classification of 247 tiles distributed in the areas of Fig. 2(a) and (b). A human operator has provided ground truth classification for each of this tile in order to have a reliable ground truth comparison. 147 tiles have been classified as in good conditions, whereas the remaining ones have been classified as in bad conditions.

The proposed procedure allowed to correctly identify 222 tiles. 24 classification errors are distributed as follows: 10 type I errors (false positive, i.e. tiles recognized as damaged while being in good conditions) and 14 type II errors (i.e. tiles recognized as in good status while being damaged). For what concerns the estimation of the number of tiles to be restored, 96 tiles has been estimated to be restored (4% error with respect to the correct number, 100).

Fig. 9 show two examples of (type II) errors. Most of these errors are typically due to tiles that are very close to be planar even if damaged (see Fig. 9 (a)). A correct classification can be difficult also if the tile is smaller (and hence typically better fitted by a plane) as in Fig 9 (b).

(a) (b)

Figure 9. Classification error examples.

CONCLUSIONS AND FUTURE WORKS:

The proposed system has been validated on an area containing 247 tiles on the façade of a University building. 2D image analysis have provided a good support in order to properly identify and separate the tiles. This allowed us to identify the corresponding 3D points on the reconstructed photogrammetric point cloud. Analysis of 3D points in order to obtain a reliable classification of the tile status has been a quite challenging problem. Indeed, the signal to noise ratio is quite low (magnitude order of reconstruction error is almost at the same level of that of tile deformations). A similar issue has been encountered also when dealing with the TLS reconstruction: in this case measurement accuracy has not been sufficient for obtaining usable results. The proposed classifier, based on a spatial averaging process and on an hypothesis test, allowed to correctly classify 90.3% of the tiles, whereas the remaining tiles have been distributed among of type I errors (4%, tiles recognized as damaged while being in good conditions), and type II errors (5.7%, tiles recognized as in good status while being damaged). 4% error has been obtained on the number of tiles to be restored.

The following future works are foreseen in order to complete the work:

- acquisition of images close also to the upper part of the building façade with UAV,
- use of a more accurate terrestrial laser scanner in order to make also this option available to technicians interested in the use of the system,
- increase the number of tiles considered in the validation process (at least 4 times more). Validation areas from other parts of the building façade shall be considered as well,
- use of different classifiers, and of calibrated camera in the photogrammetric case, will be also considered in order to obtain better classification performance.
- integration of TLS and photogrammetry will be also investigated in order to improve current results (Nex, 2009; Masiero, 2015).

REFERENCES:

1 . Ajmar, A, Balbo, S., Boccardo, P., Giulio Tonolo, F., Piras, M., Princic, J. 2013, A Low-Cost Mobile Mapping System (LCMMS) for field data acquisition: a potential use to validate

aerial/satellite building damage assessment, International Journal of Digital Earth, 6 (SUPPL.2), pp. 103-123.
2. Chiang, KW, Tsai, ML, El-Sheimy, N, Habib, A, Chu, CH. 2015, New Calibration Method Using Low Cost MEM IMUs to Verify the Performance of UAV-Borne MMS Payloads, Sensors, 15 (3), pp. 6560-6585.
3. El-Sheimy, N, 2005, An overview of mobile mapping systems, Proceedings of the FIG Working Week, pp. 16-21.
4. Masiero, A, Guarnieri, A, Pirotti, F, Vettore, A. 2015, Semi-automated detection of surface degradation on bridges based on a level set method. The International Archives of Photogrammetry, Remote Sensing and Spatial Information Sciences, 40(3), 15.
5. Nex, F, Remondino, F. 2014, UAV for 3D mapping applications: a review, Applied Geomatics, 6 (1), pp. 1-15.
6. Nex, F., Rinaudo, F. 2009, New integration approach of Photogrammetric and LIDAR techniques for architectural surveys. The International Archives of Photogrammetry, Remote Sensing and Spatial Information Sciences, 38.3.
7. Pirotti, F, Guarnieri, A, Vettore, A. 2013, State of the art of ground and aerial laser scanning technologies for high-resolution topography of the earth surface, European Journal of Remote Sensing, 46, pp. 66-78.
8. Remondino, F, Fraser C. Digital camera calibration methods: considerations and comparisons. International Archives of Photogrammetry, Remote Sensing and Spatial Information Sciences 36.5 (2006): 266-272.

Localization using Region-based Convolution Neural Network: A Comparison Study

C. K. Toth[a], Z. Koppanyi[a], Haowei Xu[a], Dorota Brzezinska[a]
[a] OSU, SPIN Lab, The Ohio State University, Bolz Hall, 2036 Neil Ave, Columbus, Ohio, USA, 43210
(toth.2, koppanyi.1)@osu.edu, xuhaoweiself@gmail.com, grejner-brzezinska.1@osu.edu

Commission VI, WG VI/4

KEY WORDS: Indoor localization, Object detection, Convolutional Neural Network, Location-based services

ABSTRACT:

This study is the part of our ongoing research to use objects detected on images and object-level representation of the environment for indoor localization. The localization concept consists of three major steps. First (1), the user takes an image inside a building in order to determine its own position. Then, in the second step (2), this image is passed to a trained object detector that recognizes and localizes various types of objects in the image. The final localization step (3) requires prior knowledge obtained by blueprint or surveying, with the location of the objects. The user position can be obtained based on the similarity of the detected image objects and the objects located on the map. In our previous study, we used Region-based Convolutional Network (R-CNN) for object detection in (2). In this paper, we assess the object detection and localization performance of the previously proposed R-CNN network, cascade detector and template matching approaches. A test was conducted in a typical yet challenging building. 300 images of selected objects were taken around the test area and organized into a database. This database was used for training the R-CNN and the cascade detector as well as used for template matching. Then, for the validation dataset, 42 images were also captured at randomly chosen, but known locations. The results indicate that the cascade detector trained on this dataset cannot be used due to the large number of false positive detections. The R-CNN outperforms the template matching method with 13% in terms of success rate, however the latter provides 9.3% less wrong localizations. The combination of the two methods provides 52% success rate with 90.5% rate of the fail safe solutions.

1. INTRODUCTION

Image-based localization provides cost efficient alternative in those indoor applications, where the goal is to provide approximate locations within a building; for instance, finding rooms in hospitals, nursing rooms, universities and institutions, or providing location-based information about objects, areas at museums or conferences. One of the main advantage of the image-based localization solutions that smartphones equipped with cameras are commonly available, and thus, no special hardware is required on the user side.

This study presents our ongoing research to apply object detection on images and use this information for indoor localization (Xu et al., 2017). The high level concept of the proposed localization framework is shown in Figure 1. The localization workflow is the following. A user captures an image with a dedicated mobile app installed on his/her smartphone in order to determine its location within a building. Then this image is uploaded to a webserver that processes it. Objects in the image with their relationships are extracted. The map of the objects is available on the server, thus the extracted image objects can be matched to the map and the user location can be obtained.

One possible way to derive location based on a single image, is to take images at different locations around the area and store in a database with their location descriptors or coordinates. Then, when the location request from a use with an image is received, the server can match this image to those stored in the database. The similarity metric can be based on the concept of Word of Visual Bags (Fei-Fei and Perona, 2005). These techniques are feature-based, not object-based. Note that these solutions require large number of images taken around the area. In contrast, the approach presented by this study does not require this kind of pre-survey around the area, if the object detector is able to recognize various type of objects around the area, and these objects are also known on a map. In other words, the network can be trained on large image datasets independently from the area, and thus, it is able to identify large number of various objects, irrespective to the specific area. The concept only requires the map of the possible objects that can be derived from blueprints or building models. Thus, this system also offers faster deployment as opposed to other techniques.

In our previous study, we examined this concept using a version of Region-based Convolution Neural Network (R-CNN) for object detection. In this study, we compare this approach to two other object detectors, namely, cascade object detector and template matching (TM).

Figure 1 The high level concept of the proposed localization system.

The paper is structured as follows. In the "Methods" section, the structure of the localization system, the object detectors and the localization algorithm are presented, briefly. In order to validate the object detectors, test data were collected, and the "Test" section presents the description of our experiment. The "Results" and "Discussions" section provides performance analysis of the object detectors. Finally, the "Conclusion" section summarizes our findings and future plans.

2. METHODS

The indoor localization method applied in this study was introduced earlier in our paper (Xu et al., 2017). Here, we briefly present the concept; for more details, see our previous study. The general workflow of the proposed localization framework is presented in Figure 2. In the offline phase, the object detector is trained (2). The general idea is to train the classifier on large number of images, i.e. training dataset (1), obtained from the internet or other source. In this study, we used images taken from the test area. The training dataset is the set of images taken from typical objects that are presented indoor. Then, these trained detectors are deployed on a server. The map of the objects also has to be created during the offline phase. Since, we use high-level representation of the scene, i.e. objects, this map is easy to create (3).

During the online phase, users capture images (4) and send them to the server. At this point, the objects are extracted using the object detector trained during the offline phase. The localization algorithm (6) takes these detected objects as inputs and calculates the user's location (7) based on matching them to the map. In the next subsections, the three applied object detectors with the localization algorithm are presented briefly.

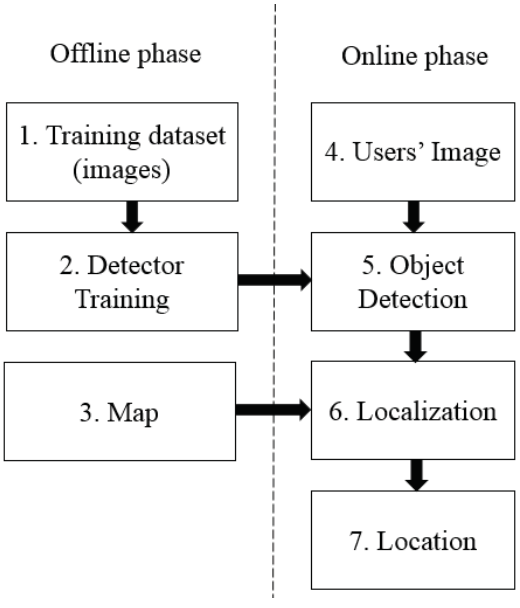

Figure 2 Workflow of the proposed localization framework

2.1 Object Detection with R-CNN

Convolutional Neural Networks (CNNs or ConvNets) are commonly used for image classification. This problem, in general, is to recognize what is on the picture. According to this problem definition, the input layer of CNN is the array of image pixels, and the output vector contains the scores or weights that indicates the class or label as probability to which the image belongs. CNN typically classifies the whole image and does not segment it into smaller objects. Region-based CNN (R-CNN), proposed by (Girshick et al., 2014), enables segmenting the image into regions, and thus, multiple objects can be localized, detected, and recognized in a single image.

Several R-CNN implementations exist, such as Fast R-CNN and Faster R-CNN algorithms (Ren et al., 2015; Ross, 2015). In this study, Faster R-CNN is used for detecting objects in images taken by a single smartphone. The latest version of Faster R-CNN consists of a Region Proposal Network (RPN) and a Fast R-CNN. RPN is used to provide proposals and distinguish between background and objects for the Fast R-CNN. Due to this structure, feature extraction, classification and proposal position refinement are integrated into one deep network, which further leads to improved detection rate and training speed. In this study, we used the *Caffe* neural network library and framework (Jia et al., 2014)

In order to improve the object detection performance, in our previous study, several Faster R-CNN networks are trained separately for each object class. During the detection, all Faster R-CNNs process the image in parallel, and the results of the R-CNNs are merged to provide a composite output with all detected classes. Different training and testing parameters are investigated for each R-CNN. In addition, when a new class is needed to be detected, instead of having the traditional Faster R-CNN re-trained by the whole dataset requiring large computation, another parallel sub-Faster R-CNN is added to the system, which is trained by a small training set containing only the specific class. For more details, see out previous study (Xu et al., 2017).

2.2 Object Detection with Cascade Classifier

Cascade classifiers are typically used for object detection on images. Here, the OpenCV library's cascade classifier implementation is used for training. The classifier can use Haar and local binary pattern (LBP) features (Liao et al., 2007; Viola and Jones, 2001). Both features are examined in this study. Detectors are trained for each object classes. The training requires positive and negative samples. The positive samples are created with manually selecting the areas of the object on images from the training dataset. The negative or background images are those images from the training dataset that do not contain any of that object which the detector is trained for. 2000 negative images are used during the training.

2.3 Object Detection with Template Matching

The template matching requires an inventory of the typical objects; these are the clipped image areas of the object created similar to the cascade classifier. Thus, we have images of doors, lights, etc. organized in a database. Then, we use these templates to find them on an image. For the object detection, first, the feature descriptors are extracted from the user's and the template images, then these descriptors are compared. The descriptor pairs are created based on whether the difference between the descriptor is lower than a predefined threshold. In addition, the matching can be further evaluated using homography constraints between the image region and the sample. The bounding box of the detected object is calculated with applying homography transformation on the template image corners.

An example is presented in Figure 3. The template image of a trash bin can be seen in the up right corner of the figure. The user's image is the larger image in the left side of the figure. The light blue circles are the detected features. SURF and SIFT features are applied in this study. The blue line connects the matched feature pairs. The bounding box calculated as the homography transformation of the template image are depicted with red rectangle.

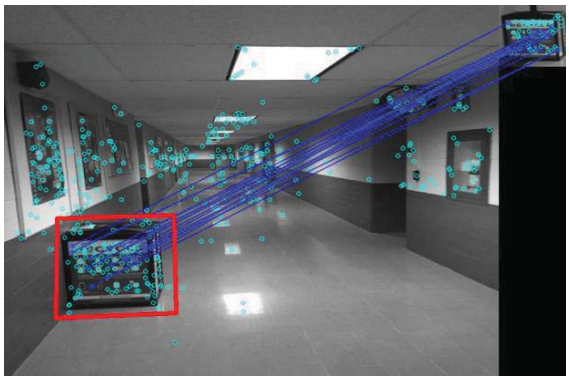

Figure 3 An example of template matching

2.4 Localization Algorithm

The localization algorithm takes the bounding boxes of the objects as inputs provided by the object detector. This algorithm is introduced earlier in details (Xu et al., 2017); here, we only briefly present it. First, the spatial relationships (e.g., up, down, right, left) of the detected image objects are derived based on the relative locations of the bounding boxes with respect to each other. This relationship is represented as a directed graph, where the directions of the graph edges indicate the relationship; these relationships are whether an object is on the right, left or up, down from the other object. This directed graph is called image graph.

The location of the objects are also known on the map. Assuming a fixed position and orientation of a virtual camera on this map, and knowing the objects' coordinates, a virtual image can be created with projecting the object coordinates onto the virtual camera plane. The virtual image contains the locations of the objects on the image as if it was taken at that fixed position and with a certain orientation. During the offline phase, a directed graph can be derived from the virtual image similar to the image graph. This graph is called position graph. The virtual camera are placed to, and thus, these position graphs are calculated at various points on the map; note that the density of these points determines the resolution of the localization. Also, note that the derivation of these graphs may require intensive computation; but, it only needs to be calculated once prior to using the system, during the offline phase. Each position graph is stored with the position and orientation of the virtual camera in a database. Finally, the user location can be obtained with measuring the similarity between the image graph and the stored position graphs. This similarity metric was proposed in our previous study.

One of the advantage of using graph concept that neither the map nor the camera parameters does not have to be defined metrically. Thus, it's enough if we have only a photo of the building's blueprint. In addition, the method is still applicable when the camera is not calibrated. This allows handling various types of images without assuming any camera model. Alternatively, if metric map is available as well as the camera parameters are known, this camera model can be used for projecting the map's objects onto the virtual image plane. Then, instead of position graphs, these images are stored in the database. During the online phase, instead of using the graph concept, one can, for instance, use the average of the Euclidean distance between the objects on the user's image and the stored virtual images for measuring the similarities.

TEST

In order to compare the performance of the object detectors for localization, a test was conducted on the 2nd and 3rd floors of the Bolz Hall at The Ohio State University. For the training dataset, 600 images were taken randomly with a smartphone camera. 9 classes, were labelled in the images. Table 1 shows the objects, the labels that was used for labelling the objects for visualization and the numbers of samples. Note that objects often presented around the area have larger number of samples. Parallel Faster R-CNN, cascade detector with Haar and LBP features are trained on this dataset. For the cascade object detector 2000 negative samples were used. The template matching algorithm with using SURF and SIFT descriptors are also worked on the same dataset. In the case of all three methods, the same object might be detected multiple times resulting in overlapping bounding boxes over one object. These boxes are merged together, if the ratio of the overlapping and the bounding box area exceeds 30%.

Table 1 Training dataset by objects

Object	Label	Samples
Coke machine	a	17
Door	d	532
Fire exhauster	f	94
Clock	k	130
Lights	l	384
Locker	o	60
Bench	r	229
Trash bins	t	185
Water fountain	w	90

For the map database, 142 objects digitized on a blueprint for both floors, see Figure 4. In the fire, lights, doors and other objects are depicted with blue, red and black triangles, respectively. Note that the floors are very similar in terms of object locations and diversity, and thus, it is a challenging environment for the localization algorithm. In order to create the position graph database, the virtual camera positions are placed along the center of the corridors with an about 5 m separation to derive position graphs. At certain positions, the virtual camera direction was also changed by 25º steps around the vertical axis to complete a 360º turn. Thus, the database contains 3154 position graphs. For validation, 42 images were taken randomly around the area with a single smart phone.

RESULTS

The results indicate that the cascade object detector cannot be used for localization due to the large number of positive falses, nevertheless whether Haar or LBP features are used. An example is presented in Figure 5. Note that in Figure 5a, however, the exit sign is selected properly, but all other regions are misclassified. Figure 5b presents a typical problem with this type of object detector. Although the light on the ceiling is selected correctly, but its reflection on the floor is also detected.

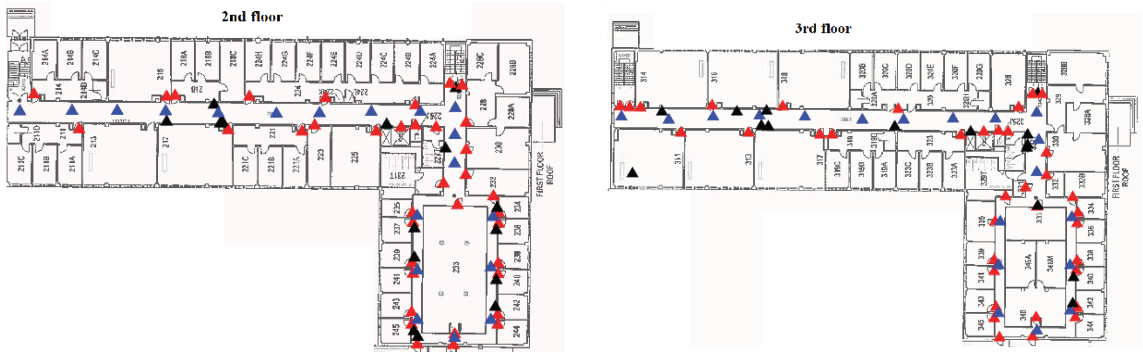

Figure 4 The digitized objects on the blueprints for the two floors.

(a) (b)

Figure 5 Objects provided by the cascade detector, (a) shows many misclassified regions, and (b) presents a case when the reflection of the light on the floor is also segmented as object.

The large number of misclassification might be caused by the small training dataset; more positive samples are required for the proper training. In this study, we want to compare the various detectors on the same training dataset. Thus, we did not intent to extend the training set to provide enough input data for the cascade training algorithm. Thus, the localization results of R-CNN and template matching are assessed further.

Four examples out of 42 validation images are presented in Figure 6 with applying R-CNN and template matching-based object detection. The first column shows the detected objects in the user's image for R-CNN and the second column for the template matching. The third column presents the obtained locations, where the blue dots depicts the R-CNN and the red dots the template matching solutions.

In the case of the example presented in the first row, both approaches extracted two objects, and because these objects and their relative positions on the image are unique, the location is successfully found on the map. The second row presents an example, when the template matching algorithm finds one more object, i.e. the trash, than the R-CNN. Thus, multiple locations are found using the objects detected by R-CNN, but with this extra object extracted by the template matching specifies the exact location. Clearly, better localization result can be achieved if more objects are detected on the image. In the third row, the R-CNN is able to extract the exit sign at the end of the corridor, above the door, and thus, provide a single location. In contrast, the template matching cannot segment this object, and the localization algorithm provides multiple solution. Only four exit signs are located on the two floors, thus if one can be detected, that significantly decreases the number of the possible locations. In general, our experience is that the template matching is not able to extract objects when they are small in the images. It often occurs when the object is located in the background, far from the camera. This is because the descriptors use window to capture the local gradients of a given image pixel. If the window is large, than the feature extractor algorithm also uses the background not just pixel points of the object. In addition, less features are extracted from a smaller area. Finally, the last row presents an example, when the localization fails, nevertheless which object detector is used. However, the R-CNN correctly finds three objects, those are not enough unique to solve the localization problem correctly. The template matching does not provide any acceptable results.

Table 2 presents the statistics for all 42 images. The table distinguishes five cases. The 'Success' column shows those cases, when only one location is found and that location is within 10 m radius of the ground truth. The wrong solutions are the false positives; thus, only one location is found, but this is outside from this 10 meter radius. Multiple solution means that no exact location can be provided; this is the case of Figure 6l. Floor ambiguous solutions have two locations due to the similar structure of the two floors. Thus, one location is obtained for the 2nd and another for the 3rd floor. Finally, no solution is obtained when no object is detected.

(a) Image 1, R-CNN object detection

(b) Image 1, TM-based object detection

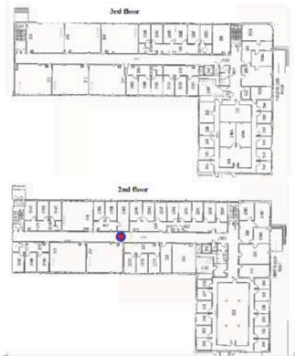

(c) Localization result for Image 1 R-CNN (blue) and TM (red)

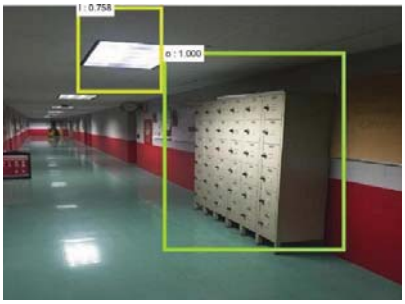

(d) Image 2, R-CNN object detection

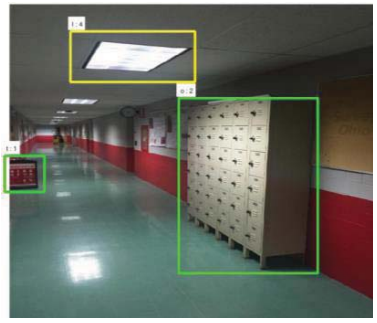

(e) Image 2, TM-based object detection

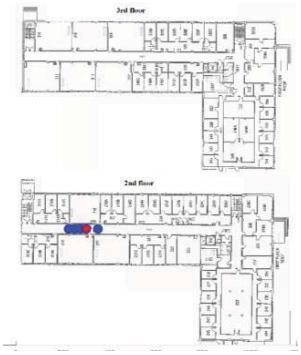

(f) Localization result for Image 2 R-CNN (blue) and TM (red)

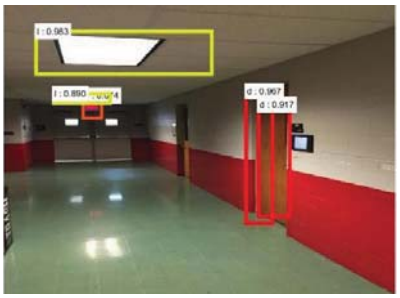

(g) Image 3, R-CNN object detection

(h) Image 3, TM-based object detection

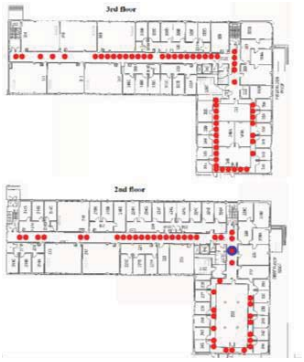

(i) Localization result for Image 3 R-CNN (blue) and TM (red)

(j) Image 4, R-CNN object detection

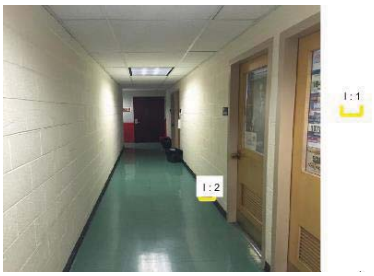

(k) Image 4, TM-based object detection

(l) Localization result for Image 4 R-CNN (blue) and TM (red)

Figure 6 Four example of the localization solutions: one solution (first row from top, a-c), template matching aids R-CNN (second, d-f), template matching does not provide solution (third, g-i) and ambiguous for both object detections (fourth, j-l)

Table 2 Solution types and rates (*- 100% - False positives)

Solution Type	Success	Wrong (False positives)	Multiple	Floor Ambiguous	No solution	Fail safe*
R-CNN	40.5%	11.9%	23.8%	23.8%	0.0%	88.1%
Template Matching	27.5%	2.5%	15.0%	12.5%	42.5%	97.5%
Combined	52.4%	9.5%	21.4%	16.7%	0.0%	90.5%

DISCUSSION

Multiple, floor ambiguous and no solution cases are detectable, and in these cases, the system is able to notify the user to take another image at a different location or from another angle. This extra images can provide further information to find the correct location. Thus, these cases are fail safe. The rate of the fail safe cases can be calculated as 100% minus the false positives; this value is presented in the last column of Table 2.

Comparing the methods, the R-CNN outperforms the template matching with 13%, however the template matchings' fail safe rate is better with 9.4%. The template matching has significantly smaller false positives (2.5% vs. 11.9%) due to filtering based on the homography constrain, but the object detection rate per image is lower than the R-CNN. Based on this, we can combine the two object detector. In the combined approach, first, the object detection based on template matching is performed. Then, if this method is not able to provide a single location, than the R-CNN is used. The combined solution achieves 52.4% success rate with 90.5% fail safe rate on the test dataset. This combined approach is better than the original localization method using only R-CNN for object detection.

CONCLUSION

This paper presented the latest results of our ongoing research on indoor localization based on object detection and with using high-level description of the environment (Xu et al., 2017). Such a framework offers faster system deployment, and does not require complex survey of the indoor environment. This study covered the question of the localization's success rate applying different object detectors. R-CNN, cascade detector and template matching approaches have been investigated. All detectors are trained on the same dataset. The cascade detector cannot be used for localization due to the low number of samples. The comparison of R-CNN and template matching indicated that the R-CNN outperforms the template matching, however, the latter provided less positive false results. The best localization can be achieved with the combination of the two; the success rate is 52.4% and the rate of the fail safe solutions is 90.5% in this case.

The main research directions in the future are the followings. First, we want to extend our localization algorithm to be able to handle the changes of the environment. These changes occur, for instance, when the objects are replaced or removed. These changes can be detected, if all images captured by the users is stored on the server side. Once these changes are recognized successfully, the system might be able to refresh the map, and thus, the system can be adaptive. Second, the combination of this localization approach with other, for instance, WiFi fingerprinting can improve the success rate as well as enables better adaptivity. Finally, the system is expected to be tested on larger or outdoor datasets.

REFERENCES

Fei-Fei, L., and Perona, P., 2005. A Bayesian hierarchical model for learning natural scene categories. In: *2005 IEEE Computer Society Conference on Computer Vision and Pattern Recognition (CVPR'05)*, pp. 524–531

Girshick, R., Donahue, J., Darrell, T., and Malik, J., 2014. Rich Feature Hierarchies for Accurate Object Detection and Semantic Segmentation. In: *Proceedings of the 2014 IEEE Conference on Computer Vision and Pattern Recognition*, pp. 580–587.

Jia, Y., Shelhamer, E., Donahue, J., Karayev, S., Long, J., Girshick, R., Guadarrama, S., and Darrell, T., 2014. Caffe: Convolutional Architecture for Fast Feature Embedding. In: *MM '14 Proceedings of the 22nd ACM International Conference on Multimedia*, pp. 675–678.

Liao, S., Zhu, X., Lei, Z., Zhang, L., and Li, S. Z., 2007. Learning Multi-scale Block Local Binary Patterns for Face Recognition. *Advances in Biometrics*, Springer, Berlin, pp. 828–837.

Ren, S., He, K., Girshick, R., and Sun, J.. 2015. Faster R-CNN: Towards Real-Time Object Detection with Region Proposal Networks. *IEEE Transactions on Pattern Analysis and Machine Intelligence*, (99), pp. 91–99.

Ross, G., 2015. Fast R-CNN. In: *Proceedings of the IEEE International Conference on Computer Vision*

Viola, P., and Jones, M. (2001). Rapid object detection using a boosted cascade of simple features. In: *Proceedings of the 2001 IEEE Computer Society Conference on Computer Vision and Pattern Recognition. CVPR 2001*, pp. 511-518

Xu, H., Koppanyi, Z., Toth, C.K., and Grejner-Brzezinska, D., 2017. Indoor Localization using Region-based Convolutional Neural Network. In: *Proceedings of the 2017 International Technical Meeting of ION*, Monterey, CA, USA

SWARM MAPPING: INVESTIGATION ON STRATEGIES TO EXPLORE BUILDING INTERIORS

Z. Koppanyi [a], C. K. Toth [a], D. Grejner-Brzezinski [a]
[a] OSU, SPIN Lab, The Ohio State University, Bolz Hall, 2036 Neil Ave, Columbus, Ohio, USA, 43210
(koppanyi.1, toth.2, grejner-brzezinska.1)@osu.edu

Commission VI, WG VI/4

KEY WORDS: exploration strategies, collaborative mapping, distributed mobile mapping, indoor mapping, first responders

ABSTRACT:

Swarm robotics is an emerging research field due to the large number of applications where this technology can be applied. One possible application in mapping is to discover building interiors to create map and identify dangerous spots inside a building to support first responders or military activities. Finding the optimal strategy for the exploration is critical in these time-sensitive scenarios. Such a strategy has to be robust, scalable, fault tolerance and distributed using local decisions. The strategy has to consider communication limitation among the swarm robots, and other mapping related issues, such as sensor noises. Furthermore, robots in a swarm are typically resource-limited platforms in terms of computation and memory. In this study, we compare three exploration strategies, namely closest frontier, maximum information gain, and bidding control policies, to determine the benefits of a more complex and computation intensive policy over a simpler one in terms of exploration time. The assessment of the strategies require statistical approach: the steps needed to explore an interior have to be calculated on large number of floorplans. For this reason, we developed a 2D simulation framework that enables us to run large number of simulations in relatively short time. During the simulations, robotic swarms with 1, 3, 6, 12 entities are placed in 20 different various-sized floorplans. Global and limited communication assumptions are also applied in the simulations. Overall, 480 scenarios are simulated and evaluated. The results indicate that the more complex bidding policy just slightly outperforms the maximum information gain strategy. Increasing the size of the swarm, this difference disappears. Clearly, a simple policy allows for real time implementation on resource-limited small platforms typically applied in swarm robotics.

1. INTRODUCTION

In the last couple of years, various novel and exciting small platforms have been introduced by the robotics community that may have potentials in mapping applications in the future (Michael et al., 2010). For instance, autonomous cheap micro-UAVs may open new research and application directions for mapping in confined or indoor areas (Morris et al., 2010; Wang et al., 2013). A group of these small platforms with utilizing swarm intelligence enables cooperative mapping. From the mapping's point of view, the group of swarm robots can be interpreted as a distributed mobile mapping system. There are several applications where these solutions can be applied, such as, aiding first responders in rescue operations, hostage situation, or supporting military activities. In civilian applications, these systems can be used for building inspections, mining activities, or for other mapping demands.

Currently, one of the main challenges to apply a group of micro-UAVs for mapping is the limited power, sensor, computation and communication resources available on these small, pocket-sized platforms (Rocha, 2006). For this reason, it is crucial to apply efficient control policies that minimize the usage of resources, but, at the same time, provide optimal control to achieve the swarm's common goal.

In this paper, we examine three control policies for collaborative robot mapping. This problem is commonly called as multi robot exploration. The main question of multi robot exploration problem is how to control a team of robots to competitively or cooperatively discover unknown areas under various restrictions, such as communication, sensor and platform limitations. Indoor environment is especially challenging for these systems due to the limited navigation capabilities. Such a control policy has to find an optimal path for fast exploration, but, at the same time, this path has to help the robot to navigate. For instance, if robots in the team use visual odometery or SLAM technique during the exploration, landmarks or keypoint locations have to be consider during the path planning to keep a consistent map of the environment, and thus, provide reliable navigation information (Fox et al., 2006).

In our ongoing research, as the first step to address the previous problem, we develop a simulation framework for investigating various multi-robot exploration strategies. Several control policy exist in the literature. The performance of these policies may depend on the environment structure, and thus, the statistical analysis of these policies is required. This analysis is important for platforms with limited resource to decide how much extra gain can be achieved using a more complex control policy than a simpler one. Because, however, a more complex control policy might achieve the common goal faster, but this gain might not be that high, which indicates to use extra computation resources; thus, a simple control policy might be more attractive for the system designer.

The contribution of this paper, as the first results of our ongoing research, is to provide statistical analysis of three control policies based on running simulation on 20 different floorplans. This analysis may provide information for mechanism design of micro-UAV swarm systems.

2. BACKGROUND

Multi robot exploration has been studied for almost three decades. Researchers developed various control policies for optimally explore areas considering various limitations and factors. These control policies can be divided into centralized and decentralized approaches (Khamis et al., 2015). In a centralized framework, the system has a higher authority to which the robots report their current states, such as discovered areas and location. Then, the authority controls the behaviour of each robots with respect to other robots' states. In the case of decentralized approach, each robot makes a decision based on their local information. The main advantage of the decentralized approaches that there is no direct link between the authority, and thus, the system is more robust, however, the computational needs might be higher on the robots' side that can be critical for platforms with limited resources. The focus of this study is on decentralized multi robot exploration problems.

In general, multi robot exploration is a game, where the global objective function is to explore the area efficiently. In this sense, game theory, more particular, mechanism design provides theoretical framework for designing distributed control policies (Li and Marden, 2013). In the next paragraphs, we briefly present some common strategies that was developed in the last decades, and which are in the scope of this study. For more details, see Sharma and Tiwari, 2016, where the authors give a longer survey on multi robot coordination (Sharma and Tiwari, 2016).

A simple cooperation can be realized, when each robot share its map among the others. Exchanging maps have a large communication load, however there are several algorithm that enables decreasing this load (Rocha, 2006). When maps are shared, robots can use control strategies developed for single robot environment. One of the main advantage of this system is to be able to handle heterogeneous robots, which may follow different control policies, since the map exchange protocol is defined.

A basic, but widely applied single robot control policy is to find a path for the closest undiscovered areas. This undiscovered area is commonly called frontier (Rajesh M. et al., 2014; Yamauchi, 1998). The definition of "closest" is critical for the system. Note that the closest distance is mostly not Euclidean distance between the robots current position and the closest frontier due to obstacle, walls or the presence of other robots. Path planning approaches give a solution to determine the exact distance (Sariff and Buniyamin, 2006). Such an algorithm may also consider the limited manoeuvrability of the robot; these algorithms typically have high computation burden. In addition, the path planning can be extended with additional constraints, such as considering that somewhat information is maximum along the path. For instance, due to sensor limitations, some locations of the map are just partially discovered during the exploration. Thus, a certainty metric can be defined for smaller areas. A path planner can consider this uncertainty and provide a feasible path, which leads the robot to the closest frontier, and, at the same time, maximize the information gain along the path to increase the reliability of the current map (Visser and Slamet, 2008).

Although the closest frontier method always solves the robot exploration problem, but it is a greedy algorithm. It tends to go to the closest area along a certain direction, and thus, those areas that is also close, but not along that direction are left behind, and thus, the robot mostly has to return to these locations. This problem can be partially addressed with creating a goal set that covers a larger area, for example a room. Thus, the robot does not leave this area before explore it (Zlot et al., 2002).

Beyond the map sharing mechanism, the level of cooperation can be increased with sharing the current robot coordinates. The behaviour-based strategy generates a "social potential field" considering the distance of obstacles, undiscovered cells and other robots, and the path is planned based on this potential field to achieve the largest exploration area (Gu Fang et al., 2005). This approach can stuck in a local minimum that has to be detected and the policy has to enforce the robot to leave this location.

More complex distributed cooperative policies can be designed with estimating other robots future positions. In this case, if all robots' policies are well-known among them, for instance, because the group is heterogeneous, one robot can calculate other robots mostly likely paths. Thus, this robot can take the others into consideration and plan its path accordingly. Typically these path are modelled as Markov Decision Processes. Using this stochastic framework, researchers introduced the concept of distributed value functions that enables to predict other robots intention when the shared map is uncertain or not updated due to short communication outages (Matignon et al., 2012a, 2012b).

Another popular solution is based on auction among the communicating agents. In this case, each robot generates a goal set; these are certain locations on the map, and they bid on them. The valuation of these locations may depend on the distance from the current robot pose, or other metrics. Then, they share their bids to a central authority and that decides the winner based on first-price auction format (Bererton et al., 2004). Note that this method requires a central unit, and thus, it is centralized. However, this research direction might be promising for designing decentralized policies in the future, because the robots do not have to share maps, just bids, and thus, the communication load is significantly lower. In addition, the auction format for resource allocation is well-known in mechanism design.

3. METHODS

The main goal of this paper is to assess the performance of various distributed control policies with respect to the environment structure, communication restriction and the size of the robotic swarm using simulation. However, several simple and sophisticated robotic simulation software and environment are available, such as Player/Stage, Gazebo, or MRXT.(Gil et al., 2015; Staranowicz and Mariottini, 2011), in this study, we present our simulation framework that is developed and optimized for playing multi robot exploration scenarios on large number of floorplans. The code is open-source and can be download from GitHub[1].

3.1 Platform and sensor models

The platform is modelled as follows. The control of the platform is 3 degree of freedom. The $A \in [a_f, a_l, a_r]^n$ is the action set, where, a_f, a_l, a_r are the atomic control commands; these are move forward, turn right with 45º or left with 45º. A $[a_1, a_2, \dots, a_r], a_i \in A$ sequence of actions realizes a path. Note that these control constraints have to be built in the control

[1] https://github.com/zkoppanyi/CooperativeMappingSimulator, March 14, 2017

policies for finding the feasible path. We assume that the platform is equipped with a range finder that is able to make a 360-degree scan around the robot. This range finder can be LiDAR or acoustic sensor. Besides mapping, these data streams are also used for navigation, see SLAM-based algorithms. The simulated sensor is assumed to have 6 m maximums ranging distance. This parameter is similar to the Hokuyo URG-04LX-UG01 range finder. The reliability of the sensor is decreasing linearly with the distance. We also assume that the georeferencing and the sensory data is perfect, thus no measurement error presents, and the points obtained by the sensor are defined in a global frame.

3.2 Communication models

The paper examines two types of communication model. The global communication model assumes that the robots can communicate with each other at all time. We also define a limited communication model, where the robots can communicate with each other within 50 m range.

3.3 Control policies

In this section, we present the implementation of three control policies that are investigated in this study. These policies are well known from the literature. Here, we adopt these approaches for our simulation environment.

In this study, we use 2D occupancy grid or raster to represent the map of the robot. This grid is represented by $M \in [0..1]^{n \times m}$ matrix, and thus, $M_{i,j} \in [0..1]$. If $M_{i,j}$ is 0, it means that the area represented by the cell is free, and if $M_{i,j}$ is 1, then it is occupied by wall or obstacle. Any other $M_{i,j}$ between 0 and 1 represents the certainty whether the cell is free or occupied. This allows for considering the uncertainty of the data obtained by the range finder. Note that when $M_{i,j}$ is 0.5, then the robot does not have any information about the area, and thus, the cell is undiscovered.

For simplicity, we use the following notation. $p \in [1..n, 1..m] = P$ is a cell or position over map M. Thus, P is all cell index pairs over M. $M[p]$ is the $M_{i,j}$ value at $p = [i, j], i = 1..n, j = 1..m$. $P_e = \{p \mid M[p] < t_e, p \in P\}$ is the set of empty cells, where t_e is a threshold for discovered empty cells. $P_w = \{p \mid M[p] > t_w, p \in P\}$ is the set of occupied cells, where t_w is the threshold of discovered occupied cells (walls). The $P_u = P \setminus P_e \setminus P_w$ is the undiscovered cells, and $P_d = P_e \cup P_w$ is the discovered cells. $P_f \subset P$ frontier cells are defined as those P_u undiscovered cells that has at least one P_d neighbour. $P_r \subset P$ is the cells occupied by other robots.

Closest frontier control policy. If $p^r \in P$ is the robot current position, and $\gamma: P \times P \to \{a_1, .., a_r\}, a_i \in A$ is a function that generates the sequence of robot actions for all feasible path between two cells on map M. Thus, the $\hat{p}$ closest frontier or the target cell is

$$\hat{p} = \underset{p^f \in P_f \setminus P_r}{\operatorname{argmin}} \sum\nolimits_{a_i \in \gamma(p^r, p^f)} 1. \qquad (1)$$

Note that $\sum_{a_i \in \gamma(p^r, p^f)} 1$ expression is the length, i.e. number of actions, of the feasible path between p^r and p^f. Thus, the action sequence of the robot to reach $\hat{p}$ target cell is $\gamma(p^r, \hat{p})$.

Note tha γ function is a graph search algorithm. For this study, we implemented a A* graph search algorithm over the action space that expands those nodes first from the available node list, which are closer to p_f target frontier based on Euclidian distance. When the $\hat{p}$ target is achieved, in other words, $\hat{p}$ is expanding in the graph, the algorithm terminates, thus the algorithm returns before the whole graph explored. For larger maps, this approach is still time consuming. For this reason, the A* algorithm is performed within a certain radius around the robot, and thus, the set or frontier cells P_f contains those positions that are within this radius. This radius is defined as 3-times of the sensor's maximum ranging distance; thus, it is 18 m. If there is no frontier cell within this range, because the map is explored locally, then a faster Jump Point Search (JPS) algorithm is used for path planning (Harabor et al., 2011). JPS considers the symmetry of the various feasible path to reduce the problem space. Unfortunately, in order to consider these symmetries, this algorithm was not designed for creating action sequences, but sequence of positions between the source and target cells. Because position sequences have to be converted to action sequences, the solution might not be optimal. But note that this algorithm is only used for global planning to navigate the robot from explored to unexplored areas, and thus, this small non-optimality can be neglected.

In addition, the path planning is not performed at each step to decrease the running time. Once the action sequence is calculated, the robot follows these commands. During the execution of the action sequence, the robot checks whether the target cell, i.e. $M[\hat{p}]$, is changed in the map, or there is any robot in the next cell. If one of these conditions are satisfied, then the robot replan the path according to the previous paragraph.

Maximum information gain control policy. The maximum information gain control policy plans such a action sequence that not just considers the length of the sequence, but also the information gained along the path. For this control policy, the $\hat{p}$ target cell is defined as

$$\hat{p} = \underset{p^f \in P_f \setminus P_r}{\operatorname{argmin}} \sum\nolimits_{a_i \in \gamma(p^r, p^f)} 1 - \alpha M[\delta(a_1 \dots a_i)], \qquad (2)$$

where, $\delta: A \times A \times \dots \times A \to P$ is a function that calculates the last position of the robot following an action sequence. $\alpha \in \mathbb{R}$ is a scaling factor; this value is important for the efficient control. If α is too small, the policy degrades to the closest frontier search, if it is too large, then the length of the path is not considered. For this policy, instead of the presented A*, breadth first search (BFS) algorithm is used without any heuristics. Here, we do not use early termination due to the second term of Equation 2, thus we discover the whole graph, and consequently, the algorithm runs slower than A*.

Bidding control policy. For the presented two control policies, the cooperation is realized only through the shared map, and the locations and decisions of other robots are not considered. The bidding control policy implemented for this study is the combination of auction and MDP methods presented earlier in Section 2. This policy apply the following steps.

1. Robots shared their map and locations among each other.
2. Each robot calculates the $\hat{p}$ target cell based on Equation 2, but not only for itself, also for all other robots located within the communication range.
3. The policy determines a $P_G \subset P_u$ goal set, which is the adjacent undiscovered cells around $\hat{p}$ target cell within 3-times of the sensor's maximum ranging distance. The distance here is measured considering obstacles based on the explored area, thus the JPS has to be used

for finding the accessible cells. These goal set is also calculated for all $\hat{p}_i$ target cells of ith robot resulting in $P_{G,i}, i = [1..k]$ goal sets, where k is the number of robots within the communication range.

4. At this step, the auction is played. We define the valuation function and allocation rule for the auction. The valuation function gives that how important a cell for a robot. The allocation rule determines which cell will be given to which robot. Here, the valuation function of a $p \in P_{G,i}$ cell is the inverse Euclidean distance of p from the p_r robot position. The policy calculates the valuation of all cells in all $P_{G,i}$ goal sets. Then, if there is any $P_{G,i} \cap P_G$ positions, which are the overlapping goal cells between the robots, then an overlapping cell is allocated to that robot of which valuation is higher; i.e. has the highest bid. Finally, the maximum information gain mechanism is used to generate the action sequence, but instead of using P_f frontier set, p^f has to be chosen from the P_G goal set, i.e.

$$\hat{p} = \underset{p^f \in P_G \setminus P_r}{\operatorname{argmin}} \sum_{a_i \in \gamma(p^r, p^f)} 1 - \alpha M[\delta(a_1 \dots a_i)]. \quad (3)$$

5. The frontiers are chosen from P_G and perform maximum information gain policy based on Equation 3, until there is no undiscovered cell in P_G. This allows for local exploration. When all cells are discovered in P_G, then the policy redefines the goal set, thus it goes back to Step 1.

Table 1 presents the comparison of the implemented control policies in terms of applied graph search algorithms, running time and degree of cooperation. Closest frontier control policy uses a more efficient A* algorithm to reach the closest undiscovered area for local search. The heuristic of this A* algorithm cannot be applied for the maximum information gain policy, thus, instead, BFS is used. The bidding control policy applies the maximum information gain approach to calculate the feasible path of all other robots, and thus, it also applies BFS. When the local area around the robot is explored, than all policies switch to global search and apply JPS for path planning. In the table, the running time is presented relatively to the unit time of the closest frontier method. The running time of this algorithm is around 50 ms on a 64-bit Intel Core i7 3.4 GHz PC. This running time is the time to find a feasible path. The maximum information gain control policy takes the double time due to the lack of heuristics in the search. The running time of bidding control policy is k-times longer then in the case of the maximum information gain policy, where k is the number of robots, because the policy has to play all robot scenarios. However, the bidding control policy is the only examined policy of that cooperation is not just realized through map sharing, but also considering the position and expected future path of other robots.

Table 1 Overview of the implemented control polices

	Closest Frontier	Maximum Information Gain	Bidding
Local graph search	A*	BFS	BFS
Global graph search	JPS	JPS	JPS
Running time	1	2	2k
Degree of cooperation	*	*	**

RESULTS

Three control policies have been investigated on 20 different floorplans. The floorplan sizes vary from a small apartment to a whole level of a building. An example floorplan of a building level is shown in Figure 1a. The simulations run with 1, 3, 6, 12 robots and with global or limited communication models resulting in 480 separate simulation scenarios. A screenshot captured during the simulation can be seen in Figure 1b. The computation of each robot run parallel on 8 cores. The total time of all simulations was around 5 days with a 64-bit Intel Core i7 3.4 GHz PC. Thus, the average running time of a scenario is 15 mins.

Figure 2 shows the simulated trajectories of 12 robots for the same floorplan in the case of the three policies. Each robot trajectory is depicted with different colors. In the case of the closest frontier policy, in Figure 2a, The trajectories are crossing and close to each other. In contrast, in Figure 2b, the maximum information gain policy provides distinct trajectories. This indicates not just the latter outperforms the previous in terms of steps to discover the area, but also, that a given area is mostly not visited multiple times.

(a) (b)

Figure 1 Floorplan of a building (a), and the simulation in the same area with 12 robots (b). Blue dots are the robot positions.

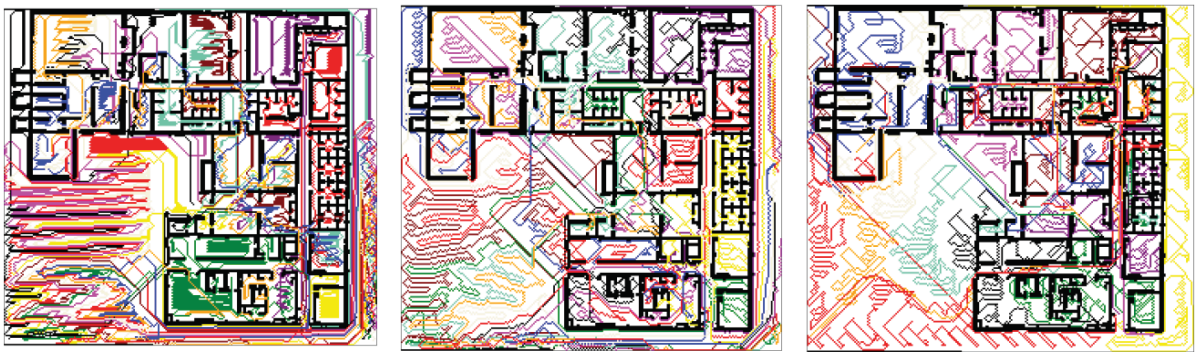

(a) Closest Frontier (b) Maximum Information Gain (c) Bidding

Figure 2 Trajectories of 12 robots for the three control policies in a building floorplan.

Figure 2c shows the robot trajectories for the presented bidding control policy. Note that the trajectories are not as long as in the case of maximum information gain policy presented in Figure 2b. This indicates that the bidding policy provides better area coverage. Also note that, inside rooms, in Figure 2c, there is mostly one robot trajectory due to the allocation rule applied in the policy.

DISCUSSION

In the discussion section, we compare the three control policies, and try to answer the question: is it worth to apply a more complicated and resource intensive strategy than a simple one?

Figure 3 shows the aggregated results from the 20 floorplans. The figure is separated into two parts; the upper part presents the results using limited and the bottom part shows the results using global communication model. For both solutions, all four (1, 3, 6, 12) robot scenarios are presented. Each subfigure shows the explored areas with respect to the normalized steps. Thus, these figures illustrates the dynamics of the swarm or robot team exploration. The steps, i.e. the number of actions, in the X axis are normalized based on the maximum number of steps with a given robot set-up and communication model. This allows for comparing results of floorplans with different sizes. Each control policy is depicted with different colors; the closest frontier policy with red, the maximum information gain with green and the bidding policy with blue. The weak lines are the solutions for each floorplan; the thick line represents the aggregated curve calculated as the median value of the individual floorplan solution.

This representation clearly illustrates the dynamics of the exploration of the control policies. In Figure 3a, the curve of the frontier control policy depicted with red is linear. It means that the robots explore the area uniformly. The steepness of the line, or gradient for curves, gives us the speed of the exploration. This is the rate of discovering undiscovered cells as the function of action steps. When the line is steeper, then the exploration is faster. Note that the graphs of maximum information gain and bidding policies have curved tail at the end. This is caused by that the robots have to return farther locations. In detail, during the exploration, the robots discover local areas and tend to go in a certain direction, and thus, undiscovered areas in the other direction are left behind. When all close frontiers are discovered, the robots have to return to these undiscovered, but farther direction that decrease the speed of the exploration. The curve at the end of the graphs clearly show this decrement in speed. Consequently, based on these graphs, we can define the optimal exploration dynamics for a control policy. We expect from a control policy to have the steepest linear exploration curve.

The results clearly present that the maximum information gain and bidding control policy outperforms the simplest closest frontier exploration strategy. But note that the bidding control policy just slightly outperforms the maximum information gain policy. In the case of global communication model and 12-robot scenario, the bidding policy shows the same performance as the information gain strategy, see Figure 3h. Clearly, the bidding policy is a more complex strategy. It considers other robots locations and future steps to apply allocation rules for providing efficient area coverage. It requires significantly larger computation resources as opposed to the maximum information gain policy. Answering to our question presented in the beginning of this section, our simulation indicates that the advantage of bidding policy is very small over the information gain policy in terms of exploration time. This gain disappears with increasing the size of the swarm.

Analysing further the subfigures, it is clear that the difference between the communication models are small in terms of the dynamics of the exploration. But, the steps are not normalized across the models, and thus, actual comparison of the communication models regarding the exploration time cannot be done based on these figures. Note the results of a single robot simulation scenarios, presented in Figure 3a and Figure 3e, are the same for both communication model, because, practically, a single robot cannot share any information.

RELATED WORKS

Other authors mostly use small number of robots and 2-5 floorplans for the proof-of-concept of their study. Gil et al. presents their simulation software and the analysis of seven control policies with various numbers of robots, but they did not change the environment and did not investigate the impact of communication limitations (Gil et al., 2015). The authors of this study does not know any other research that investigated large number of simulation scenarios to compare control policies for multi robot exploration.

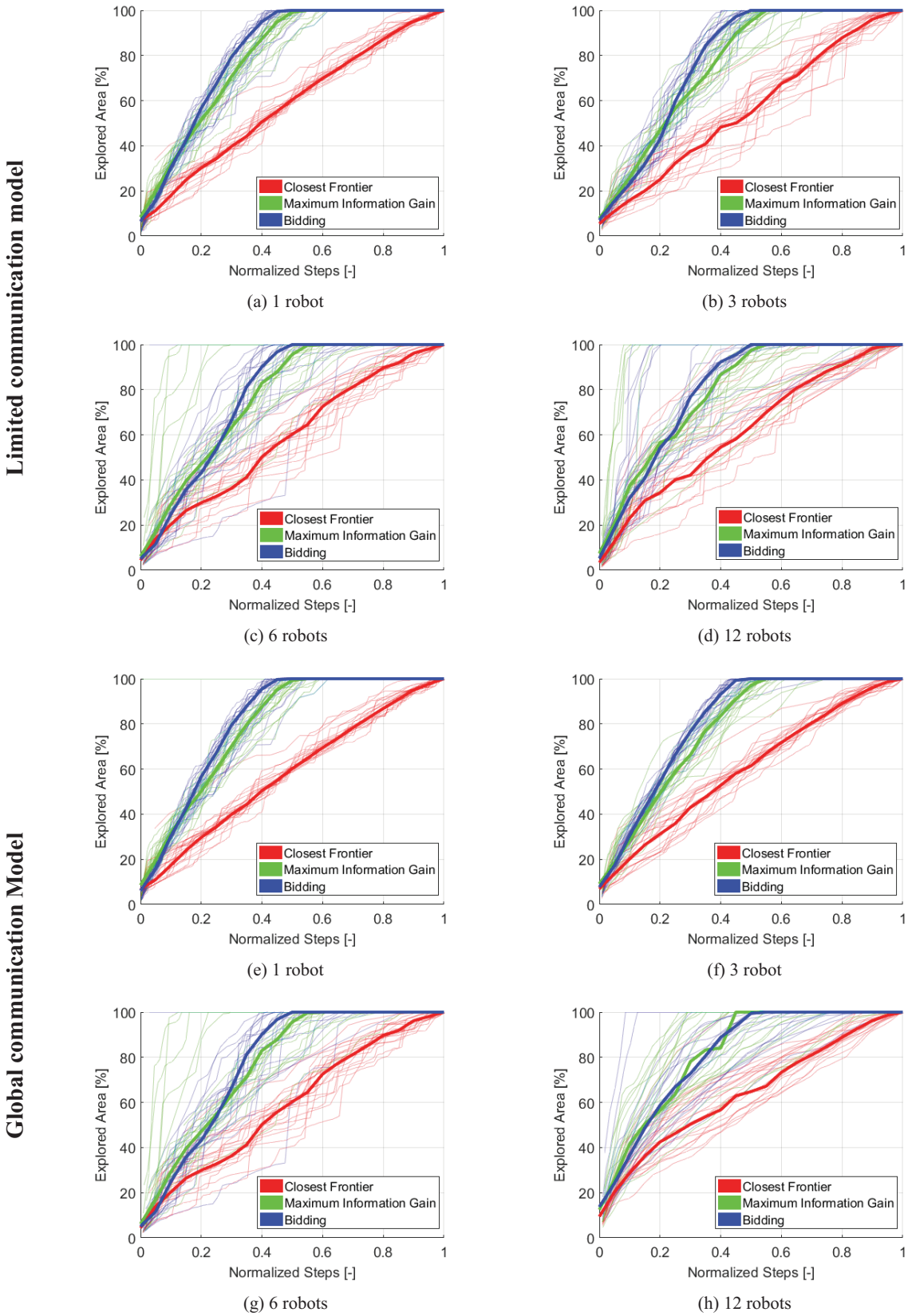

Figure 3 Exploration of 1-12 robots with respect to the normalized steps for limited and global communication models

CONCLUSION

In this paper, we investigated the exploration dynamics of three different control policies. 480 simulation scenarios are simulated on 20 different floorplans. The results indicated that the bidding control policy just slightly outperforms the maximum information gain strategy, but the bidding strategy has significantly larger computational demands. In general, this comparison allows understanding the benefits of a more complex and computation intensive control policy over a simpler one. Applying a simple policy allows for real time implementation on hardware-limited small platforms typically applied in swarm robotics.

The simulation presented in this study is rather simple, and thus, it is limited. Only 2D scenarios were investigated and the sensor's observation errors and other SLAM-specific issues could not be considered. In the future, we plan to improve our simulation framework to use different communication and sensor models, such as cameras, and other uncertainties carried by the observations.

REFERENCES

Bererton, C., Gordon, G.J., and Thrun, S., 2004. Auction Mechanism Design for Multi-Robot Coordination. In: *Advances in Neural Information Processing Systems*, pp. 879–886.

Fox, D., Ko, J., Konolige, K., Limketkai, B., Schulz, D., and Stewart, B., 2006. Distributed multi-robot exploration and mapping. *Proceedings of the IEEE* 94(7), pp. 1325-1139

Gil, A., Juliá, M., and Reinoso, Ó., 2015. MRXT: The Multi-Robot Exploration Tool. *International Journal of Advanced Robotic Systems* 12(4).

Gu Fang, Dissanayake, G., and Lau, H., 2005. A behaviour-based optimisation strategy for multi-robot exploration. In: *Proceedings of the 2004 IEEE Conference on Robotics and Automation*, Singapore, Dec 1-3, 2004, pp. 875–879.

Harabor, D.D., Grastien, A., 2011. Online Graph Pruning for Pathfinding On Grid Maps. In *Proceedings of the Twenty-Fifth AAAI Conference on Artificial Intelligence*, pp. 1114-1119.

Khamis, A., Hussein, A., and Elmogy, A., 2015. Multi-robot Task Allocation: A Review of the State-of-the-Art. Chapter. *Cooperative Robots and Sensor Networks*, Springer International Publishing, pp. 31–51.

Li, N., and Marden, J. R., 2013. Designing games for distributed optimization. *IEEE Journal of Selected Topics in Signal Processing* 7(2), pp. 230–242.

Matignon, L., Jeanpierre, L., and Mouaddib, A.-I., 2012a. Coordinated multi-robot exploration under communication constraints using decentralized markov decision processes. In: *Proceedings of the Twenty-Sixth AAAI Conference on Artificial Intelligence, 2012*, pp. 2017–2023.

Matignon, L., Jeanpierre, L., and Mouaddib, A.-I., 2012b. Distributed Value Functions for the Coordination of Decentralized Decision Makers. In: *Proceedings of the 11th International Conference on Autonomous Agents and Multiagent Systems - Volume 3*, pp. 1209–1210.

Michael, N., Mellinger, D., Lindsey, Q., and Kumar, V., 2010, The GRASP Multiple Micro-UAV Testbed. *IEEE Robot. Autom. Mag*. 17, pp. 56–65.

Morris, W., Dryanovski, I., Xiao, J., and Member, S., 2010. "3D indoor mapping for micro-uavs using hybrid range finders and multi-volume occupancy grids" RSS 2010 Workshop on RGB-D: Advanced Reasoning with Depth Cameras.

Rajesh M., Jose, G. R., and Sudarshan T. S. B., 2014. Multi robot exploration and mapping using frontier cell concept. In: *India Conference (INDICON), 2014 Annual IEEE*, Dec 11-13, 2014, pp. 1–6.

Rocha, R., 2006. Efficient information sharing and coordination in cooperative multi-robot systems. In: *Proc. of II European-Latin-American Workshop on Engineering Systems* (SELASI'2006), Porto, Portugal

Sariff, N., and Buniyamin, N., 2006. An Overview of Autonomous Mobile Robot Path Planning Algorithms. In: *4th Student Conference on Research and Development*, pp. 183–188.

Sharma, S., and Tiwari, R., 2016. A survey on multi robots area exploration techniques and algorithms. In: *2016 International Conference on Computational Techniques in Information and Communication Technologies (ICCTICT)*, pp. 151–158.

Staranowicz, A., and Mariottini, G.L., 2011. A Survey and Comparison of Commercial and Open-source Robotic Simulator Software. In: *Proceedings of the 4th International Conference on PErvasive Technologies Related to Assistive Environments*, New York, NY, USA, pp. 56:1–56:8.

Visser, A., and Slamet, B.A., 2008. Balancing the Information Gain Against the Movement Cost for Multi-robot Frontier Exploration. In: *European Robotics Symposium 2008*, pp. 43–52.

Wang, F., Cui, J. Q., Chen, B.-M., and Lee, T. H., 2013. A Comprehensive UAV Indoor Navigation System Based on Vision Optical Flow and Laser FastSLAM. *Acta Automatica Sinica* 39(11), Nov, 2013, 1889–1899.

Yamauchi, B., 1998. Frontier-based Exploration Using Multiple Robots. In: *Proceedings of the Second International Conference on Autonomous Agents*, New York, NY, USA, pp. 47–53.

Zlot, R., Stentz, A., Dias, M.B., and Thayer, S., 2002. Multi-robot exploration controlled by a market economy. In: *Proceedings 2002 IEEE International Conference on Robotics and Automation*, pp. 3016–3023.

LOW-COST MAGNETOMETERS CALIBRATION USING THE PROPORTIONAL INTEGRATOR TECHNIQUE FOR MOBILEDEVICES

Abdelrahman Ali [a,*], Salwa A.K. Mostafa [a], Naif Alsubaie [b], Naser El-Sheimy [b]

[a] Dept. of Electrical Engineering, Faculty of Engineering, Port-Said University, Egypt- (abdelrahman.saad@eng.psu.edu.eg)
[b] Dept. of Geomatics Engineering, Schulich School of Engineering, University of Calgary, Canada

Commission VI, WG VI/4

KEY WORDS: Geomagnetic Sensors, PI controller, Systems, Measurement, Calibration

ABSTRACT:

Different absolute navigation systems (such as Global Navigation Satellite Systems (GNSS)) are essential for navigation solution. However, most of these sources are not available for indoor navigation or when navigating in urban canyons due to multipath and signal blockage. In these scenarios, sensor-based navigation systems are candidates to be used. Heading information is one of the most important aspects of navigation solutions, whether it is pedestrian or vehicle navigation. An absolute heading can be derived using 3D magnetometer data. Though, the magnetic field measurements, which are obtained with low-cost sensors are corrupted by several errors, including manufacturing defects and external electromagnetic fields. Therefore, a proper calibration of the magnetometer is required to achieve high accuracy heading information. This paper presents an algorithm for calibrating magnetometers in the magnetic field domain. This algorithm calculates the calibrated magnetometer data directly. Thus, this new algorithm can be used to calibrate a full three-axis magnetometer triad. The calibration algorithm uses a proportional integrator controller for the magnetometer's calibration. The proportional integrator gains are tuned to improve the efficiency of the proposed algorithm. Different experimental magnetic field data are collected using a smartphone to evaluate the performance of the proposed technique. A major improvement in the estimated heading accuracy after the calibration process is noticed.

1. INTRODUCTION

In recent years, inertial sensors are becoming more popular for navigation in cluttered indoor environments, which are challenging for the GNSS due to signal blockage. Smart devices have become a favorite tool around the world and even an important part of the daily life activities. There are millions and millions of smartphones are sold worldwide every year, with increasing in the annual demand. The global smartphone market grew 1.1% year over year in 2016Q3, with 363.2 million shipments, based on the information from the International Data Corporation (IDC) Worldwide Quarterly Mobile Phone Tracker. Shipments grew 5.2% QoQ, compared to the 345.5 million units in the second quarter of 2016 (IDC, 2016).

The decline in the cost of smart device parts allows growth in the emerging markets of these devices. Sensors have been used in smartphones since they were presented. Accelerometers, gyroscopes, geomagnetic, light, and proximity sensors are examples of the embedded sensors in the smartphones. The microphone is used for recording sounds while cameras are used for capturing images and videos. New smart mobile devices such as smartphones, tablets, and smartwatches are powerful computing devices which are always held or carried around and have access to a wireless connection (Cerutt, 2010). Every day the smart devices are getting more capabilities to be added to the present ones. So, the user carries only one device, a smartphone, instead of carrying different devices each of which has an individual task. The rapid progress in smartphone technology allows the emerging of new applications. Nowadays, most of the smartphones are equipped with self-contained, low cost, small size, and power-efficient sensors, such as magnetometers, gyroscopes, and accelerometers. Smart device technology is continually advancing and growing, attracting developers to new application trends. All of these factors lead to a real opportunity to embed them in many practical applications, such as navigation and mapping.

All of these factors lead to a real opportunity to embed them in many practical applications, such as navigation and mapping. Figure 1 shows the axes definition for the device frame. In addition to the accelerometers and gyroscopes, magnetometers can be used to derive the user heading, by sensing the earth's magnetic field.

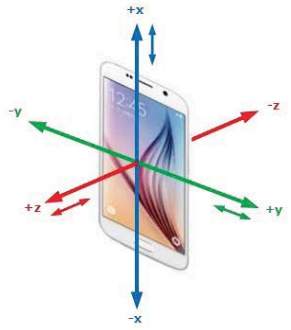

Figure 1 Smartphone axes definition

Mobile Mapping System (MMS) based on Smartphone is one of the newest innovative applications for such trend. This application can provide low cost direct geo-referencing 3D data using multi overlapped images as shown in Figure 2. The positions of the captured mapping images, are collected directly using the low-cost GPS chip. Whereas, the orientations of the involved camera are collected at the time of the camera exposure, using the IMU and magnetometer built in smartphone. Hence, accelerometers are used to provide the Roll and Pitch angles, where magnetometers are used to provide the Azimuth angles (Al-hamed et al, 2014) and (Alsubaie et al., 2010). Probable and

reliable calibration for all sensors, especially magnetometer is necessary for obtaining reliable 3D data and thus the importance of this paper.

Figure 2. Mapping application with smartphone

In the literature, the calibration of magnetometers was either accomplished in the heading domain (Guo et al., 2005) or in the magnetic field domain (Crassidis et al., 2005; Gebre and Elkaim, 1995). In the magnetic field domain, there is no dependency on the heading of the sensor before calibration. In this approach, calibration is done in the magnetic field domain depending on the fact that the error-free locus made by the compass is a circle when it makes a full rotation in 2D or a sphere when rotated in 3D covering all possible orientations (Caruso, 2000). In some implementations, it is assumed that the locus of the magnetometer readings forms a translated hyperbolic shape in 2D or translated hyperboloid shape in 3D when rotated in normal operation conditions in the presence of ferrous interference (Camps et al., 2009). For a given region, the Earth's total magnetic field is constant and obtained from the International Geomagnetic Reference Field (IGRF) model. This model provides the reference values to develop any geomagnetic sensors calibration technique in the magnetic field domain (Ali et al., 2012).

Section 2 discusses the different components of the magnetic field with the error sources and the perturbation effect on the measurements. The proposed technique for magnetometer calibration using the Proportional Integrator (PI) is described in section 3. The calibration test results with magnetometer data are presented and discussed in section 4. The paper ends with a conclusion in section 5.

2. EARTH'S MAGNETIC FIELD (EMF)

The Earth's Magnetic Field (EMF), as measured at any point on the Earth's surface, is a combination of several magnetic contributions generated by various sources. The geomagnetic field can be fully described by measuring its intensity and two angles or three orthogonal components (Mandea et al., 2006). The two angles are the declination angle and the inclination angle while the orthogonal components are the three axes x, y, and z for the directions towards geographic North, East and Vertical down, respectively. Nowadays, with the progress in sensors technology, the EMF can be precisely measured using the magnetometer. Valuable information can be extracted from the magnetometer measurements with the proper transformation of the field components such as the geomagnetic heading.

Magnetometers measure the vector components of the magnetic field. The magnetic field is characterized by different components including the strength of the magnetic field (F), the vertical and horizontal components (V, H), East and North (E, N) components, and inclination and declination angles (I, D). The values of these parameters can be considered roughly constant over a small area, which is normally covered by a walking person. These values are used as a reference for the magnetometer measurements.

Three parameters are required to describe the magnetic field at any point on the surface of the Earth, which can be sensed by an orthogonal arrangement of magnetometers as shown in Figure 3 where $\boldsymbol{B_x}$, $\boldsymbol{B_y}$, and $\boldsymbol{B_z}$ represent the measured components of the magnetic field vector. D is the declination angle referenced to true North, which indicates the difference between the true north and magnetic north. This declination angle has a range from 0 to 360 degrees depending on the user location.

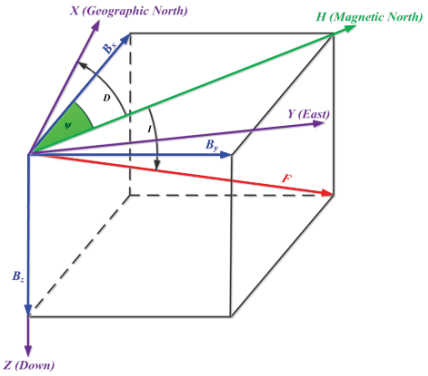

Figure 3. Geomagnetic field components and vectors.

The field also has a vertical contribution, which is represented by the inclination angle. This angle is located between the horizontal and the magnetic field direction. Magnetic inclination angle varies from 90 degrees (perpendicular to the surface) at the poles to 0 degrees (parallel to the surface) at the equator. The magnitude of the magnetic field varies from 650 *mGauss* at the poles to about 300 *mGauss* at the equator.

The heading value w.r.t. the True North can be estimated as:

$$\theta = \tan^{-1}\left(\frac{B_x}{B_y}\right) \pm D \qquad (1)$$

Equation 1 shows that the estimated magnetic heading is sensitive to any disturbance or perturbation in the horizontal magnetic field components.

The norm of the magnetic field measurements represents the strength of the magnetic field. Any significant deviations from the expected values for the different magnetic field components may be presented as disturbances. Unfortunately, small random variations can occur in the environment when someone is moving. The magnetic field can be characterized by four major components:

- Total Field Strength: F = || B_x + B_y + B_z ||
- Horizontal Field Intensity: H = || Bx + By ||
- Vertical Field Intensity: V = || Bz ||
- Field Inclination Angle: I = tan-1(V/H)

The expected values for the different magnetic field parameters are shown in Table 1. These values depend on the user location at the time of the data acquisition, which in this study is the city of Calgary, Alberta, Canada.

Component	Symbol	Ref. Value	Unit
Total Field	F	561	*mGauss*
Horizontal	H	161	*mGauss*
East (Y)	E	39.5	*mGauss*
North (X)	N	156	*mGauss*
Vertical (Z)	V	538	*mGauss*
Inclination Angle	I	73.1	*Degree*
Declination Angle	D	14.2	*Degree*

Table 1. EMF components reference values

The different values in Table 1 can be obtained from International Geomagnetic Reference Field (IGRF). Every five years, the International Association of Geomagnetism and Aeronomy (IAGA) revises and updates the IGRF parameters values. The latitude, longitude, and height of the area where the EMF intensity is measured are required. The 12th generation IGRF accepts years ranging from 1900 to 2020. The accuracy of the reference value based on this model is within 10 (nT) Nano Tesla (or 100 *mGauss*); more details about IGRF-11 in (Thébault et al., 2015).

2.1 EMF Measurements Error Source

Distortion in the magnetic field can occur due to different metallic objects in the surrounding environment. Even in well-designed handheld devices, these sources create external fields with high magnitudes. Designers of such devices should not assume that the calibration process will always be correct for a poor layout. Magnetometers' measurements are influenced by several types of errors, which can be grouped in one way mathematically (Takahashi, 2010). The scale factor can be modeled together with hard and soft iron effects, as they have the same mathematical consequence (Foster, 2008). The scale factor and bias, therefore, become the primary calibration parameters to be considered. Such parameters have a significant effect on the overall performance of the magnetometer and should be corrected (Granziera, 2006). The temperature can also be considered as one of the distortion sources for the magnetic field (Titterton, 2004). However, with an efficient calibration technique, there is no need to have a particular method for thermal effect correction as the recalibration process for the different parameters can be sufficient. In general, hard iron effect causes much larger contribution for the resulted distortions. It is important to understand the different effects, of hard and soft iron, to estimate the appropriate and necessary parameters. The following subsections describe the different source of distortion for the magnetic sensor.

2.1.1 Ideal case without distortions

In the absence of any disturbance, the plot of the measurements in the horizontal plane should form a perfect circle. The circle is centered on the origin, (0, 0), with a radius equal to the magnitude of the magnetic field. Figure 4 presents the resulted track from plotting the magnetometer x vs. magnetometer y and rotating the device in the horizontal plane two turns at 360 degrees around the z-axis. The result shows a circle at the origin as no distortion effects in the surrounding environment.

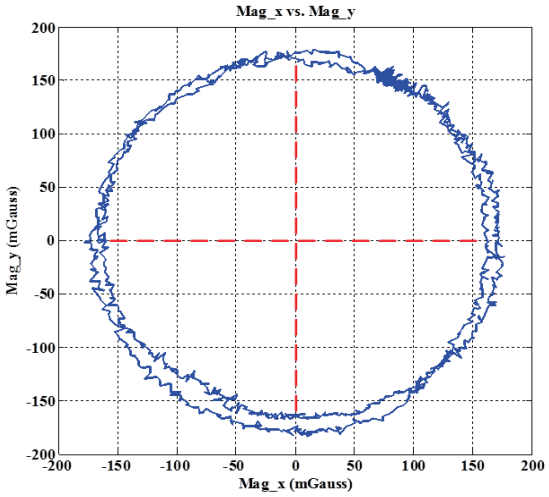

Figure 4. Distortion-free magnetometer data.

However, the perturbation in the magnetic field occurs in the presence of any hard or soft iron effect. The disturbance shifts the center of the data at another point rather than (0, 0) in the case of hard iron effects while soft iron effects cause the plotted data to appear deformed as the circle shape becomes an ellipse with a different offset angle.

2.1.2 Hard Iron Effect

Hard iron distortions generated by the objects that produce a constant and additive magnetic field to the EMF. Thus, the generated magnetic field is presented by a constant permanent bias in the output of each magnetometer. The hard iron distortions shift the origin of the produced circle out from (0, 0) as shown in Figure 5. The figure indicates that the center point is moved to (70, 65), which means that there is a 70 *mGauss* hard iron bias in x magnetometer's measurements and 65 *mGauss* hard iron bias in y magnetometer's measurements. However, the hard iron effect does not change the shape of the circle. Consequently, compensation for the hard iron distortion is accomplished by estimating the offset in the x-direction and y-direction. The estimated values are then subtracted from the measurements. It is important to convert the measured data into the horizontal plane before determining the hard iron corrections.

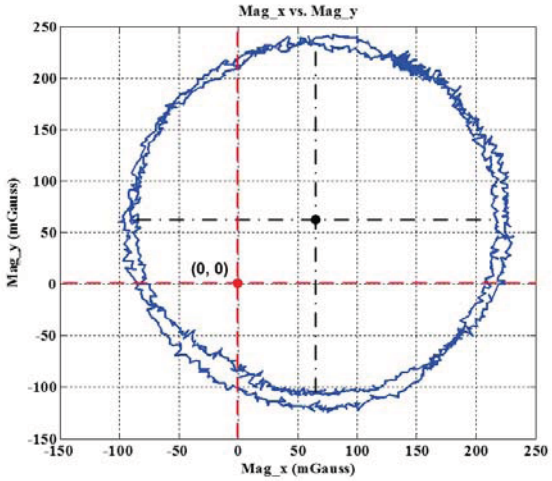

Figure 5. Magnetometer data with hard iron distortion.

2.1.3 Soft Iron Effect

Soft iron effects happen by the interaction of an external magnetic field with ferromagnetic materials surrounding the magnetometer (Vasconcelos, 2011). In other words, soft iron distortion is commonly produced by elements that influence or distort a magnetic field but that do not necessarily generate a magnetic field, such as nickel and iron. Only the magnitude and direction of the applied magnetic field on the soft iron material affect the resulting magnetic field. Therefore, it is not additive distortion and can be considered as deflections in the actual EMF. The effect of the soft iron materials depends on the direction in which the field acts related to the magnetometer. Thereby, the compensation of the soft iron is more complicated than for the hard iron distortion and not as straightforward. As made evident by Figure 6, the typical effect of a soft iron distortion is exhibited as a deformation of the circle into ellipse at (0, 0).

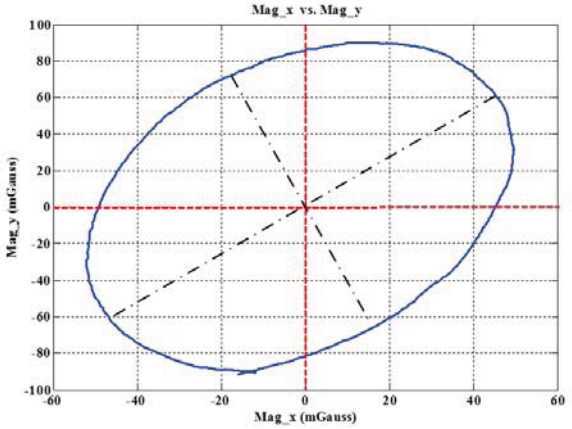

Figure 6. Magnetometer data with soft-iron distortion.

2.1.4 Case with Hard and Soft Iron Distortions

Figure 7 shows a combined hard and soft iron distortion where the circle has been distorted into an ellipse. The center of the ellipse is shifted from (0, 0) into (17, 68) in the presence of the hard iron distortions.

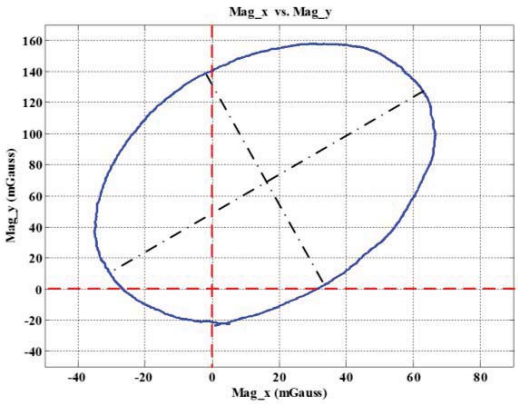

Figure 7. The effect of soft and hard iron effects.

Due to these factors, most magnetometer calibrations degrade over time, and regular re-calibration is a necessary step to ensure the integrity of the measurements. Even in well-designed handheld devices, these sources create external fields with high magnitudes. Designers of such devices should not assume that the calibration process will always be correct for a poor layout.

2.2 Perturbation Effect

Due to the fluctuations in the magnetic field, it is necessary to smooth the measurements using a low-pass filter to have the signal around the reference value of the magnetic field. Different techniques use a threshold value as a standard margin for the signal variation to recognize any perturbations in the measurements. A threshold value of 30 *mGauss* has been roughly defined as the root mean square value of the magnetic field during three steps (Ladetto, 2002). Thus, any signal bigger than this value is considered as a perturbation where the last estimated heading value will be held until the field becomes normal again. The effect of the disturbances decreases as the user is moving away from the source of the distortion. However, the results of the distortion are visible only for a few meters.

The effect of the perturbation vector on the different magnetic field components should be taken into consideration for any magnetometer anomaly detector. When a pedestrian is walking in areas of dense infrastructure or even indoors, it causes changes in the measured magnetic field. Such changes affect the different parameters and consequently lead to inaccurate heading estimation (Faulkner, 2010). The perturbation problem becomes difficult and more complicated if the external disturbance source affects different magnetic field parameters in various ratios. In contrast, the perturbation effect is ignored if the external source affects the magnetic field components equally. The only change, in this case, is that the measured values of the parameters differ from the reference values. Thus, the detector should compare the change in components individually and assess their ratios. The magnetometer-based heading estimate is considered free of perturbation if the differences between the reference and the measured values are within the predefined thresholds.

Figure 8 and Figure 9 describe two different parts of a trajectory with distorted and not distorted areas. As shown in Figure 8(a), magnetic field strength variation is much larger than the expected value and creates an inaccurate heading estimation as illustrated in Figure 8(b). Only few samples of the measurements successfully met the conditions of correct heading estimation.

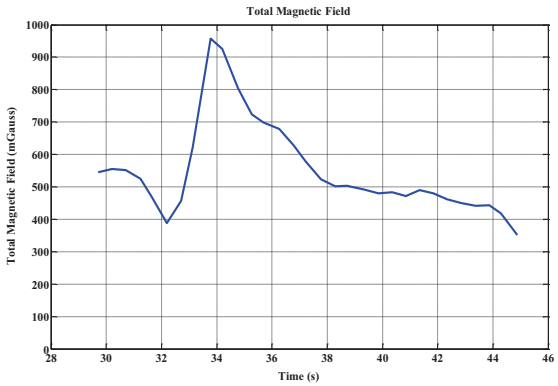

(a) The total magnetic field in a perturbed area.

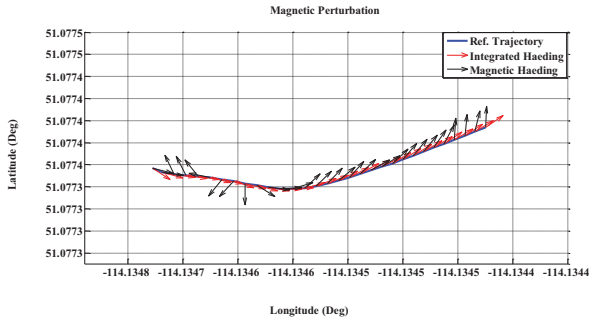

(b) The expected heading vectors in the perturbed area.

Figure 8. The estimated heading values in a troubled area.

In contrast, Figure 9 shows that the magnetic field does not have an abrupt change in the value, which indicates an area without perturbation.

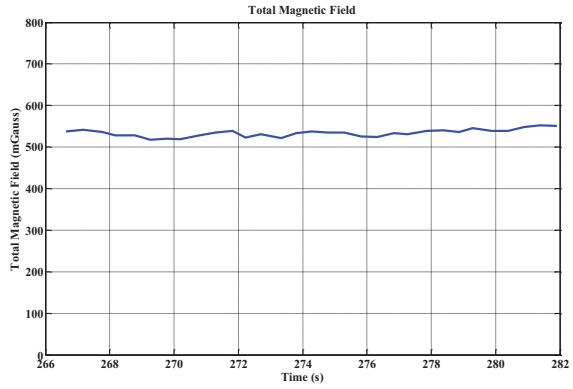

(a) The total magnetic field in the non-perturbed area.

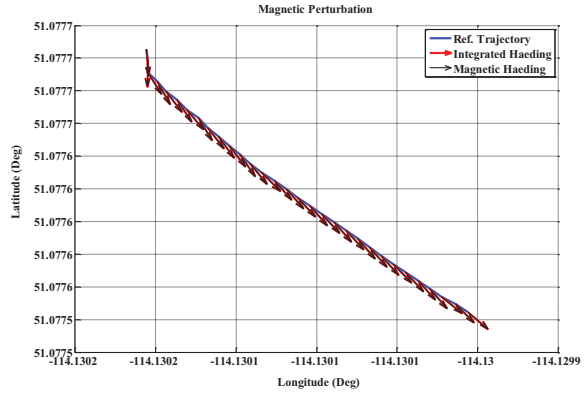

(b) The expected heading vectors in the non-perturbed area.

Figure 9. Estimated heading in a non-perturbed area.

The quality of the magnetometer based heading estimate can be observed and assessed based on the proposed anomaly detection. The technique determines the different associated errors with the magnetic parameters. Thus, this can lead to significantly reduced heading errors and improved position accuracy by rejecting distorted magnetic measurements efficiently in real-time.

3. PI-BASED CALIBRATION TECHNIQUE

The proposed algorithm is used to compensate for the different error sources effects. The compensation can be done by estimating gain values to map the measured EMF values to the reference values of the EMF at certain location. The estimated parameters or gains for the calibration process are evaluated by minimizing the difference between the measured magnetic field using a 3D magnetometer and the true (reference) magnetic field derived from IGRF model as shown in Table 1. Unlike the other calibration technique, the proposed technique used the individual component of the EMF not the total strength of the magnetic field. The proposed technique calibrates each parameter with its reference value. In this system, it is required to obtain the optimum values for the gains to set the error between the measured value and the reference value to be zero.

The proposed magnetometer calibration technique uses the principles of the Proportional and Integral (PI) controller. The proposed method adjusts some variable to hold the measurement close to the reference value. Equation 2 gives the regular form the PI controller.

$$u(t) = k_c e(t) + \frac{k_c}{\tau_I} \int_0^t e(t)\, dt \qquad (2)$$

where e = error between the measured and reference values
k_c = the controller gain
τ_I = the integral time constant
u = the controller output

The equation can be rewritten as:

$$u(t) = k_p e(t) + k_i \int_0^t e(t)\, dt \qquad (3)$$

where $k_p = k_c$
$k_i = k_c/\tau_I$

The Tuning part adjusts the values of the proportional controller gain and the integral controller gain. The value of $\boldsymbol{k_c}$ is a multiplier on the proportional error and integral term. A higher value makes the controller more aggressive at responding to errors away from the reference value. The reference value is the target value where the raw value is the measured value that may deviate from the reference value. The error from the reference value is the difference between the reference value and the measured value.

Equation 3 shows a time continuous form of the PI controller. Another discrete form of the PI controller is needed to provide an approximate value for the integral part of the error. This is necessary to replace the continuous integral part with a summation of the error and use the term $\boldsymbol{\Delta t}$ as the time between sampling instances and $\boldsymbol{n_t}$ as the number of sampling instances. Equation 4 shows a discrete form of the PI controller.

$$u(t) = k_p e(t) + k_i \sum_{i=1}^{n_t} e_i(t)\, \Delta t \qquad (4)$$

Figure 10 shows a block diagram for PI controller error compensation scheme. This type of compensation scheme is introduced by using a controller which produces an output signal consisting of two terms, one is for the proportional term, and the other is for the integral term. The $\boldsymbol{X_{ref}}$ term refers to the reference value while the $\boldsymbol{X_{raw}}$ term refers to the measured value of the magnetic field. Gain tuner block is used to provide a tuned value for the controller gains. The output feedback controller adapts the

output of the controller to be feedback to the measured magnetic field values.

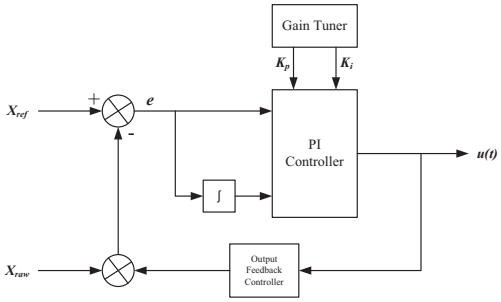

Figure 10. Block diagram of the tuned PI controller.

Controller tuning is the process of selecting the appropriate parameters to achieve a given performance specification. A heuristic tuning method is formally known as the Ziegler–Nichols method, introduced by John Ziegler and Nathaniel Nichols in the 1940s can be used to tune the controller parameters. The method suggested rules for tuning PID controller (mean to set the values of k_p, k_i, and k_d) based on the experimental step response or based on the value of k_p. The following part discusses the Ziegler-Nichols tuning rules. These rules are useful when the mathematical model of a process is not known. In such a case, it needs a series of fine adjustments until an acceptable result is obtained. In fact, the Ziegler-Nichols tuning rules give an educated guess for parameter values and provide a starting point for fine tuning (Ziegler & Nichols, 1942). In the beginning, the values of the k_i is initialized with zero. Then the proportional gain increases until it reaches the ultimate gain value, k_u, at which the output of the loop starts to oscillate. The values of k_u and the oscillation period P_u are used to set the gains as shown in Table 2:

Control Type	K_p	K_i	K_d
P	$0.50K_u$	-	-
PI	$0.45K_u$	$1.2K_p/P_u$	-
PID	$0.60K_u$	$2K_p/P_u$	$K_pP_u/8$

Table 2. Ziegler-Nicholas method

The proposed algorithm is based on two steps; finding the optimal parameters for the controller, and calculate the calibrated magnetic field using these parameters. Figure 11 illustrates the main steps of the proposed technique using the tuned PI controller. First, the collected data is manipulated with the device orientation to provide a leveled data for the magnetometer measurements. The leveling process requires the knowledge of the device orientation, roll and pitch, which can be estimated from the accelerometer and gyroscope data.

After obtaining the appropriate parameters to fit the measured magnetic field data to the reference values, these parameters are used to calculate the calibrated magnetometer data.

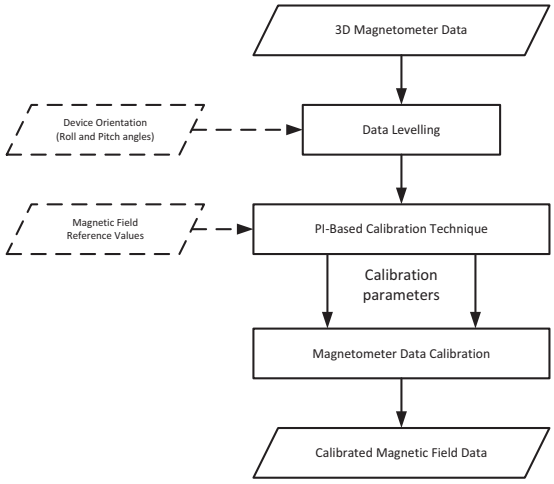

Figure 11. The proposed magnetometer calibration technique.

Referring to Equation 4, the output u(t) should be almost around zero value to have the measured data values close to the reference values. To obtain the calibrated data, Equation 4 is rewritten to use the calibrated term instead of the reference term.

$$k_P e(t) + k_i \sum_{i=1}^{n_t} e_i(t)\,\Delta t \approx 0 \tag{5}$$

In Equation 5, the error is defined as the difference between the measured values and the calibrated values.

$$k_P(B - B_{cal}) + k_i \sum_{i=1}^{n_t} e_i(t)\,\Delta t \approx u(\mathrm{t}) \tag{6}$$
$$k_P(\mathrm{B} - B_{cal}) + k_i(B - B_{cal})\Delta t + k_i \sum_{i=1}^{n_t-1} e_i(t)\,\Delta t \approx u(\mathrm{t})$$
$$k_P B - k_P B_{cal} + k_i B\Delta t - k_i B_{cal}\Delta t + k_i \sum_{i=1}^{n_t-1} e_i(t)\,\Delta t \approx u(\mathrm{t})$$
$$(k_P + k_i\Delta t)B - (k_P + k_i\Delta t)B_{cal} + k_i \sum_{i=1}^{n_t-1} e_i(t)\,\Delta t \approx u(\mathrm{t})$$

$$B_{cal} = B + \frac{k_i\Delta t}{k_P + k_i\Delta t}\sum_{i=1}^{n_t-1} e_i(t) - \frac{1}{k_P + k_i\Delta t}u(t) \tag{7}$$

where B_{cal} = calibrated data
B = measured data

Equation 7 is used to calculate the calibrated data from the measured data using the obtained parameters from the PI controller. Each component of the magnetic field treated individually to obtain its calibrated data.

4. RESULTS

The total magnitude value of the measured magnetic field should be equal to the reference value of the EMF in case of an open not-perturbed area. This value can be extracted from a specific geomagnetic model such as the IGRF model as shown in Table 1. Different field tests are conducted to evaluate the performance of the proposed calibration technique. A Samsung S4 smartphone is used to collect the magnetometer data. For the 2D calibration, the magnetometer was rotated 360◦ in the horizontal plane and then the heading was computed using the calibrated data. In the case of 3D calibration, the device is moved in the space with the form of figure eight. In all cases, the proposed technique successfully converges to a good estimate of the calibrated magnetic field which is close to the reference value of the EMF. The calibrated data based estimated heading showed an improvement in terms of heading accuracy after the calibration.

4.1 2-D Magnetometer Calibration

The first set of results is a 2D calibration for magnetic field measurements. The device is moved in the space and held in hand after that. The magnetometer data is calibrated in the horizontal plane as the most affected components for the heading are coming from the North and East parts. Table 1 provides the necessary values for the North and East reference values. Figure 12(a) shows the raw magnetic field in the x and y directions while the total horizontal raw and calibrated magnetic fields are shown in Figure 12(b). The calibrated magnetic field readings demonstrate the constancy of the estimated magnetic field, which is close to the true EMF value. Figure 12(c) shows the resulted estimated heading using Equation 1 after calibration. The device was held in the direction of 230 degrees after the calibration period.

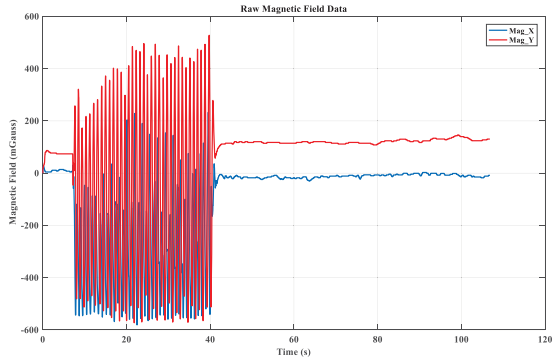

(a) The raw magnetic field readings.

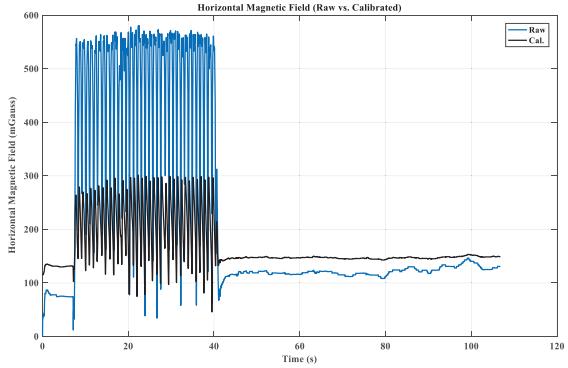

(b) The horizontal raw and calibrated magnetic field.

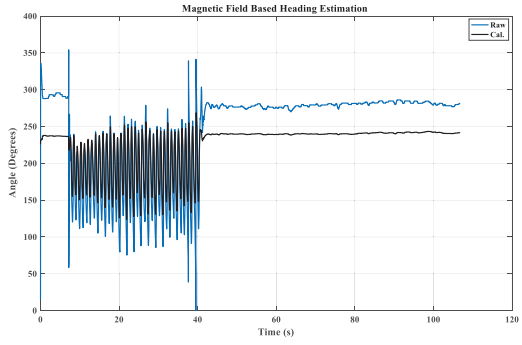

(c) Heading estimation

Figure 12. 2D PI-based magnetometer calibration technique

4.2 3-D Magnetometer Calibration

A free movement test is conducted to testify the performance of the proposed method in the 3-D space calibration. Technically, the 3-D calibration is more convenient for the user where there is no restriction for the way of carrying the device. The total magnetic field is calculated and calibrated with the reference of the total EMF value which is 561 *mGauss* as shown in Table 1. The calibration technique uses the collected data from the 3-axis magnetometer.

Figure 13 shows the calibration results for the magnetic field sensors where both the un-calibrated as well as the calibrated magnetic fields are plotted in 3D. The mesh globe shows the expected 3D magnetic field, which differs much from the measured one in the un-calibrated case. After calibration, the measured field components are coincident with the expected ones, thus showing calibration success.

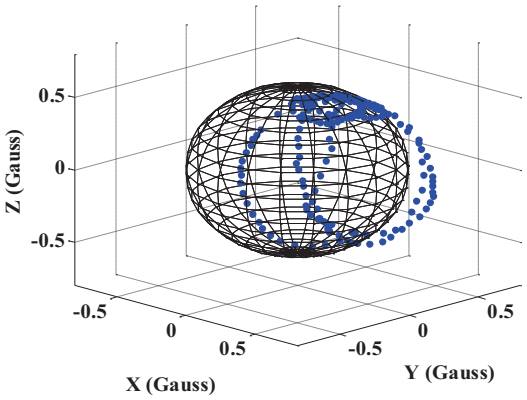

(a) The raw data

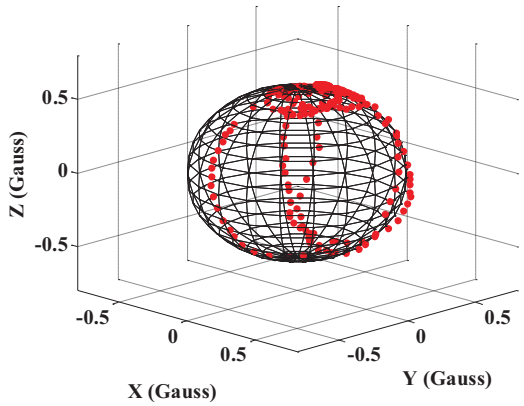

(b) The calibrated data

Figure 13. 3D PI-based magnetometer calibration technique

5. CONCLUSION

In this paper, a tuned PI-based calibration algorithm is presented to estimate the values of the controller gains to calculate the calibrated data for low-cost magnetometers data. The main advantage of this technique is the use of the individual components of the magnetic field which does not need any error modeling or awareness of the nonlinearity. The estimated gains from the proposed algorithm improved the heading accuracies, and the results are also statistically significant. This technique would help in the pedestrian navigation to decrease the heading

error of the user. Also, it can assist in the development of the portable or mobile navigation devices when combined with the inertial sensors and any available absolute positioning systems, especially in the indoors environments.

6. REFERENCES

Ali, A., Siddharth, S., Syed, Z. and El-Sheimy, N., 2012. Swarm optimization-based magnetometer calibration for personal handheld devices. Sensors, 12(9), pp.12455-12472.

Al-Hamad, A. and El-Sheimy, N., 2014. Smartphones Based Mobile Mapping Systems. The International Archives of Photogrammetry, Remote Sensing and Spatial Information Sciences, 40(5), p.29.

Alsubaie, N. and El-Sheimy, N., 2016. The Feasibility of 3d Point Cloud Generation from Smartphones. ISPRS-International Archives of the Photogrammetry, Remote Sensing and Spatial Information Sciences, pp.621-626.

Camps, F., Harasse, S. and Monin, A., 2009, June. Numerical calibration for 3-axis accelerometers and magnetometers. In Electro/Information Technology, 2009. eit'09. IEEE International Conference on (pp. 217-221). IEEE.

Caruso, M.J., 2000. Applications of magnetic sensors for low cost compass systems. In Position Location and Navigation Symposium, IEEE 2000 (pp. 177-184). IEEE.

Cerutt, S., Magenes, G., and Bonato, P. 2010. Special Section on Smart Wearable Devices for Human Health and Protection, Guest Editorial. Information Technology in Biomedicine, IEEE. Transactions on 14.3.

Crassidis, J. L., Lai, K.L., and Harman, R. R., 2005. Real time attitude-independent three axis magnetometer calibration. Journal of Guidance Control, 28(1), pp. 115–120.

Faulkner, W.T., Alwood, R., Taylor, D.W. and Bohlin, J., 2010, January. GPS-denied pedestrian tracking in indoor environments using an IMU and magnetic compass. In Proceedings of the 2010 International Technical Meeting of the Institute of Navigation (pp. 198-204).

Foster, C.C. and Elkaim, G.H., 2008. Extension of a two-step calibration methodology to include nonorthogonal sensor axes. IEEE Transactions on Aerospace and Electronic Systems, 44(3).

Gebre-Egziabher, D., and Elkaim, G. H., 2006. Calibration of strapdown magnetometers in magnetic field domain. ASCE Journal of Aerospace Engineering, 19 (2), pp 6-16.

Granziera Jr, F., 2006. Simulation and implementation of a real time attitude determinator using micro-manufactured sensors. Universidade Estadual de Londrina.

Guo, P., Qiu, H., Yang, Y., and Ren, Z. 2008. The Soft Iron and Hard Iron Calibration Method using Extended Kalman Filter for Attitude and Heading Reference System. In: Proceedings of IEEE/ION PLANS, Monterey, CA, USA, pp 1167-1174.

IDC, 2016. http://www.idc.com/promo/smartphone-market-share/vendor.

Ladetto, Q., Van Seeters, J., Sokolowski, S., Sagan, Z. and Merminod, B., 2002. Digital magnetic compass and gyroscope for dismounted soldier position and navigation. In NATO-RTO meetings.

Mandea, M., Lühr, H., Korte, M., Balasis, G., Linthe, H.J., Hemant, K., Pulz, E., Ritter, P., Rother, M., Stolle, C. and Thébault, E., 2004. A comprehensive view of the Earth's magnetic field from ground and space observations. Zweijahresbericht GeoForschungsZentrum Potsdam, 2005, p.2007.

Siddharth, S., Ali, A.S., Goodall, C.L. and El-Sheimy, N., 2011, November. Investigating Aspects of Heading Estimation Error in Pedestrian Navigation. In Proceedings of the 2011 International Technical Meeting of The Institute of Navigation (pp. 635-642).

Takahashi, N.S., Santana, T.A., Granziera Jr, F. and Tosin, M.C., 2010. Accelerometer and Magnetometer Auto-Calibration Algorithm for Attitude Determination. Journal of Aerospace Engineering, 2(3), p.11.

Titterton, D. and Weston, J.L., 2004. Strapdown inertial navigation technology (Vol. 17). IET.

Thébault, E., Finlay, C.C., Beggan, C.D., Alken, P., Aubert, J., Barrois, O., Bertrand, F., Bondar, T., Boness, A., Brocco, L. and Canet, E., 2015. International geomagnetic reference field: the 12th generation. Earth, Planets and Space, 67(1), pp.1-19.

Vasconcelos, J.F., Elkaim, G., Silvestre, C., Oliveira, P. and Cardeira, B., 2011. Geometric approach to strapdown magnetometer calibration in sensor frame. IEEE Transactions on Aerospace and Electronic Systems, 47(2), pp.1293-1306.

Ziegler, J.G. and Nichols, N.B., 1942. Optimum settings for automatic controllers. trans. ASME, 64 (11).

REMOTE SENSING IMAGES SELF RECOVERY AUTHENTICATION WATERMARKING TECHNIQUE

Salwa A. K. Mostafa [a*], Abdelrahman Ali [a], Naser El-Sheimy [b]

[a] Dept. of Electrical Engineering, Faculty of Engineering, Port-Said University, Egypt
salwaabdelkader@ eng.psu.edu.eg
[b] Dept. of Geomatics Engineering, Schulich School of Engineering, University of Calgary, Canada.

Commission VI, WG VI/4

KEY WORDS: Watermarking, Integer Wavelet Transform, Authentication, Tamper Detection, Self-Recovery, Remote Sensing Image.

ABSTRACT:

With the increasing demand of the satellite images applications, it has become a necessity to store and transmit them over the internet. The process of detecting any illegitimate change on the content of these images becomes a challenging problem for the owners and the distributors. Different digital watermarking schemes are presented to authenticate the remote sensing (RS) images to overcome this challenge. These techniques are based on adding a watermark into the image to produce an authenticated version of this image. So, any attempts to change the content of the authenticated image will result in a change of the watermark itself. Moreover, it can detect the tampered area and recover the contents of this area to its original. In this paper, a new watermarking technique for image authentication is proposed based on integer wavelet transform (IWT). The watermark is the second level approximation wavelet sub-band. It decomposes into bit-planes and inserted into the bit-planes of the IWT detail sub-bands of the RS image color bands. Experimental results show a good imperceptually of the proposed scheme. The scheme can successfully authenticate the image by detecting the tampering region correctly and recover the tampered area with good image quality.

1. INTRODUCTION

Remote Sensing (RS) images have recently attracted the attentions of the researchers and the industrial community as a crucial source of data for geographical information systems. With the wide spreading of RS images and growing of their uses and applications in different fields (such as archaeology, agriculture, military, homeland security..., etc.), the process of detecting any illegal alteration on these images contents becomes a vital issue. Also, RS images are different from general images as they have sophisticated features and valuable data as military images and the acquisition of these images is a costly operation used expensive devices as satellites. Therefore, the demand to copyright and authenticate these images is increased. The digital watermarking techniques have been suggested to overcome this problem.

The aim of digital watermarking is to add digital message called watermark to digital contents called host data (images, audio or video) in an imperceptible and secure manner. It is used in many applications including copyright protection, fingerprinting, copy protection, broadcast monitoring and data authentication. Therefore, the watermark differs according to the applications and the role the watermark will play. For authentication application, which is the scope of this work, the watermark embedded into the digital image verify the integrity of the image. The basic concept is that any attempt to modify the content of the image will also modify the watermark itself so it can confirm if the image is tampered or not and locate the tampering area. There are two types of watermarking for this application, fragile watermark and semi-fragile watermark. The fragile watermark is sensitive to any modification of the original data (Wu et al., 2013; Fan et al., 2015) while the semi-fragile watermark can tolerate some modifications (LV. Et al., 2012; Qi et al., 2015).

In (MeenakshiDevi et al., 2009), the original grayscale image is decomposed using integer wavelet transform. The HH sub-band wavelet coefficient is chosen to embed the watermark using odd-even mapping. The watermark is a logo repeated several times to match the HH sub-band size and to increase the security. Also, it is scrambled using a shared secret key. Experimental results demonstrated that the scheme is able to localize image tampering at the pixel level. The work in (Preda, 2013) presented a secure semi-fragile watermarking technique. The watermark is a binary random sequence generated using the secret key. It is embedded into the discrete wavelet transform (DWT) coefficients of the second level detail sub-bands (LH – HL – HH). The selected wavelet coefficients are randomly permuted using a secret key then they are divided into groups. Every watermarking bit is embedded in every group using quantization. The scheme can detect and locate malicious tampering in images and is also robust to unintentional mild to moderate JPEG compression by using a low watermark payload.

Besides the tamper localization, the recent researches have tended to increase the functionality of the watermarking techniques by self-recovery of the image. In (Noriega et al., 2011) two different watermarks are used. One watermark is used for only detect the modified areas in the image and is generated as a random sequence. The second watermark is used for recovery phase and is produced using discrete cosine transform (DCT) which compressed using an arithmetic code. Both watermarks are added in the integer wavelet transform (IWT) domain. The system can locate the modified areas accurately in the image and the recovered image with high quality. Also, it is robust to noise insertion; it is able to tolerate close to 5% errors produced by salt and pepper noise. An authentication watermarking technique using DWT is presented in (Som et al.,

2015). The watermark is generated from the image itself by dividing the host image into 2x2 blocks and one dimension DWT is applied to each block. The generated watermark is embedded in four regions of the image to enhance the restoration process and make the approach more robust.

Some research has used the digital watermark for copyright protection application of satellite images as in (Kim,2011; Abugharsa, 2013; Nazmudeen, 2014), but using it in authentication application is still limited. The proposed technique for secure semi-fragile watermarking in (Chamlawi et al., 2009) embeds two watermarks in the DWT bands; one is for authentication and the other is for recovery. The scheme is applied to the greyscale image.

In this paper, a watermarking technique for self-recovery authentication of multispectral RS images is proposed based on integer wavelet transform (IWT). The visible bands of RS images; Red, Green, and Blue (RGB) are utilized to embed the watermark. The three visible bands are decomposed by two levels integer wavelet transform producing four sub-bands (LL_2, LH_2, HL_2, HH_2) for R, G and B components, where LL sub-band is the approximation version of the original image and LH, HL and HH are the detail high-frequency sub-bands. As the LL sub-band has the approximation information of the original image in lower resolution, it can be used as the watermark to hold the authentication and recovery information. The three LL sub-bands corresponding to R, G, and B are formed the three watermark components. Each component is rotated by 180 degrees and expanded to 8 bit-planes. To satisfy more security, the bit-planes are XORed with pseudo number sequence with different keys. The bit-planes of three watermarks are embedded into the bit-planes of the detail sub-bands coefficients of the corresponding visible band.

The contents of the paper is organized as following: Section 2 presents the basics of IWT. The watermarking algorithm is discussed in Section 3, and the experiment results under some attacks on RS images are presented and discussed in section 4. Finally, the conclusion is given in Section 5.

2. INTEGER WAVELET TRANSFORM (IWT)

The old versions of the wavelet transform was a floating point transform. If an image with integer pixel values is transformed to wavelet domain and some process are performed on the wavelet coefficients (as embedding watermark), the resulting image after inverse transform will not have integer values. Some truncation will be conducted to have integer pixel values again, thus the image will not reconstruct exactly. Also, the computation of this technique is costly and complicated. The second generation of the wavelet transformation solves this problem using Lifting Wavelet Transform (LWT) proposed by (Sweldens,1998) which is integer to integer mapping.

Using the lifting method instead of the convolution method provides many advantages than conventional wavelet transform such as perfect reconstruction, less memory requirement, and speed computation. The lifting scheme consists of three steps as shown in Figure 1:

- Split Stage: this step is only to sub-sample the original signal into even elements and odd elements.
- Predict Stage: in this step the even elements are used to predict the odd elements using a prediction function (detail coefficient).
- Update Stage: this stage updates the even elements to preserve the average value of the smaples (approximate coefficient).

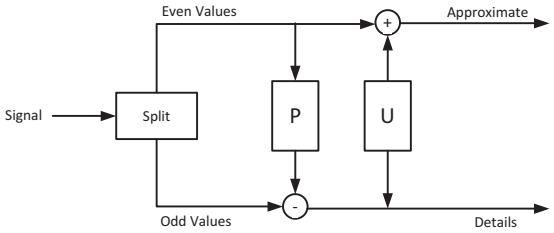

Figure 1. Lifting wavelet transform

3. PROPOSED SCHEME

The whole watermarking scheme will be discussed in the following sections.

3.1 Watermark Generation

The RS image of size MxN is decomposed into three independent images I_R, I_G, I_B corresponding to Red, Green and Blue channels. Each channel is decomposed with two level IWT producing four sub-bands (LL_2, LH_2, HL_2, HH_2), where LL is the approximation sub-band, HL is the Horizontal, LH is vertical, and HH is diagonal detail sub-bands. The three approximation sub-bands LL_2^R, LL_2^G and LL_2^B are selected as the watermark for their corresponding channels. The watermarks are first rotated by 180 degrees or cut into parts and scrambled. This operation is necessary for the image restoration process. After that, each watermark W_l^R, W_l^G, and W_l^B component is decomposed into a series of 8 bit-planes (8 binary images). The 1st bit-plane is the least significant bit (LSB) and 8th bit-plane is the most significant bit (MSB). The MSB image contains the most important features of the image and decreases gradually until the LSB image. Each binary plane image is XORed with pseudorandom binary sequence PN1, PN2, PN3 generated by different keys for different watermarks to form the final watermarks $\widetilde{W}_l^R$, $\widetilde{W}_l^G$, $\widetilde{W}_l^B$ as shown in the following equations:

$$\widetilde{W}_l^R = W_l^R \oplus PN1 \quad (1)$$

$$\widetilde{W}_l^G = W_l^G \oplus PN2 \quad (2)$$

$$\widetilde{W}_l^B = W_l^B \oplus PN3 \quad (3)$$

where $\oplus$ is the exclusive-OR operation and l =7, 6, ..., 0 is the pit-plane number of the watermark.

3.2 Watermark Embedding

In the watermark embedding stage, the pre-prepared watermarks are added in the RS image for authentication application as shown in Figure 2. After applying a second level IWT on the given I_R, I_G, and I_B images, the HL_2^k, LH_2^k, and HH_2^k sub-bands are selected for the watermark to be embedded where k represents the three R, G, and B color channels. The watermark is embedded in the detail sub-bands because they have the detail and edge components of the image which are less sensitive to the human eye. So, any change in the coefficients of these sub-bands should not cause any significant degradation in the quality of the resulted image. The selected sub-bands are decomposed into 8 bit-planes $\{P_{0,k}^n, P_{1,k}^n, \dots, P_{7,k}^n\}$ where P is the pit-plane, n is the

sub-band $HL_2, LH_2,$ or HH_2. The bit-planes of each watermark component is distributed over the bit-planes of the detail sub-

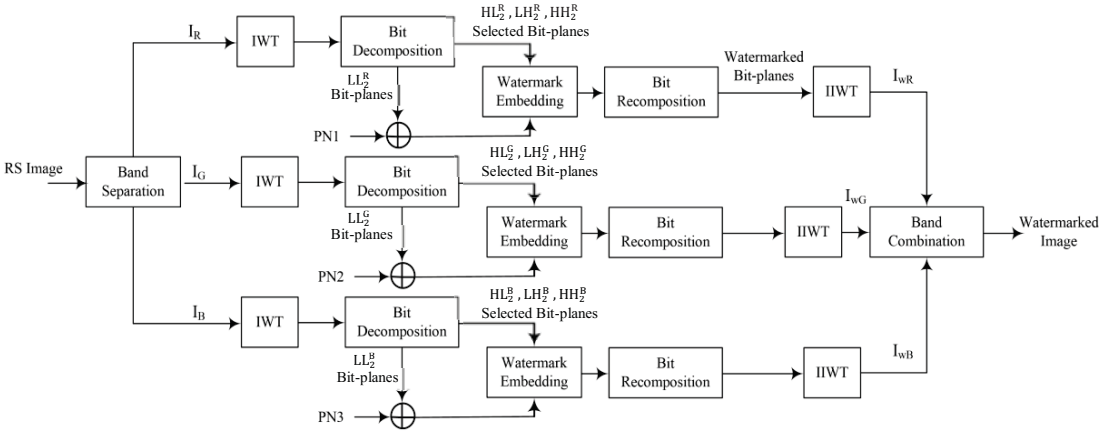

Figure 2. Watermark Embedding Scheme

bands which belongs to the corresponding channel. Adding the watermark in the high bit-planes leads to more degradation in the image quality while adding the watermark in the low bit-planes leads to less robustness. Thus, the middle bit-planes are chosen to hide the watermark to compromise between the quality and the robustness. For each channel, the watermarking embedding rule is defined as the following:

$$Pw_{m,k}^{n}(i,j) = \begin{cases} comp(b_{m,k}^{n}(i,j)) & \text{if } \widetilde{W}_k^l(i,j) = 1 \text{ and } xor\left(P_{m,k}^{n}(i,j), P_{m+1,k}^{n}(i,j)\right) = 1 \\ & \text{or } \widetilde{W}_k^l(i,j) = 0 \text{ and } xor\left(P_{m,k}^{n}(i,j), P_{m+1,k}^{n}(i,j)\right) = 0 \\ P_{m,k}^{n}(i,j) & \text{otherwise} \end{cases} \quad (4)$$

where $Pw_{m,k}^{n}(i,j)$ is the watermarked bit at the pixel position (i, j) in the m^{th} bit-plane of sub-band n and comp is the complement of $B_{m,k}^{n}(i,j)$. Once the embedding process is completed, the watermarked bit-planes are recomposed into watermarked sub-bands. Finally, the inverse integer wavelet transform (IIWT) is applied to the modified coefficients to obtain the watermarked RS image with watermarked color bands I_{wR}, I_{wG}, and I_{wB}.

3.3 Tamper detection and localization

The watermarked image can be tampered by cropping parts of the image or adding objects to the image. Also, the contents of the image could be changed by moving some parts of the image in place of other parts. To verify the tampering or integrity of the image, the watermark must be extracted first where only the keys k1, k2, and k3 must be known in the extraction operation. The watermark extraction procedure is the inverse operation of the watermark embedding procedure.

Consider that I'_{wR}, I'_{wG} and I'_{wB} are the three visible watermarked bands of the RS image corresponding to red, green, and blue bands, respectively.

- First, I'_{wR}, I'_{wG}, and I'_{wB} are decomposed using 2-level IWT to their sub-bands.
- Second, The detail sub-bands $HL_2^{k\prime}, LH_2^{k\prime}$ and $HH_2^{k\prime}$ used for watermark embedding are decomposed into 8 bit-planes $\{P_{0,k}^{n}{}', P_{1,k}^{n}{}', \dots, P_{7,k}^{n}{}'\}$ where P is the pit-plane, and n is the watermarked sub-band HL_2', LH_2', or HH_2'.
- Third, the bit-planes used in watermark embedding are separated and used to extract the bit-planes of the watermark using the rule in Equation 5:

$$W_k^{l\prime}(i,j) = \begin{cases} 1 & \text{if } P_{m,k}^{n}{}'(i,j) = P_{m+1,k}^{n}{}'(i,j) \\ 0 & \text{if } P_{m,k}^{n}{}'(i,j) \neq P_{m+1,k}^{n}{}'(i,j) \end{cases} \quad (5)$$

where $W_k^{l\prime}(i,j)$ is the extracted watermark bit at the pixel position (i, j) in the l^{th} bit-plane of the k^{th} watermark component.

- Fourth, the secret keys are used to obtain the final watermark by XORed the extracted watermark bit-planes with the corresponding PN sequence as in the following equations:

$$\widetilde{W}_R^l{}'' = W_R^l{}' \oplus PN1 \quad (6)$$

$$\widetilde{W}_G^l{}'' = W_G^l{}' \oplus PN2 \quad (7)$$

$$W_B^l{}'' = W_B^l{}' \oplus PN3 \quad (8)$$

The watermark bit-planes are combined to generate the extracted watermark components W_R'', W_G'', and W_B''.

- Finally, the three watermark components images are rotated back to their original form.

To analyze the authentication of the received RS image, the extracted watermark components are compared with the approximation sub-bands $LL_2^{R\prime}, LL_2^{G\prime}$, and $LL_2^{B\prime}$ to calculate the difference between them. A black difference image means that the RS image doesn't expose to any alteration attempt; otherwise, the image is altered. Thus, the different regions are traced in the difference image and extracted separately. These regions are correlated with the corresponding regions in the approximation sub-bands. The regions with high correlated coefficients are detected and localized as tempered regions.

3.4 Image Recovery

The detection of the tampered region can be done using one of the watermark components while the restoration process needs the three watermark components. After finishing the tamper detection process, the tampered regions are recovered by replacing the tampered pixels in $LL_2^{R'}, LL_2^{G'}$, and $LL_2^{B'}$ with the corresponding watermark components pixels. The inverse integer wavelet transform (IIWT) is applied using the reconstructed approximation sub-band to produce the recovered image. Rotating the watermark components before embedding them in the image makes the effect of any counterfeit happens at a different place away from the original place by 180 degrees. Consequently, the watermark components images still have the original information.

4. RESULT AND DISSCUSION

The effectiveness of the proposed algorithm is tested and evaluated with different RS images. The algorithm is evaluated in terms of imperceptually, authentication, tamper localization and ability to self-recovery the tampered region. Two color satellite images with different contents and size are selected as test images. The first one is part of Saint-Louis, in Missouri, USA with size 1296 x 976 and the second one is Quickbird satellite image taken for a place in Ukraine with size 1584 x 1136. The first experiment is to measure the visual quality of the watermarked images using Peak-Signal-To-Noise Ratio (PSNR). The PSNR measures the difference between the original image and the watermarked image. The PSNR is calculated as shown in Equation 9:

$$PSNR = 10\, log \frac{255^2}{MSE} \tag{9}$$

where MSE = the mean squared error between the original and distorted image.

The MSE is defined as in Equation 10:

$$\text{MSE} = \frac{1}{\text{mn}} \sum_{i=1}^{m} \sum_{j=1}^{n} [I(i,j) - I'(i,j)]^2 \tag{10}$$

where mn = give the size of the image
$I(i,j), I'(i,j)$ = the pixel values at location (i, j) of the original and distorted image.

Figure 3(a), (b) show the original and watermarked "Saint-Louis" image with average PSNR for the three bands equal to 39.7718 dB and Figure 5(a), (b) show the original and watermarked "Ukraine" image with average PSNR 40.0197 dB. It is hard to discriminate between the original and watermarked image by nicked eye.

The detection, localization, and recovery of tamper region are evaluated in the second experiment. The watermarked images are exposed to crop an object from the image and replace it with a piece of the background that surrounded the object. Accordingly, the image will appear as if it was no object in this place before. In Figure 3(c), parts from the green background are selected and inserted over the dark area which is marked by the red arrow. However, In Figure 5(c), the ship is cut and replaced by part of the water background. The proposed technique can perfectly detect the tampered regions of the images which are marked them by black blocks as shown in Figure 3(d) and Figure 5(d).

(a)

(b)

(c)

(d)

(e)

Figure 3. (a) Original Saint-Louis image. (b) Watermarked image. (c) Tampered image. (d) Tampered region detection. (e) Recovered image.

The tampered region is successfully recovered as shown in Figure 3 (e) and Figure 5 (e) with PSNR values 38.4117 dB and 39.781 dB respectively.

Figure 4 (a) indicates the extracted R component watermark for Saint-Louis image which is one-quarter of the original image size. The red circle is drawn around the place of tampered region as appear in the watermark. Figure 4 (b) is the $LL_2^{R'}$ approximation sub-band. The difference between these two images results the image in Figure 4 (c) which is used in the localization and recovery process. The red circle highlights the recovered object in this image. The same process is done for the G and B components.

Figure 6 (a) indicates the extracted R component watermark for Ukraine, (b) is the $LL_2^{R'}$ approximation sub-band while (c) is the difference image where the red circle highlights the recovered ship.

(a)

(b)

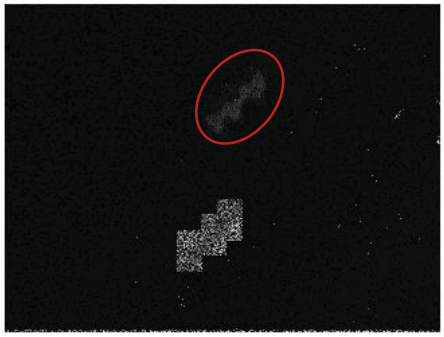

(c)

Figure 4. (a) The watermark Red component. (b) The $LL_2^{R'}$ approximation sub-band. (c) The difference Image.

(a)

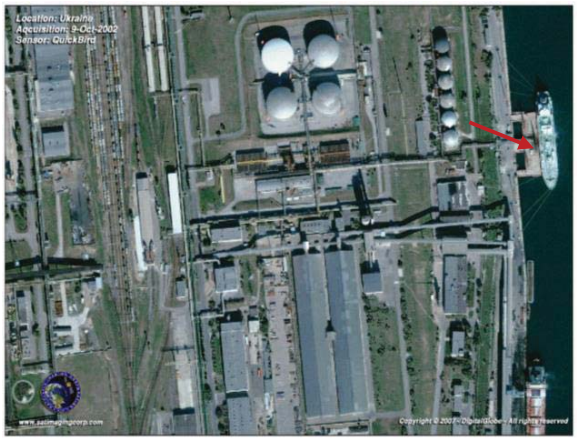

(b)

(c)

(d)

(e)

Figure 5. (a) Original Ukraine image. (b) Watermarked image. (c) Tampered image. (d) Tampered region detection. (e) Recovered image.

(a)

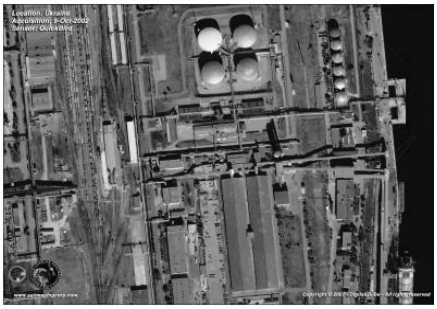

(b)

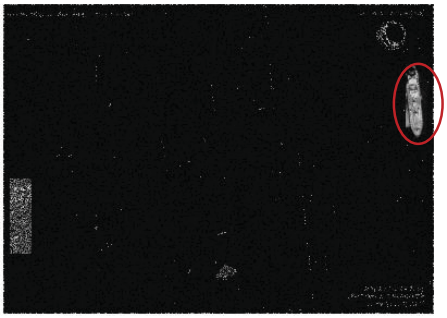

(c)

Figure 6. (a) The watermark Red component. (b) The $LL_2^{R\prime}$ approximation sub-band. (c) The difference Image.

5. CONCLUSION AND FUTURE WORK

In this paper, an image content authentication algorithm for color satellite images is presented. The proposed algorithm shows an accurate performance in the detection of the altered region and the recovery capability for these areas. It uses the same watermark for the localization and restoration functions which leads to decrease the payload and preserve the visual quality of the image at an acceptable level. The approximation sub-band of IWT which contains the necessary information of the original image is used to help in the recovery process. The watermark is embedded into the detail sub-bands so it is spread all over the image which helps in the localization process. Moreover, using IWT in embedding process reduces the computational cost. The experimental results show that the system detects correctly the place that the image has been modified, and recovers the image with a good quality. In the future work, we will focus on reducing the payload of the watermark with preserving the capability of both tamper localization and recovery.

REFERENCES

Wu, C.M. and Shih, Y.S., 2013. A simple image tamper detection and recovery based on fragile watermark with one parity section and two restoration sections. Optics and Photonics Journal, 3(02), p.103.

Qi, X. and Xin, X., 2015. A singular-value-based semi-fragile watermarking scheme for image content authentication with tamper localization. Journal of Visual Communication and Image Representation, 30, pp.312-327.

Fan, Y.C. and Hsu, Y.Y., 2015. Novel Fragile Watermarking Scheme using an Artificial Neural Network for Image Authentication. Appl. Math, 9(5), pp.2681-2689.

LV, L., FAN, H., WANG, J. and YANG, Y., 2012. A semi-fragile watermarking scheme for image tamper localization and recovery. Journal of Theoretical and Applied Information Technology, 42(2), pp.287-291.

MeenakshiDevi, P., Venkatesan, M. and Duraiswamy, K., 2009. A fragile watermarking scheme for image authentication with tamper localization using integer wavelet transform. Journal of Computer Science, 5(11), p.831.

Preda, R.O., 2013. Semi-fragile watermarking for image authentication with sensitive tamper localization in the wavelet domain. Measurement, 46(1), pp.367-373.

Noriega, J.A.M., Kurkoski, B.M., Miyatake, M.N. and Meana, H.P., 2011. Image authentication and recovery using BCH Error-correcting codes. International Journal of Computers, 5(1), pp.26-33.

Som, S., Palit, S., Dey, K., Sarkar, D., Sarkar, J. and Sarkar, K., 2015. A DWT-based Digital Watermarking Scheme for Image Tamper Detection, Localization, and Restoration. In Applied Computation and Security Systems (pp. 17-37). Springer India.

Kim, J.H., Lee, S.H. and Kown, K.R., 2011, February. A satellite image watermarkig scheme based on perspective distance. In Frontiers of Computer Vision (FCV), 2011 17th Korea-Japan Joint Workshop on (pp. 1-4). IEEE.

Nazmudeen, N.H. and Farsana, F.J., 2014. Satellite Image Security Improvement by Combining DWT-DCT Watermarking and AES Encryption. International Journal of Advanced Computer Research, 4(2), p.645.

Abugharsa M.B., Sullabi M. A., Taher A. M., 2013 . Digital Watermarking Enhancement for Satellite Images Using a DCT Algorithm. 2nd International Conference on Recent Trends in Computer and Information Engineering (ICRTCIE'2013), Dec. 20-21, Bali (Indonesia), pp. 51-54.

Chamlawi, R., Li, C.T., Usman, I. and Khan, A., 2009, January. Authentication and recovery of digital images: potential application in video surveillance and remote sensing. In Consumer Electronics, 2009. ICCE'09. Digest of Technical Papers International Conference on (pp. 1-2). IEEE.

Sweldens, W., 1998. The lifting scheme: A construction of second generation wavelets. SIAM J. Math. Anal.,29(2), pp. 511–546.

MODERN TRAMWAY TRACK GEOMETRIC QUALITY INSPECTION BY AIDED INS

Qijin Chen [a] , Xiaoji Niu [a,*], Lili Zuo [b]

[a] GNSS Research Center, Wuhan University, No.129, Luoyu Road, Wuhan, Hubei, China – xjniu@whu.edu.cn
[b] Wuhan Municipal Construction Group Co., Ltd, No.6, Chunxiao Road, Zhuankou economic development zone, Wuhan, China.

KEY WORDS: Tramway track geometry surveying; railway track irregularity; inertial surveying; relative measurement

ABSTRACT:

Tramway track geometric quality inspection is very important for track maintenance and for assuring passenger comfort. Conventional lightweight track geometry measuring trolley based on optical measuring equipment, total station for example, is still slow for the track geometric quality inspection. Railway track measuring method based on GNSS/INS has recently been proposed to be used in this field to improve the measuring speed. This paper presents an overview on the track geometry measuring trolley based on aided INS and its application in tramway track geometry surveying. The measuring principle and the architecture of the track geometry measuring track based on A-INS is introduced. Field test result analysis is followed to illustrate the performance of the proposed method, and the results show it can meet the accuracy requirements for the tramway track inspection.

1. INTRODUCTION

Tramway is a kind of rapid urban transits that the trams run on grooved rails on normal streets. The first modern tramway in Wuhan city is under construction, which is design to run with low noise level at a top speed of 70 km/h. It is the first modern catenary-free tramway that powered by super-capacitors in China, as shown in Figure 1. Good tramway track condition is important and the precondition for the passenger comfort. While the tramway track condition tends to deteriorate due to some external factors, such as error of rail setting out, frequent passage of train and deformation of the track bed, which finally resulted in track deformation. Track deformation, i.e. track irregularity, is one of the most important factors that effects passenger comfort. So the track geometry measurement and deformation identification if a task of fundamental importance for the track maintenance.

The technical standards for high speed railway track geometry measuring are adapted to the tramway construction in Wuhan since there is no related standards available. These standards specify the requirements that shall be met by measuring system fitted on lightweight track geometry measuring trolley (TGMT), which is designed for accurate measurement of specific track geometric parameters. Amberg GRP1000 by Amberg Technologies and Trimble GEDO CE are two typical and well-known products of the high-precision track geometry measuring trolley that have been widely deployed in China for the railway track geometry measuring in both the railway construction and operating maintenance stages. This kind of TGMTs usually use the motorized total station to measure the 3D coordinates of the rails relative to the control network points, and use other sensor to measure other track geometry parameters such as gauge and cross level. The TGMT equipped with high-precision total station are claimed able to measure the deviation of the railway track from its designed geometry with 1 millimeter accuracy in the stop-and-go mode. The TGMT based on total station is currently the predominant approach for accurate railway track measurement. It is accurate enough for the rail staking out in the construction stage, but has two main shortcomings when used in track condition inspection: a) low measuring speed, e.g. only about 150-m track can be inspected each hour by this method; b) this optical measuring equipment, e.g. total station, is easily affected by the external condition, such as temperature and light condition(Chen, Niu et al. 2015).

In this case, a flexible and rapid railway track geometry measuring system is desirable for completing the inspection task within a short time. So we propose a method based on the aided inertial navigation system (A-INS) to measure the track geometry parameters in kinematic mode to improve the surveying speed.

In previous works, inertial technique has been widely utilized for railway track surveying and track condition monitoring. Inertial sensors, e.g. accelerometers and gyroscopes, are usually equipped in the railway track surveying equipment to detect the track irregularity and monitor the track condition by sensing the acceleration and angular rate change of the specific platform. Typically the inertial sensors are mounted on the rigid structures of the train, such as the axle-box, bogie and car-body to detect the vertical and lateral track irregularities(Westeon, Ling et al. 2007, Weston, Ling et al. 2007, Alfi and Bruni 2008, Naganuma, Kobayashi et al. 2010, Boronakhin, Podgornaya et al. 2011, Heirich, Lehner et al. 2011, Wang, Qin et al. 2012). The accelerations are first converted to displacement by double integration; then the track irregularities are detected with the displacement. But in this case, the solutions suffer from two issues: a) the inertial sensor drift is difficult to be well compensated; b) the double integration of sensor noise and bias causes uncontrolled error in the resulting displacement, so band-pass filters have to be applied, which may harm the real motion signal when the equipment moves at low speed along the track.

Aided INS technique can overcome these two shortcomings mentioned above by fusing the GNSS position and other update information with the inertial outputs in a well-designed Kalman filter (Chen, Niu et al. 2015). The basic measuring principle and aided INS algorithm is described in section 2. Section 3 introduces the architecture of the track geometry measuring trolley and the related data processing software design. And this is followed by the field test and results analysis in section 4.

Figure 1 Wuhan Tramway in construction

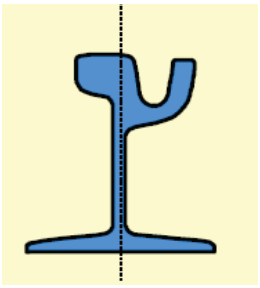

Figure 2 grooved rail for the tramway track (refer to (Esveld 2001))

2. METHODOLOGY

2.1 Principal tramway track geometric parameters

The principal track geometric parameters the TGMT should measure include track gauge, cross level, twist, alignment and longitudinal level. Track gauge is the smallest distance between lines perpendicular to the running surface intersecting each rail head profile in a range from 0 to 14 mm (for the tramway track) below the running surface, and can be measured using a contact or noncontact distance measuring sensor. Cross level, namely cant, refers to the difference in height of the adjacent running tables computed from the angle between the running surface and a horizontal reference plane. Cross level is determined by measuring either the angle between the running surface and the horizontal reference plane or the difference in height between the two running tables. Twist is the algebraic difference between two cross levels taken at a defined distance apart, usually expressed as a gradient between the two points of measurement. Alignment and longitudinal level refer to the deviation in lateral and vertical direction from the related mean position (reference line) respectively(EN 2008, EN 2011). The measuring accuracy requirement for the track geometric parameters can be found in (EN 2008, EN 2011, Chen, Niu et al. 2015) .

For the TGMT with total station, the alignment and longitudinal level can be determined from the 3D position coordinates measurement of consecutive positions on rails. Track geometry can be described in terms of track curvature, alignment, elevation (cant), and gauge as functions of distance along the track. Track irregularity refers to the deviation of railway track from its designed geometry and smoothness, usually expressed in two separate layouts for horizontal and vertical directions. Five typical track irregularities are defined: alignment irregularity, vertical irregularity, cross level, i.e. super-elevation, twist and gauge deviation.

The accurate measurement of track gauge, cross level and twist is technically easy to realize in kinematic inspection mode. The challenge of tramway track geometry measuring lies in the measurement of alignment and longitudinal level, since the position coordinates measurement shall be with submillimetre relative accuracy(Glaus 2006, Chen, Niu et al. 2015).

2.2 Measuring principle of TGMT based on A-INS

Rail and track centerline is actually a three-dimensional curve, and track irregularities can be regarded as the relative deviation of the rail from its nominal smoothness. Thus railway track deformation inspection and identification is inherently an issue of spatial-relative measurement of the track position and angles. In other word, once the track position and orientation are determined with enough precision, the 3D track geometry can be reconstructed and based on which the track defect and irregularities could be identified.

Inertial navigation system (INS) is well known capable of providing position and attitude measurements with extremely high relative accuracy in short time range. Aided INS can take advantage external update information, such as GNSS position and velocity, to correct the navigation error accumulation of the INS so as to maintain its relative measurement accuracy in a longer time range.

For the railway track irregularity measuring, as long as the wheels of the track trolley without suspension connection can keep continuous contact with the railway track, the track geometric parameters can be derived from the trolley motion information. For example, the rail position coordinates can be determined from the TGMT trajectory and attitude measurements, and the cross level can be derived from the roll angle measurement of the TGMT. The trolley motion information can be obtained by the aided INS. The trolley wheels are used to link A-INS and the rails mechanically which

allow the inertial sensors to "sense" the track geometry and defect. Tramway track irregularity inspection is based on the response of the track trolley to the track irregularity, which would cause the motion state fluctuation of the trolley moving on the rails. These response signal can be captured by aided INS. Based on the position and attitude measurements by A-INS, the track geometry can be reconstructed and the track geometric parameters can be quantitatively identified. Figure 3 illustrates the track irregularity measuring principle of the track trolley based on the A-INS.

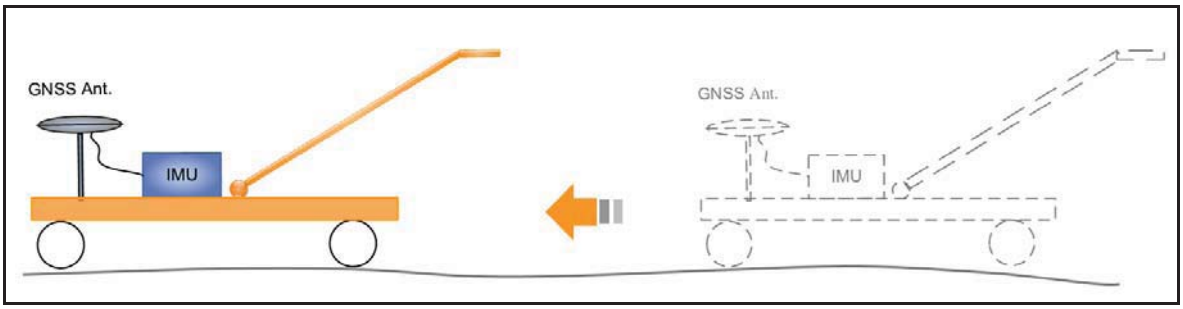

Figure 3 Illustration of the railway track trolley based on GNSS/INS system.

2.3 Aided INS algorithm

Analysis above tells that the accuracy of the position and attitude measurement determines how accurate we can measure the track geometric parameters, namely the aided INS accuracy determines the system accuracy. The Kalman filter algorithm for the aided INS data fusion is designed. And to improve the surveying accuracy of GNSS/INS system, non-holonomic constraint (NHC) and zero velocity updates are carried out for error control in the GNSS/INS integration algorithm (i.e. Kalman filter). Non-holonomic constraint refers to the fact that unless the track trolley jumps off or slides laterally on the track, the velocity of the track trolley in the plane perpendicular to the track alignment centerline is zero. Non-holonomic constraint is proved to be useful for improving the heading and pitch accuracy, especially for the low and medium grade inertial navigation system (Chen, Niu et al. 2015).

2.3.1 Kalman filter design

As the basis of the aided INS integration algorithm, a typical Kalman Filter of 21-dimensional error states is designed. The INS errors are analyzed in the computer frame(Shin 2005) and the results are expressed in terms of the $\boldsymbol{\psi}$ -angles error model(Benson 1975, Britting 2010). The errors of inertial sensors including the bias and the scale factor error of the gyros and accelerometers are augmented into the KF states and estimated through the difference of GNSS and INS solutions. The 21-dimensional states equation in terms of $\boldsymbol{\psi}$ -angle error model can be expressed as:

$$\dot{\boldsymbol{x}} = \mathbf{F}\boldsymbol{x} + \mathbf{G}\boldsymbol{w} \tag{1}$$

Where $\mathbf{F}$ is the dynamic matrix, $\mathbf{G}$ is the design matrix of the system noise(Shin 2005), $\boldsymbol{x}$ is the error state vector:

$$\boldsymbol{x} = \begin{bmatrix} \delta\boldsymbol{r}^c & \delta\boldsymbol{v}^c & \boldsymbol{\psi} & \boldsymbol{b}_g & \boldsymbol{b}_a & \boldsymbol{s}_g & \boldsymbol{s}_a \end{bmatrix}^T \tag{2}$$

Where, $\delta\boldsymbol{r}^c, \delta\boldsymbol{v}^c, \boldsymbol{\psi}$ are the position error, velocity error and attitude error, respectively. $\boldsymbol{b}_g$, $\boldsymbol{b}_a$ are the bias of gyros and accelerometers; $\boldsymbol{s}_g$ and $\boldsymbol{s}_a$ are the scale factor error of gyros and accelerometers, respectively.

2.3.2 Measurement model

The differences between the GNSS position and velocity solution and those derived from the INS system are used as the update information in the Kalman filter, as:

$$\boldsymbol{z} = \begin{pmatrix} \boldsymbol{r}_{INS} - \boldsymbol{r}_{GPS} \\ \boldsymbol{v}_{INS} - \boldsymbol{v}_{GPS} \end{pmatrix} \tag{3}$$

The data fusion is implemented through the loosely-coupled closed-loop aided INS integration algorithm, as shown in Figure 4 . Please refer to (Shin 2005) for more detail about the inertial mechanization algorithm and the Kalman filter design.

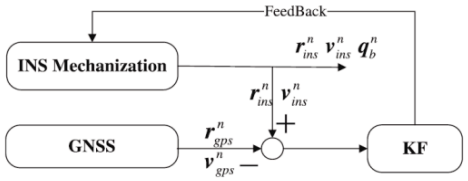

Figure 4 Kalman Filter structure for the GNSS/INS integration

The motion of the track trolley on the rails is governed by two non-holonomic constraints (NHC), since the trolley does not jump off and sideslip on the rails, which means the velocity of the trolley in the plane perpendicular to the forward direction is almost zero. Non-holonomic constraint is proved to be effective in improving the accuracy of the heading and pitch angles, especially for the low- and medium-end inertial navigation system. Non-holonomic constraints can be considered as measurement updates to the Kalman filter.

$$\begin{aligned} \boldsymbol{v}^v_y &\approx 0 \\ \boldsymbol{v}^v_z &\approx 0 \end{aligned} \tag{4}$$

Where, $\boldsymbol{v}^v_y$ and $\boldsymbol{v}^v_z$ represent the velocity of the track trolley in the plane perpendicular to the forward direction, expressed in the vehicle frame. The computed velocity in the body frame can be expressed as:

$$\hat{\boldsymbol{v}}^v = \hat{\mathbf{C}}^v_n \hat{\boldsymbol{v}}^n \tag{5}$$

By perturbing equation (5) and considering only the first order term, the computed error model of velocity in body frame can be expressed as(Chen, Niu et al. 2015):

$$\delta \boldsymbol{v}^{v} = \mathbf{C}_{n}^{v}\delta \boldsymbol{v}^{n} + \mathbf{C}_{n}^{v}(\boldsymbol{v}^{n}\times)\boldsymbol{\varepsilon}^{n} \tag{6}$$

Where, $\delta \boldsymbol{v}^{v}$: velocity error in vehicle frame; $\delta \boldsymbol{v}^{n}$: velocity error in navigation frame; $\mathbf{C}_{n}^{v}$: direction cosine matrix that transform vector from navigation frame to vehicle frame; $\boldsymbol{v}^{n}\times$: cross-product form of velocity vector in navigation frame; $\boldsymbol{\varepsilon}^{n}$: attitude error vector.

We should point out that non-holonomic constraint is a kind of velocity constraint in vehicle frame (the track trolley frame), not in n-frame (e.g. North-East-Down). It should be well valid at any point of the railway track from the vehicle frame perspective considering the track always has a smooth and continuous shape. On the other hand, the irregularity of the track is the displacement of the track relative to the ground, i.e. n-frame, essentially caused by the unexpressed angle changes of the track along the yaw and pitch directions. We find that the contribution of non-holonomic constraints for the further accuracy improvement is indeed very limited for high-grade GNSS/INS system (like navigation grade). The use of NHC requires precise calibration of the angle misalignment between the IMU body frame and the track trolley frame. For the low- and medium-grade inertial navigation system, non-holonomic constraints plays an important role in the relative accuracy improvement in the application of railway track surveying(Chen, Niu et al. 2015).

2.3.3 Optimal smoothing algorithm

Smoothing algorithm is applied to obtain an optimal estimation utilizing all the past, current and future measurements, since the tramway track measurement data is allowed to be post-processed for accuracy improvement. In this paper, the well-known Rauch-Tung-Striebel (RTS) algorithm is used (Brown and Hwang 1997):

$$\begin{aligned}
\hat{\boldsymbol{x}}_{k/N} &= \hat{\boldsymbol{x}}_{k/k} + \mathbf{A}_{k}\left[\hat{\boldsymbol{x}}_{k+1/N} - \hat{\boldsymbol{x}}_{k+1/k}\right] \\
\mathbf{P}_{k/N} &= \mathbf{P}_{k/k} + \mathbf{A}_{k}\left[\mathbf{P}_{k+1/N} - \mathbf{P}_{k+1/k}\right]\mathbf{A}_{k}^{T} \\
\mathbf{A}_{k} &= \mathbf{P}_{k/k}\boldsymbol{\Phi}_{k}^{T}\mathbf{P}_{k+1/k}^{-1}
\end{aligned} \tag{7}$$

Where, $\mathbf{A}_{k}$ is the smoothing gain, $\boldsymbol{\Phi}$ is the state transition matrix, $\mathbf{P}$ is the state error covariance, and subscript N is the total number of measurement.

3. TGMT BASED ON A-INS AND DATA PROCESSING

The TGMT based on aided INS consists of four type of sensors: IMU, GPS receiver, gauge sensor and odometer, as illustrated in Figure 5.

3.1 TGMT based on A-INS

3.1.1 Track trolley

A rigid and accurate track trolley hardware without suspension support is used as the basis of the system to where all sensors are integrated, as shown in Figure 5. As mentioned above, the response of the platform to rails defect is the premise of track geometry survey, thus the wheels of the trolley should be able to keep reliable and continuous rigid contact with the rails when moving on rails. It requires the trolley does not jump off respect to rails in the vertical direction and not slide laterally. The two flange wheels on the left hand of the trolley are pressed against a chosen rail (e.g. the inner rail in the curved section) through the springs used in gauge sensor, and the distance between INS and the chosen reference rail maintain constant. To reduce friction, landside wheels are used in the reference side of the trolley instead of wheels with flanges.

The lightweight trolley can be pushed or hauled by human force or by a special motor machine through a lever arm mounted in a bearing at a rigidly vertical axis as shown in Figure 5. It is designed able to move at a top speed of 10 m/s. Under this speed, the three wheels of the trolley are able to keep reliable and continuous contact with the rail, thus the wheels can rigidly track the track geometry and be responsive to the track irregularities. The lever arms of sensors and wheels with respect to the IMU measurement center is calibrated.

Figure 5 Track geometry measuring trolley based on aided INS

3.1.2 IMU

Inertial measurement unit (IMU) is the core sensor of the whole system. A navigation grade IMU *POS830* manufactured by Wuhan MAP Space Time Navigation Technology co.,LTD (short as MAP Inc.) is integrated. It contains a linear quartz accelerometers triad and a ring laser (RLG) gyros triad, and measures acceleration and angular velocity in three mutually orthogonal direction centered at the IMU measuring center, and outputs datasets as incremental velocity and angles. A NovAtel OEMV-2 receiver is built in this system to provide raw GNSS observations at 1 Hz sampling rate. The IMU performance specifications are listed in Table 1.

Table 1 Specifications of POS830

Component Name	Specifications
IMU	• Sampling rate: up to 200 Hz • Gyro bias: 0.01 deg/hr • Accel. bias: 10μg

3.1.3 GNSS

GNSS provides positioning solution with centimeter precision by performing differential positioning processing based on carrier phase measurement (Groves 2013). A GNSS reference station shall be set for carrier phase based differential GNSS processing to provide position solutions with centimeter accuracy. GNSS position would always be the first option for

the measuring trolley system to provide absolute geo-reference and integrate with INS whenever GNSS signal is available in the survey circumstance. But we would point out that GNSS is only an option for the trolley system, which means when the GNSS signal is not available, the trolley system also works by initialized with an absolute position through other approach to establish the relationship to the track survey network.

3.1.4 Gauge measuring sensor

Gauge is measured using a high-precision mechanical distance measuring system. The gauge is measured as the sum of the offset between the gauge sensor with respect to the reference rail plus the distance measured by gauge sensor to the other running rail edges. The gauge sensor shall sample at a sufficiently high data rate when the TGMT based on A-INS working in kinematic mode. For example, if the trolley runs at a speed of 5 m/s, and the gauge sensor samples at 20 Hz, then the distance interval of the gauge samples would be 0.25m. In addition, gauge measurement should be synchronized with IMU in time.

3.1.5 Odometer

Odometer sensor, such as Hall-effect wheel transducer and optical distance encoder, is used to measure the longitudinal distance travelled by the trolley along rails. Two Hall-effect transducers are installed on the same wheel side of the trolley in a specific manner, the longitudinal distance and travel direction can be determined. Time tags are attached to each pulses so as to synchronize with the IMU raw data. The distance measured by odometer sensor contains cumulative error which is proportional to the longitudinal travel distance due to the uncertainty in wheel radius, resolution of the odometer and possible slippage. Velocity derived from odometer/ wheel sensor is an important auxiliary information and constraint for the inertial navigation, which can effectively improve the accuracy of the navigation solution in the integrated system, especially when GNSS signal are interfered or blocked. Complementary to the non-holonomic constraint, the odometer signal can be regarded as the velocity update along the forward (along-track) direction. Therefore, the non-holonomic constraint and the odometer compose a complete three dimensional velocity update in the vehicle frame.

3.2 Data Processing Software

The raw datasets acquired by the TGMT based on aided INS and GNSS reference stations are feed into the data post process software InsRail, as shown in Figure 6, which is developed at GNSS Research Center at Wuhan University. The InsRail contains three function modular include: post GNSS positioning process, aided INS data fusion, and railway track geometry analysis.

The GNSS positioning engine is developed by the navigation group at GNSS Research Center at Wuhan University cooperated with MAP Inc. The GNSS positioning modular supports standard positioning processing (SPP), differential GNSS, and carrier-phase based differential positioning processing.

The fusion of the GNSS solutions and the raw inertial dataset are implemented in loosely coupled manner. As the basis of integrated processing modular of InsRail, the extended Kalman filter is designed based on 21-dimensional error states vectors. Moreover, Rauch-Tung-Striebel (RTS) backward smoothing algorithm is applied in the software to achieve high accuracy in the smoothed solutions. InsRail also supports other aiding information for INS such as zero velocity update (ZUPT) and non-holonomic constraints to improve the aided INS performance.

The main functions of the railway track geometry analysis modular are listed as: 1) provide the 3D position coordinates of rails and tramway track centerline, attitude measurements (including roll, pitch and azimuth angle), and mileage measurement based on the aided INS navigation solutions. 2) calculate all kinds of tramway track geometric parameters including: rail deformation magnitude in both horizontal and vertical directions, alignment and longitudinal irregularities, cross level, gauge and twist et al. The InsRail can associate the precise location to the measured data and track geometric parameters, such as mileage with centimeter precision. The rail geometry analysis reports output from the InsRail can be used for track geometry quality monitoring and safety assurance with respect to track geometry on track sections where maintenance will be carried out, e.g. rail adjustment.

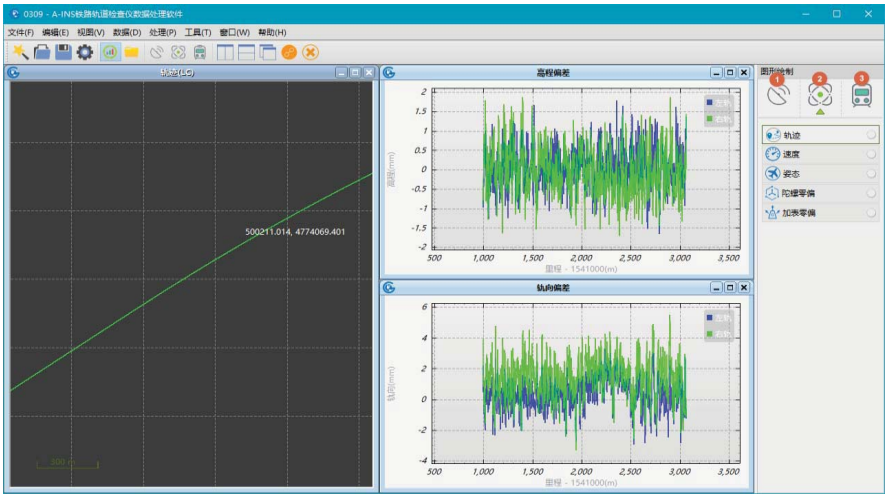

Figure 6 TGMT based on A-INS data processing software – InsRail

FIELD TEST AND RESULTS

This section presents some tramway track inspection experiment results obtained by the TGMT based on A-INS. As shown in Figure 7, the grooved rail of tramway track is inspected by TGMT based on A-INS. A Trimble NetR9 receiver sampling at 1 Hz was located at a control point of the railway construction control network as the GNSS reference station. The base station has favorable observation circumstance and the length of the baseline between base station and the trolley is less than 2 kilometers. In this experiment, three different runs over the same section of tramway track have been was carried out to check the repeatability of the surveying result as analyzed in the following section. The track segment surveyed by GNSS/INS system is about 1.3 kilometers, which covers the tangent (i.e. straight lines), curved and transitional segment.

Figure 7 Tramway track inspection on Wuhan modern tramway

The performance of the TGMT based on A-INS can be validated by comparing measurement of different runs on the same section of track(EN 2011), namely the measurement repeatability analysis. Statistical analysis of the measured parameter data can be used to compare recording runs. Analysis has been made for the important tramway track geometric parameters, and the calculation and analysis consist of the following steps: 1) precise spatial synchronization of the measurement; 2) measurement plot and calculation of the measurement difference. Figure 8 to Figure 11 show the comparison of different kind of tramway track geometric parameters measurement between different runs, including alignment, longitudinal level, gauge, cross level. The subplot (a) in each figure shows the measurement of related track geometric parameter in the 1st run and the subplot (b) shows the difference of the related measurement of the 2nd and the 3rd runs with respect to the 1st run which illustrates the measurement repeatability.

The comparisons show that the measurement repeatability of the alignment deformation and longitudinal level deformation is smaller than 0.3 mm and smaller than 0.2 mm for the gauge and cross level measurement. Figure 12 shows the result of track irregularity of reference rail in horizontal and vertical direction respectively, the repeat measurement accuracy is better than 0.3 mm. The results show that the TGMT based on A-INS can meet the accuracy requirement for the tramway track geometry inspection.

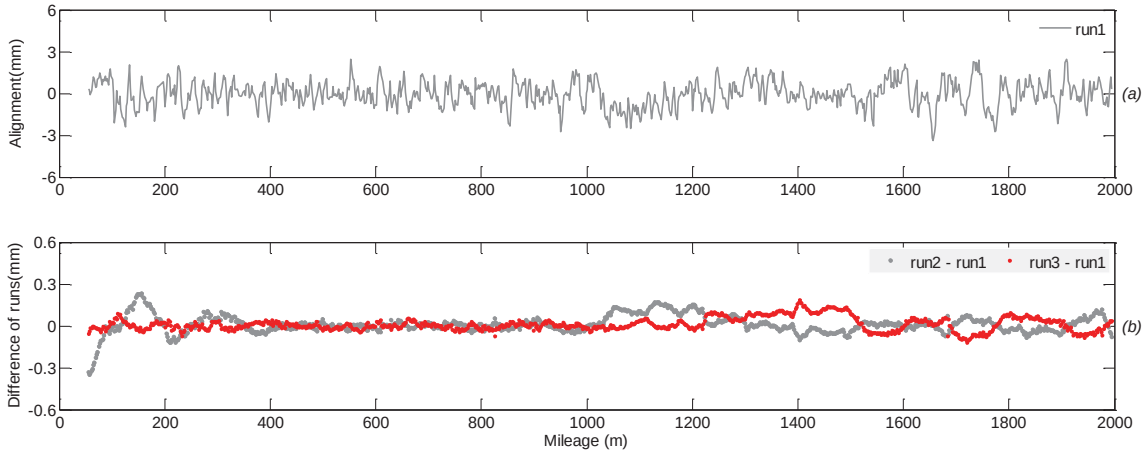

Figure 8 Alignment measurement repeatability of reference rail: (a) measurement of the 1st run; (b) difference of measurement of the 2nd and the 3rd runs with respect to the 1st run

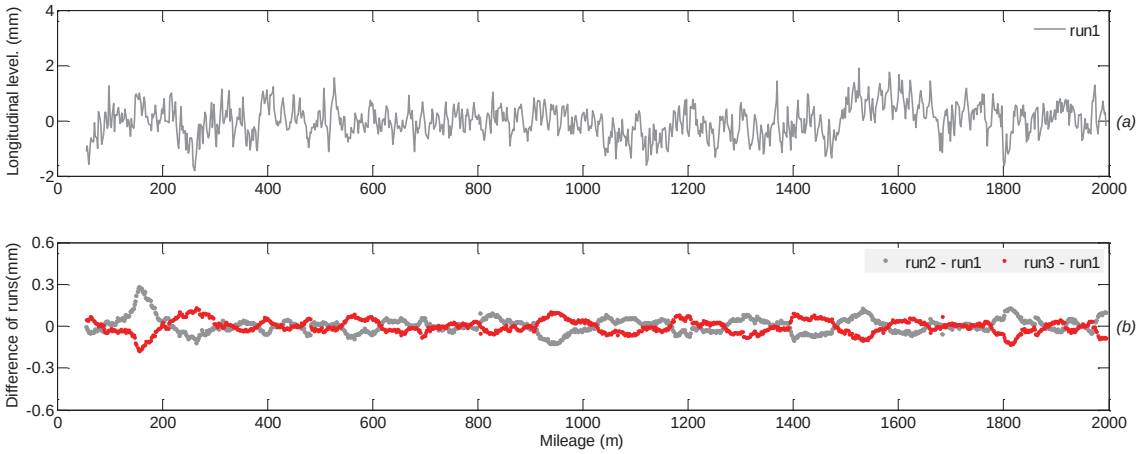

Figure 9 Longitudinal level measurement repeatability of reference rail: (a) measurement of the 1st run; (b) difference of measurement of the 2nd and the 3rd runs with respect to the 1st run

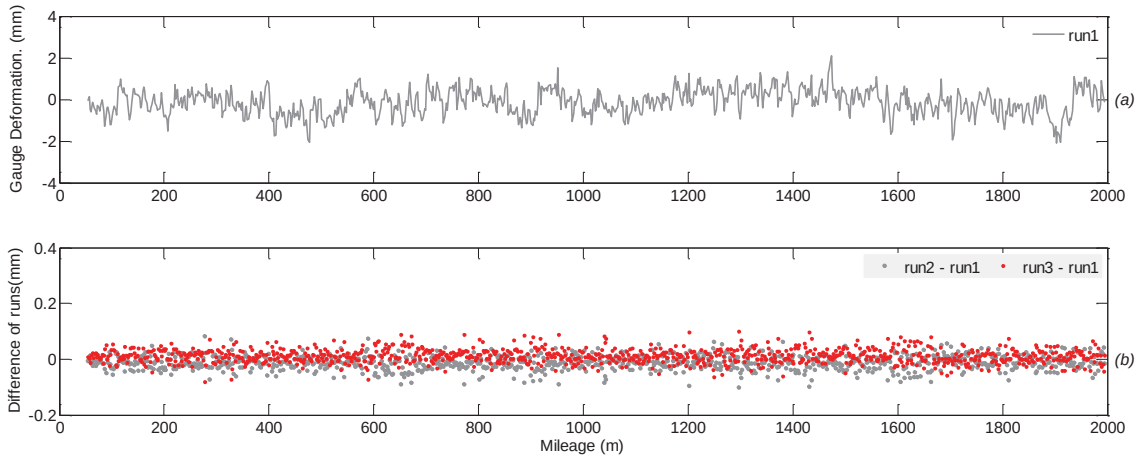

Figure 10 Gauge measurement repeatability: (a) measurement of the 1st run; (b) difference of measurement of the 2nd and the 3rd runs with respect to the 1st run

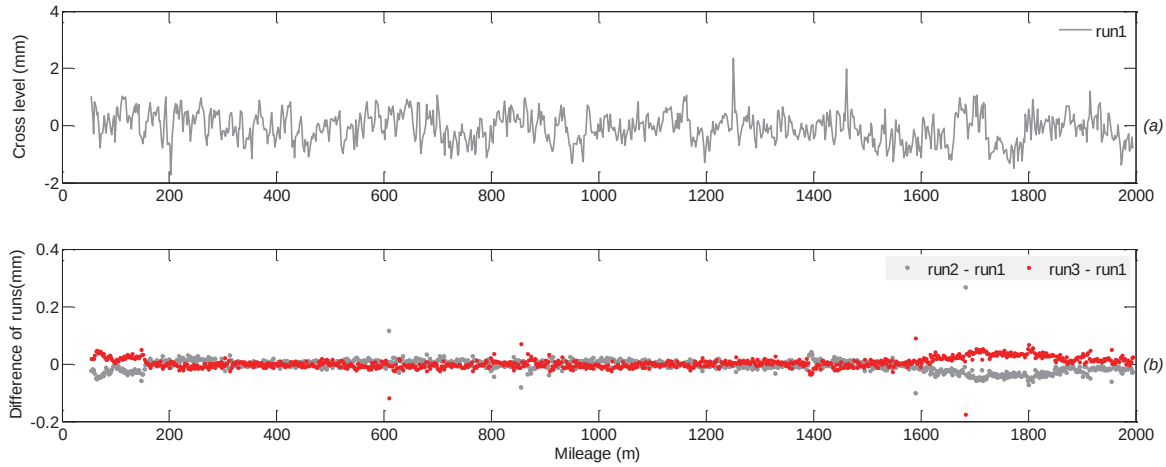

Figure 11 Cross level measurement repeatability: (a) measurement of the 1st run; (b) difference of measurement of the 2nd and the 3rd runs with respect to the 1st run

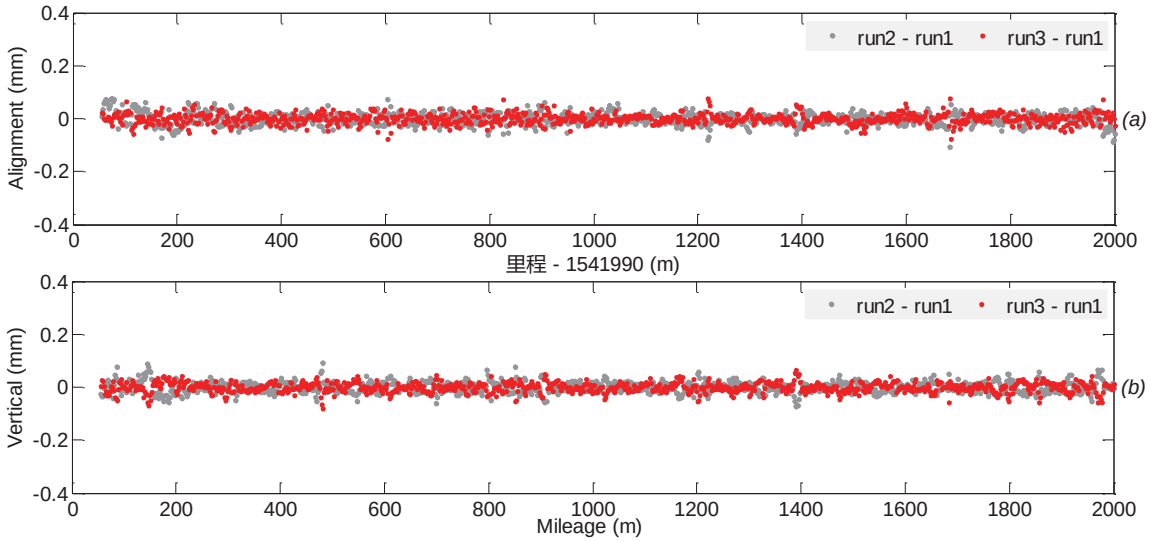

Figure 12 Shortwave length track irregularity measurement repeatability of reference rail: (a) difference of alignment irregularity measurement of the 2nd and the 3rd runs with respect to the 1st run; (b) difference of vertical irregularity measurement of the 2nd and the 3rd runs with respect to the 1st run

4. SUMMARY

This paper has presented the railway track geometry measuring trolley based on aided INS and its application on tramway track quality inspection. Field test has been conducted to demonstrate performance of the TGMT based on A-INS. Results show that the TGMT based on A-INS can measure the whole principal track geometric parameters and can meet the accuracy requirement for the tramway track construction. Results show that the proposed method can meet the accuracy requirement of the irregularity measuring for the tramway and even for high speed line. Additionally, the new method proposed in this paper is much more efficient compared to the conventional method based on total station.

ACKNOWLEDGE

This work is funded by the National Natural Science Foundation of China (NSFC) project 41674038, *study on the theory and method of aided INS in precise engineering surveying*. The project is also funded by Wuhan Municipal Construction Group Co., Ltd project *Wuhan modern tramway track geometric quality evaluation and track condition monitoring*. Finally, the authors would like to thank Wuhan MAP Space Time Navigation Technology co., LTD for providing the IMU – POS830 and the support in field tests.

REFERENCE

Alfi, S. and S. Bruni (2008). Estimation of long wavelength track irregularities from on board measurement. Railway Condition Monitoring, 2008 4th IET International Conference on, IET.

Benson, D. O. (1975). "A comparison of two approaches to pure-inertial and Doppler-inertial error analysis." Aerospace and Electronic Systems, IEEE Transactions on(4): 447-455.

Boronakhin, A. M., L. N. Podgornaya, E. D. Bokhman, N. S. Filipenya, Y. V. Filatov, R. B. Shalymov and D. Y. Larionov (2011). "MEMS-based inertial system for railway track diagnostics." Gyroscopy and Navigation **2**(4): 261-268.

Britting, K. R. (2010). Inertial navigation systems analysis.

Brown, R. G. and P. Y. Hwang (1997). Introduction to random signals and applied Kalman filtering: with MATLAB exercises and solutions. New York:, Wiley.

Chen, Q., X. Niu, Q. Zhang and Y. Cheng (2015). "Railway track irregularity measuring by GNSS/INS integration." Navigation, Journal of the Institute of Navigation **62**(1): 83-93.

EN, B. (2008). Railway applications/Track-Track geometry quality-Part1:Characterisation of track geometry. BS EN 13848-1:2003+A1:2008.

EN, B. (2011). Railway applications-Track-Track geometry quality-Part 4: Measuring systems — Manual and lightweight devices. BS EN 13848-4:2011.

Esveld, C. (2001). Modern railway track.

Glaus, R. (2006). The Swiss Trolley-a modular system for track surveying, Inst. für Geodäsie und Photogrammetrie.

Groves, P. D. (2013). Principles of GNSS, inertial, and multisensor integrated navigation systems, Artech House.

Heirich, O., A. Lehner, P. Robertson and T. Strang (2011). Measurement and analysis of train motion and railway track characteristics with inertial sensors. Intelligent Transportation Systems (ITSC), 2011 14th International IEEE Conference on, IEEE.

Naganuma, Y., M. Kobayashi and T. Okumura (2010). "Inertial measurement processing techniques for track condition monitoring on shinkansen commercial trains." Journal of Mechanical Systems for Transportation and Logistics **3**(1): 315-325.

Shin, E.-H. (2005). Estimation techniques for low-cost inertial navigation, The University of Calgary.

Wang, Y., Y. Qin and X. Wei (2012). Track irregularities estimation based on acceleration measurements. Measurement,

Information and Control (MIC), 2012 International Conference on, IEEE.

Westeon, P., C. Ling, C. Roberts, C. Goodman, P. Li and R. Goodall (2007). "Monitoring vertical track irregularity from in-service railway vehicles." Proceedings of the Institution of Mechanical Engineers, Part F: Journal of Rail and Rapid Transit **221**(1): 75-88.

Weston, P., C. Ling, C. Goodman, C. Roberts, P. Li and R. Goodall (2007). "Monitoring lateral track irregularity from in-service railway vehicles." Proceedings of the Institution of Mechanical Engineers, Part F: Journal of Rail and Rapid Transit **221**(1): 89-100.

COMPARATIVE ANALYSIS OF WHEAT AREA ESTIMATION USING LANDSAT AND SENTINAL-2 SATELLITE IMAGERY

Abdelraouf M. Ali1a,*, Ayman F. Habibb, Mohamed A. Aboelghar[a] and Mohamed A. El-shirbeny[a]
a Agriculture application Department, National Authority of Remote sensing and space science (Narss), 23 Joseph Tito.st., El-nozha Elgedidah, Cairo Egypt (raouf_shoker85@yahoo.com)
b Lyles School of Civil Engineering, Purdue University, 550 Stadium Mall Drive, HAMP 4108, West Lafayette, IN 47907, (ahabib@purdue.edu)

KEY WORDS: Crop Area Estimation, NDVI time serious, Landsat-8, Sentinal-2

1. ABSTRACT:

Estimating crop area is a foremost requirement of any crop-monitoring program, which is an agricultural application where spatial information along with crop area estimates is needed. Having the information on previous year's crop area and estimates of area change is sufficient for decision makers concerned with crop monitoring. The objective of this study is to investigate changes in cropland areas by using remote sensing satellite imagery with difference spatial resolutions from a single date. The evaluation criterion is based on the Normalize Different Vegetation Indices time series ($NDVI_{Ts}$) for estimating wheat crop area. The study is focusing on using accuracy assessment from maximum likelihood classification methods applied to multi-spatial resolution scenes (30m, 20m and 10 meters) derived from Landsat8 and Sentinel-2 satellites. More specifically, ($NDVI_{Ts}$) estimates from Landsat 30m, Sentinel-2 20m, and Sentinal-2 10m spatial resolution are compared. The study area is located in Elmenia governorate, Egypt. The result showed that the accuracy for using ($NDVI_{Ts}$) data from different products showed higher accuracy than using one single date. The NDVITs estimate from theSentinal-2 (10m) has an overall accuracy of 81% and Kappa coefficient of 0.74.The Sentinal-2 (20m) data has an overall accuracy of 69.38% and Kappa coefficient of0.58.Landsta8 (30m), on the other hand, has an overall accuracy of 64.38% and Kappa coefficient of 0.51.

2. INTRODUCTION

With over a quarter of the Egyptian population living under the poverty line, assuring the food security of all citizens is a key challenge for the government. Wheat is the most important grain crop in Egypt and grains are, in turn, the most important crop group. Wheat represents almost 10%of the total value of agricultural production and about 20% of all agricultural imports. Egypt is also the world's biggest wheatimporter. Itisthus understandable that wheat is a product of paramount importance to Egypt and wheat policy is a priority for the government [1]. Therefore, timely and costly effective statistics regarding to wheat yield is essential for food security and sustainable agricultural development. These statistics enable the governmental agencies and crop producers to manage wheat production process including: planning harvest, storage, importation, local and international marketing activities. Wheat monitoring and wheat yield prediction is considered to be one of the most challenging tasks in Egyptian agricultural sector.

In the countries with well-organized agricultural system, crop area estimates are usually available few months after harvest. The traditional approach of crop-yield forecasting, the use of ground based data collection is costly, time-consuming and labor-intensive. Having reliable statistics attached with spatial distribution of

crop area month/s before harvest is a major challenge in the area of remote sensing agricultural applications. Crop-yield prediction using remotely sensed data recently represents a wide field of research and application [2, 3, 4]. Satellite remote sensing technology is now providing accurate statistical and spatial information for yield and production forecast, however, crop classification as an essential step for yield monitoring and mapping is still problematic. Traditional methods that have proven to be successful such as: area sampling, list sampling, point sampling with or without a grid [5], however, continuous research is necessary to establish more accurate method. It is essential for the proposed method to be applicable under local agricultural conditions that might be different from a country to another and sometimes are different even within the same country.

Moderately to high spatial resolution images were used frequently for crop monitoring and to identify cropland areas [6], or on the use of spectral linear mixture models applied to time series for vegetation cover identification [7]. The moderate resolution imaging spectro-radiometer (MODIS) with 250 m spatial resolution, is proven to be suitable for identifying large crop fields in regions with widespread use of mechanized agriculture [8, 9] (Wardlow et al., 2006; Ren et al., 2008). In Egypt, developing a remotely sensed based system for crop mapping is a big challenge because of the highly intensive cultivated lands and the diversity of agricultural production systems at different technological stages, ranging from traditional small farmers to highly mechanized commodity crop production operations. Therefore, processing of multi temporal and higher spatial resolution satellite imagery is an issue of high necessity.

Sentinel-2 (S2) carries an innovative wide-swath, high-resolution, multispectral imager (MSI) with 13 spectral bands; this is going to offer unprecedented perspectives on our land and vegetation [10]. The combination of high resolution (up to10 m), novel spectral capabilities (e.g., three bands in the red-edge plus two bands in the SWIR), wide coverage (swath width of 290 km) and minimum five-day global revisit time (with twin satellites in orbit) is expected to provide extremely useful information for a wide range of land (and coastal) applications [11].

3. OBJECTIVES:

The objective of this study is to compare the suitability and effectiveness of multi-spectral bands of two types of high resolution satellite imagery landsat-8 and Sentinal-2 and normalized difference vegetation index (NDVI) to monitor and map wheat cultivation in high intensive agricultural area in upper Egypt.

4. METHODOLOGY:

4.1. Study area

El-Minya governorate is one of the most highly populated governorates of Upper Egypt. It contains 9 cities; 3,375 villages; and 10,875 hamlets. The nine cities from north to south are: Abu Qirqas, El Idwa, Minya, BeniMazar, DayrMawas, Maghaghah, Mallawi, Matay and Samalut. Figure (1) shows El-Minya governorate with the administrative boundaries of the different cities. Al-Minya has a desert climate. There is virtually no rainfall during the year. The Köppen-Geiger climate classification is BWh. The average annual temperature is 21.3 °C. The average annual rainfall is 1 mm. The driest month is January with 0 mm. With an average of 1 mm most precipitation falls in February. The warmest month of the year is July with an average temperature of 28.2 °C. January has the lowest average temperature of the year with only 12.2 °C. The difference in precipitation between the driest month and the wettest month is 1 mm. The difference in precipitation between the driest month and the wettest month is 1 mm and the average temperatures vary by 16.0 °Figure (1) shows the location of the study area.

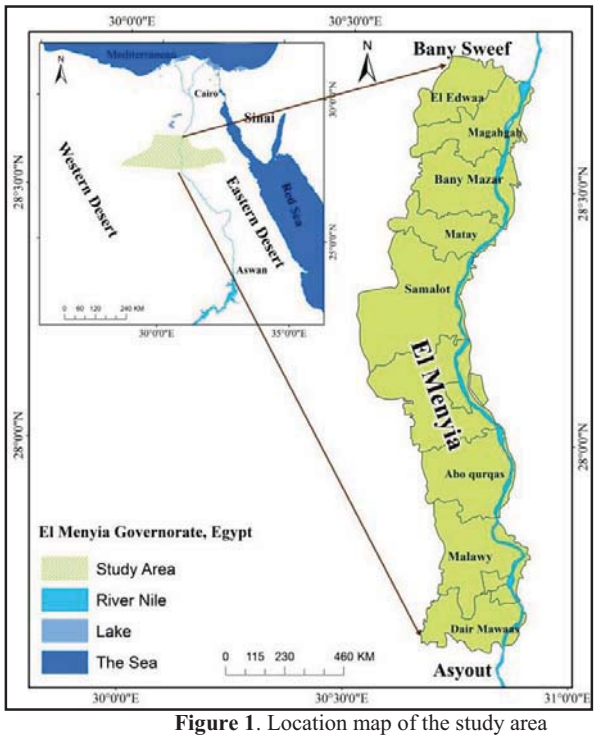

Figure 1. Location map of the study area

4.2. Remote Sensing dataset

Sevenlandsat-8 imagery (Path 177 Row 40 and Path 176 Row 41) with 30 meter spatial resolution and five sentinal-2 data with 10 meters spatial resolution covering the winter season of (2015 - 2016) were used to produce the detailed crop maps. Types of the data, acquisition dates and the spatial resolution are shown in table (1).

Table 1. Data acquisition and spatial resolution

Acquisition Date	Landsat-8	Sentinal-2	
		10 meter spatial resolution	20 mater spatial resolution
Dec/15/2015			
Jan/10/2016			
Jan/16/2016			
Feb/01/2016			
Feb/09/2016			
Feb/17/2016			
Feb/19/2016			
March/04/2016			
March/30/2016			
Apr./5/2016			
Apr./19/2016			
Apr./21/2016			

The data was geometrically corrected. Spectral bands for each dataset together with NDVI were then stacked as one file. Atmospheric correction was carried out using (FLAASH - ENVI) module. Images were mosaicked to cover the study area. Subletting was carried out in order to exclude most of uncultivated areas.

4.3 NDVI variables

Normalized difference vegetation index (NDVI) was calculated for each single image. This index is a dimensionless one that expresses the presence and density of vegetation, and is calculated according to the following equation [1]:

$$NDVI = \frac{\rho_{ir} - \rho_r}{\rho_{ir} + \rho_r} \quad (1)$$

Where; ρr and ρir are reflectance values corresponding to red and near-infrared wavelengths respectively. All NDVI images were stacked to produce NDVI multi-temporal image. Maximum and minimum values with variance were calculated from NDVI dataset. Then, the composite NDVI image was used to create a mask for cultivated areas and isolate these areas from the other land cover types (figure 2). Maximum likelihood classification was carried out for the different datasets: each single date of Landsat data, each single date of Sintenal data and NDVI composite data. Out of (300) ground check points that were collected during winter season, (200) points were used for classification while (100) points were used for accuracy assessment. Accuracy assessment was carried out using Kappa analysis. This analysis is a discrete multivariate technique used to assess classification accuracy from an error matrix. It generates a Kappa coefficient that has a possible range from 0 to 1.

$$K = \frac{N\sum_{i-1}^{r} x_{ii} - \sum_{i-1}^{r}(x_{i+}.x_{+i})}{N^2 - \sum_{i-1}^{r}(x_{i+}.x_{+i})} \quad (2)$$

There is one possible interpretation of Kappa Coefficient: poor agreement = less than (0.20), fair agreement = (0.20) to (0.40), moderate agreement = (0.40) to (0.60), good agreement =

(0.60) to (0.80), very good agreement = (0.80) to (1.00).

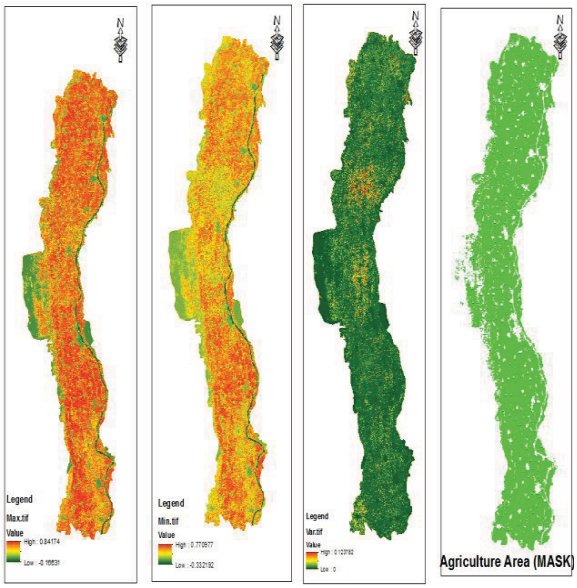

Figure 2. Masking process to isolate cultivated lands

5. RESULTS AND DISCUSSION

Overall accuracy and Kappa coefficients between single date of (Sentinal-2 10m) and times series ($NDVI_{Ts}$) generated from (Sentinal-2 10m) as shown figure (3) indicated that ($NDVI_{Ts}$) was the optimal dataset with (81%) overall accuracy and (0.74) kappa coefficient. ($NDVI_{Ts}$) generated from (Sentinal-2 20m) also showed the highest overall accuracy (69.38 %) and highest kappa coefficient (0.58) when compared with single date of (Sentinal-2 20m) as shown in figure 4. Differently, Landsat-8 data of January 16 was better than the other single dates imagery and better than ($NDVI_{Ts}$) of landsat-8 data with (76%) overall accuracy and (0.62) kappa coefficient as shown in figure 5.

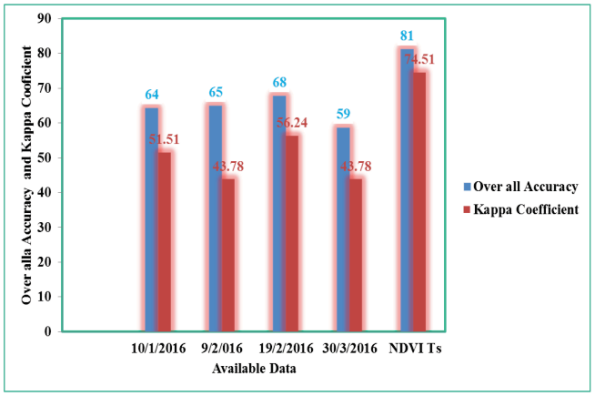

Figure 3. Overall accuracy and Kappa coefficient for Single dates of Sentinal-2 10m and the generated NDVI

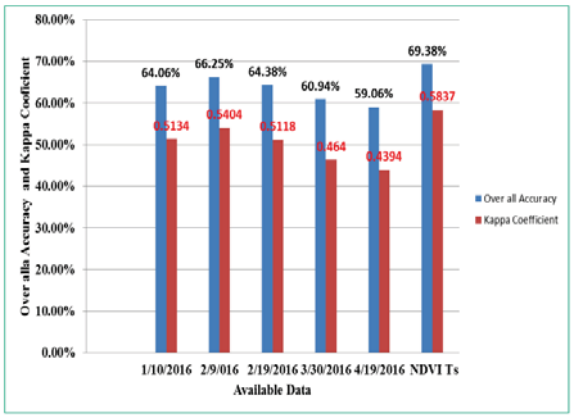

Figure 4. Overall accuracy and Kappa coefficient for Single dates of (Sentinal-2 20m) and the generated NDVI

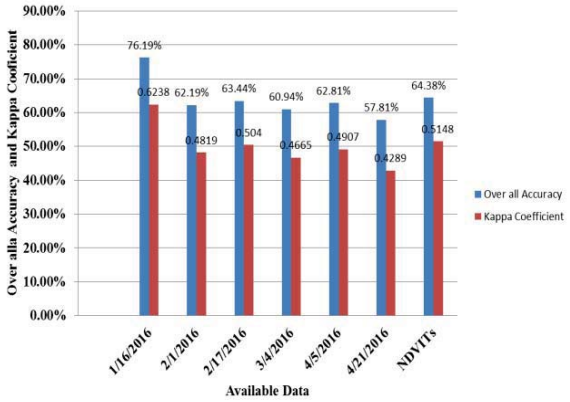

Figure 5. Overall accuracy and Kappa coefficient for Single dates of (Landsat-8) and the generated NDVI

It was found that ($NDVI_{Ts}$ of Sentinal-2 10 m) is the optimal dataset to isolate wheat cultivation in El-Minya governorate. According to the result of Maximim likelihood classification of Sentinal-2 data (figure 6), the total wheat area was 62940.4Ha. Clover occupies the largest crop area 81399Ha while orchards (mainly Citrus and Grape) cover a total area of 34530 Ha

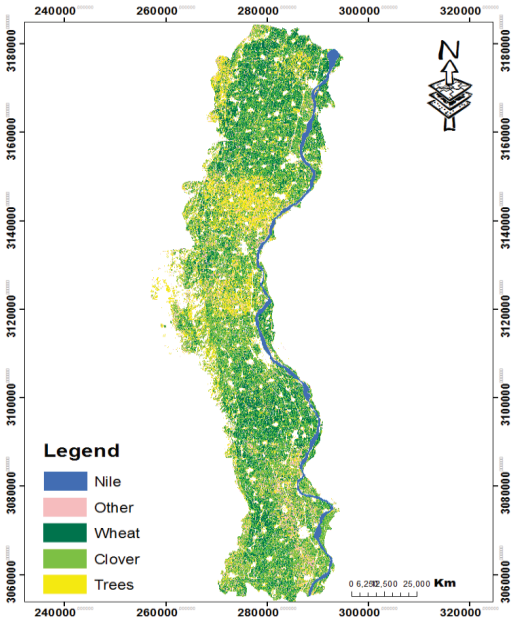

Figure 6. Maximim likelhood classification result of NDVI Ts of Sentinal-2 data

Conclusions

Comparative analysis was carried out in order to identify the optimal dataset that could be used ti isolate wheat cultivation in the study area that represents the most agricultural productive governorate in Upper Egypt. The data cover the whole winter season starting from December 2015 to April 2016. Sentinal-2 and landsat-8 data were tested to isolate wheat cultivation. Also, using single image was tested versus multi-temporal NDVI for crop classification. The result showed that NDVI Ts of Sentinal-2 data with 10 meter spatial resolution was the optimal to isolate wheat crop as explained from overall accuracy and kappa coefficient. Maximum likelihood classifier was then applied on ($NDVI_{Ts}$) of (Sentinal-2 data 10 m) and the area of the different crops were identified.

6. ACKNOWLEDGEMENT

The authors particularly appreciate USGS based GLOVIS data repository for providing free access to Landsat 8 data and special thanks to Europian space agency for sentinel-2 data.

7. REFERENCES:

[1] Food and Agricultural Organization of the United Nations (2015) Egypt : wheat sector review, 1-88.

[2] Prasad AK, chai L, singh RP, kafatos M (2006) Crop yield estimation model for Iowa using remote sensing and surface parameters. International Journal of Applied Earth Observation and Geoinformation 8: 26–33.

[3] Manjunath KR, potdar MB, purohit NL (2002) Large area operational wheat yield model development and validation based on spectral and meteorological data. International Journal of Remote Sensing 23: 3023–3038.

[4] Salazar L, kogan F, roytman L (2007) Use of remote sensing data for estimation of winter wheat yield in the United States. International Journal of Remote Sensing 28: 3795–3811.

[5] Pickup, G.; chewings, V.H.; nelason, D.J. Estimating changes in vegetation cover over time in arid rangelands using Landsat MSS data. Remote Sensing of Environment, v.43, p.243-263, 1993.

[6] Epiphanio, R. Dalla V.; formaggio, A.R.; rudorff, B.F.T.; maeda, E.E.; luiz, A.J.B. Estimating soybean crop areas using spectral-temporal surfaces derived from MODIS images in MatoGrosso, Brazil. Pesquisa Agropecuária Brasileira, v.45, p.72-80, 2010.

[7] Silva, G.B.S. DA; formaggio, A.R.; shimabukuro, Y.E.; adami, M.; sano, E.E. discriminação da cobertura vegetal do cerradomatogrossensepormeio de imagens MODIS. PesquisaAgropecuáriaBrasileira, v.45, p.186-194, 2010.

[8] Wardlow, B.D.; kastens, J.H.; egbert, S.L. Using USDA crop progress data for the evaluation of green up onset date calculated from MODIS 250-meter data. Photogrammetric Engineering and Remote Sensing, v.72, p.1225-1234, 2006.

[9] Ren, J.; chen, Z.; zhou, Q.; tang, H. Regional yield estimation for winter wheat with MODIS-NDVI data in Shandong, China. International Journal of Applied Earth

Observation and Geoinformation, v.10, p.403-413, 2008.

[10] Drusch, M.; del bello, U.; carlier, S.; colin, O.; fernandez, V.; gascon, F.; hoersch, B.; isola, C.; laberinti, P.;martimort, P.; et al. Sentinel-2: ESA's Optical High-Resolution Mission for GMES Operational Services.Remote Sens. Environ. 2012, 120, 25–36.

[11] Malenovský, Z.; rott, H.; cihlar, J.; schaepman, M.E.; garcía-Santos, G.; fernandes, R.; berger, M. Sentinelsfor science: Potential of Sentinel-1, -2 and -3 missions for scientific observations of ocean, cryosphere, andland. Remote Sens. Environ. 2012, 120, 91–101.

RANDOM LINEAR NETWORK CODING OVER CLOUD COMPUTING NETWORK IN DATA TRANSMISSION

O.F. Younis [a] , R. A. Sadek [b], H.S. ElHennawy [c]

[a] Dept. of Electronics and Communication, Engineering faculty, Ain Shams University, Cairo, Egypt - omaima_younis@aast.edu
[b] Dept. of Information Technology, Computer Science and Information, Helwan University, Cairo, Egypt - rowayda_sadek@yahoo.com
[c] Dept. of Electronics and Communication, Engineering faculty, Ain Shams University, Cairo, Egypt - helhennawy@ieee.org

KEY WORDS: Cloud computing, Network coding, Infrastructure Performance, Service Broker, Load Balancing Algorithms, RLNC

ABSTRACT:

Cloud computing is always defined as a virtualized resource used to reduce the cost and dynamic allocation of resources. This paper is focusing on the cloud computing based on the network coding in small scale internet environment where Random Linear Network Coding (RLNC) has been selected mainly because the RLNC does not depend on the nature of the network and can re-encode the data before receiving all data transmitted (Early Encoding). This type of Network Coding is selected in proposed system especially for multicast and broadcast data to enhance the data center processing time where the RLNC encoder is implemented at the data center controller while the RLNC decoder is implemented at the user side. The analysis is mainly addressing small scale internet environment based on comparing the performance using the three main service broker policies configured at the cloud side to the three main load balancing algorithms configured at the virtual machine load balancer at the data center with and without the use of the RLNC. The results has been compared to the normal analysis of service broker and load balancing in cloud computing and comes up with a conclusion that the best results when using RLNC in small scale environment are achieved with a suitable cost by using optimized response time-based policy with throttled load balancing algorithm. It gives much better data processing time with an approximate of 0.22% although it has a slightly higher overall response time than the throttled load balancing with Proximity based routing policy.

1. INTRODUCTION

Cloud computing is a model for enabling access to a shared pool of configurable computing resources (e.g., servers, applications, storage and services) with minimal management effort. This cloud model supports availability and consists of three services and four deployment models. The service models are cloud software as a services (SaaS), cloud platform as a service (PaaS) and cloud infrastructure as a service (IaaS). The deployment models are private cloud, community cloud, public cloud and hybrid cloud. Cloud computing has many advantages such as cost efficient, unlimited storage, backup and recovery, easy access to information, quick deployment and automatic software integration, etc. There are number of performance parameters like network performance, application performance and infrastructure performance, etc. Service broker and load balancing are two key areas to improve the performance of computing. A lot of algorithms have been proposed in those areas by researches to improve the performance (Peter Mell and Tim Grance, 2011) (Sunny Nandwani, Mohit Achhra, Raveena Shah, Aditi Tramrakar, KK Joshi, Sowmiya Raksha, 2015).

Network coding is a method of optimizing the flow of data in the network. It can allow more efficient uses of network resources by combining data instead of the traditional method of store and forward. Network coding can be classified into two types, physical linear network coding (PLNC) and digital network coding (DNC). PLNC such as (amplify and forward) and (decode and forward). DNC such as XOR, Reed Solomon (RS) and random linear network coding (RLNC). Network coding has a lot of benefits such as reliability, throughput, security, low complexity, and distributed nature, etc. (Xiangbo LI, Mohsen Amini Salehi, Magdy A, Bayoumi, Rajkumar Buyya, 2016) (Saeed, Basil, 2011). This paper focuses on the RLNC. RLNC uses Glasis Field (GF) to select the random coefficients which are used to encode the required data and send it. At the receiver side, the decoder uses Gaussian Elimination to obtain the main data from the received one. So, RLNC doesn't depend on the nature of the network (completely distributed operation), it can re-encode the data before receiving all data transmitted (early encoding) and It can correct missing or corrupted data packets. So, this type of Network Coding is very suitable for cloud computing.

This paper focuses on analyzing and comparing the main existing algorithms and compare them with the proposed system results to identify the best algorithm performance when using RLNC over cloud computing data transmission (Sunny Nandwani, Mohit Achhra, Raveena Shah, Aditi Tramrakar, KK Joshi, Sowmiya Raksha, 2015). The paper also discusses the Cloud Computing and network coding in Section 2, Cloud Computing performance and main existing algorithms in section 3, Proposed Cloud Computing system based on RLNC in Section 4, Implementation Results and Discussion in Section 5, Conclusion in Section 6.

2. CLOUD COMPUTING AND NETWORK CODING

This section covers cloud computing and network coding overview and usages.

2.1 Cloud Computing

Cloud Computing is a flexible environment that gives a number of users the required access for selected services where any

information can be available at anytime and anywhere in the world. There are lots of possibilities to access the public and private information by using the internet. The user needs to use a private cloud for data confidentiality and public cloud for normal or shared data depending on the distributed architecture that provides computing resources over the internet. Cloud computing services are considered as a metaphor for the internet, where the user can access the cloud but doesn't care how his data is processed inside providing pay on consumption basis and reducing the cost of operating system and networks (John Harauz, Lorti M. Kaufinan. Bruce Potter, 2009) (Cloud standards customer council, 2015). No need to purchase hardware and software licenses. Other benefits such as unlimited processing power, storage capacity, high efficiency. Cloud computing enables virtually network access and services that combine a lot of distributed resources all over the world. Service broker and load balancing are two key areas to improve the performance. A lot of algorithms and policies are used to improve the performance as shown in details in section 3.

2.2 Network Coding (RLNC)

Network coding can be classified into two types; physical linear network coding (PLNC) and digital network coding (DNC). RLNC is one of the types of DNC. BY using RLNC in cloud computing it gives us better data security and increasing the throughput. Most of the papers are using it as a security tool or in database storage but not on the data transmission. The benefits of using random linear network coding within the cloud storage providers are to minimize the required bandwidth needed for the adaptation steps and to ensure recoverability which enhances the data transmission performance. Measurements show the performance increase and bandwidth saving (Lo'ai Tawalbeh, Nour S. Darwazeh, Raad S. Al-Qassas, Fahd AlDosari, 2015). Also used for efficient confidentiality-based cloud storage framework that enhances the processing time and assures confidentiality and integrity through data classification and applying Security algorithms based on the type of classified data. Simulation results show better processing time while assuring data confidentiality and integrity (Lo'ai Tawalbeh, Nour S. Darwazeh, Raad S. Al-Qassas, Fahd AlDosari, 2015).

Multimedia cloud computing is using network coding to enhance the performance to minimize the required bandwidth and increase the throughput. This idea is used only in data storage over cloud computing. Till now no one examined it on network data transmission. The main focus of this paper is to determine the best service broker policy and load balancing algorithms when using network coding and implement it in small scale internet environment and compare the proposed system results using the network coding with the results without using it (Sunny Nandwani, Mohit Achhra, Raveena Shah, Aditi Tramrakar, KK Joshi, Sowmiya Raksha, 2015) (Lo'ai Tawalbeh, Nour S. Darwazeh, Raad S. Al-Qassas, Fahd AlDosari, 2015).

3. CLOUD COMPUTING PERFORMANCE AND MAIN EXISTING ALGORITHMS

Cloud computing requires proper implementation of certain components without these components, cloud computing can't be easily implemented. The main components are the client (the end user), the services which are the functions in the cloud computing, the application which is the backbone of the service, the platform which is the soft infrastructure for the application, the storage which is the warehouse of the cloud computing and finally the infrastructure which is the backbone of the cloud computing. To examine the performance of the cloud environment in a real environment in a repeatable manner is not that easy because, it requires cost and huge amount of resources for a long period of time, it does not provide the flexibility to reconfigure the parameters quickly and easily, also does not support repeating the experiments (Rodrigo N. Calheiros, Rajiv Ranjan, Anton Beloglazov, cesar A. F. De Rose and Rajkumar Buyya, 2011). Simulation tools enable the Cloud providers to evaluate the different kinds of resource and scenarios under varies loads and pricing distribution. It allows the customers to test their own services in a repeatable and controllable environment free of charge. Also, it identifies the performance issues before the actual deployment on the real cloud. Cloud computing tools like CloudSim Simulator, CloudAnalyst, GreenCloud, etc.

3.1 CloudAnalyst (Implementation Tool)

This paper used CloudAnalyst simulator as an implementation tool (Bhathiya Wickremasinghe, 2009). Simulation allows the customers to test their services in a repeatable and controllable environment free of charge to identify the performance issues before actual deployment on a real cloud. CloudAnalyst is a graphical toolkit. It is developed by using java. It has a friendly user interface, high degree of configurability and flexibility, the results are presented in tables and dashboards, it is easy to repeat the simulation and modify in it because it is an open source simulator. It has eight components; regions, internet, cloud application service broker, user base, data center controller, VM load balancer, internet cloudlet and GUI. It helps to evaluate the parameters and improve the quality of service (Sunny Nandwani, Mohit Achhra, Raveena Shah, Aditi Tramrakar, KK Joshi, Sowmiya Raksha, 2015) (Dhaval Limbani and Bhavesh Oza, 2012) (Nandwani S, Achhra M, Shah R, Tamrakar A, Joshi KK, Rasksha S, 2015). Cloud application service broker and VM load balancing have been the most commonly used algorithms as shown in section 3.2 and 3.3.

3.2 Service Broker Algorithms

Service Proximity-Based Routing: It selects the closest data center with the least network latency. If two or more data centers are available, the selection is done randomly. In this algorithm, it does not take the load and cost into consideration.

Performance Optimized Routing: In this routing policy, service broker actively monitors the performance of all data centers, and based on that, routes the traffic to the data center with best response time. In this algorithm, it does not take cost into consideration. (B. Wickremasinghe, R.N. Calheiros and R. Buyya, 2010) (Sunny Nandwani, Mohit Achhra, Raveena Shah, Aditi Tramrakar, KK Joshi, Sowmiya Raksha, 2015).

Dynamically Reconfigurable Router: This is an extension to the proximity based routing, where the routing logic is similar, but service broker has an additional responsibility of scaling the application deployment based on its load. This policy increases and decreases the number of VMs allocated to the data centers.

3.3 Load Balancing Algorithms

Round Robin Load Balancer: This is one of the simplest method for distributing client requests across a group of servers. Going down the list of servers in the group, the load balancer forward the client request to each server in turn. When it reaches the end of the list, load balancer loops back and goes down the list again (sends the next request to the first listed server, the one after that to the second server, and so on).

Active Monitoring Load Balancer: In this algorithm, an index table of VMs is maintained which contains the numbers of requests allocated to each VM. Initially, all the VMs have zero allocation. When the request arrives, the index table is parsed and the least loaded VM is assigned the request and correspondingly the table is updated regarding new allocations. There is an overhead of parsing the index table before assigning the request.

Throttled Load Balancer: This algorithm also prepares an index table as the one of the previous algorithm but notes whether a particular VM is available or not. When the request arrives the index table is parsed and the first available VM is selected (B. Wickremasinghe, R.N. Calheiros and R. Buyya, 2010) (Sunny Nandwani, Mohit Achhra, Raveena Shah, Aditi Tramrakar, KK Joshi, Sowmiya Raksha, 2015).

4. PROPOSED CLOUD COMPUTING SYSTEM BASED ON RLNC

The proposed system describes the cloud computing based on RLNC in data transmission and the efficiency of RLNC especially in multicast on small internet environment (David Szab, Attila Csoma, Peter Megyesi, Andras Gulyas, Frank H.P. Fitzek, 2015) (Melbourne cloud labs, 2013). Also measure the overall response time for each user, data center processing time for each data center and compare the results with original system to verify the accuracy and performance. The main reasons to use RLNC is the highest values of Packet Delivery Ratio (PDR), the lowest values of latency (delay), completely distributed operation and the correction for missing or corrupted data packets. The proposed system as shown in Figure 1 and 2. It divided it into six steps:

Step1: The user requests a specific application and send the request to the internet.
Step 2: The internet routes the information and routes the request successfully by using the Service Broker. The Service Broker defines the Data Center Selection because the Service Broker includes all data center lists, contents metafile, internet proximity of region, etc. Not only that but also it selects the policy based on the user request and sends the request to the selected data center by the internet.
Step3: The Data Center Controller receives the request. Depends on the virtual machine (VM) Load balancer, it determines which load balancing policy will be used.
Step4: The Data center controller assigns the user request to the selected virtual machines.
Step5: The virtual machines achieve the request, execute it and sends it to the Data Center Controller. The Data Center Controller encodes the data which is requested and send it to the User by using the internet.
Step 6: The user receives the required data encoded and decodes it.

This proposed system selected the RLNC especially for multicast and broadcast data transmission to enhance the data center processing time where the RLNC encoder is implemented at the data center controller and RLNC decoder is implemented at the user side.

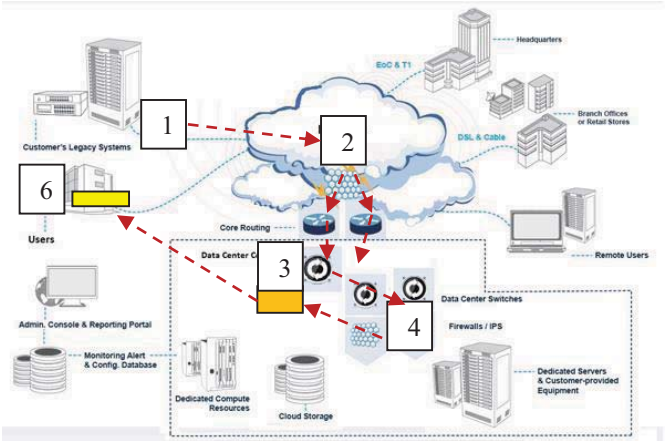

Figure 1. Proposed Cloud computing system based on RLNC

4.1 Proposed System Implementation

The RLNC is implemented in Java Language. The Cloud computing environment is simulated on the CloudAnalyst. The CloudAnalyst is an open source simulator and is using the Java Language. The Cloud Analyst is modified by RLNC code; The encoder at data center controller and the decoder at the user side as shown in Figure 2. The user base generates traffic in simultaneous bursts according to the configurable data size per request (Bhathiya Wickremasinghe, 2009). Importing real known data and exporting it to verify the results is one of our contribution which was not there at the CloudAnalyst. The Proposed system input real text file (273 bytes), user request the text file, the internet routes it by the service broker to the selected data center, the selected data center controller receives the request and assigns this request to virtual machines, the virtual machine handles the request (text file) and executes it then sends it to the data center controller, the data center controller encodes it by RLNC and sends it to the user by using the internet, the user receives it and decode it by using RLNC decoder to obtain the requested data.

5. IMPLEMENTATION RESULTS AND DISCUSSION

The proposed system has been examined through different scenarios to select the best one. Experiments have been carried out to examine the service broker policies with the load balancing algorithms by different scenarios which is identified in section 5.2. Some scenarios will do comparison with the original work for main policies others will input real multimedia data and examine its output to verify the accuracy.

Implementation results were conducted on a machine intel ® core TM i7 - 4500U CPU @ 1.8 GHZ 2.4 GHZ internal RAM 8.00 GB, system type 64 bit operating system, 64- based- processor, Windows 8.1 (2013)Microsoft Corporation.

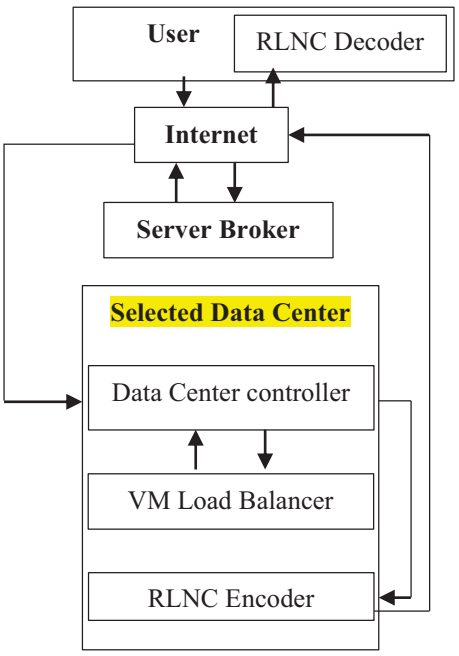

Figure 2. Proposed Flow Graph

5.1 Simulation Configuration

I. Simulation Duration: 24 Hours

II. User bases: as shown in Table 1

User Base	Region	Request per user per Hr	Data Size per request (bytes)	Peak Hours Start GMT	Peak Hours End GMT	Average Online Users During Peak	Average Online Users During Off
UB	0	60	100	12	14	5000	500
UB2	1	60	100	14	16	1000	100
UB	2	60	100	19	21	3500	350
UB4	3	60	100	0	2	1500	150
UB	4	60	100	20	22	500	50
UB	5	60	100	10	12	800	80

Table 1: User bases Configuration

III. Other parameters configured as below:

The Delay Matrix and the Bandwidth Matrix are the same as it is in the cloud Analyst simulator.

Parameter	Value Used
VM Image Size	10000
VM Memory	512
VM bandwidth	1000
Data Center – Architecture	X86
Data Center – OS	Linux
Data Center – VMM	Xen
Data Center – Number of DCs	3
Data Center – Regions	0/1/2
Data Center –VMS	5/5/50
Data Center – Memory per Machine	204800
Data Center – Storage per Machine	100000K
Data Center – Available BW per Machine	1000000
Data Center – Number of processors per machine	4
Data Center – processor speed	10000 MIPS
Data Center – VM Policy	Time Shared
User Grouping Factor	500
Request Grouping Factor	250
Executable Instruction Length	200

To calculate the Response time in the cloud computing, it is calculated by the following equations:

$$\text{Response Time} = \text{Fint} - \text{Arrt} + \text{Tdelay} \quad (1)$$

where Arrt is the arrival time of user request
Fint is the finish time of user request
Tdalay is the transmission delay

Tdelay can be calculated as equation 2:

$$\text{Tdelay} = \text{Tlatency} + \text{Ttransfer} \quad (2)$$

where Tlatency is the network latency.
Ttransfer is the time taken to transfer the size of data of a single request (D) from source location to destination.

Ttransfer can be calculated as equation 3:

$$\text{Ttransfer} = \text{D} / \text{Bw per user} \quad (3)$$

where Bw per user = Bw total / Nr
Bw total is the total available bandwidth (held in the Internet Characteristics)
Nr is the number of user requests currently in transmission.

5.2 Assumption and Scenarios

The Cloud Analyst, Service broker policy has three main policies and the load balancing has three main algorithms, so nine assumptions are available, each one has four results to four scenarios. Table 2 shows the main nine assumptions and in each assumption a result of four outputs to four scenarios.

Scenario 1 (S1): The output configuration of the paper (Sunny Nandwani, Mohit Achhra, Raveena Shah, Aditi Tramrakar, KK Joshi, Sowmiya Raksha, 2015).

Scenario 2 (S2): The implementation of the same configuration of scenario1 but using another computer specifications which was illustrated before.
Scenario 3 (S3): The implementation of the same configuration of Scenario 2 but by using multimedia (text data file) instead of unknown data traffic simulated by the simulator.
Scenario 4 (S4): The implementation of the same configuration of scenario 3 but by using the RLNC; encoder in data center and decoder at user side.

5.3 Scenario Results and discussion

Scenario 1 shows that the cost for implementing Proximity based routing and optimized response time-based service broker policies differs by a very small amount within the three load balancing algorithms. The cost for implementing the dynamically reconfigurable service broker policy is much higher than the others (Sunny Nandwani, Mohit Achhra, Raveena Shah, Aditi Tramrakar, KK Joshi, Sowmiya Raksha, 2015). Although the values of the optimized response time-based service broker policy is slightly higher than those of the proximity based routing it shows lower data center processing time with suitable cost. This is because Proximity based policy passes all the requests to the closest data center, but the Optimized response time-based policy sends most of the requests to the closest data center not all and selects the data center with the least response time for remaining requests (Sunny Nandwani, Mohit Achhra, Raveena Shah, Aditi Tramrakar, KK Joshi, Sowmiya Raksha, 2015). This scenario is a meaningless in such comparison but it is a main part in the method, configuration and conclusion.

Scenario 2 Based on the scenarios carried out, table 2 results verify that all the conclusions of scenario 1 results were verified but by using another computer specification which was illustrated before. When comparing Scenario 3 results with scenario 2 results, it shows slightly less overall response time and less data center processing time. That's because the used text file size was 273 bytes the data size per request configured as 100 bytes so when sending data it will be divided into two data requests one with 100 bytes and another with 73bytes but when CloudAnalyst simulator generate traffic automatically it will send each data request by 100 bytes.

Scenario 3 Results are higher than scenario 2 results when using reconfigure dynamically (service broker policy) with any type of load balancing algorithms, which means that scenario 3 used extra resources and not used efficient because the data is less than the full capacity so it reflected the overall response time and the data center response time.

Scenario 4 Results illustrated that the best combination algorithms are the throttled load balancing algorithm with the optimized response time algorithm when using RLNC although it is slightly higher than the throttled load balancing algorithm with Proximity-Based Routing policy but gives more better data center processing time with an approximate of 0.22% better within a reasonable cost in small scale environment.

It has been noticed that by Reconfigure dynamic service broker policy it gives high values with any type of load balancer algorithms, because it depends on scaling the application deployment based on its load. This policy increases and decreases the number of VMs allocated to the data centers, which means high overall response time, high data center processing time and high cost comparable with proximity based routing and optimize response time.

			Service Broker Policies		
			Proximity based routing	Optimize response time	Re-configure dynamically
Round Robin	Overall Response time	S1	93.72	93.74	1199.40
		S2	121.55	121.70	1091.77
		S3	121.47	121.60	1099.63
		S4	121.47	121.66	1107.73
	Data center processing time	S1	10.40	10.35	819.90
		S2	19.10	19.04	797.22
		S3	19.07	19.01	711.22
		S4	19.07	19.01	805.33
	Cost	S1	173.64	173.64	738.06
		S2	173.64	173.64	737.88
		S3	146.98	146.98	710.65
		S4	146.98	146.98	711.54
Equally spread current execution load	Overall Response time	S1	93.73	93.76	722.17
		S2	121.57	121.71	504.18
		S3	121.49	121.60	512.70
		S4	121.47	121.59	521.26
	Data center processing time	S1	10.42	10.40	452.16
		S2	19.11	19.06	324.12
		S3	19.07	19.02	337.39
		S4	19.07	19.04	337.44
	Cost	S1	173.64	173.64	738.06
		S2	173.64	173.64	737.88
		S3	146.98	146.98	711.22
		S4	146.98	146.98	711.54
Throttled	Overall Response time	S1	92.10	**92.15**	731.64
		S2	120.38	**120.52**	497.31
		S3	120.29	**120.41**	520.80
		S4	120.30	**120.41**	520.86
	Data center processing time	S1	9.30	**9.29**	458.43
		S2	18.18	**18.15**	318.77
		S3	18.15	**18.15**	337.07
		S4	18.15	**18.11**	337.12
	cost	S1	173.64	**173.64**	738.14
		S2	173.64	**173.64**	737.88
		S3	146.98	**146.98**	711.54
		S4	146.98	**146.98**	711.22

Table 2 Output Results

6. CONCLUSION

This paper concluded that by using the RLNC for cloud computing in data transmission, best results have been achieved by selecting throttled virtual machine load balancer algorithm working with the Optimize response time algorithm. By this combination it gives much better data center processing time with an approximate of 0.22% while it has a slightly higher overall response time than proximity policy based routing results. In future, Modification of the proposed system (based on RLNC) applied in large scale internet applications instead of small scale environment will be done.

REFERENCES

Bhathiya Wickremasinghe, 2009. Cloud Computing Environments MEDC Project Report, Distributed Computing Project, CSSE Dept., University of Melbourne, Australia.

B. Wickremasinghe, R.N. Calheiros and R. Buyya, 2010. Cloudanalyst: A cloudsim-based visual modeller for analysing cloud computing environments and applications, AINA 2010, Perth, Australia, pp.446-452.

Cloud standards customer council, 2015. Security for cloud computing ten steps to ensure success http://www.cloud-council.org/deliverables/CSCC-Security-for-Cloud-Computing-10-Steps-to-Ensure-Success.pdf (March 2015).

David Szab, Attila Csoma, Peter Megyesi, Andras Gulyas, Frank H.P. Fitzek, 2015. Network Coding as a Service, ACM SIGCOMM (DEMO).

Dhaval Limbani and Bhavesh Oza, 2012. A Proposed Service Broker Strategy in Cloudanalyst for Cost-effective Data Center Selection, International Journal of Engineering Research and Applications, India, 2 (1), pp. 793-797.

John Harauz, Lorti M. Kaufinan. Bruce Potter, 2009. Data Security in the World of Cloud Computing, IEEE Security & Privacy, Co-published by the IEEE Computer and Reliability Societies (August 2009).

Lo'ai Tawalbeh, Nour S. Darwazeh, Raad S. Al-Qassas, Fahd AlDosari, 2015. A Secure Cloud Computing Model based on Data Classification, Procedia Computer Science, MCSMS, pp. 1153-1158.

Márton Sipos, Janus Heide, Daniel E. Lucani, Morten V. Pedersen, Frank H.P. Fitzek,, Hassan Charaf, 2015. Adaptive Network Coded Clouds: High Speed", IEEE Transaction on Cloud Computing, VOL. 3.

Melbourne cloud labs, 2013. CloudSim: A Framework for Modeling and Simulation of Cloud Computing Infrastructures and Services, Laboratory University of Melbourne, Australia, http://www.cloudbus.org/cloudsim.

Nandwani S, Achhra M, Shah R, Tamrakar A, Joshi KK, Rasksha S, 2015. Analysis of service broker and load balancing algorithm in cloud computing, ISSN (PRINT): 2393-8374, 2 (4), (ONLINE): 2394-0697.

Peter Mell, Timothy Grance, 2011. The NIST Definition of Cloud Computing Reports on Computer Systems Technology, http://nvlpubs.nist.gov/nistpubs/Legacy/SP/nistspecialpublication 800-145.pdf (Sep. 2011)

Rajkumar Buyya, Rajiv Ranjan and Rodrigo N. Calheiros, 2011. Modeling and Simulation of Scalable Cloud Computing Environments and the CloudSim Toolkit: Challenges and Opportunities, software – practice and experience, 41(1), pp. 23 - 50.

Rodrigo N. Calheiros, Rajiv Ranjan, Anton Beloglazov, cesar A. F. De Rose and Rajkumar Buyya, 2011. CloudSim: a toolkit for modeling and simulation of cloud computing environments and evaluation of resource provisioning algorithms, 41, pp. 23–50.

Saeed, Basil, 2011. Performance Evaluation of Multimedia Broadcast Applications with Network Coding in Ad hoc Wireless Mesh Networks, Thesis, Carleton University Ottawa, Ontario, Canada.

Sunny Nandwani, Mohit Achhra, Raveena Shah, Aditi Tramrakar, KK Joshi, Sowmiya Raksha, 2015. Analysis of service broker and load balancing in cloud computing, 2(4), ISSN (PRINT): 2393-8374, (ONLINE): 2394-0697.

Xiangbo LI, Mohsen Amini Salehi, Magdy A, Bayoumi, Rajkumar Buyya, 2016. CVSS: A Cost-Efficient and QoS-Aware Video Streaming Using Cloud Services, IEEE Computer Socity, CCGrid, pp. 106-115.

MULTIMEDIA CLOUD COMPUTING BASED NETWORK CODING

O.F. Younis [a] , R. A. Sadek [b], H.S. ElHennawy [c]

[a] Dept. of Electronics and Communication, Engineering faculty, Ain Shams University, Cairo, Egypt - omaima_younis@aast.edu
[b] Dept. of Information Technology, Computer Science and Information, Helwan University, Cairo, Egypt - rowayda_sadek@yahoo.com
[c] Dept. of Electronics and Communication, Engineering faculty, Ain Shams University, Cairo, Egypt - helhennawy@ieee.org

KEY WORDS: Cloud computing, Network coding, Multimedia, CloudAnalyst., RLNC

ABSTRACT:

Nowadays cloud computing promises infinitely low cost resources which means a great value for the information technology sector. Ever-increasing demands for bandwidth and database storage are boasting the market for multimedia performance over the network. The proposed system is focusing on the overall performance of the Random Linear Network Coding (RLNC) Codec in Multimedia. It studied the overall response time, performance, throughput and quality of service of the cloud computing network in large scale internet applications such as Facebook. Also, it is very important in real time multimedia and video-conferencing. This is achieved by implementing two RLNC codec distributed at both data center and user side to increase the throughput and the quality of service. It is fulfilled by decreasing the overall response time and saving the network bandwidth in broadcasting or multicasting environment. Also, reliability and suitable security level for distributed nature are achieved. The average overall response time is improved by 0.33% compared to the currently used cloud computing networks and the average data center processing time is improved by 1.27% which decreases the cost by 32.34% compared to the cost without using the RLNC Codec.

1. INTRODUCTION

Cloud computing is a type of Internet-based computing that provides shared computer processing resources and data to computers and other devices on demand with the minimal management effort. Cloud computing is classified based on the cloud location either public, private or hybrid cloud depending on the personal requirements of businesses. It has many benefits where you can pay as you go while accessing the cloud resources, high availability and Performance Oriented Infrastructure, disaster recovery and automatic software updates, etc. Many organizations have selected to use this technology to minimize the cost and achieve the best performance.

Internet is having a significant impact on the media-related industries which are using it as a medium to enable delivery of their content to end-users e.g. text, image, sound, video, etc. Multimedia cloud computing content is growing exponentially cloud computing. Many vendors predicted that the streaming traffic will increase up to 80% of the whole internet traffic by 2019 (Anand Mohan, 2013) (Cho, Chin-Feng Lai, 2014) (Xiangbo Li, Mohsen Amini Salehi, Magdy A. Bayoumi, Rajkumar Buyya,, 2016). Multimedia has three main categories either static media which is a time independent discrete media such as text and images or dynamic multimedia which is a time dependent and continuous media such as sound and video or dimensional media such as 3D games.

Network coding is a network technique in which the transmitted data is encoded and decoded to increase the network throughput, reduce delays and make the network more robust. It is classified into physical linear network coding and digital network coding (Saeed, Basil, 2011) (David Szab, Attila Csoma, Peter Megyesi, Andras Gulyas, Frank H.P. Fitzek, 2015). Random Linear Network Coding (RLNC) is classified as digital network coding. It uses Glasis Field (GF) to select the random coefficients to encode the required data and transmit it. At receiver side, the decoder uses Gaussian Elimination to obtain the main data from the received one. RLNC is a totally distributed operation. It can re-encode the data before receiving all the transmitted one (early encoding) and it can correct the missing or corrupted data packets so, it is very suitable for use.

This paper focuses on the static media only which is time-independent, i.e. text and Images. In this category, the main requirement is to enhance this type of communication performance and reducing the overall response time (delay) over the network suffering limitation of bandwidth. The Proposed system uses Random Linear Network Coding (RLNC) to overcome the bandwidth limitations, provides reliability, and enhance throughput with less cost on cloud computing. This paper will discuss the Multimedia, Network Coding and Cloud Computing in Section 2, a new proposed multimedia cloud computing system based on RLNC in Section 3, proposed system Results in Section 4, and Conclusion in Section 5.

2. MULTIMEDIA, NETWORK CODING AND CLOUD COMPUTING

This section is an overview on multimedia, cloud computing and network coding. All Previous researches examined three combination sectors; The Multimedia and Cloud computing sector, the network coding and cloud computing sector and finally the network coding and multimedia sector. Some researches combine between multimedia, network coding and cloud computing in data storage only. This paper is focusing on the combination between them but in the network data transmission.

2.1 Cloud computing and multimedia

The multimedia database is the most popular and widely used database in the IT sector known as the data storage. And it has many applications. These applications include digital libraries such as text documents, images, audio, video, etc. So, we have different ways and requirements for storing the multimedia data used over the Cloud Computing (Anand Mohan, 2013). Experimental results for adaptive multimedia cloud computing on the H.264 streaming gives a bandwidth prediction error rate about 6% (Cho, Chin-Feng Lai, 2014). Also, experiments measure the video average delay time based on a bandwidth prediction model using selective bandwidth and balancing mechanism of stream nodes (Cho, Chin-Feng Lai, 2014). This study designs a video quality scalable streaming mechanism for the media cloud computing center, and constructs communication and management mechanisms for the media cloud, including the construction of a bandwidth measurement center and load monitoring mechanisms for nodes of specific purposes. It also designs a balancing mechanism for node resources in the media cloud (Cho, Chin-Feng Lai, 2014). Being aware that the main target is to achieve a Cost-efficient and quality of Service on the video Streaming over Cloud Services the architecture for on-demand transcoding of video streams using cloud resources includes a scheduling method that is aware of Quality of Service demands of video streams. It also includes a cost aware dynamic provisioning policy to allocate cloud resources. So, it decreases the startup delay of video streams and minimizes the cost of cloud resources. Experimental results showed that when the video demand rate is not high, it reduces the cost up to 70% in comparison with the static policies (Xiangbo Li, Mohsen Amini Salehi, Magdy A. Bayoumi, Rajkumar Buyya, 2016). From all the previous researches it is clear that the network coding is not examined to save the bandwidth in case of multicast or broadcast in data transmission which will be our main concern and contribution in this paper.

2.2 Network coding and cloud computing

Demand on the use of network coding in cloud computing is increasing the security of data and throughput (Márton Sipos, Janus Heide, Daniel E. Lucani, Morten V. Pedersen, Frank H.P. Fitzek, Hassan Charaf, 2015) (Lo'ai Tawalbeh, Nour S. Darwazeh, Raad S. Al-Qassas, Fahd AlDosari, 2015). The benefit of using the random linear network coding with multiple cloud storage providers to create the cloud of clouds is to minimize the required bandwidth needed for the adaptation steps by doing dense recoding only for the data that ensures recoverability and sparse recoding for performance-enhancing data. Measurements show the increase of performance and bandwidth optimization (Márton Sipos, Janus Heide, Daniel E. Lucani, Morten V. Pedersen, Frank H.P. Fitzek, Hassan Charaf, 2015). Also the network coding is used for efficient confidentiality-based cloud storage framework that enhances the processing time and assures confidentiality and integrity through data classification and applying Security algorithms based on the type of classified data (Lo'ai Tawalbeh, Nour S. Darwazeh, Raad S. Al-Qassas, Fahd AlDosari, 2015). Simulation results showed better processing time while assuring data confidentiality and integrity (Lo'ai Tawalbeh, Nour S. Darwazeh, Raad S. Al-Qassas, Fahd AlDosari, 2015). From all the previous researches, it is clear that the multimedia transmission over the cloud computing network was not using the network coding to minimize the required bandwidth and increase the throughput but was used in database storage only.

2.3 Network coding and Multimedia

Multimedia performance on the Broadcasted Applications with Network Coding has been evaluated (Saeed, Basil, 2011). It explored many ways to efficiently support multimedia broadcasted applications and compared different optimized broadcasted protocols optionally with the use of network coding (RLNC). Also showed that the best protocol to be used for multimedia broadcast applications among all tested protocols is the RLNC protocol. This paper selected the RLNC type of network coding in multimedia broadcast to achieve the highest values of Packet Delivery Ratio (PDR), and achieve the lowest values of latency and jitter. So, RLNC improves the overall performance of the multimedia broadcast applications, such as audio and video streaming which definitely increases the multimedia quality of service and decrease the total amount of cost in cloud computing. (Xiangbo Li, Mohsen Amini Salehi, Magdy A. Bayoumi, Rajkumar Buyya,, 2016) (Saeed, Basil, 2011).

3. A NEW PROPOSED MULTIMEDIA CLOUD COMPUTING SYSTEM BASED ON RLNC

The proposed multimedia cloud computing system is to use the RLNC codec at the user side and another one at the data center side to improve the overall response time performance which increases the throughput and optimizes the bandwidth. The proposed system flow graph Figure 1 shows a user request for a specific application and encodes the request with the RLNC encoder then sends the encoded request to the internet. The internet routes it to the selected data center by using cloud application service broker. The Service broker uses the optimized response time algorithm policy to achieve the best response time results. The selected data center decode the request by using RLNC decoder and sends the request to a virtual machine load balancer to select one of the load balancing algorithms. The Load balancing algorithm used in this paper is the Throttled algorithm. Then it assigns the request to a virtual machines to execute the request. The Virtual machine handles the request and sends it to the datacenter controller. The data center controller encodes the data and sends it to the end user by using internet. The end user receives the data and decodes it to the original data.

3.1 Proposed system Implementation

The RLNC Codec is implemented in Java language to enter it in the cloud computing environment to simulate the performance by

using the CloudAnalyst. The CloudAnalyst is built on the CloudSim Simulator. It has many benefits: open source using JAVA, can implement PAAS, SAAS, and IAAS. It has a user friendly GUI interface. After modifying the code a problem pops up where the CloudAnalyst simulates non real data traffic. Importing real known data and exporting it to verify the results is one of our main contribution in the CloudAnalyst. The CloudAnalyst helps to simulate and evaluate the performance of the cloud and improves the quality of service (Lo'ai Tawalbeh, Nour S. Darwazeh, Raad S. Al-Qassas, Fahd AlDosari, 2015) (Melbourne cloud labs, 2013) (Dhaval Limbani and Bhavesh Oza, 2012). The CloudAnalyst depends on main four components such as the user applications, the internet, the service brokers and the data centers. Algorithm 1 shows the proposed flow graph by using CloudAnalyst simulator.

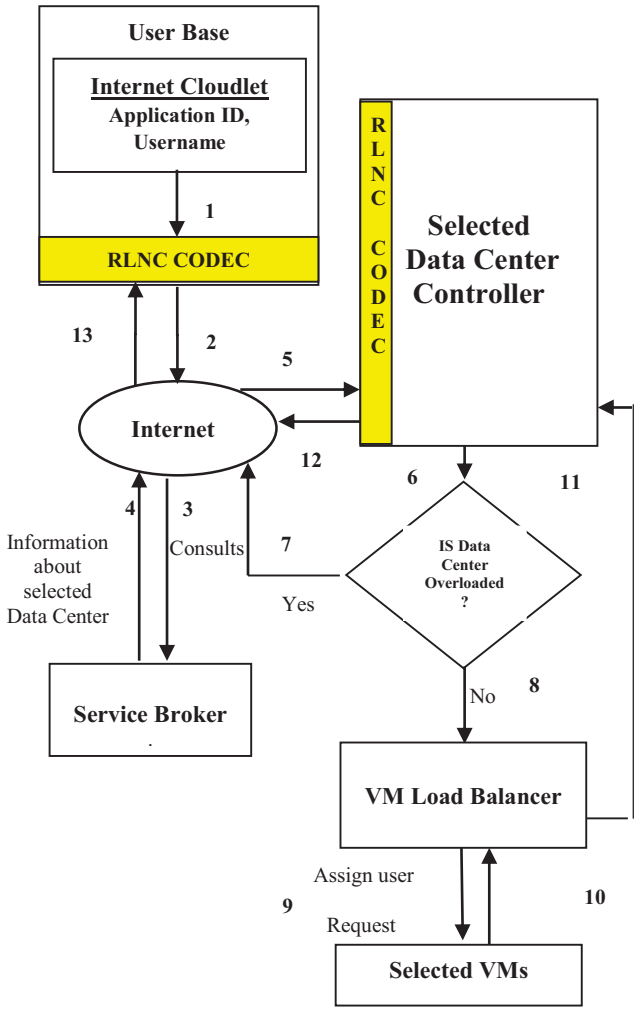

Figure 1. Proposed Flow Graph

Algorithm 1 Proposed Flow Graph

1: The user base generates the Internet Cloudlet which includes the application ID and the username in the originator field and enters the request of the multimedia application, the RLNC Codec encodes the request as shown in Figure 1.

2: The encoded request is sent to the internet while the internet uses the cloud App service broker (Service Broker) to get the routing information to route them successfully and defines the Data Center Selection.

3: The service broker includes all data center lists, contents metafile, internet proximity of the region, etc. It selects the service broker policy based on the request. There are three main policies: The Service Proximity based routing (shortest path selected), The Optimized Routing algorithm (Best response time), and the Dynamically reconfigured algorithm (based on the load, it is increasing and decreasing the number of virtual machines allocated in the data centers). The Optimized Routing algorithm is the one used in this paper.

4: The service broker sends the information about data center to the internet.

5: The internet adds appropriate network delay with the request and sends it back to the selected datacenter controller.

6: The Data Center Controller checks if it is overloaded or not and gives a decision depends on yes overloaded or not.

7: If overloaded, it retransmits it back again to the internet.

8: If not overloaded, the load balancer determines which policy of the virtual machines load balancing should be assigned to the next requests. There are three load balancing policies most used: The Round – Robin load balancer (it uses the round robin algorithm to allocate VMs), The Active monitoring load balancer (distributes equal workload on all available VMs) and The Throttled load balancer (If the request groups are more than the number of available VM's at a data center, some of the requests will have to be queued until the next VM becomes available). This paper uses the Throttled policy only.

9: Depending on the VM Load balancer which determines which load balancing policy will be used. The Data center controller assigns the virtual machine to the user request.

10: The data center controller send the request to the internet to update the metafiles.

11: The Selected VMs will handle the request and sends the response to the Data Center Controller. The Data Center Controller encodes the response data and send it to the end user by using the internet.

12: The internet uses the originator field of the cloudlet information and adds appropriate network delay with a response and sends it back to the end user.

13: The End user receives the encoded data and decodes it by using the RLNC decoder to obtain the original data.

The proposed system selected the RLNC encoder and decoder (codec) in the end user side and another RLNC codec in the Data Center side to achieve completely distributed operation, increase throughput, optimize the bandwidth especially in multicast and broadcast applications.

4. PROPOSED SYSTEM RESULTS AND DISCUSSION

The proposed system results Compare between the original multimedia cloud computing performances and the proposed multimedia cloud computing based on the RLNC Codec. Using (Facebook Case Study) MEDC Project2009 (Bhathiya Wickremasinghe, 2009) as a large scaled Internet applications. Facebook is the most popular social networking site having over 1.6 billion registered users worldwide on June 30, 2016, as shown in the (Global social network ranked, 2016). Facebook subscribers worldwide by geographic regions 2016 as shown in Figure 2 (Internet World Stats, 2016). Facebook case study 2009 results are meaning less but the method and configuration which were used are very important. In this paper data modified with new data 2016 instead of data 2009. According to Facebook subscribers worldwide by regions on June 2016, Table 1 shows Facebook users on June 2016 by region.

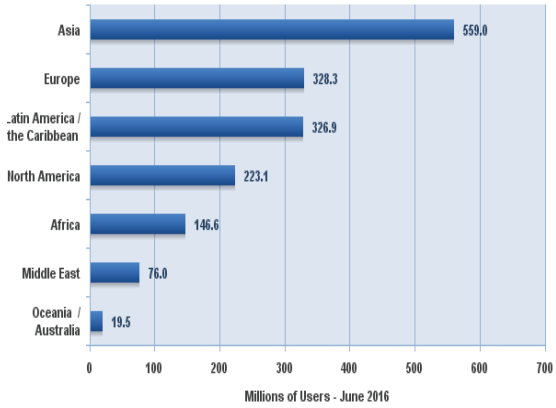

Figure 2. Facebook subscribers worldwide by geographic regions (Internet World Stats, 2016)

Region	Cloud Analyst Region ID	Facebook Users (million) (On June 2016)
North America	0	**224**
South America	1	**327**
Europe	2	**329**
Asia	3	**560**
Africa	4	**147**
Australia	5	**20**

Table 1. Facebook users on June 2016 by region

Implementation results were conducted on an intel ® core machine TM i7 - 4500U CPU @ 1.8 GHZ 2.4 GHZ internal RAM 8.00 GB, system type 64 bit operating system, 64- based- processor, Windows 8.1 (2013)Microsoft Corporation.

4.1 Simulation Configuration

For simulation let's assume a similar system but at 1/10th of the scale of Facebook. Define 6 user region based representing the above 6 regions with the following parameters:

I. Simulation Duration : 24 Hours
II. User bases as shown in Table 2

User Base	Region	Time Zone GMT	Peak Hours (Local time)	Peak Hours (GMT)	Simultaneous Online Users During Peak Hrs	Simultaneous Online Users During Off peak Hrs
UB1	0	– 6.00	7.00 – 9.00 pm	13:00-15:00	1120000	112000
UB2	1	– 4.00	7.00 – 9.00 pm	15:00-17:00	1635000	163500
UB3	2	+ 1.00	7.00 – 9.00 pm	20:00-22:00	1645000	164500
UB4	3	+ 6.00	7.00 – 9.00 pm	01:00-03:00	2800000	280000
UB5	4	+ 2.00	7.00 – 9.00 pm	21:00-23:00	735000	73000
UB6	5	+ 10.00	7.00 – 9.00 pm	09:00-11:00	100000	10000

Table 2: User bases configuration

For simplicity, each user base is contained within a single time zone and let us assume that most of the users use the application in the evenings after working hours for about 2 hours. Let us also assume that 5% of the registered users will be online during the peak time simultaneously and only one tenth of that number during the off-peak hours. Let us assume that each user makes a new request every 5 minutes when getting online.

III. Other parameters configured as below:

Parameter	Value Used
VM Image Size	100000
VM Memory	10240
VM bandwidth	10000
Data Center – Architecture	X86
Data Center – OS	Linux
Data Center – VMM	Xen
Data Center – Number of machines	20
Data Center – Memory per Machine	2048
Data Center – Storage per Machine	100000
Data Center – Available BW per Machine	10000
Data Center – Number of processors per machine	4
Data Center – processor speed	10000 MIPS
Data Center – VM Policy	Time Shared
User Grouping Factor	1000
Request Grouping Factor	100
Executable Instruction Length	250

The Delay Matrix and Bandwidth Matrix are the same as it is in the cloudAnalyst.

4.2 Assumption Scenarios

The used algorithms in the Service broker policy is the Optimize response time while the load balancing algorithm across the VM's in Data Center is throttled.

Assumed three Scenarios within the implementation:
Scenario1: Using the RLNC Encoder at the User base side and the RLNC Decoder at the data center controller.
Scenario2: Using the RLNC Encoder at the Data center controller and the RLNC Decoder at the User base side.
Scenario 3: Using the RLNC codec at the User base side and the RLNC codec at the Data center controller.

4.3 The Implementation Results and Discussion

Scenario 1 compares the results of the original work of multimedia cloud computing (without using the network coding) with the results of the multimedia cloud computing using the RLNC Encoder at the User base and the RLNC Decoder at the data center controller as shown in Table 3. The results shows that when using the RLNC in large scale internet application (like Facebook) in cloud computing, it improves the average data center processing time by 0.83% and degrade the average overall response time by 0.2% Also, increased the cost by approximately 12.57% more than the work without using network coding.

Scenario 2 compares the results of the original work of the multimedia cloud computing system with the results of the multimedia cloud computing using the RLNC Encoder at Data center controller and the RLNC Decoder at the User base side as shown in Table 3. The results shows that when using the RLNC in large scale internet application (like Facebook) in cloud computing network, it degrade the average overall response time by 0.042% with no change in the cost and it improves the average data center processing time by 0.33% .

Scenario 3 compares the results of the original work of the multimedia cloud computing system with the results of the multimedia cloud computing using the RLNC codec at the User base side and another one at the Data center controller side as shown in Table 3. The results show that when using the RLNC Codec in large scale internet applications (like Facebook), it improves 0.33% in average overall response time, 1.27% of the average data center processing time and decrease the cost by 32.34% than the original work.

The comparison of the three scenarios comes up with the fact that scenario 3 is the best scenario while using the multimedia cloud computing. It gives lower average overall response time, lower average data center processing time and lower cost. The RLNC codec achieves better throughput than other scenarios, it increases the quality of service (Qos), decreases the delay and optimizes the bandwidth especially if the bandwidth is limited. Also, it decreases the data center processing time and the cost of the service for end users.

		Service Broker used policy (Optimize response time algorithm)		
		Avg. overall response time (ms)	Avg. data center processing time (ms)	Cost ($)
VM load balancing algorithm used Throttled policy	Original multimedia work	142.85	18.11	561.99
	Scenario 1	143.18	17.96	642.78
	Scenario 2	142.91	18.05	561.99
	Scenario 3	142.38	17.88	380.23

Table 3. Proposed system implementation results

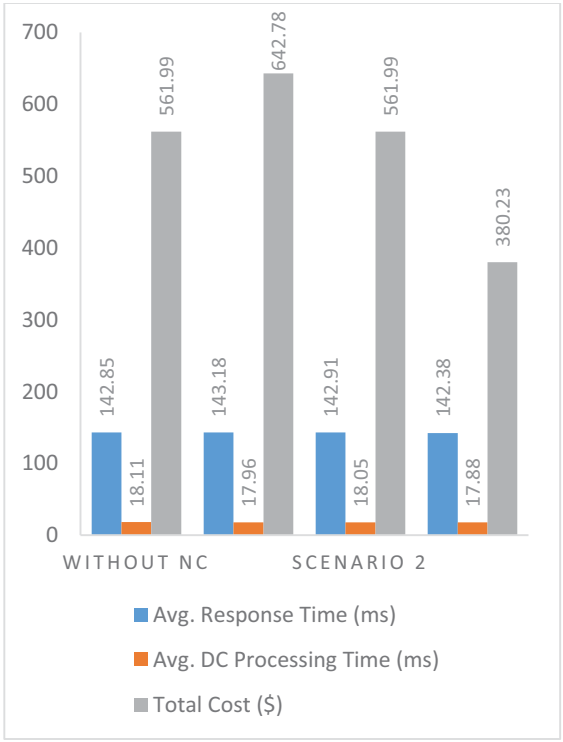

Figure 3. Proposed systems results

5. CONCLUSION

The proposed random linear network coding Codec in Multimedia cloud computing increases the throughput and the quality of service by decreasing the overall response time. It optimizes the network bandwidth in broadcasting and multicasting environment. It also achieves high reliability, security and distributed nature. It improves the average overall response time and the average data center processing time by 0.33% and 1.27 % respectively. It decreases the cost by 32.34% compared with other scenarios. Using the multimedia cloud computing with the RLNC Encoder at the User base and the RLNC Decoder at the data center controller the average data center processing time has been improved by 0.83%. The average overall response time has been degraded by 0.2% but the cost has been increased by 12.57% approximately compared to the original multimedia work. Regarding the use of the RLNC Encoder at the Data center controller and its Decoder at the User base side the average overall response time is degraded by 0.042% without any change in the cost compared to with the original work. The average data center processing time has been improved by 0.33%. The proposed system was proven that it is effective in large scale applications of internet. In conclusion the application of dynamic multimedia (audio, video, video conferencing, etc.) cloud computing based on RLNC codec could be of a great importance promising a good performance of the overall response time, data center processing time and the cost. This will be examine in the future.

REFERENCES

Anand Mohan, 2013. Impact of Multimedia Database and their Issues on Cloud Computing, IJIEASR, 2(6), ISSN: 2319-4413.

Bhathiya Wickremasinghe, 2009. Cloud Computing Environments MEDC Project Report, Distributed Computing Project, CSSE Dept., University of Melbourne, Australia.

Cho, Chin-Feng Lai, 2014. Adaptive Multimedia Cloud Computing Center Applied on H.264/SVC Streaming, LNICST 133, pp. 14–26.

David Szab, Attila Csoma, Peter Megyesi, Andras Gulyas, Frank H.P. Fitzek, 2015. Network Coding as a Service, in ACM SIGCOMM (DEMO).

Dhaval Limbani and Bhavesh Oza, 2012. A Proposed Service Broker Strategy in Cloudanalyst for Cost-effective Data Center Selection, International Journal of Engineering Research and Applications, India, 2 (1), pp. 793-797.

Global social network ranked, 2016. http://www.smartinsights.com/wp-content/uploads/2016/05/statistic_id272014_global-social-networks-ranked-by-number-of-users-2016.png

Internet World Stats, 2016. Facebook Users in the world http://www.internetworldstats.com/facebook.htm

Lo'ai Tawalbeh, Nour S. Darwazeh, Raad S. Al-Qassas, Fahd AlDosari, 2015. A Secure Cloud Computing Model based on Data Classification, Procedia Computer Science, MCSMS, pp. 1153-1158.

Márton Sipos, Janus Heide, Daniel E. Lucani, Morten V. Pedersen, Frank H.P. Fitzek,, Hassan Charaf, 2015. Adaptive Network Coded Clouds: High Speed", IEEE Transaction on Cloud Computing, VOL. 3.

Melbourne cloud labs, 2013. CloudSim: A Framework for Modeling and Simulation of Cloud Computing Infrastructures and Services, Laboratory University of Melbourne, Australia, http://www.cloudbus.org/cloudsim.

Saeed, Basil, 2011. Performance Evaluation of Multimedia Broadcast Applications with Network Coding in Ad hoc Wireless Mesh Networks, Thesis, Carleton University Ottawa, Ontario, Canada.

Xiangbo Li, Mohsen Amini Salehi, Magdy A. Bayoumi, Rajkumar Buyya,, 2016. CVSS: *A Cost-Efficient and QoS-Aware Video Streaming Using Cloud Services, IEEE* Computer Society, CCGrid,, pp. 106-115.

Abstracted Papers

The benefit of using high-rate GNSS in precise kinematic positioning

Ming Yang, Feng-Yu Chu, Shu-Chen Cheng

National Cheng Kung University, Taiwan, myang@mail.ncku.edu.tw
National Cheng Kung University, Taiwan
Southern Taiwan University of Science and Technology, Taiwan, kittyc@stust.edu.tw

Keywords: Global Navigation Satellite Systems (Gnss), High-Rate, Kinematic Positioning, Centimeter-Level

ABSTRACT:

High-rate (1Hz) Global Positioning System (GPS) precise kinematic positioning has been widely applied to mobile mapping technology. Currently besides GPS, GLONASS and BeiDou Navigation System (BDS) are the two other officially operational Global Navigation Satellite Systems (GNSS). Although many studies indicate that combining multiple systems can strengthen satellite geometry and improve ambiguity resolution (AR) performance, the influence of using high-rate combined GNSS data on AR performance has not yet been thoroughly assessed yet. This study will examine and discuss the benefit of using high-rate GNSS data in centimeter-level kinematic positioning and present experimental results.

FRAMEWORK FEATURE EXTRACTION OF BUILDING INTERIORS USING INDOOR MOBILE MAPPING SYSTEMS

Shiwei Hou [a], Chenglu Wen [a, *], Zheng Gong [a], Cheng Wang [a], Jonathan. Li [a,b]

[a] School of Information Science and Engineering, Xiamen University 422 Siming Road South, Xiamen, Fujian 361005, China
clwen@xmu.edu.cn
[b] GeoSTARS Lab, Department of Geography and Environmental Management, University of Waterloo
200 University Avenue West, Waterloo, Ontario N2L 3G1, Canada
junli@uwaterloo.ca

Commission I, WG I/6

KEY WORDS: Indoor Mobile Mapping, Point Clouds, Framework Feature, Building

ABSTRACT:

In recent years, indoor mobile mapping is with rapid pace of development. The indoor mobile mapping provides a useful three-dimensional (3D) structure via an indoor map for many applications, such as disaster searching and rescue inside buildings, virtual reality displaying and restoring the complex internal structure of buildings, etc. As we know, the common structural information includes plane, straight line, curvature line, skeleton, cylinder, surface, etc. As two of the most common features in the man-made environments, straight lines and planes provide important information regarding the geometric content and topological structure of point clouds. The traditional ways to get a 3D structural model of a building mainly rely on artificial hand-drawing or reconstructing based on design data. These ways have some limitations, such as incorrect and inaccurate data obtained when dealing with buildings of complex internal structures.

In this paper, we introduced two prototype systems for non-GPS indoor mobile mapping, which are backpacked indoor mapping system and wearable indoor mobile mapping system. The systems are capable of building a 3D point cloud map of an indoor environment, and can work as complementary. Moreover, the mapping systems provide a fast framework structure extraction of the building based on 3D point clouds obtained. The framework of lines and planes can be extracted, and the result provides a fast overview of the building interior for further application.

The backpacked mobile mapping system consists of three 2D laser scanners (as shown in Figure 1 (a)). A horizontally mounted laser scanner, which achieves 2D horizontal scan profiles, is used to build a 2D map of the building based on a particle filter-based SLAM (Simultaneous localization and Mapping) algorithm. At the same time, the system provides 2D pose information of the mapping system at each location. Two vertically mounted laser scanners are used to achieve 3D point clouds of the indoor environment. The two laser scanners are mounted to face to the two sides of the wall, and they are well calibrated. When the operator walks in the building carrying the system, our system can obtain point clouds of ceiling, floor and both sides of the walls in real-time.

Based on the backpacked system, we developed a new mobile mapping system, which we call it wearable indoor mapping system (WearSLAM). Comparing with the old system, the new system is much lighter, more accurate and with better results. The WearSLAM system (as shown in Figure 1 (b)) consists one Velodyne 16-line laser scanner and one IMU (Inertial Measurement Unit) device. In most of the existing indoor mobile mapping systems, the localization algorithms used are based on an assumption that the system moves only on 2D plane, and these localization algorithms limit the exploring ability of the mapping system in real 3D space. For example, the backpacked system is carried by a person, and there will be a significant roll and pitch motion during the movement. Especially, for certain indoor applications, for example disaster searching and rescue, the significant roll and pitch motions of the system rise the need for 6 degree of freedom (DOF) (x, y, z positions and roll, yaw, pitch angles) pose estimation of the mapping system. To achieve the pitch and roll inclination of the mapping system, an MEMS inertial measurement unit (IMU) (Xsens MTi-100) is mounted on the platforms, and the IMU sensor provides static accuracy of the pitch and roll measurements of 0.5 *deg* and dynamic accuracy of 2*deg* RMS. For this system, we developed a 6-DOF localization algorithm for system pose tracking when the systems are exploring a 3D space. The localization algorithm fuses 2D laser scanner data and IMU data by an extended Kalman filter (EKF) method. IMU accurately measures each roll and pitch angle of the system to achieve more accurate 3D system pose. For the backpacked system, the 6-DOF pose give a full 3D estimation of the system pose, and can be used to accelerate the map alignment process as initialized transformation and align the two maps directly when there is few or no

* Corresponding author.

overlapping area between the maps. For WearSLAM system, it registers the 3D point data directly with the help of the IMU device, and the system does not need to build a 3D map based on the 2D map. The mapping process is more quickly and more accurate than the backpacked mobile mapping system.

Furthermore, we extract the framework structures of the building's interiors from the point clouds using the method presented in our previous work. Firstly, the original point cloud space is partitioned by horizontal slicing, line extracting, and cell decomposing. A point set, near a straight linear structure, is extracted simultaneously. Then the 3D line-support region is fitted by our Line-Segment-Half-Planes (LSHP) structure (Figure 2(b) and (d)), which provides a geometric constraint for a line segment, making the line segment more reliable and accurate. Finally, the output will be a mesh of indoor point clouds data on the surface. The planar surfaces of the walls and ceiling are extracted, and the intersection lines between the planes are extracted as well, which finally helps to build a framework structure of an indoor environment.

Our main experiments are conducted in the following aspects: (1) a 3D point cloud map of an indoor environment is built with calibrated laser scanners referring the accurate 3D pose of the system given by the 6DOF localization algorithm; (2) a framework structure of the indoor environment is obtained, including lines between the walls, ceiling, and floor planes (Figure 2(d) and (e)). More experimental results will be given for more complicated indoor scenes.

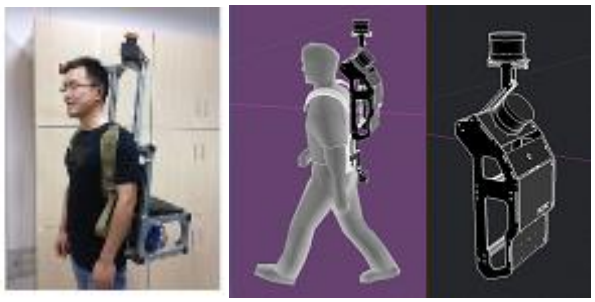

(a) (b)

Figure 1. (a) Backpacked indoor mapping system. (b) wearable indoor mapping system

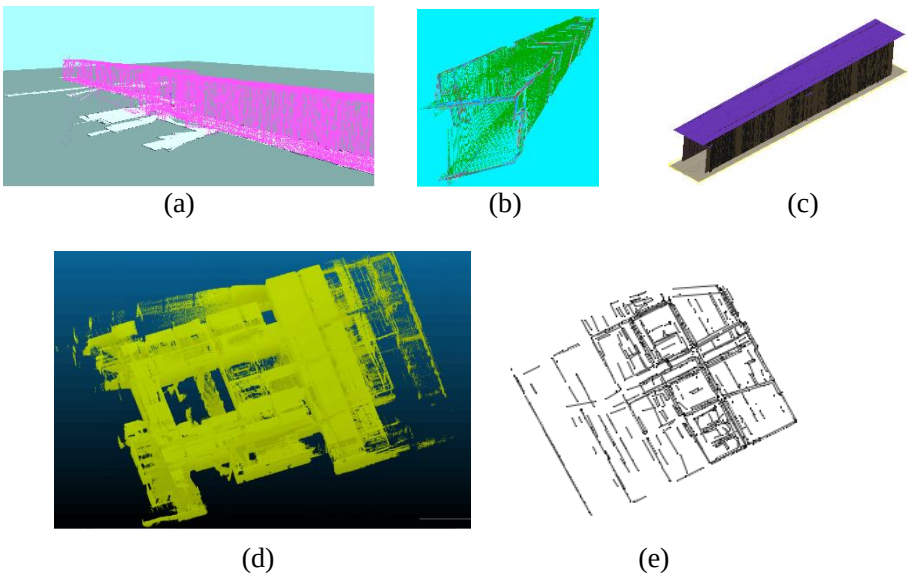

(a) (b) (c)

(d) (e)

Figure 2. (a) Original Point clouds using backpacked indoor mapping system. (b) Line extraction using backpacked indoor mapping system. (c) Planes extracted using backpacked indoor mapping system. (d) Original Point clouds using WearSLAM. (e) Line extraction using WearSLAM.

A BACKPACK MOBILE MAPPING SYSTEM BASED ON VELODYNE LIDAR

Zheng Gong , Jonathan Lia, Cheng Wang , Chenglu Wen

Xiamen University, China, junli@xmu.edu.cn
Xiamen University, China, cwang@xmu.edu.cn
Xiamen University, China, clwen@xmu.edu.cn

Keywords: Mobile mapping, multi-sensor system, SLAM

ABSTRACT:

In order to obtain the 3D spatial information quickly and effectively, we designed a mobile laser scanning system based on multi-sensor integrated technology. The system uses Velodyne VLP-16 laser scanners and one XSENS 9 DOF AHRS system.It is mainly composed of laser scanner, CCD camera to assist in the formation of a complete three-dimensional environment scanning system. Multiple sensors in the embedded computer system under the control of measurement data to complete the synchronous acquisition and storage. The post-processing method(SLAM)is adopted to match and integrate all kinds of data to complete the 3D real scene modeling of the city buildings and the indoor environment.

AN IMU/LIDAR/PCG-MAP INTEGRATED 2D POSITIONING METHOD FOR 3D INDOOR MOBILE MAPPING

Jian Tang, Chuang Qian, Xiaoji Niu, Rong Zou
wuhan university, China, tangjian@whu.edu.cn
wuhan university, China, qc_gnss@whu.edu.cn
wuhan university, China, xjniu@whu.edu.cn
China University of Geosciences (Wuhan), China, zourong@cug.edu.cn

Keywords: Mobile Mapping, PCG-Map, IMU, LIDAR, SLAM, Integration

ABSTRACT:

With the development of information industry, widespread use of smartphones and pads, equipped with different miniature navigation and positioning sensors, boost the demanding of Location-Based Services (LBS). Various smartphone based positioning solutions have also been investigated to enhance accuracy of indoor positioning, and then indoor Location Based Service (LBS) are thriving in recent years. The growing interest and the market of indoor LBS are driving a huge demand for building and updating indoor maps. The eagerness for a high-efficient, low-cost, high-accuracy indoor mapping technology in establishing a framework for the LBS is becoming more necessary than the past. However, traditional static surveying and mapping methods can't fulfill the requirements of efficiency and productivity in large, detailed and complicated indoor environment.

SLAM (Simultaneous Localization and Mapping) technology becomes more and more popular for navigation and mapping application in GNSS-denied areas, especially, in indoor area. It is considered to be an effective method for resolving positioning and environment-recognizing problems. In this paper we proposed an IMU/LiDAR/Polar Coordinate Grid Map (PCG-Map) Integrated SLAM positioning method for Indoor 2D/3D Mapping. In our system, a hardware platform which consists of two LiDARs and an IMU are horizontally and vertically installed on a cart to collect data; the horizontal LiDAR and IMU were utilized for 2D positioning and the vertical LiDAR is utilized for 3D mapping. Gauss-newton scan matching based on PCG-Map algorithm is adopted to estimate the heading change and positioning, with the prior attitude provided by IMU. At Last, a static Terrestrial Laser Scaner (TLS) mapping solution offers the reference to evaluate positioning result of our proposed method indirectly. From the results of our tests, the method has been proved to be an effective, quick and accurate solution for positioning and mapping method in indoor area.

FPGA FOR INTELLIGENT CONTROL SYSTEMS: SMART AGENT FOR ELDERLY PEOPLE SUPPORT

Nahla El-Araby, Sahar Hamed, Abdelhalim Mohamed, Islam Gamal, Mosatafa Nageeb

Dept. of Communications & Electronics Engineering, Canadian International College - CIC, Egypt
(nahla_alaraby, sahar_hamed, abdel_halim, islam_gamal, moustafa_nageeb)@cic-cairo.com

KEY WORDS: Artificial intelligence, Smart Home, FPGA, Intelligent control

ABSTRACT:
Early research focuses on the control of home appliances but current trends are moving into a creation of self-thinking home. The objective of this paper is to investigate the usage of Field Programmable Gate Array (FPGA) as a powerful processing and flexible hardware to implement intelligent control systems. A proof of concept case study was the implementation of an intelligent agent for home automation to serve and help the elderly owner of a smart home. Unsupervised elder people support is considered a great need in today's daily life. Smart home can be considered a good solution and can provide an intelligent way out for elderly people who lack personal care and supervision. A complete intelligent system is designed; it is divided into four subsystems: Temperature Control System, Security System, Abnormal Events System and The Daily Life system. The FPGA based intelligent system plays the role of controlling and updating the system in order to adapt with any abnormal events that may occur. The intelligent system updates its knowledge base by learning and observing the changes in the home environment.

INTRODUCTION/SIGNIFICANCE OF THIS WORK:
Smart Home technology started for more than a decade to introduce the concept of networking devices and equipment in the house. Smart home technology is the integration of technology and services through home networking for a better quality of living [1].
A smart home appears intelligent because its computer systems can monitor many aspects of daily life. Smart house can also provide a remote interface to home appliances or the automation system itself, via telephone line, wireless transmission or the internet, to provide control and monitoring via a smart phone or web browser [2].
Therefore, elderly individuals can rely on their smart home appliances. An intelligent interface that monitors the residents' movements, and learns to recognize their habits, can notify if the habits are interrupted or changed [3]. In addition, a smart home has the capability of monitoring the vital signs of residents. If an elderly person has a medical condition that could be of concern, the vital signs can be routinely sent to the appropriate medical facility. The smart home equipped with artificial intelligence will learn to distinguish dangerous readings and alert medical personnel immediately.
Nowadays, homes are being built with a variety of smart devices for the control of appliances throughout the home. FPGAs provide a powerful and flexible programmable platform for implementing controllers of a smart home. Some of the FPGA advantages are the efficient use of

energy and how it requires minimum programming by the home owner. Also, both power consumption and costs can be reduced by using FPGA.

In this paper, an intelligent control system is implemented using the FPGA in order to serve the elderly people. The system is divided into four subsystems: Temperature Control System, Security System, Abnormal Events System and The Daily Life system. The main advantage of the proposed system is that it observes the actions and updates itself to have a suitable reaction with every action.

OBJECTIVES:

A complete end to end solution for elderly people is proposed. The solution is based on an intelligent system which observes, learns, and updates itself according to everyday changes. The intelligent system is implemented using the FPGA in order to benefit from both flexibility and parallel hardware and in the same time reduce cost and power consumption.

METHODOLOGY:

A smart home is one that has highly advanced automatic systems. Most of the smart homes are made for luxury or to ease the life of normal people, the work in [4] and [6] is an example. This work investigates the use of smart home technologies for unsupervised elderly people support. Artificial intelligence algorithms are used to develop a self-learning system that updates its operation according to the daily life changes [3]. Field programmable gate array – FPGA is used for the control circuitry [5], as FPGAs provide high speed processing since it is considered a parallel processing hardware. Also the flexibility of reconfiguration provided by FPGAs enabled the hardware implementation of artificial intelligent algorithms. The work presented in [7] uses FPGA for task organizing in smart home.

The Home Intelligence (HI) module of the smart home, offers important added-value to the intelligent behavior of the smart-home environment. The HI creates an integrated environment in which the Artificial Intelligence (AI) algorithm can infer and suitably react according to changing conditions and events. The intelligent control module detects all daily life events and identifies abnormal or unexpected events, this information is then analyzed and used for AI learning and to improve the system's reasoning mechanisms and can provide an immediate automatic response if desired. Because of the complexity of the systems, their diverse areas of control and supervision, the variety of information technologies and learning mechanisms, and the reasoning capabilities used in updating the information system, FPGAs are used in this work to provide powerful and flexible high speed hardware [8], [9].

EXPERIMENTS AND CONCLUSION:

A case study was used to prove the efficiency of using both artificial intelligence algorithms and FPGA hardware in developing a smart home model that can provide complete support for unsupervised elderly people. The case study used in experiments was represented by smart home using FPGA control circuitry implementing an intelligent algorithm. The presented system is composed of four subsystems: Security system, Daily life, Abnormal events, and Temperature

control system. The operation of each subsystem is analyzed and described using flowcharts where the decision making was through accumulating saved data and processing a learning scheme. The control and decision making algorithms was then integrated into the design of the intelligent agent which is described through hardware description language, VHDL. The description was simulated to test different scenarios using ModelSIM simulation tool. Synthesis and implementation using Xilinx ISE showed good time delay and acceptable hardware utilization. A hardware realization was developed through configuring a Spartan 3A Xilinx FPGA (XC3A700e4) [10].

Through the system of intelligent smart home we could use those applications of smart home and the flexibility of FPGA controllers to design and implement a complete solution to serve the unsupervised elderly people in a comfortable, helpful and secure way.

The design of the system is based on learning and observing the environment of the home and the daily life events of the occupant and consequently provides an intelligent agent for decision making to issue the proper commands.

REFERENCES:

1. Rosslin John Robles1 and Tai-hoon Kim. Applications, Systems and Methods in Smart Home Technology: A Review, International Journal of Advanced Science and Technology Vol. 15, (pp.37- 48), February, 2010.
2. Jong Hyuk Park & Ching-Hsien Hsu & Hamid R. Arabnia. Intelligent systems and smart homes, Inf Syst Front, vol:11, (pp.481–482), Springer 2009.
3. Reaz, Mamun Bin Ibne. Artificial Intelligence Techniques For Advanced Smart Home Implementation. Acta Technica Corviniensis-Bulletin of Engineering, vol: 6.2, 2013.
4. Jie Zhang. Development and Implementation of Smart Home Monitoring System in Embedded Environment, International Conference on Advances in Mechanical Engineering and Industrial Informatics (AMEII 2015), (pp.1930-1933), 2015.
5. Kuon, Ian, and Jonathan Rose. Measuring the gap between FPGAs and ASICs. IEEE Transactions on computer-aided design of integrated circuits and systems, vol: 26.2, (pp. 203-215), 2007.
6. R. Panna, R. Thesrumluk and C. Chantrapornchai . Development of Energy Saving Smart Home Prototype, International Journal of Smart Home Vol. 7, No. 1, (pp. 47-66), January, 2013.
7. Marufuzzaman, Mohd, Mamun Bin IbneReaz, and Mohammad Tariqul Islam. FPGA based Distributed Task Organizing Agents in Smart Home. Proc. of the 2nd International Conference on Research in Science, Engineering and Technology (ICRSET'2014), Dubai. 2014.
8. Sweatha, K. N., M. Poornima, and M. H. Vinutha. Advance Home Automation Using FPGA Controller. International Journal of Advanced Research in Computer and Communication Engineering vol: 2.7, 2013.

9. Jesús García-Guzmán, Edgar O. Moctezuma-Monge and Farah H. Villa-López. FPGA implementation of a smart home lighting control system, IEEE Fourth International Conference on Consumer Electronics – Berlin (ICCE-Berlin), (pp. 419-420), 7-10 Sept. 2014.
10. Erjavec, Tim. Introducing the Xilinx targeted design platform: fulfilling the programmable imperative. Xilinx White Paper WP306, 2009.

A LOW-COST BOAT-BASED MOBILE MAPPING SYSTEM FOR MAPPING COASTAL REGIONS

Abdullah Arslan [a,b], Ayman F. Habib [a]

[a] Dept. of Civil Engineering, Purdue University, USA (arslan, ahahib)@purdue.edu
[b] Dept. of Geomatics Engineering, Istanbul Technical University, Turkey (arslanab)@itu.edu.tr

KEY WORDS: LiDAR (Light Detection and Ranging), Bathymetry, Shoreline, Data Fusion

ABSTRACT:
Mobile Mapping Systems can be based on different platforms such as cars/vans/trucks, unmanned aerial or surface vehicles, and backpacks carried by individuals. Manned and unmanned boats equipped with various sensors, depending on the payload capacity, can be used to study coastal regions. This study investigates the performance of the low-cost Boat-based Mobile Mapping System (BoMMS), which has an OEM GPS and a gimbal instead of a GNSS/IMU unit. The aim of the data collection was to acquire suitable data for detecting shorelines deriving from a hybrid point cloud that includes both underwater and shoreline topography. Previous BoMMS studies have mostly used a terrestrial laser scanner equipped with a GNSS/IMU unit. In this study, a Velodyne VLP-16 laser scanner was mounted on a specially designed gimbal. The gimbal compensates for the platform's roll and pitch angles. A hybrid point cloud is produced after reconstruction, georeferencing, and fusion of the LiDAR with bathymetry data. According to the preliminary results, the possibility of obtaining hybrid point cloud representing the coastal area and underwater topography is demonstrated.

AN OGC STANDARD-BASED INTERNET OF THINGS PROTOTYPE FOR VEGETATION RECOVERY MONITORING IN NORTHERN ALBERTA

Steve Liang, Sara Saeedi, James Badger, Luo Kan

University of Calgary, Canada, steve.liang@ucalgary.ca
University of Calgary, Canada, ssaeedi@ucalgary.ca
University of Calgary, Canada, jpbadger@ucalgary.ca
University of Calgary, Canada, kan.luo@ucalgary.ca

Keywords: gis, internet of things, sensor networks, ogc

ABSTRACT:

This paper describes an end-to-end Internet of Things (IoT) prototype system that uses open source hardware, and interoperable IoT standard for environmental monitoring. The system was designed to monitor the physical conditions of a boreal ecosystem in northern Alberta. In summer 2016, eleven IoT sensor nodes were deployed in three different sites in a boreal forest environment. Real-time ambient environmental data were sent back from the remote area via 2.5G mobile networks to an Open Geospatial Consortium (OGC) Sensor Things API cloud server. This research demonstrates the IoT prototype system based on the OGC architecture is power and data transmission efficient and can survive in a harsh deployment environment. To our best knowledge, this deployment is world's first real-world evaluation of the OGC Sensor Things API for environmental monitoring applications.

Author Index

A Potsiou, Chryssy 3
A. Aboelghar, Mohamed 439
A. Shawky, Mahmoud 224
Abd El Azeem, Mohamed 275
Abd Rabbou, Mahmoud 134, 153, 211, 384
Abdelazeem, Mohamed 178
Abou Galala, Mohammed 83
Ahmed, Kamal 139
Ahmed, Mokhtar 327
Ahmed, Salwa 415, 423
Alaa, Islam 42, 112
Alenezi, Sultan 234
Ali, Abdelrahman 415, 423
Alkadi, Abdullah 10
Almagbile, Ali 146
Alrajhi, Muhamad 8
Alsubaie, Naif 415
Arslan, Abdullah 467
Asal, Fahmy 161
Attiya, Gamal 268, 327

Badger, James 468
Baraka, Moustafa 69
Berveglieri, Adilson 122
Bullock, Darcy 349

Campos, Mariana 308
Chang, Hsiu-Wen 77, 314
Chapman, Michael 379
Chen, Qijin 430
Chen, You Liang 62
Cheng, Shu-Chen 458
Chiang, Kai Wei 62
Chiang, Kai-Wei 12, 35, 48, 55
Chu, Chien-Hsun 12
Chu, Feng-Yu 458

de La Fortelle, Arnaud 101
Dong, Zhen 239
Dorota, Grejner-Brzezinska 408

El Hennawy, Hadya 445, 451, 333
El Kadi, Omar 97
El Shazly, Adel Hassan Youssef 97
El-Araby, Nahla 463
El-Ashmawy, Nagwa 24
El-Desoky, Abdalla 333
El-Fishawy, Nawal 327
El-Gamil, Nancy 302

El-Ghazaly, Mohamed 139
El-Rabbany, Ahmed 178, 280, 384
El-Shazli, Alaa 302
El-Shazly, Adel 134, 139, 153, 211
El-Sheimy, Naser 55
Elbahnasawy, Magdy 217, 349
Elbooz, Sheren 268
Eldieb, Amr 42, 112
Elfishawy, Nawal 268
Elhabiby, Mohamed 333, 357
Elhifnawy, Hassan 224
Elkaffas, Saleh Mesbah 234
Elsheimy, Naser 287
Elshirbeny, Mohammed 439
Ettlinger, Andreas 232

Farouk Younis, Omayma 445, 451
Fathy, Cherine 109
Fawzy Habib, Ayman 439
Fayed, Ibrahim 327
Fissore, Francesca 192, 391
463
Gamal, Islam 232
Gikas, Vassilis 91
Givigi, Sidney 127
Goel, Salil
Gong, Zheng 459, 461
Grejner-Brzezinska, Dorota 402
Guarnieri, Alberto 192

Habib, Ayman 170
Hamed, Sahar 463
Hamza, Essam 224
Hanafy, Hany 321
Hassanein, Mohamed 295
He, Fangning 187, 204, 217
Heipke, Christian 1
Hofer, Hannes 232
Honkavaara, Eija 308
Hou, Shiwei 459
Huang, Ronggang 252
Huang, Shih-Huan 12, 35
Huang, Tsung-Che 18
Hussien, Allaa 109

Jiuchao, Qian 260
Joly, Cyril 101

Kamel, Ahmed 333
Kan, Luo 468
Karamat, Tashfeen 91
Kealy, Allison 127, 232
Khedr, Maan 287, 373

Koppanyi, Zoltan 402, 408
Kun, Liu 260
Kuo, Yun-Tzu 48

Li, Deren 5
Li, Jianping 252
Li, Jonathan 459, 461
Li, Qingquan 7, 379
Li, You 244
Liang, Fuxun 239
Liang, Steve 468
Liao, Jhen-Kai 12, 35, 48
Lin, Yun-Jou 182, 204, 349
Ling, Pei 260
Lohani, Bharat 127

Mahar, Khaled 234
Mahmoud, Mostafa 112
Mansour, Ahmed 153
Masiero, Andrea 192, 391
Massoud Ali, Abdelraouf 439
Miller, Megan 170
Min, Cao 379
Mohamed, Abdelhalim 463
Mohamed, Essam 118, 321
Mohamed, Haytham 357
Mohammed Zidan, Zaki 83
Morsy, Salem 280
Mostafa, Mostafa 366
Mousa Rabah, Mostafa 83
Moussa, Adel 357, 366

Nageeb, Mostafa 463
Niu, Xiaoji 430, 482
Noureldin, Aboelmagd 91, 112

Obex, Franz 232
Oweis, Mohamed 275

Peilin, Liu 260
Pirotti, Francesco 391

Qian, Chuang 482

Radi, Ahmed 244
Rahman, Muhammed Tahsin 91
Rashad, Osama 42
Rashid Kaloop, Mosbeh 83
Ravi, Radhika 349
Rayan, Omar 42
Retscher, Guenther 127, 232
Ricaud, Bruno 101

S. Elsharkawy, Ahmed 224
Sadek, Rowayda 445, 451
Saeedi, Sara 468
Sakr, Mostafa 341
Saleh, Esalm 139
Sesay, Abu 244
Sesay, Abu B 366
Sesay, Abu-Bakarr 357
Shaker, Ahmed 24, 280
Shamseldin, Tamer 217, 349
Su, Tz-Chiau 314
Swelam, Wael 275

Tang, Jian 482
Tommaselli, Antonio 122, 308
Toth, Charles 402, 408
Tsai, Guang Je 62
Tsai, Guang-Je 55
Tsai, Min Chuan 62
Tsai, Min-Chuan 55
Tseng, Yi-Hsing 18

Vettore, Antonio 192, 391

Wang, Cheng 459, 461
Wang, Jinling 146
Wassal, Amr 42, 112
Wen, Chenglu 459, 461
Wenxian, Yu 260
Xiong, Weifeng 187, 217
Xu, Haowei 402

Yang, Bisheng 239, 252
Yang, Ming 458
Youssef, Ahmed 69
Youssef, Sheren 321
Youssef, Sherin 109, 118, 302

Zhang, Deijin 379
Zhang, Hai 373
Zhantao, Deng 260
Zhou, Qifan 373
Zou, Rong 482
Zou, Xianghong 252
Çelik, Rahmi Nurhan 178

Conference Committees

Honory Chair

Prof. Dr. Ismail Abdel Ghafar (AASTMT President)

Organization Committee

Prof. Dr. Nasser El-Sheimy (Canada) (Chair)

Scientific Committee

Prof. Dr. Gamal Selim (AASTMT) (Chair),
Prof. Dr. Ayman Habib (Purdue univeristy, USA) (Co-Chair)

Local Scientific Committee

Prof. Dr. Attala Hashad (AASTMT),
Prof. Dr. Allaa AbdElBary (AASTMT),
Prof. Mohamed Eltouky (Ains Shams University),
Prof. Moustafa Baraka, (The German University in Cairo),
Prof. Ibrahim Shaker (Ain Shams University),
Prof. Adel El-Shazly (Cairo University),
Prof. Amr Ali (AASTMT),
Prof. Sherin Youssef (AASTMT),
Prof. Mohamed E. Khedr (AASTMT),
Prof. Adel Belal (AASTMT),
Prof. Mohamed Ibrahim Zahran (Banha University),
Prof. Amr Hanafi Ahmed Ali (Banha University),
Prof. Abdel MonemSanad (AASTMT),
Dr. Saleh Mosbah (AASTMT)

International Technical Committee

Prof. Dorota Brzezinska, (Ohio State University, USA),
Prof. Stefan Hinz (The Karlsruhe Institute of Technology, Germany),
Prof. Boris Jutzi (The Karlsruhe Institute of Technology, Germany),
Prof. Charles Toth (The Ohio State University, USA),
Prof. NorbetHala, (Stuttgart University, Germany),
Prof. Allison Kealy, (University of Melbourne, Australia),
Prof. Jonathan Li (Waterloo University, Canada),
Prof. Cheng Wang (Xiamen University, China),
Prof. Kai-Wei Chiang (National Cheng Kung University, Taiwan),
Prof. Xiang Niu (Wuhan University, China),
Prof. Mike Chapman, (Ryerson University, Canada),
Prof. Retscher Guenther, (Technical University of Vienna, Austria),
Prof. Antonio Vettore (University of Padua, Italy),
Prof. Ahmed Shaker, Ryerson University (Canada),
Prof. Jan Skaloud, (Swiss Federal Institute of Technology, Switzerland),
Prof. Jinling Wang, (UNSW Australia, Sydney, Australia),
Prof. AboelmagdNoureldin, (Queens University, Canada),
Prof. Pedro Arias-Snchez, (University of Vigo, Spain),
Prof. Ruizhi Chen, (Texas A&M University Corpus Christi, USA),
Prof. Wu Chen, (Hong Kong Polytechnic University, China),
Prof. Clive Fraser, (University of Melbourne, Australia),
Dr. Alberto Gonalves,(University of Porto, Portugal),
Prof. Pierre Grussenmeyer, (INSA Strasbourg, France),
Prof. Murat YAKAR, University of Selcuk, Turkey,
Dr. Alberto Guarnieri, (University of Padova, Italy)

Program Chair (ISPRS WG I/7)

Prof. Sherin Youssef (AASTMT),
Kai-Wei Cheng (Taiwan)

Publication Committee

Khalid Saqr (AASTMT)
Sherif Eldiasty (AASTMT)

The 10th International Conference on Mobile Mapping Technology

Mobile Mapping For Sustainable Development

Designed & Printed by

Design and Printing Department

Educational Recources Center

Arab Academy for Science, Technology & Maritime Transport